PROCEEDINGS OF THE 1999 PARTICLE ACCELERATOR CONFERENCE

REPORT DOCUMENTATION PAGE

Public reporting burden for this collection of information is estimated to average 1 hour per response, including the time for reviewing instructions, searching existing data sources, gathering and maintaining the data needed, and completing and reviewing the collection of information. Send comments regarding this burden estimate or any other aspect of this collection of information, including suggestions for reducing this burden, to Washington Headquarters Services, Directorate for Information Operations and Reports, 1215 Jefferson Davis Highway, Suite 1204, Arlington, VA 22202-4302, and to the Office of Management and Budget, Paperwork Reduction Project (0704-0188), Washington, DC 20503.

1. AGENCY USE ONLY (Leave Blank)	2. REPORT DATE June 1999	3. REPORT TYPE AND DATES COVERED Final; March 27- April 2, 1999

4. TITLE AND SUBTITLE
Proceedings of the 1999 Particle Accelerator Conference
Volumes 1 through 5

5. FUNDING NUMBERS
G

6. AUTHORS
A. Luccio, W. MacKay - editors

7. PERFORMING ORGANIZATION NAME(S) AND ADDRESS(ES)
Brookhaven National Lab
P.O. Box 500
Upton, NY 11973

8. PERFORMING ORGANIZATION REPORT NUMBER

9. SPONSORING / MONITORING AGENCY NAME(S) AND ADDRESS(ES)
U.S. DOE
National Science Foundation
Office of Naval Research

10. SPONSORING / MONITORING AGENCY REPORT NUMBER

11. SUPPLEMENTARY NOTES

12a. DISTRIBUTION / AVAILABILITY STATEMENT
Available to public

12b. DISTRIBUTION CODE

13. ABSTRACT (Maximum 200 words)
Papers for the eighteenth biennial Particle Accelerator conference, an international forum on acceleator science and tehnology held March 27-April 2, 1999 in New York City, organized by Brookhaven National Lab.

14. SUBJECT TERMS

15. NUMBER OF PAGES
3779

16. PRICE CODE

17. SECURITY CLASSIFICATION OF REPORT Unclassified	18. SECURITY CLASSIFICATION OF THIS PAGE Unclassified	19. SECURITY CLASSIFICATION OF ABSTRACT Unclassified	20. LIMITATION OF ABSTRACT UL

20000209020

IEEE

The
American
Physical
Society

Proceeding of the 1999

Particle Accelerator Conference

(Editors: A. Luccio, W. MacKay)

Volume 1 of 5

Pages 1 – 648

20000229 020

Proceedings of the
1999 IEEE Particle Accelerator Conference

Additional copies of this publication are available from:

IEEE Service Center
445 Hoes Lane
Piscataway, NJ 08854-4150, USA

1-800-678-IEEE (1-800-678-4333)
1-732-981-1393
1-732-981-9667 (FAX)
e-mail: customer.service@ieee.org

FOREWORD

The 18th Particle Accelerator Conference was held at the Marriott Marquis Hotel, New York City, New York, from March 29 to April 2, 1999, under the joint auspices of the Nuclear and Plasma Sciences Society of the IEEE, and the Division of Physics of Beams of the APS.

Here is a bit of history of the Particle Accelerator Conference as related by Louis Costrell of the National Institute of Standards and Technology and a member of the PAC Organizing Committee. In 1963 Bob Livingston of the Oak Ridge National Laboratory, who was then President of the IEEE Nuclear Science Society (NSS) now the Nuclear and Plasma Sciences Society (NPSS) called Lou to discuss the feasibility of initiating an IEEE/NSS series of conferences on Particle Accelerator Engineering. They then proceeded to organize the first such conference that was held March 10-12, 1965 at the Shoreham Hotel in Washington DC and drew 750 participants. In 1993 the IEEE/NPSS and American Physical Society, Division of Physics of Beams, signed a Memorandum of Understanding for joint sponsorship of the Particle Accelerator Conference, beginning with PAC'95. Concerning the locations: the first three conferences were held in Washington DC, then the conference started rotating between the East, Central and Western areas. The location statistics up to 1997 are as follows: Washington, 6. San Francisco, 3. Chicago, 3. Vancouver, 2. Santa Fe, 1. Dallas, 1.

PAC'99 was the first time the meeting has been held in New York, and Brookhaven National Laboratory was honored to have been chosen as host. The attendance (1338) was as anticipated, up 10% from the 1997 Vancouver meeting and up 25% from the 1995 Dallas meeting, indicating the continuing vitality of the discipline even in these fiscally stringent times. The international component is also growing, with 34% of the delegates coming from 29 countries outside North America.

PAC'99 marks the completion of the construction of the BNL Relativistic Heavy Ion Collider (RHIC) which started its commissioning about the time of the conference. Physicists from around the world will use the Relativistic Heavy Ion Collider to explore some of Nature's most basic -- and most intriguing -- ingredients and phenomena.

Scientific Program: The opening plenary session, chaired by Ilan Ben-Zvi of BNL, covered four highlights of the conference: Commissioning of B-Factories, commissioning results from RHIC, accelerators for cancer therapy and technology challenges of linear colliders. The first two asymmetric electron-positron B-Factory colliders were finished in the past year: PEP-II at SLAC in the USA and KEKB at KEK in Japan. These two accelerators use many novel accelerator advancements to allow high design luminosities, as reported by John Seeman of SLAC. Michael Harrison of BNL presented the progress on the commissioning and highlights of RHIC. Accelerators for cancer therapy, an area in which accelerators benefit society in a highly visible way, were presented by James Slater of Loma Linda University, who observed that designing the clinical accelerator requires a highly orchestrated design effort involving the entire facility. The last presentation of the Opening Plenary session, on the technology and challenges of linear colliders, was invited from Bjoern Wiik, the director of DESY. Four weeks before PAC'99, the world's scientific community learned about the tragic loss of this internationally acclaimed accelerator scientist, a compassionate colleague and an outstanding director of DESY. The chair of the session, John Peoples of Fermilab eulogized Bjoern. Then he introduced Reinhard Brinkmann of DESY, who rose to the challenge of reviewing the design challenges of a high energy, high luminosity e^+e^- linear collider in a very short time. Reinhard discussed various technical options and presented the status of the R&D effort underway at several laboratories.

Commissioning results were reported on the Fermilab main injector. Plans for major upgrades were presented such as a five-fold luminosity upgrade of HERA. The progress made in the acceleration of polarized protons to high energy at the AGS led to plans for polarized beams in RHIC and HERA. The Large Hadron Collider (LHC), the largest machine under construction, incorporates many technological innovations in order to achieve its design objectives at the lowest cost. Lower costs are also the main challenge for the Very Large Hadron Collider that is under initial consideration. Light source talks were evenly divided between storage ring results and Free-Electron Lasers. The storage ring talks included the performance of SPring 8 by Hiromichi Kamitsubo and a look into the future provided by Albin Wrulich. FEL presentations included the high power lasing results of the TJNAF FEL by Steve Benson and a look towards future x-ray FELs by Li Hua Yu.

Interesting advances were reported in all areas of accelerator technology. Self-bunching electron guns based on secondary emission have been developed at FM Technologies, Inc., and a pulsed photoinjector operating at GV/m field was reported by BNL. Very short period undulators were described using either a superconducting magnet (Karlsruhe) or microwave resonant structures (ANL). Ron Scanlan reported on superconducting accelerator magnet advances towards fields higher than 10T, including Nb_3Al as well as the high temperature superconductors in both tape and cable configurations. Vincenzo Palmieri introduced the production of seamless niobium cavities, and many talks covered various technological aspects of very high current proton accelerators.

Accelerators are versatile tools for the production of various beams: protons, electrons, neutrons, x-rays, heavy ions, muons, neutrinos, and other secondary beams. These beams serve not just basic research in nuclear and high-energy physics, but also a multitude of applications: cancer therapy, neutron radiography, sterilization, production of isotopes, medicine, material science, contraband detection and much more. Gary Hogan described the use of protons for producing radiographic motion pictures of dense, exploding objects, and Jose Alonso talked about the Spallation Neutron Source (SNS).

The final plenary session offered a look to the future of the major uses of accelerators: William Marciano described the future of High Energy Physics, and Nathan Isgur that of Nuclear Physics. Wayne Hendrickson presented the impact of synchrotron radiation on structural biology, and Andrew Taylor the physics potential of MW class spallation sources.

In all, 1602 abstracts were submitted, for 79 invited and 120 contributed talks, and 1403 posters. In addition, a very successful 3-day industrial exhibition was held, featuring 40 exhibitors, and over thirty satellite topical and committee meetings were scheduled.

Social Program and Awards: The social program began on Sunday evening with a reception. The conference banquet was held in the Marriott Marquis Hotel on Tuesday evening and attended by 669 - a good number even in view of the culinary and cultural attractions of downtown New York! Following the conference, 187 participants attended a tour of Brookhaven National Laboratory on Saturday.

Awards were presented at the conference banquet. The APS Robert R. Wilson Prize was awarded to Robert Palmer, (BNL) for his many diverse contributions and innovations in particle accelerator and detector technologies.

Of the IEEE/PAC Technology Awards, the first went to Ilan Ben-Zvi (BNL) for contributions to high-brightness electron beams and superconducting rf and for leadership of BNL's Accelerator Test Facility. The second award went jointly to William Foster and Gerald Jackson, (FNAL) for the development of the first large-scale application of permanent magnet technology.

The US Particle Accelerator School Prizes were given to Robert Gluckstern, (UMD) for contributions to the understanding of fundamental processes in high-intensity beams and to Bruce Carlsten, (LANL) for the concept of emittance compensation.

The APS Award for Outstanding Doctoral Thesis Research went to Zhirong Huang (Stanford U) for his analysis of radiation damping and quantum excitation in novel accelerator configurations.

A large number of companions registered, about 310, owing no doubt to the attractions of New York City. Many companions and participants enjoyed the tours, theaters, shows and museum visits assisted by a week of good weather.

Proceedings: As at PAC'95 and PAC'97, electronic publication was the norm. The abstracts were collected on the web site together with author information that went to the conference database. Authors enjoyed the ability to edit the submitted abstracts and apply corrections (that somehow are always needed). The papers were sent by electronic means with few exceptions. Completed papers were placed on the PAC'99 web site as soon as they were processed, with the majority of the papers being on the web by the end of the conference. The proceedings are being published by IEEE in both book and CD-ROM form, and are also available on a combined PAC/EPAC/APAC Web site (http://www.cern.ch/accelconf/). The number of CD-ROMs ordered was double that of books. Publication has been supported by generous grants from the US Department of Energy, National Science Foundation and Office of Naval Research.

Acknowledgements: Space is unfortunately too short to thank individually all those people whose dedicated efforts, often over a period of many months, were responsible for the success of the conference - especially the members of the Organizing Committee, Program Committee, Local Organizing Committee, and BNL staff. Exceptions must be made however for Mary Campbell, the Conference Secretary whose hand was everywhere, John Smith, the computer and electronic data group leader who made it all possible, Pauline Pearson who must have exchanged e-mails and solved problems of every single author, and Chris Ronick, the Hotel Coordinator who managed this enormous event calmly and confidently.

Bill Weng
Conference Chairman

Ilan Ben-Zvi
Program Chairman

1999 Particle Accelerator Conference Committees

Organizing Committee:

M. Allen	SLAC (NPSS)
J. Ball	ORNL
W. Barletta	LBNL
I. Ben-Zvi	NSLS, BNL
Y. Cho	ANL
L. Costrell	NIST
M.K. Craddock	UBC & Triumf
W.K. Dawson	TRIUMF (IEEE)
D. Finley	FNAL
D. Friesel	IUCF
D. Hartill	Cornell U.
C. Joshi	UCLA
M. Kihara	KEK (APAC)
S. Krinsky	BNL
C. Leeman	TJNAF
J. Peoples	FNAL (DPB)
M. Reiser	U. Maryland
B. Ripin	APS (APS)
C. Robertson	ONR
S. Schriber	LANL
R. Siemann	SLAC
D. Sutter	DOE
S. Tazzari	U. Roma & INFN-LNF (EPAC)
W.T Weng	BNL, Chairman
G. Westenkow	LLNL
R. York	NSCL

Local Organizing Committee:

J. Becker	Treasurer
I. Ben-Zvi	Vice-Chairman
M. Campbell	Conference Secretary
H. Kirk	Coordinator, Poster & Exhibits
J. Laurie	Printing / Publisher
E. Lowenstein	BNL Tour
P. Lucas	Publishing
A. Luccio	Editor, Publishing
W.W. MacKay	Editor, Publishing
C. Ronick	Hotel Coordinator
J. Smith	Electronic Publishing
P. Yamin	Social & Spouse Activities, Aid
W.T. Weng	Chairman

Program Committee:

J. Alonso	LBNL
V. Balakin	BINP
W. Barletta	LBNL
I. Ben-Zvi	BNL, Chairman
M. Berz	MSU
J. Bisognano	TJNAF
E. Blackmore	Triumf
J. Byrd	LBNL
G. Caporaso	LLNL
B. Carlsten	LANL
J. Cary	U. Colorado
S. Chattopadhyay	LBNL
Y. Cho	ANL
P. Colestock	FNAL
J. Collins	IUCF
J. Corlett	LBNL
M. Craddock	Triumf
P. Debenham	DOE
G. Decker	ANL
G. Dutto	Triumf
E. Esarey	NRL
D. Finley	FNAL

J. Fox	SLAC
J. Galayda	ANL
J. Gallardo	BNL
D. Gilpatrick	LANL
E. Gluskin	ANL
S. Gourlay	LBNL
A. Hahn	FNAL
R. Hamm	AccSys
W. Herrmannsfeldt	SLAC
A. Hutton	TJNAF
A. Jackson	LBNL
A. Jason	LANL
T. Katsouleas	USC
P. Kneisel	TJNAF
G. Krafft	TJNAF
S. Krinsky	BNL
A. Krisch	U. Michigan
J. L. Laclare	CEA
S. Y. Lee	IUCF
W. Leemans	LBNL
M. Lynch	LANL
F. Marti	MSU
M. McAshan	FNAL
W. McDowell	ANL
D. McGinnis	FNAL
M. Month	BNL
S. Myers	CERN
W. Namkung	Pohang U.
J. Nolen	ANL
J. Noonan	ANL
P. O'Shea	Duke U.
D. Olsen	ORNL
W. Oren	TJNAF
H. Padamsee	Cornell U.
S. Peggs	BNL
C. Pellegrini	UCLA
J. Peoples	FNAL
N. Phinney	SLAC
T. Raubenheimer	SLAC
M. Reiser	U. Maryland
J. Rogers	Cornell U.
J. Rosenzweig	UCLA
T. Roser	BNL
D. Rubin	Cornell U.
R. Ryne	LANL
S. Schriber	LANL
R. Sheffield	LANL
R. Siemann	SLAC
D. Sutter	DOE
M. Thuot	LANL
A. Todd	Advanced Energy Systems
J. Tompkins	FNAL
G. Vignola	Frascati
P. Wanderer	BNL
S. Wang	IHEP
W.T. Weng	BNL
M. White	ANL
D. Whittum	SLAC
F. Willeke	DESY
M. Wilson	DOE
Y. Yamazaki	KEK
Y. Yan	SLAC
A. Zolfaghari	MIT
M. Zumbro	LANL

Registrants

Abrar, Muhammad H. abrar@kfupm.edu.sa
King Fahd University of Petrolelum & Minerals, Department of Physics, P.O. Box 1110, Dhahran, 31261, Saudi Arabia

Adamenko, Stanislav V. bulyak@kipt.kharkov.ua
CemEx, 19, Vasilenko Str Apt.39, Kiev, 252124, Ukraine

Adams, Dean J dean.adams@rl.ac.uk
Rutherford Appleton Laboratory, CCLRC, CCLRC, Rutherford Appleton Laboratory, Didcot, Oxfordshire, OX110QX, United Kingdom

Adderley, Philip A Adderley@jlab.org
TJNAF, Accelerator Division; MS 16A, 12000 Jefferson Ave, Newport News , Va., 23606, USA

Adolphsen, Chris E star@slac.stanford.edu
SLAC, SLAC, MS 65, 2575 Sand Hill Road, Menlo Park , CA, 94025

Agafonov, Alexey V. agafonov@sci.lpi.ac.ru
P.N.Lebedev Physical Institute, Lebedev Physical Institute, Leninsky Prospect, 53, Moscow, 117924, GSP, Russia

Ahle, Larry E ahle1@llnl.gov
LLNL, LLNL, L-481, PO Box 808, Livermore, CA, 94551, USA

Ahn, Hyo Eun heahn@nanum.kaeri.re.kr
Korea Atomic Energy Research Institute, Nuclear Physics and Engineering Team KAERI, PO Box 105 , Yusong, Taejon, 305-600, South Korea

Akiyoshi, Hiromichi akiyoshi@postman.riken.go.jp
RIKEN, Cyclotron Laboratory, 2-1 Hirosawa, Wako, Saitama, 351-0198, Japan

Aleksandrov, Alexandre V Aleksandrov@inp.nsk.su
BINP, Institute of Nuclear Physics, Lavrentieva - 11, Novosibirsk, 630090, Russia

Alessi, James G. alessi@bnl.gov
BNL, AGS Department, Building 930, Upton, NY, 11973, USA

Alexahin, Yuri alexahin@sunse.jinr.ru
Joint Institute for Nuclear Research, PPL, Dubna, Moscow region, 141980, Russia

Alexeff, Igor ialexeff@earthlink.net
University of Tennessee, Electrical Engineering Department, Ferris 315, Middle Drive, Knoxville, TN, 37996-2100, USA

Allen, Matthew A. matallen@slac.stanford.edu
SLAC, 325 Chatham Way, Mountain View, CA, 94040, USA

Allen, Lawrence J allen@fnal.gov
FNAL, Beams Div. Proton Source MS 307, Box 500 , Batavia, IL, 60510, USA

Alonso, Jose R AlonsoJR@ORNL.gov
ORNL, SNS , 104 Union Valley Road, Mailstop 8218, Oak Ridge, TN, 37830-8218, USA

Altiparmakov, Dimitar V. alti@eunet.yu
VINCA Institute of Nucelar Sciences, Laboratory of Physics (010), P.O.Box 522, Belgrade, 11001, Yugoslavia

Amatuni, Andrey gayane@jerewan1.yerphi.am
Yerevan Physics Institute, Yerevan Physics Institute, 2 Alikhanian Brothers' Street, Yerevan, 375036, Armenia

Ambrosio, Giorgio giorgioa@fnal.gov
FNAL, T/D Development & Test Department, P.O. Box 500, MS 316, Batavia, IL, 60510, USA

Anatoli, Zelenski N zelenski@triumf.ca
TRIUMF, 4004 Wesbrook Mall, Vancouver, BC, V6T2A3, Canada

Anderson, Scott G anderson@physics.ucla.edu
UCLA, UCLA Dept. of Physics and Astronomy, 1-129 Knudsen Hall, 405 Hilgard Ave, Los Angeles, CA, 90095, USA

Anderson, David E deanderson@lanl.gov
LANL, DX-8 M/S P939, Bikini Atoll Road, Los Alamos, NM, 87545, USA

Anderson, James L jla@lanl.gov
LANL, APT/TPO, Ms H816, Los Alamos National Laboratory, Los Alamos, NM, 87544, USA

Anderson, Oscar A OAAnderson@LBL.gov
LBNL, Bldg 47, 1 Cyclotron Road, Berkeley, CA, 94720, USA

Anderson, Edwin B eba1@cornell.edu
Cornell U., Department of Physics, Cornell University, Ithaca, NY, 14853

Andrews, David ER. AndrewsDE@ox.com
Oxford Instruments, 600 Milik, Carteret, NJ, 07009, USA

Andrianov, Serge Serge.Andrianov@pobox.spbu.ru
St.Petersburg S.U., Department of Applied Mathematics and Control Processes, Bibliotechnaja pl. 2, Bela Kuna str. 2-3-126, St.Petersburg, Russia, 198904, Russia

Anerella, Michael D mda@bnl.gov
BNL, RHIC Department, Building 902, Upton, NY, 11973, USA

Anferov, Vladimir A anferov@umich.edu
U. of Michigan, Physics Department, University of Michigan, Ann Arbor, MI, 48109-1120, USA

Angert, Norbert N.Angert@gsi.de
GSI, Accelerator Division, Postfach 11 05 52, Darmstadt, 64220, Germany

Aoki, Yasushi yss_aoki@shi.co.jp
Sumitomo Heavy Ind., Ltd., Research and Development Center, 2-1-1 YATO-CHO, TANASHI, TOKYO, 188-8585, Japan

Asaka, Takao asaka@haru01.spring8.or.jp
SPring-8, Linac Group, SPring-8, Mikazuki, Sayo, Hyogo 679-5198, Sayo, 679-5198, Japan

Ashton, John EU john.ashton@eev.com
EEV, Waterhouse Lane, CHELMSFORD, ESSEX, CM1 2QU, United Kingdom

Assadi, Saeed assadi@fnal.gov
FNAL, Main Injector, P.O. Box 500, MS 341, Batavia, IL, 60510, USA

Ausset, Patrick ausset@ipno.in2p3.fr
Institut de Physique Nucleaire, SERVICE RDA, UNIVERSITE PARIS SUD, ORSAY, 91406 Cedex, France

Averill, Robert J averiall@bates.mit.edu
MIT-Bates, 15 Meltiah Road, Falmouth, MA, 02540, USA

Baartman, Rick A krab@triumf.ca
TRIUMF, 4004 Wesbrook Mall, Vancouver, BC, V6T2A3, Canada

Badea, Sorin-Viorel badea@bnl.gov
BNL, AGS Department, Bldg. 911A, Upton, New York, 11973, USA

Bagley, Richard E pac99@bnl.gov
Process Systems International, 20 Walkup DriveWes, Westborough, MA, 01581, USA

Bai, Mei mbai@indiana.edu
Indiana U., Physics Department, AGS Dept. Bldg. 911B, Brookhaven National Lab., IUCF, India, Upton, NY, 11973, USA

Bakker, Rene J bakker@bii.bessy.de
BESSY, BESSY II, BESSY II, Geb. 14.51, Rudower Chausee 5, Berlin, Berlin, 12498, Germany

Balakin, Vladimir Egorovich balakin@vlepp.serpukhov.su
BINP, BINP, Protvino, Moscow region, 142284, Russia

Balbekov, Valeri I balbekov@fnal.gov
FNAL, Beams division, Muon Collider, FNAL, MS220, P.O.Box 500, Batavia, Illinois, 60510, USA

Ball, Penny penny@onramp.net
M J B Plus, Inc., Suite 304, 119 Executive Way, De Soto, TX, 75115, USA

Balon, Anthony J balon@bnl.gov
BNL, Bldng. 725D, Brookhaven National Lab., Upton, NY, 11973, USA

Banna, Samer Samer@tx.technion.ac.il
Tech-X Corporation, Electrical Engineering, Department of Electrical Engineering - Thecnion - Haifa , Nazareth 319/13 - Zip code 16000, Haifa, Israel , 32000, Israel

Baranauskas, Vitor VB vitor@dsif.fee.unicamp.br
State University of Campinas, Faculdade de Engenharia Elétrica e Computação, Av. Albert Einstein N.400, UNICAMP, Campinas, SP, 13083-970, Brazil

Barletta, William wbarletta@lbl.gov
LBNL, Accelerator and Fusion Research Division, One Cyclotron Road, 50-4049, Berkeley, California, 94720, USA

Barnard, John J jjbarnard@llnl.gov
LLNL/LBNL, L-645, Lawrence Livermore National Laboratory, Livermore, CA, 94550, USA

Barnes, Jr., Peter D. pdbarnes@llnl.gov
LLNL, N Division, Mail Stop L-50, 7000 East Ave., Livermore, CA, 94550, USA

Barov, Nikolai batov@vesta.ohysics-ucla.edu
UCLA/Fermilab, X Gallery, Kirk & Pine Rds, Batavia, IL

Barry, Walter Walter_Barry@lbl.gov
LBNL, Engineering Division, One Cyclotron Road, MS: 71-259, Berkeley, CA, 94720, USA

Barton, Donald S dsbarton@bnl.gov
BNL, AGS/RHIC, Bldg 911C, PO Box 5000, Upton, NY, 11973-5000

Batskikh, Gennady I mamaev_g@mail.sitek.ru
Moscow Radiotechnical Institute, 132, Warshawskoe shosse, Moscow, 113519, Russia

Batygin, Yuri K batygin@rikaxp.riken.go.jp
RIKEN, Radioactive Isotope Beam Factory Project Office, 2-1 Hirosawa, Wako-shi, Saitama, 351-01, Japan

Bauer, Pierre   pbauer@fnal.gov
FNAL, T/D Development & Test Department, P.O. Box 500, MS 316, Batavia, IL, 60510, USA

Bechtold, Alexander   A.Bechtold@iap.uni-frankfurt.de
Institut fur Angewandte Physik, Institut fuer Angewandte Physik, Johann Wolfgang Goethe-Universitaet, Robert-Mayer-Str. 2-4, Frankfurt am Main, D-60054, Germany

Becker, Reinard   rbecker@physik.uni-frankfurt.de
Universitaet Frankfurt, IAP, Institut fuer Angewandte Physik, der Universitaet Frankfurt, Fach 182, Frankfurt am Main, D-60054, Germany

Beczek, Kevin J   beczek@aps.anl.gov
ANL, ASD Vacuum Group, 9700 S. Cass Avenue, Building 401, Argonne, Illinois, 60439-4800, USA

Bedau, Juergen   jb@bruker.de
Bruuer Germany, Wikingerstr 13, Karlsruhe, 76189, Germany

Beebe, Edward N   BEEBE@BNL.GOV
BNL, AGS Dept., Bldg. 930, 16 Fifth Ave., Upton, NY, 11973, USA

Beebe-Wang, Joanne J.   bbwang@bnl.gov
BNL, AGS Dept., Bldg.. 911-A, Upton, NY, 11973, USA

Beetham, Gary   Gary.Beetham@cern.ch
CERN, Div. SL, 1211 Geneva 23, Switzerland

Belicev, Petar   p_belicev@hotmail.com
Faculty of Science, P.O.Box 162, Skopje, FYR Macedonia, 91000, Yugoslavia

Belomestnykh, Sergey A   sab@lns62.lns.cornell.edu
Cornell U., Laboratory of Nuclear Studies, Newman Lab., Cornell University, Ithaca, NY, 14853, USA

Ben-Zvi, Ilan   ilan@bnl.gov
BNL, National Synchrotron Light Source, P.O. Box 5000, Building 725C, Upton, NY, 11973-5000, USA

Bendall, Robin G   R.G.Bendall@rl.ac.uk
Rutherford Appleton Laboratory, ISIS Facility, Rutherford Appleton Laboratory, Chilton, DIDCOT, Oxon, OX11 0QX, United Kingdom

Benson, Stephen V   felman@jlab.org
TJNAF, Free Electron Laser, Accelerator Division, 12000 Jefferson Avenue, Mail Stop 6A, Newport News, Virginia, 23606, USA

Bergoz, Julien   bergoz@bergoz.com
Bergoz Instrumentation, Rue du Jura, Crozet, (Ain), 01170, France

Bernal, Santiago   sabern@plasma.umd.edu
U. of Maryland, Institute for Plasma Research, University of Maryand, College Park, MD, 20742, USA

Bertolini, Louis R.   bertolini1@llnl.gov
LLNL, Lawrence Livermore National Laboratory, 7000 East Ave. L-287, P.O. Box 808, Livermore, Ca., 94551-0808, USA

Bertsche, Kirk J   kbertsche@smsocs.com
Siemens Medical Systems, 4040 Nelson Ave., Concord, CA, 94520, USA

Bhatia, Tarlochan S   BHATIA@LANL.GOV
LANL, LANSCE-1, MS H808, LANL, LOS ALAMOS, NM, 87545, USA

Biallas, George H   biallas@jlab.org
TJNAF, FEL Dept., Mail Stop 4A, 12000 Jefferson Ave., Newport News, VA, 23606, USA

Bickley, Matthew H   bickley@jlab.org
TJNAF, 85A, 12000 Jefferson Ave, Newport News, VA, 23606, USA

Biedron, Sandra G.   biedron@aps.anl.gov
ANL, APS, 9700 S. Cass Avenue, Bldg. 401, Argonne, IL, 60439, USA

Bieler, Michael f   bieler@desy.de
DESY, MIN, DESY, Notkstrasse 85, 22603 Hamburg, Germany

Bieniosek, Frank   FMBieniosek@lbl.gov
LBNL, Accelerator Fusion Research Dept., One Cyclotron Rd., MS 47-112, Berkeley, CA, 94720, USA

Billen, James H   jbillen@lanl.gov
LANL, LANSCE-1, Mail Stop H817, Los Alamos, NM, 87545, USA

Biryukov, Valery M   biryukov@mx.ihep.su
Institute of High Energy Physics, Beam Dep, Pobedy 1, Protvino, Moscow Region, 142284, Russia

Biscari, Caterina   biscari@lnf.infn.it
INFN - Frascati, ACCELERATOR DIVISION, C.P.13, Frascati (Roma), 00044, Italy

Bisognano, Joseph J.   bisognano@jlab.org
TJNAF, Accelerator Division, 12000 Jefferson Avenue, MS 7A, Newport News, Virginia, 23606, USA

Blackmore, Ewart W   ewb@triumf.ca
TRIUMF, TRIUMF, 4004 Wesbrook Mall, Vancouver, BC, V6T 2A3, Canada

Blaskiewicz, Michael M   blaskiewicz@bnl.gov
BNL, AGS Department, BNL 911B, Upton, NY, 11973-5000, USA

Blaugrund, A.E.   FNBLA@Weizmann.Weizmann.AC.IL
Weizmann Institute of Science, Weizmann Institute of Science, Rehovot Israel, Rehovot, Israel, 76100, Israel

Blell, Udo   u.blell@gsi.de
GSI, BEN, Planckstr 1, Darmstadt, 64291, Germany

Bleser, Edward J   bleser@bnl.gov
BNL, AGS Deparment, Building 911B, Upton, New York, 11973, USA

Bluem, Hans P   bluem@grump.com
Advanced Energy Systems, 29 Airpark Rd., Princeton, NJ, 08540, USA

Blum, Eric B   blum@bnl.gov
BNL, NSLS, Bldg. 725C, Upton, NY, 11973-5000

Blume, Martin   blume@aps.org
BESSY, One Research Rd., Ridge, NY, 11961, USA

Bocchetta, Carlo J   carlo.bocchetta@elettra.trieste.it
Sincrotrone Trieste, s.s. 14 km 163.5, Basovizza, Trieste, 34012, Italy

Boellmann, J. F   sigmaphi@dial.oleane.com
Sigmaphi,

Bogacz, S. Alex   bogacz@cebaf.gov
TJNAF, Beam Physics & Instrumentation Dept., 12000 Jefferson Ave. MS 5A, Newport News, Virginia, 23608, USA

Bogart, Locke   elbogart@aol.com
PEPCC, 2364 Altisma Way, Ste C, Carlsbud, CA, 92009, USA

Bohlen, Heinz P   heinz.bohlen@mpp.cpii.com
CPI Inc., MPP Division, 811 Hansen Way, M/S B-450, P.O. Box 50750, Palo Alto, CA, 94303-0750, USA

Bohn, Courtlandt L.   clbohn@jlab.org
TJNAF, Accelerator Division, 12000 Jefferson Avenue, Mail Stop 6A, Newport News, Virginia, 23606, USA

Bolme, Gerald O   gbolme@lanl.gov
LANL, LANSCE Division, Los Alamos National Laboratory, LANSCE-5 MS-H827, Los Alamos, New Mexico, 87545, USA

Bondarev, Boris I.   lidos@aha.ru
Moscow Radiotechnical Institute, 132 Warshavskoe Shosse, Moscow, Russia, Russia

Borburgh, Jan   Jan.Borburgh@cern.ch
CERN, PS Division, 1211 Geneva 23, Switzerland

Bordry, Frederick   frederick.bordry@cern.ch
CERN, CERN, Geneve 23, 1211, Switzerland

Boriskin, Victor N.   boriskin@nik.kharkov.ua
National Science Center, Kharkov Institute of Physics and Technology, 1 Academicheskaya str., Kharkov, 310108, Ukraine

Borisov, Oleg   borisov@nu.jinr.ru
Joint Institute for Nuclear Research, Laboratory of Nuclear Reactions, Joliot Curie 6, Dubna, Moscow region, 141980, Russia

Borland, Michael D   borland@aps.anl.gov
ANL, Advanced Photon Source, Bldg 401, B2201, 9700 South Cass Avenue, Argonne, IL, 60439, USA

Borovina, Dan L   dlborovina@aol.com
U. of New Mexico, Electrical and Computer Engineering, EECE Rm. 125, University of New Mexico, Albuquerque, NM, 87131, USA

Bosch, Robert A   bosch@src.wisc.edu
SRC, U. of Wisconsin- Madison, 3731 Schneider Drive, Stoughton, Wisconsin, 53589-3097, USA

Boscolo, Ilario   ilario.boscolo@mi.infn.it
Milan University, Physics Department, via Celoria 16, Milano, Italy, 20133, Italy

Botman, Jan   j.i.m.botman@tue.nl
Eindhoven University of Technology, Cyclotron Laboratory, P.O.Box 513, Den Dolech 2, Eindhoven, 5600 MB, Netherlands

Bourque, Robert F   robert.bourque@gat.com
General Atomics, APT Project, 135B Central Park Sq., Los Alamos, NM, 87544, USA

Boussard, Daniel   Daniel.Boussard@cern.ch
CERN, SL-HRF, CERN CH-1211 GENEVA 23, GENEVA, Switzerland, 1211, Switzerland

Bovet, Claude B.C.   madeleine.catin@cern.ch
CERN, Division SL, CERN (Prevessin), Geneva 23, Switzerland, 1211, Switzerland

Bowler, Darrin   darrin.bowler@eev.com
EEV, 106 Waterhouse Lane, Chelmsford, Essex, CM12QU, United Kingdom

Bradley III, Joseph T.   j_bradley@lanl.gov
LANL, M.S. H827, PO Box 1663, Los Alamos, NM, 87545, USA

Braeutigam, Werner   w.braeutigam@fz-juelich.de
Forschungszentrum Juelich, Institut fuer Kernphysik, Postfach 1913, Juelich, D-52425, Germany

Brennan, Joseph M   Brennan@bnl.gov
BNL, AGS Department, Building 911B, Upton, NY, 11973, USA

Bricault, Pierre   BRICAULT@TRIUMF.CA
    TRIUMF, 4004 Wesbrook Mall, Vancouver, British Columbia, V6T 2A3,
    Canada
Briggs, Richard J.   Richard.J.Briggs@cpmx.saic.com
    S.A.I.C., SAIC, 7041 Koll Center Parkway, Suite 260, Pleasanton, CA,
    94566, USA
Brinkmann, Reinhard   reinhard.brinkmann@desy.de
    DESY, MPY, Notkestr. 85, Hamburg, D-22603, Germany
Brown, Bruce C.   bcbrown@fnal.gov
    FNAL, Beams Division, MS 341, PO Box 500, Batavia, IL, 60510, USA
Brown, Kevin A.   kbrown@bnl.gov
    BNL, AGS Dept., Bldg. 911a, BNL, Upton, NY, 11973, USA
Brown, Winthrop J   brown@psfc.mit.edu
    Plasma Science and Fusion Center, MIT Plasma Science and Fusion
    Center, 167 Albany St., Cambridge, MA, 02139, USA
Bruhwiler, David L   bruhwile@txcorp.com
    Tech-X Corporation, 1280 28th St., Suite 2, Boulder, CO, 80303, USA
Brunelle, Pascale   brunelle@lure.u-psud.fr
    LABORATOIRE LURE, UNIVERSITE PARIS-SUD BAT209A, BP 34,
    ORSAY, 91898, France
Bruno, Donald   bruno@bnl.gov
    BNL, RHIC Project, Building 830M, Upton, New York, 11795, USA
Bryan, David A   bryan@jlab.org
    TJNAF, Beam Applications Team, 12050 Jefferson Ave., MS5A, Newport
    News, VA, 23602, USA
Bulfone, Daniele   bulfone@elettra.trieste.it
    Sincrotrone Trieste, s.s. 14 km 163.5, Basovizza, Trieste, 34012, Italy
Bulyak, Eugene V.   bulyak@kipt.kharkov.ua
    NSC KIPT, 1, Academicheskaya Str., Kharkov, 310108, Ukraine
Burger, Al   al_burger@atdc.northgrum.com
    Advanced Energy Systems, Inc., 199 Smith Ave., Holbrook, NY, 11741
Burla, Paolo A   Paolo.Burla@cern.ch
    CERN, Div. LHC/CRI, 1211 Geneva 23, Switzerland
Burns, Michael J   burns_michael_j@lanl.gov
    LANL, DARHT Project Office, Mail Stop P941, Los Alamos National
    Laboratory, Los Alamos, NM, 87545, USA
Burov, Alexey V   burov@fnal.gov
    FNAL, BD/EC, m.s.221, Batavia, IL, 60510, USA
Butler, Sharon E   sbutler@fnal.gov
    FNAL, Batavia, IL 60510, USA
Butler, Michael   pac99@bnl.gov
    DOE, Upton, NY, 11973, USA
Buxton, Wesley E   Buxton@bnl.gov
    BNL, AGS, 35 Lawrence Drive Bldg 911C, Upton, NY, 11973, USA
Byrd, John M   JMByrd@lbl.gov
    LBNL, 80-101, 1 Cyclotron Road, Berkeley, CA, 94720, USA
Böge, Michael   Michael.Boege@psi.ch
    Paul Scherrer Institut, Swiss Light Source, OBBA/4, Villigen PSI, CH-
    5232, Switzerland
Calabretta, Luciano   calabretta@LNS.INFN.IT
    INFN-LNS, Vio S. Sofia, Catania, I-95123, Italy
Cameron, Peter   cameron@bnl.gov
    BNL, RHIC, bldg 1005-4, upton, ny, 11973, USA
Campisi, Ricky   neil@jlab.org
    TJNAF, FEL Dept., Accelerator Div., 12000 Jefferson Avenue, Mail Stop
    6A, Newport News, Virginia, 23606, USA
Campisi, Isidoro E.   campisi@jlab.org
    TJNAF, 12000 Jefferson Ave., Newport News, VA, 23606, USA
Caporaso, George   caporaso1@llnl.gov
    LLNL, Lawrence Livermore National Laboratory, 7000 East Ave. L- 645,
    P.O.Box 808, Livermore, Ca., 94550-0808, USA
Cardman, Lawrence S   cardman@jlab.org
    TJNAF, Physics Division, MS-12H, 12000 Jefferson Ave, Newport News,
    VA, 23606, USA
Carlsten, Bruce E.   bcarlsten@lanl.gov
    LANL, LANSCE-9, MS H851, Los Alamos National Laboratory, Los
    Alamos, NM, 87545, USA
Carneiro, Jean-Paul   CARNEIRO@FNAL.GOV
    FNAL, BEAM DIVISION, MS 306, P.O. BOX 500, ASPEN EAST,
    ROOM 208, BATAVIA, ILLINOIS, 60510, USA
Carr, Larry   carr@bnl.gov
    BNL, 75 Brookhaven Avenue, Upton, NY, 11973, USA
Cary, John R   cary@colorado.edu
    University of Colorado, Department of Physics, Campus Box 390, Boulder,
    CO, 80309-0390, USA

Casey, Jeffrey A.   casey@divtecs.com
    Diversified Technologies, Inc., Diversified Technologies, Inc., 33 Wiggins
    Ave., Bedford, MA, 01730, USA
Caspi, Shlomo   s_caspi@lbl.gov
    LBNL, Superconducting Magnet Program/AFRD, 1 Cyclotron Rd., MS 46-
    161, Berkeley, CA, 94720, USA
Cassel, Richard   RLC@SLAC.Stanford.edu
    SLAC, Power Conversion Department, P.O.Box 4349, M/S 49, Stanford, CA,
    94309, USA
Castellano, Michele   michele.castellano@lnf.infn.it
    INFN - Frascati, INFN-LNF Divisione Ricerca, via E. Fermi 40, Frascati,
    00044, Italy
Castle, Michael W   castle@eng.umd.edu
    U. of Maryland, Institute for Plasma Research, University of Maryland,
    College Park, MD, 20742, USA
Castro, Pedro   pcastro@mail.desy.de
    DESY, MPY Group, Notkestrasse 85, Hamburg, 22603, Germany
Catalan-Lasheras, Nuria   Nuria.Catalan.Lasheras@cern.ch
    BNL, c/o Alt. Gradient Synchrotron , Bldg. 911B, P.O. Box 5000, Upton,
    NY, 11973, USA
Catravas, Palmyra E   PECatravas@lbl.gov
    LBNL, Center for Beam Physics, MS 71-259, 1 Cyclotron Rd., Berkeley, CA,
    94720, USA
Celata, Christine M   CMCelata@lbl.gov
    LBNL, Mailstop 47-112, Lawrence Berkeley National Laboratory, 1
    Cyclotron Road, Berkeley, California, 94720, USA
Cennini, Enrico   Enrico.Cennini@cern.ch
    CERN, ST DIVISION ACCESS CONTROL SECTION, 1211 GENEVE 23,
    GENEVA, 1211 GENEVE 23, Switzerland
Champion, Mark S   champion@fnal.gov
    FNAL, Beams Division / RF & Instrumentation, PO Box 500, MS 306,
    Batavia, IL, 60510, USA
Chan, Kwokchi D   KCCHAN@LANL.GOV
    LANL, APT-TPO, H816, Los Alamos, New Mexico, NM 87545, USA
Chang, Suk S   sschang@postech.ac.kr
    Pohang Accelerator Laboratory, Accelerator Department, San 31 Hyoja-
    Dong, Pohang, Kyungbuk, 790-784, Korea
Chao, Alex W   achao@slac.stanford.edu
    SLAC, MS 26, SLAC, P.O. Box 4349, Stanford, CA, 94309, USA
Chao, Yu-Chiu   chao@cebaf.gov
    TJNAF, Accelerator, 12000 Jefferson Avenue, Newport News, VA, 23606,
    USA
Chapelle, Sonja   chapel@gat.com
    General Atomics, 3550 General Atomics Ct, San Diego, California, 92121
Chargin, Anthony K.   chargin1@llnl.gov
    Lawrence Livermore National Laboratory, PO Box 808 MS L-050, 7000 East
    Avenue, Livermore, CA, 94550, USA
Chattopadhyay, Swapan   chapon@lbl.gov
    LBNL, Center for Beam Physics, Mail Stop 71-259, 1 Cyclotron Road,
    Berkeley, CA, 94720, USA
Chen, Teng   chen@phy.duke.edu
    Duke University FEL Lab, Physics Department, P.O.Box 90319, Durham,
    NC, 27708-0319, USA
Chen, Szu-yuan   sychen@umich.edu
    U. of Michigan, Center for Ultrafast Optical Science, 1006 IST Bldg., 2200
    Bonisteel Blvd., Ann Arbor, MI, 48105, USA
Chen, Chiping   chenc@psfc.mit.edu
    MIT , MIT Plasma Science and Fusion Center, 167 Albany Street,
    Cambridge, MA, 02139, USA
Chen, Pisin   chen@SLAC.Stanford.EDU
    SLAC, SLAC; MS-26, P.O. Box 4349, Stanford, CA, 94309, USA
Chen, Zukun   zchen@lanl.gov
    LANL, Engineering Sciences & Applications Division, Los Alamos National
    Lab, P.O.Box 1663, MS H821, Los Alamos, NM, 87545, USA
Chen, Ju   leon7@llnl.gov
    LLNL, Lawrence Livermore National Laboratory, 7000 East Ave. L-645,
    P.O.Box 808, Livermore, Ca, 94551-0808, USA
Chen, Yu-Jiuan   chen6@llnl.gov
    LLNL, Lawrence Livermore National Laboratory, 7000 East Ave. L-645,
    P.O. Box 808, Livermore, Ca., 94551-0808, USA
Chen, Judy   chen29@llnl.gov
    LLNL, Lawrence Livermore National Laboratory, 7000 East Ave. L- 645,
    P.O.Box 808, Livermore, Ca., 94550-0808, USA
Chen, Jiaer   chence@pku.edu.cn
    Peking University, Office of the President, Peking University, Hai Dian,
    Beijing, 100871, China, Peoples Republic of

Cheng, Daniel W   dwcheng@lbl.gov
LBNL, Engineering, 1 Cyclotron Road, MS 5-119, Berkeley, , CA, 94720, USA

Cheng, Hung-Ming   hmcheng@srrc.gov.tw
Synchrotron Radiation Research Center, Utility Group, No.1 R&D Road VI, Hsinchu Science-Based Industrial Park, Hsinchu, 300, Taiwan

Cherenshchykov, Sergiy A.   bulyak@kipt.kharkov.ua
National Science Center, Kharkiv Institute of Physics and Technology, 1, Academichna Str., Kharkiv, 310108, Ukraine

Cherepakhin, Anatoli A   cherepakhin@fnal.gov
FNAL, Antiproton Source Department, PO Box 500 Fermilab MS 341, Batavia, Illinois, 60510-500, USA

Chernin, David P   chernin@apo.saic.com
S.A.I.C., 1710 Goodridge Dr. MS 2-6-9, McLean, VA, 22102, USA

Chesnokov, Yuri A   chesnokov@mx.ihep.su
Institute of High Energy Physics, Beam Dep, Pobedy 1, Protvino, Moscow Region, 142284, Russia

Chiang, I-Hung   Chiang@bnl.gov
BNL, AGS Depart, Buil.911B, Brookhaven National Lab., Upton, LI, New York, 11973, USA

Chichili, Deepak R.   chichili@fnal.gov
FNAL, Technical Division / Engineering and Fabrication, P.O. Box 500, M.S. 316, Batavia, IL, 60510, USA

Chihiro, Ohmori   chihiro@insuty.tanashi.kek.jp
KEK, Tanashi, 3-2-1 Midori-cho, Tanashi, Tokyo, 188, Japan

Chin, Yong-Ho   yongho.chin@kek.jp
KEK, Accelerator Laboratory, 1-1 , Oho, Tsukuba-shi, Ibaraki-ken, 305-0801, Japan

Cho, Yanglai   yc@aps.anl.gov
ANL, APS, Bldg. 401, 9700 S. Cass Avenue, Argonne, IL, 60439, USA

Cho, Yong-Sub   choys@nanum.kaeri.re.kr
KAERI, P.O. Box 105, Yusong, Taejon, 305-600, Korea

Chohan, Vinod   Vinod.Chohan@cern.ch
CERN, PS Division, PS Division, CERN, 1211 Geneva 23, Switzerland

Chojnacki, Eric P   epc1@cornell.edu
Cornell U., Newman Laboratory, Ithaca, NY, 14853, USA

Chou, Weiren   chou@fnal.gov
FNAL, Beams Division, Fermilab, P.O. Box 500, Batavia, IL, 60510, USA

Chow, Ken P.   kpchow@lbl.gov
LBNL, Superconducting Magnet Program/AFRD, 1 Cyclotron Rd., MS 46-161, Berkeley, CA, 94720, USA

Christiansen, David W.   david.christiansen@gat.com
General Atomics, 135B Central Park Square, Los Alamos, New Mexico, 87544, USA

Chu, Chungming P   cmchu@iucf.indiana.edu
Indiana U., Cyclotron Facility, 2401 Milo B. Sampson Ln., Bloomington, IN, 47405, USA

Ciriani, Paolo   ciriani@cern.ch
CERN, ST division EL group, CERN, geneva , switzerland, Switzerland

Clarke, James A   j.a.clarke@dl.ac.uk
Daresbury Laboratory, Daresbury Laboratory, Daresbury, Warrington, Cheshire, WA44AD, Ukraine

Clayton, Christopher E.   cclayton@ucla.edu
UCLA, 56-125B Engineering IV Bldg., Los Angeles, CA, 90095, USA

Clendenin, James E   clen@slac.stanford.edu
SLAC, SLAC, MS-18, P.O. Box 4349, Stanford, CA, 94309, USA

Cline, David B.   dcline@physics.ucla.edu
UCLA, Physics and Astronomy Dept., 405 Hilgard Ave., Los Angeles, CA, 90095-1547, USA

Colestock, Patrick L.   colestock@adcalc.fnal.gov
FNAL, Femilab, Mail Statiaon 306, P.O. Box 500, Batavia, IL, 60510, USA

Collins, John C   collins@iucf.indiana.edu
Indiana U., Cyclotron Facility, 2401 Milo B. Sampson Lane, Bloomington, IN, 47408-1368, USA

Comunian, Michele   comunian@lnl.infn.it
Legnaro National Laboratories LNL, Divisione Acceleratori, Via Romea,4, Legnaro, Padova, 35020, Italy

Conde, Manoel   conde@hep.anl.gov
ANL, 9700 S. Cass Ave. Bldg. 362, Argonne, IL, 60439, USA

Connolly, Roger   connolly@bnl.gov
BNL, Brookhaven National Laboratory, RHIC Project - 1005S-4, P.O. Box 5000, Upton, NY, 11973-5000, USA

Cook, Don   colson@sandia.gov
Sandia National Laboratory, Pulsed Power Sciences Center, MS-1190, P. O. Box 5800, Albuquerque, NM, 87185-1190, USA

Cooke, Simon J   cooke@mmace.nr.navy.mil
S.A.I.C., Naval Research Laboratory, Code 6840, 4555 Overlook Ave. S.W., Washington, D.C., 20375, USA

Corbett, William J.   corbett@ssrl.slac.stanford.edu
SLAC, SLAC/SSRL, P.O. Box 4349, Stanford, CA, 94309-0210, USA

Corlett, John N   jncorlett@lbl.gov
LBNL, MS 71-259, Lawrence Berkeley National Laboratory, 1 Cyclotron Road, Berkeley, CA, 94611, USA

Cornacchia, Max   cornacchia@ssrl.slac.stanford.edu
SLAC, SSRL, P.O. Box 4349, MS/69, Stanford, CA, 94309, USA

Cornelis, Karel   karel.cornelis@cern.ch
CERN, SL-division, Geneva, Switzerland

Cornelius, Wayne D.   ssolutions@compuserve.com
Scientific Solutions, P.O. Box 500207, San Diego, CA, 92150, USA

Corredoura, Paul L   PLC@SLAC.Stanford.edu
SLAC, Klystron/Microwave Department, P.O. Box 4349, mail stop #33, Stanford, CA, 94309, USA

Costrell, Louis   costrell@nist.gov
NIST, National Institute of Standards and Technology, Route 270 and Qunice Orchard Road, Gaithersburg, MD, 20899, USA

Courant, Ernest D   courant@bnl.gov
BNL, RHIC, 40 W 72 St, Apt 41, New York, NY, 10023, USA

Coutrakon, George R   coutrak@proton.llumc.edu
Loma Linda Univ. Med. Center, 11234 Anderson St., Rm. B-121, Loma Linda, CA, 92354, USA

Craddock, Michael K   craddock@triumf.ca
UBC & TRIUMF , TRIUMF, 4004 Wesbrook Mall, Vancouver, B.C., V6T 2A3, Canada

Craft, Benjamin C.   bcraft@univ1.sncc.lsu.edu
CAMD, 6980 Jefferson Hwy., Baton Rouge, LA, 70806, USA

de Loos, Marieke J   gpt@pulsar.nl
Pulsar Physics, De Bongerd 23, Soest, NL, 3762 XA, Netherlands

D'yachkov, Mikhail   dyachkov@triumf.ca
TRIUMF, Accelerator Technology Division, 4004 Wesbrook Mall, Vancouver, B.C., V6T2A3, Canada

Dabrowski, John J   dabrowsk@bnl.gov
BNL, NSLS, BNL, Bldg.725B, Upton, N.Y., 11973, USA

Dahl, Per F.   pfdahl@aol.com
LBNL, Not Applicable, USA

Danared, Hakan   danared@msi.se
Manne Siegbahn Laboratory, Manne Siegbahn Laboratory, Frescativagen 24, Stockholm, 10405, Sweden

Daniels, Kevin   kdaniels@tritonetd.com
Triton Electron Technology, 3400 Charlotte Ave, P.O. Box 100, Easton, PA, 18044-0100, USA

Danilov, Viatcheslav V   danilovs@ornl.gov
ORNL, SNS, 104 Union Valley Road, Oak Ridge, TN, 37830, USA

Danly, Bruce G   danly@nrl.navy.mil
NRL, Electronics Science & Technology Division, Code 6840, 4555 Overlook Ave., SW, Washington, DC, 20375, USA

Davidson, Ronald C.   rdavidson@pppl.gov
Princeton University, Plasma Physics Laboratory, Princeton University, P.O. Box 451, Princeton, New Jersey, 08543, USA

DeFord, John F.   john.deford@staarinc.com
STAR, Inc., 11520 N. Port Washington Rd., Ste. 101B, Mequon, WI, 53092

DeSantis, Stefano   sdesantis@lbl.gov
LBNL, ALS, One Cyclotron Road, MS:80-101, Berkeley, CA, 94720, USA

DeVries, Jan   GJDeVries@lbl.gov
LBNL, Engineering Division, One Cyclotron Road, MS: 46-125, Berkeley, CA, 94720, USA

Debenham, Philip H.   phil.debenham@science.doe.gov
DOE, SC-224; U.S. Department of Energy, 19, 901 Germantown Road, Germantown, MD, 20874, USA

Decker, Glenn A   decker@aps.anl.gov
ANL, ASD/401, 9700 S. Cass Avenue, Argonne, Illinois, 60439-4800, USA

Decker, Franz-Josef   Decker@SLAC.Stanford.edu
SLAC, P.O. Box 4349, MS 18, Stanford, CA, 94309, USA

Degen, Chris   degen@bnl.gov
BNL, Bldg. 1005, Upton, NY, 11973, USA

Dehler, Micha M.   Micha.Dehler@psi.ch
Paul Scherrer Institut, Swiss Light Source, OBBA/6, Villigen PSI, CH-5232, Switzerland

Dehning, Bernd D.B.   Madeleine.Catin@cern.ch
CERN, Div. SL/BI, CERN, GENEVA 23, 1211, Switzerland

Dejus, Roger J   dejus@aps.anl.gov
ANL, The Advanced Photon Source, Argonne National Laboratory, 9700 S. Cass Avenue, Argonne, IL, 60439, USA

Delahaye, Jean-Pierre   Jean-Pierre.Delahaye@cern.ch
CERN, PS Division, CERN, Geneva 23, 1211, Switzerland

Delayen, Jean R.   delayen@jlab.org
TJNAF, Accelerator Division, 12000 Jefferson Avenue, Mailstop 7A, Newport News, Virginia, 23606, USA

DenHartog, Patric K.   PDenHartog@anl.gov
ANL, APS Division, 9700 S. Cass Avenue, Bldg. 401/B3177, Argonne, IL, 60439, USA

Dey, Joseph E   dey@fnal.gov
FNAL, Beams Division RFI, P.O. Box 500, MS 306, Batavia, IL, 60510, United Kingdom

Dias, Joao M   pcp848@alfa.ist.utl.pt
Instituto Superior Tecnico/GoLP, Centro de Fisica de Plasmas-Complexo/IST, Av. Rovisco Pais, 1, Lisboa, 1096, Portugal

Dickson, Richard W   dickson@jlab.org
TJNAF, Controls Dept., 12000 Jefferson Ave, Bldg 85, Newport News, VA, 23606, USA

Dietrich, Juergen   j.dietrich@fz-juelich.de
Forschungszentrum Juelich, Institut fuer Kernphysik, P.O.Box 1913, Juelich, D-52425, Germany

Dimitrov, Dimitar   ladec@plovdiv.techno-link.com
Ladec Ltd., 48 Svoboda, Flat 22, Plovdiv, 4002, Bulgaria

Ding, Xiaodong   ding@ucla.edu
U. of California, Los Angeles, Department of Physics, Knudsen Hall 4-108, 405 Hilgard ave., Los Angeles, California, 90095-1547, USA

Diviacco, Bruno   diviacco@elettra.trieste.it
Sincrotrone Trieste, s.s. 14 km. 163,5 - Area Science Park, Basovizza (Trieste), 34012, Italy

Dohan, Donald A   dohan@aps.anl.gov
ANL, Accelerator Systems Division, Bldg 401, C2252, 9700 S. Cass Avenue, Argonne, Il, 60439, USA

Dolbilov, Gennady V.   dol@sunse.jinr.ru
Joint Institute for Nuclear Research, Particle Physics Laboratory, 141980, Dubna, Moscow region, Russia, Dubna, Moscow Region, 141980, Russia

Dolbilovb, Gennagy V.   dol@sunse.jinr.ru
Joint Institute for Nuclear Research, PPL, 141980, Dubna, Moscow Region, Dubna, Moscow Region, 141980, Russia

Doll, David W.   david.doll@gat.com
General Atomics, Electromagnetic Systems, P.O. Box 85608, San Diego, California, 92121-1194, USA

Domer, Gregory A   gdomer@kcp.com
AlliedSignal FM&T, Department ME3, P.O. Box 419159, Mail Stop FQ24, Kansas City, MO, 64141, USA

Donahue, Joey B   jdonahue@lanl.gov
LANL, Group LANSCE-7, Mail Stop H840, P.O. Box 1663, Los Alamos, New Mexico, 87545, USA

Donaldson, Anthony R   ARDAT@SLAC.STANFORD.EDU
SLAC, Power Conversion Department, 2575 Sand Hill Road MS49, Menlo Park, Ca., 94025, USA

Donley, Lawrence   lidonley@anl.gov
ANL, IPNS, 9700 S. Cass Ave., Bldg. 360, A132, Argonne, IL, 60439, USA

Dooling, Jeffrey C   jcdooling@anl.gov
ANL, Intense Pulsed Neutron Source (IPNS), 360 IPNS, C-125, 9700 S. Cass Avenue, Argonne, IL, 60439, USA

Doolittle, Lawrence R.   ldoolitt@jlab.org
TJNAF, Accelerator Division, 12000 Jefferson Avenue, MS 58, Newport News, Virginia, 23606, USA

Dorfan, Jonathan M   jonathan@slac.stanford.edu
SLAC, PEP-II Division, P.O. Box 4349, Stanford, CA, 94309, USA

Dovbnya, Anatoliy   dovbnya@nik.kharkov.ua
NSCKIPT, NSC KIPT 1, Akademichiskay, 310108 Kharkov, Ukraine

Doyuran, Adnan   adoyuran@ic.sunysb.edu
SUNY, ATF BNL, Bldg. 820, Upton , NY, 11973, USA

Drago, Alessandro   drago@lnf.infn.it
INFN-LNF, Istituto Nazionale de Fisica Nucleare, Via E. Ferhi 40, Frascati (RM), 00044, Italy

Dragt, Alex J   dragt@physics.umd.edu
U. of Maryland, Department of Physics, Department of Physics, University of Maryland, College Park, MD, 20742, USA

Drees, K. A.   drees@bnl.gov
BNL, RHIC Project, P.O. Box 5000, Bldg. 1005S, Upton, NY, 11973-5000, USA

Driouichi, Chafik   d_chak@mailcity.com
Universite Hassan II, LPNP - Faculte des Sciences, LPNPA8- Faculte des Sciences,Ain Chock., (ChezA. Hassnaoui). 6 Rue Jamila 05. , 20450-Casablanca., Casablanca, 20450, Morocco

Drozhdin, Alexandr I   drozhdin@fnal.gov
FNAL, Beams Physics, Beams Division, FNAL, FNAL, MS220, P.O.Box 500, Batavia, Illinois, 60510, USA

Drury, Michael A.   drury@jlab.org
TJNAF, Accelerator Division, 12000 Jefferson Avenue, Newport News, Virginia, 23606, USA

Duda, Brian J   bjduda@physics.ucla.edu
UCLA, 1-130 Knudsen Hall, Los Angeles, CA, 90095, USA

Dugan, Gerald F   gfd1@cornell.edu
Cornell U., Newman Laboratory, Cornell University, Ithaca, New York, 14853, USA

Duke, Jonathan P   j.p.duke@rl.ac.uk
Rutherford Appleton Laboratory, ISIS, Rutherford Appleton Laboratory, Chilton, Didcot, OXON., 0X11 0QX, United Kingdom

Dunbar, Anne   Dunbar@bnl.gov
BNL, AGS, Building 911A, Upton, NY, 11973, USA

Dutto, Gerardo G.   DUTTO@TRIUMF.CA
TRIUMF, Cyclotron Division, 4004 Wesbrook Mall, Vancouver, British Columbia, V6T 2A3, Canada

East, Gary W.   east@iucf.indiana.edu
Indiana University Cyclotron Facility, 2401 Milo Sampson Lane, Bloomingron , In., 47408, USA

Eberhardt, Marvin L   marvin.eberhardt@eimac.cpii.com
CPI Inc., Eimac Division, 301 Industrial Road, San Carlos, CA, 94070, USA

Economou, Dimitris   deco@rtm.iasa.uoa.gr
Institute of Accelerating Systems and Applications (IASA), 21 Filikis Etaireias St, 152 32 Halandri, Athens, Greece

Efstathiadis, Efstratios   stratos@sun2.bnl.gov
Boston University, Brookhaven National Lab., Physics Dept., (Bldg.# 510A), P.O.Box 5000, Upton, NY, 11973-5000, USA

Eickhoff, Hartmut   H.Eickhoff@gsi.de
GSI, Accelerator Development, Planckstr. 1, Darmstadt, Hessen, 64291, Germany

Einfeld, Dieter   einfeld@anka.fzk.de
Forschungszentrum Karlsruhe, ANKA (PEA), Postfach 3640, Karlsruhe, D-76021, Germany

Elias, Luis R.   elias@creol.ucf.edu
CREOL-School of Optics-FEL-UCF, 4000 Central Florida Blvd., Orlando, FL, 32816-2700, USA

Emamian, Mark   marke@fel.duke.edu
Duke University, Free Electron Laser Lab., P.O. Box 90319, Durham NC. 27708-0319, 300 Mimosa Dr, Chapel Hill, NC, 27514, USA

Emery, Louis   emery@aps.anl.gov
ANL, ASD, 9700 South Cass Avenue, Argonne, IL, 60439, USA

Endo, Akira   aendo@fesra.or.jp
Femtosecond Research Assoc., 5-5 Tokodai, Tsukuba, 300-2635, Japan

Eppley, Kenneth R   keppley@bos.saic.com
S.A.I.C., SAIC, Suite 130, 20 Burlington Mall Rd., Burlington, MA, 01803, USA

Erickson, John L   jerickson@lanl.gov
LANL, MS H821, Los Alamos National Lab, Los Alamos, NM, 87545, USA

Erickson, Andrew   erickson_a@lanl.gov
LANL, MS-H851, P.O. Box 1663, Los Alamos, NM, 87545, USA

Esarey, Eric   EHEsarey@lbl.gov
LBNL, Center for Beams Physics, 1 Cyclotron Road, Berkeley, CA, 94720, USA

Evans, Lyndon R.   evans@mail.cern.ch
CERN, DG - M219000, CH - 1211 Geneva 23, Geneva, CH - 1211, Switzerland

Evans, Kenneth Jr.   evans@aps.anl.gov
ANL, ASD, Bldg. 401, C2245, 9700 S. Cass Avenue, Argonne, IL, 60439

Eylon, Shmuel   S_Eylon@LBL.gov
LBNL, MS 47-112, 1 Cyclotron Rd., Berkeley, CA, 94720, USA

Fabris, Alessandro   fabris@elettra.trieste.it
Sincrotrone Trieste, Sincrotrone Trieste, ss.14 km 163,5 Basovizza, Trieste, 34012, Italy

Facco, Alberto   facco@lnl.infn.it
INFN - Laboratori Nazionali di Legnaro, Divisione Acceleratori, Via Romea 4, Legnaro, Padova, I-35020, Italy

Fagan, Matthew J.   fagan@lanl.gov
LANL, ESA-DE, P.O.Box 1663, Mail Stop H821, Los Alamos, NM, 87545, USA

Fahmie, Michael P.   mpfahmie@lbl.gov
LBNL, MS46-125 LBNL, 1 Cyclotron Road, Berkeley, CA, 94720, USA

Faltens, Andris   a_faltens@lbl.gov
LBNL, 47 - 112 LBNL, 1 Cyclotron Rd., Berkeley, CA, 94720, USA

Fan, Mingwu   mingwu@mipsa.ciae.ac.cn
China Institute of Atomic Energy, P.O. Box (1), Beijing, 102413, PR China

Fan, Kuanjun   kjfan@ustc.edu.cn
National Synchrotron Radiation Lab, USTC, National Synchrotron
Radiation Lab, USTC, P.O.Box 6022, Hefei, Anhui, 230029, PR China

Fang, Jyan-Min   fang@beamer8.physics.yale.edu
Columbia University, Department of Applied Physics, 272 Whitney
Avenue, Beam Physics Laboratory, New Haven, CT, 06511, USA

Fang, Si   cjf@fnal.gov
FNAL, P.O. Box 500 MS 308, Batavia, IL, 60510, USA

Farkas, Zoltan D   zdf@slac.stanford.edu
SLAC, Stanford, CA 94309, USA

Fartoukh, Stephane   stephane.fartoukh@hep.saclay.cea.fr
CEA, 139 Rue des PYRENEES, Paris, 75020, France

Faugeras, Paul   Paul.Faugeras@cern.ch
CERN, AC, CH - 1211 Geneva 23, Geneva, CH - 1211, Switzerland

Faugier, André   Andre.Faugier@cern.ch
CERN, SL division, GENEVA, Switzerland

Favale, Anthony J.   tony_favale@atdc.northgrum.com
Advanced Energy Systems, Inc., Northrop Grumman Bldg. 14, Bethpage,
NY, 11714, USA

Fawley, William M   William_Fawley@lbl.gov
LBNL, Accelerator Fusion Research Division, lawrence Berkeley National
Laboratory, One Cyclotron Road, M.S. 71J, Berkeley, CA, 94720, USA

Fazio, Michael V.   mfazio@lanl.gov
LANL, LANSCE-9 , MS-H851, Los Alamos, NM, 87545, USA

Fedorova, Antonina N   anton@math.ipme.ru
IPME RAS, Mathematical Methods in Mechanics Group, V.O.Bolshoj
pr.,61, St.Petersburg, 199178, Russia

Fedotov, Alexei V.   fedotov@physics.umd.edu
U. of Maryland, Dynamical Systems & Accel. Theory Group, Physics
Department, University of Maryland, College Park, MD, 20742, USA

Feher, Sandor   fehers@fnal.gov
FNAL, T/D Development & Test Department, P. O. Box 500, MS 316,
Batavia, IL, 60510, USA

Feikes, Joerg   feikes@bii.bessy.de
BESSY, MB, Rudower Chaussee 5, Berlin, Berlin, 12489, Germany

Feinberg, Ben   b_feinberg@lbl.gov
LBNL, Advanced Light Source, MS 80-101, 1 Cyclotron Rd., Berkeley,
CA, 94720, USA

Feldl, Erich J   feldl@jlab.org
TJNAF, Accelerator Division, Engineering, 12050 Jefferson Ave., Newport
News , VA, 23606, USA

Feng, Shuchen Kate   feng1@bnl.gov
BNL, NSLS, 725D, NSLS, Upton, NY, 11973, USA

Ferguson, Patrick E.   mdsfer@aol.com
MDS Company, 1955 Mountain Blvd., Suite 101, Oakland, CA, 94611

Fernow, Richard C   fernow@bnl.gov
BNL, Physics Department, Bldg. 901A, 59 Cornell Ave., Brookhaven
National Labaoratory, Upton, NY, 11973-5000, USA

Ferrario, Massimo M   FERRARIO@LNF.INFN.IT
INFN - Frascati, RICERCA Divisione Ricerca, Via E. Fermi 40, Frascati
(Roma), 00044, Italy

Finley, David A   finley@fnal.gov
FNAL, Beams Division, MS221, PO Box 500, Batavia, IL, 60510, USA

Fiorito, Ralph B   rfiorito@rocketmail.com
Catholic University of America, Dr. Ralph B. Fiorito, 3 Lauer Terrace,
Silver Spring, MD, 20901, USA

Fischer, Wolfram   Wolfram.Fischer@bnl.gov
BNL, RHIC Project, P.O. Box 5000, Bldg. 1005S, Upton, NY, 11973-
5000, USA

Fisher, Alan S.   AFisher@SLAC.Stanford.edu
SLAC, Accelerator Department, Mail Stop 18, P.O. Box 4349, Stanford,
CA, 94309, USA

Fitch, Michael J.   mjfitch@pas.rochester.edu
FNAL and Univ. of Rochester, Fermilab Beams Division, MS 306 Box
500, Batavia, IL, 60510-0500, USA

Fitze, Hans R   Hansruedi.Fitze@psi.ch
Paul Scherrer Institut, GFA, Villigen-PSI, CH-5232, Switzerland

Fitzgerald, Daniel H.   fitzg@lanl.gov
LANL, LANSCE-2, MS H838, Los Alamos National Laboratory, Los
Alamos, NM, 87545, USA

Flanagan, John W   john.flangan@com
KEK, 1-1 OHO, Tsukuba- Sh1, I-BARAKI -KEN, Japan

Flanz, Jacob B   Flanz@HADRON.MGH.Harvard.edu
Massachusetts General Hospital, Dept of Radiation Oncology, Northeast
Proton Therapy Center, 30 Fruit Street, Boston, MA, 02114, USA

Flechtner, Donald D   ddf1@cornell.edu
Cornell U., Lab. of Plasma Studies, 369 Upson Hall, Ithaca, NY, 14853

Flippo, Kirk A.   kflippo@umich.edu
Michigan S.U., 1835 Pointe Crossing #304, Ann Arbor, MI, 48105, USA

Floersch, Richard H   dfloersch@kcp.com
AlliedSignal FM&T, P.O. Box 4191159, Kansas City , Mo, 64141-6159

Foerster, Conrad L   FOERSTER@BNL.COM
BNL, NSLS, Bldg.725c, Upton, New York, 11973,

Fontana, Jorge R.   jorgef@rain.org
University of California, 4375 Via Glorieta, Santa Barbara, CA, 93110-2113

Foster, (Bill)   gwf@fnal.gov
FNAL, MS #323, Fermilab, PO Box 500, Batavia, IL, 60510, USA

Fox, John D.   jdfox@SLAC.Stanford.EDU
SLAC, ARD-A, SLAC, MS-26, P.O. Box 4349, Stanford, CA, 94309, USA

Franchetti, Giuliano   G.Franchetti@gsi.de
GSI, Hochstrombeschleuniger, Plankstrasse 1, Darmstadt, Germany, 64291,
Germany

Franks, Mark   franks1@llnl.gov
LLNL, Accelerator Technology Engineering Group, 7000 East Avenue, Mail
Stop L-287, Livermore, CA, 94551, USA

Friedrichs, Carl C   friedrichs@lanl.gov
LANL, LANSCE-5, MS H827, Los Alamos, NM, 87545, USA

Friedsam, Horst   horst@aps.anl.gov
ANL, ASD, 9700 S. Cass Avenue, Bldg. 401, Argonne, IL, 60439, USA

Friesel, Dennis L.   Friesel@IUCF.Indiana.EDU
Indiana University Cyclotron Facility, 2401 Milo B. Sampson Lane,
Bloominngron, In., 47408, USA

Fromowitz, Daniel B   dbf5@cornell.edu
Cornell U., Wilson Laboratory, Dryden Rd, Ithaca, NY, 14853-8001, USA

Fujieda, Miho   miho@insuty.tanashi.kek.jp
KEK, KEK-Tanashi, Midori-cyo 3-2-1, Tanashi, Tokyo, 188, Japan

Fukuda, Mitsuhiro   fukuda@taka.jaeri.go.jp
JAERI, Takasaki, Advanced Radiation Center, 1233 Watanuki, Takasaki,
Gunma, 370-1292, Japan

Fung, Ka-Man   kafung@indiana.edu
Indiana U., Indiana University Cyclotron Facility, 2401 Milo B. Sampson
Lane, Bloomington, IN, 47408, USA

Furman, Miguel A   mafurman@lbl.gov
LBNL, Lawrence Berkeley Natl. Lab., mail stop 71-259, 1 Cyclotron Rd.,
Berkeley, CA, 94720, USA

Furst, Mitchell L   furst@nist.gov
NIST, NIST, 100 Bureau Drive, Stop 8411, Gaithersburg, Maryland, 20899-
8411, USA

Fuss, Brian   ruland@slac.stanford.edu
SLAC, 2575 Sand Hill Rd., Bldg. 282, Menlo Park, CA, 94025, USA

Gai, Wei   wg@hep.anl.gov
ANL, ANL, High Energy Physics Division, 9700 S. Cass Ave.,, Argonne, IL,
60439, USA

Galambos, John D   jdg@ornl.gov
ORNL, ORNL, SNS Building, MS-8218, Oak Ridge, TN, 37831-8218, USA

Galayda, John N   asd-div@aps.anl.gov
ANL, Advanced Photon Source, Argonne National Lab Building 401, 9700
South Cass Avenue, Argonne , IL, 60439-4800, USA

Galimberti, Andrea   galimberti@elettra.trieste.it
Sincrotrone Trieste, Strada Statale 14 per Basovizza km 163.5, Trieste, TS,
34012, Italy

Gallardo, Juan C.   gallardo@bnl.gov
BNL, Bldg. 901-A, Physics Department, BNL, Upton, NY, 11973, USA

Gallo, Alessandro   Alessandro.Gallo@lnf.infn.it
INFN - Frascati, Accelerator Division, P.O. Box 13, Frascati (Rome), 00044,
Italy

Galstjan, Eugene A   galstjan@aha.ru
Moscow Radiotechnical Institute, Warshavskoe Shosse 132, Moscow,
113519, Russia

Gammino, Santo   gammino@lns.infn.it
INFN-LNS, INFIN via S. Sofia 44, Catania, 95123, Italy

Gao, Jie   gao@LAL.IN2p3.FR
Laboratoire de l,Accelerateur Lineaire, Laboratoire de LAccelerateur
Lineaire, B.P.Box 34, Orsay Cedex, Cedex, F-91898, France

Gardelle, Jacques M   pac99@bnl.gov
CEA/CESTA, BP2 , LeBarp, 33114, France

Gardner, Chris J   cgardner@bnl.gov
BNL, AGS Department, Building 911 B, P.O. Box 5000, Upton, New York,
11973-5000, USA

Garnett, Robert W   rgarnett@lanl.gov
LANL, LANSCE Division, Group LANSCE -1, MS H817, Los Alamos
National Laboratory, Los Alamos, NM, 87545, USA

Garren, Alper A   aagarren@lbl.gov
UCLA and LBNL, Center for Beam Physics, 259 Bldg. 71, LBNL, 1
Cyclotron Road, Berkeley, CA, 94720, USA

Gassner, David M   gassner@bnl.gov
BNL, AGS, Building 911B, Upton , NY, 11973, USA

Gaudreau, Marcel P.J.   marcel@divtecs.com
Diversified Technologies, Inc., Diversified Technologies, Inc., 33 Wiggins
Ave., Bedford, MA, 01730, USA

Gebre-Amlak, Kassatihun D   gebre@physics.cennas.nhmfl.gov
FAMU, FAMU, PO Box 6851, Tallahassee, FL, 32314-6851, USA

Geitz, Marc A   geitz@sun52a.desy.de
DESY, FDET, Notkestr. 85, Hamburg, 22603, Germany

Gelfand, Norman M   gelfand @fnal.gov
FNAL, Beam Physics, MS 220, P. O Box 500, Kirk and Pine St., Batavia,
Il, 60510, USA

Geng, Rongli   rg58@cornell.edu
Cornell U., Institute of Heavy Ion Physcics, Peking University, Beijing,
100871, China, Peoples Republic of

Gentzlinger, Robert C.   gentzlinger@lanl.gov
LANL, Los Alamos National Lab, P.O. Box 1663, M/S H821, Los Alamos,
NM, 87545, USA

Ghigo, Andrea   GHIGO@LNF.INFN.IT
INFN - Frascati, Accelerator.Division, C.P.13, Frascati (Rome) , 00044,
Italy

Ghosh, Anindita   ghosh@jlab.org
Thomas Jefferson National Accelerator Facility, Accelerator Operations,
12000 Jefferson Ave, Newport News, VA, 23606, USA

Gilad, Pinchas   pinglad@netvision.net.ie
RAFI, 6 Kipnis Street, Rehovot, 76305, Israel

Gilchrist, Donna A   gilchris@jlab.org
TJNAF, Free Electron Laser Dept., Accelerator Division, 12000 Jefferson
Avenue, Mail Stop 6A, Newport News, VA, 23606, USA

Gillespie, George H.   ghga@ghga.com
G. H. Gillespie Associates, Inc., 10855 Sorrento Valley Rd., Suite 201, San
Diego, CA, 92121, USA

Gilpatrick, John D   gilpatrick@lanl.gov
LANL, LANSCE-1, M.S. H808, LANL, Los Alamos, NM, 87545,

Gioia, Jack G.   gioiaj@gat.com
General Atomics, LANL, TA-53, MS H836, Los Alamos, NM, 87544

Giovannozzi, Massimo   Massimo.Giovannozzi@cern.ch
CERN, PS Division, GENEVA, 1211, Switzerland

Glenn, Joseph W   glenn@bnldag.bnl.gov
BNL, AGS, 911B, Upton, NY, 11973, USA

Gluckstern, Robert L.   rlg@physics.umd.edu
U. of Maryland, Physics, Department of Physics, University of Maryland,
College Park, MD, 20742, USA

Gluskin, Efim   gluskin@aps.anl.gov
ANL, Advanced Photon Source, Bldg.401, 9700 S.Cass Ave., Argonne, IL,
60439, USA

Godlove, Terry F   tgodlove@cpcug.org
FM Technologies, 9713 Manteo Court, Ft Washington, MD, 20744, USA

Gofman, Yury I.   hoffmany@avoda.jct.ac.il
51/3 Shahal st., Jerusalem, 93721, Israel

Gold, Steven H.   gold1@ppdu.nrl.navy.mil
NRL, Naval Research Lab; Code 6793, 4555 Overlook Ave. SW,
Washington, D.C., 20375-5346, USA

Goldstein, William H   goldstein3@poptop.llnl.gov
LLNL, Physics & Space Technology Directorate, P.O. Box 808, L-051,
Livermore, California, 94550, USA

Golkowski, Czeslaw   cg18@cornell.edu
Cornell U., Lab. Plasma Studies, 369 Upson Hall, Ithaca, NY, 14853, USA

Goodzeit, Carl   clg@onramp.net
M J B Plus, Inc., 119 Executive Way, Suite 304, DeSoto, TX, 75115, USA

Gordon, Daniel F.   gordond@ucla.edu
UCLA, 11155 Montana, Los Angeles, CA, 90049, USA

Gorev, Vladimur V   gorev@polyn.kiae.su
Institute of Physical Ballistics, 1,Kurchatov sq., Moscow, 123182, Russia

Gorski, Anthony J   gorski@aps.anl.gov
ANL, ASD, 9700 S. Cass Avenue, Bldg. 401, Argonne, IL, 60439, USA

Gourlay, Steve A.   sagourlay@lbl.gov
LBNL, Superconducting Magnet Program/AFRD, 1 Cyclotron Rd., MS 46-
161, Berkeley, CA, 94720, USA

Grafstrom, Per G.P   Madeleine.Catin@cern.ch
CERN, Div. SL-EA, CERN (Prevessin), Geneva 23, 1211, Switzerland

Grames, Joe M   grames@jlab.org
University of Illinois / TJNAF, Thomas Jefferson National Accelerator
Facility, MS-12H, 12000 Jefferson Avenue, Newport News, VA, 23606

Granatstein, Victor L   vlg@eng.umd.edu
U. of Maryland, Dept. Electrical Engineering, University of Maryland,
College Park, MD, 20742, USA

Grand, Pierre   pgrand@IBM.net
Tech Source, Inc., P.O.Box 31057, 301 N. Guadalupe St., Ste 204, Santa Fe,
NM, 87594, USA

Graves, William S   wsgraves@bnl.gov
BNL, NSLS, Building 725D, Upton, NY, 11973, USA

Grechko, Vladimir V.   grechko@al20.inr.troitsk.ru
Russian Academy of Siences, Institute for Nuclear Research, Moscow Meson
Factory Linac, Moscow, 60th October Anniversary Prospect, 7a, 117312,
Russia

Green, Mike A.   magreen@lbl.gov
LBNL, Superconducting Magnet Program/AFRD, 1 Cyclotron Rd. MS 46-
161, Berkeley, CA, 94720, USA

Greninger, Paul   grenin@gat.com
General Atomics, 135 B Central Park Sq., Los Alamos, NM, 87544, USA

Griffiths, Stephen A   s.a.griffiths@dl.ac.uk
Daresbury Laboratory, Daresbury, Warrington, Cheshire, WA44AD, Ukraine

Grimm, Terry L.   GRIMM@NSCL.MSU.EDU
NSCL, National Superconducting Cyclotron Laboratory, Michigan State
University, E. Lansing, MI, 48824, USA

Grishin, Vladislav Konstantinovich   grishin@depni.npi.msu.su
Institute of Nuclear Physics of Moscow Lomonosov St. University, Moscow
Lomonosov St. University, Institrute of Nuclear Physics, Vorobievy Gory,
Moscow, 119899, Russia

Grote, David P   grote1@llnl.gov
LLNL, X-Div/HIF project, L-645, P.O.Box 808, Livermore, CA, 94550, USA

Grunder, Hermann A.   grunder@jlab.org
TJNAF, Director's Office, 12000 Jefferson Avenue, Newport News, Virginia,
23606, USA

Gu, Shaoting   shgu@eecs.umich.edu
U. of Maryland, 1006 I.S.I.Building , 2200 Bonisted Blvd, Ann Arbor, MI,
48109, USA

Gueye, Paul L   gueye@jlab.org
Hampton U/TJNAF, Jefferson Lab, TC16B/Physics Division , 12000
Jefferson Ave., Newport News, VA, 23606, USA

Guharay, Samar K   guharay@plasma.umd.edu
U. of Maryland, Institute for Plasma Research, Institute for Plasma Research,
University of Maryland, College Park, MD, 20742, USA

Guidee, Philippe J.   philippe.guidee@tte.thomson-csf.com
THOMSON Tubes Electroniques, 18 , avenue du Maréchal Juin, Meudon la
Foret Cedex , 92366, France

Guidi, Vincenzo   guidi@fe.infn.it
University of Ferrara, Dipartimento di Fisica , Dipartimento di Fisica, Via
Paradiso 12, Ferrara, I-44100, Italy

Guiducci, Susanna   guiducci@lnf.infn.it
INFN - Frascati, LNF-INFN, P.O.Box 13, Frascati, 00044, Italy

Guignard, Gilbert F   Gilbert.Guignard@cern.ch
CERN, SL Division, 1211 GENEVA 23, Geneva, 1211, Switzerland

Guo, Zhiyuan   guozy@bepc3.ihep.ac.cn
Institute of High Energy Physics, P. O. Box 918-9, Beijing, 100039, China,
Peoples Republic of

Gupta, Ramesh C   rgupta@lbl.gov
LBNL, Superconducting Magnet Group, MS 46-161, Lawrence Berkeley
Lab, 1 Cyclotron Road, Berkeley, CA, 94720, USA

Gurd, Dave   gurd@lanl.gov
LANL, LANSCE-8, MS H820, LANL, Los Alamos, NM, 87544

Hafizi, Bahman   hafizi@ppdu.nrl.navy.mil
NRL, Code 6790, 4555 Overlook Av. SW, Washington, DC, 20375, USA

Hahn, Harald   hahnh@bnl.gov
BNL, Brookhaven National Laboratory, RHIC - Bldg. 1005S, P.O. Box 5000,
Upton, NY, 11973-5000, USA

Hahn, Alan A   ahahn@fnal.gov
FNAL, Fermilab, MS221, P.O.Box 500, Batavia, Il, 60510, USA

Haimson, Jacob -   haimson@aol.com
Haimson Research Corporation, 3350 Scott Blvd Bldg 60, Santa Clara, CA,
95054-3104, USA

Hamm, Robert   rhamm@linacs.com
Acc Sys Technology Inc, 1177A Quarry Lane, Pleasanton, CA, 94566, USA

Hammen, Addo   a.f.j.hammen@tue.nl
Eindhoven University of Technology, Cyclotron Laboratory, P.O.Box 513,
Den Dolech 2, Eindhoven, 5600 MB, Netherlands

Hancock, Steven B   Steven.Hancock@cern.ch
CERN, PS Division, Geneva, 1211, Switzerland

Hanke, Klaus   klaus.hanke@cern.ch
CERN, SL division, Geneva 23, 1211, Switzerland

Hanna, Samy M.   shanna@smsocs.com
Siemens, Oncology Care Systems, 4040 Nelson Avenue, Concord, CA, 94520, USA

Hardekopf, Robert A   hardekopf@lanl.gov
LANL, SNS Project Office, MS H-824, Los Alamos National Laboratory, Los Alamos, NM, 87545, USA

Harding, David J.   harding@fnal.gov
FNAL, Development and Test, MS343, P.O. Box 500, Batavia, IL, 60510, USA

Hardy, Laurent   hardy@esrf.fr
European Synchrotron Radiation Facility, Machine Division-Operation Group, BP220 Avenue des Martyrs, Grenoble, 38043, France

Harkay, Katherine C   harkay@aps.anl.gov
ANL, Argonne National Laboratory, ANL - ASD/401, 9700 S. Cass Ave., Argonne, IL, 60439, USA

Harkins, Joseph P   jpharkins@lbl.gov
LBNL, Lawrence Berkeley National Laboratory, #1 Cyclotron Rd., Mail Stop 80-101, Berkeley, California, 94720, USA

Harriott, Lloyd R   lrh@lucent,com
Bell Labs, 600 Mountain Ave, Murray Hill, NJ, USA

Harrison, Michael A.   harrison@bnl.gov
BNL, RHIC Project, P.O. Box 5000, Bldg. 1005S, Upton, NY, 11973-5000, USA

Hartemann, Fred V   hartemann1@.llnl.gov
LLNL, Institute for Laser Science & Applications, LLNL, PO Box 808, L-411, Livermore, CA, 94550, USA

Hartman, Neal D   NHartman@lbl.gov
LBNL, LBNL, MS 46-161, 1 Cyclotron Road, Berkeley, CA, 94720, USA

Hartmann, Peter   hartmann@jlab.org
TJNAF, Accelerator Division, 12000 Jefferson Ave., Newport News, VA, 23606, USA

Hartmann, Heather   hartman1@bnl.gov
BNL, AGS, Building 911C, 35 Lawrence Drive, Upton, NY, 11973, USA

Hartung, Walter H.   Hartung@FNAL.Gov
FNAL, Beams Division, Fermilab, Mail Station 306, P.O. Box 500 , Batavia, Illinois, 60510, USA

Hartunni, Edward P.   hartunnil@llnl.gov
LLNL, P.O. Box 808, L-050, Livermore, CA, 94550, USA

Harwood, Leigh H.   harwood@jlab.org
TJNAF, Accelerator Division, 12000 Jefferson Avenue, MS: 7A, Newport News, Virginia, 23606, USA

He, Duohui   HDH@ustc.edu.cn
Univ Sci. and Tech. of China, University of Science and Technology of China, National Synchrotron Radiation Lab., P. O. Box 6022, Hefei, Anhui 230029, Hefei, Anhui, 230029, China, Peoples Republic of

He, Ping   phe@sun2.bnl.gov
UCLA, Physics Department, B.820/ATF, BNL, Upton, NY, 11973, USA

Heese, Richard   heese@bnl.gov
BNL, National Synchrotron Light Source, P.O. Box 5000, Building 725C, Upton, NY, 11973-5000, USA

Hemker, Roy G   hemker@physics.ucla.edu
UCLA, Department Of Physics and Astronomy UCLA, Los Angeles, Ca, 90095, USA

Henderson, Stuart D   sdh9@lns62.lns.cornell.edu
Cornell U., Laboratory of Nuclear Studies, Wilson Laboratory, Cornell University, Ithaca, NY, 14853, USA

Henderson, Thomas F   TFHenderson@lbl.gov
LBNL, #1 Cyclotron Road, Mail Stop 161, Berkeley, California, 94720

Hendrickson, Linda J.   ljh@slac.stanford.edu
SLAC, SLAC Controls Dept, 2575 Sand Hill Road, MS 46, Menlo Park, California, 94025, USA

Henke, Heino   henke@tu-berlin.de
Technische U. Berlin, Technische Universitaet,Einateniufer 17,EN-2, Berlin, 10587, Germany

Heron, Mark T   m.t.heron@DL.AC.UK
Daresbury Laboratory, Daresbury Laboratory, Daresbury, Warrington, Cheshire, WA44AD, Ukraine

Herrmannsfeldt, William B   wbhap@slac.stanford.edu
SLAC, SLAC, MS-26, P.O. Box 4349, Stanford, CA, 94309, USA

Hershcovitch, Ady   hershcovitch@bnldag.bnl.gov
BNL, AGS, Building 911B, Upton, New York, 11766, USA

Herwig, Ingo   ingo@sunkist.physik.uni-frankfurt.de
Institut fur Angewandte Physik, Johann Wolfgang Goethe-Universitaet, Robert-Mayer-Strasse 2-4, Frankfurt am Main, D-60325, Germany

Hess, Mark H   mhess@psfc.mit.edu
Plasma Science and Fusion Center, Physics Department, PSFC/NW16-168, 167 Albany Street, Cambridge, Massachusetts, 02139-4294, USA

Hesselson, Stuart L.   shesselson@eevinc.com
EEV, 4 Westchester Plaza, Elmsford, NY, 10523, USA

Hill, Barrey W.   bhill@ghga.com
G. H. Gillespie Associates, Inc., 10855 Sorrento Valley Rd., Suite 201, San Diego, CA, 92121, USA

Hilleret, Noel   noel.hilleret@cern.ch
CERN, LHC DIVISION, , GENEVA 23, 1211, Switzerland

Hillman, Al   hillmana@aps.anl.gov
ANL, APS Division, 9700 S. Cass Ave., Bldg. 401, Argonne, IL, 60439

Hirata, Kohji   hirata@post.kek.jp
KEK, Accelerator Theory Group, KEK, 1-1 OHO , Tsukuba Ibaraki, Japan

Ho, Darwin D   ho1@llnl.gov
LLNL, Los Alamos National Laboratory, 7000 East Avenue, P.O. Box 808, L031, Livermore, California, 94551, USA

Ho, Ching-Hung   CHH@SRRC.GOV.TW
SRRC, Light Source Division, No.1 R&D Road VI, Hsinchu Science-Based Industrial Park, Hsinchu, 30077, Taiwan

Hock, Jon c   hock@bnl.gov
BNL, AGS, 911a, Upton, NY, 11973, USA

Hockman, Jeff   hockman1@llnl.gov
LLNL, Lawrence Livermore National Laboratory, Accelerator Technologies Engineering Group, P.O. Bosx 808, L-287, Livermore, CA, 94550, USA

Hoeft, Roger   rhoeft@bnl.gov
BNL, Bldng 725D, Brookhaven National Lab., Upton, NY, 11973, USA

Hoeltermann, Holger   hoeltermann@rz.uni-frankfurt.de
Universitaet Frankfurt/Main, Institut fuer Angewandte Physik, Robert-Mayer Str. 2-4, Frankfurt, 60054, Germany

Hoffman, Bruce C.   bhoffman@tctus.com
Thomson Components and Tubes Corp., 40G Commerce Way, Totowa, NJ, 07511; USA

Hoffstaetter, Georg H   hoff@mail.desy.de
DESY, MPY, Notkestrasse 85, Hamburg, 22603, Germany

Hofle, Wolfgang   Wolfgang.Hofle@cern.ch
CERN, SL-RF, CERN, Geneva 23, Switzerland, 1202, Switzerland

Hogan, Mark J   hogan@slac.stanford.edu
SLAC, SLAC - M/S 07, Stanford University, P.O. Box 4349, Stanford, CA, 94309, USA

Hogan, Gary E   hogan_gary@lanl.gov
LANL, P-25, MS H846, Los Alamos National Laboratory, Los Alamos, NM, 87545, USA

Holmes, Stephen D   holmes@fnal.gov
FNAL, Fermilab M.S. 306, P.O. Box 500, Batavia, IL, 60510, USA

Holmes, Jeffrey A   jzh@ornl.gov
ORNL, Oak Ridge National Laboratory, SNS Building, MS 8218, Oak Ridge, TN, 37831-8218, USA

Holtzapple, Robert L   rlh@cesr10.lns.cornell.edu
Cornell U., Wilson Laboratory, Ithaca, New York, 14853-8001, USA

Homscheidt, Michael   homscheidt@anka.fzk.de
Forschungszentrum Karlsruhe, PEA, P.O. Box 3640, Karlsruhe, 76021, Germany

Hori, Toshitada   Tst_Hori@shi.co.jp
Sumitomo Heavy Ind., Ltd., Research and Development Center, 1-1 Yato-machi 2-chome, Tanashi, Tokyo, 188-8585, Japan

Hosokai, Tomonao   thosokai@hikari.tokai.jaeri.go.jp
JAERI, Advanced Photon Research Center, Tokai-mura,, Naka-gun, Ibaraki-ken, 319-1195, Japan

Houck, Timothy L.   houck1@llnl.gov
LLNL, Lawrence Livermore National Laboratory, 7000 East Ave., P.O. Box 808, Livermore, Ca., 94551-0808, USA

Hoyer, Egon H   EHHoyer@lbl.gov
LBNL, Engineering, 1 Cyclotron Road, MS 46 - 161, Berkeley, California, 94720, USA

Hseuh, Hsiao-Chaun   hseuh@bnl.gov
BNL, RHIC Project, Building 817, Brookhaven National Laboratory, Upton, New York, 11973, USA

Hsi, Wen-chien   wchsi@iucf.indiana.edu
Indiana U., Indiana University Cyclotron Facility, 2401 Milo B. Sampson Lane, Bloomington, Indiana, 47408, USA

Hsu, Ian C   ichsu@faculty.nthu.edu.tw
National Tsing Hua Univ. & SRRC, Taiwan, Dept. of Nuclear Science, National Tsing Hua University, Hsinchu, 30013, Taiwan

Huang, Haixin   HUANG@BNLDAG.BNL.GOV
BNL, AGS DEPARTMENT, BUILDING 911-B, UPTON, NEW YORK, 11973-5000, USA

Huang, Zhirong   zrh@aps.anl.gov
ANL, Argonne National Laboratory, 9700 S. Cass Ave., Bldg. 401-B2202, Argonne, IL, 60439, USA

Hubbard, Edward L Ed_Hubbard@compuserve.com
General Atomics, Electromagnetic Systems, PO Box 85608, San Diego, CA92816, 5527 Chelsea Ave., La Jolla, California, 92037, USA

Hubbard, Richard E. hubb@ppdu.nrl.navy.mil
NRL, Code 6791, Naval Research Lab., Washington, DC, 20375-5346

Huelsmann, Peter peha@sunkist.physik.uni-frankfurt.de
Institut fur Angewandte Physik, Johann Wolfgang Goethe-Universitaet, Robert-Mayer-Strasse 2-4, Frankfurt am Main, D-60325, Germany

Hughes, Thomas P tph@mrcabq.com
Mission Research Corp., 1720 Randolph, S.E., Albuquerque, New Mexico, 87106, USA

Humphries, Stanley humphrie@unm.edu
U. of New Mexico, Dept. Elec. and Computer Engr., University of New Mexico, Albuquerque, New Mexico, 87131, USA

Hurh, Patrick G hurh@fnal.gov
FNAL, Beams - Mechanical Support Department, P.O. Box 500 , MS 340, Batavia, IL, 60510, USA

Huttel, Erhard huttel@anka.fzk.de
Forschungszentrum Karlsruhe, ANKA (PEA), Postfach 3640, Karlsruhe, D-76021, Germany

Hutton, Andrew M. andrew@jlab.org
TJNAF, Accelerator Division, 12000 Jefferson Avenue, MS12A2, Newport News, Virginia, 23606, USA

Ingrassia, Peter F ingrassia@bnl.gov
BNL, AGS Department, Building 911A, P.O. Box 5000, Upton, NY, 11073-5000, USA

Irwin, John irwin@slac.stanford.edu
SLAC, Accelerator Research Department - A, 2575 Sand Hill Road, Menlo Park, CA, 94025, USA

Isgur, Nathan Isgur@jlab.org
Jefferson Lab, 12000 Jefferson Ave. MS12H2, Newport News, Va., 23606

Issinsky, Igor B. Issinsky@sunhe.jinr.ru
Joint Institute for Nuclear Research, Laboratory of High Energies, Joliot Curie str. 6, Dubna, Mascow Region, 141980, Russia

Ivanov, Ivan Tsakov itsak@inrne.bas.bg
NRNE, Inst. for Nuclear Research and Nuclear Energy of Bulgarian Academy of Sciences, Particle Physics, 72 Tsarigrad Rd., Sofia, 1784, Bulgaria

Ivers, Jim jdi2@cornell.edu
Cornell U., Lab. Plasma Studies, 369 Upson Hall, Ithaca, NY, 14853, USA

Iwashita, Yoshihisa iwashita@kyticr.kuicr.kyoto-u.ac.jp
Kyoto U., Accelerator Lab., NSRF, Inst. for Cem. Res., Gokanosho, Uji, Kyoto, 611-0011, Japan

Jaber, Zakaria jaber@in2p3.fr
corpuscular physical laboratory (LPC), Clermon-Ferrand, IN2P3/CNRS - University Blaise Pascal7, 24, Av des Landais, Aubiere, Cedex France, 63177

Jackson, Alan ajackson@lbl.gov
Lawrence Berkeley National Laboratory, Accelerator and Fusion Research Division, One Cyclotron Road, MS 50-4049, Berkeley, California, 94720

Jacob, Jorn jacob@esrf.Fr
ESRF, Avenue des Martyrs BP 220, Grenoble, 38043, France

Jain, Animesh K jain@bnl.gov
BNL, Building 902A, Upton, NY, 11973, USA

Jansson, Andreas K R Andreas.Jansson@cern.ch
CERN, PS Division, Geneva, 1211, Switzerland

Jenner, David L djenner@indiana.edu
Indiana U., 2401 Milo Sampson, Bloomington, Indiana, 47408, USA

Jensen, Peter Jensenp@mail.desy.de
DESY, MKK, Notkestrasse 85, D 22603 Hamburg, Germany, Germany

Jensen, Chris C ccjensen@fnal.gov
FNAL, Beams Division EE Department, P.O. Box 500, MS 308, Batavia, IL, 60510, USA

Jensen, Erk Erk.Jensen@cern.ch
CERN, PS/RF, CERN, Mailstop G00710, CH - 1211 Geneva 23, 1211, Switzerland

Jeon, Dong-o jeond@ornl.gov
ORNL, SNS Bldg MS-8218, 104 Union Valley Rd, Oak Ridge, TN, 37831-8218, USA

Jett, Nelson D djett@kcp.com
AlliedSignal FM&T, D/173, 1A32, P. O. Box 419159, 2000 E. Bannister Road, Kansas City, Mo., 64131, USA

Jex, Graham Graham.Jex@eev.com
EEV, Power Tube Sales, 106 Waterhouse Lane, Chelmsford, Essex, CM1 2QU, United Kingdom

Jiang, Daoman kjfan@ustc.edu.cn
National Synchrotron Radiation Lab, USTC, P.O.Box 6022, Hefei, Anhui, 230029, PR China

Jin, Yuming jin@nsrl.ustc.edu.cn
University of Science and Technology of China (USTC), National Synchrotron Radiation Laboratory (NSRL), P.O.Box 6022, Hefei, Anhui, 230029, China, Peoples Republic of

Johnson, Neil neil@skatter.usask.ca
Saskatchewan Accelerator Laboratory, Saskatchewan Accelerator Laboratory, 107 North Road, Saskatoon, Saskatchewan, S7N 5C6, Canada

Johnson, Brant brant@aps.org
American Physical Society/PRSTAB, 1 Research Road, Ridge, NY, 11961

Johnson, David E dej@fnal.gov
FNAL, Beams Division/Main Injector Dept., P.O.Box 500 MS 323, Batavia, Il, 60510, USA

Johnstone, Carol J cjj@fnal.gov
FNAL, Fermilab, M.S. 220, P.O. Box 500, Batavia, IL, 60510, USA

Jones, Frederick W fwj@triumf.ca
TRIUMF, 4004 Wesbrook Mall, Vancouver, B.C., V6T 2A3, Canada

Jones, Ted G. ted.jones@nrl.navy.mil
Naval Research Laboratory, Naval Research Laboratory, Code 6795, Washington, DC, 20375, USA

Jones, William P jones@iucf.indiana.edu
Indiana U., Indiana University Cyclotron Facility, 2401 Milo B. Sampson Lane, Bloomington, IN, 47408, USA

Jones, Justin jones@aps.anl.gov
ANL, ASD, 9700 S. Cass Avenue, Bldg. 401, Argonne, IL, 60439, USA

Jordan, Kevin jordan@jlab.org
TJNAF, Accelerator Division, 12000 Jefferson Avenue, Mail Stop 6A, Newport News, Virginia, 23606, USA

Joshi, Chan joshi@ee.ucla.edu
UCLA, Department of Electrical Engineering, Dept. Electrical Eng., 405 Hilgard Ave., Engr. IV Bldg., Los Angeles, CA, 90095-1594, USA

Joshi, Chad H chad@energen.net
Energen, Inc., 17 D Sterling Road, Billerica, Ma, 01862, USA

Jowett, John M John.Jowett@cern.ch
CERN, SL Division, CERN, 1211 Geneva , 23, Switzerland

Kabel, Andreas C andreas.kabel@desy.de
DESY, MPY, Notkestrasse 85, Hamburg, 22607, Germany

Kahn, Stephen A kahn1@bnl.gov
BNL, AGS Department, Building 902A, Brookhaven National Laboratory, Upton, NY, 11973, USA

Kaiser, Karl H. kaiser@kph.uni-mainz.de
Instit. fur Kernphysik/Universitat Mainz, Germany, Becher-Weg 45, Mainz, 55099, Germany

Kajiyama, Yoichi y_kajiyama@lbl.gov
LBNL, Engineering Dept., B88-229 #1 Cyclotron Road,, Building 88 Cyclotron, #1 Cyclotron Road, Berkeley,, CA, 94720, USA

Kako, Eiji kako@mail.kek.jp
KEK, Accelerator Laboratory, 1-1, Oho, Tsukuba, Ibaraki, 305-0081, Japan

Kaltchev, Dobrin kaltchev@triumf.ca
TRIUMF, 4004 Wesbrook Mall , Vancouver, BC, V6T 2A3, Canada

Kamitsubo, Hiromichi kamitsub@sp8sun.spring8.or.jp
SPring-8, Japan Synchrotron Radiation Research Institute, 323-3 Mihara, Mikazuki-cho, Sayo-gun, Hyogo, 670-5198, Japan

Kamps, Thorsten tkamps@ifh.de
DESY, Zeuthen, Platanenallee 6, Zeuthen, D-15738, Germany

Kanai, Yasumori kanai@mail.kek.jp
Tohoku U., physics, aobaku aramaki aza aoba tokuhoku daigaku, cyclotron and RI center, sendai, miyagi, 980-8578, Japan

Kanaya, Noriichi noriichi.kanaya@kek.jp
KEK, Photon Factory, High Energy Accelerator Research Organization, 1-1, Oho,, Tsukuba, 305-0801, Japan

Kanazawa, Mitsutaka kanazawa@nirs.go.jp
NIRS, Division of Accelerator Physics and Engineering, 9-1, Anagawa 4-chome, Inageku, Chiba, 263-8555, Japan

Kando, Masaki kando@hikari.tokai.jaeri.go.jp
JAERI, Advanced Photon Research Center, 2-4 Shirakata-shirane, Tokai-mura, Naka-gun, Ibaraki, 319-1106, Japan

Kang, Yoon W ywkang@aps.anl.gov
ANL, Advanced Photon Source, 9700 S. Cass Ave., Building 401, Argonne, IL, 60439, USA

Karn, Jeff S karn@jlab.org
TJNAF, Mechanical Engineering Group, 12000 Jefferson Ave., MS 16A, Newport News, VA, 23606, USA

Kashikhin, Vladimir   kash@fnal.gov
FNAL, Technical Division / Engineering and Fabrication, P.O. Box 500,
M.S. 316, Batavia, IL, 60510, USA

Kashiwagi, Shigeru M   kasiwagi@kekvax.kek.jp
KEK, Department of Accelerator Science, School of Mathematical and
Physical Science , 1-1 Oho , Tsukuba, Ibaraki, 305-0801, Japan

Kato, Sydhei   pac99@bnl.gov
Maison Okamoto 1402, Motoyamakimachi 4-7-59, Higashinada, Kobe,
Japan

Katonak, David J   katonak@lanl.gov
LANL, ESA-DE, PO Box 1663 MS H821, Los Alamos National Lab, Los
Alamos, NM, 87544, USA

Katsouleas, Tom   katsoule@usc.edu
University of Southern California, EE-Ep Dept., Los Angeles, CA, 90089-
0484, USA

Kaye, Robert A   kaye@anlphy.phy.anl.gov
ANL, Physics Division, 9700 S. Cass Ave., Argonne, IL, 60439, USA

Kazakov, Sergey Yurievich   kazakov@vlepp.serpukhov.su
BINP, BINP, Protvino, Moscow region, 142284, Russia

Keane, John   keane@bnl.gov
BNL, National Synchrotron Light Source, Brookhaven National
Laboratory, Bldg. 725B, Upton, NY, 11973, USA

Keesee, Marie S   keesee@jlab.org
TJNAF, Accelerator Division, 12000 Jefferson Ave., MS 85A, Newport
News, Virginia, 23693, USA

Kehne, David M   dkehne@gmu.edu
FM Technologies, Inc., 1702 Broadfield Lane, Vienna, Virginia, 22182

Keil, Eberhard   Eberhard.Keil@cern.ch
CERN, SL Division, CERN, Geneva 23, 1211, Switzerland

Keller, Roderich   r_keller@lbl.gov
LBNL, AFRD, MS 71-259, 1 Cyclotron Road, Berkeley, CA, 94720, USA

Kempkes, Michael A.   kempkes@divtecs.com
Diversified Technologies, Inc., Diversified Technologies, Inc., 33 Wiggins
Ave., Bedford, MA, 01730, USA

Kerner, Thomas M   kerner@bnl.gov
BNL, RHIC/AGS/CAD, Bldg 911C, Upton, NY, 11973, USA

Kerr, John W.   john.kerr@eev.inc.com
EEV, Waterhouse Lane, Chelmsford, Essex, Ch12QU, United Kingdom

Kessel, Eric D.   ekessel@owlcontrol.com
Owl Control Systems, LLP, 165M New Boston St.; Suite 244, Woburn,
MA, 01801, USA

Kesselman, Martin   kesselman@bnl.gov
BNL, AGS, Bldg 911B, Upton, NY, 11973, USA

Kewisch, Jorg   jorg@bnl.gov
BNL, RHIC Project, P.O. Box 5000, Bldg. 1005S, Upton, NY, 11973-
5000, USA

Kezerashvili, Guramy   guramkez@inp.nsk.su
BINP, Lavrentev 11, Novosibirsk, 630090, Russia

Khachatryan, Arsen   khachatr@moon.yerphi.am
Yerevan Physics Institute, Dept. of Theoretical Physics, Yerevan Physics
Institute, Alikhanian Brothers St. 2, Yerevan, 375036, Armenia, Yerevan,
375036, Armenia

Khan, Shaukat   khan@bii.bessy.de
BESSY, BESSY, Rudower Chaussee 5, Geb. 14.51, Berlin, 12489,
Germany

Khan, Sameen a   khan@pd.infn.it
INFN - Padova, Dipartimento di Fisica Galileo Galilei, Via Marzolo 8,
Padova, , 35131, Italy

Kim, Kwang-Je   kwangje@aps.anl.gov
ANL, ASD 401/C4265, 9700 S. Cass Avenue, Argonne, IL, 60439, USA

Kim, Jin-Soo   kimjs@far-tech.com
FARTECH, Inc., 3146 Bunche Avenue, San Diego, CA, 92122-2247, USA

Kim, Eun-San   eskim@beams.lbl.gov
University of California, Berkeley, 1 cyclotron road, MS 71-259, LBNL,
Berkeley, CA, 94720,

Kim, Young-hwan   hessee@paragon.snu.ac.kr
Seoul National University, Department of Nuclear Engineering, San 56-1,
Shinlim, Kwanak, Seoul, 151-742, Korea

Kim, Jong-Won   jwkim@rikaxp.riken.go.jp
Cyclotron Lab., RIKEN, Cyclotron Lab., RIKEN, Hirosawa 2-1, Wako-shi,
Saitama, 351-0198, Japan

Kimura, Wayne D.   wkimura@stioptronics.com
STI Optronics, Inc., 2755 Northup Way, Bellevue, WA, 98004-1495, USA

King, Bruce J   bking@bnl.gov
BNL, Center for Accelerator Physics, Brookhaven National Laboratory, PO
Box 5000, Upton, NY, 11973-5000, USA

King, Quentin A.   Quentin.King@CERN.CH
CERN, SL Division, CERN, 1211 , GENEVA 23, Switzerland

Kirbie, Hugh C.   kirbie1@llnl.gov
Lawrence Livermore National Laboratory, 7000 East Ave. L-645, P.O.Box
808, Livermore, Ca, 94551-0808, USA

Kirk, Harold G   hkirk@bnl.gov
BNL, Dept. of Physics, 901A, Upton, New York, 11973-5000, USA

Kishek, Rami A.   ramiak@ebte.umd.edu
IPR/University of Maryland, IPR, Energy Research Bldg. (#223), University
of Maryland, College Park, MD, 20742, USA

Kishiyama, Keith   kishiyama1@llnl.gov
Lawrence Livermore National Laboratory, Accelerator Technologies
Engineering Group, P.O. Bosx 808, L-287, Livermore, CA, 94550, USA

Klaisner, Lowell A.   klaisner@slac.stanford.edu
SLAC, Technical Division, P.O. Box 4349, M/S 24, Stanford, California,
94309, USA

Kleeven, Willem   Kleeven@iba.be
Ion Beam Applications, 3 Chemin lu Cyclotron, 1348 Louvain La Beuve,
Belguim

Klein, Hans-Udo M   klein@accel.de
ACCEL Instruments GmbH, Friedrich-Ebert-Str.1, Bergisch Gladbach, D-
51429, Germany

Knapp, Edward A   eak@santafe.edu
World Physics Technologies, 19 Bishops trail, Santa Fe, NM, 87501, USA

Ko, Kwok   kwok@SLAC.Stanford.EDU
SLAC, 2575 Sand Hill Road , Mail Stop 26, Menlo Park, CA, 94309, USA

Koeth, Timothy w   koeth@physics.rutgers.edu
FNAL, Rutgers University - Dept. of Physics, Busch Campus, Frelynghuysen
Road, Piscataway, New Jersey, 08855, USA

Konrad, Gerhard T.   gkonrad@smsocs.com
Siemens, 787 Kirkcrest Road, Danville, CA, 94526, USA

Koontz, Roland   rfkap@slac.stanford.edu
SLAC, Klystron Department, Bin # 33, Stanford Linear Accelerator Center,
Stanford, CA, 94309, USA

Korenev, Sergey   A.Sergey@korenev.com or Sergey_Korenev@steris.com
STERIS Isomedix Services, 11 Apollo Drive, Whippany, NJ, 07981, USA

Koscielniak, Shane R   shane@triumf.ca
TRIUMF, 4004 Wesbrook Mall, Vancouver, B.C., V6T 2A3, Canada

Kourbanis, Ioanis   IOANIS@FNAL.GOV
FNAL, Beams Division, MI department, MS 341, P.O Box 500, Batavia, IL.,
60510, USA

Koutchouk, Jean-Pierre S.   Jean-Pierre.Koutchouk@cern.ch
CERN, SL Division, CH-1211 GENEVA 23, Switzerland

Kovach, Paul E   kovach@bnl.gov
BNL, Building 902A, Upton, NY, 11973, USA

Kozawa, Takahiro   kozawa@sanken.osaka-u.ac.jp
Osaka University, The Institute of Scientific and Industrial Research , 8-1
Mihogaoka, Ibaraki, Osaka, 567-0047, Japan

Kponou, Ahovi E   akponou@sun2.bnl.gov
BNL, AGS Dept, Bldg 930, Upton, NY, 11973-5000, USA

Krafft, Geoffrey A.   krafft@jlab.org
TJNAF, Accelerator Division, 12000 Jefferson Avenue, Mail Stop 6A,
Newport News, Virginia, 23606, USA

Kramer, Stephen L   kramer@bnlls1.bnl.gov
BNL, NSLS, Bldg. 725C, Upton, NY, 11973, USA

Kravchuk, Leonid V.   kravchuk@al20.inr.troitsk.ru
INR MOSCOW, Vice-Director, 60-th October Anniversary pr.,7a , Moscow,
Russia, 117312, Russia

Kreischer, Kenneth E   kek@psfc.mit.edu
Plasma Science and Fusion Center, MIT NW16-174, Cambridge, MA, 02139,
USA

Krienen, Frank   krienen@bnl.gov
Boston University, 22927 Drake Lane, Summerland Key, FL, 33042-4313

Krietenstein, Bernd   kstein@temf.tu-darmstadt.de
Technische U. Darmstadt, FB 18 / FG TEMF, Schlossgartenstrasse 8,
Darmstadt, 64289, Germany

Krinsky, Samuel   krinsky@bnlls1.nsls.bnl.gov
BNL, Bldg. 725B, Upton, NY 11973 USA

Krisch, A. D.   krisch@umich.edu
U. of Michigan, Randall Lab of Physics, Univ. of Michigan, Ann Arbor,
Michigan, 48109-1120, USA

Krischel, Detlef   krischel@accel.de
ACCEL Instruments GmbH, Friedrich-Ebert-StraDFe 1, Bergisch Gladbach,
51429, Germany

Krishnan, Mohan   yohann@umich.edu
Michigan S.U., 2200 Bonisteel Blvd. Rm. 1006, Ann Arbor, MI, 48109-2680

Kroll, Norman M   nkroll@ucsd.edu
UCSD, Dept. of Physics, 9500 Gilman Drive, La Jolla, CA, 92093-0319
Krupnick, Jim   jtkrupnick@lbl.gov
LBNL, Advanced Light Source, #1 Cyclotron Rd. MS80-101, Berkeley, California, 94720, USA
Kubo, Kiyoshi   kiyoshi.kubo@kek.jp
KEK, Accelerator Lab., 1-1, Oho, Tsukuba, Ibaraki, 305-0801, Japan
Kugler, Hartmut   Hartmut.Kugler@cern.ch
CERN, PS Division, PS Division, CERN, 1211 Geneva 23, Switzerland
Kuhn, Hans-Karl E.   hans-karl.kuhn@cern.ch
CERN, CERN-LHC Division, Group IAS, CERN, Geneva 23, 1211, Switzerland
Kumada, Masayuki   kumada@nirs.go.jp
NIRS, Heavy Ion Physics and Engineering, 4-9-1 Anagawa, Inage, Chiba, Chiba, 263-8555, Japan
Kuo, Chang Hor   longmild@srrc.gov.tw
SRRC, Instrument and Control, No. 1 R&D Road VI Hsinchu Science-Based Industrial Park, Hsinchu 300, Taiwan, R. O. C
Kurakin, Vyacheslav   kurakin@sgi.lpi.msk.su
Lebedev Physical Institute, Leninsky Prosp., 53, Moscow, 117924, Russia
Kurennoy, Sergey S   kurennoy@lanl.gov
LANL, Los Alamos National Laboratory, LANSCE-1, MS H808, Los Alamos , NM, 87545, USA
Kurita, Nadine R   KURITA@SLAC.STANFORD.EDU
SLAC, SSRL, 2575 SAND HILL ROAD, MS 69, MENLO PARK, CALIFORNIA, 94025, USA
Kurokawa, Shin-ichi   shin-ichi.kurokawa@kek.jp
KEK, Accelerator Laboratory, 1-1 Oho, Tsukuba-shi, Ibaraki-ken, 305-0801, Japan
Kurz, Stefan   stefan.kurz@ite.uni-stuttgart.de
University of Stuttgart, Institut for Theory of Electrical Engineering, Pfaffenwaldring 47, Stuttgart, 70550, Germany
Kuske, Bettina   kuskeb@bii.bessy.de
BESSY, Geb. 14.51, Rudower Chaussee 5 , Berlin-Adlershof, 12489, Germany
Kuske, Peter M   Kuske@turtle.acc.bessy.de
BESSY, Geb. 14.51, Rudower Chaussee 5, Berlin-Adlershof, 12489, Germany
Kuzminski, Jozcf   jozef.kuzminski@gat.com
General Atomics, 2237 Trinity Dr., Los Alamos, NM, 7544, USA
Kwan, Joe W   jwkwan@lbl.gov
Lawrence Berkeley National Laboratory, Fusion Energy Program, MS 47-112, 1 Cyclotron Road, Berkeley, CA, 94720, USA
Kwan, Thomas J.T.   tjtk@lanl.gov
Los Alamos National Laboratory, P. O. Box 1663, MS-B259, Los Alamos, NM, 87545, USA
Kwiatkowski, Slawomir   slawomir@bnl.gov
BNL, RHIC RF, Building 1005, Upton, NY, 11973, USA
Kwon, Hyeok-jung   khj27@paragon.snu.ac.kr
Seoul National University, Department of Nuclear Engineering, San 56-1, Shinlim, Kwanak, Seoul, 151-742, Korea
Kwon, Young   ykkwon@can.ac.kv
Chung University, Nuclear Physics Lab., Huk-suk dong , Dong Jak Gn, Seoul, Korea
Kwon, Myeun   kwonm@postech.ac.kr
Pohang Accelerator Laboratory, Accelerator Department, San-31 Hyoja-Dong, Pohang, Kyungbuk, 790-784, Korea
LaPointe, Michael A   lapointe@omega-p.com
Omega-P, Inc, 202008 Yale Station, New Haven, CT, 06520-2008, USA
Laclare, Jean-Louis JLL   laclare@sol.cnrs-gif.fr
SOLEIL, DRIF du CNRS - Avenue de la Terrasse, B0.000000E+002timent 5, GIF-SUR-YVETTE, 91190, France
Lagniel, Jean-Michel L   jmlagniel@cea.fr
CEA, CEA-Saclay DSM-DAPNIA-SEA, CEA-Saclay, DSM-DAPNIA-SEA, Gif-sur-Yvette CEDEX, 91191, France
Lamanna, Giuseppe   giuseppe.lamanna@ba.infn.it
INFN-Bari, Dipartimento di Fisica, Via Amendola 173, Bari, 70125, Italy
Lambiase, Robert F   lambiase@bnl.gov
BNL, Building 817, Upton, NY, 11973, USA
Lamont, Mike   Mike.Lamont@cern.ch
CERN, SL Division, CERN, Geneva, CH-1211, Switzerland
Landahl, Eric C   landahl@wente.llnl.gov
Lawrence Livermore National Laboratory, 7000 East Avenue L-411, Livermore, CA, 94550, USA
Lantz, Stephen A.   slantz@pcc-york.com
Precision Components Corporation, 500 Lincoln Street, York, PA, 17404, USA

Larionov, Alexandre Viktorovich   larionov@vlepp.serpukhov.su
BINP, BINP, Pronvino, Moscow region, 142284, Russia
Larsen, Raymond S.   larsen@slac.stanford.edu
SLAC, 409 Greenbrier Road, Hartmoon Bay, Ca, 94019, USA
Lau, Wai-Keung   wklau@bd08.srrc.gov.tw
SRRC, Light Source Division, No.1 R and D Road VI,, Hsinchu, Taiwan, 30077, Taiwan
Laverty, Michael P   mapl@triumf.ca
TRIUMF, 4004 Wesbrook Mall, Vancouver, BC, V6T 2A3, Canada
Lawrence, George P   glawrence@lanl.gov
LANL, APT/TPO, Mail Stop H816, Los Alamos National Laboratory, Los Alamos, NM, 87544, USA
Laxdal, Robert E   lax@triumf.ca
TRIUMF, 4004 Wesbrook Mall, Vancouver, BC, V6T 2A3, Canada
Lazarev, Yuri N   yu.n.lazarev@vniitf.ru
RFNC-Institute of Technical Physics, Department of Theoretical Physics and Applied Mathematics, P.O.Box245, Snezhinsk, Chelyabinsk region, 456770, Russia
LeDuff, Joel R.   Leduff@LAL.IN2P3.FR
Laboratoire de l,Accelerateur Lineaire, Laboratoire de l'Acelerateur Lineaire, B.P.34, Orsay Cedex, Orsay Cedex, 91898, France
LeMaire, Jean-Louis R   jlemaire@bruyeres.cea.fr
CEA-Bruyeres, DIF/DPTA/SP2A, BP 12, BRUYERES -LE- CHATEL, 91680, France
Lebedev, Valeri A   lebedev@jlab.org
TJNAF, Accelerator Physics, 12000 Jefferson Ave., Newport News, VA, 23693, USA
Leboutet, Hubert   hubertleboutet@minitel.net
CEA, 16 Residence Beausoleil, ST Cloud, 92210, France
Lebrun, Paul L.   lebrun@fnal.gov
FNAL, Computing Division, P.O. Box 500, M.S. 234, Batavia, Ill, 60510
Lee, Yong Y   yylee@bnl.gov
BNL, AGS Department, Building 911B, Brookhaven National Laboratory, Upton, New York, 11973, USA
Lee, W. W.   wwlee@pppl.gov
PPPL, P.O. Box 451, Princeton Plasma Physics Lab., Princeton, NJ, 08540, USA
Lee, S.Y.   shylee@indiana.edu
Indiana U., Department of Physics, 2401 Milo B. Sampson Lane, IUCF, Bloomington, IN, 47408-1398, USA
Lee, Yvette Y   YYLee@lbl.gov
LBNL, Plasma and Ion Source Group, 1 Cyclotron Rd. MS 5-121, Berkeley, CA, 94720, USA
Lee, Peter J   lee@engr.wisc.edu
University of Wisconsin-Madison, ASC, Applied Superconductivity Center, 939 ERB, 1500 Engineering Drive, Madison, WI, 53706-1687, USA
Lee, Seung   seunglee@usc.edu
USC, Electrical Engr./Electrophysics, University of Southern California, LA, CA, 90089-0271, USA
Leemann, Christoph W.   leemann@jlab.org
TJNAF, Accelerator Division, 12000 Jefferson Avenue, Mailstop 7A, Newport News, Virginia, 23606, USA
Leemans, Wim   wpleemans@lbl.gov
LBNL, Center for Beam Physics, 1 Cyclotron Road, MS 71-259, Berkeley, CA, 94720, USA
Lehrach, Andreas   a.lehrach@fz-juelich.de
Forschungszentrum Juelich, Institut fuer Kernphysik (COSY), Leo-Brand Str., P.O. Box 1913, Juelich, Nordrhein-Westfalen, D-52425, Germany
Lei, Ge   leige@jlab.org
TJNAF, Software, 12000 Jefferson Ave., MS 85, Newport News, VA, 23606
Leitner, Matthaeus   MLeitner@lbl.gov
LBNL, Accelerator and Fusion Research Division, 1 Cyclotron Road, Mailstop 5-119, Berkeley, CA, 94720, USA
Len, L.K.   llen@gmu.edu
FM Technologies, 10529-B Braddock Road, Fairfax, VA, 22032, USA
Lenkszus, Frank R.   frl@aps.anl.gov
ANL, ASD, Bldg. 401, C2263, 9700 S. Cass Avenue, Argonne, IL, 60439
Leonhardt, William   WJLeonhardt@bnl.gov
BNL, Bldg 510A, room 1-161, Box 5000, Upton, NY, 11973-5000, USA
Lesrel, Jean   lesrel@ipno.in2p3.fr
Institut de Physique Nucleaire, SERVICE RDA CAVITES, UNIVERSITE PARIS SUD, ORSAY, 91406, France
Letchford, Alan   A.Letchford@rl.ac.uk
Rutherford Appleton Laboratory, Room 101, Bldg. R2, Rutherford Appleton Laboratory, Chilton, Didcot, Oxon, OX11 0QX, United Kingdom
Lettry, Jacques   jacques.lettry@cern.ch
CERN, ISOLDE, CERN Geneva 23 EP C26700, Geneva , 1211, Switzerland

Leung, Ka-Ngo   knleung@lbl.gov
LBNL, IBT/AFRD, 1 Cyclotron Road MS/5-119, Berkeley, CA, 94720,
USA

Level, Marie-Paule MPL   level@sol.cnrs-gif.fr
SOLEIL, DRIF du CNRS-Avenue de la Terrasse, B0.000000E+002timent
5, GIF-SUR-YVETTE, 91190, France

Levichev, Eugene   levichev@inp.nsk.su
BINP, Synchrotron Radiation Laboratory, Lavrentiev av.11, Novosibirsk,
630090, Russia

Levush, Baruch   levush@mmace.nrl.navy.mil
NRL, 4555 Overlook Ave. SW, Washington, DC, 20375, USA

Lewis, Stephen A   SALewis@lbl.gov
LBNL, IBT Group, Mail Stop 71-259, 1 Cyclotron Rd, Berkeley, CA,
94720, USA

Lewis, Paul S.   lewis@lanl.gov
LANL, LANSCE-DO, Mail Stop H848, TA-53, Bldg. 1, Los Alamos, New
Mexico, 87544, USA

Li, Nanyang   N_Li@lbl.gov
LBNL, #1 Cyclotron Road, Berkeley, CA, 94720, USA

Li, Zenghai   lizh@SLAC.Stanford.EDU
SLAC, P.O. Box 4349, Mail Stop 26, Stanford, CA, 94309, USA

Li, Derun   DLi@lbl.gov
Center for Beam Physics, Lawrence Berkeley National Laboratory,, #1
Cyclotron Road, MS 71-259, Berkeley, CA, 94720

Li, Yun   liyun@glue.umd.edu
U. of Maryland, Institute for Plasma Reesearch, P.O. Box 83, College Park,
MD, 20742, USA

Li, Rui   lir@jlab.org
TJNAF, Accelerator Division, 12000 Jefferson Avenue, Mail Stop 6A,
Newport News, Virginia, 23606, USA

Liaw, Chong-Jer   liaw@bnl.gov
BNL, AGS Department, Building 911A, Upton, New York, 11973, USA

Libkind, Marcus   libkind1@llnl.gov
LLNL, Mechanical Engineering, Accelerator Technologies Engineering
Group, P.O. Bosx 808, L-287, Livermore, CA, 94550, USA

Lidestri, Joseph   pac99@bnl.gov
HHMI/Columbia U, Buichemistry, 630 West 168th Street, Neww York,
NY, 10032, USA

Lidia, Steven M   SMLidia@lbl.gov
LBNL, MS 58-201, Berkeley, CA, 94720, USA

Liechtenstein , Vitaly   liechten@qq.nfi.kiae.su
Kurchatov Institute, Institute of Nuclear Fusion, Kurchatov Sq.1, Moscow,
123182, Russia

Lill, Robert M   blill@aps.anl.gov
ANL, APS/ASD/DIA, 9700 South Cass, Building 401, Argonne, IL,
60439-4800, USA

Limborg, Ceule G.   limborg@ssrl.slac.stanford.edu
SLAC, P.O. Box 4349, Mail Stop 69, Stanford, CA, 94309, USA

Limon, Peter J   pjlimon@fnal.gov
FNAL, Technical Division, MS316, P.O. Box 500, Batavia, IL, 60510

Lin, Xintian E.   eddie@slac.stanford.edu
SLAC, MS 7, SLAC, Stanford University, P.O.BOX 4349, Stanford, CA,
94309-4349, USA

Lindroos, Mats A   Mats.Lindroos@cern.ch
CERN, PS Division, Geneva, 1211, Switzerland

Lisowski, Paul W   lisowski@lanl.gov
LANL, Accelerator Production of Tritium, MS-H813, Los Alamos
National Laboratory, Los Alamos, NM, 87545, USA

Little, Robert   robert.little@cpmx.saic.com
S.A.I.C., W/2, 10260 Campus Point Drive, San Diego, CA, 92121, USA

Litvinenko, Vladimir N.   vl@phy.duke.edu
Duke University, Department of Physcis, FEL Lab Box 90319 Duke
University, Durham, NC, 27708-0319, USA

Liu, Jinying   hdh@mail.nsrl.ustc.edu.cn
Univ. of Science & Technologu of China, Modern Physics Department,
Hefei, Anhui, 230026, China, Peoples Republic of

Liu, Yabo   yliu@phpysics.ucla.edu
UCLA, Physics Dept., 405 Hilgard Ave., Los Angeles, CA, 90095-1547

Liu, Yuan   liuy@ornl.gov
ORNL, Physics Division, Bldg. 6000, MS-6368, P.O. Box 2008, Oak
Ridge, TN, 37831-6368, USA

Liu, Lin   liu@lnls.br
LNLS, Fisica de Aceleradores, Caixa Postal 6192, Campinas, SP, 13083-
970, Brazil

Lo, Chu-Chung   CCLo@lbl.gov
LBNL, Engineering Division, One Cyclotron Road, MS: 46-125, Berkeley,
CA, 94720, USA

Lodesto, Vincent   lodestro@bnl.gov
BNL, P.O. Box 5000, Bldg. 930, Upton, NY, 11973, USA

Loew, Gregory A   galoew@slac.stanford.edu
SLAC, Technical Division, P.O.Box 4349, MS33, Stanford, CA, 94309, USA

Lombardi, Augusto   Alombardi@lnl.infn.it
INFN Laboratori Nazionali di Legnaro, INFN Laboratori Nazionali di
Legnaro, via Romea 4, Legnaro, Padova, I35020, Italy

Losito, Roberto   roberto.losito@cern.ch
CERN, Div. SL, Geneva, 1211, Switzerland

Loulergue, Alexandre   aloulergue@cea.fr
CEA, DSM/DAPNIA/SEA, Gif-sur-Yvette CEDEX, 91191, France

Lowenstein, Derek I.   lowenstein@bnl.gov
BNL, AGS Department, Building 911B, Upton, NY, 11973-5000, USA

Lucas, Peter W.   lucas@fnal.gov
FNAL, MS 220, PO Box 500, Batavia, IL, 60510, USA

Luccio, Alfredo U   luccio@bnl.gov
BNL, AGS , 911B, Upton, NY, 11973-5000, USA

Ludewig, Hans   ludewig@necs01.dne.bnl.gov
BNL, Department of Advanced Technology, Building 475B, 12 South Upton
Road, Upton, NY, 11973, USA

Ludlam, Thomas W.   ludlam@bnl.gov
BNL, RHIC, BROOKHAVEN NATIONAL LABORATORY, BUILDING
1005-4, UPTON, NY, 11973-5000, USA

Luiten, Jom   o.j.luiten@tue.nl
Eindhoven University of Technology, Cyclotron Laboratory, P.O.Box 513,
Den Dolech 2, Eindhoven, 5600 MB, Netherlands

Lujan, Richard E   relujan@lanl.gov
LANL, Los Alamos National Laboratory, P.O. 1663 MS H821, Los Alamos,
New Mexico, 87545, USA

Lumpkin, Alex H   lumpkin@aps.anl.gov
ANL, ASD/401, 9700 S. Cass Avenue, Argonne, Illinois, 60439-4800, USA

Lund, Steven M   lund@hif.llnl.gov
LLNL, Y-Division, Lawrence Livermore National Laboratory, PO Box 808,
L-645 , Livermore, CA, 94550, USA

Lyles, John T. M.   jtml@lanl.gov
LANL, LANSCE, Post Office Box 1663, Mail Stop H827, Los Alamos, New
Mexico, 87545, USA

Lynch, Michael T.   mtlynch@lanl.gov
LANL, Bikini Road, MS-H827, Los Alamos, Nm, 87545, USA

MacKay, W. W.   mackay@bnl.gov
BNL, RHIC Project, P.O. Box 5000, Bldg. 1005S, Upton, NY, 11973-5000

MacKinnon, Barry A.   barrymac@ix.netcom.com
ISYS- Ion Beam Systems, 283 Brokaw Road, Santa Clara, CA, 95050, USA

MacLaren, Stephan A   samaclaren@lbl.gov
Lawrence Berkeley National Laboratory, MS 47-112, One Cyclotron Rd,
Berkeley, CA, 94720, USA

Macek, Robert J   macek@lanl.gov
LANL, LANSCE-DO, MS-H848, Los Alamos, NM, 87545, USA

Machida, Shinji   shinji.machida@kek.jp
KEK, Accelerator, Midori-cho 3-2-1, Tanashi-shi, Tokyo, 188-8501, Japan

Machuzak, John S   machuzak@psfc.mit.edu
Massachusetts Institute of Technology, MIT Plasma Science and Fusion
Center, Room NW16-116, 167 Albany Street, Cambridge, MA, 02139, USA

Maeng, Aehee   mah@postech.ac.kr
Pohang Accelerator Laboratory, PAL, San 31, Hyojadong, Pohang,
Kyungbuk, 790-784, Korea

Magerl, Marty J   marty.magerl@us.nycomed-amersham.com
Nycomed-Amersham, Cyclotron, 3350 N. Ridge, Arlington Heights, Illinois,
60004, USA

Maggs, Peter N.   peter.maggs@eev.com
EEV, EEV LTD Waterhouse Lane, CHelmsford, Essex, CM12QU, United
Kingdom

Mahler, George J   Mahler@bnl.gov
BNL, AGS, Building 911-A, Upton, NY, 11973, USA

Makita, Yo   yo@wel.crl.melco.co.jp
Mitsubishi Electric Co., Dep. of Electromechanical Systems Advanced
Technology R and D Center, 8-1-1 Tsukaguchi-Honmachi, Amagasaki-shi,
Hyogo, 661-8661, Japan

Mako, Frederick M   fmako@erols.com
FM Technologies, Inc., 10529-B Braddock Rd., Fairfax, VA, 22032, USA

Maksimchuk, Anatoly M.   tolya@umich.edu
University of Michigan, Rm. 1006,IST Bldg., 2200 Monisteel Blvd., Ann
Arbor, MI, 48109, USA

Malenfant, Jerome   jm@aps.org
American Physical Society/Physical Review Letters, 1 Research Road, Ridge,
NY, 11961, USA

Molodojentsev, Alexander molod@sunse.jinr.ru
Joint Institute for Nuclear Research, Accelerator Division , Particle Physics
Laboratory, Dubna, Moscow region, 141980, Russia

Molvik, Arthur W. molvik1@llnl.gov
LLNL, L-645, P.O. Box 808, Livermore, CA, 94550, USA

Mondelaers, Wim WIM.MONDELAERS@RUG.AC.BE
University of Gent, DEPT.OF SUBATOMIC AND RADIATION
PHYSICS, PROEFTUINSTRAAT 86, GENT, B-9000, Belgium

Mondelli, Alfred A mondelli@apo.saic.com
S.A.I.C., SAIC, T2-3-1, 1710 Goodridge Drive, McLean, VA, 22102, USA

Month, Melvin month@bnl.gov
BNL, Building 902A, P.O. Box 5000, Upton, New York, 11973, USA

Moog, Elizabeth R Moog@ANL.GOV
ANL, XFD-401 9700 S. Cass Ave., Argonne, IL, 60439, USA

Moore, Craig D cmoore@fnal.gov
FNAL, Beams Division, M.S. 221, P.O. Box 500, Batavia, IL, 60510, USA

Morcombe, Peter H peterm@acpub.duke.edu
U. of Dortmund, FEL Laboratory, LaSalle Street Extension, Durham, NC,
27708, USA

Mori, Yoshiharu moriy@mail.kek.jp
KEK, Accelerator Laboratory, KEK-Tanashi,3-2-1,Midori-cho, Tanashi-
shi, Tokyo, 188-8501, Japan

Mori, Warren B. mori@physics.ucla.edu
UCLA, 1-130 Knutsen Hall, Los Angeles, CA, 90095, USA

Morimoto, Hiroshi hiroshi.morimoto@hal.hitachi.com
Hitachi,Ltd., Procurement & Technical Service Div., 50 Prospect Ave.,
Tarrytown, NY, 10591-4698, USA

Morris, William A. ADRIAN.MORRIS@RL.AC.UK
Rutherford Appleton Laboratory, Rutherford Appleton Laboratory, Chilton,
Didcot, Oxon, United Kingdom

Morris, John T. jtm@bnl.gov
BNL, RHIC/AGS, Building 911C, P.O. Box 5000, Upton, NY, 11973

Mortazavi, Payman payman@bnl.gov
BNL, Building 725C, P.O.Box 5000-725C, Upton, N.Y., 11973-5000

Moser, Herbert O. moser@anka.fzk.de
FZ Karlsruhe/ANKA , FZK/PEA, Postfach 3640, Karlsruhe, D-76021,
Germany

Mosnier, Alban Am mosnier@sol.cnrs-gif.fr
SOLEIL, DRIF du CNRS-Avenue de la Terrasse, B0.000000E+002timent
5, GIF-SUR-YVETTE, 91190, France

Mostacci, Andrea Andrea.Mostacci@cern.ch
Universita' di Roma, , Dipartimento di Energetica, Via Antonio Scarpa 14,
Roma, 00161, Italy

Muggli, Patrick muggli@ee.ucla.edu
USC, 56-125B ENG IV UCLA-EE, Los Angeles, Ca, 90095, USA

Mukherjee, (Sam) K SKMukherjee@lbl.gov
Ion Beam Tech. Div., Lawrence Berkeley National Laboratory, Berkeley,
CA, 94720, USA

Muller, Anke-Susanne Anke-Susanne.Muller@cern.ch
CERN, Division SL/OP, Geneva 23, CH-1211, Switzerland

Mullier, Benoit mullier@iba.be
Ion Beam Applications, 3 Chemin du Cyclotron, 1348 Louvain La Neuve,
Belgium

Muratore, Joseph F muratore@bnl.gov
BNL, Building 902A, Upton, NY, 11973, USA

Murokh, Alex Y alex@stout.physics.ucla.edu
UCLA, Department of Physics and Astronomy, 405 Hilgard Avenue, Los
Angeles, CA, 90095-1547, USA

Muroya, Yusa muroya@tokai.t.u-tokyo.ac.jp
U. of Tokyo, NERL, Graduated school of Engineering, University of
Tokyo, 2-22, Shirakata-shirane, Tokai, Naka, Ibaraki, 319-1106, Japan

Murphy, James B jbm@bnl.gov
BNL, National Synchrotron Light Source, P.O. Box 5000, Bldg. 725C,
Upton, NY, 11973-5000, USA

Musson, John musson@jlab.org
TJNAF, Accelerator Division, 12000 Jefferson Avenue, MS 58, Newport
News, Virginia, 23606, USA

Myers, Stephen M Stephen.Myers@cern.ch
CERN, SL Division, CERN, 1211 GENEVE , 23, Switzerland

Müller, Roland M. mueller@bii.bessy.de
BESSY, Accelerator Division, Bld. 14.51, Rudower Chaussee 5, Berlin, D-
12489 , Germany

Nadji, Amor An nadji@sol.cnrs-gif.fr
SOLEIL, DRIF du CNRS-Avenue de la Terrasse, Batiment 5, GIF-SUR-
YVETTE, 91190, France

Nagaitsev, Sergei nsergei@fnal.gov
FNAL, Fermilab MS 307, Batavia, IL, 60510

Nagaoka, Ryutaro nagaoka@esrf.fr
ESRF, ESRF BP220 F-38043, Polygone Scientific Louis Neel Avenue des
Martyrs, Grenoble, 38043, France

Nakagawa, Nobuhiko nobuhiko.nakagawa@mecc.mee.com
Mitsubishi Electric Europe BV, European Alliance Sourcing Office, Power &
Inductrial System Group, 18th Floor, Centre Point, 103 New Oxford Street,
London, WC1A 1EB, United Kingdom

Namkung, Won namkung@postech.ac.kr
POSTECH, Physics Department, San-31, Hyoja-dong, Pohang, 790-784,
Korea

Nath, Subrata snath@lanl.gov
LANL, LANSCE-1, LANL, MS H817, Los Alamos, NM, 87545, USA

Nation, John A JAN4@cornell.edu
Cornell U., Electrical Engineering, 325 Rhodes Hall, Ithaca, NY, 14853

Nawrocky, Roman J nawrocky@bnl.gov
BNL, NSLS, Building 725B, Upton, NY, 11973, USA

Nelson, Scott D. nelson18@llnl.gov
Lawrence Livermore National Laboratory, 7000 East Ave. L-645, P.O.Box
808, Livermore, Ca, 94551-0808, USA

Nelson, Eric M enelson@lanl.gov
LANL, MS B259, Los Alamos, NM, 87545, USA

Neri, Filippo fneri@lanl.gov
L-1, MS 808, Los Alamos National Laboratory, Los Alamos, NM, 87545,
USA

Neuffer, David V. neuffer@fnal.gov
FNAL, MS-220, P.O. Box 500, Batavia, IL, 60532, USA

Neuman, Charles P neuman@bnl.gov
BNL, NSLS, NSLS, Bldg. 725-D, Upton, NY, 11973-5000, USA

Neurath, Rene neurath1@llnl.gov
LLNL, Lawrence Livermore National Laboratory, 7000 East Ave. L-535,
P.O.Box 808, Livermore, Ca, 94551-0808, USA

Newman, Ernest W. enewman@lanl.gov
Los Alamos Naitonal Laboratory, P.O. Box 1663, MS H821, Los Alamos,
NM, 87544, USA

Nezhevenko, Oleg A. nezhev@omega-p.com
Omega-P, Inc, 345 Whitney Ave. , Suite 100, New Haven, CT, 06511, USA

Ng, King Y ng@fnal.gov
FNAL, Beams Physics, Fermilab MS 220, PO Box 500, Batavia, IL, 60510

Nguyen, Minh N MNN@SLAC.STANFORD.EDU
SLAC, Power Conversion Dept., M/S 49, 2575 Sand Hill Rd., Menlo Park,
CA, 94025, USA

Nguyen, Dinh C dcnguyen@lanl.gov
LANL, Mail Stop H851, Los Alamos, NM, 87545, USA

Nguyen, Viet nguyen@jlab.org
TJNAF, MS 58B, 12000 Jefferson Avenue, Newport News, VA, 23606, USA

Niell, Fred M fmniell@midway.uchicago.edu
FNAL, 1005 E. 60th , Rm645, Chicago, IL, 60637, USA

Nielsen, Bjarne R brn@danfysik.dk
Danfysik A/S, Mollehaven 31, DK-4040 Jyllinge, Denmark

Ninin, Pierre Pierre.Ninin@cern.ch
CERN, ST/MO , 1211 Geneva 23, Switzerland

Noda, Akira noda@kyticr.kuicr.kyoto-u.ac.jp
Kyoto U., Institute for Chemical Research, Gokanosho, Uji-city, Kyoto, 611-
0011, Japan

Nolden, Fritz f.nolden@gsi.de
GSI, ESR, Planckstr.1, Darmstadt, D-62491, Germany

Nolen, Jerry A nolen@anl.gov
Physics Division, D-203, Argonne National Laboratory, Argonne, IL, 60439,
USA

Nomura, Masahiro nomura@oec.jnc.go.jp
System Engineering Tecchnology Division, OEC, JNC, Oarai-machi, Narita-
cho, 4002, Ibaraki, 311-1393, Japan

Noonan, John R. noonan@aps.anl.gov
ANL, APS/ASD, 9700 S. Cass Avenue, Bldg. 401, Argonne, IL, 60439

Norem, James H norem@hep.anl.gov
ANL, High Energy Physics, Bldg 362, Argonne, IL, 60439, USA

Novokhatski, Alexandre novot@temf.tu-darmstadt.de
Technische U. Darmstadt, TEMF, Schlossgartenstrasse 8, Darmstadt, D-
64289, Germany

O'Shea, Patrick G. POSHEA@ENG.UMD.EDU
U. of Maryland, IPR-Energy Research Facility, Universitiy of Maryland,
College Park, MD, 20742-3511, USA

Obina, Takashi obina@mail.kek.jp
KEK, Light Source Division, 1-1 Oho, Tsukuba, 305-0801, Japan

Oerter, Brian R. oerter@bnl.gov
BNL, AGS, Building 911C, Upton, NY, 11973, USA

Ogitsu, Toru ogitsu@fnal.gov
FNAL, T/D Development & Test Department, P.O. Box 500, MS 316, Batavia, IL, 60510, USA

Oh, Saewoong M soh@galaxy.postech.ac.kr.
POSTECH, Depatment of Physics, San-31 Hyojadong, Pohang, Kyungbuk, 790784, Korea

Ohkuma, Haruo ohkuma@spring8.or.jp
Japan Synchrotron Radiation Research Institute(JASRI, SPring-8), Accelerator Div., JASRI, 323-3, Mikazuki, Sayou-gun, Hyogo, 679-5198, Japan

Oide, Katsunobu oide@acsad1.kek.jp
KEK, Accelerator Division, Oho, Tsukuba, Ibaraki, 305, Japan

Okamura, Masahiro okamura@bnl.gov
AGS, 911B, Brookhaven National Laboratory, Upton, NY, 11973, USA

Okugi, Toshiyuki okugi@phys.metro-u.ac.jp
Tokyo Metropolitan University, Department of Physics, Minami-Osawa 1-1, Hachioji, Tokyo, 192-0364, Japan

Oleg, Borisov borisov@nu.jinr.ru
Joint Institute for Nuclear Research, Laboratory of Nuclear Reactions, Joliot Curie, Dubna, Moscow region, 141980, Russia

Olsen, David olsendk@ornl.gov
SNS Project, 104 Union Valley Rd, ORNL PO 2008 MS 8218, Oak Ridge, TN, 37830, USA

Onillon, Emmanuel F onillon@bnl.gov
BNL, Bldg 911B, Upton, NY, 11973, USA

Onischenko, Leonid olm@nusun.jinr.ru
JP Accelerator Works, Inc., Laboratory of Nuclear Problems, Joliot Curie, Dubna , Moscow Region, 141980, Russia

Oren, William oren@jlab.org
Accelerator Division, TJNAF, MS 7A, 12000 Jefferson Av, Newport News, VA, 23606, USA

Ormond, Kern W kwo1@cornell.edu
Cornell U., Laboratory of Nuclear Studies, Wilson Lab, Cornell University, Ithaca, NY, 14853, USA

Orris, Darryl orris@fnal.gov
FNAL, T/D Development & Test, P.O. Box 500, MS 316, Batavia, IL, 60510, USA

Orsini, Fabienne orsini@hep.saclay.cea.fr
CEA, DSM/DAPNIA/SEA, Batiment 701, 91191 Gif sur Yvette, France, France

Oshatz, Daryl P. daryl_oshatz@lbl.gov
LBNL, One Cyclotron Road, MS 71-259, Berkeley, CA, 94611, USA

Oster, Gene pac99@bnl.gov
Oster Magnetics, Inc., 2042 Bering Dr., San Jose, CA, 95131, USA

Ostiguy, Jean-Francois ostiguy@fnal.gov
FNAL, Beam Physics/Beams Division, MS 220, P.O. Box 500, Batavia, IL, 60510, USA

Ostojic, Ranko Ranko.Ostojic@cern.ch
CERN, LHC Division, 1211 Geneva 23, Switzerland

Ott, Klaus ott@exp.bessy.de
BESSY, Rudower Chaussee 5, Berlin, Berlin, 12489, Germany

Ovsyannikov, Alexander ovs@apcp.apmath.spbu.ru
St.Petersburg S.U., Faculty of Applied Mathematics - Control Processes, St.Petersburg, 198904, Russia

Ovsyannikov, Dmitri A. Dmitri.Ovsyannikov@pobox.spbu.ru
St.Petersburg S.U., Institute of Computational Mathematics and Control Processes, Petrodvorets, Bibliotechnaya pl.2, NII VM and PU, St.Petersburg, 198904, Russia

Ozaki, Toshiyuki ozaki@post.kek.jp
KEK, Acceleraor Laboratory, KEK, Oho 1-1, Tsukuba-shi, Ibaraki-ken, 305-0801, Japan

Ozaki, Satoshi ozaki@bnl.gov
Brookhaven National Laboratory, RHIC, Building 1005, P.O. Box 5000, Upton, NY, 11973, USA

Pagani, Carlo carlo.pagani@mi.infn.it
INFN - Milano, LASA, Via Fratelli Cervi, 201, Segrate (Milano), I-20090, Italy

Pai, Chien pai@bnl.gov
Brookhaven National Laboratory, AGS Department, Upton, New York, 11973, USA

Pakter, Renato pakter@psfc.mit.edu
Plasma Science and Fusion Center, 167 Albany Street, MIT Building NW-16, Cambridge, MA, 02139, USA

Palmer, Dennis T dtp@slac.stanford.edu
SLAC, ARDB, P.O. Box 4349, Mail Stop # 07, CA, 94309, USA

Palmer, Robert B. palmer@bnl.gov
BNL, 901A, P.O. Box 5000, Upton, NY, 11973-5000, USA

Palmieri, Vincenzo PALMIERI@LNL.INFN.IT
INFN - Legnaro National Laboratories, INFN - LNL Superconductivity Laboratory, Via Romea 4, Legnaro (Padua), I - 35020, Italy

Pamasee, Hansan HSP3@CORNELL.EDU
Cornell U., Newman Lab, NY, USA

Papaphilippou, Yannis yannis@mail.cern.ch
CERN, SL Division (AP), Geneva 23, CH-1211, Switzerland

Pappas, Chris pappas@slac.stanford.edu
SLAC, PCD, 2575 Sandhill Rd. , MS 49, Menlo Park, CA, 94025, USA

Parietti, Lucie M parietti@lanl.gov
Los Alamos National Laboratory, PO Box 1663, MS H821, Los Alamos, NM, 87544, USA

Park, Hee park@phy.duke.edu, park@fel.duke.edu
Duke University, Duke Free Electron Laser Lab, Department of Physics, LaSalle st. extension, Box 90319, Durham, NC, 27708-0319, USA

Park, Sanghyun spark@slac.stanford.edu
SLAC, SSRL, P.O.Box 4349, Stanford, CA, 94309, USA

Parker, Brett L parker@bnl.gov
Building 902A - RHIC, Brookhaven National Laboratory, Upton, NY, 11973

Parsa, Zohreh parsa@bnl.gov
Physics Dept., 901A , Brookhaven National Laboratory, Upton, NY, 11973

Pasquinelli, Ralph J pasquin@fnal.gov
FNAL, Fermilab, P.O. Box 500 MS 341, Batavia, Illinois, 60510, USA

Paterson, Alan JAPaterson@lbl.gov
LBNL, Engineering Division, One Cyclotron Road, MS: 46-161, Berkeley, CA, 94720, USA

Paul, Peter ppaul@bnl.gov
BNL, Director's Office, Bldg. 460, Upton, NY 11973USA

Payne, Chris G cpayne@jlab.org
TJNAF, Accelerator Operations, Jefferson Lab, 12000 Jefferson Avenue, MS 85A, Newport News, Virginia, 23606, USA

Pedersen, Flemming Flemming.Pedersen@cern.ch
CERN, PS Division, PS Division, CERN, 1211 Geneva 23, Switzerland

Peggs, Stephen G. peggs@bnl.gov
BNL, RHIC Project, P.O. Box 5000, Bldg. 1005S, Upton, NY, 11973-5000

Peiniger, Michael peiniger@accel.de
ACCEL Instruments GmbH, Friedrich-Ebert-STR 1, Bergisch Gladbach, D-51429, Germany

Pekeler, Michael J michael.pekeler@desy.de
DESY, FDET, DESY, Notkestr. 85, Hamburg, 22607, Germany

Pellegrini, Claudio PELLEGRINI@PHYSICS.UCLA.EDU
UCLA, Dept. Physics & Astronomy, Box 951547, Los Angeles, CA, 90095-1547, USA

Pellico, William A pellico@fnal.gov
FNAL, Proton Source, Beams Division, Box 500 , Batavia, IL, 60510, USA

Penn, Gregory gpenn@socrates.berkeley.edu
UC Berkeley, Berkeley Lab, Mail Stop 71-259, 1 Cyclotron Road, Berkeley, CA, 94720, USA

Peoples, John -- peop@fnal.gov
Fermilab, Directors Office, P.O. Box 500, M.S. 105, Batavia, Illinois, 60510, USA

Perelstein, Elkuno A. perel@nu.jinr.ru
Joint Institute for Nuclear Research, Lab. of Nuclear Problems, JINR, Lab. of Nucl. Probl., Dubna, Moscow region, 141980, Russia

Perez, Francisco perez@anka.fzk.de
Forschungszentrum Karlsruhe, ANKA (PEA), Postfach 3640, Karlsruhe, D-76021, Germany

Perin, Romeo V. romeo.perin@cern.ch
CERN, SPL Division, CERN, CERN-SPL Division, Geneve, 1211, Switzerland

Perkins, Michael M.Perkins@rl.ac.uk
Rutherford Appleton Laboratory, Rutherford Appleton Laboratory, Building R12, Chilton, Didcot, Oxfordshire, OX11 0QX, United Kingdom

Peters, Gerald J. jerry.peters@science.doe.gov
US Department of Energy, SC-GTN 19901 Germantown Road, Germantown, Md., 20874-1290, USA

Petillo, John J jpetillo@bos.saic.com
S.A.I.C., Applied Physics Operation, Suite 130, 20 Burlington Mall Rd., Burlington, MA, 01803, USA

Petracca, Stefania petracca@vaxsa.csied.unisa.it
University of Salerno, Dept. Scienze Fisiche E.R.Caianiello, Universita di Salerno, via S.Allende, Baronissi (Salerno), ITALY, 84081, Italy

Pflueger, Joachim joachim.pflueger@desy.de
DESY, HASYLAB, Notkestr. 85, Hamburg, 22607, Germany

Phillips, Larry phillips@jlab.org
TJNAF, Accelerator Division, 12000 Jefferson Avenue, Mail Stop 58, Newport News, Virginia, 23606, USA

Phinney, Nan nan@slac.stanford.edu
 SLAC, SLAC, MS 66, Stanford, CA, 94309, USA

Piaszczyk, Christopher chris_piaszczyk@atdc,northgrum.com
 Advanced Energy Systems, Inc., 3 Barberry Rd., West Islip, NY, 11795

Pichoff, Nicolas npichoff@cea.fr
 CEA, Centre CEA de Saclay, DSM/DAPNIA/SEA, bat 701, Gif-sur-Yvette cedex, 91 191, France

Pickett, Mike pac99@bnl.gov
 Process Systems Int'l., 20 Walkup Dr., Westboro, MA, 01581, USA

Pico, Randolph E. pico2@llnl.gov
 LLNL, 7000 East Ave. L-280, Livermore, CA, 94550, USA

Piel, Christian piel@accel.de
 ACCEL Instruments GmbH, Friedrich-Ebert-Straße 1, Bergisch Gladbach, Germany, D-51429, Germany

Pikin, Alexander pikin@bnl.gov
 BNL, AGS, 690 Fort Washington Ave, Apt. #1M, New York, NY, 10040

Pilat, Fulvia pilat@bnl.gov
 BNL, RHIC Project, Bldg. 1005S, Upton, NY, 11973-5000, USA

Piller, Maurice F piller@jlab.org
 TJNAF, Accelerator, 12000 Jefferson Avenue, MailStop 58B, Newport News, VA, 23606, USA

Pinayev, Igor pinayev@fel.duke.edu
 Duke University, FEL Laboratory, P.O.Box 90319, Durham, NC, 27708-0319, USA

Ping, Wang wang@fel.duke.edu
 Duke University, FEL Lab, Physics Department, P. O. Box 90319, LaSalle Street Extention, Durham, NC, 27708-0319, USA

Pinto, Innocenzo M pinto@vaxsa.csied.unisa.it
 University of Salerno - ITALY, D.I.I.I.E. Facoltà di Ingengeria, Unversity of Salerno, via ponte Don Melillo, Fisciano - Salerno, ITALY, 84084, Italy

Piquemal, Alain piquemal@bruyers.cea.fr
 CEA, Centre d tudes de Bryers-le-thalef, Bruyers le chatel, 91680, France

Pisent, Andrea pisent@lnl.infn.it
 INFN-LNL, via Romea 4, Legnaro, Padova, I-35020, Italy

Pivarc, Juraj fyzipiv@savba.sk
 Institue of Physics of the Slovak Academy of Sciences, Dubravska cesta 9, Bratislava, SK-842 28, Slovac Republic

Plate, David W. dwplate@lbl.gov
 LBNL, #1 Cyclotron Road, MS 46/161, Berkeley, CACA, 94720, USA

Plawski, Eugeniusz Mr plawski@ipj.gov.pl
 Andrzej Soltan Institute for Nuclear Studies, Accelerators Physics Depart. P-10, 05-400 Otwock-Swierk, Otwock-Swierk, Poland

Plettner, Thomas tplettne@leland.stanford.edu
 Stanford Univ., Dept. of Applied Physics, Stanford University, CA, 94305

Plotnikov, Sergey V. plotnikov@vitep5.itep.ru
 ITEP, Applied Linacs Group, B.Cheremushkinskaya 25, Moscow, 117259, Russia

Plum, Michael A plum@lanl.gov
 LANL, LANSCE-2, Mail Stop H838, Los Alamos, NM, 87545, USA

Podlech, Holger hjp@daniel.mpi-hd.mpg.de
 Max-Planck-Institut fuer Kernphysik, Saupfercheckweg 1, Heidelberg, 69117, Germany

Podobedov, Boris boris@slac.standford.edu
 SLAC M/S 07, Stanford University, Standford University, Ca, 94309

Poirier, Roger L POIRIER@TRIUMF.CA
 TRIUMF, Cyclotron Div., 4004 Wesbrook Mall, Vancouver, BC, V6T 2A3, Canada

Poncet, Alain alain.poncet@cern.ch
 CERN, DIVISION LHC, 1211 GENEVA 23, GENEVA , GENEVA , 1211, Switzerland

Poole, Brian R. poole1@llnl.gov
 LLNL, Lawrence Livermore National Laboratory, 7000 East Ave. L-645, P.O.Box 808, Livermore, Ca, 94551-0808, USA

Popov, Gennadiy F popov@pht.univer.kharkov.ua
 Kharkiv State University , Physics & Technology Department, P.O. Box 60, Kharkiv , 310052, Ukraine

Portmann, Greg GJPortmann@lbl.gov
 LBNL, Engineering Division, One Cyclotron Road, MS: 80-101, Berkeley, CA, 94720, USA

Power, John g jp@hep.anl.gov
 ANL, HEP, Bldg 362, 9700 S Cass Ave, Argonne, IL, 60439, USA

Power, John F. jpower@lanl.gov
 LANL, P.O. Box 1663, MS H808, Los Alamos, NM, 87505, USA

Powers, Thomas J. - powers@jlab.org
 TJNAF, Accelerator Division, 12000 Jefferson Avenue, MS58, Newport News, Virginia, 23606, USA

Pozdeyev, Eduard G. pozdeev@nscl.msu.edu
 NSCL, NSCL, Michigan State University, East Lansing, MI, 48824, USA

Pozimski, Juergen K juergen@mikro1.physik.uni-frankfurt.de
 Institut fur Angewandte Physik, Institut für Angewandte Physik, Robert-Mayer-Str. 2-4, Frankfurt am Main, 60489, Germany

Preble, Joseph P. preble@jlab.org
 TJNAF, Accelerator Division, 12000 Jefferson Avenue, MS 58, Newport News, Virginia, 23606, USA

Prelec, Krsto prelec1@bnl.gov
 BNL, AGS Department, Bldg. 911-B, Upton, New York, 11973, USA

Pritzkau, David P pritzkau@slc.standford.edc
 SLAC, SLAC M/S 07 Stanford University, P.O. Box 4349, Standford, Ca., 94309, USA

Prodell, Albert G votruba@bnl.gov
 BNL, Building 902A, Upton, NY, 11973, USA

Proudlock, Paul Paul.Proudlock@cern.ch
 CERN, AC, Ch - 1211 Geneva 23, Geneva 23, CH - 1211, Switzerland

Provenzano, Gary Transgary@aol.com
 Transtechnik Corp. USA, Mahwah Division, 97 McKee Drive, Mahwah, New Jersey, 07430, USA

Pruss, Stanley M pruss@fnal.gov
 FNAL, Main Injector Dept., Fermilab MS 341, PO Box 500, Batavia, Illinois, 60510, USA

Ptitsyn, Vadim vadimp@bnl.gov
 BNL, RHIC Project, P.O. Box 5000, Bldg. 1005S, Upton, NY, 11973-5000, USA

Purser, Robert K rpurser@owlcontrol.com
 Owl Control Systems, LLP, 165M New Boston St.; Suite 244, Woburn, MA, 01801, USA

Pusterla, Modesto pusterla@pd.infn.it
 INFN - Padova, Dipartimento di Fisica, Univ. di Padova, Via Marzolo 8, Padova, 35131, Italy

Putnam, Ernest T pac99@bnl.gov
 9672 RT 365, Holland Patent, NY, USA

Qiang, Ji jiqiang@lanl.gov
 LANL, Ms H817, Lansce-1, Los Alamos National Laboratory, Los Alamos, NM, 87545, USA

Qin, Hong HongQin@pppl.gov
 Princeton Plasma Physics Lab, Princeton University, Princeton Plasma Physics Lab, Princeton University, Princeton, NJ, 08543, USA

Quimby, David C dcq@stioptronics.com
 STI Optronics, Inc., 2755 Northup Way, Bellevue, WA, 98004-1495, USA

Rakowsky, George rakowsk1@bnl.gov
 BNL, NSLS, Bldg. 725-D, P.O.Box 5000, Upton, NY, 11973-5000, USA

Ramamoorthy, Susila susila@bnl.gov
 N.S.L.S., Bld. 725B, Brookhaven National Lab., Upton, New York, 11973

Ramsell, Christopher T. Ramsell@NSCL.MSU.edu
 NSCL, Cyclotron Lab, Michigan State University, East Lansing, MI, 48824-1321, USA

Raparia, Deepak raparia@bnl.gov
 BNL, AGS Department, Building 911-A, Upton, New York, 11973, USA

Rasson, Joseph JERasson@lbl.gov
 LBNL, One Cyclotron Rd, MS-46A-1123, Berkeley, CA, 94720, USA

Rathke, John W john_rathke@atdc.northgrum.com
 Advanced Energy Systems, Inc., PO Box 249, Bethpage, New York, 11714, USA

Ratti, Alessandro aratti@lbl.gov
 LBNL, LBNL, 1 Cyclotron Road, MS 71-259, Berkeley, CA, 94720, USA

Ratzinger, Ulrich U.Ratzinger@gsi.de
 GSI, Accelerator Division, Planckstr. 1, Darmstadt, 64291, Germany

Read, Michael E.' read@psccorp.com
 Physical Sciences, Inc., 5705A General Washington Dr., Alexandria, VA, 22312, USA

Reardon, Paul L maryc@bnl.gov
 Proton Corp. of America, 32 Lochatomy Road, West Trenton, NJ, 08628

Reass, William A WREASS@LANL.GOV
 LANL, LANCE-5, H-827, PO Box 1663 , Los Alamos, NM, 87545

Redin, Sergei i redin@bnldag.bnl.gov
 Physics, Bld 510, g-2, BNL, Upton, NY, 11973, USA

Reece, Kenneth reece@bnl.gov
 AGS Dept., Bldg. 911C, Brookhaven National Laboratory, Upton, NY 11973

Regan, Amy H. aregan@lanl.gov
 Los Alamos National Lab., P.O. Box 1663; MS H827, Los Alamos, NM, 87545, USA

Reginato, Louis L LLReginato@lbl.gov
 LBNL, Accelerator Electronics, Engineering, One Cyclotron Road MS: 46A-1123, Berkeley, CA, 94720, USA

Regler, Meinhard   regler@hephy.oeaw.ac.at
Institute of High Energy Physics, Austrian Academy of Siences, Nikolsdorfer Gasse 18, Vienna, A-1050, Austria

Reijonen, Jani P   reijonen@mh1.lbl.gov
LBNL, Accelerator and Fusion Research Division, 1 Cyclotron Road, MS 5-132, Berkeley, CA, 94720, USA

Reiniger, Klaus   Reiniger@triumf.ca
TRIUMF, Cyclotron Division, 4004 Wesbrook mall, Vancouver, British Columbia, V6T2A3, Canada

Reiser, Martin P.   mreiser@glue.umd.edu
U. of Maryland, Institute for Plasma Research, Energy Research Facility, College Park, MD, 20742-3511, USA

Revol, Jean-Luc   revoljl@esrf.fr
ESRF, Machine Division /RF, Avenue Des Martyrs, BP220, Grenoble, 38043, France

Richards, Mitchell C   mrichards@lanl.gov
WSRC, M.C. Richards, P.O. Box 267, Canton, Ga, 30114, USA

Richardson, Roger A.   richardson8@llnl.gov
Lawrence Livermore National Laboratory, 7000 East Ave. L-153, P.O.Box 808, Livermore, Ca, 94551-0808, USA

Rimmer, Robert A   RARimmer@lbl.gov
LBNL, AFRD, CBP, Mail Stop 71-259, LBNL, 1 Cyclotron Rd., Berkeley, CA, 94596, USA

Ristau, Uwe   ristau@anka.fzk.de
Forschungszentrum Karlsruhe, ANKA (PEA), Postfach 3640, Karlsruhe, D-76021, Germany

Rivkin, Leonid   rivkin@psi.ch
Paul Scherrer Institut, SLS, Villigen PSI, CH-5232, Switzerland

Roberson, Charles W   robersc@onr.navy.mil
Hahn-Meitner-Institut Berlin, Physical Sciences Division, Code331, 800 N. Quincy St., Arlington, Virgina, 22217, USA

Robin, David S   dsrobin@lbl.gov
LBNL, MS 80-101, 1 Cylotron Road, Berkeley, CA, 94720, USA

Rodenas, Jose   jrodenas@iqn.upv.es
U. Politecnica de Valencia, Dpto. Ingenieria Nuclear, Universidad Politecnica de Valencia, Apartado 22012, Valencia, E-46071, Spain

Rodriguez, Carmelo   Carmelo.Rodriguez@gat.com
General Atomics, Accelerator Production Of Tritium, 2237 Trinity Drive, Bldg. 2, Floor 3, Los Alamos, New Mexico, 87544, USA

Romanoff, Scott D   scott.romanoff@us.nycomed-amersham.com
Nycomed-Amersham, Cyclotron, 3350 N. Ridge Ave., Arlington Heights, Illinois, 60004, USA

Romo, Louis G   louisr@magnetsales.com
Magnet Sales & Manufacturing, Engineering Division, 11248 Playa Court, Culver City, California, 90230, USA

Ropert, Ammick   ropert@esrf.fr
ESRF, ESRF BP220, Cedex 09, Grenoble, 38043, France

Rose, James T   rose@bnl.gov
BNL, RHIC, Building 1005, Upton, New York, 11973, USA

Rosenzweig, James B   rosen@stout.physics.ucla.edu
U. of Maryland, Department of Physics & Astronomy, Dept. Physics & Astronomy, UCLA, Los Angeles, CA, 90095, USA

Roser, Thomas   roser@bnl.gov
BNL, AGS Department, Bldg. 911B, Upton, NY, 11973-5000, USA

Ross, Marc C   mcrec@slac.stanford.edu
SLAC, NLC Project Group, PO Box 4349, MS66, Stanford, CA, 94309

Rossmanith, Robert   rossmanith@anka.fzk.de
Forschungszentrum Karlsruhe, ANKA, Postfach 3640, Karlsruhe, D-76021, Germany

Rothemund, Karsten   karsten.rothemund@etechnik.uni-rostock.de
U. Rostock, Institut f. Allgemeine Elektrotechnik, Albert Einstein-Strasse 2, Rostock, 18051, Germany

Rothman, Jeffrey   jrothman@bnl.gov
BNL, NSLS, P.O. Box 5000, Building 725B, Upton, NY, 11973-5000

Rovelli, Alberto   rovelli@lns.infn.it
INFN, Laboratori Nazionali del Sud, via S. Sofia 44/a, Catania, Italy, 95123, Italy

Rrhioua, Bdeslem   abrrhioua@sciences.univ-oujda.ac.ma
University Mohammed Ist, Faculty of science,department of physics, LPTP, Oujda Morocco. , University Mohammed Ist, Faculty of science,department of physics, LPTP, Oujda Morocco., Rue Haifa, A/9, Lot Houar, Oujda 60000, Morocco, University Mohammed Ist, Faculty of science,department of physics, LPTP, Oujda 60000 Morocco., Oujda, 60000, Morocco

Rrhioua, Abdeslem   abrrhioua@sciences.univ-oujda.ac.ma
University Mohammed Ist, Faculty of Science, Department of Physics, LPTP, Oujda Morocco

Rubin, David L   dlr@cesr10.lns.cornell.edu
Cornell U., Newman Lab, Cornell University, Ithaca, NY, 14853, USA

Ruggiero, Alessandro G   agr@bnl.gov
BNL, AGS, Brookhaven National Laboratory, PO BOX 5000, AGS -- 911B, UPTON, New York, 11973, USA

Rusnak, Brian   brusnak@lanl.gov
Los Alamos National Lab, PO Box 1663, LANSCE-1 MS H817, Los Alamos, NM, 87544, USA

Russell, Steven J   srussell@lanl.gov
MS H851, Los Alamos National Laboratory, Los Alamos, NM, 87545, USA

Russenschuck, Stephan H   stephan.Russenschuck@cern.ch
CERN, LHC-ICP, 1211 Geneva 23, Geneva , 1211, Switzerland

Ruth, Ronald D.   rruth@slac.stanford.edu
SLAC, MS 26, SLAC, PO Box 4349, Stanford, CA, 94309, USA

Rutherford, Robert J   burlepwm@burle.com
Burle Industries, 1000 New Holland Ave., Lancaster, PA, 17601, USA

Rutkowski, Henry L   HLRutkowski@lbl.gov
Accelerator Fusion Research Division, Lawrence Berkeley National Laboratory, One Cyclotron Road, M.S. 71J, Berkeley, CA, 94720, USA

Ryan, William   ryan@bnl.gov
BNL, Bldg 10055, Upton, NY, 11973, USA

Ryne, Robert D   ryne@lanl.gov
LANL, LANSCE Division, Mail Stop H817, Los Alamos, NM, 87545, USA

Sabado, Maurice M   maurice.m.sabado@cpmx.saic.com
S.A.I.C., W/2, 10260 Campus Point Drive, San Diego, CA, 92121, USA

Saban, Roberto I   Roberto.Saban@cern.ch
CERN, LHC Division, CERN, 1211 Geneva 23, Switzerland

Sabbi, Gianluca   sabbi@fnal.gov
FNAL, T/D Development & Test Department, P. O. Box 500, MS 316, Batavia, IL, 60510, USA

Safranek, James A   safranek@slac.stanford.edu
SLAC, SSRL, PO Box 4349, bin 69, Stanford, CA, 94309, USA

Sagan, David   dcs16@cornell.edu
Cornell U., Cornell University, Wilson Lab, Cornell University, Ithaca, NY, 14853, USA

Sah, Richard C   sah@srrc.gov.tw
SRRC, No.1 R&D Rd VI, SBIP, Hsinchu 300, Taiwan

Sajaev, Vadim V   sajaev@bnl.gov
ANL, ASD/APS, ANL, bldg 401, South Cass Av, Argonne, IL, 60439, USA

Sakai, Fumio   Fmo_Sakai@shi-co-jp
Sumitomo Heavy Industries Ltd, 2-1-1 Yatocho, Tamashi, Tokyo, 188-8585, Japan

Saleh, Ned R   nedsaleh@umich.edu
CUOS/U. Michigan, 2200 Bonisteel, Ann Arbor, MI, 48109,

Salimov, Rustam   veis@inp.nsk.su
BINP, Industrial Accelerators Laboratory, 11, Ac. Lavrenyev ave., Novosibirsk, 630090, Russia

Samios, Nicholas P.   samios@bnl.gov
Physics Dept., Bldg. 510A, BNL, Upton, NY, 11973-5000, USA

Sampayan, Steve   houston2@llnl.gov
Lawrence Livermore National Laboratory, 7000 East Ave., P.O. Box 808, Livermore, Ca., 94551-0808, USA

Sampson, William B   votruba@bnl.gov
BNL, Building 902A, Upton, NY, 11973, USA

Sandberg, Jon   sandberg@bnldag.bnl.gov
Brookhaven National Laboratory, AGS Dept., Upton, NY, 11973, USA

Sander, Oscar R   osander@lanl.gov
LANL, LANSCE Division, MS H838, PO Box 1663, Los Alamos, NM, 87545, USA

Sanders, Ralph T.   rsanders@bnldag.bnl.gov
Brookhaven National Laboratory, P.O. Box 5000, AGS Dept., Bldg. 911-A, Upton, NY, 11973, USA

Sasao, Mamido   sasao@nifs.ac.jp
NIFS, Oroshi, Tokai, GIFU, 509-5292, Japan

Sassowsky, Manfred   Manfred.Sassowsky@cern.ch
CERN, SL Division, Site Meyrin, Geneva 23, CH-1211, Switzerland

Sato, Hikaru   hikaru.sato@kek.jp
KEK, Accelerator Dep., 1-1 Oho, Tsukuba-shi, Ibaraki-ken, 305-0801, Japan

Satogata, Todd   satogata@bnl.gov
BNL, RHIC Project, P.O. Box 5000, Bldg. 1005S, Upton, NY, 11973-5000

Scandale, Walter   Walter.Scandale@cern.ch
CERN, LHC, 1211 Geneva 23 Switzerland, Geneva, Switzerland, 1211, Switzerland

Scanlan, Ron M.   magreen@lbl.gov
LBNL, Superconducting Magnet Program/AFRD, 1 Cyclotron Rd., MS 46-161, Berkeley, CA, 94720, USA

Scaramelli, Alberto A   Alberto.Scaramelli@cern.ch
CERN, CERN, Division ST, Geneve, 1211 Geneve 23, Switzerland

Schachter, Levi   pac99@bnl.gov
Technion, Dept of EE, Technion, Haifa, 32000, Israel

Schempp, Alwin   a.schempp@em.uni-frankfurt.de
Institut fur Angewandte Physik, Robert Mayer Str. 2-4, D-60054 Frankfurt,
D-60054, Germany

Schieler, Harald   schieler@anka.fzk.de
Forschungszentrum Karlsruhe, ANKA (PEA), Postfach 3640, Karlsruhe,
D-76021, Germany

Schmalzle, Jesse D   Jesses@bnl.gov
BNL, Building 902A, Upton, NY, 11973, USA

Schmor, Paul W.   SCHMOR@TRIUMF.CA
TRIUMF, 4004 Wesbrook Mall, Vancouver, British Columbia, V6T 2A3,
Canada

Schnase, Alexander   A.Schnase@fz-juelich.de
Forschungszentrum Juelich, Institut fuer Kernphysik, Leo-Brand-Str.,
Juelich, Nordrhein-Westfalen, D-52425, Germany

Schneider, J. David   jdschneider@lanl.gov
LANL, APT-TPO, P.O. Box 1663, MS H836, Los Alamos, New Mexico,
87545, USA

Schneider, William   schneide@jlab.org
TJNAF, 12000 Jefferson Avenue, Newport News , VA, 23606, USA

Schoessow, Paul   pvs@hep.anl.gov
Argonne National Laboratory, 9700 S Cass Ave, 362/HEP, Argonne, IL,
60439, USA

Schrage, Dale L.   dls@lanl.gov
Los Alamos National Laboratory, MS H817, Los Alamos, NM, 87545,
USA

Schreiber, Siegfried R   siegfried.schreiber@desy.de
DESY, FDET, Notkestr. 85, Hamburg, Germany

Schriber, Stanley O   sschriber@lanl.gov
LANL, MS H845, P.O. Box 1663, Los Alamos, New Mexico, 87545, USA

Schroeder, Carl B   carl@physics.berkeley.edu
University of California - Berkeley, LBNL, MS 71-259, 1 Cyclotron Road,
Berkeley, CA, 94720, USA

Schuett, Petra   schuett@temf.tu-darmstadt.de
Technische U. Darmstadt, FB 18, Theory of Electromagnetic Fields,
Schlossgartenstrasse 8, Darmstadt, D-64289, Germany

Schulte, Daniel   Daniel.Schulte@cern.ch
CERN, CERN, PS-LP, Geneva 23, CH-1211, Switzerland

Schultheiss, Carl M.   carls@bnl.gov
Brookhaven National Laboratory, Building 817, Upton, NY, 11973, USA

Schulze, Martin   schulz@gat.com
General Atomics, LANL MS-H816, Los Alamos, NM, 87545, USA

Schumburg, Niels F   schumburg@bnl.gov
Brookhaven National Laboratory, BLD 911C, Upton, NY, 11973, USA

Schwartz, Charles   csch@aps.anl.gov
ANL, RF Group, Accelerator Systems Division, 9700 S. Casss, 401,
Argonne, IL, 60439, USA

Schwarz, Carl   c.schwarz@elsevier.nl
Elsevier Science, Physics & Astronomy Department, P.O. Box 103,
Amsterdam, 1000 AC, Netherlands

Schönauer, Horst O.   Horst.Schonauer@cern.ch
CERN, PS Division, Geneva 23, Switzerland, CH 1211,

Scott, John P.   Scott.john@mayo.edu
Mayo Clinic, Mayo Clinic, 200 First Street, SW, Rochester, MN, 55905

Sebek, James J   sebek@slac.stanford.edu
SLAC, SSRL/SLAC MS99, PO Box 4349, Stanford, Ca, 94309, USA

Seeman, John T   seeman@slac.stanford.edu
SLAC, Accelerator,Technical, 2575 Sand Hill Road, MS 18, Menlo Park,
CA, 94025, USA

Seidel, Mike G   Mike.Seidel@desy.de
DESY, Machine Department, Notkestr. 85, Hamburg, 22603, Germany

Seidl, Peter A   paseidl@lbl.gov
LBNL, AFRD, 47-112, Berkeley, CA, 94720, USA

Sellyey, William c   sellyey@lanl.gov
LANL, LANSCE-1, TA-53, Bldg-6, MS: H808, Los Alamos (County),
NM, 87545, USA

Semertzidis, Yannis   semertzidis@bnl.gov
Physics Dept., Bldg. 510A, Brookhaven National Laboratory, PO Box
5000, Upton, NY, 11973, USA

Sen, Tanaji   tsen@fnal.gov
Fermilab, MS 220, P.O. Box 500, Batavia, IL, 60510, USA

Senichev, Yurij V.   senichev@dfi.aau.dk
Aarhus University, ISA, Ny Munkegade, Aarhus C, DK-8000, Denmark

Senti, Mark W   msenti@gsma.com
Advanced Magnet Lab., Inc., 2730 Kirby Ave. - Bldg. 5, Palm Bay, FL 32905

Sereno, Nicholas S   sereno@aps.anl.gov
ANL, Advanced Photon Source ASD, 9700 S. Cass Ave. Bldg 401, Argonne,
IL, 60439-4800, USA

Sergeev, Anatoly P   apserg@sunse.jinr.ru
Joint Institute for Nuclear Research, Particle Physics Laboratory, Dubna,
Moscow region, 141980, Russia

Serio, Mario   mario.serio@lnf.infn.it
INFN - Frascati, LNF, Div. Acc., C.P. 13, Frascati (RM), 00044, Italy

Serov, Valery   sharamen@al20.inr.troitsk.ru
Institute of Nuclear Research of the Hungarian Academy of Sciences, Linear
Accelerator Division, 60-th October Anniversary Prospect, 7a, Moscow,
117312, Russia

Serre, Christian A.   Christian.Serre@cern.ch
CERN, PS Division, CERN, 1211 Geneva 23, Switzerland

Sery, Andrey A   sery@fnal.gov
FNAL, Beams Division, MS 221, PO Box 500, Batavia, IL, 60510, USA

Sessler, Andrew M   amsessler@lbl.gov
LBNL, Center for Beam Physics, Staff, 1 Cyclotron Road MS 71-259,
Berkeley, CA, 94720, USA

Shang, Lei   lshang@ustc.edu.cn
National Synchrotron Radiation Lab, USTC, P.O.Box 6022, Hefei, Anhui,
230029, PR China

Shapiro, Michael A   shapiro@psfc.mit.edu
Plasma Science and Fusion Center, MIT, Plasma Science and Fusion Center,
Bldg NW16-172, MIT, Cambridge, MA, 02139, USA

Sharamentov, Sergey   sharamen@al20.inr.troitsk.ru
Institute for Nuclear Research of the Russian Academy of Science, Linear
Accelerator Division, 60-th October Anniversary prospect 7a, Moscow,
117312, Russia

Sharma, Sushil   sharma@aps.anl.gov
ANL, ASD, 9700 S. Cass Avenue, Bldg. 401, Argonne, IL, 60439, USA

Sharp, William M   wsharp@llnl.gov
LLNL / LBNL, LLNL, P. O. Box 808 L-645, Livermore, CA, 94551, USA

Shasharina, Svetlana G.   sveta@txcorp.com
Tech-X Corporation, Tech-X Corporation, 1280 28th Street, Suite 2, Boulder,
Colorado, 80303, USA

Shatunov, Yuri M.   shatunov@inp.nsk.su
BINP, Budker Institute of Nuclear Physics, 11, Lavrentiev str., 630090,
Russia

Shea, Thomas J   shea@bnl.gov
BNL, Building 1005, Upton, NY, 11973, USA

Sheffield, Richard L   sheff@lanl.gov
LANL, LANSCE-4, MS H851, Los Alamos, NM, 87544, USA

Sheldrake, Ronald -   Ron.Sheldrake@eev.com
EEV, Thyratron Section, EEV Ltd., 106 Waterhouse Lane, Chelmsford,
Essex, CM1 2QU, United Kingdom

Shemyakin, Alexander V.   shemyakin@fnal.gov
FNAL, Beam Division, Fermilab, MS307, Batavia, IL, 60510, USA

Shen, Stewart   shen2@llnl.gov
LLNL, Mechanical Engineering, ATEG, P.O. Box 808, L-287, Livermore,
CA, 94550, USA

Shepard, Kenneth W.   kwshepard@anl.gov
ANL, Physics Division B203, 9200 South Cass Ave, Argonne, Il, 60439

Sheppard, John C.   jcs@slac.stanford.edu
SLAC, SLAC, P.O. Box 4349 M.S. #66, Stanford, CA, 94309, USA

Sheynin, Sam   Sam.Sheynin@gat.com
General Atomics, Electromagnetic Systems, 3550 General Atomics Court,
San Diego, California, 92121-1194, USA

Shiltsev, Vladimir D.   shiltsev@fnal.gov
FNAL, Beams Division, FNAL, PO Box 500, MS 221, Batavia, IL, 60510

Shintake, Tsumoru   tsumoru.shintake@kek.jp
KEK, Accelerator , 1-1 Oho, Tsukuba, Ibaraki, 305-0801, Japan

Shirai, Toshiyuki   shirai@kyticr.kuicr.kyoto-u.ac.jp
Kyoto U., Institute for Chemical Research, Gokasho, Uji, Kyoto , 611-0011,
Japan

Shoaee, Hamid   hamid@slac.stanford.edu
LAC, MS 46, P.O.Box 4349, Stanford, CA, 94309, USA

Shoaff, Phillip V.   shoaff1@llnl.gov
Lawrence Livermore National Lab, PO Box 808, L-287, Livermore, CA,
94551

Shu, Deming   shud@aps.anl.gov
ANL, APS/XFD, Bldg. 401 Room C1255, 9700 S. Cass Ave., Argonne, IL,
60439, USA

Shuman, Derek B   DBShuman@lbl.gov
LBNL, Mailstop 47-112, 1 Cyclotron Rd, Berkeley, CA, 94720, USA

Shvets, Gennady   gena@pppl.gov
Princeton University, Plasma Physics Laboratory, Forestall Campus, Princeton, NJ, 08543, USA

Sieber, Thomas A   Thomas.Sieber@physik.uni-muenchen.de
University of Munich, Sektion Physik, Am Coulombwall 1, Garching, Bavaria, 85748, Germany

Siemann, Robert H   siemann@slac.stanford.edu
SLAC, SLAC, MS 07, 2575 Sand Hill Rd, Menlo Park, CA, 94025, USA

Sigg, Peter K   Peter.Sigg@psi.ch
Paul Scherrer Institut, RF/ABE/GFA, WBGA/25, Villigen , CH-5232, Switzerland

Sikora, John P   jps@lns62.lns.cornell.edu
Cornell U., Dept. of Nuclear Studies, Wilson Laboratory, Cornell University, Ithaca, NY, 14853, USA

Silvestrov, Grigory I.   G.I.Silvestrov@inp.nsk.su
BINP, 11 Lawrentiew pr., Novosibirsk, 630090, Russia

Simon, Daniel J.   Daniel.Jean.Simon@cern.ch
CERN, PS Division, CERN, 1211 Geneva 23, Switzerland

Simonin, Alain   simonin@drfc.cad-cea.fr
CEA, CE Caderache DRFC-SCCP, 13105 St Paul-les Duranie, FRANCE 13108, France

Sinclair, Charles K.   sinclair@jlab.org
TJNAF, Accelerator Division, 12000 Jefferson Avenue, Newport News, VA, 23606, USA

Singh, Om V   singh@aps.anl.gov
ANL, ASD/401, 9700 S. Cass Avenue, Argonne, Illinois, 60439-4800

Skelly, Joseph   skelly@bnl.gov
BNL, AGS, P.O. Box 5000, 911C, Upton, NY, 11973, USA

Slater, James M.   jmslater@dominion.llumc.edu
Loma Linda University Medical Center, Department of Radiation Medicine, CSP, A-1010, 11175 Campus Street, Loma Linda, Ca., 92345

Smart, Loralie A   loralie@bnl.gov
BNL, RHIC Project, Building 830M, Upton, NY, 11973-5000, USA

Smedley, John M   smedley@bnl.gov
BNL, Instrumentation, Bldg 535B, Upton, NY, 11973, USA

Smirnov, Alexei V.   sav@smisav.msk.ru
Kurchatov Institute, KSRS, Bazovskaya St., #14, Apt. 228, Kurchatov Sq., #1, RRC , Moscow, Russian Federation, 127635, Russia

Smith, H. Vernon   hvsmith@lanl.gov
LANL, APT/TPO, Mail Stop H838, P.O. Box 1663, Los Alamos, NM, 87545, USA

Smith, Robert J   r.j.smith@dl.ac.uk
Daresbury Laboratory, CLRC Daresbury Laboratory, Keckwick Lane Daresbury, Warrington, Cheshire, WA44AD, Ukraine

Smith, Gary A.   smith8@bnl.gov
Brookhaven National Laboratory, Bldg. 911-A, P.O. Box 5000, Upton, NY, 11973, USA

Smith, John D   jsmith@bnl.gov
BNL, NSLS, Bldg. 725B, Brookhaven Ave., Upton, NY, 11973, USA

Smith, Kevin S   ksmith@bnl.gov
BNL, AGS RF, Bldg 911B, Upton, NY, 11973, USA

Smolyakov, Nikolay V.   nick@sci.hiroshima-u.ac.jp
Hiroshima University, Particle Beam Science Laboratory,, Faculty of Science, Hiroshima University, , Kagamiyama 1-3-1, Higashi-Hiroshima, 739-8526, Japan

Sokolowski, Jerzy S.   Fnsoko@weizmann.weizmann.ac.il
The Weizmann Institute of Science, Particle physics, Rehovot, Israel, 76100, Israel

Solomon, Lorraine   lsolomon@bnl.gov
BNL-NSLS, Bldg. 725D, Upton, NY, 11973, USA

Solyak, Nikolay Antonovich   solyak@vlepp.serpukhov.su
BINP, Protvino, Moscow region, 142284, Russia

Song, Joshua J.   jsong@aps.anl.gov
ANL, APS, 9700 S. Cass Av. 401, Argonne, IL, 60439, USA

Song, Jinhu   jinhu@bnl.gov
BNL, NSLS, Building 725B, P.O. Box 5000, Upton, NY, 11973, USA

Sonnemann, Florian   Florian.Sonnemann@cern.ch
CERN, LHC Division, CERN, Geneva 23, CH-1211, Switzerland

Sonnendrucker, Eric   ESonnendrucker@lbl.gov
LBNL, MS 47-112, 1 cyclotron Road, Berkeley, CA, 94720, USA

Soukas, Anastasios   soukas@bnl.gov
Brookhaven National Laboratory, P.O. Box 5000, Building 911-A AGS Department, Upton, NY, 11973, USA

Soutome, Kouichi   soutome@spring8.or.jp
Japan Synchrotron Radiation Research Institute(JASRI, SPring-8), Accelerator Div., JASRI, 323-3, Mikazuki, Sayou-gun, Hyogo, 679-5198, Japan

Spalek, George   spalek@gat.com
General Atomics, 1311 Lejano Lane, Santa Fe, Nm, 87501, USA

Spentzouris, Panagiotis   spentz@fnal.gov
FNAL, Computing Division/PAT, P.Spentzouris, MS234, POBOx 500, Batavia, IL, 60510, USA

Spentzouris, Linda K   klamp@fnal.gov
FNAL, Beams Division, L.Spentzouris, MS306, PoBox 500, Batavia, IL, 60510, USA

Spiller, Peter   P.Spiller@gsi.de
GSI, Beschleunigerentwicklung, Planckstr. 1, Darmstadt, 61267, Germany

Sprangle, Phillip A   sprangle@ppd.nrl.navy.mil
Naval Research Laboratory, Plasma Physics Division, 4555 Overlook Avenue, S.W., Washington DC, 20375, USA

Spyropoulos, Vassilios   vspyro@mail.ariadne-t.gr
Medical Instrumentation Technology Department, TEI Athens, Agiou Spyridonos Street, Egaleo, Athens, GR 12210, Greece

Srinivasan-Rao, Triveni   triveni@bnl.gov
BNL, Instrumentation Division, Bldg. 535 B, Upton, NY, 11973, USA

Staats, Joachim   staats@temf.tu-darmstadt.de
Technische U. Darmstadt, Institut fuer Hochfrequenztechnik, FG Theorie Elektromagnetischer Felder, Schlossgartenstrasse 8, Darmstadt, 64289, Germany

Staples, John W   JWStaples@lbl.gov
Accelerator and Fusion Research Division, Building 71, Room 205, Lawrence Berkeley National Laboratory, Berkeley, California, 94720, USA

Stassen, Rolf   r.stassen@fz-juelich.de
Forschungszentrum Jülich, IKP / COSY, Postfach 1913, Jülich, 52425, Germany

Steck, Markus   M.STECK@GSI.DE
GSI, ESR, Planckstr. 1, Darmstadt, D-64291, Germany

Sten, Stewart   sten2@llnl.gov
LLNL, L-287 LLNL, Livermore, CA, 94550, USA

Steski, Dannie B.   STESKI@bnl.gov
BNL, AGS Dept., Bldg. 901A, 59 Cornell Avenue, Upton, NY, 11973-5000

Stevens, Alan   a.f.stevens@rl.ac.uk
Rutherford Appleton Laboratory, ISIS Facility, Linac/RFQ Group, , Room G19, Bld. R2, Chilton, Didcot, Oxfordshire, OX11 0QX, United Kingdom

Stover, Gregory D.   gdstover@lbl.gov
LBNL, Advance Light Source - Electronics Engineering, M/S 46-125, 1 Cyclotron Rd., Berkeley, Ca, 94720, USA

Strasburg, Sean D   sstrasbu@pppl.gov
Princeton Plasma Physics Laboratory, Sean Strasburg, The Graduate College, Princeton University, NJ, 08543, USA

Stratienko, Volodymyr O.   bulyak@kipt.kharkov.ua
NSC KIPT, 1, Academicheskaya Str, Kharkov, UA-310108, Ukraine

Strauss, Bruce P   bruce.strauss@science.doe.gov
DOE, 14311 Cartwright Way, North Potomac, MD, 20878-4810, USA

Stringfield, Ray M   stringfield_r@lanl.gov
LANL, LANSCE Division, Mail stop H851, Los Alamos , NM, 87545, USA

Strubin, Pierre M   Pierre.Strubin@cern.ch
CERN, LHC-VAC, GENEVA 23, CH 1217, Switzerland

Sugahara, Jun   jun@tokai.t.u-tokyo.ac.jp
NERL,Graduate School of Engineering,University of Tokyo, 2-22 Shirakara,Shirane, , Tokai,Naka, Ibaraki, 319-1106, Japan

Suk, Hyyong   suk@stout.physics.uccla.edu
Department of Physics, University of California at Los Angeles, 405 Hilgard Ave, Los Angeles, Ca, 90095, USA

Suller, Victor P   suller@DL.AC.UK
Daresbury Laboratory, Keckwick Lane, Warrington, Cheshire, WA44AD, Ukraine

Sullivan, Michael K   Sullivan@SLAC.Stanford.edu
SLAC, MS 17, P.O. Box 4349, Stanford, CA, 94309, USA

Sun, Yin-e   yinesun@midway.uchicago.edu
Univ. of Chicago, 1414 E. 59th. St., Rm. 719, Chicago, IL, 60637, USA

Sun, Baogen   bgsun@ustc.edu.cn
NSRL, USTC, Accelerator, P.O.Box 6022, Hefei, Anhui 230029, P.R.China, Hefei, Anhui, 230029, China, Peoples Republic of

Sundelin, Ronald M   sundelin@jlab.org
TJNAF, Office of Technical Performance, MS12A3, 12000 Jefferson Avenue, Newport News, VA, 23606, USA

Sura, Jozef   sura@ipj.gov.pl
Soltan Institute for Nuclear Studies, Swierk, Poland, Accelerators Physics Department P-10, 05-400 Otwock-Swierk, Poland, Otwock, Poland

Sutter, David F.   hep-tech@science.doe.gov
DOE, 1510 Blue Meadow Road, Potomac, MD, 20854, USA

Swenson, Donald A   DASwenson@aol.com
Linac Systems, 2167 N. Highway 77, Waxahachie, TX, 75165, USA

Syphers, Michael J — syphers@fnal.gov
FNAL, M.S. 341, Fermilab, P.O. Box 500, Batavia, IL, 60510, USA

Tajima, Tsuyoshi — tsuyoshi.tajima@kek.jp
KEK, Accelerator Facility, Oho 1-1, Tsukuba, Ibaraki, 305-0801, Japan

Takahashi, Hiroshi — takahash@bnl.gov
BNL, DAT, Bldg. 475 B, P.O. Box 5000, Upton, NY, 11973-5000, USA

Takanaka, Masao — takanaka@insac7.tanashi.kek.jp
RIKEN, MUSES project, Hirosawa 2-1, Wako-shi, 351-0198, Japan

Takayama, Yasuhiro — takayama@phys.metro-u.ac.jp
Department of Physics, Tokyo Metropolitan, 1-1 Minami-Ohsawa,
Hachioji-shi, Tokyo, 192-0397, Japan

Takeshi, Toyama — takeshi.toyama@kek.jp
KEK, Accelerator Department, Oho 1-1, Tsukuba, Ibaraki , 305, Japan

Takeuchi, Takeshi — takeuchi@rcnp.osaka-u.ac.jp
Konan University, Department of Physics, Okamoto 8-9-1, Higashinada-
ku, Kobe, Hyogo, Japan

Tallerico, Thomas N — tallerico@bnl.gov
BNL, AGS Dept., Building 911B, Upton, NY, 11973, USA

Tallerico, Paul — tallerico@lanl.gov
Los Alamos Nat. Lab, PO Box 1663, MSH827, Las Almos, NM, 87544

Talman, Richard M. — talman@lns62.lns.cornell.edu
Cornell U., 309 Winthrop Dr., Ithaca, NY, 14850, USA

Tanabe, Toshiya — ttanabe@postman.riken.go.jp
RIKEN, RI-Beam Factory Project Office, 2-1 Hirosawa, , Wako, Saitama,
351-0198, Japan

Tanabe, Eiji — aetaus@webjapan.com
AET, 20370 Town Center Lane, Suite 252, Cupertino, CA, 95014, USA

Tanaka, Hitoshi — tanaka@spring8.or.jp
Japan Synchrotron Radiation Research Institute(JASRI, SPring-8),
Accelerator Div., JASRI, 323-3, Mikazuki, Sayou-gun, Hyogo, 679-5198,
Japan

Tang, Johnny Y — jtang@bnl.gov
Brookhaven National Lab, NSLS Bldg. 725B, Upton, NY, 11973-5000

Tang, Yong-nian — yntang@bnl.gov
NSLS, Bldg 725B, NSLS, Brookhaven National Lab., Upton, NY, 11973

Taniuchi, Tsutomu — taniuchi@spring8.or.jp
SPring-8, Accelerator Division, 323-3, Mihara, Mikazuki, Sayo-gun,
Hyogo, 679-5198, Japan

Tantawi, Sami C. — tantawi@SLAC.Stanford.EDU
SLAC, MS-26, P.O. Box 4349, Stanford, CA, 94309, USA

Tavares, Pedro F. — PEDRO@LNLS.BR
LNLS, Accelerator Division , CX Postal 6192, Campinas, Sao Paulo ,
13083-970, Brazil

Taylor, Andrew — A.D.Taylor@rl.ac.uk
ISIS Facility, Rutherford Appleton Laboratory, Chilton, Didcot, Oxon,
OX11 0QX, United Kingdom

Taylor, Thomas M — tom.taylor@cern.ch
CERN, LHC, Geneva 23, Geneva, 1211, Switzerland

Tazzari, Sergio — tazzari@roma2.infn.it
Univ. ROMA II and INFN, Dipartimento di Fisica, Universita di Roma -
Tor Vergata , V.le della Ricerca Scientifica 1, ROMA, RM, 00133, Italy

Tecchio, Luigi B. — tecchio@lnl.infn.it
INFN-Laboratori Nazionali di Legnaro, Accelerator Division, Via Romea,
4, Legnaro (PD), 35020, Italy

Tecker, Frank — tecker@fnal.gov
FNAL, MS #341, P.O. box 500, Batavia, IL, 60510, USA

Temkin, Richard J — temkin@psfc.mit.edu
MIT, Plasma Science and Fusion Center, MIT Building NW16-186, 167
Albany St., Cambridge, MA, 02139, USA

Tenenbaum, Peter — quarkpt@slac.stanford.edu
SLAC, SLAC Mail Stop 66, PO Box 4349, Stanford, California, 94309

Teng, Lee C. — teng@aps.anl.gov
ANL, Advanced Photon Source, 9700 S. Cass Ave., Argonne, IL, 60439

Tepikian, Steven — tepikian@bnl.gov
BNL, RHIC, P.O. Box 5000, Bldg. 1005S, Upton, NY, 11973-5000

Terebilo, Andrei G — terebilo@ssrl.slac.stanford.edu
University of California Los Angeles, Physics, 846 Riley Dr, Albany, CA,
94706, USA

Terechkine, Iouri — terechki@fnal.gov
FNAL, Technical Division / Engineering and Fabrication, P.O. Box 500,
M.S. 316, Batavia, IL, 60510, USA

Terrell, Robert — terrell@jlab.org
TJNAF, 12000 Jefferson Ave., MS 89, Newport News, VA, 23606, USA

Thomae, Rainer W. — rwthomae@lbl.gov
LBNL, Accelerator and Fusion Division, 1 Cyclotron Road, MS 5-132,
Berkeley, CA, 94720, USA

Thomas, Richard A — thomas@bnl.gov
BNL, Building 902A, Upton, NY, 11973, USA

Thomas, Sherry L — sthomas@jlab.org
TJNAF, Accelerator Division, 12000 Jefferson Avenue, Mail Stop 58,
Newport News, VA, 23606, USA

Thompson, Patrick A. — thompson@bnl.gov
BNL, RHIC Project, P.O. Box 5000, Bldg. 1005S, Upton, NY, 11973-5000

Thuot, Mike E. — mthuot@lanl.gov
LANSCE-8, MS H820, Los Alamos National Laboratory, P.O. Box #1663,
MS H820, Los Alamos, NM, 87545, USA

Tiefenback, Michael G. — tiefen@jlab.org
TJNAF, Accelerator Division, 12000 Jefferson Avenue, Mail Stop 6A,
Newport News, Virginia, 23606, USA

Tighe, Richard C. — rtighe@slac.stanford.edu
SLAC, MS 33, PO Box 4349, Stanford, CA, 94309, USA

Tilley, Kevin — k.tilley@rl.ac.uk
ISIS, Rutherford Appleton Laboratory, Chilton, Didcot, Oxfordshire, OX11
0QX, United Kingdom

Timm, Martin — timm@temf.tu-darmstadt.de
Technische U. Darmstadt, Theorie elektromagnetischer Felder,
Schlossgartenstrasse 8, Darmstadt, D-64289, Germany

Ting, Antonio C. — ting@ppd.nrl.navy.mil
Naval Research Laboratory, 4555 Overlook Ave. SW, Washington, DC,
20375, USA

Tkatchenko, Andre — tkatchen@ipno.in2p3.fr
Institut de Physique Nucleaire, Service RDA.FE, Universite Paris Sud ,
ORSAY, 91406 ORSAY CEDEX, France

Todd, Alan M — todd@grump.com
Advanced Energy Systems, 29 Airpark Road, Princeton, New Jersey, 08540,
USA

Tolmachev, Nikolaj G. — bulyak@kipt.kharkov.ua
TMM, 7 Chkalova Str, Kharkov, 310070, Ukraine

Tommasini, Davide — davide.tommasini@cern.ch
CERN, LHC-MMS, GENEVA 23, 1211, Switzerland

Tooker, Joseph F. — tooker@gat.com
General Atomics, 2237 Trinity Dr., Los Alamos, NM, 87544, USA

Tor, Raubenheimer O. — tor@slac.stanford.edu
SLAC, P.O. Box 4349, Stanford, CA, 94309, USA

Torikoshi, Masami — torikosi@nirs.go.jp
NIRS, Anagawa 4-9-1, Inage, Chiba, Chiba, 263-8555, Japan

Tosi, Lidia — tosi@elettra.trieste.it
Sincrotrone Trieste, s.s. 14 - KM 163.5 - in Area Science Park, Basovizza,
Trieste, 34012, Italy

Towne, Nathan A — towne@bnl.gov
BNL, National Synchrotron Light Source, Bldg 725B, Upton, NY, 11973

Toyama, Takeshi — takeshi.toyama@kek.jp
KEK, Accelerator Department, Oho 1-1, tsukuba, Ibaraki, 305, Japan

Trakhtenberg, Emil M. — emil@aps.anl.gov
ANL, APS, 9700 S. Cass Ave., Argonne, IL, 60439, USA

Trbojevic, Dejan — dejan@bnl.gov
BNL, RHIC Project, P.O. Box 5000, Bldg. 1005S, Upton, NY, 11973-5000,
USA

Tremaine, Aaron — tremaine@physics.ucla.edu
UCLA, Department of Physics, Knudsen Hall 1-129, 405 Hilgard, Los
Angeles, California, 90095, USA

Trendler, Robert C. — trendler@fnal.gov
FNAL, Particle Physics Division, M.S. 222, P.O. Box 500, Batavia, Illinois,
60510-0500, USA

Troha, Anthony L. — altroha@ucdavis.edu
ILSA at LLNL & Dept. Applied Science, UC Davis, L-411, Lawrence
Livermore National Laboratory, 7000 East Avenue, Livermore, CA, 94550

Tsoupas, Nicholaos — tsoupas@bnl.gov
AGS Dept., Bldg. 911B, Brookhaven National Laboratory, Upton, NY 11973

Tsuchiya, Kimichika — tsuchiya@mail.kek.jp
KEK, Photon Factory,Light source division, 1-1 OHO TSUKUBA,
IBARAKI ,JAPAN, Tsukuba, Ibaraki, 305-0801, Japan

Tsukishima, Chihiro — tsuki@wel.crl.melco.co.jp
Mitsubish Electric Corporation, Advanced R&D Center, 8-1-1 tsukaguch-
honmachi, Amagasaki, Hyogo pref., Japan

Tung, Louann — tung2@llnl.gov
Lawrence Livermore National Laboratory, Accelerator Technologies
Engineering Group, P.O. Bosx 808, L-287, Livermore, CA, 94550, USA

Tuozzolo, Joseph — tuozzolo@bnldag.bnl.gov
AGS Dept., Bldg. 911B, Brookhaven National Laboratory, Upton, NY 11973

Tur, Yuriy D.   tur@nik.kharkov.na
  NSCKIPT, NSC KIIPT, 1 Akadmicheskaya, 310108 Kharkov, Ukraine
Turner, Stuart   Stuart.Turner@cern.ch
  AC Division, CERN, 1211 Geneva 23, Switzerland
Uesaka, Mitsuru   uesaka@tokai.t.u-tokyo.ac.jp
  U. of Tokyo, Nuclear Engineering Research Laboratory, 2-22, Shirakata-
  Shirane, Tokai, Naka, Ibaraki, 319-1106, Japan
Umezawa, Masumi   umezawa@erl.hitachi.co.jp
  Hitachi,Ltd., Power and Industrial Systems R and D Division, 7-2-1,
  Omika-cho, Hitachi-shi, Ibaraki-ken, 319-1221, Japan
Unser, Klaus B.   unser@bergoz.com
  Bergoz Instrumentation, Rue du Jura, Crozet, (Ain), 01170, France
Ursic, Rok   rok@i-tech.si
  Instrumentation Technologies, Srebrnicev Trg 4a, Solkan, Slovenia, 5250,
Uythoven, Jan   jan.uythoven@cern.ch
  CERN, SL - Division, CH 1211 Geneva 23, Switzerland
van der Geer, Bas   gpt@pulsar.nl
  Pulsar Physics, De Bongerd 23, Soest, NL, 3762 XA, Netherlands
Vaerenbergh, Pierre   vanvaer@esrf.fr
  ESRF, IDs Group, Av. des Martyrs; BP220, Grenoble Cedex 09, 38043,
  France
Valdiviez, Robert   valdiviez@lanl.gov
  LANSCE Division, LANL, M/S H817, Los Alamos, New Mexico, 87545,
  USA
Valentini, Marco   marco.valentini@cern.ch
  PS/LP 18-2-44 L19910, CERN, Geneva 23, 1211, Switzerland
Valero, Saby   valero@ccars.in2p3.fr
  CEA, DSM/DAPNIA/SEA Saclay, Gif-sur-Yvette CEDEX, 91191,.France
Van Zeijts, Johannes   johannes@bnl.gov
  BNL, RHIC Project, P.O. Box 5000, Bldg. 1005S, Upton, NY, 11973-5000
Van Asselt, Willem   VANASSELT@BNL.GOV
  BNL, AGS Dept., Bldg.. 911B, Upton, NY, 11973-5000
Van Bibber, Karl A.   kvanbibber@llnl.gov
  Physics & Space Technology Directorate, L-050, LLNL, P.O. Box 808,
  Livermore, CA, 94550, USA
Van Steenbergen, Arie   avanst@bnl.gov
  BNL, NSLS, Building 725B, Upton, NY, 11973, USA
Variale, Vincenzo   vincenzo.variale@ba.infn.it
  INFN-Bari, INFN-sez. Bari, Via Amendola 173, Bari, 70126, Italy
Vasserman, Isaac B.   isaac@aps.anl.gov
  ANL, APS, 9700 S. Cass Ave., Argonne, IL, 60439, USA
Veness, Raymond J M   veness@cern.ch
  CERN, LHC Division, CERN, Geneva 23, CH-1211, Switzerland
Venturini, Marco   venturin@physics.umd.edu
  Physics Department, University of Maryland, College Park, MD, 20742
Verbeke, Jerome M   JMVerbeke@lbl.gov
  LBNL, Ion Beam Technology, MS 5-101, 1 Cyclotron Road, Berkeley,
  CA, 94720, USA
Verdier, Andre   andre.verdier@cern.ch
  CERN, SL Division, Geneva SWITZERLAND, 1211 MEYRIN,
  Switzerland
Verzilov, Viktor   verzilov@lnf.infn.it
  INFN - Frascati, Laboratori Nazionali di Frascati dellINFN, Via E.Fermi
  40, Frascaty (RM), 00044, Italy
Vetter, Arthur M   arthur.m.vetter@boeing.com
  Boeing, Space and Communications Group, Free Electron Laser Program,
  P.O. Box 3999, MC 2T-50, Seattle, Washington, 98124-2499, USA
Vier, David C.   dvier@ucsd.edu
  U of California - San Diego, Department of Physics 0319, 9500 Gilman
  Dr., La Jolla, CA, 92093-0319, USA
Vignola, Gaetano   gaetano.vignola@lnf.infn.it
  INFN - Frascati, LNF, Div. Acc., C.P. 13, Frascati (RM), 00044, Italy
Virostek, Steve P.   spvirostek@lbl.gov
  LBNL, One Cyclotron Road, M/S 71-259, Berkeley, CA, 94549, USA
Vlieks, Arnold E.   aev@slac.stanford.edu
  SLAC, MS-33, 2575 Sand Hill Road, Menlo park, CA, 94025, USA
Vogel, Hanspeter   vogel@accel.de
  ACCEL Instruments GmbH, ACCEL Instruments GmbH, Friedrich-Ebert-
  Straße 1, Bergisch Gladbach, Germany, D-51429, Germany
Volfbeyn, Paul   psvolfbeyn@lbl.gov
  LBNL, MS 71-259, 1 Cyclotron Rd, Berkeley, CA, 94720, USA
Volkov, Vladimir N   V.N.Volkov@inp.nsk.su
  BINP, Radiophysics Division, RF Group, Lavrentev Ave., 11, Novosibirsk,
  630090, Russia

Volkov, Valery I.   volkov@sunhe.jinr.ru
  Joint Institute for Nuclear Research, Laboratory of High Energies, Laboratory of
  High Energies, Joint Institute for Nuclear Research, Dubna, Moscow Region,
  141980, Russia
Von Holtey, Georg   georg.von.holtey@cern.ch
  CERN, SL Division, CERN Meyrin, CH-1211 GENEVE 23, Switzerland
Vorobiev, Leonid G.   vorobiev@nscl.msu.edu
  NSCL, NSCL, Michigan State University, East Lansing, MI, 48824-1321
Voss, Gustav-Adolf   ga.voss@mail.desy.de
  DESY, Notuestr.85, DESY 22603 HH, HH, 22603 HH, Germany
Vsevolozhskaya, Tatiana A.   T.A.Vsevolozhskaya@inp.nsk.su
  BINP, 11 Lawrentiew pr., Novosibirsk, 630090, Russia
Vuola, Olli   olli.vuola@cern.ch, cc: christine.sivori@cern.ch
  CERN, CERN/EP, CH-1211 Geneva 23, Switzerland
Vysotskii, Vladimir I.   viv@vhome.kiev.ua
  Kiev Shevchenco U., Radiophysical Faculty, Vladimirskaya St. 64, Kiev,
  252033, Ukraine
Vysotskii, Vladimir I.   viv@vhome.kiev.ua
  Kiev Shevchenco U., Radiophysical Faculty, 64 Vladimirskaya st., Kiev,
  252033, Ukraine
Wait, Gary D   wait@triumf.ca
  TRIUMF, 4004 Wesbrook Mall , Vancouver, B.C., V6T 2A3, Canada
Waldron, William L   WLWaldron@lbl.gov
  Engineering Division, Lawrence Berkeley National Laboratory, One
  Cyclotron Road, MS 71J, Berkeley, CA, 94720, USA
Walker, Ian J   ian@gmw.com
  GMW Associates, PO Box 2578, Redwood City, CA, 94064, USA
Walstrom, Peter L.   walstrom@lanl.gov
  Los Alamos National Laboratory, MS H808, Los Alamos, NM, 87545, USA
Walters, Dean R   drw@aps.anl.gov
  ANL, Advanced Photon Source, 9700 South Cass Ave., Bld #401, Argonne,
  ILL, 60439, USA
Wan, Weishi   wan@fnal.gov
  FNAL, Beams Division/BeamPhysics Dept., M. S. 220, Batavia, IL, 60510-
  0500,
Wanderer, Peter J   wanderer@bnl.gov
  BNL, RHIC Project, Building 902, PO Box 5000, Upton, NY, 11973-5000
Wang, Haipeng   haipeng@bnl.gov
  BNL, Center for Accelerator Physics, Building 901A, Physics Department,
  Upton, NY, 11973-5000, USA
Wang, Fusheng   wangfsh@ee.ucla.edu
  UCLA, 3290 Sawtelle Blvd, #203, Los Angeles, CA, 90066, USA
Wang, Fuhua   fwang@bates.mit.edu
  MIT, Bates Linear Accelerator Center, Post Office Box 846, Middleton , MA,
  01949, USA
Wang, Min-Huey   mhwang@srrc.gov.tw
  SRRC, Light Source Division, No. 1 R&D Road VI, Hsinchu SBIP, Hsinchu,
  30077, Taiwan
Wang, Yi-Ming   ymwang@lanl.gov
  LANL, P.O. Box 1663, MS H827, Los Alamos, NM, 87545, USA
Wang, Chunxi   wangcx@SLAC.Stanford.EDU
  SLAC, P.O. Box 4349; Mail Stop 26, Stanford , CA, 94309, United States
Wang, Changbiao   beamlab@riviera.physics.yale.edu
  Yale University, Physics Department/WNSL, P.O. Box 208124, New Haven,
  CT, 06520-8124, USA
Wang, Juwen   jywap@SLAC.Stanford.EDU
  SLAC, MS 26, Stanford, CA, 94036, USA
Wang, Jiuqing   wangjq@post.kek.jp
  KEK, Accelerator Laboratory, 1-1 Oho, Tsukuba-shi, Ibaraki-ken, Tsukuba,
  Ibaraki, 305-0801, Japan
Wang, Ju   juw@anl.gov
  Argonne National Laboratory, 9700 S. Cass Avenue, ASD/401-C3244,
  Argonne, IL, 60439, USA
Wang, J.G.   jgwang@bnl.gov
  AGS, BNL, Bldg. 911B, Upton, NY, 11973, USA
Wang, Tai-Sen F   TWANG@LANL.GOV
  LANSCE-1 Group, MS H808, Los Alamos National Laboratory, Los
  Alamos, New Mexico, 87545, USA
Wang, Pingshen   wang@lps.cornell.edu
  Cornell U., Lab. Plasma Studies, 369 Upson Hall, Ithaca, NY, 14853, USA
Wang, Lifang   wanglf@svr.bimp.pku.edu.cn
  Institute of Heavy Ion Physics, Peking Univ., P. R. China, RF SC Group,
  IHIP, Peking Univ., Beijing, 100871, China, Peoples Republic of
Wang, Lisa   wang22@llnl.gov
  LLNL, Lawrence Livermore National Laboratory, 7000 East Ave. L-645,
  P.O.Box 808, Livermore, Ca, 94551-0808, USA

Wang, Xijie   xwang@bnl.gov
Building 725 C,NSLS, Brookhaven National Lab, Upton, NY, 11973, USA

Wang, Xiangqi   xwang@ssrl.slac.stanford.edu
National Synchrotron Radiation Lab, USTC, National Synchrotron
Radiation Lab, USTC, P.O.Box 6022, Hefei, Anhui, 230029, PR China

Wangler, Thomas P.   twangler@lanl.gov
LANL, LANSCE 1, MS-H817, Los Alamos, NM, 87545, USA

Washio, Masakazu   washiom@mn.waseda.ac.jp
Waseda University, Advanced Research Institute for Science and
Engineering, 3-4-1 Okubo, Shinjuku-ku, , Tokyo, 169-8555, Japan

Webber, Robert C   webber@fnal.gov
FNAL, Fermilab MS341, P.O. Box 500, Batavia, Illinois, 60510, USA

Weggel, Robert J   weggel@bnl.gov
Brookhaven National Laboratory, Building 901A, Upton, NY, 11973-5000

Wei, Jie   jwei@bnl.gov
BNL, RHIC Project, P.O. Box 5000, Bldg. 1005S, Upton, NY, 11973-
5000, USA

Weihreter, Ernst   weihreter@bessy.de
BESSY, Rudower Chaussee 5, Berlin, D-12489, Germany

Weir, John T.   weir2@llnl.gov
Lawrence Livermore National Laboratory, 7000 East Ave., P.O. Box 808,
Livermore, Ca., 94551-0808, USA

Weiss, Daniel   dweiss@bnl.gov
BNL, RHIC Project, Building 830, Room 24, Upton, NY, 11973-5000

Welch, James J   welch@lns.cornell.edu
Wilson Laboratory, Cornell University, Ithaca, NY, 14853, USA

Weng, Wu-Tsung   weng@bnl.gov
Brookhaven National Laboratory, AGS Dept. Bldg. 911B, P.O. Box 5000,
Upton, NY, 11973, USA

Westenskow, Glen A.   westenskow1@llnl.gov
Lawrence Livermore National Laboratory, 7000 East Ave. L-645, P.O.Box
808, Livermore, CA 94551-0808, USA

White, Gregory R   greg@slac.stanford.edu
Controls Software Group, MS 46, MCC, SLAC, 2575 Sand Hill Road,
Menlo Park, CA, 94025, USA

White, Karen S   karen@jlab.org
TJNAF, Accelerator Division, 12000 Jefferson Avenue, MS 85, Newport
News, VA, 23606, USA

White, Marion M   mwhite@aps.anl.gov
ANL, APS - ASD , Building 401-B2178, 9700 South Cass AV, Argonne,
IL, 60439, USA

Wienands, Ulrich   Uli@slac.stanford.edu
SLAC, Accelerator Dept., Technical Div., 2575 Sand Hill Road, MS 18,
Menlo Park, Calif., 94025, USA

Wiik, Bjoern H.   bjoern.wiik@desy.de
DESY, GD, Notkestrasse 85, Hamburg, Germany, 22607, Germany

Wildman, David W   wildman@fnal.gov
FNAL, Mail Stop 306, P.O. Box 500, Batavia, IL, 60510, USA

Wilhelmsson, Mats M   Mats.Wilhelmsson@cern.ch
CERN, Division ST, Geneve, 1211 Geneve 23, Switzerland

Willeke, Ferdinand   ferdinand.willeke@desy.de
DESY, Germany

Willen, Erich H   willen@bnl.gov
BNL, B902, Upton, NY, 11973, USA

Williams, Malcom D   mdwilliams@lbl.gov
LBNL, Ion Beam Technology, 1 Cyclotron Rd., MS 5-119, Berkeley, CA,
94720, USA

Williams, Ronald L.   pac99@bnl.gov
Florida A&M University, 2114 Broad St., Tallahassee, FL, 32301, USA

Wilson, Edmund J.N.   ted.wilson@cern.ch
CERN, AC Division, CERN, Geneva 23, 1211, Switzerland

Wilson, Mark A. D.   mark.wilson@science.doe.gov
DOE, SC-224, 19901 Germantown Rd., Germantown, MD, 20874-1290

Winick, Herman   winick@slac.stanford.edu
SLAC, USA

Winn, David R.   winn@fair1.fairfield.edu
Fairfield University, Department of Physics, Bannow 118, N. Benson Rd.,
Fairfield, CT, 06430-5195, USA

Wiseman, Mark   wiseman@jlab.org
TJNAF, Accelerator, 12000 Jefferson Avenue, MS4A, Newport News, VA,
23606, USA

Wisnivesky, Daniel   daniel@lnls.br
LNLS, Caixa Postal 6192, Campinas, S.P., 13083-970, Brazil

Witkover, Richard L   witkover@bnl.gov
AGS, Brookhaven National Lab, Bldg 911b, Upton, NY, 11973, USA

Wolcott, Alan P   cwolcott@mit.edu
MIT, 21 Manning Rd., Middleton, MA, 01949, USA

Wolski, Andrzej   a.wolski@dl.ac.uk
Daresbury Laboratory, Daresbury, Warrington, Cheshire, WA44AD, Ukraine

Woodle, Martin H.   woodle1@bnl.gov
BNL, Bldg. 725 C, Upton, NY, 11973-5000, USA

Wrulich, Albin   albin.wrulich@psi.ch
Paul Scherrer Institut, Swiss Light Source, OVGA/201B, Villigen PSI, 5232,
Switzerland

Wu, Xiaoyu   xwu@nscl.msu.edu
NSCL, NSCL, Michigan State University, S. Shaw Lane, East Lansing, MI,
48824, USA

Wu, Ying   .wu@fel.duke.edu
Duke University, Department of Physcis, Box 90319 FEL Laboratory Duke
University, Durham, NC, 27708-0319, USA

Wu, Guan-Hong   HONG@FNAL.GOV
FNAL, AD/BD MS-341, P.O.Box 500, Kirk & Pine, Batavia, IL, 60510

Wuensch, Walter U   walter.wuensch@cern.ch
CERN, PS Division, CERN, Geneve 23, CH-1211, Switzerland

Wutte, Daniela   daniela_wutte@lbl.gov
LBNL, Nuclear Science Division, 1 Cyclotron Road MS 88-208, Berkeley,
CA, 94720, USA

Wyss, Carlo   carlo.wyss@cern.ch
CERN, LHC-MMS, GENEVA 23, 1211, Switzerland

Xiao, Meiqin   xiao@rikaxp.riken.go.jp
CNS,U. of Tokyo/RIKEN, Cyclotron Lab, Riken , Hirosawa, Wako-shi,
Saitama-ken , 351-0106, Japan

Xiaofang, Wang   xfw@llcs.umich.edu
University of Michigan, Rm. 1006 IST, 2200 Bonisteel Blvd., Ann Arbor,
MI, 48105, USA

Xie, Ming   mingxie@lbl.gov
LBNL, MS.71-259, 1 Cyclotron Road, Berkeley, CA, 94720, USA

Xu, Shenglan   xus@aps.anl.gov
ANL, APS, 9700 S. Cass Ave., Argonne, IL, 60439, USA

Yagi, Katsuyasu   yagi-ajc@ktx.or.jp
ACCESS Japan Corporation, 17-3, , Kami-Ishihara 3-chome,, Chofu-shi, ,
Tokyo, 182-0035, Japan

Yakimenko, Vitaly   yakimenko@bnl.gov
BNL, NSLS, Bldg.725C, Upton, NY, 11973, USA

Yakovlev, Vyacheslav P   slava@omega-p.com
Omega-P, Inc, Omega-P,Inc., 345 Whitney Ave, #100 , New Haven, CT,
06511-2316, USA

Yamada, Hirorari   rironari@seritsumei.ac.jp
Ritsumeikau University, 1-1-1 Nojihigashi, Kusatu City, Shiga, 525, Japan

Yamamoto, Robert M.   yamamoto1@llnl.gov
Lawrence Livermore National Laboratory, Livermore, Ca., 94550, USA

Yamamoto , Noboru   noboru.yamamoto@kek.jp
KEK, Acclerator Lab., 1-1 Oho, Tsukuba, Ibaraki, 305-0801, Japan

Yamazaki, Yoshishige   yoshishige.yamazaki@kek.jp
KEK, Accelerator Laboratory, 1-1 OHO, Tsukuba-Shi, Ibaraki-Ken, 305-
0801, Japan

Yamin, Peter   yamin@bnl.gov
Director's Office, Bldg. 510F, Brookhaven National Lab, Upton, NY, 11973

Yan, Chen   yan@jlab.org
TJNAF, Physics Division, MS12H, 12000 Jefferson Avenue, Newport News,
Virginia, 23606, USA

Yan, Chen   yan@jlab.org
TJNAF, Hall C, Physics division, MS 12H, 12000 Jefferson Avenue, newport
news, virginia, 23606, USA

Yan, Yin   yanyin@YYLabs.com
.Y. Labs, Inc., P.O. Box 597, Fremont, CA, 94537-0597, USA

Yang, Bingxin   bxyang@aps.anl.gov
ANL, ASD/401, 9700 S. Cass Avenue, Argonne, Illinois, 60439-4800, USA

Yang, Ming-Jen   yang@fnal.gov
FNAL, BD/MID, MS 221, PO BOX 500, Batavia, IL, 60510, USA

Yarba, Victor A.   yarba@fnal.gov
FNAL, Technical Division / Engineering and Fabrication, P.O. Box 500,
M.S. 316, Batavia, IL, 60510, USA

Yen, Boris T   yen2@llnl.gov
Bechtel Nevada, Electro-Optics, P.O.Box 2710, Livermore, Ca 94551, L535,
Bldg. 4475, Rm. 1000, LLNL, Livermore, Ca, 94550-9234, USA

Yeremian, Anahid D   anahid@slac.stanford.edu
SLAC, P. O. Box 4349, BIN 33, Stanford, California, 94309, USA

Yoder, Rodney B   rodney.yoder@yale.edu
Yale University, Physics Dept., PO Box 208124, New Haven, CT, 06520-
8124, USA

Yoon, Moohyun   moohyun@postech.ac.kr
POSTECH, Department of Physics, POSTECH, San 31, Hyoja Dong, Nam
Gu, Pohang, Kyungbuk, 790-784, 790-784, Korea

Yoon, Jong C   jc0927@postech.ac.kr
Pohang Accelerator Laboratory, Accelerator Department, San 31 Hyoja-Dong, Pohang, Kyungbuk, 790-784, Korea

York, Richard C.   york@nscl.msu.edu
NSCL, NSCL, 153 Cyclotron Lab, Michigan State University, East Lansing, MI, 48824-1321, USA

Yoshii, Masahito   masahito.yoshii@kek.jp
KEK, High Energy Accelerator Research Organization, 1-1 Oho, Tsukuba, Ibaraki, 305-0801, Japan

Young, Lloyd M   lyoung@lanl.gov
LANL, LANSCE-1, MS-H817, Los Alamos, NM, 87545, USA

Yourd, Ron   rbyourd@lbl.gov
LBNL, 1 Cyclotron Road, MS 71-259, Berkeley, CA, 94720, USA

Yovchev, Ivailo G   igy@eng.umd.edu
Institute for Plasma Research, University of Maryland, College Park, MD, 20742, USA

Yu, David U.L.   duly@technologist.com
DULY Research Inc., 1912 MacArthur Street, Rancho Palos Verdes, CA, 90275-1111, USA

Yu, Li-Hua   lhyu@bnl.gov
BNL, NSLS, P.O. Box 5000, Building 725C, Upton, NY, 11973-5000

Yu, Simon S   SSYu@lbl.gov
Accelerator Fusion Research Division, Lawrence Berkeley National Laboratory, One Cyclotron Road, MS 71J, Berkeley, CA, 94720, USA

Yudin, Ivan   yudin@cv.jinr.ru
Joint Institute for Nuclear Research, Lab.of SuperHigh Energies, Dubna 141980, Moscow region, Russia, Russia

Yunn, Byung   yunn@jlab.org
TJNAF, Accelerator Division, 12000 Jefferson Avenue, MS: 6A, Newport News, Virginia, 23606, USA

Zadorozhny, Vladimir   zvf@umex.istrada.net.ua
Ukraine,Kiev,str.Teremkovskaya13,ap.53, Kiev, Ukraine

Zagel, James R   zagel@fnal.gov
FNAL, Beams Division - RFI, P.O. Box 500 , MS 308, Batavia, IL, 60510

Zaidman, Ernest G   ezaidman@erols.com
FM Technologies, Inc, 10529-B Braddock Rd., Fairfox, Va., 22032-2236

Zaltsman, Alexander   zaltsman@bnl.gov
BNL, AGS, BLDG. 911-B, UPTON, NY, 11973, USA

Zaplatine, Evguenii   e.zaplatine@fz-juelich.de
Forschungszentrum Juelich, IKP, Forschungszentrum Juelich, Juelich, D-52425, Germany

Zaugg, Thomas J   tzaugg@lanl.gov
LANL, Box 1663, MS-H838, Los Alamos, NM, 87545, USA

Zeitlin, Michael G   zeitlin@math.ipme.ru
IPME RAS, Mathematical Methods in Mechanics Group, V.O.Bolshoj pr.,61, St.Petersburg, 199178, Russia

Zelenski, Anatoli N.   zelenski@triumf.ca
TRIUMF, 4004 Wesbrook Mall, Vancouver, B.C., V6T2A3, Canada

Zeno, Keith L   zeno@bnl.gov
BNL, AGS, bldg 911A, Upton, NY, 11973, USA

Zhang, Min   zhangm@temf.tu-darmstadt.de
DESY/CST, CST GmbH, Lauteschaegerstr. 38, Darmstadt, 64289, Germany

Zhang, Fengqing   zhangfq@mail.kek.jp
KEK, Accelerator Laboratory, 1-1 Oho, Tsukuba, Ibaraki 305-0801 Japan, Tsukuba, Ibaraki, 305-0801, Japan

Zhang, Tianjue   tjzhang@mail.phy.ornl.gov
Oak Ridge National Lab., Bethel Valley Rd, Oak Ridge , TN, 37831-6368

Zhang, Wu   arling@bnl.gov
BNL, AGS, 911A, AGS, BNL, Upton, NY, 11973, USA

Zhang, Wenwei   wwz@glue.umd.edu
Institute for Plasma Research, University of Maryland, College Park, MD, 20742, USA

Zhang, SY   syzhang@bnl.gov
BNL, AGS Department, 911B, Upton, NY, 11973, USA

Zhang, Yunxiang   yxz@ustc.edu.cn
NSRL, USTC, P.O.B. 6022, Hefei, Anhui, P.R.China, NSRL,USTC, Hefei, Anhui, P.R.China, Hefei, Anhui, 230029, China, Peoples Republic of

Zhao, Yongxiang   yxz@bnl.gov
Physics Dept., Brookhaven National Laboratory, Physics Dept. Bldg. 901-A, Upton, NY, 11973-5000, USA

Zhao, Zhentang   zhaozt@bepc3.ihep.ac.cn
SSRF, P.O.Box 800-204, Shanghai Institute of Nucler Research, Shanghai, 201800, China, Peoples Republic of

Zhao, Kui   kzhao@pku.edu.cn
I nstitute of Heavy Ion Physics, Peking Univ., P. R. China, RF SC Group, IHIP, Peking Univ., Beijing, 100871, China, Peoples Republic of

Zholents, Alexander A   AAZholents@lbl.gov
LBNL, Center for Beam Physics, MS 71-259, 1 Cyclotron Rd., Berkeley, CA, 94720, USA

Zisman, Michael S.   mszisman@lbl.gov
LBNL, Accelerator And Fusion Research Division, Mail Stop 71J, One Cyclotron Road, Berkeley, CA, 94720, USA

Zlobin, Alexander   zlobin@fnal.gov
FNAL, T/D Development & Test Department, P.O. Box 500, MS 316, Batavia, IL, 60510, USA

Zobov, Mikhail   Mikhail.Zobov@lnf.infn.it
INFN - Frascati, Accelerator Division, LNF INFN, Via Enrico Fermi, 40, Frascati (Roma), C.P. 13 - 00044, Italy

Zolfaghari, Abbi   abbi@mit.edu
Massachusetts Institute of Technology, Lab.for Nuclear Science/Bates Laboratory, 21 Manning Road-P.O. Box 846, Cambridge,MA 02139

Zou, Peng   pzou@hep.anl.gov
ANL, G-108, Bldg. 362, 9700 S. Cass Ave, Argonne, IL, 60439, USA

Zou, Yun   yunzou@glue.umd.edu
U. of Maryland, IPR, 120313 Energy Research Bldg. #223, University of Maryland, College Park, MD, 20783, USA

FIVE-VOLUME CONTENTS

Volume 1: ORAL, pp. 1-648

LIGHT SOURCES AND FREE-ELECTRON LASERS -- *Chairs: Jean-Louis Leclare, Kwang-Je Kim*

EXTREMES OF BEAMS -- *Chair: David Sutter*

LINEAR COLLIDERS -- *Chair: Vladimir Balakin*

SPECIAL SESSION -- *Chair: Robert Siemann*

LEPTON ACCELERATORS AND COLLIDERS -- *Chairs: Stephen Myers, Robert Palmer*

ADVANCED CONCEPTS -- *Chair: Chris Clayton*

CONTROLS AND COMPUTING -- *Chairs: David Gurd, John Cary*

SINGLE-PARTICLE BEAM DYNAMICS AND OPTICS – *Chairs: Joseph Bisognano, John Irwin*

RADIO-FREQUENCY SYSTEMS -- *Chairs: Daniel Boussard, Ron Sundelin*

ACCELERATOR TECHNOLOGY -- *Chairs: Horst Friedsam, Tsumoru Shintake*

APPLICATION OF ACCELERATORS -- *Chairs: Stanley Schriber, Anthony Favale*

PULSED-POWER AND HIGH-INTENSITY BEAMS -- *Chair: Craig Olsen*

INSTABILITIES AND FEEDBACK -- *Chair: John Byrd*

Volume 2: POSTER, pp. 649 – 1476

ACCELERATOR RING CONTROL SYSTEMS

ROOM TEMPERATURE RF

SUPERCONDUCTING RF

RF POWER SOURCES

FEEDBACK SYSTEMS

BEAM INJECTION/EXTRACTION, TRANSPORT AND TARGETRY

ALIGNMENT AND SURVEY

SUBSYSTEMS, TECHNOLOGY AND COMPONENTS

Volume 3: POSTER, pp. 1477 – 2258

PULSED POWER TECHNOLOGY

LINEAR AND NON LINEAR ORBIT THEORY

TRANSVERSE AND LONGITUDINAL INSTABILITIES AND CURES

BEAM-BEAM INTERACTION

BEAM COOLING

HIGH CURRENT DYNAMICS

PARTICLE SOURCES

RF GUNS AND LINACS INJECTORS

BEAM DIAGNOSTICS INSTRUMENTATION

Volume 4: POSTER, pp. 2259 - 2962

LOW- AND MEDIUM-ENERGY CIRCULAR ACCELERATORS

SYNCHROTRON RADIATION FACILITIES

FREE-ELECTRON LASERS

ACCELERATOR APPLICATIONS

RADIATION MONITORING AND SAFETY

HIGH ENERGY HADRON ACCELERATORS AND COLLIDERS

INSERTION DEVICES

COMPUTER CODES

BEAM DYNAMICS, OTHER

POST DEADLINE

Volume 5: POSTER, pp. 2963 - 3779

ELECTRON STORAGE RINGS AND CIRCULAR ACCELERATORS

ACCELERATORS AND STORAGE RINGS, OTHER

SUPERCONDUCTING MAGNETS

PULSED POWER ACCELERATORS

HIGH INTENSITY ACCELERATORS

ROOM TEMPERATURE MAGNETS

ELECTRON LINEAR COLLIDERS

LINEAR ACCELERATORS

NEW ACCELERATION TECHNIQUES

POWER SUPPLIES

COMMISSIONING RESULTS OF THE
KEKB AND PEP-II B-FACTORIES[*]

J. T. Seeman[#], MS 18, SLAC, Stanford, CA 94309

KEKB *Abstract*

KEKB [1-6] is a two ring asymmetric electron-positron collider at 3.5 x 8 GeV being built in the TRISTAN tunnel at the Japan National Laboratory for High Energy Physics KEK in Tsukuba. The five year KEKB construction project was approved by the Japanese government in April 1994. The parameters are listed in Section 1 and the overall layout of KEKB shown in Fig. 1. The two beams will collide in the Tsukuba experimental hall where the BELLE detector will be located. The salient features of KEKB are side-by-side rings, +/- 11 mrad crossing angles at the collision point with non-radiating straight incoming beams, new RF cavities: copper cavities with high stored energy (ARES) and superconducting cavities both designed to reduce the strength of the bunch-by-bunch feedback systems, many bunches (5000), high stored beam currents (2.6 A x 1.1 A), superconducting IR quadrupoles, novel 2.5π lattice design for flexibility, and an upgraded linac for full energy injection of both beams with new transport lines.

Beam commissioning started for the KEKB High Energy Ring HER in December 1998 and January 1999 for the Low Energy Ring LER. The present peak current in the LER is 380 mA and the HER 420 mA. A luminosity of 1.2x10**31/cm**2/s was achieved in March 1999 with 200 bunches with 13 mA x 65 mA.
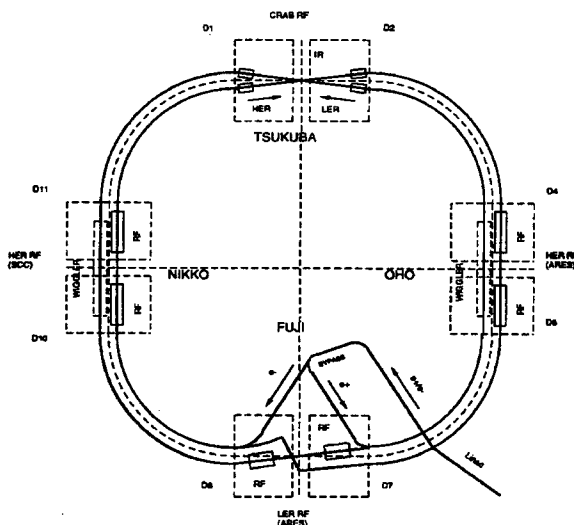
PEP-II *Abstract*

PEP-II [7-12] is a two ring asymmetric electron-positron collider at 3.1 x 9.0 GeV being built in the PEP tunnel at the Stanford Linear Accelerator Center SLAC. The five year PEP-II construction project was approved by the Department of Energy of the United States government in January 1994. A collaboration of SLAC, Lawrence Berkeley National Laboratory LBNL, and Lawrence Livermore National Laboratory LLNL designed and constructed PEP-II. The parameters are listed in Section 3 and the overall layout of PEP-II is shown in Fig. 2. The beams will collide in the IR2 hall of the PEP tunnel where the BABAR detector will be located. The salient features of PEP-II are LER-above-the-HER, head-on collisions but with dipoles bends near the collision point, new copper RF cavities, strong bunch-by-bunch feedback systems, many bunches (1658), high stored charges (2.1 A x 0.75 A), permanent magnet IR quadrupoles and dipoles, and use of the existing SLAC linac as an injector but with new transport lines.

PEP-II HER commissioning started in June 1997 and LER commissioning in July 1998. The present maximum current in the HER is 750 mA in 1658 bunches which is the design value. The LER has stored 1171 mA, which is believed to be a world record for a positron ring. A luminosity of 5.2x10**32/cm**2/s was achieved in February 1999 with 786 bunches with 354 mA x 680 mA (HER x LER). Bunch trains of 1, 11, 291, 522, 786, 1048, and 1571 have been collided. An average luminosity of 2x10**32/cm**2/s was maintained over 72 hours.

Figure 1: KEKB B-Factory Overview
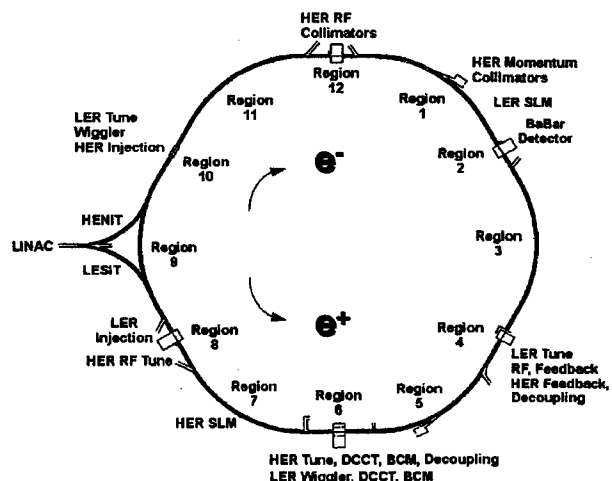
Figure 2: PEP-II B-Factory Overview

1 KEKB DESIGN PARAMETERS

Parameter	LER	HER
Beam energy (GeV)	3.5	8.0
CM energy (GeV)	10.58	
Particle type	e+	e-
Circumference (m)	3016.3	
Crossing angle (mrad)	+/- 11.0	
Luminosity	10^{34} cm^{-2}sec^{-1}	
Beam-beam tune shift (y)	0.052	
Beam-beam tune shift (x)	0.039	
$\beta y^*/\beta x^*$ (cm/cm)	1./33.	1./33.
Optimum coupling (%)	2.0	2.0
Emittance (nm-rad) (y/x)	0.36/25.	0.36/25.
IP rms beam σ_y/σ_x (mm)	1.9/90.	1.9/90.
Number of bunches	5000	5000
Particles per bunch	3.3 x 10^{10}	1.4x 10^{10}
Bunch spacing (m)	0.59	0.59
Bunch length (mm)	4.0	4.0
Damping times (ms) (x/z)	23	23
ΔE/turn (MeV)	1.5	3.5
Radiation power (MW)	4.0	3.8
HOM power (MW)	0.57	0.14
Total beam power (MW)	4.5	4.0
Total current (A)	2.6	1.1
RF frequency (MHz)	508.9	508.9
Harmonic number	5120	5120
Ion clearing gap (buckets)	---	120
RF voltage (MV)	8	20
Rel. energy spread ($10^{-3)}$	0.71	0.67
Synchrotron tune	0.012	0.011
Betatron tune (ν_x/ν_y)	45.71/44.49	44.51/42.29
Linac injection rate (Hz)	50	50
Full injection time (min)	13-14	3
Detector solenoid field (T)	1.5	

3 PEP-II DESIGN PARAMETERS

Parameter	LER	HER
Beam energy (GeV)	3.1	9.0
CM energy (GeV)	10.58	
Particle type	e+	e-
Circumference (m)	2199.318	
Crossing angle (mrad)	0.0	
Luminosity	3 x 10^{33} cm^{-2}sec^{-1}	
Beam-beam tune shift (y)	0.03	
Beam-beam tune shift (x)	0.03	
$\beta y^*/\beta x^*$ (cm/cm)	1.5/50.	1.5/50.
Optimum coupling (%)	3.0	3.0
Emittance (nm-rad) (y/x)	1.5/49.	1.5/49.
IP rms beam σ_y/σ_x (mm)	4.7/157.	4.7/157.
Number of bunches	1658	1658
Particles per bunch	6.0 x 10^{10}	2.8x 10^{10}
Bunch spacing (m)	1.26	1.26
Bunch length (mm)	10.0	11.0
Damping times (ms) (x/z)	62.5/30	37./18.3
ΔE/turn (MeV)	0.75	3.6
Radiation power (MW)	1.62	3.58
HOM power (MW)	0.23	0.15
Total beam power (MW)	1.85	3.73
Total current (A)	2.16	0.75
RF frequency (MHz)	476.	476.
Harmonic number	3492	3492
Ion clearing gap (buckets)	---	176
RF voltage (MV)	5.1	14.0
Gap voltage/cavity (MV)	0.85	0.7
Rel. energy spread (10^{-3})	0.77	0.61
Synchrotron tune	0.0334	0.0449
Betatron tune (ν_x/ν_y)	38.57/36.64	24.62/23.64
Linac injection rate (Hz)	60	120
Detector solenoid field (T)	1.5	

2 KEKB MILESTONES

Date		Milestone or Commissioning
1994	April	Start of KEKB construction
1995	December	Start removing TRISTAN
1995	July	Bids out for LER construction
1996	May	Bids out for HER construction
1996	July-Nov.	Beam tests in Accum. Ring
1996	December	Start bypass tunnel constr.
1997	February	Start magnet installation
1997	October	Complete new bypass tunnel
1998	May	Commission fully upgraded linac and transport lines
1998	Nov. 30	KEKB installation complete
1998	Dec. 13	HER beam first stored
1999	Jan. 14	LER beam first stored
1999	Jan. 26	First beam-beam collisions
1999	March 26	Luminosity of 1.2x10**31
1999	May	BELLE detector to be installed
2000		Nine month run planned

4 PEP-II MILESTONES

Date		Milestone or Commissioning
1994	January	Start of PEP-II Construction
1995	October	e- injection transport studies
1997	April	HER injection studies
1997	June	HER installation complete
1997	June 16	HER beam first stored
1997	June	e+ injection transport studies
1998	January	LER injection (part turn)
1998	July 10	LER construction complete
1998	July 16	LER beam first stored
1998	July 23	First collisions
1998	Dec. 8	8 x10**31 luminosity
1998	Feb. 8	5.2 x 10**32 luminosity
1999	May	BABAR detector to be installed
2000		Ten month run planned

5 KEKB COMMISSIONING RESULTS

(as of 3/30/1999)	LER	HER
Beam energy (GeV)	3.5	8.0
Maximum total current (mA)	380	420
Single bunch current (mA)	2.3	4.0
Number of bunches	1024	640
βy^* (cm)	1.0	1.0
βx^* (cm)	100	100
Bunch length (mm)	6.4	5.6
Injection rate (Hz)	50	25
RF voltage	4.0	9.0
Number of ARES RF cavities	12	6
Number of SC cavities	0	4
νx	45.57	44.26
νy	44.62	42.21
Max. injection efficiency (%)	70	80-100
Injection charge (nC)	0.18	1.0
Beam lifetime in collision (min)	40	200
Bunches collided (max)	200 x 200	
Collided currents (mA)	65	13
Maximum luminosity (1/cm^2/s)	1.2 x 10**31	
IP beam sizes (microns) (x,y)	197/5.6	
Integrated current (A-hr)	28	20

6 PEP-II COMMISSIONING RESULTS

(as of 3/30/1999)	LER	HER
Beam energy (GeV)	3.1	9.0
Maximum total current (mA)	1171	750
Single bunch current (mA)	7.0	12.0
Number of bunches	1658	1658
βy^* (cm)	1.4	1.3
βx^* (cm)	50	50
Bunch length (mm)	---	12.
Injection rate (Hz)	10	10
RF voltage (max) (MV)	3.2	14
Number of cavities	4	20
νx	38.63	24.58
νy	36.59	23.62
Bunch ion gap (%)	10	10
Max. injection efficiency (%)	90-100	95-100
Injection charge (max) (nC)	3	3
Injection rate at 10Hz (mA/sec)	2.1	2.2
Beam lifetime at 300 mA (min)	150	420
Bunches collided (max)	1571 x 1571	
Collided currents (max) (mA)	1007	354
Luminosity (max) (1/cm^2/s)	5.2x10^{32}	
Current at max luminosity (mA)	680	354
IP beam sizes (microns) (x,y)	160/6.1	
Integrated current (A-hr)	153	115

7 KEKB COMMISSIONING ISSUES

The magnetic lattices for KEKB have noninterleaved 2.5π phase advance cells with local chromaticity correction near the interaction point. The measured lattice functions are close to the design and the IP vertical beta functions are 1.0 cm which is a world record level for an e+e-collider.

The KEKB LER uses ARES cavities. The ARES system has a HOM-damped copper accelerating cavity coupled to a high-Q energy storage cavity via a coupling cavity. The HER will use a combination of ARES and superconducting (SC) cavities. The SC cavities are single cells with room temperature beam line ferrite HOM absorbers. The KEKB RF systems worked well during commissioning. The measured synchrotron frequencies are correct. The superconducting cavities have had very few trips over the first few months. No longitudinal instabilities have been seen even without feedback.

The vacuum chambers for both rings of KEKB are extruded copper with Helicoflex seals. The HER chambers are racetrack shaped and have distributed NEG pumping. The LER chambers are circular to reduce the resistive wall instability and have NEG cartridges every meter. During commissioning the vacuum systems started with somewhat higher pressures than expected but with beam scrubbing the gas desorption rate and resulting pressures have quickly approached values expected at this commissioning phase. See Fig. 3.

The existing KEK linac has been upgraded to inject at full energy into KEKB. The upgrade involved adding more linac accelerating sections, newly designed SLED energy doublers, higher power klystrons, improved diagnostics, new positron target, and a new gun. The positron production per pulse has increased a factor of twenty. New transport lines were also built. Long term beam stability issues are under study for the injection complex.

Transversely, the beams are stable with bunch-by-bunch feedback. Without feedback, an instability starts in the LER at about 100 mA for bunch spacings less that 8ns. The cause is under study. Instability in the HER appears as centroid motion at the end of a long bunch train at currents of about 190 mA. In both rings growth times approach a few milliseconds at high currents.

In KEKB the LER and HER beams are brought into collision horizontally with +/- 11 mrad crossing angles. The first quadrupoles QCS which are superconducting including skew quadrupole and x-y dipole windings have been fully tested. Farther away, several special iron septum quadrupoles are needed in both rings to complete the IP doublet optics and to allow the two beams to separate. The compensation of the detector solenoid done by a pair of reverse solenoids near the collision point and with small trim skew quadrupoles in the interaction region has also been tested.

KEKB has had about four days of colliding beam experiments. The beams were first steered into collision using position monitors. Then, beam-beam scans are used to center the beams and measure their sizes. The scans were done magnetically in the vertical plane and longitudinally with the LER RF phase for horizontal

scans. See Fig. 4. Most studies have been with single bunches but 200 bunches have been collided. The vertical and horizontal beam sizes are near the design values. A slow orbit drift of unknown origin affects IR steering.

Backgrounds near the IP have been measured by the BEAST detector. The backgrounds are high at this early phase but collimator and beam steering are starting to reduce the levels.
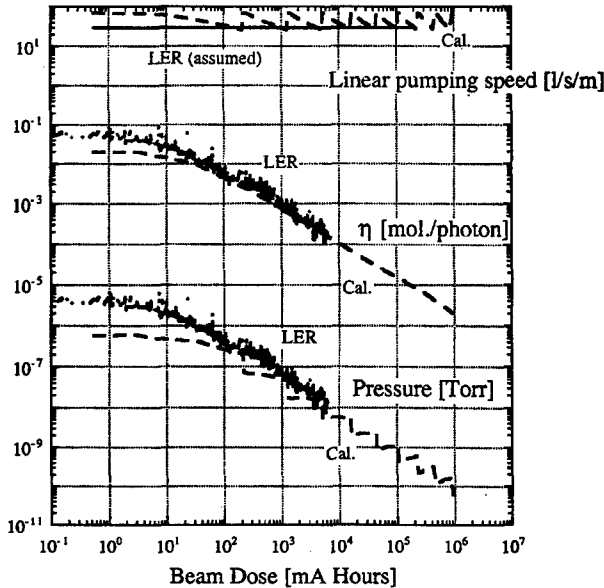
Figure 3: KEKB vacuum pressure and desorption versus beam dose. Scrubbing is following expectations (- - - -).
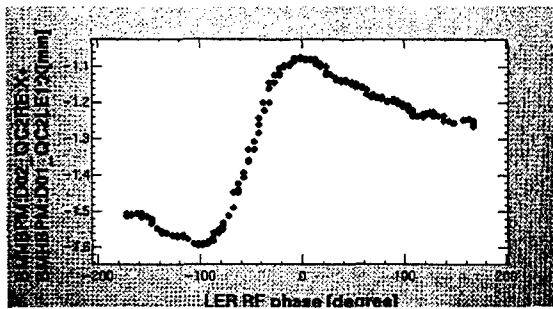
Figure 4: KEKB horizontal beam-beam deflection scan.

8 PEP-II COMMISSIONING ISSUES

The PEP-II magnetic lattices for the HER and the LER are significantly different. The HER has a 60 degree per cell lattice in the arcs with standard interleaved sextupole chromaticity correction. The chromaticity correction in the HER interaction region is made using "beta-beats" (high single plane betas at the sextupoles) in the nearby arcs. The LER has a 90 degrees per cell lattice in the arcs with a noninterleaved sextupole correction scheme. In the LER interaction region the chromaticity correction is semi-local with the y correction done in the IR and the x correction made in the nearby arcs. Both HER and LER

lattices as measured are within a few percent of the design. The IP betas are correct horizontally and about 10% low vertically which helps the beam-beam effect.

The PEP-II RF system uses single cell copper cavities with three HOM absorbers. The HER has four cavities per klystron and the LER two. The cavities are E-beam welded with staged machining and tuning steps. The high power RF windows are ceramic with a stainless steel compression ring and are coated with TiN. The low level RF control system includes feedback loops, comb filters, fast interlocks, network analysis, beam aborts, phase control, high voltage and drive control, and EPICs overall control. Both the HER and LER RF systems are fully functional with nearly full gradient. There are only a few trips per day for the full system. The RF feedback systems are well tuned, reliable, and useful diagnostics.

In PEP-II the HER arc vacuum chambers are extruded copper, the LER arc chambers are aluminum with antechambers, and the straight sections have water cooled cylindrical stainless steel pipes. The HER vacuum chambers are made to absorb over 100 W/cm of synchrotron radiation and pumped using distributed ion pumps. The synchrotron radiation in the LER is absorbed in Glidcop (grooved) photon stops located in the pumping chamber antechamber. The beam results show that the HER pressure rise with current is within a factor of two of the desired value and should scrub quickly. The LER vacuum pressure is decreasing more slowly than desired and is now at 10 nT/A. An investigation is underway to determine if the TiN coating, small leaks, or the antechamber outgassing contributes. More vacuum pumping is being installed and the small leaks are being fixed. At above 600 mA in the LER there is evidence for electron multipacting which depends on the bunch current and the number of bunches resulting in pressure increases.

The existing 50 GeV SLAC linac as modified for the SLC with damping rings is used for PEP-II injection. Intensities per pulse can range up to 4 x 10^10. The injection systems are working well often with 100% injection efficiency. The e+ beam has a modest transverse mismatch which is under study.

All beams are stable with bunch-by-bunch feedbacks. Without feedback the LER is stable longitudinally to about 330 mA and the HER to about 500 mA, agreeing with predictions. Transversely, the LER instability threshold is at least 100 mA, again near the prediction. However, the HER transverse threshold is about 10 to 20 mA which is much lower that predicted. The data do not point to ions nor resonances cleanly although there is some agreement with each. Without transverse feedback very short trains in either ring are unstable at low currents with the tail of the train oscillating. In the HER, different mode numbers occur at different bunch currents.

In PEP-II the LER and HER beams are collided head-on requiring horizontal separation near the interaction point using strong dipoles. These first dipoles and quadrupoles are permanent magnets with 10^-4 field

tolerances and off-axis beams. The next several magnets are special iron septum quadrupoles to complete the doublet focusing. The compensation of the BABAR solenoid is done with six strong skew quadrupoles on each side of the interaction region per ring.

PEP-II has had collisions 20 days so far with several different bunch trains. Position monitors 72 cm from the IP are very useful in bringing the beams into collision. The bunch timing is measured to a few ps and held constant with RF phase feedback. Beam-beam scans are done magnetically in both planes. A vertical scan is shown in Fig. 5. Raising the HER bunch charge above 0.4 mA reduces the LER bunch lifetime. Raising the LER bunch charge even to 3 mA has not yet hurt the HER bunch lifetime but does reduce its own lifetime. The optimum ratio of bunch charges is near 0.35 mA HER to about 1.3 mA LER which is about the design. No significant parasitic collision effects have been seen. The multi-bunch luminosity scales correctly from single bunch luminosity. The luminosity measured over several days is shown in Fig. 6 and the luminosity versus current product in Fig. 7. The specific luminosity is about 60% of the design. The best luminosity has been achieved with 786 bunches, spaced every four RF buckets. The achieved beam-beam tune shifts are about 0.032 horizontally and 0.013-0.017 vertically, with the horizontal e+ as the only operational limit so far. There is an IP orbit drift associated with air temperature and the HER beam current.

The backgrounds at the IP for the HER now match the new simulations but are a factor of 5 to 7 larger than the original design. The backgrounds for the LER are 10 to 20 times the design. Twelve collimators are being installed.

9 REFERENCES

[1] "KEKB B-Factory Design Report", KEK Report 95-7, (1995).

[2] "Design Report on PF Injector Linac Upgrade for KEKB", KEK Report 95-18, (1996).

[3] K. Oide, "Commissioning Results from KEKB," PAC99 proceedings, March 1999.

[4] K. Egawa, etal, "Modeling of the KEKB Colliding Rings," PAC99 proceedings, March 1999.

[5] T. Tajima, "Superconducting Cavity System for KEKB," PAC99 proceedings, March 1999.

[6] M. Tobiyama and E. Kikutani, "Commissioning of the KEKB Bunch Feedback Systems," PAC99 Proceedings, March 1999.

[7] "PEP-II Conceptual Design Report", SLAC Report 418, LBL-PUB-5379, June (1993).

[8] M. Sullivan, "Beam-Beam Collisions at PEP-II," PAC99 proceedings, March 1999.

[9] P. Corredoura et al., "Low-level RF System for the PEP-II B-Factory", PAC95, p. 2672 (1995) and PAC99 proceedings, March 1999.

[10] M. Zisman, "Commissioning Results of the PEP-II LER," PAC99 proceedings, March 1999.

[11] J. Seeman, "KEKB and PEP-II B Factories," Proceedings of Flavor Physics Conference, Nuc. Phys. B 59 (1997), p. 51.

[12] J. Fox, "Multi-Bunch Instability Diagnostics via Digital Feedback Systems," PAC99 proceedings, March 1999.
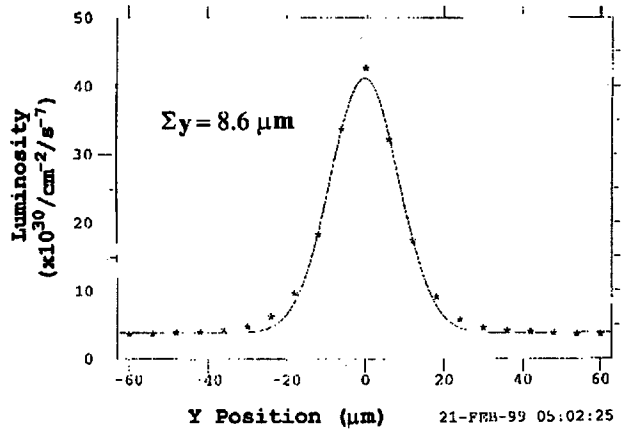
Figure 5: PEP-II vertical beam scan showing luminosity vs beam position. The width gives the combined beam size. The design Σy is 6.7 microns.
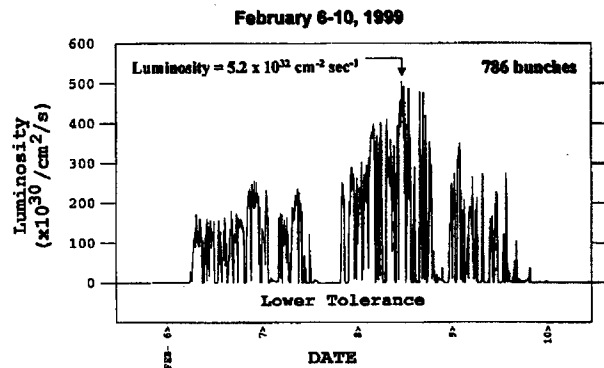
Figure 6: PEP-II Luminosity measured over 72 hours in February 1999 with an average of 2x10**32/cm**2/s.
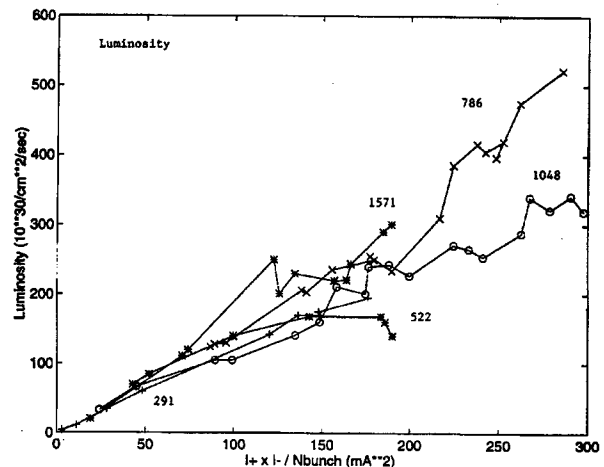
Figure 7: PEP-II measured luminosity versus the product of the beam currents divided by the number of bunches (indicated). At low currents the specific luminosities are nearly the same but at high currents some spot size enlargements occur.

THE COMMISSIONING STATUS OF RHIC[*]

M. Harrison[#], BNL, Upton, NY

Abstract

The construction and commissioning status of the Relativistic Heavy Ion Collider, RHIC, is discussed. Those novel features of a heavy ion Collider that are distinct from conventional hadron Colliders in general are noted. These features are derived from the experimental requirements of operation with a variety of ion species over a wide energy range including collisions between ions of unequal energies. The paper notes other challenging issues for the Collider including intrabeam scattering, interaction-region error compensation, magnet alignments, and matched transition-energy jump. The project is in the final few months of a seven-year construction cycle and is entering the commissioning phase. A review of the superconducting magnet program is given together with the status of the machine construction and commissioning.

1 INTRODUCTION

The primary motivation for colliding heavy ions at ultra-relativistic energies is the belief that it is possible to create macroscopic volumes of nuclear matter at such extreme conditions of temperature and energy density that a phase transition will occur from hadronic matter to a confined plasma of quarks and gluons. The main goal of the Relativistic Heavy Ion Collider (RHIC is to provide head-on collisions at energies up to 100 GeV/u per beam for very heavy ions, which are defined to be gold $^{197}Au^{79+}$, but the program also calls for lighter ions all the way down to protons and polarized protons. Luminosity requirements for the heaviest ions are specified to be in the 10^{26-27} cm^{-2} s^{-1} range. The higher Au-Au total cross section results in interaction rates comparable to p-p Colliders although this luminosity is several orders of magnitude lower than those machines. A short interaction point (IP) length (<20 cm rms.) is desirable for optimum detector design. The final, though most influential, experiment requirement has been the need for collisions of different ion species (most notably p-Au) at the same center of mass energies per nucleon. This necessitates accommodating mass-to-charge ratios (A/Z) in the range of 1 (p) to 2.5 (Au). Stabilizing the collision point involves equalizing the rotation frequencies of the two beams, which also requires the two rings to operate at different magnetic fields. The complications in the interaction region (IR) where the beams must pass through common magnets dictate a lattice design different from conventional hadron Colliders.

Based on these general requirements, the detailed RHIC machine parameters were derived and are outlined in Table 1. Operation of the RHIC Collider at relatively low energies together with the enhanced intrabeam scattering (IBS), which scales as Z^4/A^2, results in beams of large transverse and longitudinal dimensions. This in turn has ramifications for the lattice (short cells, strong focusing) and magnet aperture. This consideration and the short IP length also determine the rf system requirements. Colliders, unlike fixed target machines, are designed to operate for extended periods at high energies. The economics of power consumption argue strongly for superconducting magnets. RHIC is such a superconducting machine.

Table 1: Major Parameters for the Collider

Kinetic Energy, Inj.-Top, Au	10.8-100	GeV/u
(each beam), protons	28.3-250	GeV
No. of bunches/ring	60	
Circumference	3833.845	m
Number of crossing points	6	
β^*, injection, H/V	10	m
β^*, low-beta insertion, H/V	1	m
Betatron tunes, H/V	28.18/29.18	
Magnetic rigidity, injection	97.5	T-m
top energy	839.5	T-m
Number of dipoles (192/ring + 12 common)	396	
Number of quadrupoles (276 arc + 216 insertion)	492	
Dipole field at 100 GeV/u,Au	3.45	T
Arc dipole effective length	9.45	m
Arc quadrupole gradient	71.2	T-m

2 MACHINE DESIGN AND LAYOUT

The complete RHIC facility is a complex set of accelerators interconnected by beam transfer lines. The collider, shown schematically in Fig. 1, is located in the existing 3.8 km tunnel north of the AGS.
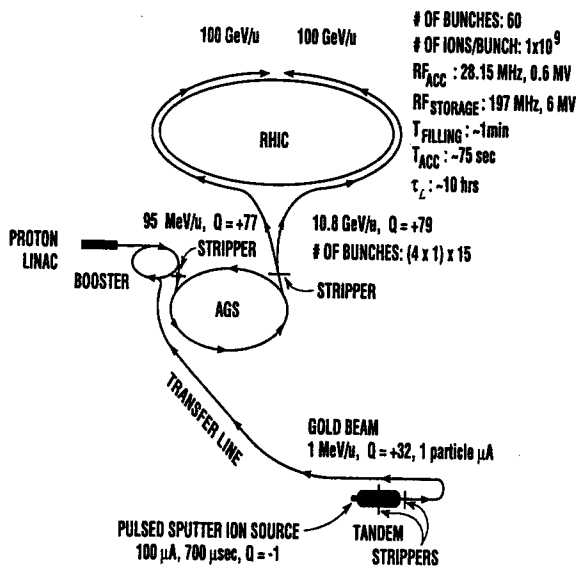
Figure 1: The RHIC Complex

It is comprised of two identical, quasi-circular rings separated horizontally by 90 cm, and oriented to intersect with one another at six locations. Having a 3-fold symmetry, each ring consists of three inner and three outer arcs and six insertion regions joining them. Each arc consists of 11 FODO cells, with each half-cell consisting of a single dipole and a spool-piece assembly containing a quadrupole, sextupole, and concentric correction elements. Fig. 2. shows the Collider layout together with the standard cell schematic.
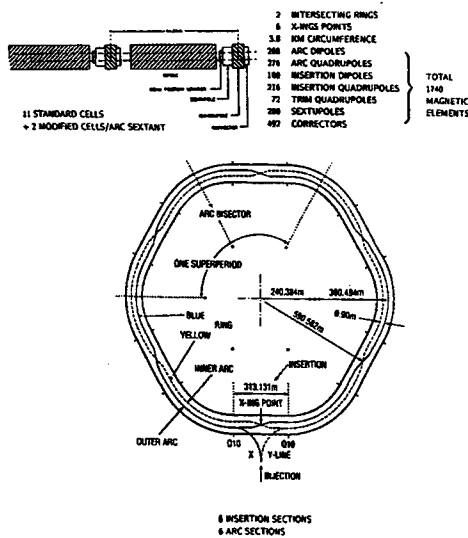
Figure 2: Collider layout and standard cell

The nominal design magnetic rigidity of the dipoles is 840 T-m which corresponds to a design field of 3.45 T at 100 GeV/u. Injection takes place at 97.5 T-m. The half-cell length of 15 m has beta-functions in the range from 10.5 m to 50 m, and a dispersion from 0.8 m to 1.8 m. These relatively small values are dictated by the need to minimize the physical size of a beam (i.e. maximize dynamic aperture and thus intensity lifetime) with relatively large emittances (40πmm-mr normalized 95% transverse, 1.2 eV-s/u longitudinal). The dipole coil inner diameter (i.d.) of 8 cm is determined both by the beam size at injection and by the projected emittance growth which occurs during a store at the lowest collision energy of 30 GeV/u. The quadrupoles, also having a coil i.d. of 8 cm, operate at a maximum gradient of 72 T/m. A cross-section of a dipole of length 9.45 m is shown in Fig 3. The magnets are conceptually similar to the HERA dipoles with a "cold-iron" design and cryogenic transfer lines located in the cryostat.
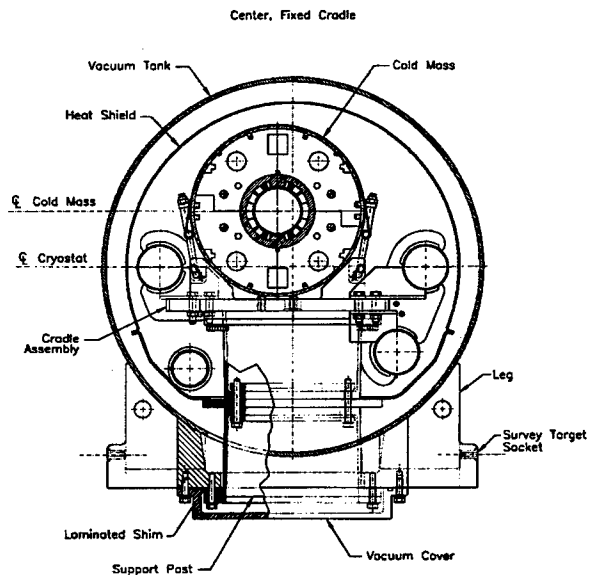
Figure 3: RHIC dipole cross section

Collisions of the beams take place at the crossing point of the insertions. These regions contain the optics necessary for producing small betatron amplitude functions β^*, a zero dispersion at the crossing point, and the magnet steering to bring the beams into head-on collisions. The "non-arc" regions also contain the only warm regions of the machine where the machine utilities reside such as injection, beam abort, rf station, collimators, and specialized instrumentation. Locations available for these devices are the 30 m section between Q3 and Q4, the missing dipole between Q7 and Q8, and the section adjacent to the short D9 dipole. The magnetic elements in the region from Q10 to Q4 are identical in cross-section but different in length to those in the standard cell. The final focus triplet (Q1, Q2, and Q3), and bending magnets (D0 and DX) are non-standard magnets with apertures of 13 cm, 10 cm, and 18 cm, respectively. The focusing is

7

relaxed at injection with a β^* value of 10 m. During collisions at top energy, a β^* of 1 m can be attained resulting a maximum β of about 1400 m in the triplet quadrupoles. The maximum focusing strength of 48 T/m is determined by both the physical beam size in the triplet and the strength of the trim quadrupoles at Q4, Q5, and Q6. The lattice functions in the IR's are shown in Fig. 4. Each insertion is independently adjustable and can be matched over a machine tune range of ±1 unit. The phase advance across the insertion is almost constant during the squeeze, as is the triplet excitation.
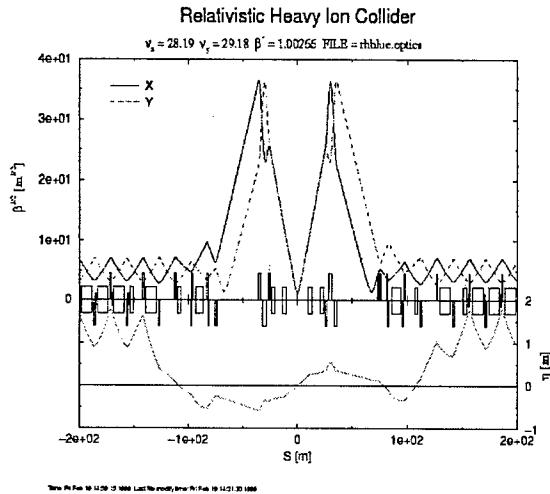
Figure 4: Lattice functions in the interaction regions

3 DESIGN FEATURES

3.1 Unequal Energies

Probing the dynamics of a quark-gluon plasma benefits greatly by the ability to varying the initial conditions which in the context of RHIC means collisions between unequal particle species and energies in addition to merely varying species and collision energy. This requirement precluded a common final focus and the RHIC beams are separated before the final focus. The quadrupole triplet is thus moved further away from the interaction point impacting the aperture requirements. The closest magnet to the interaction point is a large aperture (18cm) dipole operating at 4T. Particle trajectories vary considerably in this magnet.

3.2 Intrabeam Scattering (IBS)

Emittance growth caused by intrabeam scattering [1] is of concern during both injection and storage of the heavy ion beams. At injection, the IBS longitudinal growth time is only 3 minutes. Injection needs to be accomplished in 60s to avoid difficulty in transition crossing and rf

rebucketting due to increased longitudinal beam size. At storage, emittance growth occurs in both transverse and longitudinal planes with transverse emittances growing from the initial 10π mm-mr to more than 40π mm-mr during the first several hours of a store. Longitudinal bunch area exceeds the bucket area of 1.2 eV-s/u in about an hour. Collimation systems are designed to intercept particles escaped from the rf buckets. Increasing peak rf voltage only modestly improves the luminosity performance, since transverse growth is so significant. The ultimate improvement can be made if cooling methods are adopted. Maximizing machine performance with large emittance beams required an unusually short cell length to minimize the physical beam size in the arcs.

3.3 IR Error Compensation

In order to maximize the instantaneous luminosity the final focus triplets are designed to enable the collision β^* to be reduced to 1m. Dipoles and triplets of quadrupoles of large bore are placed on both sides of the IP. The $\beta_{\mu\alpha\xi}$ of 1400m, along with the strong IBS growth, results in the 5σ beam size increasing from 35% to about 70% of the triplet magnet coil radius. In order to optimize the field quality in these elements, sophisticated compensation techniques have been developed [2] including individual error correction with tuning shims, amplitude dependent body-ends compensation, low β magnet sorting, and lumped triplet multi-layer corrector packages.

3.4 Transition Crossing

RHIC will be the first superconducting accelerator to cross transition energy. Due to the slow ramping rate of the superconducting magnets, both chromatic nonlinear effects and beam self-field effects are strong at crossing. In addition the superconducting machine environment makes operation vulnerable to magnet quenching arising from beam losses should they occur. A "matched first order" transition jump scheme has been implemented [3] to effectively increase the crossing rate by a factor of 8 during the 60 ms time around transition. With such a scheme the longitudinal emittance growth can be limited to less than 20% at transition while keeping the beam spot size constant to avoid particle losses.

4 SUPERCONDUCTING MAGNET PROGRAM

The Superconducting magnet program for the Project is now complete with the last magnet delivered to the ring in November 1998. The ring magnets naturally fall into two types; the 8cm elements which are used throughout the arc regions and constitute the majority of the magnets, and the smaller number of variable aperture magnets used in the immediate vicinity of the IP. A list of the various magnet types is given in Table 2.

Table 2: RHIC Superconducting Magnet Inventory

8 cm dipoles	360
8 cm quadrupoles	420
IR trim quadrupoles	72
sextupoles	288
8 cm multilayer correctors	420
13 cm IR final focus quadrupoles	72
13 cm IR correctors	72
10 cm IR dipoles	24
18 cm IR dipoles	12

The 8cm dipoles, quadrupoles, and sextupoles were all produced industrially. The low-current correctors, final-focus triplet quadrupoles and beam splitting dipoles were produced internally by BNL. BNL also performed the integration of the quadrupoles, sextupoles, and correctors into a single cryogenic module. The dipole magnets, produced by the Northrop-Grumman Corporation in a build-to-print contract, were complete cryogenic elements suitable for immediate installation.

The crucial aspects of superconducting accelerator magnets are field quality and quench threshold [4]. Since it was decided that cold testing of each magnet was not realistic, field quality was measured at room temperature. It therefore became important to establish a good correlation between warm and cold magnetic field measurements at the 10^{-5} level. An analysis of the complete data set demonstrated that after compensating for yoke saturation effects, good warm/cold field correlations could be obtained at this accuracy. Figure 5 shows a plot of the fractional field deviation on the mid-plane as a function of position.
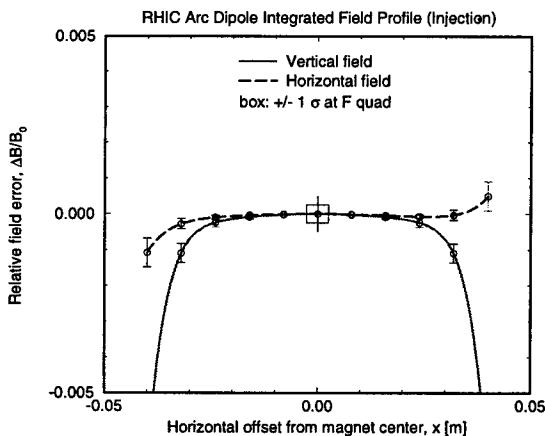
Figure 5: Arc dipole field variation at injection

The magnet set demonstrates excellent field quality with very small random multipole field components by virtue of tight mechanical tolerances on the cable dimensions [5]. The systematic component of the field harmonics is optimized for low-field performance at injection with

yoke saturation apparent in the allowed harmonics at high field. During collisions the dynamic aperture is determined by the triplet quadrupoles. The quench performance of the 8 cm dipole magnets is shown in Fig. 6 with the minimum and plateau quench currents for a set of 60 magnets.
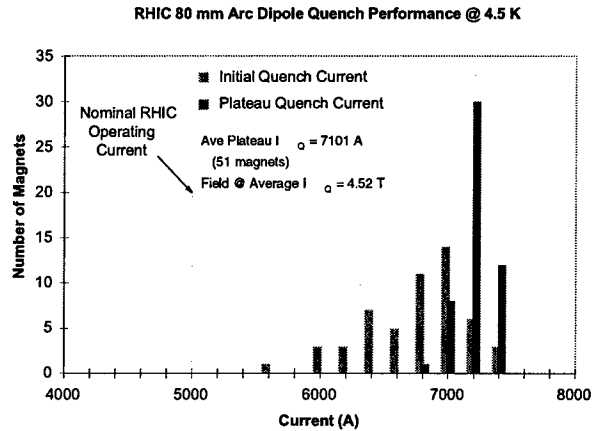
Figure 6: Arc dipole quench performance

Since only 20% of the magnets are measured cold, it is important to demonstrate sufficient operating margin to make limited testing viable. None of the magnets tested to date have had an initial quench current less than the nominal operating level. The plateau quench level demonstrates a healthy 30% operating margin. For the IR magnets however the situation was not so pristine. The large aperture dipole magnets did indeed have an initial quench threshold below the nominal operating point of 6KA. The plateau level on these elements has only a ~10% operating margin and did show some loss of training on a thermal cycle. The data on these magnets is shown in Fig 7.
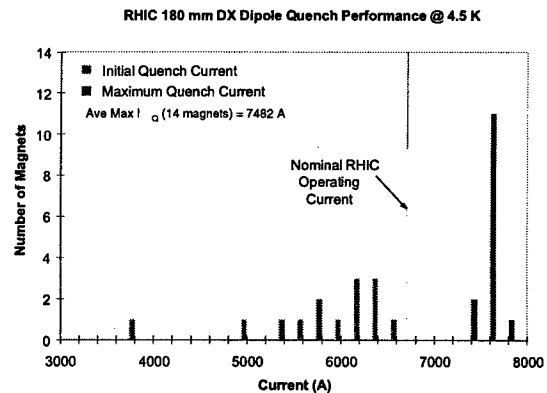
Figure 7: Beam separation dipoles quench performance

5 COMMISSIONING STATUS

The final magnet was delivered to the ring in November 1998. At this point mechanical installation was

completed in the arc regions and activities were confined to the beam separation and final focus regions. Installation of the interaction regions was completed two months after the last magnet delivery. Each magnet interconnect requires 20 welded connections and while a local vacuum leak check was performed as part of the installation the necessary leak check sensitivity to ensure an acceptable vacuum at cryogenic temperatures can only be performed when the cryostat is closed up and an insulating vacuum can be established in the cryostat. Leak checking of the system at both low and high pressures in all five cryogenic circuits together with the associated repair took over 10 weeks to complete. With in excess of 25,000 welded joints in the installation process we were pleased to find that we experienced a relatively small number (~25) of helium leaks from the internal piping to the insulating vacuum. Locating and repairing these leaks proved to be relatively slow going since access had to be made through the external cryostat before the repair could be made. In addition, the final focus assembly is mechanically quite complex and precisely locating very small leaks proved difficult on occasion. Another factor that proved to be significant was large leaks masking smaller ones. The machine vacuum was finally certified 'ready-to-go' by the end of March 99 after a few false starts. The main refrigerator was then brought on-line and a purification of the helium circuits was done with a pump/purge cycle. At the time of this conference the cooldown process is just starting. The schedule calls for the rings to be cooled to 50K (the shield temperature) for some helium spill tests and then cryogenic temperatures by the end of April. The first beam tests are scheduled for the end of May after the power supply and quench protection systems are commissioned. We then plan for beam commissioning to continue for two months until the end of July. We goal for this initial operation is to demonstrate collisions of gold ions. The machine will then have a three month summer shutdown when detector equipment will be installed and the first full running period of 37 weeks will start in November 1999. The goals for this run are 10% of design luminosity and 50% up time.

6 REFERENCES

[1] J. Wei, The Evolution of Hadron Beams under Intrabeam Scattering, Proc. 1993 PAC, p. 3653.

[2] J. Wei, Error Compensation in Insertion Region Magnets, Particle Accelerators, 55, p. 439-448, (1996).

[3] S. Peggs, S. Tepikian, D. Trbojevic, A First Order Transition Jump at RHIC, Proc. 1993 PAC, p. 168.

[4] J. Wei, et. al., Field Quality Evaluation of the Superconducting Magnets for the Relativistic Heavy Ion Collider, Proc. 1995 PAC, p. 461.

[5] R. Gupta, Estimating and Adjusting Field Quality in Superconducting Magnets, Particle Accelerators, 55, p. 375, 1996.

ACKNOWLEDGMENTS

DESIGN CONSIDERATIONS FOR MEDICAL PROTON ACCELERATORS

George Coutrakon, Ph.D., James M. Slater, M.D., F.A.C.R.,
Abiel Ghebremedhin, Ph.D. Loma Linda University Medical Center 11234 Anderson Street
Loma Linda, CA 92354, e-mail: coutrak@proton.llumc.edu

Abstract

The design requirements for current heavy-particle accelerators operated within a hospital to deliver radiation therapy must satisfy both clinical and research needs. Advances in dedicated beam delivery systems for clinical utilization and biological studies add requirements that previous accelerators did not have. Eight years experience using the Loma Linda University proton facility has emphasized that the most important requirements are safety, reliability, beam stability, low energy consumption, and efficiency of beam delivery to the treatment rooms. In the future, raster scanning techniques will add further demands on the control of beam energy, intensity, and position stability. Rapid and precise flexibility in changing beam parameters is essential for satisfying clinical needs; electronic rather than mechanical control is clearly preferable for clinical use. Biological research increases the need to expand the margins of some clinical requirements, such as beam size, intensity, and energy ranges. Both clinical and research activities require a totally integrated control system, beginning with the ion source and continuing through the accelerator and switchyard to multiple rooms and each beam delivery system therein. Accordingly, designing the clinical accelerator requires a highly orchestrated design effort, involving the entire facility. Detailed design requirements addressing these issues will be presented.

1 INTRODUCTION

More than forty years have passed since protons were first used in treating localized tumors in humans. In the meantime, twenty facilities worldwide have treated more than 23,000 patients with proton beams.[1] Until 1990, all of these facilities used previously existing accelerators, which were designed for physics research and later modified for medical use. From 1987 to 1990, the first medical proton accelerator was designed and built for the Loma Linda University Proton Accelerator Facility[2] (LLUPAF) in Loma Linda, CA. This project was a cooperative effort between Loma Linda University, Fermi National Accelerator Laboratory (Fermilab), and Science Applications International Corporation (SAIC). Since 1990, over four thousand patients have been treated with protons at LLUPAF. To date, four more hospital-based facilities are under construction: one in Boston, MA and three in Japan. In addition, many new facilities are in the planning stages in the US, Europe, and Japan.

The advantages of a hospital-based facility over a laboratory-based facility are great. In a hospital, health care professionals can work as a team more efficiently and more effectively in planning, preparing and executing high precision radiotherapy treatments for each patient. In addition, the expensive ancillary equipment (such as CT) and hospital staff are already in place for patient preparation and treatment. Beam time can be dedicated for medical use, which is not the case at physics research laboratories. Finally, anesthetized and other non-ambulatory patients can be treated only in a hospital setting. In many of the new facilities, basic research in radiation biology will also need to be included in the facility requirements as well. In this paper, we examine the primary requirements that any new proton or light ion accelerator will face in a hospital or clinical setting.

2 PROTON DOSIMETRY

The primary advantage of protons over therapeutic x-rays is shown in dose vs. penetration data (Fig.1). One sees that protons give a higher dose at deeper sites and a lower dose near the entrance to the body, where healthy tissue is likely to be. Unlike x-rays, protons have no "exit dose," which spares healthy tissue beyond the Bragg peak.
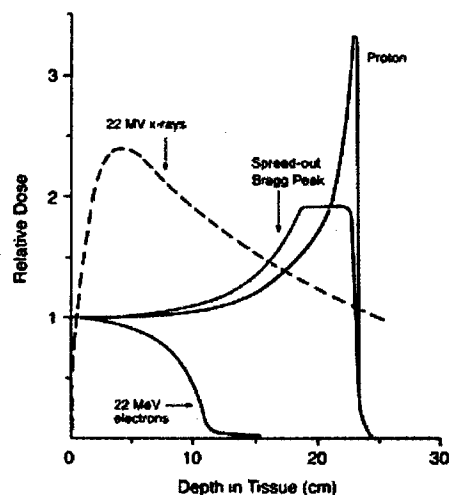
Fig. 1: Dose vs. depth for therapeutic proton, x-ray, and electron beams. The mono-energetic Bragg peak is the narrow one on the right. The spread-out Bragg peak (SOBP) is generated from mono-energetic peaks as shown in Fig. 2. The maximum depth of beam penetration and width of the SOBP can be controlled by the beam energy.

The energy of the proton beam can be so adjusted from the accelerator that protons penetrate to the correct depth for each tumor. By adding Bragg peaks of successively lower

energies and intensities (Fig. 2) a SOBP can be generated which has uniform dose over the entire depth of the tumor. The energy accuracy for each Bragg peak is quite precise and dictates the energy accuracy requirement for the accelerator, as is discussed later. The ability to achieve dose uniformity in depth as well as transverse to the beam direction within the tumor volume is a primary requirement in all radiotherapy treatments.

8 cm SOBP, 155 MeV, 4 mm peak
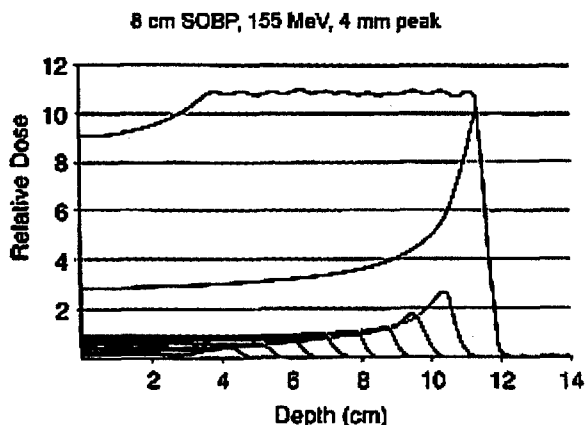
Fig.2: A spread-out Bragg peak (SOBP) generated from the addition of mono-energetic Bragg peaks. The dose uniformity in the SOBP between 4 cm and 12 cm is less than +/-2% with no energy or intensity errors.

3 ACCELERATOR SYSTEM REQUIREMENTS

The primary function of any proton therapy accelerator is to provide treatment rooms with a specified energy and intensity (or dose rate) throughout each treatment. In addition, accelerator or beam transport magnets must be capable of terminating beam to within 1% of the prescribed dose for each treatment. The emittance from the accelerator should be as small as possible, to allow use of smaller magnet apertures and smaller magnets in the beam transport lines and rotating gantries. Typical emittance values for several classes of accelerators are presented in Table 2. The accuracy requirements for energy and intensity will depend largely on the type of beam delivery system that the treatment room uses. For example, scanning the target volume with a narrow pencil beam and rapid energy changes from the accelerator will have much tighter accelerator energy, intensity, and spot position requirements than a beam delivery system that uses lead foils to passively enlarge the beam. Of course, active scanning will offer superior sparing of normal tissues and is a clear goal for all proton and light ion facilities. Examples of active and passive beam delivery systems are shown in Fig. 3a and 3b. For active beam scanning, the accelerator control system must contain a library of energy ramp sets that can be executed in rapid succession to generate SOBPs (Fig.2) at the patient. The exact sequence of energies and intensities must be transmitted electronically from the treatment planning computer for each patient.
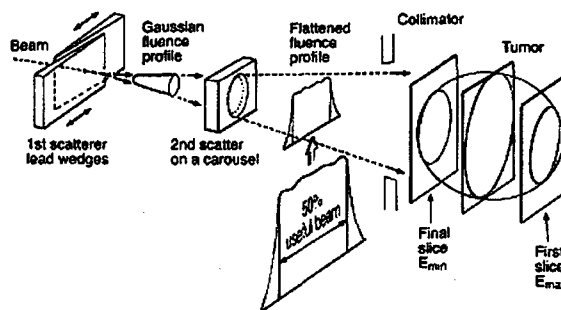
Fig. 3a: Lead foil scattering system to enlarge the beam laterally after transport to the treatment room. Oftentimes, another passive device (not shown) in the treatment room, called a range modulator, is used to degrade parts of the beam to various ranges, which generate the SOBP. This is used in lieu of multiple energy changes from the accelerator. The time structure of the extracted beam is not important in this case.
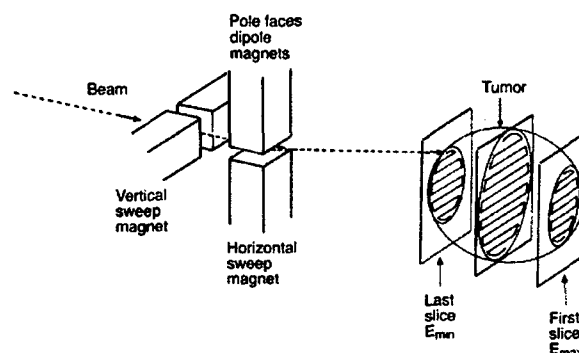
Fig. 3b: Raster scan magnet system to sweep a small (1 cm) beam across the tumor volume. Here, the energy of the beam must be varied from the accelerator.

Fig. 4a and 4b show the ranges of energy and intensity that are required for proton therapy. The energy range most often specified for a therapy accelerator is 70 to 250 MeV, which corresponds to 3 to 40 cm range in water or soft tissue. Fig. 4b shows the fluence requirements in units of protons/cm²/Gy and should be scaled using the appropriate field size, dose rate, and modulation depth that is desired. The ideal facility should have efficient beam extraction and beam delivery systems which will require the minimum beam current (protons/min) to achieve treatment times below several minutes with doses of approximately 2 Gray. This minimizes the risk of an inadvertent overdose to the patient.
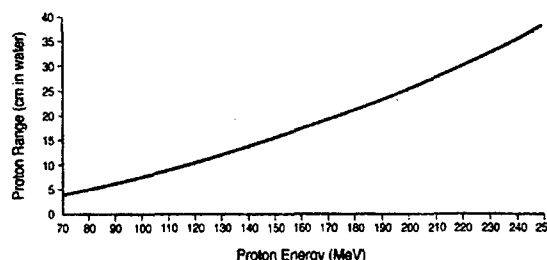
Fig. 4a : Proton energy vs. range in water[3]

(protons/cm²/Gy)x10⁹

Modulation Depth of Bragg Peak (cm)
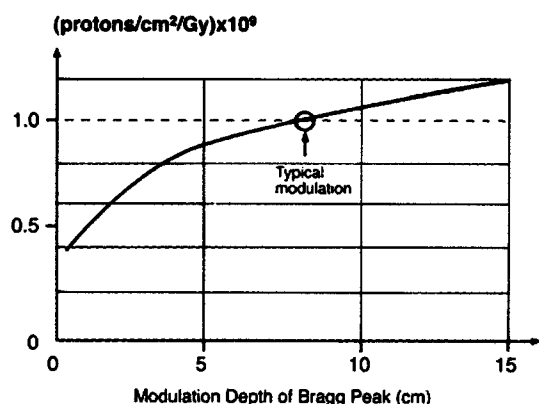
Fig. 4b: Proton fluence/Gray versus width of SOBP for 155 MeV maximum energy[4]. The proton fluence per Gray for 250 MeV maximum energy is about 30% higher than this curve and about 30% less for SOBPs with 100 MeV maximum energy.

4 GENERAL REQUIREMENTS

Some obvious requirements only need mentioning for completeness, but require careful attention for a successful facility. Accelerator reliability is one of the top priorities for all therapy operations. For example, the LLUPAF synchrotron has enjoyed 98% uptime for patient treatments with five treatment days per week and 24-hour operations.

The proton synchrotron services four treatment rooms and one research room. The high reliability has been accomplished with the help of a maintenance team that monitors various systems to perform preventive maintenance before failures occur, particularly with magnet power supplies, vacuum components and water cooling systems. Accelerator reliability is extremely important, particularly for patients in the middle of three- or four-week treatment schedules. Clinical data have shown that patients whose treatments have been interrupted for two or more weeks have increased risk of tumor recurrence compared to patients who keep regularly scheduled treatments. Most of the accelerator down time (2%) over the past three years was due to power outages that caused vacuum failures and magnet power supply problems related to chilled water systems. Oftentimes, any missed treatments can be made up on weekends or by increasing daily dose fractions.

A new facility must be designed for high patient throughput to be financially solvent and to rapidly acquire statistically significant clinical data for each disease site being treated. High patient throughput requires a large number of activities to run smoothly. On the accelerator end, the ability to switch beam energies and treatment room destinations quickly and reliably is crucial to reducing patient waiting times. For the same reason, the dose rate (or intensity) from the accelerator must also be sufficiently high to avoid limiting patient throughput.

At LLUPAF, the average treatment time per patient is about two minutes and the time to switch treatment rooms less than one minute. Since the time to align the patient requires typically ten to fifteen minutes, the accelerator performance does not currently limit the patient throughput. The Loma Linda facility has demonstrated patient throughput as high as 125 patients in a 16-hour day.

Attention should also be given to power supply stability in accelerator systems. This affects energy, intensity, and position stability of extracted beams. In beam transport lines, dipole bending magnet stability effects position stability of the beam in the treatment rooms. Typical values of beam position tolerance require fluctuations less than ± 1mm in the treatment rooms, at the end of a beam line that may be 50 meters from the accelerator. In some cases, the current output from a bending magnet power supply in the beam lines may require current stability to the magnets better than 0.1%. Reproducible and stable current output to all beam transport magnets is crucial to avoid beam losses during treatment and to maintain correct beam position in the treatment rooms.

Efficiency of beam extraction from the accelerator is an area where higher efficiency will lower the radiation activation of accelerator components and make serviceability much easier. Shielding requirements for personnel will also be lower. Higher beam transport efficiency through the switchyard will lower the required intensity from the accelerator, thereby reducing neutron exposure to personnel and the general public. Typical values for beam extraction efficiency and beam transport efficiency at LLUPAF are 90%, with extracted beam currents less than 5 nA (time averaged). This leads to very low equipment activation and low exposure to personnel.

5 REQUIREMENTS FOR BIOLOGICAL STUDIES

A large NASA program has begun at Loma Linda to investigate the health effects of space radiation on astronauts on long missions. These experiments present requirements that differ from therapy beam requirements. In general, they require very low dose exposures, extending from one day to several weeks. To accommodate these requirements, the accelerator must have intensity control that is roughly 100 times lower than therapy beams with energies from 20 to 300 MeV. Small energy changes (< 4 MeV) of once per second would be required to cover this large dynamic range. Many of these irradiations must be done between patient treatments and therefore require a separate room with semipermanent biologic setups. Accelerator and beam line controls must be able to switch between a treatment room and the research room fast enough (less than one minute) so that patient wait times are low. In addition, measurements of mammalian cell damage on the sharp distal edge falloff of the Bragg peak (see Fig. 1) require energy stability of 0.1% from the accelerator. Fortunately, this is within accuracy and stability limits of modern proton therapy accelerators. These are only two examples of a large class

of research requirements that need to be satisfied by the accelerator and control system.

6 INTENSITY REQUIREMENTS FOR BEAM SCANNING

The stacked Bragg peaks in Fig. 2 show that the integrated dose for each peak is different. A dynamic range of 20:1 is required to obtain the desired dose uniformity throughout the SOBP. Approximately ten to twenty energies will be required for each treatment to generate the desired dose uniformity over the entire depth of the tumor. Studies have shown[5] that it is much more time efficient to vary the accelerator intensity for different proton energies than to vary the dwell time for individual energies to achieve the 20:1 range of doses between Bragg peaks. Variable intensity control is, therefore, desirable. The ability to control the beam current from the accelerator with an accuracy of ± 10% over the 20:1 dynamic range also is desirable. For beam scanning applications, it is desirable to have the intensity as uniform as possible as the beam is swept across a target volume, to "paint" a uniform dose distribution. The detailed requirement depends on the beam spot size, σ in the patient and the sweep speed, v, of the scanning magnets. In general, all frequencies below f = v/σ should have intensity ripple below ± 3% to have dose errors less than ± 3% in the plane transverse to the beam direction. For example, a typical beam diameter of 1 cm and magnet sweep speed of 1 cm/ms, yields an intensity stability requirement of ± 3% for frequencies below 1 kHz.

7 ENERGY CONTROL REQUIREMENTS FOR BEAM SCANNING

Due to the sharp falloff at the distal edge of a mono-energetic Bragg peak, each energy must be delivered very precisely relative to the preceding one to generate a superposition of Bragg peaks (or SOBP) with good dose uniformity throughout the depth of the target. When the mono-energetic beams are generated from the accelerator and not from passive devices in the treatment room beam delivery system, much tighter energy control is required. A minimum targeted dose uniformity throughout the tumor volume is currently ± 3%. Note that the distal dose falloff is sharper at lower energies due to lower energy straggling for particles of less range in tissue. Therefore, the dose uniformity, in depth, is more sensitive to range errors at low energies than at high energies. The effects of a 0.7 MeV error (or equivalently 1 mm of range) from one of the Bragg peaks can be clearly seen in Fig. 5, where the dose non-uniformity has increased to 10% near the distal edge. Further simulations have shown that an energy accuracy of ± 0.1 MeV to ± 0.3 MeV (see Table 1, below) is necessary to insure ± 3% dose uniformity in the SOBP.

Depth Dose Uniformity
8 cm SOBP, 155 MeV, 4 mm peak spacing
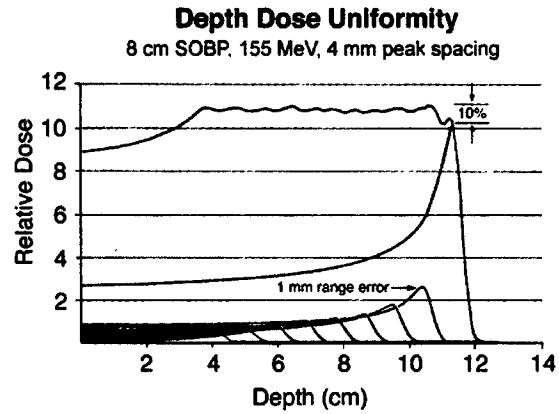
Fig. 5 Effects of 0.5 MeV (1 mm range) energy error on the uniformity of the SOBP. Note that the clinical tolerance of ± 3% has been exceeded.

Table 1: Energy accuracy to achieve ± 3% Dose Uniformity in the SOBP

Energy (maximum)	Allowed Energy Error	Corresponding Range Error	Distal Dose Falloff of Bragg peak (90%-10%)
100 MeV	± 0.1 MeV	± 0.1 mm	1.8 mm
155 MeV	± 0.2 MeV	± 0.4 mm	4.3 mm
250 MeV	± 0.3 MeV	± 0.8 mm	10.0 mm

Fig. 6 shows the dose uniformity as a function of range error for SOBPs with 100 MeV, 155 MeV and 250 MeV maximum energies. The graph is a compilation of 1000 SOBPs with random range errors selected from a gaussian error distribution. The dose uniformity is indicated for the 95 percentile group of the 1000 SOBPs which were generated for each gaussian range error. The range error for ± 3% dose uniformity is consistent with the values shown in Table 1.

Beam Energy (range) Error Analysis
Depth dose uniformity vs. range error for stacked Bragg peaks

r.m.s. Range Error (mm)
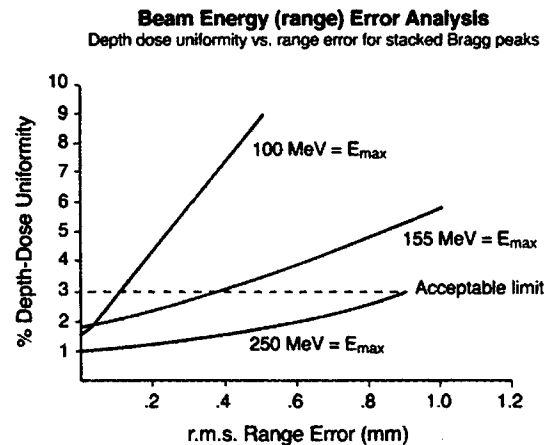
Fig. 6: A monte carlo analysis of 1000 SOBPs for each gaussian error function. Each mono-energetic Bragg peak is given an error and the uniformity of the SOBP is calculated. The curves indicate the upper limit of non-uniformity for 95% of the cases.

Comparison of the three basic accelerator types for proton therapy is outlined in Table 2. All three designs have been shown to work for therapy applications and all

three are currently being built or used for therapy facilities around the world. The parameters listed above are those that customers examine most when selecting an accelerator. Vendors of proton therapy synchrotrons include Mitsubishi Electric Corp. in Kobe, Japan and Optivus Technology, Inc. of San Bernardino, CA. The intensity limit for synchrotrons in Table 2 is taken from the Hitachi accelerator, which uses multiturn injection.

The cost for each type of accelerator has not been included because it depends on the vendor's amortization schedule and the quantity of units to be sold. For example, the cost of development, engineering and overhead may be included differently among vendors. This dependence is probably larger than the difference between economical and more expensive designs. Roughly speaking, cost ranges can be expected to fall between eight and fifteen million dollars (in 1999 dollars) for the three accelerator types, with maximum energy capabilities between 220 to 270 MeV.

Table 2: Accelerator comparisons

	Synchrotron	Cyclotron	LINAC
Vendor(s)	Fermilab/ Optivus Technology (USA) Hitachi (Japan)	IBA (Belgium)	ENEA(Italy)
Energy level selection	continuous	fixed*	continuous
Intensity limit (ave.)	5×10^{12}/min.	AHAN**	AHAN**
Size (diam. or length)	6 meters	4 meters	37 meters
Ave. power consumed (beam on)	370 kW	300 kW	320 kW
Beam emittance (unnormalized, 67% of beam)	1-3 π mm-mrad	10 π mm-mrad*	0.1 π mm-mrad
Rapid energy changes	4 MeV/s	4 MeV/s	4 MeV/ms
Duty factor (% beam on time)	20% at 0.5Hz	100% or CW	0.1% at 300Hz
Beam intensity uniformity (for scanned beams)	adequate***	good	good
Beam extraction efficiency	90%	N/A	N/A
Energy spread (typ)	± 0.1%	± 0.5%	± 0.1%
Energy stability	± 0.1%	N/A	± 0.1%

N/A Not (yet) available

IBA – Ion Beam Applications, Inc.

* While the energy extracted from the cyclotron is fixed, a variable thickness plastic wheel, which intercepts the beam, can reduce the energy to the desired level in a continuous fashion. The main penalties are higher emittance from multiple scattering and higher intensity losses from the energy degrading process which contribute to higher shielding requirements.

** AHAN – As High As Necessary. These intensities can exceed 100 μA but they can be hardware limited at the ion source to the 30 to 300 nA range.

*** Beam intensity uniformity for active beam scanning generally requires intensity regulating feedback loops to achieve uniform intensity. First demonstrated use of a scanning beam system occurred at the Berkeley synchrotron[6] in 1992. Adequate spill uniformity was achieved using intensity control feedback loops.

8 SUMMARY

The design effort for developing a hospital-based heavy-charged-particle facility mandates a highly orchestrated program that requires the hospital personnel teams to work closely with the architects, physicists, and engineers of the vendors involved in the facility. The clinical beam delivery systems and the integrated control systems needed for the facility are complex and are, in general, less well developed than the accelerators, making an orchestrated development effort all the more necessary to ensure that all systems, including the accelerator, function for the benefit of the patient.

9 ACKNOWLEDGEMENTS

The authors take full responsibility for any inaccuracies which may have been reported here about the accelerators discussed. The reader is urged to contact the institutions directly for any accelerator questions which might arise.

10 REFERENCES

[1] J. Sisterson, Particles Newsletter, No. 23, Jan. 1999, Massachusetts General Hospital, Dept. Radiation Oncology, Boston, MA, Web site, http://www.neurosurgery.mgh. harvard.edu/hcl/ptles.htm

[2] J.M. Slater et al., "The Proton Treatment Center at Loma Linda University Medical Center", Int. J. Radiation Oncology, Biology and Physics, Vol. 22, p.383-389 (1992).

[3] J.F. Janni, "Proton Range—Energy Tables; 1KeV-10GeV," Atomic and Nuclear Data Tables, Vol. 27, No.2-5, p.147-529 (1982).

[4] Private communications, A. Koehler, Harvard Cyclotron Laboratory, Cambridge, MA

[5] J. Debus et al., "Proposal for a Dedicated Ion Beam Facility for Cancer Therapy", Internal report, Gesellschaft fur Schwerionenforschung (GSI), Darmstadt, Germany.

[6] W.T. Chu et al., "Instrumentation in Medical Systems", Proceedings of the 1995 Particle Accelerator Conference, p.2394-2398, (1995).

TECHNOLOGY AND CHALLENGES OF LINEAR COLLIDERS

R. Brinkmann

DESY, Notkestr. 85, D-22603 Hamburg, Germany

Abstract

In this talk I'll briefly review the design challenges of a high energy, high luminosity e+e- linear collider and discuss the layout and performance of various technical options. I'll then present the status of the R&D effort and review the performance of the integrated system tests now underway at several laboratories.

1 INTRODUCTION

With the approved LHC project at CERN the energy frontier of Particle Physics will be pushed into new territory, almost an order of magnitude higher than the reach of presently operating collider facilities. In the international community of High Energy Physics there is widespread agreement that an e+e- Linear Collider of 500 GeV center-of-mass energy (upgradable to about 1 TeV) should be the next project to continue the complementary research with hadron and lepton machines, which has proven extremely important and fruitful in the past. Studies towards a next generation Linear Collider are being pursued at several High Energy Physics Laboratories [1]. At present, one can distinguish three different approaches for such a future linear accelerator. The conventional concept of NLC/JLC (SLAC/KEK study) using travelling wave copper structures driven by high peak-power klystrons, similar to the SLC, but at X-band frequency (four times the 3 GHz frequency of the SLAC linac) in order to reach higher gradients. Second, the CLIC study (CERN) still using similar structures but at even higher frequency and replacing the klystrons by a relativistic high power drive beam from which the rf power is extracted. The third concept, pursued by a broad international collaboration centered at DESY, is the TESLA approach of a superconducting linear accelerator. In the following, a brief overview of the different linear collider concepts will be given and the status of the technical developments will be summarised.

2 MACHINE PARAMETERS

The key parameter (in addition to the center-of-mass energy) of a linear collider is the luminosity

$$L = \frac{f_{rep} n_b N_e^2}{4\pi \sigma_x \sigma_y} \qquad (1)$$

where f_{rep} denotes the pulse repetition frequency of the linear accelerator, n_b the number of bunches per pulse, N_e the bunch charge and $\sigma_{x(y)}$ the horizontal (vertical) beam size at the interaction point (IP for short). It can be shown that the luminosity is essentially limited by the AC-power P_{AC} taken from the grid, the overall efficiency η of converting P_{AC} into beam power, the energy loss δ_B due to beamstrahlung at the IP and the normalized vertical beam emittance $\gamma \varepsilon_y$:

$$L \propto \eta P_{AC} \sqrt{\frac{\delta_B}{\gamma \varepsilon_y}} \qquad (2)$$

The power consumption has to remain within reasonable limits and the beamstrahlung has to be limited to a few percent of the beam energy in order to maintain good energy resolution and small background in the interaction region. Thus the only remaining free parameters to optimize the machine performance in terms of the luminosity are the efficiency and the emittance.

An overview of the basic parameters for the X-band, CLIC and TESLA 500 GeV designs is given in Table 1. A common feature of all approaches is operation with long trains of bunches per rf-pulse, necessary to achieve a high rf-to-beam power transfer efficiency. Due to the extremely low power losses in the walls of the superconducting resonators, the pulse length in TESLA can be several orders of magnitude larger than in a conventional accelerator, resulting in a low rf-peak power requirement. Furthermore, in that case the time structure of the beam with large spacing between bunches allows to apply energy and orbit feedback [2] on a bunch-to-bunch basis, thus making the superconducting linac almost immune with respect to pulse-to-pulse drift and jitter effects. The spot size at the IP is two orders of magnitude below what is routinely achieved at the SLC. In addition to a special magnet lattice for beam size demagnification (Final Focus System, see below), good control of emittance dilution in the linac is indispensable to achieve this ambitious goal [3-5]. Wakefields excited by the beam in the accelerating structures are the main cause of emittance blow-up. Since wakefields are strongly dependent on the linac frequency (the transverse wakefield scales approximately proportional to the 3rd power of the frequency), it is no surprise that the alignment tolerances and the needs for frequent orbit optimization and tuning are more stringent for the high-frequency conventional linacs than for TESLA (e.g. for the structure alignment 10 – 15μm as compared to

0.5mm). The realistically achievable beam emittance at the IP is thus lower for TESLA, which, together with the high efficiency, leads to a higher design value of the luminosity. On the other hand, the site length for the X-band and two-beam machines can be shorter thanks to the higher accelerating gradient.

Table 1: Main parameters of the TESLA, X-Band and Two-beam linear colliders at 500 GeV center-of-mass energy.

	TESLA	X-band	CLIC
Frequency [GHz]	1.3	11.4	30
Gradient [MV/m]	22	57	100
AC power [MW]	95	99	68
Efficiency η [%]	23	10	14
Emittance $\gamma\varepsilon_{x,y}$ [μm]	10, 0.03	5, 0.1	2, 0.1
Spot at IP $\sigma_{x,y}$ [nm]	553, 5	335, 4.5	196, 4.5
Beamstrlng. δ_B [%]	3	4	3.6
Lumin. [10^{33}cm^{-2} s^{-1}]	31	7	5
Peak power [MW/m]	0.2	31	230
# of klystrons	616	3312	-
Pulse length [ns]	$9\cdot10^{5}$	224	100
Rep. Rate [Hz]	5	120	200
Bunch spacing [ns]	337	2.8	0.67
# of bunches pp	2820	95	150
Bunch charge [10^{10}e]	2	0.95	0.6

Complete conceptual designs for the X-band [6,7] and TESLA [8] colliders have been worked out, including all sub-systems such as Final Focus, injection systems, etc. The layout of the sub-systems takes the possibility of energy upgrade into account. For TESLA E_{cm}= 800GeV can be reached within the foreseen 32km site with improved performance of the s.c. cavities at g = 34 MV/m. For X-band, the 30km site length accommodates an upgrade to 1 TeV, eventually extendable to 1.5 TeV.

The CLIC group has recently been focusing much attention on the two-beam linac layout and parameters in the very high energy regime, 3 – 5 TeV [9].

As part of the TESLA project study [8], the integration of a coherent (FEL) X-ray user facility in the Angstroem wavelength regime is foreseen. DESY as the co-ordinating laboratory of the TESLA collaboration has taken over the charge to investigate a site next to DESY suitable for the integrated Linear Collider/Free Electron Laser facility. A detailed study of the required civil construction work and the preparations for the legal procedure necessary for project approval are in progress.

3 TEST FACILITIES

The development of the technology required for the next generation linear collider is pursued in the framework of test facilities at several laboratories, see Table 2. The SLC as the only existing linear collider is included in this list. The experience gained from years of successful operation of the SLC in many fields of accelerator physics and technology has proven invaluable for the development of future linear collider projects. Furthermore, the 50 GeV SLC linac has been used to test a beam optical system (Final Focus system) required to provide de-magnification of the spot size to the tiny values foreseen for the next generation machine.

Table 2: Overview of linear collider test facilities

SLC	Only existing L.C.	SLAC
FFTB	Final Focus System	SLAC/int. coll.
NLC-TA	400 MeV X-band linac	SLAC
ASSET	structure test (wakefields, HOM)	SLAC
ATF	1.54 GeV low-ε damping ring	KEK
TTF	s.c. cavity development, 500 MeV linac	DESY/int. coll.
CTF	two-beam test acc.	CERN

3.1 FFTB

The Final Focus Test Beam experiment, set up at the end of the SLAC two-mile linac, was constructed in international collaboration of institutes from 6 countries
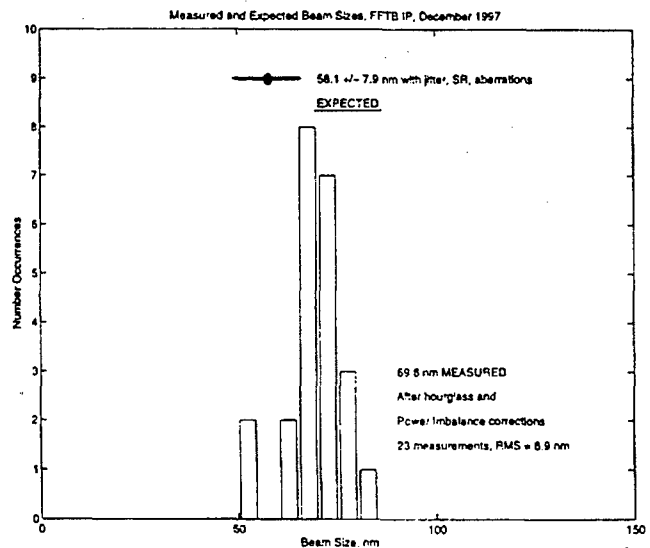
Figure 1: Vertical spot size measurements at the FFTB in comparison with the expected value (58±8nm).

led by SLAC. It comprises a complete beam line very similar to the system required for a future machine, except, of course, for the lower beam energy. First successful operation of the FFTB took place in 1994 [10].

Evaluation of measurements done in Dec. 1997 yield a vertical spot size of about 70nm in reasonable good agreement with the expected value (see Fig. 1). In the analysis, a measured orbit jitter of 40nm was taken into account.

3.2 NLCTA, ASSET

The X-band linac technology is under development at SLAC in collaboration with KEK. The 400 MeV test linac of NLCTA [11] represents a full integrated system test of of the components for the X-band collider. Beam acceleration with a maximum gradient of 40MV/m was achieved at 50% of the design intensity (600mA) and reduction of the multi-bunch energy spread to 0.3% peak-to-peak with beam loading compensation was successfully demonstrated. High power klystrons have been developed with periodic permanent magnet (ppm) focusing (Fig. 2), avoiding the considerable power consumption otherwise due to the focusing solenoid. With a peak power of 50MW at 2μs pulse length and an efficiency of 55% all specifications have been met. Work on a 75MW ppm focused klystron is in progress both at SLAC and KEK. RF-pulse compression by more than a factor of three was achieved with a SLED-II system. The application of a delay line distribution system for pulse compression is foreseen for the future [12,13]. It is also planned to replace the present conventional modulator concept by a more efficient and lower cost induction type device based on solid state technology.

Several 1.8m long X-band structures have been built and tested. The concept of detuning and damping of higher order modes (HOM) is applied to provide a sufficiently strong suppression of long-range wakefields. Beam tests of X-band structures at ASSET [14] (see Fig. 3) have demonstrated the wakefield suppression as well as the possibility to use the HOM signal for precise beam-based alignment of the structures as required for beam stability. Furthermore, the challenge of obtaining a structure straightness at the 10μm level has been addressed [15].

3.3 ATF

The accelerator test facility at KEK comprises a 1.54GeV electron beam injector linac and damping ring and represents an (almost) full size model of a low emittance injection system for the X-band linear collider. So far, operation took place at 1.29 GeV and with damping wigglers off, leading to a damping time of 30ms as compared to the design value of 9ms. With single bunch operation at $6 - 8 \cdot 10^9$ bunch charge, the measured emittances are approaching the ambitious design goals of $3 \cdot 10^{-6}$ m (horizontal, normalised) and $3 \cdot 10^{-8}$ m (vertical, norm.) [16].
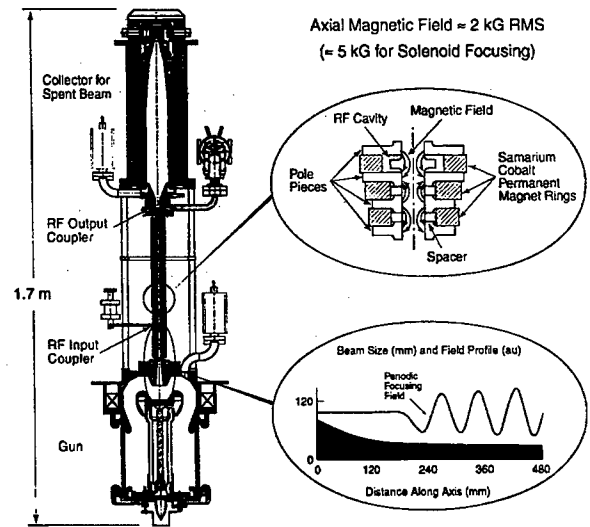
Figure 2: The ppm focused X-band klystron developed at SLAC.
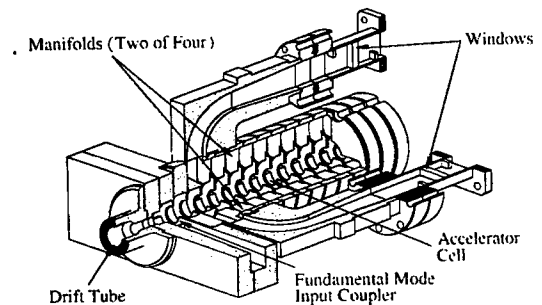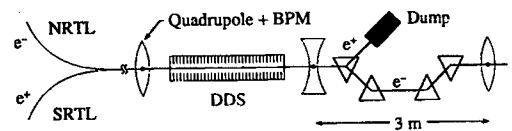
Figure 3: Sketch of the accelerating structure set up (top) at the SLC linac and of the X-band damped-detuned structure (bottom).

3.4 CTF

The main objective of the CLIC test facility at CERN is the demonstration of the two-beam acceleration concept at a frequency of 30GHz. The CTF drive beam line uses a high intensity RF-laser gun, S-band accelerating section and bunch compressor. In 1998 a bunch train with total charge up to 450nC was sent through the 30GHz decelerating/power transfer structure, generating up to 50MW of RF-power [9,17]. The maximum field produced in the main beam accelerating structure was 69MV/m. First test of an active alignment system for the linac components achieved a position stability of 2μm (rms).

For the future, it is planned to upgrade the CTF for a full system test of the newly developed drive beam generation scheme [18,19], as it would be used in a multi-TeV two-beam linear collider facility.
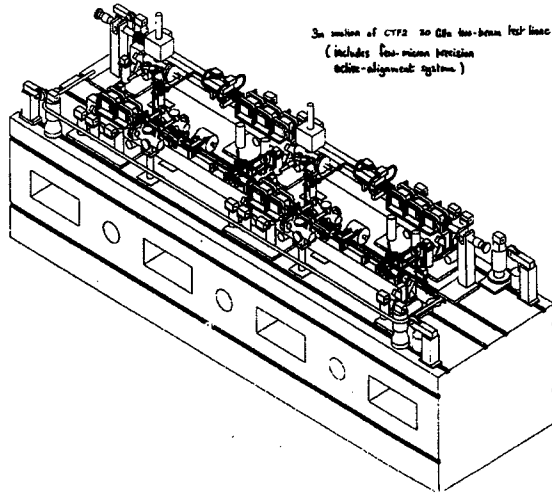
Figure 4: One section of the two-beam accelerator at CTF.

3.5 TTF

The development of high-performance 9-cell superconducting Niobium cavities (Fig. 5) is pursued by the international TESLA collaboration (involving more than 30 institutes from 9 countries) in the framework of the TESLA test facility at DESY.
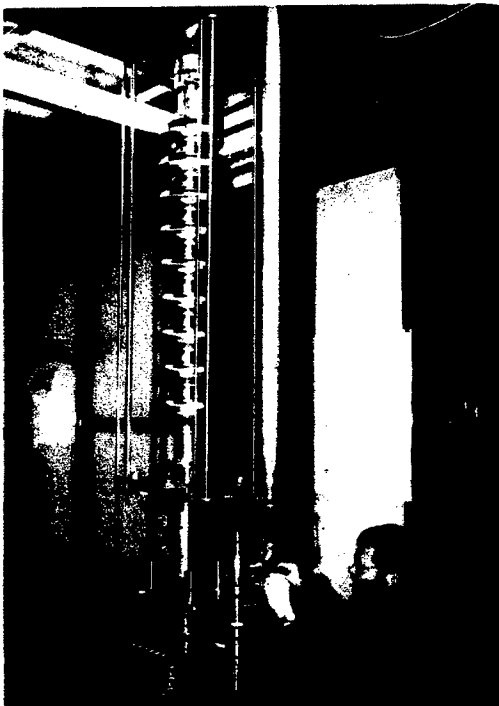
Figure 5: One of the TESLA Niobium resonators being prepared for CW-RF test in the vertical test stand.

The TTF includes the complete infrastructure for cavity processing (clean rooms, chemical and high-temperature treatment, high-pressure rinsing with ultra-pure water), vertical and horizontal test stands for CW- and pulsed-RF operation of the 1.3GHz resonators and a 500MeV linac for a full integrated system test of the accelerator modules with beam. The evolution of the achieved accelerating gradients in vertical test over the last years is shown in Fig. 6. High gradients above 20MV/m were reached already at an early stage, but the failure rate (cavities with poor performance due to fabrication errors) was rather high at that time. The results from the more recent production series shows a strong improvement in the performance statistics, so that the gradient of 22MV/m required for the 500GeV collider is now achieved on average (see ref. [20] for more details). Cavities equipped with RF- and HOM-couplers underwent pulsed power tests in the horizontal test stand. No systematic degradation of performancecompared to the vertical test was observed (Fig. 7).
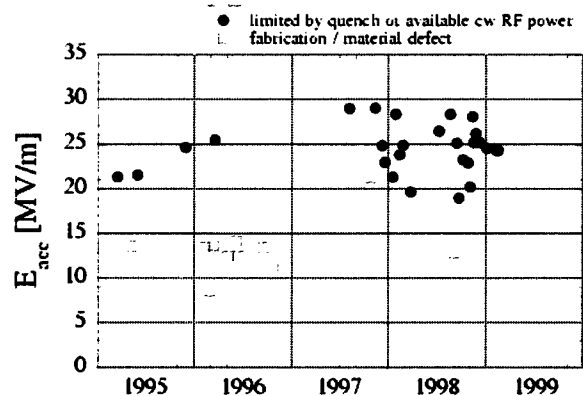
Figure 6: Evolution of accelerating gradient achieved with TESLA cavities on the vertical test stand.
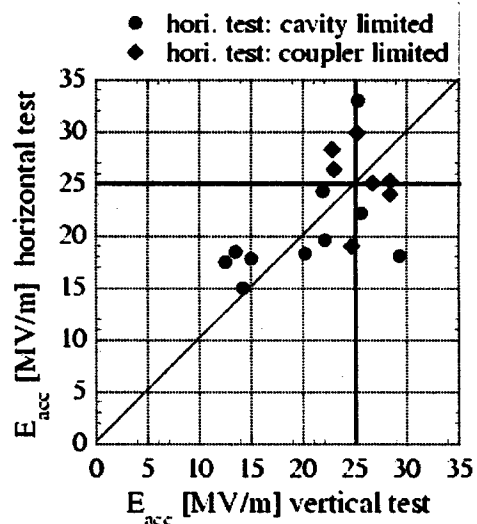
Figure 7: Horizontal vs. vertical test stand results.

Eight 9-cell cavities are assembled into a string and mounted in an accelerator module, which also contains focusing and beam diagnostics devices. So far two of these modules have been installed in the TTF linac and tested with beam. The 1st module reached a gradient of 16MV/m in May 1997. The 2nd module was tested early this year and showed a gradient of 18.5MV/m measured with beam and 20.8 MV/m obtained from RF-measurement, in both cases limited by insufficient RF-power coupler conditioning. From cryogenic measurements a resonator quality factor of $1.3 \cdot 10^{10}$ at T=2K, exceeding the TESLA design goal of 10^{10}, could be deduced. A 3rd module is presently being installed, replacing module #1, and expected (from test stand results for the individual resonators) to yield an average gradient of 25MV/m. The TTF beam line is also being prepared for a first test of the SASE FEL concept, which will take place after beam operation resumes in summer this year.

Accelerating gradients above 30MV/m have already been achieved with some of TESLA cavities (the record value being 33MV/m at full pulse length and rep. rate in the horizontal test stand). The TESLA cavity R&D will continue to define a reliable procedure, suitable for mass production, for obtaining an average gradient of 34MV/m as required for the energy upgrade to 800GeV. One very promising improvement of resonator performance was recently obtained by electro-polishing [21], with gradients up to 37MV/m obtained in single cell L-band cavities.

4 CONCLUSIONS

The technical developments towards a next generation linear collider are far advanced and the X-band and TESLA groups will present technical proposals, incuding cost estimates and schedule, within the next two years.

The recent progress of the CLIC group on both the test facility and the conceptual design of the two-beam linear collider is remarkable. These developments, to my mind, should be seen on a longer time scale. At present the two-beam approach appears to be the most promising concept for a multi-TeV lepton collider, which may be realised as a facility following the next generation linear collider.

Being left with two concepts for the next machine, the obvious question is which one to choose. This decision will have to involve a detailed comparison of the scientific potential as well as the cost of the X-band and TESLA facilities.

5 ACKNOWLEDGEMENT

6 REFERENCES

[1] G. A. Loew (ed.), International Linear Collider Technical Review Committee Report, SLAC-R-471, 1995.

[2] I. Reyzl and R.-D. Kohaupt, contribution to this conference TUA41.

[3] T. O. Raubenheimer, contribution to this conference TUDR1.

[4] K. Kubo, T. Higo and K. Yokoya, contribution to this conference FRA22.

[5] S. Fartoukh, A. Mosnier and O. Napoly, contribution to this conference FRA10.

[6] NLC Zeroth Order Design Report, SLAC-R-474, 1996.

[7] JLC Design Study, KEK 1997.

[8] R. Brinkmann, G. Materlik, J. Roßbach and A. Wagner, Conceptual Design of a 500GeV e+e- Linear Collider with Integrated X-ray Laser Facility, DESY-1997-048.

[9] J.-P. Delahaye et al., contribution to this conference TUDR3.

[10] D. Burke et al., Proc. 4th EPAC London 1994, Vol. I, p. 23.

[11] C. Adolphsen et al., Proc. 17th PAC Vancouver 1997, Vol. I, p. 439.

[12] S. G. Tantawi, R. D. Ruth and P. B. Wilson, contribution to this conference THAL3.

[13] Y. H. Chin et al., contribution to this conference FRA15.

[14] M. Seidel, Proc. 17th PAC Vancouver 1997, Vol. I, p. 434.

[15] T. Higo et al., contribution to this conference FRA16.

[16] T. Okugi et al., contribution to this conference TUDR5.

[17] R. Bossart et al., CLIC note 382, CERN 1998.

[18] R. D. Ruth, Proc. 6th EPAC Stockholm 1998, Vol. I, p. 248.

[19] R. Corsini, contribution to this conference FRA17.

[20] M. Pekeler, contribution to this conference TUDR2.

[21] E. Kako et al., contribution to this conference THAL6.

LHC ACCELERATOR PHYSICS AND TECHNOLOGY CHALLENGES

L.R. Evans, CERN, Geneva, Switzerland

Abstract

The Large Hadron Collider (LHC) incorporates many technological innovations in order to achieve its design objectives at the lowest cost. The two-in-one magnet design, with the two magnetic channels integrated into a common yoke, has proved to be an economical alternative to two separate rings and allows enough free space in the existing (LEP) tunnel for a possible future re-installation of a lepton ring for e-p physics. In order to achieve the design energy of 7 TeV per beam, with a dipole field of 8.3 T, the superconducting magnet system must operate in superfluid helium at 1.9 K. This requires further development of cold compressors similar to those first used at CEBAF. The LHC will be the first hadron machine to produce appreciable synchrotron radiation which, together with the heat load due to image currents, has to be absorbed at cryogenic temperatures. Finally, the LHC is the first major CERN accelerator project built in collaboration with other laboratories. A brief review of the machine design is given and some of the main technological and accelerator physics issues are discussed.

1 INTRODUCTION

The Large Hadron Collider, now under construction at CERN will provide proton-proton collisions with a centre-of-mass energy of 14 TeV and an unprecedented luminosity of 10^{34} cm^{-1} s^{-2}. In order to achieve this it must operate with more than 2800 bunches per beam and a very high intensity. The machine will also operate for heavy (Pb) ion physics at a luminosity of 10^{27} cm^{-1} s^{-2}.

Many accelerator physics issues must be taken into consideration in the machine design. The first is a sound and flexible optics, robust against inevitable lattice perturbations and able to cater for changes in layout demanded by hardware builders and particle physicists. The interaction of the beam with its immediate environment and with the other beam can produce many undesirable effects. Incoherent single particle effects include the beam-beam interaction due to the influence of the electromagnetic field of one beam on the particles in the other, and intrabeam scattering, multiple Coulomb scattering between the particles in the same beam. Collective effects include single bunch instabilities driven by short range wakefields and coupled bunch effects due to the large number of bunches and small separation. Since the unavoidable imperfections in superconducting magnets produce non-linear field errors, the issue of dynamic aperture, the maximum useful betatron amplitude of particles over a long time duration, is also of fundamental importance.

The attainment of 7 TeV in the existing LEP tunnel also presents some considerable technological challenges. The small tunnel cross section as well as the need for cost reduction imposes a two-in-one magnet design for the main dipoles and quadrupoles. The 8.3 T operating field can only be obtained at an acceptable cost by cooling the magnets to 1.9 K, below the lambda point of helium. This presents serious challenges to both the magnet designers and cryogenic engineers.

After a brief description of the machine layout and status, some of these issues are discussed.

2 MACHINE LAYOUT

The basic layout mirrors that of LEP, with eight long straight sections, each approximately 500 m in length available for experimental insertions or utilities. Two high luminosity insertions are located at diametrically opposite straight sections, Point 1 (ATLAS) and Point 5 (CMS). A third experiment, optimised for heavy ion collisions (ALICE) will be located at Point 2. A fourth experiment (LHCb) has now been approved and will be located at Point 8. The two detectors at Points 1 and 5 require a substantial amount of new civil engineering infrastructure, whilst the other two will be integrated into existing LEP caverns. The beams cross from one ring to the other only at these four locations. Points 2 and 8 also contain the injection systems for the 450 GeV/c beams provided by the SPS.

The other four long straight sections do not have beam crossings. Points 3 and 7 are practically identical and are used for collimation of the beam halo in order to minimise the background in the experiments as well as the beam loss in the cryogenic parts of the machine. Consequently they only contain classical warm magnets robust against the inevitable beam loss and secondary shower from the collimators. Point 4 contains the RF systems which are independent for the two beams, where the beam separation must be increased from 194 mm in the regular arcs to 420 mm in order to provide the transverse space needed. Finally, Point 6 contains the beam abort system, where the two beams are extracted using a combination of fast pulsed magnets and steel septa and transported to the external beam dumps.

3 OPTICS

The regular arc cell is 106.9 m in length and contains six dipoles, each of 14.3 m magnetic length. The lattice quadrupoles, 3.1 m in length, are integrated into "short

straight sections" containing a combined orbit correction dipole and chromaticity sextupole and space for another short corrector, either a trim quadrupole, skew quadrupole or octupole, depending on its position in the lattice. The dipoles and quadrupoles are powered independently, with different gradients in the two quadrupole apertures allowing a tune split of up to ten units in order to render the machine insensitive to linear coupling.

The four collision insertions have a similar layout. Moving out from the interaction point (IP), one first encounters the inner triplet. The distance from the IP to the first element of the triplet is 23 m, with the IP at Point 8 displaced longitudinally by 11.25 m with respect to the centre of the experimental hall due to the asymmetric geometry of the LHCb detector. After the triplet, the beams are separated. In the high luminosity insertions 1 and 5, the separation dipoles are not superconducting due to the very high particle flux from the IP. In the other two insertions they must be superconducting due to the restricted longitudinal space available because of the presence of the injection systems.

The long straight section terminates with a twin aperture dipole to bring the beams into the two magnetic channels and a set of four independently powered matching quadrupoles. Between the long straight section and the regular arc there is a dispersion suppressor approximately 171 m long, where the dispersion function is matched to that of the arc. The first three quadrupoles in the dispersion suppressor are also independently powered in order to increase flexibility.

4 ACCELERATOR PHYSICS ISSUES

4.1 The Beam-Beam Interaction

The beam-beam interaction is an inevitable consequence of bringing the beams into collision. The particle trajectories in one beam are perturbed by the electromagnetic field of the other beam. This non-linear interaction excites betatron resonances and also produces a variation of tune with amplitude, generating a tune spread in the beams which makes it more difficult to steer clear of these resonances.

Experience in the SPS has shown that the beam lifetime is strongly reduced when particles straddle resonances of order less than 12. The tune footprint, the image of the beam in the tune diagram, must therefore be small enough to fit in between these resonances. The LHC working point can safely be placed close to the diagonal between 3rd and 10th order resonances provided the tune footprint stays below 0.01. The value of the beam-beam parameter of .0034 with two insertions illuminated is very close to that achieved routinely in the SPS collider.

4.2 Intrabeam Scattering

Intrabeam scattering, or multiple Coulomb scattering between particles in the same bunch, can give rise to a redistribution of the energy of oscillation between the different degrees of freedom. Roughly speaking, the bunch can be thought of as a relativistic gas which is not in thermal equilibrium. Due to the Lorenz contraction, the longitudinal phase plane is much "colder" than the transverse planes, so a transfer of energy takes place between betatron and synchrotron motions. This should result in slow damping of transverse emittance and increase in energy spread. However, due to the dispersion, there is a heating term in the radial phase plane that dominates the damping term. Intrabeam scattering therefore results in an increase in radial emittance that can rapidly degrade the luminosity unless remedial action is not taken. The transverse emittance growth can be strongly reduced by diluting the 6-dimensional phase space density by artificially increasing the longitudinal emittance. In the LHC, the emittance will be increased from its injection value of 1 eV.s to 2.5 eV.s at collision energy. This fixes the maximum RF voltage of 16 MV per beam in order to give sufficient bucket area.

4.3 Dynamic Aperture

The beam-beam interaction generates resonances due to the non-linear nature of the beam-beam force and can limit the available aperture during collision. However, superconducting magnets also have non-linear field errors coming from many sources including persistent currents, small errors in coil geometry and redistribution of current between the strands during ramping. These errors are dominant at the injection field level where the beam must survive for many minutes. The dynamic aperture is defined as the maximum stable amplitude of oscillation in the presence of these errors combined with other effects such as tune ripple and closed orbit distortion.

At the present time the only quantitative ways to investigate the dynamic aperture is by computer simulation and by experiments on existing machines. For the LHC, a computer farm has been dedicated to this activity, where particles are tracked through sample machines where the non-linearities are statistically distributed, for up to 10^6 turns.

In order to check the reliability of the results, extensive experiments have been launched at the CERN SPS and at HERA. They have shown that the simulations agree with the experimental results at the level of 10-20% if all known details like closed orbit errors, coupling and tune ripple are taken into account.

The final objective is to obtain a dynamic aperture from the simulations of at least 12 sigma in order to be sure that in the real machine particles will be stable up to the collimator settings of 6 sigma. This requires a very close

interaction between accelerator physicists and magnet designers in order to define the tolerable errors during series production of the magnets and to define the small correctors needed to compensate for systematic non-linearities, especially the sextupole and decapole fields generated by persistent currents.

4.4 Collective Effects

Collective effects can be broadly separated into single bunch effects, where bunch instability is driven through the short range wakefields generated by the interaction of the beam with its environment, and multibunch instabilities generated by the long range wakefields .

The most common of the single bunch instabilities is the transverse slow head-tail instability. This can be suppressed for the rigid dipole mode m=0 by operating the machine with a small positive chromaticity. Another instability driven by the broadband impedance is caused by coupling between transverse modes and is potentially much more dangerous since it cannot be suppressed in this way. However this instability, unlike the head-tail, shows a threshold behaviour, which occurs at about twice the nominal beam current for the LHC. The longitudinal equivalent of the transverse mode-coupling instability is known as the microwave instability. Due to the very low coupling impedance, the threshold for onset of this instability is also well above the nominal bunch current.

The most important multibunch effect in the LHC is the transverse resistive wall instability. Its growth rate is proportional to the square root of the resistivity of the beam pipe and to the inverse cube of its radius. The instability exhibits no threshold behaviour but its growth rate can be reduced by coating the inside of the beam screen with a 50 μm layer of copper and cooling it to below 20 K where its resistivity is further reduced. The e-folding time for the most dangerous mode at a frequency of a few kHz then exceeds 100 turns, which can easily be damped with an active feedback system.

5. TECHNOLOGICAL CHALLENGES

5.1 Superconducting Magnets

The LHC will require more than 8000 superconducting magnets of different types. The most challenging are the 1232 superconducting dipoles which must operate reliably at the nominal field of 8.3 Tesla, corresponding to the centre-of-mass energy of 14 TeV, with the possibility of being pushed to an ultimate field of 9 Tesla.

In the early days of magnet development, two technologies for the attainment of fields above 9 Tesla were investigated. The first of these was using Nb_3Sn at 4.2 K. Indeed a dipole model with a first quench at 11 Tesla was built using this technology. However, the coils are very difficult and expensive to manufacture and are not suitable for economic mass production.

Nevertheless this technology is still being pursued on a small scale for possible use in selected areas, for example for second generation low-beta quadrupoles.

The other, more economical alternative is to use conventional NbTi technology at reduced temperature. This suffers from the drawback that the specific heat of the superconducting material and its associated copper matrix falls rapidly as the temperature is reduced. For example, the specific heat of copper falls by about a factor of 5, to 0.03 J/kg.K between 4.2 K and 1.9 K. This makes the coil much more prone to premature quenches due to small frictional movements of conductor strands since the adiabatic temperature rise for a given amount of frictional energy is much higher at 1.9 K than at 4.2 K. One can therefore expect more training of these magnets at the highest field levels than at 4.2 K. The important thing is that there is no retraining below the ultimate operational field of 9 Tesla.

The special properties of superfluid helium can be used in part to compensate for this disadvantage. The most well known property of this material is the absence of viscosity but for the purpose of superconducting magnet design, the most important properties are the very large specific heat (about 4000 J/kg.K) and the enormous thermal conductivity at low heat flux. The cable insulation is therefore designed to be as porous as possible to allow penetration of helium whilst maintaining good electrical insulation properties. In this way the helium can contribute to absorbing energy and transporting heat away from the coils.

The development of two-in-one superconducting dipoles and quadrupoles has proved to be a considerable challenge. For the dipoles, this work has been done both at CERN and in industry where a number of long dipoles have been constructed. Recently the coil geometry has been modified from the original 5-block design to improve the field quality and to allow more flexibility for small changes during series production. A number of models using this modified 6-block geometry have performed very well, with first quenches well above 9 Tesla and fast training to the conductor limit of 10 Tesla (Fig. 1). A final full-length prototype with this coil geometry is presently being prepared for testing. Another important outcome of the R&D programme is that the level of compressive prestress applied to the coils can be considerably lowered without loss of performance. This has opened up the possibility of changing from aluminium to stainless steel collars, reducing tolerances and simplifying magnet assembly during series production.

The lattice quadrupoles are designed by CEA/Saclay in collaboration with CERN. To produce the required gradient of 223 T/m the same cable as for the outer layer of the dipole is used in a two-layer geometry. Two prototypes are under construction and the first will be tested before the end of the year.
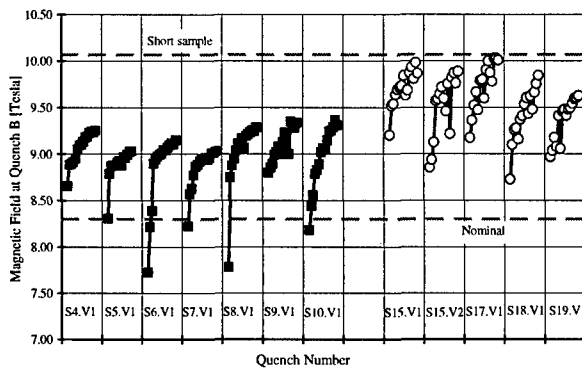
Figure 1: Quench performance of 5-block versus 6-block (open circles) dipole models.

The procurement of some 1200 tons of superconducting cable is a critical path item for the dipole fabrication. The cable will be procured by CERN and supplied to the magnet manufacturers. Contracts for the full supply have been placed with firms in Europe, Japan and the USA. As part of the US contribution to the LHC construction a test facility has been set up at BNL for cable measurement and quality control.

The long straight sections and insertion regions contain many specialised magnets, the most demanding of which are the high gradient (220 T/m), large (70 mm) aperture quadrupoles for the inner triplets of the low-beta insertions. Two versions of this quadrupole have been designed, and prototype models built at KEK and Fermilab. The final integration of both Japanese and US magnets into the inner triplets will be done at Fermilab.

5.2 Cryogenics

Cooling more than 31000 tons of material spread over 26.7 kms to below 2 K presents a considerable technological challenge. The most convenient way to cool helium to below its critical temperature is to reduce the vapour pressure above the liquid bath. At 50 mbar the liquid crosses the lambda point at 2.17 K and it is necessary to reduce the pressure to below 20 mbar to reach the 1.9 K operating temperature. In practice, the LHC will operate in a static bath of pressurised superfluid helium at 1.9 K cooled with flowing saturated superfluid helium at 15 mbar through a linear heat exchanger extending over each full 107 m long cell of the machine. In view of the high thermodynamic cost of refrigeration at such a low temperature, most of the system heat loads are intercepted at higher temperature. As a result, the LHC requires a mix of refrigeration duties at several temperature levels. The machine will be cooled by eight cryoplants, each with an equivalent capacity of 18 kW at 4.5 K. Four of these will be the existing LEP refrigerators upgraded in capacity from 12 kW to 18 kW and adapted for LHC duty. The other four new plants, unlike those of LEP, will be entirely installed on the surface, reducing the need for additional underground infrastructure.

In order to create the superfluid helium at 1.9 K, it is necessary to compress cold helium gas from 15 mbar up to atmospheric pressure by the use of cold hydrodynamic compressors attached to the 4.5 K cryogenic plants. CERN has conducted a vigorous R&D effort with three industrial partners with the aim of investigating technological alternatives and validating efficient reliable solutions for these machines. In order to achieve this, three scale 1:5 prototype compressors for the first stage of compression from 10 to 30 mbar have been built and successfully tested (Fig. 2). Orders have now been placed for the eight full-size cold compressors, each handling 125 g/s of helium.
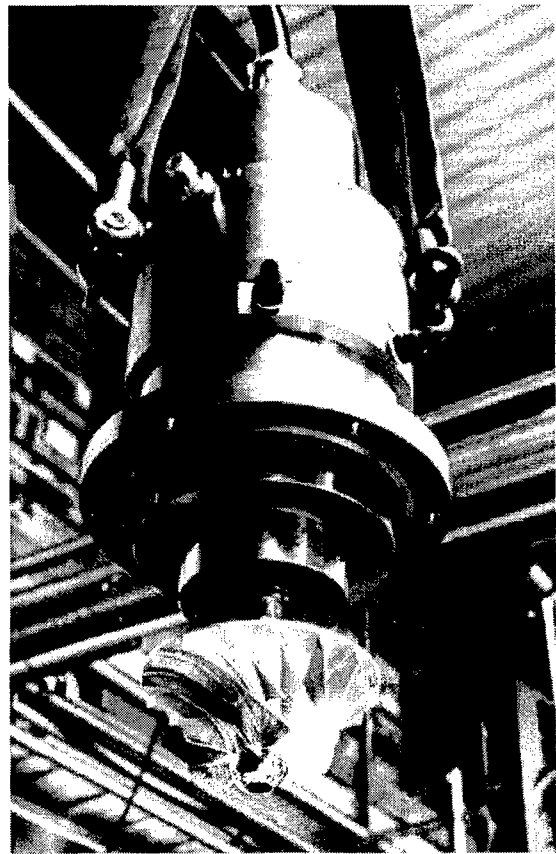
Figure 2: The impeller of a prototype cold compressor stage.

Among the other cryogenic components under development, it is worth mentioning the high-temperature (HTS) current leads. The superconducting magnets have to be fed with a total current of more than 3.5 MA with current ratings from 13 kA (main dipoles and quadrupoles) to 100 A (orbit correctors). The leads for the higher currents, 13 kA to 0.6 kA, will be made using HTS technology in order to reduce the refrigeration requirements for lead cooling. Prototype pairs of such current leads have been ordered from industry. The first of these has been successfully tested up to the design current of 13 kA (Fig. 3).
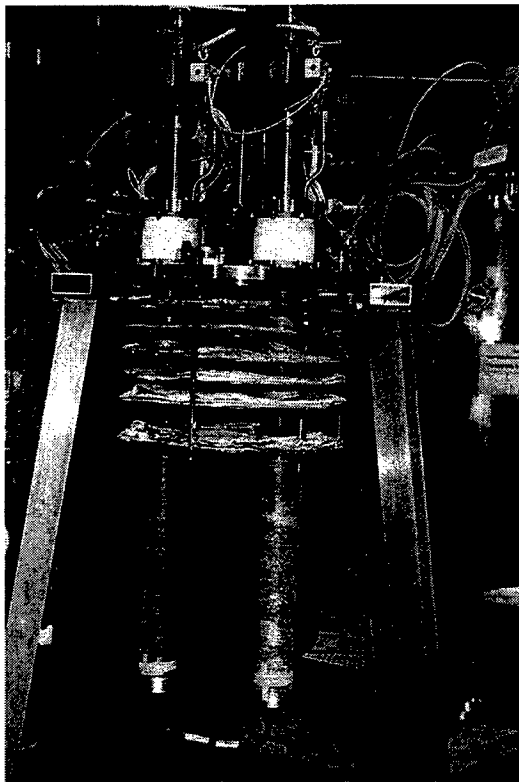
Figure 3: 13 kA HTS current leads.

5.3 Vacuum

The high intensity beams in the LHC will deposit heat into the cryogenic surface surrounding the beam through a number of effects. The most important of these are image currents (up to about 0.8 W/m) and synchrotron radiation (0.6 W/m). These heat loads cannot be taken at 1.9 K and will be intercepted by a beam screen fitted inside the magnet cold bore and cooled by circulation of supercritical helium between 5 K and 20 K. Gas desorbed by the synchrotron radiation cannot be efficiently cryo-pumped by the screen at this high temperature. In order to avoid a catastrophic pressure rise, the screen is punched with small holes over about 2% of its surface so that the cold bore can pump away the gas while being protected from the heat source.

Another effect producing heat is inelastic scattering of protons with the residual gas molecules. This cannot be intercepted by the screen and must be transported away by the superfluid. Recently an additional heat source has been identified, secondary and photoelectrons accelerated across the beam pipe due to the bunched nature of the beam. Under unfavourable conditions, this could result in a resonant build-up of the electron cloud (multipactor), heavily loading the cryogenic system and causing beam instability. In order to avoid this, the secondary emission coefficient of the screen surface must be kept below about 1.4.

5.4 Radiofrequency

The RF frequency, 400.8 MHz, is the highest multiple of the SPS RF frequency (200.4 MHz) compatible with the length of the SPS bunches at transfer. Each beam has a separate system necessitating an increase of the beam separation from 194 mm to 410 mm. Eight single-cell cavities per beam are needed. The maximum operating voltage per cavity (2 MV) corresponds to a very conservative average accelerating gradient of 5 MV/m. The cavities are made from copper with a thin film of niobium sputtered on the inside surface, identical to those of LEP. In order not to lose the technology transferred to firms during the LEP project, these cavities are now being manufactured and the first complete two-cavity unit has been assembled and tested (Fig. 4). The RF coupler is the most critical cavity component with a forward power of 180 kW. It will be an upgraded version of the LEP coupler with a d.c. bias on the inner conductor to suppress multipactoring in the coaxial part.
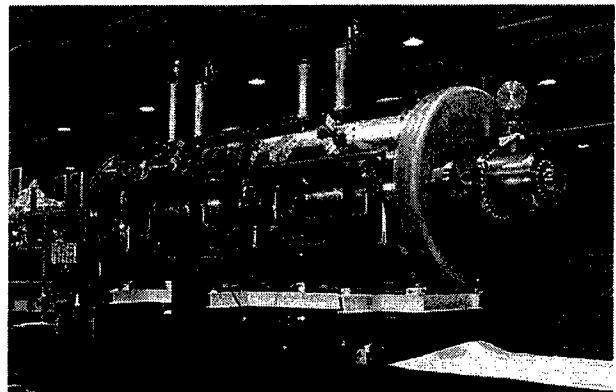
Figure 4: Two LHC 400 MHz superconducting cavities.

5 CONCLUSIONS

From the point of view of accelerator physics, the LHC machine design rests on a sound base, with a great deal of accumulated knowledge from previous projects to guide the choice of parameters and the steps needed to combat undesirable effects. On the hardware side, the LHC represents a technological step forward, stimulated by the need to achieve the best possible performance within the constraints of the existing infrastructure and at the lowest possible cost.

6 ACKNOWLEDGEMENTS

ACCELERATION OF POLARIZED PROTONS TO HIGH ENERGY *

T. Roser[†], BNL, Upton, NY 11973, USA

Abstract

High energy polarized beam collisions will open up the unique physics opportunities of studying spin effects in hard processes. However, the acceleration of polarized beams in circular accelerators is complicated by the numerous depolarizing spin resonances. Using a partial Siberian Snake and a rf dipole that ensure stable adiabatic spin motion during acceleration has made it possible to accelerate polarized protons to 25 GeV at the Brookhaven AGS. Full Siberian Snakes and polarimeters are being developed for RHIC to make the acceleration of polarized protons to 250 GeV possible. A similar scheme is being studied for the 800 GeV HERA proton accelerator

Figure 1: The evolution of the spin tune during the crossing of a resonance with strength ϵ

1 SPIN DYNAMICS, RESONANCES AND SIBERIAN SNAKES

Accelerating polarized beams requires an understanding of both the orbital motion and spin motion. Whereas the effect of the spin on the orbit is negligible the effect of the orbit on the spin is usually very strong. The evolution of the spin direction of a beam of polarized protons in external magnetic fields such as exist in a circular accelerator is governed by the Thomas-BMT equation [1],

$$\frac{d\overrightarrow{P}}{dt} = - \left(\frac{e}{\gamma m} \right) \left[G\gamma \overrightarrow{B_\perp} + (1 + G) \overrightarrow{B_\parallel} \right] \times \overrightarrow{P}$$

where the polarization vector P is expressed in the frame that moves with the particle. This simple precession equation is very similar to the Lorentz force equation which governs the evolution of the orbital motion in an external magnetic field:

$$\frac{d\overrightarrow{v}}{dt} = - \left(\frac{e}{\gamma m} \right) \left[\overrightarrow{B_\perp} \right] \times \overrightarrow{v}.$$

From comparing these two equations it can readily be seen that, in a pure vertical field, the spin rotates $G\gamma$ times faster than the orbital motion. Here $G = 1.7928$ is the anomalous magnetic moment of the proton and $\gamma = E/m$. In this case the factor $G\gamma$ then gives the number of full spin precessions for every full revolution, a number which also called the spin tune ν_{sp}. At top RHIC energies this number reaches about 400. The Thomas-BMT equation also shows that at low energies ($\gamma \approx 1$) longitudinal fields $\overrightarrow{B_\parallel}$ can be quite effective in manipulating the spin motion, but at high energies transverse fields $\overrightarrow{B_\perp}$ need to be used to have any effect beyond the always present vertical holding field.

The acceleration of polarized beams in circular accelerators is complicated by the presence of numerous depolarizing spin resonances. During acceleration, a spin resonance is crossed whenever the spin precession frequency equals the frequency with which spin-perturbing magnetic fields are encountered. There are two main types of spin resonances corresponding to the possible sources of such fields: imperfection resonances, which are driven by magnet errors and misalignments, and intrinsic resonances, driven by the focusing fields.

The resonance conditions are usually expressed in terms of the spin tune ν_{sp}. For an ideal planar accelerator, where orbiting particles experience only the vertical guide field, the spin tune is equal to $G\gamma$, as stated earlier. The resonance condition for imperfection depolarizing resonances arise when $\nu_{sp} = G\gamma = n$, where n is an integer. Imperfection resonances are therefore separated by only 523 MeV energy steps. The condition for intrinsic resonances is $\nu_{sp} = G\gamma = kP \pm \nu_y$, where k is an integer, ν_y is the vertical betatron tune and P is the superperiodicity. For example at the AGS, $P = 12$ and $\nu_y \approx 8.8$.

Close to a spin resonance the spin tune deviates away from its value of $G\gamma$ of the ideal flat machine. For a resonance with strength ϵ, which is the total spin rotation due to the resonance driving fields, the new spin tune is given by the equation

$$\cos \left(\pi \nu_{sp} \right) = \cos \left(\pi G\gamma \right) \cos \left(\pi \epsilon \right).$$

Fig. 1 shows the solutions of this equation with and without a resonance. A similar calculation can be done for the effective precession direction or, as it is now often called, the stable spin direction. The stable spin direction describes those polarization components that are repeated every turn. Note that both the stable spin direction and the spin tune are completely determined by the magnetic structure of the

† Email: roser@bnl.gov

accelerator and the beam energy. The magnitude and sign of the beam polarization, however, depends on the beam polarization at injection and the history of the acceleration process.

The spin tune and stable spin direction calculations apply only to a time-independent static situation or if parameters are changed adiabatically. Far from the resonance the stable spin direction coincides with the main vertical magnetic field. Close to the resonance, the stable spin direction is perturbed away from the vertical direction by the resonance driving fields. When a polarized beam is accelerated through an isolated resonance at arbitrary speed, the final polarization can be calculated analytically [2] and is given by

$$P_f/P_i = 2e^{-\frac{\pi|\epsilon|^2}{2\alpha}} - 1,$$

where P_i and P_f are the polarizations before and after the resonance crossing, respectively, and α is the change of the spin tune per radian of the orbit angle. When the beam is slowly ($\alpha \ll |\epsilon|^2$) accelerated through the resonance, the spin vector will adiabatically follow the stable spin direction resulting in spin flip as is indicated in Fig. 1. However, for a faster acceleration rate partial depolarization or partial spin flip will occur.

Traditionally, the intrinsic resonances are overcome by using a betatron tune jump, which effectively makes α large, and the imperfection resonances are overcome with the harmonic corrections of the vertical orbit to reduce the resonance strength ϵ [3]. Both of these methods aim at making the resonance crossing non-adiabatic. They require very accurate adjustments at every resonance crossing which can become very difficult and time consuming.

Over the last ten years new techniques to cross both imperfection and intrinsic resonances adiabatically have been developed. The correction dipoles used to correct the imperfection resonance strength to zero were replaced by a localized spin rotator or 'partial Siberian snake' which makes all the imperfection resonance strengths large and causes complete adiabatic spin flip at every imperfection resonance [5]. The tune jump quadrupoles were recently replaced at the AGS by a single rf dipole magnet which increased the strength of the intrinsic resonances by driving large coherent betatron oscillations.

At higher energies a 'full Siberian snake' [4], which is a 180° spin rotator of the spin about a horizontal axis, will keep the stable spin direction unperturbed at all times as long as the spin rotation from the Siberian snake is much larger than the spin rotation due to the resonance driving fields. Therefore the beam polarization is preserved during acceleration. An alternative way to describe the effect of the Siberian snake comes from the observation that the spin tune with the snake is a half-integer and energy independent. Therefore, neither imperfection nor intrinsic resonance conditions can ever be met as long as the betatron tune is different from a half-integer.

A local spin rotator can be constructed by using either a solenoid at lower energies or at high energy by a sequence
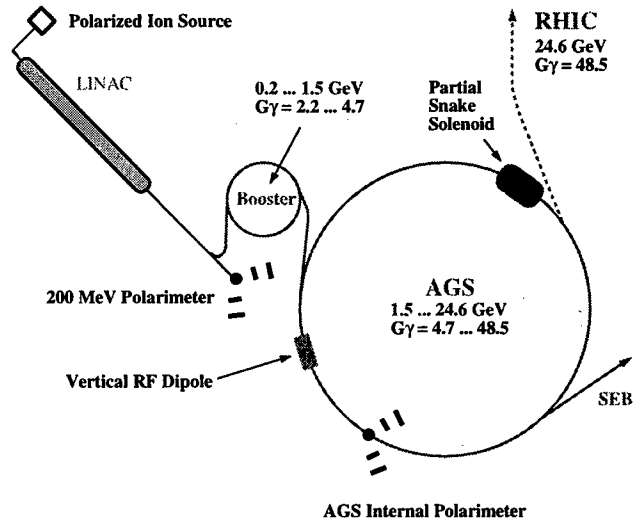
Figure 2: Layout of the AGS accelerator complex showing the location of the partial Siberian snake, the vertical rf dipole, and the AGS internal polarimeter

of interleaved horizontal and vertical dipole magnets producing only a local orbit distortion. Since the orbit distortion is inversely proportional to the momentum of the particle, such a dipole snake is particularly effective for high-energy accelerators, e.g. energies above about $30\,GeV$.

2 RECENT RESULTS FROM AGS, IUCF AND COSY

Polarized proton beam experiments at the AGS have demonstrated the feasibility of polarized proton acceleration using a 5% partial Siberian snake. Fig. 2 shows a layout of the AGS accelerator complex highlighting the necessary hardware for polarized beam acceleration in the AGS. It was shown that a 5% snake is sufficient to avoid depolarization from imperfection resonances without using the harmonic correction method up to the required RHIC transfer energy of about 25 GeV. Fig. 3 shows the evolution of the beam polarization as the beam energy and therefore $G\gamma$ is increased [6]. As predicted the polarization reverses its sign whenever $G\gamma$ is equal to an integer. At this relatively low energy polarization is preserved even without snake but is partially lost at energies close to integer values of $G\gamma$.

More recently a novel scheme of overcoming strong intrinsic resonances using a rf dipole magnet was successfully tested [8]. Full spin flip can be achieved with a strong artificial rf spin resonance excited coherently for the whole beam by driving large coherent vertical betatron oscillations. If the rf spin resonance location is chosen near the intrinsic spin resonance, the spin motion will be dominated by the rf resonance and the spin near the intrinsic resonance will adiabatically follow the spin closed orbit of the rf spin resonance. With the rf dipole, a new dominant resonance near the intrinsic resonance is introduced to flip the spin, in-
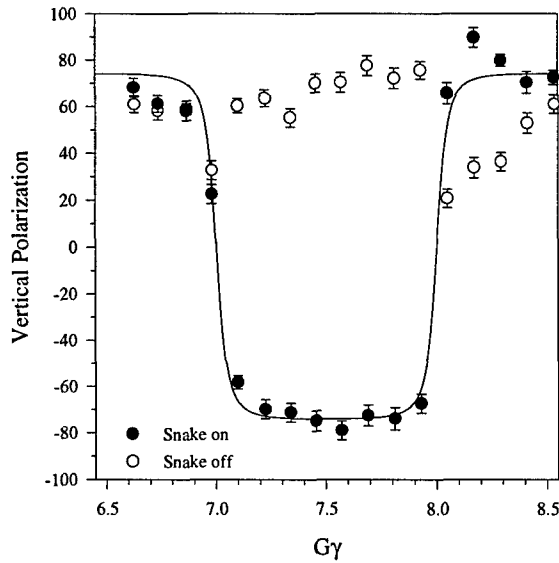
Figure 3: The measured vertical polarization as a function of $G\gamma$ for a 10% snake is shown with and without a snake. The solid line is the predicted energy dependence of the polarization.

AGS Polarization

Figure 4: Vertical polarization versus $G\gamma$ measured in the AGS. The lower curve is the result of a spin tracking calculation for the experimental conditions. The upper curve simulates the use of a helical partial snake in the AGS.

stead of enhancing the intrinsic resonance, as has been proposed earlier [7], which would also enhance the strength of the nearby coupling resonance. Fig. 4 shows the new record proton beam polarization achieved during the last AGS polarized beam experiment. The rf dipole was used to completely flip the spin at the four strong intrinsic resonances $0+\nu_y$, $12+\nu_y$, $36-\nu_y$, and $36+\nu_y$. The lower curve shown going through the data points was obtained from a spin tracking calculation simulating the experimental conditions. Most of the remaining polarization loss is caused by the coupling resonances. A new AGS partial snake using a helical dipole magnet would eliminate all coupling resonances. Spin tracking simulations of this condition are depicted by the upper curve in Fig. 4.

During the last year the Cooler Synchrotron (COSY) at the Forschungszentrum in Juelich, Germany, has successfully accelerated polarized protons to $2.7\,GeV/c$ [9]. With the low acceleration rate used at COSY stable full spin flip at the few imperfection resonances can easily be achieved with small harmonic orbit distortions. The intrinsic resonances were crossed with a pulsed quadrupole using the tune jump method.

The studies of polarized proton acceleration and storage are also continuing at the IUCF Cooler. Most recently it was shown that an artificial spin resonance can be used to flip the spin of a store polarized beam even in the presence of a full Siberian snake[10]. In this as in all other experiments that use artificial spin resonances a simple oscillating field is used to drive the spin resonance. Even though an oscillating field is in fact the sum of two counter rotating fields, only one is generally in resonance with the beam precession frequency. However, with a full Siberian snake the spin tune is a half-integer and therefore the two
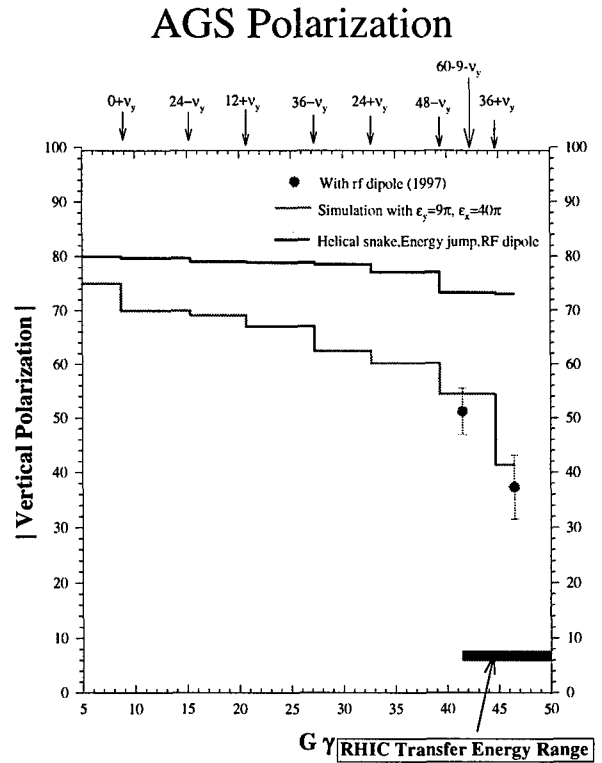
counter-rotating fields are both in resonance and interfere so that effectively only half of the beam around the ring circumference sees a driving field. The IUCF experiment showed successfully that it is possible to slightly reduce the snake strength to avoid this degeneracy. A spin flip efficiency of 91% was achieved. This result is very encouraging for polarized proton colliders such as RHIC where the long storage times would make it necessary to reverse the polarization of the stored beam frequently to reduce systematic errors[11]. The efficiency reachable at the IUCF experiment is limited by the fact that both the snake and the rf resonance driving field are solenoids which can cause synchrotron sideband spin resonances close to the main artificial spin resonance. This would not be an issue at a high energy machine where transverse fields would be used for snakes and for driving spin resonances.

3 PLANS FOR RHIC AND HERA

By using Siberian snakes the stage is set for the acceleration of polarized proton beams to much higher energies. With snakes all depolarizing resonances should be avoided since the spin tune is a half-integer independent of energy. However, if the spin disturbance from small hori-

Polarized Proton Collisions at BNL
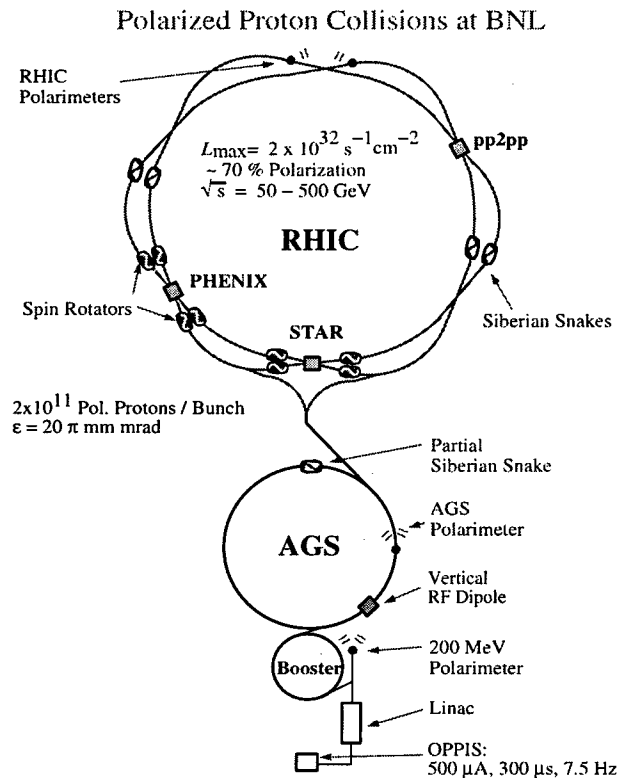
Figure 5: The Brookhaven hadron facility complex, which includes the AGS Booster, the AGS, and RHIC. The RHIC spin project will install two snakes per ring with four spin rotators per detector for achieving helicity-spin experiments.

Figure 6: Schematic picture of the superconducting helical dipole shows the 16 helical current blocks and half of the iron yoke

zontal fields is adding up sufficiently between the snakes depolarization can still occur. This is most pronounced when the spin rotation from all the focusing fields add up coherently which is the case at the strongest intrinsic resonances. A simplistic rule of thumb would then suggest that as long as the total spin rotation of all the Siberian snakes is much larger than the total spin rotation per turn caused by the strongest spin resonance the polarization should be preserved during acceleration. This rule holds for the AGS partial Siberian snake with regard to the imperfection resonances. It would also predict that for a beam with a normalized 95% emittance of $20\,\pi\,mm\,mrad$ at least two snakes are needed for RHIC and four snakes for HERA.

Polarized protons from the AGS are injected into the two RHIC rings to allow for up to $\sqrt{s} = 500\,GeV$ collisions with both beams polarized [12]. Fig. 5 shows the lay-out of the Brookhaven accelerator complex highlighting the components required for polarized beam acceleration.

Of particular interest is the design of the Siberian snakes (two for each ring) and the spin rotators (four for each collider experiment) for RHIC. Each snake or spin rotator consists of four $2.4\,m$ long, $4\,T$ helical dipole magnet modules each having a full 360 degree helical twist [13]. Using helical magnets minimizes orbit excursions within the extend

of the snake or spin rotator which is most important at injection energy. Nevertheless the bore of the helical magnets has to be 10 cm in diameter to accommodate the 3 cm orbit excursions. Superconducting helical dipoles have been successfully tested at BNL using thin cable placed into helical grooves that have been milled into a thick-walled aluminum cylinder. A schematic picture of the helical dipole magnet is shown in Fig. 6. The first full length magnet has recently been successfully tested[14].

To verify that full polarization is preserved during acceleration in RHIC an elaborate spin tracking program was developed[15]. The acceleration through the energy region of the strongest resonance was simulated in great detail including a 1 mm rms misalignment of the quadrupoles, and sextupoles as well as the corrector dipoles used to correct the closed orbit. The result is shown in Fig. 7 for a beam with a normalized 95% emittance of $20\,\pi\,mm\,mrad$. The upper and lower curve show the result for the full beam and the particles at the edge of the beam, respectively. Although there is a significant decrease of the polarization at the energy of the resonance at $G\gamma = 5 \times 81 + (\nu_y - 12) =$
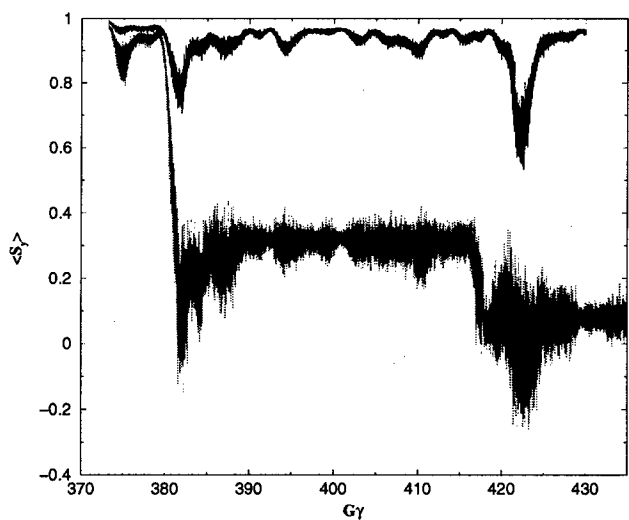
Figure 7: Result of spin tracking through the region of the strongest resonance in RHIC. The closed orbit was corrected with residuals of less than 0.2 mm.

422.18, the polarization of the full beam is restored after accelerating completely through the resonance region. The simulation also shows that there is significant polarization loss at the edge of the beam. This fact highlights the need for a polarimeter that can measure polarization profiles.

Measuring proton polarization at high energies has been the focus of several workshops and experiments. The analyzing power of only very few reactions has been measured at high energies and the magnitudes are typically rather small. Polarization sensitive interaction with an external electromagnetic field is also much smaller than for the much lighter electron for which Compton back scattering is typically used for high energy polarization measurement. Two methods are presently being considered for RHIC. Inclusive pion production from both hydrogen and carbon targets has been shown to have large analyzing power. Magnetic spectrometers are being designed for RHIC to allow for high rate data acquisition. The second method is based on the relatively large, energy independent analyzing power predicted for very small angle elastic scattering where the magnetic interaction interferes with the spin independent nuclear interaction[16]. Tests are presently in progress to demonstrated the possibility of detecting the recoil carbon nucleus from a ultra thin carbon fiber. For both methods the carbon fiber target could be scanned through the circulating beam to measure polarization profiles.

The HERA collider consists of a 30 GeV electron ring and a 820 GeV proton ring. Electron beam polarization of about 70 % has been achieved and spin rotators are successfully being used to produce longitudinal polarization for the HERMES fixed target experiment. Recently, there is interest to examine the possibility to also polarize the HERA proton beam [17]. With a top energy of 820 GeV the acceleration of polarized protons in HERA would need at least four snakes. However the high energy will require very detailed studies to determine the beam emittance and magnet alignments that are required to successfully accelerate polarized protons. HERA faces an additional complication from the vertical excursions that were included at the interaction regions with the electron beam. Additional snakes are needed to make these excursions spin transparent.

4 CONCLUSIONS

With all the recent advances in the understanding of spin dynamics and the development of techniques for spin manipulation, polarized beam operation could become more of an integral part of future high energy accelerators. In particular, polarized proton beam capabilities are being developed for RHIC It is anticipated that, for the expected turn-on of RHIC late in 1999, one ring will be equipped with two snakes and a polarimeter which will allow for initial commissioning of polarized beam acceleration. The remaining snakes and all the spin rotators for the two detectors STAR and PHENIX will be in place for the first RHIC spin physics run starting after October 2000.

5 REFERENCES

[1] L.H. Thomas, Phil. Mag. **3**, 1 (1927); V. Bargmann, L. Michel, V.L. Telegdi, Phys. Rev. Lett. **2**, 435 (1959).

[2] M. Froissart and R. Stora, Nucl. Instr. Meth., **1**, 297 (1960).

[3] T. Khoe et al., Part. Accel. **6**, 213 (1975); J.L. Laclare et al., J. Phys. (Paris), Colloq. **46**, C2-499 (1985); H. Sato et al., Nucl. Inst. Meth., Phys. Res. Sec A**272**, 617 (1988); F.Z. Khiari, et al., Phys. Rev. D**39**, 45 (1989).

[4] Ya.S. Derbenev et al., Part. Accel. **8**, 115 (1978).

[5] T. Roser, AIP Conf. Proc. No. 187, ed. K.J. Heller p.1442 (AIP, New York, 1988).

[6] H. Huang et al., Phys. Rev. Lett. **73**, 2982 (1994)

[7] T. Roser, in Proc. of the 10th Int. Symp. on High Energy Spin Physics, Nagoya, Japan, p. 429 (1992).

[8] M. Bai et al., Phys. Rev. Lett. **80**, 4673 (1998)

[9] A. Lehrach, Ph.D. thesis, Forschungszentrum Juelich, Germany, 1997

[10] D.D. Caussyn et al., Phys. Rev. Lett. **73**, 2857 (1994), B.B. Blinov et al., Phys. Rev. Lett. **81**, 2906 (1998)

[11] M. Bai, 'Beam manipulations with an rf dipole', these proceedings; B. Parker et al., 'Design of an ac-dipole for use in RHIC', these proceedings.

[12] Design Manual - Polarized Proton Collider at RHIC, Brookhaven National Laboratory, July 1998, http://www.ags.bnl.gov/ rhicspin .

[13] V.I.Ptitsin and Yu.M.Shatunov, Helical Spin Rotators and Snakes, Proc. 3. Workshop on Siberian Snakes and Spin Rotators (A.Luccio and T.Roser Eds.) Upton, NY, Sept. 12-13,1994, BNL-52453, p.15;

[14] E. Willen et al., 'Construction of helical magnets for RHIC', these proceedings.

[15] A.U. Luccio et al., 'Development of the spin tracking program SPINK', these proceedings.

[16] J. Schwinger, Phys. Rev. **73**, 407 (1948)

[17] 'Acceleration of Polarized Protons to 820 GeV at HERA', University of Michigan Report HE 96-20, 1996

FERMILAB MAIN INJECTOR COMMISSIONING STATUS

P.S. Martin* and C.S. Mishra for the Main Injector Commissioning Team
Fermi National Accelerator Laboratory**
Batavia, Illinois 60510

Abstract

The Fermilab Main Injector construction project is nearing completion. The commissioning of the Main Injector began in late 1998. The status of the beam studies and fulfillment of the project commissioning milestones is presented.

1 INTRODUCTION

The Main Injector accelerator is a 150 GeV proton synchrotron constructed to replace the original Fermilab Main Ring as the injector into the Tevatron and as a high intensity, fast-cycling accelerator for antiproton production and for supporting a fixed target program using 120 GeV protons. The Main Injector project received first funding in FY92, and its final funding in FY98. Completion of the Main Injector ring civil construction occurred in 1997, and fabrication and installation of the technical components for the ring was completed in 1998. The civil construction for the beamline enclosure connecting the Main Injector to the Tevatron and Antiproton Source began in September 1997, at which time removal of the Main Ring components for refurbishing and reuse in the Main Injector began. Installation of the beamline equipment continued into late 1998.

The 750-m beamline enclosure connecting the Booster to the Main Injector was constructed earlier, and components were installed in 1996. This beamline is comprised primarily of permanent magnets as a prototype for fabrication of ring-quality permanent magnets for the Recycler Ring. Commissioning of the MI-8 beamline was begun in February 1997.

2 COMMISSIONING SCHEDULE

The commissioning of the Main Injector (MI) ring began in September 1998. At this time, the MI ring installation was complete (except for resonant extraction devices) but installation activities continued both on the Recycler ring and on the MI-Tevatron beamlines. Therefore, MI commissioning activities were carried out on weekends only, with installation activities during the week.

In addition to weekend running, there have been three extended periods of MI commissioning (i) November 22-29; (ii) December 19-January 13, and (iii) January 24-February 14.

3 COMMISSIONING GOALS

There are seven commissioning goals associated with the Main Injector, which are to be fulfilled to satisfy the project milestones with the Department of Energy. These goals relate to the energy and intensity of the beam to be delivered to another machine or user (the Tevatron, the Antiproton Source, or a fixed target beamline) and to the repetition rate at which this beam is accelerated and extracted. Due to the various accelerator improvement projects underway in the Tevatron and the Antiproton Source, beam could not be delivered to either of them during this commissioning period. Similarly, there are as of now no 120 GeV beamlines constructed and ready for beam. Therefore, the definition of the milestones requires only that beam is accelerated in the Main Injector, not delivered to the ultimate intended designation. The milestones are as follows, along with the status.

1. 150 GeV proton energy for injection into the Tevatron. *This milestone was accomplished on November 28.*
2. 2×10^{13} protons injected per Tevatron cycle. *This milestone was accomplished on January 6. (Since the Tevatron is filled via two successive MI cycles, this corresponds to 1×10^{13} protons per MI cycle.)*
3. 75% proton/antiproton transmission efficiency. *This milestone was accomplished (with protons) on November 28.*
4. 120 GeV proton energy for antiproton production and test beam. *This milestone was accomplished on November 27.*
5. 2.5 second cycle time to 120 GeV. *This milestone was accomplished on November 27.*
6. 2×10^{12} protons to antiproton target per cycle. *This milestone was accomplished on December 31. (As noted above, this milestone was satisfied by accelerating beam of the desired intensity in the Main Injector, but delivering the beam to the MI abort.)*
7. 2×10^{13} protons resonantly extracted per cycle. *This milestone is yet to be accomplished.*

The last milestone, which requires both the highest intensity and the commissioning of the equipment for the resonant extraction, is by far the most challenging. Some progress has been made on both of these issues. The resonant extraction equipment (electrostatic septa and
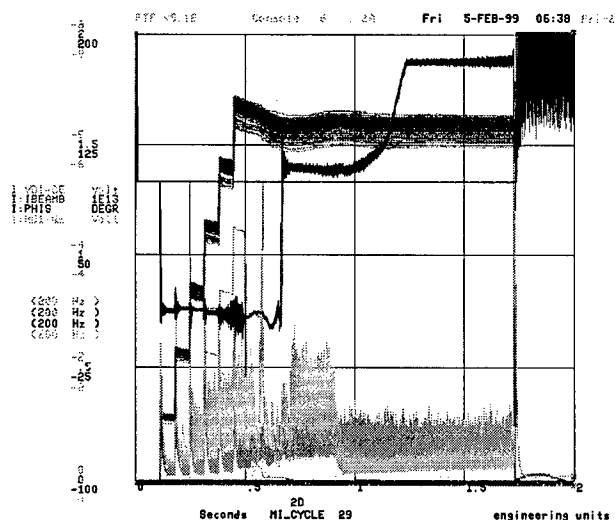
Figure 1. Beam intensity at the best performance of the Main Injector to date. Six Booster cycles are injected and accelerated to 120 GeV.

special quadrupoles for improving the spill quality) were installed in January, and preliminary studies were conducted in February. During this same time period, the intensity was increased to 1.6×10^{13} protons per cycle, as shown in Figure 1. In this figure, the four signals being fast-time plotted are the beam intensity (I:IBEAMB), the synchronous phase angle (I:PHIS), and the error signals from the horizontal and vertical narrow band 1-Q dampers. As can be seen in the figure, the overall efficiency in the Main Injector is in the vicinity of 90%. The large step in synchronous phase mark transition, after which there are no losses. The slight rise in the intensity signal after transition is an instrumentation problem, which is not understood.

The commissioning goals, including the last one, are still conservative with respect to the operational goals of the Main Injector. The nominal design goals of the MI include accelerating 5×10^{12} protons per cycle for antiproton production, and 3×10^{13} protons per MI cycle for both Tevatron and MI fixed target programs. To achieve the design goals will require the Fermilab Booster to push its intensity about 25% above its previous record performance. While that goal appears achievable without major upgrades, it will likely require considerable time to fine-tune the Booster. This effort is underway, including realignment activities to optimize the transmission and intensity performance.

4 COMMISSIONING HIGHLIGHTS

The commissioning was begun in a step-by-step process requiring the approval of the Beams Division Head (and advisory committees) before proceeding to the next step. The first weekend was devoted to Booster extraction set-up, tuning the 750-m long MI-8 beamline and into the MI-10 straight-section, through the injection Lambertson magnet and to the end of the MI-10 straight. The second weekend was spent on one-half turn beam, taking beam from MI-10 around to the beam abort at MI-40. This included timing in and adjusting the level of the injection kickers at MI-10. Finally, on the third weekend, circulating beam was attempted. Happily, circulating beam was accomplished within the first hour of attempting to circulate. Successive weekends were devoted to turning on the rf, adjusting the orbit, tune and chromaticity, power supply studies to improve regulation, and finally, to accelerate beam.

Concurrent with beam commissioning, shifts were devoted to power supply commissioning, beginning at low rms currents and eventually ramping the magnets to the full design peak and rms currents. A DOE milestone related to the full power testing of the dipole circuit was accomplished on December 21.

As the push for higher intensity began, so did vacuum avalanching. As more intense beams were injected, there was a rise in the pressure by one to two orders of magnitude. This pressure rise was related primarily to the bunch intensity, but also depended more weakly on the total intensity in the ring. The rise was sufficient to cause the vacuum valves to close. This situation has since been changed by using the much-higher pressure Pirani gauges for the vacuum sector permits rather than the ion pump pressures. At the slow repetition rate for most of the commissioning (in interest of keeping the residual activation levels in the ring as low as reasonably achievable), typically one beam cycle every 15-30 seconds, the ion pumps were able to recover most of the pressure rise between beam pulses, although the background level did rise slowly. For reference, the typical pressures without beam are in the low 10^{-8} Torr range. The pressure bump was also confirmed to be due to beam intensity and not beam loss. With subsequent running, the pressure rise was observed to decrease, and it is not believed that this will be a long term problem, even at the nominal cycle time as short as every 1.5 seconds. Figure 2 shows a vacuum burst near the end of the running period.

The need for dampers became apparent also as we pushed the intensity up. Longitudinal dampers were commissioned first, and transverse dampers have been installed and are in the process of being commissioned. Without transverse dampers, the MI has been operating with large chromaticities (~-30) before transition.
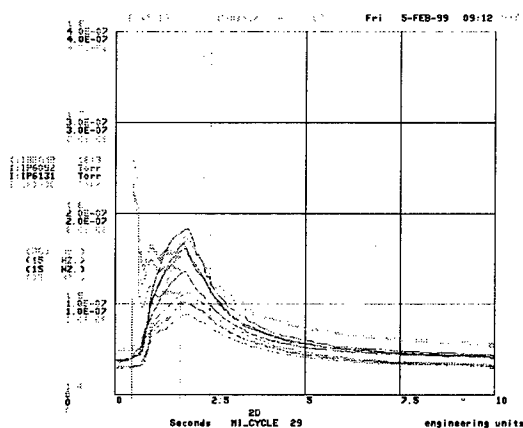
Figure 2. Pressure rise due to high intensity beam.

The optics of the Main Injector ring have been measured and compared with the design lattice. The details of measurement and online-model calculations can be found in Ref 2-3. The measurements are in very good agreement with the design values of the Main Injector lattice functions. Figure 3 shows the measured and calculated dispersion in the Main Injector at 8 GeV. The vertical dispersion is close to zero everywhere, and the horizontal dispersion is near zero in the straight sections.
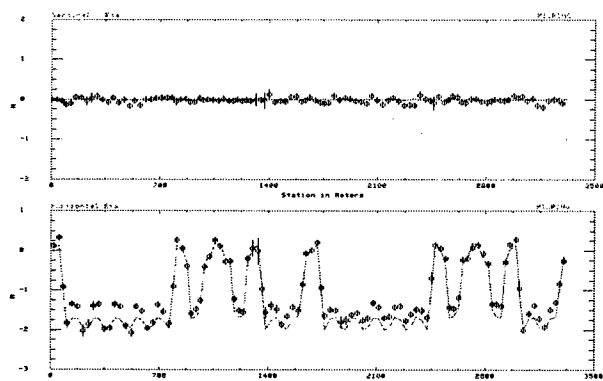
Figure 3. Measured and design values of the Dispersion functions in the Main Injector.

The commissioning of the beamlines between the Main Injector and the Tevatron and Antiproton Source has also begun. The P1 line connects the Main Injector to the F-0 location in the Tevatron. Beam can be injected into the Tevatron by energizing four Lambertson magnets at F-0, or, with the Lambertson magnets turned off, beam continues upwards into the P2 line, which is a modified section of the old Main Ring, connecting to the Antiproton Source line at F-17. The P1 line is designed to handle 1) 8 GeV proton beam from Main Injector to the Antiproton Source for commissioning studies, or antiprotons from the Source to the Main Injector, 2) 120 GeV protons for antiproton production or for the 120 GeV

fixed target program, 3) 150 GeV protons to the Tevatron and 4) 150 GeV antiprotons from the Tevatron, for deceleration in the MI and recooling in the Recycler. Eight GeV protons have been delivered to the Antiprotons Source, but neither the P1 nor P2 lines have been commissioned at higher energies. The optics of both the MI-8 line and the P1 line (at 8 GeV) agree well with the design lattices[2].

5 ACKNOWLEDGEMENTS

6 REFERENCES

1. S.D. Holmes, et al. "Status of the Main Injector and Recycler", Proceedings of the 1997 Particle Accelerator Conference.
2. M-J. Yang, et al. "The Optics measurement and analysis of Fermilab 8 GeV transfer line to Main Injector." Proceeding of PAC99.
3. M-J. Yang, et al. "The optics measurement and analysis of Fermilab Main Injector". Proceeding of PAC99 and reference therein.

LUMINOSITY UPGRADE OF HERA

M. Seidel (DESY) for the HERA Upgrade Group

Abstract

After six years of operation the electron proton collider HERA had reached a luminosity of $1.4 \cdot 10^{31}\,\mathrm{cm}^{-2}\mathrm{s}^{-1}$, very close to the design value. We present an overview on the HERA upgrade project that pursues the goal to further increase the luminosity three-fold by the year 2000. The increase is achieved by reducing the beam cross sections at the IP to $120 \times 30\,\mu\mathrm{m}^2$ (RMS values). If furthermore design currents can be reached in both machines the improvement factor is up to 5. The upgrade involves a complete rebuild of the interaction regions as well as lattice modifications in the electron ring. Major issues of the project are superconducting magnets that will be installed inside the colliding beam detectors, unconventional normalconducting magnets, the handling of synchrotron radiation in the IR, and electron beam dynamics.

1 CONCEPT AND PARAMETERS

HERA is a 6.3 km long electron/proton collider, presently running at 27.5 GeV for the electrons and 920 GeV for the protons. The proton machine uses superconducting magnets in the arcs. The machine is equipped with four interaction regions (IR's), two of them for electron proton collisions with the detectors ZEUS and H1. The HERA luminosity can be written as follows:

$$\mathcal{L} = \frac{N_p I_e}{4\pi e \varepsilon_x^p \sqrt{\beta_x^p \beta_y^p}} \tag{1}$$

Here it has been assumed that both beams are matched, i.e. $\sigma_{x,y}^e = \sigma_{x,y}^p$. This condition is necessary to minimize the effect of the beam-beam interaction. For the electron beam a linear tuneshift limit of 0.04 should not be exceeded, whereas the proton beam suffers from nonlinear diffusion caused by the beam-beam force in case the electron beam is too small. Furthermore it holds $\varepsilon_x^p = \varepsilon_y^p$ for the proton beam emittances. It is difficult to decrease the proton emittances or to increase the proton bunch population N_p due to limitations in the pre-accelerator chain. The electron current I_e is limited ultimately by the available RF power. The most promising way to increase the luminosity is therefore the reduction of the spotsizes by stronger focusing, thus smaller β-functions $\beta_{x,y}^{p,e}$. In case of the electron beam a reduction of the beam emittance is anticipated in addition. The emittance reduction is achieved by increasing the phase advance per FODO cell from 60° to 72° and a combined shift of the RF frequency. Details on the parameter choice for the electron machine as well as implications on the beam dynamics can be found in [1].

The limitations for this way to increase the luminosity are mainly given by aperture restrictions and the beam-beam tune shift for the electrons. Additional limitations are caused by the so called hourglass effect for the protons since the vertical β-function comes close to the longitudinal beam size, and dynamic aperture problems for the electrons. Smaller β-functions at the interaction point (IP) imply a steeper increase of the beam dimensions with distance from the IP:

$$\sigma(s) = \sqrt{\sigma_0^2 + \varepsilon^2 s^2/\sigma_0^2} \approx \frac{\varepsilon}{\sigma_0} s \tag{2}$$

Consequently the spotsize at the IP is limited by the available aperture in the final focus quadrupoles and the distance to the IP at which those quadrupoles can be installed. The linear beam-beam tuneshift for the electrons is given by the following expression:

$$\begin{aligned}
\Delta\nu_{x,y}^e &= \frac{r_e N_p \beta_{x,y}^e}{2\pi\gamma_e(\sigma_x^p + \sigma_y^p)\sigma_{x,y}^p} \\
&= \frac{r_e N_p \sqrt{\beta_{x,y}^p}}{2\pi\gamma_e \varepsilon_{x,y}^e \left(\sqrt{\beta_x^p} + \sqrt{\beta_y^p}\right)}
\end{aligned} \tag{3}$$

Here r_e is the classical electron radius and γ_e the relativistic factor. The beam matching condition has been used to obtain the second line. As one finds from (3) the tuneshift can always be controlled by an appropriate choice of the electron beam emittance. After fixing the emittance, the beam sizes can be matched by adjusting the electron β-functions, which is possible as long as the available aperture allows this.

The concept of the HERA upgrade is based on an early separation of the two beams with combined function magnets that are installed inside the experimental detectors, 2 m from the IP. The following electron final focus magnets are passed by both beams. The first exclusive proton focusing magnet is positioned at 11 m distance, which has to be compared with a distance of 26 m at which it is installed in the present scheme. A summary of the upgrade parameters is shown in table 1, details are discussed in [2]. The luminosity can be raised by a factor 4.7 compared to the original HERA design. This assumes that design currents can be stored in both machines, which has to be achieved by independent improvements. The present machine has already achieved the original design luminosity, even without the full beam intensity, by pushing the aperture margins of the final focus quadrupoles to a considerably larger extend than foreseen for the upgrade (which provides space for 12 rms widths of the proton beam, compared to 9 rms widths in the present HERA operation). Since the parameters for the

Figure 1: Schematic layout of the upgraded HERA interaction region. Beam envelopes of the proton beam (12 σ) and the electron beam (20 σ) are indicated.

Figure 2: Left superconducting magnet, GO, top view (courtesy: BNL).

upgrade we adopted an unconventional solution that foresees to move the IP transversally by 8 mm for positron operation. With this offset the p(e$^+$) beam penetrates the p(e$^-$) beam at the end of the second proton final focus quadrupole. At this position we install a small septum like dipole magnet that corrects the remaining angle. The positron orbit is matched to the electron orbit by small transverse movements of the electron final focus magnets, which can be done without modifying the vacuum system.

2 NEW COMPONENTS

Superconducting magnets. The early beam separation and focusing of the electron beam is done with superconducting magnets. We use two types of sc. magnets, left and right from the IP. The magnets are being designed and manufactured at BNL [3]. Because of the absent iron yoke those magnets can be build with very small outer diameters but relatively large apertures, which is important for the safe passage of synchrotron radiation (SR). The small outer diameter makes it possible to install the magnets directly inside the detectors. Both magnets have four coils: horizontal dipole, vertical dipole, quadrupole and tilted quadrupole. The vertical dipole is used for orbit correction and the tilted quadrupole for coupling correction of the electron beam.

Normalconducting magnets. In total we need 56 new magnets for the HERA interaction region. Most of the new magnets are being build at the Efremov Institute in St. Petersburg, Russia [4]. Many of these magnets have special features, resulting from the close beam orbits of the two machines, or synchrotron radiation issues. Examples are the electron final focus magnets that exhibit gaps between the coils to provide space for the SR fan and NEG pumps above and below the beam pipes. The first two proton quadrupoles are half quadrupoles with mirror plates to let the electron beam pass closely without affecting it. Another example is the above mentioned septum dipole magnet for the proton beam which has stringent requirements for the stray field that the electron beam experiences, at a distance of only 120 mm from the protons.

Vacuum system. Totally 448 m of UHV vacuum system have to be build new for the HERA upgrade. Since the beam separation is done in the detector, background induced by beam-gas interaction is more critical now and consequently the requirements on the vacuum quality are higher. At every possible location we are planning to equip

HERA upgrade have been chosen it was possible to raise the p-beam energy from 820 GeV to 920 GeV in routine operation. This further improved the specific luminosity. The luminosity upgrade parameters and aperture margins are still based on the larger 820 GeV p-beam emittance. All magnets, however, are strong enough for 920 GeV operation. For these reasons the luminosity upgrade parameters appear to be sound (if not conservative). Further improvement of specific luminosity by pushing the aperture margins and exploiting the smaller p-beam emittance may be feasible.

	e-Beam	p-Beam
energy [GeV]	30	820
beam current [mA]	58	140
emittance [nm]	22	5000/γ
emittance ratio $\varepsilon_y/\varepsilon_x$	0.18	1
beta-function β_x^* [m]	0.63	2.45
beta-function β_y^* [m]	0.26	0.18
spot s. $\sigma_x \times \sigma_y$ [μm^2]	118 × 32	118 × 32
rms b. length [mm]	15	130
bb tune shift/IP $\Delta\nu_{x,y}$	0.027, 0.041	0.002, 0.0005
min. aperture [σ]	20	12
Luminosity	7.00 · 10^{31}cm^{-2}s^{-1}	

Table 1: Goal parameters for the HERA upgrade.

The layout of the IR should not only allow electron/proton collisions but also positron/proton collisions. In that case the separator magnets switch polarity, and consequently the proton beam receives a small kick in the opposite direction, when compared to the electron case. In the present machine lattice this kick is compensated locally by special septum corrector magnets. However, this comfortable solution costs luminosity because it increases the distance between the IP and the focusing magnets. For the

the chambers with NEG pumps. In addition there are getter pumps and Ti-sublimation pumps installed in-between the magnets. The synchrotron radiation has to be guided relatively far from the detector to avoid too much backscattered photons. On the electron-downstream side we have foreseen key-hole shaped stainless steel chambers which are up to 250 mm wide. From 11 m on the outer SR fan is transported in a separate pipe. The critical septum absorber is discussed in [5].

3 CRITICAL ISSUES

Synchrotron radiation. The bend radius of the beam separation magnets has been decreased from 1200 m to about 400 m. Consequently the total SR power in the IR is increased to about 28 kW. Since the beam separation is done inside the detectors it is not possible anymore to collimate SR before the beams enter the detectors, as it is done in the present layout. In the new scheme the SR has to pass the detector safely without loosing even small fractions in the detector area ($P_{loss} < 10^{-8} \cdot P_{tot}$). To predict or to guarantee such small losses without collimation is difficult since the particle distribution in the e-beam tails is not precisely known. We are planning to do detailed beam tail studies by scraper measurements in the present machine.

Particle background. Another implication of the beam separation in the detectors is that all low energy electrons, produced by bremsstrahlung interactions with residual gas molecules in the straight IR section, will ultimately hit the detector beam pipe and cause background. This qualitative difference to the present scheme would cause a large increase in the particle background. To reduce this effect the lattice incorporates a dispersive chicane upstream of the detectors to collimate low energy electrons. However, there are still some meters of beamline between this collimation scheme and the detectors, where the beam-gas induced background will depend sensitively on the achievable residual gas pressure.

Sc. magnets inside detectors. The installation of the sc. magnets inside the detectors has two unpleasant implications. One is that magnetic detector components disturb the field quality of the magnets. Simulations predict for the magnet on the right side in ZEUS a sextupole component of several 10^{-3}. According to the simulations this could be reduced to acceptable $2 \cdot 10^{-4}$ by installing purposely additional iron parts that symmetrize the geometry. It is planned to verify the simulations experimentally by field measurements in realistic environments. The second difficulty arises from the interaction of the magnet end fields with the detector solenoid fields. At H1 one expects a magnetic force of about 5000 N on one end of the left sc. magnet, which is much larger than the weight force of the magnet of about 750 N. Unfortunately the magnet cannot be fixed very rigidly in the detector environment. While the electron beam is ramped from 12 to 30 GeV we expect a vertical movement of the magnet of 700 μm. This motion has to be corrected by a ramp table for the vertical correc-

tion dipole.

Electron beam polarization. The electron machine of HERA operates routinely with polarized beam, typically $50\% - 60\%$, which is used by the internal fixed target experiment HERMES in hall east. Spin rotators are installed in the IR east to provide longitudinally polarized electrons at the IP. In order to minimize the depolarizing effect of the solenoid fields of the other detectors, so called anti-solenoids are installed next to them for local correction. Because of space requirements those correctors will be removed for the upgrade. The beam coupling has to be corrected non-locally by tilted quadrupoles. Additional spin rotator pairs will be installed in the north and south interaction regions, primarily with the purpose to provide longitudinally polarized electrons also for the ep experiments. Without the anti-solenoids these rotators become essential also for the over-all achievable polarization degree since a longitudinally oriented spin is not disturbed by a solenoid field. A further complication arises from the partial superposition of detector solenoid field with the dipole fields of the sc. magnets. In summary it will be more difficult to achieve comparable polarization levels as in the present machine.

4 SUMMARY AND SCHEDULE

The HERA upgrade is an ambitious project that tries to push the design of the interaction regions to the possible limits. The qualitatively new scheme to separate the beams already inside the detectors will make the machine operation more critical. To guarantee safe passage of more than 10 kW synchrotron radiation through the detectors the machine controls and interlocks have to be refined.

The projects makes good progress, all components are still on schedule and the first five normalconducting magnets have been delivered already to DESY. The shutdown for installation of components in the tunnel and modifications of the ep detectors is scheduled for May 2000 and will take about 9 months.

5 REFERENCES

[1] G. Hoffstätter et al., Electron Dynamics in the HERA Luminosity Upgrade Lattice of the Year 2000, these proceedings

[2] U. Schneekloth (editor), The HERA Luminosity Upgrade, DESY internal report

[3] B. Parker et al., Superconducting Magnets for Use Inside the HERA ep Interaction Regions, EPAC (1998); http://www.cern.ch/accelconf/e98/PAPERS/TUOA02A.PDF

[4] E. Bondarchuk et al., Normalconducting QI/QJ/QN/QM Magnets for the HERA Luminosity Upgrade, EPAC (1998); http://www.cern.ch/accelconf/e98/PAPERS/TUP48C.PDF; TUP49C.PDF; TUP50C.PDF

[5] M. Bieler et al., Design of a High Power Synchrotron Radiation Absorber for HERA, these proceedings

PROCESSING AND ANALYSIS OF THE MEASURED ALIGNMENT ERRORS FOR RHIC*

F. Pilat, M. Hemmer, V. Ptitsin, S. Tepikian, and D. Trbojevic, BNL, NY

Abstract

All elements of the Relativistic Heavy Ion Collider (RHIC) have been installed in ideal survey locations, which are defined as the optimum locations of the fiducials with respect to the positions generated by the design. The alignment process included the presurvey of all elements which could affect the beams. During this procedure a special attention was paid to the precise determination of the quadrupole centers as well as the roll angles of the quadrupoles and dipoles. After installation the machine has been surveyed and the resulting as-built measured position of the fiducials have been stored and structured in the survey database. We describe how the alignment errors, inferred by comparison of ideal and as-built data, have been processed and analyzed by including them in the RHIC modeling software. The RHIC model, which also includes individual measured errors for all magnets in the machine and is automatically generated from databases, allows the study of the impact of the measured alignment errors on the machine.

1 MEASUREMENT TECHNIQUES

The centers of the RHIC quadrupoles were determined in two ways: by ferrofluidic colloidal cell and by antenna measurements. The *colloidal cell* [1] uses a collimated light passing through two polarizers at the opposite sides of the magnet. This light cannot be seen with the telescope if there is no magnetic field around the cell. In the presence of field, small particles in the colloidal solution orient themselves along the magnetic field lines producing the field picture at the telescope. The *antenna* [2] [3] is a special coil harmonic with several windings to measure harmonic and feed down terms. Fiducials are placed on the antenna to locate the magnetic centers relative to the magnet fiducials.

Information about the survey instruments and data collection can be found in [4].

2 FINDING THE OPTIMAL MAGNET POSITIONS

A set of programs have been developed to ensure that all RHIC magnets are installed as close as possible to their design position, in the "ideal" position, [5]. *Mechanical* and *optical survey* data are collected, structured in a relational database (SYBASE) and analyzed. For all magnets, the mechanical roll angle measurements were very well correlated with the field roll measurements. The *cold mass*

fiducials, welded near the ends of the laminations, are accessible during optical survey in the production phase and during magnet positioning in the tunnel. The position of the cold mass fiducials are located with respect to the *cryostat fiducials* and to the horizontal gravitational plane. We will describe in more detail what has been done for the main magnet systems, dipoles and quadrupoles, with particular emphasis on the Interaction Region quadrupoles.

Arc dipoles have 4 cold mass fiducials. The dipole magnet centers were determined by a combination of the *optical survey* and *mechanical* dial gauge indicator measurements. The roll of the dipoles was controlled by a combination of the rotating coil measurements and the optical survey measurements. The field angle of the dipoles is determined by the rotating coil measurements with respect to the gravitational plane. The optical survey measurements were performed at room temperature with only a few magnets measured at 4 K. The warm to cold correlation for the field angle has a standard deviation of 0.20 mrad. The systematic error as well as the reproducibility of the measurement is estimated to be ±0.2 mrad.

Arc quadrupoles have also 4 fiducials and their magnetic centers were determined by the best linear fit over a few positions along the length of the magnets. This was used to define the *beam axis* vector. The systematic error in the location of the quadrupole magnetic center along the magnets, measured by two methods (cell and antenna), was estimated to be within ±60 μm.

Special attention was paid to the properties and alignment of the **Interaction Region (IR) magnets**, the strong focusing quadrupoles (triplets), dipoles, and harmonic correctors since the IRs dominate the beam dynamics at storage. There are three packages of multi-layer correction magnets between the triplet magnets [3]. Two are directly attached to Q3 while one is attached to the Q2 magnet. Q1, the shorter cold mass, has 4 fiducials, Q2 and Q3 respectively have 10 and 12 fiducials since they are longer and at a more critical position. The quanties relevant to the alignment and positioning of the IR assemblies are summarized in Table 1. Mechanical measurements such as the sag and

Table 1: Measured quantities in IR assemblies

Mechanical	Correction package	Survey data
Sag	FA between layers	QC along length
Roll angle	FA to quad	FA along length
CM fiducials	FC along length	CM fiducials
CM length	FC each layer	CR fiducials
		BPM offset

---

roll angle along the length,the cold mass (CM) fiducials with respect to the mechanical center, and the CM length from end plate to end plate were taken during production. The second column lists quantities relevant to the correction package assembly, the field angle (FA) between layers, the residual FA relative to the quadrupole FA, the position of the field centers (FC) along the length, the position of FC of each layer. The third colums lists survey and field data, the quadrupole center (QC) and FA along the length, the CM fiducial and cryostat (CR) fiducials in the local coordinate system. Table 2 shows the average FA and standard deviation for the IR triplet and special dipoles. Table 3 shows the standard deviations of the magnetic centers for the same magnet assemblies, radial, along the magnet axis and vertical respectively. The positions of the two beam

Table 2: Measured Field Angle for RHIC IR assemblies

Magnet	FA mean [rad]	FA sigma [rad]
CQ1	-0.001101	0.001227
CQ2	-0.000553	0.001013
CQ3	-0.000726	0.001219
D0+	-0.000385	0.000931
D0-	-0.000476	0.000924
DX	-0.001236	0.000768

Table 3: Measured Centers for RHIC IR assemblies

Magnet	x [in]	y [in]	z[in]
CQ1	0.0178	0.1086	0.0092
CQ2	0.0965	0.0783	0.0182
CQ3	0.0929	0.0710	0.0196
D0+	0.3278	0.0288	0.0106
D0-	0.3165	0.0285	0.0148
DX	0.1554	0.1101	0.0285

position monitors (BPM) were also measured with respect to the quadrupole centers by a separate RF antenna system. The accuracy of the BPM position with respect to the outside fiducials is estimated to be $\pm 0.13mm$. The survey and alignment of the high beta elements were performed by using eight theodolites at the same time, electronically connected to a portable computer. Adjustments of the magnet positions are performed until the difference between the required and established positions in readings of at least four instruments are less than $\pm 25 \ \mu$m. Other details about the surveying procedure were presented elsewhere [4].

3 ANALYSIS OF RHIC MISALIGNMENT

Magnets were installed in their ideal positions, as determined by the ideal fiducials. Once installed, all magnets have been surveyed and the real position of the fiducials have been measured (as-built fiducials). For each magnet we calculate the difference (delta) between the ideal and the as-built values at each fiducial, and we define as magnet

misalignment the average over the deltas. The goal of the analysis is to evaluate the impact of the misalignment on the machine performance, notably the closed orbit, to establish if the dipole corrector system is able to compensate for it and to recommend resurveying of specific magnets if necessary. We pursued two methods of analysis: the first directly correlates the errors to the strengths of neighboring corrctors as a first check. The second includes the same misalignment data in the detailed model of RHIC allowing the first turn and the correction of the closed orbit to be realistically simulated. The analysis of the vertical alignment will be described in the following, the horizontal analysis is work in progress.

3.1 Correlation of errors to correctors

Figure 1 shows the vertical alignment for both Yellow and Blue RHIC rings. These main cause of errors is ground settlement in the tunnel. The correlation between Blue and Yellow is very good. Although the data exibit long wavelength oscillations, the real source of the beam orbit perturbation are short range local irregularities or spikes corresponding to big *relative* misalignments of individual quadrupoles. In order to quantatively characterize the
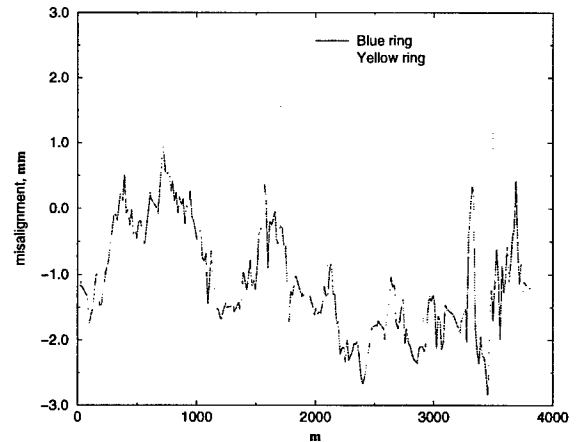
Figure 1: Vertical misalignment data for quadrupoles

strength of the orbit perturbation produced by the errors we used the concept of *effective corrector strength*. That is, the value of the corrector strength, (adjacent to the quadrupole) which is required to locally correct the beam orbit. This involves the relative misalignments of 3 neighboring quadrupoles. Figures 2 and 3 show the effective corrector strengths expressed in terms of the orbit kick angle for vertically misaligned quadrupoles. The dashed lines mark the effective region ($\pm 90 \mu$rad) inside which we would like to limit the corrector strength at top energy. The required strengths in the region between 3000 m and 4000 m is notably worse than in other areas. Quadrupoles here
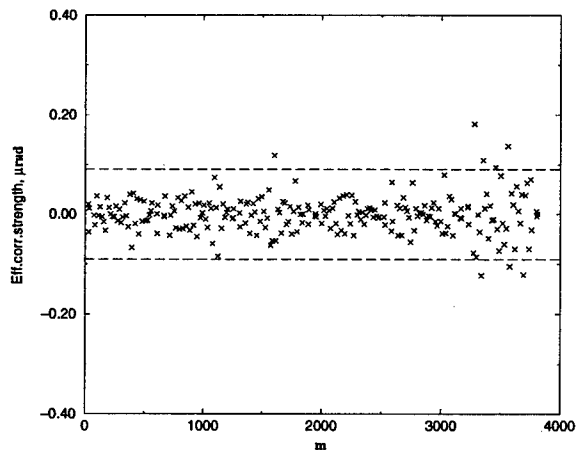
Figure 2: Effective corrector strengths for the Blue Ring

were the first to be installed, and on the basis of the present analysis the magnets in this sector have been realigned. A
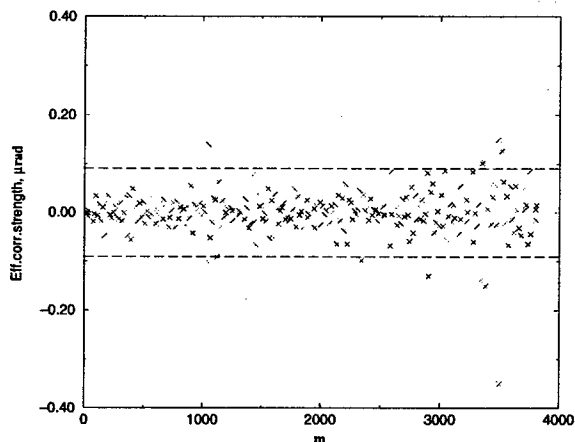
Figure 3: Effective corrector strengths for the Yellow ring

good example is the point in Figure 3 that requires about -350μrad corrector strength, far beyond the available corrector strength at the top energy. This quadrupole, $O04Q20$ needed to be realigned by about 3 mm. It is remarkable that the same realignment value was calculated on the basis of beam loss monitor data taken with beam during the RHIC sextant test [7].

3.2 Modeling of RHIC

A software model has been developed for RHIC that uses UAL [8], a modular environment which provides an accelerator object model and physics libraries interfaced via Perl Scripts, and SXF [9], an ascii external machine representation which includes errors together with lattice information. The model includes individual measurement field harmon-

ics assigned to all measured magnets in the ring. The RHIC model is automatically generated from the lattice, magnet and survey databases by a collection of stored procedures, C++ code, and Perl scripts. We extended the model to include the measured misalignments by assigning the data to the magnets via a filter that reads, manipulates and writes out a RHIC SXF file. The resulting machine has been simulated by TEAPOT++ with particular focus on the first turn and closed orbit correction. The study confirmed that the measured alignment errors in RHIC can be handled by the closed orbit correction system. Figure 4 is an example of the vertical beam orbit during the first turn before and after correction (by the sliding bump method system that will be used for real first turn steering in RHIC [6]).
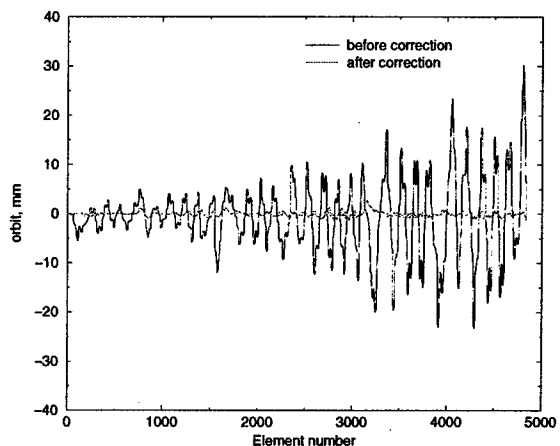
Figure 4: Correction of the vertical orbit (first turn).

4 CONCLUSIONS

The positioning of all magnets in RHIC has been optimized and all magnets have been eventually surveyed. The impact of the measured vertical misalignment on the closed orbit was found, after resurveying of a few quadrupoles, in within the capability of the dipole correction system.

5 REFERENCES

[1] M.A. Goldman, et. al., PAC93, Washington , pp.2916-2918

[2] D. Trbojevic et.al., PAC95, Dallas, pp.2099-2101

[3] D. Trbojevic et al., PAC97, Vancouver, pp.3651-3654

[4] F.X.Karl et.al, PAC93, Washington, pp.2919-2921

[5] W. Mackay, S. Peggs, RHIC/AP/12, Nov. 1993.

[6] W.Fischer et al.,"The RHIC Injection System", PAC99, New York City

[7] P.Thompson, private communication

[8] N.Malitsky, R.Talman, AIP 391, 1996

[9] H.Grote, et.al., RHIC/AP 155

IMPACT OF AND PROTECTION AGAINST FAILURES
OF THE LHC INJECTION KICKERS

O.Brüning, A.Hilaire, J.B.Jeanneret, V.Mertens[*], S.Péraire, P.Sala-Ferrari, E.Weisse

CERN, Geneva, Switzerland

Abstract

The LHC injection systems consist of horizontally deflecting steel septum magnets and vertically deflecting kickers. A mobile beam stopper is placed downstream of the kickers for setting up with single bunches and to protect the superconducting machine elements during normal injection in the event of a malfunctioning of the kickers. The effects of various potential kicker failures and their impact on the machine have been investigated. The injection parameters, the design principles of the stopper and additional protection measures are discussed.

1 INTRODUCTION

Two new beam transfer lines with a combined length of 5.6 km and using over 700 room-temperature magnets, TI 2 and TI 8, are being built at CERN to transport 450 GeV/c protons from SPS to LHC [1]. An overview of these lines is given in [2].

TI 2 leads to the injection into LHC ring 1 near intersection 2 (IP2), TI 8 to the injection into ring 2 near intersection 8 (IP8). Civil engineering for both lines has started in 1998. First injection tests are foreseen for autumn 2003 (TI 8) and mid 2005 (TI 2).

A schematic plan view of an injection region is given in

Figure 1: Schematic plan view of IP2 injection

Fig. 1. The beam to be injected passes through 5 horizontally deflecting steel septum magnets (MSI) with a total deflection of 12 mrad and a vertically deflecting kicker (MKI), consisting of 4 modules, with a nominal total kick strength of 0.85 mrad [3]. A mobile beam stopper (TDI), consisting of 2 absorber blocks positioned a few mm above and below the nominal LHC orbit, will be placed some 70 m downstream of the MKI, at a phase distance of $\Delta\mu_y = 90°$. Its main role is to protect the immediately following (cold) separation dipole D1 against miskicked bunches and to receive intentionally

beam during commissioning and verification/re-adjustment of the injection before each fill.

The main beam and kicker parameters are given in Table 1. The destructive power of the beam imposes high precision and very good protection when injecting beam into the small aperture, superconducting LHC. The quench limit (through instantaneous energy deposition in a coil) is assumed to 38 mJ/cm^3 [4], the damage limit to 87 J/cm^3 [5].

Table 1: Beam and kicker parameters at injection

Beam (proton) momentum	450 GeV/c
Nominal single bunch intensity	$1.1*10^{11}$ p
Nom. batch intensity (3*81 bunches)	$2.67*10^{13}$ p
Ultim. batch intensity (3*81 bunches)	$4.13*10^{13}$ p
Bunch distance	25 ns
Nom. norm'd transverse emittance	3.5 μm rad
Nominal kick strength	0.85 mrad
Kicker rise time	0.9 μs
Kicker flat top length	6.6 μs
Kicker fall time	3 μs

In the following the various modes of using the MKI/TDI ensemble, either intentionally or accidentally, will be described. Then, results of simulations are presented leading to a preliminary design of an appropriate TDI. Finally, the impact of particles escaping the TDI on the LHC is looked at, discussing the benefit from supplementary protection elements.

2 OPERATIONAL AND FAILURE MODES

Various circumstances of using the MKI/TDI ensemble have been investigated and listed in Table 2, grouped into "cases" with the same total kick strength seen by the beam, in order of decreasing expected occurrence. Operational (intentional) uses (marked shaded) imply normally the use of single bunches, accidental or emergency uses have to proceed from the assumption of full batch intensity.

Case 2 (sweep) occurs when the passage of beam to be injected or circulating beam coincides with the rise or fall slope of the kicker pulse. The latter case results in close to 100 bunches put on various places of the TDI and close to 20 bunches escaping the TDI (assuming linear kick slope). One of the reasons for a beam sweep is a possible

prefire of one of the kicker modules. Special precautions are foreseen to make this very unlikely, or to reduce its consequences, e.g. applying the high voltage only very shortly before the trigger pulse to the thyratron switches or firing rapidly the other three kicker modules if one produces a prefire.

Table 2: Operational (shaded) and failure modes of the MKI/TDI ensemble

Case	Kick [%]	Reason(s) [expected rate]
1	0	Setting-up [during commissioning] Verification/re-adjustment [before each fill] SPS extraction launched but LHC not ready [occasional] Trigger missing (MKI internal or external) [rare]
2	0-100	Beam sweep: Wrong timing (MKI internal or external) [occasional] Prefire of one MKI module, followed by firing the other 3 [rare]
3	75	One MKI module full fault [rare]
4	75-125	One MKI module flashover or equiv. [extremely rare] (grazing case ≈ 86 %)

Fig. 2 shows a simplified side view (left) of the injection region (not to scale), with an enlarged front view (right) of the upper TDI block, showing schematically the beam impacts for the different cases.
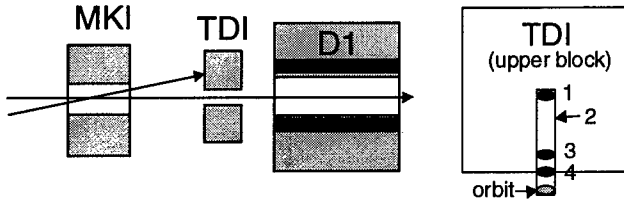
Figure 2: Schematic side view (left) of injection area (case 1 shown); enlarged beam view (right) of upper TDI block with schematic beam impacts for various cases (case 4 shown for grazing impact).

Case 1 corresponds to an impact distance from the bottom edge of about 30 mm, case 3 to about 3.5 mm. The lower TDI block (not shown) is foreseen to receive miskicked circulating beam in mirrored positions. At injection the TDI blocks are supposed to be ± 8.5 σ (tangential to the machine aperture) or less distant from the LHC orbit (corresponding to about ± 4.3 mm).

3 TDI/D1 SIMULATION RESULTS

The TDI/D1 ensemble has been simulated using FLUKA [6]. For the most frequent case 1 the length and the composition of the TDI was varied. The results are shown

in Fig. 3, plotted as maximum energy deposition in the D1 coil against the number of interaction lengths of the TDI. The transverse dimensions were kept fixed at 8*8 cm. Even though the counter-rotating beam imposes a space limitation in the horizontal plane, these dimensions reveal to be sufficient with a contribution from lateral leaking of only ≈5*10^{-7} GeV/cm^{3}p.
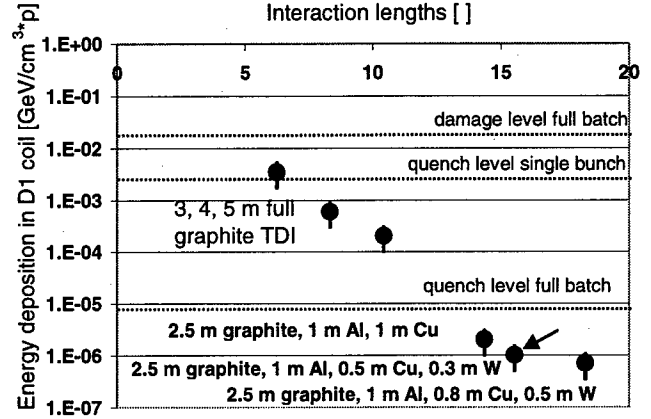
Figure 3: Energy deposition in D1 coil as a function of the number of interaction lengths of the TDI (case 1).

Sandwich constructs of appropriate materials have the benefit over full graphite to stay below the quench limit even for full batches, at a comparable length. A sequence of 2.5 m graphite, 1 m aluminium, 0.5 m copper and 0.3 m tungsten (marked with arrow) has been chosen as "reference TDI". In a next step it has been investigated what protection this TDI procures to D1 in the various cases. The results are given in table 3.

Table 3: Energy deposition in D1 coil (preliminary) for various cases (reference TDI)

Case	Error [%]	Energy deposition in D1 coil [J/cm^3]		
		1.1*10^{11}p	2.67*10^{13}p	4.13*10^{13}p
1	50	1.8*10^{-5}	4.3*10^{-3}	6.7*10^{-3}
2	50		6.8	10.5
3	50	2.3*10^{-2}	5.6	8.7
4	25	0.25	60.3	93.3

Case 1 leads to no quench, even with highest intensities. Full batches in cases 2 and 3 will, without additional measures, quench D1. Case 4 (values given for grazing impact) approaches the damage limit for a nominal full batch and surpasses it slightly for the ultimate intensity. To test the effect from additional shielding a copper cylinder (25 ≤ r ≤ 140 mm, 1m long) has been introduced in the simulation 3 m in front of D1. This reduced the energy deposition by about a factor 120, thus excluding damage to D1 under all circumstances. Whereas such a shield would only be mandatory for case 4 with highest intensity, it is also beneficial in the other cases. The

figure for the sweep case at nominal batch intensity is then close to the quench level. Some further shield optimisation will probably allow to fall short of the quench level for this case.

A perspective sketch of the preliminary design of the reference TDI is given in Fig. 4. Each TDI block has 2 servo motors allowing a vertical adjustment with a precision of better than 0.1 mm. The enlargement in Fig. 4 (upper left corner) shows the front face of the TDI in more detail. The main absorber material is shrink-mounted into an aluminium frame, attached to an iron beam which in turn is moved by the motors. The required vertical movement is relatively small in IP8 but in IP2 it must take into account the opening requirements of the ALICE Zero Degree Calorimeter [7].
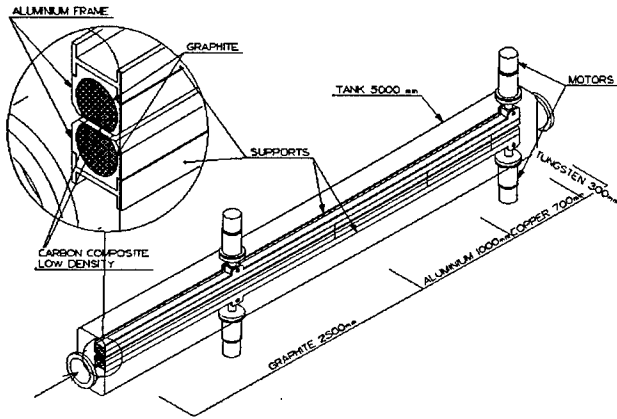
Figure 4: Perspective sketch of the TDI assembly (preliminary).

4 OTHER IMPACTS THAN ON D1

4.1 Triplets / Dispersion Suppressors / Arcs

The effect of injected bunches missing the TDI on other parts of the LHC than D1 has also been looked at. Two worst cases are considered:

Firstly, the case 2 where close to 20 bunches could be swept between the orbit and the TDI edge, starting to oscillate around the orbit. The mean particle density is about $2*10^{10}$ p / 0.1 σ. The damage level is estimated to be 10^{12} p lost per m, the quench level 10^9 p lost per m. Damage seems therefore excluded, but to avoid a quench the TDI must be set such that it covers entirely the machine aperture of 8.5 σ.

Secondly, the case 4 with a full batch just missing the TDI edge. Here the worst case particle density is about $1.6*10^{12}$ p / 0.1 σ (peak). Excluding machine damage with certainty would again require a sufficient closure of the TDI.

Two additional collimators, positioned at a phase advance $\Delta\mu \approx \pm 20°$ from the TDI (at around Q6/Q7 on the other side of the injection insertions), with the same

aperture, would provide the same protection as the TDI in the presence of phase errors.

4.2 Cleaning Sections

Badly injected particles oscillating around the LHC orbit between 8.5 σ (TDI) and 7 σ (primary cleaning collimators) will end up in the LHC cleaning sections. This does not cause problems for a few bunches, but if a full batch is lost in this area, the collimators are likely to be damaged.

4.3 Experiments

Since the aperture of the experimental vacuum chambers is large compared to the machine aperture, it seems excluded that parts of the detectors can be hit directly by misinjected bunches. However particles leaking out of the TDI or supplementary protection elements or scattered particles may reach the experiments in IP2 and IP8. Their impact is however at present estimated to be insignificant compared to the radiation from normal operation. More detailed studies are required to confirm this assumption.

5 CONCLUSIONS

The destructive beam power and the LHC characteristics as superconducting, small-aperture machine require highest care at injection. Mishaps can have severe consequences. Although the injection kickers are being built for utmost reliability, failures are not entirely excluded. Simulations of these failures reveal that a beam stopper with supplementary shielding and collimators can, appropriate setting assumed, provide sufficient protection, except in very rare cases where the warm aperture limiting cleaning collimators can be affected.

6 ACKNOWLEDGEMENTS

7 REFERENCES

[1] The LHC Study Group, "The Large Hadron Collider Conceptual Design", CERN/AC/95-05 (LHC) (1995).

[2] A. Hilaire, V. Mertens, E. Weisse, "Beam Transfer to and Injection into LHC", Proc. EPAC'98, Stockholm (1998) and CERN/LHC Project Report 208 (1998).

[3] L. Ducimetière et al., "Design of the Injection Kicker Magnet System for CERN's 14 TeV Proton Collider LHC", Proc. IEEE Pulsed Power Conference, Albuquerque, USA, July 10-13, 1995.

[4] J. B. Jeanneret et al., CERN/LHC Project Report 44 (1996).

[5] O. Brüning, J. B. Jeanneret, CERN/LHC Project Note 141 (1998).

[6] A. Fassò, A. Ferrari, J. Ranft, P. Sala, "FLUKA: Present Status and Future Developments", Proc. Int. Conf. on Calorimetry in High Energy Physics, La Biodola (Is. d'Elba), Italy, September 20-25, 1993, Eds. A.Menzione and A.Scribano, World Scientific, p.493.

[7] ALICE Technical Design Report of the Zero Degree Calorimeter (ZDC), CERN/LHCC 99-5 (1999).

TEVATRON PERFORMANCE GOALS FOR THE COMING DECADE

Stephen D. Holmes, Fermi National Accelerator Laboratory*, P.O. Box 500, Batavia, IL 60510

Abstract

Fermilab is in the midst of a program to raise the luminosity in the Tevatron proton-antiproton collider by at least a factor of five above the currently achieved level of 1.6×10^{31} cm^{-2}sec^{-1}. Components of this program include the construction of a new synchrotron, the Main Injector, a new antiproton storage ring, the Recycler, and a variety of improvements to the existing Antiproton Source and Tevatron. Commissioning of these components will be underway in early 1999 with the next Tevatron collider run scheduled to start in April 2000. Initial commissioning experience with these systems will be described, along with developments underway to support further Tevatron luminosity enhancements over the coming decade.

1 PROGRAM GOALS

The Fermilab Tevatron is the highest energy collider operating in the world today and will remain so until the initiation of LHC operations. The goal of the Tevatron collider program over the upcoming decade is to exploit the capabilities of this facility to the fullest extent possible while it retains this unique position. In support of this goal a new proton accelerator, the Fermilab Main Injector, and a new antiproton storage ring, the Recycler Ring, have recently been constructed. These facilities are now nearing completion and will support reinitiation of Tevatron collider operations in early 2000.

Table 1 lists operational parameters achieved in the most recent collider run, "Run IB", and those expected in the upcoming run, "Run II". Two sets of Run II parameters are presented: one based on operations with 36 proton and 36 antiproton bunches and a second based on 140 proton and 121 antiproton bunches. Bunch configurations during Run II will be chosen to maintain fewer than three interactions per crossing as seen by the two experimental detectors. Initial operations during Run II will be with the 36×36 bunch configuration, rising to 140×121 as the luminosity surpasses 1×10^{32} cm^{-2}sec^{-1}. The primary source of improved performance relative to Run IB is an increase in the number of antiprotons in the collider, directly attributable to the Main Injector. Achievement of luminosities beyond 1×10^{32} cm^{-2}sec^{-1} are expected once the recovery of antiprotons at the ends of stores is implemented. The initial programmatic goal for Run II is to deliver 2 fb^{-1} of integrated luminosity by the end of 2002.

Table 1: Tevatron Collider operational parameters achieved in the most recent collider run (Run IB) and expected in the upcoming run (Run II).

RUN	IB	II (36×36)	II (140×121)	
Protons/bunch	2.3×10^{11}	2.7×10^{11}	2.7×10^{11}	
Pbars/bunch	5.5×10^{10}	3.0×10^{10}	3.0×10^{10}	
Total Pbars	3.3×10^{11}	1.1×10^{12}	3.6×10^{12}	
Pbar Production Rate	6.0×10^{10}	2.0×10^{11}	2.0×10^{11}	
Proton Emittance	23π	20π	20π	mm-mr
Pbar Emittance	13π	15π	15π	mm-mr
β^*	0.35	0.35	0.35	m
Energy	900	1000	1000	GeV
Bunches	6	36	121	
Bunch Length	0.60	0.37	0.37	m
Crossing Angle	0	0	136	μrad
Luminosity	1.6×10^{31}	8.6×10^{31}	1.6×10^{32}	cm^{-2}s^{-1}
Integrated Luminosity	3.2	17.3	32.5	pb^{-1}/week
Bunch Spacing	3500	396	132	nsec
Interactions/crossing	2.5	2.3	1.3	

2 ELEMENTS OF RUN II

The luminosity in the Tevatron is given by the expression,

$$L = \frac{3\gamma f N_p (B N_{\bar{p}})}{\beta^* (\varepsilon_p + \varepsilon_{\bar{p}})} F(\sigma_z / \beta^*, \phi) \qquad (1)$$

where γ is the relativistic factor, f is the revolution frequency, B is the number of bunches in each beam, N_p ($N_{\bar{p}}$) is the number of protons (antiprotons) in a bunch, ε_p ($\varepsilon_{\bar{p}}$) is the 95% normalized transverse beam emittance, σ_z is the rms bunch length, β^* is the beta function at the interaction point, and F is a form factor dependent on the ratio of the bunch length to β^* and to the crossing angle, ϕ. Potential performance limitations are related to the number of protons per bunch, N_p, and the total number of antiprotons in the collider, $B N_{\bar{p}}$. While the number of protons per bunch is limited due to beam-beam effects, the primary performance limitation in the Tevatron has been, and will remain, the availability of antiprotons. The current round of modifications to the Tevatron complex are aimed at providing more antiprotons to the collider. The scope of changes to the complex includes construction of the Main Injector and Recycler, and modifications to the Antiproton Source and Tevatron.

2.1 Main Injector and Recycler

The Main Injector is a 3319 meter circumference, 150 GeV, conventional-magnet-based accelerator [1]. The Main Injector replaces the recently decommissioned Main Ring accelerator. The Main Injector will fill all duties previously assigned to the Main Ring with significantly improved performance. In particular the Main Injector has been constructed to provide an improved (by at least a factor of three) antiproton production targeting rate, a modest increase in the proton bunch intensity, and a new capability for delivery of high intensity (>3×10^{13} protons every 1.9 sec.) 120 GeV protons to support fixed target experiments.

The Reycler is a 3319 meter, 8.9 GeV, permanent-magnet-based antiproton storage ring [2]. Construction of the Recycler was formally incorporated into the Main Injector project in April 1997. The Recycler will become the third antiproton storage ring supporting the Tevatron complex. The Recycler has been constructed to relieve the existing Antiproton Accumulator of responsibility for maintaining high stacking rates at high stacks, to double the effective antiproton stacking rate through the recovery of unspent antiprotons from the collider, and to provide a platform for further improvements to the complex. As constructed the Recycler Ring will utilize stochastic cooling and should be capable of supporting stacks containing 3×10^{12} antiprotons and a stacking rate of 2×10^{11} antiprotons/hour. An electron cooling research and development program is currently underway to support future performance enhancements.

2.2 Antiproton Source

Significant modifications have been undertaken to the Antiproton Source to capitalize on the increased intensity delivered from the Main Injector for antiproton production. The goal is to achieve a stacking rate of 2×10^{11} protons per hour for stacks containing up to approximately 4×10^{11} antiprotons. Modifications to achieve this performance include: 1)doubling the bandwidth of the Accumulator stack-tail stochastic cooling system to 2-4 GHz; 2)increasing the transition gamma of the Accumulator by one unit (to 6.4), to accommodate this increase in the cooling bandwidth [3]; and 3)doubling the bandwidth of the Debuncher stochastic cooling system to 4-8 GHz, accompanied by the introduction of cryogenically cooled amplifiers [4].

2.3 Tevatron

The Tevatron has been reconfigured to support the experimental program enabled by the new Main Injector and Recycler rings. Primary modifications include: 1)a modest number of magnet replacements and relocations aimed at supporting 1 TeV beam operations; 2)introduction of new injection equipment to accommodate relocation of Tevatron injection from E-0 to F-0 and 36 bunch operations; and 3)construction of a new experimental hall at C-0 for possible future experiments.

3 INSTALLATION AND COMMISSIONING STATUS

Figure 1 shows the Main Injector enclosure with the Main Injector installed near the floor and the Recycler installed near the ceiling. The Main Injector installation is now complete. Recycler installation is currently in its final phase with completion scheduled for early April. At the time this is written the entire Recycler ring is installed and under vacuum, with work on the abort line and instrumentation in process. Installation of the stochastic cooling systems is scheduled for late in 1999.

The Antiproton Accumulator lattice modification is complete and the increased bandwidth stack-tail cooling system will be installed by early April. Debuncher cooling system fabrication will continue through the summer with installation late in 1999.

The Tevatron has been reconfigured to support the new beam transfers at F-0. Cooldown of the Tevatron will be initiated in March in anticipation of 800 GeV fixed target run startup in mid-April. A changeover from fixed target to collider configuration will be required following completion of the fixed target run later this year.

Figure 1: The Main Injector enclosure showing the installed Main Injector (lower) and the permanent-magnet-based Recycler (upper).
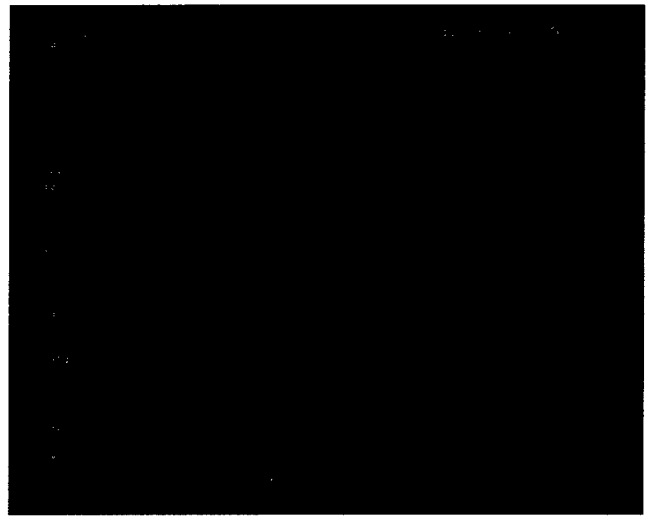
Figure 2: Main Injector beam orbit for the first circulating beam observed at the 8 GeV injection energy. The horizontal orbit position is given on top, vertical position in the middle, and beam intensity on the bottom.

3.1 Main Injector and Recycler Commissioning

Main Injector commissioning with beam was formally initiated on September 26, 1998 with the first transmission of protons from the Booster through the 8 GeV transfer line and into the Main Injector injection channel. Beam was transmitted through the first two half-cells at which point it was absorbed. The first attempt at circulating beam at the 8 GeV injection energy was made on October 10. Circulating beam was achieved within one hour of the initiation of beam transfers from the Booster. Figure 2 shows the first beam orbit observed in the Main Injector. This achievement was followed by acceleration of beam to the 120 GeV antiproton production energy on November 15 and to the 150 GeV Tevatron injection energy on November 23. Figure 3 shows a typical 150 GeV acceleration cycle achieved in early January 1999. Six Booster batches are injected and a total intensity slightly in excess of 1×10^{13} protons is accelerated to 150 GeV.

In parallel with these efforts beam transfers from the Main Injector to the Antiproton Source and the partially installed Recycler ring were also initiated in January. 8 GeV protons were transported through approximately one-third the circumference of the Recycler to a temporary beam absorber on January 11, and the first transfer of 8 GeV beam from the Main Injector to the Antiproton Source was accomplished on January 26.

The Main Injector and Recycler are currently shutdown for completion of the final Recycler installation phase. Current performance may be summarized as follows:

- 1.6×10^{13} protons routinely accelerated to 120 GeV with 90% acceleration efficiency. This is to be compared with the full design goal of 3×10^{13}.
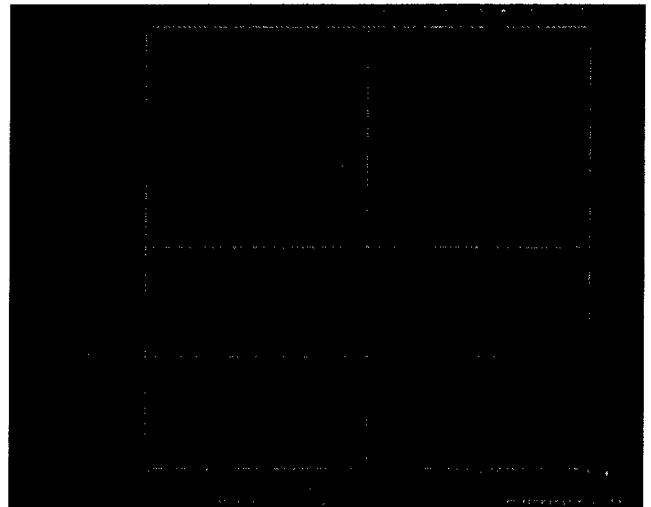
Figure 3: Typical acceleration of protons to 150 GeV during early commissioning of the Main Injector. A total beam intensity of slightly more than 1×10^{13} protons is injected over six Booster acceleration cycles and accelerated to the full design energy of 150 GeV.

- The full design operating energy of the Main Injector, 150 GeV, has been achieved with beam.
- Antiproton targeting cycles with beam have been run with an average repetition rate of 2.5 seconds. The full design goal is 1.5 seconds.
- Low intensity proton beams have been resonantly extracted from the Main Injector.
- The Main Injector optics are well understood with excellent agreement between measured and modeled lattice functions.

Operations of the Main Injector and first circulating beam commissioning of the Recycler are expected to recommence in early April. At that time we expect to bring the Main Injector up to its full operational performance goals over a period of several months.

3.2 Antiproton Source Installation and Commissioning

The reconfigured Antiproton Source is currently being installed. However, commissioning of the new Antiproton Accumulator lattice was initiated in January 1999 without the new stochastic cooling systems completely installed. Proton beams delivered from the Main Injector have been used to recommission the Accumulator as a storage ring with observed beam lifetimes consistent with vacuum lifetime. Currently the Antiproton Source is shutdown with complete installation of the upgraded Accumulator stack-tail cooling systems scheduled for early April, and the upgraded Debuncher cooling system scheduled for fall. Commissioning of the Antiproton Source is expected to recommence in April and continue through 1999.

3.2 Tevatron Installation and Commissioning

Tevatron reconfiguration and reinstallation is now essentially complete. Following cooldown and power supply commissioning the first introduction of beam from the Main Injector is expected in mid-April.

4 ACCELERATOR SCHEDULE

The current schedule of activities leading up to the initiation of Collider Run II is as follows:

April 1999	Complete Recycler installation (except for stochastic cooling). Initiate beam transfers from Main Injector to Recycler, Tevatron, and Antiproton Source.
May	Start Tevatron 800 GeV fixed target run.
November	Complete Tevatron 800 GeV fixed target run.
December	Complete installation of Debuncher and Recycler stochastic cooling systems. Start collider changeover.
February 2000	Collider startup.

4 BEYOND RUN II

Initial goals for Tevatron Collider Run II include a luminosity of ~1×10^{32} cm^{-2}sec^{-1}, accompanied by a total delivered integrated luminosity of 2 fb^{-1} by the end of 2002. Improvements in performance beyond these values will require increasing the number of antiprotons in the

collider and controlling the beam-beam forces experienced by the antiprotons as the number of proton bunches grows. A number of development projects currently underway at Fermilab are targeting these two areas.

4.1 Improved Antiproton Availability

Increasing the number of antiprotons in the collider beyond the quantities given in Table 1 requires the production and storage of more antiprotons. Fortunately the improvements to the Antiproton Source cooling systems described above are sufficient to support a factor of three increase in the antiproton flux into that facility. As a result increasing antiproton availability will depend on: 1)producing more antiprotons; and 2)providing a place to store them.

Increasing the antiproton production rate is anticipated as being achieved through increases in the acceptance of the Antiproton Source and in the proton targeting rate for antiproton production. The former is possible because the apertures of the beam transfer line downstream of the antiproton production target and of the Debuncher ring are limited in a few well-known locations. A program of identifying such locations and opening the aperture could yield a 50% increase in acceptance. In addition a liquid lithium lens development program now underway at the Budker Institute will, if successful, increase the accumulated yield from the target by up to 30%.

Increasing the number of protons on the antiproton production target will require raising the proton intensity delivered from the Main Injector. One possibility that has been studied is a technique called "slip stacking" [5]. This technique, which was first demonstrated at CERN in the 1970s [6], involves stacking beams in longitudinal phase space. Two subsequent Booster batches are injected into the Main Injector and captured at different energies (different radial positions) by subsets of the rf cavities running one harmonic number above and below the nominal harmonic number of the accelerator (h=588). The two batches "slip" with respect to each other and are recaptured in the h=588 system once they are aligned with each other. A simulation indicates that the beam intensity can be nearly doubled via this process. Of course, the longitudinal beam emittance is also doubled in the process.

The combination of Antiproton Source aperture improvements and slip-stacking should lead to a factor of approximately three increase in the antiproton stacking rate. Unfortunately, the stochastic cooling systems in the Recycler Ring will not be capable of supporting the increased flux coming from the Antiproton Source and so implementation of electron cooling will be required.

4.2 Electron Cooling

An R&D program aimed at providing electron cooling of 8.9 GeV/c antiprotons is currently underway at

Fermilab [7]. The electron beam requirements for such a system include a 4.4 MeV beam energy and a current of 200 mA (dc). The electron beam is to be provided by a 5 MV electrostatic generator. Because of the inability of the generator to source more than a few hundred watts, highly efficient beam recovery is a important feature of any such system. The program to date has concentrated on definition of required electron beam properties and the achievement of a sustained high dc current in a 1.5 MV electrostatic generator (known as a "Pelletron") at the National Electrostatics Corporation in Middleton, Wisconsin. The program at NEC is nearly complete, with sustained currents of 200-500 mA demonstrated, and procurement of a 5 MV electrostatic generator is in process. It is anticipated that a demonstration electron beam line could be assembled in 2001, with implementation in the Recycler possible in late 2002.

4.3 Electron Beam Compensation

Once the number of proton bunches in the Tevatron rises to the vicinity of 100, the impact on the antiprotons in the collider, even in the presence of separated orbits, is significant. Each antiproton bunch experiences more than 200 long-range beam-beam encounters with high intensity proton bunches in addition to the two head-on encounters at the interaction points. Because of the lack of uniformity of proton populations in all possible buckets, bunch-to-bunch variations in closed orbit, tune, and tune spread can be induced in the antiproton beam. If these variations become too large performance will suffer. Minimization of the bunch-to-bunch variations is currently foreseen as being achieved through control of the proton bunch configuration in the collider.

However, an alternative approach is under study that relies on a low energy electron beam, current modulated at the bunch crossing frequency (7.5 MHz) in order to provide an additional focusing force that cancels the lowest order (tune variation) effect within the antiproton beam [8]. A system consisting of a 6.7 KV, 3 A electron beam has been constructed and tests are now underway to demonstrate the ability to program current pulses at 7.5 MHz. If successful implementation could occur in the Tevatron as early as 2001.

5   SUMMARY

After a six year construction period the Main Injector is now complete and the Recycler Ring is nearing completion. Commissioning of the Main Injector has been underway since October 1998 and the accelerator is currently performing at about 60% of its ultimate design goal. Significant reconfigurations of the Antiproton Source and Tevatron are also nearly complete in anticipation of the reinitiation of collider operations in early 2000. The Fermilab goal is to operated the collider at an energy of 2000 GeV (center-of-mass) and a luminosity in the range $0.5\text{-}1\times10^{32}$ $cm^{-2}sec^{-1}$, accumulating a total of 2 fb^{-1} of integrated luminosity by the end of 2002. Further improvements to collider performance are possible based on increasing the availability of antiprotons and control of the beam-beam interaction. Possible improvements under study include Antiproton Source aperture improvements, a higher gradient lithium lens, slip-stacking in the Main Injector, electron cooling of antiprotons at 8.9 GeV/c, and electron beam compensation of the beam-beam tune shift. Implementation of these new technologies affords the possibility of achieving luminosities in excess of 1×10^{32} $cm^{-2}sec^{-1}$ before the LHC becomes operational in the middle of the next decade.

5   REFERENCES

[1] Stephen D. Holmes, Status of the Main Injector and Reycler, Proceedings of the 1997 Particle Accelerator Conference, Vancouver.

Information is also available at http://www-fmi.fnal.gov

[2] G. Jackson, editor, The Fermilab Recycler Ring Technical Design Report, Fermilab-TM-1991

[3] S. O'Day, The Fermilab Accumulator Ring Lattice Upgrade, Proceedings of the 1997 Particle Accelerator Conference, Vancouver.

[4] D. McGinnis, The 4-8 GHz Stochastic Cooling Upgrade for the Fermilab Debuncher, Paper submitted to this conference.

[5] S. Shukla et al, Slip Stacking for the Fermilab Luminosity Upgrade, Proceedings of the 1997 Particle Accelerator Conference, Vancouver.

[6] D. Boussard and Y. Mizumachi, Production of Beams with High Line-Density by Azimuthal Combination of Bunches in a Synchrotron, CERN-SPS/ARF/79-11; 1979 IEEE Particle Accelerator Conference (1979).

[7] S. Nagaitsev, Status of the Fermilab Electron Cooling Project , Paper submitted to this conference.

[8] V. Shiltsev et al, Compensation of Beam-Beam Effects in Tevatron Collider with Use of Electron Beam, Paper submitted to this conference.

VERY LARGE HADRON COLLIDER R&D*

G. Dugan, Laboratory of Nuclear Studies, Cornell University, Ithaca, NY 14853

Abstract

This article discusses the present state of R&D for a post-LHC very large hadron collider (VLHC). Such a machine can be built with today's technology; the thrust of the R&D is to reduce the cost of the machine, through development of new ideas and utilization of new technologies. R&D issues in the areas of accelerator physics, magnets, and general accelerator technologies, will be reviewed. Finally, the outlook for future R&D will be presented.

1 INTRODUCTION

1.1 Description of the VLHC

During Snowmass'96, the concept of a post-LHC hadron collider, with a center-of mass energy of 100 TeV, and a peak luminosity of 10^{34} cm^{-1}s^{-1}, was explored [1]. Two distinct approaches to the problem were studied.

In one approach, which was first investigated in detail at a workshop [2] at Indiana in 1994, and discussed at the 1995 PAC [3], the machine uses high field (>12 T) superconducting magnets, and produces considerable synchrotron radiation. At these fields, and for beam energies of greater than 30 TeV, the radiation damping time can be considerably less than the luminosity lifetime; this is very beneficial for the beam dynamics. The major disadvantage of this approach is the need to absorb this radiation at cryogenic temperatures, which complicates the design of the cryogenic and vacuum systems.

The crucial R&D issue for the high-field VLHC is the development of a high-field magnet. This magnet requires a practical, low-cost conductor, able to operate at fields in the 12 T range, and a robust design that can be built with this conductor to the specifications of the collider.

The other approach, developed at Fermilab [4] in 1996, proposes the use of a low-field (2 T) superconducting magnet. The magnet is a "double-C" iron-dominated device with a warm vacuum chamber, driven by a superconducting transmission line; its simplicity offers the possibility of a very low magnet system cost per unit energy. The principal disadvantage of this scheme is the very large circumference required for a 50 TeV per beam collider with low field magnets.

The low-field VLHC has a number of challenging R&D issues in the accelerator physics area, such as emittance preservation and emittance growth limitation, beam stability, and abort and beam loss handling. The need for the development of low cost tunneling technologies, to allow an affordable large-scale ring, is also crucial.

1.2 Developments since Snowmass '96

Since Snowmass '96, considerable additional R&D has been carried out at several national laboratories, primarily Fermilab. In the summer of 1998, a steering committee was created to coordinate R&D efforts for the VLHC. The Directors of Fermilab, Brookhaven, Lawrence Berkeley Laboratory and Cornell's Laboratory of Nuclear Studies formed the committee, and its membership contains representatives from those institutions.

Under the sponsorship of the committee, three workshops have been held, on the topics of magnets, accelerator technologies, and accelerator physics. Some of the results from these workshops are presented in the sections below. The committee anticipates continued sponsorship of these workshops on an annual basis in future years. An annual meeting will also be held to summarize progress and plan for the future.

2 CURRENT R&D ISSUES

2.1 Accelerator Physics

2.1.1 Lattice design and single particle dynamics

To maximize the simplicity of the magnet system, the low-field VLHC design has adopted a combined function magnet. The high-field VLHC is generally thought of as a separated function machine. Nevertheless, a topic for further study is the possibility of achieving the correct damping partition numbers without requiring separated function magnets, such as in a non-isomagnetic configuration [5].

The major issues in the design of the lattice itself are the phase advance per cell and the cell length [6]. The cell length is a key parameter. Longer cell lengths increase reliability and may reduce costs, as the number of components decreases. However, longer cell lengths lead to larger lattice functions, which in turn imply larger beam sizes and hence increased field quality requirements on the magnets.

Detailed considerations on single-particle dynamic aperture, and its relation to magnet aperture and field errors, have yet to be undertaken. There may be an important role for nonlinear beam dynamics experiments at existing colliders, such as the Tevatron and RHIC. For the low-field magnet, beam stability considerations (see section 2.1.4) may play the most important role in determining the magnet aperture. New types of high-field magnet designs using new conductors (see section 2.2) may also have very different field errors than conventional cos-θ NbTi magnets.

2.1.2 Interaction region design

Many of the problems in the interaction region design are common to both the high-field and low-field VLHC. However, the design of the final focus quadrupoles may be different for the two versions of the VLHC. The radiation damping present in the high-field VLHC can result in a beam which is "flat" (small dimension vertical)[7], whereas the low-field VLHC will have a conventional "round" beam. The final focus design for flat beams is less demanding than for the round beams: a quadrupole doublet, rather than a triplet, is usually adequate. For the same minimum beta, the peak value of the beta function is also usually smaller in flat beam optics, than with round beams.

2.1.3 Emittance control

Transverse emittance is a key parameter for any high luminosity, high-energy hadron collider. At fixed intensity, luminosity is inversely proportional to emittance. Any mechanism that causes an increase in the emittance will reduce the luminosity. Consequently, there is a great premium on maintaining the design emittance.

2.1.3.1 The injector

The Snowmass '96 designs focused on an injection energy of 3 TeV. The most challenging requirement on the injector is the beam emittance.

Preserving the emittance of the beam has historically been a crucial issue in the luminosity performance of high-energy colliders. This issue will be as important for the low-field VLHC as it is in today's hadron colliders. For the high-field VLHC, the existence of significant radiation damping shortens the beam's memory and relieves much of the pressure for emittance preservation.

Considerable work has been done at Fermilab on the design of a 3 TeV injector[8], which would use the low-field magnet technology. This machine would be a demonstration project for that technology, as well as serving as the VLHC injector.

Higher injection energies than 3 TeV are also being examined. One possibility is to build the collider as a fixed-energy (high-field) machine [9]. This could allow much simpler, small aperture, high field magnets, which might dramatically reduce their cost. A full energy injector (low field) would be required.

Another variant is to use an 8-10 TeV injector in the same tunnel as the collider. A particularly elegant implementation of this idea is to combine the low-field and high-field magnets into a single four-aperture device [10]. The low field magnet is iron-dominated, with a 20 mm aperture; the high field insert has a 40 mm aperture. The combination could have a dynamic range of 150.

2.1.3.2. Radiation damping and beam cooling

The energy and field parameters of the high field VLHC are specifically chosen to insure that the radiation damping time is a fraction of the luminosity lifetime. There are a number of benefits to this choice.

Since the injected beam will damp to the equilibrium emittance, the luminosity does not depend sensitively on the injected emittance. The quality of the magnetic field at injection may be reduced, since some level of emittance growth can be tolerated. In collision, radiation damping will immunize the beam against some forms of long-term emittance growth.

Although significant, these benefits must be carefully weighed against the clear disadvantages that appear in magnet, cryogenic, and vacuum systems, due to the substantial synchrotron radiation load.

Partition number manipulation with Robinson wigglers, a standard technique in electron machines, should be investigated for the VLHC. It may allow significant enhancement of damping times.

Bunched beam stochastic cooling schemes have been attempted for hadron colliders, with limited success [11]. Also under study is optical stochastic cooling [12], which has great potential because of the enormous available bandwidth.

2.1.3.3 Emittance growth

Emittance growth that occurs in the collider results in a direct reduction in the luminosity lifetime, which can lead to poor integrated luminosity performance.

There are many possible mechanisms for emittance growth. All have the general feature that they drive the beam at one of its resonant frequencies. Phase space filamentation then results in effective emittance growth. Possible sources of the driving terms are power supply ripple (coupled to the beam through the dipoles) and ground vibrations (coupled to the beam through the quadrupoles).

Because of its large circumference, the beam in the VLHC will have a lower resonant frequency than beams in today's hadron colliders. This is particularly true for the low-field VLHC. Usually, sources of vibration and ripple have power spectra that increase as the frequency decreases [13]. As a result, emittance growth from these sources will be more of an issue than in current machines.

2.1.4 Multiparticle dynamics

Because of the relatively low beam intensities, collective effects are not expected to play a limiting role in the high-field VLHC. The usual care will be required to keep the impedance of the machine low, but no special problems are anticipated. Radiation damping in the longitudinal plane will result in a rather high longitudinal density, considerably higher than required for design luminosity performance. This high density will, in fact, be a problem, resulting in severe intrabeam scattering. Consequently, it will be necessary to artificially maintain a reduced longitudinal density.

The situation is quite different for the low-field VLHC. With its larger circumference, the machine requires a much larger number of bunches than the high-field machine. In addition, the warm vacuum chamber in the combined function magnets constitutes a very large resistive wall impedance. At low frequencies, this impedance drives a strong coupled-bunch instability, with a rise time of a fraction of a turn. At the high frequencies characteristic of the bunch, despite the decrease of the resistive wall impedance as $\omega^{-1/2}$, the impedance is still large enough that the threshold for the transverse mode coupling instability can be approached with intensities a few times larger than nominal.

Although making the diameter of the vacuum chamber larger can reduce the resistive wall impedance, this

increases the cost and complexity of the magnets. Consequently, other remedies for the stability problem are under investigation. A distributed damping system has been proposed to solve the coupled bunch problem [14]. The long-wavelength collective motion is sampled at several points around the ring, and feedback is applied to damp the motion.

The transverse mode coupling instability is a more difficult problem. Schemes to raise the instability threshold using radio-frequency quadrupoles (similar to BNS damping), and asymmetric vacuum chambers, are under consideration [15].

2.2 Magnet System

This is the most important accelerator system for the VLHC. For the high field variant, the principal issues are obtaining a low-cost superconductor that can carry a high current density, at as high a temperature as possible, while satisfying the demanding mechanical and magnetic requirements; and designing a magnet which can sustain the large electromagnetic forces.

2.2.1 Field quality

The question of the required harmonic purity of the VLHC magnets is a crucial ingredient for any magnet design. Contrary to expectations prior to the SSC, both the prototype SSC magnets, and the full production magnets made for RHIC, show that, with current manufacturing processes, systematic errors dominate over random errors. Mature design techniques, improved tooling, excellent cable and coil size control, better measurement techniques, and a flexible, experimental approach mean that even early prototypes can now be made with the desired (geometric) field errors. This applies to both high field and low field magnets. Systematic persistent current errors, and saturation effects, will thus be the principal sources of error fields.

In this event, relatively simple analytic estimates [16] of the tune shifts caused by systematic errors can provide some guidance for magnet designers. A key issue is the magnitude of the tune shift that the beam can tolerate [17].

2.2.2 Conductor

The conductors that are being studied for use in high-field VLHC magnets are of two general classes. The first class is A15-compound low temperature superconductors: Nb_3Sn and Nb_3Al. These conductors would be operated at 4.5°K. The second class includes copper-oxide high temperature superconductors (HTS), such as BSCCO-2212, BSCCO-2223, and YBCO-123 [18]; these conductors could be operated from 4.5°K to 20-30°K, with some reduction in critical current at the higher temperatures.

Although Nb_3Sn has a high critical field, this material has several disadvantages. Small filament diameters and high current density are difficult to achieve simultaneously in Nb_3Sn, since high-density filaments tend to grow together after reaction. Nb_3Sn is also much less strain tolerant than NbTi.

Target specifications for conductor which would be useful in high-field VLHC magnets correspond to a critical current density of about 2000-3000 A/mm² at 12

T, 4.2°K, with a filament diameter <20 µm. Currently available material has a critical current density in the 950-1100 A/mm² range, with an effective filament diameter of 7-14 µm.

Rapid-quench Nb_3Al has less strain sensitivity than Nb_3Sn, with comparable current density performance. However, the rapid-quench method has yet to be developed into a viable industrial process. Nb_3Al is being considered as the conductor for the low-field transmission line magnet [19]; this conductor would allow a higher operating temperature than NbTi.

The high temperature superconductor BSSCO-2223 is the only form of HTS commercially available in large quantities at this time. This material is made in the form of oxide-powder-in-tube tapes. Small samples can have superconductor current densities (at 1 µV/cm) in excess of 700 A/mm² at 10 T, 4.2°K. Long (400 m) tapes have an engineering current density of about 100 A/mm². These materials, being basically ceramics, do not have a great deal of stress tolerance; in this regard, they are similar to the A15 compounds.

Another high temperature superconductor, BSCCO-2212, has been fabricated in the form of round multi-filamentary strands. Cables made from this material have operated above 600 A/mm² at 10 T, 4°K. As is typical of the high temperature superconductors, there is little degradation with fields up to at least 30 T.

The most promising (but least developed) of the copper-oxide superconductors is YBCO-123. Thin (1-5 µm) films of this material, up to 1 m in length, have been made in the form of a copper, superconductor and buffer layer sandwich. In this form, superconductor current densities of 10,000 A/mm² have been observed at 20 T, 4°K.

The processes by which the buffer layer and the superconductor are deposited onto the copper are complex, typically requiring the use of ion beams. Groups at ORNL, LANL, and BNL are working to simplify these processes. The most challenging task appears to be deposition of the buffer layer, which is needed to obtain the alignment of the YBCO crystals required for high current density.

2.2.3 Magnet design and prototyping

There are four major high-field magnet R&D programs underway. BNL, LBL, and Texas A&M (TAMU) are focusing on block designs; Fermilab is studying a conventional cos-θ design. The Fermilab, LBL, and TAMU programs are concentrating on Nb_3Sn conductor. BNL is looking at BSCCO and YBCO.

2.2.3.1 Fermilab program: High field magnets

Fermilab's goal is a magnet in the 11 T range. In collaboration with KEK and LBL, they are designing a 50-mm bore, Nb_3Sn two-shell cos-θ dipole [20]. This approach is motivated by recent progress in Nb_3Sn conductor performance, and utilizes the well-understood cos-θ technology developed for the SSC and LHC.

Facilities to react and study Nb_3Sn are being installed at Fermilab. Component tests will be done in a 15 T solenoid, at 4°K. The first prototype magnet is expected in

the summer of 2000. The program will also study Nb$_3$Al, and common-coil block designs.

2.2.3.2 LBL program

High-field magnet development, using Nb$_3$Sn, has been ongoing at LBL for many years. The most recent success has been the 13 T D20 dipole [21]. The conductor performed well in this magnet: an assembly flaw limited the magnet performance. The success of this magnet shows that brittle materials can be used in high-field magnets.

LBL's future plans for high-field dipoles are concentrated on common-coil [22] block magnet designs using Nb$_3$Sn. Such designs have a number of attractive features. They are simple, robust, and compact; the Lorentz forces are easier to contain than for a cos-θ dipole.

They use flat racetrack coils, which are quite easy to fabricate. The geometry is very friendly to brittle materials, such as Nb$_3$Sn or the copper oxides. The design can be fully modular, with modules independently preloaded. In the development phase, the modular design allows different conductors to be tested in the inner high-field regions. Because of the simplicity of the design, tooling and labor costs tend to be moderate, and a relatively low-cost magnet may be expected.

A 1-m long prototype Nb$_3$Sn dipole of this form has been built, using ITER conductor [23]. It reached 6 T (short sample) with no training. Subsequent magnets will use improved conductor, with an ultimate field target of 15 T.

2.2.3.3 BNL program

BNL is also focusing their R&D efforts on a modular common-coil block dipole [24]. They plan to use the magnet as a test vehicle for BSCCO at 20-30°K, and eventually YBCO. It will be a 1m long, 4-cm bore hybrid magnet, with NbTi background field coils and HTS (or Nb$_3$Sn) inserts. The goals of the program are to gain experience with HTS tape conductors and the common-coil design, and to develop techniques for magnetic measurements, quench protection, splices, and joints. This will lead eventually to an all HTS magnet.

2.2.3.4 TAMU program

The high field magnet program at TAMU [25] is focused on a 16 T dipole, which will use Nb$_3$Sn. The dipole has a scaleable-aperture segmented block coil design (with apertures from 1-5 cm) and emphasizes stress management techniques. Laminar inconel springs are used to intercept stress, preventing it from being applied to the conductor. Shear release is accomplished through the use of mica sheets, which prevent stick/slip friction at the coil-rib interface.

2.2.3.5 Low field magnets

Fermilab's development of the combined function transmission-line dipole for the low-field VLHC is much further advanced than the high-field magnets. A short (1 m) prototype has been built and tested with a drive current of 43 kA [26]. The latest design has a 20 mm gap, NbTi conductor with a drive current of 75 kA, a peak field of 2 T, and a good field region of 18 mm at 10^{-4}. Crenellated laminations (material missing in every 10th lamination) will be used to get to 2 T without saturation [27]. This

should fully suppress the saturation quadrupole and sextupole fields. Proposed transmission line magnets for the 3 TeV injector use SSC cable [28]. A long prototype magnet and string is planned for this year or the next.

A cold iron, low field magnet is being considered at JINR. It is a 2.2 T, 1-turn, dual bore combined function magnet, with a 34 kA drive current, having a window frame conductor arrangement. The cold bore has a beam screen capable of handling up to 1.5 W/m. JINR is planning to make a prototype.

2.2.4 Magnet cost issues

For the VLHC magnet system to be affordable, it must be much more cost-effective than those of past or current large hadron colliders. A systematic attack on this problem starts with an analysis of the cost drivers and the cost tradeoffs in the scalable parameters: conductor, bore, field, length, etc.

For previous superconducting magnet systems, labor has been the major part of the cost, followed by the cost of the conductor. A cost analysis [29] for intermediate field (3-10 T) magnets has been carried out, based on RHIC dipole costs. The dipole costs have been scaled to 18 m dipoles with a single 40 mm aperture, appropriate for the VLHC. This scaling gives a dipole cost of $1400/T-m.

High-field VLHC magnets would need fields above 10 T, where either an A15 compound or a copper oxide material would be used. These materials are currently considerably more expensive than NbTi. For example, Nb$_3$Sn conductor now costs about $10/kA-m at 12 T, vs. $1/kA-m at 5 T for NbTi. Copper oxide superconductors are even more expensive. Costs of YBCO cannot be estimated, as no material is commercially available yet. For BSCCO materials at 4°K and zero field, the costs range from about $50/kA-m (2212) to close to $1000/kA-m (2223).

Because of its simplicity and advanced state of development, a relatively reliable cost estimate can be made for the Fermilab low-field transmission-line magnets [30]. Two-thirds of the cost is in the iron yoke. In FY97$, the total cost for a 13 m magnet is about $14,000. At 2 T, this corresponds to $540/T-m.

2.3 Accelerator Technologies

A general survey of the challenging issues in the broad range of technologies needed for the VLHC were reviewed in a recent workshop [31]. The workshop covered the topics of instrumentation, alignment, cryogenics, vacuum, rf and feedback.

The cost vs. operating temperature tradeoffs for the high-field VLHC cryogenic systems were studied for the Snowmass '96 workshop [32]. For the low field VLHC transmission-line magnet, which uses NbTi conductor, the low current density and low field allow operation at temperatures above 4°K. A higher operating temperature (6.5-7.5°K) results in a much simpler cryogenic system.

Both the high field and low field VLHC have challenging vacuum systems [33]. The large synchrotron radiation load in the high field requires a beam screen intercept operating in the 10-20°K region. The screen must be integrated with a cryosorber, which pumps the

desorbed gases released by the synchrotron radiation. The warm-bore vacuum system for the low field machine is much like that of a low-energy electron machine. A distributed pumping system, using an antechamber, together with frequent localized lumped pumps, will be required.

2.4 Civil construction

Both variants of the VLHC would benefit from the minimum possible tunnel costs, but this is particularly important for the low-field VLHC. Considerable work was done on this topic at Snowmass [34], and studies have continued at Fermilab. For tunnels excavated with present-day technology tunnel boring machines (TBM), the minimum cost tunnel has a bore diameter in the range of 8-10 ft.

The overall SSC main tunnel costs were estimated in 1991 at about $5500/m. Recently, a cost estimate [35] gave $4000/m for a TBM-style tunnel for a 3 TeV low-field injector to the VLHC, sited at Fermilab. This cost may be reduced with continued R&D and tunneling technology improvements in the future.

3 CONCLUSION AND OUTLOOK

A post-LHC very large hadron collider, with a center-of-mass energy of 100 TeV and a luminosity of 10^{34} cm^{-1}s^{-1}, can be built with today's technology, but would be unaffordable.

The principal thrust of the R&D is to reduce the cost. The R&D on magnet systems, which is the most critical, has received the most attention to date. The low-field VLHC uses a simple low-cost magnet. In the next several years, one may hope that a good low-cost candidate also emerges for the high-field VLHC magnet. During this same period, many of the other issues mentioned above, related to the accelerator physics and the technologies of the accelerator systems, will receive more detailed study.

With this information in hand, a sound and affordable baseline design, and a detailed cost estimate, could be undertaken. If this can be completed by the time that physics results from the LHC begin to become available, the high-energy physics community would then be in a position to decide if and when it makes sense to embark on this project.

4 REFERENCES

[1] G. Dugan, P. Limon and M. Syphers, "Really Large Hadron Collider Working Group Summary", *1997 DPF/DPB Summer Study on New Directions for High Energy Physics*, 251, (Snowmass, 1996)

[2] *Proceedings of the Workshop on Future Hadron Facilities in the US*, Fermilab TM-1907 (1994)

[3] M. J. Syphers et. al., "Beyond the LHC: A Conceptual Approach to a Future High Energy Hadron Collider", *PAC-95*, 431(Dallas, 1995)

[4] G. W. Foster, E. Malamud, "Low Cost Hadron Colliders at Fermilab", Fermilab TM-1976 (1996)

[5] A. Hoffman, B. Zotter, "Combined Function Electron Storage Rings", *IEEE Trans. On Nucl. Sci.*, NS-24, 1875 (1977)

[6] S. Peggs et. al., "Lattices for a High Field 30 TeV Hadron Collider", *1997 DPF/DPB Summer Study on New Directions for High Energy Physics*, 354 (Snowmass, 1996)

[7] S. Peggs et. al., "Flat Beams in a 50 TeV Hadron Collider", *PAC-97*, 95 (Vancouver, 1997)

[8] C. S. Mishra, "Lattice Design of the 3 TeV Low Field Injector for the VLHC", *PAC-99*, paper TUP39 (New York, 1999)

[9] G. Dugan, M. Syphers, "50 TeV High-field VLHC with a Low-field Full Energy Injector, *PAC-99*, paper THA9 (New York, 1999)

[10] R. Gupta, Field Quality in a Common Coil Design Magnet System", *PAC-99*, paper THP120 (New York, 1999)

[11] R. Pasquinelli, "Bunched Beam Cooling for the Fermilab Tevatron", *PAC-95*, 2379 (Dallas, 1995)

[12] M. Zolotorev, A. Zholents, *Phys. Rev. E*, **50N4**, 3087 (1994)

[13] B. Bakalov et. al., "Ground Motion Measurements for Fermilab Future Collider Projects", *PAC-99*, paper TUA133 (New York, 1999)

[14] J. Marriner, "Transverse Instabilities and Dampers for the VLHC", in *Accelerator Physics Issues for Future Hadron Colliders*, Mini-Symposium at 1998 APS Meeting (Columbus, OH, 1998)

[15] V. Danilov, et. al., "Beam Instabilities in Very Large Hadron Colliders", *PAC-99*, paper FRBR5 (New York, 1999)

[16] S. Peggs, F. Dell, "Tolerable Systematic Errors in Really Large Hadron Colliders", *1997 DPF/DPB Summer Study on New Directions for High Energy Physics*, 329 (Snowmass, 1996)

[17] M. Harrison et. al. "Sustainable Tune Shifts during Collisions in a High Field Hadron Collider", *PAC-99*, paper TUP92 (New York, 1999)

[18] P. Lee, D. Larbalestier, "Prospects for Use of HTS in High Field Accelerator Magnets", *PAC-99*, paper TUBR4 (New York, 1999)

[19] E. Barzi et. al., "Nb$_3$Al Conductor Development for the Low-Field VLHC Magnet", *PAC-99*, paper THP155 (New York, 1999)

[20] T. Arcan et. al., "Conceptual Design of the Fermilab Nb$_3$Sn High Field Dipole Model", *PAC-99*, paper TUBR3 (New York, 1999)

[21] A. McInturff et. al., "Operational Characteristics, Parameters, and History of a 13 T Nb$_3$Sn Dipole", *PAC-99*, paper THP118 (New York, 1999)

[22] R. Gupta, "A Common Coil Design for High Field 2-in-1 Accelerator Magnets", *PAC-97*, 3344, (Vancouver, 1997)

[23] K. Chow et. al., "Fabrication and Test Results of a Prototype, Nb$_3$Sn Superconducting Dipole Magnet", *PAC-99*, paper TUBR2 (New York, 1999)

[24] A. K. Ghosh et. al., "A Common-coil Magnet for Testing High Field Superconductors", in *PAC-99*, paper THP117 (New York, 19999)

[25] C. Battle et. al., "Block-coil Dipole for Future Hadron Colliders", *PAC-99*, paper THA149 (New York, 1999)

[26] G. W. Foster et. al., "Design and Operation of an Experimental 'Double-C' Transmission-line Magnet", *PAC-95*, 3392 (Dallas, 1995)

[27] G. W. Foster et. al., "Measurements of a Crenellated Iron PoleTip for the VLHC Transmission Line Magnet", *PAC-99*, paper THP154 (New York, 1999)

[28] G. W. Foster et. al., "Tests of a Rutherford-Cable-in-Conduit Transmission Line Magnet Conductor Based on Leftover SSC Cable", *PAC-99*, paper TUBR5 (New York, 1999)

[29] E. Willen, "Superconducting Magnets", in *Hadron Colliders at the Highest Energy and Luminosity*, 141 (Erice, 1996)

[30] W. Fowler, "Cost Studies for Low-Field Magnets", in *Workshop on Magnets for a Very Large Hadron Collider* (Pt. Jefferson, NY, 1998)

[31] J. Marriner, V. Shiltsev, "Accelerator Technology for the VLHC", *PAC-99*, paper THA11 (New York, 1999)

[32] M. MacAshan, P. Mazur, "Cryogenic Systems for the High Field RLHC Study Cases", *1997 DPF/DPB Summer Study on New Directions for High Energy Physics*, 316, (Snowmass, 1996)

[33] W. Turner, "Beam Tube Vacuum in Low Field and High Field Very Large Hadron Colliders, *1997 DPF/DPB Summer Study on New Directions for High Energy Physics*, 341, (Snowmass, 1996)

[34] J. E. Friat et. al., "Pipetron Tunnel Construction Issues", *1997 DPF/DPB Summer Study on New Directions for High Energy Physics*, 286, (Snowmass, 1996)

[35] J. Lach et. al., "Cost Model for a 3 TeV VLHC Booster Tunnel", Fermilab TM-2048 (1998)

NEW PROJECTS OF CRYSTAL EXTRACTION AT IHEP 70 GeV ACCELERATOR

A.G.Afonin, V.M.Biryukov, V.N.Chepegin, Y.A.Chesnokov, V.I.Kotov, V.I.Terekhov,
E.F.Troyanov, Yu.S. Fedotov
Institute for High Energy Physics, Protvino, Russia
Yu.M.Ivanov, *Nuclear Physics Institute, St.Petersburg, Russia*
W.Scandale, *CERN, Geneva*; M.B.H.Breese, *University of Surrey, UK*

Abstract

Using channeling in a 5-mm crystal with bending angle of 0.65 mrad, a record high efficiency, over 60%, of particle extraction from accelerator was achieved. The extracted beam intensity was up to 5.2×10^{11} protons per spill of $\sim$0.5 s duration. Also, the first proof-of-principle experiment on 'crystal collimation' was performed where crystal - serving as a scraper - has reduced the radiation level in the accelerator by a factor of two. The measurements agree with Monte Carlo predictions.

1 INTRODUCTION

Crystal can channel a charged particle if it comes within so-called critical angle θ_c, about ± 5 μrad/$\sqrt{p(TeV)}$ in silicon. This restricts crystal efficiency in divergent beams. However, it's been argued theoretically[1] that a breakthrough in crystal efficiency can be due to multiple character of particle encounters with a crystal installed in a circulating beam, where particle may scatter in inefficient encounters and have new chances on later turns. The importance of multi-pass mechanism of extraction was first shown in CERN SPS experiment[2]. To benefit from the "multi-pass" channeling, the crystal must be short enough to reduce beam losses in multiple encounters with it.

The Protvino experiment on slow extraction of 70 GeV protons from IHEP accelerator employs, as a primary element of the extraction system, a very short bent silicon crystal. To gain extraction efficiency from an increased number of proton encounters with the crystal, it is necessary to use crystals as short as possible.

Bending a short crystal to be installed in the accelerator vacuum chamber is not easy. The first crystal Si(111) was performed as a short plate of a big height, $0.5 \times 40 \times 7$ mm^3 (thickness, height, and length along the beam direction, respectively). It was bent transversally with a metal holder which had a hole of 20 mm size for beam passage, and gave the channeled protons a deflection of 1.7 mrad. Despite an angular distortion (a "twist") in that design, encouraging results on beam extraction were obtained in our first run in December 1997, Figure 1. The peak extraction efficiency reached about 20% and the extracted beam intensity was up to 1.9×10^{11} [3]. Here and later on in the paper, the extraction efficiency is defined as the ratio of the extracted beam intensity as measured in the external beamline to all

the beam loss in the accelerator.

To further increase the extraction efficiency, further crystals (without twist) were made from a monolithic Si piece in a shape of "O" at the Petersburg Nuclear Physics Institute, as described in Ref. [4]. The crystals Si(110) used in our recent runs had the length along the beam direction of only 5 mm. The bent part of the crystal was just 3 mm long, and the straight ends were 1 mm each.

Such a crystal, with bending angle of 1.5 mrad, was successfully tested in March 1998 and has shown extraction efficiencies over 40% [4]. In the mean time we have changed the crystal location in order to use another septum magnet (with partition thickness of 2.5 mm instead of 8 mm as in the old scheme) where a smaller bending angle is required from a crystal. This change was also motivated by the intention to test even shorter crystals (two of them, 2.5 and 3.0 mm long, are already prepared for the tests). The crystal used in this location was new, but of the same design and dimensions as earlier described[4]. The bending angle used in our recent run was 0.65 mrad. Below we consider the results of the studies with this crystal.

2 EXPERIMENT

The general schematics of beam extraction by a crystal is shown in Ref.[4]. As the small angles of deflection are insufficient for a direct extraction of the beam from the accelerator, a crystal served as a primary element in the existing scheme of slow extraction. Crystal was placed in straight section 106 of the accelerator upstream of a septum-magnet of slow-extraction system. The accuracy of the crystal horizontal and angular translations was 0.1 mm and 13.5 μrad, respectively. The horizontal emittance of the circulating proton beam was about 2π mm$\times$mrad, and the beam divergence at the crystal location was 0.6 mrad. A local distortion of the orbit by means of bump windings in magnets moved the beam slowly toward the crystal. To obtain a uniform rate of the beam at crystal, a monitor for close loop operation based on a photomultiplier with scintillator was used to automatically adjust the orbit distortion. We used also function generator to control current in bump windings.

The beam deflection to the septum and its transmission through the beam line of extraction were supervised with a complex system of beam diagnostics, including TV system,

53

loss monitors, profilometers, intensity monitors[4]. All the diagnostics devices were firstly tested in fast-extraction mode and calibrated with beam transformers. The background conditions were periodically measured with and without crystal. According to the measurements, the fraction of background particles (e.g. elastically scattered protons) together with the apparatus noise did not exceed 4% of the useful signal level. This background was subtracted from the efficiency figures shown in the paper. The fraction of the beam directed to the crystal was defined as the difference between the measurements of the circulating beam intensity done with beam transformers before and after the beam extraction, with the systematic error of 1%. The extraction efficiency was evaluated in every cycle of acceleration.

3 RESULTS

The accelerator beam intensity during the experiment was about 1.3×10^{12} protons per cycle. The fraction of the circulating beam incident on the crystal ΔI was varied from 20 to 90%. The spill duration of the channeled beam in the feedback regime was on the order of 0.5 s. The plateau of the IHEP U-70 accelerator magnet cycle is 2 s long while the overall cycle of the machine is 9.6 s. Figure 1 shows the efficiency of extraction averaged over the spill, as measured in our three experiments of 1997-98. In the last one, the efficiency was about 50% even when all the accelerator beam was directed onto the crystal. The spill-averaged efficiency figures were reproducible with 1% accuracy from run to run. The dependence of the extracted beam intensity on orientation of the crystal was about the same as in Ref.[4] and not shown here. The highest intensity of the extracted beam, for 1.15×10^{12} protons incident at the crystal in a cycle, was equal to 5.2×10^{11}.

As the beam moves radially toward the crystal, the proton incidence angle drifts at the crystal. For this reason the extraction efficiency varies in time during the spill (Fig. 2), especially for a large beam fraction used. The peak extraction efficiency in a spill was always greater than 60%. Figure 2 shows also a minor 'satellite peak', present in some cases and unexplained yet. The absolute extraction efficiency as obtained in our Monte Carlo simulations agree with the measurements to accuracy of about 5% for spill-averaged figures. The time dependence calculations (Figure 2) are more sensitive to the details of beam direction methods.

4 CRYSTAL COLLIMATION EXPERIMENT

Bent crystal, situated in the halo of a circulating beam, can be the primary element in a scraping system, thus serving as an 'active' collimator. In this case, the only difference from extraction is that channeled particles are bent onto a secondary collimator instead of the extraction beamline. The bent particles are then intercepted (with sufficiently big
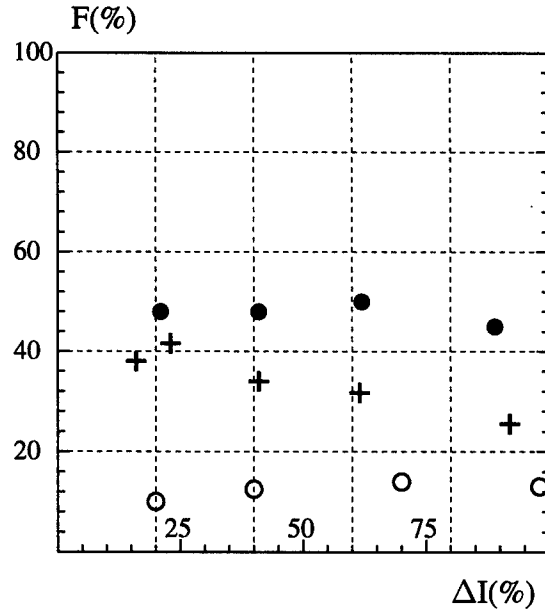
Figure 1: Spill-averaged efficiency of extraction as measured with 5-mm crystal 0.65 mrad bent (●), December 1998; 5-mm crystal 1.5 mrad bent (+), March 1998; 7-mm twisted crystal 1.7 mrad bent (o), December 1997; plotted against the beam fraction taken from the accelerator.
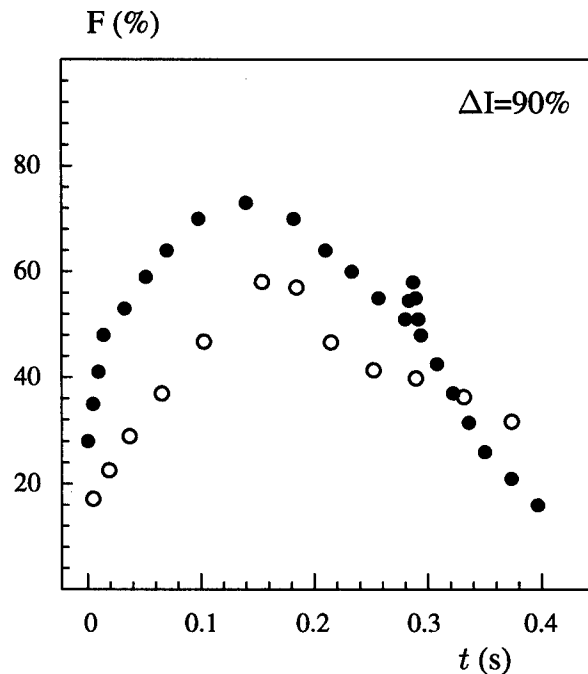
Figure 2: Extraction efficiency measured with 0.65-mrad crystal (●) as a function of time during the spill, for $\Delta I=90\%$. Also shown are simulated absolute figures of efficiency (o) in the assumption of uncompensated angular drift.

impact parameter) at the secondary element and absorbed there.

We have performed the first demonstration experiment on crystal-assisted collimation. A bent crystal, with the same dimensions as the extraction crystals described above and with bending angle of 1 mrad, was positioned upstream of a secondary collimator (stainless steel absorber 4 cm wide, 18 cm high, 250 cm long) "FEP" and closer to the beam in the horizontal plane. As the horizontal betatron tune is 9.73 in our accelerator, it was most convenient to intercept the bent beam at FEP not immediately on the first turn, but after 3 turns in the accelerator. In this case the deflection angle of 1 mrad transforms into more than 20 mm horizontal offset, and so the bent beam enters the FEP collimator at some ~15 mm from the FEP edge. The optimal horizontal position of the crystal w.r.t. the FEP edge was found to be ~10 mm.

The radiation level was monitored at 3 places along the ring in the vicinity of FEP. Figure 3 shows how the radiation level depends on the angular alignment of the crystal. At the best crystal angle, preferable for channeling, the radiation levels decrease by up to factor of ~two in the places of monitoring. This is explained by the fact that ~50% of the incident beam is channeled by the crystal and deflected to the depth of FEP where absorbed. In the case when crystal was out and the beam was scraped directly by FEP, the radiation at the monitors was at about the same level as in the case of disaligned crystal.
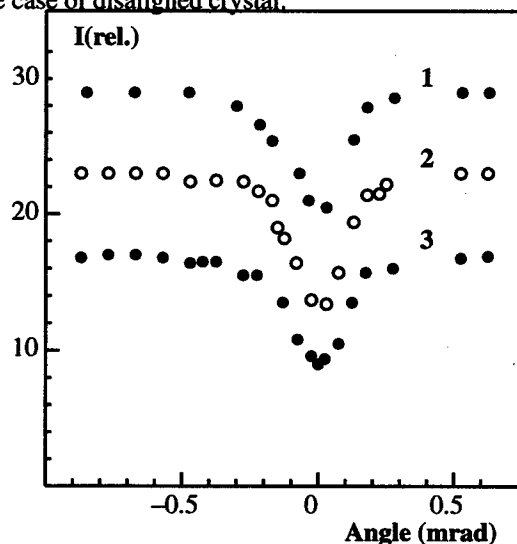
Figure 3: Measured irradiation in detectors 1, 2, 3 as function of crystal angle.

We were able to check the crystal efficiency figure by alternative means, measuring the profile and intensity of the particles incident at the FEP entry face. The channeled beam had a narrow profile and was well distanced from the FEP edge, as shows Figure 4 where this profile is shown in comparison with the profile of the accelerator beam deflected onto FEP by a kicker magnet. From comparison of the two profiles, from crystal and from kicker, we again

derived the crystal efficiency, which was found to be about 50%, in agreement with the radiation monitoring figures and with the earlier shown figures of extraction efficiency with crystal in straight section 106.
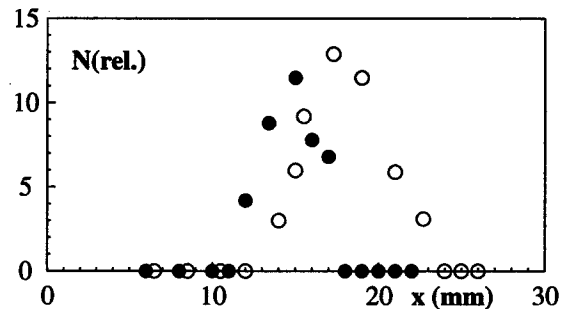
Figure 4: Profiles measured at FEP entry face: channeled beam (•) and beam (o) deflected by kicker magnet.

5 CONCLUSIONS

The crystal-assisted method of slow extraction demonstrates peak efficiency in the order of 60-70%, now comparable to alternative techniques of slow extraction, and shows reliable, reproducible and predictable work. A crystal can channel at least $5-6 \times 10^{11}$ ppp without cooling measures taken and without degradation seen. The basis for the efficiency boost was the multiple character of the particle encounters with a short crystal.

In our experiment this technique was for the first time demonstrated for scraping of the beam halo. Such application has been studied by computer simulation for several machines, notably RHIC [5] and Tevatron [6]. We have shown that radiation levels in accelerator can be significantly decreased by means of channeling crystal incorporated into beam cleaning system as a primary element.

We plan to continue tests with crystals 2.5-3.0 mm long, where Monte Carlo predicts ~80% extraction efficiency. The ultimate efficiency in our 70 GeV experiment can be obtained with a crystal shortened to ~1 mm. We study different techniques to prepare bent crystal lattices with required size, one of the most interesting approaches is described in Ref.[7].

6 REFERENCES

[1] V.Biryukov. NIM B 117 (1996) 463 and refs therein.

[2] X.Altuna et al., Phys.Lett. B 374 (1995) 671

[3] A.G.Afonin et al., JETP Lett. 67 (1998) 741.

[4] A.G.Afonin et al., Phys. Lett. B 435 (1998), 240.

[5] V.M.Biryukov, Y.A.Chesnokov, V.I.Kotov, D.Trbojevic, A.Stevens. "Optimization of the Parameters in the RHIC Single Crystal Heavy Ion Collimation", these Proceedings.

[6] A.I.Drozhdin, N.V.Mokhov, V.M.Biryukov. "On Possible Use of Bent Crystal to Improve Tevatron Beam Scraping", these Proceedings.

[7] M.B.H.Breese, NIM B 132 (1997) 540

TEVATRON RUN-II BEAM COLLIMATION SYSTEM *

M. Church, A. I. Drozhdin, A. Legan, N. V Mokhov[†], R. Reilly, FNAL, Batavia, IL

Abstract

Based on realistic Monte-Carlo simulations a two-stage beam collimation system is designed to minimize the beam loss in the Fermilab Tevatron for fixed target and collider Run II. Thin primary collimators are used to increase particle amplitude and their impact parameter on the downstream secondary collimators. This results in a significant reduction of the total beam loss in the machine, decreases collimator overheating and mitigates requirements to collimator alignment. A set of collimators will originally be installed for fixed target operation and for antiproton beam recycling studies. The collimation system improvement will continue into the collider Run II and intensity upgrade.

1 INTRODUCTION

Even in good operational conditions, a finite fraction of the beam will leave the stable central area of accelerator because of beam-gas interactions, intra-beam scattering, proton-antiproton interactions in the IPs, RF noise, ground motion and resonances excited by the accelerator elements imperfection. These particles produce a beam halo. As a result of halo interactions with limiting aperture, hadronic and electromagnetic showers are induced in accelerator and detector components causing accelerator related background in the detectors. A new collimation system has been designed for the Tevatron Run II to localize most of the losses in the straight sections D17, D49, EØ, F17, F48, F49 and AØ. In the beginning of Run II a set of collimators will be installed for magnet protection at Fixed Target operation, and for antiproton beam recycling studies. The collimation system improvement will continue for the Collider run and intensity upgrade. A multi-turn particle tracking through the accelerator and beam halo interactions with the collimators are done with the STRUCT[1] code. Using the calculated beam loss distribution, Monte-Carlo hadronic and electromagnetic shower simulation, secondary particle transport in the accelerator and detector components, including shielding with real materials and magnetic fields are done with the MARS[2]code.

2 RUN-II COLLIMATION SYSTEM

The collimation system consists of horizontal and vertical primary collimators and a set of secondary collimators placed at an optimal phase advance, to intercept most of particles out-scattered from the primary collimators during the

---

first turn after beam halo interaction with primary collimators. An impact parameter on the primary collimators is of the order of $1 \mu m$[3]. Our studies show that in the Tevatron, a 5-mm thick tungsten primary collimator positioned at 5σ from the beam axis in both vertical and horizontal planes would function optimally, reducing the beam loss rates as much as a factor of 4 to 10 compared to the system without such a scatterer. Secondary collimators located at the appropriate phase advances, are a 1.5 m long L-shaped steel jaw positioned at 6σ from the beam axis in horizontal and vertical planes. They are aligned parallel to the envelope of the circulating beam.
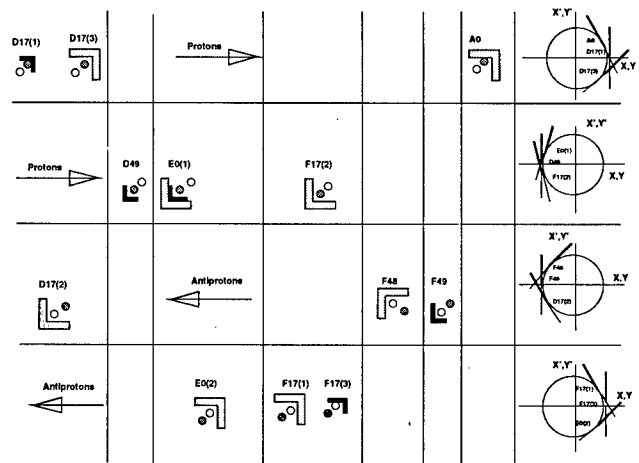
Figure 1: Tevatron Run II beam collimation system.

Based on the Tevatron experience[4, 5, 6], numerous optimization studies, designed helix separation[7] and available space in the Tevatron lattice, the collimation system shown in Fig. 1 is proposed for Run II. A proton primary collimator is placed at the beginning of the D17 straight section outward and up of the closed orbit (Fig. 2). It intercepts the large amplitude protons and a positive off-momentum beam.

Protons scattered from this collimator are presented by a vertical line in the transverse phase diagram (Fig. 1). Protons with a positive angle are intercepted by a D17(3) secondary collimator at the end of the D17 straight section. An AØ secondary proton collimator positioned outward and up of the circulating beam is intended to intercept the negative angle protons emitted from the primary collimator. A primary collimator D49 and secondary collimators EØ(1) and F17(2) are used to deal with the protons with negative momentum deviations. Antiproton beam cleaning consists of primary collimators F49, F17(3) and secondary collimators D17(2), F48, F17(1) and EØ(2).
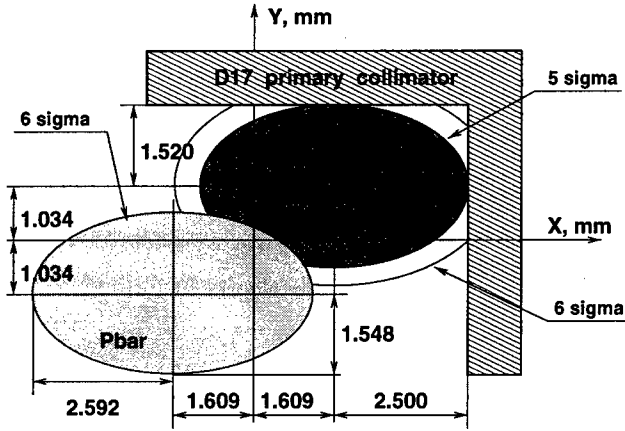
Figure 2: Proton primary collimator D17(1).

Figure 3: Beam halo horizontal phase space in D17(3) for positive off-momentum collimation.

3 COLLIMATOR PERFORMANCE

The source of beam halo intercepted by the collimation system is elastic and diffractive $\bar{p}p$ collisions in BØ and DØ, intra beam scattering, beam-gas interactions, ground motion, RF noise and resonances. The inelastic and elastic $\bar{p}p$ cross sections at 2 TeV are equal to 60 mb and 15 mb, respectively. The average luminosity is assumed to be equal to 10^{32}cm^{-2}s^{-1} and antiproton intensity reduction of 60% over the store (10 hours). Table 1 represents our assumptions on the Tevatron intensity evolution.

Table 1: Tevatron intensity evolution over the store

	proton, 10^{11}	antiproton, 10^{11}
Initial intensity	97.2	10.8
Inelastic interactions in DØ and BØ	4.32	4.32
Elastic interactions in DØ and BØ	1.08	1.08
60% intensity drop		6.48
A drop fraction due to elastic beam-gas interactions, ground motion and resonances		6.48-4.32-1.08 = 1.08 10% of the beam
10% drop for proton beam	9.72	
Total proton intensity drop	9.72+4.32+1.08= = 15.12	
Intensity at the end of the store	82.08	4.32
Number of particles intercepted by collimators	1.08+9.72 = 10.8	1.08+1.08 = 2.16
Scraping rate	3×10^7 p/s	6×10^6 p/s

Halo particles first hit the primary collimator with a 1 to 3 μm impact parameter. On the next turns, the impact parameter–as a result of scattering–increases to about 0.3 mm. The halo horizontal phase space at the D17(3) secondary collimator is shown in Fig. 3 for the off-momentum protons. The ellipse represents a 6σ envelope of the equilibrium energy beam. The vertical line shows the collimator jaw position. After the first interaction with primary collimator high amplitude particles are intercepted by the secondary collimators, but large number of particles survive.

Some fraction of the halo is not intercepted by a primary/secondary collimator pair and will interact with a primary collimator on the next turns. On average, halo pro-

tons interact with the primary collimator 2.2 times. Particles with the amplitudes $\leq 6\sigma$ are not intercepted by the secondary collimators and do survive for several tens of turns until they increase amplitude in the next interactions with the primary collimator. The tail of halo is extended above 6σ (Fig. 4). Large amplitude particles, which escape from the cleaning system at the first turn, are able to circulate in the machine, before being captured by the collimators on the later turns. This defines the machine geometric aperture. Calculated beam loss distribution in the Tevatron is presented in Fig. 5 for the proton and antiproton directions.
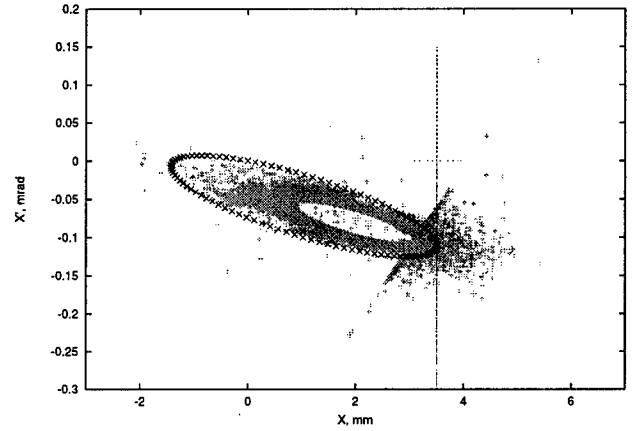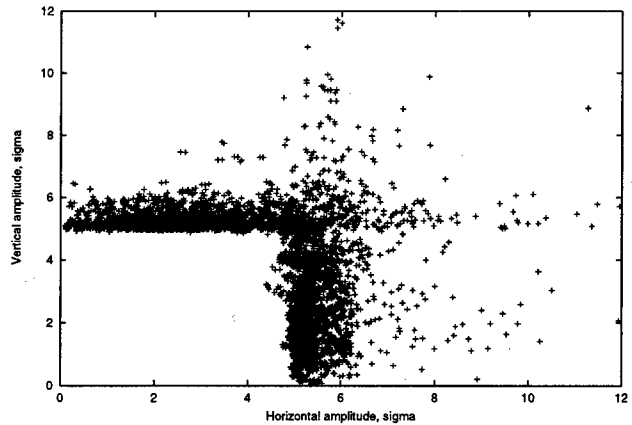
Figure 4: Proton beam halo in the Tevatron aperture.

The studies[6] have shown that the accelerator related background in the DØ and CDF collider detectors is originated by the beam halo loss in the inner triplet region. In addition to the optically small aperture at β_{max} location, the aperture restrictions in this area are the DØ forward detector's Roman pots placed at 8σ and the BØ Roman pots placed at 10σ at the entrance and exit of the beam separators. Beam loss in the BØ and DØ depends strongly on the secondary collimator offset with respect to the primary
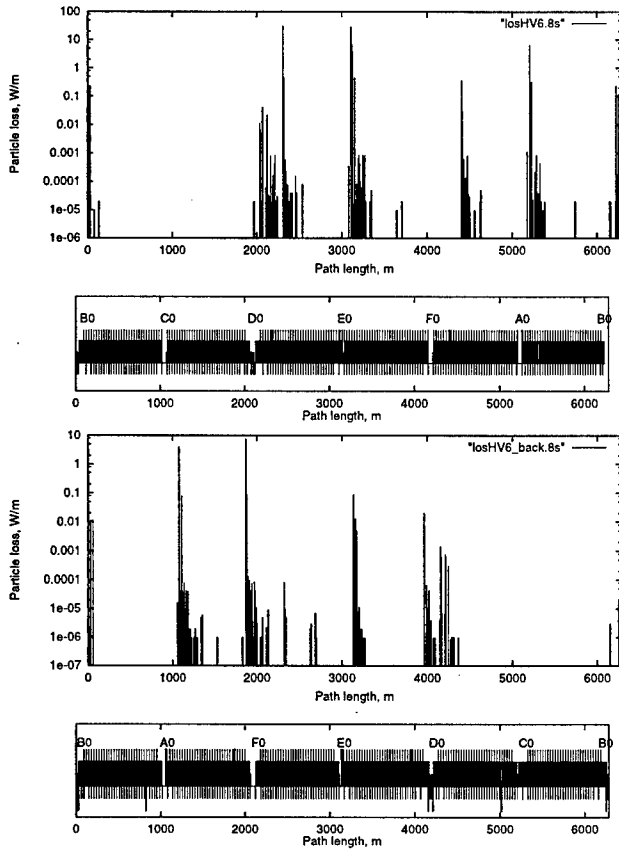
Figure 5: Beam loss in Tevatron at collimation with primary collimators at 5σ and secondary collimators at 6σ for proton (top) and antiproton (bottom) directions.

collimators. Table 2 gives the number of particles passed through the Roman pot detectors for different positioning of the secondary collimators. Beam loss at DØ goes down by a factor of 3 and 6 with the secondary collimators moved from 7σ to 6σ and 5.5σ, respectively.

Before being intercepted by the secondary collimators some of halo particles can pass through the Roman pot detectors several times creating false hits there and additional background in the main CDF and DØ detectors. Background is decreased by a factor of 1.8 if the DØ Roman pots are moved from $8\sigma_x$ to $9\sigma_x$, and by a factor of 1.6 in the CDF detector if the Roman pots at BØ are moved from $9\sigma_x$ to $10\sigma_x$ (Table 2). This would certainly decrease the Roman pot acceptances, therefore their transverse positions have to be chosen as a compromise between the main detector background and forward detector acceptance. The efficiency of collimation in the Tevatron Run II calculated as a ratio of background in the detectors without collimation and with collimation is equal to 150.

4 COLLIMATOR POSITION CONTROLS

The stepping motors (200 steps/turn) will be used to control position of the primary collimators and upstream and downstream ends of the secondary collimators in horizon-

Table 2: Halo hit rate (in $10^5 p/s$) at the DØ and CDF Roman pots for several secondary collimator and pot positions with respect to the closed orbit

Collimators	$5.5\sigma_{x,y}$	$6\sigma_{x,y}$	$7\sigma_{x,y}$	$6\sigma_{x,y}$	$6\sigma_{x,y}$
DØ pots	$8\sigma_{x,y}$			$9\sigma_{x,y}$	$8\sigma_{x,y}$
CDF pots	$10\sigma_{x,y}$			$10\sigma_{x,y}$	$9\sigma_{x,y}$
ROMAS	2.86	5.67	17.9	3.23	5.83
ROMAQ	2.69	5.27	16.5	2.91	5.34
ROMPQ	2.29	4.13	12.3	2.19	4.11
ROMPS	2.31	4.31	12.4	2.39	4.35
CDFPQ	3.11	5.62	9.40	5.75	9.15
CDFPS	4.02	7.49	13.2	7.83	12.5
CDFAS	5.84	10.7	23.5	11.7	17.1
CDFAQ	4.18	8.38	17.2	8.68	13.9

tal and vertical plane independently. The motors will be geared so that the collimator can be moved at a maximum speed of 2.5 cm in 10 seconds, which is approximately the distance from the full out position to the beam axis. This gearing will yield a minimum step size of 3 μm, which is never larger than about 1/80th of the beam sigma. Position read-back is provided for primary and secondary collimators. Limit switches will protect hardware from damage. Local fast feedback for the motion control will be provided by standard Tevatron loss monitors, placed downstream and upstream of each collimator.

5 ACKNOWLEDGMENTS

6 REFERENCES

[1] I. Baishev, A. Drozhdin, and N. Mokhov, "STRUCT Program User's Reference Manual", SSCL–MAN–0034 (1994).

[2] N. V. Mokhov, "The MARS Code System User Guide, Version 13(95)", Fermilab-FN-628 (1995); N. V. Mokhov et al., Fermilab-Conf-98/379 (1998); LANL Report LA-UR-98-5716 (1998); nucl-th/9812038 v2 16 Dec 1998; http://www-ap.fnal.gov/MARS/.

[3] M. Sidel, "Determination of Diffusion Rates in the Proton Beam Halo of HERA", DESY-HERA 93-04 (1993).

[4] A. I. Drozhdin, M. Harrison, and N. V. Mokhov, "Study of Beam Losses During Fast Extraction of 800 GeV Protons from the Tevatron", Fermilab-FN-418 (1985).

[5] S. M. Pruss, "A Design for a Beam Halo Scraper System for the Tevatron Collider", Proceedings of the 1991 IEEE Particle Accelerator Conference, p. 2340-2341, May 6-9, San Francisco, California (1991).

[6] J. M. Butler, D. S. Denisov, H. T. Diehl, A. I. Drozhdin, N. V. Mokhov, D. R. Wood, "Reduction of TEVATRON and Main Ring Induced Backgrounds in the DØ Detector", Fermilab-FN-629 (1995).

[7] P. Bagley, "Beam Separation for the Tevatron Run-II", Private communication (1998).

The 4-8 GHz Stochastic Cooling Upgrade for the Fermilab Debuncher[*]

D. McGinnis[#], FNAL, Batavia, IL

Abstract

During the Fermilab Collider Run II, the Main Injector is expected to provided a three-fold increase in flux of the proton beam sent to the antiproton production target as compared to the previous Collider Run Ib. This increase in antiproton production rate to 20×10^{10} antiprotons/hour will be handled by upgrading the stochastic cooling systems in both the Debuncher and Accumulator rings of the Fermilab Antiproton Source. In the Debuncher ring, the upgrade calls for increasing the stochastic cooling system bandwidth from 2-4 to 4-8 GHz. The effective front-end noise temperature of the cooling systems will also be lowered from 125K to 35K. This paper will discuss some details of the system design of the new 4-8 GHz cooling systems in the Debuncher Ring.

1 INTRODUCTION

The original horizontal, vertical, and momentum Debuncher cooling systems covered a bandwidth of 2-4 GHz. The pickups and kickers each consisted of 128 100Ω stripline pickups with an octave bandwidth. The signals were combined (or split) with a binary combiner tree. The pickups were cooled to 77K and had an overall front-end system temperature of 125K. The kickers were powered with 1600 Watts per plane. These systems were power limited and operated well below optimum cooling gain. These systems could cool 45×10^6 8 GeV particles from 25 π-mm-mrad (95% un-normalized) to 5 π-mm-mrad in 2.4 seconds.

The original upgrade plan called for the same cooling bandwidth of 2-4 GHz but with a reduction in noise temperature of the front-end to 35K. This was to be accomplished by cooling the pickup arrays and amplifiers to 10K with liquid helium as a coolant. Also the plan called for the arrays to plunge (change the transverse spacing of the pickups) during the cooling cycle so that system gain would increase as the beam size decreased for a fixed amount of kicker power. The combined result of both components of the upgrade was to cool 80×10^6 8 GeV particles from 30 π-mm-mrad to 5 π-mm-mrad in 1.5 seconds. This would have been sufficient for the anticipated Run II antiproton flux of 20×10^{10} antiprotons/hour.

However, for stacking rates beyond 20×10^{10} antiprotons/hour, the Debuncher cooling systems would near optimum cooling gain and further increases in

stacking rate would be limited by cooling bandwidth. [1]

Also, the 2-4 GHz system left little margin for design error. If the design plunging aspect ratio could not be achieved (due to factors such as closed orbit variations for example) or the front-end signal-to-noise ratio was smaller than anticipated (due to larger than expected combining losses or lack of pickup sensitivity), Run II stacking rates would not be achieved. To provide a future upgrade path and give larger design margins, the upgrade plan was changed to increase the Debuncher cooling bandwidth to 4-8 GHz.

2 NARROW BAND SYSTEM DESIGN

For Run 1b, all of the stochastic cooling pickup and kicker arrays at Fermilab consisted of stripline or planar loop electrodes. The signals from these electrodes are combined with a binary combiner tree formed by microstrip or stripline transmission lines. With a binary combining scheme, there must be no waveguide modes traveling down the beam pipe that would provide an alternate (uncontrollable) signal path in parallel to the binary combiner tree.

The nominal Debuncher transverse aperture is 30 π-mm-mrad (95% un-normalized). To account for closed-orbit variations, the design aperture of the cooling arrays was set at 40 π-mm-mrad. With lattice beta functions on the order of 10 meters, the transverse dimensions of the beam pipe will be about 40 mm which will propagate waveguide modes above 4 GHz. The presence of travelling waveguide modes in the beam pipe will limit the workable fractional bandwidth of the cooling arrays.

The solution was to divide the 4-8 GHz bandwidth into 4 narrower bands with each band having a bandwidth of about 1 GHz. The cooling arrays are built with slot coupled "slow-wave" waveguide structures as shown in Figure 1. The structure consists of two rectangular waveguides that are coupled to a rectangular beam pipe by a series of slots. The transverse signal is derived from the difference between the two waveguides and the momentum signal is derived from the sum of the two waveguides.

The image current that flows along the walls of the beam pipe due to a charged particle beam travelling in the center of the beam pipe excites electromagnetic magnetic waves in the slots which in turn excite travelling waveguide modes in the side waveguides and beampipe. Since the phase velocity of the unperturbed waveguide modes is faster than the beam velocity, the slots also act to "slow down" the waveguide modes by multiple reflections so that the phase velocity of the waveguide modes along the structure matches the beam

velocity. These structures are similar to the ridged waveguide pickups used for bunched beam cooling in the CERN SPS.[2]
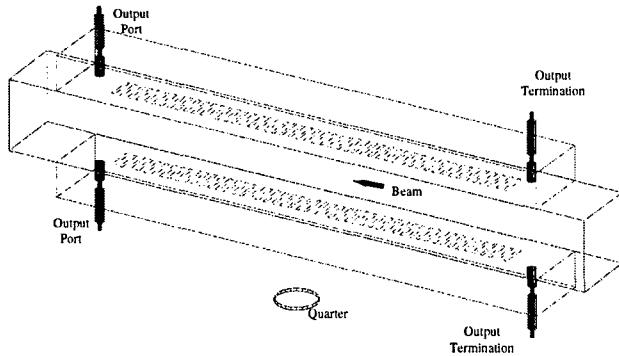
Figure 1: Conceptual drawing of a slow wave pickup.

The gain of the structure is proportional to the number of waveguide slots or the length of the array. However, the bandwidth of the structure is inversely proportional to the length of the array. For a 40 π-mm-mrad aperture in the 4-8 GHz range, a 0.7-meter long array provides about 1 GHz of bandwidth. In the Debuncher ring, there is 11.4 meters of space available per plane for either pickup or kicker, which leaves enough room for 16 arrays per plane (or 4 arrays per band). Because the fractional bandwidth of each band is still relatively large, it is desirable from a perspective of power balance to power each kicker array with one power amplifier. Because of the large fractional bandwidth per band and the frequency range of 4-8 GHz, the natural choice for power amplifier is a travelling wave tube (TWT). The TWTs chosen can provide 150 Watts per tube, which results in an available power of 2400 Watts per plane. The Run II design goals for a 4-8 GHz system require about 1200 Watts per plane, which leaves plenty of room for future upgrades or design margin. [1]
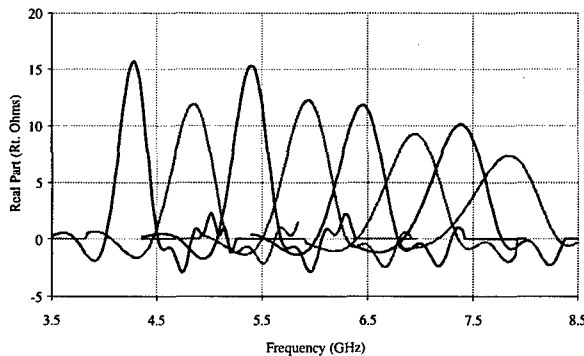
Figure 2: Pickup impedance for all 8 sub-bands. The blue trace is the lower sub-band. The red trace is the upper sub-band.

The pickup arrays will be cooled with liquid helium to a temperature of about 10K. Before the pickup signals can be brought out to room temperature, they must be amplified with low noise cryogenic amplifiers, which are

also cooled with liquid helium. The noise temperature of these amplifiers is about 25 K, which brings the total front-end noise temperature to 35 K.

Figure 3: The kicker response for all 4 bands. The green
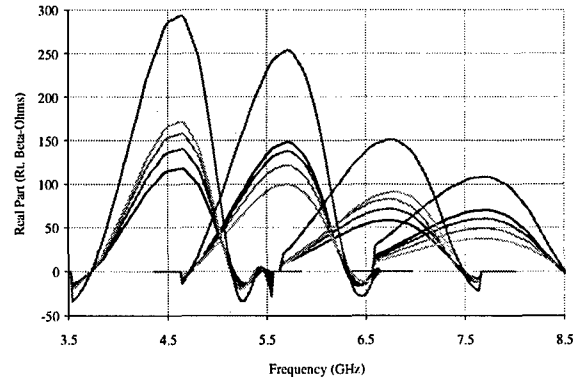
traces are the response of individual arrays while the red traces are the power sums of all the individual arrays in a band.
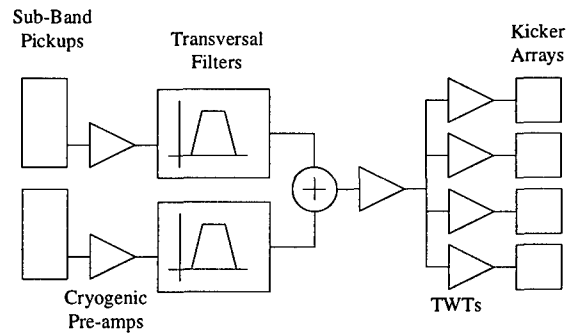
Figure 4: Simple schematic of components in a single band.
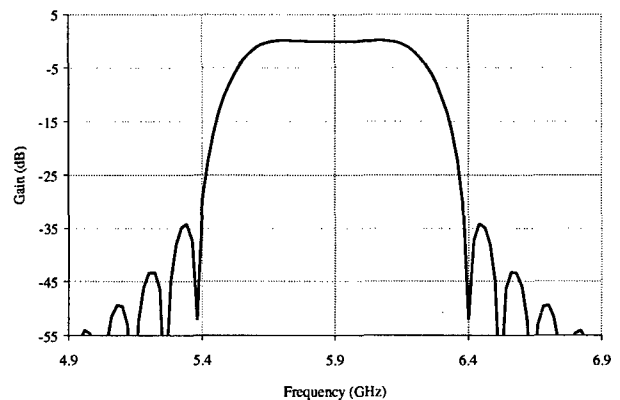
Figure 5: Response of a transversal filter for Band 2b.

If the pickup arrays have the same bandwidth as the kicker arrays, this would require eight cryogenic amplifiers per plane per band (4 for transverse, 4 for momentum). For reliability reasons, it is undesirable to have this many cryogenic amplifiers in the same vacuum vessel. The number of cryogenic amplifiers per band per

plane could be reduced by adding a combiner board inside the cryogenic vacuum tank that adds the signals of a number arrays together. However, this combiner board would add extra loss to the pickup array resulting in a reduction in signal to noise ratio. Also the combiner board would be relatively large and make the cryogenic vacuum tank much more costly and difficult to assemble and repair.
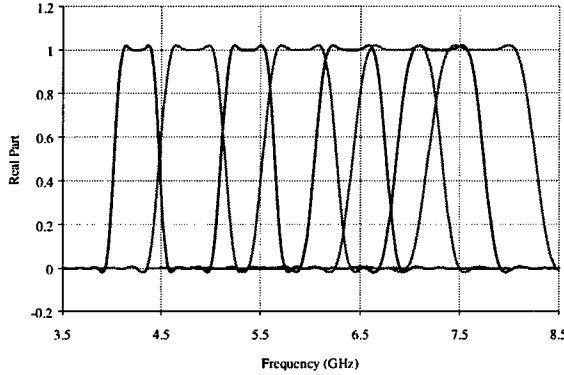
Figure 6: Transversal filter response for all 8 sub-bands. The blue trace is the lower sub-band . The red trace is the upper sub-band.

The alternative that was pursued was to divide each 1 GHz band into two 0.5 GHz sub-bands with a center to center spacing of about 0.5 GHz. The length of the pickup arrays was increased to 1.4 meters so that there was only one pickup array per sub-band per plane. This resulted in four cryogenic amplifiers per band per plane (1 transverse amplifier x 2 sub-bands per band + 1 momentum amplifier x 2 sub-bands per band) and no cryogenic combiner boards.

The transverse impedance of the pickup array is defined as:

$$P_\Delta = \frac{1}{2}(Z_\Delta)i_b^2 \frac{\varepsilon_b}{1\pi - mm - mrad}$$

Where P_Δ is the signal power obtained from the pickup, i_b is the beam current and ε_b is the emittance of the beam. The kicker impedance is defined as:

$$P_\Delta = \frac{1}{2}\frac{\left(\sqrt{\beta_k}\frac{\Delta pc}{q}\right)^2}{Z\beta_{\Delta kr}}$$

Where Δpc the change in transverse momentum going through the kicker for a particle with charge q and $\beta_{\Delta kr}$ is the lattice beta function at the kicker. The array impedance is defined in this manor so as to incorporate the lattice beta functions easily into cooling rate calculations. A plot of the pickup impedance for all 4 bands is show in Figure 2. A plot of the kicker impedance for all 4 bands is show in Figure 3.

The two sub-bands for each band were added together as shown in Figure 4. Because the noise power spectral

density of the cryogenic amplifier and pickup array covered a frequency range much wider than the bandwidth of the pickup, a narrow-band filter has to be added to each sub-band before the sub-bands are added together.

This narrow-band filter has to have "brick-wall" characteristics of flat phase and gain in the filter pass-band with very high rejection outside the pass-band. These characteristics can be accomplished with a transversal filter made with many sections of weakly coupled striplines. The response of such a filter is shown in Figure 5. The responses of all the filters in the 4-8 GHz band are shown in Figure 6.

The total system impedance for all 4 bands is shown in Figure 7. The predicted transfer efficiency from the Debuncher to the Accumulator for Run II intensities is using the impedance profile shown in Figure 7 is shown in Figure 8.
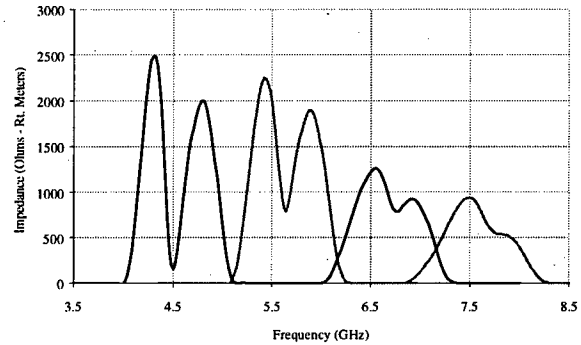
Figure 7: The total system impedance for all 4 bands. Bands I and III are the black traces. Bands II and IV are the purple traces.
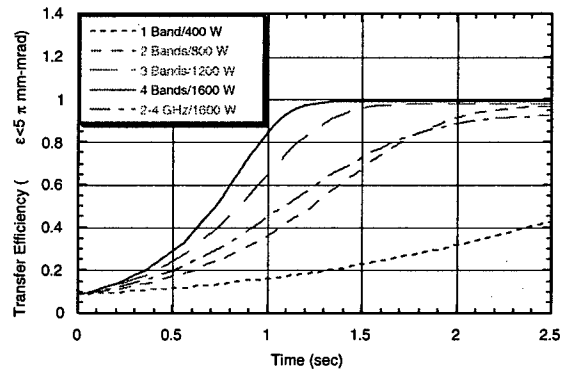
Figure 8: Debuncher to Accumulator transfer efficiency for Run II parameters using the 4-8 GHz narrow band system.

3 REFERENCES

[1] J. Marriner,"Debuncher Stochastic Cooling Upgrade for Run II and Beyond", Fermilab PBAR Note 573, April, 1998.

[2] D. Boussard, G. Di Massa, "High Frequency Slow Wave Pickups",CERN SPS/86-4, February 1986

COHERENT MODE OF A HIGH INTENSITY BEAM IN A SYNCHROTRON

S. Machida[1], T. Uesugi, KEK-Tanashi, Tanashi, Tokyo, 188-8501, Japan

M. Ikegami, JAERI, Tokai, Ibaraki, 319-1195, Japan

Abstract

As one of major sources which cause emittance growth and beam loss in high intensity hadron synchrotrons, we have investigated coherent mode oscillations in a beam. Using Sacherer's envelope equations, mode frequencies of a bunched beam are derived. Multi-particle simulation shows that emittance growth occurs when the oscillation frequency of a coherent mode hits a resonance. The present status of a beam experiment at HIMAC is also mentioned, which is expected to show the direct observation of a resonance crossing of a coherent mode and beam loss.

1 INTRODUCTION

Emittance growth and beam loss in high intensity accelerator draw more and more attention recently because of several projects, such as JHF, SNS, ESS, where high intensity accelerators are the essential components and their radioactivation has to be minimized. Study of a parametric resonance in linear accelerator has been successful for last few years [1]. In which, motion of particles in the tail of a beam core is treated in semi self-consistent way, so-called particle-core model. In fact, similar mechanism may occur not only in linear accelerators but also in circular machines [2,3].

Stability of a coherent mode itself, not only as a driving force of halo formation, is one of major topics in a circular machine. In particular, an envelope mode and its stability in connection with resonances excited by field errors has been studied for long time based on envelope equations.

The envelope stability analysis can be found in his dissertation work of Sacherer [4]. He clearly stated that incoherent motion is not the one which causes beam loss. Using envelope equations, he showed that when a coherent mode frequency hits a resonance, the envelope becomes unstable and cause emittance growth and beam loss.

Although Sacherer's analysis holds in general, the real situation is rather complicated in a circular machine. First, there is an effect of dispersion functions in a circular machine. Much work has been done and shows that essentially the same form of envelope equations can be applicable to dispersion [5].

Secondly, a beam in an accelerator is bunched in 3D configuration space unlike the model assumed by Sacherer in his dissertation. In fact, the mode frequency is derived for an azimuthally symmetric 3D beam by Barnard et. al.

[6] and for a bunched beam in a linac with some approximations by Pabst et. al. [7]. However, for long bunch in a synchrotron, three mode frequencies are different from those results as we show later.

The ultimate confirmation of the model should be done by beam experiments. Although there are some experiments which detect coherent quadrupole mode, its connection with emittance growth and beam loss is still not clear.

In this paper, we first discuss envelope equations of a 2D and 3D beam. In order to estimate 3D potential due to a beam, elliptical integral is numerically estimated. Then, we quickly introduce a beam experiment at HIMAC. Finally, we will show some simulation results to support the model.

2 COHERENT MODES

As shown by Sacherer [8], 2D envelope equations for any particle distribution can be written in a self-consistent way if one takes rms beam size and emittance evolution is known.

$$\frac{d^2\tilde{x}}{d\phi^2} + \left(\nu_{0x}^2 - \frac{N_2 r_0 R^2}{\beta^2 \gamma^3} \frac{1}{\tilde{x}(\tilde{x}+\tilde{y})}\right)\tilde{x} = \frac{(R\varepsilon_x)^2}{\tilde{x}^3} \quad (1)$$

where N_2 is the line density of particles, r_0 the classical proton radius, R the average radius of a machine, β and γ Lorentz factors. Similar equation for y. When the bare tune of two planes are split, two equations are practically independent and two mode frequencies are mostly determined by two bare tunes and tune shift of each plane, respectively.

On the other hand, when the two bare tunes are nearly equal, the two modes are coupled. One calls the higher mode as breathing mode and the lower one as quadrupole mode because the former mode oscillates in phase and the latter does out of phase in two planes.

The envelope equations are easily extended to include longitudinal mode. In fact, Sacherer showed that once one takes rms beam size, the envelope equations for a bunched beam also hold almost independently of the detailed particle distribution just like a 2D beam [8]. However, analytically treatment becomes difficult since the force term remains as elliptical integral. The 3D envelope equations are

$$\frac{d^2\tilde{x}}{d\phi^2} + \left(\nu_{0x}^2 - \frac{N_3 r_0 R^2}{\beta^2 \gamma^3}\lambda_3 g(\tilde{x},\tilde{y},\gamma\tilde{z})\right)\tilde{x} = \frac{(R\varepsilon_x)^2}{\tilde{x}^3} \quad (2)$$

---
[1] E-mail address: shinji.machida@kek.jp

where N_j is the total number of particles, λ_j a factor defined by Sacherer indicating small difference among distributions, and g elliptical integral as shown below. Similar equations for y and z.

$$g(a,b,c) = \frac{3}{2} \int_0^\infty \frac{ds}{(a^2+s)^{3/2}(b^2+s)^{1/2}(c^2+s)^{1/2}} \quad (3)$$

We numerically integrate elliptical integral and derive three mode frequencies and eigen vectors [9]. As a result, we can show that in a long bunch such as the one in a synchrotron, the two transverse modes of a bunched beam are almost identical to the ones of a 2D beam. That approximation holds unless the longitudinal bare tune becomes similar to the transverse one, which never occurs in synchrotrons. Third mode presents longitudinal oscillations.

3 EXPERIMENT AT HIMAC

Now we know that the difference of transverse mode frequencies between a 2D and 3D beam are negligible in a synchrotron. In order to verify the Sacherer's model and study mechanism of emittance growth and beam loss, or halo formation due to core oscillations, we started a beam experiment in HIMAC.

HIMAC is a heavy ion synchrotron and we use He^{2+} beams because the tune shift becomes largest. Main machine parameters are shown in Table 1.

Table 1: Main machine parameters of HIMAC.

item	number	units
Energy	6	MeV/u
Intensity	$1\ 10^{11}$	ppp
Particle	He^{2+}	
Emittance	264(H)/10(V)	π mm-mrad

A pickup with four electrodes was designed and installed. It was expected to detect coherent signal of a quadrupole mode. An RF quadrupole kicker is also used to excite a quadrupole mode in a beam.

Up to now, we have observed coherent signals. The quadrupole coherent tune shift is $-0.082/10^{11}$ppp while the expected value is $-0.059/10^{11}$ppp. A part of the discrepancy can be attributed to uncertainty of emittance. The relation between beam loss and resonance of coherent mode is not clear yet. More detailed descriptions on the experiment are found in another paper [9].

4 SIMULATION RESULTS

A multi-particle tracking is the other way to verify the mode frequency with space charge force and also to see its relation to beam emittance and loss. In a conventional way of single particle tracking, space charge force is included as a momentum kick at every time step [10]. The time step is chosen as small enough such that space charge force is evaluated smoothly according to a beam

envelope. That is necessary in order to estimate a frequency of asymmetric mode such as quadrupole one. As a model lattice, HIMAC is adopted, where about 380 space charge kicks are applied per turn while the beam envelope oscillates 12 times (essentially 12 FODO cells in a whole ring.)

First, we look at oscillation frequencies of second moments in a 2D beam without space charge. The vertical bare tune is lowered as a function of time by decreasing strength of defocusing quadrupoles. The initial bare tune is (3.65, 3.60) and the vertical one is varied at the rate of -0.10 per 2000 turns. Figure 1 shows four modes of coherent motion of second moments, which correspond to $2\nu_x$, $2\nu_y$, $\nu_x+\nu_y$, and $\nu_x-\nu_y$.
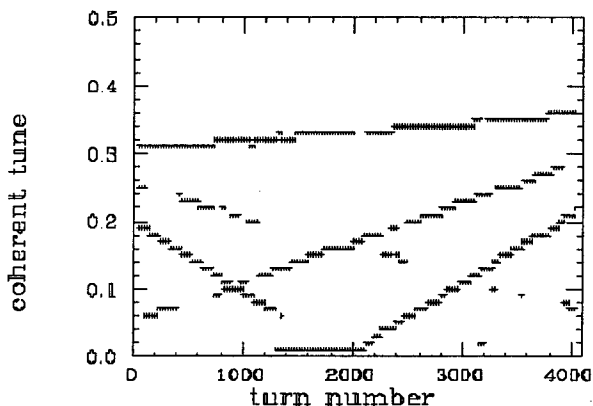
Figure 1: Tune of coherent modes of second moments. Space charge force is not included.

The line starting from 0.3 corresponds to $2\nu_x(=2\ 3.65-7)$, which is slightly increasing because of defocusing quadrupole change. The one starting from 0.2 and going down as the turn number increases is $2\nu_y(=2\ 3.60-7)$, which crosses zero and going down although the figure shows its reflection. The other two lines starting from 0.25 and 0.05 show $\nu_x+\nu_y$, and $\nu_x-\nu_y$, respectively.

There are some quadrupole errors included in the model lattice. The half-integer resonance with a width of 0.005 is excited at $\nu_y=3.5$. Figure 2 shows rms emittance under the same condition of time-varying quadrupole as Fig. 1.

Initial values of horizontal and vertical rms emittance (normalized) are $7.3\ 10^{-6}$ and $2.8\ 10^{-7}$, respectively. When the vertical bare tune crosses a half-integer resonance at 3.5 (and also coherent tune becomes integer of 7), vertical rms emittance suddenly grows. The decrease of emittance right after the crossing is due to beam loss (once a particle satisfies loss criterion, that particle is no longer counted to calculate emittance.)
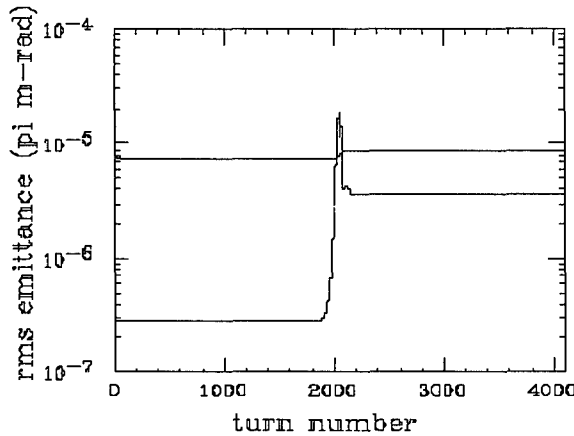
Figure 2: Horizontal and vertical rms emittance when the bare tune is varied in the same way of Fig. 1.

Figure 4: Horizontal and vertical rms emittance when the vertical bare tune is lowered.

Now, we include space charge effects. We first examine KV distribution in which space charge force is linear. The beam intensity was chosen to be 1×10^{11}ppp, which makes the vertical incoherent tune shift of -0.06 (much smaller shift in horizontal because of its larger emittance.)
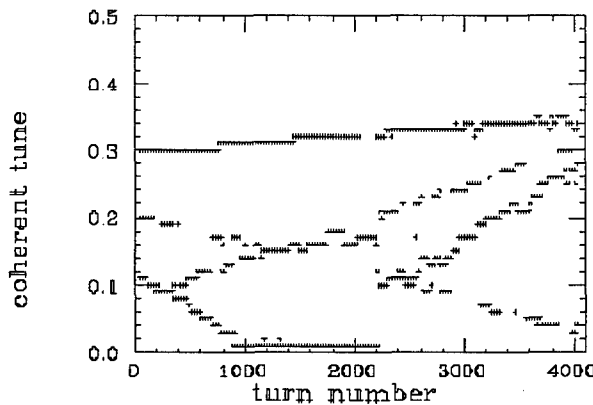
Figure 3: Tune of coherent modes with space charge force.

Figure 3 shows same four modes of Fig. 1. Because of space charge defocusing force, the coherent tune which is determined by vertical motion is lowered. The lowered coherent tune is no longer twice of loaded incoherent tune as the envelope equations states. At the turn number of around 1200, the coherent mode of $2\nu_y$ becomes zero. If one looks at rms emittance, one can notice that the rms emittance starts increasing right after coherent tune crosses integer (in this case 7.) The growth continues up to the turn number of 2000, where the bare tune hits the resonance.

That behavior is weakly dependent of particle distribution. The waterbag and gaussian distributions give almost same results.

Finally, let me mention the simulation results of a 3D beam. Since long term (~1,000 turns) tracking with space charge is very time consuming, we have not confirmed the emittance growth and beam loss due to a resonance crossing of a coherent mode yet. However, a mode frequency is identified. Under the condition of the same incoherent tune as Fig. 3 (without tune ramping), the coherent tune of $2\nu_y$ becomes 0.12. That is in good agreement with our previous findings, namely 2D and 3D mode frequencies are similar.

5 REFERENCES

[1] See, for example, T. P. Wangler, *et. al.,* "Particle-core model for transverse dynamics of beam halo", Phys. Rev. ST-AB, 1, 1998.

[2] S. Machida, "Coherent mode analysis of high intensity beams in synchrotrons", Proc. of 1998.

[3] J. A. Holmes, *et. al.,* "A particle core model for space charge dynamics in rings", *ibid.*

[4] F. J. Sacherer, "Transverse space-charge effects in circular accelerators", Ph.D, Thesis, UCRL-18454, October, 1968.

[5] S. Y. Lee and H. Okamoto, "Space-charge dominated beams in synchrotrons", Phys. Rev. Lett. 80, 1998.

[6] J. J. Barnard, *et. al.,* "Theory of longitudinal beam halo in RF linacs: I. Core/test-particle formation", Proc. of 1997 PAC.

[7] M. Pabst, *et. al.,* "Progress on intense proton beam dynamics and halo formation", Proc. of 1998 EPAC.

[8] F. J. Sacherer, "RMS envelope equations with space charge", IEEE trans. Nucl. Phys., 1991.

[9] T. Uesugi, *et. al., in this proceedings.*

[10] S. Machida, "Simulation of space charge effects in a synchrotron", AIP Conf. Proc. 448, 1998.

RECENT ADVANCES IN POLARIZED ELECTRON SOURCES*

Charles K. Sinclair[+], Jefferson Laboratory, Newport News, VA

Abstract

Current experimental physics programs at a number of electron accelerator laboratories worldwide require the delivery of high average current highly polarized electron beams for long periods of time. The polarized electrons are produced by near bandgap photoemission from certain semiconductor photocathodes. We observe the quantum efficiency of these cathodes to be inversely related to the total charge they have delivered. Recent developments in ultrahigh vacuum technology, electron trajectory control, photocathode preparation, and lasers have led to operationally reliable delivery of many hundreds of coulombs of polarized electrons, at rates as high as 8 coulombs/day. Currently, our photocathode operational lifetime is almost completely dominated by ion backbombardment. Further gains in the high average current lifetime of these cathodes may be expected, which will allow photoemission electron guns to be used for accelerator applications other than polarized sources.

1 INTRODUCTION

During most of the past decade, polarized electron source development efforts have concentrated on developing cathodes to provide electron beam polarization above the ~40% available from GaAs; on reducing the "charge limit" effect; and on establishing ultrahigh vacuum conditions in the polarized electron guns sufficient to provide reasonable photocathode operational lifetimes. The charge limit effect is a current dependent reduction in the effective cathode quantum efficiency, caused by space charge accumulation at the surface of the semiconductor cathode. This effect is important in injectors for low duty factor accelerators. Most of the ultrahigh vacuum work centered on the development of various load-lock schemes, which allowed photocathodes to be activated outside the high voltage section of the gun, and installed in the electron gun without the need for a vacuum bakeout. These developments have led to a number of polarized electron injectors which deliver beam polarizations of about 80% from cathodes with initial quantum efficiencies in the 0.1 to 0.3% range at the instantaneous currents used. Cathode "dark" lifetimes of 1000 hours or greater are routinely obtained in most laboratories, while at average beam currents of about 20 μA, the cathode lifetimes are typically an order of magnitude shorter. To date, all cathodes which deliver very high electron polarization have the unfortunate side effect of showing significant polarization correlated beam intensity and position changes, complicating their use in physics experiments

With the advent of CW electron accelerators, the demand for much higher average beam currents and much higher total charge delivery per experiment arose. In addition, the need to do experiments with the highest practical beam polarization requires that the polarization correlated systematic effects be either eliminated or carefully controlled. The means to control these effects are under active study at the present time, and will not be discussed further here. The polarized source technologies in place as of early 1997 were unable to meet the high average current and high total charge requirements while providing acceptable photocathode operational lifetimes. Over the past two years, several developments have taken place which now allow the delivery of hundreds of coulombs of highly polarized electrons, at rates up to 8 coulombs/day.

The term "operational lifetime" is used to describe the length of time that the cathode can be used to deliver beam meeting established requirements, rather than a cathode quantum efficiency decay constant. This operational lifetime is the convolution of many system parameters and physical effects, such as the initial quantum efficiency and the available laser power; the total pressure and residual gas composition of the static vacuum in the gun; vacuum degradation during operation with beam; electron losses between the photocathode and the experimental target; the useful photocathode area, etc.

2 VACUUM ISSUES

There are two classes of vacuum issues associated with photoemission electron gun operation. The first of these is degradation of the cathode quantum efficiency by chemical poisoning of its surface. The photocathode is prepared, or "activated", by exposure of the clean semiconductor surface to monolayer quantities of cesium and an oxidant. The dark lifetime of the finished cathode is strongly affected by exposure to tiny quantities of chemically active gases, such as water, oxygen, and carbon dioxide. It is generally suspected that additional oxidation of the cathode is involved in this degradation, but convincing evidence is difficult to establish rigorously, as the quantities of gases involved are exceptionally small [1]. Experience at many laboratories has shown that it is possible to prepare good quantum efficiency cathodes in a polarized gun with dark lifetimes of one thousand to several thousand hours. This indicates that to the extent that chemical poisoning of the cathode is responsible for reduced cathode operating life, it is caused by gases released by electron-stimulated desorption.

The electrons responsible for this desorption may arise either from field emission from the gun electrode structures, or electron beam losses in areas which can communicate, vacuum-wise, with the cathode. Generally speaking, it is practical to eliminate field emission as a source of cathode lifetime degradation [2]. Note that chemical poisoning should degrade the cathode quantum efficiency uniformly over its entire area.

The second vacuum related issue is ion backbombardment of the cathode. Depending on the ion mass and energy, the damage to the cathode may range from generation of defects in the cathode semiconductor to sputtering of the oxidized cesium surface layer. While ion damage may depend somewhat on the ion mass, it does not depend on the chemical nature of the ion. Thus the total system pressure, rather than the residual gas composition, is the more relevant parameter in quantifying this damage mechanism.

In many polarized electron guns, the photocathode is not uniformly illuminated. In these cases, ion backbombardment would be expected to affect only the area of the cathode between the illuminated spot on the cathode and the electrostatic center of the cathode. In the case of a fully illuminated cathode, ion backbombardment would preferentially damage the region around the electrostatic center of the cathode. Thus, by comparing maps of the cathode quantum efficiency before and after operation with beam, one should be able to discriminate between chemical poisoning and ion backbombardment problems. It is worth noting that to the extent that the cathode lifetime is limited by ion backbombardment, it is far more meaningful to express the lifetime in terms of the delivered charge per unit illuminated area of the cathode, rather than clock hours or calendar days.

Evidence of cathode degradation at the illuminated site was first reported by groups at Mainz and Bates [3], and the Mainz group first reported the ion backbombardment interpretation of this [4]. An example of a quantum efficiency map showing clear evidence of ion backbombardment damage is shown in figure 1, taken from the 100 kV Jefferson Lab polarized gun.
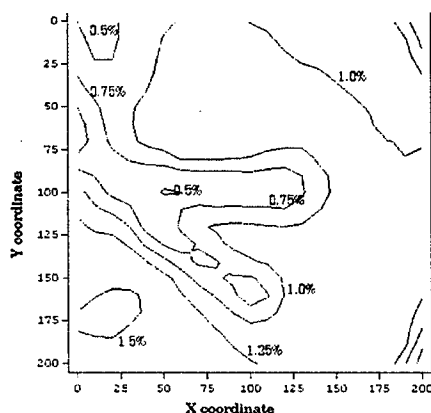
Figure 1. A quantum efficiency map of a cathode damaged by ion backbombardment

Here, a small diameter (~250 μm) laser beam illuminated the cathode in the two indicated locations. The damage region between the illuminated spots and the electrostatic center of the cathode is clear. Some fraction of this damage can be repaired by heat cleaning and re-activating the cathode. Ion backbombardment damage is an important effect in polarized electron guns operating at MAMI and Bates, and is the dominant cathode damage mechanism at Jefferson Lab. In the present Jefferson Lab polarized gun, a 1/e reduction of the quantum efficiency in the ion damaged area corresponds to the delivery of ~10000 coulombs/cm^2.

There is some evidence that cathodes which produce the highest beam polarization also have better operational lifetimes than ordinary GaAs cathodes. The reason for this may be that all high polarization cathodes developed to date are very thin — typically about 100 nm. Ions of the highest energy, which might be expected to do the greatest damage to the cathode, pass through this thin layer and deposit the majority of their energy in the underlying substrate. For example, hydrogen ions with energies above ~15 keV will pass through a 100 nm layer of GaAs. It also appears true that the quantum efficiency loss caused by backbombardment with lower energy ions may be recovered more readily by heat cleaning and reactivation.

The only beam produced ions which have much likelihood of being accelerated back to the cathode must originate in the cathode-anode gap. Most polarized guns constructed to date have not had particularly good pumping speed in the cathode-anode gap region. At Jefferson Lab, we have constructed a gun in which the cathode has been extended into a chamber containing a massive array of NEG pumps [5]. When fully activated, these pumps provide a pumping speed in the cathode chamber of over 4000 l/sec for H$_2$ and ~1700 l/sec for CO. In its first test, this gun reached a base pressure, measured by an extractor gauge located in the chamber downstream of the anode aperture, of ~ 2 x 10^{-12} torr. The sensitivity limit of this gauge is claimed by the manufacturer to be ~ 1 x 10^{-12} torr. RGA scans indicate that the pressure in the gun is higher when the gauge filament is powered. Thus we believe that we have achieved a very excellent static vacuum in this gun. This gun has been in service for 14 months, and has consistently provided the excellent cathode charge delivery reported above. This gun is shown in figure 2.

Gases may reach the cathode-anode gap region from higher pressure regions downstream of the gun. In the Jefferson Lab injector the pressure in these downstream areas gradually increases to about 10^{-9} torr several meters from the cathode. These regions are isolated by sputter ion pumps and a NEG based differential pump module. In an effort to further decrease the pressure in the cathode-anode gap, we have sputter coated the inner wall of the
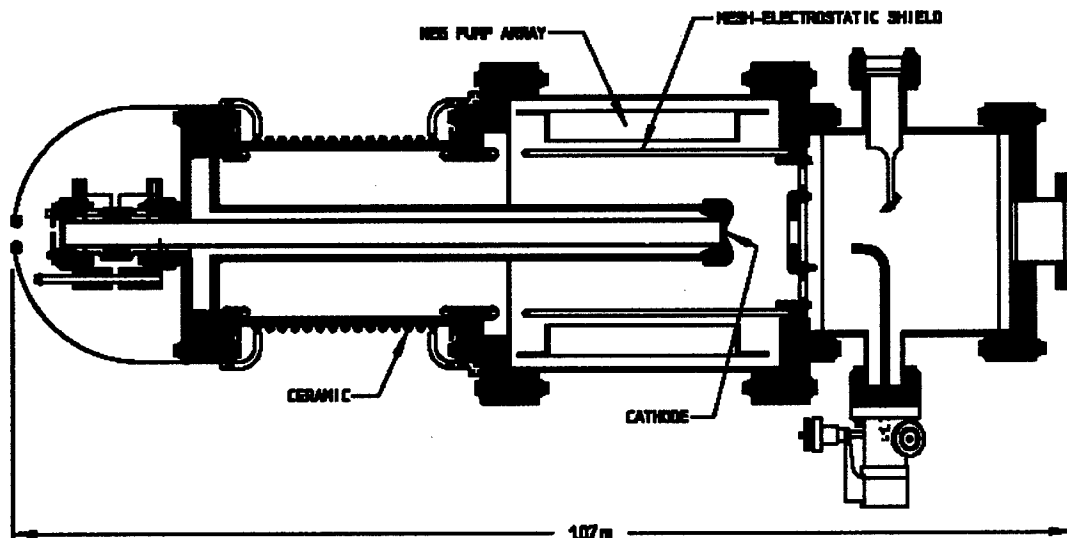
Figure 2. Schematic view of the Jefferson Lab polarized gun.

vacuum tube downstream of the gun with a Ti/Zr getter, following the method of Benvenuti et al. [6]. This coated beam tube provides three distinct vacuum advantages. It provides a high pumping speed for chemically active gases; it is a diffusion barrier to gases diffusing from or permeating through the beam tube wall; and it is expected to have dramatically lower electron stimulated desorption [7]. We have found Benvenuti's method straightforward to reproduce, and a gun incorporating a coated beam tube is presently in test.

3 ELECTRON TRAJECTORY CONTROL

During early use of the Jefferson Lab polarized source, good operational lifetimes were obtained with average currents in the range of 10-20 µA. At currents of 100-150 µA, lifetimes were substantially shorter. At these higher currents, we observed a significant rise in the vacuum pressure in the beamline following the polarized gun, and sensitive Geiger tubes placed along this beamline showed an elevated counting rate with beam on. These are clear indications of electron beam striking the beamline vacuum chambers. This was initially difficult for us to understand, since the 12.8 mm diameter cathode was illuminated by a 0.2 mm diameter laser spot placed close to the cathode center. The beam spot observed on all downstream viewscreens was very small, as anticipated, and modelling results indicated that the beam originating from the directly illuminated area of the cathode should be far from all vacuum system walls. We concluded that a small number of beam electrons must be originating from large radius areas of the cathode. These large radius electrons follow extreme trajectories, ultimately striking the beam tube walls. The extreme trajectories were the result of small transverse fields at the edge of the cathode; short focal lengths of some beamline elements; and field aberrations in the solenoids.

Modelling with PARMELA, using the actual fields of these elements, demonstrated that these extreme trajectories struck the vacuum walls [8].

Initially, we thought that the electrons originating at large radius were due to reflections from the window admitting laser light into the gun. Replacement of this window with an AR coated version produced no change in the beam loss, where a factor of eight reduction would have been expected were these reflections the source of the problem. We presently believe that the large radius electrons originate from photoemission caused by recombination light in the semiconductor cathode itself. This recombination light, which is close to the bandgap energy of the semiconductor, is weakly absorbed and thus can reach the large radius areas of the cathode wafer.

To reduce the number of electrons originating at large radius on the cathode, we prepared cathodes with the quantum efficiency deadened at large radius. Initially we reduced the quantum efficiency by masking the large radius area during atomic hydrogen cleaning. More recently, we have grown a thick anodic oxide on the large radius region of the cathode. The anodized region has zero quantum efficiency at the illumination wavelength. The previously observed pressure rise and Geiger tube counting rate were dramatically reduced in the first test with a cathode deadened at large radius. Unfortunately, this improvement was introduced at the same time as the massive NEG pump array, and we do not know the relative contributions of these two changes to the cathode lifetime improvement.

In the gun system now in test, noted above, we have changed to a horizontal gun mounting, eliminating a 90 degree bend magnet which had both short focal lengths and a relatively small gap. We have increased the bore of the downstream vacuum tube as well as coating it with NEG material. The solenoid closest to the gun now has an increased bore, reducing its aberrations. Finally, we

67

have altered the shape of the cathode electrode, and increased the anode aperture, reducing the small transverse fields in the cathode area. We anticipate that each of these changes will further improve the operational lifetime of the cathode.

4 REDUCTION OF ELECTRON LOSSES BETWEEN PHOTOCATHODE AND EXPERIMENTAL TARGET

It is clear that even with the improvements obtained by providing exceptional vacuum conditions, it is desirable to produce only electrons which can be transported to the ultimate user. For accelerators requiring single or widely spaced bunches, and where high accelerator energy and/or damping rings provide adequate beam quality, subharmonic bunching provides an effective solution, as at the SLC. For CW or high duty factor accelerators, this technique is not applicable. Furthermore, in these latter machines, it is normal to limit the emittance growth associated with bunching by RF chopping the beam before the buncher. Typically, 65% to 85% of the beam leaving the cathode is lost in such chopping systems.

To avoid the chopping losses, it is necessary to produce the electrons already bunched at the cathode, and/or to extend the fraction of the RF cycle over which the buncher can compress the beam without degrading the beam quality. Both schemes are now employed at CW machines.

At MAMI, two buncher cavities are used, the first operating at the fundamental frequency and the second at the second harmonic. With the two cavities separated by the correct distance, the bunching field is effectively linearized over about 50% of the RF cycle. Using this technique, the MAMI injector increased the acceptance of their chopper-buncher system from ~15% to ~50% [9].

At Jefferson Lab, we have developed an RF gain-switched diode laser oscillator-amplifier system [10]. Variations of this laser have been demonstrated to operate reliably between 125 MHz and 3 GHz. At Jefferson Lab, three such lasers, each operating on the third subharmonic of the 1497 MHz fundamental accelerator frequency, produce three interleaved bunch trains, which are delivered to three independent experimental halls with the aid of third subharmonic RF separators. Longitudinally polarized electron beams have been delivered to all three experimental halls simultaneously with this scheme. MAMI has adopted this laser system as well, and in conjunction with its two frequency bunching system, now delivers ~95% of a 20 μA CW beam from its photocathode to the experimental target. At Jefferson Lab, where the polarized beam current to a single experimental hall has been as high as 110 μA CW, a pre-buncher is used ahead of the chopper system to optimize the transmission. 75% transmission from cathode to target has been achieved to date at this high current, with higher transmission obtained at lower current. Future

experiments planned at Jefferson Lab will require six times the present peak microbunch current. Additional effort will be necessary to accomplish this.

It is worth noting that with RF structure present at the cathode, standard BPMs can be used in the low energy region of the injector. Such BPMs have been implemented at Jefferson Lab, and are very useful for beam setup.

5 IMPROVING CATHODE PREPARATION

All else being equal, a high initial quantum efficiency will deliver the longest cathode operational lifetime. For the highest quantum efficiency, the semiconductor surface should be clean on an atomic scale prior to the activation with cesium and oxidation. Some surface contaminants, such as carbon and some oxides, are difficult or impossible to remove by conventional heat cleaning. All cathodes developed to date to provide high beam polarization are too thin (~100 nm) to tolerate wet chemical cleaning. We have developed a cathode cleaning technique based on exposure of the cathode surface to atomic hydrogen, which is well known to produce atomically clean surfaces on many semiconductors. The atomic hydrogen is produced in a small RF discharge chamber [11]. The dangling bonds at the surface of atomically clean GaAs are saturated by atomic hydrogen exposure, so the surface is effectively passivated and can be transferred through air into an electron gun structure [12]. Whether this is true for other semiconductors remains to be demonstrated. Using atomic hydrogen cleaning, we have consistently produced high quantum yield photocathodes on both strained and unstrained GaAs surfaces.

The excellent results we have had using atomic hydrogen cleaning have led us to examine the importance of the cathode dopant density on the maximum quantum efficiency. It has been shown that a high dopant density, at least near the cathode surface, is important to reduce the charge limit effect [13]. However, since a high dopant density is responsible for electron depolarization in the cathode in several theoretical models, it may be possible to improve the polarization by lowering the dopant density in applications where the charge limit is not important. To determine the importance of the dopant density, we procured a set of six different epitaxial GaAs wafers of varying thickness and dopant density. The GaAs layers were grown on a thick layer of GaAlAs, with the aluminum fraction chosen so that for wavelengths longer than about 670 nm, all photoemission was from the thin GaAs layer only.

The quantum efficiency of one of these thin GaAs samples is shown in figure 3. This sample was 0.27 μm thick, and was p-doped at 5.8×10^{17} cm^{-2}.
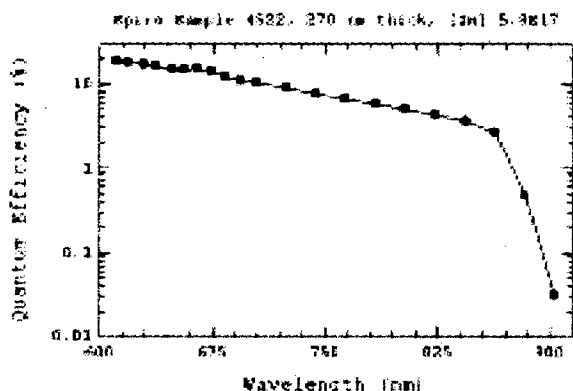
Figure 3. Quantum efficiency versus wavelength for a thin, lightly doped GaAs sample.

A two parameter fit to the 700 to 850 nm wavelength region, using the known absorption coefficient and its variation with photon energy, yields an electron surface escape probability of 0.26 [14]. This escape probability is considerably higher than both modelled and measured values for the surface escape probability reported in the literature [15]. We do not know if this excellent esape probability is a result only of the atomic hydrogen cleaning process. However, we have obtained escape probabilities comparably higher than those reported in refs. 15 from three other thin, lightly doped samples. Further measurements on these samples are planned to determine the effect of dopant density on polarization.

6 SUMMARY

Prior to 1998, polarized electron injectors were delivering several tens of coulombs to experimental programs during an entire calendar year. The future experimental program planned at Jefferson Laboratory requires the delivery of many hundreds of coulombs annually from high polarization cathodes. Both the Bates Lab and Jefferson Lab demonstrated during 1998 the delivery of several hundred coulombs to their experimental programs during two to three month periods from bulk and thin GaAs photocathodes. At Jefferson Lab, excellent operational lifetime at high average current from high polarization cathodes has recently been demonstrated. These accomplishments have been made without the use of complex load-locked electron guns, although well designed load-locked guns offer clear operational versatility which is difficult to achieve otherwise.

Ion backbombardment of the cathode is presently the dominant limiting factor in the operational lifetime of photoemission cathodes for polarized electron delivery. State-of-the-art ultrahigh vacuum technology and the elimination of electron stimulated desorption by careful control of extreme electron trajectories in the polarized gun and its associated beamline can reliably provide very long cathode operational lifetimes. Methods to maximize the fraction of the photoemitted electrons which reach the experimental target, such as RF gain-switched lasers and

improved bunching schemes, are also very useful. At Jefferson Lab, 1/e quantum efficiency degradation due to ion backbombardment from the delivery of ~10000 coulombs/cm^2 has been demonstrated. With additional improvements in the operating vacuum in the cathode-anode gap of the electron gun, considerably greater charge delivery appears possible.

7 ACKNOWLEDGMENTS

8 REFERENCES

[1] H. Fischer et al.,Proceedings of the Workshop on Photocathodes for Polarized Electron Sources for Accelerators, SLAC Report 432 Rev, SLAC, Stanford, CA, 1994, p. 249

[2] At Jefferson Lab, we have obtained very good high voltage performance from electrodes made of Ti-6Al-4V alloy.

[3] C. K. Sinclair, in High Energy Spin Physics, AIP Conference Proceedings No 187, AIP, New York, p. 1412.

[4] K. Aulenbacher et al., Proceedings of the Workshop on Photocathodes for Polarized Electron Sources for Accelerators, SLAC Report 432 Rev. SLAC, Stanford, CA 1994, p.1.

[5] NEG pumps are commercially supplied by SAES Getters.

[6] C. Benvenuti et al., J. Vac. Sci. Technol. A16, 148 (1998).

[7] J. J. Welch and C. K. Sinclair, Proceedings of the 1986 Linear Accelerator Conference, SLAC Report 303, SLAC, Stanford, CA, p.87.

[8] B. Dunham, private communication.

[9] V. T. Shvedunov et al., EPAC96, p. 1556.

[10] M. Poelker, Appl. Phys. Lett. 67, 2762 (1995).

[11] M. Poelker et al., Nucl. Instr. Meth. A364, 58 (1995).

[12] Y. Okada and J. S. Harris, J. Vac. Sci. Technol. B14, 1725 (1996).

[13] K. Togawa et al., Nucl. Instr. Meth. A414, 431 (1998).

[14] J. S. Blakemore, J. Appl. Phys. 53, R123 (1982).

[15] D. G. Fischer et al., J. Appl. Phys. 43, 3815 (1972); G. Vegara et al., J. Vac. Sci. Technol. A8, 3676 (1990).

SELF-BUNCHING ELECTRON GUNS*

L. K. Len and Frederick M. Mako#

FM Technologies, Inc., 10529-B Braddock Road, Fairfax, VA 22032

Abstract

This paper presents several new approaches for producing bunched electron beams. The need for higher power injectors and microwave sources for various applications has in turn created the need for higher emission current density electron guns with a means for bunching at the gun. Four different cathode/gun approaches are presented. The first three utilize external methods of bunching. They are based on: field emission, photoemission and ferroelectric emission. The fourth is based on secondary emission and utilizes self-bunching. The latter is emphasized in this presentation. This self-bunching electron gun produces naturally bunched electron beams with the use of microwave fields to generate secondary emission and multipacting of electrons. This type of electron gun is called the Micro-Pulse Gun+ (MPG). One wall of an RF cavity is made opaque to an input RF electric field but is partially transparent to electrons in order to extract the beam. FMT has studied using simulation codes the resonant bunching process which gives rise to high current densities ($0.01–5$ kA/cm^2), high charge bunches (up to 500 nC/bunch), and short pulses (1–100 ps) for frequencies from 1 to 12 GHz. The beam pulse width is nominally ~5% of the RF period. Experimental verification of self-bunching, cold electron emission, long life, and tolerance to contamination has been achieved. Measurements of current density, bunch length and lifetime are presented for the MPG.

1 INTRODUCTION

The creation of high-current, short-duration pulses of electrons has been a challenging problem for many years. High-current pulses are widely used in injector systems for electron accelerators, both for industrial linacs as well as high-energy accelerators for linear colliders. Short-duration pulses are also used for microwave generation, in klystrons and related devices, for research on advanced methods of particle acceleration, and for injectors used for free-electron laser (FEL) drivers [1,2]. Future linear colliders based on two-beam accelerator schemes [3,4] may require individual RF sources capable of 50–75 MW of RF power with a corresponding pulse width of 0.15–0.3 µs at a frequency of up to 30 GHz and at repetition rates of 60–180 Hz. Because the cost of the RF sources will be a large fraction of the cost of the accelerator, there is a

need for high-power microwave sources capable of reliable multi-megawatt performance at high efficiency.

Recent cathode advances have been driven by the need for ultra-high-power devices. These devices require higher emission current densities than thermionic cathodes provide and could benefit from direct modulation of the electron beam at the gun. Direct modulation of the emitted beam can improve the gain and efficiency and reduce the size of microwave amplifiers [5]. In addition direct modulation of the beam to produce a train of short pulses is of interest for use as a buncher for injection into RF linacs. Current density and direct modulation are addressed in the following sections by four different cathode/gun schemes.

2 FIELD EMISSION

In this section we present recent developments in field emission and direct modulation of electron beams using field-emission arrays (FEAs). Field-emission cathodes have been fabricated using a variety of materials and methods. Single tips with a radius of curvature about 60 nm to 90 nm have been used to generate current densities of more than 10^8 A/cm^2 [6,7]. Arrays of tips have generated current densities of 2.5–40 A/cm^2 (DC) to 2,000–2,400 A/cm^2 (pulsed) [8-10], which exceed current densities available from thermionic cathodes. Emission from gated FEAs can be initiated by the application of gate voltages of less than 100 Volts. Among the advantages envisioned for FEAs are the ability to address and control the emission spatially and to directly modulate emission current. Beam emittance from single tips is estimated to be much smaller than any other type of cathode. Normalized beam brightness from single tips with total currents of 10 µA is estimated to be on the order of 10^{15} $A/(m^2$-steradian) [11,12], or about two to three orders of magnitude better than thermionic cathodes. The emittance from arrays of tips is, however, poor without integrated lenses on each tip [13-16].

NEC Corporation demonstrated two miniaturized TWTs using: lateral resistor-stabilized Spindt-type FEAs [17] and arc-resistant Spindt-type FEAs [18,19]. The arc-resistant FEA type TWT achieved 5,000 hours of operation and was terminated by a cause other than arc failure. The electron beam in the TWT is modulated in the conventional manner (not gate modulated). Gate modulation is complicated by the large input capacitance caused by the small distance between the gate and the substrate. A large transconductance, defined as the ratio of the change in emitted current to the change in gate voltage, will help alleviate this problem. Several groups have demonstrated

---

emission modulation on top of a DC beam current at frequencies of up to 10 GHz [8-10, 20-26]. This device offers a compact and potentially highly efficient microwave source.

3 PHOTOEMISSION

During recent years, considerable effort has been applied to the development of laser-initiated photocathode injectors [27-34]. The best photocathodes have achieved ten's of nanocoulombs per microbunch with a train limited by the available laser systems to contain less than one hundred bunches [34]. Photoemitters have been used mainly until recently as sources of prebunched electron beams in RF linacs. In a typical photoinjector, the photocathode forms an integral part of the first RF cavity before the main linac structure. The photoelectrons from the cathode are quickly accelerated in field gradients of 50–100 MV/m so that the electrons reach relativistic velocities within a centimeter from the cathode surface. Thus, debunching effects due to space charge are minimized. Current interest for photocathode injectors is in high power RF generation. Potential applications include devices such as two-beam accelerators [3,4] which have been proposed to generate tens of megawatts at frequencies of 11.4–34.2 GHz. RF power generation relies on the laser to generate a bunch train to form the electron beam. With photocathodes, the charge, bunch length, spatial and temporal distribution of the electrons could be controlled by varying the laser energy, its pulse duration and its spatial and temporal profile. The CLIC facility [34] at CERN combines both injector and RF source aspects of bunched electron emission in its two-beam accelerator. In this device the drive beam consists of 24 bunches of electrons each with ~3 nC charge, ~1.5 mm bunch length and bunch repetition rate of 3 GHz. The prebunched, pre-accelerated beam was decelerated in a slow wave structure to produce 60 MW of RF power at 30 GHz in a ~15 ns pulse.

4 FERROELECTRIC EMISSION

Ferroelectric emission falls broadly into two categories. The first involves a phase transition from ferroelectric to antiferroelectric state [35,36]. The second involves rapid changes in the ferroelectric state [37-42] but does not involve a phase transition. The former can be described by considering the free charge that exists on the surface of a pre-poled ferroelectric cathode. This free charge screens the extremely large electrostatic field from the surrounding electron gun vacuum due to the material polarization. When a rapidly changing electric field is applied across the ferroelectric material, it modifies the amount of surface charge required to produce the electrostatic screening. The resulting surplus charge is ejected into the gun and is available for the production of pulsed electron

beams. In the second mode of emission, depending on the polarity of the trigger pulse used to initiate emission it is also possible to generate the electron beam from the metallic grid on the front surface of the ferroelectric. In this configuration the ceramic acts as a high dielectric constant ($\varepsilon_r \sim 1000$), which serves to enhance the field causing the emission at the triple points on the front surface of the ferroelectric ceramic. In this mode of use the emission is similar to that found in FEA arrays, where the application of the emission trigger pulse to the gate electrode in the FEA is replaced by pulsing of the rear surface of the ferroelectric emitter. Unlike the previous two emission schemes, relatively little work has been done to date on beam modulation, and work has focused on the understanding of the physics of the emission process. Experiments have been carried out by changing the material (e.g. PLZT) from an antiferroelectric to a ferroelectric state [35,36], and in other cases by cycling a ferroelectric material (e.g. PZT) around a minor hysteresis loop [37-42]. Beam currents up to 350 A and electron energies in the range of 200–550 keV with pulses in excess of 200 ns have been achieved [43]. The ferroelectric emission mechanism can easily generate electron beam currents which are suitable for ultra-high-power microwave sources.

5 SECONDARY EMISSION GUNS

The electron guns to be described below are based on a natural bunching process which eliminates the need for bunching section(s), timing system, and laser. In this method, short (~10 ps) high-current pulses are formed by the resonant amplification of an electron current utilizing multipacting from the walls of a microwave cavity. One narrow bunch is transmitted every RF period. This cavity-type bunching electron gun is called the Micro-Pulse Electron Gun or MPG [44]. The MPG is capable of generating high-current and short bunches with low emittance as required for many accelerators and microwave devices. Studies of the multipacting process [45-47] have concentrated on the theoretical aspects of the phenomenon and the RF driver interaction. Bunch stability and its effect on current saturation are treated in reference [48]. References [44] and [49-51] discuss the saturation process, peak currents, and frequency scaling characteristics.

Micropulses are produced by resonantly amplifying a current of secondary electrons in an RF cavity operating in, for example, a TM_{010} mode (see Fig. 1). Bunching occurs rapidly and is followed by saturation of the current density in ten to fifteen RF periods. Bunching occurs automatically by a natural phase selection of resonant particles. Localized secondary emission in the MPG is determined by material selection. The reason for the name "Micro-Pulse Gun" is the fact that the pulse width is only a few percent of the RF period, in contrast to usual RF guns where it is equal to half the RF period.
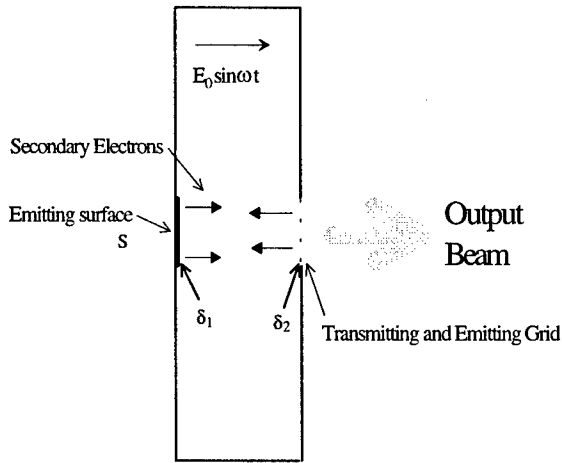
Figure 1: MPG concept for generation of bunched beams. Side view of MPG cavity showing emitting and transmitting grid surfaces. Figure is not to scale.

Radial space charge expansion in the MPG cavity is controlled by a combination of electric and magnetic focusing. The grid not only allows transmission of bunches but also provides an emitting surface for electron multiplication. Emittance growth from the grid in the MPG can be very small due to a unique feature of the MPG. Briefly, the resonant particles are loaded into the wave at low phase angles. They reach the opposite grid 180° later, and thus exit at low phase angles, thereby experiencing a reduced transverse kick from the grid wires. This minimizes the emittance growth from the grid in the MPG.

5.1 Experimental Demonstration of the MPG

Figure 2 shows the macropulse operation of an L-band MPG experiment. The L-band MPG cavity is designed for a TE_{101} mode and is powered by an L-band (~1.3 GHz) magnetron. The magnetron is operated at 300 Hz repetition rate. Each microwave pulse lasts for 5 μs (at the base) and contains about 6,313 electron bunches (1 for each RF period). The top trace is the RF power in the cavity and the bottom trace is the transmitted macropulse beam current from the MPG on a 1 μs/div. time scale. The RF power delivered to the beam is about 50 kW and the beam current is about 2 A or about 2 A/cm² in the macropulse. The current and current density are not limited to the above values but were the design values for this particular experiment. Note the clean current trace over the full RF pulse length.

When a fast (50 GHz) sampling oscilloscope is used and a 5 ns slice of the macropulse as indicated in Figure 2 is examined, the micropulses can be observed. Figure 3 shows a measurement of the bunches on a 500 ps/div. time scale. The bunches appear with the periodicity of the RF field (~792 ps), in excellent agreement with simulation [44,49,50]. The pulse amplitude appears to decrease

slightly in time because of the location of the 5 ns slice in the macropulse. More detailed measurements show that the actual bunch length is about 40 ps (FWHM) which is about 5% of the RF period. In Figure 3 the micropulse current density is about 22 A/cm² and is in good agreement with simulation. For this result there is about 1.1 nC or ~7 × 10⁹ electrons per RF period. Lifetime testing has been carried out for about 18 months at almost 24 hours per day with a repetition rate of 300 Hz and 5 μs macropulses. During that time, approximately 5.8 × 10¹³ microbunches or 62,000 coulombs (82,000 C/cm²) have passed through this gun and it is still working flawlessly.
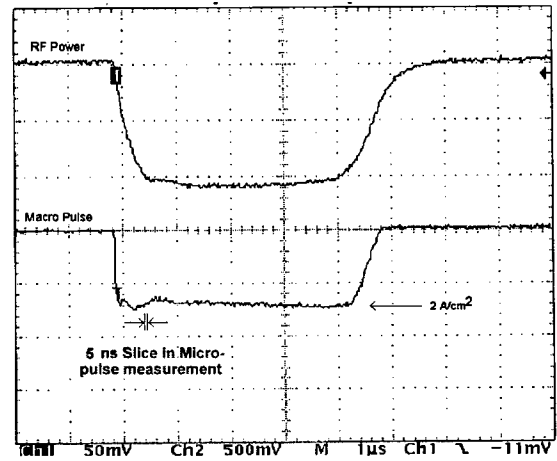
Figure 2: Oscilloscope traces of macropulse operation of the L-band experiment. Top trace: the RF power in the cavity. Bottom trace: the transmitted beam current.
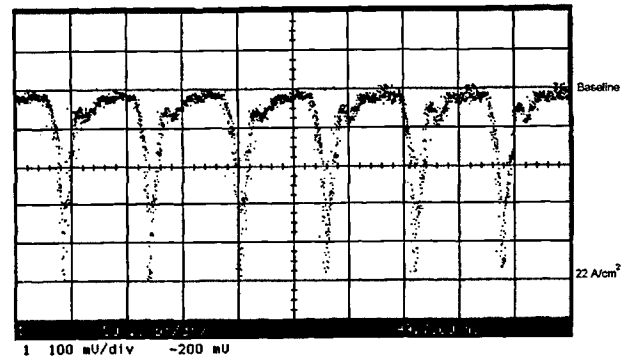
Figure 3: Experimental data showing the current trace of the MPG microbunches.

Figure 4 shows a MPG experiment at S-band (2.85 GHz). The micrometer that is vertical in Figure 4 is used to adjust the current. The diagonal micrometer is used to tune the TE_{101} cavity. The macropulse operation is shown in Figure 5 where the top trace is the RF power in the cavity and the bottom trace is the transmitted macropulse beam current, both on a 0.5 μs/div. time scale. The RF

72

power is about 400 kW and the macropulse current is about 18 A. The corresponding micropulse or bunch current is 360 A. The macropulse current density is about 10 A/cm² and the corresponding micropulse or bunch current density is 200 A/cm². The S-band MPG has been operating at a repetition rate of 50–300 Hz with a 2.25 µs macropulse and 6.3 nC per microbunch. There are 6,412 microbunches or 40.5 µC per macropulse. Note also the clean current trace over the full RF pulse length. The S-band work is presently being extended to give a 4.5 µs pulse at a frequency of 2.995 GHz.
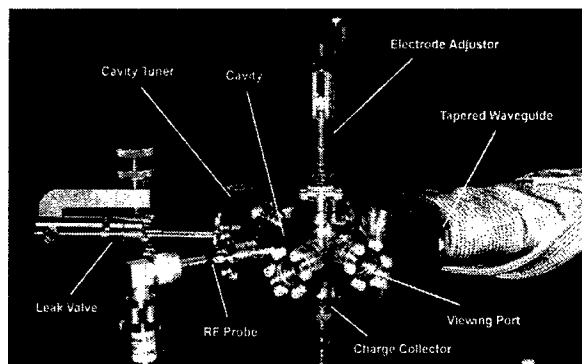
Figure 4: Close-up of the S-band experiment showing the tapered waveguide and the MPG. RF power is fed to the cavity via the tapered waveguide (wrapped in heating tape) from the right. The micrometer on top provide adjustability to the electrode. A charge collector is attached to the coaxial feed-through at the bottom. A port with an RF probe and one with a leak valve are on the left. The micrometer in the back is for cavity tuning.
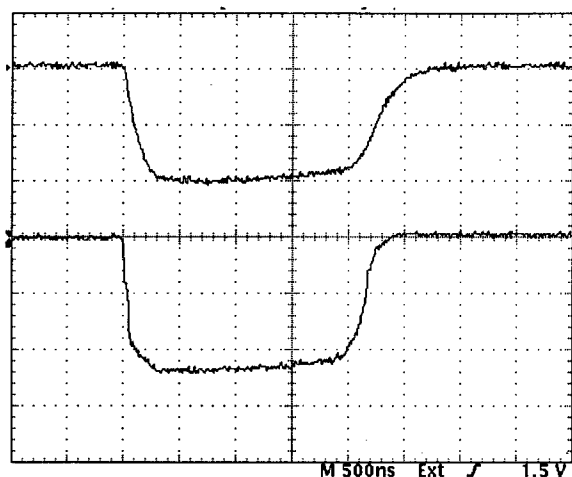
Figure 5: Oscilloscope traces of macropulse operation of the S-band experiment. Top: The RF power in the cavity. Bottom: The transmitted beam current macro pulse.

6 SUMMARY

In the last several years, considerable progress has been made in advancing cathode sources of electrons. Extensive work has been done on the field emission source and prototype microwave tubes are being fabricated using field emission arrays. Field emission arrays hold the promise of direct modulation of emission, but this feature has yet to be demonstrated in a practical device. High current densities have been achieved in electron emission from ferroelectrics. In this case, the physics of the emission process is not completely understood on a materials level. These sources show potential for use in high current source applications such as high power microwave tubes. Further work is required to study the useful life of the sources especially at high current, long pulse and high repetition rate. Like field emission arrays, direct modulation of emission is difficult which due to the high capacitance.

An extensive amount of work has been done with photoemitters on the production of single pulses and on the generation of a short train of pulses. The main application has been as injectors for accelerators. Their use in RF generation is at present limited to relatively short duration pulses. Photocathodes are complementary to the MPG device since they can provide a flexible assortment of pulses.

Finally, we have described the MPG, a device which uses secondary emission in an RF cavity to produce a train of picosecond long electron pulses. In contrast to photoemission sources the MPG can easily produce multi-microsecond long macropulses. When driven with a klystron, it can form a very compact and high gain RF system. The fact that the MPG produces prebunched pulses, and doing so before post-accceleration, makes it extremely attractive for use in many applications including RF generation, radiography, radiation therapy, radiation sterilization, and in injector for high-energy accelerators. Its proven long lifetime is a big advantage.

Research and development of new electron emitters has advanced substantially in the last several years. However, these novel emission schemes have not yet received widespread use. Additional research and development is still required to provide improved electron gun solutions for practical applications.

The electron emission schemes presented in this paper are described in more detail in reference [51].

7 ACKNOWLEDGMENTS

8 REFERENCES

1. J. L. Adamski et al., *IEEE Trans. Nucl. Sci.* NS-32 (5), 3397 (1985).
2. T. F. Godlove and P. Sprangle, *Particle Accelerators,* 34, 169, (1990).
3. H. Braun et al., CLIC Note 364, The CLIC RF Power Source, (1998).
4. H. Braun et al., CLIC Note 367 *Proc. EPAC 98*, CERN/PS 98-014(LP) .
5. E. G. Zaidman and M. A. Kodis, *IEEE Trans. El. Dev.*, ED-38, p. 2221-2228 (1991).
6. W. A. Mackie, R. L. Hartman and Paul R. Davis, *Applied Surface Science* 67, p. 29-35 (1993).
7. W. A. Mackie, R. L. Hartman, M. A. Anderson and P. R. Davis, *J. Vac. Sci. Technol. B* 12, p. 722-726 (1994).
8. L. Parameswaran et al., submitted to *Proc. of Vacuum Electronics Review*, San Diego, May (1997).
9. C. O. Bozler et al., *J. Vac. Sci. Technol. B* 12, p. 629 (1994).
10. C. A. Spindt et al., *J. Vac. Sci. Technol. B* 14, p. 1986 (1996).
11. C. A. Brau, presented at 9th Interntional Free Electron Laser Conf., Beijing, China, August, 1997.
12. C. A. Brau, presented at Gargnano Electron Beam Workshop, 1997.
13. C. M. Tang, M. Goldstein, T. A. Swyden and J. E. Walsh, *Nucl. Instrum. and Methods A* 358, pp. 7-10 (1995).
14. Y. Liu and Y. Y. Lau, *J. Vac. Sci. Technol. B* 14, p.2126-2129 (1996).
15. C. M. Tang, 1995 Particle Accelerator Conf., Dallas, TX, p. 70-74 (1995).
16. C. M. Tang and T. A. Swyden, Society for Inform. Display Intl. Sym. Digest of Tech. papers, Vol. XXVIII., p. 115-118 (1997).
17. H. Makishima et al., *Technical Digest of IVMC'97* Kyongju, Korea, p. 194-199 (1997).
18. H. Imura et al., *Technical Digest IEDM*, Intl. Electron Devices Meeting, Wash. D.C., Dec. 7-10, 1997 p.721-724.
19. H. Takemura et al., *Technical Digest IEDM*, Intl. Electron Devices Meeting, Wash. D.C., Dec. 7-10, 1997 p.709-712.
20. S. G. Bandy et al., *1997 IEEE Intl. Conf. on Plasma Science, IEEE Catalog No. 97CH36085*, May 19-22, p. 127 (1997).
21. K. L. Jensen, J. E. Yater, E. G. Zaidman, M. A. Kodis and A. Shih, *Tech. Digest IVMC'97*, Kyongju, Korea, p.186-189 (1997).
22. D. Palmer et al., *J. Vac. Sci. Technol. B* 13, p. 576-579 (1995).
23. R. K. Parker, K. L. Jensen and R. H. Abrams, *Technical Digest IVMC'97*, Kyongju, Korea, p. 92-97 (1997).
24. C. A. Spindt, C. E. Holland, P. R. Schwoebel and I. Brodie, *J. of Vac. Sci. Technol. B* 14, p. 1986-1989 (1996).
25. C. A. Spindt, C. E. Holland, P. R. Schwoebel and I. Brodie, *Technical Digest of IVMC'97*, Kyongju, Korea, p. 200-207 (1997).
26. J. P. Calame, H. F. Gray and J. L. Shaw, *J. Appl. Phys.* 73, p. 1485-1504 (1993).
27. P. Schoessow et al., *Proc. of the 2nd European Particle Accel. Conf.*, p. 606 (1990).
28. K. Batchelor, et al., *Nucl. Instr. and Meth. in Phy. Res.* A318, p. 372 (1992).
29. S. C. Hartman et al., presented at 1993 Part. Accel. Conf., *IEEE Cat. 93CH3279-1*, p. 561 (1993).
30. I. Ben-Zvi, presented at 1993 Part. Accel. Conf., *IEEE Cat 93CH3279-1*, p. 2962 (1993).
31. I. S. Lehrman, I. A. Birnbaum, M. Cole, R. L. Heuer, E. Sheedy, Part. Accel. Conf., *IEEE Cat. 93CH3279-1*, p. 3012 (1993).
32. C. Travier et al., *Nucl. Instr. and Meth. in Phy. Res.* B89, p. 27 (1994).
33. I. Ben-Zvi, Adv. Accel. Concepts, CF 398, 40, AIP Press, NY (1997).
34. R. Bozart et al., CLIC Note 29, PS/RF Note 95-25, CERN, Switzerland.
35. H. Gundel, H. Riege, E.J.N. Wilson, J. Handerek and K. Zioutas, *Nuclear Instru. and Methods in Phy. Research* A 280 p.1 (1989).
36. T. C. Cavazos, W.L. Wilbanks, C.B. Fleddermann and D.A. Shiffler, *Appl. Phys. Lett.* 65, p. 2612 (1994).
37. A. Sh. Airapetov, A.K. Krasnykh, I.V. Levshin and A. Yu. Nikitskii, *Sov. Tech. Phys. Lett.* 35, p.182 (1990).
38. J.D. Ivers, L. Schachter, J.A. Nation, G.S. Kerslick and R. Advani, *J. Appl. Phys.* 73, p. 2667 (1993).
39. L. Schachter, J.D. Ivers, G.S. Kerslick and J.A. Nation, *J. Appl. Phys.* 73, p. 8097 (1993).
40. B. Jiang, G. Kirkman and N. Reinhardt, *Appl. Phys. Lett.* 66, p. 1196 (1995).
41. S.E. Sampayan et al., *Nuclear Instruments and Methods in Physics Research* A 340, p. 90 (1994).
42. M. Okuyama, J. Asano and Y. Hamakawa, *Jpn. J. Appl. Phys.* 33, p. 5506 (1994).
43. J.D. Ivers et al., submitted for publication to IEEE Trans. on Plasma Science (1998).
44. F. Mako and W. Peter, Part. Accel. Conf., *IEEE Cat. 93CH3279-1* p. 2702 (1993).
45. A. S. Gilmore, *Microwave Tubes* (Artech House, Norwood, MA 1986), p. 474.
46. J. R. M. Vaughan, *IEEE Trans. Electron Devices* 35 (7), p. 1172 (1988)
47. R. Kishek and Y. Y. Lau, *Phys. Rev. Lett.* 75, 6, p. 1218, (1995).
48. S. Riyopoulos, D. Chernin and D. Dialetis, *Phys. Plasmas* 2 (8), p. 3194 (1995); also IEEE, Trans. Elec. Devices, 44, p. 489 (1997).
49. F.M. Mako and L.K. Len, to be published in the Proceeding of RF98 Conference (1998).
50. F. Mako, L.K. Len and W. Peter, to be published in the Proceedings of the 8th Workshop on Advanced Accelerator Concepts, 1998.
51. J. A. Nation et al., *Proc.of the IEEE*, vol. 87, no. 5, May 1999.

SIMULATION, GENERATION, AND CHARACTERIZATION OF HIGH BRIGHTNESS ELECTRON SOURCE AT 1 GV/M GRADIENT

T. Srinivasan-Rao, J. Schill, I. Ben-Zvi, Brookhaven National Laboratory, Upton, NY 11973,
K. Batchelor, J. P. Farrell, Brookhaven Technology Group, Inc. Stony Brook, NY, 11790,
J. Smedley, State University of New York, Stony Brook, NY 11790
X. E. Lin, A. Odian, SLAC, Stanford, CA 94309

Abstract

This paper describes computer simulations and measurements on an electron bunch from a pulsed, high gradient gap. MAFIA and PBGUNS were used to calculate the emittance, brightness and energy spread of the electron beam for peak currents ranging from 10 A to 1 kA and pulse durations ranging from 0.3 ps to 10 ps. Under optimum conditions, normalized emittance of 10^{-7} pi m-rad, beam brightness of 3×10^{15} A/(m-rad)^2 and energy spread of 0.15 % were obtained. A pulsed high voltage with 1 MV amplitude, and ~ 1 ns duration was applied to the diode with an interelectrode gap ranging from 2 mm to 0.5 mm. Copper cathodes with three different surface preparations, diamond polished, diamond cut and chemically cleaned, have been tested for their voltage hold-off properties under this high gradient and the Fowler-Nordheim plots were generated. The diamond polished OFC class II copper was shown to consistently produce lower dark current and higher hold-off voltage. Photoemission studies have been made using light from a KrF excimer. The field enhancement factor for photoemission was calculated to be 5, an order of magnitude smaller than the dark current beta for a similar surface.

1 SIMULATIONS

Two simulation codes, MAFIA and PBGUNS were utilized. Agreement between these codes has been demonstrated [1]. PBGUNS was then used to perform the bulk of the optimization, with only those issues that required time dependence being resolved with MAFIA.
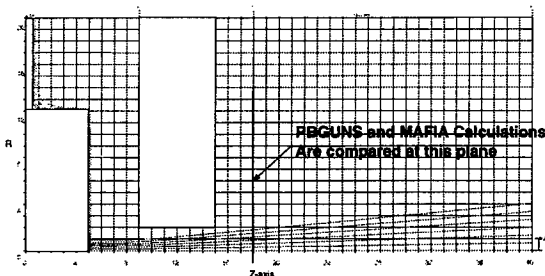
Fig 1. PBGUNS Geometry and particle trajectories

Figure 1 shows the standard geometry used in simulation. In all cases, output data from simulation was taken at 3.25 mm from the surface of the cathode. A 1 mm accelerating gap was used, with a potential of 1 MV on the cathode. The emitting spot had a radius of .25 mm and the initial transverse and longitudinal current densities were constant. Table 1 displays the emittance and brightness as a function of initial current and pulse duration, obtained using MAFIA results.

Current	Charge	Bunch length	Emittance	Brightness
A	nC	ps	π mm mrad	A/(mm^2mrad^2)
100	1	10	0.167	3571
100	0.3	3	0.088	12854
100	0.1	1	0.062	26014
100	0.03	0.3	0.073	18868
500	0.5	1	0.207	11668
250	0.25	1	0.132	14348
50	0.05	1	0.039	33557
10	0.01	1	0.045	5027

Table 1. 1-σ normalized slice emittance and brightness as a function of pulse duration and charge.

PBGUNS is a DC code and therefore does not provide information on longitudinal variation. Hence, slice emittance values were used in the optimizations to allow for a direct relationship with PBGUNS. The MAFIA results for the particle's r and p_r are used to calculate the 1-σ normalized slice emittance (using the center 1% of the beam for the emittance calculation), using the expression:

$$\varepsilon = 2\sqrt{\langle r^2 \rangle \langle p_r^2 \rangle - \langle r \cdot p \rangle^2} \qquad (1)$$

For the 100A, 10 ps case, the full beam 1-σ normalized emittance was found to be .385 π mm-mrad. The slice emittance for the center 1% of the beam under the same conditions was .167 π mm-mrad. It is important to note that the above results assume no random energy distribution at the source (such as might result from thermal effects or photon energy in excess of the work function). A random initial energy of 1eV places a lower bound of .17 π mm-mrad on the emittance, and leads to brightness of 3×10^{15} A/(m-rad)^2. Beyond 500A the transverse beam spreading due to space charge leads to clipping at the anode aperture.

PBGUNS has been used to investigate the effect of curving the cathode emission region to compensate for the divergence induced by the anode hole. Cathodes with radii of curvature of 1, 1.5 & 2 mm were used for a 100 A beam. It was found that by altering the cathode curvature, a collimated beam could be obtained or a focus could be provided at a desired location beyond the anode.

Simulations have also been done to study the longitudinal energy spread of the beam. Figure 2 shows a MAFIA plot of longitudinal position vs longitudinal momentum for a charge of 1nC and a pulse duration of 10 ps. The RMS energy spread is .15%.

Longitudinal Momentum Spread
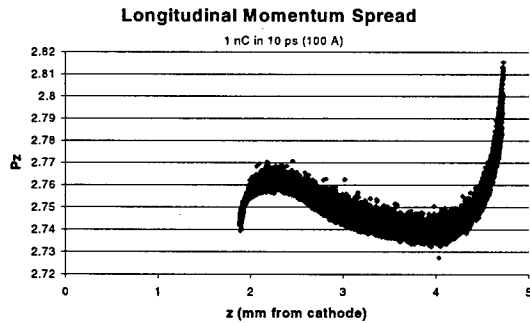
Fig 2. Charge induced longitudinal momentum spread. Pz is in $\beta_z\gamma$.

MAFIA was also used to investigate the longitudinal variation of the transverse emittance. Figure 3 shows the r vs r' curves for three 1% slices taken from the front, middle and back of a 10ps bunch, all at 3.25 mm from the cathode.

Transverse Phase Space
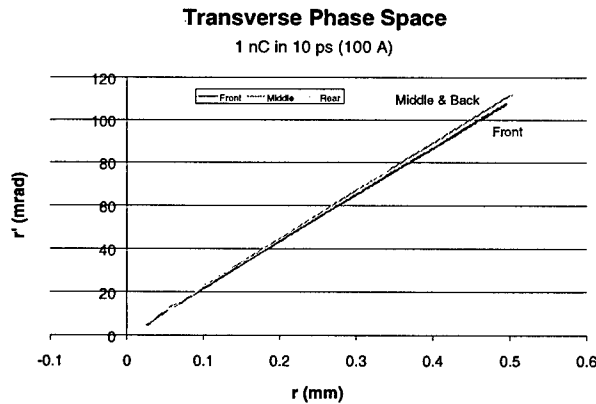
Fig 3. Longitudinal variation of the transverse phase space.

2 EXPERIMENTAL RESULTS

2.1 Dark Current

One advantage of a pulsed power gun is the ability to maintain higher field gradients. Experiments have shown that higher breakdown thresholds of materials can be obtained under short pulse conditions as compared to DC [2]. With our generator pulsed voltages up to 1 MV with a 1 ns duration can be applied to diodes with interelectrode spacing ranging from 2-0.5 mm. Details of the pulse generator and the experimental arrangement can be found elsewhere[3]. The dark current and maximum field before breakdown were measured for chemically cleaned (prepared using SLAC specification C01a.1 without steps 8-9), single point diamond turned and diamond polished (preperation described in [4]) OFC copper cathodes.

The cathodes were installed in a vacuum gap with 1.5 mm interelectrode spacing. The voltage amplitude on the cathode was slowly increased from 300 kV to 800 kV, allowing the cathode to condition. The field on the conditioned cathode was then gradually reduced. The dark current from the cathode, collected on a faraday cup positioned 5 mm from the cathode, is then measured as a function of the applied voltage. The gap was then reduced to 1 mm and the process was repeated. The criterion for breakdown was assumed to be a sudden, irrevocable increase in the dark current accompanied by a visible flash. A Fowler-Nordheim[5] plot was generated using the data prior to breakdown for the chemically cleaned cathode (1.5 mm interelectrode spacing) and the diamond polished cathode (1 mm and 1.5 mm spacing). The field enhancement factor, β, has been calculated for each case, assuming a cathode work function of 4.65 eV[6]. For the diamond turned sample, surface could not be conditioned using the standard technique, and no dark current measurements were taken for this sample. The field enhancement factor β for chemically cleaned copper, conditioned to ~500 MV/m was measured to be 76. β for the diamond polished sample under similar conditions was 46. The same sample when conditioned up to 800 MV/m field had an enhancement factor of 30. This reduction in β from a 1.5 mm to 1 mm electrode spacing for the polished sample is likely an effect of the conditioning process.
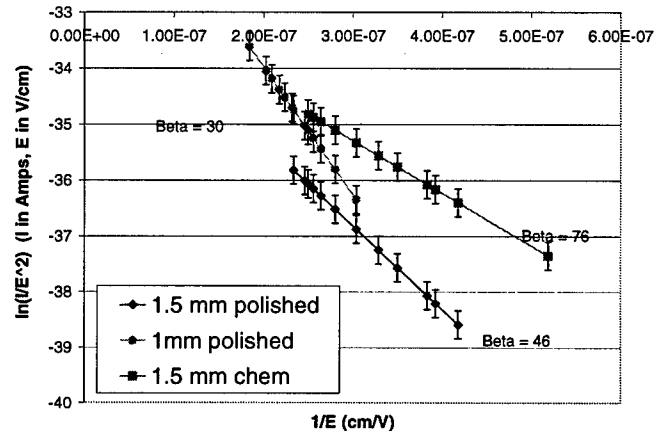
Fig 4. Fowler Nordheim plot for chemically cleaned and diamond polished Cu cathodes.

Both the chemically cleaned and diamond turned samples suffered breakdown when the electrode spacing was set to 1mm, and both had significantly higher currents. Of the three surface preparation methods tested, diamond polish seemed to have a lower dark current and higher hold-off voltage. A similarly prepared surface was tested to hold-off field gradients up to 1.66 GV/m [1]. Further increase in the field was limited by our experimental arrangement.

2.2 Photocurrent

Photoemission measurements have been made by illuminating the cathode with light form a KrF excimer (248 nm, photon energy of 5 eV) laser. The laser spot illuminated the center 1 mm diameter of the cathode at normal incidence. The interelectrode spacing was set at 2 mm, and voltage amplitudes from 200kV to 500 kV were applied to the cathode coincident with the laser pulses. The cathode was diamond polished, and was conditioned to 250 MV/m. The emitted charge was then collected on the Faraday cup in the same manner as the dark current. At these applied fields, the dark current was negligible and did not contribute to the photocurrent. Collected charge was measured as a function of laser energy and voltage amplitude. The laser pulse duration was 23 ns FWHM, much longer than the voltage pulse duration of 1 ns. For this measurement, the pulser was run in self-triggered mode leading to a jitter with respect to the laser of 20 ns. Only those shots falling into a 3 ns window at the peak of the laser pulse are considered in this analysis. The charge collected was found to have a linear dependence on the laser energy for a constant applied voltage. This finding is in agreement with the expected dependence for a laser with a photon energy greater than the work function of the copper cathode (4.65 eV), in the space charge free regime.
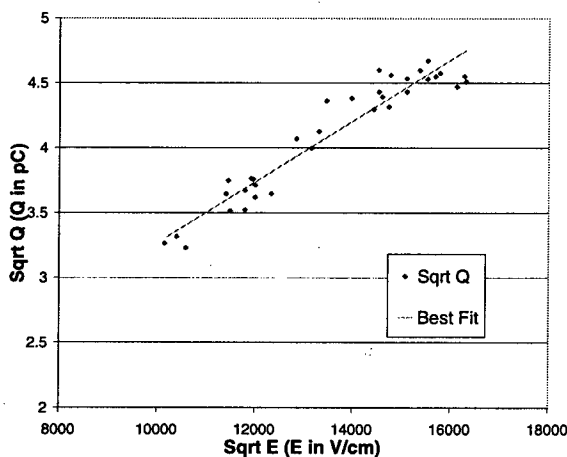
Fig 5. Sqrt of applied field vs Sqrt of measured charge (corrected for variation in laser energy). The slope is 2.35e-4 and intercept is .915.

In the presence of an applied field, the charge emitted from the cathode can be written as [5]:

$$Q = A(h\nu-\phi+\alpha(\beta E)^{1/2})^2$$

Here A is a constant of proportionality which includes the laser energy, $\alpha=(e/4\pi\varepsilon_0)^{1/2}$, $h\nu$ is the photon energy, ϕ is the work function, E is the applied field and β is the field enhancement factor of the surface for photoemission. Figure 5 shows a plot of $E^{1/2}$ vs $Q^{1/2}$ for constant laser energy. The ratio of the slope to the intercept is then:

$$\text{Slope/intercept} = \alpha(\beta)^{1/2}/(h\nu-\phi)$$

For a work function of 4.65 eV, the slope and the intercept obtained from Figure 5 result in a field enhancement factor of 5 for photoemission, significantly smaller than that for the dark current. The origin of this difference is not yet fully understood. More systematic analysis of the photoemission data and measurement of dark current from this surface under higher applied fields are currently underway to help better understanding.

3 CONCLUSION

Simulations have been performed to study the beam parameters at the output of a 1 MeV pulsed power gun. It was found that emittance of .2 π mm-mrad and brightness of 3×10^{15} A/(m-rad)^2 were predicted, with an energy spread of 0.15% for a 100A beam with 10 ps pulse duration.

Measurements of dark current have been made on copper cathodes with three different surface preparations. The behavior of the polished sample was significantly superior in terms of lower dark current and higher breakdown threshold. Field enhancement values for field emission were measured to be ~30 for the polished surface and 76 for the chemically cleaned surface.

Measurements of photocurrent were performed with a KrF excimer. The emitted charge was measured to be linear with the laser energy. Dependence of the charge on the applied field indicate a field enhancement factor of 5 for photoemission, significantly lower than the dark current field enhancement factor for a similar surface.

4 ACKNOWLEDGEMENTS

5 REFERENCES

[1]T. Srinivasan-Rao, et al, presented at 8th Workshop on Advanced Accelerator Concepts, , Baltimore, MD, 6-11, July (1998)

[2] G. A. Mesyats and D. I. Proskurovsky, Pulsed Electrical Discharge in Vacuum, (Springer-Verlag, 1989), p.109

[3]T. Srinivasan-Rao, J. Smedley, Advanced Accelerator Concepts workshop, AIP Conference Proceedings 398, NY 1997, P. 730.

[4] T. Srinivasan-Rao, J. Yu, X. J. Wang, BNL report 62626, Brookhaven National Lab, (1996)

[5]M. Cardona and L. Ley, Photoemission in Solids 1, (Springer-Verlag,, 1978), pp. 21-29

[6]CRC Handbook of Chemistry and Physics, edited by R. C. Weast, (CRC Press, Inc, 1984), pg. E-76

EXPERIMENTAL STUDY OF GaAs PHOTOCATHODE PERFORMANCE IN RF GUN*

A.V.Aleksandrov, N.S.Dikansky, R.G.Gromov, P.V.Logatchov, BINP, Novosibirsk, Russia

Abstract

A prototype of S-band RF photogun with GaAs photocathode has been built and tested at Novosibirsk. The main goal of this prototype is to check a possibility of long time operation for GaAs photocathode in a strong accelerating field of RF cavity. The first experimental results concerning dark current and lifetime of GaAs photocathode in NEA condition under high RF power are presented. The dark current observed is much higher than predicted. Possible mechanism of large dark current emission from NEA surface is suggested and discussed.

1 INTRODUCTION

Nowadays GaAs polarized electron source is the best available because it has intrinsic advantages in performance of intensity, quantum efficiency, degree of polarization compared with other type of polarized electron sources. Combining all these advantages with a significant interest to polarized electron beams which comes from a high energy physics, we have chosen a GaAs photocathode for our RF photogun project. Unfortunately there was no experimental confirmation of possibility to use this cathode inside a cavity with high gradient accelerating field. In order to investigate a performance of GaAs photocathode in S-band RF gun the experimental bench was build in our laboratory. The detailed description of the installation can be found in [1].

2 EXPERIMENTAL RESULTS

2.1 GaAs photocathode with small quantum efficiency

The first experiments started in autumn of 1997 with the bulk GaAs cathode activated to quantum efficiency about .01% - .05% on HeNe laser wavelength. It corresponds to positive electron affinity (PEA) state of a cathode. The aim of that run was to test all systems and measure cathode properties for different levels of RF power in the cavity. Dark current and lifetime were measured for the accelerating field strength up to 100MV/m. The detailed description of experiment and results can be found in [2]. In this experiment dark current after activation increased about two orders of magnitude. Measured dependence of dark current on cathode field strength was well in accordance with Fowler-Nordheim low. We observed

decreasing of cathode lifetime from 200min in absence of RF power to about 30 min in 30MV/m accelerating field. This effect could be explained by vacuum worsening in the cavity due to dark current. After experiment we observed significant damage on the cathode surface.

2.2 GaAs photcathode with large quantum efficiency.

New cathode was installed at the end of 1997. After 50 hours of baking at 300°C pressure $2 \cdot 10^{-10}$ torr was established. Only ion pumps were used at this stage. Cathode was activated following usual "yo-yo" algorithm. Typical quantum efficiency on HeNe laser wavelength was 3%-5% that ensures that cathode surface is in negative electron affinity (NEA) condition. Lifetime was 7-8 hours in activation chamber and practically the same in the cavity with RF switched off. Then cathode was moved to the cavity and RF power increased slowly step by step while dark current was controlled to prevent RF breakdowns causing cathode damages. Lifetime of a cathode in this case was just several seconds therefore we reduced repetition rate of RF pulses to .5 Hz. Signal from Faraday cup was measured by ADC and stored in computer after each RF pulse. Photocathode was moved to activation chamber after each 10-15 pulses for measurement of quantum efficiency. Typical record of experimental run is shown in Fig.1.
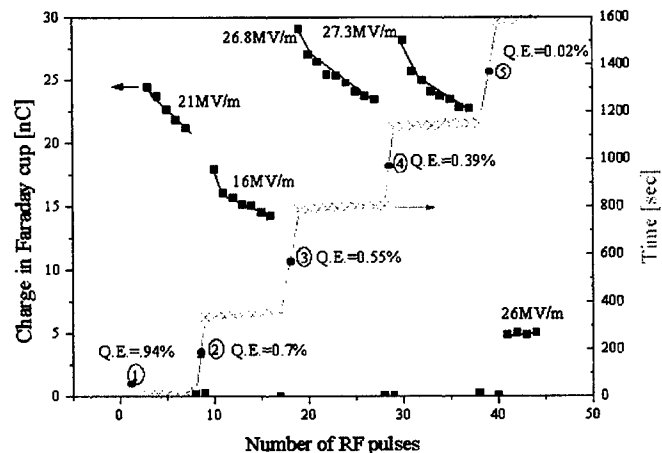
Figure 1. Dependence of charge in Faraday cup and quantum efficiency upon number of RF pulses.

One can see from fig.1 that dark current depends on quantum efficiency of the cathode and on the strength of RF field. The dependence of dark current upon field strength on the cathode is shown in Fig.2 in Fowler-Nordheim (FN) coordinates.
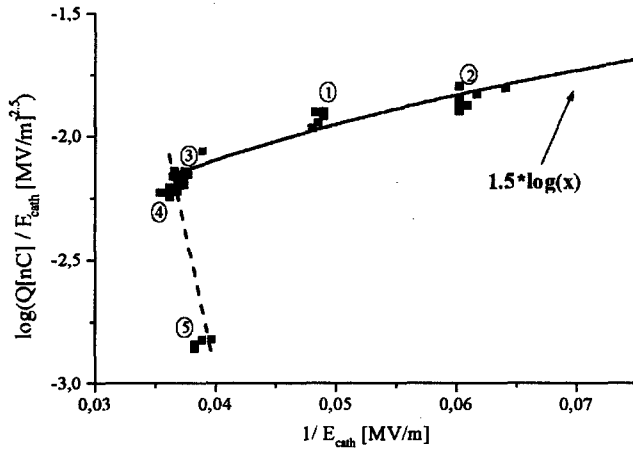
Figure 2. Fowler-Nordheim plot

In principle, Fowler-Nordheim low describes a field emission from a metal surface, however experimentally measured dark current from semiconductor PEA photocathode satisfies this low as well [2,3]. It is not true in our case as seen from Fig. 2. Indeed, there are two branches: 4 -5 has normal negative slope and 1-3 has anomalous positive slope, which probably coincide to PEA and NEA regimes of the photocathode respectively. Indeed, a dark current dependence upon electric field strength can be described as:

$$I = I_0 \cdot (\beta E_C)^{2.5} \cdot \exp(-\frac{\alpha \varphi^{1.5}}{\beta E_C}) \quad , if \ \varphi > 0$$
$$I = I_0 \cdot E_C^{\gamma} \quad\quad\quad\quad , if \ \varphi \leq 0$$

Here E_C is field strength on the cathode, α, β are FN parameters, φ is cathode work function, γ is constant. In FN coordinates x =1/E_C, y = log (I/$E_C^{2.5}$) this set of equations becomes:

$$y = \log(I_0 \beta^{2.5}) - \log e \cdot \frac{\alpha \varphi^{1.5}}{\beta} \cdot x \quad , if \ \varphi > 0$$
$$y = \log I_0 + (2.5 - \gamma) \cdot \log x \quad , if \ \varphi \leq 0$$

It corresponds well to experimental points if γ = 1.0 as demonstrated by fitting curve in fig.2.

3 MECHANISM OF DARK CURRENT GENERATION

The observed dependence of dark current on electric field can be understood if one assume that free electrons present in conduction band of a photocathode even in absence of illuminating light. When work function is positive these electrons penetrate through a surface barrier in accordance with usual FN theory. In opposite case of NEA condition there is no barrier and electrons escape from a crystal immediately as they reach its surface resulting in weak dependence of current on strength of accelerating field. As we show below, back bombardment, inherent for RF gun operation, can be responsible for charge build up in a cathode in NEA state.

3.1 Charge build-up Due to Back Bombardment

Lets assume that there is some charge q_n in a conduction band of a cathode after n RF pulses, then electrons can travel to crystal surface and escape to vacuum with probability Y. After emission some electrons are accelerated to gun exit other returned back to the cathode with probability k_r depending on RF phase of electric field. Returned electrons can excite large number M of additional electrons from valence to conduction band. (It is well known that NEA semiconductors have very large secondary emission coefficient [4].) Again these new electrons may excite electrons after emission in proper RF phase providing rapid growth of charge inside a cathode. Charge after the next RF pulse can be found as:

$$q_{n+1} = q_n \cdot e^{\frac{-T}{\tau}} + (Y \cdot q_n) \cdot k_r \cdot M =$$
$$= q_n \cdot (e^{\frac{-T}{\tau}} + Y \cdot k_r \cdot M) \approx q_n \cdot g \cdot k_r$$

Here q_n, q_{n+1} is a charge inside a cathode on a successive RF pulses, T is RF period, τ is electron lifetime in a bulk of a cathode, Y-quantum efficiency, k_r is back bombardment coefficient depending only on configuration of e/m fields and cavity geometry , M is multiplication factor, g=YM is secondary emission coefficient depending on cathode properties only.

Solution of this equation is

$$q_n = q_0 \cdot (g \cdot k_r)^n \quad \Rightarrow \quad q(t) \propto (g \cdot k_r)^{\frac{t}{T}}$$

One can see that charge inside crystal grows exponentially if $gk_r > 1$. Typical cathode parameters Y≈005, M≈200-2000, k_r≈.25 give estimation for gk_r≈.25–2.5 It is near a critical value providing that back bombardment can be responsible for dark current generation and even small variation of gk_r have to enhance or suppress dark current significantly.

Computer simulation of charge build up in a cathode was done using model of pillbox cavity. Typical result of this simulation for some values of secondary electron emission coefficient g is shown in fig.3. The maximum charge multiplication is observed on the edges of RF pulse where back bombardment coefficient is maximal.
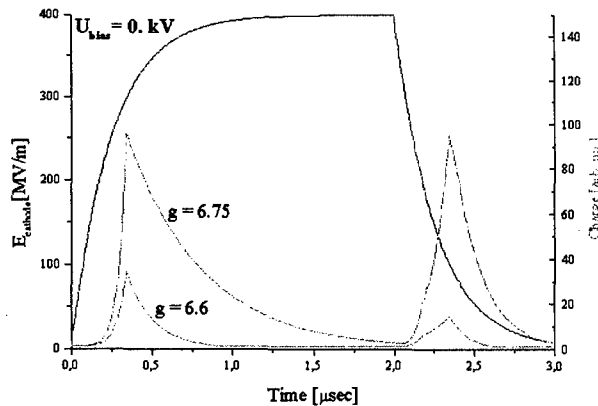
Figure 3. Build up of a charge in a cathode during RF pulse.

4 CONCLUSIONS

The experimental results reported above allow making the following conclusions:

- GaAs photocathode can operate in a RF cavity with accelerating electric field strength up to 30MV/m without irreversible damages. After degradation due to bad vacuum conditions it can be activated again using standard procedure.
- Dark current from an activated to NEA bulk GaAs photocathode exceeds by 2 – 3 orders of magnitude dark current of PEA photocathode in a field of the same strength.
- The dependence of dark current from GaAs photocathode activated to quantum efficiency about 1% upon electric field strength doesn't satisfy Fowler-Nordheim low
- Back bombardment of a cathode in RF gun combined with large secondary electron emission from NEA surface can be responsible for emission of large dark current In this case reducing of back bombardment coefficient and (or) secondary emission coefficient can suppress dark current considerably. Non-uniform magnetic field and (or) low voltage cathode bias may be used for reduction of number of returned electrons. Reducing cathode thickness that is favorable also from the point of view of maximum achievable polarization can reduce secondary electron emission coefficient.

5 FUTURE DEVELOPMENTS

More experimental data are needed for further investigation dark current from GaAs photocathode in RF gun therefore we have made modernization of our installation:

1) The main problem for experiment is very short lifetime of activated cathode under high gradient RF field. We believe that reason is intense gas release in Faraday cup that is very close to the cathode location. Now distance from the cavity to Faraday cup is increased and additional pumping is placed between them. Differential pumping will separate vacuum near cathode from vacuum in Faraday cup chamber.

2) Wall current monitor with 100ps resolution is installed into beamline to observe a shape of dark current pulse. We can compare it with predictions of back bombardment model and check validity of this model.

3) A coil producing non-uniform magnetic field is installed near the gun cavity to reduce number of returned electrons. If back bombardment model is correct reducing number of returned electrons will lead to significant reduction of dark current.

All modernisation is completed and we plan to make next experimental run in April-May of 1999. The main goal of this run is to check validity of back bombardment mechanism of charge generation.

6 AKNOWLEGEMENTS

7 REFERENCES

[1] A.V.Aleksandrov et al, "A Prototype of RF photogun with GaAs photocathode for injector of VEPP-5", EPAC'96, Sitges, June 1996.

[2] A.V.Aleksandrov et al, "High power test of RF gun with GaAs photocathode", LC'97, Zvenigorod, September 1997.

[3] C.Travier et al, "CANDELA photo-injector high-power test.", NIM B89 (1994) 27-32.

[4] R.L.Bell, Negative Affinity Electron Devices, Clarendon, Oxford,1973.

A HIGH GRADIENT 17 GHz RF GUN FOR THE PRODUCTION OF HIGH BRIGHTNESS ELECTRON BEAMS

W. J. Brown, K. E. Kreischer, M. Pedrozzi, M. A. Shapiro, R. J. Temkin, X. Wan

Plasma Science and Fusion Center, M.I.T., Cambridge, MA 02139 USA

Abstract

We report on the design and construction of a new, tuneable, 1.5 cell 17 GHz RF gun and improved beamline. Emittance compensation in the new beamline is achieved with a 6.5 cm long, 0.5 T solenoid placed immediately after the RF Gun. Simulations predict a normalized rms emittance of 0.5 πmm-mrad for a 1 ps, 0.1 nC, 2.4 MeV beam. Emittance measurement diagnostic slits have also been designed and constructed. This gun will operated with 50 ns, approximately 5 MW, pulses from a 17.13 GHz klystron amplifier built by Haimson Research Corp. Initial cold tests of the new gun have been performed. The on axis field profile of the RF gun has recently been measured using a "bead hang" technique developed at MIT to forgo the need of a hole in the cathode as required by the more conventional "bead pull" measurement. A balanced field profile was obtained.

1 INTRODUCTION

The MIT 17 GHz photocathode RF gun is a 1.5 cell electron accelerating structure consisting of two coupled TM_{010} like cavities excited by side wall coupled microwaves from a WR-62 waveguide (Fig. 1). The goal of the MIT 17 GHz RF gun experiment is to examine the advantages of operating an electron source at high frequency, and thereby produce an ultra-high quality electron beam capable of meeting the demands of future applications such as short wavelength free electron lasers. The scaling with RF frequency of the quality of the beam from an RF gun has previously been derived [1]. This study suggests that the emittance of the beam will scale inversely with RF frequency provided the charge and size of the beam are also scaled inversely with RF frequency (constant peak current) and the accelerating gradient is increased proportional to frequency. This implies a quadratic increase in the beam brightness.

Initial experiments demonstrating beam production have been completed at MIT and are summarized in the next section. This was the first RF gun experiment to operate above 3 GHz. In order to demonstrate an ultra-high brightness electron beam, a new emittance compensated RF gun and beamline with emittance diagnostics will begin operation in the near future.
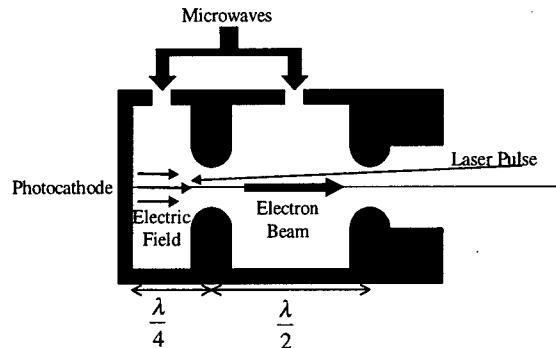
Figure 1: Schematic of RF Gun

2 OPERATION OF ORIGINAL GUN

The original MIT 17 GHz RF gun consists of 3 pieces of OFHC copper which are clamped together and attached to WR-62 coupling waveguide. Cold tests of the gun revealed a π mode frequency of 17.145 GHz, a coupling coefficient $\beta = 1.56$, and an ohmic $Q = 2700$. More recent field profile measurements (see section 4) showed that the electric field strength in the half cell is about 15-20% larger than that in the full cell. In high power tests, the gun was driven with up to 8 MW of RF power from the 17 GHz relativistic Klystron Amplifier built by Haimson Research Corporation [2], corresponding to peak accelerating fields of 300 MV/m. Breakdown in the RF gun occurring on some shots with incident power exceeding 5 MW, however, usually limited operation to a lower incident power and peak fields of 200-250 MV/m. The electron beam was produced by 1 ps, 20 μJ, 0.5 mm radius UV laser pulses created by frequency tripling 2 ps, 1.0 mJ, 800 nm pulses produced from a Ti-Sapphire regenerative amplifier.

2.1 Experimental Results

Results of beam measurements are listed in Table 1. These results have previously been reported in greater detail [3]. The bunch charge measurements (yielding values up to 0.1 nC) were made with a high speed Faraday cup placed downstream of the gun. The laser was injected into the gun with a prism placed inside the collector portion of the Faraday cup. The energy measurements were made with a Browne-Buechner [4] style magnetic spectrometer placed about 30 cm away from the RF gun. The measured rms energy spread at

the position of the spectrometer is in good agreement with PARMELA [5] simulations of the RF gun and beam transport, and is consistent with an rms energy spread of about 1.5 % at the RF gun exit.

Table 1: Beam measurement results

Parameter	Measurement
Bunch Charge	0.1 nC
RF Injection Phase	10 - 40 °
Initial Bunch Length	1 ps (Laser Measurement)
Initial Bunch Radius	0.5 mm (Laser)
Cathode Electric Field	≈ 200 MV/m
Beam Energy	1.05 MeV
Energy Spread (rms)	2.5% (at Spectrometer)

3 NEW GUN AND BEAMLINE

A new RF gun and beamline are in development in order to provide an emittance measurement demonstrating an ultra high brightness beam. The new RF gun is a 1 1/2 cell structure similar to the original gun, but is equipped with tuners in order to optimize field balance, allowing for maximum electron beam energies. The tuners consist of small plungers which retract from or fill up a small hole in both the half and full cells, but fall short of actually protruding into the cavity. This provides about 10 MHz of tunability.

The gun will be installed into the beamline shown in Fig. 2. Emittance compensation is performed with a 6.5 cm long, 5 kG peak field solenoid. The edge of the magnet will be placed 2.0 cm from the RF Gun cathode, resulting in a maximum magnetic field at the cathode of about 25 Gauss. The additional normalized emittance resulting from this magnetic field at the cathode is only 0.04 πmm-mrad for a 0.5 mm radius beam. The emittance will be measured by breaking the beam into individual beamlets using an emittance mask, made from laser drilled 70 μm slits in a thin (0.125 mm) tantalum foil placed about 200 μm apart. The beamlets will then be imaged downstream of the mask in order to reconstruct the phase space.

It is expected from PARMELA simulations that a 0.1 nC, 1 ps, 2.4 MeV beam with a normalized rms emittance of 0.4-0.6 πmm-mrad can be produced with this experiment. For a 1 1/2 cell gun, peak accelerating fields of 350 MV/m will be required to obtain these parameters. In order to alleviate the necessity for such high fields, a 2 1/2 cell gun could be easily inserted in the beamline, bringing the needed peak field value down to 218 MV/m. The normalized rms brightness of the beam, defined by

$$B = \frac{I_{peak}}{\varepsilon_n^2} ,$$ (1)

can reach values of about 500 A/(πmm-mrad)^2. If this value is achieved, it will represent a significant improvement over previous high current electron injectors.
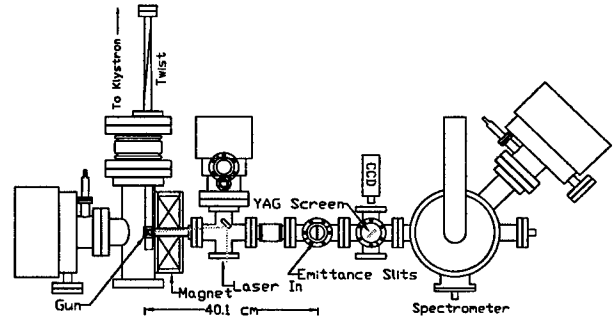
Figure 2: Schematic of New Beamline.
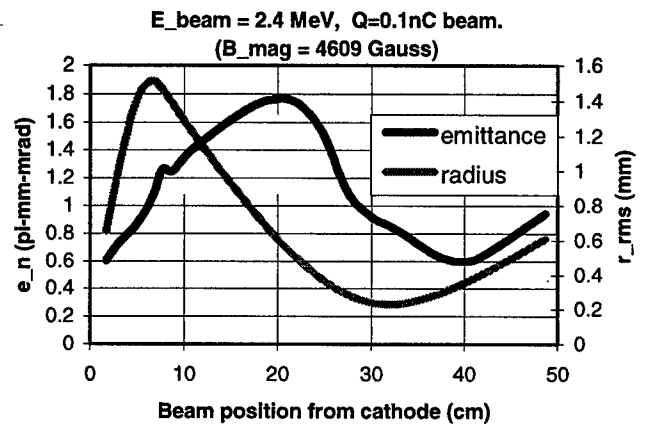
Figure 3: PARMELA Simulation of emittance compensation for 1 1/2 cell gun.

4 FIELD PROFILE MEASUREMENTS

In order to perform field profile measurements of the excited mode in the MIT RF gun, a "bead hang" method was developed. This is similar to "bead pull" measurements [6], but has a key difference in that the perturbing element is simply hung down into the RF cavity as opposed to being pulled all the way through it. The advantage of this method is that there is no need to have a hole in the cathode, allowing for the exact structure used in high power experiments to be measured. Ideally, the axial electric field profile in the gun can then be determined by mapping out the perturbation in the resonant frequency of the excited mode as a function of the position of the bead, i.e.

$$|E(z)|^2 \propto \frac{\Delta f(z)}{\alpha_{bead}} .$$ (2)

where α_{bead} is the electric polarizability of the bead.

In reality, the line used to hang the bead into the cavity also has a position dependent effect on the

resonant frequency as a result of the fact that the bead is simply being hung as opposed to pulled all the way through. This non-local perturbation, which can be expressed as,

$$\Delta f_{line}(z) \propto \int^z |E(\xi)|^2 d\xi \qquad (3)$$

where the integral is along the length of the support line up to the position of the bead, should be subtracted out of the measurement in order to obtain accurate results. This is especially necessary for smaller, high frequency structures like the MIT 17 GHz RF gun in which the line will have a more significant effect. The measured value for the electric field profile is then given by

$$|E(z)|^2 \propto \frac{(\Delta f(z) - \Delta f_{line}(z))}{\alpha_{bead}} \qquad (4)$$

Results of a bead hand measurement of the new cavity are shown in Fig. 4. The bead used in the measurement was a 0.5 mm long, 0.2 mm diameter piece of copper wire. The support line used in the measurement was a short piece of 76 μm diameter fishing line (1.5 lb. tensil strength). As expected, at the position of the iris between the half and full cell, the frequency perturbation due to the bead is zero.

Eventually, we plan to perform measurements of the azimuthal asymmetry of the field caused by the coupling holes. Initial measurements yield qualitative agreement with numerical simulations, with the value of E_z being slightly larger off axis at the azimuthal position of the coupling holes. Quantitative results, however, have proven difficult to obtain since a very large perturbation in the fields has been required in order to resolve the variations in the azimuthal dependence of the field.

5 CONCLUSIONS

A first round of experiments on a 17 GHz 1 1/2 cell RF Gun have been completed, demonstrating 1 MeV electrons with peak accelerating fields greater than 200 MV/m. A new, tunable, RF Gun has been designed and built, and the on axis field profile has been measured using a "bead hang" technique, demonstrating good field balance between the half and full cells. This gun will be installed in a new and improved beamline which includes an emittance compensating solenoid and a slit based emittance measurement scheme. We hope to demonstrate a record high quality electron beam with an rms normalized emittance $\varepsilon_n \approx 0.5$ πmm-mrad and peak current $I_{peak} \approx 100A$, corresponding to a rms normalized brightness of about 500 A/πmm-mrad. Operation will begin by June, 1999.

6 ACKNOWLEDGEMENTS

Figure 4: Measurement of the on axis field profile of the new RF gun.

7 REFERENCES

[1] J. Rosenzweig, E. Colby, "Charge and Wavelength Scaling of RF Photoinjector Designs," *Advanced Accelerator Concepts*, P. Schoessow, editor, AIP Conf. Proc. 335, AIP Press, Woodbury, NY pp. 724-737 (1995).

[2] J. Haimson and B. Mecklenburg, "Initial Performance of a High Gain, High Efficiency 17 GHz Traveling Wave Relativistic Klystron for High Gradient Accelerator Research," *Pulsed RF Sources For Linear Collider*, Richard C. Fernow, editor, AIP Conf. Proc. 337, AIP Press, Woodbury, NY, pp. 146-159 (1995).

[3] W. Brown, et. al., "Experimental and Theoretical Investigations of a 17 GHz RF Gun," to be published in Nucl. Instr. and Meth. A, April 1999.

[4] C.P. Browne and W. W. Buechner, "Broad-Range Magnetic Spectrograph", The Review of Scientific Instruments, Vol. 27, No. 11, pp. 899-907 (1956).

[5] J.H. Billen, PARMELA User's Manual, Los Alamos Accelerator Code Group (LAACG), LA-UR-96-1835.

[6] S. Hanna, et. al. "Development of Characterization Techniques for X-Band Accelerator Structures", Proceedings of the 1997 Particle Accelerator Conference, vol.1, pp.539-41 (1998).

FIRST EXPERIMENTS WITH THE RF GUN BASED INJECTOR FOR THE TESLA TEST FACILITY LINAC

S. Schreiber* for the TESLA Collaboration, DESY, 22603 Hamburg, Germany

Abstract

During 1997 and 1998 a first accelerator module was tested successfully at the TESLA Test Facility Linac (TTFL) at DESY. Eight superconducting cavities have accelerated the beam to an energy of more than 120 MeV. The injected 10 MeV electron beam was produced by a sub-harmonic injector using a thermionic gun, a buncher cavity, and one standard superconducting acceleration cavity. Since the achieved single bunch charge is not as high as required for a TESLA Linear Collider, a laser driven rf gun has been developed and been brought in operation late fall 1998. The aim of the new injector is to achieve the TESLA bunch charge and time structure, i.e. 8 nC bunches with 1 MHz repetition rate in 0.8 ms long bunch trains. This allows beam dynamics experiments in the TTFL. An overview of the injector is given and results of first experiments are described.

1 INTRODUCTION

The TESLA Test Facility (TTF) built by an international collaboration [1] is a test bed situated at DESY to prove that superconducting cavities as proposed for a TeV scale linear e^+e^- collider can be assembled into a linac test string (TTFL), and that accelerating gradients above 15 MV/m are consistently obtainable [2], [3].

During the running periods in 1997 and 1998, a low bunch charge injector with full beam current of 8 mA and full pulse length of 800 μs has been used to establish beam acceleration and stable operation of the acceleration modules. Among basic measurements of the beam parameters [4], beam induced high order modes in cavities of the acceleration module have been investigated [5].

In 1998, the injector has been upgraded with a laser-driven rf gun [6] to generate high bunch charges up to 8 nC with 1 MHz repetition rate to match as close as possible the TESLA beam structure. This is necessary to perform various experiments at the TTFL concerning higher order mode losses, space charge, and wake field effects. In addition, the new injector will be used for the proof-of-principle experiment of the proposed free electron laser TTF-FEL [7].

The rf gun has been commissioned end of 1998 together with a second acceleration module [8] and is being operated since then.

2 OVERVIEW

A schematic overview of the TTF injector is shown in Fig. 1, further details can be found in [9].

* E-mail: siegfried.schreiber@desy.de

The electron source is a laser-driven 1 1/2-cell rf gun operating at 1.3 GHz using a Cs_2Te cathode. A load lock cathode system allows mounting and changing of cathodes while maintaining excellent ultra-high vacuum conditions. The cathode is illuminated by a train of UV laser pulses generated in a mode-locked solid-state laser system synchronized with the rf.

The gun section is followed by a superconducting capture cavity, a bunch compressor, a dispersive arm, and a section to match the beam optics to the accelerating structures. The capture cavity is identical to a 9-cell TESLA accelerating structure. It boosts the beam energy up to 20 MeV. For some beam experiments, the magnetic chicane bunch compressor is used to compress the bunch length by a factor of 2. Several diagnostic instruments allow to measure basic beam parameters as well as to perform dedicated experiments.

The design parameters of the injector are listed in Table 1 together with parameters required for TTF-FEL operation.

Table 1: Injector design parameters for TTFL and TTF-FEL operation.

Parameter		TTFL	FEL
RF Frequency gun/booster	GHz	1.3	
Rep. Rate	Hz	10	
Macro Pulse Length	μs	800	
Macro Pulse Current	mA	8	9
Bunch Frequency	MHz	1	9
Bunch Charge	nC	8	1
Bunch Length (rms)	mm	1	0.8
Emittance, norm. (x,y)	10^{-6} m	20	2
$\Delta E/E$ (single bunch, rms)		$1 \cdot 10^{-3}$	
$\Delta E/E$ (bunch to bunch, rms)		$2 \cdot 10^{-3}$	
Injection Energy	MeV	20	

3 THE RF GUN

The rf gun consists of a 1 1/2 cell TM_{010} π-mode structure operated at 1.3 GHz. The design is based on work reported in [10], and has been adapted to L-band and to specific requirements for TTF, especially to the long rf pulse (1 ms) operation [11]. The gun has been built and tested in the framework of the TESLA collaboration at the A0 Test Facility at Fermilab [12], where a second gun is being tested now. At DESY, a low emittance gun dedicated to FEL operation is in development [13].

The geometrical dimensions, like the iris radius (2 cm) and the half cell length (5/4 λ/2) have been optimized to
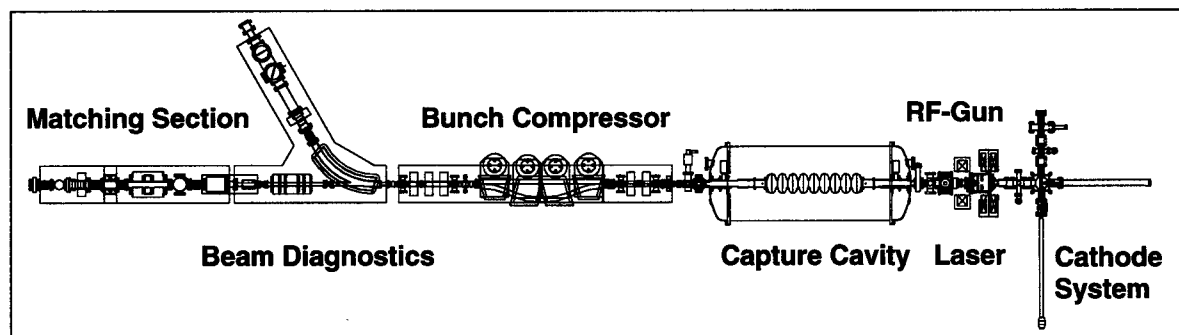
Figure 1: Schematic overview of the rf gun based TTF injector. (The laser system is not shown.)

improve the beam quality and to minimize the rf induced emittance growth. Although the rf is coupled transversely into the full cell, the distortion of the accelerating field is kept small. The focusing kick from a pair of solenoids is used to compensate [14] for space charge induced emittance growth. A 5 MW Klystron together with a modulator delivers rf pulses up to 1.2 ms length. The klystron power allows an accelerating gradient close to 50 MV/m. An extensive water cooling system is required for operation at full power. Since the gun is operated with very long rf pulses, a low level rf control system has been developed to stabilize amplitude and phase during the rf pulse. A system based on digital signal processors similar to the system used for the accelerating modules is used [15].

A summary of rf gun design and typical operating parameters is shown in Tab. 2.

Table 2: Some RF gun design parameters compared to typical operating values during the last runs.

Parameter		Design	Operated at
Ave. Gradient	MV/m	35	35 ... 43
Klystron Power	MW	2.2	2.2 ... 3.3
Av. Diss. Power	kW	22	0.11 ... 3.5
Rep. Rate	Hz	10	1 ... 5
RF Pulse Length	μs	800	50 ... 800
Bunch Charge	nC	8	1 ... 8
Bunch Spacing	μs	1	1
Bunch Length (rms)	mm	2	2 ... 4

4 THE CATHODE SYSTEM

Operating an rf gun with multiple high peak current bunches per train, a cathode with a high quantum efficiency is required to reduce the effort in laser construction. Cs_2Te was chosen, because high quantum efficiency for ps pulses (1 %) and high charge extraction over a reasonable operating time (more than 1000 h) was already obtained elsewhere [16]. Furthermore, the cathode response time is below 1° of 1.3 GHz (2 ps) [17], and is operated at a UV wavelength accessible to standard solid-state lasers ($\approx$ 260 nm).

However, its lifetime depends strongly on the vacuum quality, namely impurities like oxygen, CO_2, water, and hydrocarbons can considerable lower the lifetime. Their partial pressure has to be kept below $1 \cdot 10^{-11}$ mbar [18]. Therefore, a load-lock system has been developed allowing insertion and replacement of cathodes while maintaining ultra-high vacuum conditions. A prototype system has been built and is in operation at Fermilab [19].

The system at DESY was brought into operation in May 1998. It consists of three 3 major parts: a separate preparation chamber to prepare a stack of up to five cathodes, a transport chamber to transfer the fresh cathodes to the loading system, which is itself connected to the rf gun. Up to now, the transfer of cathodes was performed two times. One cathode was used from the first stack. It obtained a stable quantum efficiency of 0.5 % during the whole running period from December 1998 to March 1999. The second stack prepared in December 1998 contained a cathode of a novel type: the Molybdenum surface was polished to mirror quality prior to coating with Cs_2Te. This cathode was tested in the last week of the run. It reached a remarkable 5.9 ± 0.6 % efficiency with beam in the rf gun, stable over the whole test period. Furthermore, the dark current was reduced by a factor of 100 compared to the first cathode to less than 20 μA at 35 MV/m.

5 THE LASER SYSTEM

The laser design is challenged by the unusual requirement of providing synchronized ps UV pulses in very long trains of 1 ms length with ambitious stability requirements. The UV pulse energy has to be adapted to the charge required and the quantum efficiency obtained with the cathode: up to 800 pulses with 5 μJ for 8 nC and 1 % efficiency at 10 Hz. The decision for the specific design was also driven by the requirement of an operational system with a very high reliability and an up-time close to 100 % during running periods.

The laser is based entirely on the well known solid-state material Nd:YLF pumped with flash lamps. This material has a long fluorescence lifetime, high induced emission cross section, and very small thermal lensing. In a pulse train oscillator (PTO) a 2 ms long 54 MHz pulse train

is generated. The pulses are locked to the TTF master rf oscillator. An electro-optic modulator driven with 1.3 GHz enhances the phase stability to 1 ps (min/max). A pulse to pulse energy stability of better than 1 % (rms) before amplification is achieved. A Pockels-cell based pulse picker reduces the 54 MHz bunch train to 1 MHz with variable train length. This train is amplified by three single pass amplifiers to 250 μJ per single pulse. The UV (262 nm) generation with two nonlinear crystals has an efficiency of 10 %. A feed-forward system is applied to preset the shape of the flash lamp current pulse to obtain a flat pulse train [20]. A UV shot-to-shot energy variation integrated over 10 micro pulses of 2 % (rms) is achieved. The UV pulse length was measured with a streak camera [21] to be $\sigma_t = 8\pm1$ ps. The system was running 24 h per day during the last 3 month running period. The laser was available for beam 98 % of the running time.

6 EXPERIMENTAL RESULTS AND RUNNING EXPERIENCE

Since the rf gun has already been tested at Fermilab, the rf conditioning at DESY went smooth. The design field gradient of 35 MV/m was routinely achieved during the whole running period. For some experiments, the gradient was raised to 43 MV/m. The rf pulse length was limited to 50 μs and 1 Hz during the run for machine safety reasons, although the gun was conditioned at Fermilab up to 800 μs. It is planned to go to full rf pulse length at DESY during the next running period.

The charge transmission of the gun is linear up to 16 nC for nominal field and a hard edge laser spot size on the cathode of $r = 5$ mm. For charge densities above 20 nC/cm^2 we start to loose transmission. From Gauss' law we expect the limit at 35 nC/cm^2, were the space charge field compensates the acceleration field.

The beam energy has been measured with and without capture cavity: 3.8$\pm$0.1 MeV and 16.5$\pm$0.1 MeV resp. This corresponds well to the expected gradients deduced from the forward power. The view screen used for the energy spread measurements at 16.5 MeV allows at the moment only an estimate of the upper limit of $2.5 \cdot 10^{-3}$.

Two different techniques have been used to measure the emittance: a tomographic reconstruction of the phase space using the quadrupole doublet [22], and a slit system to mask out small bunchlets. From the bunch size and the divergence of the drifting bunchlets the emittance can be reconstructed. Both method use transition radiation created on aluminum foils to measure the bunch profiles. The data are still in evaluation, preliminary results for a 1 nC beam show a transverse emittance in the order of 5 to $8 \cdot 10^{-6}$m depending on the solenoid field settings.

7 REFERENCES

[1] For a list of members of the TESLA collaboration see ref [8].

[2] "Proposal for a TESLA Test Facility", TESLA Report 93-1, DESY 1992.

[3] TESLA-Collaboration, ed. D.A. Edwards, "TESLA Test Facility Linac – Design Report", DESY Print March 1995, TESLA 95-01.

[4] T. Garvey et al., "First Beam Tests of the TTF Injector", Proc. of the 1997 Particle Accelerator Conference, Vancouver, B.C., Canada, 12-16 May 1997.

[5] S. Fartoukh et al., "Evidence for a strongly coupled dipole mode with insufficient damping in TTF accelerating module", these proceedings (MOP110).

[6] The injector is based on Injector I built by IN2P3/LAL and IN2P3/IPN, Orsay and CEA/DSM DAPNIA, Saclay. Major contributions to the new installation at DESY are from Fermilab, Max Born Inst. Berlin, INFN Milano, DESY, INFN Frascati, INFN/Univ. Roma II, UCLA Dep.of Physics.

[7] "A VUV Free electron Laser at the TESLA Test Facility at DESY – Conceptual Design Report", DESY Print, June 1995, TESLA-FEL 95-03.

[8] M. Pekeler, "Experience of Superconducting Cavity Operation in the TESLA Test Facility", these proceedings (MOP111).

[9] S. Schreiber, "The RF-Gun based Injector for the TESLA Test Facility Linac", Proc. of the 6th European Particle Accelerator Conference, Stockholm, Sweden, June 22-26, 1998, p. 1462.

[10] I. S. Lehrman et al., Nucl. Instr. and Meth. A318 (1992) 247.

[11] E. Colby, "Design, Construction, and Testing of a Radiofrequency Electron Photoinjector for the Next Generation Linear Collider", PhD-Thesis, UCLA 1997.

[12] J.-P. Carneiro et al., "First Results of the Fermilab High-Brightness Photo-Injector", these proceedings (WEA60).

[13] B. Dwersteg et al., "RF Gun Design for the TESLA VUV Free Electron Laser", Proc. of the 18th International FEL Conference, Rome, Italy, Aug 26-30, 1996.

[14] B. E. Carlsten et al., Nucl. Instr. and Meth. A285 (1989) 313.

[15] G. v. Walter, Diploma Thesis, RWTH Aachen, to be published.

[16] E. Chevallay et al., Nucl. Instrum. Meth. A340 (1994) 146; G. Suberlucq, CERN-CLIC-NOTE-299, May 1996.

[17] R. Bossart et al., "CTF Developments and Results", Proc. of the 1995 Particle Accelerator Conference, Dallas, TX, May 1-5, 1995, pp. 719-721.

[18] P. Michelato et al., "Cs$_2$Te Photocathode for the TTF Injector II", Proc. of the 5th European Particle Accelerator Conference, Sitges, Spain, June 10-14, 1996, p. 1510.

[19] E. Colby et al, "Experimental Testing of the TTF RF Photoinjector", Proc. of the 1997 Particle Accelerator Conference, Vancouver, B.C., Canada, 12-16 May 1997.

[20] I. Will et al, "Feedback-stabilized Nd:YLF amplifier system for generation of picosecond pulse trains of an exactly rectangular envelope", Journal of Quantum Electronics 34 (1998), 2020-2029.

[21] The streak camera (ARP, Kehl, Germany) was made available to us by LAL, Orsay (France).

[22] M. Geitz, G. Schmidt, "Phase Space Tomography at the TESLA Test Facility", these proceedings (WEA132).

ION-SOURCE AND LOW-ENERGY BEAM-TRANSPORT ISSUES FOR H⁻ ACCELERATORS*

R. Keller

E. O. Lawrence Berkeley National Laboratory, Berkeley, CA

Abstract

H⁻ ions are being used in high-energy accelerators and spallation neutron-sources because of the efficiency with which they can be converted into protons at high energy, a mechanism utilized in schemes that provide injection into a ring by means of charge. This paper discusses new trends and recent developments in the field of H⁻ plasma generators, extraction systems, and Low-Energy Beam-Transport (LEBT) systems, with emphasis on low-emittance systems delivering beams in the 50-mA range.

1 INTRODUCTION

H⁻ ion beams have been utilized for many years with high-energy accelerators that include a synchrotron or storage ring because charge-exchange injection is an elegant way to eliminate the problems associated with extreme ramping requirements for injection kickers encountered with positive-ion facilities. Accelerator based spallation neutron-sources are likewise taking advantage of the property of H⁻ ions to efficiently undergo charge exchange into protons at energies up to a few GeV. Historically, magnetron-type [1] and H⁻-Penning-type [2] ion sources were the first ones to generate intense beams for this kind of accelerators.

A completely different line of H⁻ sources was developed in neutral-injection systems for magnetically confined fusion plasmas. These multi-cusp, or "bucket" sources were derived from proton sources when the desired beam energies started exceeding the 100-keV level where the charge-exchange process from protons to neutral hydrogen atoms is less efficient than the one from H⁻ to neutrals. Substantial progress has been made in the neutral injection field with the understanding of extraction and beam-formation processes in general, including beam transport and space-charge compensation phenomena. This knowledge is by now making its way into the former fields, leading to novel designs of accelerator front ends.

A review paper on H⁻ ion sources [1] has been recently published, covering a larger variety of source types and providing a useful general background. The present paper is narrower in focus and discusses recent work with H⁻ ion sources, and Low-Energy Beam-Transport (LEBT) systems, mostly involving bucket sources that are, or are planned to be, installed in spallation-neutron sources and high-energy accelerators.

Since the term "ion source" is subject to some ambiguity because it may or may not include an extraction system we will here distinguish between plasma generators that create the ions and extraction systems that provide beam formation. Extraction systems will be discussed in a separate chapter.

2 PLASMA GENERATORS

There are two basic mechanisms that lead to the generation of H⁻ ions, i. e., surface and volume production.

2.1 Surface Production Generators

Surface production essentially relies on the small electron affinity of alkaline metals, especially cesium, and plasma generators utilizing this mechanism have some or all inner surfaces coated with a cesium layer. Two representatives of this class are the magnetron and H⁻-Penning sources mentioned above. Maintaining an adequate cesium coverage, especially at higher duty factors is one of the challenges seen with these devices.

Another variety of surface-production H⁻ plasma generators [4] is lined with an external multi-cusp magnet configuration that ensures stable and quiet plasma confinement. The discharge is filament driven, and a converter electrode in the center of the discharge vessel is covered with cesium and biased by about -300 V with respect to the plasma potential. The converter attracts positive ions that are abundantly created in the hydrogen discharge, changes a fraction of them into H⁻ ions, and pre-accelerates and at the same time focuses them towards the outlet aperture. Figure 1 shows a schematic of these sources. A recent converter source [5] is quoted as generating 47 mA beam current at 12% duty factor, with 7.8 kW discharge power. In this device, the axial position of the converter electrode can be optimized on-line, and the discharge-chamber walls are designed to run at approximately 100° C, so as to impede condensation of cesium.

2.2 Volume Production Generators

Volume production of H⁻ ions relies on a very special plasma condition where vibrationally excited H_2 molecules are exposed to a flux of cold electrons and converted into atoms and H⁻ ions by dissociative electron attachment or H_2^+ and H_3^+ ions undergo dissociative recombination, again leading to H⁻ ions [6]. Unfortunately, this plasma

condition is not generally encountered in discharges that would produce high particle densities, suitable for the creation of intense ion beams. By separating the discharge plasma into two varieties, however, it became possible to consolidate these two contradicting requirements. This separation is achieved by introducing a magnetic dipole filter into the discharge vessel; only cold electrons and all ions can penetrate this filter at considerable rates, whereas faster electrons that are produced in the main chamber and sustain its plasma are repelled [7].
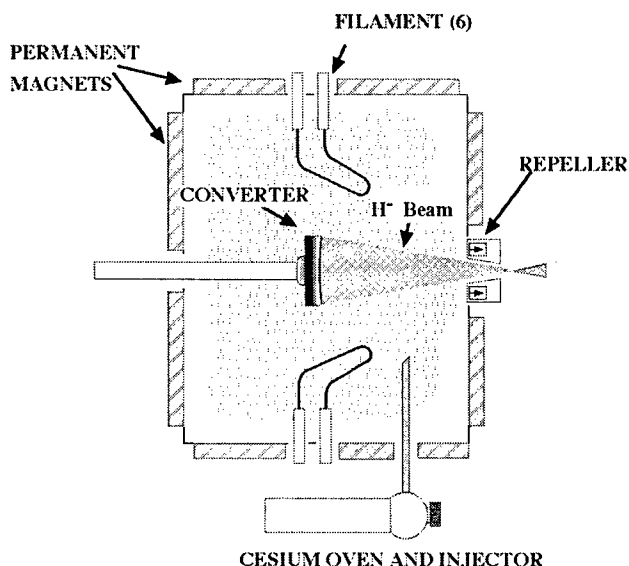
Figure 1. Schematic of a filament-driven converter plasma generator of the LBNL type [5]. The repeller electrode carries magnets that impede electrons from leaving the discharge vessel.

Volume-production H⁻ discharge-vessels are usually lined with multi-cusp magnets as well, offering the same benefits as in the case of converter devices. Recent versions of this plasma generator type, however, utilize rf power of 2 or 14 MHz frequency instead of filaments to maintain the discharge [8]. The power is coupled to the discharge by an internal antenna, using a variable impedance-matching network that can be adapted to the required plasma density.

Addition of a minute amount of cesium to the chamber surfaces near the outlet aperture enhances the production rate of H⁻ ions by about a factor of four, proportionally reducing the power needs to achieve a given beam intensity [9]. This technique in essence combines surface and volume production processes and also significantly reduces the electron density in the discharge, mitigating the electron-dumping problem that will be discussed below in more detail.

A schematic of a cesium-enhanced, rf driven, multicusp H⁻ ion source is shown in Fig. 2. One specimen of such a source is reported to have achieved 45 mA beam current at 6% duty factor from a 6.2-mm diameter outlet aperture [10].
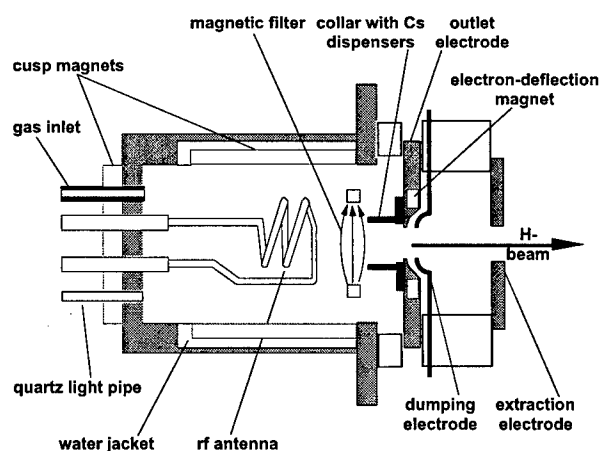
Figure 2. Schematic of an rf driven H⁻ ion source.

In principle, rf discharges offer higher lifetimes than those found with filament-driven plasmas because the rate of the sputtering process to which the thermionic filaments are subject can be reduced by covering the rf antenna with an insulating coating such as porcelain. Good electrical conductivity between metal and plasma is not needed in the case of an rf antenna. Application of such a coating, however, appears not yet to be fully controlled in all cases, and antennas used in rf-driven plasma generators have shown a wide range of lifetimes [3].

A significant improvement in antenna lifetime (2800 hours operation at 0.05% duty factor without any sign of wear) was achieved by widening the coil, thereby moving the conductor close to the discharge-chamber wall, and covering the entire coil on its inner perimeter by an alumina screen [3].

One research group has recently reversed the main trend for H⁻ plasma generators, exchanging their rf antenna for conventional thermionic filaments to drive a cesium-enhanced discharge in a multi-cusp vessel. The ion source and diagnostic layout is shown in Fig. 3. A beam current of 120 mA from is reported to be extracted from a 10-mm diameter aperture, when operating a 47.5-kW discharge power at 6% duty factor [11].

3 BEAM EXTRACTION

3.1 Electron Suppression

Extraction of a negative ion beam from a plasma presents a peculiar challenge not encountered with positive ions because large amounts of electrons are being extracted as well, and their space charge tends to deteriorate the quality of the ion beam. Furthermore, these electrons form a particle beam of substantial power that drains the extraction power-supply, and whose power load has to be absorbed by a target electrode. Accelerator H- ion sources therefore use various kinds of magnetic field configurations to suppress these electrons.
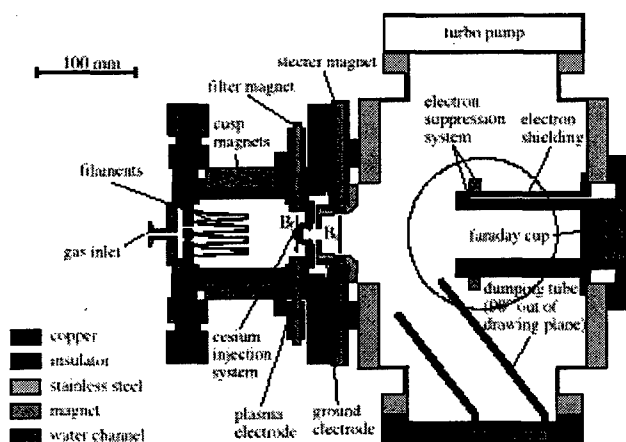
Figure 3. Layout of the Frankfurt H⁻ source with electron dump and Faraday cup.

Magnetic suppression can be achieved either at full beam energy, separating the electrons from the ion beam somewhere downstream of the extractor electrode as illustrated in Fig. 3, or by repelling them still within the discharge plasma itself. The latter way is being used in converter sources where one can take advantage of the higher ion energy provided by the converter bias-voltage. For volume-production sources, suppression of the electrons in an area where the ions have extremely low velocities would lead to serious problems with space-charge density, essentially inhibiting the formation of high-quality beams.

In a recent approach [10], the electrons are deposited on an intermediate, "dumping" electrode in the main extraction gap near the outlet electrode, as shown in Fig. 2. The separation of the electrons from the ion beam is achieved by inserting permanent magnets in the outlet electrode that generate a transverse dipole field in a location where the ions have already acquired some elevated speed. With this arrangement, the electrons can be entirely removed from the ion beam and deposited at the comparatively low energy of 5 keV.

Utilization of an electron-dumping field has its own price because this field exercises a weak steering action on the ion beam. This action could in principle be counteracted by yet another magnet field, but the simpler remedy consists in mechanically tilting the entire plasma generator with respect to the ideal beam axis through the adjacent LEBT. Model calculations let expect that no offset is needed, additionally to the tilt, to steer the beam onto the ideal axis [10]. The first ion source that is being built on the base of these calculations will have an adjustable tilt angle to avoid having to rely on code predictions.

3.2 Beam Simulation Issues

Apart from the steering angle introduced by the electron-dumping field, extraction systems for H⁻ ion-beams in general are rather conventional. Unfortunately, to this date there is no widely accepted code available that would allow simulating all essential physical processes that occur during the formation of an H- beam being extracted from a plasma. However, there are again two basic ways to deal with this problem, both involving the use of simulation codes for positive ions.

In the simple approach, the purpose of the calculations is reduced to minimizing the ion-optical aberrations of the extraction, or LEBT, system under the full space-charge load of the expected beam current. This approach appears to be more promising when the ions enter the extraction region already with considerable energy, as is the case with a converter source, because then the trajectories will be less influenced by the exact shape of the plasma meniscus that cannot be properly simulated. Examples of extraction/LEBT systems developed according to this principle are given in Refs. [12] and [13], applied to the plasma generator shown in Fig. 1. Results of beam simulations from Ref. [13] are displayed in Fig. 4.
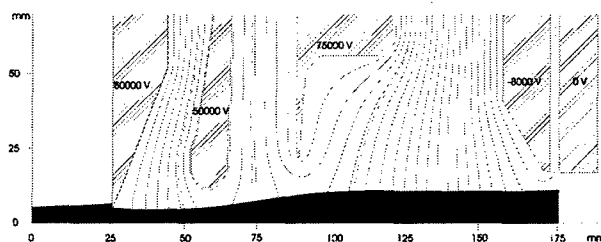
Figure 4. Optimized extraction/LEBT configuration for the LANSCE plasma generator, based on beam simulations using the code IGUN [14]. Electrode potentials as marked in this figure apply to a positive ion beam.

A more refined method makes new use of the fact that many modern simulation codes allow splitting the problem under investigation into smaller parts, with the aim of enhancing the resolution in more critical areas while not making excessive demands on computer memory and processing times where it is not warranted. Trajectory data obtained at the border of the first area are simply transferred as initial conditions into the subsequent area. In the case of negative-ion extraction from a plasma, the full ion and electron space-charge (electrons are best represented by their proton-current equivalent) is being considered in a zone near the outlet electrode, and trajectory data as well as equipotential shapes are computed.

The border between this zone and the subsequent one is chosen at a location where complete removal of the electrons from the ion beam can be reasonably assumed. In the second part of the problem, only the ion-beam space-charge is considered to be present [15].

With this method, even results from different codes can be merged, for example, introducing trajectories obtained from a 3-d code that is able to accommodate the influence of a magnetic electron-dumping field into a simpler one that assumes cylindrical symmetry of the in-

vestigated problem, with the benefit of higher resolution and greater speed in the latter part [10].

3.3 Current Measurements

One diagnostic issue related to extraction systems deserves careful attention, i. e. measurement of the extracted beam current in a Faraday cup. In the presence of an intense electron population within the beam, it is very easy to underestimate the danger of measuring electrons together with the negative ions, or of not fully suppressing secondary electrons. A simple validity check can be performed by operating the H⁻ plasma generator with helium gas, while still using a positive extraction voltage [10]. In this case electrons only will be extracted because helium does not form negative ions, and no signal should be measured in the cup if the electron separation from the main beam works as intended.

4 LEBT SYSTEMS

Low-Energy Beam-Transport (LEBT) systems for the ion sources under discussion usually have to perform multiple tasks. Their main function is to match the extracted H⁻ beam into the subsequent accelerator structure, such as an RFQ or a high-voltage column, giving the beam the desired radial size and angle. To be able to handle a variety of input conditions and allow empirical tuning to optimize the beam transport downstream of the LEBT, a wider range of decoupled matching parameters is convenient, but it requires at least two independent lenses. At the same time, the LEBT should include some beam-steering elements which may be magnetic, electrical, or simply of mechanical nature and provide adjustments of axis offset and tilt angle.

Facilities where the beam ultimately has to be extracted from a ring accelerator at GeV-level energies, such as spallation neutron sources, use beam chopping to avoid excessively activating their extraction septum. In view of the fact that a considerable fraction of beam is separated from the useful portion and has to be deposited somewhere, the main chopping function is most conveniently performed in the LEBT where the beam power is lowest, leaving the clean-up task where pulse flanks with nanosecond-range rise and fall times are shaped to some other beam-line structure.

As another set of requirements, a variety of diagnostics, notably of current and emittance, may be required from the LEBT in order to fully characterize the low-energy beam before it is injected into the subsequent accelerating structure.

Last not least, efficient pumping of the gas emitted from the plasma generator has to occur in the LEBT, the first place in the entire accelerator system where it can be performed. The art of the LEBT designer consists in fulfilling all these demands while keeping the beam emittance from growing excessively. And, in fulfilling those

tasks, compromises have to be made sacrificing less important features for the really essential ones.

4.1 Magnetic LEBT

The classic LEBT configuration for high-current ion beams easily reaches 1-m length or more and essentially consists of wide-bore magnetic lenses such as solenoids or quadrupole multiplets, diagnostic chambers, and vacuum pumps. The possibility of obtaining complete space-charge compensation in these structures by bleeding in a controlled amount of auxiliary gas used to be the desirable feature that led to this choice, allowing for relatively modest focusing-strength requirements.

Designers of H⁻ beam lines have adapted this concept, but the recent trend with beam currents around 40 mA goes towards much shorter structures. Apart from severe emittance growth, one problem will occur as soon as fast-rising pulse flanks are needed because of the finite time it takes to establish full space-charge compensation. Those parts of the beam whose space charge is not fully compensated will be focused differently than the main part and will be lost along the subsequent transport line.

A magnetic test LEBT using two solenoids [16] is shown in Fig. 5. This LEBT is rather short, and its diagnostic elements are supplemented by several instruments installed in a separate diagnostic chamber at its exit. In an operational beam line, insertion of such a chamber would severely degrade the beam quality; therefore it could only be used during commissioning, but this is a price to be paid in any case when highly efficient transport structures for high-current, high-brightness beams are designed. In this LEBT, compensating particles can be removed by six clearing electrodes.
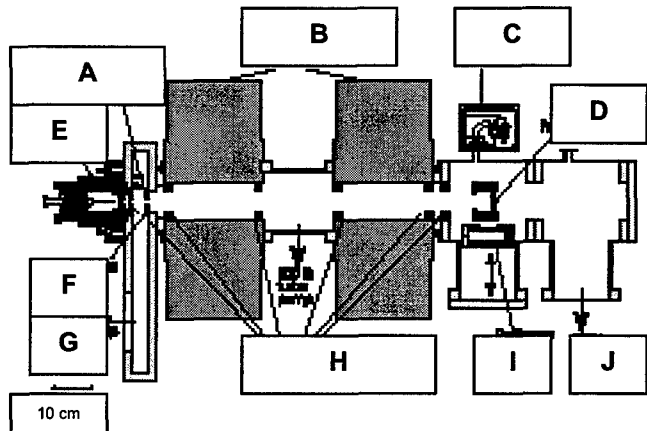
Figure 5. Short magnetic LEBT. A, Faraday cup, profile monitor. B, solenoids of 0.73 T, maximum. C, residual-gas ion-energy analyzer. D, Faraday cup. E, ion source. F, beam scraper. G, 500 l/s turbo pump. H, clearing electrodes. I, emittance scanner. J, 500 l/s turbo pump. A 200 l/s turbo pump is installed between the two solenoids.

4.2 Electrostatic LEBT

From a particle-optical standpoint there is not too much difference between magnetic and electrostatic lenses; a variety of design tools is available to optimize the geometrical shapes of either kind. Some practical issues, however, can determine a choice of one over the other. Electrostatic LEBTs can be built as "open" configurations, providing larger cross-sectional area for pumping than magnetic LEBTs. On the other hand, frequent sparking used to be a serious draw back associated with electrostatic transport systems that have to approach breakdown limits to achieve the intended properties.

Beam simulation codes are again helpful in developing optimized electrostatic structures that fulfill the optical requirements without compromising operational performance.

Fig. 6 shows a very compact electrostatic LEBT [17] designed for the Spallation Neutron Source presently under construction. Its main features include extraction at 81 kV for a final beam energy of 65 keV and two lenses separated by a ground electrode, with the second one being split into four isolated quadrants to facilitate dc steering as well as beam chopping with about 50-ns rise time [18]. The last of the electrodes acts as target for the chopped beam portions and is split into four quadrants as well, allowing to measure transverse beam offset on-line. To compensate for transverse offset against the ideal beam axis, the entire LEBT can be mechanically shifted with respect to the subsequent RFQ structure.
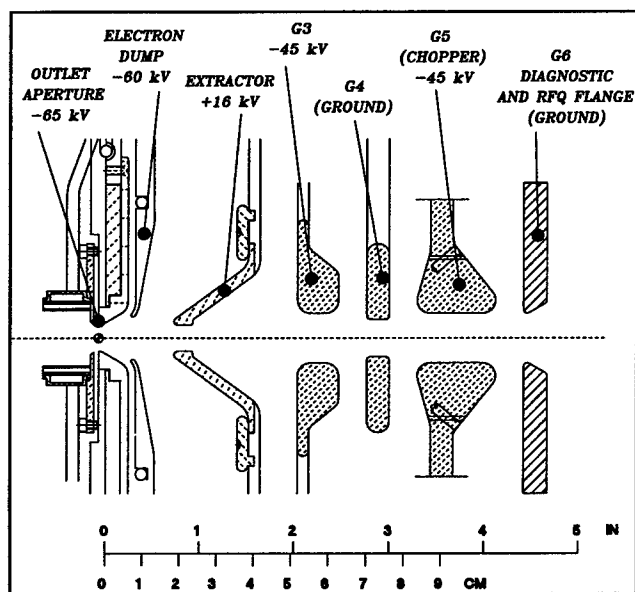
Figure 6. Electrostatic SNS LEBT [17].

5 ACKNOWLEDGMENTS

6 REFERENCES

[1] Yu.I. Belchenko, G.I. Dimov, and V.G. Dudnikov, Nuclear Fusion 14 (1974).

[2] V.G. Dudnikov, Proc. 4th All-Union Conf. On Charged Particle Accelerators, Moscow, 1974 – NAUKA vol. 1, p. 323 (1975).

[3] J. Peters, "Review of negative hydrogen high brightness/high current ion sources," Proc. 1998 Linac Conf., Chicago, IL.

[4] K.N. Leung and K.W. Ehlers, Rev. Sci. Instrum. 53, 803 (1982).

[5] M.D.Williams, R.A. Gough, R. Keller, K.N. Leung, D. Meyer, A. Wengrow, O. Sander, W. Ingalls, B. Prichard, and R. Stevens, "Ion Source Development for LANSCE Upgrade," Proc. 1998 Linac Conf., Chicago, IL.

[6] K.N. Leung, "Negative Ion Sources," in I.G. Brown, ed., "The Physics and Technology of Ion Sources," Wiley, New York, 1989.

[7] K.N. Leung, K.W. Ehlers, and M. Bacal, Rev. Sci. Instrum. 54, 56 (1983).

[8] K.N. Leung, "Radio Frequency Driven Multicusp Sources," Rev. Sci. Instrum. 69, 998 (1998).

[9] K. Saadatmand, J. Hebert, N. Okay, Rev.Sci.Instr. 62, 1173 (1994).

[10] M.A. Leitner, D.W. Cheng, S.K. Mukherjee, J.Greer, P.K. Scott, M.D. Williams, K.N. Leung, R. Keller, R.A. Gough, "High-Current, High-Duty-Factor Experiments with the RF Driven H- Ion Source for the Spallation Neutron Source," Submitted to 1999 Particle Accelerator Conf., New York.

[11] K. Volk, A. Maaser, H. Klein , "The Frankfurt H⁻ Source for the European Spallation Source," Proc. 1998 Linac Conf., Chicago, IL.

[12] R. R. Stevens, W. Ingalls, O. Sander, B. Prichard, and J. Sherman, "Beam Simulations for the H- Upgrade at LANSCE," Proc. 1998 Linac Conf., Chicago, IL.

[13] R. Keller, J.M. Verbeke, P. Scott, M. Wilcox, L. Wu, and N. Zahir, "A Versatile Column Layout for the LANSCE Upgrade," Submitted to 1999 Particle Accelerator Conf., New York.

[14] R. Becker, "New Features in the Simulation of Ion Extraction with IGUN," Proc. EPAC 98, Stockholm, Sweden (1998)

[15] M.A. Leitner, D. C. Wutte, and K.N. Leung, "2D Simulation and Optimization of the Volume H⁻ Ion Source Extraction System for the Spallation Neutron Source Accelerator," Proc. Int. Conf. On Charged Particle-Beam Optics, Delft, Netherlands (1998).

[16] A. Lakatos, J. Pozimski, A. Jakob, and H. Klein, "Extraction and Low Energy Transport of Negative Ions," Proc. 1998 Linac Conf., Chicago, IL.

[17] D.W. Cheng, M.D. Hoff, K.D. Kennedy, M.A. Leitner, J.W. Staples, M.D. Williams, K.N. Leung, R. Keller, and R.A. Gough, "Design of the Prototype Low Energy Beam Transport Line for the Spallation Neutron Source," Submitted to 1999 Particle Accelerator Conf., New York.

[18] J.W. Staples, J.J. Ayers, D.W. Cheng, J.B.Greer, M.D.Hoff, and A.Ratti, "The SNS Four-Phase LEBT Chopper," Submitted to 1999 Particle Accelerator Conf., New York.

REVIEW OF ION-SOURCE DEVELOPMENTS FOR RADIOACTIVE ION-BEAM FACILITIES

J. A. Lettry   CERN, Geneva

Abstract

The ion-sources dedicated to the production of radioactive ion beams (RIB) shall be highly efficient, selective and fast. This efficiency is mandatory since only limited amounts of radionuclides are produced. Chemical selectivity is needed to confine other elements near to the production site and to suppress isobaric contaminants. Eventually, the ion-source shall only delay the radioisotopes by a fraction of their half-life to reduce decay losses. The world wide spread RIB facilities came up with a large variety of solutions to meet part or all of these requirements such as: ion traps, surface, plasma, sputtering, electron cyclotron resonance and laser ion-sources.
In this review, the latest developments are presented and their applications to charge states breeder systems proposed for post-acceleration are discussed.

1 INTRODUCTION

Around the world, 23 radioactive ion beam facilities are currently in operation construction or planned [1-4]. Among them, the new generation facilities aims at more than one order of magnitude increased RIB intensities. Most of these schemes rely on an equivalent increase of the driver beam and on the development of targets able to cope with the deposited energy [4-8]. In Isotope Separation On Line (ISOL) facilities the isotopes are produced and stopped in the target and then transported as atoms by diffusion and effusion processes into the ion source (section 1.2-1.3). In Ion Guide Isotope On Line (IGISOL) facilities, the highly charged fragments recoiling from a thin target are stopped in a noble gas catcher where they rapidly decrease to the 1^+ charge state and keep this for a few milliseconds. In the mean time, they are transferred by the gas flow to the extraction and thus do not require any ion source. To overcome the missing chemical selectivity inherent to the IGISOL principle, the solution chosen by the Leuven group is to let the ions recombine in the gas catcher and then selectively reionize the wanted element (section 2.1).

The energy of the radioactive ion beam is dictated by the physics case requirements. A few eV for mass measurement, keV for solid state physics and atomic physics and many MeV/nucleons to reach and pass the coulomb barrier. The later requires a post acceleration of the low energy extracted ions. Cost effective post acceleration schemes requires a charge to mass ratio (q/M) in the region of ¼, the proposed charge state

1.1 RIB production mechanisms

The radioisotopes are produced by nuclear reactions between a projectile and a target [9]. The energy involved begins near the coulomb barrier with the fusion-evaporation reactions (complete fusion is at the origin of the super heavy elements). Neutron induced fission of heavy elements produces two neutron rich nuclei. At thermal energies, the isotopic distribution is the classical double peak of nuclear reactor (centered around A=95 and 140), which become broader with increasing neutron energy. The fragmentation of relativistic nuclei on a light target, or of heavy nuclei by relativistic light projectiles (called spallation in the case of relativistic protons) produces radioisotopes over the complete periodic table up to uranium. Obviously, the choices of the projectile, its energy and of the target material are crucial, witnessed by the efforts made in the computation and measurement of cross sections [10,11].

1.2 General criteria for target and ion-sources

The target region will become radioactive, its radio toxicity depends mainly on the proton number of both projectile and target and its activity on the projectile beam intensity and duration. Already on existing facilities, the exchange of target and ion source has to be remote controlled and repair works have to be made in hot cells and with manipulators. In addition, these works are preferably done after a few weeks to allow the short-lived elements to decay. Therefore, targets and ion sources shall be very reliable or designed as consumable items.

The ion source shall be highly efficient since the production rate is limited by the facility and cannot be increased. This is a major difference compared to ion sources producing beams of stable elements that are tuned to maximise the ion current.

The ion source shall be chemically selective to increase the beam purity and to confine the unwanted radioactive species near to the target area.

The emittance and the energy spread have to be small to match the requirements of the first separation stage (often a "simple" dipole magnet) and the acceptance of the post acceleration.

1.3 Selected ion sources used for the production of radioisotopes

A figure of merit of the 1^+-ion sources for RIB is presented in figure 1 as a function of the ionization potentials. Major deviation from the presented trends is the result of the chemical or metallurgical bounds, which may exist between the ion source material and the element to be ionized. Or simply due to the low mobility of the refractory elements even at very high temperature. Developments of chemical processes currently attempting to circumvent these limitations are described in this section.

High temperature surface ion sources: Saha and Langmuir described the ionizing properties of a hot surface. Positive ions are produced when the minimal energy needed to remove an electron from a surface (its work function) is larger than the ionization potential and negative ions are produced when the work function is smaller than the electron affinity of the atom impacting on the surface at thermal energies. The amplification effect (multiple hits on the surface) and the trapping after themalisation in a hot cavity (density $\approx 5\times10^{14}/cm^3$) filled with Xe were demonstrated by Kirchner [12,13]. Both techniques increase the efficiencies when compared to the prediction of the Saha-Langmuir model. Surface ionization remains the most efficient ionization scheme for low ionization potential radioisotopes (alkalis and some lanthanides) that are currently produced with W, WO_3 and Re surfaces. Negative chlorine, bromine, iodine and astatine have been efficiently produced on LaB_6 Surfaces [14]. The work function (and thus the ion source efficiency) depends on crystal orientation, temperature and cleanliness [15,16].

Electron Cyclotron Resonance (ECR) ion sources are known to produce very high currents of highly charged stable elements (e.g. $100e\mu A$ of Pb^{27+} for LHC [17]) and to very efficiently ionize gaseous elements (H_2, N_2, O_2, Cl_2 and noble gases). The extension of ECR to condensable or reactive radioisotopes is demonstrated in the following examples: The production-ionisation of condensable B and Be was achieved via a volatile fluorine molecular side band (BF^+ and BeF_2^+) [18]. The 2.2% efficiency obtained for $^7BeF_2 \rightarrow {}^7BeF_2^+$ is one order of magnitude below the results of the same ion source for gaseous elements (12% to 48% for 1^+ states) [19]. Using a volatile fluoromethane to transport ^{18}F, produced via the $^{18}O(p,n)^{18}F$ reaction, to the ECR, an efficiency of 0.3% was obtained for $^{18}F^+$ and 0.12% for $^{18}F^{2+}$ [20]. These successful applications of ECR ion sources to produce highly condensable or reactive materials also reveal the efficiency drop, tribute to the chemical nature of these elements.

Forced Electron Beam Induced Arc Discharge (FEBIAD) [21,22] are known for their efficient ionisation of gaseous and condensable elements (up to refractory and highly reactive like F and O) the ionisation occurs in a high temperature cavity by collision with 100-200eV electrons. The electrons are produced by a hot cathode and accelerated via a grid into a typically $1cm^3$-plasma chamber under low magnetic field. The production of 2×10^7 $^{17}F^+$/s via the $^{16}O(d,n)^{17}F$ reaction was achieved via a AlF molecular side band obtained by Al vapors diffusing through the HfO target and ionized with a FEBIAD type ion source. The efficiencies were 5%, 1.3% and 4% for the ^{19}F, ^{18}F (109.7m) and ^{17}F (64.8s) isotopes respectively. These values include the decay losses in the target [23].
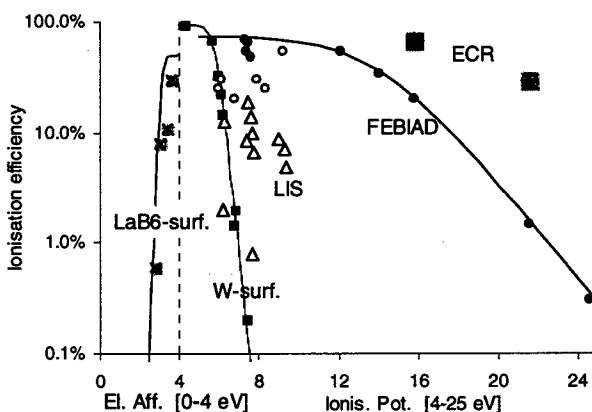
Figure 1 : 1^+ Ionization efficiencies measured with surface (black squares), plasma-FEBIAD (circles), laser (triangles) and ECR ion sources. The lines drawn to guide the eye represent the cases for which no chemical reaction occurs between the ion source materials and the element to be ionized. i.e. full and empty circles show the difference between the high and low temperature FEBIADs for condensable and volatile elements.

2 LASER ION SOURCES

Laser ion sources (LIS) are the last born of the RIB ion sources. The excitation energies are a unique fingerprint of each element. This is the origin of the high selectivity of resonant laser ionization methods [24]. Two LIS applications are described in the following sections.

2.1 Ion Guide Laser Ion Source (IGLIS)

The IGLIS developed at the LISOL separator [25] relies on the resonant laser ionization in a noble gas cell of the thermalized and neutralized recoil products [26]. The thin target sits in a gas cell filled with 500mbar helium or argon. Fission recoils have a wide energy distribution (up to 100MeV) which reduces the nearly 100% stopping efficiency down to 50%. The constant flow of the carrier

gas transports the radionuclides within typically 40ms from their stopping point to the region of ionization that is located in front of the opening hole. The purity of the gas is mandatory to suppress molecular sidebands. As a matter of fact, this method would allow detection of impurities in nobles gases at the ppt level. The release time-constant after laser ionization measured with stable ^{58}Ni is 10ms with a He carrier. Off line tests with argon showed that a fraction of the Ni$^+$ ion recombine before reaching the outlet, the effect is correlated with the observation of (NiAr)$^+$, (NiAr$_2$)$^+$ and (NiArH$_2$O)$^+$ charged molecules [27]. A major improvement in IGLIS systems was the replacement of the skimmer electrode used to separate the ions from the carrier gas by a sextupole ion guide (SPIG) [28]. The efficiency increased by a factor of 2 and the resolving power of the LISOL separator stepped from 300 up to 1450. Furthermore, a SPIG surrounded by a set of annular electrodes that are set at different potentials delivered ion bunches after 10ms confinement with an off line efficiency of 7% [29].

The IGLIS coupled to a SPIG or SPIG-trap is the system showing the least dependence on the chemistry of the recoiled element. The short time needed for transport and ionization essentially depends on the gas carrier. It had its first milestone with the successful production and ionization of the $^{54\text{-}55}$Ni (^{54}Ni: $T_{1/2}$ = 106ms [30]) and $^{68\text{-}74}$Ni isotopes and opens the door for the production of elements for which the laser ionization scheme is known (Ti, Ni, Co and Rh isotopes are currently produced). The IGISOL-SPIG combination is an elegant production scheme for all refractory elements (ionization potentials between 6.8 and 9.1eV).

2.2 Laser ion-sources in hot cavities

Stepwise resonant laser ionization in hot cavities is used for RIB production in ISOLDE [31] and ISIS [32]. The 2 to 3 laser beams are collinear to the axis of the metallic tube where the atoms effuse out of the target container. Dye lasers pumped by copper vapor lasers produce them. The UV light required for some transitions is obtained via frequency doubling or tripling of the dye laser light in non linear BBO crystals [33]. The lasers are pulsed at a frequency of 10 kHz, which corresponds to the typical 100µs needed for an atom of mass 10 to be pumped through the cavity. The electrons emitted from the cavity surface generate a negative potential well, which confines the positive ions. The ions then drift along the tube towards the extraction hole thanks to the electrical field generated by the ohmic heating of the cavity. The width of laser ionized bunches is typically 40µs FWHM for m=100amu. LIS-ions trapped in the high temperature cavity are confined in a 3×30mm size W- or Nb-tube at temperatures between 2100 and 2500K and released even 100 µs after ionisation [34]. Very short ^{139}La$^+$ ion bunches of 0.4µs duration were produced [35] which seems to correspond to LIS ionization restricted to the

ions localized in the extraction field region. The very high selectivity of the resonant laser ionization towards other elements is somewhat perturbed by the surface ionized elements. The choice of a low work function cavity like Nb and the micro gating of the LIS ion bunch effectively improves the selectivity.

Table 1. Off-line LIS ionisation efficiencies in high temperature cavities obtained by integrating the ion current of a typically 10µg sample. The sample was vaporised in a Ta-oven sealed to the rear of the LIS cavity. Radioisotope beams of each of these elements (but Mg) were produced.

Be	7.0%	[24]	Ag	14.0%	[39]
Mg	9.8%	[36]	Cd	8.8%	[34]
Mn	19.2%	[37]	Sn	8.5%	[40]
Ni	0.8%	[38]	Tm	2.0%	[41]
Cu	6.6%	[34]	Yb	12.5%	[41]
Zn	4.9%	[34]			

Hyperfine splitting (HFS) of the energy levels may exceed the line width of the laser (typically 5GHz) and reduce the efficiency. On the other hand, by reducing its line width, the LIS can be used to select between the spin states of a given isotope. This was experimentally shown on the ^{107m,g}Ag [42] and used for physics of the ^{70m,g}Cu [43], ^{155}Yb and ^{154}Tm [44,45] isotopes.

The fine-tuning of the laser frequencies shall also account for the isotope shift. Therefore, measurement of the isotope shift (thus on the mean square charge radius of heavy nuclides) is done by scanning the laser frequencies while recording the radioisotope production. The isotope shift of all Be isotopes [42] and of Yb and Tm isotopes [44] were measured with this technique. The efficiencies of hot cavity laser ion sources are given in table 1.

3 CHARGE STATE BREEDING 1$^+$/N$^+$

Post acceleration schemes require charge states with q/A of the order of ¼. In GANIL, in the framework of the SPIRAL [46] project, an ECR ion sources is foreseen for the ionization of high charge state radionuclides of noble gases, oxygen and nitrogen. However, for condensable elements, the charge state breeding of low energy 1$^+$-ion beams is a natural thought which is foreseen by TRIUMF, GANIL and ISOLDE. The 1$^+$/n$^+$ technique would dramatically reduce the activity deposited in the ECR or EBIS (Electron Beam Ion Source) breeders and thus ease their maintenance.

3.1 ECR based charge state breeding

The first experimental proof of an ECR based 1$^+$/n$^+$ scheme [47] showed the high sensitivity of the breeding efficiency on the energy of a condensable Rb$^+$ ion beam.

A Rb^+ beam must be decelerated from 18kV to 15±3eV in order to be captured in the ECR plasma, while for noble gases, the ionisation is at a flat maximum between 30 and 90eV. The losses resulting from the mismatch of the 1^+ beam emittance to the breeder acceptance were estimated as the ratio of the n^+ ionization efficiencies of the $1^+/n^+$ to the neutral/n^+ schemes and yields 50% for Argon [8]. The injection efficiency of the 1^+ beam into the ECR plasma at very low velocities was investigated with the $Cr^{1+} \rightarrow Cr^{11+}$ breeding. The emittance of the 18kV 1^+ beam was set from 40 to 6 πmm.mrad thus also reducing the total 1+ion current from 210 to 13 nA. The efficiency increased from 0.7% to 3.5% [48] as shown in figure 2. This result sets stringent requirement on the 1^+ beam emittance which shall be of the order of 5 πmm.mrad at 18kV.

The ECR Ion Trap (ECRIT) [49,50] operating in the after glow mode [51] is under development to bunch the high charge state ions as required by pulsed post acceleration schemes. The storage half-life of confined ions is typically $\tau_{1/2}$=360ms. The after glow ion bunch has a 1ms peak followed by a 5ms tail (pulse duration ~20ms). The efficiency measured for Rb^{15+} is a factor 2 lower than that of an ECR in continuous mode. 10^{11} Rb ions were simultaneously trapped in the ECRIT (full charge spectrum).
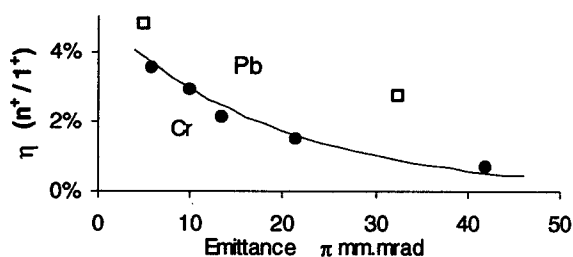
Figure 1. Cr^{11+} and Pb^{24+} Breeding efficiency (ECR continuous mode) vs. 1^+ ion beam emittance (18kV)[49].

Table 2 Charge state breeding efficiencies: $\eta(n^+/1^+)$ including the injection losses of the 1^+ beam. The confinement time τ in the breeder is given. The trapping efficiency of the penning trap is not included in the EBIS measurement (*).

	$\eta(n^+/1^+)$	τ ms			$\eta(n^+/1^+)$	τ ms	
Rb $^{9+}$	2.8%	50	[47]	Pb $^{24+}$	4.2%	200	[51]
Kr $^{9+}$	6.5%	60	[47]	Rb $^{15+}$	5.0%	200	[51]
Xe $^{14+}$	4.0%	70	[47]	Cr $^{11+}$	3.5%	200	[49]
Kr $^{9+}$	9.2%	100	[51]	*N $^{7+}$	30.0%	40	[53]
Ar $^{8+}$	9.0%	100	[51]	*Ar $^{14+}$	9.4%	40	[53]
Zn $^{9+}$	3.5%		[51]				

3.2 EBIS based charge state breeding

The REX-ISOLDE [52] experiment aims to accelerate the low energy ion beams of the ISOLDE facility up to 2.2MeV/u and perform in its first phase nuclear structure studies of the neutron rich isotopes of Na, Mg, K and Ca. EBIS provides high charge states, excellent beam quality and tunable time structure [53]. At a repetition rate of 50Hz, the EBIS is designed to deliver 10μs ion bunches of up to 2×10^7 ions. The emittance of the 60kV ISOLDE ion beams, typically 30π·mm·mrad has to be reduced to match the design acceptance (3π·mm·mrad) of the EBIS. A penning trap [54] working with low noble gas pressure of 0.01mbar was designed to accept, thermalize the ISOLDE beam decelerated to 70eV and deliver the ions as bunches with an emittance below 3π·mm·mrad. The trapping losses shall be overcompensated by the improved capture in the EBIS. The lifetime of trapped ions mainly depends on the purity of the gas, for Cs trapped in Ar, the lifetime yields 400ms independently of the total Ar pressure between 0.2 and 2.6 10^{-4} mbar [55]. The 1^+ confinement time in the REX trap is of the order of 10ms. The chemistry of the trapped element and its ability to bind to the rest gas traces should affect its trapping lifetime. The noble gas of the trap is therefore purified with a set of Zr-V-Fe non-evaporable getters. A summary of the available breeding data is shown in figure 3.
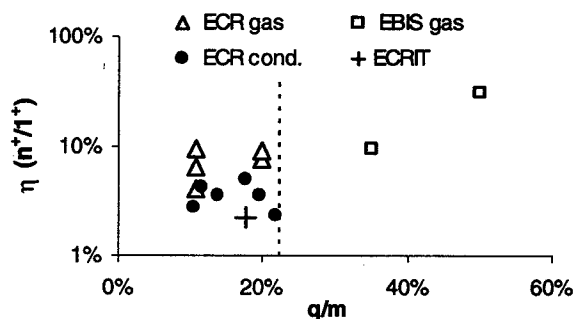
Figure 3 Charge state breeding efficiencies (including the injection losses) as a function of the charge to mass ratio. The values from table 2 are represented with triangles for gaseous, full dots for condensable or reactive elements ionized in an ECR breeder and squares for gaseous elements tested in the DIONE EBIS (Orsay). The q/m=1/4.5 dotted line is the specification of the REX-ISOLDE experiment.

4 CONCLUSION / SUMMARY

Complementary production mechanisms are available for the enthusiastic RIB community. The fast, efficient, and selective ion sources that exist for most elements are now tuned to specifically match the desired isotope. Beside the physics of ion sources and high temperature chemistry which rules the selectivity of ISOL ion sources, the ion guide and trap technologies [56-59] are

95

now a growing part of the equipment of RIB facilities. They adapt the phase space of high emittance ion beam to the acceptance of charge state breeder and linear accelerators. Last but not least, the intersection of nuclear medicine, biophysics, fundamental interactions studies, solid state, atomic, nuclear and astrophysics is research with radioactive ion beams and the origin of these fruitful developments.

5 REFERENCES

[1] A. C. Mueller, ENAM 98 AIP conf. proc. **455**, 933 (1998).

[2] I. Tanihata, ENAM 98 AIP conf. proc. **455**, 943 (1998).

[3] J. A. Nolen, ENAM 98 AIP conf. proc. **455**, 952 (1998).

[4] H. L. Ravn, Radioactive ion-beam projects based on the two accelerator or ISOL principle, Phil. Trans. R. Soc. Lond. A **365**, 1955 (1998).

[5] W.L. Talbert, T. A. Hodges, H.-H. Hsu and M. M. Fikani, Rev. Sci. Instr. **68**, 3019 (1997).

[6] W.L. Talbert,. CAARI 98, Denton AIP conf. Proc., 1998, to be published.

[7] J. R. J. Bennett, Nucl. Instrum. and Meth. B **126**, 105 (1997).

[8] L. Maunoury, PhD thesis univ. Caen France, 1998.

[9] H. Geissel, G. Münzenberg and K. Riisager, Ann. Rev. Nucl. Part. Sci. **45**, 163 (1995).

[10] J. Benlliure, F. Farget, A. R. Junghans, K. H. Schmidt, ENAM 98 AIP conf. proc. **455**, 960 (1998).

[11] M. V. Ricciardi, S. Monti, Tech. Report ENEA DT-SBD-0005, (1998).

[12] R. Kirchner, Nucl. Instrum. and Meth. A **292**, 203 (1990).

[13] R. Kirchner, Rev. Sci. Instr., **67**, 928 (1996).

[14] B. Vosicki, T. Björnstad, L. Carraz, J. Heinemeier and H. Ravn, Nucl instrum. and meth. **186**, 307 (1981).

[15] Handbook of thermoionic properties, V.S. Fomenko, Ed. G.V. Samsonov, Plenum press data division, Ney York (1966).

[16] Solid surface physics, J. Hölzl, F.K. Schulte and H. Wagner, Springer verlag Berlin, Heidelberg, New York (1979).

[17] C. Hill, and K. Langbein, Rev. Sci. Instr., **69**, 643 (1997).

[18] K. Jayamanna, Z. Zyuzin, L. Buchmann, G. Cojocaru, M. Dombski, T. Kuo, M. McDonald, P. W. Schmor, and D. Yuan. Rev. Sci. Instr., **69**, 756 (1997).

[19] K. Jayamanna, Z. Zyuzin, L. Buchmann, G. Cojocaru, M. Dombski, T. Kuo, M. McDonald, P. W. Schmor, and D. Yuan. Rev. Sci. Instr., **69**, 753 (1997).

[20] M. Cogneau et al., Nucl. Instrum. Meth. A **420**, 489 (1999).

[21] R. Kirchner and E. Roeckl, Nucl. Instrum. and Meth. **133**, 187 (1976).

[22] R. Kirchner, K. H. Burkard, W. Hüller and O. Klepper, Nucl. Instrum. and Meth. **186**, 295 (1981).

[23] ORNL http://www.phy.ornl.gov/hribf/beamdevel/yields.htm
http://www.phy.ornl.gov/hribf/ribinjector/ionsource/sor.htm

[24] V. N. Fedoseyev, CAARI 98, Denton AIP conf. Proc., 1998, to be published.

[25] M. Huyse et al., Nucl. Instrum and Meth. B **70**, 50 (1992).

[26] Y. Kudriavtsev, A. Andrzejewski, N. Bijnens, S. Franchoo, J. Gentens, M. Huyse, A. Piechaczek, J Sezerypo, I. Reusen, P. Van Duppen, P. Van den Bergh, L. Vermeeren, J. Wauters and A. Wöhr, Nucl. Instrum. and Meth. B **114**, 350 (1996).

[27] Y. Kudriavtsev, S. Franchoo, J. Gentens, M. Huyse, R. Raabe, I. Reusen, P. Van Duppen, P. Van den Bergh, L. Vermeeren and A. Wöhr, Rev. Sci Instr., **69**, 738 (1997).

[28] P. van den Bergh, S. Franchoo, J. Gentens, M. Huyse, Yu. A. Kudriavtsev, A. Piechaczek, R. Raabe, I. Reusen, P. Van Duppen, L. Vermeeren, A. Wöhr. Nucl. Instrum. and Meth. B **126**, 194 (1997).

[29] S. Fujitaka, M. Wada, H. Wang, J. Tanaka, H. Kawakami, I. Katayama, K. Ogino, H Katsuragawa, T. Nakamura, K. Okada, S

[30] I. Reusen, A. Andreyev, J. Andrzejewski, N. Bijnens, S. Franchoo, M. Huyse, K. Kruglov, Y. Kudriavtsev, W. F. Muller, A. Piechaczek, R. Raabe, K. Rykaczewski, J Sezerypo, P. Van Duppen, L. Vermeeren, J. Wauters and A. Wöhr, Submitted to Phys. Rev. C (1998).

[31] V.I. Mishin, V.N. Fedoseyev, H.J Kluge,V.S. Letokhov, H.L. Ravn, F. Scheerer, S. Sundell, Y. Shirakabe, O. Tengblad. Nucl. Instrum. and Meth. B **73**,550 (1993).

[32] A. E. Barzakh, V.P. Denisov, D.V. Fedorov, S. Yu. Orlov, M.D. Seliverstov, Nucl. instrum. and meth. B **126**, 85 (1997).

[33] N. Erdmann, V. Sebastian, V.N. Fedoseyev, M. Hannawald, G. Huber, T. Kautzsch, K.-L. Kratz, V.I. Mishin, M. Nunnemann, G. Passler, N. Trautmann , European Physical Journal A **66**, 431 (1998).

[34] J. Lettry, R. Catherall, G.J. Focker, O. C. Jonsson, E. Kugler, H. Ravn, C. Tamburella, V.N. Fedoseyev, V.I. Mishin., G. Huber, V. Sebastian, M. Koizumi, U. Köster, Rev. Sci Instrum., **69**, 761 (1997).

[35] M. Koizumi, A. Osa, T. Sekine, M. Kubota, Nucl. Instrum. and Meth. B **126**, 1997, 100.

[36] Mg LIS, ISOLDE Collaboration, mars 98 to be published .

[37] V.N. Fedoseyev, K.Bätzner, R. Catherall, A.H.M. Evensen, D. Forkel-Wirth, O.C. Jonsson, E. Kugler, J. Lettry, V.I. Mishin, H.L. Ravn, G. Weyer, Nucl. Instrum. and Meth. B **126**, 88 (1997).

[38] A. Jokinen et al., Nucl. Instrum. and Meth. B **126**, 98 (1997).

[39] Y. Jading, R. Catherall, V.N. Fedoseyev, A. Jokinen, O.C. Jonsson, T. Kautzsch, I. Klöckl, K.L. Kratz, E. Kugler, J. Lettry, V.I. Mishin, H.L. Ravn, F. Scheerer, O. Tengblad, P. Van Duppen, W.B. Walters, A. Wöhr, Nucl. Instrum. and Meth. B **126**, 76 (1997).

[40] V. N. Fedoseyev Res. Ion. Spectr. AIP conf. Proc. **329**, 465.

[41] V.I. Mishin et al., Nucl. Instrum. and Meth. B **73**, 550 (1993).

[42] V. Sebastian, R. Catherall, G. Huber Y. Jading, O. Jonsson, M. Koizumi, K.-L. Kratz, E. Kugler, J. Lettry, V.I. Mishin, H. Ravn, C. Tamburella, A. Wöhr. ENAM 98, AIP conf. Proc. **455**, 126 (1998).

[43] U. Köster et al., to be published in Nucl. Instrum. and Meth.

[44] A.E. Barzakh, I.Y. Chubukov, D.V. Fedorov, V.N. Panteleev, M.D. Seliverstov, Y.M. Volkov, ENAM 98 AIP conf. Proc. **455**, 94 (1998).

[45] A.E. Barzakh, I.Y. Chubukov, D.V. Fedorov, F.V. Moroz, V.N. Panteleev, M.D. Seliverstov, Y.M. Volkov, The European Physical Journal A Abstract Vol. **1**, 3 (1998).

[46] SPIRAL, GANIL report R-94-02, Caen 1994.

[47] C. Tamburella, J. L. Belmont, G. Bizouard, J. F. Bruandet, R. Geller, G. Simond, B. Vignon, Rev. Sci. Instr. **68**(6) 2319 (1997).

[48] J.F. Bruandet, N.Chauvin, J.C. Curdy, T. Lamy, P. Sortais. Rapport Interne: R.I. ISN Grenoble 98.99.

[49] N. Chauvin, J.F. Bruandet, J.C. Curdy, R. Geller, T. Lamy, P. Sortais, Nucl. Instrum. Meth. A, **419**, 185 (1998).

[50] J.-L. Bouly, J.F. Bruandet, N.Chauvin, J.C. Curdy, R. Geller, T. Lamy, P. Sole, P. Sortais. EPAC98, Stockholm conf. Proc. 1403 (1998).

[51] P. Sortais, Rev. Sci. instr. **63**, 2087 (1992).

[52] D. Habs et al., proposal to the ISOLDE committee CERN-ISC 94-25.

[53] M. P. Stockli et al., Rev. Sci. instr. **69**, 665 (1998).

[54] F. Ames, G. Bollen, G. Huber, P. Schmidt, Proc. of ENAM 98, 927 (1998).

[55] S. Schwarz, PhD thesis 98-24, Univ. Mainz (1998).

[56] G. Savard, Nucl. instrum. and meth. B **126**, 361 (1997).

[57] H. Raimbault-Hartmann, B. Beck, G. Bollen, M. König, H.-J. Kluge, E. Schark, J. Stein, S. Schwarz, J. Szerypo, Nucl. Instrum. and meth. **126**, 378 (1997).

[58] G. Bollen et al., ENAM 98, AIP conf. proc. **455**, 981 (1998).

[59] A. Jokinen, J. Äystö, P. Dendoven, V. S. Kolhinen, J. Huikari, A. Nieminen and K. Peräjärvi, ENAM 98, AIP conf. proc. **455**, 981 (1998).

FREQUENCY UPGRADING OF THE SUPERCONDUCTING ECR ION SOURCE SERSE

G. Ciavola, S. Gammino, M. Castro, L. Celona, F. Chines, S. Marletta,
INFN-LNS, Via S. Sofia 44, 95123 Catania, Italy

Abstract

The installation of the superconducting ECR ion source SERSE at LNS and its commissioning have been successfully accomplished during last year. The problems related to LHe supply and high voltage insulation have been solved and the source is now fully operational with currents that are equal or greater than any other already operating ECR ion source.

Recently the upgrading to higher field and frequency (from 14.5 GHz to 18 GHz) has been carried out, in order to increase further the plasma density and then the beam currents. The preliminary results of the study of magnetic field scaling are reported, along with the experimental evidence of the "two frequency heating" (14.5 and 18 GHz), according to the experience of LBNL source.

The source is going to be coupled to the K-800 Superconducting Cyclotron and it will allow a significant increase of the intensity (one to two order of magnitude) and of the energy of the extracted beams, with respect to the injection of beams from 15 MV Tandem, used up to now.

1 INTRODUCTION

The design of the superconducting Electron Cyclotron Resonance (ECR) ion source SERSE is described in previous papers [1,2,3]. Tab. 1 describes its main features. SERSE was designed on the basis of the concept of High B mode [1,4] that relates the performance of the ECR ion sources to the frequency and to the strength of the magnetic confining trap, with a scheme, which is complementary to the Geller's scaling laws [5].

The source construction has begun in fall 1993 and in 1995 all the components were operational, except the hexapole, which was able to attain only 70% of the nominal field, a value which did not meet our request to operate the source in High B mode (i.e. with a magnetic field exceeding the value of $2 \cdot B_{ECR}$, where B_{ECR} is the resonance magnetic field, corresponding to 0.52 T for the frequency of 14.5 GHz and 0.64 T for the frequency of 18 GHz).

Therefore we could not accept the magnets and we ordered a new set of superconducting magnets, which resulted in a delay of almost two years for the whole project. Finally in spring 1997 the magnets were ready and operating above the specification [2] and in summer 1997 the first beams of highly charged ions were obtained, with already excellent performance [3]. The tests on the bench site of Grenoble were completed in March 1998 and the source was moved to LNS, where it was operated at 14.5 GHz for a few months.

Table 1: The main features of SERSE

Frequency	18 GHz + 14.5 GHz
Type of launching	WR62, off-axis
Axial maxima distance	490 mm
B_{max} (injection side)	2.7 T
B_{min}	0.3 to 0.6 T
B_{max} (extraction side)	1.6 T
Resonance zone length	< 100 mm
Hexapole length	700 mm
B_{rad} (at chamber wall)	1.55 T maximum
ϕ plasma electrode	8 mm
ϕ puller	12 mm
Extraction voltage	30 kV max

Figure 1 - The source SERSE.

In fig. 1 the source is shown; the stainless steel plasma chamber (ϕ=130 mm) is surrounded by the hexapole, which is enclosed into a structure on which the solenoids are placed. Both the hexapole and the solenoids are made by superconducting wires. On the right there are the microwave and gas inputs and on the left the three-electrode extraction system. A biased disk is placed on-axis at the injection side and can be moved along the same axis. Pumping units at the injection and extraction side provide an operational vacuum of about 2 to $5 \cdot 10^{-8}$ mbar, without plasma (typical values with gas and plasma are 1 to $4 \cdot 10^{-7}$ mbar).

2 FREQUENCY UPGRADING

In a recent paper [6] we estimated that the source SERSE, operated with a 18 GHz generator, should increase its plasma density of about 60% as compared to 14.5 GHz operations and then an increase of current of the same order of magnitude was expected. The condition for the upgrading is that the magnetic field is also scaled by the same factor as the frequency, being B_{ECR} proportional to the frequency.

In fig. 2 the axial magnetic field is shown; the radial confining field was also increased from 1.1 T to 1.45 T.

Except for a few cases, a significant increase of currents was observed, as described in tab. 2.

It needs to be pointed out that the test with increased frequency were carried out with a lower available power (our 18 GHz generator is able to give only 1100 W, in spite of nominal 1500 W). We focused our attention on the production of Xenon high charge states, which beams were at least a factor 1.6 larger with respect to the ones measured at 14.5 GHz. This increase was not only obtained with the higher frequency but even other factors played a role, as the improvement of chamber conditioning and the use of ^{18}O as mixer, according to the experience gained at KVI with the "anomalous isotope effect" [7], which increased the currents of about 20%.

Figure 2 – Axial magnetic field of SERSE.
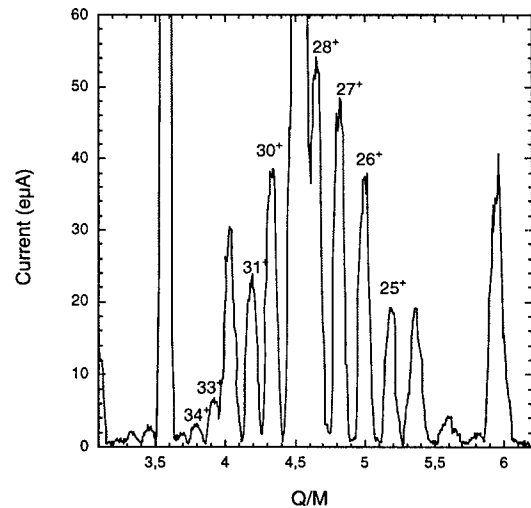
Figure 3 – A charge state distribution for Xenon, optimized for 30^+.

We also operated the source with the "two frequency heating" [8] and the results were not clear, although the currents were higher. The two frequency heating was more effective in the case that the volume of the second resonance was narrow and the amount of power was poor (50 to 90 W). In this case an average increase of 20 to 50% of the xenon currents was measured for the highest charge states, because of the higher plasma density and of the presence of two resonance surfaces.

In fig. 3 a typical charge state distribution for Xe is shown (power was 1040 W at 18 GHz and 60 W at 14.5 GHz). Charge states up to 38^+ were obtained just by decreasing the gas input.

Table 2: Typical currents (in eμA) produced by SERSE

	14.5 GHz	18 GHz
O^{7+}	200	208
O^{8+}	40	55
Ar^{14+}	80	84
Ar^{16+}	17	21
Ar^{17+}	1	2.6
Ar^{18+}	0.05	0.4
Kr^{22+}	46	66
Kr^{25+}	20	35
Kr^{27+}	4.5	7.8
Xe^{27+}	45	78
Xe^{30+}	12	38.5
Xe^{33+}	1.5	9.1
Xe^{34+}	1	5.2
Xe^{36+}	0.4	2
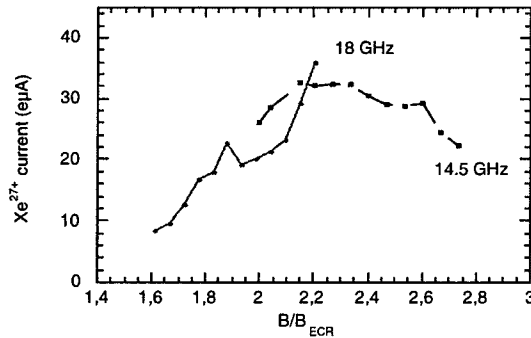
Figure 4 – Xe^{27+} currents for different radial field, with gas mixing and biased disk.
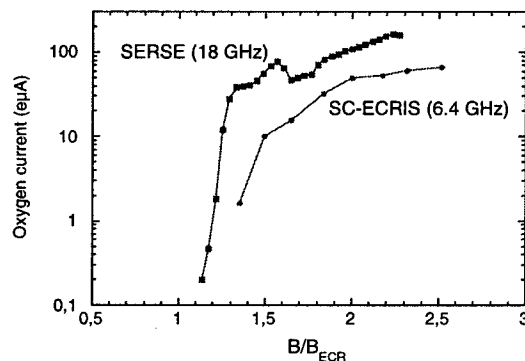
Figure 5 – O^{7+} current for SC-ECRIS (6.4 GHz) and SERSE (18 GHz) for different radial field.

3 MAGNETIC FIELD SCALING

Systematic tests about the magnetic field scaling for the operations at 14.5 GHz and 18 GHz were carried out with the same procedure already used for SC-ECRIS at Michigan State University [9]. The trend that was observed for SERSE was quite similar to the one reported in [9], as it is shown in fig. 4.

The currents increase up to value around $2 \cdot B_{ECR}$ then they remain stable or decrease. Similar results have also been obtained for axial field scaling: a larger axial field than $4 \cdot B_{ECR}$ on the injection side improves the plasma stability, as already observed for SC-ECRIS at Michigan State University [9].

In fig. 5 the comparison between the results of SERSE and the ones of SC-ECRIS is presented for O^{7+}. It can be seen that, except for the absolute values of the current, the shape of the curves is quite similar for the two sources.

The maximum current is not scaled with the square of frequency, as it is foreseen by the Geller's scaling laws, because space charge effects at the extraction play a role (total current is above 4 mA for SERSE, through an extraction hole of 8 mm).

4 CONCLUSIONS

It can be concluded that:
- a radial field above $2 \cdot B_{ECR}$ is necessary to have an optimum confinement and to improve the production of highly charged ions;
- axial field above $4 \cdot B_{ECR}$ for the axial field at injection and $2 \cdot B_{ECR}$ to $3 \cdot B_{ECR}$ are needed too;
- the frequency scaling is effective, provided that the magnetic field is high enough, as we underlined some years ago [4].

The results that we have obtained with SERSE have confirmed the validity of our choice to build an ECR ion source with superconducting magnets, even if the time for the construction has been long and the investments have been relatively high. In fact, the operations of the K-800 Superconducting Cyclotron [10] will benefit of the performance of SERSE, which allows to boost the currents extracted from the cyclotron and also to rise the energy, especially for the heaviest ions.

The former result is particularly important, because the EXCYT project [11] needs high currents of fully stripped light ions (up to 5 pµA) that cannot be provided with the radial injection by means of the Tandem, and that can be provided with the axial injection by means of SERSE.

5 ACKNOWLEDGEMENTS

6 REFERENCES

[1] G. Ciavola, S. Gammino, Rev. Sci. Instr. 63(4), (1992) 2881
[2] P. Ludwig et al., Rev. Sci. Instr. 69(2), (1998) 653 and references therein
[3] P. Ludwig et al., Rev. Sci. Instr. 69(12), (1998) 3312
[4] S. Gammino, G. Ciavola, Plasma Sources Science & Technology 5, (1996), 19
[5] R. Geller et al., Proc. of the 8th Workshop on ECR ion sources, East Lansing (1987) 1
[6] S. Gammino, G. Ciavola, Rev. Sci. Instr. 69(8), (1998), 3081
[7] A.G.Drentje et al., Rev. Scient. Instrum. 67(3), (1998), 953
[8] D. Xie, C.M. Lyneis, Rev. Sci. Instr. 66(8), (1995) 4218
[9] S. Gammino et al., Rev. Sci. Instr. 67 (12), (1996) 4109
[10] D. Rifuggiato et al, "First years of operation with the Superconducting Cyclotron", Proc. of the 15th Conf. on Cyclotrons and Appl., Caen, June 1998, in press
[11] G. Ciavola et al., these proceedings

A 500 MeV-100μA PROTON TARGET FOR THE ISAC RADIOACTIVE ION BEAM FACILITY

Pierre Bricault, Marik Dombsky, Paul Schmor, Guy Stanford, Ian Thorson and Jaroslav Welz

TRIUMF, 4004 Wesbrook Mall, Vancouver, BC, Canada

Abstract
The construction phase of the ISAC radioactive ion beam (RIB) facility is now completed. The ISAC RIB facility utilizes the Isotopic Separation On Line (ISOL) production method. The ISAC facility includes: a new building with 5000 m^2 of floor space, a beam line with adequate shielding to transport up to 100 μA of proton at 500 MeV from the H⁻ TRIUMF cyclotron to two target stations, remote handling facilities for the targets, a high resolution mass separator, a linear accelerator and experimental facilities. A novel approach for the target/ion source station is described. The target/ion source assembly and heavy ion optic components are located in a shield canyon under 2 m of steel shielding plug. A separator is to be coupled with either a low energy experimental area or to a linear accelerator for post-acceleration up to 1.5 A MeV.

1 INTRODUCTION

The TRIUMF's ISAC uses the isotope separation on line (ISOL) technique to produce radioactive ion beams (RIB). The ISOL system consists of a primary production beam, a target/ion source, a mass separator, and a separated beam transport system. These systems together act as the source of radioactive ion beams to be provided to the accelerator or the low-energy experimental areas. We utilize the 500 MeV - 100μA primary proton beam extracted from the H- cyclotron [1]. A new beam line has been built to transport this beam to one of the two target stations followed immediately by a residual proton beam dump. The target station contains proton beam monitoring equipment, production target and ion source, a beam dump, and the front-end heavy ion beam optics. A strategy has been adopted in which the target station is contained in a heavily shielded building connected directly to a hot cell facility. This approach is based on the successful experience at TRIUMF of vertically servicing and remote handling of modular components embedded in a close-packed radiation shield, coupled with the requirement for quick access to the production target and of containment of any mobile activity. Careful design of both the modular components and the remote-handling systems was carried out to ensure the operational viability of this system.

The effective operation of the ISOL system is crucial to the overall ISAC facility performance. It is therefore essential that we build in as much flexibility as possible. The target/ion source module is the key component. It must be serviced, or modified and exchanged on a regular basis to satisfy the varying demands of the physics program. Its design addresses many difficult aspects, including high voltage services, containment of radioactivity, accommodation of different target/ion source combinations, radiation-hard components, and ease of remote handling.

Existing target designs can accommodate up to 10 μA beam intensities and the available intensities of many radionuclides can be expected to scale with the proton beam currents. But, production targets capable of withstanding proton beam intensities up to 100 μA without compromising the yield of radioactive isotopes will be a future challenge. Several approaches to the dissipation of the power deposited in such targets by the proton beam have been investigated and a realistic solution for the removal of the heat from the target container seems possible. The heat transfer within the target material itself, however, is highly target dependent and it is clear that 100 μA operation will be limited at least initially to only a few target's materials. Some of the problems may have to be addressed near the 10 μA level but, in general, heat has to be supplied to the target system to maintain the prescribed temperature. The development of high power target is the subject of a development program at TRIUMF.

2 TARGET STATION

The ISAC target-handling concept and the ISAC target facility is based on fifteen years of experience at operating meson factories. The meson production target and beam stop areas of these facilities have power dissipation and radiation levels similar to, or greater than, those expected at ISAC. Meson factory experience shows that the correct approach to handle components in high-current and thick-target areas is to place them in tightly shielded canyons. Access to the components is done vertically and repair and service is made in dedicated hot cells.

Three important factors not encountered in the meson factory targets have to be addressed. These are: the containment of large amounts of mobile radioactivity; the high voltage required for beam extraction; and quick routine replacement of short-lived target systems. In the present design these issues are solved by placing the target in a sealed self-contained module which can be transferred directly to the hot cell facility for maintenance.

The target stations are located in a sealed building serviced by an overhead crane. The target maintenance facility includes a hot cell, warm cell, decontamination facilities and a radioactive storage area. The target area is sufficiently shielded so that the building is accessible during operation at the maximum proton beam current.

Beam-line elements near the target are installed inside a large T-shaped vacuum chamber surrounded by close-packed iron shield. This general design eliminates the air activation problem associated with high current target areas by removing all the air from the surrounding area. Figure 1 shows a plan view of the target stations area. The design breaks naturally into modules; an entrance module containing the primary beam diagnostics, an entrance collimator and a pump port; a beam dump module containing a water cooled copper beam dump; a target module containing the target/ion source, extraction electrodes and first steering component and heavy ion diagnostics; and two exit modules containing the optics and the associated diagnostics for the transport of heavy ion beams. Figure 2 shows a three-dimensional view of the target/ion-source module. Each module represents 2 m of shielding steel. The target and the two exit module are identical in size and each of them has a service cap and a containment box where most of the volatile contamination will be contained. Figures 3 and 4 show a section view along the proton beam and heavy-ion beam axis respectively. On those figures we can notice the close

packed iron and concrete shielding which will allow us to operate the target at 100 μA.

The vacuum design seeks to eliminate the need for radiation-hard vacuum connections at beam level by using a single vessel approach. The front-end components, with their integral shields, are inserted vertically into the T shaped single large vacuum vessel. Most vacuum connections are situated where elastomer seals may be used. Only two beam-level connections exist: one at the proton beam entrance and one at the heavy ion beam exit.

Target Hall
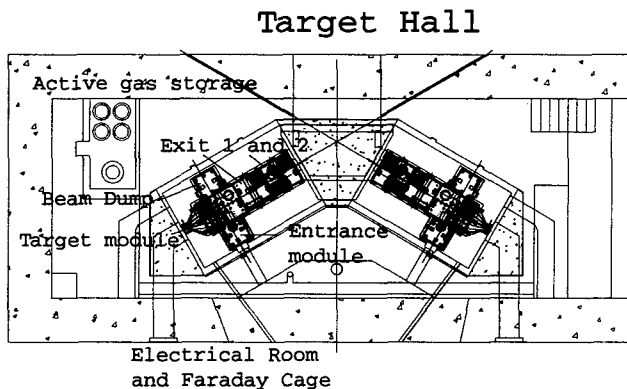
Fig. 1 – Plan view of the ISAC two target stations.
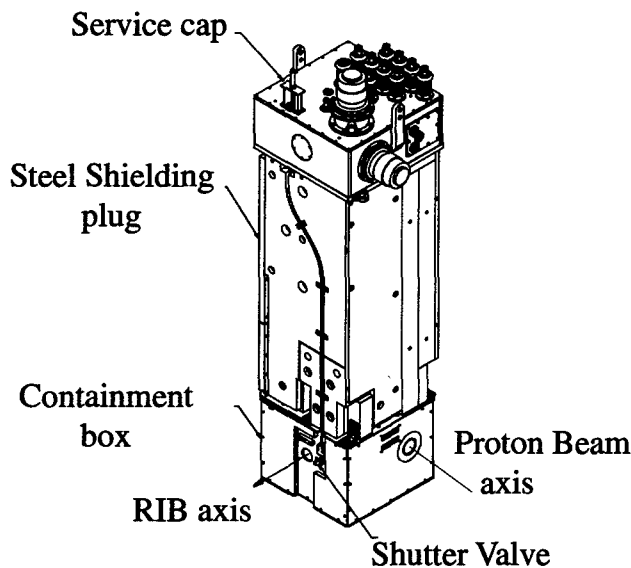
Fig. 2 – Three dimensional view of the target/ion source module.

3 REMOTE HANDLING

An effective remote handling and servicing system will be required to bring about quick and frequent target changes. All modules in the target area will have high levels of residual activity and will be potentially contaminated with mobile activity. Both aspects are considered in the handling design.

Target component maintenance involves disconnecting services and craning the module to the hot cell. Removing the concrete blocks covering the target station gives the overhead crane access to the modules. While the target module is pulled out of the canyon personnel are excluded from the target hall. Target module transfers to the hot cell must therefore be done completely remotely. The connection and disconnection of the target module

services can be done manually since the shielding of the module is thick enough to allow hand-on operation.

Section view along the proton beam axis of the target station
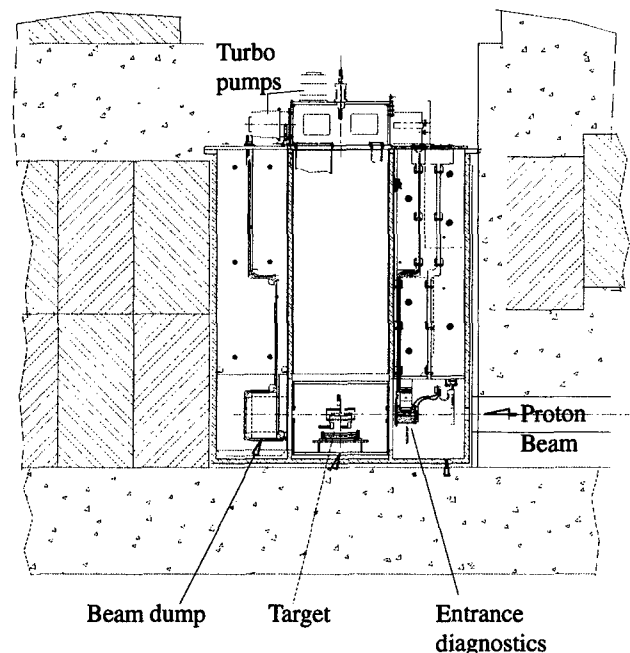
Fig. 3 – Section view of the target station along the proton beam axis.

Section view along the heavy ion beam axis of the target station
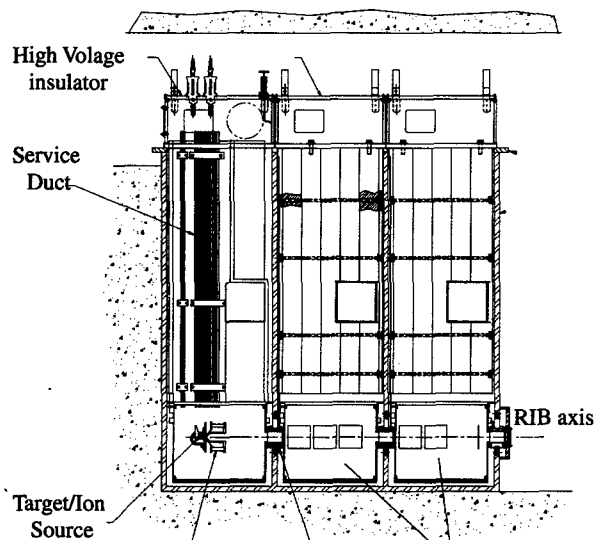
Fig. 4 – Section view of the target station along the heavy ion beam axis.

The mobile contamination produced in the target area is normally contained within the target module. The target module and the two exit modules are equipped with a containment box, which is sealed with pillow-seals to avoid migration of the mobile activity. Nevertheless, contamination of the target building is considered possible. This building must therefore be considered as an extension of the hot cell complex and all entrances must be controlled and provided with appropriate

contamination control. The air within the building must be maintained at reduced pressure and HEPA-filtered. The interior surfaces are painted to allow easy decontamination. All fluid drains will go to sump tanks for monitoring before disposal. See reference [2] for more detail on the procedure.

A module storage area is located between the hot cell and the target station. One silo will be provided with the necessary services for the testing and preconditioning of targets before installation for a beam run. This area is fully accessible during beam operation; servicing and testing of modules will therefore be possible during beam production.

The hot cell provides facilities to remotely maintain; replace, decontaminate or inspect the highly radioactive components removed from the target area. It is a conventional design with concrete shielding walls, lead glass viewing windows and sealable roof ports to allow crane access to the hot cell. Personnel access to the top of the cell is possible, if required. The hot cell bay is provided with direct actuated master slave manipulators. The mechanical bay includes remote viewing, service equipment and an elevating turntable to support and position the component being serviced. The hot cell is kept under negative pressure by its own HEPA-filtered air handling system.

A support annex houses the remote handling control room, offices, personnel change rooms, radiation safety monitoring equipment and target hall entry air-locks. All the equipment needed to control the remotely operated crane, viewing systems and other devices is in the control room. Cameras are mounted in strategic locations throughout the building and on the cranes. An air lock is provided for transfer of equipment into the target hall.

4 TARGET SERVICES

4.1 Vacuum System

The vacuum system of the target station consists of two separated vacuum stages; the primary vacuum which will contain all the exhaust gasses escaping the target/ion source and a secondary vacuum which will surround the target and the extraction and the heavy ion beam transport system installed into the two exit modules. The primary vacuum is expected to be very contaminated by radioactive species produced in the target while the secondary vacuum is expected to be less contaminated. All the exhaust will be stored into two tanks.

4.2 Ventilation

In addition to supplying fresh air and removing stale or contaminated air, the ventilation systems for ISAC building will maintain the prescribed pressure differentials that will prevent the inadvertent leakage of airborne radioactivity. These are the short-lived hadron spallation products of oxygen and nitrogen in the air around the high power targets. There are two exhaust systems for the radioactive areas. A small one of 100 m^3/min, which is dedicated to maintain a depression in the proton beam, line tunnel.

The other is the main ventilation system for the ISAC building. It is designed to exhaust 660 m^3/min of air from

six independently regulated exhaust pick-up points each with a capacity of 110 m^3/min. The air flows through HEPA filtration system.

4.3 Cooling system

The power in the beam line and target will be dissipated in a raw water evaporator. All the cooling circuits for components will use de-ionized water in closed loop systems that transfer their heat to the raw water through heat exchangers. This design maintains water purity and prevents the release of any radioactivity that is produced by nuclear reactions in the cooling circuit. There are three de-ionized water systems. They cool equipment as follows:
- non-active low conductivity water,
- active low conductivity water,
- high-active low conductivity water.

The first system cools all components which are considered non-radioactive or where the radioactivity contamination probability is expected to be very low. The system services all water-cooled power supplies and vacuum pumps and mass separator beam line components. The second system cools all components, which are radioactive, but not in direct contact with the target/ion source vacuum chamber and thus is not exposed to high level of neutron radiation fields. This system services the primary proton beam line, the high-active heat exchanger, the target assembly components outside the vacuum tank, the target module storage area, the pre-separator magnet, and the high voltage lines from the Faraday cage to the target. The third system cools all components inside the target assembly vacuum tank. As this water is exposed to the intense radiation fields from the target bombardment, it will contain tritium at concentrations similar to those in the existing meson production target cooling systems.

5 STATUS OF THE ISAC PROJECT

The T-shaped vacuum tank was installed last September, and pumped down to 5×10^{-7} mbar in less than 2 days. First stable beams were extracted from a surface ion source September 24th. In November 3rd first high resolution mass scan was obtained in the mass separator. Stable beam of ^{39}K was tuned to the low energy experimental area by November 19th. November 30th a proton beam of 1µA was tuned on the production target and first radioactive beams were produced at ISAC. A week later, December 5th/1998, we started delivering potassium beams to the TRINAT experiment at 15 keV extraction energy. The beam intensities were 6.6×10^6 for ^{37}K and $6. \times 10^8$ for ^{38}K at 1µA proton beam intensity. The second round of experiments will resume April 8th with ^{38}K for TRINAT and $^{37-38}$K for _ decay experiment.

6 REFERENCE

[1] P. G. Bricault, M. Dombsky, P. W. Schmor, and G. Stanford, *Radioactive ion beams facility at TRIUMF*, Nuclear Instruments and Methods, **B126** (1997) p. 213.
[2] L. E. Moritz, Radiation protection considerations in the design of accelerated radioactive beam facilities. Proc. Cyclotron and theirs applications conf. Caen, France, 1998, to be published

CERN PS LASER ION SOURCE DEVELOPMENT

P. Fournier, G. Grégoire, H. Haseroth, H. Kugler, N. Lisi, A. Lombardi, C. Meyer, P. Ostroumov,
W. Pirkl, J.-C. Schnuriger, R. Scrivens, V. Tenishev, F. Varela-Rodriguez (CERN, Geneva, CH)
S. Kondrashev, I. Roudskoy, B. Sharkov, A. Shumshurov (ITEP, Moscow, Russia)
S. Khomenko, K. Makarov, V. Roerich, Y. Satov, A. Stepanov (TRINITI, Troitsk, Russia)

Abstract

CERN, together with ITEP and TRINITI (Russia), is developing a CO_2 laser ion source. The key design parameters are: 1.4×10^{10} ions of Pb^{25+} in a pulse of 5.5 µs, with a 4-rms emittance of 0.2×10^{-6} rad m, working at a repetition rate of 1 Hz. This device is considered as one candidate source for LHC heavy ion operation. The status of the laser development, the experimental set-up of the source consisting of the target area and its illumination, the plasma expansion area and extraction, beam transport and ion pre-acceleration by an RFQ, will be given.

1 INTRODUCTION

In 1996 a laser ion source with beam transport (LEBT) and RFQ came into operation. This system was designed for multi-charge, heavy ($A \approx 200$) ion currents >50 mA, charge states around 25+ [Fig. 1], [1]. The source generated 8 mA of Ta20+, 28% were transported into the aperture of the RFQ. A coarsely matched beam was accelerated by the RFQ to 100 keV/u. A current of 1 to 2 mA of Ta20+ was obtained, starting an intense effort to improve this result [2].
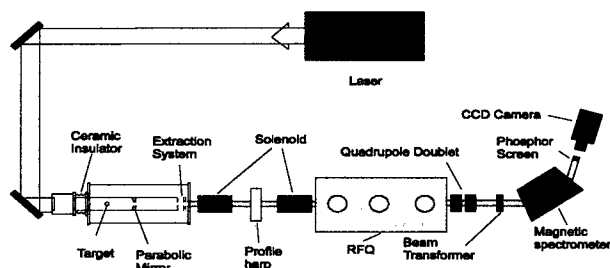
Figure 1: Scheme of the CERN Laser Ion Source

2 WORK AT THE SOURCE

2.1 Matching of Plasma Density and Extraction

The border between plasma and extracted ions together with the electric fields of the extraction electrodes and beam space-charge define the optics. Matching of the plasma and extraction is reached if the beam is smoothly focused to the LEBT. The current (I) of a Faraday cup with an aperture of 30 mm, was measured as function of

extraction voltage (U), 300 mm after extraction. The current density of ions in the plasma was varied by changing the target to extraction distance for laser energies of 6 and 30 J. Figure 2 shows a measurement, $I = I (U)$, at 30 J. Two areas can be identified, current increasing with U and a flat-top, separated by a "knee-voltage", U_k. For a charge-state of 20+ and an atomic number of 181, the relation $U_k = 0.45\times10^6\times I^{2/3}$ is found. U_k gives the source working point.
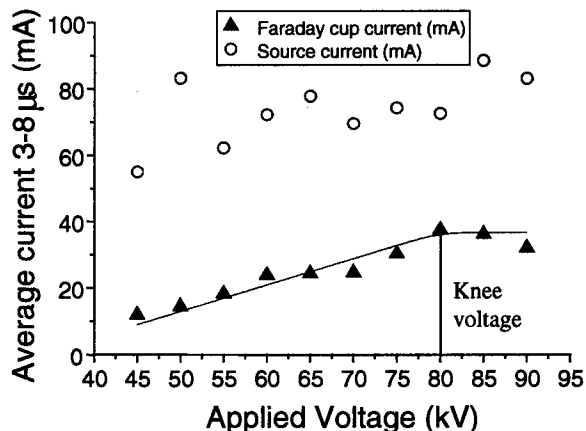
Figure 2: Characteristics of Current Transmission and Source Potential

2.2 Emittance Measurements

Figure 3 shows the emittance as function of extraction aperture ϕ at a density from 8 to 12 mA/cm², U = 60 kV. The distance between the extraction electrodes and the apertures was kept equal. It was observed that during the beam pulse, the orientation of the phase space ellipse changes (Fig. 4) and different shaping of the source outlet electrode led to different emittances. For the present extraction geometry and a source current of 60 to 80 mA, one finds for the ensemble of about 10 charge-states, around Ta20+ at 7 keV/u, a total 4rms-emittance of 300 mrad mm, normalized 1.2×10^{-6} rad m, a value which requires improvement. At 7 keV/u, measurements of the emittance using a multi-slit and phosphor screen at high currents suffer from space-charge effects. More reliable measurements of emittance can be expected at 100 keV/u, after the RFQ.
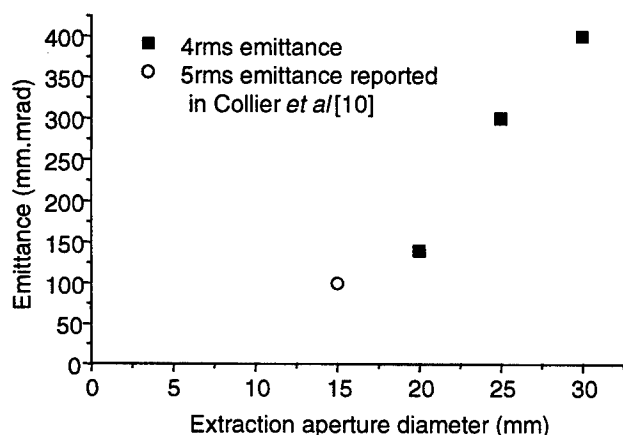
Figure 3: Emittance as a Function of Extraction Aperture
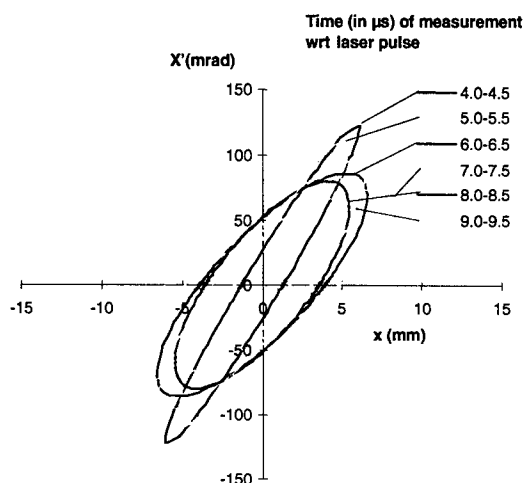
Figure 4: Emittance as a Function of Time

configuration		param.	96	Fall 98 [8]	Fall 98 [9]
φ FC = 30	1 sol	R30	33/58 = 57%	44/77 = 57%	
	2 sol	R30	26/58 = 45%	33/63 = 52%	
φ FC = 6.5	1 sol	R6.5		17/69 = 25%	17/63 = 27 % (18)
		T6.5		40%	43% (50)
		A6.5		5/80 = 6%	7/70 = 10 % (5)
		Y		11%	16% (20)
	2 sol	R6.5	10/60 = 17%	13/76 = 17 % (13), ((11))	
		T6.5	28%	28% (30), ((40))	
		A6.5		6/81 = 7 % (3), ((4))	
		Y		12% (11), ((11))	
remarks		transfer from source to outlet of RFQ 12%	good alignment plasma/extraction matched d=100 for 1 sol, d = 192 for	d = 30	
		EF = 1.66, U = 60	EF = 1.66, U = 80	EF = 1.6, U = 60	
Legend		Rab : I ab Faraday Cup / I source [%]		Y : Yield = A6.5 * EF [%]	
		T6.5 : R6.5 * EF [%]		U : Extraction voltage [kV]	
		A6.5 : I through double aperture / I source [%]		φFC : Faraday Cup aperture [mm]	
		d : image distance from solenoid [mm]		I : Average current [mA]	
		EF : Enhancement Factor allows for the change of charge states distribution at transport			

Table 1: Transfer Rates and Yields of Solenoid LEBTs

3 WORK ON THE LEBT

3.1 Magnetic LEBT, Experiments and Numerical Simulations

To improve transmission, alignment facilities for the solenoids were up-graded from 1D to 3D. In some experiments the LEBT was reduced to a single solenoid line, as beam simulations [3] suggested a strong improvement of the transfer rate. The best transmission rate which could be obtained was 43%. However the best particle yield was only 16%, when a double aperture device was inserted at RFQ position, simulating RFQ acceptance.

The programs PATH [4], CPO [4] and KOBRA3 [4] have been used. The latter treats magnetic and electrostatic elements or fields and it allows the introduction of electrons. Simulations included the study of a LEBT with super-conducting (sc) solenoids.

3.2 Results

Experimental and numerical results are summarised in Table 1. Simulations for warm solenoids are given in single parenthesis and for sc solenoids in double parenthesis. None of the configurations (whether tried out in an experiment or simulated with our different programs) led to a yield (particles in the xx'yy' acceptance of the RFQ) above 20 %. The reason is the strong non linear space charge effect from the "chained" focal points in a beam of ions of different charge states, leading to strong emittance blow-up (>2, in some cases 8 times), intrinsic to all solenoids. In the beam, ring structures were observed in the transverse plane (Fig. 5).
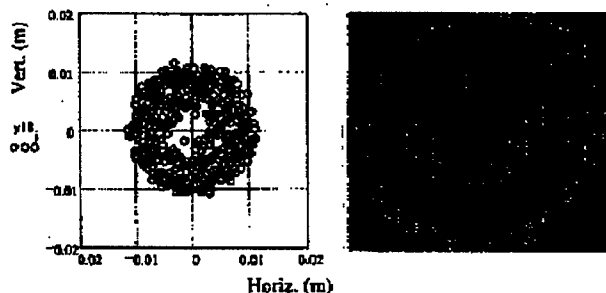
Figure 5: Ring Structures, Simulation and Experiment

3.3 Electro-static LEBT with Grids (GEL)

The GEL has been designed at CERN [5] and manufactured by INR, Moscow. Due to the lack of charge separation, strong non-linear space-charge effects should not appear and one expects high transfer rates compared to solenoid LEBTs. The mechanical layout of the GEL is shown in Fig. 6.

The result from beam simulations for an extracted beam of 60 mA , and an input emittance of 320 mrad mm, is shown in Fig. 7. Simulations give emittance growth <1.5, current transfer >50 %, a yield of 35 %. Experiments have started recently. An average current of 40 mA (for solenoid LEBTs it was 17 mA, see Table 1) has been observed in the Faraday cup of φ = 6.5 mm. The source current was then 70 mA. Inserting the double aperture device gave a yield of 30 %. Near the focal plane,

emittance measurements confirmed the predicted low emittance growth.
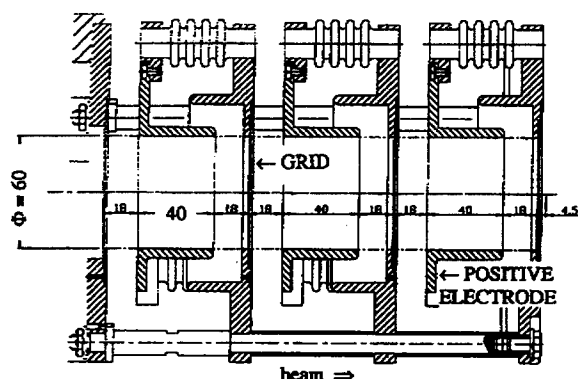
Figure 6: Mechanical Lay-out of the GEL
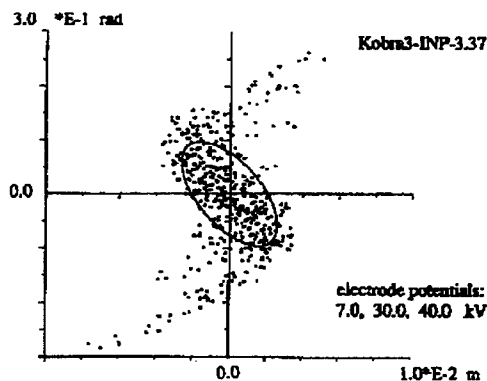
Figure 7: GEL Beam Simulations

4 LASER DEVELOPMENTS

4.1 Work at TRINITI, ITEP

In 1995, experiments with CO_2 laser oscillators of 30 J (CERN) and 80 to 130 J (TRINITI) suggested that a 100 J laser system, consisting of a master-oscillator and power-amplifier (MO/PA) should provide more than 10^{10} ions of Pb25+ within 6 μsec [6]. A master-oscillator was built by ITEP and TRINITI in 1996 and run in at CERN. It produces single transverse mode, single longitudinal mode pulses of 150 mJ in 60 to 70 ns at 3 Hz. The realisation of a 100 J laser amplifier with 1 Hz repetition rate [7] started in December 1997. This is a joint project of ITEP and TRINITI, supported by an ISTC grant. The amplifier will be delivered to CERN by the end of 2000. The first phase of the project included the characterisation

of the ion yield to define the final laser parameters. Many configurations, 13 to 65 J, at pulse-lengths of 15 to 80 ns, have been run. Ion yields were measured and scaled to the 100 J energy level according to ion beam pulse length and current density at extraction. Extrapolating from a system, running at 13 J and 20 ns leads, with a power density of 8×10^{13} W/cm^2 at the target, to 1.3×10^{10} Pb25+.

4.2 Work at CERN

The 30 J laser delivers one pulse per 30 sec. To get hands-on experience with a 1 Hz system, a low level 1 Hz oscillator has been converted to an amplifier for the master-oscillator pulses. It provides 2 J of energy. This energy is sufficient to study LEBT performances at high currents, with light elements such as Al.

5 NEXT STEPS

The RFQ will be re-installed, together with the electro-static LEBT. Effort will be invested in the reduction of the source emittance if the results, obtained at 6 to 7 keV/u, are confirmed by measurements at 100 keV/u. Shaping of the extraction electrodes and modulation of extraction voltage may help. Immediate acceleration of the ions after extraction, to reduce space charge effects at transport and matching of the beam to the RFQ, is under study.

6 REFERENCES

[1] H. Haseroth and 21 co-authors, "Laser Ion Source Development for Heavy Ions", Proceedings of the XVIIIth International Linear Accelerator Conference, Geneva, August 1996, CERN 96-07.

[2] Thesis R. Scrivens, University of Wales, Swansea,U.K., to be published this year.

[3] B.H. Breese and J.-C. Schnuriger, "PATH Simulations of a Solenoid LEBT", PS/HP/Note 99-03 (Tech.), 1999.

[4] PATH is a program, developed at LANL, now maintained by one of the authors of this report, A. Lombardi.
CPO and KOBRA3 are commercially available programs.

[5] P. Ostroumov, "LIS LEBT on the Base of Electrostatic Gridded Lenses", PS/HP/Note 99-04 (Tech.)

[6] ILP paper, "Investigation of Highly-Charged Heavy Ion Generation", Troitsk, August 1995.

[7] S.V. Khomenko and 4 co-authors ,"Master-Oscillator-Power Amplifier Laser System for Laser Ion Source", TRINITI Report 0045-A, August 1998.

[8] N. Lisi and 3 co-authors, "Experimental Characterisation of Solenoid LEBT for LIS Source", PS/HP/Note 98-14 (Tech.), 1998.

[9] P. Fournier and 4 co-authors, "Experimental Characterisation of Solenoid LEBT for LIS Source: Short Solenoid to Extraction Distance", PS/HP/Note 99-02 (Tech.), 1999.

[10] J. Collier and 4 co-authors, "Emittance Measurements on the CERN Laser Ion Source", PS/HI/Note 95-07 (Tech.), 1995.

OPTICALLY-PUMPED POLARIZED H⁻ ION SOURCES FOR RHIC AND HERA COLLIDERS

A.N.Zelenski[*][+], V.Klenov, Yu.Kuznetsov, V.Zoubets, INR, Moscow

G.Dutto, S.Kadantsev, C.D.P.Levy, G.W.Wight, P.Schmor, TRIUMF

J.Alessi, BNL, Y.Mori, KEK, M.Okamura, RIKEN, T.Takeuchi, Konan Univ., Kobe, Japan.

Abstract

The TRIUMF OPPIS (Optically Pumped Polarized Ion Source) provides high quality polarized H⁻ ion beam for studies of hadronic structure via the parity-violating weak interaction. High-current polarized H⁻ ion source development is now underway at TRIUMF for the new generation of polarization facilities at RHIC and HERA. The required 2×10^{32} /s cm^2 luminosity in RHIC can be obtained with a 0.5 mA injected H⁻ ion beam intensity. Such an intensity was already produced in dc operation of the TRIUMF OPPIS, and a similar KEK OPPIS is being upgraded at TRIUMF for future installation at RHIC. Much higher 10-20 mA polarized H⁻ ion beam intensity is necessary for the proposed polarized proton-electron collider at HERA (DESY). The feasibility of such pulsed current has been proven earlier and the first results of polarization measurements are presented here.

1 INTRODUCTION

The OPPIS technique for polarized H⁻ ion beam production was developed in the early 80's at KEK (Japan), INR Moscow (Russia), LAMPF (USA) and TRIUMF (Canada). This technique is based on spin-transfer collisions between a proton or atomic hydrogen beam of a few keV beam energy and optically-pumped alkali metal vapors [1,2]. The modern technology involved -- a super-conducting solenoid, a 28 GHz microwave generator and high power tunable solid state lasers -- is essential for this development. Achievement of 0.55 mA dc H⁻ ion current with 85% polarization and 1.0 mA current with 75% polarization (limited by the available dc laser power) was reported at PAC95 [3] and in excess of 20 mA pulsed H⁻ ion current was obtained in experiments with the atomic hydrogen injector [4]. At present, OPPIS development is continuing only at TRIUMF where the OPPIS is heavily used for parity violation studies in pp collisions at 220 MeV. The source operation is very reliable and spin-correlated current, position and beam energy modulations are very small, meeting the stringent requirements of the parity experiment [5].

2 OPPIS FOR RHIC

The polarization facility at RHIC will provide 70% polarized proton-proton collisions at energies up to sqrt(S)=500 GeV with luminosity of 2×10^{32} /cm^2 s [6]. This luminosity will be obtained with 57 bunches of polarized proton beam having 2×10^{11} particles/bunch in each ring. The polarized source must produce in excess of 0.5 mA H⁻ ion current during a 300 μs pulse, or current×duration ≥150 mA μs, within a normalized emittance of less than 2 π mm mrad. This current corresponds to 9×10^{11} particles/pulse. Assuming 50% beam losses in the LEBT, RFQ, LINAC, and injection to the AGS Booster, that gives 4.5×10^{11} polarized protons per booster bunch and finally 2×10^{11} particles for the RHIC bunch. The polarization preservation during acceleration is described in a talk by T.Roser at this conference.

The first ECR-type OPPIS was constucted at KEK [7]. Polarized beam is not presently required at KEK, and the KEK OPPIS is on loan to BNL to produce polarized H⁻ ion beam for RHIC. The source is now being upgraded at TRIUMF to meet the RHIC requirements. Table I. compares the RHIC requirements and the KEK OPPIS parameters with what has been obtained at TRIUMF.

Table I.

	KEK	TRIUMF	RHIC
Peak current I (mA)	0.1	0.5-1.0	0.5-1.5
Pulse duration t (μs)	100	dc	100-300
Charge/pulse (mA μs)	10	150 (in 300 μs)	≥150
Polarization (%)	75	75-85	≥80
Normalized emittance (mm mrad)	2 π	2 π	≤2 π
Repetition rate (Hz)	25	dc	7.5

2.1 ECR primary proton source upgrade

A 28 GHZ ECR source is used at TRIUMF vs. 18 GHz at KEK. In the KEK OPPIS the protons are produced in a 6.4 kG field and extracted at a 27 kG field which is necessary to obtain high polarization. With the 28 GHz frequency at TRIUMF the resonance field is 10 kG. It is believed this gives a factor of 2-3 current gain, other

---

conditions being similar, for the TRIUMF OPPIS. In dc operation, the extraction grids are hot which prevents Rb deposition and provides practically spark-free operation (sparking was a serious problem in the pulsed KEK source operation). After modification to 28 GHz dc operation, a 0.6 mA H⁻ ion current was obtained with a 120 hole extraction system (and 1.0 mA with 199 holes) within the specified emittance. The same extraction system produced twice as much current in the TRIUMF OPPIS. The difference is partly due to the longer distance between the ECR source and the ionizer (the KEK OPPIS superconducting solenoid has a room temperature yoke and the TRIUMF OPPIS has a cold yoke). In addition the large hole in the KEK solenoid yoke disturbs the magnetic field symmetry and might be responsible for a transverse field component which missteers the proton beam. The displacement was observed by direct measurements of the atomic H beam profile, produced after proton beam neutralization in a Rb cell. The biggest problem was the degradation of the source performance, within 12 hrs, to 50% or less of the initial current obtained with the fresh grids and cavity assembly. After systematic tests the explanation has been found in the ECR gas composition. With the fresh source assembly there is water vapor contamination to the hydrogen in the discharge tube. Water desorbs from the boron-nitride cups which isolate the plasma from the copper cavity walls. As the cavity dries out by discharge and cryopumping, the ECR current goes through a maximum (in a few hours) and then drops after about 12 hrs. of operation. A controlled water vapor supply was set up , comprising a water reservoir at 0° C , needle valves and bypass pumping by an oil-free diaphragm pump. Optimal ECR operation is quite sensitive to the hydrogen:water ratio. When properly tuned, the H⁻ ion current recovered to its best value and remained stable for hundreds of hours of operation. Another remarkable feature was very quiet ECR operation. Similar behaviour was previously observed in ECR sources of multiply-charged ions. It was speculated that an oxygen admixture helps to activate the wall surface for better electron emission to the ECR plasma. We also observed current recovery with an oxygen admixture to the hydrogen supply.

2.2 Sodium-jet ionizer cell

The polarized H⁻ ion beam emittance is completely determined by the ionizer cell aperture diameter and ionizer magnetic field. A field of 1.5 kG is necessary to reduce polarization losses during ionization to below 2.5%. Therefore, the specification for beam emittance of 2.0 π mm mrad gives the limit for the sodium cell aperture diameter of 2.0 cm. The sodium vapor flow and corresponding sodium consumption, deposition and, more important, penetration into the low field region is proportional to the cube of the cell diameter in an oven-type cell. The laser beam diameter and corresponding

diameter of the proton beam and extraction system is limited by the ionizer cell because the laser beam must pass through the ionizer cell. The neutral atomic beam enters the ionizer, and H⁻ ions produced in the cell can be accelerated to 35 keV energy (which is required for injection to the RFQ) by ionizer biasing to -31.0 kV. A large cell aperture is essential for this purpose because the neutral beam collimated to 2.0 cm in diameter before the cell must not touch the biased cell parts, otherwise secondary emission will cause sparking. A new jet-type ionizer cell with transverse sodium flow was developed to allow large apertures (see Fig.1). Sodium- and lithium-jet cells with apertures up to 20×10 cm² were originally developed by D'yachkov [8]. In our case the aperture diameter is 20 mm. The reservoir is loaded with 100-150 g of sodium and heated to 480° C. At this temperature the sodium vapor pressure is about 5 torr and the vapor density is about 10^{17} atoms/cm³. The vapor is delivered through a hot transport tube to the nozzle assembly, which produces a horizontal vapor jet having an effective thickness of about $5×10^{15}$ atoms/cm², sufficient for H⁻ ion yield saturation. A nozzle slit 0.2 cm wide and 2.0 cm tall was used in initial tests (a Laval nozzle with an expanding cone is prepared for the next test). The transport tube and nozzle temperatures are maintained at 485° C.
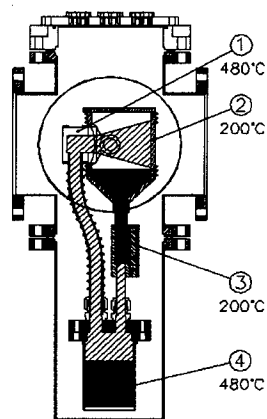
Figure 1: Sodium jet ionizer cell: 1-nozzle; 2-collector; 3-return line; 4-sodium reservoir.

The sodium vapor condenses at the collector walls, which are air-cooled to about 200° C. At this temperature the sodium vapor density is $2×10^{12}$ atoms/cm³ and the sodium viscosity is low. Liquid sodium flows down the return tube and back to the reservoir. The return tube temperature is kept at about 200-250° C by an attached cooling line. The backstream vapor flow through the return tube is negligible due to the low conductance at 200° C. Sodium in the jet-cell circulates along the path reservoir-nozzle-collector-return line-reservoir and the system provides continual, stable operation for hundreds of hours with 100-150 g of sodium. Without the circulation the cell works for only 3 hours, measured in a

test with the collector water-cooled to 29° C. The frozen sodium in the collector had a volcano shape perfectly confined within the 10 cm collector length. The sodium flow outside the cell was much less than with an oven-type cell. The whole ionizer assembly including the solenoid magnet is attached to the rest of the OPPIS by 5.0 cm thick Delrin isolation flanges, and is ready for the biasing tests.

3 PULSED OPPIS FOR POLARIZED HERA COLLIDER

Polarization of a 820 GeV proton beam in HERA, in addition to the existing longitudinally polarized electron beam, would signficantly expand the kinematic range for proton spin-structure studies and will allow measurements of the gluon contribution to the proton spin, provided that the luminosity of the polarized beam is the same as the unpolarized beam [9]. The bunch intensity should be 1.0×10^{11} protons/bunch, i.e. half that in RHIC , but the capture time to the DESY III booster ring is only 33 μs at the 50 MeV linac energy. This pulse is split into 10 bunches which eventually become HERA bunches. Therefore, the peak polarized H⁻ ion current out of the source must be almost 100 times higher than for RHIC. At least 20 mA current in a 50 μs pulse within 2.0 π mm mrad is required from the polarized HERA injector. A pulsed H⁻ current in excess of 20 mA was demonstrated in experiments with an atomic hydrogen injector in an INR-type OPPIS . At present, the atomic H injector is installed at the extended TRIUMF OPPIS test-bench. The ECR proton source is replaced with a pulsed He ionizer cell, and a new 45 cm long Rb cell has been installed. The proton polarization is measured by a low energy Lamb-shift type polarimeter, which was tested and calibrated with the well known dc polarized beam from the TRIUMF OPPIS. The source operates at a 1 Hz repetition rate and about 100 μs pulse duration. The optical pumping is produced by the pulsed Ti:sapphire laser as described above.

The TRIUMF OPPIS superconducting solenoid is designed for ECR source application. While the total length is 105 cm, the flat section of 24.5 kG produced by the main coil is only 30 cm long. The fields of the other two coils are limited, and to produce a more or less flat field 60 cm long, only 10.0 kG is achievable. The low field in the optically-pumped Rb cell causes about 40% polarization losses due to the spin-orbital interaction in the hydrogen excited states. The ideal magnet would produce a 25-30 kG field with a flat top 80 cm long.

Preliminary results of polarization measurements are shown in Fig.2. Results can be compared with polarization calculations by T. Sakae for spin exchange plus charge-exchange polarization with the He-ionizer cell [2]. The cell thickness is limited by radiation trapping to about 2.5×10^{14} atoms/cm² in a 10 kG field and can be at least doubled in a higher 25 kG field and 60 cm long cell.

The use of Cs vapor instead of Rb, or a Cs-Rb mixture with the pumping of both is also promising due to the expected large spin-exchange cross-section and higher radiation trapping limit of Cs vapor. The expected charge-exchange polarization with the He-ionizer is reduced significantly in the 10 kG field. The experimental results are to be compared with the dashed curve in Fig.2, which is reduced by a factor 0.65 compared to the solid line calculated neglecting depolarization. This neglect is valid for a magnetic field in the Rb cell higher than 25 kG. The polarized H⁻ ion current is reduced to 6.0 mA with the He ionizer in operation because of nonhomogeneity of the magnetic field in the cell.
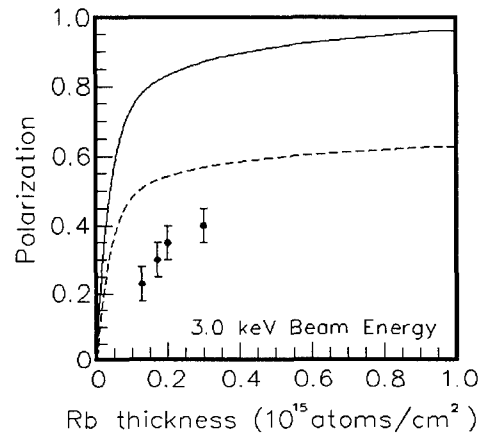
Figure 2: Solid line – expected polarization in the high 25 kG field; Dashed line – polarization for 10 kG field.

4 ACKNOWLEDGEMENTS

5 REFERENCES

[1] L.W.Anderson, Nucl. Instr. Meth. 167, p.365, (1979).

[2] A.N.Zelenski, Proc. Int. Workshop on Polarized Beams and Polarized Gas Targets (Cologne, 1995), (World Scientific, Singapore, 1995), p. 111.

[3] A.N.Zelenski et al., Proc. 1995 IEEE PAC, Dallas, 1995, p.864.

[4] A.N.Zelenski et al., AIP Conf. Proc. 421, p. 372, (1997).

[5] A.N.Zelenski et al., AIP Conf. Proc. 412, p. 328, (1997).

[6] J.Bunce et al., Particle World, v.3, p. 1 (1992).

[7] Y.Mori et al., AIP Conf. Proc. 117, p. 123, (1983).

[8] C.M.D'yachkov et al., Pribory I Technika Exsp., No. 2, p. 35, 1974.

[9] Prospects of the Spin Physics at Hera, Desy-Zeuten, DESY Report, 95-200, (1995).

SIMULATION STUDIES OF SPACE-CHARGE-DOMINATED BEAMS IN SPALLATION NEUTRON SOURCES *

J. A. Holmes, J. D. Galambos, D. Jeon, V. V. Danilov, D. K. Olsen, ORNL, Oak Ridge, TN,
M. Blaskiewicz, BNL, Upton, NY, S. Y. Lee, Indiana University, Bloomington, IN

Abstract

Uncontrolled beam losses due to space-charge-induced halo generation are a concern in the accumulator rings of spallation neutron sources, such as SNS and ESS. Such rings are characterized by high beam intensities and low uncontrolled beam loss requirements. It is therefore important to investigate the dynamics of space charge in high intensity rings. We have done this extensively by using a particle tracking approach with a self-consistent particle-in-cell code. We have found that the inclusion of space charge forces is essential in simulating not only the dynamics of halo generation, but also the formation of the observed beam profile shapes under typical conditions. Our results extend the understanding of fundamental space charge physics, which has been developed for linear accelerators, to rings.

1 INTRODUCTION

Accumulator rings for spallation neutron sources represent a new regime for the study of space charge dynamics. In comparison with linear accelerators, for which much understanding of space charge dynamics has been gained [1], space charge forces are modest in rings, with tune shifts of only a few percent of the bare tunes. However, beams remain in accumulator rings much longer than in linacs, and have significant time to become destabilized. Furthermore, the lattice periodicities and dispersion phenomena peculiar to rings couple to space charge effects to enrich and complicate the dynamic picture.

The motivation to study space charge dynamics in high intensity rings is related to their extremely low beam loss requirements. For example, to facilitate hands-on maintenance in the SNS accumulator ring, uncontrolled losses from the 1 GeV proton beam are limited to < 1 nA/m, or about 1 part in 10^4 [2]. Consequently, uncontrolled beam losses due to space-charge-induced halo generation are an important concern.

We have extensively examined the effects of space charge in high intensity rings using a particle tracking approach with a self-consistent particle-in-cell code, ORBIT [3]. Section 2 briefly presents the computational model used in our studies. A more complete description can be found in Ref. [4]. Section 3 presents a detailed comparison of calculated and measured beam profiles for the PSR accumulator ring at LANL [5]. The calculations match as closely as possible the actual injection scheme and beam accumulation process occurring in PSR. These

results serve not only to benchmark ORBIT, but also to emphasize the necessity of including space charge forces in the calculations. Section 4 describes some new results on the role of space-charge-driven lattice resonances in creating rms mismatch in initially matched beams [6]. This mismatch can then drive the parametric resonance in the usual way, resulting in large halo formation [7]. Section 5 presents the results of injection studies for the SNS ring including a survey of halo formation as a function of vertical tune and a comparison of results for comparable FODO and doublet lattices. Finally, our conclusions are presented in Sect. 6.

2 COMPUTATIONAL MODEL

High intensity rings are characterized by the separation of longitudinal and transverse scales. In SNS, for example, the longitudinal bunch length is on the order of 100 m, compared with transverse beam dimensions of a few cm; and the longitudinal tune is about 10^{-3}, compared with transverse tunes of about 5.8. For this reason it is possible, with good approximation, to separate the longitudinal and transverse dynamics in high intensity rings and, for the study of space charge effects, to consider the transverse dynamics. In ORBIT, the particle tracking is carried out in six dimensional phase space and, although transverse canonical coordinates couple strongly into the longitudinal equations, the only coupling of longitudinal dynamics into the transverse equations is through the momentum deviation $\delta \equiv \Delta p / p_0$ and the modulation of the space charge density along the bunch. For the remainder of this paper we will concentrate on space charge in transverse phase space.

The model adopted in the ORBIT code is a particle-tracking approach. The essence of the transverse phase space treatment is the following dynamic equation for the macroparticle coordinate $u = x$ or y:

$$u'' = F_u^{lin} + F_u^{sc} + F_u^{nl} , \qquad (1)$$

where prime denotes differentiation with respect to the longitudinal coordinate s, F_u^{lin} are the linear magnet forces, F_u^{sc} are the space charge forces, and F_u^{nl} are the nonlinear magnet forces. The linear focusing forces and nonlinear magnet forces are dependent on the lattice and are evaluated independently for each macroparticle using first and second order transport matrices, respectively, generated by either MAD [8] or DIMAD [9]. The space

charge forces are collective, involving the interacton of all the macroparticles, and are evaluated self-consistently:

$$F_u^{sc} = P \sum_{i=1}^{N} \frac{u - u_i}{(x - x_i)^2 + (y - y_i)^2} , \qquad (2)$$

where the summation is over the number of macroparticles, N, and P is the generalized perveance of the beam [10].

The integration scheme is chosen to be explicit second order symplectic, with a transport matrix representation of all external magnet forces and the inclusion of space charge forces as kicks. Our treatment of space charge uses a particle-in-cell (PIC) model [11] with fast Fourier transforms (FFTs) to evaluate the forces. Further details of the algorithms are given in Ref. [4]. The inclusion of nonlinear magnet forces in the model is recent, and we do not utilize this feature in the present results. Consequently, the space charge potential provides the only nonlinearity in these calculations.

The study of space charge using this numerical model involves a number of parameters: N, the number of macroparticles; N_{FFT}, the spatial resolution (grid parameter for the FFT algorithm); and N_{az}, the number of azimuthal integration steps. Convergence studies have shown that the accuracy of the solution depends both on having a sufficient number of macroparticles, N, and enough FFT gridpoints, $N_{FFT} \times N_{FFT}$, but that the numerical stability of the integration scheme depends only on having a sufficiently fine azimuthal grid, as determined by N_{az}. The results presented here were obtained using $N = (2\text{-}10) \times 10^4$ macroparticles and $N_{FFT} \times N_{FFT} = 64 \times 64$ FFT grid points. For numerical stability we used $N_{az} = 480$ integration points, which corresponds to about 20 points per FODO cell or step sizes of about ½ meter. Such calculations typically require about 10 hours on a 500 MHz Dec Alpha workstation.

3 BENCHMARK WITH PSR

As a benchmark of the ORBIT code, we now present comparisons of simulated and experimentally measured transverse beam profiles at the end of injection in the Los Alamos Neutron Science Center, LANSCE, Proton Storage Ring, PSR. Experimental beam profiles were generated using H⁻ foil injection from an 800 MeV linac. Injection was carried out for a duration of 825 s, or 2305 turns, for two painting schemes and three beam intensities. Subsequently, the beam was extracted in a single turn and transported to a wire scanner beam profile diagnostic in the extraction beam line.

In the benchmark calculations, care was taken to match the full PSR lattice parameters, injection scenarios, and beam intensities [5]. Because the absolute transverse location of the wire scanner was not precisely known, the comparison was carried out by matching the centers of the calculated and experimental distributions. The shift required to align these proved to be independent of beam intensity. Also, because the calculated and measured distributions were obtained in different arbitrary units, the vertical scales of the distributions were adjusted so that the calculated height matched that from the wire scanner data at the center of the distribution. We emphasize that the width and shape of the calculated distribution were not adjusted. Comparisons were made for two injection scenarios, both with and without a vertical closed orbit bump at the foil. The PSR does not have bump magnets to paint in the horizontal direction, but a horizontal spread is provided through the injected beam energy distribution since there is a dispersion of 1.4 m at the foil location.

The overall results reveal very good agreement between the measured and calculated transverse profiles. For both injection scenarios, there is a noticeable broadening of the vertical distribution with increasing beam intensity in both the experimental measurements and calculated profiles. The horizontal profiles are much less sensitive to increasing beam intensity, both for the experimental and calculated results.
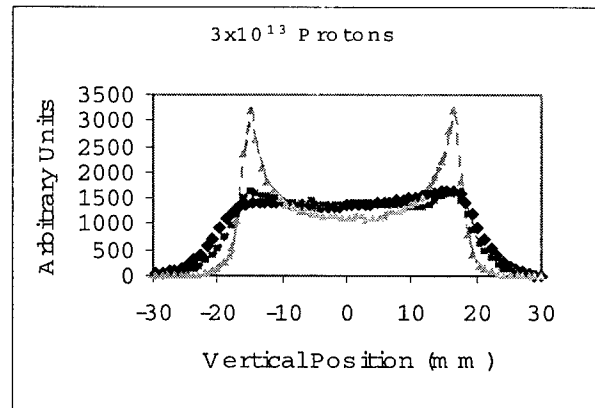
Figure 1. The effect of the space charge force on the calculated beam profiles, for the highest intensity case with no closed orbit bumps during injection. Blue curve – experiment; red curve – calculation with space charge; green curve – calculation without space charge.

Furthermore, this good agreement is very dependent on including the space charge force in the calculations. This is demonstrated emphatically in Fig. 1, which shows the experimental and calculated vertical beam profiles at full intensity, calculated both with and without the space charge force. For this case the injection is offset vertically with no bumps. This is reflected by the "horns" on the profile calculated without the space charge force, which occur at the location of injection with peak width corresponding to the linac beam size. In both the experiment and the calculation with space charge, space charge forces spread these "horns", causing the distribution to fill in and to broaden. The transverse space charge model predicts most of the observed beam

broadening. This comparison provides a benchmark that the space charge calculations are correct, particularly considering that the intensity of the PSR beam at high currents is comparable to that in proposed spallation neutron sources.

4 LATTICE RESONANCES AND HALO FORMATION

It is well established, both in linacs and rings, that a primary cause of space-charge-induced halo formation is rms beam mismatch [1,7]. This mismatch leads to envelope oscillations at approximately twice the coherent tune which, driven by space charge forces, manifest as the parametric resonance. Beam particles with large action in the phase plane of the resonance can diffuse across the separatrix and become halo particles. Although it is necessary to have well-matched beams to avoid halo formation, we now show that this may not be sufficient. Depending on the operating point in tune space, space charge forces can drive resonances that lead to beam mismatch, even for initially rms-matched beams. The presentation here is brief, and greater details can be found in Ref. [6, Jeon et al].

In order to illustrate these phenomena clearly, we calculate three cases in the fourfold symmetric SNS ring lattice using initially matched beams with K-V distributions. For these cases the initial transverse rms beam emittances are chosen to be $120\,\pi\,mm\text{-}mrad$, the proton beam energy is 1 GeV, the beam intensity is set so that the initial tune shift is about 0.08 giving a tune depression of 1.4%, and the initial horizontal bare tune is $v_x = 5.82$. The three cases are identical except for varying the choice of vertical bare tune v_y, which is taken to be $v_y = 5.67, 5.82,$ and 5.77.

Before proceeding, we note that an ideal K-V distribution supports only even terms in the space charge potential. However, in general, all terms will be present if there are asymmetric nonuniformities in the beam distribution. Because the numerically-generated K-V beams used in these calculations are created with random numbers, the resulting distributions contain small non-uniformities. If the operating point in tune space is sufficiently close to certain resonances, it is possible for the space charge nonuniformities to excite these resonances and destabilize the beam. As shown below, this will apply even for the case of an rms matched beam.

Considering first the case, $v_y = 5.67$, the operating point is such that no lattice resonances are excited. In a calculation tracking the rms matched beam for 1250 turns, the transverse rms emittances are observed to remain constant, envelope fluctuations remain small, and the beam phase space plots show no halo. To observe halo generation for this operating point, it is necessary to mismatch the initial envelope radii by more than about 5%, beyond which the extent and population of the halo increases with increasing mismatch.

We next consider the case of $v_x = v_y = 5.82$. This point in tune space lies atop the difference resonance $v_x - v_y = 0$. Difference resonances $v_x - v_y = n$ are not usually regarded as dangerous to the operation of accelerators because of the conservation of $J_x + J_y$, where $J_{x(y)}$ is the $x(y)$ action. However, it has been shown [12] using self-consistent Vlasov-Poisson equations that the space charge potential can support an odd mode contribution $\propto xy$ capable of exciting the difference resonance. Given the presence of such a driving term, the difference resonance, $v_x - v_y = 0$, facilitates halo generation in two ways: (1) by increasing the strength of the 2:1 parametric resonance through the coupling of the horizontal and vertical envelope oscillations; and (2) by helping particles, through coupling, to cross the separatrices of the 2:1 parametric resonance.
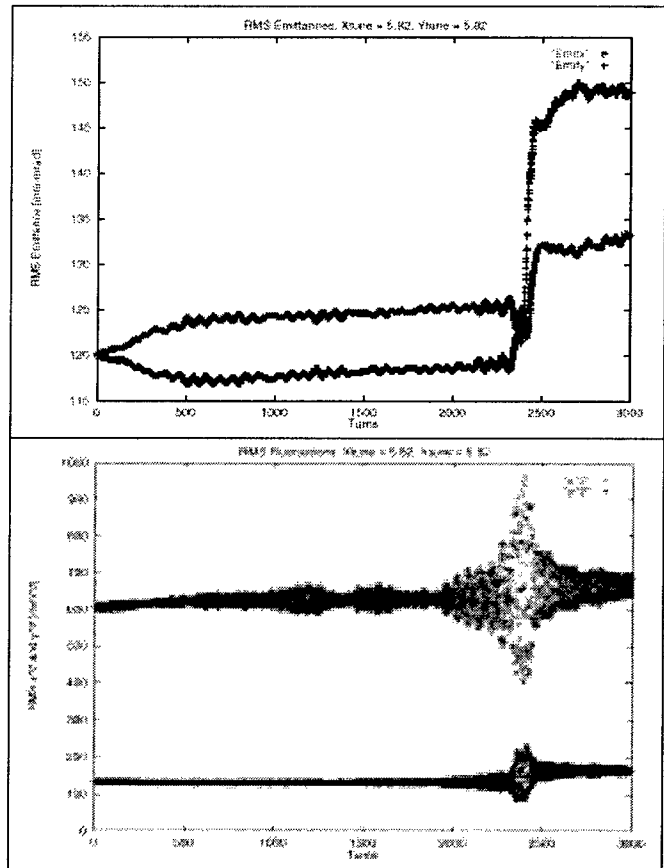
Figure 2. Evolution of rms emittances and second moments $<\Delta x^2>$ and $<\Delta y^2>$ for $v_x = v_y = 5.82$.

Figure 2 shows the evolution of the transverse rms emittances and envelope fluctuations for the case of a well-matched beam at $v_x = v_y = 5.82$. The small initial oscillations in the second moments reflect the quality of the match. Even though the odd mode contribution $\propto xy$

is small in the potential of the numerical K-V distribution, this term excites the difference resonance. Evidence of this is clear in the anticorrelation of the horizontal and vertical emittances in Fig. 2. This leads to rms mismatch, as shown by the increasing oscillation amplitudes of $< \Delta x^2 >$, and ultimately to the strong excitation of the 2:1 parametric resonance. Little halo formation is observed for this case for over 2000 turns, but ultimately substantial halo formation accompanies a large emittance increase at around 2300 turns. The strength of this process is due to the difference resonance enhancing the parametric resonance by coupling the horizontal and vertical envelope oscillations and by helping particles to cross the separatrix through $x - y$ coupling.

Let us now consider the case of $v_x = 5.82$ and $v_y = 5.77$. In this case the fourth order resonance $4v_y = 23$ is excited by the fourth order even mode term, $a_0 x^4 + a_2 x^2 y^2 + a_4 y^4$, in the space charge potential. Again, for an initially well-matched beam, this induces a mismatch that leads to significant halo formation. Unlike odd mode terms in the space charge potential, which are skew terms in the Hamiltonian that are usually small in lattices with midplane symmetry, even mode terms can be significant. Consequently, when the space charge potential is the driving force in such lattices, the $4v_y = n$ resonance associated with the fourth order even mode potential term is significantly more excited than the $3v_y = n$ resonance associated with the third order odd mode term, $a_1 x^2 y + a_3 y^3$ [12].

When the coherent tune is near a lattice resonance [13] associated with an even mode space charge potential, the excited resonance can generate a mismatch, even though the initial beam is well matched. This mismatch can drive the 2:1 parametric resonance and expedite halo formation. Figure 3 illustrates this process for the case with $v_x = 5.82$ and $v_y = 5.77$. The moderate y rms emittance increase around 200 turns is due to the excitation of the fourth order $4v_y = 23$ resonance. This can be seen in the upper right plot, which is a snapshot of the particle distribution in y phase space taken at 250 turns. An rms beam mismatch is generated by this resonance as can be seen in the plot of the beam moments at the lower left. This mismatch leads to the excitation of the 2:1 parametric resonance and to the subsequent large increase in the y emittance. Because the tune difference is only $v_x - v_y = 0.05$, the difference resonance also contributes to the strength of the process. This can be seen in the anticorrelation of the x and y emittances, an effect that is due to coupling. The y phase space plot at lower right superposes the beam distribtuions at 1000 turns and 1250 turns, and shows the 1:2 parametric resonance structure and halo. Clearly, it is advantageous to avoid nonlinear resonances associated with even mode space charge

potentials when choosing an operating point for intense beam circular accelerators. This is especially true when the horizontal and vertical tunes are close.
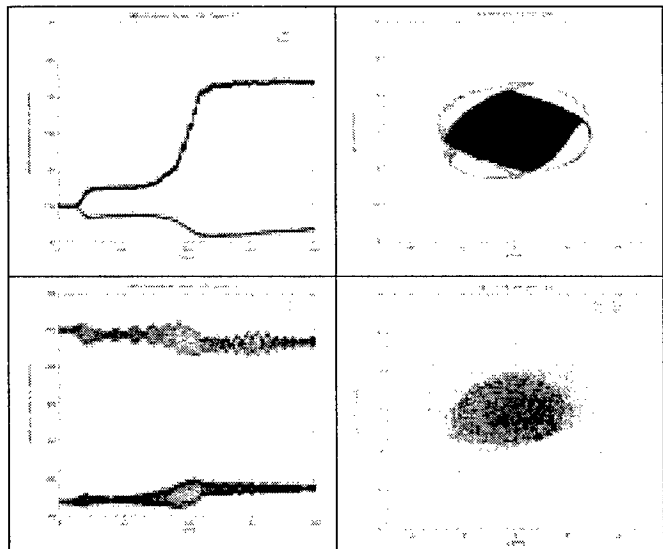
Figure 3. Evolution of rms emittances and second moments $< \Delta x^2 >$ and $< \Delta y^2 >$ for $v_x = 5.82$, $v_y = 5.77$. Phase space plots in vertical plane for 250 turns and superposition of 1000 and 1250 turns.

The main conclusion of this section is that, depending on the operating point in tune space, space charge forces can excite resonances that lead to beam mismatch. This mismatch can then excite the parametric resonance, thus leading to substantial halo formation, even for initially matched beams. Furthermore, if the x and y tunes are close together the resulting coupling can contribute to the destabilization of the parametric resonance and the resulting halo formation.

5 INJECTION STUDIES

We have carried out a number of injection studies for the SNS ring, including optimization of the injection scheme for minimum halo formation [14]. The most recent injection studies include a survey of vertical tune space for fixed horizontal tune, $v_x = 5.82$, and a comparison of doublet and FODO lattices having the same global parameters, including length, beam size, and bare tunes. These studies track the entire injection process, including such features as incident linac beam distribution, foil stripping model, and bumping schemes, for 1158 turns. More details of the injection model are presented in Reference [14].

Figure 4 shows the results of the vertical tune survey by plotting the percentage of particles with x or y emittance exceeding 180π mm-mrad as a function of bare tune at the end of injection. The resolution of this tune scan is coarse, with cases separated by $\Delta v_y = 0.05$ in the range from $4 < v_y \lesssim 6$, but it is clear that halo formation is sensitive to the operating point in tune space. It is

interesting that, although bare tunes of exactly 5 or 6 give low halo formation, the worst operating points flank these integral values. The divergence of the results as v_y approaches 4 is due to the structure resonance with the fourfold symmetric SNS lattice. We also note that there are a number of operating points at which none of the particles exceed $180\,\pi$ mm-mrad, indicating that it may be possible to avoid producing halo through proper choice of operating point.
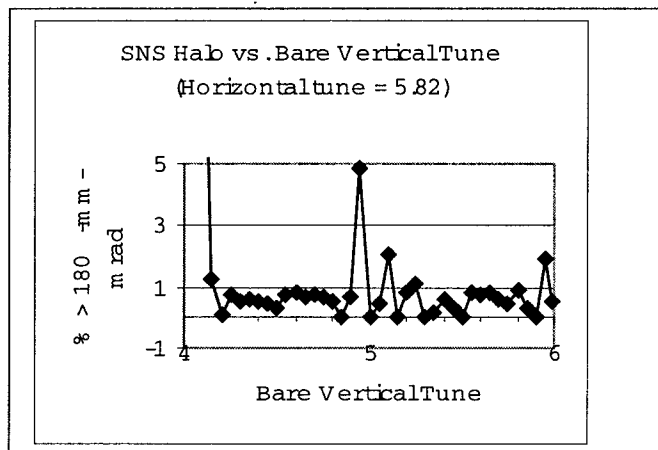
Figure 4. Halo production as a function of vertical tune for injection into SNS lattice with $v_x = 5.82$.

Finally, calculations were carried out comparing halo formation for doublet and FODO lattices having the same global parameters. For both lattices, the results are sensitive to the tune values, but in some cases the doublet lattice produces less halo and in other cases the FODO lattice produces less.

6 CONCLUSIONS

We have demonstrated by benchmark comparison with experiment that the inclusion of space charge forces is a necessary component in any beam-dynamic model of high intensity rings. We have also shown that nonlinear space charge forces can excite various lattice resonances that lead to rms beam mismatch. This can trigger a two-stage process in which the mismatched beam in resonance with the lattice excites the parametric resonance, resulting in substantial halo formation. These results, along with realistic injection studies surveying the tune dependence of halo formation, emphasize the sensitivity of beam stability to the operating point in tune space. Comparison of halo formation in FODO and doublet lattices with the same global parameters shows that results are sensitive to the tune, but reveal no performance bias for one or the other. Future work will involve the study of space charge dynamics in the presence of nonlinear magnetic forces, such as errors, fringe fields, and higher multipoles, which have recently been incorporated into the ORBIT Code.

7 REFERENCES

[1] P.M. Lapostolle, IEEE Trans. Nucl. Sci. NS-18, 1101 (1971); F.J. Sacherer, ibid. NS-18, 1105 (1971); J.D. Lawson P.M. Lapostolle, and R.L. Gluckstern, Part. Accel. 5, 61 (1973); E.P. Lee and R.K. Cooper, ibid. 7, 83 (1976); C. Chen and R.C. Davidson, Phys. Rev. E 49, 5679 (1994); Phys. Rev. Lett. 72, 2195 (1994); S.Y. Lee and A. Riabko, Phys. Rev. E 51, 1609 (1995); A. Riabko, et al, Phys. Rev. E 51, 3529 (1995); R.A. Jameson, Proceedings of the 1993 Particle Accelerator Conference (IEEE, Piscataway, NJ, 1993), p.3926 (unpublished); J.S. O'Connell, T.P. Wangler, R.S. Mills, and K.R. Crandall, Proceedings of the 1993 Particle Accelerator Conference, (IEEE, Piscataway, 1993), p.3657; J.M. Lagniel, Nucl. Instr. Meth. A345, 46 (1994); A345, 405 (1994); I. Hofmann, L.J. Laslett, L. Smith, and I. Haber, Part. Accel. 13, 145 (1983); Struckmeier and M. Reiser, Part. Accel. 14, 227 (1983); R. L. Gluckstern, Phys. Rev. Lett. 73 (1994) 1247..

[2] National Spallation Neutron Source Conceptual Design Report, Volumes 1 and 2, NSNS/CDR-2/V1,2, (May, 1997); at http://www.ornl.gov/~nsns/CDRDocuments/CDR.html

[3] Galambos, J.D., Holmes, J.A., and Olsen, D.K., ORBIT User Manual, Version 1.01, SNS/ORNL/AP TECHNICAL NOTE Number 011, (March, 1999).

[4] J.A. Holmes et al, Proceedings of International Computational Accelerator Physics Conference, (Monterey, CA, September 1998); F. Jones, Users' Guide to ACCSIM, TRIUMF Design Note, TRI-DN-90-17 (1990).

[5] J.D. Galambos et al, submitted to PRSTAB, (1999).

[6] S. Machida and Y. Shoji, in Space Charge Dominated Beams and Applications of High Brightness Beams, AIP Conf. Proc. 377, ed. S.Y. Lee, 161 (1995); D. Jeon et al, submitted to Phys. Rev. Lett., (1999).

[7] S. Machida, in Workshop on Space Charge Physics in High Intensity Hadron Rings, AIP Conf. Proc. 488, ed. A.U. Luccio, W.T. Weng, 73 (1998); J.A. Holmes et al, Proceedings of the European Particle Accelerator Conference, paper THP24C, (Stockholm, June 1998).

[8] H. Grote and F. Christoph Iselin, The Mad Program, Version 8.19, User's Reference Manual, CERN/SL/90-13 (Geneva, 1996).

[9] R.V. Servranckx, K.L. Brown, L. Schachinger, and D. Douglas, User's Guide to the Program DIMAD, SLAC Report 285 UC-28 (A), (May, 1985).

[10] Thomas P. Wangler, in Space Charge Dominated Beams and Applications of High Brightness Beams, AIP Conf. Proc. 377, ed. S.Y. Lee, 3 (1995).

[11] R.W. Hockney and J.W. Eastwood, Computer Simulation Using Particles, Adam Hilger, IOP Publishing Ltd. (New York: 1988); C.K. Birdsall and A.B. Langdon, Plasma Physics via Computer Simulation, McGraw-Hill Book Company (New York: 1985).

[12] I. Hofmann, Phys. Rev. E 57, 4713 (1998).

[13] R. Baartman, Proceedings of Workshop on Space Charge Physics in High Intensity Hadron Rings (Shelter Island, NY, 1998), p.56.

[14] J.D. Galambos, J.A. Holmes, and D.K. Olsen, Proceedings of the Particle Accelerator Conference, ,(Vancouver, 1997).

BEAM ECHO MEASUREMENTS*

L. K. Spentzouris, P. L. Colestock and C. Bhat

Fermi National Accelerator Laboratory

P. O. Box 500, Batavia, IL 60510, USA

Abstract

Beam echo measurements provide a sensitive way to obtain the diffusion rate in storage rings. Often intrabeam scattering is the dominant diffusion mechanism degrading a beam. The analytical formalism of beam echoes will be reviewed, followed by a summary of current experimental data and their analysis. A specific case study of scattering rates below transition in the Fermilab antiproton storage ring will be presented.

1 INTRODUCTION

A beam echo is a weakly nonlinear wave mixing phenomenon, whereby a large, coherent response arises at the difference frequency of two previous excitations. Often the large beam motions due directly to the prior excitations have long since damped away, so that the echo seemingly comes out of nowhere. Although the response to each initial excitation has Landau damped, the particles remain correlated, the 'memory' of the kick remaining in the beam. The recoherence which is the echo is made possible by the mixing of the two sets of correlations at different frequencies.

Echoes arise at a specific time which is directly proportional to the time separation of the excitations. In the case of echo measurements, these kicks are externally applied so that the time of the echo can be well controlled. It is this feature which allows echoes to be exploited as a means of measuring the diffusion coefficient in a beam. Any source of particle collisions has the effect of degrading particle correlations. Once particle correlations from the applied kicks have been sufficiently destroyed, echo reconstruction is no longer possible. Scattering rates within a beam may be measured by examining the degradation of echo amplitude as a function of the time at which the echo occurs. This method of determining diffusion rates is very sensitive and requires little machine time compared with more conventional techniques. Scattering rate measurements using longitudinal echoes in unbunched beams have been done successfully at both Fermilab and CERN [1, 2].

The potential of echoes as a diagnostic is in the early stages. The use of echoes has been explored experimentally primarily in the longitudinal degree of freedom in unbunched beams. However, longitudinal beam echoes in bunched beams have been observed, and a corresponding

theory developed [5]. Transverse beam echoes have been theoretically described [3, 4]. There is also a wealth of information in the shape of each individual echo. Echo shape is dependent on the beam distribution, and as such, can be used to determine the beam profile or related information. For example, longitudinal echoes in an unbunched Gaussian beam have been used to measure its energy spread [6]. There is much to be gained from the continued study of echoes.

2 THEORY AND MEASUREMENT

An expression for the longitudinal echo current in an unbunched beam can be found analytically. In the absence of wakefields, but allowing for scattering processes, the current has the following form,

$$I_{echo} = A J_1(k_1 \delta \Delta t) \exp\left(-c\nu t^3\right)$$
$$\times \int d\varepsilon \frac{df_0(\varepsilon)}{d\varepsilon} \exp\left(ig(\varepsilon)[t - \frac{h_2}{h_2 - h_1}\Delta t\right) \quad (1)$$

where A, k_1, and c are constants depending on various machine parameters, and the definition of the rest of Eq. 1 will follow.

The CERN group of Brüning, et al. [2] have coined the second line of Eq. 1 as the form factor of the echo response, because it determines the shape of an individual echo. The sinusoidal term in the integrand determines the temporal location of the echo. Its average causes the integral to go to zero, except at the time $t_{echo} = [h_2/(h_2 - h_1)]\Delta t$, where h_1 is the harmonic number of the frequency of the first applied kick, h_2 is the harmonic number of the frequency of the second applied kick, and Δt is the time separation between the two kicks. The derivative of the unperturbed beam distribution, $f_0(\varepsilon)$, with respect to the energy deviation ε is what determines the shape of the echo. A Gaussian beam will thus have a two-lobed echo with a notch that goes to zero in the center. Such echoes are typical of the ones seen in the Fermilab Accumulator, an example of a single echo is shown in Fig. 1. The CERN group has sometimes observed four-lobed echoes in their SPS machine, and have successfully modeled it using a parabolic function for the beam distribution [2].

Since the echo occurs at a time dependent on the applied kick separation, it is possible to do scans of echo amplitude versus time-to-echo, by systematically varying kick separation. The superposition of echoes from such a scan is shown in Fig. 2. The envelope function of an echo scan is

---

given by line one in Eq. 1 and consists of a Bessel function multiplied with an exponential having a time cubed dependence. The argument of the Bessel function depends on the kick strength, δ, and time ($\Delta t \propto t_{echo}$). The exponential comes from including diffusion into the beam description, ν is the collision rate. In the echo scan of Fig. 2, the beam parameters were such, and the diffusion rate high enough, so as to prevent echo reconstruction before reaching the first zero of the Bessel function. In contrast, echo scans in the CERN SPS clearly showed the first several lobes of the Bessel function dependence.
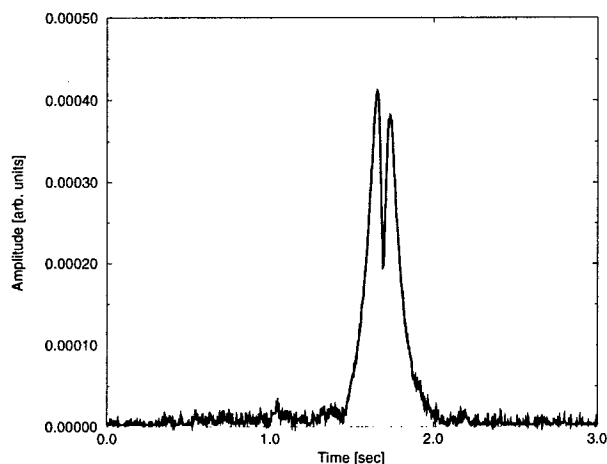
Figure 1: Amplitude of a single echo versus time, as seen in the Fermilab Accumulator.
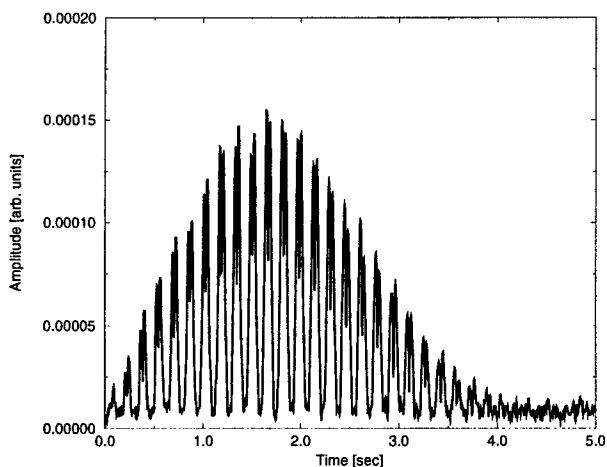
Figure 2: Results of an echo scan done in the Fermilab Accumulator. The data shows echo amplitude versus time-to-echo.

3 SIMULATION

The effect of diffusion on beam echo response has been studied with simulation at Fermilab. The simulation is a particle tracking code using the difference equations for unbunched longitudinal motion. The single frequency excitations are applied as short kicks which modify the energies of the individual particles in accordance with their phase space coordinates.

The available outputs of the program show the time evolution of the phase space coordinates of each particle, the projection of the phase space onto the spatial axis (the current modulation of the beam around the machine), and the amplitude of oscillation of selected Fourier components in the beam. The amplitude of oscillation at the echo frequency may thus be viewed, and mirrors the experimentally observed time development of an echo.

An echo scan may be simulated by superposing the outputs of the amplitude of motion at the echo frequency from successive runs in which the time separation of the applied kicks is varied. This mimics the actual experimental procedure of an echo scan, and the results of the simulation agree well with experimental results. A simulated echo scan, without the intentional introduction of a diffusional term is shown in Fig. 3. There is a noise floor apparent in Fig. 3, which is due to the finite number of particles in the tracking code. This is essentially Schottky noise, and does not affect the echo decay.
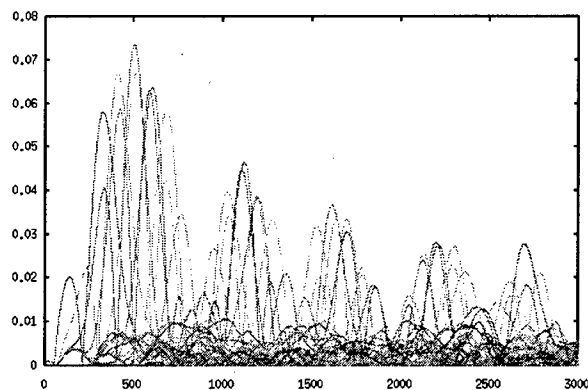
Figure 3: Simulated echo scan, the case of no diffusion.

A simulated echo scan with the intentional introduction of a diffusional term is shown in Fig. 4. Here, a 1% noise level has been injected into the particle dynamics in order to model a random scattering process. The amplitude of the echoes becomes degraded, with the echoes suffering more as they become later in time. The clearly visible Bessel function dependence of Fig. 3 has been eroded by the randomizing process. It is worthwhile to note that echoes can be used in this manner to determine true random processes in numerical simulations.

115
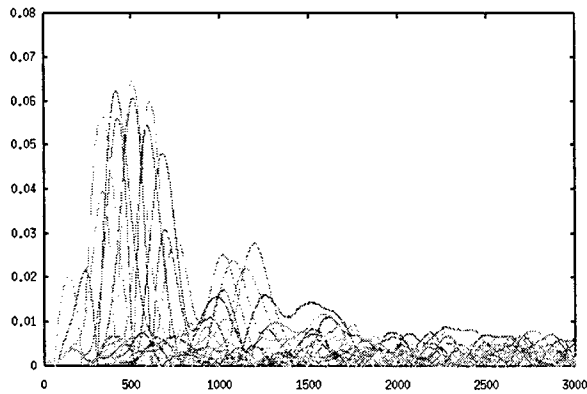
Figure 4: Simulated echo scan, with diffusion introduced.

Figure 5: Comparison of the theory to experiment for longitudinal scattering rates. The dashed lines represents agreement.

4 DIFFUSION COEFFICIENT MEASUREMENTS

Through the use of echo scans, scattering rate measurements have been done in the FNAL Accumulator and the CERN SPS. The scattering rate (or diffusion coefficient, $D = \nu(\Delta\varepsilon/\varepsilon_0)$) may be extracted by fitting the amplitude envelope of a scan with the function given in the first line of Eq. 1. It is difficult to know the kick strength δ, as seen by the beam, so there are two free parameters in the fit. The constant c in the exponent depends on known quantities, and can be written as,

$$c = (2\pi\Delta f)^2 \frac{1}{3}\left(\frac{(h_2 - h_1)h_1}{h_2}\right)^2$$

where Δf is the sigma of the beam distribution in frequency (this can be measured with a Schottky pickup), and where h_1 and h_2 are the harmonic numbers of the first and second applied excitations.

The CERN group found that a typical diffusion coefficient in the SPS was $D = 10^{-13}s^{-1}$. In addition, they measured the diffusion coefficient as a function of externally applied noise amplitude, and found that echo measurements had two orders of magnitude greater sensitivity than did Schottky measurements [2].

At Fermilab, a series of scattering rate measurements was undertaken after the beam was decelerated below the transition energy in the Accumulator ring [7]. The purpose was to determine whether the scattering rate was consistent with the prediction for intrabeam scattering in a ring below transition [8, 9]. The results are shown in Fig. 5.

Conveniently, the Accumulator has a number of stochastic cooling systems, for both longitudinal and transverse cooling. Once they are turned off, the beam emittances will grow in free expansion. The diffusion coefficients can be determined either from the growth rates during the expansions, or by using the echo scan measurement technique.

A comparison between experiment and intrabeam scattering theory below transition is done in Fig. 5 by plotting the measured scattering rate versus the theoretically predicted scattering rate for various beam emittances. If there were no errors in the measured parameters, the points would fall on a straight line with a slope of one. However, there is a systematic error due to the uncertainty in the beta functions below transition which could be as high as 20%. Therefore, as long as the measured points fall along a straight line, having a slope consistent with the systematic error, the data can be considered to be in good agreement with the theory. The open circles in Fig. 5 correspond to free expansion data, and the filled circles to the echo measurement data. Not only is there good agreement with the theory, but once again the echo measurement data is seen to have greater sensitivity than is possible with the more conventional methods. The free expansion data lies along the theoretical curve, but begins to fall off at low scattering rates. In contrast, the echo measurements show good agreement with theory even at the lowest measured scattering rates.
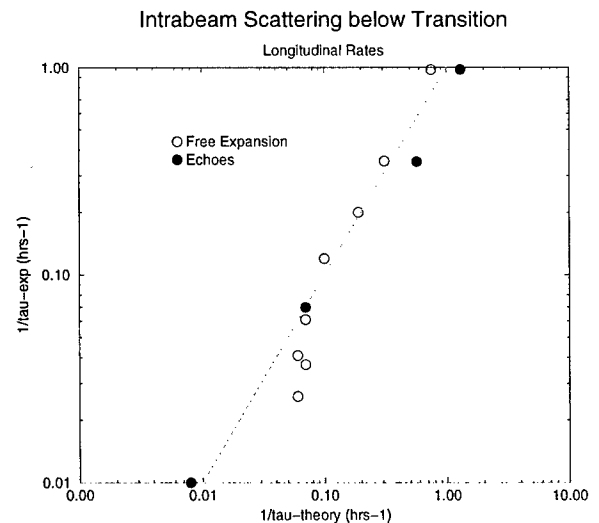
5 DISCUSSION

Longitudinal beam echo scans with an unbunched beam have been shown to be a useful way of measuring the scattering rate. Both at CERN and at FNAL, echo scans were able to measure smaller scattering rates than other methods. Echo scans are fast as well as sensitive, the measurement itself taking on the order of minutes. Even with this success, the potential use of echoes is still largely unexplored. Full application of diffusion rate measurements in bunched beams and in the transverse plane has yet to be done. There are also possibilities of using echoes in other ways, since the echo shape is dependent on the beam profile.

6 REFERENCES

[1] L. K. Spentzouris, *et al., Phys. Rev. Lett.* **76**, 4 (1996)

[2] O. Brüning, et al. AIP conf. proc. 395, Arcidosso, (1996)

[3] G.V. Stupakov, Superconducting supercollider laboratory report No. SSCL-579, 1992.

[4] G.V. Stupakov and K. Kauffmann, Superconducting supercollider laboratory report No. SSCL-587, 1992.

[5] P.L. Colestock and S. Assadi, conf. proc. PAC'97, Vancouver (1997)

[6] L.K. Spentzouris and P.L. Colestock, conf. proc. PAC'97, Vancouver (1997).

[7] C. Bhat, L.K. Spentzouris and P.L. Colestock, conf. proc. PAC'99, New York (1999)

[8] A. Piwinski, Proc. 9th Int. Conf. on High Energy Accelerators, Stanford, p. 406, (1974)

[9] J. D. Bjorken and S. K. Mtingwa, Particle Accelerators, Vol. 13, p. 115 (1983)

THE IMPACT OF COHERENT SYNCHROTRON RADIATION ON THE BEAM TRANSPORT OF SHORT BUNCHES*

R. Li

Thomas Jefferson National Accelerator Facility, 12000 Jefferson Ave., Newport News, VA 23606

Abstract

Designs for next-generation accelerators, such as future linear colliders and short-wavelength FEL drivers, require beams of short (mm-length or smaller) bunches and high charge (nC-regime). As such a high charge microbunch traverses magnetic bends, the curvature effect on the bunch self-interaction, by way of coherent synchrotron radiation (CSR) and space charge force, may cause serious emittance degradation. This impact of CSR on the beam transport of short bunches has raised significant concern in the design of future machines and led to extensive investigations. This paper reviews some of the recent progress in the understanding of the CSR effect, presents analysis of and computational work on the CSR impact on short bunch transport, and addresses remaining issues.

1 INTRODUCTION

The designs of future accelerators often require creation and manipulation of beams with high phase space densities. This incorporates short bunches with high charge being circulated or compressed by magnetic bending systems [1, 2]. The strong requirement of these designs on the preservation of small emittances makes it crucial to understand the evolution of beam phase space as a high charge microbunch traverses magnetic bends.

When an electron bunch goes through a bend, each electron gives out synchrotron radiation. When the radiation wavelength is longer than the bunch length, the radiations from individual electrons add constructively to form coherent synchrotron radiation (CSR). This coherent synchrotron radiation is a result of the curvature induced electromagnetic self-interactions within the bunch. These self-interactions may have detrimental effects on beam phase space: the longitudinal collective self-force could induce energy spread on the bunch, which further causes dispersive displacement of the particles due to the nonzero dispersion in the bend region, whereas the transverse collective self-force could directly drive the transverse motion nonuniformly across the bunch. Both the longitudinal and transverse self-interaction forces can cause emittance growth. Even when the bunch is transported through an achromatic system, since the curvature induced energy deviations occur *during* the bends, emittance degradation could still be a potential problem.

The problems related to the CSR effect in bends are: What are the curvature induced longitudinal and transverse self-interaction forces? What are their parametric dependence, their transient and steady state behavior? What is the effect of shielding by the vacuum chamber surrounding the beam? What is the impact of the curvature induced self-interaction on the short bunch transport through magnetic bending systems? What is the present understanding of the cancellation of the centrifugal space-charge force (CSCF) with the particle potential? What is the role of the non-inertial space-charge force? How does one simulate the bunch dynamics in a curved trajectory with the presence of the CSR effect? How does one handle the retardation and singularity which is intrinsic to the problem? How does one model the beam so as to maintain self-consistency of the simulation? How do the simulation results benchmark with analysis? Finally, how do the analysis and simulation compare with experiments?

This paper reviews some of the main results in the analysis, discusses the self-consistent simulation of the CSR impact on bunch dynamics, and highlights recent experiments.

2 OUTLINE OF THE CSR PROBLEM

First we outline the fundamental equations governing the curvature induced bunch self-interaction.

Consider a source electron with charge e, velocity v and acceleration $\dot{v}$. The electromagnetic field generated by the source electron at its retarded space-time (r', t') on a test electron at (r, t) is described by the Liénard-Wiechert formula: $\mathbf{E}_0 = \mathbf{E}_0^c + \mathbf{E}_0^r, \mathbf{B}_0 = \mathbf{B}_0^c + \mathbf{B}_0^r$,

$$\mathbf{E}_0^c = e \left[\frac{\mathbf{n} - \boldsymbol{\beta}}{\gamma^2 (1 - \boldsymbol{\beta} \cdot \mathbf{n})^3 R^2} \right]_{\text{ret}}, \quad \mathbf{B}_0^c = (\mathbf{n} \times \mathbf{E}_0^c)_{\text{ret}}, \quad (1)$$

$$\mathbf{E}_0^r = \frac{e}{c} \left[\frac{\mathbf{n} \times \{(\mathbf{n} - \boldsymbol{\beta}) \times \dot{\boldsymbol{\beta}}\}}{(1 - \boldsymbol{\beta} \cdot \mathbf{n})^3 R} \right]_{\text{ret}}, \quad \mathbf{B}_0^r = (\mathbf{n} \times \mathbf{E}_0^r)_{\text{ret}}, \quad (2)$$

where $\boldsymbol{\beta} = \mathbf{v}/c, \dot{\boldsymbol{\beta}} = \dot{\mathbf{v}}/c, \gamma = (1 - \beta^2)^{-1}, \mathbf{R} = \mathbf{r} - \mathbf{r}'$, $R = |\mathbf{R}|$, and $\mathbf{n} = \mathbf{R}/R$. The subscript "ret" denotes the retardation condition

$$t' = t - |\mathbf{r} - \mathbf{r}'|/c, \quad (3)$$

which requires the fields to travel from source to test electron with the velocity of light c. Here $\mathbf{E}_0^c$ and $\mathbf{B}_0^c$ are the Coulomb fields, and $\mathbf{E}_0^r$ and $\mathbf{B}_0^r$ are the radiation fields caused by the acceleration $\dot{\boldsymbol{\beta}}$ of the source electron. The

Lorentz force applied on the test electron by the single source electron is therefore $\mathbf{F}_0(\mathbf{r}, t) = \mathbf{F}_0^c + \mathbf{F}_0^r$, with

$$\mathbf{F}_0^c = e(\mathbf{E}_0^c + \boldsymbol{\beta} \times \mathbf{B}_0^c), \quad \mathbf{F}_0^r = e(\mathbf{E}_0^r + \boldsymbol{\beta} \times \mathbf{B}_0^r). \quad (4)$$

Given the above single particle forces, we can now move on to discuss the collective forces generated by a bunch. For a bunch moving on a circular orbit, let s denote the initial offset of a particle from the bunch center, and the particle's trajectory as $\mathbf{r}_0(\mathbf{s}, t)$. Then the bunch density distribution $n(\mathbf{r}, t)$ can be expressed in terms of its initial density distribution $\lambda(\mathbf{s})$ with respect to the bunch centroid: $n(\mathbf{r}, t) = \int ds\, \lambda(\mathbf{s}) \delta(\mathbf{r} - \mathbf{r}_0(\mathbf{s}, t))$. A test electron in the bunch will then experience the collective self-interaction forces, which are the integral of the single particle Coulomb and radiation forces in Eq. (4) generated by all the electrons in the bunch,

$$\begin{cases} \mathbf{F}^{cc}(\mathbf{r}, t) = \int \mathbf{F}_0^c(\mathbf{r}, t, \mathbf{s}')\lambda(\mathbf{s}')ds' \\ \mathbf{F}^{cr}(\mathbf{r}, t) = \int \mathbf{F}_0^r(\mathbf{r}, t, \mathbf{s}')\lambda(\mathbf{s}')ds' \end{cases} \quad (5)$$

where $\mathbf{F}^{cc}$ stands for the *collective Coulomb force*, and $\mathbf{F}^{cr}$ for the *collective radiation force*. The two collective forces have distinctive features. For steady-state circular motion, $\mathbf{F}^{cc}$ is negligible at high energy while $\mathbf{F}^{cr}$ is still effective. However, even at high energy, both are important for transient interaction. Therefore they should both be included when considering the feedback to the bunch dynamics

$$d(\gamma m \dot{\mathbf{v}})/dt = \mathbf{F}^{ext} + \mathbf{F}^{cc} + \mathbf{F}^{cr}, \quad (6)$$

where $\mathbf{F}^{ext}$ stands for the external force.

Instead of the integration of single particle Liénard-Wiechert fields as described above, it is often easier to analyze the bunch self-interaction forces in terms of the potentials

$$\mathbf{F} = -e\nabla(\Phi - \boldsymbol{\beta} \cdot \mathbf{A}) - ed\mathbf{A}/cdt. \quad (7)$$

However, associating the potential approach with the Liénard-Wiechert approach often can help us identify the nature of a potential term — if it is originated from the collective Coulomb force $\mathbf{F}^{cc}$ or the radiation force $\mathbf{F}^{cr}$.

3 ANALYSIS OF SELF-INTERACTION

In this section we study the curvature induced bunch self-interaction of a rigid Gaussian line-bunch on a circle in free space, with the particle density function

$$\lambda(s, \sigma_s) = e^{-s^2/2\sigma_s^2}/\sqrt{2\pi}\sigma_s. \quad (8)$$

Here s is the longitudinal distance from the bunch center, and σ_s is the rms bunch length. The radius of the circle is ρ and the number of electrons in the bunch is N. The velocity of the bunch is v, and $\beta = v/c$.

3.1 Steady-State Results in Free Space

The longitudinal collective force on the bunch is [3, 4, 5]

$$F_\theta(s) \simeq \frac{2Ne^2}{\sqrt{2\pi}(3\rho^2\sigma_s^4)^{\frac{1}{3}}} \int_0^\infty \frac{d\phi_1}{\phi_1^{\frac{1}{3}}} \frac{\partial}{\partial \phi_1} e^{-\frac{(s/\sigma_s - \phi_1)^2}{2}}. \quad (9)$$

This equation shows that the longitudinal force is bigger for smaller bend radius and shorter bunch length, and it causes energy spread by accelerating the bunch head and decelerating the bunch tail. For example, for $\rho = 1$ m, $\sigma_s = 1$ mm, and $N = 10^9$, we have $|F_\theta|_{max} \sim 8$keV/m. The steady-state CSR power in free space (fs) is [5, 6]

$$P^{fs} = -\int F_\theta(s)\lambda(s)ds \simeq \frac{N^2e^2c}{\rho^{2/3}\sigma_s^{4/3}} \frac{3^{1/6}\Gamma^2(2/3)}{2\pi}. \quad (10)$$

Using Eq. (7), the transverse collective force yields

$$F_r = -e\frac{\partial(\Phi - \boldsymbol{\beta} \cdot \mathbf{A})}{\partial r} - e\frac{dA_r}{cdt} + e\mathbf{A} \cdot \frac{d\mathbf{e}_r}{cdt}, \quad (11)$$

where the third term on the right of the equation contains the rate of change of the transverse direction, which is purely due to the curvature effect. For circular motion, this term gives the centrifugal space-charge force (CSCF) [7]:

$$F^{CSCF} = e\mathbf{A} \cdot \frac{d\mathbf{e}_r}{cdt} = e\frac{\beta_\theta A_\theta}{r} \quad (12)$$

with r the distance of the test particle from the center of the design circle. It can be shown that F^{CSCF} is dominant in F_r of Eq. (11). For a rigid 2D Gaussian ribbon-bunch on a circular orbit with density distribution $\lambda(s, \sigma_s)\lambda(z, \sigma_z)$, with $\lambda(s, \sigma_s))$ given in Eq. (8) and z being the vertical offset from design orbit, one has [8]

$$A_\theta(s, z = 0) \simeq Ne\lambda(s, \sigma_s) \ln\left[\frac{(\rho\sigma_s^2)^{2/3}}{\sigma_z^2}(1 + \frac{\sigma_z}{\sigma_s})\right]. \quad (13)$$

For example, for $\rho = 1$ m, $\sigma_s = 1$ mm, $\sigma_z = 1$ mm, $N = 10^9$, we have $|F^{CSCF}|_{max} \sim 3$ keV/m. Similar to the coasting beam case [7], the logarithmic dependence of F^{CSCF} with respect to the transverse offset $x = r - \rho$ also exists for a bunched beam. This highly nonlinear behavior with transverse offset makes its impact on the transvese dynamics worrisome for machine designers. This topic will be further discussed in Sec. 4.1.

3.2 Shielding of Steady-State CSR

The mechanism of shielding of steady-state coherent synchrotron radiation by two parallel conducting plates is well understood [9, 10, 11]. Denoting the gap size between the two plates being h, and the shielding factor as

$$\eta = \sqrt{\frac{2}{3}} \left(\frac{\pi\rho}{h}\right)^{3/2} \left(\frac{\sigma_s}{\rho}\right), \quad (14)$$

we can show [12] that for strong shielding ($\eta \geq 1$), the ratio of the shielded CSR power P^{sh} to free-space steady-state CSR power P^{fs} (Eq. (10)) is given by

$$P^{sh}/P^{fs} \simeq 4.2\eta^{5/6}e^{-2\eta}. \quad (15)$$

The behavior of P^{sh}/P^{fs} vs. η is depicted in Fig. 1. The free-space case corresponds to $h = \infty$, or $\eta = 0$, where $P^{sh}/P^{fs} = 1$. As the gap becomes narrower, η grows bigger, and the CSR is gradually shut off. For example, for $\rho = 1$ m, $\sigma_s = 1$ mm, $h = 2$ cm, we have $\eta = 1.6$, and $P^{sh}/P^{fs} = 0.25$.
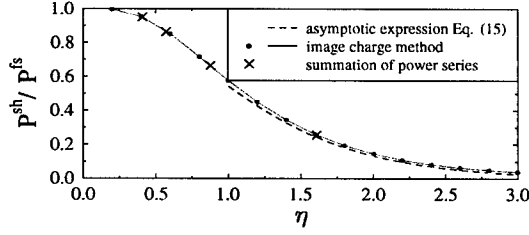
Figure 1: Steady-state CSR power with shielding, with free-space case corresponding to $\eta = 0$.

3.3 Transient Self-Interaction with Shielding

The free-space transient self-interaction for a bunch entering a bend from a straight path was recently studied by Saldin [13]. Later we studied the transient self-interaction in the presence of shielding [14]. To illustrate the duration and magnitude of the transients, we plot in Fig. 2 the instantaneous power $P^{sh}(t)$ (normalized by P^{fs} in Eq. (10)) radiated by a line Gaussian bunch as a function of θ, which is the angle of the bunch center entering the bend from a straight path. Here we use the typical parameters $\rho = 1$ m, $\sigma_s = 1$ mm. Fig. 2 shows that the free-space power increases from zero and saturates to its steady-state value as the bunch moves into the bend. For $h = 2$ cm, the transient power oscillates and saturates to its steady-state value after $\theta = 30°$. For machine designs intending to reduce the CSR effect by using a narrow gap size, one should notice that in a certain bend region, the transient interaction with shielding has much bigger amplitude than its steady-state counterpart, as shown by the $h = 2$ cm curve in Fig. 2 around $\theta \sim 10°$.
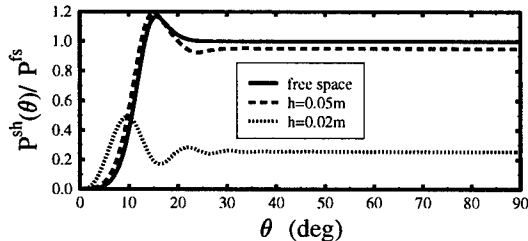
Figure 2: Transient power loss of an ultrarelativistic bunch, due to the curvature-induced self-interaction in the presence of two parallel plates, with $\rho = 1$ m, $\sigma_s = 1$ mm, and various plate spacing h. Here θ is the angle of the bunch center entering the bend.

Our study [14] also shows that the collective Coulomb force from the straight path upstream of a bend makes an important contribution to the transient self-interaction of the bunch. This is because when the bunch turns into the arc, the pancake-shaped Coulomb field from the straight path shines right upon a portion of the bunch just turned into the arc, causing the transient collective Coulomb effect comparable in magnitude with the transient collective radiation effect.

4 IMPACT ON BUNCH DYNAMICS

4.1 General Formalism

In the previous section, we discussed the curvature induced bunch self-interaction forces. These forces feed back on the bunch dynamics through the equation of motion in Eq. (6). Let θ be the angle of an electron into the bend, E_0 be the design energy, $x = (r - \rho)/\rho$ be the relative offset from the design orbit, and the design bending field be the only external field. Then the first order equation for the transverse motion of an electron in the bunch is [8]

$$\frac{d^2x}{d\theta^2} + x = \frac{\Delta E}{E_0} + \frac{\rho F_r}{E_0}, \tag{16}$$

where F_r is given by Eq. (11), and denoting the initial potential of the electron as Φ_0, one has

$$\Delta E = \int_0^\theta \Delta F_\theta \rho \, d\theta' - e(\Phi - \Phi_0), \quad \Delta F_\theta = e\frac{\partial(\Phi - \boldsymbol{\beta} \cdot \mathbf{A})}{c \partial t}. \tag{17}$$

It is instructive to further write Eq. (16) as

$$\frac{d^2x}{d\theta^2} + x = \frac{e\Phi_0}{E_0} + \frac{\rho}{E_0}\left[\int_0^\theta \Delta F_\theta \, d\theta' + G\right]. \tag{18}$$

Here G is the residual function in which the logarithmic A_θ term (Sec.3.1) in F_r is largely cancelled with the potential Φ in Eq. (17), as shown by the underlined term:

$$G \equiv F_r - \frac{e\Phi}{\rho}$$
$$= -e\frac{\partial(\Phi - \boldsymbol{\beta} \cdot \mathbf{A})}{\partial r} - e\frac{dA_r}{c \, dt} + e(\underline{\frac{\beta_\theta A_\theta}{r} - \frac{\Phi}{\rho}}) \tag{19}$$
$$= G_0 + G_1 x + \dots$$

for $G_0 = G|_{x=0}$ and $G_1 = \frac{\partial G}{\partial r}\big|_{x=0}$.

The general formula in Eq. (18) applies to both the coasting beam case and the bunched beam case. For a coasting beam with constant density λ, one can show that

$$\Delta F_\theta = 0, \quad G_0 = \text{constant}, \tag{20}$$

$$G_1 = O\left[\frac{\lambda}{\rho^2}\right] \ll \frac{\partial F_r}{\partial r}\bigg|_{x=0} \tag{21}$$

as studied by E. Lee [15]. For a bunched beam, in steady state, the driving terms in Eq. (18) are

$$\Delta F_\theta = F_\theta \quad (F_\theta \text{ as in Eq. (9)})$$
$$G \simeq -e\frac{V_0}{\rho} - e\frac{\partial V_0}{\rho \partial x} - e\frac{\beta_\theta A_\theta}{\rho} x \tag{22}$$

with $V_0 \equiv \Phi - \beta_\theta A_\theta$. Note that unlike the coasting beam, where G_0 is a constant which only modifies the equilibrium orbit, here for a bunched beam, $G_0(s)$ and $G_1(s)$ are non-uniform across the bunch, so they both could cause emittance growth. Using the result of V_0 [8], one has

$$\frac{|G_0|_{\max}}{|\Delta F_\theta|_{\max}} \sim \left(\frac{\sigma_s}{\rho}\right)^{1/3}, \quad \frac{|G_1|_{\max}x}{|\Delta F_\theta|_{\max}} \sim \frac{x}{\rho}\left(\frac{\sigma_s}{\rho}\right)^{-1/3}. \tag{23}$$

120

For $\sigma_s/\rho \sim 10^{-6}$ to 10^{-3}, one often has

$$x \ll (\sigma_s/\rho)^{1/3} \ll 1. \qquad (24)$$

It then yields

$$\frac{|G_0|_{\max}}{|\Delta F_\theta|_{\max}} \ll 1 \quad \text{and} \quad \frac{|G_1|_{\max} x}{|\Delta F_\theta|_{\max}} \ll 1. \qquad (25)$$

With the comparisons of G and ΔF_θ in Eqs. (23) and (25), one should keep in mind that in Eq. (18), the effect of the residual function G on the transverse motion should be compared with the *integral* of ΔF_θ over the bend angle $\int \Delta F_\theta d\theta'$. Therefore the comparison of the effects of G and ΔF_θ varies with different machine designs. Also note that similar to the initial energy spread, Φ_0 in Eq. (18) does not cause emittance growth for an achromatic bending system. For a line charge moving *on-axis* from a straight path to a circle, i.e., $x = 0$, the nonvanishing $(\Phi - \Phi_0)$ is purely the transient effect due to the collective Coulomb forces from the straight path [14]. Therefore the fact that Φ is largely cancelled by A_θ in Eq. (19) indicates that the on-axis A_θ undos part of the transient effects.

4.2 Noninertial Space-Charge Force

The role of the "noninertial space-charge force" [16] can be understood in the context of the big picture discussed in the above sections. This force arises from the analysis of the longitudinal collective force exerted on an off-axis $(x \neq 0)$ test particle from a finite uniform bunch on a circle.

We start with the single particle force exerted on an observation particle O by a source particle S orbiting on a circle. Let the distances from S and O to the center of the circular orbit C be R_s and R_o respectively, $c\tau$ be the distance from S to O, and γ_s be the Lorentz factor of S. In the cylindrical coordinate, at the observation time t, O is at (R_o, θ_o) and S is at (R_s, θ_s). The corresponding retarded time for S is t' when S is at (R_s, θ'_s). The angular distances of O and S from the bunch center are $\phi_o = \theta_o - \beta_s ct/R_s$ and $\phi' = \theta'_s - \beta_s ct'/R_s$ respectively. Let $s_o = R_s\phi_o$, $s' = R_s\phi'$ and $\theta = \theta_o - \theta'_s$. For $\Delta s = s_o - s'$, the retardation relation requires

$$R_s\theta = \Delta s + \beta_s c\tau, \quad c\tau = \sqrt{R_s^2 + R_o^2 - 2R_sR_o\cos\theta}. \qquad (26)$$

The *single particle* longitudinal force from S on O is

$$F_{\theta 0} = -e\frac{\partial\Phi}{R_o\partial\theta} - e\frac{\partial A_\theta}{c\partial t} =$$

$$-e^2\frac{\partial}{\partial\Delta s}\left[\frac{\frac{R_s}{\gamma_s^2 R_o} + \beta_s^2\left(\frac{R_s}{R_o} - 1\right) + \beta_s^2(1 - \cos\theta)}{c\tau - \beta_s R_o\sin\theta}\right] \qquad (27)$$

where θ and τ are implicit functions of Δs via Eq. (26).

The *collective* longitudinal force on the test particle O is

$$F_\theta(s_o) = \int_{s_r}^{s_f} F_{\theta 0}(s_o - s')\lambda(s')ds'$$

$$\simeq e^2\lambda\left[\frac{\frac{R_s}{\gamma_s^2 R_o} + \beta_s^2\left(\frac{R_s}{R_o} - 1\right) + \beta_s^2(1 - \cos\theta)}{c\tau - \beta_s R_o\sin\theta}\right]_{s_o-s_r}^{s_o-s_f} \qquad (28)$$

with λ the constant bunch density, and s_r and s_f standing for the rear and front of the line bunch respectively. Comparing the *single particle* force in Eq. (27) with the Liénard-Wiechert fields in Eqs. (1) and (2), one finds that on the right-hand side of Eq. (27)), the first term is the Coulomb field and the second and third terms are the radiation field. Therefore in the *collective* force of Eq. (28), the first term is the collective Coulomb force and the second and third terms are the collective radiation force.

The longitudinal collective force can also be analyzed using the potential approach. For $\beta_o = \beta_s$ one has

$$F_\theta(s_o) = e\left[\frac{\partial(\Phi - \boldsymbol{\beta}_o \cdot \mathbf{A})}{c\partial t} - \frac{d\Phi}{cdt}\right] \qquad (29)$$

$$\simeq e^2\lambda\left[\frac{\frac{1}{\gamma_s^2} + \left(\frac{R_s}{R_o} - 1\right) + \beta_s^2(1 - \cos\theta)}{c\tau - \beta_s R_o\sin\theta}\right]_{s_o-s_r}^{s_o-s_f} \qquad (30)$$

Notice that Eq. (30) is equivalent to Eq. (28) but slightly varied in expression. In the literature [16], for the terms on the right-hand side of Eq. (30), the first term is called the "usual Coulomb force", the second term is named the "noninertial space-charge force" and the third term is called the " usual CSR force". One can show that the "noninertial space-charge" term is nothing but the $-ed\Phi/cdt$ term in Eq. (29), which integrated over time gives the term $-e(\Phi - \Phi_0)$ in Eq. (17) for the energy change. As we've shown in Eq. (19), the effect of the potentials Φ in the energy change is largely cancelled by the term A_θ in F_r, and only the residual of their cancellation, the function G, acts as one of the driving factors to the transverse motion. Therefore we remark that the effect of the "noninertial space-charge force" on the transverse motion must be considered *together* with the radial force (Talman's force) so as to have a complete and proper description of the dynamical system.

5 SELF-CONSISTENT SIMULATION

The analyses in the previous sections are based on the rigid-line-bunch model. In reality, a bunch has finite transverse size, and its dynamics responds to the curvature induced self-interaction. In order to study the actual dynamical system, we have developed a *self-consistent* simulation [17] based on a 2-dimensional macroparticle model. This simulation integrates numerically the following equation of motion around a design orbit

$$\frac{d(\gamma\beta_r)}{cdt} - \beta_\theta\left(\frac{\gamma\beta_\theta}{r} - \frac{\gamma_0\beta_0}{r_0}\right) = \tilde{F}_r \qquad (31)$$

$$\frac{d(\gamma\beta_\theta)}{cdt} + \beta_r\left(\frac{\gamma\beta_\theta}{r} - \frac{\gamma_0\beta_0}{r_0}\right) = \tilde{F}_\theta, \qquad (32)$$

where β_0, γ_0 are the design parameters, r_0 the design radius, $B_{\text{ext}} = -e\gamma_0\beta_0\mathbf{e}_z/r_e r_0$ for $r_e = e^2/mc^2$, and $\tilde{\mathbf{F}} = (e/mc^2)(\mathbf{E} + \boldsymbol{\beta} \times \mathbf{B})$ is the curvature induced self-interaction force in free space. The algorithm for the computation of the curvature induced self-interaction force $\tilde{\mathbf{F}}$

and its benchmark with analytical results are described in Ref.[17], which shows that the macroparticle model handles the retardation and self-consistency in a straightforward manner.

In Ref.[17] it is shown that the fields from each macroparticle are 2-dimensional integrals over the area surrounding the previous path of the source macroparticle. The singularities in the integrands are intrinsic to the Green's function and are readily removed by integration by parts using the finite 2-dimensional size of the macroparticles. By doing this, one finds that as the result of the retardation relation, the integrand of F_r has a narrow spike near the observation point (in addition to the long range behavior), which has nontrivial contribution to the integration. Therefore extra care is needed for the numerical integration to compute F_r.

The above described simulation can handle both transient (including entrance and exit) and steady-state self-interaction self-consistently. It also takes care of cases involving the coupling of two or more bends, where the radiation generated in an earlier bend can influence the bunch when it is at succeeding bends. The disadvantage of the above scheme is that it takes extra numerical work to calculate the radial force correctly, while this force is actually largely canceled with Φ, which is hidden in γ of Eq. (31) as part of ΔE. Therefore this scheme *indirectly* handles the cancellation of F_r and Φ.

To overcome the disadvantage in the above scheme, we are currently improving the simulation by numerically integrating the following reduced form of the equation of motion:

$$
\begin{cases}
\dfrac{d(\gamma + \tilde{\Phi})\beta_r}{cdt} - \beta_\theta \left[\dfrac{(\gamma + \tilde{\Phi})\beta_\theta}{r} - \dfrac{\gamma_0\beta_0}{\rho} \right] \\
\qquad = -\dfrac{\partial \tilde{V}_0}{\partial r} + \beta_\theta \dfrac{\delta \tilde{A}_\theta}{r} - \dfrac{d\delta \tilde{A}_r}{cdt} \\[2mm]
\dfrac{d(\gamma + \tilde{\Phi})\beta_\theta}{cdt} + \beta_r \left[\dfrac{(\gamma + \tilde{\Phi})\beta_\theta}{r} - \dfrac{\gamma_0\beta_0}{\rho} \right] \\
\qquad = -\dfrac{\partial \tilde{V}_0}{\rho\partial\theta} - \beta_\theta \dfrac{\delta \tilde{A}_r}{r} - \dfrac{d\delta \tilde{A}_\theta}{cdt} \\[2mm]
\dfrac{d(\gamma + \tilde{\Phi})}{dt} = \dfrac{\partial \tilde{V}_0}{\partial t}
\end{cases}
\tag{33}
$$

where the reduced potentials are

$$
\tilde{\Phi} = \frac{e}{mc^2}\Phi \qquad \tilde{V}_0 = \frac{e}{mc^2}(\Phi - \boldsymbol{\beta} \cdot \mathbf{A})
$$

$$
\delta \tilde{A}_{r,\theta} = \frac{e}{mc^2}(A_{r,\theta} - \beta_{r,\theta}\Phi).
\tag{34}
$$

In this new scheme, $\delta \tilde{A}_\theta$ is the residual of the cancellation of Φ and A_θ, whose effect on the transverse dynamics can be clearly identified. With the initial potential $\Phi(t = 0)$ known, one can obtain at each step $(\beta_r, \beta_\theta, \gamma + \tilde{\Phi})$ as the result of the driving factors $\nabla \tilde{V}_0$ and $\delta \mathbf{A}$. These driving factors are computed from the macroparticle model as 2-dimensional integrals in a similar way as the field calculation in Ref.[17]. Notice that due to the above mentioned

cancellation, when computing the driving factors in Eq. (6), the retardation-caused local spikes in the integrands have now negligible contribution to the integrals; therefore they are numerically much easier to compute than the radial force F_r in the previous scheme. Our numerical computation shows that for a line charge, the numerical results of the driving factors agree with their analytical counterparts. These numerical results are not sensitive to the macroparticle size as long as it is much less than the real bunch size. Development of simulation based on this new scheme is still continuing.

6 RECENT EXPERIMENTS

Recently there are some experimental results on the CSR effect in bends. One example is the measurement of the transverse emittances as a function of bending angle carried out on the CLIC bunch compressor [18], which shows that among all the possible causes of transverse phase space dilation, the CSR effect can best explain the measured emittance growth. On the Jefferson Lab FEL beamline, we are in the process of measuring the emittance growth through the first 180° arc as a function of the cryomodule phase. The latter rotates the longitudinal phase space and affects the bunch length along the beamline in a complex way. Currently we are carrying out parametric studies of the CSR effect using the simulation, and systematic benchmarking of the simulation with experiment is underway at Jefferson Lab.

7 REFERENCES

[1] M. Cornacchia, SLAC-PUB-7433, 1997.

[2] E. T. d'Amico, et al., CLIC Note 355, 1998.

[3] L. V. Iogansen and M. S. Rabinovich, Sov. Phys. JETP 37(10), 83 (1960).

[4] Ya. S. Derbenev, et al., DESY Report No. TESLA-FEL-95-05, 1995.

[5] B. Murphy, S. Krinsky, and R. L. Gluckstern, BNL-63090, (1996).

[6] L. I. Schiff, Rev. Sci. Instr. 17, 6-14, (1946).

[7] R. Talman, *Phys. Rev. Letts.* 56, 1429 (1986).

[8] Ya. S. Derbenev and V. Shiltsev, Fermilab-TM-1974 (1996).

[9] J. S. Nodvick and D. S. Saxon, Phys. Rev. 96, 180 (1954).

[10] R. L. Warnock and P. Morton, Part. Accel. 25, 113 (1990).

[11] S. Heifets and A. Michailichenko, SLAC Note AP-83 (1990).

[12] R. Li, C. L. Bohn, and J. J. Bisognano, Proceedings of the Particle Accelerator Conference, Vancouver, 1997.

[13] E. L. Saldin, E. A. Schneidmiller, and M. V. Yurkov, DESY-TESLA-FEL-96-14, (1996).

[14] R. Li, C. L. Bohn, and J. J. Bisognano, Proc. SPIE, San Diego (1997).

[15] E. P. Lee, *Particle Accelerators*, 25, p.241 (1990).

[16] B. E. Carlsten, *Phys. Rev. E*, 54, p.838 (1996).

[17] R. Li, Proc. of 1998 European Partical Accelerator Conf., Stockholm (1998); *Nucl. Instr. and Meth. in Phys. Res. A*, to be published.

[18] H. Braun, et al., CLIC Note 389, 1999.

THEORY AND MEASUREMENT OF THE ELECTRON CLOUD EFFECT[#]

K. C. Harkay [+], Advanced Photon Source

Argonne National Laboratory, Argonne, IL 60439 USA

Abstract

Photoelectrons produced through the interaction of synchrotron radiation and the vacuum chamber walls can be accelerated by a charged particle beam, acquiring sufficient energy to produce secondary electrons (SEs) in collisions with the walls. If the secondary-electron yield (SEY) coefficient of the wall material is greater than one, a runaway condition can develop. In addition to the SEY, the degree of amplification depends on the beam intensity and temporal distribution. As the electron cloud builds up along a train of stored bunches, a transverse perturbation of the head bunch can be communicated to trailing bunches in a wakefield-like interaction with the cloud. The electron cloud effect is especially of concern for the high-intensity PEP-II (SLAC) and KEK B-factories and at the Large Hadron Collider (LHC) at CERN. An initiative was undertaken at the Advanced Photon Source (APS) storage ring to characterize the electron cloud in order to provide realistic limits on critical input parameters in the models and improve their predictive capabilities. An intensive research program was undertaken at CERN to address key issues relating to the LHC. After giving an overview, the recent theoretical and experimental results from the APS and the other laboratories will be discussed.

1 INTRODUCTION

Electron cloud (EC) effects involve the interaction between high-energy beams and low-energy electrons produced in the vacuum chamber. These interactions are essentially nonresonant in nature, unlike the well-known phenomenon of ion-trapping [1], widely observed in electron and anti-proton storage rings. A major contribution to the electron cloud in high-energy, multibunch lepton rings are photoemitted electrons (PE) produced through the collision of synchrotron radiation photons and the vacuum chamber walls. Ionization of the residual gas is a negligible source of electrons for typical vacuum pressures. The surface condition, material, and geometry of the vacuum chamber are important considerations in the photoelectron yield, Y, as is the photon energy and incident angle. The electron cloud distribution further depends on the photon reflectivity, R. The published Y, R data differ in some details [2][3]; other uncertainties in predicting EC effects lie in choosing realistic parameters for the photon energies and incidence angles. The most severe effects are expected in chambers without an antechamber, such as in the

PEP-II interaction region [4]. Even with an antechamber to pass most of the high-energy photons, a storage ring chamber is typically designed with a number of absorbers to intercept photons to protect downstream surfaces such as flanges and ceramic chambers. The absorbers can serve as a dominant source of PE, as observed at the APS [5].

The photoelectrons can be accelerated by a charged particle beam, acquiring sufficient energy to produce secondary electrons in collisions with the walls. If the secondary-electron yield (SEY) coefficient of the wall material is greater than one, the runaway condition of beam-induced multipacting can develop. In addition to the SEY, the degree of amplification depends on the beam intensity and the temporal distribution. The former determines the incident electron energies and the latter determines whether a resonance condition is satisfied between the bunch spacing and the wall-to-wall time-of-flight of the electrons. Beam-induced multipacting was first observed 20 years ago in the Intersecting Storage Ring (ISR), at which time a fast pressure rise of an order of magnitude was seen due to electron-induced desorption [6]. Photoemission can be thus be important in ~TeV hadron machines such as the LHC, primarily because of multipacting effects and heating of the superconducting magnet liners [7]. To avoid multipacting, a minimum SEY, close to unity, is desired. Photon reflectivity (R) also plays a key role in determining the electron distribution in regions with a dipole field [8]. Uncertainties in calculating the minimum SEY and maximum R involve the assumed energy and angular distribution of the incident cloud electrons.

As the electron cloud builds up along a train of stored bunches, a wakefield of sufficient magnitude can be produced through the local perturbation of the cloud by transverse offsets of the leading bunches. The effective wakefield is short-ranged, but for a large bunch number, the oscillation amplitude in the tail of the train can grow exponentially. Also called the beam-photoelectron instability or "Ohmi" effect, ECI was first described by K. Ohmi (KEK) in 1995 [9] after experimental evidence for it was found at the KEK Photon Factory (PF) [10]. The possibility of ECI at the KEK-B lead to a collaboration between KEK and IHEP (China) to undertake experiments at BEPC, where results similar to those at PF were obtained and a detailed study of the dependence of the instability on machine parameters was made [11]. Although results from theoretical simulations are qualitatively consistent with these observations, the electrons had not been directly measured. The goal of studies at the APS was to directly characterize the electron cloud. The SEY for the oxidized Al chamber in the storage ring is >2 for incident electrons up to 1 keV [4][12], so a large effect was expected.

In this overview, the initial experimental evidence for electron cloud instabilities is reviewed, including relevant observations on phenomena involving trapped electrons. Recent analytical results, including refinements of the models, are presented. Recent experimental results from CERN, APS, PEP-II, and BEPC are then described. Table 1 gives the parameters for the machines discussed.

2 EXPERIMENTAL OBSERVATIONS

The most convincing evidence for ECI are similarities between theoretical predictions and experiments performed at the PF, BEPC, and CESR, which include positron vs. electron behavior, growth rate, effect of bunch spacing, and effect of bunch current on spectrum.

In machine experiments at PF [10] and BEPC [11], vertical coupled-bunch instabilities were observed with positrons and electrons, but with different instability thresholds and characters. For electrons, the threshold was higher, excitation of rf cavity HOMs were seen, and the betatron sideband spectrum was narrow. For positrons, the threshold was lower, no HOM signals were seen, and the sideband spectrum was broad. The threshold was not affected by the operation of the distributed ion pumps (DIPs). At the PF, the peaks of the betatron spectrum shifted with beam current, unlike what would be expected with a conventional coupling impedance. The instability was not completely suppressed with a bias voltage applied to the position monitors (clearing electrode), but could be overcome using octupoles. At the BEPC, a fit to the betatron spectrum shows the range of the wakefield to be 2-4 bunches. The instability was very sensitive to vertical chromaticity, emittance, bunch spacing, and rf frequency (horizontal orbit position), and weakly dependent on the energy. The damping effect of high chromaticity is thought to involve a combination of head-tail and Landau damping [9]. The instability threshold increased by a factor of 4 after increasing the bunch spacing by a factor of 2.

A horizontal coupled-bunch instability involving PE electrons trapped in the combined quadrupole electrostatic leakage field from the DIPs and bending magnet field was observed at CESR [13]. The transverse position of the beam modulates the trapped charge density, which in turn produces a time-dependent force on the beam, similar to

ECI. Calculations show that the wakefield is long-range, but that SE are unimportant at the nominal bunch spacing (280 ns). No ECI-like effects were seen for spacings > 14 ns, but preliminary data at a 2-ns spacing shows a betatron sideband signature similar to PF and BEPC [14].

A broadly studied beam-electron interaction in a machine very different from these is the "e-p" instability at the Proton Storage Ring (PSR) at LANL [15]. Plans for very high-intensity proton drivers ($>10^{14}$ protons/pulse) for the spallation neutron source and muon collider have generated renewed interest in understanding the e-p effect. Experiments indicate that coupled oscillations of low-energy electrons and beam protons develop when electrons are trapped in the beam potential well. Charge collected on electrodes when the beam becomes unstable is believed to have a contribution from beam-induced multipacting. The peak in the unstable frequency spectrum depends on the current and bunch length. Clearing electrodes have minimal effect on increasing the instability threshold. There is some recent evidence that an e-p instability has been observed at the CERN Proton Source [16].

Transverse coupling between bunches mediated by the free electrons in ECI is similar to the dynamics with free ions in the fast beam-ion instability (FBII), first proposed theoretically, and then observed at Pohang Light Source (PAL), Advanced Light Source (LBNL), and TRISTAN (KEK) [17]. FBII persists even with a gap much longer than is necessary to clear classically trapped ions.

3 THEORY/SIMULATION

The three major numerical models for electron cloud effects were developed by K. Ohmi at KEK [9], M. Furman and G. Lambertson at LBNL [4], and F. Zimmermann at SLAC [18], the latter further developed by O. Brüning at CERN [19]. Simulation studies are complemented by analytical work by S. Heifets at SLAC [20] and N. Dikansky at BINP [21]. The codes give qualitatively similar results. First, the electron cloud is established by synchrotron photons emitted by a train of bunches, the distribution balanced between production and absorption processes. In the range of 10-100 eV photon energy, for example, the normal incidence Y for Al ranges between 0.2 and 0.06 [2]. Both the yield and the photon reflectivity, R, increase

Table 1: Machine parameters

	PF	BEPC	CESR	APS	PEP-II	KEKB	LHC	PSR
E (GeV)	2.5	2.2	5.3	7	3.1/9*	3.5/8*	7000	0.8
max. # bunches, N	312	160	1281	1296	1658	5120	2835	1
min. bunch spac. (m)	0.6	1.5	0.6	0.85	1.26	0.59	7.5	–
I (max.) (mA)	300	20-30	300*	100	2140/980	2600/1100	540	2×10^{13} p
photon critical E (keV)	4	2.3	3.7	19.5	4.8&	6&	0.044	–
chamber radius or semi-axes (h × w) (mm)	א	29×60	25×45	21×42	25×45&	48&	22	50
chamber material	Al	Al	Al	Al	TiN,Cu,SS	Cu	Cu	SS

* LER (e+) / HER (e-)　　& LER only　　* N = 27　　א not available

for smaller incident angles. The force of the beam on the electrons is then computed, and the electrons are allowed to drift between bunch passages. In the impulse approximation, the momentum kick of an electron at a radial position, r, is $\Delta p_e = 2m_e c r_e N_b / r$, where $r_e = 2.8 \times 10^{13}$ cm is the classical electron radius and N_b is the number of beam particles. For better accuracy in the models, the beam is sliced longitudinally and the force on the electrons is computed for each slice. Space charge is included in the calculations, as is the contribution by the image charges on the wall. When an electron reaches a wall, SE are generated using the appropriate SEY coefficients, given the electron energy and incident angle [12].

To calculate coupled-bunch effects, the first bunch is displaced transversely, which drags the electron cloud with it. The following bunch feels a kick due to the potential of the offset cloud, perturbing the cloud further, and so on. The forces are either represented by an effective wakefield or calculated on a finite-element grid. The instability growth rates of the transverse, coherent, multi-bunch modes are then computed in the usual way [22].

The greatest variations in the cloud saturation levels and growth rates predicted in the codes involve the assumptions made in the electron production processes and the presence of an external magnetic field. The EC buildup is limited by space charge. The distribution in a field-free region is more uniform than in a dipole field, where the electrons are confined to move in tight vertical helices. The main consequence is the severe suppression of the horizontal component of the momentum transferred to the cloud electrons [4]. In this case, the electrons near the beam orbit are produced by photons scattered from the mid-plane to the upper and lower chamber surfaces. Given a large SEY, even electrons produced by ionization of the residual gas by the beam are sufficient to start a chain reaction. For PEP-II, it was found that coating the Al chamber with TiN, thereby lowering the SEY, reduced the instability growth time by a factor of ~20-40. The SEY for oxidized Al is >2 for primary electrons up to 1 keV, while for Ti, it is <1 [4][12]. This result is important in the case of LHC, also. Calculations indicated that depending on assumptions about Y, SEY, and R, the EC-induced heat load on the beam liner could far exceed the cryogenic budget of 1 W/m. As a result, an intensive research program at CERN to measure the relevant physical quantities, validate the theoretical estimates, and propose remedies has been initiated [7][23]. A minimum SEY of 1.3 was defined to prevent multipacting [8][19].

The buildup of the electron cloud depends on so many factors that it is not obvious that simple scaling rules can be found to apply the results from one machine to another [4]. The PE alone may be sufficient to cause a beam instablity, as is likely to be the case in PF, KEKB, and BEPC. Even if the SEY is high, all the secondaries are lost if the bunch spacing is large; then only the PE are important. At a smaller bunch spacing, the SE can dominate for large SEY. In this case, primary PE may no longer be important, and even ionization electrons can lead to blowup, as in the ISR [6].

In the case of coupled-bunch instabilities, the range of the wakefield sets an upper limit to the bunch spacing at which ECI is important. This appears to be the case at both BEPC, where the ECI threshold increased for twice the bunch spacing, and at CESR, where an EC-like betatron spectrum was seen only when the bunch spacing was < 14 ns. The range of the wakefield is determined by both the average electron kinetic energy and by their density distribution. But if secondary emission and hence multipacting are unimportant, then the range of the wakefield is critically dependent only on their kinetic energy [24]. Therefore, while electron cloud effects are essentially nonresonant in nature, beam-induced multipacting effects can be important. It is observed that both multipacting and ECI could be important in both positively and negatively charged beams [5][6][9][24].

4 RECENT MEASUREMENTS

Of particular interest for recent measurements is to provide realistic limits on critical input parameters in the models to improve their predictive power. For example, a better knowledge of the fraction of photons diffused away from the forward direction and of the secondary electron energy distribution is required to understand the beam-induced multipacting heat load for LHC [7]. Comparison of independent codes (Furman and Zimmermann) has led to a convergence in the results at the 20% level for LHC simulations.

4.1 CERN

Photon irradiation tests were performed using an existing Electron-Positron Accelerator beamline at CERN to study the photoelectron yield, Y, and photon reflectivity, R [8]. A 4.2-m-long SS test chamber was irradiated at a grazing incidence (11 mrad) by 45 eV and 194 eV photons. The Cu liners inserted were of varying surface preparation and roughnesses, including a sawtooth structure with 0.5-mm steps quasi-perpendicular to the incident photons. Both Y and the forward scattering R were smallest for the sawtooth surface. Surface treatments such as TiN deposition, air oxidation, electron bombardment, and standard *in situ* baking are considered options for reducing the SEY, although the latter is rather difficult in the cold arcs of LHC. The use of a ribbed chamber wall for the purpose of shadowing top and bottom faces of the beam screen from reflected photons is being investigated [25]. The coupling impedance of such a surface is also under investigation.

Multipacting tests were performed using a resonant coaxial cavity [26]. A peak rf voltage of ~4.5 kV at 500 MHz could be achieved between the inner and outer conductor; the minimum expected voltage required for the multipacting threshold is 1.5 kV. Varying the rf voltage is equivalent to changing the beam current (i.e., accelerating potential). An amplitude-modulated signal was used to

detect the onset and rise time of multipacting with and without a dipole field while varying a solenoidal magnetic field. It was found that a 50-G solenoidal field can lower the secondary yield in the drift spaces, but it is ineffective with a strong dipole field. It is hoped that these data may provide direct information on SEY and, possibly, the energy distribution of the SE. A sharp decrease in the multipacting threshold was observed when the dipole field has an intensity such that the electron cyclotron frequency is equal to the resonant frequency of the coaxial cavity.

4.2 APS

To measure the properties of the electron cloud, a special 5-m vacuum chamber, equipped with rudimentary electron energy analyzers, beam position monitors (BPMs), and targets, was installed in a field-free region in the APS storage ring [5]. Two detectors are shown mounted on a standard-aperture vacuum chamber in Figure 1. A removable, water-cooled target is shown inserted in the antechamber channel. Data were collected by measuring the collector current with a pico-ammeter as a function of bias applied to the retarding grid.
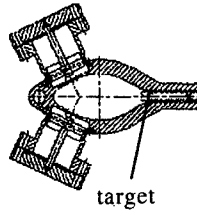
Figure 1: Cross-section schematic showing mounting of detectors.

The dependence of the detector current, normalized to the total positron beam current, on the detector location is seen in Fig. 2. In this example, 20 mA are stored in 10 bunches spaced at either 128 (0.36 µs) or 7 rf buckets (20 ns). As expected, a downstream Cu end absorber (EA6) is the primary source of electrons, dominating the signal at the detectors < 0.3 m away. The normalized electron current at the larger spacing is identical to that with a single bunch; therefore, this current vs. voltage (I-V) signature is believed to be determined mostly by the PE.

A **dramatic** amplification of the signal is observed at the 7-bucket bunch spacing. This can be attributed to the SE contribution. Detectors >1.4 m from EA6 show a higher amplification, which we speculate comes from multiple scattering of electrons originating from the absorber. A scan in the bunch spacing (10 bunches total) gave a peak in the normalized electron current at a spacing between 8-10 buckets. There is additional factor of 2.6 amplification in the normalized signal when the beam current increases from 10 to 20 mA. These data give evidence of a beam-induced multipacting effect [6]; the bunch spacing at the peak current equals the wall-to-wall time-of-flight in the vertical direction of electrons with an average energy of 8-12 eV.

The electron energy distribution is extracted from the derivative of the I-V curves and is dominated by low- energy electrons. The bunch spacing affects the shape of the high-energy tail, giving a longer tail for the multipacting conditions.
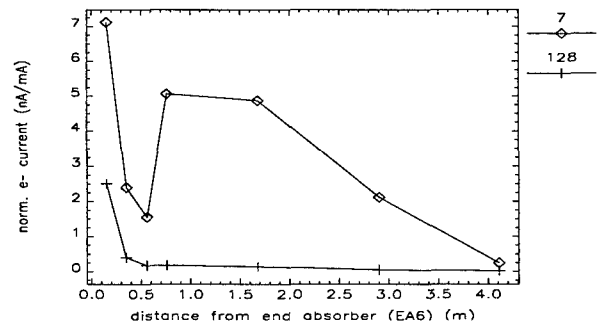
Figure 2: Total, normalized electron current per detector vs. distance from downstream end absorber as a function of bunch spacing (10 bunches, 20 mA).

The measured buildup of the electron cloud was most pronounced at the 7-bucket spacing, and the most dramatic increases occurred for detectors farthest from EA6. Figure 3 shows the normalized detector current 3 m from EA6 for bunch trains of varying length, with 1-2 mA/bunch. The total amplification at 2 mA/bunch is a factor of 360 in normalized current. A local pressure rise of a factor of 20 was observed for these conditions, indicative of enhanced desorption induced by the secondary electrons, and giving independent evidence of the multipacting effect [6]. A saturation effect is observed after a certain number of bunches, beyond which the increases becomes linear.
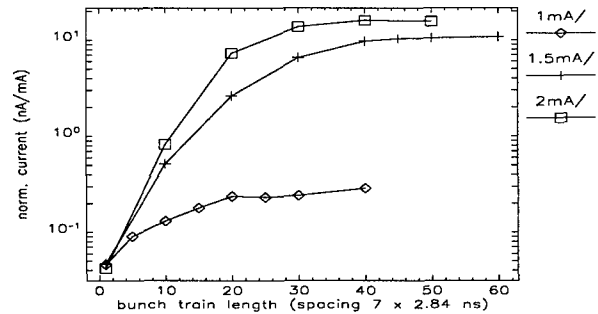
Figure 3: Amplification of EC over bunch trains.

More modest amplifications were seen for long electron bunch trains, but at a spacing of 11 buckets. The buildup of the electron cloud was also observed over long trains of electron bunches, with a similar saturation effect. Preliminary results with targets of different materials show a SE reduction for Cu or TiN surfaces compared to oxidized Al.

4.3 PEP-II LER

An initial search for electron cloud effects was made, with no clear evidence of ECI [27]. There is, however, fairly clear evidence for beam-induced multipacting, accompanied by a significant pressure rise with 500-1000 bunches and currents above 1 mA/bunch [24].

4.4 BEPC

Further refinements of ECI rise times have been made with time-domain measurements using a single-pass BPM

system [29]. The measured value of ~6 ms compares well with the predicted value of 3 ms.

5 DISCUSSION

Independent experimental results at CERN, APS, and PEP-II regarding electron cloud effects are beginning to converge. Evidence of beam-induced multipacting at APS with long trains of bunches spaced at 20 ns and 2 mA/bunch was accompanied by a significant local pressure rise. The pressure rise with 1 mA/bunch was not significant. Evidence of multipacting at PEP-II shows a very similar bunch-current-dependent pressure rise effect, with a threshold at 1 mA/bunch. The vertical aperture and 20-ns bunch spacing at APS are nearly the same as the LHC aperture and bunch spacing, for which calculations predict that multipacting conditions are satisfied. Even though the maximum energy of photoelectrons impinging on the walls by the impulse approximation are very different, 200 eV at LHC vs. 10 eV at APS, the peak of the SE energy distribution of ~5 eV is nearly independent of material and incident electron energy [12].

Electron bombardment of the chamber surface was measured in bench tests to lower the SEY. At SLAC, a 25% reduction was seen after a dose of ~10^{18} e/cm^2 (15 A-h equivalent in PEP-II) [4], and at CERN a dose of 10^{-3} C/cm^2 reduced the Cu SEY to below 1.3, the critical value for multipacting [28]. Data with the APS Al chambers show that the SE-dominated signal was reduced by 45% after 62 A-h of stored beam.

Saturation effects due to space charge and the dependence on the bunch current and other critical parameters (Y, R, SEY) have been studied in simulations and analytical work [4][18][20][21]. A bunch-current-dependent saturation effect was measured with long bunch trains at the APS (Fig. 3); these data may provide a benchmark for calculations of the equilibrium electron cloud density. Comparisons of these and other APS data with simulations are planned, with the view of perhaps developing an empirical model for realistic chamber geometries.

Remaining questions include: how far can active damping and passive control (necessary in LHC) raise the threshold for electron cloud effects? A solenoidal B-field is only effective in field-free regions [26]. Clearing electrodes have not shown promise as being effective (PF, PSR, etc). Quantitative measurements of the growth rate at BEPC [29] suggest that a feedback system may be effective. There is a need for a more quantitative theory. For example, only vertical blowup is seen in ECI, while the present theory does not favor either plane. ECI is not a resonant phenomenon *per se*, but beam-induced multipacting appears to be an important effect in the buildup of the electron cloud. What is the role of other resonant effects, such as when the EC cyclotron frequency in the dipoles equals the betatron frequency or the resonant frequency of a structure in the vacuum chamber? Calculations have been made of the influence of quadrupoles on

the SEY [19]. However, electron trapping in quadrupoles, such as occurs in the DIP-induced instability at CESR [13], may be important. A kinetic description of the e-p effect as an electron-ion two-stream instability may be a promising theoretical approach for understanding the broader array of electron cloud effects [30].

6 ACKNOWLEGEMENTS

The author would like to thank R. Rosenberg, J. Galayda, S. Milton, L. Teng, M. Furman, S. Heifets, Z. Guo, O. Brüning, and J. Rogers for their generous assistance.

7 REFERENCES

[1]   Y. Baconnier and G. Brianti, CERN Report No. CERN/SPS/80-2 (DI) (1980)

[2]   O. Gröbner et al., J. Vac. Sci. Technol. A7, 223 (1989); R. B. Cairns and J. A. R. Samson, J. Opt. Soc. 56, 1568 (1966); B. L. Henke, J. P. Knauer, K. Premaratne, J. Appl. Phys. 52 (3), 1509 (1981); R. H. Day et al., J. Appl. Phys. 52 (11), 6965 (1981)

[3]   B.L. Henke, E.M. Gullikson, J.C. Davis, Center for X-ray Optics, Web page: www-cxro.lbl.gov/optical_constants/mirror2.html

[4]   M. Furman, Proc. of MBI97, KEK Proc. 97-17, 170 and 234 (1997) and Proc. of 1997 PAC, 1617 (1998)

[5]   K. C. Harkay and R. A. Rosenberg, "Measurements of the Electron Cloud in the APS Storage Ring," these proceedings

[6]   O. Gröbner, Proc. of 10th Int'l Conf. on High Energy Accel., Protvino, 277 (1977)

[7]   V. Baglin et al., Proc. of 1998 EPAC, 359 (1998)

[8]   V. Baglin et al., Proc. of 1998 EPAC, 2169 (1998)

[9]   K. Ohmi, Phys. Rev. Lett. 75, 1526 (1995); Proc. of 1997 PAC, 1667 (1998); and KEK Report 97-7 or IHEP/BEPC/AP/97-09

[10]   M. Izawa, Y. Sato, T. Toyomasu, Phys. Rev. Lett. 74, 5044 (1995)

[11]   Z. Y. Guo et al., Proc. of 1997 PAC, 1566 (1998) and Proc. of 1998 EPAC, 957 (1998)

[12]   W. H. Kohl, Handbook of Materials and Techniques for Vacuum Devices, AIP Press (1995); Seiler, Phys. 54 (11) (1983)

[13]   T. Holmquist and J. T. Rogers, Phys. Rev. Lett. 79, 3186 (1997)

[14]   J. T. Rogers, KEK Proc. 97-17, 42 (Dec. 1997)

[15]   M. A. Plum et al., Proc. of 1997 PAC, 1611 (1998)

[16]   B. Zotter, in private communication from R. Cappi (1998)

[17]   T. O. Raubenheimer and F. Zimmermann, Phys. Rev. E 52, 5487 (1995); J. Y. Huang et al., Phys. Rev. Lett. 81, 4388 (1998); J. Byrd et al., Proc. of 1997 PAC, 1563 (1998); H. Fukuma et al., Proc. of 1997 PAC, 1596 (1998)

[18]   F. Zimmermann, SLAC-PUB-7425 (1997) and Proc. of MBI97, KEK Proc. 97-17, 221 (1997).

[19]   O. Brüning, Proc. of 1998 EPAC, 332 (1998)

[20]   S. Heifets, Proc. of CEIBA95, KEK Proc. 96-6 (1996)

[21]   A. V. Burov, N. S. Dikansky, KEK Proc. 97-17, 200 (1997)

[22]   A. W. Chao, Physics of Collective Beam Instabilities in High Energy Accelerators, Wiley (1993)

[23]   F. Ruggiero, "Electron Cloud in the LHC" Web page: wwwslap.cern.ch/collective/electron-cloud/electron-cloud.html

[24]   M. Furman, private communication (1999)

[25]   O. Brüning et al., "Electron Cloud and Beam Scrubbing in the LHC," these proceedings

[26]   O. Brüning et al., Proc. of 1998 EPAC, 356 (1998)

[27]   M. Furman et al., "Search for the Electron-Cloud Effect in PEP-II," these proceedings

[28]   O. Brüning, private communication (1999)

[29]   Z. Y. Guo et al., "Recent Studies on Beam-Photoelectron Instability in BEPC," these proceedings

[30]   R. C. Davidson et al., "Kinetic Description of Electron-Proton Instability in High-Energy Linacs and Storage Rings," these proc.

MODELING OF SPACE-CHARGE PHENOMENA IN MULTI-TURN TRACKING

R.A. Baartman, M. D'yachkov, and F.W. Jones
TRIUMF, 4004 Wesbrook Mall, Vancouver, V6T 2A3, Canada

Abstract

Although many space-charge simulations have been developed for linacs, beamlines, and idealized rings, there are relatively few simulation codes applicable to multi-turn tracking with space charge in a realistic synchrotron or accumulator/storage ring lattice. Recently the program ACCSIM, used for accumulator-ring injection studies and other applications, has been upgraded with improved transverse space charge models: one using a conventional multiple-Fourier-transform (MFT) method and another using a new hybrid fast-multipole (HFM) algorithm. After an overview of their implementation in the ACCSIM code, we present tests and observations of how well various space-charge phenomena can be reproduced by the HFM models.

1 INTRODUCTION

In the class of tracking codes devoted to multi-particle simulations in synchrotrons or accumulator/storage rings, there are several that incorporate space-charge effects, but in the past the use and development of these codes have been curtailed by the intensive computational resources required by the space-charge algorithms, which for most applications have escalated the codes to the supercomputer realm.

Recently, the need for such simulations has increased due to a new generation of intense-beam proton machines that are under study, in the proposal stage, or under construction. These machines must reach new intensity frontiers and be able to operate with extremely low losses, which sets a new standard of accuracy and generality for the simulation codes. Fortunately, at the same time the available computing resources, on the desktop or on modestly-priced compute servers, have increased dramatically and have spurred a new effort to refine and extend the simulation codes.

We have utilized one such code, ACCSIM, to explore some space-charge phenomena with various simulated particle ensembles in an idealized continuous-focusing model. Application to a real machine, the CERN PSB, is described in another paper[1].

2 TRANSVERSE SPACE CHARGE IN ACCSIM

The code ACCSIM[2] has been used to study injection and accumulation scenarios for a number of different proton rings, both existing and proposed, as well as being applied to miscellaneous simulation tasks such as rf capture, esti-mation of diagnostic signals, and collimation systems. The numerous simulation features are all built on top of a basic 3D (6 phase-space variables) tracking engine using transfer matrices to represent the magnet lattice.

Recently, the first self-consistent treatment [1] of transverse space-charge was added to the code, using the standard field-solve/particle-push integration method to incorporate space-charge forces in the tracking. In addition to a conventional FFT-based field solver, based on routines contributed by ACCSIM users at BNL and ORNL [3], a new Hybrid Fast-Multipole solver has been developed. It combines a Particle-In-Cell grid with a Fast-Multipole field evaluation, and can offer advantages in speed and/or accuracy in cases such as few-turn betatron stacking or multi-turn injection with halo formation. A comparison of the computational efficiencies of the two methods can be found in Reference [4].

3 TESTS

In 2D, the only exactly solvable distribution is the Kapchinsky-Vladimirsky distribution. For simplicity, we have run cases approximating 'smooth-focusing': one thin stigmatic lens every $\sim 10°$ of betatron phase advance, and one space charge calculation at every lens. The rms sizes in x and y are calculated and an FFT performed on these. Even with no seeding and matched initial distributions, there is enough numerical noise to give clean spectra. See Fig. 1. Runs were made for equal x- and y-emittances and for fixed bare tune in x ($\nu_{0x} = 5.817$) and varying tune in y (ν_{0y}). The tune shift in all cases was $\Delta\nu_x = 0.175$. Fig. 2 shows these tracking results as points. The curves on this figure are the theoretical envelope eigenmode frequencies given by the well-known formula[6, e.g.]

$$\nu^2 = 2\nu_{0x}^2 + 2\nu_{0y}^2 - 5\nu_{0x}\Delta\nu_x +$$
$$\pm\sqrt{(2\nu_{0x}^2 - 2\nu_{0y}^2)^2 + (\nu_{0x}\Delta\nu_x)^2}. \quad (1)$$

The agreement between tracking and theory is strikingly good. For comparison, we also show twice the bare tunes and twice the incoherent tunes.

In 1971 Sacherer[5] proved that the KV envelope equations apply to any distribution, provided that the beam size is replaced by twice the rms size and the emittance by 4 times the rms emittance. Although the resulting equations are still correct, they are no longer closed, since rms emittance is not a conserved quantity in the presence of nonlinear forces. In practice, however, this turns out to only cause difficulty if one wishes to study the evolution of an
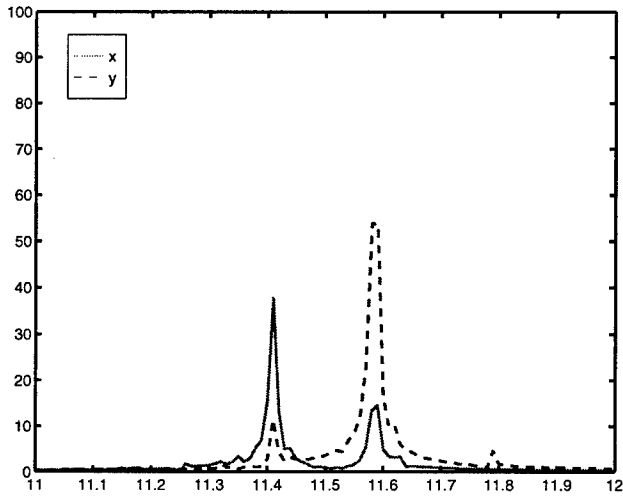
Figure 1: FFT spectra of rms envelopes for KV case. 10,000 macro-particles. The bare tunes are 5.817 in x and 5.894 in y. The tune shift is 0.175.
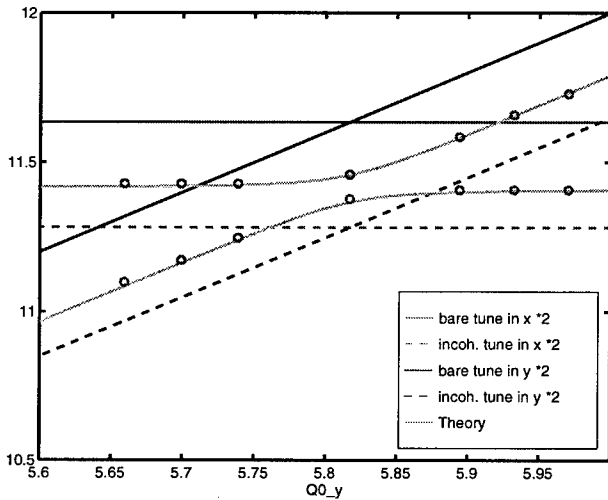
Figure 2: Envelope mode frequencies found from tracking KV beams with 10,000 macro-particles (points) compared with theory (curves) and twice the bare tunes (solid) and twice the incoherent tunes (dashed) plotted against bare tune in y. Bare tune in x is 5.817.

Figure 3: FFT spectra of rms envelopes for gaussian case with 10,000 macro-particles. The bare tunes are 5.817 in x and 5.894 in y. The rms emittance is the same as the rms emittance that was used for the KV case. This results in a peak incoherent tune shift of 0.35.
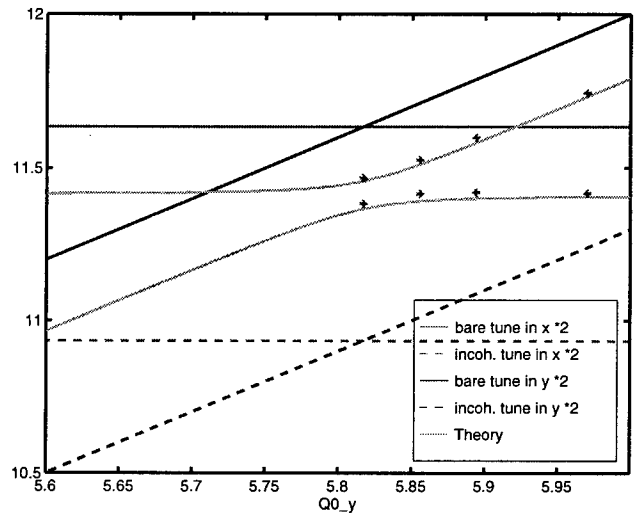
Figure 4: Envelope mode frequencies found from tracking gaussian beams with 10,000 macro-particles (points) compared with theory (curves) and twice the bare tunes (solid) and twice the incoherent tunes (dashed) plotted against bare tune in y. Bare tune in x is 5.817.

unstable distribution. This was tested in ACCSIM by simulating a gaussian beam. See Fig. 3; the spectra are not as clean as in the KV case, but the modes are still identifiable. These are the points denoted as '+'-symbols in Fig. 4. Again, there is good agreement with the theoretical tunes given by eqn. 1.

Another test is against the known fact that the KV distribution is stationary. This artificial distribution is an infinitesimally thick shell in 4D phase space. Knowing the matched distribution, each particle can be assigned an 'action' (J_x in x and J_y in y), which is in fact the emittance traced out in phase space as the particle undergoes betatron

oscillations. All the particles in the KV distribution therefore lie on the line $J_x + J_y =$ constant. In fact, the finite resolution in tracking a finite number of macro-particles results in deviations from this rule so that eventually there is a distribution in $J_x + J_y$. See Fig. 5. The width of this distribution is plotted in Fig. 6 as a function of turn number. We see that the extra emittance grows quickly to a level which varies as the square root of the number of macro-particles, and thereafter grows only very slowly. This is an 'acid'-test for the tracking method, since the KV case has hard edges

that require very high resolution to maintain. Tracking with similar parameters and gaussian distributions, for example, yields no detectable diffusion.
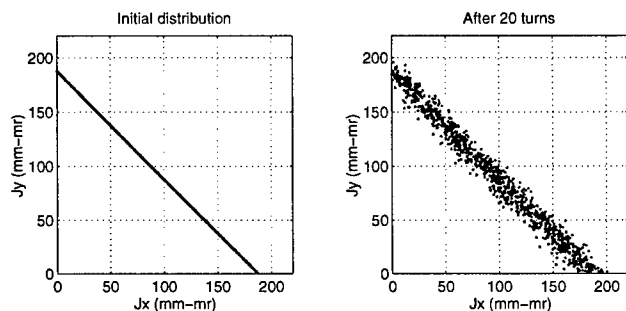
Figure 5: Numerical diffusion of an initial KV beam. 40,000 particles, of which only every 40th has been plotted.
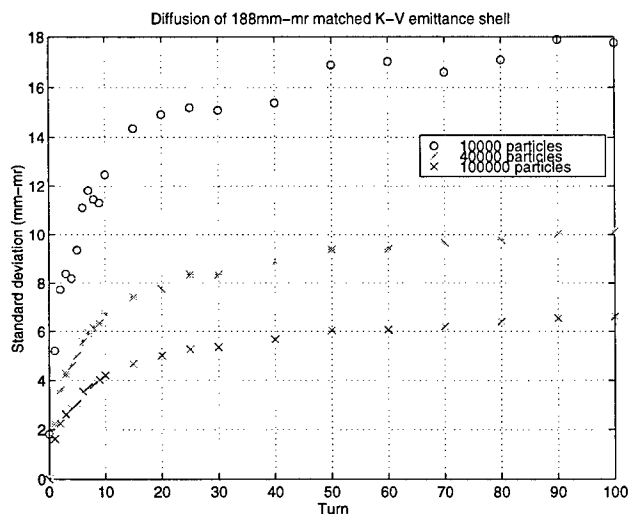
Figure 6: Numerical diffusion of an initial KV beam of emittance 188 πmm-mrad, for three different numbers of macro-particles.

4 CONCLUSION

Tracking with the new hybrid fast-multipole algorithm shows good agreement with analytical results.

5 REFERENCES

[1] F.W. Jones and H.Schönauer, "New Space-Charge Methods in ACCSIM and Their Application to Injection in the CERN PS Booster," these proceedings.

[2] F.W. Jones, "Developments in the ACCSIM Multi-particle Tracking and Simulation Code," *Proc. 1997 Particle Accelerator Conference*, Vancouver, 1997, p. 2597.

[3] J.A. Holmes et al., "A Particle-In-Cell Model for Space-Charge Dynamics in Rings," *Proc. European Particle Accelerator Conference*, Stockholm, 1998.

[4] F.W. Jones, "A Hybrid Fast-Multipole Technique for Space-Charge Tracking With Halos," *Workshop on Space Charge Physics in High Intensity Hadron Rings*, Shelter Island NY, May 1998, AIP Conf. Proc. **448** p. 359.

[5] F. Sacherer, *RMS Envelope Equations with Space Charge* IEEE Trans. Nucl. Sci. **NS-18** (PAC 1971) p. 1105.

[6] R. Baartman, "Betatron Resonances with Space Charge," *Workshop on Space Charge Physics in High Intensity Hadron Rings*, Shelter Island NY, May 1998, AIP Conf. Proc. **448** p. 56.

[7] ACCSIM home page, http://www.triumf.ca/compserv/accsim.html.

SINGLE AND MULTIBUNCH BEAM DYNAMICS IN THE DAΦNE MAIN RINGS

C. Biscari, A. Drago, A. Gallo, A. Ghigo, F. Marcellini, M. Migliorati, M. Preger, F. Sannibale,
M. Serio, A. Stella, G. Vignola, M. Zobov, LNF-INFN, Frascati, Italy
J. Fox, S. Prabhakar, D. Teytelman, A. Young, SLAC

Abstract

We describe the results of single bunch measurements and observations of the multibunch beam behavior in the DAΦNE electron-positron collider main rings. In single bunch mode the nominal current of 44 mA has been exceeded, reaching 110 mA in both electron and positron rings without any harmful single bunch instability. We have measured the bunch length as a function of the bunch current at different RF voltages. According to the data the longitudinal normalized impedance is lower than 0.6 Ohm. The estimated transverse broad band impedance is small. This is confirmed by the fact that the head-tail instability threshold without sextupoles is as high as 13 mA. The measured transverse tune shift at the nominal current is a small fraction of the synchrotron tune. The longitudinal feedback systems have been successfully commissioned in both main rings allowing to store routinely high multibunch currents and observe the beam behavior for different multibunch fills. In particular, such observations have helped us to identify some parasitic High Order Modes trapped within vacuum chamber elements and capable to drive rather fast multibunch instabilities, both longitudinal and transverse.

1 INTRODUCTION

The Frascati electron-positron collider DAΦNE is the first Φ-Factory [1,2] in operation. After a total beam time of six months devoted to commissioning without experiments, it is ready to start the operation for physics with the experimental detector KLOE [3]. At the commissioning stage all the machine subsystems such as vacuum, RF, cooling system etc., have been checked and proved to be reliable. Since the final goal of the factory is to achieve a luminosity as high as $5 \cdot 10^{32}$ cm^{-2} s^{-1} with 5 A of average current distributed over 120 bunches, several machine shifts have been dedicated to study high current beam dynamics. A separate paper at this conference deals with the luminosity optimisation [4].

In this paper the observations and measurement results obtained in single bunch and multibunch regimes are described and compared with the analytical models and numerical simulations. In particular, Section 2 is dedicated to single bunch dynamics; the bunch lengthening in DAΦNE is discussed, the microwave instability observations are compared with analytical predictions and the broad band impedance is evaluated. Section 3 describes multibunch performance, with emphasis on measures

undertaken to damp coupled bunch instabilities. The powerful longitudinal feedback systems have been successfully commissioned in both rings and the experience gained with the system during the DAΦNE multibunch runs is reported in this section. The High Order Mode (HOM) trapped in the injection kicker was also identified as that responsible for coupled bunch vertical oscillations. Special measures, proposed to avoid the transverse instability, are discussed.

2 SINGLE BUNCH DYNAMICS

The DAΦNE Main Rings commissioning started with single bunch. After careful orbit adjustment and chromaticity correction the single bunch current was routinely exceeding 110 mA in both rings. Despite this value is by a factor of 2.5 higher than the nominal project current of 44 mA, no destructive single bunch instability has been observed.

2.1 Bunch lengthening and impedance estimate

A comprehensive study of the longitudinal single bunch dynamics for DAΦNE [5] including numerical simulations, analytical estimates and experimental measurements has been performed. In order to simulate the bunch lengthening process a computer code modelling a large number of macroparticles (up to 600000), interacting through the machine wakefield and tracked over 4 damping times has been used.

The wake potential of a short Gaussian bunch with $\sigma_z = 2.5$ mm (much shorter than the nominal bunch length) has been used as a machine wake function. The wake potential has been calculated with 2D and 3D numerical codes during the machine vacuum chamber design. In addition, all the vacuum chamber components that could give a significant contribution to the DAΦNE impedance and wake potential in the time domain were measured in the laboratory with the wire method.

Below the results of the simulations are compared with the beam measurements.

Bunch length measurements in the DAΦNE positron ring have been performed during single bunch operation at different currents. The bunch signal from a broad band button electrode connected with a low attenuation cable, 8 m long, to a sampling oscilloscope Tektronix 11801A, equipped with a sampling head SD-24 with a rise time of 17 psec and an equivalent bandwidth of 20 GHz, has been analysed. The waveform has been digitized and sent via a GPIB interface to the control system for storage and

off-line processing. The bunch distribution has been reconstructed by processing the button electrode signal taking into account the button transfer impedance and the cable attenuation. The measurements were performed for different single bunch stored currents in the range from ~ 0 to 48 mA (note that the nominal design current is 44 mA) at RF voltages of 100 kV and 150 kV.

Figure 1 shows the bunch length measurements together with the numerical calculation results for an RF voltage of 100 kV. The agreement is good except at low current (< 5 mA). This small discrepancy is due to the fact that for short bunches, with length comparable to the button size, the bunch spectrum covers a frequency range where the button transfer impedance undergoes cutoff and the measurement are no longer reliable. The measurements will be repeated with a fast fotodiode (25 GHz bandwidth), which should resolve short longitudinal bunch dimensions. In Figure 2 the measured bunch current distribution at an RF voltage of 100 kV is compared with the numerical simulations for a current of 26 mA.
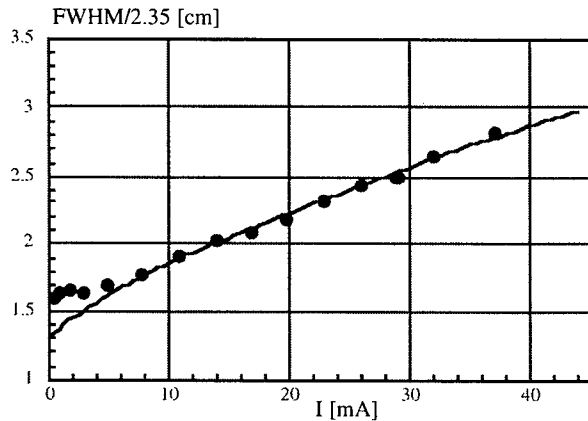
Figure 1: Bunch length at 100 kV RF voltage. Solid line - numerical calculations; circles - measurement results.
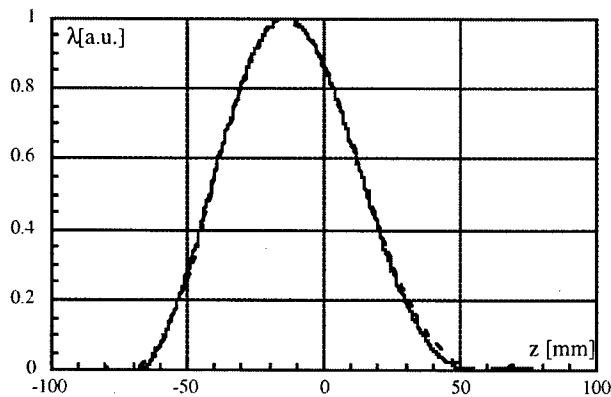
Figure 2: Bunch current distribution at 100 kV (I = 26 mA). Solid line - measured signal; dotted line - simulation.

The bunch distribution is wider than a Gaussian one due to the interaction with the imaginary part (mainly inductive) of the impedance. The bunch centroid is shifted and the distribution is slightly distorted because of the power loss. The normalized coupling impedance $|Z/n|$ has been

evaluated by making the Fourier transform of the machine wake field. In the frequency range up to 20 GHz the absolute value of the impedance does not exceed 0.6 Ω.

2.2 Microwave instability

The microwave instability is caused by the bunch longitudinal coherent mode coupling. The instability can manifest itself either through the coupling among the azimuthal modes or the radial ones having the same azimuthal number. A double water bag distribution model [6] which allows to treat analytically the mode coupling taking into account splitting of each azimuthal mode in two radial modes has been applied.

So far the theoretical model predictions of the longitudinal mode coupling coincide well with experimental observations. According to the model, at lower voltages (V_{RF} = 100 kV for DAΦNE) the microwave instability is driven by the radial mode coupling of the quadrupole (m = 2) and sextupole (m = 3) azimuthal modes. At higher RF voltages the instability arises from coupling of the higher azimuthal modes. The conclusion is that an RF voltage higher than 150 kV would be preferable for DAΦNE operation in order to avoid the radial mode coupling of the lowest azimuthal modes (dipole, quadrupole, sextupole) which could lead to a strong bunch shape modulations harmful for beam-beam interactions.

Indeed, experimentally, at V_{RF} = 100 kV an appearance of pure quadrupole synchrotron sidebands has been detected at stored current of ~25 mA, while the onset of the dipole mode was observed only at about 35 mA. Increasing the RF voltage to 150 kV, the quadrupole mode threshold shifted to 38 mA while the dipole mode was stable up to the nominal bunch current. For higher RF voltages the coupling of the low coherent modes has not been observed below the nominal value. Exactly the same threshold current were calculated by applying the above theoretical model.

2.3 Transverse single bunch dynamics

No special measurements have been so far dedicated to transverse single bunch dynamics but some indirect observations have shown that the transverse impedance is small. The following possible single bunch transverse instabilities do not seem to be dangerous for DAΦNE:

a) Head tail instability without sextupoles: a very high current has been stored in the single bunch without sextupoles when the orbit is corrected in the machine. A maximum value of 13 mA, that is almost 1/3 of the nominal bunch current, has been achieved. The instability threshold decreases rapidly by changing the orbit.

b) Transverse mode coupling instability: when the chromaticity is corrected, the observed vertical tune shift versus stored current is a small fraction of the synchrotron tune. In the range from ~ 0 to 80 mA the frequency shift was ~ 9 kHz compared to a synchrotron frequency of 35 kHz, demonstrating that DAΦNE is far from the transverse mode coupling threshold.

3 MULTIBUNCH BEAM DYNAMICS

During the DAΦNE commissioning several shifts were dedicated to the multibunch operation. A current of 540 mA has been stored in 30 bunches configuration in both electron and positron rings without transverse feedback installed. Despite some coherent multibunch oscillations have been observed they were not limiting the current. The poor vacuum in the temporary Day-One interaction regions is the main current limiting factor.

3.1 Longitudinal

A very high current in many bunches must be stored in each ring. Special cares have been undertaken while designing the RF cavity and other vacuum chamber elements to damp the HOMs capable to drive unstable coupled bunch oscillations. Their effectiveness have been confirmed by the measurements on prototypes. Nevertheless, residual low impedance HOMs couple the bunches and a rise time faster than the radiation damping time can occur. The rise time during injection transients can be very fast. A very powerful longitudinal feedback capable to damp all the coupled bunch instabilities has been developed. A bunch-by-bunch feedback scheme in which any bunch is kicked proportionally to the time derivative of its longitudinal position error has been adopted [7].
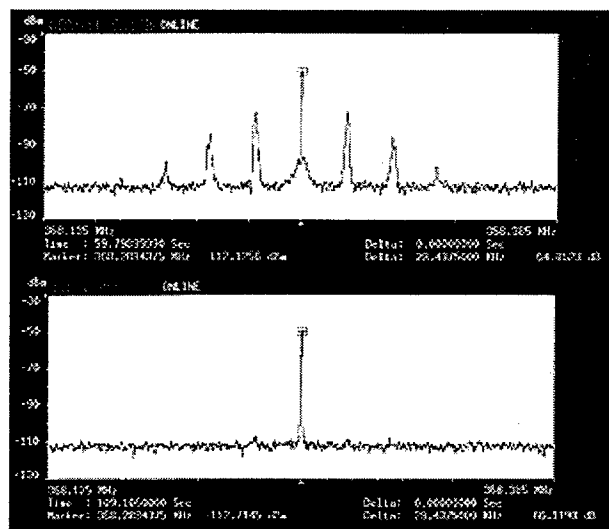
Figure 3: Longitudinal pick-up signal spectrum of 30 bunches with feedback off - feedback on.

In this system a time gated phase detector measures the bunch position; a bank of parallel filters produce the correction kick signals; a broad band power amplifier transfers the correction kick to the bunch by means of a broad band kicker [8]. The synchronization with the bunches (better than 50 psec), in particular of the back end part, has been accurately set in order to kick the bunches with the maximum efficiency. Sinusoidal digital filters with different downsampling factor have been tested and the optimum filter uses 6 taps to reconstruct the signal and with proper regulation of the gain, the system was able to manage up to 120 injected bunches.

In the commissioning phase the longitudinal feedback systems have been successfully commissioned allowing to store in both electron and positron ring routinely high current in any filling configuration. A damping time of ~ 200 μs has been achieved.

A current larger than 540 mA has been stored in each ring in 30 bunches configuration without any significant longitudinal oscillations. At these current levels the feedback is not yet saturated. Figure 3 shows that the synchrotron sidebands disappear with the feedback on.

3.2 Transverse

The first transverse multibunch instability has been observed while tuning the machine to a working point with fractional part close to the integer (5.09,5.07). The beam transverse motion was studied by digitizing a beam position monitor signal with the front end of the longitudinal feedback of the other ring and storing the turn by turn motion of each bunch in its memory. The off-line analysis of the bunch motion, consisting in the Fourier analysis of the time domain bunch signal, permitted to identify the mode 55 as the one responsible for the instability.

In order to understand where the dangerous mode is trapped, local orbit displacements (bumps) were made around suspected HOMs sources: RF cavity, transverse kickers, injection kickers. We have found a clear dependence of the transverse multibunch instability threshold on a bump localized in one of the injection kickers. Indeed, the unstable line of mode 55 coincides with the frequency of the HOM (1304 MHz) trapped in the injection kicker, that was found both in the simulations and bench transverse impedance measurements. To overcome the problem, the present working point has been moved elsewhere thus shifting the mode line away from the HOM frequency. For the future a transverse feedback system has been envisaged and a study to damp the incriminated mode by inserting an antenna has been performed. Impedance measurements confirm the successful HOM damping.

4 ACKNOWLEDGMENTS

5 REFERENCES

[1] G. Vignola and DAΦNE Team, Proceedings of EPAC '96, p. 22.

[2] S. Guiducci and DAΦNE Team, DAΦNE Operating Experience, these Proceeding.

[3] The KLOE collaboration, KLOE a General Purpose Detector for DAΦNE, Frascati Internal Note LNF-92/109, Aprile 1992.

[4] M.E. Biagini et al., Optimization of DAΦNE beam-beam performance, these Proceeding.

[5] M. Zobov et al., Bunch lengthening and microwave instability in the DAΦNE Positron Ring, DAΦNE Technical Note BM-3, Frascati, (June 98)

[6] A. Chao et al., Proceedings of PAC 95, p.3040.

[7] M. Serio et al., Proceedings of EPAC '96, p.148.

[8] R. Boni et al., Proceedings of EPAC '96, p.1881.

Investigation of Coherent Emission from the NSLS VUV Ring

G.L. Carr[†], S.L. Kramer, J.B. Murphy, BNL, Upton, NY

J. LaVeigne, R.P.S.M. Lobo, D.H. Reitze, D.B. Tanner, Univ. Florida, Gainesville, FL

Abstract

Bursts of coherent radiation are observed from the NSLS VUV ring near a wavelength of 7 mm. The bursts occur when the electron beam current (I) exceeds a threshold value (I_{th}), which itself varies with ring operating conditions. Beyond threshold, the average intensity of the emission is found to increase as $(I-I_{th})^2$. With other parameters held nearly constant, the threshold current value is found to increase quadratically with synchrotron frequency, indicating a linear dependence on momentum compaction. It is believed that the coherent emission is a consequence of micro-bunching of the electron beam due to the microwave instability.

1 INTRODUCTION

Synchrotron radiation is produced when electron bunches traverse the magnetic guide structure of an accelerator or storage ring. For wavelengths shorter than the bunch length, the incoherent superposition of each electron's radiated field results in an intensity that scales linearly with the number of electrons, N. For wavelengths longer than the bunch, the resulting superposition has a large coherent term which scales as N^2. The spectral content of this coherent emission is the product of the standard synchrotron radiation flux and the Fourier transform of the longitudinal electron density[1,2]. Thus, for a Gaussian bunch of width σ_L, the spectral range for coherent emission is also Gaussian with width $\sigma_\omega = c/2\pi\sigma_L$. A 10 cm electron bunch (300 ps duration) emits coherently for frequencies up to ~ 1 GHz. Such emission is difficult to observe since the radiation must propagate out from the ring chamber to a point where a detector is situated. The ring chamber is a waveguide[1], and the dimensions of most chambers are such that the effective cutoff frequency is above 10 GHz. However, if the electron bunch is small enough (i.e., ~ 10 ps duration) or a short period modulation of the bunch density can be imposed, coherent emission at higher frequencies should be observed.

In addition to intentional modifications of the electron bunch, instabilities can lead to variations in the bunch shape and density, which in turn may lead to coherent emission. This work presents evidence for the emission of coherent synchrotron radiation from the NSLS VUV ring. The radiation occurs in bursts of less than 1ms in duration at a wavelength of 7 mm; much shorter than the nominal electron bunch length. This and other evidence suggest that the emission is a consequence of micro-bunching (a density modulation within a bunch) that is characteristic of the microwave instability.

2 EXPERIMENT

2.1 NSLS VUV Ring

Our measurements were conducted using the VUV ring at the National Synchrotron Light Source (NSLS/BNL). This storage ring operates as a dedicated synchrotron radiation source. It has a Chasman-Green lattice consisting of 4 superperiods. The bending radius is 1.91 m in each of the 8 dipole magnets. The rf accelerating system operates at 52.88 MHz and the ring orbit frequency is 5.7 MHz. Though the ring energy can be varied from below 500 MeV up to 800 MeV, we conducted most of our studies at the injection energy of 737 MeV. In the standard mode of operation, the synchrotron tune is near 11.8 kHz, corresponding to a momentum compaction $\alpha = 0.0235$. By varying α, the synchrotron tune can be changed by more than an order of magnitude, and α can be set to both positive and negative values.

2.2 U12IR beamline

The presence of short wavelength coherent emission is detected at U12IR, one of 6 infrared beamlines at the NSLS built to extract infrared radiation from a bending magnet port. The U12IR beamline extracts 90 mr by 90 mr through a 6 cm square aperture, which is somewhat larger than the interior dimension of the ring chamber itself. Infrared light is transported by both mirror and waveguide optics to a lamellar grating interferometer and ℓHe cooled bolometric detector. The longest detectable wavelength for this system is ~ 20 mm. The detector response has a fall time between 200 and 800 μs. The rise time is less well known, but is substantially shorter (a few microseconds).

2.3 Coherent bursts

Under normal operations of the VUV ring, the far IR power is temporally smooth and varies linearly with beam current, as expected for incoherent synchrotron radiation. When the beam current exceeds a threshold value (which depends on the ring's operating parameters), bursts of

radiation are emitted. An example of these bursts is shown in Figure 1. The time structure is rather complex, and varies with operating conditions. Typically, bursts occur with varying amplitude, and at time intervals ranging from ~ 1 ms to ~ 10 ms. The growth rate of these particular bursts is faster than the resolution of our detector (a few microseconds). The decay time is also detector limited at ~ 200 μs. As the current is increased beyond the threshold value, the magnitude of a typical burst increases. Figure 2 shows that the time-average power increases as the square of the excess beam current (i.e., current over threshold).

Figure 3: Power spectral content of the coherent emission, relative to the incoherent synchrotron spectrum.
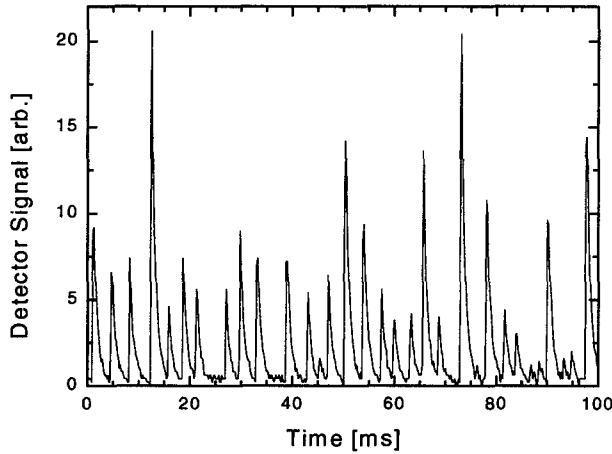
Figure 1: Far infrared detector output versus time showing emission bursts for $I > I_{th}$.
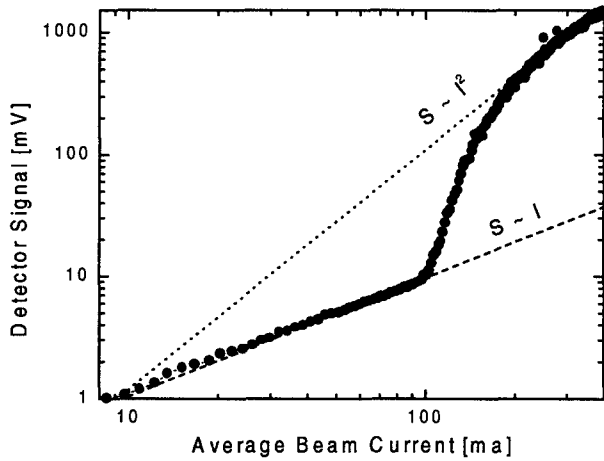
Figure 2: Measured output power versus average beam current in a single bunch, showing the onset of coherent emission at $I_{th} = 100$ ma.

We measured the coherent emission spectral content using a lamellar grating interferometer, which has a lower frequency limit of ~ 0.5 cm^{-1} ($\lambda = 20$ mm). Spectra for both coherent and normal (incoherent) emission were recorded and ratioed, thus eliminating characteristics associated with the instrument's own response. The result is a peak close to 7 mm wavelength (42 GHz) (see Fig. 3).

3 DISCUSSION

3.1 Microwave instability

The wavelength of the emission bursts and the unusual time-structure suggest a process related to the so-called microwave instability[3]. This particular type of longitudinal instability can result when electrons interact with each other through their wake field. The wake field interaction is characterized by a complex impedance determined by the beam pipe, rf cavities, and other structures such as beam ports and bellows. The threshold condition for the microwave instability has been given by a number of authors. For unbunched (coasting) beams, the Keil-Schnell criteria for stability[4] gives

$$eI_{ave}\frac{Z_n}{n} \le 2\pi\alpha E\sigma_E^2 \qquad (1)$$

where I_{ave} is the average beam current, Z_n is the impedance for disturbance with mode number n, α is the momentum compaction, E is the electron energy and σ_E is the energy spread. The parameter that is most readily varied over a wide (> 2 orders of magnitude) range is α. Expressed in terms of a threshold current, one finds that

$$I_{th} \propto \alpha \sim f_{s0}^2 \qquad (2)$$

i.e., the threshold current scales linearly with the momentum compaction, or as the synchrotron frequency squared. The average current in Eq. 1 can be replaced with the peak value in order to accommodate bunched beams[5], which brings in a factor of the bunch length σ_L. Neglecting bunch lengthening due to rf potential well distortion and assuming other parameters are fixed, σ_L depends only on the momentum compaction, and the resulting threshold condition has an additional factor of $\alpha^{1/2}$. Thus, in terms of the synchrotron frequency $f_s \sim \alpha^{1/2}$,

we expect the threshold current to follow f_s^3 for bunched beams.

3.2 Single bunch threshold current versus f_s

To study the variation in the single bunch threshold current the momentum compaction of the ring was varied over a wide range ($-\alpha_0 \leq \alpha \leq +2\alpha_0$) while holding the RF cavity voltage fixed. The measured threshold current behavior is shown in Fig. 4, which gives a log-log plot of the threshold current vs. synchrotron tune (in the zero current limit). The storage ring was operated under conditions of positive and negative α. In both situations, a quadratic (as opposed to cubic) dependence of threshold current on synchrotron frequency is observed.
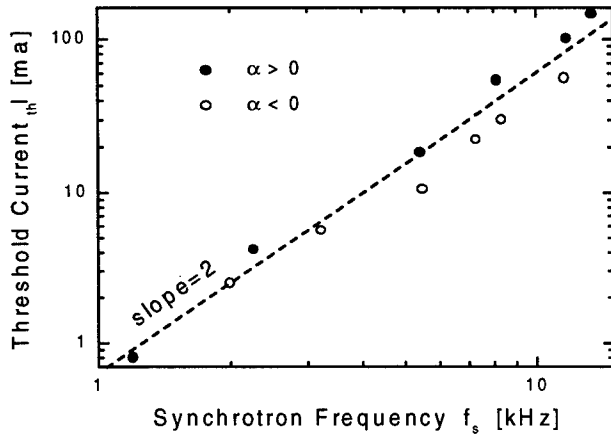
Figure 4: Measured single bunch threshold current versus synchrotron frequency for both positive (solid circles) and negative (open circles) momentum compaction. The dashed line represents the behavior $I_{th} \sim f_s^2$.

As noted above, the rate at which the instability grows and decays is typically faster than our detector can resolve. However, we did observe a decreased growth rate for coherent bursts as f_s (i.e., α) was reduced. In particular, for $f_s \sim 1$ kHz the growth rate had a rise-time of ~100 μs. This is shown in Figure 5, which compares the burst behavior for high (12 kHz) and low (1 kHz) values of f_s. While the decay rate was never resolved, we know that it must be faster than ~200 μs, which is more than an order of magnitude shorter than the synchrotron damping time (~10 ms). Thus, the decay is not attributed to synchrotron radiation damping. At present we do not understand what determines the time structure of the bursts. Additional studies are needed to assess the impact of potential well distortions on the threshold current.

3.3 Beam chamber impedance

The instability threshold depends on the beam impedance due to the storage ring vacuum chamber and any other structures subjected to the beam wake field. In practice, this impedance is difficult to characterize given the complexities of the rf cavities and other ring structures.

But the characteristic 7 mm wavelength of the emission matches the corrugation period of several bellows situated around the ring chamber, and an analysis of their effective impedance at these frequencies is presently underway.
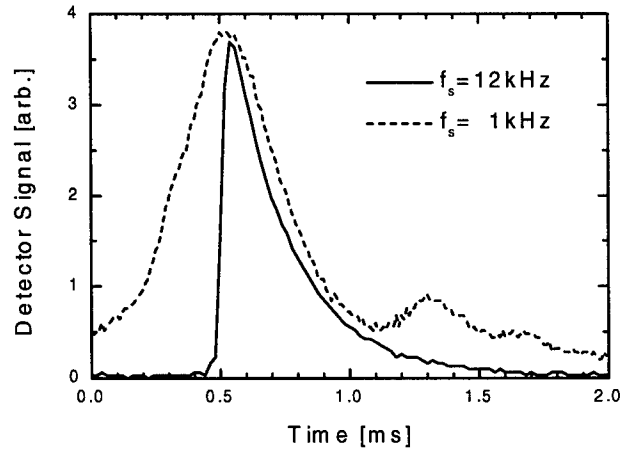
Figure 5: Coherent bursts for 2 different values of the synchrotron frequency, showing the decrease in burst risetime as the synchrotron frequency is reduced.

4 SUMMARY

The NSLS VUV ring produces coherent emission with a wavelength of 7 mm. The emission appears in bursts of duration shorter than 200 μs, and at intervals of a few ms. Emission bursts occur only when the beam current exceeds a threshold value. The dependence of this threshold on momentum compaction is consistent with some aspects of the microwave instability, and we attribute the coherent emission to an instability-driven longitudinal density modulation. The 7 mm emission wavelength matches the bellows sections found at numerous locations around the ring orbit, suggesting these components produce the impedance characteristics leading to the instability. Finally, we note that bursts of coherent microwave emission have also been reported[6] by the group at SURF II (NIST).

5 ACKNOWLEDGEMENTS

6 REFERENCES

[1] S. Nodvick & D.S. Saxon, *Phys. Rev.* **96**, 180 (1954).

[2] G.P. Williams et al., *Phys. Rev. Lett.* **62**, 261 (1989); C.J. Hirschmugl et al., *Phys. Rev.* **A44**, 1316 (1991).

[3] J-M Wang & C. Pellegrini, BNL 51236 (1979); J-M Wang, *Phys. Rev.* **E58**, 984 (1998).

[4] E. Keil & W. Schnell, CERN-ISR-TH-RF/69-48 (1969).

[5] D. Boussard, CERN LABII/RF/INT/75-2 (1975).

[6] A.R. Hight Walker, et. al., *SPIE* v.3153, p.42 (1997).

COHERENT COUPLING CRITERION FOR THREE-DIMENSIONAL HALO FORMATION

I. Hofmann, GSI, Ji Qiang, R. Ryne, LANL

Abstract

In this paper we study coupling between the transverse and longitudinal degrees-of-freedom in intense, rms mismatched charged particle beams. We find that a coherent (2:1, i.e. parametric) resonance beween the transverse and longitudinal mismatch eigenmodes has the effect that a transverse "breathing mode" mismatch can excite a longitudinal mismatch and halo. If the resonance condition is not satisfied we find practically no coupling. We compare results obtained with the 3D rms envelope equations in a uniform focusing channel with those obtained using large scale, 3D parallel Particle-In-Cell (PIC) simulations.

1 INTRODUCTION

The study of halos in beams for new high intensity accelerator applications has so far focused mainly on two-dimensional models of the transverse halo. In recent work on three-dimensional effects the presence of coupling phenomena was recognized for a special class of fully self-consistent equipartitioned equilibria, where it was claimed that longitudinal or transverse halo results for small mismatch (10%) if the mismatch in the other plane is large [1].

In this paper we examine the coupling issue using the 3D rms envelope equations and PIC simulations. Unlike Ref. [1] we allow our beams to be non-equipartitioned. In practical linac design the requirement of strict equipartitioning [2] appears to be unnecessarily stringent; a recent study of anisotropy effects showed that "temperature" ratios of 2-3 between different degrees of freedom do not necessarily give rise to instability and energy exchange [3]. We therefore investigate these more general anisotropic equilibria subject to rms mismatch. The matched bunches are not equilibria in a strict sense (i.e. functions of the Hamiltonian), but our simulations show — confirming the 2D analysis of Ref. [3] — that within the constraint of modest anisotropy the rms quantities remain practically constant.

2 ENVELOPE MODEL

For simplicity we assume constant focusing and bunched beams with a rotational axis, which restricts the analysis to the transverse "breathing mode" [4] generalized by the presence of longitudinal motion, as well as a longitudinal mode.The rms envelope equations can be written as

$$\frac{d^2a}{dt^2} + k_{0,x}^2 a - \frac{3Nr_c}{2\beta^2\gamma^3ac}\left(1 - f/\gamma^2\right) - \frac{\epsilon_x^2}{a^3} = 0 \quad (1)$$

$$\frac{d^2c}{dt^2} + k_{0,z}^2 c - \frac{3Nr_c}{\beta^2\gamma^5a^2}f - \frac{\epsilon_z^2}{c^3} = 0 \quad (2)$$

The geometry factor f depends on the aspect ratio $p \equiv c/a$,

$$f \equiv \frac{p\,\text{arccosh}(p)}{(p^2 - 1)^{3/2}} - \frac{1}{(p^2 - 1)} \quad (p > 1), \quad (3)$$

with $p^2 - 1$ replaced by $1 - p^2$ for $p < 1$. The transverse "quadrupolar" mode may be included, if desired, using separate equations for x and y and a more general form of f.

For matched beams we assume vanishing time derivatives. The resulting algebraic equations determine the rms matching conditions, which are also used to initialize PIC simulations. It is convenient to introduce the space charge shifted wavenumbers $k_{x,z}$ according to

$$k_x^2 = k_{0,x}^2 - \frac{3Nr_c}{2\beta^2\gamma^3a^2c}\left(1 - f/\gamma^2\right) \quad (4)$$

$$k_z^2 = k_{0,z}^2 - \frac{3Nr_c}{\beta^2\gamma^5a^2c}f \quad (5)$$

For small perturbations the rms equations can be linearized about the matched values c_0, a_0, which yields the two eigenmodes of coupled envelope oscillation with corresponding eigenfrequencies $\omega_{tr,lo}$. For vanishing space charge the "transverse" eigenmode oscillates with $2k_{0,x}$, and the "longitudinal" eigenmode with $2k_{0,z}$. As is typical for systems with two degrees of freedom, results can be represented in terms of three dimensionless parameters which can be chosen conveniently. In Fig. 1 we show the envelope frequencies for fixed $c_0/a_0 = 1.5$ and $k_{0,z}/k_{0,x} = 0.6$. Note that the space charge limit is reached
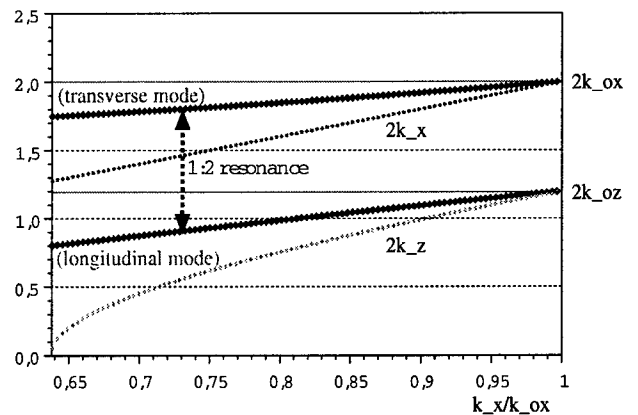
Figure 1: Envelope mode frequencies (normalized to $k_{0,x}$) for fixed aspect ratio and zero-current focusing constants as function of tune depression in x.

for vanishing k_z, which occurs near $k_x/k_{0,x} = 0.64$, and which corresponds to vanishing longitudinal emittance.

The point of interest here is that the dispersion of mode frequencies allows a 2:1 coherent resonance condition which enables coupling between the transverse and longitudinal eigenmodes. Obviously, this particular type of coherent resonance condition is lost if $k_{0,z}/k_{0,x} < 0.5$.

We can easily explore this coherent resonance behaviour by using the nonlinear envelope equations. For the parameters at the 2:1 resonance condition of Fig. 1, Fig. 2 shows the results based on an initial transverse envelope mismatch, $MM_{xy} = 1.5$, and an initial longitudinal mismatch, $MM_z = 1.0$ (i.e. no initial longitudinal mismatch). For convenience we have arbitrarily chosen $a_0 = 1$. We have defined the initial mismatch factor according to

$$MM_{xy} \equiv (a_0 + \delta a)/a_0, \tag{6}$$

where the initial value of the transverse rms envelope is $a_0 + \delta a$. A similar definition holds for z. Later we will have occasion to describe the resulting mismatch observed in an envelope or PIC simulation due to an initial mismatch; we will define the resulting mismatch according to

$$MM_{xy} \equiv \max(a(t)/a_0), \tag{7}$$

where $a(t)$ is the rms size, a_0 is the matched size, and where the maximum is over the duration of the simulation. Returning to Fig. 2, note that there is a resonant exchange

Figure 3: Maximum axial mismatch factors induced by coupling in nonlinear envelope model for fixed $k_{0,z}/k_{0,x} = 0.6$, $k_x/k_{0,x} = 0.7$ and $MM_{xy} = 1.5$ as function of c_0/a_0.

ratio. The maximum longitudinal amplitude is, however, slightly shifted towards smaller frequency ratios, a nonlinear effect that is reduced with decreasing mismatch.

While the 2:1 resonance can provide mismatch coupling from the transverse to the longitudinal direction, the opposite is also possible in terms of a 1:2 resonance. This direction of coupling is, however, found to be less efficient.

3 3D SIMULATIONS

This study used a parallel PIC code called IMPACT which was developed as part of a DOE Grand Challenge in Computational Accelerator Physics [5]. For this study we used a second-order accurate, split-operator integration algorithm which involves solving Poisson's equation once in the middle of each step. This is accomplished using standard PIC techniques, namely: (1) depositing charge on a numerical grid, (2) solving Poisson's equation on the grid and obtaining the associated self-field, and (3) interpolating the field from the grid to the particle's positions. The free-space potential is found by convolving the charge density with the Green's function using FFT's and the method of Hockney to analytically move the boundaries to infinity [6].

Figure 2: Solutions for δa, δc from the nonlinear envelope equation at parametric coherent resonance with initial mismatch $MM_{xy} = 1.5$ and $a_0 = 1$.

between the transverse and longitudinal mismatch. The latter reaches large amplitude, after which the oscillation energy flows back into the transverse mismatch and the picture repeats. The fact that δc exceeds δa is attributed to the weaker axial focusing.

A more complete picture of the maximum axial mismatch factors induced by this coupling process is shown in Fig. 3 for fixed $k_{0,z}/k_{0,x} = 0.6$, $k_x/k_{0,x} = 0.7$, initial $MM_{xy} = 1.5$, and the aspect ratio c_0/a_0 as free parameter. There is a stopband for the coupling process around the linear theory parametric resonance condition $\omega_{lo}/\omega_{tr} = 0.5$. The width of the stopband is about $\pm10\%$ in this frequency

We present calculations for parameters associated with Fig. 3. We have chosen an initial 6D waterbag distribution matched by means of the rms equations. The simulation was run for a total of 160 units of time using 4000 integration steps and 20 million simulation particles. At each step a 128^3 grid was placed around the particles for the space charge calculation (though the code actually used an augmented 256^3 grid to solve the free space Poisson equation). To ensure that the bunch was sufficiently stationary, we tracked the initial distribution for 60 units of time prior to applying the envelope mismatch. (In our units, one unit of "time" equals one period of zero current transverse oscillation, i.e. one period corresponding to $k_{o,x}$). We ran 4 cases corresponding to 4 different points in Fig. 3: the exact linearized theory resonance condition (case A1,

$\omega_{lo}/\omega_{tr} = 0.5$); the point of maximum envelope coupling for the value of $MMxy = 1.5$ (case A2); and points at the upper and lower edge of the stopband where practically no coupling is expected (cases A3 and A4, respectively). After applying the mismatch at $t = 60$ we observe the coupling and compare results with the envelope model. See Table 1. For cases A1 and A2 the mismatch observed in the simulations is quite close to that predicted by the rms equations, and the results are in qualitative agreement for case A3. Since the development of density inhomogeneity and halo are beyond the envelope model, and since the rms emittances change in the simulations following the mismatch, we do not expect precise agreement.

case	A1	A2	A3	A4
$k_z/k_{0,z}$	0.42	0.33	0.60	0.19
k_z/k_x	0.36	0.28	0.51	0.16
c/a	1.55	1.46	1.88	1.37
ω_{lo}/ω_{tr}	0.50	0.48	0.55	0.46
$MM_{xy}^{\text{envelope}}$	1.50	1.50	1.50	1.50
$MM_{xy}^{\text{simulation}}$	1.50	1.48	1.48	1.4
MM_z^{envelope}	1.79	1.95	1.06	1.12
$MM_z^{\text{simulation}}$	1.76	1.87	1.25	1.6
$X_{\max}/a_0$	6.6	6.5	6.1	5.9
$Z_{\max}/c_0$	5.3	5.4	3.7	4.9

Table 1: Summary of 3D rms envelope results and 3D PIC simulation results for $k_{0,z}/k_{0,x} = 0.6$ and $k_x/k_{0,x} = 0.7$.

Besides showing that the coupling predicted in the rms equations is also present in PIC simulations, these results indicate that rms-matched, non-equipartitioned beams in certain parameter regimes may propagate stably for long periods with little-or-no change in the rms quantities. Fig. 4 shows the rms emittances for case A1. Prior to the mismatch at $z = 60$ there is almost no emittance growth; the variation is roughly $\pm 0.3\%$ for the transverse emittances and $\pm 0.7\%$ for the longitudinal emittance. Fig. 5 shows the
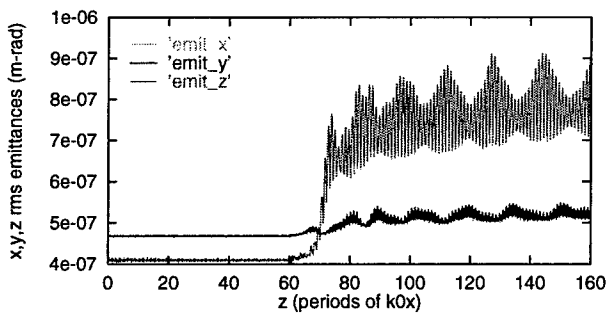
Figure 4: rms emittances vs. z for case A1

rms beam sizes for case A1. There is obvious coupling between the horizontal and transverse planes, with the transverse size reaching a minimum when the longitudinal size is maximum, and vice-versa. By comparison, the corresponding figure for case A3, Fig. 6, shows less coupling.
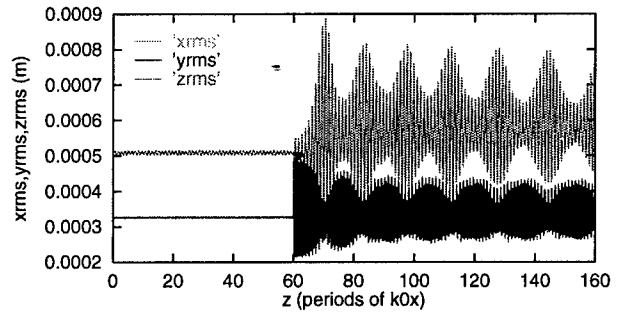
Figure 5: rms beam sizes vs. z for case A1
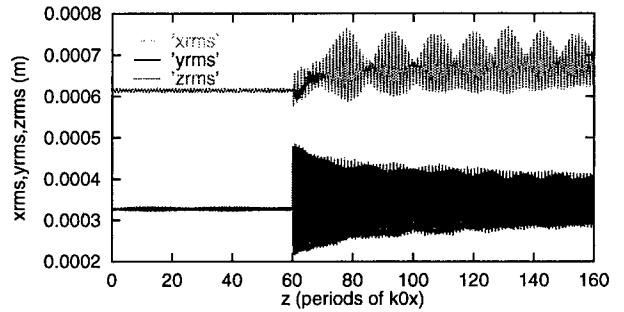
Figure 6: rms beam sizes vs. z for case A3

Case A4 is in fact unstable; we observed significant changes in the rms emittances shortly after the start of the simulation. Note that the initial temperature anisotropy given by $\frac{T_z}{T_x} = \frac{ck_z}{ak_x}$ results in a value of 0.56 for the case at resonance (A1), 0.37 for the case of maximum coupling (A2), 0.95 (close to equipartitioned) for case A3, and 0.23 for case A4. The stability of the beams in cases A1, A2, and A3, and the instability of case A4, confirms the findings of analytical work in Ref. [3].

4 ACKNOWLEDGEMENTS

5 REFERENCES

[1] R.L. Gluckstern et al., *Phys. Rev. E,* **58**, 4977 (1998)

[2] N. Brown and M. Reiser, *Phys. Plasmas* **2**, 965 (1995)

[3] I. Hofmann, *Phys. Rev. E,* **57**, 4713 (1998)

[4] J.S. O'Connell, T.P. Wangler, R.S. Mills and K.R. Crandall, Proc. 1993 Part. Accel. Conf., Washington DC, 3651 (1993)

[5] R. Ryne *et al.*, Proc. 1998 Linac Conf., Chicago, IL (1998)

[6] R.W. Hockney and J.W. Eastwood, *Computer Simulation Using Particles*, (Adam Hilger, NY, 1988)

Variable Momentum Compaction Lattice Studies[*]

S.L. Kramer[#] and J.B. Murphy, BNL, Upton, NY 11973

Abstract

The VUV storage ring at the National Synchrotron Light Source was used to study the impact of changes in the momentum compaction factors over a large range from positive to negative values. Changes in bunch length and synchrotron tune were measured versus current and RF parameters for these different lattices. By controlling both the first and second-order momentum compaction factors, a lattice was developed in which a pair of alpha buckets was created within the energy aperture of the vacuum chamber and beam was stored simultaneously in both buckets.

1 INTRODUCTION

The longitudinal equations of motion for electrons are given as,

$$\dot{\phi} = -\omega_{rf}(\alpha_1 - \alpha_2\delta)\delta \quad ,$$

$$\dot{\delta} = \frac{eV_{rf}\mathrm{Sin}(\phi+\phi_s)-U(\delta)}{E_0 T_0} \quad (1)$$

where $\delta \equiv \Delta E/E_0$, and α_1, α_2 are the first and second-order momentum compaction factors respectively. The need to consider higher order terms in the momentum compaction has its origins in the problem of transition crossing in proton machines [1]. In fact graphic illustrations of the so-called alpha buckets can be found in these early references. More recently several groups at electron storage ring facilities have attempted to develop short electron bunches by reducing α_1 [2& refs. therein].

Although this approach can yield short bunches at low currents, it has so far failed at high currents due to increases in the energy spread of the stored beam resulting from a lower threshold for the microwave instability [3]. The infrared users of the VUV ring at the NSLS desire shorter bunch lengths for pump-probe experiments. This requirement motivated a study of the possibility of variable α_1 lattices and their impact on the bunch length for high current beams in this ring. The VUV ring is normally operated as a medium emittance (160 nm) double bend achromatic lattice and a low frequency (53 MHz) RF system.

2 VARIABLE α LATTICES

The achromatic condition for the VUV ring is controlled by a single quadrupole family (Q3) in the dispersion region between the two-dipole magnets. By increasing the strength of this quadrupole family the dispersion function can be made negative in a portion of each dipole magnet

resulting in a reduction in α_1. In order to maintain injection, the betatron tunes are restored using the remaining two quadrupole families (Q1 & Q2). Varying the Q3 quadrupole over a range of 40% allowed the α_1 to be varied over a wide range, $-\alpha_{1o} < \alpha_1 < 2\alpha_{1o}$, where $\alpha_{1o} = 0.0235$ is the value for the achromatic lattice. The value of α_1 was determined for each lattice by measuring the synchrotron frequency (excited by a kicker), $f_s \propto \sqrt{\alpha_1}$, for $I \approx 1$ ma; the low current was chosen to eliminate the effects of potential well distortion. Figure 1 shows these values for $|\alpha_1|$ as a function of the magnetic field measured in a Q3 magnet.

For $\alpha_1 \geq \alpha_{1o}/10$ we attempted an independent measurement of α_1 by using the lattice modeling code LOCO [4]. Since this program required measurements of the beam response matrices, we were able to use it only where sufficient current could be stored. We also measured lattices with $\alpha_1 = -\alpha_{1o}$ where the sextupoles were turned off to store high current, since the head-tail instability was not a problem for negative (natural) chromaticity. The values of α_1, calculated by MAD using the LOCO determined lattice, are also shown in Figure 1. Although the LOCO calculations yield results close to the values estimated by the synchrotron tune measurements, there remains some significant differences. For the remainder of the studies we adopted the synchrotron tune measurement scheme to determine α.

As the magnitude of α_1 is reduced, we needed to consider the impact of α_2. For $\alpha_2 \neq 0$, a stable off energy RF bucket exists at $\delta_c = \alpha_1/\alpha_2$ in addition to the "normal" one at $\delta_0 = 0$. As α_1 decreases two things happen: 1) the energy deviation, δ_c, decreases so that the two buckets approach one another and 2) the height of each bucket increases as $\delta_{rf0} \propto \sqrt{V_{rf}/\alpha_1}$. Collision of the two buckets occurs when $\delta_{rf0} = \alpha_1/\sqrt{3}\alpha_2$. After collision, the energy acceptance of the buckets depends only on α_1/α_2 and the phase acceptance of the buckets is given by

$$\Delta\phi \approx 2\frac{1}{\sqrt{3}}\frac{\alpha_1}{\alpha_2}\sqrt{\frac{2\pi h \alpha_1 E_0}{eV_{rf}\cos\phi_s}} \quad . \quad (2)$$

By controlling α_2 using the SF chromaticity correcting sextupole magnets we were able to store beam in lattices with $\alpha_1 \approx \alpha_{1o}/200$.

[#] Email address: kramer@bnlls1.bnl.gov
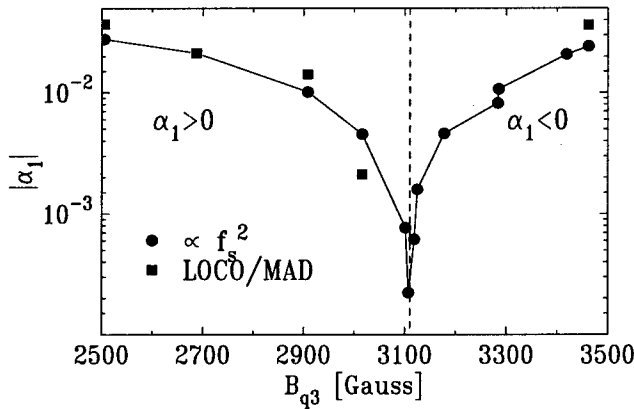
Figure 1: Variation of $|\alpha_1|$ with the magnetic field in the Q3 quadrupole family, Q1 and Q2 are varied to maintain constant tunes.

The values for α_2 were measured by varying the RF frequency, f_{rf}, using the relationship [2]

$$f_s^4 = f_{s0}^4 \left(1 + 4 \frac{\alpha_2}{\alpha_1^2} \frac{\Delta f_{rf}}{f_{rf}} \right). \tag{3}$$

3 STORED BEAM IN ALPHA BUCKETS

On March 16, 1999, we successfully stored electrons in a pair of alpha buckets; either bucket alone or both simultaneously. This was achieved not by reducing α_1 to the smallest values ($\alpha_1 \approx \alpha_{1_0}/10$), but by increasing α_2 such that the value $\delta_e \leq 1\%$, a value devised to maintain the off energy bucket inside the vacuum chamber aperture on the off energy closed orbit. To provide adequate phase acceptance, V_{rf} was reduced by at least a factor of 3-4. Figure 2 shows the two bunches as measured on a stripline BPM; superimposed is the waveform of the 53MHz RF cavity field. The time separation for the two alpha bunches is 6.75 ns or $\Delta\phi = 128.5°$ of the RF wave. This spacing is $\Delta\phi = \pi - 2\phi_s$ and was tunable by changing V_{rf}. Note that the separation between "normal" RF buckets in the VUV ring is 18.9 ns. In Figure 3 the 2-D images of the two bunches are visible on a synchrotron radiation monitor. The separation $\Delta x = 3.3$ mm for the left image is proportional to the energy difference of the two bunches with δ_0 on the left and δ_e on the right, the reverse of the scope trace in Figure 2. The dispersion is not well known at this beam port, however using two different BPM measurements of Δx and the calculated dispersion from the LOCO model we determine $\delta_e = \Delta x/D_x = 0.66\%$. The Δx separation was tunable by changing α_2 with the SF sextupole, as shown in the right image of Fig. 3 where $\delta_e \approx 0.4\%$. It can also be seen that there is a vertical separation of the beam spots, which indicate the presence of vertical

dispersion in the ring. To arrive at the alpha bucket lattice that we could inject into we'd greatly increased the strength of SF to increase α_2. We believe the horizontal chromaticity was pushed far positive while sending the vertical chromaticity negative putting us at odds with the head-tail instability. In normal operation the VUV ring can store roughly 15 ma without any sextupoles (head-tail limit) and this jives with the current limit we could attain in the on energy alpha bucket. At present we were limited to 2 ma in the off energy bucket.
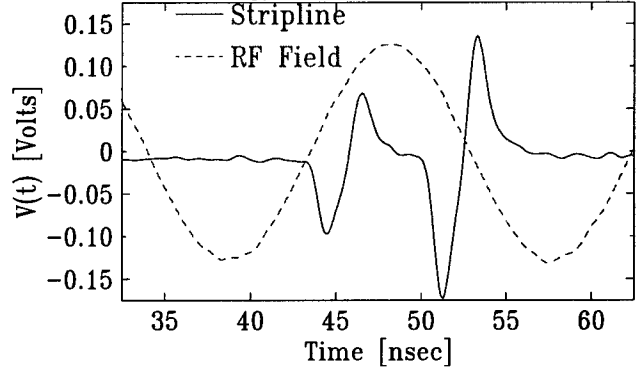
Figure 2: Scope traces of the RF field and beam bunch signals from a stripline BPM showing beam stored in the two alpha buckets separated by 6.75 ns.
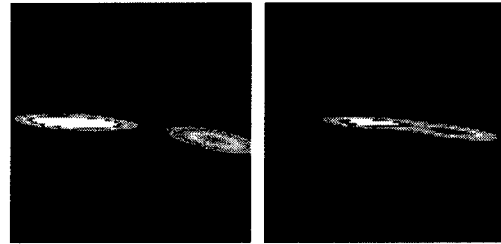
Figure 3: Synchrotron light monitor images showing the two alpha buckets for two values of α_2. The horizontal bunch spacing, $\Delta x = 3.3$ and 2.0 mm for left and right images respectively, are proportional to δ_e.

4 BUNCH LENGTH MEASUREMENTS

The bunch length was first measured with a fast photo-diode and a 20 GHz sampling scope. The response of the diode and scope was measured with a 2 psec laser pulse and gave a Gaussian risetime of 28 psec. The measured risetime, σ_t, assuming a Gaussian leading edge to the bunch, was obtained by subtracting in quadrature the delta function response from the measured bunch risetime. A second method used a fast transient digitizer to measure the bunch shape in a single passage of the bunch [5]. This used a beam position monitor, BPM, to obtain a large coupling to the beam. The resulting signal was deconvolved using a measured response function determined at low current by assuming a Gaussian bunch shape as measured by the diode.

Figure 4 shows the measured σ_t of the bunch as a function of current. This data shows the reduction in the

zero current bunch length $\sigma_t(I=0) \equiv \sigma_0$ as α_1 was reduced. However, the rate of increase with current is greater for smaller values of α_1. The values of σ_t measured for $\alpha_1 = \pm\alpha_{1o}$ agreed closely. The data for α_{1o} was fit to a bunch lengthening model used for SPEAR data [6], gave a broad-band impedance of $\left|\dfrac{Z}{n}\right| = 1.8\,\Omega$ and a high frequency cutoff parameter a=–0.78 (a=–0.68 for SPEAR). This predicted a threshold for the microwave instability of about 82 mA. However, extrapolating the microwave lengthening to σ_0 gave a threshold current value of $I_m \approx 113\,\text{mA}$. It's clear from Figure 4 that I_m decreases as α_1 decreases.

$\alpha_1 > 0$	I_c[mA]	I_m[mA]	$\alpha_1 < 0$	I_c[mA]	I_m[mA]
0.030	148	140	-.026	60	127
0.0235	100	113	-.023	56	113
0.0109	54	56	-.012	30	
0.0049	18.5	17	-.005	10.5	
0.0008	4.2		-.0007	2.5	
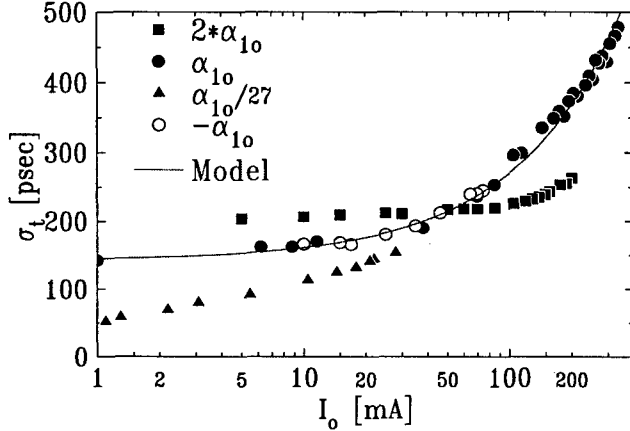
Figure 4: Gaussian risetime measured as a function of bunch current for several values of α_1.

The measured Gaussian risetime doesn't show the detailed information on the impedance seen by the beam. The reconstructed bunch current distributions using the BPM signal are presented in Figure 5 and show that the FWHM bunch length is larger for $\alpha_1 > 0$ than for the same magnitude of $\alpha_1 < 0$. This appears to be the result of a sharper trailing edge to the bunch distribution rather than from the leading edge, risetime show in Figure 4. This is qualitatively consistent with a resistive impedance plus and inductive term which should contribute to bunch lengthening for $\alpha_1 > 0$ and shortening for $\alpha_1 < 0$ [7].

5 IR COHERENT SR THRESHOLDS

Infrared users on the VUV Ring have seen large bursts of far-infrared synchrotron radiation being emitted by the beam. These signals are most prominent above a well-defined current threshold, I_c and increase in intensity proportional to the bunch current squared [8]. For the achromatic lattice, I_c agrees with I_m calculated using the bunch length data. Since this threshold should depend on the bunch length and therefore α_1, we compare I_c with I_m for the different α_1 lattices in the following table. For $\alpha_1 > 0$, $I_c \approx I_m$, but for $\alpha_1 < 0$, $I_c < I_m$. This agrees with the shorter FWHM bunches for $\alpha_1 < 0$.

6 ACKNOWLEDGEMENTS

7 REFERENCES

[1] A.A. Kolomenski & L.L. Sabsovich, p. 112, CERN 56-25 (1956), and N. Vogt-Nilsen, CERN PS/NVN-2 (1958).

[2] D. Robin, et. al., "Experimental Results on Low Alpha Electron Storage Rings", AIP Conf. proceedings 367, p. 150 (1996).

[3] C. Limborg, "A Review of Difficulties in Achieving Short Bunches in Storage Rings", Proc. EPAC-98, p. 151 (1998).

[4] J. Safranek, "Experimental Determination of Storage Ring Optics Using Orbit Response Measurements", Nuc. Instr. and Meth., A388, p.27 (1997).

[5] S.L. Kramer, et. al. , "Bunch Current Density Measurements in the VUV Light Source", proceedings of EPAC-94, p. (1995).

[6] P. Wilson, et. al., "Bunch Lengthening and Related Effects in SPEAR II", IEEE Trans. Nuc. Sci., NS-24, p.1211 (1977).

[7] Karl L.F. Bane, "Bunch Lengthening in the SLC Damping Rings", SLAC-PUB-5177, (1990).

[8] G.L. Carr, et. al., "Investigation of Coherent Emission from the NSLS VUV Ring", this proceedings (1999).
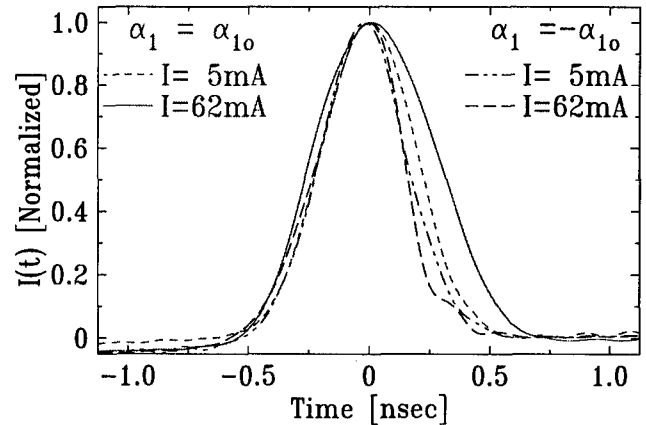
Figure 5: Bunch current distribution measured for two beam currents (5 and 62 mA) and for $\alpha_1 = \pm\alpha_{1o}$.

NEW TECHNIQUE FOR BUNCH SHAPE FLATTENING

A. Blas, S. Hancock, M. Lindroos, F. Pedersen, CERN, Geneva, Switzerland,

S. Koscielniak, TRIUMF, Vancouver B.C., Canada

Abstract

A technique for increasing the bunching factor (B_f) is described. Typically in booster-type synchrotrons, it is important to reduce the transverse space-charge tune shift. One means to achieve this is to increase the ratio of average to peak longitudinal charge density. Essentially, the idea is to create hollow bunches by sweeping high-harmonic empty buckets into the particle beam prior to bunching and acceleration. Successful beam experiments are reported with supporting LONG1D simulation studies performed on the CERN PS Booster for both single and dual rf cases. The longitudinally hollow bunches also benefit the receiving ring during the double batch transfer where half of the PS has to wait 1.2 seconds at low energy for the second injection. A 15th harmonic rf system was used to form the empty buckets. Simulations show that for the single harmonic case, B_f is increased from 0.28 to 0.38, and for the dual harmonic one, B_f is increased from 0.45 to 0.55 (values at 100 MeV). The flattening technique has been tested successfully with the first harmonic to 1 GeV and to 100 MeV for dual harmonic acceleration.

1 INTRODUCTION

Phase space displacement acceleration of a coasting beam by decelerating empty buckets through it has been described by Dome [1]. Perhaps the best picture is to think of the beam particles sliding up between the empty buckets as these descend, Figure 1. Depositing empty buckets into the core of a coasting beam and then turning the rf off will give rise to a double peaked energy spectrum, Figure 2. Capture of this beam into a low harmonic bucket and subsequent filamentation will give rise to a hollow phase space distribution, Figure 4. This technique was tested at the Booster in 1979 [2], but was limited by intensity-related problems. Since that time, rf feedback has been implemented; $h=1$ replaced $h=5$; and the bucket area doubled, so the enhanced space charge from a hollow bunch is more tolerable. Further, in 1992 hollow distributions were accelerated in the PS [3] providing the incentive to renew attempts in the Booster.

1.1 Slew rate

Let $\Delta\omega$ be the angular frequency sweep, T the duration of the sweep and ω_s the angular synchrotron frequency at the high harmonic. All the standard formulae for rf buckets can be adopted parametrized in terms of the synchronous phase given by $\sin\Phi_s = -\Delta\omega/[\omega_s^2 T]$.

Here $\Delta\omega$ must be sufficient to place the initial buckets outside the beam and so, for given voltage, T is the only free variable with which to control the height and width of the buckets and the adiabaticity of the process. T is limited by the need to accelerate away from space-charge induced transverse betatron resonances. Longitudinal space charge also has an influence: it reduces the size of full buckets and increases the size of empty ones.
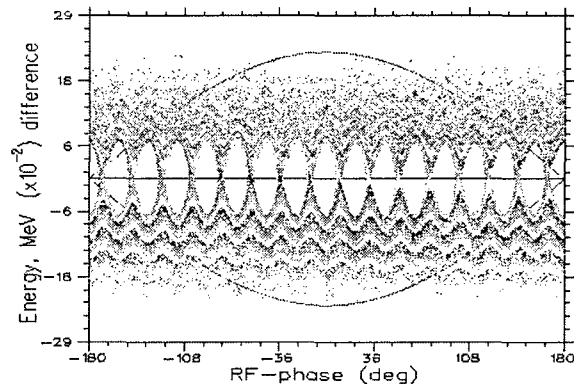
Figure 1: Computer simulation of longitudinal phase space after deposition of $V_{16}= 1$kV empty buckets; $T = 5$ms.

1.2 CERN PS Booster

The PS Booster has three rf systems: C02 $h=1$, C04 $h=2$ or $h=4$, and the C16 system capable of producing harmonics from 10-27 at 50 MeV. C02 and C04 operate at up to 8 and 5 kV, respectively. For C16 at 1 to 4 kV, sweeps of 20-30 kHz in 20 to 5 ms are appropriate, followed by capture in 2 to 6 ms depending on how short is the 50 MeV injection porch. To achieve a uniform phase depopulation, it is preferable to use a high harmonic number for the buckets; the strong rf feedback on the C16 system makes this an easier proposition.

2 BTFM

In principle, the C16 rf manipulations can and have been carried out [4] using dead reckoning. However, in the PS Booster it is possible to use a beam transfer function measurement [5], BTFM, to diagnose the precise energy at which the buckets are deposited via the notch introduced into the energy spectrum of the coasting beam, Figure 2. The C04, $h=4$, cavity is used to tickle the beam with noise. The beam response is proportional to the derivative of the particle density distribution per unit energy. Reconstructing the distribution requires integration of a very noisy response spectrum and leads to a stochastically varying baseline.
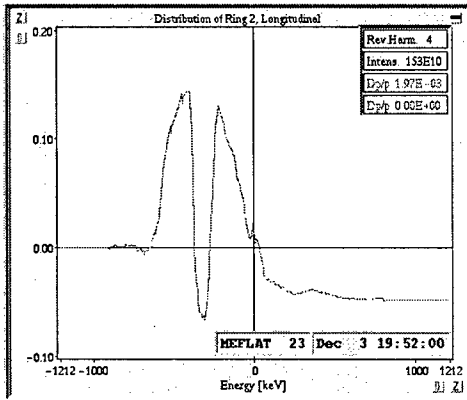
Figure 2: Energy spectrum (from BTFM) after deposition of empty buckets with V_{15}= 4kV, 8 ms frequency sweep.

2.1 Initial energy spectrum

Based on the principle that one cannot introduce a notch where there are no particles, one may calibrate the BTFM by sweeping small empty buckets (e.g., V_{16}= 0.5 kV) of known rf into the periphery of the beam and looking for the notches. After calibration, the BTFM with C16 off can be used to obtain the beam energy spectrum versus injected intensity. Figure 3 shows three measures of width: 100% full width, full width without tails and FWHH.
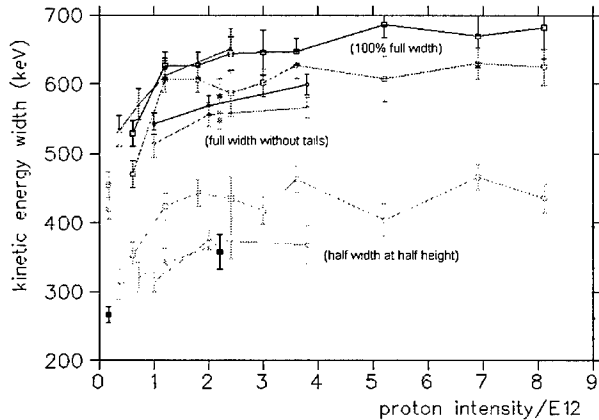
Figure 3: Beam energy width versus injected intensity.

It is clear that the beam is initially much wider than the 370 keV measured by spectrometer, at the exit from the linac, and assumed in the computer simulations.

3 SINGLE HARMONIC

The hollow bunch technique has been refined in several machine development periods and complemented with computer simulations [6]. Experimental work has benefited greatly from another diagnostic technique: beam tomography [7] of bunch shape data that spans at least half a synchrotron period. The following data, acquired in experiments spanning several months, shows successful capture and acceleration of the hollow beam to 1 GeV. Results are not always reproducible, though the BTFM

has helped in this respect. One cause of variability that has been identified is the 180° phase jump of the fundamental during locking to the beam after the C16 modulation produces slightly asymmetric double-peaked bunch shapes.
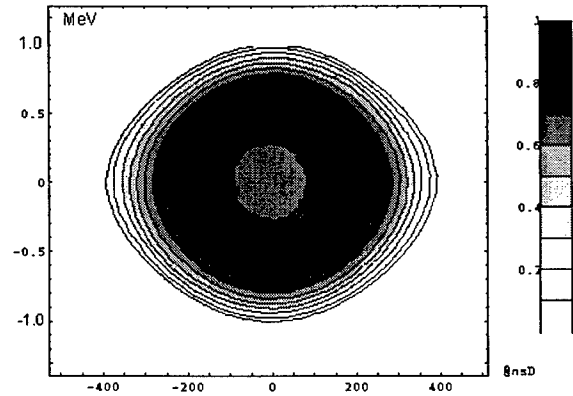
Figure 4: Tomographic reconstruction of phase space after h=1 capture and acceleration to 100 MeV flat top; V_{16}= 2kV, frequency sweep in 20ms, intensity 7×10^{12} ppp.
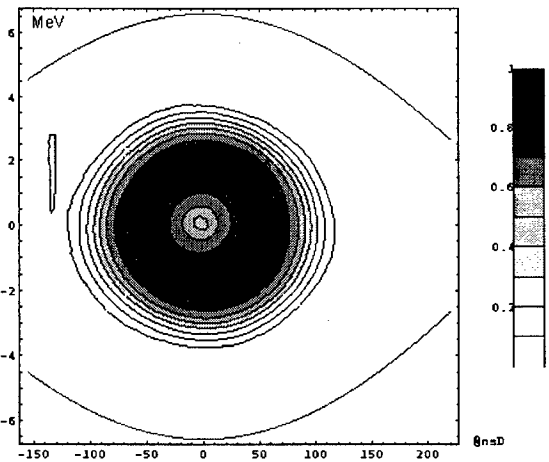
Figure 5: Tomographic reconstruction of phase space after acceleration to 1 GeV, V_{15}= 3kV, 8 ms sweep, 6×10^{12} ppp.

Because of the increased emittance and the typically flat or double-peaked bunch shape, the peak charge densities are reduced and the bunching factor increased.

Table 1: Bunching factors at 100 MeV, single harmonic.

C16	B_f prediction	B_f measurement
Off	0.29	0.32—0.34
On=1kV	0.36	0.37
On=2kV	0.39	0.37—0.39
On=4kV	?	0.39—0.41

4 DUAL HARMONIC

Setting up for dual harmonic operation is complicated by the fact that the C04 system is to be used both for the BTFM (h=4) and the second harmonic (h=2), though not in the same magnetic cycle. Adjustment of the empty bucket deposition is more delicate and, typically, a dipole

component remains after capture by the dual harmonic rf, Figure 6. Acceleration to 100 MeV is possible at low intensity, Figure 8, but a longitudinal instability hinders further acceleration due to losses. Up to this energy, experimental data compares quite favourably with simulation [6], Figure 8, Figure 9 and Table 2.
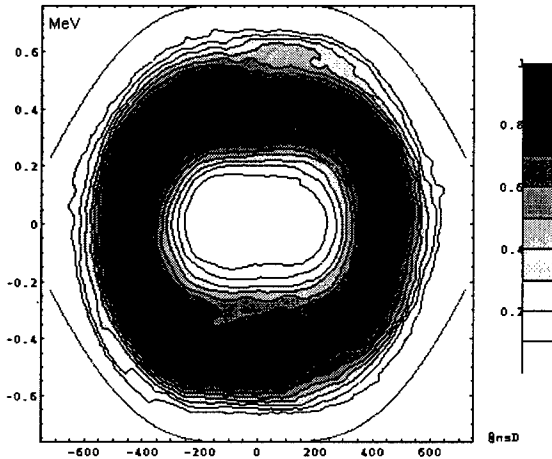
Figure 6: Tomographic reconstruction at 50 MeV, 20 ms filamentation V_{15}= 4kV, 8 ms sweep, intensity 2×10^{12} ppp.

Table 2: Bunching factors at 100 MeV, dual harmonic.

C16	B_f prediction	B_f measurement
Off	0.44	0.44—0.46
On=2kV	0.51	0.46—0.48
On=4kV	0.55	0.46—0.52
On=6kV	0.59	0.53—0.57

4.1 Longitudinal instability
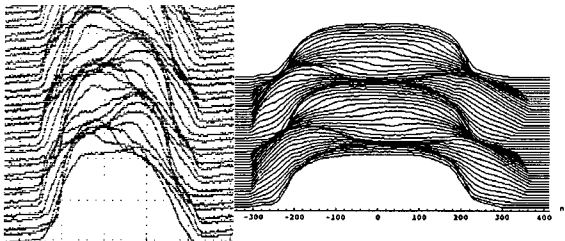
Figure 7: Sextupole mode at 120 ms, octupole at 160 ms.

Careful observations show the instability to be present even when C16 is turned off and the bunches are not hollow, but in this case the instability is less severe and usually the losses are not significant. The upward ramp of the Booster magnet cycle lasts ≈ 500 ms. The instability starts at ≈ 50 ms and stops at ≈ 250 ms. During this time, at least two within-bunch oscillation modes appear to be present: first sextupole and then octupole, Figure 7. It is suspected that the hollow amplitude distribution contributes unfavourably to the growth rate. When the instability is over, the distribution of the surviving particles is monotonically decreasing with amplitude. The instability appears related to the control loop which

synchronises second harmonic to the fundamental waveform. Opening this loop calms the instability, but loss of h=1,2 relative phasing eventually leads to beam loss.
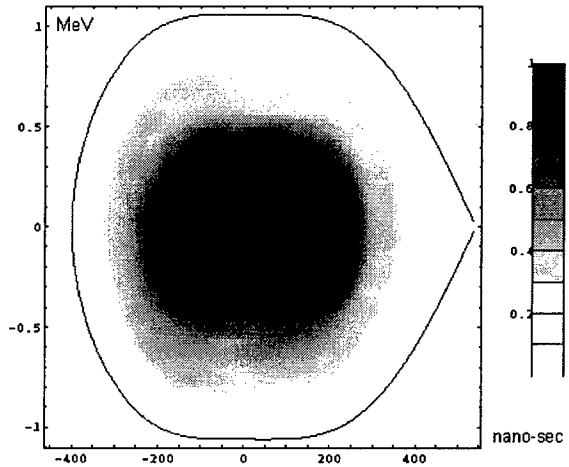
Figure 8: Tomographic reconstruction of phase space at 120 MeV, V_{15}= 4 kV, 6 ms frequency sweep, 10^{12} ppp.
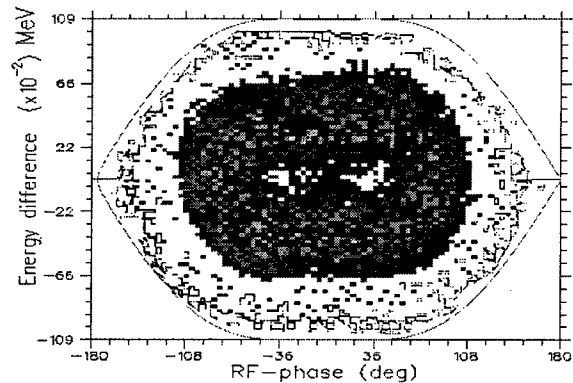
Figure 9: Computer simulation, 105 MeV flat top, V_{16}= 2 kV, 8 ms frequency sweep, intensity 3×10^{12} ppp.

5 CONCLUSION

With relatively little effort, this technique of bunch flattening has been successfully applied to single harmonic acceleration. Progress with dual-harmonic hollow bunches has been compromised by an instability. However, the evidence suggests that this problem is particular to the PS Booster low-level rf and may not be a hindrance at other machines.

6 REFERENCES

[1] G. Dome: Theory of rf acceleration, CERN 87-03.
[2] J. Delahaye et al: Shaping of proton distribution, Proc 11th Int. Conf. on High-Energy Accels, Geneva, pp.299-304, 1980.
[3] R. Cappi et al: Proc. 1993 PAC, Washington D.C., p.3570.
[4] A. Blas: CERN/PS/RF/Note 98-14 (MD).
[5] H. Schonauer: PS/OP/Note 96-18 & PS/OP/Note 97-52.
[6] S. Koscielniak: TRI-DN-99-13 & TRI-DN-99-14.
[7] S.Hancock, M.Lindroos, E.McIntosh, M.Metcalf: Tomo-graphic measurements of longitudinal phase space density, accepted for publication in Computer Physics Communications.

SIGNALS FROM MICROWAVE UNSTABLE BEAMS IN THE SLC DAMPING RINGS [†]

Boris Podobedov and Robert Siemann

Stanford Linear Accelerator Center, Stanford University, Stanford, CA 94309

Abstract

The longitudinal microwave instability is present in the SLC damping rings during routine operations. Experimental studies of the instability at nominal conditions have been reported previously [1]. To complement those studies and better understand the properties of the instability a series of dedicated experiments were performed under a broad range of operating parameters. These experiments included spectral measurements of BPM signals as well as time domain diagnostics using a custom detecting circuit. This paper describes the techniques, the results and discusses possible interpretations of these measurements.

1 INTRODUCTION

Two SLC damping rings operate to increase the brightness of 1.2 GeV electron and positron beams before their further acceleration in the linac. Nominal store times in the rings are 8.3 ms for electrons and 16.6 ms for positrons. During normal operations both rings store two bunches each. The RF frequency is 714 MHz and typical accelerating voltage is $V_{RF} \sim 800$ kV. This results in a low current synchrotron frequency of about $v_s \sim 100$ kHz and an rms bunch length of $\sigma \sim 17$ ps. Other design and operating parameters for the SLC damping rings are described elsewhere [2].

It was reported previously [3] that above a threshold of about 2×10^{10} particles per bunch (ppb) stored beams become longitudinally unstable. The instability develops a few milliseconds after injection which is comparable to the longitudinal damping time. Since the instability saturates quickly it does not prevent successful operation for stored currents as high as $4\text{-}5 \times 10^{10}$ ppb. However, it has been measured that the instability somewhat compromises the damping ring performance as an injector resulting in the beam jitter in the linac downstream [4].

The properties of instability can be summarized as follows. Instability is due to a single bunch; it contains a quadrupole or a sextupole mode and is rather sensitive to the accelerating voltage.

The simplest diagnostics for the instability is a spectrum analyzer connected to a BPM electrode. Above the threshold, high frequency revolution harmonics acquire sidebands that are displaced by roughly 2 or 3 times the unperturbed synchrotron frequency v_s indicating a quadru-

pole or a sextupole mode. The amplitude of the sidebands often varies slowly on a millisecond scale in a peculiar manner. This variation can be seen with a spectrum analyzer if it is set to zero span as a receiver at the sideband frequency. However, this is not a convenient measurement for longer stores when the instability sideband frequency changes as the stored charge decreases. A better way of seeing this variation is by demodulating the instability signal from the sidebands and observing the resulting low frequency signal with an oscilloscope. In addition to a slowly varying envelope this method gives a fast (roughly 2 or 3 v_s) signal that is characteristic of the phase-space orientation of the structure associated with the instability [1].

On the other hand, dependence of the instability frequency on current as well as the amplitude dependence of a specific sideband can be measured much easier with a spectrum analyzer. Indeed, to extract the frequency from the time-domain data one needs to have large memory depth due to high ratio of the characteristic time of the envelope variation (ms) to the instability period (3-5 μs).

Although some instability properties can be measured during routine operation a dedicated experiment with a single bunch stored and flexibility in stored charge and RF voltage has more value. In this paper we report the results of a series of such experiments performed in the positron damping ring. Qualitatively similar results were obtained at a different time in the electron ring. However, since the positron ring studies were much more detailed we chose to present the positron ring results alone.

2 SETUP AND HARDWARE
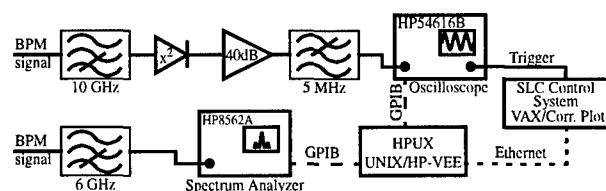
Figure 1. Experimental setup.

As shown in Fig. 1 BPM signals were simultaneously measured with two instruments i) a spectrum analyzer and ii) a digitizing oscilloscope after some initial processing. The processing circuit is described in more detail in [1]. To summarize, the front end high pass filter cuts off the bulk of the RF power coming from the BPM. A square law detector demodulates the instability signal from the side-

bands to high frequency revolution harmonics. This signal is subsequently amplified, and higher order mixing products are removed by a low pass filter. During our experiments the major settings were as follows. The central frequency of the spectrum analyzer was set to the 1149th revolution harmonic which is roughly 9.77 GHz. The span was 500 kHz, and the resolution and video bandwidths were 1 kHz. This results in the sweep time of 2 s and, moreover, two subsequent sweeps were video averaged. The oscilloscope was AC coupled. It was set to 1 ms/div and the trace length was 2000 points.

The oscilloscope and the spectrum analyzer were controlled through the GPIB bus from a UNIX host running HP-VEE. This program was saving the data onto the local disk and also communicated with the SLC control system VAX via Ethernet. That host was in turn running the correlation plot routine that recorded the values of the stored current as well as various RF system parameters. In addition, prior to recording each data point the control system was sending a trigger that we used for the oscilloscope. The spectrum analyzer was free running but the HP-VEE program guaranteed that the data was acquired synchronously with the oscilloscope trace. This procedure allowed us to attach the value of beam current to every pair of traces recorded. The data taking rate was a fraction of a Hz which was adequate for a typical beam lifetime of several minutes.

3 MEASUREMENT RESULTS

In the course of our measurements several dozen beam stores at various accelerating voltages were recorded. Each store lasted about seven minutes that allowed initial beam current of ~3.5×10^{10} ppb to decay roughly a factor of two and to a value below the instability threshold. Detailed analysis of the data including the dependence of instability properties on the RF voltage will be presented elsewhere [5]. In this paper we will illustrate some of the most interesting aspects of our measurements using the data for the RF voltage of V_{RF}=690 kV as determined from the measured synchrotron frequency.
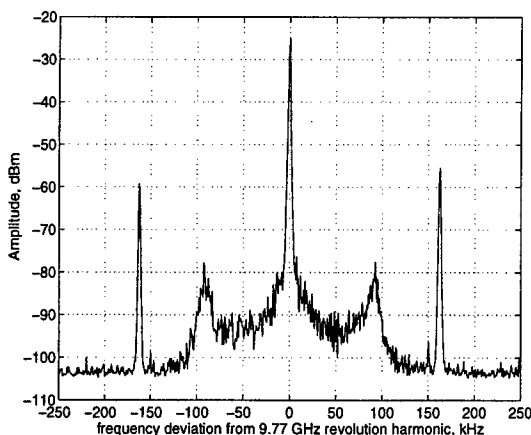
Figure 2. Typical spectrum at N=3×10^{10} ppb.

The typical spectrum analyzer sweep when the quadrupole mode of the instability is present is shown in Fig. 2. One can clearly see the instability sidebands to the revolution harmonic displaced by about 160 kHz. This is roughly 10% lower than twice the zero current synchrotron frequency at this RF voltage. To represent the change of the instability spectrum with current we use a contour plot of all the spectrum analyzer sweeps for each store as shown in Fig. 3.
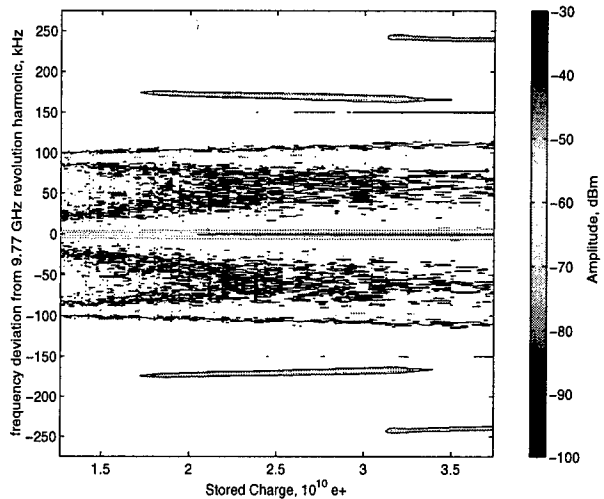
Figure 3. Spectrum analyzer data vs. stored charge.

One can see how the instability jumps from sextupole to a quadrupole mode in the region of 3.2-3.4×10^{10} ppb. The quadrupole mode threshold is about 1.7×10^{10} ppb. Note that other than this mode switching the instability behavior with current seems to be mundane. The frequency of the quadrupole mode is linearly decreasing at a rate of ~5 kHz/10^{10} ppb. Such a behavior is usually attributed to the inductive portion of the ring impedance.
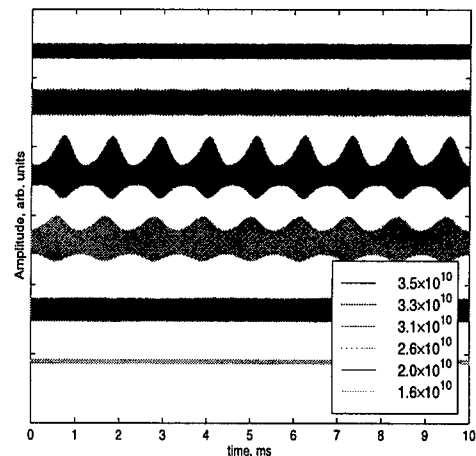
Figure 4. Oscilloscope traces of the instability signal for different values of stored charge.

The picture, however, becomes more interesting if along with the spectrum analyzer data we consider oscillo-

scope traces taken concurrently. Several such traces taken for the same case as Fig. 3 are shown in Fig. 4. The top trace that corresponds to the highest current shows a constant amplitude sextupole mode. The second trace from the top relates to the case when both sextupole and quadrupole modes coexist. At even smaller values of current (two traces in the middle) instability becomes pure quadrupole but it acquires the characteristic bursting behavior. As seen from Fig. 4 the bursts repeat in time with a period of about 1 ms. Finally, below 2.5×10^{10} ppb bursts disappear and the quadrupole mode oscillates with constant amplitude.
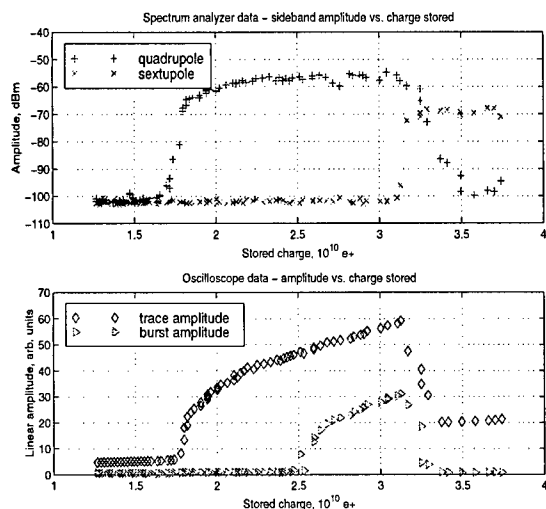
Figure 5. Instability amplitude behavior.

It is interesting to compare the amplitude dependence of the signals measured by the spectrum analyzer and the oscilloscope. The results for all the traces for this particular store are shown in Fig. 5. From the spectrum analyzer data we again clearly see the transition between the quadrupole and sextupole mode. It appears that the sextupole mode has a clear threshold of 3.2×10^{10} ppb while the quadrupole mode makes a slower transition in that region. In order to summarize the oscilloscope data we derived the amplitude information from the traces by simply taking the standard deviation of the whole trace (trace amplitude) and its envelope (burst amplitude). Although the oscilloscope data does not directly distinguish the two modes, the transition between them is clearly seen as the amplitude jump on the upper trace. The lower trace shows the region where instability is bursting. Note, that the thresholds seen from oscilloscope data slightly exceed the ones observed with the spectrum analyzer which can be attributed to better sensitivity of the latter. Still the agreement between the two plots in Fig. 5 is quite good.

Finally we should point out that the relative amplitudes of the quadrupole and sextupole modes seen from the spectrum analyzer or the oscilloscope data do not reflect the ratio of the quadrupole and sextupole components in the beam phase space. This is due to the fact that the amplitude of any instability sideband is not only pro-

portional to the corresponding moment of charge density but it also has a form factor that is slowly varying with frequency. These form factors are different for each azimuthal mode and usually have the highest peak at frequency of $m/(2\pi\sigma)$ where m=2,3 for quadrupole and sextupole modes respectively [6]. This is at least partially responsible for lower signal we observe for the sextupole mode that has the maximum response outside the bandwidth of the BPM pickup. One way to quantify what a particular signal means in terms of the changes to the beam phase space is to simultaneously employ a streak camera to show a variation of the beam profile with the instability signal [1].

4 DISCUSSION

Utilizing both frequency and time domain techniques we have developed a convenient way to characterize single bunch instability behavior.

It appears that some features of the data obtained e.g. frequency dependence on current or the quadrupole mode threshold can be explained in terms of conventional theory that is usually based on the linearized Vlasov equation. For example, in reference [7] simulations with a numerically obtained wake-function yielded values similar to those measured. However, some aspects of the measurement results clearly go beyond the linear theory. Those are 1) the fact that instability saturates, 2) occasional bursting behavior and 3) switching between the modes. There have been some theoretical models published [8-10] that could at least in principle lead to 1) and 2). It appears that item 3) is the most unusual. Indeed it is common to see more than one azimuthal mode go unstable as intensity increases. What is surprising is that the mode that first goes unstable becomes stable again. Furthermore, this stability switch happens near the intensity value at which the other mode becomes unstable. This suggests some mechanism of coupling between these azimuthal modes. On the other hand it is commonly thought that as long as frequency shifts are small compared to ν_s then different azimuthal modes are independent and instability can only arise as a result of other mechanisms e.g. radial mode coupling.

More theoretical work and computer simulations are required to understand this instability.

REFERENCES

[1] B. V. Podobedov, R. H. Siemann, Proc 1997 PAC, 1629 (1997).
[2] SLC Design Handbook, SLAC, (1984).
[3] K. Bane et al, Proc 1995 PAC, 3105 (1995).
[4] F.-J. Decker et al, Proc Linac 96, Geneva, 143 (1996).
[5] B. V. Podobedov, Ph.D. thesis, Stanford University (to be published).
[6] R.H. Siemann, AIP Conf. Proc. 184, 430 (1989).
[7] K. Bane, K. Oide, Proc 1995 PAC, 3112 (1995).
[8] R. Baartman, M.D'Yachkov, Proc 1995 PAC, 3119 (1995).
[9] S. Heifets, Phys. Rev. E, 54, 2889 (1996).
[10] G. Stupakov et al, Phys. Rev. E, 55, #5, (1997).

LHC ARC DIPOLE STATUS REPORT

C.Wyss, CERN, Geneva, Switzerland [#]

Abstract

The LHC, a 7 Tev proton collider presently under construction at CERN, requires 1232 superconducting (SC) dipole magnets, featuring a nominal field of 8.33 T inside a cold beam tube of 50 mm inner diameter and a magnetic length of 14.3 m.
To achieve such high fields whilst retaining the well-proven fabrication methods of cables made with NbTi superconductors, it is necessary to operate the magnets at 1.9 K in superfluid helium. For reasons of space and economy, the two dipole apertures are incorporated into a single iron yoke and cryostat (two-in-one concept). The design considerations and the experimental results, which have led to the design adopted for series manufacture, are presented and discussed. The aims and status of the short model and full size prototype dipole programmes are subsequently reported. Finally, the major milestones of the schedule of the dipole magnets series manufacture are given and commented.

1 DESIGN REQUIREMENTS

The LHC dipole design aims at a nominal field of 8.33 T and at an ultimate one of 9 T. The first training quench of each magnet should be above the first value and the second one be reached with limited training. After cold tests and installation, no retraining up to 9 T should occur. The field quality at injection (0.54 T) is critical for machine performance and should be as close as technically feasible to beam optics requirements, to minimise imperfections at their source and limit the size and complexity of corrector magnets schemes. The design must be suitable for series production by several contractors: this implies robustness with regard to mechanical tolerances in view of a simple, fast and reliable cold mass assembly, relative independence of assembly steps, a sufficient range for fine tuning of field quality without major tooling modifications. Last but not least, at the required performance the cost of components and labour is to be minimised.

2 DESIGN AND R&D WORK

The considerations which lead to the choice of the above field levels and basic magnet design can be found in the LHC Yellow Book (YB)[1]. The resulting dipole magnet main features are a twin-aperture structure, a margin of about 15% with regard to SC cables nominal short sample critical value reached at a dipole field of 9.65 T, an operating temperature of 1.9 K, an active protection system driving a fast quench propagation to the whole coils to avoid damages because of the high stored energy.

Further, at the injection field, the effects on field of the strand persistent currents [2] and their time decay drive the choice of the SC filaments diameter and impose a tight control on the characteristics of the SC strands. Field quality considerations require also to limit the effect of eddy current effects during field ramping, imposing to control the cables inter-strand resistance [3] to within some 10 μΩ around its design value. The main magnet parameters are given in table 1.

	Value	Unit
Inj. field (0.45 TeV beam energy)	0.54	T
Nom. field (7 TeV beam energy)	8.33	T
Nominal current	11'800	A
Operating temperature	1.9	K
Magnetic length at 1.9 K	14.300	m
Stored energy (both apertures) at 7 TeV	7.1	MJ
Ultimate operational field	9.00	T
Nominal short sample field limit	9.65	T
Distance between aperture axis at 1.9 K	194.00	mm
Bending radius at 1.9 K	2804	m
Aperture axis distance at 293 K	194.52	mm
Approx. bending radius at 293 K	2812	m
Inner coil diameter at 293 K	56.00	mm
Outer coil diameter at 293 K	118.60	mm
Conductor blocks / pole	6	
Turns / pole, inner layer	15	
Turns / pole, outer layer	25	
E.m. forces/coil quadrant at 8.3 T Hor. force (inner and outer layer) Vertical force (inner layer) Vertical force (outer layer)	1.7 -0.14 -0.60	MN/m MN/m MN/m
Axial electromagnetic force on both ends at nominal field	0.50	MN
Cold bore inner diameter at 293 K	50.00	mm
Cold bore outer diameter at 293 K	53.00	mm
Cold mass length at 293 K (active part)	15'180	mm
Cold mass diameter at 293 K	570.0	mm
Overall length with ancillaries	16.8	M
Cold mass weight	≈ 30	tonne

Table 1: Main parameters and characteristics of the LHC dipole magnet cold mass

The magnet structure shown in Fig. 1 is the result of concomitant design studies and experimental work. The design studies addressed topics like optimum coil cross-section, field quality tuning range and sensitivity of field

---

[#] Carlo.Wyss@cern.ch
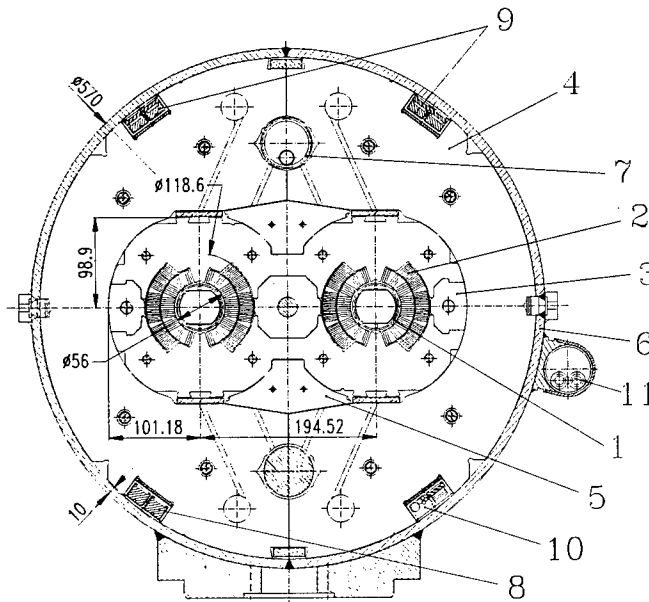
Figure 1: Series-manufacture cross-section of LHC dipoles. 1-beam tube; 2-SC coils; 3-austenitic steel collars; 4-iron yoke; 5-iron yoke "insert"; 6-shrinking cylinder / He II vessel; 7-heat exchanger tube; 8-dipole bus-bars; 9-arc quadrupole and "spool-pieces" bus-bars; 10-wires for magnet protection and instrumentation; 11-bus-bars for auxiliary magnets in the LHC arc short straight sections.

quality to the tolerances of coil components [4], stability at high field of the cold mass structure with respect to collar material and tolerances, yoke lamination tolerances, variations of coil pre-stress and shrinking cylinder stress [5, 6]. The experimental work comprised numerous 1-m long single aperture models, four 10-m long models of the YB design and one full size prototype, also of the YB design.

The aim of the ongoing 1-m model program [7] started in October 1995, is to assemble and test at CERN some 12 to 14 magnets per year, allowing to have fast answers on questions raised in design studies and/or experimental work. These questions include coil cross-section (5-and 6-blocks), SC cable characteristics, geometry and materials of coil components (e.g. end- and interlayer- spacers, quench heaters, cable and ground insulation, collar material), design of transition areas (e.g. inner layer "jump" and splice to the outer layer, transitions from straight to curved sections), optimum layer pre-stress level, manufacturing procedures (coil winding, layer curing and layer-end impregnation).

The 10-m, YB-design model program, initiated in 1996 and terminated in spring 1998, allowed to achieve several goals. The first was to continue to carry out coil winding and collaring in industry, so as to check tooling and manufacturing procedures in view of series production and foster know-how exchange with industry. The second was to assemble at CERN the collared coils into complete cold masses, gathering hands-on experience on issues like collared-coils and yoke interface, assembly procedures,

welding technologies and procedures, cold mass geometry, cold mass assembly into cryostats delivered by industry. The third was obviously to assess the performance of the YB design in view of series production.

The first 15-m prototype, also of the YB design, jointly funded by CERN and INFN (Italy), was initiated in spring 1995 and delivered by end 1997. It allowed to gain experience with the manufacture of full-length components, assembly of a complete cold mass and its cryostating in industry, transport to CERN of the cryostated prototype, and to assess its performance. A comprehensive summary of the results from the four 10-m models and the above prototype is given in ref. [8].

The main design choices resulting from the above activities are reported in the following.

2.1 Coil cross-section

A 6-block coil cross-section, optimised thanks to the recent availability of genetic algorithms [9] allowing to consider discrete and continuous parameters at the same time, is chosen [10]. With regard to the previous 5-block coil design, it features a wider tuning range, a more stable mechanical behaviour because of a more favourable geometry and distribution of electromagnetic forces, a
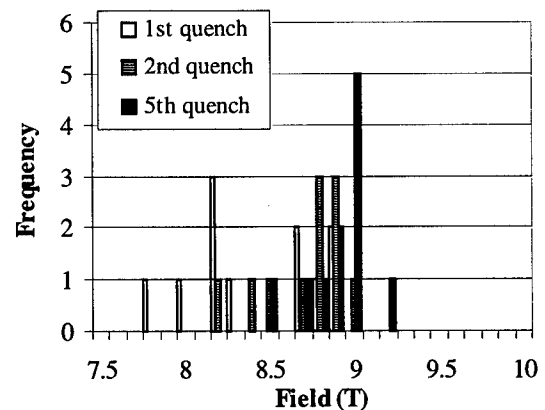
Figure 2: Quench levels in 1-m models with 5-block coil design
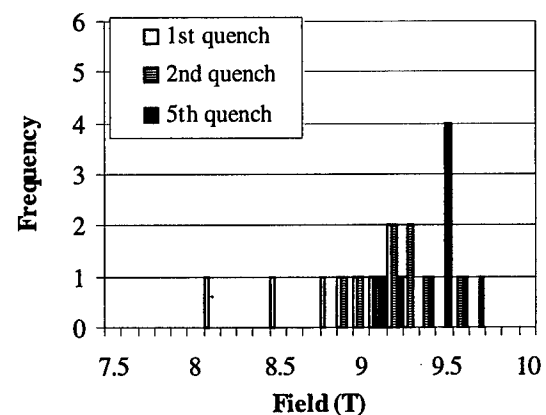
Figure 3: Quench levels in 1-m models with 6-block coil design

150

lower field at the inner layer turn which is submitted to the S-bend transition to the outer layer. The possible increase in winding time because of the additional wedge spacer in the inner layer is about compensated by the fact the 6-block design has one turn less in the outer layer. The training performance of 1-m long single-aperture models equipped with 5- and 6-block coils is shown in Figs. 2 and 3. It can be seen that the 6-block design consistently reaches a 0.5 T higher field than the 5-block one.

2.2 Collar-yoke "vertical" interface

The 10-m models and the prototype of the YB design feature a racetrack-shaped collar, containing an iron insert (needed for field quality reasons), fitted into the collar pairs prior to the assembly of the collar packs.
Experience has shown that small variations in the fitting of the soft iron insert and its possible plastic deformation during collaring lead to irreversible changes of the vertical dimensions of the collared coils. The achievement of the design value of these dimensions is critical, as they control the interference, necessary up to the highest field, between the yoke and the collared coil. This interference is essential for the stiffness of the cold mass structure and hence for the mechanical stability of the coil, particularly if alloyed aluminium (AA) is chosen as collar material. It was therefore decided to make the insert independent of the collars and shape it so as to provide inclined boundaries between collars and yoke (see Fig. 1). This geometry of the collar-insert-yoke interface, already used in a highly successful short twin-aperture model [11], leads to an increase by a factor 3 of the contact forces between collared coil and yoke.

2.3 Layer pre-stress and choice of collar material

Several short models were devoted to the study of the influence of coil pre-stress on training behaviour. These studies have shown that for the LHC dipoles, nominal pre-stresses of 30 MPa and 40 MPa at 1.9 K for the inner and outer layer, respectively, allow to reach field levels in excess of 9 T within a few quenches, and eventually field levels of up 10 T after 15 quenches. Pre-stress values some 10 MPa lower than the above may lead to an erratic training behaviour above 9 T, while values higher by 10-20 MPa may lead to slower training and lower final field levels. A few more short models will be assembled to complete the definition of the admissible pre-stress window. The above values of nominal pre-stress lead to an unloading of the inner and outer layer at about 8.4 T and 9 T, respectively. They are comfortably lower than the 50 to 60 MPa which were sought in previous work, where it was considered important to maintain some 10 MPa pre-stress up to field levels above 9 T. A lower collaring force and hence a lower collar deformation after collaring are thus possible, easing at the same time the collaring operation and the matching of collar and yoke geometries throughout magnet assembly, cool down and operation. Moreover, and most important, the above

values of nominal pre-stress allow to consider austenitic steel as collar material. Because of the lower integrated thermal contraction coefficient of austenitic steel (AS) with respect to that of alumimium, the letter being close to that of the SC coil layers, the loss of coil pre-stress during cold mass cool-down from 290 to 1.9 K is of 10-15 MPa and about 30 MPa for AA and AS collars, respectively. Coil prestresses at room temperature higher than 80 MPa lead to creep of the polyimide SC cable insulation and are therefore to be avoided, thus limiting for AS collars the maximum design layer prestress at 1.9 K at 40-45 MPa, values which turned out to be compatible with a satisfactory training performance. The possibility to consider AS for the collar material has far reaching consequences on the design and assembly of the cold mass structure, as shown later.

2.4 Structure behaviour with regard to components and assembly tolerances

Considering that series manufacture is likely to take place at three different sites at an expected rate of some 20 cold masses per month, in two-shift work, design simplicity and robustness are considered to be of highest importance in view of minimising labour cost and maximising the likelihood that each magnet be well within the specified requirements.
In a first phase, the impact of the dimensional tolerances of collars, laminations and collared coil on the distribution of forces between collared coils and yoke, and hence on structural stability, was studied by means of F.E computations. The component tolerances lead to variations of the nominal gap/interference, before longitudinal welding the shrinking cylinder half-shells, between yoke halves and between collared coils and yoke. The width of latter gaps was scanned, one at a time, in steps of 0.05 mm. Three designs were considered at this stage: combined AA collars and combined AS collars of identical geometry, and separated AS collars optimised for minimum material usage. It was thus shown that the collar material plays a major role: the higher E-modulus and lower thermal expansion coefficient of AS with respect to AA collars entail smaller displacements and deformations. Whilst maintaining positive contact forces among collared coils and yoke up to ultimate field, combined and separated AS collars designs allow for tolerances of about ±0.2 mm and ±0.3 mm for the fitting of the collars and laminations transmitting horizontal and vertical forces, respectively. Combined AA collars allow for ± 0.1 mm only in both directions. These values are to be compared with the ± 0.1 mm obtained when summing up the nominal tolerances (not achieved in the 10-m long models) on collars, laminations and their assemblies.
Computations showed that the choice of separated AS collars would not bring decisive advantages over AS combined ones, in terms of field level and quality. Moreover, a complete new qualification and tooling programme with its inherent costs and time schedule would be necessary to assess in detail such a major design

change. It was therefore chosen not to depart from the combined collar design. Strong AS-combined collars, with the same geometry of the AA ones, entail only minor changes to existing tooling and drawings. Moreover, they minimise the coupling between collared coils and cold mass assembly, so as to make field quality and cold mass behaviour only weakly dependent on assembly history, which is a positive feature for a large series production.

In a second phase, the widths of the horizontal gaps between yoke halves, above (upper gap) and below (inner gap) the heat exchanger tube were varied simultaneously. These widths were determined by assuming a linear sum of components ($3\sigma = 0.02$ mm) and assembly ($3\sigma = 0.05$ mm) design tolerances.

Statistical draws from data provided by a deterministic multidimensional F.E. model, showed (see Fig. 4) that for AA collar the 1σ width of the tolerance of the above gaps must be < 0.05 mm (instead of 0.1 mm for AS collars) in order to guarantee (probability $P = 1$ in the above figure) a positive mating force between yoke halves at high field, i.e. prevent an opening of the yoke and subsequent mechanical instabilities of the collared coil.

Finally, the influence of actual tolerances, as observed in 10-m models, of 11 main parameters (various dimensions of collars, inserts, laminations, coils, and stress in the shrinking cylinder) to be controlled in the cold mass assembly, were evaluated by a Monte Carlo analysis of the F.E. model of the cold mass. The outcome of this work is summarised in Fig. 5, which shows the probabilistic distribution of the mating force at nominal field at the "inner" yoke gap. For AA collars, for about 25% of the magnets this force is likely to be non-existent and its average value is 230 N per mm of magnet length. For AS collars, the mating force is always present and its average value is about four times higher.

Moreover, because of relative differences of the thermal expansion coefficients of collared coils and yoke, AA collars require, after assembly at room temperature, an horizontal gap of about 0.5 ± 0.05 mm between yoke halves. This in order not to damage the coils by overstressing them and to obtain then at 1.9 K the required contact forces between collars and yoke in the horizontal plane. Experience has shown that this gap is difficult to measure and control.

By choosing AS collars, the yoke halves can be made to mate (no gap) already after assembly at room temperature, making the cold mass to behave as a continuous, stiff structure throughout thermal and excitation cycles. Considering all the above, austenitic steel was chosen as collar material for series manufacture.

2.5 Field quality, analysis and control

Further to the field quality characteristics of the YB 10-m models and prototype reported in ref. [8], the study made in ref [12] gives insight on the links between field quality and coil geometry in the YB long models. Methods to ease field quality analysis in view of its reliable fine tuning during series productions are being investigated [13].
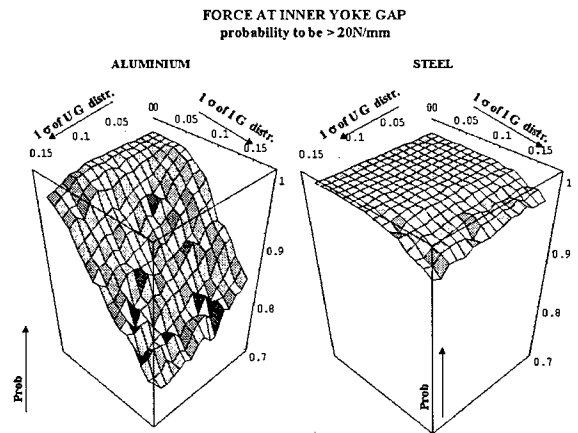
Figure 4: Estimated probability of conformity of the forces along the inner gap in function of the tolerances of dimensions (mm) of the upper (UG) and inner gap (IG)
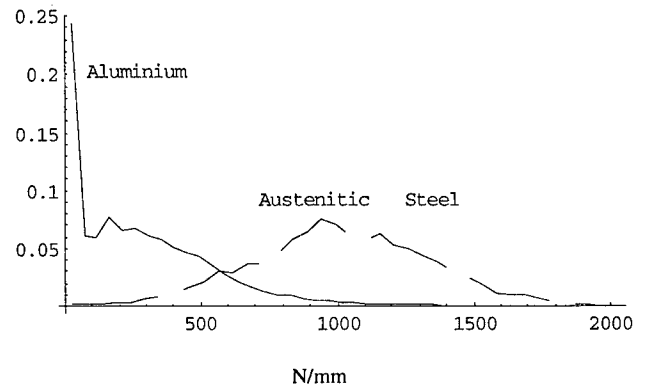
Figure 5: Probability distribution of the force (at 8.33 T) along the inner gap, following Monte Carlo analysis

3 NEXT PROTOTYPES

CERN has launched in summer 98 the manufacture by industry of 3 x 2 full-length prototype collared coils, featuring 6-block coil cross-section, inclined interface between collars and yoke, AS collars (but for the first of them, which still has AA collars for reasons of component availability). These collared coils are assembled into cold masses at CERN; the first of them (called MBP2N1) was completed on 21 February 1999. Its geometry is within the expected values of imposed horizontal sagitta and natural vertical deflection (see Figs. 6 and 7), apart for the ends, where improvements of the procedure for welding the beam pipe to the cold mass end-covers are being studied. A second prototype, MBP2N2, equipped with AS collars, will be assembled as from end April and tested this July. Two of the four remaining prototypes will be tested in autumn 99 and the two last one in February and March 2000.
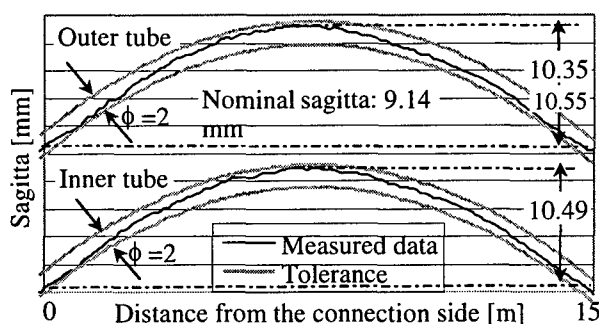
Figure 6: MBP2N1 prototype: horizontal sagitta of the beam tubes axis
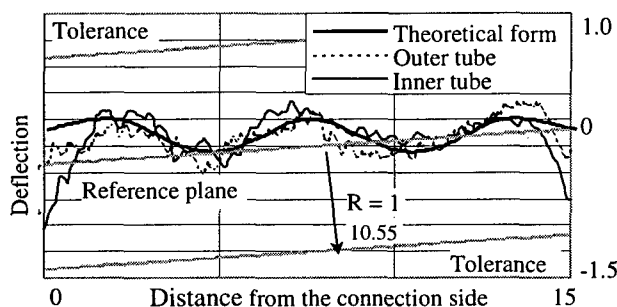
Figure 7: MBP2N1 prototype: deflection in the vertical plane of the beam tubes axis

4 TOWARDS SERIES PRODUCTION

4.1 Procurement of SC cables

Invitation to tenders were issued in August 1997 for the supply of NbTi bars and Nb sheet (funded by the U.S.A. contribution to the LHC project) and that of a total of 6840 km of SC cables, of two different types. The arc dipoles use about 2370 km of "Cable 1" for the inner layer and about 3740 km of "Cable 2" for the outer layer, while the arc quadrupoles use only "Cable 2". The corresponding contracts were placed in the course of 1998. The deliveries of the raw materials (by now about 15 tonnes) by one US firm started in autumn 1998. The supply of Cable 1 was entrusted to two European firms, that of Cable 2 also to two European firms for a total of 3320 km and one US and one Japanese firm, each for a length of 575 km. The SC strand pilot production is starting, by the end of 1999 a pilot cable production corresponding to 1% of the European supplies is expected. The cable supply is scheduled to finish by end 2004. A new test facility for the reception tests of SC strands and cables [14] is being set-up at CERN, it will be operational in the next months.

4.2 Procurement of cold masses

A call for tender for the supply of a total of 468 cold masses for three LHC octants was issued on 17 December 1998. The bids will be in by 31 March 1999. It is expected to present the adjudication proposals to the CERN Finance Committee in June 1999. It is likely that three different contractors be retained; under best conditions, the first cold masses are expected in the first months of the year 2000. During the first 2 years, the cold mass contracts will be carried out under a cost reimbursement (with ceiling) and fixed benefit scheme. The contractors will subsequently be asked by spring 2001 to bid fixed prices for up to four octants, including the octant already being manufactured. Present planning foresees the end of the cold mass deliveries by early 2005.

5 CONCLUSION

The R & D program for the LHC dipole magnets is approaching its completion, the design chosen for series manufacture is being validated this year with a set of six full-length prototypes. Industrial production of SC cable has begun, that of dipole cold masses is expected to start by autumn 1999.

6 ACKNOWLEDGMENTS

The work described here is the result of the ingenuity, professional competence, enthusiasm, untiring efforts of a large number of colleagues in the LHC and EST divisions, and of the firm and inspiring support of L. Evans.

7 REFERENCES

[1] The Large Hadron Collider CERN/AC/95-05(LHC), October 1995

[2] S. Le Naour et al, "Magnetization measurements on LHC superconducting strands", ASC'98, Palm Spring, September 1998

[3] D. Richter, J.D. Adam, D. Leroy, L. Oberli, "Strand coating for the superconducting cables of the LHC main magnets", ASC'98, Palm Spring, September 1998

[4] S. Russenschuck, "Comparative study of different coils for the LHC main dipoles", LHC Project Report 159, December 1997

[5] D. Perini, R. Vuillermet, C. Wyss, "Comparative study of different designs of the mechanical structure of the LHC main dipoles", LHC Report, to be published

[6] P. Fessia, D. Perini, "Statistical evaluation of the behaviour of the mechanical structure of the LHC main dipoles depending on collar material", LHC Report, to be published

[7] N. Andreev et al, "State of the short model program for the LHC", EPAC'98, Stockholm, June 1998

[8] J. Billan et al, "Test results on the long models and full scale prototype of the second generation LHC arc dipoles", ASC'98, Palm Spring, September 1998

[9] S. Ramberger, S. Russenschuck, "Genetic algorithms for the optimal design of superconducting accelerator magnets", EPAC'98, Stockholm, June 1998

[10] N. Andreev et al, "Performance of five and six block coil geometries in short superconducting dipole models for the LHC", this Conference

[11] D. Leroy, L. Oberli, D. Perini, A. Siemko, G. Spigo, "Design features and performance of a 10 T twin aperture model dipole for LHC", MT'15, Beijing, October 1997

[12] O. Pagano, W. Scandale, E. Todesco, "Field-shape variation induced by thermal cycling and excitation in the LHC dipole", this Conference.

[13] P. Ferracin, W. Scandale, E. Todesco, P. Tropea, "A method to evaluate the field-shape multipoles induced by coil deformations", this Conference.

[14] A. Verweij, J. Genest, A. Knezovic, D.F. Leroy, J.P. Marzolf, L.R. Oberli, "1.9 K test facility for the reception of the superconducting cables for the LHC", ASC'98, Palm Spring, September 1998

PERFORMANCE OF FIVE AND SIX BLOCK COIL GEOMETRIES IN SHORT SUPERCONDUCTING DIPOLE MODELS FOR THE LHC

N.Andreev, K.Artoos, L.Bottura, F.Rodriguez-Mateos, S.Russenschuck, N.Siegel, A.Siemko, F.Sonnemann, D.Tommasini, I.Vanenkov CERN, Geneva, Switzerland

Abstract

A series of similar one meter long superconducting dipole models for the LHC is being manufactured and tested since 1995 for exploring design variants and assembly parameters. Until the end of 1997 all magnets of this series were based on a coil geometry subdividing the conductors in five distinctive winding blocks. In order to cope with new requirements of magnetic field distribution and coil design flexibility, one additional block has been added in the beginning of 1998.

A significant number of models of both types have been built and tested, some of them re-built in a different version, adding up in more than 40 models tested so far.

The paper reviews the performance of these two different coil designs in terms of manufacture, training behaviour and temperature margins as well as mechanical behaviour and magnetic field quality.

1 THE MODELS

The regular CERN in-house model program for the development of the LHC dipoles was started in 1995 with the fabrication of 1m-long single-aperture magnets, so-called MBSMS. The design of the MBSMS models, presented in previous conference papers [1] [2], is based on circular collars of 197 mm outer diameter placed inside a vertically split yoke, held together by a bolted shrinking cylinder for easy re-assembly of the structure.

2 COIL GEOMETRY:DESIGN FEATURES

The LHC dipole coils consist of two superposed layers, an internal layer and an external one. Each layer is subdivided in blocks of conductors separated by copper spacers. The two coil geometries tested on the models are shown in Fig.1 below.
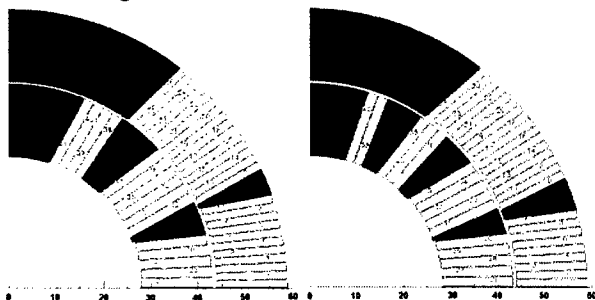
Fig. 1a : 5-block geometry   Fig. 1b : 6-block geometry

The first 13 magnets have been built with the 5-block version of the Yellow Book [3], consisting in 3 blocks of conductors in the inner layer and two in the outer layer (fig.1a). As from MBSMS15, the coil design has undergone a substantial evolution, being replaced by a 6-block one, consisting in four blocks of conductors in the inner layer and two in the outer layer (fig.1b). The last 6 magnets have been built according to this 6-block geometry.

2.1 Magnetic design

The original 5-block coil cross-section was optimized using deterministic techniques with the CERN program ROXIE [4]. First a preliminary geometric modelling was done with a given choice on cable dimensions and conductor blocks, thereafter the model was iterated to find an acceptable solution for field quality and peak field/main field ratio. This coil design however did not ensure sufficient tunability and flexibility for later field adjustments like compensating the persistent current multipoles at injection and fine-tuning of field quality. In particular a further compensation of the b3 term, if required, would have been impossible because the copper wedges would become too small at the inner edge. Moreover the performance of the magnets with 5-block coils and laboratory tests indicate that the stress distribution in the inner block of the inner layer is not favourable. With the implementation of genetic algorithms in ROXIE in 1997 [5] it was possible to make an extended the search for more appropriate designs considering all the constraints learned with the short model program based on 5 blocks. The study gave two alternative designs based on 6-block coils, all having similar field quality and quench margin, however with a different number of turns and coil-block layouts. The final choice of the geometry was based on mechanical considerations (see paragraph 2.2) and sensitivity to manufacturing tolerances [6]. Table 1 shows the optimized parameters of five and six-block geometries.

In the 6-block version the number of turns decreased by one (i.e. 40 per pole), but the margin to short sample limit increases by 0.11T, which is explained by the lower ratio of peak field to central field. Further, geometric multipoles were systematically introduced to partially compensate the persistent current effect at injection field level to ease correction scheme requirements.

154

Table 1: Design parameters of single aperture 5 and 6 block

	5 block	6 block
Turns inner layer	15	15
Turns outer layer	26	25
%load line (inner layer)	86.5	85.64
%load line (outer layer)	82.5	84.92
Peak/main field inner	1.05	1.03
Peak/main field outer	0.87	0.89
Current @ 8.36T	11.5 kA	11.8 kA
Maximum central field	9.65 T	9.76 T
Force parallel to cable broad side inner layer	34kN/m	17kN/m
b_3 geometric @ 17 mm	+ 0.3	+ 4.1
b_3 geo + pers @ 17 mm	−11.8	− 6.5

Finally the electromagnetic force parallel to the broad face of the cable has been considerably reduced.

The first two turns of the inner layer are now aligned parallel to the field direction, reducing considerably the shear stress to which they are submitted during excitation.

2.2 Radial supporting of inner layer.

In addition to a lower radial electromagnetic force on the first turns of the inner layer, the 6-block geometry provides a better radial support of these turns. This can be seen in fig 2a and 2b which show the measured distribution of radial pressure of a 5-block inner layer and a 6-block inner layer.
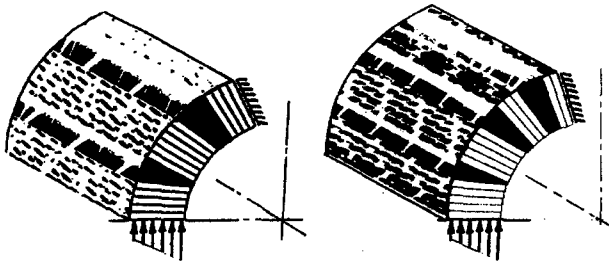
Fig. 2a : 5 blocks   Fig. 2b : 6 blocks

The imprint was obtained with a pressure sensitive tape inserted between the inner layer coil and a mould compressing the coil in the azimuthal direction with a pressure of about 50MPa. The first upper turns of the five block coil in fig. 2a are not in good radial contact with the mould, whilst the six block geometry in fig. 2b provides a more uniform radial support to all the conductors.

3 CONSTRUCTIONAL VARIANTS

Variants explored through the model fabrication concern cable types, material of collars and coil pre-stress.

3.1 Cable types.

One 5-block magnet and all 6-block are made with the 15.1mm wide cable corresponding to the present LHC specification, which is slightly less compacted and with

more rounded corners compared to the previous 15.0mm wide cable used for all other 5-block magnets [2].

3.2 Material of collars.

The MBSMS base design relied on aluminium collars, of similar rigidity as those of the twin aperture dipoles. Later, a number of magnets have been collared with austenitic steel collars, which is the present baseline for the LHC dipoles. In general, the use of austenitic steel improves the training behaviour of 5-block coils [2], but this effect is not noticeable in the 6-block coils which appear to have a more stable structure.

3.3 Coil pre-stress.

The coil stress of inner and outer layers has been measured on all models with specially developed strain gauge transducers and capacitive pressure transducers [7][8]. In terms of coil pre-stress the models made so far can be divided into two groups: one of high pre-stress in which coils are compressed by the collars up to the maximum excitation fields and the other of lower pre-stress in which the inner layer unloads from the collars before the magnet reaches 9T. To the first group belong most of 5-block magnets, and to the second group most of the 6-block magnets. Cold tests have shown that magnets of the second group have higher initial quenching fields than magnets of the first group. This effect appears to be less important for 6-block magnets. For simplicity the data presented later will not be grouped by coil pre-stress.

4 PERFORMANCE

The advantages foreseen for the 6-block coil geometry versus 5-block appear especially for the training behaviour. The dynamic behaviour and magnet protection are similar for both designs and linked to cable properties.

4.1 Training.

The 6-block magnets, both with aluminium and austenitic steel collars, show better performance compared to 5-block magnets. Fig. 3 shows the average quenching field of the 5 and 6-block magnets built so far, without distinction between collar material.
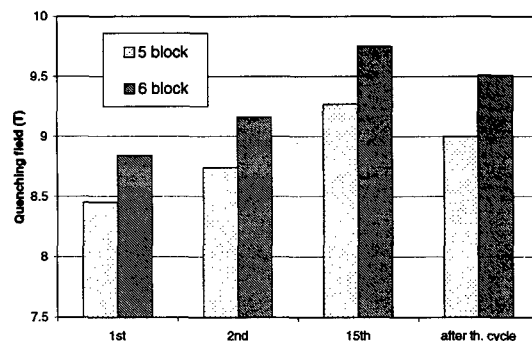
Fig.3 : average quenching field of 5 and 6-block magnets
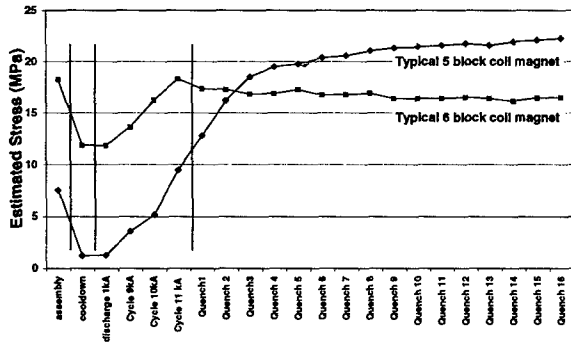
Fig.4: radial pressure between collars and inner layer conductors.

Six-block magnets allow to gain in average about 0.5T in terms of quench performance. One possible reason for this better performance of 6-block can be found in a more stable radial support of the conductors of the inner layer close to the collar pole as suggested from the test in fig. 2. This effect is confirmed by the smaller variation of the radial pressure between the collars and the first turns of the inner layer measured at zero current during the cool-down and the training tests (fig.4).

4.2 Magnetic field.

The six block geometry, having one more block of conductors in the inner layer, allows more freedom for possible adjustements of the high order field harmonics. However, in terms of sensitivity of magnetic field quality to manufacturing tolerances (in particular final coil size after collaring), the two coil geometries are identical. In table2 are shown the change of geometric field harmonics for an increase of 0.1mm in the inner layer coil size after collaring, extrapolated from measurements on 13 five-block magnets and 11 six-block magnets. Concerning the outer layer, in both cases its size has an important effect only on b3, of about 1.3 units per 0.1mm.

Table 2: Change of geometric field harmonics (units 10-4 at a reference radius of 17mm) versus a change of 0.10mm in the inner layer size,measured data.

	b3	b5	b7	b9
5 block magnets	-1.7	+0.4	-0.1	0.05
6 block magnets	-1.6	+0.4	-0.2	*

*range of b₉ for all magnets between 0.02 and 0.10 units.

Finally, the measured non allowed multipoles were similar in both cases, showing that the introduction of one more spacer does not affect the quality of assembly.

4.3 Magnet protection.

In terms of magnet protection no substantial difference was observed between 5 and 6-block design. The hot spot temperatures (fig.5) at 9T range from 200K to 270K and depend in both cases on cable parameters like RRR and Cu/Sc ratio [9].
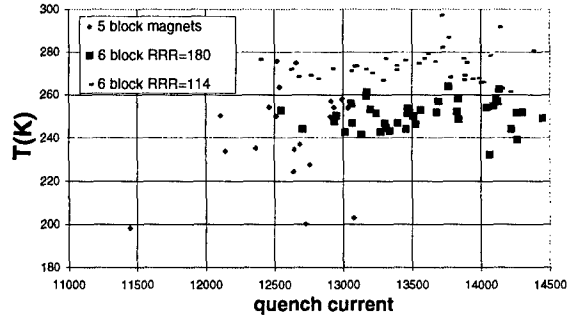
Fig. 5: hot spot temperature for 5 and 6-block magnets

Finally, at nominal current, the time between firing the quench heaters and start of quench (heater delay) was the same for 5 and 6-block magnet (about 50ms).

5 CONCLUSIONS

The advantages foreseen for the 6-block coil cross section of the LHC main superconducting dipoles have been confirmed experimentally on short models. The 6-block geometry has proven to be better performing than the 5-block in terms of mechanical stability of the conductor blocks and of quench behaviour. Concerning magnetic field reproducibility and sensitivity to coil size tolerances the two coil geometries are equivalent. Finally magnet protection parameters are very similar for the two designs, and are dominated by the cable characteristics.

6 ACKNOWLEDGEMENTS

The authors would like to thank C.Wyss and L.Evans for their support to the short dipole model program, and all the teams involved in magnet fabrication and testing.

7 REFERENCES

[1] N.Andreev et al, "The one meter long single aperture dipole coil test program for LHC", proc. of the 5th EPAC, Sitges, Spain, 10-14 June 1996.

[2] N.Andreev et al, "State of the short dipole model program for the LHC", Proc. VI European Particle Accelerator Conference,Stockholm, June 1998.

[3] "The Large Hadron Collider - Conceptual Design" CERN/AC/95-05, October 1995.

[4] S. Russenschuck et. al.: "Integrated Design of Superconducting Accelerator Magnets - A case study of the main quadrupole, The European Physical Journal, Applied Physics, 1, 1998.

[5] S. Ramberger, S. Russenschuck: Genetic algorithms for the optimal design of superconducting accelerator magnets, EPAC 98, Stockholm, Sweden.

[6] S.Russenschuck :"Comparative study of different coils for the LHC main dipoles", LHC Project Report 159, December 1997.

[7] I.Vanenkov et al."Mechanical performance of a twin aperture 56mm bore 1m long dipole model made with SSC type cables", MT-14, June 1995.

[8] N.Siegel, D.Tommasini,I.Vanenkov"Design and use of capacitive force transducers for superconducting magnet models for the LHC", MT-15, 1997.

[9] F.Sonnemann, et al. "Quench process and protection of LHC Dipole Magnets", LHC Project Note, 1999.

INSERTION DEVICES FOR 4TH GENERATION LIGHT SOURCES

J. Pflüger,
Hamburger Synchrotronstrahlungslabor HASYLAB
at Deutsches Elektronen-Synchrotron DESY
Notkestr85, 22603 Hamburg, Germany

Abstract

The next generation of light sources will consist of Free Electron Lasers (FEL's) using the principle of Self Amplified Spontaneous Emission (SASE).
They will be driven by Linacs using low emittance photocathodes. Transverse RMS beam sizes are typically 20 - 50 μm and the bunch lengths are of the same magnitude. Worldwide several projects are under construction or in a design phase to cover the whole spectral range down to 0.1 nm. Very long undulators are needed for SASE FELs in order to reach saturation.. Their lengths may easily reach 100m for the X-ray FEL's. In order to minimize the total length and maximize output power they must meet two criteria: First, tough magnetic specifications must be fulfilled in order to have optimum overlap between electron and laser beam. Second, additional external strong focusing is required in order to keep the electron beam size small over the whole undulator length. In this contribution problems related with the design of very long undulators will be addressed. Alternative ways of providing the strong focusing are outlined and special attention is given to the magnetic design of undulators with integrated strong focusing. As an example the work done at the undulator under construction for the FEL at the TESLA Test Facility in Hamburg is presented.

1 INTRODUCTION

At the begin of the 1980 's the principle of Self Amplified Spontaneous Emission (SASE) has been discovered.[1,2] In contrast to conventional FEL's a SASE FEL completely avoids the use of reflecting mirrors. With the development of low emittance RF photo guns during the past ten years SASE FEL's down to a wavelength of 0.1 nm now become technically feasible. It is now widely accepted that SASE FEL's will represent the next, the 4th generation of light sources. [3]

Several projects in the VUV region are under construction at DESY, Hamburg [4], APS, Argonne [5] and NSLS, Brookhaven [6]. Two more have been proposed in the X-ray regime : The Linear Coherent Light Source (LCLS) at Stanford [7] and the X-ray FEL at TESLA in Hamburg [8]
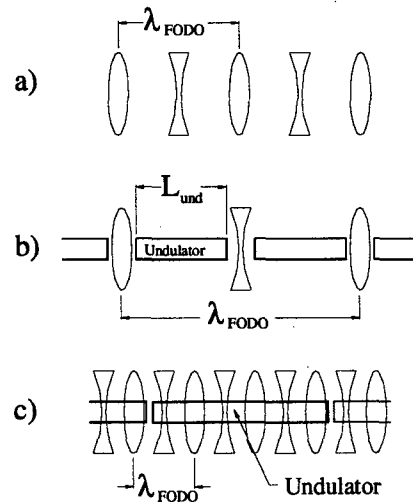
Fig 1 a) FODO Lattice schematic
   b) Separated function undulator:
   c) Combined function undulator

2 UNDULATORS FOR SASE FEL's

In contrast to Undulators for conventional Sychrotron Radiation (SR) Sources. those for SASE FEL's have to be much longer. Their length may easily reach 100m for X-ray FEL's [7,8]. Additional focusing is required in order to keep the transverse beam dimensions within a well specified variation. Most commonly a sequences of focusing and defocusing quadrupoles a so called FODO lattice is used for this purpose. This is sketched in Fig 1 a-c). Fig. 1a) shows the quad sequence of a conventional FODO lattice. It is characterized by the so called FODO cell length λ_{FODO}. The β function in a FODO lattice varies between a minimum and a maximum value which can be calculated in the thin lens approximation as :

$$\beta_{Max,Min} = 2 \cdot f \pm \lambda_{FODO} / 2 \quad ; \quad \frac{1}{f} = c \cdot e \cdot L_Q \cdot \frac{g}{E} \quad (1)$$

Here f is the focal length of the quads of length L_Q, g is the field gradient, E the kinetic energy, c the velocity of light and e the elementary charge. In order to combine a FODO lattice as sketched in Fig 1 a) with an undulator

two possibilities exist: FODO lattice and undulator may be separated, Fig. 1 b) or combined., Fig 1 c). Separated function, Fig 1 b), means that the undulator is interrupted for the quadrupoles. Therefore focusing sections and undulator modules alternate. A minimum FODO cell length of about 3.6 m seems possible assuming 1.5m for a minimum undulator length and 0.3m for the quads. For shorter cell lengths the undulators become too short and the interruptions too long. Smaller cell lengths can be realized if a combined function undulator , Fig 1 c) is considered. It utilizes a magnetic design which combines the generation of the periodic undulator field with a strong focusing quadrupole field. The advantage is now that λ_{FODO} can take very small values well below 1m and interruptions of the undulator structure are not needed at all. The undulator may even be built seamless. The price is a more sophisticated magnetic design which is considerably more complicated to implement..

For a FEL with its set of specific parameters there is a optimum β function which determines what kind of design is to be used in the undulator region. The average β function is given by the strength of the quads only, but its variation is given by $\lambda_{FODO} / 2$. The tolerable variation also called beat therefore determines the required FODO cell length. An optimum value cannot be given analytically and can only be found using numerical simulation codes. There is a trade off between other critical FEL parameters such as peak current, bunch length and beam emittance. Codes such as TDA-3D can be used to find the optimum β function as well as the influence of the β beat. As a rough rule of thumb VUV FEL's with electron beam energies in the 1 GeV range need low β values in the order of a very few meters as compared the X ray FEL's with beam energies up to 25 GeV which require β values well above 10m, The tolerable β beat may exceed 50% of its average value or even more

At energies well below 1 GeV the weak natural focusing of an undulator in the vertical plane together with horizontally focusing quads in the intersections can be used. This way has been chosen for the LEUTL project [7]. In the vertical plane therefore the focusing is similar to that of a FODO lattice, where the focusing is done by the undulator which can be considered as a thick distributed lens. The defocusing is done by the quads in between the undulators. Since in the horizontal plane the undulator acts like a drift space only a sequence of focusing quads is effective in this direction. This focusing scheme resembles the separated function approach but at comparable β beat allows for about twice the uninterrupted undulator length.

3 ALIGNMENT TOLERANCES

The closed overlap between the electron and laser beam is essential for the SASE process to take place. As an empirical rule from many simulations it has turned out that an overlap degradation which does not exceed about 20% of the RMS beam size is still tolerable and does not

deteriorate the SASE process too much. In this context it is irrelevant if the overlap is disturbed by field errors in the undulator or by misalignment of quadrupoles. Consequently this imposes tough requirements on the second field integral of the undulator field, i. e. the beam excursion as well as on the alignment of the quadrupoles of the FODO lattice.

For example the energy of the Phase I TTF FEL is 300MeV, the transverse beam size is about 60μm. The tolerance on the second field integral in this case is only 12 Tmm^2. A similar argument holds for quadrupole alignment errors. Although a number of correctors should be planned in the undulator section the requirements are still a challenge for insertion device technology as well as for magnetic measurement techniques.

Separated function means that the quads are independent of the undulators. They can be electromagnets. So correctors are straight forward to implement in the coils Quad alignment is now decoupled from the undulator Beam based alignment methods like those developed for the final focus test beam in linear colliders can be applied [9,10]. Besides of different magnetic specifications the undulator in this case has no fundamental difference to those used as light sources in storage rings.

Combined function means that undulator and quadrupoles become one entity and the field of both are superimposed. This can be achieved in two different ways. A straight forward approach is to build a pure permanent magnet structure without iron parts inside a quadrupole, with a bore diameter quite of about 100mm or more. This approach was presented in an early LCLS proposal is now used for the VISA experiment [6]. Alternatively new magnetic designs like the one described below can be found which combine the generation of the undulator and of the quadrupole field in one structure. Here tolerance requirements mix. Correctors maybe limited in strength and difficult to apply due to space limitations. This imposes more stringent tolerances on the alignment and strength of the quads. Moreover new and appropriate measurement techniques are needed to measure the quad properties in the presence of the superimposed undulator field. Beam based alignment techniques have also been developed for combined function permanent magnet undulators which in this case requires the variation of electron beam energy [11-13].

4 COMBINED FUNCTION UNDULATOR

In literature there are several proposals to combine the generation of the undulator field with a strong field gradient.. An overview is given in [13,14]. As one of the first projects of its kind the combined function undulator under construction for the FEL at the TESLA Test Facility will be described in more detail.

The small β-function of only 3m, which is needed to optimize the FEL process was a basic input for the design consideration so that there was no alternative to a combined function undulator at all. Many design

proposals found in literature were found inappropriate because they either limit or even block completely the accessibility of the gap region thus making precise magnetic measurements as well as the installation of the vacuum system after magnetic measurements very problematic. Furthermore since the focusing sections were integral parts of the undulator there was no fine tunability neither of the strength nor of the exact location of the quadrupole axis. In contrast the design proposal for the undulator for the VUV-FEL, which was given the name Four Magnet focusing Undulator (4MFU) combines the following properties :

1. It is a completely planar structure, which allows for very good access to the field region at the beam position. This is important for high accuracy field measurements but also for inserting the vacuum chamber without breaking magnetic circuits.

2. The gradient can be as large as 17 T/m. The exact value and the position of the quadrupole axis is fine tunable.

3. Undulator and focusing fields are decoupled. This means that on the quadrupole axis the sign and magnitude of the field gradient has no influence on the undulator field and vice versa.

A detailed description may be found in ref [14-17]. Here it is only briefly described and illustrated in Fig 2 : Permanent magnet (PM) technology using state of the art
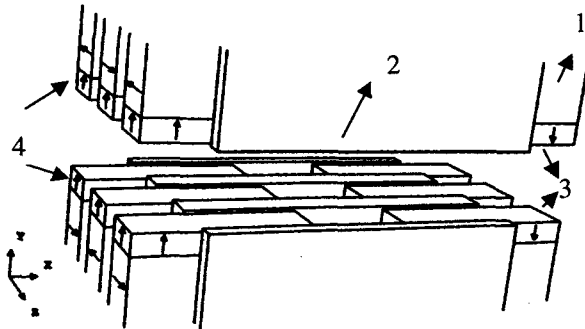
Fig. 2: The Four Magnet Focusing Undulator (4MFU) as an example for a combined function undulator .

1 : Magnets for the undulator field
2 : Poles
3, 4 focusing magnet arrays magnetized parallel antiparallel to the Y-axis

NdFeB magnet material has been chosen for the undulator. Fig 2 shows a schematic 3-D view of 1 ½ periods of the (4MFU) which has been proposed to be used for the FEL at the TTF. It is based on a regular Halbach type hybrid structure [18], consisting of the magnets creating the undulator field (1) and the poles conducting the flux (2). The gap between the poles is kept fixed at 12mm. There is no gap tunability.

In the 2.5mm recess between these magnet and the poles the focusing magnets arrays (3), (4) are placed. They are magnetized parallel / antiparallel to the Y-axis as can be seen in Fig. 2. Each of the four magnet arrays can be adjusted individually in the horizontal direction. This gives the required adjustabilty of the gradient as well as of the position horizontal and vertical quad center This is described in detail in ref. [19].

5 MAGNETIC OPTIMIZATION

Trajectory control in both transverse directions in very long undulators is a crucial problem.. In a long fixed gap device this problem can be solved in a straight forward manner. For the undulator for the TTF it is subdivided into the following steps:

1. At first the "naked" undulator in both transverse directions is optimized and error corrected. "Naked" means that there are no focusing magnets attached yet. The horizontal error field is measured using a suitable coil and integrator technique. The vertical B_y component is measured using a Hallprobe.

2. In the second step, the focusing magnet arrays are attached to the optimized undulator and the axes of the quadrupoles are aligned using the techniques described below.

Precise magnetic measurements are the basis for the verification of the specified values. Without the focusing magnets the undulator is just like any hybrid undulator. The only difference is the larger pole overhang of 2.5mm at the gap side. It has become state of the art to assemble hybrid undulators. Each magnet is individually measured characterized. The assembly of the magnet structure is made on the basis of these data. The method of "Simulated Annealing" was used to find a magnet configuration which minimizes field errors [20].

The horizontal field is measured using a 3x5x10 mm coil with about 3500 windings working in conjunction with an analog integrator. The method has been developed previously [21] and was further improved in sensitivity so that the second horizontal field integral of a 4.5 m long stricture can be measured with an accuracy of a few Tmm^2. The horizontal field errors are small. For their correction a very few horizontal shims should be sufficient. The experience with the first two out of the three undulator modules showed that 14 shims were sufficient for the first and only 3 were needed for the second which is also in accordance with the expectations from the Simulated Annealing procedure.

The vertical field has been optimized using a technique called technique called "Field Fine Tuning by Pole Height Adjustment" [22]. To do so the mechanical design of the structure is such, that all poles are height adjustable using set screws on either side of the poles which allow them to be moved in and out by few tenths of a millimeter. The optimization goal is to obtain an almost perfectly straight trajectory over the whole

undulator length. The basic idea of the adjustment method is simple but rather complex to implement for an undulator system with 327 poles. It can be subdivided into the following steps:

- The field distribution along the electron beam axis is measured. The deviation of this field distribution from a hypothetically "ideal" one resulting in a perfectly straight trajectory is calculated.
- The response of a local gap change of one pole i onto the field of a neighboring pole j is determined
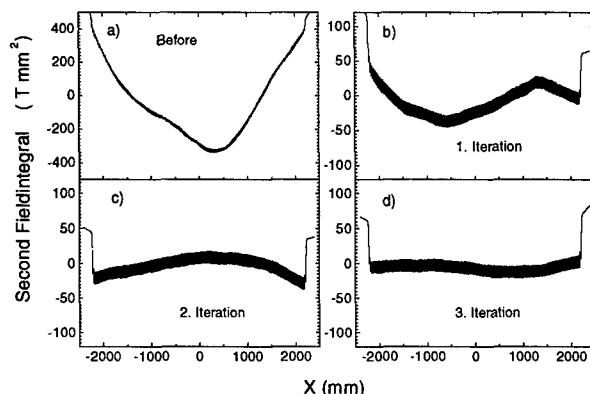
Fig. 3   Trajectory optimization of the first 4.5m long undulator module. Note the different scale in a); The results shown in b – c) have been obtained after three optimization steps

experimentally. From these data the coefficients which couple the movement of a pole i with field change on a pole j can be extracted. Experience shows that there is only short range interaction and only near neighbors interact, i.e. $i - j \leq 5$ is sufficient.

- The local gap changes of all poles, which are needed to produce the required correction, are calculated.
- Finally a list giving the pole numbers and the required local gap changes is generated.

The whole procedure is described in detail in ref [22]. Fig 3 shows the results of trajectory optimization of the first undulator module. Fig 3 a) shows the initial second field integral with an RMS value of 192 Tmm^2, note the expanded scale in Fig 3 a) Successively three iteration steps are shown. The results are self explaining. After the last step and RMS value 0f 7.1Tmm^2 has been obtained, which is already very close to the 6.5 Tmm^2 which are due to the orbit oscillation. In any case they are well below the required specification of 10Tmm^2. The optimization of one structure requires not more than 2-3 days. Experience has shown that the first iteration requires by far the most adjustments. Almost every of the 327 poles has to be tuned. The higher the iteration count the smaller were the required corrections. For the last iteration it was found useful to sum up errors over n poles and to use only the center pole of this interval for correction where n was between 10 and 20.

The alignment of the FODO quads is done using the Rectangular Coil Method (RCM) described in detail in ref [19]. This method allows for the exact location of the quad center as well the precise determination of the integrated gradient of a quad in the presence of the undulator field. Fig 4 a-c) shows results obtained on a prototype structure.

In Fig 4a) the integrated gradient strength of a FODO

Set screw setting [Turns]
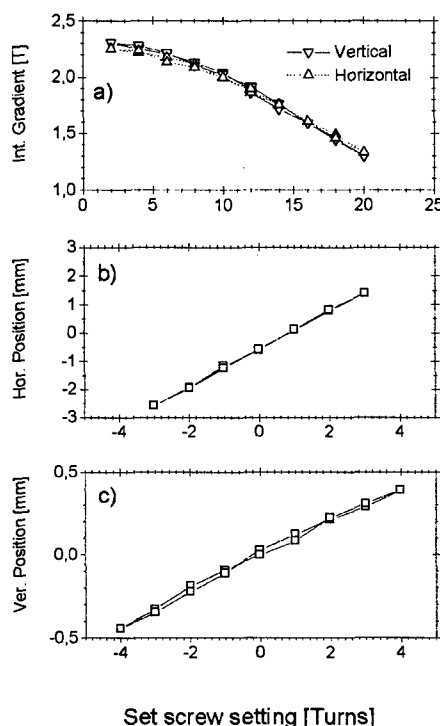
Fig 4 Quad adjustability:
a) Strength
b) Horizontal Position
c) Vertical Position

quad is shown as a function of the set screw settings. The pitch of the screws is 0.7mm. In the case of Fig 4 a) the separation distance of the focusing quads was changed. At zero turn angle there is no separation between the focusing magnets and the integrated gradient is at the maximum strength of 2.3 T. For the quads with an effective length of 0.1365m the maximum field gradient obtained is 16.85 T/m. Fig. 4 b) shows the ability to change the horizontal position of the quadrupole axis. Here a positive / negative sign of the set screw setting means movement of all magnets to the right / left, respectively. It is seen that the axis can easily be moved by +/- three turns which is more than +/- 2 mm. In a similar fashion Fig 5 c) shows the adjustability of the vertical axis. Here a positive/ negative turning sense means that the separation of the magnets in the lower / upper jaw are decreased / increased so that the quad axis is moved up / down and the average separation distance between upper and lower jaw is kept constant. The adjustment range is +/- 0.4mm. In Fig 4 a-c) the adjustments is made back and forth and gives a good impression about reproducibility A more detailed

160

analysis has shown that position measurements can be repeated within 7-8 μm RMS, while the gradient can be determined better than 0.5% RMS.

6 CONCLUSION

In this contribution the requirements on Insertion Devices for 4th generation light sources i.e. those to be used in Linac driven SASE FEL's have been investigated. Very long undulators are required with total lengths up to about 100m for the proposed X-ray FEL's . An important question is whether the focusing has be combined with the undulator or could be separated. The ultimate answer can only be obtained with simulations using FEL code such as TDA-3D, but generally in X-ray FEL's due to their higher beam energy the optimum β-functions are in the range 10-20m Therefore separated function are likely to be used in contrast to VUV - FEL's with much smaller β-functions in the order of a few meters only. Combined function undulators are a real challenge for insertion device technology since they require new developments. The work on the undulator for the TTF may serve as an illustrating example.

In contrast to this the technology for building separated function devices is state of the art and not significantly different from what has been developed for 3rd generation SR labs.

In both cases a new dimension is added by the large lengths especially of the ID's in X-ray FEL user facilities For example the TESLA FEL will consist of a number of undulators each will be up to 100m long [8] Each has about the same total length as all devices of a 3rd generation X-ray source together. The total device length of such a facility can be up to one order of magnitude larger than for the existing facilities

This simple comparison shows that efficient, economic and fast production techniques will play an important role in getting these devices built.. In order to avoid excessively long tuning and manufacturing times as well as excessive production costs new fast, economic and accurate methods have to be found. One way may be to combine modern state of the art motion control technology , i.e. robotic actuators with automated accurate magnetic measurement facility. In this way a magnetic structure can be tuned and optimized automatically.

The method of "Field fine tuning by Pole Height Adjustment" described above together with a suitable magnetic measurement bench can be one part of such a system for undulator optimization. The robotic part on a small scale has already been demonstrated at the Santa Barbara FEL [23,24]. And might serve as an example for further developments. In this way long undulators could be trajectory tuned in a short time.

7 REFERENCES

[1.]   M. Kondratenko, E. L. Saldin, Part. Accel. 10 (1980), 207

[2.]   R. Bonifacio, C. Pellegrini, L. Narducci, Opt. Comm. 50 (1984), 373

[3.]   Proceedings of the 10th ICFA Beam Dynamics Panel Workshop on 4th Generation Light sources Jan 22-25, 1996, Grenoble, , France

[4.]   "A VUV Free Electron Laser at the TESLA Test Facility at DESY – Conceptual Design Report" TESLA-FEL 95-03 ,1995

[5.]   S. V. Milton representing the LEUTL design team, Nucl. Instr. and Methods A407 (1998), 210

[6.]   L..Bertolini, R. Carr, M. Cornacchia, E. Johnson, M. Libkind, S. Lidia, H.-D. Nuhn, C. Pellegrini, G. Rakowski, J. Rosenzweig, R. Ruland, Proceedings of the FEL 98 Conference, Aug 16-22, 1998, Williamsburg, VA, USA

[7.]   LCLS Design Study Report, SLAC - R – 521, April, 1998

[8.]   Conceptual Design of a 500GeV Linear Collider with Integrated X-ray Laser Facility Vol. II Editors: R. Brinkmann, G. Materlik, J. Rossbach, A. Wagner DESY 1997-048

[9.]   T. O. Raubenheimer, R. D. Ruth, Nucl. Instr. and Methods A 302 (1991),191

[10.]   T. Tennenbaum, D. Burke, R. Helen, J. Irvin, P. Raimouch, SLAC-PUB 95-6769 (1995)

[11.]   K. Flöttmann, B. Faatz, E Czuchry, J. Roßbach, Nucl. Instr. and Methods A 416 (1998), 152

[12.]   P. Castro-Garcia, B. Faatz, K. Flöttmann Accepted in Nucl. Instr. And Methods,

[13.]   P. Castro "TTF FEL Beam based Alignmentby dispersion Correction using Micado Algorithm" TESLA FEL 97-04

[14.]   J. Pflüger, Y. M. Nikitina, Nucl. Instr. and Methods A381 (1996), 554

[15.]   J Pflüger, Y. M. Nikitina, " Undulator Schemes with focusing Properties", TESLA - FEL 96-02, 1996

[16.]   Y. M. Nikitina, J. Pflüger, Nucl. Instr. and Methods A375 (1996), 325

[17.]   Y. M. Nikitina, J. Pflüger, "Magnetic Design Optimization of the Undulator for the VUV-FEL at the TESLA Test Facility", TESLA - FEL 96-03, 1996

[18.]   K. Halbach, Journal de Physique, C1, suppl.2 , (1983) C1-211

[19.]   J. Pflüger, H.Lu, D. Köster, T. Teichmann, Nucl. Instr. and Methods A407 (1998), 386

[20.]   B. Faatz, J. Pflüger, "Sorting strategy for the TTF-FEL undulator magnets" TESLA-FEL 99-01

[21.]   J. Pflüger, Rev. Sci. Instrum. 63,1 (1992), 295

[22.]   J. Pflüger, H. Lu, T. Teichmann, Proceedings of the FEL 98 Conference, Aug 16-22, 1998, Williamsburg, VA, USA, to be published in Nucl. Instr. and Methods

[23.]   G. Ramian,Nucl. Instr. and Methods A318 (1992), 225

[24.]   G. Ramian,, J. Kaminski, S.J. Allen, Nucl. Instr. and Methods A393, (1997),220

MAGNETIC PERFORMANCE OF THE ADVANCED LIGHT SOURCE EPU5.0 ELLIPTICALLY POLARIZING UNDULATOR

S. Marks, J. DeVries, E. Hoyer, B. M. Kincaid, D. Plate, P. Pipersky, R. D. Schlueter, A. Young,

Lawrence Berkeley National Laboratory, Berkeley, CA[*]

Abstract

An elliptically polarizing undulator (EPU) has been assembled, tested, and installed in the Advanced Light Source (ALS) storage ring. It is a 2 m long pure permanent magnet device with a 5.0 cm period capable of providing polarized radiation of any ellipticity. This paper reports on the program of magnetic measurements and field tuning, and final magnetic and drive system performance. A summary of measurement results, calculated radiation spectral performance, and a description of the magnetic shimming procedure used for field tuning are included.

1 INTRODUCTION

A facility dedicated for magnetic microscopy and spectroscopy is evolving at the ALS. This facility includes two undulator stations placed in tandem within a single storage ring straight.[1] A set of three chicane magnets separate the beams from the two devices by 2.53 mrad. The first undulator, an EPU5.0, the vacuum chambers and chicane are installed, have undergone accelerator tests and are operational.

The EPU design concept was first proposed by Sasaki.[2] The magnetic structure is a pure permanent magnet (PM) type including four identical quadrants. The diagonally juxtaposed quadrants, Q1 and Q3, are coupled and allowed to translate parallel to the axis. The other two quadrants, Q2 and Q4, are fixed. By moving Q1 and Q3 relative to Q2 and Q4, field amplitudes of B_x and B_y are modulated according to the following equations.

$$B_x = B_{x0}\sin(\varphi/2); \quad B_y = B_{y0}\cos(\varphi/2) \qquad (1)$$

B_{x0} and B_{y0} are peak amplitudes for the horizontal and vertical field components, respectively, and $\varphi = 2\pi dz/\lambda$, where dz corresponds to the quadrant shift and λ is the magnetic period. Regardless of relative magnitudes, the phase difference between B_x and B_y along the axis is 90°. When $dz = 0$ and $dz = \lambda/2$, $B_x = 0$ and $B_y = 0$, respectively, the electron trajectory is sinusoidal within a plane and the resulting radiation is linearly polarized in the horizontal and vertical planes, respectively. When $B_x = B_y$ the electron follows a helical trajectory and the resulting polarization is circular. For other values of dz, the polarization has intermediate ellipticities.

The helical mode produces on-axis radiation only in the fundamental. The brightness of radiation in higher harmonics is maximum for the linear polarized states. The EPU5.0 was designed to produce radiation with high brightness in the fundamental, and third and fifth harmonics with degrees of circular polarization exceeding 80%. The design photon energy range is 90 – 1500 eV for linear polarization, and 130 – 1500 eV for circular polarization.

2 MAGNETIC SHIMMING

Preparation for installation into the storage ring included an extensive program of drive system tests and magnetic measurements and field tuning. The magnetic field is adjusted by moving the vertically oriented PM blocks vertically and horizontally by up to ±0.25 mm with the use of mechanical shims.[1] The objectives of shimming are to correct local field errors that perturb the optical phase and to smooth nonuniformities in the lateral distribution of total field integrals, I_x and I_y.

2.1 Optical Phase Errors

The high brightness of an undulator depends upon the constructive interference of radiation along the electron trajectory. An accumulation of electron path deviations leads to phase errors that degrade the brightness. An expression for path length error $\Delta s(z)$ is shown below.

$$\Delta s(z) = x_0(z)\Delta x'(z) + y_0(z)\Delta y'(z)$$
$$- \int_{-\infty}^{z}[x_0(\xi)\Delta x''(\xi) + y_0(\xi)\Delta y''(\xi)]d\xi \qquad (2)$$
$$+ \frac{1}{2}\int_{-\infty}^{z}[\Delta x'^2(\xi) + \Delta y'^2(\xi)]d\xi$$

The terms x_0 and y_0 are the unperturbed transverse coordinates, first and second derivatives correspond to velocity and magnetic field, respectively, and Δ indicates a perturbation due to field errors.

Two approaches have been used successfully to limit optical phase errors in conventional linear undulators. The first approach, as used in previous ALS hybrid devices, is to sufficiently limit RMS field errors[3] via application of appropriate magnet block and pole tolerances, and block sorting and placement. It is clear

how this strategy works; all terms in Equation 2 are locally small, thus limiting the integral accumulation. The second approach, as exemplified in undulators built for ESRF, is to place iron shims within the magnetic structure to compensate for phase errors indicated by magnetic measurements.[4] The efficacy of this approach may be understood by examining Equation 2. While all errors make a positive definite contribution to the third term, local contributions to the first and second terms may be either positive or negative. The strategy followed in the placement of iron shims is to introduce field errors of the appropriate sign and location to cancel accumulated phase errors. In contrast to the first approach, this strategy generally increases RMS field errors.

Both of these approaches are problematic for application to an EPU. The absence of iron poles coupled with the achievable block-to-block variations in PM material naturally lead to relatively high field errors, before shimming. The iron-shimming scheme can be applied to compensate for phase errors corresponding to a single configuration of quadrant offset in the same way that works with a conventional undulator. However, upon changing the polarization state, via quadrant translation, the magnetic neighborhood of each shim, and thus its local on-axis magnetic effect, will change. Also, since shim placement generally does not correspond to field error locations, the efficacy of this approach depends critically upon the positions of initial field errors relative to those introduced by shims. This relationship changes with quadrant translation, since the shims' locations on one quadrant pair will shift relative to the errors belonging to the other quadrant pair. These considerations lead to the development of an alternative magnetic shimming approach.

The input to our magnetic shimming procedure was local magnetic field errors obtained from on-axis magnetic measurements at two polarizaiton states: horizontal linear polariztion, producing pure B_y on-axis, and vertical linear polarizaiton producing pure B_x on-axis. A constrained optimization procedure was applied to minimize an objective function composed of RMS values of local optical phase errors and local first field integrals for both polarization states. The variables within the optimization were the vertical and horizontal displacements of the vertically oriented PM blocks within each quadrant pair. Movements were constrained to ±0.25mm from initial locations. The effect of PM displacements was determined from analytically derived sensitivity coefficients.

2.2 Transverse Integral Nonuniformities

Local field adjustments to Q1 and Q3 are equivalent in how they affect on-axis fields and thus optical phase. However, the block movements used for field tuning also result in changes to the lateral distribution of field integrals, which are not symmetric about the axis. Therefore,

Q1 and Q3 displacements are not equivalent in their effect on field integrals. Figure 1 shows perturbations in integral distributions due to vertical and horizontal magnet position adjustments of 0.25 mm in Q1. Adjustments to Q2, Q3, and Q4 are derived by applying appropriate symmetries.
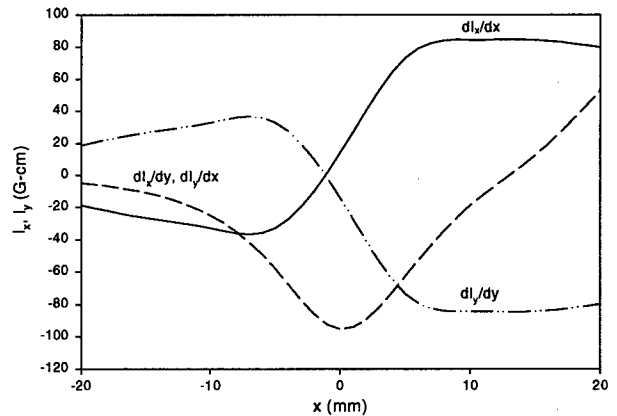
Figure 1 Change in I_x and I_y due to block motions dx and dv of 0.25 mm.

Our magnetic shimming procedure used the on-axis field optimization to identify PM block position adjustments for the Q1/Q3 and Q2/Q4 quadrant pairs. The choice between applying adjustments to Q1 or Q3, and Q2 or Q4 was made to minimize nonuniformities in lateral integral distributions.

2.2 Results of Magnetic Shimming

The RMS values, prior to shimming, for optical phase error and horizontal and vertical field integrals for the horizontal polarization mode were 10°, 147 G-cm and 95 G-cm, respectively. The values for vertical polarization were 32°, 218 G-cm, and 165 G-cm. After three tuning iterations, values for horizontal polariztion mode were reduced to 9°, 59 G-cm and 76 G-cm. The values for vertical polarization were 12°, 56 G-cm, and 64 G-cm. A fourth tuning iteration was applied for final integral adjustment. Figure 2 shows lateral integral distributions before and after shimming.
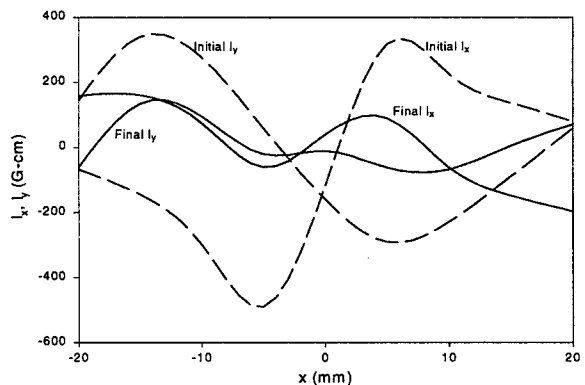
Figure 2 I_x and I_y, before and after magnetic tuning.

3 SPECTRAL CALCULATIONS

The magnetic shimming procedure used only field measurements for the two linear polarization states. Measurements were taken for other states to characterise performance over the operating range and provide assurance that optical phase errors had been adequately corrected over this range. Spectral properties were calculated done for a variety of polarization states. A computer code was developed that numerically integrates the full time domain electric field equations[5] for a single electron, without emittance and energy spread considerations.

Figure 3 summarises a comparison of spectral properties calculated from field measurements and from an error free device. The magnetic gap is 23 mm with a quadrant offset of 9 mm (an offset of 0 corresponds to the horizontal polarized configuration), corresponding to $B_y \approx 3B_x$, which produces a high degree of circular polarization with strong spectral brightness in the third and fifth harmonics. The third harmonic is at 660 eV, in the core energy range for many experiments.

Figure 3 illustrates the spectral effect due to magnetic field errors. The peak flux density ratio of the actual device (spectrum calculated from measured fields) to an ideal device (spectrum calculated from an error free device of the same magnetic structure) is graphed versus harmonic number. Notice that flux density is at or above 70% of ideal up to the ninth harmonic. Degree of circular polarization is also graphed as a function of harmonic number. In this configuration the degree of circular polarization is above 80% for all harmonics, and increases with harmonic number. Field errors do not degrade polarization.
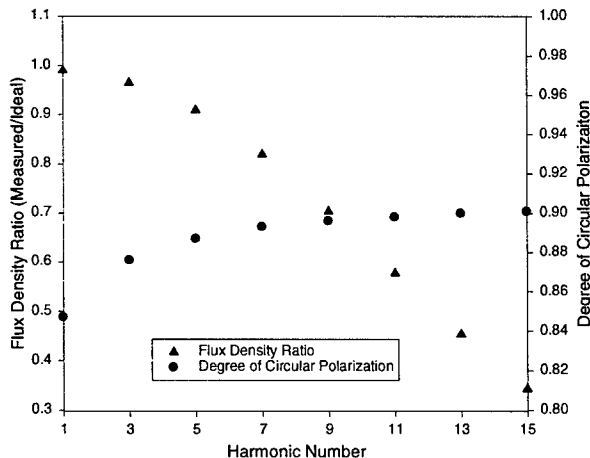
Figure 3 Flux density ratio and degree of circular polarization at 23 mm gap and 9 mm offset.

4 ON-AXIS FIELD INTEGRALS

Figure 4 shows the on-axis field integrals as a function of quadrant shift, dz, at the minimum gap of 14 mm. The change is due to the finite permeability of the PM and the change in proximity of end blocks to their neighbors. The effect on I_y is nearly canceled because the vertical magnetic structure is odd about the midpoint; the horizontal magnetic structure is even.
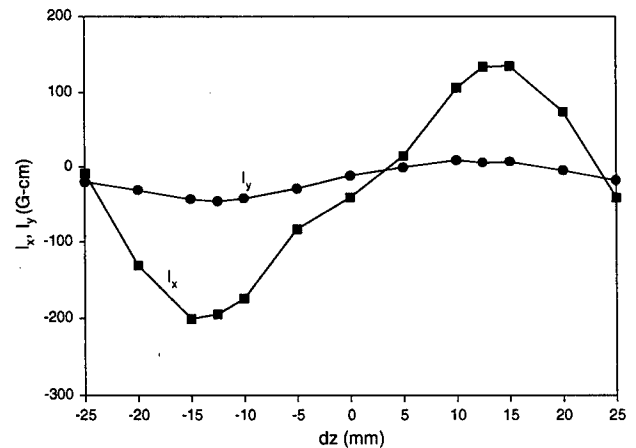
Figure 4 On-axis I_x and I_y at 14 mm gap.

5 DRIVE SYSTEM ACCURACY

Very precise and repeatable control of the magnetic gap and quadrant translation is required to achieve the required precision and repeatability in spectral energy and degree of circular polarization.[6] The drive and motion control design has been described previously.[1]

Measurements demonstrated that final position repeatability was limited only by encoder resolution of 1 μm for vertical gap and 0.25 μm for quadrant offset. Settling time following a move was measured to be within 1.5 seconds.

6 REFERENCES

[1] S. Marks, et al., "The Advanced Light Source Elliptically Polarization Undulator,"*Proc. 1997 Particle Accelerator Confernce* (1998) 3221.

[2] S. Sasaki, "Analyses for a planar variably-polarizing undulator", *Nucl. Instr. And Meth.* A347 (1994) 83.

[3] B. M. Kincaid, "Random errors in undulators and their effects on the radiation spectrum," *SPIE* Vol. 582 (1982) 72.

[4] J. Chavanne, P. Elleaume, "Undulator and wiggler shimming," *Synchrotron Radiation News* 8-1 (1995) 18.

[5] J. D. Jackson, *Classical Electrodynamics*, John Wiley & Sons (1975) 654.

[6] "EPU5.0 Elliptical Polarization Undulator Conceptual Design Report", to be published.

EXPERIMENTAL RESULTS WITH A NOVEL SUPERCONDUCTIVE IN-VACUUM MINI-UNDULATOR TEST DEVICE AT THE MAINZ MICROTRON MAMI

T. Hezel, M. Homscheidt, H. O. Moser, R. Rossmanith
Forschungszentrum Karlsruhe, Project ANKA, D-76021, Karlsruhe, Germany
Th. Schneider
Forschungszentrum Karlsruhe, Inst. for Technical Physics, D-76021, Karlsruhe, Germany
H. Backe, S. Dambach, F. Hagenbuck, K.-H. Kaiser, G. Kube, W. Lauth, A. Steinhof,
Th. Walcher
Institute for Nuclear Physics, University of Mainz, Germany

Abstract

Experimental results of beam tests with a novel superconductive in-vacuum mini-undulator test device are described. The period length is 3.8 mm and the undulator is 100 periods long. The gap height can be varied between 1 and 2 mm. The tests were performed with an 855 MeV electron beam at the Mainz Microtron MAMI. The small gap undulator has been operated up to an electron beam current of 50 μA cw. The bremsstrahlung background is almost negligible and the beam does not influence the in-vacuum superconductor. In this paper the measured X-ray spectra are presented.

1 INTRODUCTION

Undulators with a short period length (less than 10 mm), a significant number of periods (100 and more) and high magnetic fields are becoming more and more interesting both for synchrotron light sources and FELs [1-5]. Those undulators need small gaps of about 1/3 to 1/4 of the period length.

In order to maintain the largest possible aperture the field generating devices of the undulators have to be placed directly in the vacuum chamber.

In this paper an undulator with a completely new approach is described. The undulator field is generated by a current through a superconducting wire. Different to other superconductive concepts [1,2] the superconducting wire is in vacuum [6]. Since the whole undulator is cooled by liquid helium the outgassing rate is very low. This is an important advantage compared to warm bore permanent magnet undulators.

2 THE UNDULATOR

Fig. 1 shows the principal layout of the undulator. The field is generated by the current through superconductive wires. The direction of current flow is opposite in two adjacent wires generating a vertical field with alternating sign along the electron trajectory. The superconducting wire is embedded into a groove. In the undulator described here the grooves are cut into soft iron. The superconducting wires are in vacuum and are indirectly cooled by liquid helium. The cross section of the wire is rectangular so that each wire can be in reality a stack of wires with identical current flow direction. In the present undulator the stack consists of four wires.
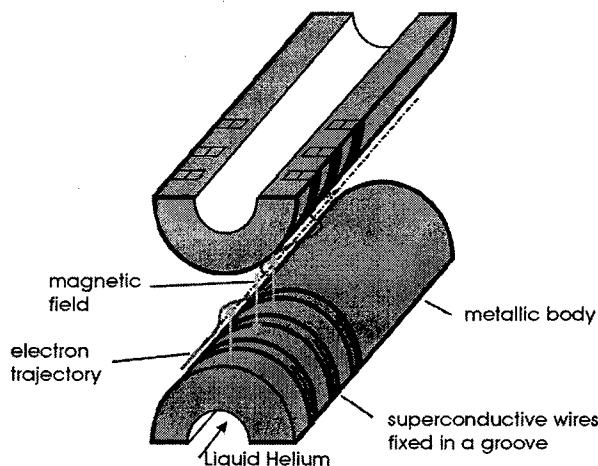
Fig. 1 Layout of the undulator. The field is generated by superconductive wires with alternating current directions. Two identical coils, indirectly cooled by LHe, are placed above and below the electron beam.

Fig. 2 shows one of the completely wound undulator coils. In the center is the tube for the liquid Helium.
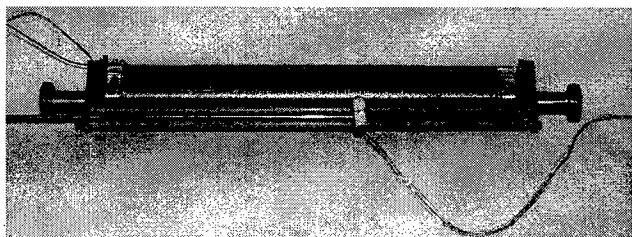
Fig. 2 One completely coiled undulator half, 38 cm long with the micro Hall probe for field measurement

3 THE MEASURED UNDULATOR FIELD

Fig. 3 shows the measured field of one undulator coil with a miniature Hall probe (active area $100 \times 100 \mu m^2$). The slight dipole component of the field can be compensated by optimizing the winding geometry at both ends of the coils.
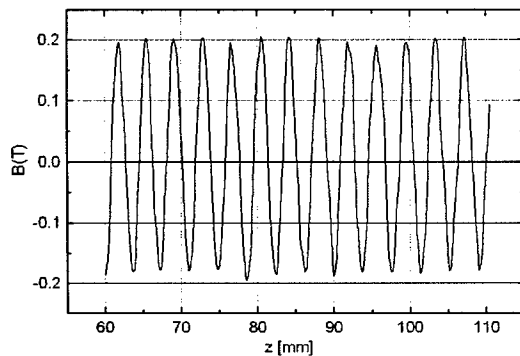
Fig. 3 Field of one undulator coil measured with a miniature Hall probe at a distance of 0.5 mm. The current was 600 A.

4 THE EXPERIMENT AT MAMI

The two undulator halfs are suspended in a vacuum vessel which is part of the normal vacuum chamber of the accelerator. Fig 4 shows the layout. The two undulator halfs are surrounded by a LHe shield. On top of the undulator is a container for LHe which provides the undulator and the shield with LHe. In order to simplify current feedthroughs the maximum current was limited to 400 A. The maximum current through the coils before quenching is 1400 A.
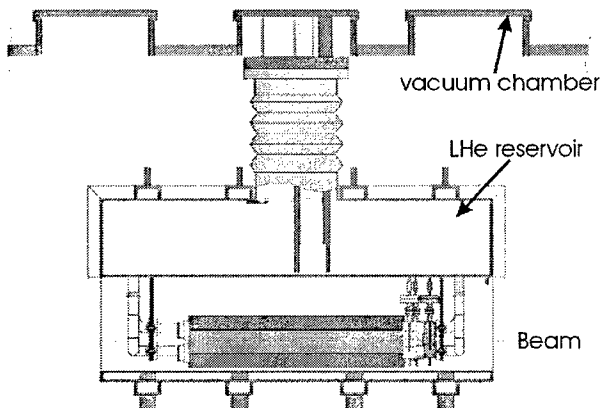
Fig. 4 The cryostat for the undulator

The measurements of the undulator radiation were performed with an 855 MeV beam at the Mainz microtron MAMI at a beam current up to $50 \mu A$ cw. The undulator is followed by a bending magnet which separates the electron and the X-ray beam (fig. 5). 12 m downstream of the undulator is a Ge detector with a 200 μm wide pinhole which can be moved perpendicularly to the beam. With this arrangement it is possible to measure the spatially resolved spectrum.
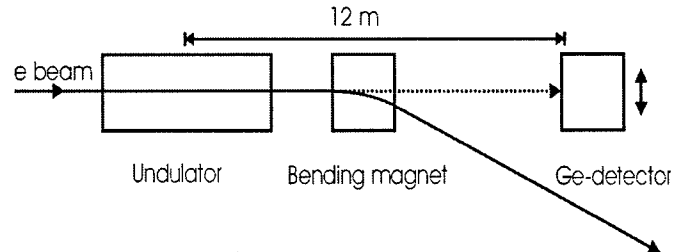
Fig. 5 Schematics of the experimental setup.

The measured spectrum on the undulator axis is shown in fig. 6. The current of MAMI was reduced so that the detector measured single photons (current of about 30 pA). The peak energy of the spectrum is close to the expected value. The FWHM is mainly determined by the detector resolution of 150 eV. The low energy tail stems from the curvature of the beam path due to the residual dipole field. As a result of the curvature of the horizontal beam path photons emitted under a larger angle and therefore lower energy can hit the detector.
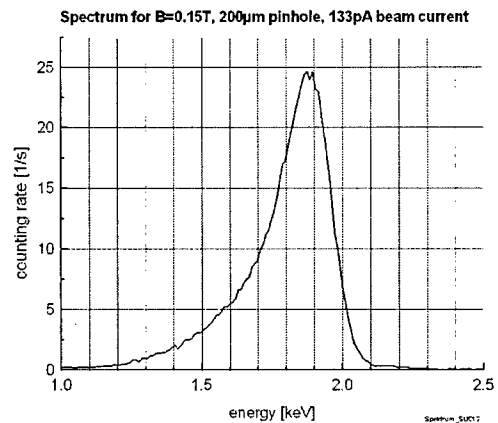
Fig. 6 The measured spectrum. The detector resolution is ca. 150 eV.

The complete spatially resolved spectrum (again measured with a Ge detector and a 200μm pinhole) is shown in fig. 7. The pinhole-detector ensemble can be moved together perpendicularly to the beam direction. The measurements were performed at a distance of 12 m

from the undulator. The data are in excellent agreement with the fundamental formula of the photon energy of an undulator

$$E_{Phot} = \frac{2hc\gamma^2}{\lambda_u} \frac{1}{1 + \frac{K^2}{2} + \gamma^2 \left(\frac{x}{d}\right)^2}$$

where, in the present case, λ_u is 0.38 cm, the period length of the undulator, K is the undulator parameter

$$K = 0.934 \, B_{max} \, [T] \, \lambda_u \, [cm]$$

B_{max} the maximum field in Tesla, d the distance between the undulator and the detector and x the vertical position of the detector (Fig. 8).
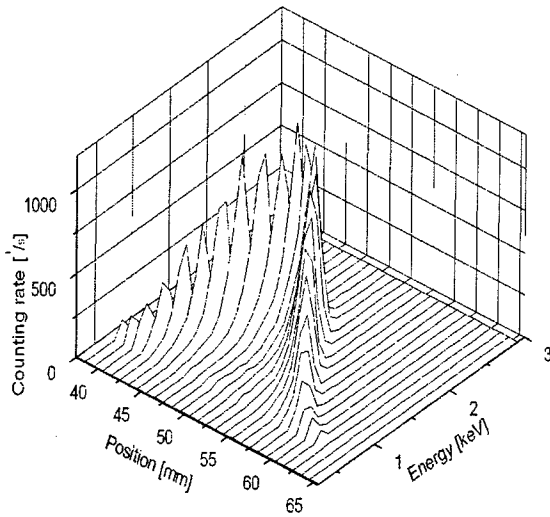
Fig. 7 Vertical spatially resolved X-ray undulator spectrum with a 200 μm pinhole and a Ge detector at a distance of 12 m from the undulator.

Due to the curvature of the horizontal trajectory which is caused by the dipole component the horizontal spectrum is, as expected, smeared out.

5 PLANNED FUTURE EXPERIMENTS AND IMPROVEMENTS

In summary it was shown experimentally that a superconductive undulator with a period length of several mm works perfectly with a beam. In a next step the dipole field of the undulator will be compensated. This can be achieved by shaping the grooves at the end of the coils and by additional trim coils.
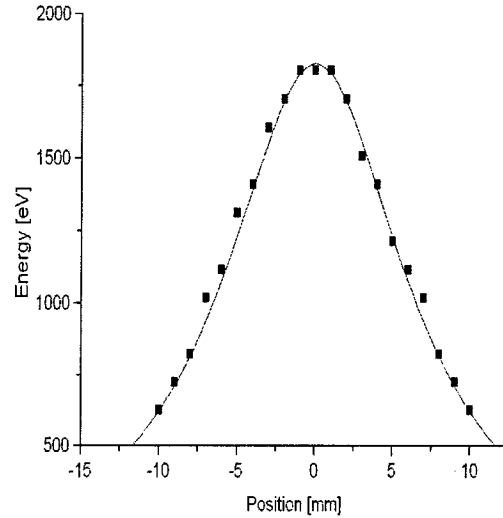
Fig. 8 Peak energy values (rectangles) compared with the undulator formula given above (solid line).

One natural application of the undulator will be in the field of X-ray and VUV FELs. The short period length allows to reach the VUV and X-ray region with relatively modest beam energies (1 to 2 GeV). Studies for a test are under way.

Finally a test with a high current beam in a storage ring is considered for the near future. In this test an undulator is envisaged which allows to tune the radiated light over a wide range purely electrically. This requires a period length in excess of 1 cm to reach K values of about 2 and allows, as a consequence, larger gaps of about 5 mm.

REFERENCES

[1] Ben-Zvi, I. et al. Nucl. Instr. Meth. A 297 (1990) 301

[2] Ingold, G. et al., Nucl. Instr. Meth. A375 (1996) 451

[3] Granatstein, V. L. et al., Appl. Phys. Lett. 47 (1985) 586

[4] Tatchyn, R., Csonka, P. L., Appl. Phys. Lett. 50(1987) 16

[5] Gomes, P. A. P., et al., Rev. Sci. Instr. 63 (1992) 352

[6] Hezel, T., et al., J. Synchrotron Rad. 5 (1998) 448

A MICROWAVE BEAM WAVEGUIDE UNDULATOR FOR A BRILLIANT ABOVE 100 KEV PHOTON SOURCE*

Y. Kang, J. Song, and R. Kustom, Argonne National Laboratory, Argonne, IL

Abstract

For generation of photons above 100 keV with a magnetic field strength in the range 0.2-0.5 Tesla, an undulator wavelength λ_u shorter than 5 mm may be needed with beam in the Advanced Photon Source (APS) storage ring. A microwave beam waveguide undulator system has been investigated for generation of such light. The waveguide structure consists of two parallel reflector surfaces that can be derived from an elliptically cylindrical waveguide. The structure can support deflecting TE_{m0} modes with very low microwave loss. A microwave ring resonator circuit employing the beam waveguide is considered to construct an undulator with the above requirement. Microwave properties of the beam waveguide structure have been investigated, and the design criteria for a microwave undulator are discussed.

1 INTRODUCTION

Undulators and wigglers that use microwave fields can have short undulator wavelength that is useful to generate high photon energy x-rays above 100 keV. A microwave undulator using a fundamental mode waveguide was reported in [1] and elsewhere. The fundamental mode waveguides can have certain limitations for a short undulator wavelength less than several millimeters due to narrow gap between metal walls and higher rf loss. The small aperture can be a problem for the beam passing through the undulator area; a microwave undulator with a physically large aperture is of interest. Using an overmoded quasi-optical beam waveguide can be useful to achieve the goal with low loss [2]. The microwave beam waveguide can support all TE and TM modes, but TE_{m0} modes (m=odd integer) are the useful modes for the undulator. With openings between the two reflectors, most unwanted modes may be damped completely. By constructing a ring resonator circuit with the beam waveguide, a microwave undulator can be possible with a reasonably low power microwave source.

Parameters of the electron beam in the Advanced Photon Source (APS) storage ring are shown in Table 1. The first harmonic synchrotron radiation spectra on beam axis ($\theta=0°$) for various undulator fields are shown in Figure 1. The calculations were made in XOP [3][4] and show brilliance vs. photon energy around 100 keV with the undulator wavelength λ_u=4.5 mm at three undulator field strengths.

Table 1: APS beam parameters

Beam Energy	7 GeV
Beam Current	100 mA
σ_x	0.342 mm
σ_y	0.091 mm
σ'_x	24 µrad
σ'_y	9 µrad
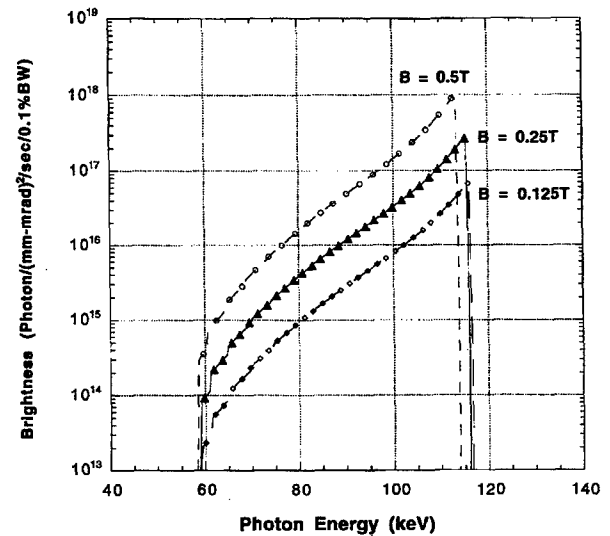
Figure 1: Brilliance vs. photon energy of first harmonic undulator radiation of the APS beam, λ_u=4.5 mm, N=400 periods, L=1.8 m.

2 BEAM WAVEGUIDE

A microwave beam waveguide and its TE_{m0} mode field distribution are shown in Figures 2(a) and 2(b). Two extruded concave reflectors are used with a gap between the two. The gap is important in order to provide damping of higher-order TE and TM modes and vacuum pumping for a practical undulator. The higher-order TE_{mn} and TM_{mn} modes (n>0) may not be supported by the open structure since the radiation loss through the openings can be significant.

The field strength needs to be uniform within a certain window area for coherent photon generation. The standing wave due to the transverse resonance has the transverse wavelength $\lambda'_g > \lambda$. For a sinusoidal field variation, ±9% window gives 1% change from the peak field. The Gaussian microwave beam waist is given as

$$\omega_o(m) = \sqrt{\sqrt{2bd - d^2} \Big/ k_{m0}(m)} \qquad (1)$$

where k_{m0} is the transverse wave number k_t for the TE_{m0} mode, b is the reflector focal length, and d is the distance between the two reflectors.

Electric Field of TE_{mn} mode
m=5, n=0

(a)

Gaussian RF Beam Envelope

(b)
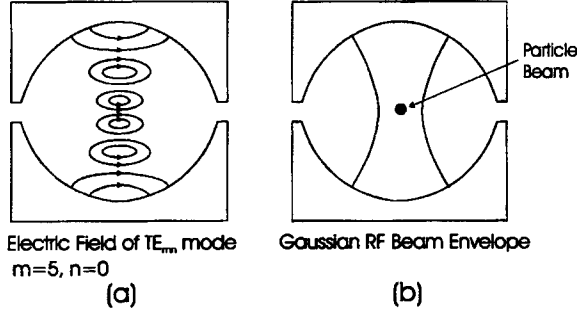
Figure 2: Cross section of a parallel reflector beam waveguide. (a) Electric field of the TE_{50} mode, (b) particle beam with respect to the microwave beam.

Beam waists at the waveguide center and on the reflector surfaces are shown in Figure 3. The waveguide system will have two distinct losses: one due to the metal surface resistance and the other due to spillover at the openings. The microwave beam waveguide can support TE modes with low loss due to its high Q factor; small diffraction and ohmic losses. The loss factors of diffraction loss and conductor loss of the beam waveguide are

$$\alpha_c \approx 2 \frac{R_s k_{mo}}{k_o h_{mo} d} \left(1 + \frac{h_{mo}^2}{2 k_{mo}^2 d} \right) \qquad (2)$$

$$\alpha_d = \frac{k_{mo}}{h_{mo}} \ln \left| \frac{1}{p} \right| \qquad (3)$$

where $h_{mo}^2 = k^2 - k_m^2$ and p is the reflected field intensity per reflection. Some properties and parameters of the beam waveguide are shown in [4].
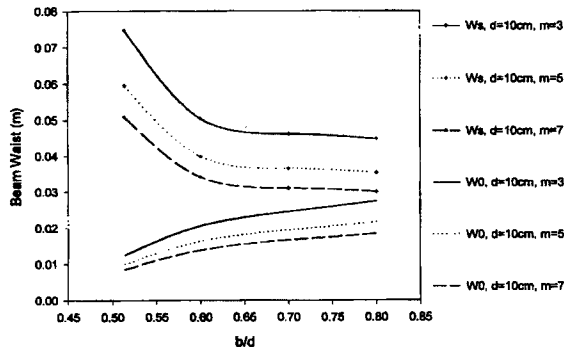
Figure 3: Beam waists of microwave in the beam waveguide. Ws and W0 are waists on the reflector and at the center, respectively, d=10 cm, λ_u=4.5 mm.

The wave functions chosen in [5] are useful for estimating electromagnetic fields and parameters of the beam waveguide. The undulator field strength vs. b/d is

shown in Figure 4. The peak field strengths can be achieved at around b/d=~ 0.6 and was ~0.3 Tesla for 1 MW microwave input power in the d=12 cm case.
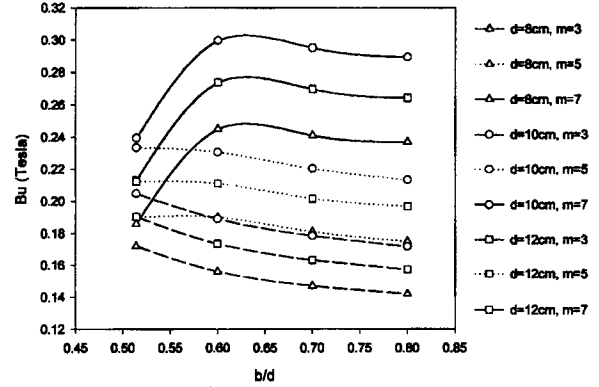
Figure 4: Undulator field strength in a beam waveguide. 1 MW microwave dissipation in 1 m, λ_u=4.5 mm.

3 PROPOSED DESIGN

A power amplification scheme known as ring resonator can be used to obtain the high field strength with low power microwave source [6]. The ring resonator consists of a closed microwave transmission line ring with a high directivity directional coupler. The beam waveguide can be used as the transmission line in the ring. The schematic diagram of the microwave ring resonator undulator is shown in Figure 5.
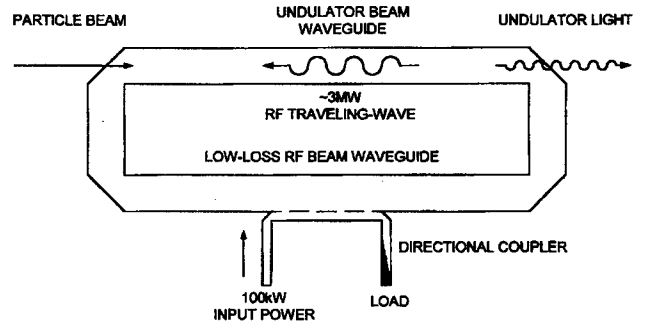
Figure 5. Schematic diagram of the microwave beam waveguide ring resonator undulator.

The ring can resonate at a frequency when the axial length is $N\lambda_g$, where λ_g is the guide wavelength. A ring resonator can provide amplified fields inside the resonator and have been used in certain high-power microwave experiments. The power gain of the system is given as [7] where c is the voltage coupling factor of the directional

$$G_p = \frac{c^2}{\left\{ 1 - 10^{-\alpha/20} (1 - c^2) \right\}^2} \qquad (4)$$

coupler and α is the one-way attenuation around the ring measured in dB. The coupling of the directional coupler determines the power amplification factor. Due to its low microwave loss, a factor of 20-100 may be possible with practical high directivity couplers at above 30 GHz, so that a realistic system could be implemented.

The attenuation factor α is the limiting factor for the power gain of such structures as shown in Eq. (4). The diffraction loss dominates and thus limits the system performance. The directivity of the directional coupler must be made high enough so that the loss does not contribute much in total system loss. Estimated microwave properties of an example design of the 1.8-m resonator made of copper for λ_u=4.5 mm is shown in Table 2. The power gain of about 50 is obtained when the path loss is < 0.05 dB with a −15-dB directional coupler. A regular waveguide to overmoded beam waveguide directional coupler can be constructed for this purpose. Note that the beam waveguide loss is much less than the loss in regular fundamental mode waveguides in the same frequency range of 0.5-1.0 dB/m. For the design $\lambda'_g \approx 20$ mm, a ±1.8-mm vertical window can give a field variation of ±0.5%. The beam waist is ~20 mm; this translates to ~ ±2 mm horizontal window for ±0.5% field variation.

Table 2: An example of microwave ring resonator undulator parameters

Operating frequency (GHz)	34
Mode of operation	TE_{50}
Reflector focal length, b (cm)	7.2
Reflector distance, d (cm)	12
Diffraction loss	0.014 dB/m
Reflector loss	0.0035 dB/m
Directional coupler coupling	−15 dB
Undulator field	0.25 T
Microwave source power	100 kW

A proposed design is shown in Figure 6. The design uses two halves of symmetrically machined plates. The entire ring resonator is made of beam waveguide to lower the microwave loss. The machined pieces are aligned with a gap between them to satisfy the mode damping and vacuum pumping as discussed above. A directional coupler is formed in the beam waveguide shown in the figure. Maintaining a resonance requires the use of tuners in the waveguide. Tuners can also be phase shifters in the form of electromagnetic, thermomechanical, or mechanical tuners. Temperature control of the waveguide structure can provide fine tuning of the resonance.

4 DISCUSSION

By using the low-loss, larger-aperture beam waveguide structure, a higher field can be obtained with sub-cm λ_u. The low-loss waveguide can help raise the power amplification factor over regular fundamental mode waveguides. The beam aperture in the microwave

standing wave field does not have uniform strength like in DC magnet systems, but still can be useful in generating a synchrotron light. In the example design, the power loss is <0.02 dB/m so the axial field uniformity in a 1.8-m structure will be better than 0.1%. If more precise field uniformity is desired, the reflecting surfaces can be tailored to match the wavelength and the field strength. By increasing the microwave frequency, photon energy much higher than 100 keV can be generated. Recently, klystron and gyrotron amplifiers have become commercially available in the above frequency range for >200 kW pulses and for 50-100 kW CW, which is considered sufficient for this application.
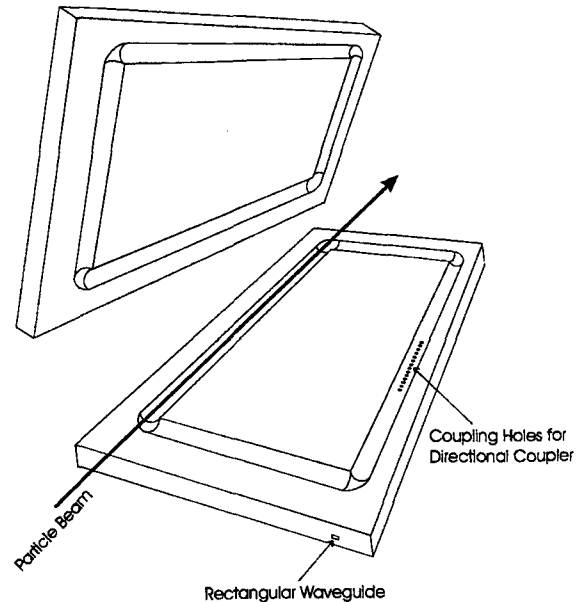
Figure 6: A proposed design of a beam waveguide microwave undulator.

5 REFERENCES

[1] T. Shintake et al., "Development of microwave undulator," Japanese Journal of Applied Physics, Vol. 22, No. 5, May 1983 pp. 844-851

[2] Y. Kang, R. Kustom, P. Matthews, and A. Nassiri, "Parallel Reflector Beam Waveguide as a Microwave Undulator," EPAC '94 proceedings, 1994

[3] M. Sanchez del Rio and R. J. Dejus, "XOP: A Multiplatform Graphical User Interface for Synchrotron Radiation Spectral and Optics Calculations," SPIE Proceedings, Vol. 3152, 1997

[4] R.J. Dejus and M. Sanchez del Rio, "XOP: A Graphical User Interface for Spectral Calculations and X-Ray Optics Utilities," Proceedings of SRI '95, Rev. Sci. Instrum. 67(9) 1996

[5] T. Nakahara and N. Kurauchi, "Guided Beam Waves between Parallel Concave Mirrors," IEEE Trans. on Microwave Theory and Techniques, Vol. MTT-15, No. 2, February 1967 pp. 66-71

[6] T Shintake, "RF Insertion Devices," 4th Generation Workshop, SLAC, February 1992

[7] K. Tomiyasu, "Attenuation in a Resonant Ring Circuit," IRE Trans. MTT-8, pp. 253-254 March 1960

FABRICATION AND TEST RESULTS OF A NB₃SN SUPERCONDUCTING RACETRACK DIPOLE MAGNET*·

K. Chow, D.R. Dietderich, <u>S.A. Gourlay</u>[+], R. Gupta, W.Harnden, A.F. Lietzke, A.D. McInturff,
G.A. Millos, L. Morrison, M. Morrison, R.M. Scanlan

Lawrence Berkeley National Laboratory, Berkeley, California, 94720

Abstract

A "proof-of-principle" Nb₃Sn superconducting dual-bore dipole magnet was built from racetrack coils, as a first step in a program to develop an economical, 15 Tesla, accelerator-quality magnet. The mechanical design and magnet fabrication procedures are discussed. No training was required to achieve temperature-dependent plateau currents, despite several thermal cycles that involved partial magnet disassembly and substantial pre-load variations. Subsequent magnets are expected to approach 15 Tesla with substantially improved conductor.

1 INTRODUCTION

Economical, high-field magnets are needed to reduce the overall cost of the next high-energy collider. Flat "racetrack" coils are believed to facilitate a reliable, cost-effective utilization of the brittle, high performance superconductors that are currently required to achieve high magnetic fields. The "Common-Coil" racetrack design (schematically shown in Fig.1), with two bores that share coils, has been proposed as a cost-effective design for future colliders [1,2]. Consequently, LBNL's high-field Nb₃Sn accelerator magnet development effort has shifted to the "Common-Coil" racetrack geometry. The ultimate goal of the program is to develop accelerator quality dipoles with fields up to 15 Tesla (T). This was approached by first building a lower field magnet (6T) to demonstrate the feasibility of the design, develop fabrication techniques and understand relevant performance parameters. Ultimate success will depend upon the development of high-quality, low-cost, high-field superconductor.

2 DESIGN

The design and early fabrication stages have been described elsewhere [3]. The physical parameters are briefly summarized in Table 1.

The conductor was manufactured by Teledyne Wah Chang Albany (TWCA) for the ITER project. Short sample
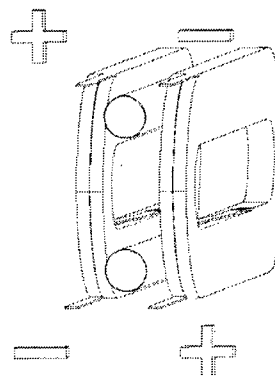
Figure. 1: Schematic of "Common-Coil" Magnet

Table 1: Racetrack Coil Specifications

Coil Geometry	Two, double-layer pancakes
Number of turns	40 turns/coil
Coil Inner-Radius	40 mm
Straight Length	500 mm
Coil-Coil Spacing	40 mm (Max. bore diam.)
Bore-Bore Spacing	150 mm
Transfer Function	0.71 T/KA (linear, no iron)
Cable	30 strand, Rutherford
Cable Size	1.45 x 12.34 mm
Strand	0.808 mm (ITER)
Manufacturer	TWCA
Jc (TWCA)	610 A/mm² at 12 T (4.2 K)
B₀ (Max, strand)	6.6 T
B₀ (Max, cable)	5.8 T
B₀ (Max, achieved)	5.9 T

measurements of single strands predicted a bore field of 6.6 T at short sample. A single measurement of a bifilar cable sample gave a lower value of 5.8 T. Additional measurements are in progress to verify the conductor performance, but as the quench data described below show, the magnet performance was more in line with the cable measurement.

The basic component of this design is the coil module, which consists of a double-layer, 40-turn coil contained in a support structure. The preliminary design was for a 10 mm aperture magnet (40 mm coil spacing) with emphasis on maintaining the simplicity of the racetrack geometry.

The coil-support system (Figure 2) permitted independent adjustment of each orthogonal pre-load, and easy modification of any coil module. Coil forces were supported within the coil module. A coil-edge pre-load was applied to the straight section via 50 mm thick Al-bronze rails running the full length of the coil package. The end-load was applied using a series of set-screws that loaded the coil end-shoes. The coil-face pre-load was applied via multiple tensioning rods, whose forces were transmitted via thick, side-by-side stainless steel bridging beams.
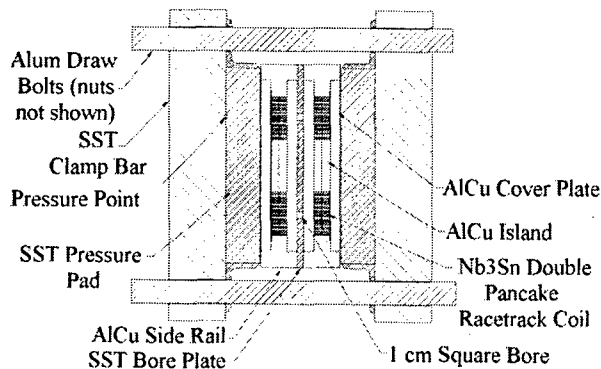
Figure 2: Magnet Cross Section

3 FABRICATION

The cable was insulated with a nominal 0.13 mm thick sleeve of woven S-2 glass. To reduce carbon deposits during reaction, the factory sizing is baked out and replaced with a palmitic acid sizing. However, there is still a minor problem with low resistivity of the epoxy. Alternatives are being considered.

Each double-layer coil was wound around a central island on a flat plate, with an inter-layer ramp to avoid an internal splice. Narrow strips of stainless-steel foil contact the cable at the intended voltage-tap locations. A 10 mm thick end-spacer was inserted after the 6th turn, to reduce the peak field in the coil ends.

After winding, the coil straight section was compressed to a predetermined size by bolting spacer-bars and side-rails onto the coil-face support-plates. End-shoes were installed, and the leads were carefully insulated and supported in their final positions. The coils were placed in a stainless-steel retort under positive Argon atmosphere and reacted according to the manufacturer's recommended reaction cycle (~2 weeks).

The reacted conductor is quite strain-sensitive, and must be protected from excessive strain. In preparation for supporting the conductor with an epoxy-glass matrix, each Nb_3Sn lead was carefully spliced to a pair of NbTi cables, and immobilized. The stainless steel side-rails and face-plates that were used during reaction were replaced with similar Al-bronze pieces that were designed to closely fit the post-reaction coil dimensions. A 1 mm thick shim was inserted between each side-rail and corresponding face-

support plate that would permit post-potting coil loading via a thinner shim. Mica paper was added between the outer turn of each coil and the associated support pieces. This improved the electrical insulation and provided a potential shear plane away from the conductor. To further facilitate shearing, all coil support pieces were mold released before potting. These shear planes were intended to reduce shear stresses while coil-face and coil-edge pre-loads were independently adjusted.

The completed coil assemblies were vacuum impregnated to provide good internal conductor support, and produce robust coil modules for insertion into the coil support structure. All surfaces in contact with the coil during potting were left undisturbed, in order to provide good surface matching, without the stringent machining tolerances that were encountered with previous Nb_3Sn magnets, another potential cost saving feature of this design. The coil modules were stacked and aligned via pins. All loads from the adjustable external loading elements were transferred through the use of bearing rods or balls. This technique greatly reduced the need for high tolerances. Minor variations in coil module thickness and uniformity were accommodated with Kapton shims under the pressure pads.

3.1 Test Configurations

One philosophy in magnet design maintains that the coils should have sufficient preload such that under Lorentz loads the conductor maintains contact with the support structure. In order to satisfy this design requirement at fields over 12 T, the required room temperature preloads approach levels that could damage the conductor. Taking advantage of the flexibility of the RD-2 design, we have performed a series of tests with reduced horizontal and vertical preload. Three pre-load combinations (Table 2) were tested.

Table 2: Tested Coil Pre-Loads

Magnet	300K Horiz.	300K Vert.	4K Horiz.	4K Vert.
RD-2-01	14 MPa	50 MPa	30 MPa	30 MPa
RD-2-02	6 MPa	50 MPa	6 MPa	30 MPa
RD-2-03	6 MPa	21 MPa	6 MPa	7 Mpa

The initial test configuration (RD-2-01) was loaded sufficiently to maintain contact between the coil and all support surfaces (although insufficient to stop slippage during high excitation).

The second configuration (RD-2-02) had the coil-face pre-load reduced enough to insure that each coil would separate from its inner (bore) face-plate during excitation. This was done by replacing the aluminum tensioning rods with stainless steel, and reducing the room temperature pre-load.

The third configuration (RD-2-03) had its coil-edge pre-load reduced enough to insure that the inner turn would separate from the island during excitation. This was accomplished by changing the straight edge shim thickness, and re-adjusting the end load.

4 TEST RESULTS

4.1 Quench Behavior

RD-2-01 required no training and achieved a thermally dependent 4.4 K plateau current of 8.29 kA on the first ramp. The mechanically modified versions of the magnet (RD-2-02 and 03) performed identically to the original load configuration, despite the sizable differences in loading and loading histories. During the initial cooldown, 18 high current quenches were used to establish training, ramp rate, and temperature dependencies. Figure 3 shows the spontaneous quench history of the RD-2 series.
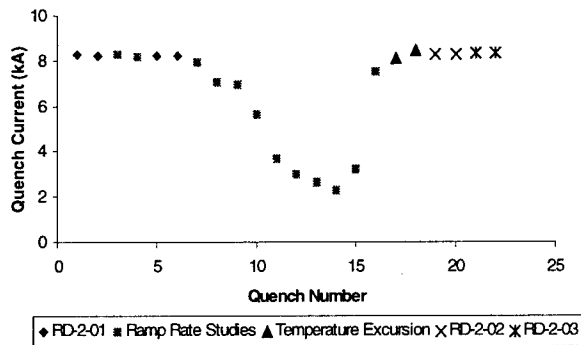
Figure 3: RD-2 Quench History

Initial ramp rates were 12 A/s. All quench initiations showed a thermal start characteristic, i.e. a gradual start with no evidence of a fast flux change, as was observed in previous Nb$_3$Sn magnet (D19 and D20) tests [4,5]. All quenches originated in the same area in coil-2, with the exception of the highest ramp rate, which occurred in coil-1. The quenches started simultaneously in both the high-field and low-field layers, within the multi-turn segments that spanned the coil's highest field region, at the approximate axial location of the inter-layer ramp, on the ramp side of the coil. Fast flux changes (probable motion voltage spikes) were monitored during the current ramps on the half-magnet balance (coil 1 – coil 2). Compared to the other Nb$_3$Sn magnets the number and magnitude of the voltage spikes were very small, exhibited unusually high frequencies and did not appear to be associated with the initiation of a quench. The magnet exhibited a monotonic-decreasing quench current as the ramp rate increased. No plateau was visible either at low ramp rates or the highest measured (540 A/s, 0.386 T/s), in contrast to the behavior of both D20 and D19. The temperature dependence at the

quench current was measured at two additional operating points, 4.68 K and 3.88 K, shown in Figure 3.

4.2 Quench Propagation

Voltage-tap signals, and signal sequences, were very similar for all quenches (neglecting current-dependent amplitude and speed variations). At any current, the propagation speeds were similar with previous Nb$_3$Sn experience (6-10m/s), but varied considerably (5 – 21 m/s) with location, indicative of sizable variations in operating margin, ohmic power density, and/or heat capacity. Propagation speeds around the island-ends appeared to be considerably (1.5-2x) faster than in adjacent straight sections.

5 DISCUSSION AND CONCLUSIONS

A 6 Tesla, Nb$_3$Sn racetrack dipole magnet has been built and systematically tested under varying preload conditions. In every configuration the magnet reached the conductor short-sample limit without training and validated the simple fabrication features of this particular magnet design. A 14 T racetrack dipole magnet, utilizing the experience gained on the 6 Tesla magnet, is currently being designed [6,7] and is scheduled for completion later this year.

6 ACKNOWLEDGEMENT

7 REFERENCES

[1] G. Danby, et al., "Proceedings of the 12th International Conference on High-Energy Accelerators," Fermilab, August 11-16, 1983.

[2] R. Gupta, "A Common Coil Design for High Field 2- IN-1 Accelerator Magnets", Particle Accelerator Conference, Vancouver, Canada, 1997.

[3] K. Chow et al., "Design and Fabrication of Racetrack Coil Accelerator Magnets," Sixth European Particle Accelerator Conference, Stockholm, Sweden, June 1998.

[4] D. Dell'Orco, et al., "A 50 mm Bore Superconducting Dipole with a Unique Iron Yoke Structure," IEEE Transactions on Applied Superconductivity, vol. 3, No. 1, March, 1993.

[5] A. D. McInturff, et al., "Test Results for a High Field (13 T) Nb$_3$Sn Dipole," Particle Accelerator Conference, Vancouver, Canada, May, 1997.

[6] K. Chow, et al., "Mechanical Design of a High Field Common Coil Magnet," These proceedings.

[7] R. Gupta., "Common Coil Magnet System for VLHC," These proceedings.

Conceptual Design of the Fermilab Nb3Sn High Field Dipole Model

G. Ambrosio, N. Andreev, T. Arkan, E. Barzi, D. Chichili, V. Kashikhin, P.J. Limon,
T. Ogitsu, J.Ozelis, I. Terechkine, J.C. Tompkins, S. Yadav, R. Yamada,
V. Yarba, A.V. Zlobin*, FNAL, Batavia, IL, USA
S. Caspi, LBNL, Berkeley, CA, USA,
M. Wake, KEK, Tsukuba, Japan

Abstract

A short dipole model with the 10-11 T nominal field based on the Nb3Sn superconducting strand is being developed at Fermilab in collaboration with LBNL and KEK as part of the R&D effort for VLHC. This paper describes the magnet conceptual design and parameters as well as the results of magnetic field, mechanical and quench protection calculations. Parameters of the superconducting strand and cable are also reported.

1 INTRODUCTION

Among the approaches for a post-LHC Very Large Hadron Collider (VLHC) of 100 TeV center-of-mass energy are designs based on superconducting High-Field Magnets (HFM). A VLHC built with HFM has the advantage of relatively small machine circumference and emittance damping due to synchrotron radiation, but has to accommodate the radiation power absorbed in the beam tube. While an optimum field range has yet to be determined, an operational field between 10 T and 12 T results in sufficient radiation damping effect without overpowering and significant complication the cryogenic and vacuum systems of the machine.

Development of HFM with the 10-12 T nominal field based on the NbTi strand is practically impossible because of the upper critical field limitation. Alternative superconductors for high field magnets are A15 alloys and Nb3Sn in particular, having higher critical magnetic field and critical temperature. Recent progress in the development of Nb3Sn superconducting strands [1] makes it possible to design cost-effective accelerator magnets with a nominal field range of 10-12 T based on a shell-type (cosθ) coil geometry. Extensive studies of shell-type designs with small bore diameter of 30-50 mm, with a different current block arrangement and cable parameters, etc., were carried out during last year. Their main goal was the determination of optimal magnet parameters, development of the robust and cost effective design and technology. The results of these studies will be reported separetelly. This paper presents the description of the conceptual design of the first Nb3Sn short models to be fabricated and tested at Fermilab in frame of High Field Magnet R&D program.

2 MAGNET DESIGN

The design of the HFM consists of two layer shell-type coil with a 44.5 mm bore and cold iron yoke. Figure 1 shows the magnet coil cross-section.
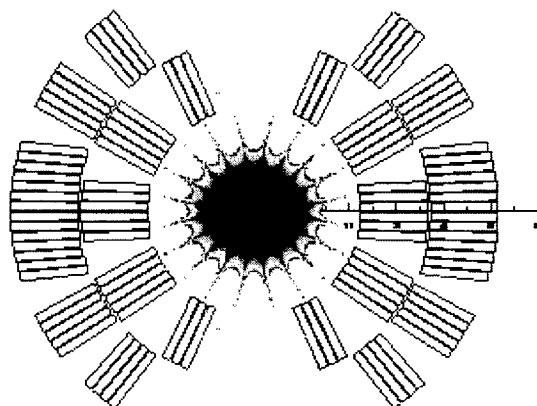
Figure 1: HFM coil cross-section.

One keystoned Rutherford-type Nb3Sn cable is used in both inner and outer layer. The cable has the width of 14.24 mm, the mid-thickness of 1.80 mm and the keystone angle of ~1 degree. Strand and cable parameters are presented in Table 3 and 4. The cable is insulated with a high temperature ceramic insulation having 125 μm azimuthal and 125 μm radial thickness [2].

Each coil consists of 27 turns, 11 turns in the inner layer and 16 turns in the outer layer. The inter-layer insulation thickness is 0.28 mm and the thickness of the mid-plane insulation is 2×0.125 mm for each layer. Each coil has four spacers per quadrant, two for each layer, which are used to minimize the low order geometrical harmonics and to ensure the radial turn position in the coil. The coil ends have also a blockwise layout of turns to reduce the maximum field and to improve the end field quality.

The iron yoke has an inner diameter of 120 mm and an outer diameter of 400 mm. The yoke inner diameter was determined by a chosen thickness of the coil/yoke spacer. The iron outer diameter was chosen based on the fringe field reduction, minimization of yoke volume and available contact tooling. No special holes are used at

this stage. The final optimization of the iron yoke cross-section will be done later.

Calculated magnet design parameters are presented in Table 1.

Table 1: Magnet design parameters

Parameter	Unit	Value
Magnet bore diameter	mm	44.5
Maximum central field	T	12.28
Short sample limit	kA	18.14
Central field transfer function	T/kA	0.7407
Coil current @ 11 T central field	kA	16.25
Stored energy @ 11 T	kJ/m	252
Magnet inductance	mH/m	1.91
Coil area	mm^2	2512

The maximum central field presented in Table 1 was calculated without the iron saturation effect and cable degradation effect. These effects reduce the maximum field by 5-10%.

The design was optimized to increase the inner coil pole width and to reduce the coil volume. The large pole width of 16.36 mm in this design is quite comfortable for the inner-layer pole-turn winding. The coil cross-section area in this design is by factor of 1.9 smaller than one in MSUT (design field is 11.4 T) [3] and by factor of 2.7 smaller than D20 coil cross-section (design field is 13 T) [4].

The design low-order harmonics for the dipole central field and harmonics RMS spread for block random displacements within ±50 um, calculated with ROXIE [5] assuming an iron yoke permeability of 1000, are reported in Table 2 at 1 cm bore radius.

Table 2: Field harmonics

n	bn	σ(an), σ(bn)
2	-	1.198
3	-0.000	0.564
4	-	0.279
5	0.000	0.103
6	-	0.047
7	-0.007	0.021
8	-	0.008
9	-0.071	0.005
10	-	0.001
11	0.103	0.003

Both geometrical (systematic) low order harmonics and their expected RMS spread are small and meet the field quality requirements for the accelerator magnets [6].

Nb3Sn strands produced using the internal tin process have quite high effective filament diameter of ~70-100 um. Expected contribution of coil magnetization for d_{eff}=70 μm to b3 is –40 units and to b5 is +5 units at 1 kA. These values are too large and must be significantly reduced by reducing the effective filament diameter to the

level less than 10-20 μm. Eddy current magnetization effects, related to the eddy currents in strands and in the cable, are not presented here. They will be reduced using small filament twist pitch and providing a high interstrand resistance in the cable.

The effect of iron saturation on the field quality is also quite large. The range of variation for b3 is within 6-7 units at 1cm reference radius for the chosen yoke cross-section. The effect on higher order harmonics is small. Iron saturation effect will be corrected in future by optimizing the hole size and position in iron yoke.

Magnet protection in case of quench provided by internal quench heaters. They are installed in between the inner and outer layers to quench all inner and outer turns. Quench analysis was done for one operating heater.

According the calculations to keep the cable maximum temperature after quench below 300 K, the quench integral has to be less than $16 \cdot 10^6 A^2 s$. At current of 16 kA the heater induced quench integral is $11 \cdot 10^6 A^2 s$. It corresponds to the coil temperature under heater 160 K in the inner layer and 120 K in the outer layer. The calculated maximum turn-to-turn voltage is less than 15 V and coil-ground voltage does not exceed 100 V for 1 m long model. As it can be seen, the quench protection scheme with inter-layer heaters provides low maximum coil temperature and low voltages in the magnet.

3 COIL SUPPORT STRUCTURE

HFM cold mass cross-section is shown in Figure 2. The coils are mechanically supported by the vertically split iron laminations locked with two aluminum or stainless steel clamps and the stainless steel helium vessel skin. Thick end plates are used to restrict the longitudinal coil motion under Lorentz forces.
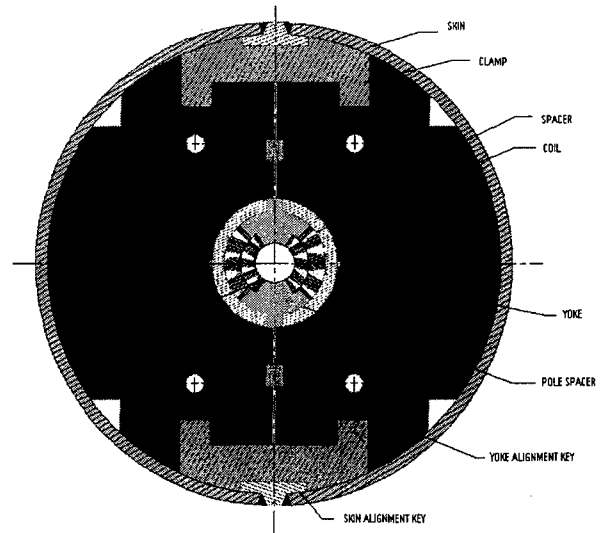
Figure 2: Cold mass cross-section.

Two 8 mm thick aluminum or brass spacers fill the space between the coil and yoke and protect the coil

during assembling. The initial coil preload during assembling and the magnet geometry (vertical gap) control at room temperature is provided by two clamps. Final coil prestress at operation temperature, necessary to reduce the radial and azimuthal turn motion under Lorentz force action, is created with the help of a two-piece iron yoke, two clamps and a welded stainless steel helium vessel skin.

Preliminary calculations show that maximum radial and azimuthal stresses applied to the cable in the coil is less than 100 MPa. Finite element analysis using ANSYS is being performed now to optimize the azimuthal coil prestress at room and at operation temperatures and to determine tolerances and maximum stresses in the major elements of magnet support structure.

4 CONDUCTOR DEVELOPMENT

The superconducting strands for the HFM first short model are being produced by IGC using internal tin process. Strand parameters are summarized in Table 2.

Table 2: Nb3Sn strand parameters

Parameter	Unit	Value
Strand diameter	mm	1.00
Effective filament diameter	μm	<70
Cu:nonCu ratio		0.85:1
Residual resistivity ratio (RRR)		>75
Twist pitch	mm	15
Ic(12T,4.2K)	A	800
Jc (12T,4.2K)	kA/mm^2	1.886

The R&D program aimed to improve the Nb3Sn strand parameters and to reduce its cost supported by U.S. Labs, universities and industry has been started. The main goal of the program is to increase a critical current density J_c(12T,4.2K) in strands up to 2000-2500 kA/mm^2 at an effective filament diameter of 20 um or less.

The main HFM cable parameters are listed in Table 3.

Table 3: Cable parameters

Parameter	Unit	Value
Number of strands		28
Strand diameter	mm	1.00
Cable width	mm	14.24
Mean thickness	mm	1.800
Minor edge	mm	1.687
Major edge	mm	1.913
Packing factor		0.884

Cable samples with different packing factor have been fabricated by LBNL and tested at Fermilab. Critical current degradation with respect to round strand measured on the strands extracted from cable as function of the cable packing factor is shown in Figure 2.
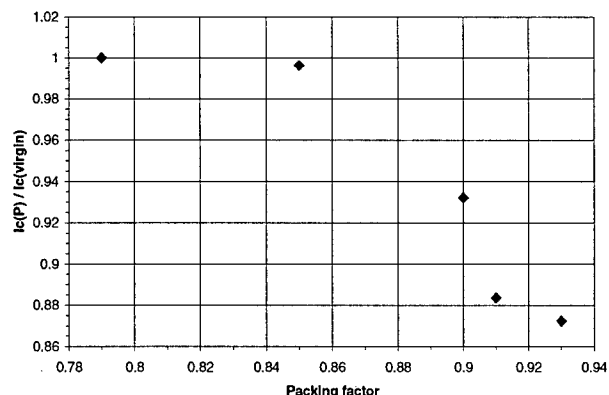
Figure 2: Effect of packing factor on the cable critical current degradation.

The data show that the critical current degradation after cabling for Nb3Sn strand could be less than 5% if cable packing factor does not exceed 88%. Based on the results of stress calculations the additional cable critical current degradation caused by the azimuthal and radial stresses applied to the cable in the coil at expected stress level will be reversible and small, less than 6% [7].

5 CONCLUSIONS

The design of Nb3Sn dipole model, developed by the Fermilab/LBNL/KEK collaboration, allows to reach the maximum field of 11-12 T with existing Nb3Sn superconducting strand and to reduce significantly the coil cross-section. The presented design concept as well as the basic technological solutions will be studied experimentally on a series of short models. The development of HFM engineering design and tooling has been started. Tests of the first short model are planned for the Fall of 2000.

6 REFERENCES

[1]. E. Gregory and T. Pyon, "Some Recent Developments In Low Temperature Superconductors For Fusion, High Energy Physics And Other Applications", Proc. of ICEC'17, Bournemouth (UK), 1998, p.399.

[2]. C. Chichili et al., "Niobium-Tin Magnet Technology Development at Fermilab ", presented at PAC'99.

[3]. A. den Ouden et al., "Application of Nb3Sn Superconductors in High-Field Accelerator Magnets", IEEE Trans. on Applied Superconductivity, Vol. 7, No. 2, June 1997, p.733.

[4]. A.D. McInturff et al., "Test Results for a High Field (13 T) Nb3Sn Dipole", PAC'97

[5]. S. Russenschuck, "A Computer Program for the Design of Superconducting Accelerator Magnets", CERN AC/95-05 (MA), September 1995.

[6]. Superconducting Super Collider, Conceptual Design, SSC-SR-2020, March 1986, p.151

[7]. H. ten Kate, "Recent Developments on PIT Nb3Sn conductors", High Field Accelerator Magnet Workshop, Erice, March 12, 1999.

PROSPECTS FOR THE USE OF HIGH TEMPERATURE SUPERCONDUCTORS IN HIGH FIELD ACCELERATOR MAGNETS[*]

D. C. Larbalestier[+] and P. J. Lee,[#]

Applied Superconductivity Center, University of Wisconsin–Madison, Madison WI

Abstract

Several future accelerators will require magnets to operate above 10 T (for example the proposed Muon and Hadron colliders). In this new domain of accelerator magnets, the pre-eminence of Nb-Ti falls away. In the time frame of new accelerator construction (10-20 years), there are strong opportunities to bring on new classes of superconductor (advanced A15, HTS), provided that serious, focused efforts start soon. Of the primary HTS superconductors, $Bi_2Sr_2CaCu_2O_x$, $(Bi,Pb)_2Sr_2Ca_2Cu_3O_x$, and $YBa_2Cu_3O_7$, the most promising for near-term high field magnet application is $Bi_2Sr_2CaCu_2O_x$ (Bi-2212). However, HTS conductors are still at an early stage of development and continued improvement over the next ten years could make other HTS superconductors available for accelerator application. Bi-2212 appears to have the highest potential today, because it can be made in round wire form with reasonably high J_c values, thus permitting access to the cabling technology developed for LTS materials. Bi-2223 and YBCO are both presently limited to wide-tape designs, for which cabling is a significant challenge. Development of less aspected conductor designs might permit YBCO coated conductors to drive out 2212 as the present conductor of choice. An alternative approach is to design magnets around the use of aspected conductor forms and anisotropic properties in order to make the most of the unique properties of HTS superconductors.

1 INTRODUCTION

It has been 13 years since the discovery of high temperature superconductors (HTS) [1] but it is likely to be at least as long until a next generation of accelerators that might fully exploit them goes into construction. Some planning and speculation as to how HTS might enter into HEP construction plans is therefore appropriate. At this time, conductors made from HTS have made considerable progress towards viability for magnets useful for utility applications, where the essential need is that HTS replace copper and iron. This means that their main present target is dominated by lower field uses (1-2 T, occasionally higher) than most LTS applications, and by cost. Today, HTS conductors made of multifilamentary Bi-2223

$((Bi,Pb)_2Sr_2Ca_2Cu_3O_x)$ (see Figure 1) are being applied to significant prototype motors, transformers, power cables, fault current limiters, and other utility applications [2]. The principal limitation on their eventual use is now seen to be primarily economic, since most electrotechnical and utility applications are already available from conventional uses of Cu, Fe and Al. Accelerator applications are generally fundamentally different, in that superconductivity is a vital enabling technology and they are also demanding in what they expect of the superconductor. Thus the HEP view of HTS is not at all the same as the utility market view of HTS

2 HEP MAGNET SYSTEMS

There are essentially two types of magnet that HEP wants, dipole and quadrupole magnets with bores of a few tens of millimeters for beam steering, and large detector magnets of many meters diameter for beam interaction analysis. Present designs of large hadron colliders (e.g. LHC) are already at 8 T for main ring dipoles and more than 10 T for specialty quadrupoles. By contrast, beam interaction analysis magnets are often meters in diameter and they continue to get bigger. However, their fields remain in the 1-2 T range, which is comfortably accessible by present day Nb-Ti conductors.
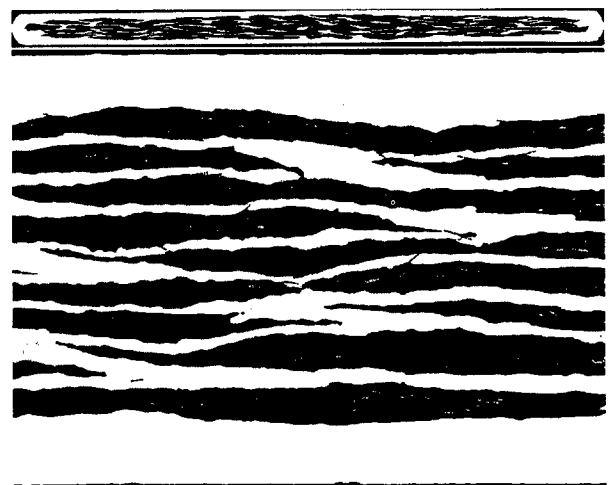
Figure 1: Cross-sectional detail of 85 Filament $(Bi,Pb)_2Sr_2Ca_2Cu_3O_x$ conductor from American Superconductor Corporation with inset overview of cross-section. Typical dimensions of such a conductor are 4 mm by 0.2 mm and the zero field critical current is about 100 A at 77 K and 500 A at 4.2 K.
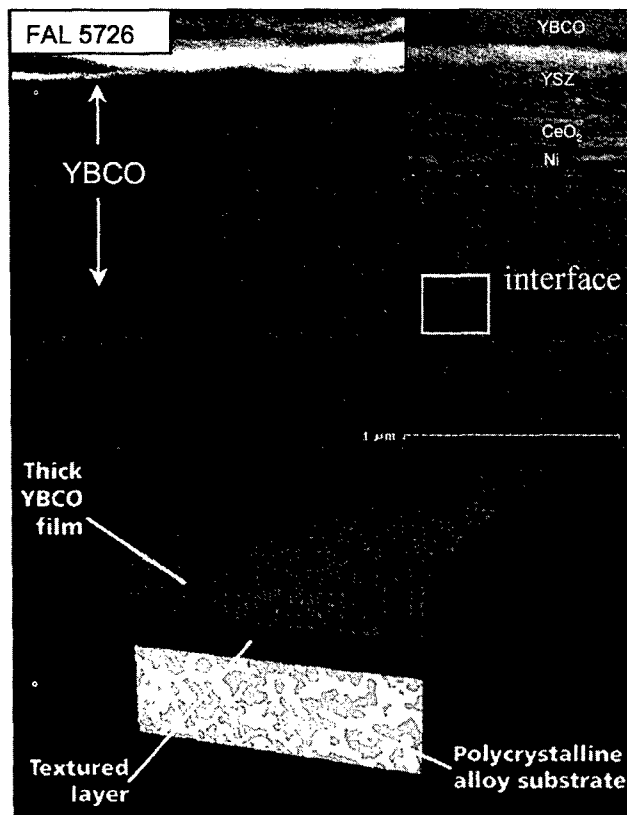
Figure 2: Y-123 coated conductors in the two presently favored formats. The upper cross-section of a rolling-assisted-biaxially-textured-substrate (RABiTS™) conductor made at ORNL and imaged by Yang and Babcock at UW shows the complex substrate ([001]-textured Ni), 3-layer buffer of CeO_2/Y_2O_3-stabilized ZrO_2 (YSZ) with superconducting YBCO overlayer. The alternate approach developed by Fujikura Electric and LANL is illustrated at bottom (courtesy S. Foltyn at LANL). In this case the substrate is untextured and the buffer layer (normally YSZ) is textured by ion-beam-assisted-deposition (IBAD) process. Both routes lead to a wide-tape, monofilament conductor. Typical dimensions are 1 cm wide, 1-2 μm thick Y-123, 1 μm thick buffer layer(s) and 100 μm thick substrate. Such a conductor can have a critical current of 100-200 A at 77 K and some 7-10 times larger at 4 K.

3 HTS CONDUCTOR OPTIONS

Today there are three HTS materials from which useful conductors can be made. They are the two micaceous Bi-Sr-Ca-Cu-O (BSCCO) compounds $Bi_2Sr_2CaCu_2O_x$ (Bi-2212) with T_c ~90 K and $(Bi,Pb)_2Sr_2Ca_2Cu_3O_x$ (Bi-2223) with T_c ~107 K, and the metallic reservoir layer compound $YBa_2Cu_3O_{7-x}$ (Y-123) with T_c of ~92 K. However, in the context of a still great worldwide interest in high temperature superconductivity (and the very recent report of surface superconductivity [3] in the Na-doped WO_3), we should still admit the possibility of the discovery of new compounds that might replace the present choices. Most of us in the superconductivity community have a mindset that postulates that new superconductors of higher T_c are going

to be more complex than any low temperature superconductor (LTS). However, there is no firm and explicit basis for his belief, and we should remain open to pleasant surprises. Those who are optimists may be heartened by the recent interest of the popular author, Tom Clancy, in superconductivity. In his 1999 book, "Carrier", he describes the discovery of superconductivity well above RT in wires of a Cu-Pt-Sc mix [4] in the year 2016! Apparently the simultaneous discovery of large Pt and Sc reserves in Sri Lanka also makes the material very affordable, halts a nuclear skirmish between India and Pakistan, and leads to the award of both the Physics and Chemistry Nobel prize to the discoverer and to instant widespread applications too!

Turning back to today's conductor designs, they are either large aspect ratio multifilaments (Figure 1), round wire multifilaments (Figure 3) or monofilament tapes (Figure 2), Bi-2223 (or Bi-2212) exemplifying the first, Bi-2212 the second, and Y-123 the third. Before going into the details of fabrication that govern their availability, we first turn to discussion of the underlying properties that determine their suitability for conductors. The key issues that must be addressed in order for HTS to be made into successful conductors are:

High critical current density.
Temperature capability.
Strength.
Length availability.
Cost and performance competitiveness with LTS conductors.

Of the above issues, only improved temperature capability by HTS conductors is fully satisfied in the competition between HTS and LTS superconductors such as Nb-Ti and Nb_3Sn. Attaining high enough overall J_c in reasonable conductor forms is the biggest present obstacle to applications and the one that we emphasize most in the limited space available here.

4 PREREQUISITES FOR HTS USE

4.1 High Critical Current Density

The most fundamental requirement of any viable conductor is that it must have a high critical current density, J_c, in the field range needed for the magnet. High normally is taken to mean values of $>10^3$ A/mm^2 flowing in the superconductor cross-section. For low temperature superconductors, we expect that J_c is primarily determined by flux pinning (filament cross-sectional variation (sausaging) may reduce the flux pinning determined J_c by factors of order 10 %), but for HTS materials this is very far from being the case. Figure 4 shows that the best HTS conductors exceed this baseline value, BSCCO at 4 K (and perhaps up to 15-20 K), while Y-123 does this comfortably at 77 K. However, a central fact of all HTS polycrystalline forms is that the supercurrent percolates, because it is im-
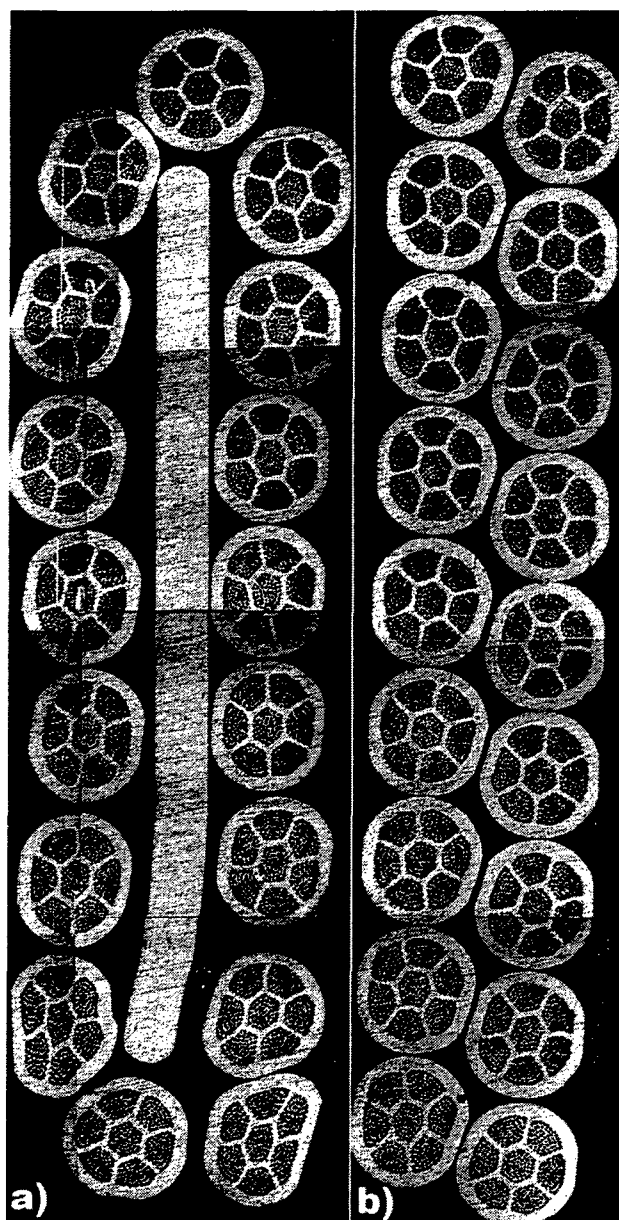
Figure 3: Cable wound at LBNL from round multifilamentary "double stack" Bi-2212 conductor made by Showa Electric a) with and b) without Ag core. The I_c values are around 280 A at 4.2 K and self field, for the 0.8 mm diameter strands. Images courtesy of D. Dietderich (LBNL).

peded by obstacles on multiple length scales. This percolation results in loss of vital information in understanding the attainable current densities in many conductor forms, because the presence of so many barriers means that the actual cross-section occupied by transport current is a continuously varying and in general unknown quantity. What can be measured to high accuracy is the critical current, I_c, but the conversion to J_c produced by dividing by the *total cross-sectional area* of superconductor contains little fundamental information.

This percolation is illustrated by representative flux penetration pictures obtained by magneto optical (MO)
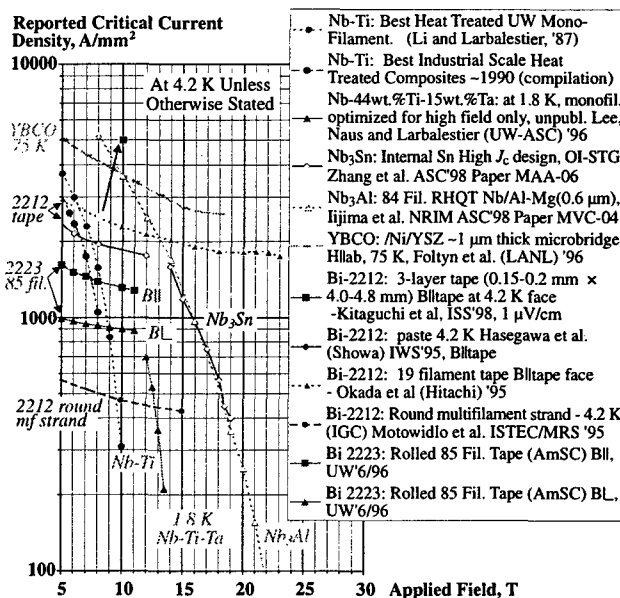
imaging of 2212, 2223, and Y-123 conductors in Figure 5 and Figure 6. The image contrast comes from the non-uniformity of flux penetrating into the superconductor. Flux obviously penetrates Bi-2212 and Bi-2223 differently. The fine network in Bi-2223 has its origin in the many cracks that populate 2223 filaments. Bi-2212, being melt processed at its final stage, suffers from porosity on a larger scale, while the origin of percolation in Y-123 is less clear at the present time. The larger length scale of the granularity is important, since it means that typical Bi-2212 conductors have overall J_c values 2-3 times those of Bi-2223 conductors at low temperatures, even though Bi-2212 has the lower T_c.

At the smallest scale, the ultimate limit to J_c is defined by the depairing current density, J_d, the current density of the Meissner sheath or the circulating current around each vortex. Since $J_d \sim 0.5\ H_c/\lambda$, where H_c is the thermodynamic critical field and λ is the penetration depth over which currents circulate, values of J_d well exceed the needed value of J_c, since they reach 10^6 A/mm^2 at 4 K and 10^5 A/mm^2 at 77 K. The flux pinning current density, J_{fp}, is typically up to 10 % of J_d. It is determined by the density of pinning sites in the microstructure and the vortex density gradient that they can support. Thus more than adequate J_c is available from flux pinning too, even if the value of order 10^4 A/mm^2 at 77 K must be derated somewhat to take account of flux creep, a phenomenon not normally considered in LTS materials.

The first barrier seen by these large values of local, *intra*granular critical current density, J_{fp}, are grain boundaries of arbitrary misorientation, which in general have significant local strain and disorder and depressed superconductivity, which makes the boundary a barrier to current flow. Although the magnitude of this effect is known well for special [001] tilt boundaries in Y-123 (the inter-
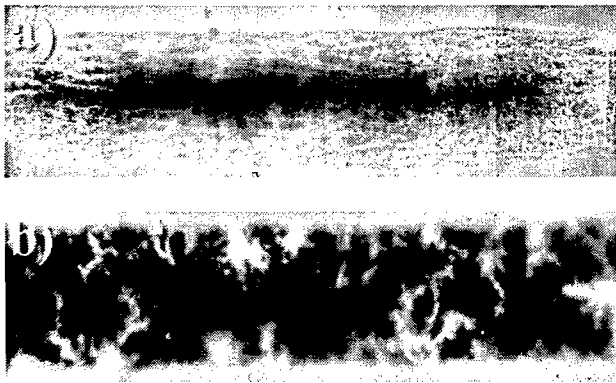
Figure 5: Magneto optical images (T = 20 K, B = 72 mT) of a) Bi-2223 and b) Bi-2212 tape conductors. Residual, preferentially oriented crack-like defects extend along the tape axis in the Bi-2223 conductor as a result of thermomechanical processing. The Bi-2212 exhibits better flux shielding because it does not undergo a heavy mechanical deformation step after heat treatment. However, the melting step inherent in its optimum processing produces larger scale defects such as pores and secondary phases. The generally better connectivity of Bi-2212 means that its low temperature critical current density is higher than that of Bi-2223, even though Bi-2223 has the higher transition temperature. Images courtesy of A. A. Polyanskii (UW).

granular J_c, J_{gb}, is depressed by about 10^3 [5,6] on increasing the misorientation from 0 to 45°), it is not well known for most boundaries and there are interesting signs that the doping state of the compound plays an important role in determining and perhaps ameliorating these strong barriers to current flow [7]. This strong dependence on misorientation is the reason for using texturing methods for making Y-123 coated conductors, as noted in Figure 2.

Larger scale barriers are cracks and voids, which are in these authors opinions [8-9] amongst the most serious contributors to the degradation of J_c in the Bi compounds, while sausaging also contributes 20 to 100 % degradations to J_c. Thus the final J_c determined by the measurements of I_c and A_{total} is a much reduced, trickledown J_c, in which an inherently high flux pinning J_c is reduced by factors of order 10 to 100 in BSCCO and perhaps 5-10 in Y-123. This is of course also a big opportunity to improve the J_c since the factors controlling J_c are not fundamental ones, but rather those affected by the processing into useful conductor forms.

We finally should note that the working J_c of the conductor is further diluted by the support structure (as seen in Figure 2, the superconductor cross-section in coated conductors is only about 1 % of the substrate and buffer layer) and the need to add a normal metal stabilizer, typically about equal to the superconductor cross-section. Thus the J_c values of Figure 4 may be seriously misleading when applied to real conductors, of which in any case only BSCCO are available in lengths beyond 1 m today.

Figure 6: Magneto Optical image (FC in 60 mT to 77 K, field then decreased to zero) of a 0.6 MA/cm^2 (77 K, 0 T) Y-123 coated conductor tape (FAL5727) showing the granular flux penetration characteristic of supercurrent percolation. Sample courtesy of A. Goyal (ORNL and image courtesy of A. Pashitski (UW).

4.2 Temperature Capability

As suggested by Figure 4, it seems that only Y-123 is viable for making strong magnets at 77 K. The determining factor is the irreversibility field H^*(T) at which the J_c goes to zero [10]. This has typical values of 5 T (Y-123) and 0.3 T (Bi-2223) at 77 K. The BSCCO compounds do not achieve H^* which exceeds 5 T until the temperature is reduced below about 25-30 K, while Y-123 has H^* exceeding 20 T at such temperatures.

4.3 Strength

Pure Ag is very soft, but it can be hardened by alloying additions. Ag doped with ~0.5-2 wt.% Mg is the most favored present alloy, permitting yield strengths up to 350-Mpa which is more than 5 times the value for Ag sheathed tapes [11].

4.4 Length Availability

Today BSCCO-2223 available in 0.5-1 km lengths from several companies world wide in conductor forms such as that shown in Figure 1. Since such wide tape conductors have I_c values of 100 A or less, they often need to be assembled in parallel. For magnets co-winding a stack of 3-5

conductors is presently the most favored method, but this is rather primitive compared to accelerator demands and expectations from LTS conductors, where the fully transposed Rutherford cable is generally favored. Full (or at least one-layer) transposition can be attained in power cables by twisting the tapes around a core, since only operation in self field is required and the loss of space (often used for cooling) in the core is not material. The Pipatron concept for making a VLHC magnet is compatible with this form of cable [12]. Since the need to make aspected conductors from HTS compounds is fundamentally driven by their layered atomic structure, there is an important need to find new ways to cable HTS conductors or to use aspected conductors in new magnet designs. Recent common coil designs may be one such approach [13].

The most promising present conductor for saddle coil applications is in fact Bi-2212. The melt processing that is applied to make 2212 permits reasonable connectivity (the main factor controlling percolation and thus J_c) in round wire form. Scanlan's group at LBNL have been developing this with several manufacturers and one such cable operating at ~4000 A at 4 K is shown in Figure 3. Such a cable is now being made in lengths of ~100 m and will soon be tested in coil designs common to Nb-Ti and Nb_3Sn conductors too, permitting a direct comparison of HTS and LTS performance.

Since Y-123 conductors are not yet available in more than 1 m lengths and their form is that shown in Figure 2, they face several problems common to Bi-2223, exacerbated for now at least by the very large fraction of substrate that so strongly reduces the overall J_c of the conductor. Much present effort world-wide is aimed at reducing this overall J_c limitation and in scaling up for long-length manufacture.

4.5 Costs

Present costs of HTS wire are high but since they are made on a still small scale with much high-priced characterization, it seems not necessary to be too strongly concerned by present costs for the long term. The raw material costs of Ag and BSCCO powder are within about a factor of two of the same for Cu and Nb-Ti, but conductor costs expressed in $/kA.m are more than a factor of 100 different. Thus raising J_c and scale up are crucial parameters to be addressed for HTS conductors.

5 CONCLUSIONS

As this very brief review has summarized, HTS conductors suitable for HEP saddle coil applications are still some way from being commodity items, because they are still primitive, of lower working overall J_c and higher cost than competing LTS conductors. But LTS conductors have had some 35 years of development, strong improvements coming even in the last 10 years, making it not appropriate either to abandon LTS or HTS conductors. HEP magnet builders with HTS interests can now start to play an im-

portant role in developing the technology, pushing the development of HTS conductors in ways that have been so productive for LTS conductors [14]. And although not discussed here, HTS current leads are likely to be applied to all future accelerators, providing the first entry point of the new technology to HEP.

7 REFERENCES

[1] J. G. Bednorz and K. A. Muller, "Possible high T_c superconductivity in the Ba-La-Cu-O system," *Zeitschrift-fur-Physik-B*, vol.64(2), pp.189-93, (1986).

[2] R. D. Blaugher, "Superconducting electric power applications," *Adv. Cryo. Eng.*, vol. 42, pp. 883-898, (1996).

[3] S. Reich and Y. Tsabba, "Possible nucleation of a 2D superconducting phase on WO_3 single crystals doped with Na^+," to be published in the *European Physical Journal B*, 1999.

[4] Tom Clancy, "Carrier: a guided tour of an aircraft carrier," Berkley Pub., 1999.

[5] D. Dimos, P. Chaudhari, J. Mannhart, " Superconducting transport properties of grain boundaries in $YBa_2Cu_3O_7$ bicrystals," *Physical-Review-B-(Condensed-Matter)*, vol.41(7), pp. 4038-49, (1990).

[6] N. F. Heinig, R. D. Redwing, J. E. Nordman, and D. C. Larbalestier, "The strong to weak coupling transition in low misorientation angle thin film YBa2Cu3O7-x bicrystals", to be published in *Physical Review B*, (1999).

[7] A. Gurevich, E. A. Pashitskii, " Enhancement of superconductivity at structural defects in high-temperature superconductors," *Physical-Review-B-(Condensed-Matter)*. vol.56(10), pp.6213-25, (1997).

[8] D. C. Larbalestier, "The road to conductors of high temperature superconductors: 10 years do make a difference," *IEEE Transactions On Applied Superconductivity*, vol. 7(2), pp. 90-97 (1997).

[9] X. Y. Cai, A. Polyanskii, Q. Li, G. N. Riley, and D. C. Larbalestier, "Current-limiting mechanisms in individual filaments extracted from superconducting tapes," *Nature*, vol. 392, pp. 906-909 (1998).

[10] D. Larbalestier, J. W. Anderson, S. E. Babcock, X. Y. Cai, S. E. Dorris, M. Feldmann, J. Jiang, Q. Li, J. A. Parrell, R. Parrella, M. Polak, A. Polyanskii, G. N. Riley Jr., M. Rupich, and Y. Wu. "New Experiments Elucidating the Current Limiting Mechanisms of Ag-Sheathed (Bi,Pb)2Sr2Ca2Cu3Ox Tapes," To appear in *Advances in Superconductivity XI*, Springer Verlag Tokyo (1999).

[11] B. Ullmann, A. Gäbler, M Quilitz, W. Goldacker, "Transport Critical Currents of Bi(2223) Tapes at 77 K Under Mechanical Stress," *IEEE Trans. Applied Superconductivity*, vol. 7(2), pp. 2042-2045, (1997).

[12] G.W. Foster, V. Kashikhin, M. S. McAshan, P.O. Mazur, H. Piekarz, J.T. Volk, R. Walker, "Conductor design for the VLHC transmission line magnet," paper TUBR5 at the 1999 Particle Accelerator Conference, these proceedings., (1999).

[13] R. Gupta, "Common Coil Magnet System for VLHC," paper THP120 at the the 1999 Particle Accelerator Conference, these proceedings.

[14] D. C. Larbalestier and P. J. Lee, "New Developments in Niobium Titanium Superconductors", in proceedings of *The 1995 Particle Accelerator Conference*, Dallas, TX, May1, pp. 1276-1281, 1996.

CONDUCTOR DESIGN FOR THE VLHC TRANSMISSION LINE MAGNET

G.W. Foster[#], V. Kashikhin, M. McAshan, P.O. Mazur, H. Piekarz, J. T. Volk, R. Walker

FNAL, Batavia, IL

Abstract

The transmission line magnet [1] is under development for the Very Large Hadron Collider (VLHC) at Fermilab with the expectation that it's cost will be several times less (per Tesla-meter) than conventional superconducting magnets. It is a dual-aperture warm-iron superferric magnet built around an 80kA superconducting transmission line. The superconductor consists of 8 Rutherford (SSC Outer) cables in an Invar pipe jacket. The conductor design requirements and development program is described. A 100kA conductor test facility based on inductive coupling is described.

Table 1: Transmission Line Magnet Parameters

Magnet Type	Warm Iron, Warm Bore
Magnet Topology	Double-C, 2-in-1
Operating Range	0.1T $\rightarrow$ 2T
Drive Conductor	Single turn, 80 kA Superconducting Transmission line
Focusing	Combined Function (no quads or spool pieces)
Normalized Gradient	3%/cm
Magnet Gap	3cm x 2cm (H x V)
Good-Field Aperture ($|\delta B_y/B_o| < 10^{-4}$)	2cm round at injection 1cm round at 2T
Iron Yoke	22cm x 24cm (H x V) Laminated Low-carbon Steel
Transmission Line	Cryopipe: 4cm OD Vacuum Jacket: 7.5cm OD
Inductance	2.8uH/m (low currents) 2.2uH/m ($2E_s/I^2$ at 75kA)

KEY FEATURES:
- Simple Cryogenic System
- Small Superconductor Usage
- Small Cold Mass
- Low Heat Leak
- Continuous in Long Lengths
- No Quads or Spool Pieces
- Warm Bore Vacuum System
- Standard Construction Methods

Figure 1 - Transmission Line Magnet

1 INTRODUCTION

When one examines the traditional cost drivers of superconducting magnets (cold mass, magnetic stored energy, superconductor usage, cryogenic heat load, etc.) the transmission line magnet (Figs. 1-2) enjoys a significant advantage over conventional designs. The simplicity of the design (low inductance single turn magnet, all-piping cryogenic system, absence of quadrupoles or complicated magnet ends, and a warm bore vacuum system which is not sensitive to synchrotron radiation) offers many advantages for large hadron accelerators. For these reasons it is being developed as an affordable magnet for the VLHC[2], a 100 TeV E_{CM} proton-proton collider under development for Fermilab. The parameters of the magnet are given in Table 1.

Fig. 2 – Transmission line magnet.

2 SUPERCONDUCTING CABLE DESIGN

The major cryogenic component of the transmission line magnet is the 80kA superconducting DC transmission line (fig. 3) that energizes the magnet. The conductor requirements are similar to a cable-in-conduit design with the following exceptions:

- Accurate positioning (±0.5mm) of the conductor must be maintained inside the iron yoke to limit magnetic decentering forces. To meet this requirement the superconductor is evenly spaced along the inner circumference of the cold pipe. This configuration also minimizes the self-field of the conductor.

- A 3cm clear bore must be maintained to allow helium transport over 4-5km. This requirement is met using a perforated Invar inner pipe around which conventional superconducting cables (leftover SSC outer coil cables) are spirally wrapped with a ~1m pitch. The cables are wrapped with copper tape and placed inside an Invar pipe jacket to contain the helium.
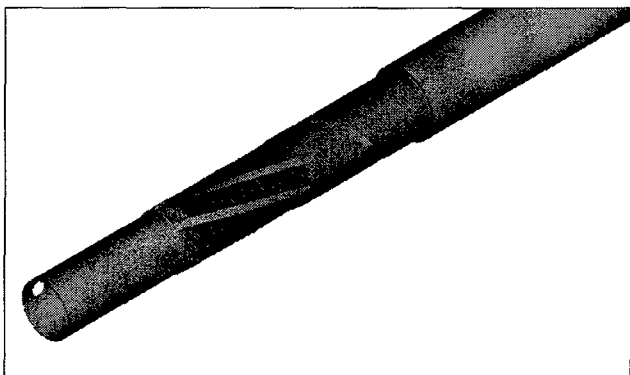
Fig. 3 – Transmission Line Conductor, including perforated Invar core, array of 8 Rutherford (SSC outer) cables, spiral wrapped copper tape (4 layers x 0.25mm), and outer Invar pipe jacket 3.81cm OD x 1.25mm wall. After assembly the inner perforated core is expanded outwards by forcing an expanding plug through the core.
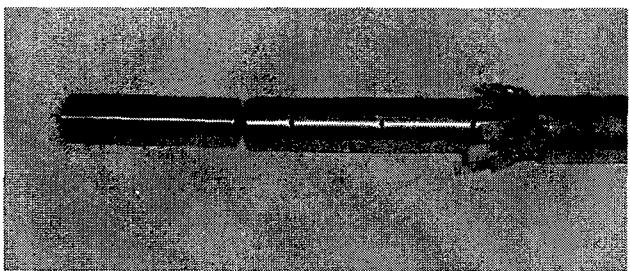
Fig. 4 – End of transmission line conductor. From right to left: Invar pipe jacket, superconducting cables, perforated Invar former, and expanding plug.

- It must operate with zero thermal contraction from 300K to 5K. This is necessary since the conductor loops around the entire ring without bellows or expansion joints. This is accomplished with an Invar jacket and by taking advantage of the longitudinal

stretchiness of the Rutherford-style superconducting cable which carries the current. To ensure reliability of the Invar cryopipe in the "zero-contraction" mode a testing program has been completed. In the test a 50 meter section of Invar pipe was cut into more than 125 pieces, re-welded together using automatic equipment, then thermal cycled 1000 times to between 300K and 80K with the ends constrained to prevent thermal contraction. After thermal cycling the pipe was checked and found to be free of leaks. The number of (welds x thermal cycles) in this test corresponds to 40 thermal cycles of the 3 TeV injector to the VLHC.

- To survive quenching, it must contain enough copper and thermal mass to allow a current dump from 100kA with a 1 second time constant. This requires ~1.5cm^2 of copper stabilizer in addition to the heat capacity of the helium and Invar piping.

- Field splices must be reasonably convenient for the conductor. A joint resistance of ~0.1nΩ (corresponding to 1W power dissipation at 100kA) is adequate. Figs. 5-6 show the techniques developed for the 100kA conductor test facility.
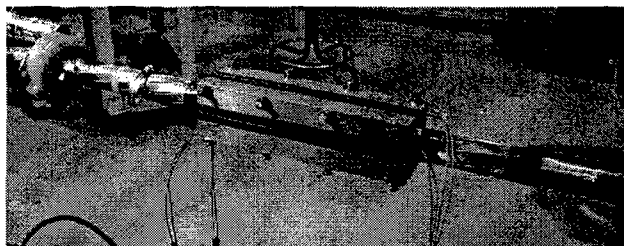
Fig 5 - Splicing technique for 100kA conductor test facility. Pre-tinned cables are interleaved and clamped in an aluminum 4-way split block with heating cartridges and temperature regulation.
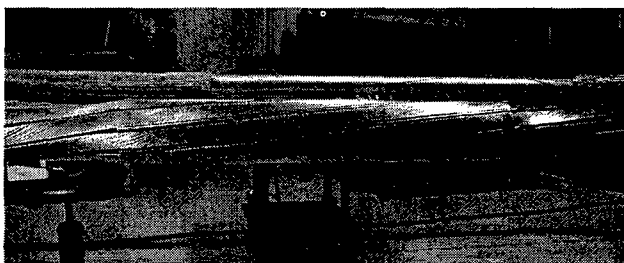
Fig. 6 – Completed splice for the conductor test loop. After soldering, the conductor is wrapped in copper tape to allow clamshell welding of the helium pipe over the splice. The vacuum jacket is made up with telescoping sections over the splice region.

3 OPERATING TEMPERATURE

The choice of operating temperature is a well-known tradeoff between superconductor costs and high-field performance (which favor a low operating temperature) and cryogenic simplicity, capital and operating costs (which favor a high operating

temperature). The trend in recent high field magnet designs is towards complicated 1.8K cryogenic systems and/or expensive conductor. In contrast, cost-optimization of the transmission line magnet resulted in conventional NbTi superconductor operating at 6.5K and a very simple single-phase cryogenic system (fig.7). The system uses no recoolers or heat exchangers and has one remotely operated valve every 4km of tunnel [3]. In contrast, high field magnet designs such as the LHC require >1 remotely operated valve per dipole.
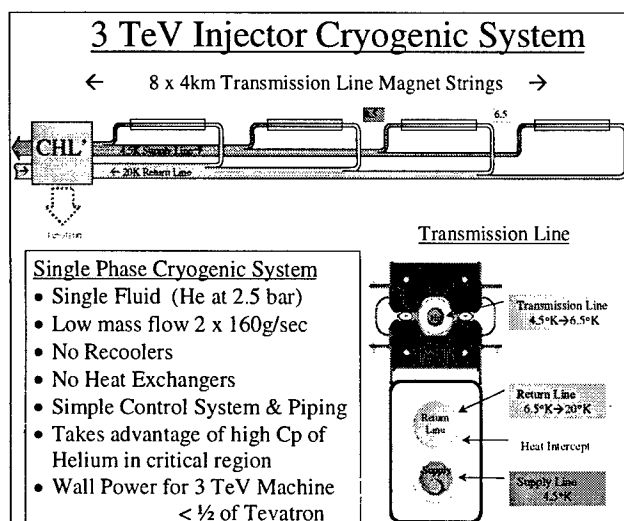
Fig. 7 – The cryogenic system of the transmission line magnets for the 3 TeV injector to the VLHC. The higher energy machine duplicates this structure, with a cryogenic plant approximately every 40km along the circumference.

Superconductor costs are only 5%(10%) of the total cost of the transmission line magnets at 4.5K(6.5k) operation. There are several reasons for this. The iron-dominated design requires fewer ampere-turns per Tesla than a conductor-dominated (cosine-theta) magnet. The conductor operates at a low field (0.9T) so that a very high current density can be achieved. The transmission line magnet does not require the micron-sized filaments needed by $\cos\Theta$ magnets, which lowers processing costs. Finally, there has been almost an order-of-magnitude increase[4] in the current-carrying capability of NbTi conductors (at low field) since the time of the Tevatron.

4 MAGNET TEST PROGRAM

A 100kA test facility is under construction at Fermilab. This is a scale up of the successfully-operated test facility reported in [5]. To avoid the expense of 100kA current leads, the facility uses a floating superconducting loop and inductive coupling through a warm-iron transformer made from an old beamline magnet. The cryogenic system is Dewar-based and consists of a pressurized and pumped loop capable of operating at temperatures between 4.5K and ~10K. Initial tests to

optimize various conductor designs [8] will use a 17m loop containing a 4m replaceable section of transmission line. The setup will then be used to power magnets of up to 50m in length.
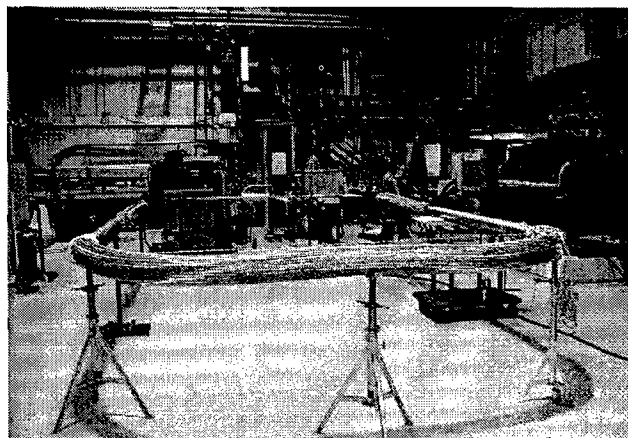
Fig. 9 – 100kA conductor test loop nearing completion. Dewar-based cryogenic system in background and drive transformer at right. The test loop contains a 4m replaceable test section of transmission line
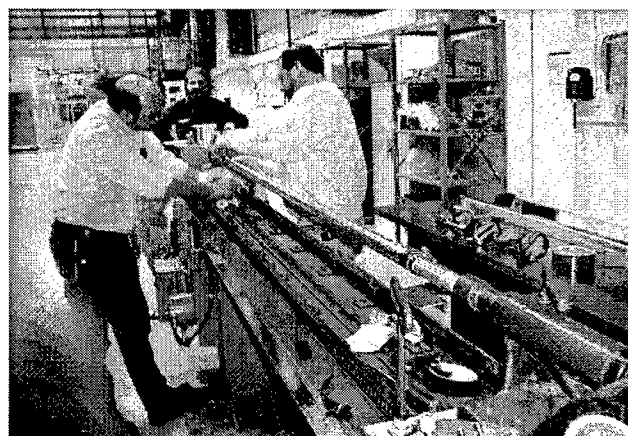
Fig. 10 – Spiral-wrapping of copper tape on prototype transmission line lengths using the wrapping machine used for Tevatron and Recycler beam pipes. The conductor design and swaging operation have been chosen to allow in-house production of 70m lengths.

5 REFERENCES

[1] "Transmission Line Magnet Status Report", G.W. Foster, VLHC Information Packet for Gilman HEPAP Subpanel, Fermilab 1998. See also [2].

[2] VLHC Project information and technical documents can be found at WWW.VLHC.ORG

[3] "Cryogenic Design of the 3 TeV Injector", M. McAshan, ibid ref [1], [2].

[4] D. Larbelestier and P. J. Lee, "New Developments in Niobium Titanium Superconductors", PAC'95.

[5] "Design & Operation of an Experimental Double-C Transmission Line Magnet", P.Mazur et. al, PAC 97

[6] E. Malamud et. al, PAC '99.

RHIC IR QUADRUPOLES AND FIELD QUALITY STATE OF THE ART IN SUPERCONDUCTING ACCELERATOR MAGNETS[*]

R. Gupta[#], Lawrence Berkeley National Laboratory, Berkeley, CA 94720, USA,

M. Anerella, J. Cozzolino, A. Ghosh, A. Jain, S. Kahn, E. Kelley, G. Morgan,

J. Muratore, A. Prodell, W. Sampson, P. Thompson, P. Wanderer, E. Willen,

Brookhaven National Laboratory, Upton, NY 11973, USA

Abstract

The interaction region (IR) quadrupoles [1] for the Relativistic Heavy Ion Collider (RHIC) [2] are the best field quality superconducting magnets ever built for any major accelerator. This field quality is primarily achieved with the help of eight tuning shims [3] that remove the residual errors from a magnet after it is built and tested. These shims overcome the limitations from the typical tolerances in parts and manufacturing. This paper describes the tuning shims and discusses the evolution of a flexible approach that allowed changes in the design parameters and facilitated using parts with significant dimensional variations while controlling cost and maintaining schedule and field quality. The RHIC magnet program also discovered that quench and thermal cycles cause small changes [4] in magnet geometry. The ultimate field quality performance is now understood to be determined by these changes rather than the manufacturing tolerances or the measurement errors.

1 INTRODUCTION

To increase the design luminosity of RHIC, the design beam size was made smaller at the crossing point [5]. An unavoidable consequence was an increase in the good field aperture required in the interaction region quadrupoles. A magnet aperture larger than the design 130 mm would have caused delay and increase in cost. A tuning shim method that extended the good field region was developed. As compared to the 80 mm aperture main arc quadrupoles, the increase in beam size in these magnets is ~400%, whereas the increase in aperture is only 63%. In the high luminosity lattice configuration, the field errors in these magnets are more critical than those in the rest of the RHIC machine magnets combined [5]. The skew (a_n) and normal (b_n) field harmonics are defined (in units) as follows:

$$B_y + iB_x = 10^{-4} G \times R \sum_{n=0}^{\infty} [b_n + ia_n] \left[\frac{x+iy}{R} \right]^n ,$$

where B_x and B_y are the components of the field at (x,y), G is the gradient at the center of the quadrupole and R is the reference radius, which is 40 mm in these magnets.
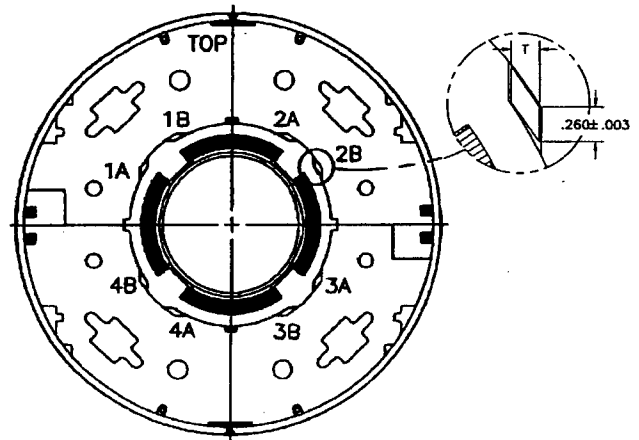
Fig. 1. Cross section of the 130 mm aperture RHIC interaction region quadrupoles. 1A, 1B, etc. are the locations of eight gaps for tuning shims. The tuning shim area at location 2B is shown in more detail.

2 MAGNET CROSS SECTION

The cross section of the 130 mm aperture insertion quadrupole is shown in Fig.1. In this design the yoke acts as a collar, a cost saving feature which is common to most RHIC magnets. An identical cross-section is used for 24 each of quadrupoles Q1 (1.44 m), Q2 (3.4 m) and Q3 (2.1 m). The parameters of these magnets are given in an earlier paper [1]. A 2-radius aperture yoke reduces the computed saturation-induced b_5 from about 17 units to less than 1 unit up to 8 kA. The design current is 5 kA and measurements performed to ~7 kA agree with these calculations. The tuning shims are inserted at eight angular locations (see Fig. 1) between the yoke and the RX630 spacers.

Another cost saving feature of all RHIC quadrupoles is the use of a 2-fold symmetric yoke design and collaring operation. This simplifies the magnet construction but breaks the 4-fold quadrupole symmetry. A large (~7 units) measured octupole (b_3) harmonic in the first

assembly was compensated by deliberately introducing an asymmetry in the coil to coil ground plane insulation (midplane gap) in later designs. This, however, generated a higher order b_7 harmonic. A proper choice of asymmetric tuning shim configuration and asymmetric midplane gaps removed both b_3 and b_7 harmonics.

3 A FLEXIBLE MAGNET PROGRAM

In a program where only a small number of magnets are required, a significant cost is associated with the magnet R&D to achieve the required quench and field quality performance. A large field margin, a flexible approach and an inherently inexpensive design were the primary factors in keeping the program cost low while producing high field quality for these insertion magnets.
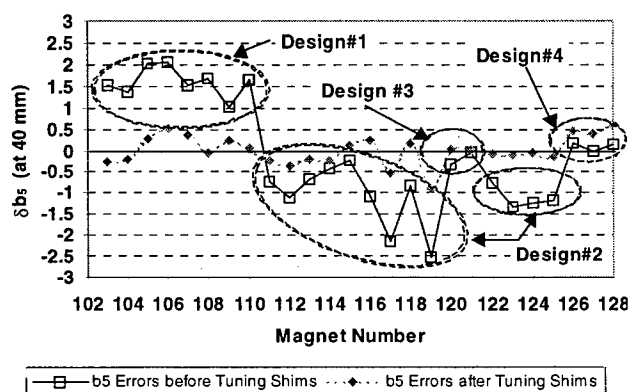
Fig. 2. A flexible design accommodated large changes in harmonics and parts without iterating the coil cross section in Q1 magnets. The figure shows the b_5 error from nominal value before (warm measurements) and after tuning shims (cold measurements at 5 kA).

At the time when this quadrupole cross section was being designed, the choice for cable insulation could not be made between two that would make the effective cable thickness differ by about 22 micron (~0.9 mil). This is about an order magnitude larger than that required before a typical magnetic design can be specified. This problem was solved by choosing a unique cross section in which such a large difference (620 micron over 27 turns) was absorbed in a rectangular wedge while maintaining a constant b_5 and pole angle. Since the pole angle did not change, the coil curing tooling and the spacer dimensions could be specified and the magnet design and construction were not delayed.

In Q1 magnets, the midplane gaps were adjusted between 150 micron and 390 micron (rather than a fixed typical value of 100 micron) and pole shims between 430 micron and 630 micron. This flexibility was used in a combination that kept the pre-stress on the coil within the desired range, while adjusting the field harmonics and accommodating variation in parts. As shown in figure 2, a large change in b_5 in design#2 and onward (required from beam dynamics considerations), a mid-

course correction for drift in b_5 (design#4), and a large 9 micron change in cable size or 243 micron in coil size (design#3), were accommodated. As mentioned in the last section, a large b_3 harmonic was also removed by adjusting midplane gaps. In the past, such changes required an iteration in the coil cross section, causing delay in production and increase in cost.

4 TUNING SHIMS

Eight tuning shims of adjustable iron thickness to adjust eight harmonics (a_2 through a_5 and b_2 through b_5) are used in each magnet. The nominal resolution of the harmonic correction, determined by the minimum thickness of iron lamination (0.125 mm) in the tuning shim package, is given in Table 1. The resolution in certain harmonics is better for certain location of tuning shim, but that may not always be realized when eight harmonics are optimized together. The resolution given in Table 1 is generally comparable to the uncertainties in the measured harmonics within a factor of 2. The reproducibility of the harmonic measurements itself was, however, an order of magnitude better than that listed in Table 1. The maximum thickness of iron in each tuning shim package is 6 mm.

Table 1. Resolution in the harmonic correction from the tuning shim package at the design current.

a_2	a_3	a_4	a_5	b_2	b_3	b_4	b_5
0.2	0.1	0.07	0.03	0.2	0.08	0.07	0.02

The iron fraction for eight tuning shims is computed to minimize the harmonics at the maximum design current (nominal value 5 kA) based on warm magnetic measurements. The tuning shim specifications required a series of tasks to be performed in a synchronous and iterative way. These tasks include: (a) an error function minimization using the weighted contributions of eight primary and eight higher order harmonics, (b) a series of non-linear iron calculations (which automatically generated input for a finite element mesh program), (c) transferring data between a number of computers, (d) generating an electronic spec-sheet for manufacturing tuning shims, and (e) computing the expected warm and 5kA harmonics after installation of tuning shims.

Each tuning shim is actually a package of fifteen (four 0.125 mm thick and eleven 0.5 mm thick) laminations - iron (magnetic) and brass (non-magnetic) – having a width of 6.6 mm. In the initial magnets, the laminations were bonded with epoxy that was found to delaminate on cool down. In the later magnets, the laminations were simply welded in the front end. The full-length tuning shims are inserted through eight holes in one end of the magnet. The magnetic forces in the iron assure a proper contact for the tuning shim iron inside the magnet once the magnet is energized.

The tuning shims significantly reduced b_5 errors in Q1 magnets (see Fig. 1). Table 2 gives the systematic and standard deviations from nominal value in normal harmonics (b_n) before and after tuning shims in all magnets. A significant improvement can be seen in harmonics b_2 through b_5. However, as a result, the higher order harmonics (b_6 through b_9) get worse, as expected, but remain of the order of 0.1 unit. A similar effect has been seen in skew harmonics also. Fig. 3 shows the standard deviations of field errors from nominal skew harmonics before and after tuning shims.

Table 2. The errors from the nominal values of the normal harmonics before and after tuning shims.

n	<b_n> (n=2 is sextupole)			$\sigma(b_n)$		
	NO-shim(W)	Shims(W)	Shims(5kA)	NO-shim(W)	Shims(W)	Shims(5kA)
2	0.41	0.01	0.05	1.74	0.41	0.56
3	0.87	-0.76	0.08	1.19	0.60	0.49
4	0.06	0.03	-0.17	0.42	0.20	0.27
5	-0.07	0.00	0.05	0.78	0.78	0.36
6	0.01	0.05	0.05	0.11	0.21	0.18
7	-0.26	-0.07	-0.14	0.04	0.17	0.14
8	0.00	0.01	0.04	0.03	0.04	0.06
9	-0.03	-0.30	-0.14	0.17	0.18	0.19
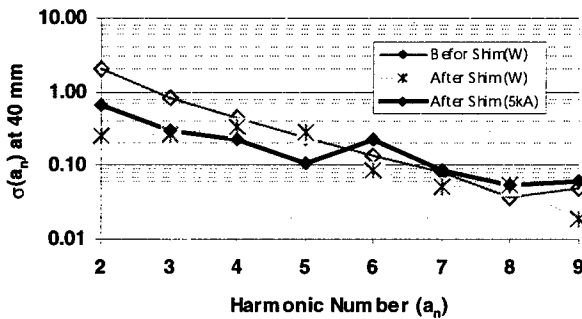
Fig. 3. Measured improvements in the Std. deviations of the lower order skew harmonics with tuning shims.

5 DYNAMIC CHANGES

The RHIC magnet program found that the field harmonics change after quench or thermal cycles [4]. Though these changes are relatively small, they are an important limitation in these high field quality magnets. An estimate of the magnitude of these changes (based on limited measurements) is given in Table 3. For non-allowed harmonics the variation is of a random nature. For the allowed b_5 harmonic and to some extent also for the semi-allowed b_3 harmonic, the change is also systematic and seems to approach an asymptotic value.

Table 3. Standard deviation (σ) of the changes in harmonics due to quench and thermal cycle in RHIC 130 mm aperture quadrupoles. σ of warm-cold (W-C) correlation is also given.

	a_2	a_3	a_4	a_5	b_2	b_3	b_4	b_5
Quench	0.4	0.3	0.1	0.01	0.4	0.1	0.1	0.1
Thermal	0.3	0.1	0.1	0.01	0.3	0.1	0.05	0.1
W-C	0.7	0.3	0.2	0.1	0.5	0.4	0.25	0.2

Similar changes have been observed in other RHIC magnets, in SSC magnets (but having smaller magnitude) and recently in 5-block LHC dipoles [6].

6 ULTIMATE FIELD QUALITY

Although the field errors in these magnets are significantly smaller than ever measured before, there is still a room for improvement. The tuning shim resolution (see Table 1) did not limit the performance and the harmonic measurement system has made large progress over time [7]. One source of remaining errors was the uncertainty due to warm-cold correlation as the tuning shim correction was based on estimating cold harmonics from the warm measurements. "W-C" in Table 6 includes the errors because of different measuring coils and a different setup of the lead configuration in two cases. In principle, this error could have been reduced, if desired, by applying harmonic correction to the cold measurements and measuring harmonics in a setup similar to that in the machine. This would, however, have improved the situation only moderately. The ultimate limit is now placed by the changes due to quench and thermal cycles, as discussed in the last section. To fully utilize the capability of the tuning shim method in future magnets, these changes must be studied systematically so that they can be made smaller. It appears that the magnitude of these changes depends on the details of magnet construction.

Sorting [8] allowed a better field quality in the critical magnets as only 2 out of 6 interaction regions will be operated in the high luminosity configuration.

ACKNOWLEDGEMENTS

The above developments would not have been possible without close interaction between the RHIC accelerator physicists and magnet scientists. In particular, discussions with Jie Wei and Steve Peggs and encouragements from Mike Harrison were critical to this development. The role of technicians is also appreciated.

REFERENCES

[1] R. Gupta, et al., "Large Aperture Quadrupoles for RHIC Interaction Region", Proc. of the 1993 Particle Accl. Conference, Washington D.C., pp 2745-7.

[2] M. Harrison, "RHIC Status", these proceedings.

[3] R. Gupta, et al., "Tuning Shims for High Field Quality in Superconducting Magnets", Proc. of MT-14, IEEE Trans. on Magnetics, Vol. 32, No. 4, 1996, pp. 2069-73.

[4] R. Gupta, et al., "Changes in Field Harmonics after Quench and Thermal Cycles in Superconducting Magnets", Proc. of the 1997 Particle Accl. Conference, Vancouver, Canada, pp 3347-9.

[5] J. Wei, et al., "Magnetic Correction for RHIC Triplets", Proc. of the 1993 Particle Accl. Conference, Washington D.C., pp 258-260.

[6] W. Scandale, et al., "Field-Shape Variation Induced by Thermal Cycling and Excitation in the LHC Dipole", these proceedings.

[7] A. Jain and P. Wanderer, BNL note RHIC-MD-281, Jan 25, 1999.

[8] J. Wei, et al., "Real World Sorting of Superconducting Magnets in the Relativistic Heavy Ion Collider", these proceedings.

PERFORMANCE AND NEW CAPABILITIES OF SPRING-8

H.Kamitsubo, N.Kumagai, SPring-8/JASRI, Mikazuki, Hyogo, Japan

Abstract

SPring-8 was commissioned in March 1997 and put into the scheduled operation in October 1997. In 1998 the storage ring was operated for 4190 hours, 62.6% of which was the user time. Presently sixteen beamlines are operational in the user service mode, five are in commissioning and seventeen are under construction. We found that specifications of the accelerators exceed the design values and it becomes clear that the storage ring has much higher performance than that we had expected in the design phase. In addition, insertion devices developed at SPring-8 have proved to be of high performance. In 1998 construction of a 30m long insertion device and beamline is started.

1 OVERVIEW OF THE SPRING-8 FACILITY

SPring-8 is the third generation synchrotron radiation source in an energy range from 0.3 to several hundreds keV. It is composed of a 1GeV injector linac, an 8GeV booster synchrotron and an 8GeV storage ring with a natural emittance of 7nmrad. SPring-8 is the national user facility enacted by the special law and is open to users not only in Japan but also from abroad.

Design studies of SPring-8 and related R&D works started in 1987. The project was decided to be promoted jointly by Japan Atomic Energy Research Institute (JAERI) and the Institute of Physical and Chemical Research (RIKEN) and the Joint Project Team was formed in 1988. The construction of the facility started in 1990 and the linac and the synchrotron were completed in August and in Decenber, 1996, respectively. Commissioning of the storage started in the middle of March and the first synchrotron radiation from a bending magnet was observed on March 23 1997. After the Dedication Ceremony held on October 6, 1997, SPring-8 entered into the scheduled operation in the user service mode [1].

The storage ring consists of 48 cells with a lattice structure of Chasman-Green type and has a circumference of 1,436m. Four of them are straight cells which are to be used for accommodation of very long insertion device. Presently the straight cell has the same arrangement of focussing magnets as the normal cell but no bending magnet. In this year, however, the construction of a beamline from a long straight section starts and beam-dynamical study to modify the magnet arrangement to realize the dispersion-free long straight sections.

Besides the long straight sections the storage ring has 40 dispersion-free straight sections of 6.5m long. One of them is used for beam injection and four are used for RF stations, each of which is composed of eight single-cell cavities of 508.6MHz. Furthermore one straight section is reserved to install harmonic cavities in future. The remaining 34 are used to accommodate standard-size insertion devices (ID). Total number of the beamlines is 62, 38 of which are ID beamlines and 23 are bending-magnet (BM) beamlines. There is one beamline for infrared spectroscopy.

The beamlines are classified into three categories; the public, the contract and the JAERI and RIKEN beamlines. Presently sixteen beamlines are operational, five are in commissioning, and seventeen are under construction.

The linac delivers 1GeV electrons to a 1.5GeV synchrotron/storage ring (New SUBARU), which is built by Himeji Institute of Technology and Hyogo Prefecture for their own use.

2 PERFORMANCE OF SPRING-8

Since the commissioning of the storage ring in March 1997, machine studies have been intensively pursued and it becomes clear that the storage ring is extremely stable and has high performance. Design values of the storage ring specifications are shown in Table 1 together with the achieved values[2].

2.1 Operation of SPring-8

Since October 1997 the storage ring has been operational in user service mode. As we had to construct more than 15 new beamlines in the past one year, we had shut down the machines in January, July and August 1998 to install their ID's and front end parts. Nevertheless we could operate the storage ring for 4190 hours in 1998 and provided photon beam to users for 2600 hours. In Table 2 is summarized the statistics of the storage ring operation in 1997 and 1998.

Presently we operate SPring-8 continuously in three weeks (one cycle). In one cycle we start the operation of the machines in Wednesday morning and usually spend one day for machine and beamline tuning and, if it is possible, machine studies. User time starts in Thursday afternoon and ends in Wednesday evening of the third week. Then machine group uses two days for machine studies. The cycle just after a long shutdown of the machines is used only for tuning of machine and new beamlines.

Currently the storage ring is operated in several filling modes, that is, a full-filling, a several-bunch and a hybrid modes. More than 62% of the user time were delivered in a full-filling mode in 1998. Recently the storage ring is operated in a 2/3-filling mode for user time.

The lifetime depends on the filling mode. At present beam lifetime at 70mA is 90 hrs in a full-filling mode and 56 hrs in the 2/3 filling mode. The reason why the beam lifetime is so long in a uniformly filling mode is that the electron beam size is grown by the instability due to an ion-trapping effect. This means that the beam quality in the full-filling mode is a little worse than that in the 2/3 filling modes so that we adopt the 2/3 filling mode for the routine operation.

Table 1: Performance of SPring-8 Storage Ring

	Designed	Achieved
Energy	8GeV	8GeV
Circumference	1435.948m	
No. of Cells (Normal / Straight)	44 / 4	
Current(Single bunch) (Multi-bunch)	5mA 100mA	12mA 100mA
Harmonic Number	2436	
Revolution Time	4.79μs	
Tunes (vx/vy)	51.22 /16.16	51.16/16.31
Chromaticities (ξ_x/ξ_y)		3.21 / 3.93
Energy Spread (ΔE/E)	0.11%	0.12%
Emittance	7nm.rad	6.8∓0.4nmrad
Coupling	<10%	0.06%
Life Time at 100mA	>10hr	~ 50hr
BunchLength (FWHM)	34.2ps	~ 40ps
Dispersion (Vertical) (Horizontal)		<0.01m <0.02m
COD (Vertical) (Horizontal)		0.05 ~ 0.1 0.05 ~ 0.1

For experiments using the time structure of the beam the storage ring is operated in the several bunch mode. Filling patterns of this mode are equally-spaced single bunches or several-bunch trains. In this case bunch purity is routinely better than 10^{-6}. Filling pattern of the hybrid mode is a mixture of equally-spaced single bunches and a long train of bunches.

The bunch length depends on the bunch current, too. We measured bunch width by a streak camera. The measured value is 40ps(FWHM) at a current lower than 1mA/bunch and, due to inductive impedance of vacuum elements such as bellows and so on, increases rapidly with the bunch current.

2.2 Emittance and Coupling

The size of the stored electron beam in the horizontal plane was measured directly in the following way: The beam is put in the bump orbit by the DC bump magnet in the injection section and then deflected by the pulse bump magnet. The amplitude of the bump orbit changes with the field strength of the DC bump magnet and a part of the beam is lost by a septum wall of the septum magnet.

Table 2: Operation Statistics of SPring-8 (October 1997 to December 1998)

	1997	1998
Total Beam Time	1290(hrs)	4190(hrs)
User Time*	980	2624
Tuning & Machine Studies**	287	1456
Loss Time due to Failures	26	110
MTBF#	43.5	43.7

* does not include loss time due to failures
** includes time for new beamline commissioning
\# mean time between failures

Horizontal charge distribution was obtained from the relation between the beam loss rate and the bump orbit. Then the horizontal emittance of the beam was determined from the width of the horizontal charge distribution and a measured beta function. The measured value of the emittance is 6.8 nmrad.

The emittance in the vertical plane depends on the coupling between the horizontal and vertical betatron oscillations. In case of the SPring-8 storage ring a skew component of the focussing magnets is very small so that the coupling is induced mainly by the nearest tune resonance of $v_x-v_y=35$. Then it is possible to estimate the coupling ratio at the normal operating point from the width of the resonance measured by detuning the horizontal tune. The other way is to extrapolate the coupling ratio from the Touschek lifetime.

The coupling ratio at the present operation point is 0.06% and the vertical emittance is smaller than 10^{-11}mrad [3]. We can change the coupling ratios from 0.05% up to 80% only by changing the operation point in the tune diagram.

Direct measurement of the photon beam emittance and accordingly the electron beam emittance is underway. Preliminary results showed the vertical beam size is around 10μm or less.

2.3 Orbit Stability

The beam stability and reproducibility in position and angle is essential for the low emittance ring. The SPring-8 storage ring and the beamlines are built on a stable rock to reduce a subsidence of the floor and ground vibrations induced outside of the SPring-8 campus. In addition, we have put a large effort to remove vibrations transmitted to the magnet girders from cooling-water pumps and to stabilize cooling water temperature. The digital feedback system is developed to stabilize the beam orbit within 0.7μm(in rms) in the horizontal plane and 0.4μm(in rms) in the vertical plane. Since the commissioning of the storage ring, a long-term variation of the circumference or the beam energy has been measured. There are two components, one with a period of 12 hours and the other with a period of one year. The former is well explained as induced by earth tide [4].

2.4 Novel Insertion Devices

High quality insertion devices are indispensable for the third generation synchrotron radiation source. We have developed various types of novel insertion devices. In Table 3 are listed the insertion devices which are currently operational and under construction. The in-vacuum undulator covers a very wide range of X-ray energy. For example, an undulator of $\lambda u = 32$mm provides X-ray from 5.2keV to 18.5keV as the fundamental radiation, 15.5keV to 51keV as the 3rd harmonics, and 26keV to 75keV as 5th harmonics [5].

The helical undulator can provide circularly polarized X-ray and has a special feature that only the fundamental radiation goes along the optical axis. Accordingly we have adopted a helical undulator as a source of the high-flux beamline. Figure-8 undulator, on the contrary, can provide linearly polarized radiation [6]. It should be pointed out that integer-harmonic radiation is horizontally polarized but half-integer harmonics is vertically polarized. In addition to these we have developed an in-vacuum mini-pole undulator of $\lambda u=11$mm for BNL, USA.

Table 3 List of Insertion Devices at SPring-8

ID (operational)		ID (constructing)	
Type of ID	λu (mm)	Type of ID	λu (mm)
in-vacuum U*	32	in-vacuum U	28 32 36 40
tandem vertical U	37	hybrid in-vacuum U	24
twin helical U	120	revolver type U	40,100
figure-8 U	120 26	long U	32 80
variably polar. U	120		
elliptical MPW	120		

* U: undulator
** variably polarizing undulator

3 NEW CAPABILITIES OF SPRING-8

At the early stage of design work, we changed the original design of SPring-8 in the following way; we increased the electron energy from 6GeV to 8GeV and changed the magnet configuration of the storage ring from 48-fold symmetric lattice to 4-fold symmetric one with 4 long straight sections. At the same time we decided to leave a possibility to lengthen several beamlines by 300m and 1000m. These modifications give new capabilities to SPring-8 and some of them are being developed.

3.1 Long Straight Section

Main purpose of the long straight sections is to install a very long insertion device to get photons of higher brilliance. By now we have organized two international workshops to discuss technical issues related to long insertion divices as well as scope of science to be done with very brilliant X-ray. Construction of the first beamline from a 25m-long undulator with $\lambda u=32$mm starts in this year. At the same time a proposal to construct the second one is prepared. Design of two long undulators is in progress. Preliminary parameters are listed in Table 4.

The magnet arrangement in the long straight sections are determined. The emittance of this lattice is the same as that of the present lattice.

The magnet arrangement will be changed in the summer of 2000. Experimental program at this beamlines is being discussed.

Table 4 Design Parameters of Long Undulators

	Long X-ray U	Long Helical U
total length	25 m	25 m
periodic length	32 mm	80 mm
period number	780	312
energy range	8 ~ 18keV (1st) 24 ~ 38keV (3rd) 40 ~ 50keV (5th)	0.2 ~ 6keV (1st)
brilliance	8×10^{20}	3×10^{20}

3.2 Long Beamline

There are three beamlines which can be lengthened by 1,000m. The first one is from a standard-size undulator, the second is from a bending magnet, and the last is from a long undulator. Construction of one long beamline from the in-vacuum undulator with $\lambda u=32$mm starts this year. The purpose of this beamline is to pursue various experiments with precise phase measurement in hard X-ray region. Experiments of ultra small angle scattering is also planned. The beamline will be completed in 2001.

Two beamlines of 200m long are under construction. One is a BM beamline and the other is an undulator beamline and both are used for medical application of synchrotron radiation. The former is in commissioning and test experiments will start in this fall. The latter will be completed in 2000. The experimental stations of these beamlines are in the building which locates 200m apart from the experimental hall of SPring-8.

3.3 High Energy X-ray and Slow Positron Source

Electron energy of 8GeV is very useful to produce high energy X-ray in a GeV region through Compton back scattering. The Research Center for Nuclear Physics, Osaka University is constructing "Laser-Electron-Photon" beamline. In the first phase high power Ar gas laser will be used. The maximum energy in this case is 2.4GeV and the expected photon intensity is 5×10^6 /sec at a stored current of 100mA. All photons are tagged by scattered electrons to determine their energy. The experiments will start in this fall.

Photons of energy higher than the threshold of $e^- e^+$ pair production can produce slow positrons. The conventional way is to produce the positrons by bombarding high energy electrons on the metal target. On the other hand, if we can produce high-intensity photons of energy higher than 1MeV, we will get slow positrons through $e^- e^+$ pair production process in converter materials. This method has an advantage of making the source activation-free. We are collaborating with Budker Institute of Nuclear Physics to develop a 10T superconducting wiggler. Total yield of slow positrons at SPring-8 is estimated as $10^{10} - 10^{11}$ from numerical simulations.

3.4 Infrared Radiation

A beamline for infrared spectroscopy is under construction at SPring-8. The advantage of using 8GeV electron beam is that more intensive infrared synchrotron radiation is emitted into narrow vertical angle from electrons in the orbit with the larger bending radius. We extract a very sharp infrared photon beam from the bent part of the dipole magnet and reflect it by copper mirror in horizontal direction. Expected energy range and photon number are 0.7 to 100 μm and 10^{11} photons/sec/0.1%b.w at 10μm, respectively.

4 SUMMARY

Machine studies and operation experience in the past two years show that the performance of SPring-8 is remarkable. We expect that new projects to build the long undulator beamline, 1km beamline and a slow positron source will open the new capability of the large scale synchrotron radiation source. It could be emphasized that high energy electron beam with ultra low emittance will create a new field of science and technology.

6 REFERENCES

[1] H.Kamitsubo, J.Synchrotron Rad. **5**(1998) 162
[2] S.Date et al. "Operation and Performance of the SPring-8 Storage Ring" presented by H.Okuma at this Conference
[3] N.Kumagai et al. "Estimation of Betatron Coupling and Vertical dDispersion for SPring-8 Storage Ring" presented by M.Takao at this Conference
[4] S.Date and N.Kumagai, N.I.M. **A421**(1999) 417
[5] T.Tanaka and H.Kitamura, N.M.I. **A364** (1995) 368

FUTURE DIRECTIONS IN THE STORAGE RING DEVELOPMENT FOR LIGHT SOURCES

Albin F. Wrulich, PSI, Switzerland

Abstract

Major performance objectives for storage-ring based light sources are small emittance and energy spread, high beam stability, and full exploitation of the photon energy from a few eV up to hard X-rays. Most of the recent- generation light sources are built up by highly optimized lattices of the Double Bend- or Triple Bend Achromat type. There is little room left to further optimize these lattices to even smaller emittances. Only a local adjustment of the optics at the source points might still bring some benefit. With decreasing emittance orbit stability is becoming more and more important. Cures for vibrations, thermal effects and ground motion have to start at the basic design of the building, the storage ring infrastructure and the magnet support system. Beam instabilities are especially harmful as they increase the energy spread and as a consequence deteriorate the higher harmonics of the undulator radiation. Well optimized beams suffer from lifetime problems due to Touschek scattering. Particular problems arise when short bunches are requested, for instance for storage ring based lasers. Medium-energy machines are able to produce high brilliance in the hard X-ray range by means of mini-undulators with small gaps. This, again, has an adverse effect on the beam lifetime due to beam gas scattering.

The current trend in storage ring development for future Light Sources is discussed. What are the crucial issues and where is improvement desirable and possible? Is there still room for improving the basic design of a light source? Are there alternatives to the 'classical' lattices which could be used for the next generation? Or is improvement possible only on the operational field?

1 INTRODUCTION

At first glance, storage-ring based light sources seem to have reached their performance limits. The optimization of the structure towards low emittance is very advanced and not much room is left for further improvements. An increase of the ring size is always an alternative, but beside the usual problem of budgetary constraints, large circumference machines working at low energies are suffering from adverse coherent effects and lifetime problems. At the last Workshop on 4th Generation Light Sources [1], an enthusiastic vote was given that linac driven SASA FELs will be the machines of the 4th generation. In this meeting and in subsequent publications [2] it was stated that 'they are fulfilling all the requirements for a next generation light source'! On the other hand, a pilot project demonstrating the SASA principle for X-rays is still missing and from there it would be still a long way to a user facility. Fundamental limits for the lasing process are reached at photon energies of 10-20 keV [3]. Stability might also be an issue, and is better under control in storage-ring based sources. Last but not least, storage ring technology is extremely well developed [4] and we can still benefit from it in the future. It is therefore necessary to think also about the future of storage ring based light sources.

2 PERFORMANCE GOALS

At the Workshop on 4th Generation Light Sources [1] the key parameters for future sources were defined to be: brilliance, coherence, short bunch lengths, high photon energies (up to 100 keV) and stability. A factor 100 in the reduction of the emittance was considered as a target goal which would allow the realization of a new class of experiments. Figure 1 shows the development of brilliance for light sources from the first generation to a possible 4th generation. A next step of a factor 100 would simply mean a reduction of the horizontal emittance to about $5 \, 10^{-11}$ rad-m. As demonstrated in Figure 1, with each new generation also the vertical emittance was simultaneously reduced by about the same ratio. For the next generation, it might be advisable to not further reduce the vertical emittance in the same way. This would alleviate problems with Coulomb scattering inside the bunch. Furthermore, already now the vertical emittance is at the diffraction limit for 10 keV photons.
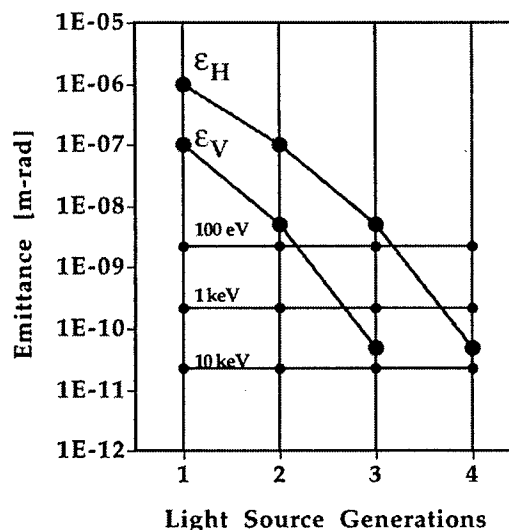
Fig. 1: Development of the brilliance in light sources with a possible future step for Fourth Generation Sources.

2.1 LOW EMITTANCE

The emittance of a storage ring is solely defined by magnet structure and energy. It should be analyzed here, which further reduction we can expect for the 4th generation and what the solutions are for that. The 'classical' structures for light sources are DBA and TBA (Double and Triple Bend Achromat structures). Structures have been developed with more magnets per achromat, since for constant deflection of an achromat, the angle of the individual magnet is reduced and correspondingly the emittance which scales with the third power of the angle. Ultimately, such an expansion leads to a FODO structure with dispersion matching towards both ends. This, of course tends to increase the length of an achromat. As figure of merit for comparing structures with the same emittance we can take the ratio of straight section length to achromat length.

All these structures have well defined limits for the emittance. They are given by the individual limits for the single bending magnets, with dispersion suppression towards both ends and the dispersion symmetry points in the middle for the inside bending magnets. For DBA and TBA the theoretical limits [5,6] are given by:

$$\varepsilon_H = \frac{C_q \gamma^3}{J_H} \cdot K \cdot \phi_B^3$$

$$\text{with} \quad K = \frac{1}{4\sqrt{15}} \text{ for DBA} \qquad K = \frac{7}{36\sqrt{15}} \text{ for TBA}$$

where γ is the Lorentz factor, J_H the horizontal damping partition number, ϕ_B the deflection of one bending magnet, and C_q, K are numerical factors.

Intrinsic matching requirements reduce the numerical factor for the TBA limit to about the value of the DBA [7]. Nevertheless, there is still the third power of the bending angle ratio that considerably reduces the emittance for an TBA as compared to a DBA. On the other hand, whereas a TBA always requires a small dispersion in the center of the structure, a DBA allows an increase of the dispersion inside the achromat by expansion, which makes the chromatic compensation with sextupoles easier. This is the reason why large machines with low individual bending angle and correspondingly small dispersion are always built up by DBA structures. For the 3rd generation sources, the ratio between actual emittance and minimum emittance is varying between 1.5-3 for DBAs and 2-4 for TBAs. Not much space is left for further reducing the emittance for these 'classical' structures, maybe a factor of two. The simplest way for reducing the emittance, as mentioned before, is to increase the number of bending magnets. Unfortunately, a machine with large circumference working at low energies reveals a couple of adverse effects which are difficult to handle. Keeping the energy fixed by increasing the length affects the energy loss per turn as $\sim 1/L$, damping time as $\sim L^2$, energy spread as $\sim 1/L^{1/2}$ and emittance as $\sim 1/L^3$ Going to the

maximum capability of such an expanded ring (i.e. with a bending magnet field as before the expansion) all the adverse effects would be eliminated and even be improved as compared to the original not expanded machine. In addition, the spectrum would be extended further into the high photon energy range. Actually, all existing machines actually are working at the maximum energy for these reasons. Another way of alleviating some of the adverse effects due to circumference increase and of further reducing the emittance is the introduction of damping wigglers in the structure. Storage ring relevant parameters would be modified [8] according to:

$$\left(\frac{\sigma_E}{\sigma_{E0}} \right)^2 = \frac{U_o}{U_w} \left[1 + \frac{4}{3\pi} \frac{L_w}{L_o} \left(\frac{\rho_o}{\rho_w} \right)^3 \right]$$

$$\frac{\varepsilon_H}{\varepsilon_{H0}} = \frac{U_o}{U_w} \left[1 + \frac{L_w}{L_o} \frac{H_w}{H_o} \left(\frac{\rho_o}{\rho_w} \right)^3 \right]$$

$$\frac{U_w}{U_o} = 1 + \frac{1}{2} \frac{L_w}{L_o} \left(\frac{\rho_o}{\rho_w} \right)^2$$

$$H_w = \left(\frac{\lambda_w}{2\pi\rho_w} \right)^2 \cdot \frac{4 \langle \beta \rangle}{15\pi}$$

L, ρ, and U are total length, bending radius and energy loss per turn for wigglers (w) and bending magnets (o). H is the Courant Snyder invariant, λ_w the wiggler period length and $< \beta >$ the average beta function in the wiggler section. As an example for an expanded structure, let us double the size of the APS [9] and use the additional 40 straight sections for the implementation of 5.2 meter long damping wigglers with 2 Tesla field and 10 cm period length. We would obtain a machine with the parameters listed in Table 1.

Table 1 Example for an 4th Generation Light Source (2 x APS)

PARAMETERS	
Energy, GeV	7
Circumference, m	2120
Natural emittance, m-rad	$5.4 \, 10^{-11}$
Energy spread	$6.8 \, 10^{-4}$
Damping times τ_x, τ_y, τ_s, ms	4, 4, 2
Momentum compaction	$6 \, 10^{-5}$
Number of straight sections	80
Straight sections with damping wigglers	40
Total damping wiggler length, m	208
Wiggler field, T	2
Wiggler period length, m	0.1

The emittance would provide diffraction-limited photons in the 10 keV range and a high degree of coherence. The 'damping' wiggler would have interesting properties for a wide field of applications. Brilliance and horizontal flux density are shown in Figures 2 and 3 (for a beam current of 100 mA). The period length could be optimized towards the experimental needs, as long as the emittance blow up due to the self dispersion is kept small. It must be notified that the power from such a wiggler would not be easy to handle (125 kW for 100 mA) and a reduction of the current would presumably be necessary, which proportionally reduces the brilliance.
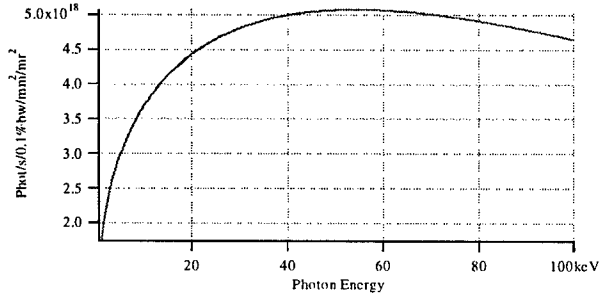
Fig. 2: Brilliance as a function of photon energy for the damping wiggler (B= 2T, λ= 0,1 m, L= 5,2 m).
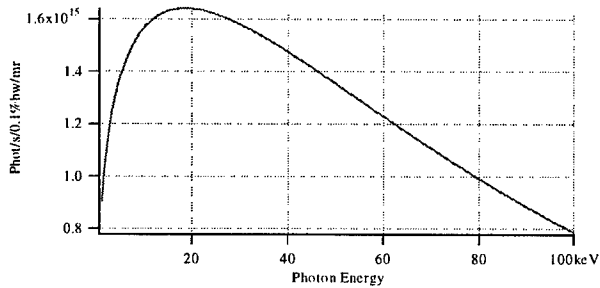
Fig. 3: Horizontal flux density as a function of photon energy for the damping wiggler.

2.2. SHORT PULSES

The direct method for achieving short light pulses is the reduction of the bunch length of the electron beam. Several methods have been discussed and tested in various places. The brute force method is to increase the RF-gradient, which according to the definition of the bunch length as:

$$Low\ current:\ \sigma_s \approx \left\{ \frac{\alpha_c \gamma^3}{\omega_{RF} V_{RF}} \right\}^{1/2} \quad High\ current:\ \sigma_s \approx \left\{ \frac{I \frac{|Z_1|}{n}}{\omega_{RF} V_{RF}} \right\}^{1/3}$$

can be done by increasing the RF-voltage (V_{RF}) or the RF-frequency (ω_{RF}). An increase of the voltage by adding

more cavities is costly. A harmonic cavity working at a multiple of the fundamental frequency combines the advantages due to voltage increase and higher frequency in order to reach higher gradients. Pulsed RF would be an alternative, but provides only a low duty cycle. The same holds for a rotation of the bunch by additional cavities. A lot of hope was put in the reduction of the momentum compaction factor (α_c) in order to reach short bunch lengths. Experiments were performed at Lure, ALS, ESRF and others. Unfortunately, the outcome is not promising. Low and negative momentum compaction effectively reduces the bunch length at low currents. For the interesting range of higher currents, however the bunch length is independent of the momentum compaction. Even if the low intensity would be acceptable for the performance of certain experiments, it creates a conflict with users preferring high brilliance and correspondingly high currents. An alternative method has been developed by [10] which does not generate this compatibility problem. There, in an ID section, the electron beam is interacting with a femtosecond laser pulse. This creates a modulation of the energy corresponding to the pulse length of the laser beam. Subsequently, the light generated by the off energy fraction of the beam can be extracted by spectral or dispersive separation. In spite of this interesting approach, one must conclude that linac-based SASE FELs will be far superior in creating pulses in the 100 fs range.

2.3 HIGH PHOTON ENERGIES

The simplest way to reach higher photon energies is to spend more money, i.e. to increase the dimensions of the storage ring and simultaneously the energy. The question here is more what can be reached within certain budgetary boundary conditions or what is the cost- optimized machine for a certain photon energy range. The new upcoming generation of medium-energy machines, DIAMOND, SLS and SOLEIL is trimmed in this direction. SLS, currently under construction in Switzerland, is the first machine of the medium energy range which will enter the regime of hard X-rays with high brilliance. This is achieved by the use of mini-undulators and the utilization of higher harmonics of the spectrum. Both aspects of this approach are posing severe conditions on machine performance and machine operation. Low gaps adversely affect the beam gas scattering lifetime, which scales inversely proportional to the square of the gap size. But not only this, also the Touschek scattering lifetime can be reduced. For the SLS, a strong nonlinear coupling of the horizontally oscillating Touschek scattered particle transfers the motion into the vertical plane where it get lost at the low- gap insertion device aperture [11]. Only a careful coupling minimization can alleviate this effect. A variation of the Touschek lifetime with vertical aperture for the SLS is shown in Figure 4.
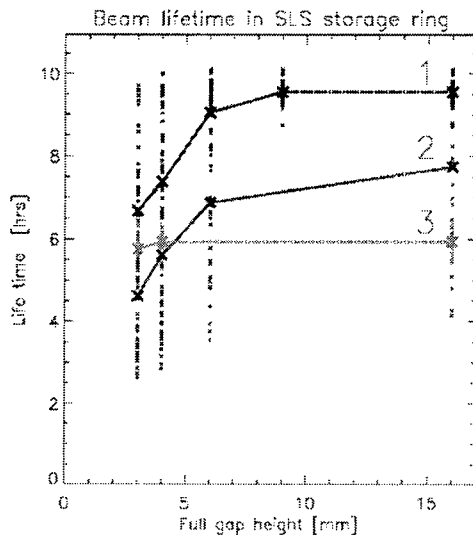
Fig. 4: Touschek lifetime as a function of vertical stay clear aperture in the undulator. The meanings of the different curves are: (1) tracking for constant energy deviation, (2,3) tracking with synchrotron oscillations and (3) with additional coupling control. The emittance coupling is 2.8 ‰ for (1,2) and 1 ‰ after minimization for (3).

The effect will presumably be increased if more circularly polarized undulators are inserted into the storage ring structure, since their horizontal magnet field will transfer motion into the vertical plane. This demonstrates that increasing the momentum acceptance is not always the way to cure Touschek scattering life time reductions. Only a reduction of the scattering events, i.e. a reduction of particle density, as reached with a bunch lengthening cavity, can improve the situation. An elegant way to alleviate the problem of reduced lifetime is continuous top-up injection. It has been tested in many laboratories and extensive studies were recently performed at the APS [12]. Such an operation mode could maintain a constant thermal load on beamline optics and storage ring vacuum systems and could have the benefit of constant signal to noise ratio for the experiments. Nevertheless, a basic good lifetime before top-up should be envisaged in order to reduce radiation safety problems caused by high particle losses. Solving the lifetime problem by top-up injection puts higher requirements on the injection system. Reliability is of paramount importance; low power consumption and small beam dimensions for a loss free injection would be highly desirable. The SLS booster for example [13] is placed inside the storage ring tunnel. The large circumference results in many small little magnets with modest field. This provides a low power consumption (230 kW for 3 Hz and correspondingly lower for less frequent top-up) and a small emittance (7 nm) for effective injection. A voltage and current controlled switch mode power supply allows a flexible adjustment of the ramp. The utilization of higher harmonics, on the other

side, requires perfect beam conditions. Especially energy blow up due to instabilities must be avoided. Longitudinal coupled-bunch instabilities must be perfectly compensated. A series of measures were developed which are ranging from measures at the source, like mode shifting by temperature tuning or HOM plungers, damping of individual modes, superconducting zero-mode cavities, to broad-band feedback systems. All of them have been proved to work satisfactory. The new upcoming generations, are well advised to keep these most harmful instability effects well under control.

2.4 STABILITY

When beam sizes becomes smaller and smaller, the stability of the electron beam becomes more and more important. Measures for stabilization start with a proper site selection and the construction of the foundation for the storage ring-tunnel. All potential vibration sources should be removed from the nearby areas of the storage ring. Whatever has to be close, must be provided with proper damping features. A crucial issue is the temperature stabilization of the tunnel to avoid thermal movement. Synchrotron radiation must be absorbed in an antechamber on lumped absorbers equipped with powerful pumps under neat. In order to allow for a compensation of the residual movement with an orbit-feedback system, a fast and accurate beam position monitor system becomes essential. For the SLS, a new development was started which combines these usually conflicting requirements. In order to be fast, multiplexing is avoided and each BPM is equipped with four detectors, one for each pick-up button. For the calibration of these devices a pilot signal is used, which gives the guaranty for a high precision reading of the orbit [14]. A precise adjustment of the individual quadrupoles is important in order to reach a small vertical emittance and to reduce orbit distortions before switching on correction dipoles. High precision can be reached by placing groups of elements on a girder. Random displacements of the girders are generating a far smaller amplification on the orbit distortion than individually supported quadrupoles. These positions of the girders can be controlled by hydrostatic systems with capacitive or ultrasonic pick-ups and optical systems. To control the horizontal position of the SLS girder, an optical system will be used [15].

3 CONCLUSIONS

In spite of the unbeatable brilliance of future linac based SASE-FEL sources, storage ring based light sources will still be of great importance in the future. Regarding intensity, brilliance beyond 10 keV photon energies and stability they are even superior. Compared with the existing 3rd generation sources, great progress will be reached with the new upcoming generation, i.e. DIAMOND, SLS and SOLEIL. These are machines of medium energy range that enter the regime of hard X-rays. To reach this goal with low undulator gaps and the use of higher har-

monics of the spectrum, special attention must be given to maintain the necessary high beam performance. Top-up injection must become routine operation for these machines. This sets more stringent requirements on the injection system regarding reliability and power consumption. The high standard in storage ring technology will guarantee that storage ring based light sources will become members of the 4th generation family.

4 ACKNOWLEDGMENTS

I would like to thank C. J. Bocchetta, M. Pool and J. L. Laclare for helping me with information material. I am also grateful to my colleagues at the SLS for providing me with some graphs, A. Streun for the Touschek lifetime and T. Schmidt for the Brilliance. H. Weyer I would like to thank for carefully reading the manuscript and making several suggestions, and M. Bugmann for typing the manuscript.

5 REFERENCES

[1] 10th ICFA Beam Dynamics Panel Workshop on 4th Generation Light Sources, Grenoble, 1996.

[2] C. Pellegrini, 'Is the X-ray Source the 4th Generation Light Source?', EPAC, Stockholm, 1998.

[3] J. Rossbach et al, 'Interdependence of Parameters of an X-ray FEL', NIM A374, 1996.

[4] J. L. Laclare, 'Light Source Performance Achievements', EPAC, Stockholm, 1998.

[5] M. Sommer, 'Optimization of the Emittance of Electron Storage Rings', LAL/RT/83-15, 1983.

[6] L. Teng, 'Minimum Emittance Lattice for Synchrotron Radiation Rings', APS LS-17, 1985.

[7] G. Wüstefeld, 'The Minimum of the Natural Emittance in the Triple Bend Achromat', BESSY TB 108/97, 1987.

[8] R. P. Walker, 'Wigglers', Sincrotrone Trieste ST/M-94-4, 1994.

[9] Conceptual Design Report of the 7GeV Advanced Photon Source, ANL-87-15, 1987.

[10] A. A. Zholents, M. S. Zolotorev, 'Femtosecond X-ray Pulses of Synchrotron Radiation, PRL, Volume 76, Number 6, 1996.

[11] M. Böge, P. Marchand, A. Streun, 'Beam Lifetime Studies for the SLS Storage Ring', this conference.

[12] L. Emery, M. Borland, 'Top-up Operation Experience at APS', this conference.

[13] C. Gough et. al., 'SLS Booster Synchrotron', EPAC, Stockholm, 1998.

[14] M. Dehler et. al., 'BPM System for the Swiss Light Source', this conference.

[15] V. Schlott, PSI Annual Report 1998.

STATUS AND COMMISSIONING-RESULTS OF BESSY II[*]

R.J. Bakker[**] for the BESSY II Project Team[***], BESSY, Berlin, Germany

Abstract

The new Storage Ring BESSY II in Berlin Germany is a dedicated third generation synchrotron radiation source for the VUV and soft X-ray spectral range [1]. On April 22nd, 1998 a 1.7 GeV electron beam was stored for the first time. Despite a relatively short time for commissioning of the synchrotron radiation source, the milestones were met as scheduled. Accelerator parameters that determine the quality of the synchrotron radiation are as designed or the design goals were even exceeded. The only parameter that is still not according to design is the beam lifetime, as the baking of the vacuum system is not completed yet. The regular scientific program started according to plan in January 1999 with experiments. The front-end for 22 additional beamlines are installed and scheduled for use before the end of next year. Thus required shutdown periods will also be used to install additional hardware to improve the performance of the ring.

1. TIME SCHEDULE

The BESSY II project was approved in 1992. At the end of 1996 the injector was assembled and the commissioning of the booster commenced [2]. On April 21st 1998, 3 months ahead of schedule, electrons were extracted out of the booster and injected into the main ring for the first time [3]. Already the next day beam storage and accumulation was achieved. Pilot user-experiments started on November 9 well before the beginning of the regular scientific program: January 11. For 1999 a three-mode schedule is planned with 9 weeks of beam-time for commissioning and machine studies, 20 weeks shut down to permit further installation of equipment, and 23 weeks of user-operation.

2. TECHNICAL DESCRIPTION

BESSY II employs a full energy injector that consists of a 70-kV DC thermionic gun, a 3 GHz racetrack microtron and a 10-Hz rapid-cycling synchrotron equipped with a

single 500 MHz rf-cavity [2]. The main ring has an extended double bend achromat lattice with 16-fold symmetry. Individually powered doublet- and triplet- focussing schemes around the dispersion-free straight sections allow for alternating high and low horizontal β-functions at the location of the insertion devices (ID's). Orbit correctors are incorporated in both the dipoles and in the 112 sextupoles. Four sextupoles also house skew quadrupoles for tuning of the global coupling.

Up to 14 straight are suited for installation of ID's of which 5 are installed: a 4-T super-conducting wavelength shifter, a 180 mm period electromagnetic undulator, and 3 hybrid undulators with variable gap (two planar polarized with a period of 49 and 125 mm, respectively, and one elliptically polarized with a period of 56 mm). The remaining straight sections are used for the rf-system and the injection [4], respectively. The former is located in one of the low-β sections and consists of four DORIS type 500 MHz single-cell cavities, fed with 75 kW DC klystron each.

Table 1. Main specifications of BESSY II

Parameter		Design	Achieved	
Energy	E	0.9-1.9	0.85-1.9	GeV
Acceptance (rms)	$\Delta E/E$	± 3	-3 / +5	%
Current	I	100	397	mA
Tune	Q_x	17.8	17.85	
	Q_y	6.7	6.72	
Nat. Chromatisity	ξ_x	-48		
	ξ_y	-23		
Max dispersion	η_x	0.44	0.42	m
Emittance[*]	ε_x	6	6	nm rad
Coupling	c	<3	<0.1	%
Comp. factor [4]	α	7.3×10^{-4}	7.3×10^{-4}	
Life time[**]	τ	>6	3.4	h
Injection rate	I_{inj}	6	6	mA/s

[*] $E = 1.7$ GeV, [**] $I = 100$ mA

The booster governs the filling of the ring. In the default mode the injection is synchronized with the 10 Hz of the booster and a bunch-train of 120 buckets out of the possible 400 are filled. It is also possible to fill in a toggled mode and in an asynchronous mode where the bunch-trains are injected at two different locations or at fully random position, respectively. Single bunch operation is presently in preparation and planned for the near future.

The performance of the ring is summarized in Tab. 1. A more complete description of the installed hardware can be found in Ref. 3.

3. COMMISSIONING RESULTS

After the beam was stored in the main ring for the first time [3] a commissioning program started which aimed

for stable operation conditions according to the design parameters as quickly as possible. During commissioning the mayor setback encountered was related to the vacuum system: two fine whiskers in the ring vacuum vessel caused unstable injection conditions. It took until the end of August before the reasons were clear and the cause of the troubles could be localized and removed. Non the less it was possible to reach the goal and a solid basic understanding of the machine is obtained. Below follows a collection of some of the results.
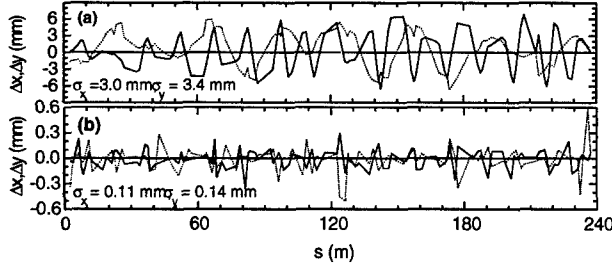
Figure 1 Original horizontal (solid line) and vertical (dotted line) closed orbit (a) compared with the present orbit (b).

3.1 Beam Optics

The beam position monitor system (bpm) [6] was already available on the first day of commissioning. The initial orbit showed large excursions in both planes, see Fig. 1a. Furthermore, the vertical tune appeared to be one unit smaller than the design tune. Both errors were adjusted with the aid of available orbit-correction algorithms [7,8] based on the closed orbit response on both corrector variations and quadrupole variations. For this, a good understanding of the linear lattice is essential and the ring was operated with sextupoles off for some time, i.e., with extremely negative natural chromaticities. As this mode causes the machine to be extremely sensitive with very short beam lifetimes, it was due to the patience and hard work of the crew that this mode of operation could be obtained. The orbit in Fig. 1b is the present one relative to the 'natural' machine orbit, i.e., the orbit that has minimal distortion on variations of the quadrupole fields [6].
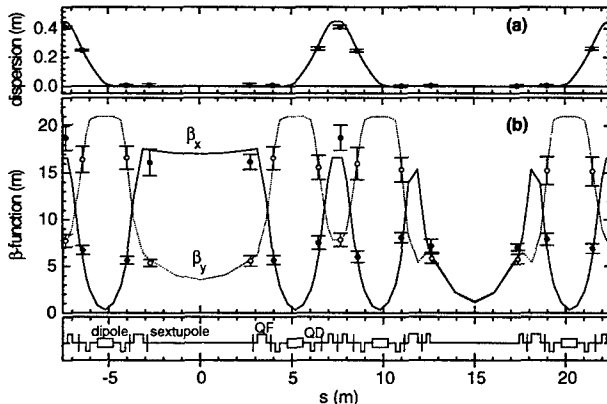
Figure 2 Comparison of the design twiss-parameters (solid curve) with the result of orbit corrector response measurements. The error bars indicate the rms variation of the parameters between the 8 sections of the ring.

The machine parameters shown in Fig. 2 depict the present understanding. The β-beating along the ring has been reduced to below 10 %.
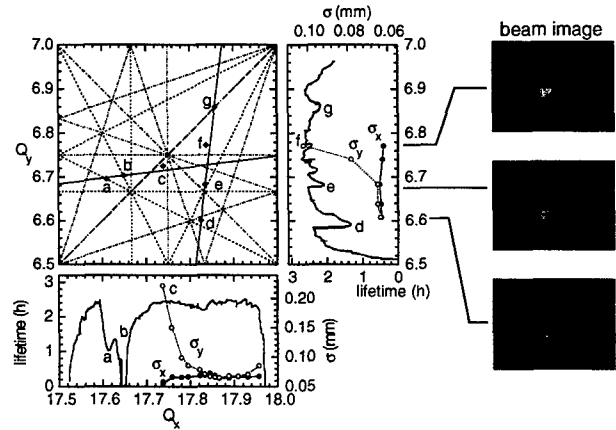
Figure 3 Lifetime and transverse beam-size as a function of the tune. The solid lines mark the path of recording through the resonance diagram. Visible resonance-crossings are labeled.

3.2 Tune dependency

Around the design tune (Q_x=17.8, Q_y=6.7) the resonance diagram was scanned to find optimum operational conditions in terms of lifetime and optical spot-size. The former was recorded with the standard current monitor available whereas the latter was obtained from an imaging system on a dipole beamline. Fig. 3 shows an example of some of the results obtained [9]. The present working point (Q_x=17.85, Q_y=6.72) is a combined optimum of stable lifetime conditions (the absence resonance lines that deteriorate the lifetime) and small optical spot-size.
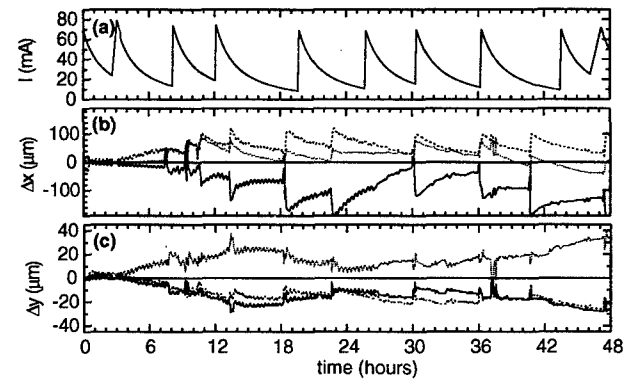
Figure 4 Typical machine performance without orbit correction, recorded on Nov. 24 and 25, 1998: (a) beam intensity, horizontal (b) and vertical (c) orbit stability recorded at 3 different positions in one sector.

3.3 Orbit Stability

The ring is equipped with 112 bpm pickup stations that can track both fast (up to single turn) and slow orbit changes [6]. In a standard mode of operation the bpm's record a closed orbit with 1 Hz and an accuracy of 1 μm. Typical log-data during a user-ring is shown in Fig. 4.

198

Without any correction the current-dependent drifts are of the order of 5 µm in the vertical, and 40 µm in the horizontal plane during the time in which the current drops from 100 to 40 mA. On a larger time-scale drifts add up to 40 µm and 150 µm, respectively. Orbit distortions are increased due to external influences such as variation of undulator gaps: e.g., the orbit distortion at t = 37.5 h in Fig. 4. The oscillations that disappear after t = 27 h could be traced back to fluctuations in the cooling water temperature on a sub degree scale.

Until now user operation has been performed in a mode as described above. However, initial tests with a slow feedback system [7] indicate that it is possible to significantly reduce these drifts and to compensate for sources of distortion. Present studies aim to minimize the correction without sacrificing the achievable orbit definition.

3.4 Beam lifetime and Vacuum

The beam lifetime is still dominated by the vacuum pressure. Until the end of 1998 only 1/3 of the ring was baked. The influence of the vacuum was intensified because the vacuum system needed to be opened on several occasions for completing machine elements and user front-ends. Consequently, desorption by the photon beam is still the dominant process in reducing the vacuum pressure and lifetime [10]. Fig. 5 displays the lifetime at 20 and 100 mA. Resets of the integrated dose curve correspond with moments on which the vacuum was broken. Note that the graph displays logged lifetime data. Hence, reduction may also be caused by non-lifetime optimized machine studies that took place at the time of logging. It is anticipated that the lifetime will increase as the vacuum improves.
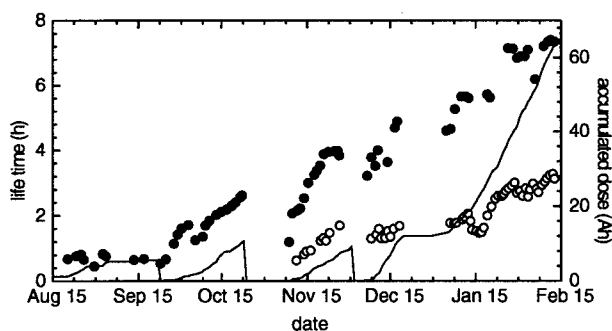
Figure 5 Lifetime at 20 mA (solid dots) and 100 mA (open dots) of beam current and accumulated dose (curve) versus time.

4. OPERATIONAL STATISTICS

From April 1998 until February 1999 a total of 2540 hours of beam time have been recorded of which 1850 hours were used for machine studies and optimization. The rest was used for the regular scientific program, which accumulated the most hours during the last 5 weeks of operation (460 hours).

During the initial nine months less than 300 hours had to be counted as downtime. Hence, already during commissioning the reliability of the machine proved to be better

than 80%. The most time consuming reasons for the down times were: a) an insufficient cooling of a coil in a transfer-line magnet which got damaged, and b) the two tiny fine whiskers mentioned before. No significant hardware failures were reported while commissioning and during the 5 weeks of user operation no downtime has been recorded at all.

5. FUTURE PLANS

Further development of BESSY II takes place on several fronts simultaneously. First more ID's will be installed and more beamlines will be built up, e.g., a 7-T wavelength shifter build by BINP/Novosibirsk. From the machine side more hardware will be installed to make operation more stable and versatile. For this year a new electron gun will come available that enables single bunch operation. Also several feedback systems are anticipated to boost the performance in the imminent future [11,12]. In collaboration with MAX-Lab/Lund, attention is focuses on the installation of 3rd harmonic cavities.

ACKNOWLEDGEMENTS

REFERENCES

[1] E. Jaeschke et al., Lattice Design for the 1.7 GeV Light Source BESSY II, 1993 IEEE Part. Acc. Conf., p 1474.

[2] E. Weihreter et al., Commissioning of the BESSY II Booster Synchrotron, Proc. EPAC98, Stockholm, Sweden, p.436 (1998)

[3]. D. Krämer et al., Start of Commissioning of the High Brlliance Synchrotron Radiation source BESSY II, Proc. EPAC98, Stockholm, Sweden, p. 262 (1998)

[4] J. Feikes et al., Measurement of BESSY II Parameters using Beam Tune Signals, this conference (WEP47)

[5] J. Feikes et al., Operational experience with the BESSY II Injection System, this conference (TUA87)

[6] P. Kuske at al., Experience with the BPM system of the BESSY II storage ring, this conference (WEA84)

[7] R. Bakker et al, Experience with commissioning software tools at BESSY II, this conference (WEP49)

[8] R. Bakker et al., Establishment of an online model in interpretation and correction tools for BESSY II, this conference (WEP48)

[9] J. Feikes at al., Dependence of the transversal Source Size of Synchrotron Radiation on Optical Parameters at BESSY II, this conference (WEP46)

[10] S. Khan, Study of the BESSY II Beam Lifetime, this conference (THA104)

[11] S. Khan et al., BESSY II Feedback System, this conference (TUA32)

[12] T. Knuth et al., Longitudinal and Transverse Feedback Kickers for the BESSY II storage ring, this conference (TUA33)

TOP-UP OPERATION EXPERIENCE AT THE ADVANCED PHOTON SOURCE *

L. Emery, M. Borland, ANL, Argonne, IL

Abstract

The Advanced Photon Source (APS) is a 7-GeV, third-generation synchrotron radiation source. To provide more stable beam for users, in September 1998 we began commissioning a new operating mode called "top-up." In this mode, the beam current does not decay but is maintained at a high level using frequent injection, while photon shutters are open and photon beams are delivered to users. The hardware, software, and safety requirements for top-up will be reported. Safety issues related to injection with open photon shutters are covered in companion papers in this conference. Present operational experience includes testing aspects of top-up injection and delivering beam to X-ray users for a few hours with fractional current stability of 10^{-3}. We expect to run several top-up operation shifts in Spring 1999. Issues of importance are orbit and emittance transients during the injection and scheduling of injection pulses for the convenience of users.

1 INTRODUCTION

Top-up injection refers to injecting with photon shutters open to deliver a near-constant stored beam current. This will improve X-ray beam stability through a constant heat load on X-ray optics and eliminate current-dependent systematics of storage ring (SR) beam diagnostics.

A relative current stability of 10^{-4} is our long-term goal. We have acheived this for a few hours of running during machine studies (shutters not necessarily open). A lower stability of 10^{-3} was achieved routinely, and has been delivered to users for several hours on a trial basis.

An equally important beam quality issue of top-up is the beam disturbance that may be caused by the injection process. Though any closed orbit or emittance disturbance is damped out after several tens of milliseconds through synchrotron radiation damping or the decay of pulsed magnet fields, these disturbances affect most X-ray experiments. We will report on steps taken to reduce the impact of these injection transients on X-ray experiments.

2 RADIATION SAFETY

Photon shutters are normally closed during injection to block any injected beam particles from escaping the SR enclosure and entering the experiment hall, where they would constitute a radiation hazard. (This might occur, say, due to a short in a dipole magnet with a photon port.) Prevention of such an accident is the main safety issue in top-up and was the subject of extensive studies [1, 2].

We found that if the dipole magnets and power supplies are operating normally, no configuration error or magnet fault can produce an accident. Simulations gave a stronger conclusion, that even with a shorted dipole and other errors, one cannot have stored beam while extracting injected beam down a photon beamline. Thus, we ensure the top-up safety with an interlock that inhibits injection with shutters open if there is no stored beam.

The simulations used a series of lattices and conservative (i.e., accident-enhancing) choices of magnet faults. All scenarios involved a shorted dipole of variable degree. Other faults considered simultaneously were hypothetical mis-set quadrupoles, worst-case dipole steering from malfunctioning nearby multipoles, and injected beam energy error. To limit the possible steering from multipoles, we ran the simulations for 6 GeV; a hardware interlock on the dipole power supply enforced this minimum energy.

Because of the importance of aperture location and dimensions in limiting the possible trajectories of the injected beam, we require controlled drawings and documents listing the relevant apertures (those used in the tracking simulations). Tolerances for the placement of apertures (determined from tracking) are also documented. Routine checks of the placement of apertures are required. Since apertures in the SR vacuum chambers and photon beamline are not visible from the outside, this is done indirectly using survey measurements of the magnets and photon beamline safety shutter, and using measurement gauges to verify the position of vacuum chambers in magnets.

3 OTHER OPERATIONAL CONCERNS

The injector produces a single bunch at 2 Hz, with a nominal charge of 1 nC and design maximum of 20 nC. For 10^{-4} current stability, the injected charge is about 0.04 nC, at the bottom range of the beam transport line diagnostics sensitivity. Beam diagnostics with higher sensitivity are planned. In the meantime, scrapers in the transport line can be used to scrape down to the required low charge.

Permanent magnets in insertion devices (IDs) can be demagnetized by a large radiation dose. Injected beam losses are highest at the ID vacuum chambers (VCs). In top-up operation the IDs are closed, almost touching the VCs. Shielding cannot reduce the dose at the downstream end of the ID since a radiation shower travels inside the beam pipe and through the thin (1 mm) Al chamber. Injection losses will have to be closely monitored. We plan to install radiation monitors on the ID VC to serve as diagnostics.

SR injection uses a four-magnet kicker bump lasting less than one turn, as well as two septa at the end of the transfer line. Poor injection efficiency is typically due to variation

of injected beam initial coordinates in the SR that causes particles to hit vertical or horizontal apertures, which are both small because of small gap undulator apertures. Automatic trajectory correction takes care of the vertical and most of the horizontal motion. However, horizontally we are affected by the pulse-to-pulse jitter of the pulsed magnets. Improved pulsed supply performance and increased injection aperture in the final septum are planned for the near future. In the meantime, virtually 100% injection efficiency can be obtained using a mismatched kicker bump that reapportions the betatron oscillation of the injected beam between the injected beam and the stored beam.

4 BEAM PERTURBATION

It is important that the injection process is transparent to the users. Stored beam centroid motion or increased emittance will reduce the X-ray brightness. The mismatched injection bump used for good injection perturbs the stored beam, imparting a betatron amplitude of a few millimeters. Decoherence (due to tune spread) occurs in about 20 turns, replacing the centroid motion with increased emittance. An increase in measured beamsize (Figure 1) is seen after injection and lasts a few damping times, during which time the synchrotron radiation brightness is greatly reduced. The beam returns to normal in about 30 ms. The blow-up is expected to be greatly reduced when aperture problems are fixed, which will allow a matched kicker bump.
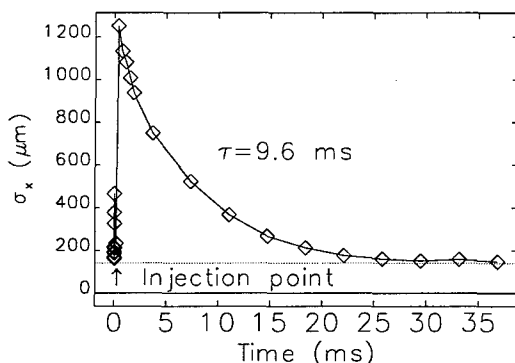
Figure 1: Beamsize blow-up after firing injection kickers

Another injection-related beam perturbation is a closed orbit distortion produced by a septum leakage field. The first, "thick" septum, pulsed with a 10 ms half sine wave, almost touches the SR vacuum chamber. Figure 2 shows the orbit disortion caused by the leakage field for the original septum and an upgraded septum. In either case the beam disturbance lasts for a total of about 25 ms. The maximum orbit distortion for the upgraded septum is about 200 μm—about 60% of the horizontal beam size. Various beamlines will experience different orbit and angle distortion depending on the phase advance from the septum.

The remaining closed orbit distortion will be corrected using the real-time orbit feedback system in feedforward mode in a time window around the injection transient. While this system cannot react quickly enough to com-
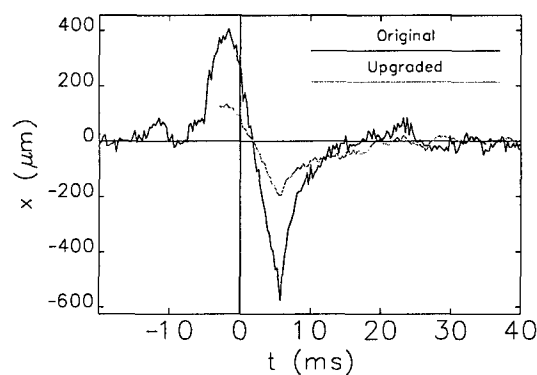
Figure 2: Closed orbit bump due to septum leakage

pletely eliminate the distortion in feedback mode, in feedforward mode its 1.6-kHz update rate should suffice.

Performance of real-time feedback was affected indirectly by the injection orbit transient because of the strong coupling in the mini-BPMs between the beam size and the y-readback for an off-centered beam in the y direction. The problem is eliminated by gating off the feedback for the duration of the injection transient.

Injection-related trigger signals are available to X-ray experimenters so that X-ray data acquisition can be blocked during a time window around the injection event. This is most useful for counting experiments. The possible blanking out of 35 ms of beam time every two minutes is not problematic, as it provides a 99.97% duty factor.

Those experimenters taking data by CCD camera imaging require uninterrupted beam for a wide range of time intervals, say 1 second to 30 minutes. Any beam disturbance that reduces X-ray brightness during a long CCD camera scan may produce an unacceptable spurious signal. Since our current injection process produces a beam perturbation, in the short term we must adopt a top-up injection time interval longer than the longest CCD camera experiment, say one to several hours following a strict schedule. This mode does not provide all the advantages of top-up, but can significantly increase X-ray availability.

5 COMMISSIONING

Commissioning of top-up operation mode involves injecting beam in the SR with the photon shutters open for the first time. The commissioning plan entails measuring radiation dose rates outside shielding walls in areas possibly occupied by personnel for various beam loss scenarios and checking that the measured doses are within the acceptable predicted values. The beam loss scenarios considered here are those that are possible assuming the proper functioning of the personnel protection system. The first scenario is an injected beam loss inside the SR enclosure; the second, an injected beam missteered at an ID vacuum chamber.

The maximum radiation hazard is expected to be produced when the injected beam is missteered into an ID vacuum chamber aperture. Bremsstrahlung photons travel through the open shutters and scatter in the front-end en-

closure (FOE), producing a dose outside the FOE. Measurements we done simulating this condition by repeatedly dumping a stored beam on different ID VCs with the corresponding beamline shutters open. The worst results were scaled to the injection safety envelope of 40 nC/s, giving a maximum credible incident of 12.5 rem/h.

The above measurement was repeated with an actual 1-nC/s injected beam dumped on two separate ID vacuum chambers with corresponding beamline shutters open. The largest dose measured around the FOE scaled to the safety envelope conditions was 0.25 rem/h. The variability of the equipment housed in the FOEs may explain the discrepancy between these two experiments.

Assuming a 100-mA beam with 10 hour lifetime, a current stability of 10^{-3} requires injection of 0.37 nC every 36 seconds. The maximum dose rate outside the SR tunnel if every pulse was lost on an ID VC would be 3.2 mrem/h.

The tracking studies of top-up safety cannot be verified easily as it would involve defeating the personnel protection system and creating difficult-to-generate magnet faults. However, we verified one aspect of the simulations. The tracking studies give a conservative limit for the negative fractional strength error (FSE) for a dipole magnet that would preclude stored beam. The tracking limit, FSE $= -0.09$, would be supported if the measured limit was smaller in absolute value. Dipole trim coils were used to simulate a negative FSE in a particular dipole. Beam was lost at FSE $= -0.050$ (-0.036) with (without) orbit correction running.

6 TOP-UP OPERATION

There are two top-up operation modes, a high current-stability mode (frequent injection) and a refill mode (injection every few hours). The relative current stability, ϵ, is defined by $|I(t) - I_0| < \epsilon I_0$ where $I(t)$ is the instantaneous current and I_0 is the target current.

In high current-stability mode we either inject on an as-needed basis or at a constant time interval. For the former, injection occurs when the beam decays below I_0. Because of typical 10% injector performance variation, injection occurs at irregular intervals. Injecting with 0.04-nC charge, we achieved 10^{-4} stability for $I_0 = 100$ mA, with an injection interval of about 7 s. A 3×10^{-4} current stability was achieved by injecting 1 nC every few minutes.

Since the unpredictability of the injection event in this mode is undesirable to users who are sensitive to the injection process, we developed a fixed-injection-interval mode. One specifies an injection interval T, a target current I_0, and set up the injector to deliver the expected charge deficit ($\Delta I = I_0 T / \tau$) in one pulse. At the end of the interval, we inject only if $I < I_0$, giving stability of $2\Delta I$.

In the refill top-up mode the beam is allowed to decay undisturbed for several hours, then beam is injected to reach the target current. For example, in one hour the 100-mA beam decays by 3 to 5 mA, depending on the bunch pattern. Refilling at 2 Hz and 0.8 nC/pulse would

take 8 to 12 seconds, giving a high duty factor (99.7%) and a low user impact. Presently standard APS operation involves filling (with shutters closed) to 100 mA every 12 or 24 hours. We plan to change this to refill-mode top-up to improve X-ray availability and get more experience with top-up injection.

Obviously when the injector becomes unavailable because of some fault condition, then the beam current in the high current-stability mode will decay below the current tolerance. When the injector is ready again, the current will be topped-up to the target current with a sequence of pulses, similar to what happens in refill mode.

In top-up injection with high current-stability, only one pulse in one bucket is injected. In general, a different target bucket is selected at every pulse to maintain the bunch pattern as well as the total current. A constant bunch pattern is desirable for BPM triggering and electrical offset stability, and for X-ray user timing experiments.

The target bucket is selected between top-up injection events, during which time the bunch pattern intensity is measured, averaged, and compared with a reference bunch pattern intensity. The bunch that has the largest charge deficit will receive the charge of the next injection. The stability of the bunch charge is of the order of ϵ times the number of bunches. For example, for a standard bunch pattern of about 80 bunches, the bunch current variation could be as high as 8%.

We measured the jitter in the timing of the injection pulses in response to user concerns of possible mistimed injection pulses. We found no missed or skipped injection pulses in several hours of testing, and measured the jitter in time to be 60 ms in a one-hour measurement [3]. This jitter is consistent with the 60-Hz line frequency drift.

We plan to implement pulse histories for the SR pulsed magnets, particularly in the kickers, in order to help diagnose possible beam dumps during top-up. Though the kickers have been very reliable, and we have no evidence of kicker-caused beam dumps in the past, it would be useful to be able to eliminate this possibility when diagnosing causes of beam dumps.

7 ACKNOWLEDGEMENTS

8 REFERENCES

[1] L. Emery, M. Borland, "Analytical Studies of Top-Up Safety at the Advanced Photon Source," these proceedings.

[2] M. Borland, L. Emery, "Tracking Studies of Top-Up Safety at the Advanced Photon Source,", these proceedings.

[3] F. Lenkszus, R. Laird, private communication.

IMPACT OF SUPERBENDS AT THE ALS[*]

H. Nishimura and D. Robin[#+], LBNL, Berkeley, CA

Abstract

To satisfy a demand for more high energy, high brightness x-ray sources at the Advanced Light Source (ALS), a plan is in place to replace three 1.3 Tesla normal conducting bending magnets with three 5 Tesla superconducting magnets (superbends) in the year 2001. In this paper we discuss the impact of the superbends on the ALS beam parameters and particle dynamics. In particular we show the effect on the emittance, energy spread, and lifetime. We find that by adjusting the dispersion to be positive in the straight section we are able to largely restore the horizontal emittance. The vertical emittance can be adjusted independently to control the lifetime. The particle dynamics are investigated through particle tracking with a frequency analysis postprocessor. We find that by placing the three superbends symmetrically around the ring there is ample dynamic aperture for injection and lifetime.

1 INTRODUCTION

For applications in protein crytallography, high pressure diffraction, and x-ray tomography there is a desire for good sources at the ALS with photon energies of 10 to 20 KeV and beyond. In principle one can create high energy sources by placing wigglers or wavelength shifters in the long straight sections. However at this time there are very few unoccupied straight sections remaining in the ring — at present of the 12 straight sections only 2.5 are empty.

A way to introduce more high energy sources without using up any straight sections is to replace some of the bending dipole magnets with shorter, higher field magnets. This is the direction that the ALS has decided to pursue. A plan is in place to replace 3 normal conducting dipole magnets with 3 superconducting dipoles (superbends).

Operating with a beam energy of 1.9 GeV, the normal dipoles have a critical photon energy of 3.1 KeV whereas the superbends have a critical photon energy of 12 KeV. This increase in critical energy means that in both flux and brightness the superbend source is almost an order of magnitude larger than the normal dipole source at 10 KeV and almost two orders of magnitude larger at 20 KeV [1].

In this paper we discuss the modifications to the ALS lattice that are necessary to include the superbends. We discuss the changes to the beam parameters and the impact on the beam dynamics — particularly injection and lifetime.

2 LATTICE MODIFICATIONS

The ALS consists of 12 sectors. A typical sector can be seen in Fig. 1 (top). Each sector has 3 dipole magnets each of which bend the beam by 10 degrees. The dipoles are combined function magnets having both dipole and quadrupole field components. The plan is to modify 3 of the 12 sectors, replacing the center dipoles in those sectors with superbends.
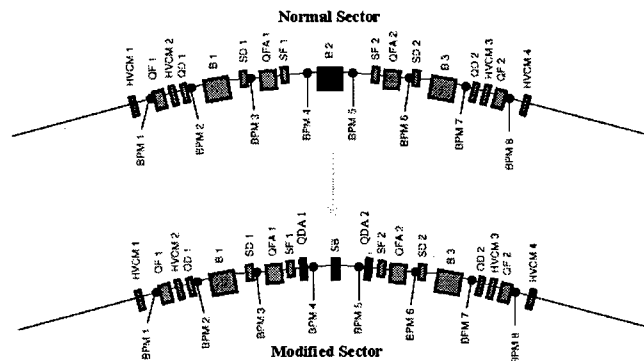
Figure 1. Magnet layout of a normal (top) and modified (bottom) sector.

In 1998 the Superconducting magnet group at LBNL in collaboration with Wang NMR successfully constructed and tested a prototype superbend coil and yoke [2]. One of the superbend field requirements, which was met by the prototype, is that the magnet bend the beam by 10 degrees while achieving a 5 Tesla field at the beamline ports.

Unlike the normal dipoles, the superbends do not have a large quadrupole focusing component. Therefore additional quadrupoles (QDAs) are placed on both sides of the superbend in order to compensate for the lack of focusing. Fig. 1 (bottom) shows a sector modified to include a superbend and two QDAs.

2.1 Matching the Lattice

Once the superbends and quadrupoles are installed, the magnetic fields of the quadrupoles and sextupoles in the ring must be adjusted to match the lattice functions. The goal of the matching is to minimize the distortion of the lattice functions as compared with that of the lattice with no superbends. The QF, QD, and QFA quadrupoles in the normal sectors are used to adjust the dispersion and betatron tunes. The QF, QD, and QDA quadrupoles in the modified sectors are adjusted to match the β-functions

and dispersion to the normal sector [3]. The *SF* and *SD*
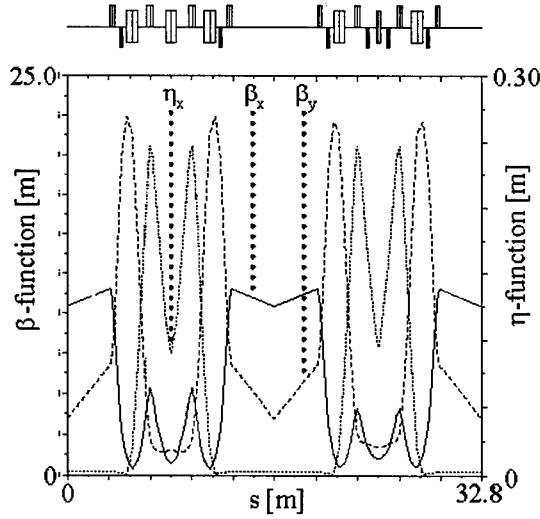
sextupoles are used to adjust the chromaticities [4].

Figure 2. Twiss functions of a normal (left) and modified (right) sector fit to zero dispersion in the straights.

In Fig. 2 the lattice functions are plotted for a normal sector (left) and a modified sector (right) after the lattice has been matched with the dispersion fit to zero in the straight sections [5]. It is also possible to fit the lattice to have positive dispersion in the straight section by slightly increasing the strengths of the *QFAs*.

2.2 Impact on the Machine Parameters

In Table 1 the parameters of the ALS are given with and without the superbends. There are 3 columns in the table. In column 1 the parameters are given for normal ALS without superbends and matched to zero dispersion,η_x , in the straights. In column 2 the parameters are given with 3 superbends and matched to zero dispersion in the straights. In column 3 the parameters are given for 3 superbends matched to 6 cm dispersion in the straights. Due to increased quantum fluctuation with the superbends, the horizontal emittance, ε_x, increases. However by operating with finite dispersion in the straight section it is possible to reduce ε_x.

Table 1: Storage ring parameters with no superbends (η_x=0), 3 superbends (η_x=0), and 3 superbends (η_x=6cm)

	No S-Bends ($\eta_x = 0$)	3 S-Bends ($\eta_x = 0$)	3 S-Bends ($\eta_x = 6cm$)
Energy	1.9 GeV	1.9 GeV	1.9 GeV
ε_x	5.5 [nm rad]	13 [nm rad]	7.5 [nm rad]
σ_E	0.08%	0.10%	0.10%
ΔE/turn	232 KeV	281 KeV	281 KeV

The vertical emittance, ε_y, which is determined by coupling and vertical dispersion can be adjusted using

skew quadrupoles. At present without powering the skew quadrupoles, the ratio of ε_x to ε_y is less than 1%. However with such a small ε_y, the lifetime, which is limited by intrabeam scattering, is unacceptably short — about 2 hours at 1.3 mA/bunch. To recover the lifetime (which in the case of the ALS is proportional to the squareroot of the product of ε_x and ε_y) ε_y is typically increased to 2%. Therefore an increase in ε_x with the superbends, allows us to operate with smaller ε_y for the same lifetime.

3 IMPACT ON BEAM STABILITY

It is important that there be no major impact on the operation of the ALS after the lattice is modified to include superbends. Therefore it is necessary to check that the region of stable motion for the particles is sufficient for good injection and lifetime. We know that the stability of the particle motion will be affected by increased resonance activity resulting from the superbends perturbing the ring's 12-fold periodicity [6] as well as introducing some nonlinear fields. The question is how big is the effect.

The condition for resonance excitation in a machine with *P*-fold periodicity is

$$\frac{N_x v_x}{P} + \frac{N_y v_y}{P} = M \tag{1}$$

where v_x, v_y are the horizontal and vertical betatron tunes, N_x, N_y, and M are integers. The order of the resonance is given by $|N_x| + |N_y|$. From Eq. 1 it is clear that reducing the periodicity allows more low-order resonances to become excited. In the lattice without superbends the degree of periodicity is 12. With 3 superbends located symmetrically around the machine the degree of periodicity is 3. If the superbends are not located symmetrically around the ring, the periodicity drops to one.

2.2 Effect of Reduced Periodicity – Tune Scans

A useful way to visualize the impact of periodicity breaking is through tune scans. This is done in the following way. We use simple 4x4 matrix code to do the tracking where the sextupoles are modeled as thin kicks. The superbends are modeled as isomagnetic sector bends with linear hard edge fringe fields [7]. The strength of the magnetic field, *B*, and length, *L*, is adjusted such that the longitudinal integral of *B* and B^2 is the same as for the true superbend fields. The chromaticity is set to zero in both planes and the dispersion fitted to zero in the straight sections. Attached to the tracking code is a frequency analysis post processor that numerically computes the fundamental frequencies of an orbit [8].

The procedure was the following: First the betatron tunes were set. Then a particle was launched with an initial offset of 10 mm horizontally and 1 mm vertically and tracked for 1024 turns or until lost. If the particle

survives 1024 turns the frequency post processor computes the fundamental frequencies for that particle. The procedure is then repeated for many different tunes. In total the machine is adjusted to 900 tunes (on an evenly spaced grid of 31x31 tunes between $v_x = 14.1$ to 14.4 and $v_y = 8.1$ to 8.4). The results are plotted in Fig.3.
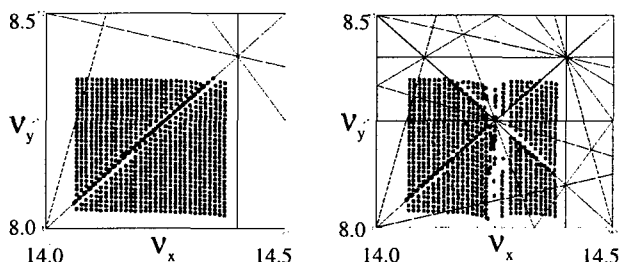
Figure 3. Tunescans: A comparison of 0 and 3 superbends.

On the left in the figure is the lattice with no superbends. on the right side of the figure is a lattice with 3 superbends evenly spaced. Superimposed on the plots are lines plotting all allowed resonances up to 5th order (Eq. 1. with $P = 12$ in the left plot and $P = 3$ in the right plot). The dots correspond to the numerically calculated frequencies. Excitation of resonances can be observed either from missing points or distortion in the point spacing.

In the case of no superbends one only sees the influence of the $2v_x - 2v_y = 12$ resonance. In the case of 3 evenly spaced superbends one sees that there are more resonances excited. In particular one sees a 4th order resonance, $4v_x = 57$, that is strongly excited and also several coupled resonances which cross at the $v_x = 14.25$ and $v_y = 8.25$. In these regions the motion of large amplitude particles is chaotic. However even in the case of 3 superbends evenly spaced there still seems to be large regions in tunespace where it is possible to operate. This is not true in the case of 3 superbends located asymmetrically around the ring. In that case the tunescans were greatly distorted with many missing points.

Based upon the tunescans for the 3 evenly spaced superbends, a working point was chosen ($v_x = 14.25$ and $v_y = 8.2$) for more detailed tracking studies.

3.2 Results of Tracking Studies

For more quantitative particle tracking studies we use a 6-D symplectic integrator. We include a ±25mm horizontal and ±4mm vertical physical aperture. Quadrupole gradient errors are included that match the existing machine producing a 5% horizontal and vertical β-beat and 1% coupling. For the superbends we included an integrated sextupole ($-5.6m^{-2}$) and decapole ($-4.1m^{-4}$) which are the values measured in the prototype [2].

At the ALS injection is made off axis in the horizontal plane. It is necessary to have at least a 7mm horizontal aperture to capture the beam. So for injection studies the particles were launched with different horizontal offsets and no energy offset and tracked for 512 turns or until lost. Without superbends the smallest aperture with errors was calculated to be 14 mm. With superbends it reduced to 11 mm. But there still exists a sufficiently large region for injection.

As previously mentioned the lifetime is determined by intrabeam scattering. Therefore it is important to insure that the momentum aperture is acceptably large. In the ALS the dynamic momentum acceptance is smallest in the arcs and largest in the straight section [9]. We were particularly concerned that a reduction in the momentum acceptance in the arcs could be less than the RF acceptance and reduce the lifetime. To determine the dynamic momentum acceptance the particles are launched with an initial horizontal offset and an energy offset and tracked with synchrotron oscillations. The results of the tracking showed that the dynamic momentum acceptance (in the arcs) reduced from 2.8% to 2.4% with superbends. However this is still larger than the RF acceptance which is 2% at 1.9 GeV. Therefore there should be no impact on the lifetime.

4. CONCLUSION

The superbends will provide excellent sources of high energy radiation for the ALS. There will be an increase in the horizontal emittance but that increase can be minimized by operating with finite dispersion. Tracking studies indicate that there should be no major impact on injection or lifetime.

5. ACKNOWLEDGEMENTS

REFERENCES

[1]H. Padmore and D. Robin, "Initial Results Considering the Impact of the Superbends on the Photon Beam Parameters" (Unpublished)

[2]C. E. Taylor et. al.,"Test of a High-Field Bend Magnet for the ALS", in the Proceedings of the 1998 Applied Superconductivity Conf.

[3]The QFAs were set to the same values in the modified and normal sectors. However they can be adjusted independently.

[4]For all results presented in the paper the chromaticity is set to zero.

[5]At present the ALS operates with the dispersion matched to zero.

[6]D. Robin, J. Safranek, and W. Decking, "Realizing the Benefits of Restored Periodicity in the ALS", to be published in Phys.Rev.S.T.

[7]Tracking simulations using a full 3-D field map were performed by E. Forest showing no significant impact on the beam dynamics.

[8]H. S. Dumas and J. Laskar, Phys. Rev. Lett.,7 (1993), 2975-2979

[9]W. Decking and D. Robin, "Momentum Aperture of the Advanced Light Source", LBNL-42462 (1998)

SPEAR 3 - A LOW EMITTANCE SOURCE FOR SSRL*

U. Beck, P. Bellomo, G. Bowden, R. Boyce, B. Choi, J. Corbett, E. Daly, D. Dell'Orco, M. Dormiani, T. Elioff, I. Evans, A. Garren, R. Hettel, J. Judkins, K. Kennedy, L. Klaisner, N. Kurita, G. Leblanc, C. Limborg, D. Martin, C. Ng, Y. Nosochkov, S. Park, T. Rabedeau, J. Safranek, H. Schwarz, B. Scott, J. Sebek, J. Tanabe, A. Trautwein, C. Wermelskirchen, H. Wiedemann, K. Wille, R. Yotam, F. Zimmermann, K. Zuo, SSRL/SLAC, Stanford, CA

Abstract

SSRL is planning to upgrade the 3 GeV SPEAR storage ring in FY 2002 to reduce the emittance from 160 nm-rad to 18 nm-rad and to increase the beam current from 100 to 200 mA, and then towards 500 mA as photon beam lines are upgraded. The core of the 'SPEAR 3' project includes new magnets and power supplies for a DBA lattice, vacuum chamber, and a mode-damped RF cavity system. Beam lines will see one to two orders of magnitude increase in performance and future high brightness insertion device beam lines are planned. The ring conversion will take place in a 6-month shutdown period to minimize the impact on the SSRL user program. SPEAR 3 lattice, beam properties, and accelerator system components are reviewed.

1 OVERVIEW

The SPEAR storage ring at the Stanford Linear Accelerator Center was constructed in 1972 for colliding beam research and then dedicated as a synchrotron radiation (SR) source in 1989. SPEAR is now scheduled for a major upgrade in FY 2002 to better serve the growing user community at the Stanford Synchrotron Radiation Laboratory [1,2]. By reducing the emittance from 160 nm-rad to 18 nm-rad and raising the beam current to 200 mA, SPEAR 3 will be comparable with 3rd generation SR facilities. The focused SR flux density at experimental stations will increase by an order of magnitude for insertion device beam lines and by two orders of magnitude at higher photon energies on bending magnet beam lines. A lifetime of >30h at 200 mA will enable 24 h beam delivery times.

As beam line components are upgraded, the SPEAR 3 current will be raised towards 500 mA, with a proportional increase in beam focused flux density and beam brightness. New insertion device beam lines that exploit the low emittance and small size of the SPEAR 3 beam are also planned [3]. These include 4 m undulators having brightnesses approaching 10^{19} in the 1-5 keV regime and a vertically polarized wiggler requiring a small horizontal vacuum chamber aperture. The SPEAR 3 conversion entails replacing the existing storage ring magnet, vacuum chamber, RF, and most power systems in a 6-month shutdown period to minimize the impact on the SSRL scientific program. A compact double bend

Table 1. Source parameters for SPEAR 2 and SPEAR 3.

	SPEAR 2	SPEAR 3
Energy	3 GeV	3 GeV
Current	100 mA	200/500 mA*
Emittance(w/ IDs)	160 nm-rad	18 nm-rad
RF frequency / h	358.5 MHz/280	476.4 MHz/372
Lifetime	30 h @ 100 mA	>30 h @ 200 mA
Critical energy	4.8 keV	7.6 keV
Tunes (x,y,s)	7.18, 5.28, .019	14.19,5.23,.007
e- σ (x,y,s) - ID	2.0, .05, 23 mm	0.43, .03, 6 mm
e- σ (x,y,s) -bend	.79, .20, 23 mm	.16, .05, 6 mm
Injection energy	2.3 GeV	3 GeV

* 200 mA phase 1; future increase to 500 mA as beam lines upgraded.

achromat (DBA) lattice has been developed that maintains the present beam line alignment and provides four enlarged 4.5 m straight sections adjacent to two 7.5m racetrack straights, in addition to twelve 3m straights. Magnet and vacuum chamber systems will be pre-assembled on new support girders (Fig. 1) to reduce installation time. Intensively cooled monochromators (including LN-cooled devices) and other absorber components will be installed on beam lines to handle the increased SR power load [3].

The upgrade project is administered by the DOE, with major funding contributions from the National Institutes of Health. Principal features of the SPEAR 3 design and beam properties are discussed below.
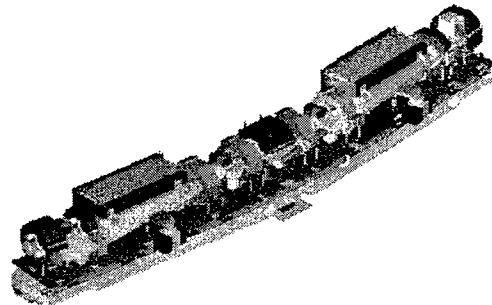
Figure 1. 8.9 m magnet girder with 2 gradient dipoles, 5 quadrupoles, 4 sextupoles, and 4 H/V correctors.

2 LATTICE

The 234 m SPEAR 3 lattice has a double bend achromat (DBA) configuration with vertical focusing in the dipoles to enhance separation of the x and y focusing and reduce sextupole strengths [4]. There are 14 standard cells and 4 matching cells flanking the two long straight sections. Straight sections have nominal beta functions of 10 m horizontally and 5 m vertically to maximize photon flux density (Fig. 2). Betas are held below 18m globally to reduce sensitivity to field errors, and minimize beam stay clear. The magnet parameters were optimized to provide optical tunability and uniform field ramping to 3.3 GeV. The optics can be modified for finite dispersion in the straights to reduce emittance by up to 30%. Vertical coupling and beam size can be adjusted using a system of 14 skew quadrupoles. The matching cells can also be tuned for future applications requiring lower betatron functions in the long straights.
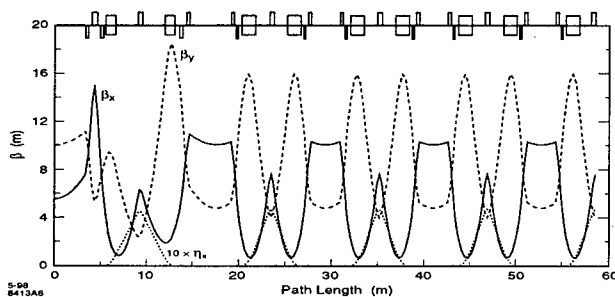
Figure 2. Lattice functions for one SPEAR 3 quadrant.

The phase advance per cell is ~1.5π horizontally and ~0.5π vertically to locally cancel chromatic betatron waves from quadrupoles and sextupoles and geometric sextupole aberrations. The layout, phase advance and sextupole strength in the matching cells leading into the two long racetrack straights were optimized to produce low beta functions and maximize off-energy dynamic aperture. Global tunes v_x=14.19 and v_y=5.23 were chosen to operate below the half integer to reduce resistive wall effects, to avoid strong resonance lines, to provide efficient injection, and to optimize dynamic aperture. Tracking data at ID locations indicate that with a full complement of magnet errors the horizontal dynamic aperture exceeds 20 mm with minimum reduction for off-momentum particles [5].

3 BEAM PROPERTIES

SPEAR 3 electron beam dimensions at photon beam source points are given in Table 1. Vertical beam size assumes 1% horizontal-vertical emittance coupling, which can be controlled by adjusting skew quadrupoles.

The goal for transverse beam stability is <10% of the photon beam size and divergence at beam line source points to maintain <0.1% intensity constancy past small apertures and precise beam alignment on small samples. This stability level can be achieved by minimizing magnet thermal motion and vibration relative to beam line optical components, and by using orbit feedback to maintain rms beam position to ~20 μm horizontally and ~5 μm vertically at BPM locations. Feedback bandwidth is on the order of 100 Hz to suppress low frequency orbit motion. Coherent longitudinal bunch oscillations must be <0.4° rms (dE/E <0.016%) to maintain transverse stability in dispersion regions and to prevent line width broadening of higher undulator harmonics.

HOMs in the mode-damped cavities and chamber are not strong enough to excite 500 mA coupled bunch instabilities[6]. Antechamber and beam duct are decoupled for modes at or below the cutoff frequencies (4.7 GHz TM and 2.1 GHz TE) by a 12 mm high, 5 cm wide slot. We are investigating <1 GHz TE modes in the wide antechamber sections that could influence BPM readings. A broadband impedance of ~1Ω is estimated using a resonator model having R_s = 12 kΩ, Q = 1, and f_{res}= 15 GHz, derived from the ~60 nH inductance caused by discontinuities and transitions in the 34 x 84 mm beam duct crossection (Fig. 3). The resistive wall instability is suppressed by setting the ring tunes below the half-integer and by head-tail damping achieved with positive chromaticity (~0.2 normalized). The threshold current is then 450 mA for a stainless steel chamber and >800 mA for a copper chamber (Sec.4). In either case the resistive wall impedance is dominated by small-gap stainless steel ID chambers.

The gas scattering lifetime is calculated to be 83 h at 200 mA assuming a 0.6 nTorr N$_2$-equivalent pressure, comprised of a 275 h Coulomb lifetime and a 120 h Bremsstrahlung lifetime. The Touschek lifetime is RF bucket-limited at 217 h for 200 mA in 279 out of 372 bunches, with 3.2 MV gap voltage, 1% coupling, and 3% energy acceptance. A 93-bucket gap (1/4 of the ring) is left empty to avoid ion trapping. The total lifetime is calculated to be 60 h at 200 mA, and ~20 h at 500 mA (assuming 1.5 nTorr N$_2$-equivalent pressure at 500 mA).

4 ACCELERATOR SYSTEMS

The SPEAR 3 lattice has 36 C-shape gradient dipoles (k = 0.33), 94 Collins-type quadrupoles, 72 closed-yoke sextupoles, 54 horizontal and 54 vertical combined function dipole correctors, and a vertical Lambertson septum magnet [2]. Magnets and vacuum chamber are mounted on new steel support girders, each resting on three existing pylons embedded 2m in the ground plus a fourth new concrete support pad to increase stability. Magnets are optimized for 3 GeV operation but can be run at 3.3 GeV. Magnet cores are made with AISI 1010 steel laminations, either glued or compressed using end plates and longitudinal rails. Chamfered ends improve integrated field quality. A straight core was chosen for the 1.45 m dipole to simplify construction at the expense

of a wider pole for the 33 mm beam sagitta. Main coils are made of water-cooled hollow copper conductor insulated with fiberglass and vacuum-impregnated with epoxy. Quadrupoles and dipoles have ~2% trim coils for beam-based alignment excitation; sextupoles have skew quadrupole trim coils. Laminated core correctors have ~200 Hz bandwidth for orbit feedback. Chopper-style power supplies will be used for all magnets. SLAC is collaborating with IHEP to build the magnets in Beijing.

An antechamber vacuum chamber design (Fig. 3) with discrete photon stops and nearby TSP vacuum pumps has been chosen to achieve low pressure and high mechanical stability under varying SR loads [7]. The 8.9 m girder chamber has three bellows-connected sections. Sloped masks and crenellated crotch-type absorbers intercept powers of 0.5-8 kW with power densities as high as 20 W/mm^2 and fan heights as small as 0.5 mm. The higher power density components employ GlidCop^{TM} to handle the thermal stresses.

Two water-cooled chamber designs having 3-5 mm wall thickness in magnet apertures are presently being evaluated. A formed stainless steel chamber with 1 mm copper cladding and copper inserts in the chamber slot downstream of each ID is passively safe to 50 mA for both dipole and ID radiation. Without copper inserts, the safe current is 6 mA for ID radiation. A machined copper chamber option is passively safe to 50 mA for ID radiation and to >500 mA for dipole radiation. An orbit interlock ensures the electron beam stays within a ±1 mm vertical and ±5 mm horizontal window at source points for potentially damaging SR beams. The number of BPMs and interlock complexity is reduced by more than a factor of two for the copper chamber. The 12 mm slot height between beam chamber and antechamber is a compromise between a small gap for choking RF modes and a large gap that increases the safe orbit window.

The penetration and transverse uniformity of AC fields from fast orbit correctors are sufficient in the stainless chamber, and can be dramatically improved in the copper chamber by reducing eddy currents with high resistivity CuproNickel^{TM} chamber inserts at corrector sites (Fig. 3). Chamber impedance is reduced by minimizing step discontinuities, providing 5:1 transitions

between different crossections, and using RF-shielded bellows and slotted pipe injection kickers [8]. BPM thermal motion is minimized using bellows and temperature-stable supports (Invar or carbon fiber).

Four PEP-II mode-damped 476.4 MHz RF cavities [9] in the West racetrack straight section will replace the present 358.5 MHz 5-cell cavity system to provide stable high current operation. The 1 MW needed to produce a 3.2 MV gap voltage for 500 mA will be supplied either by two 600 kW klystrons powered with existing HV supplies or by a single 1.3 MW PEP-II tube with a new supply. PEP-II RF controls will be used. Cooling water and cavity temperature will be stabilized to 0.1°C.

An expanded SPEAR computer control system will be enhanced with fast digital control links for orbit control and monitoring. The orbit feedback system will acquire orbit information from 92 BPMs and update setpoints for 108 correctors with a 2 kHz cycle rate. 36 orbit interlock BPMs are needed for the stainless steel chamber, while only half that many are needed for the copper chamber (2 BPMs per ID). A vertical beam size interlock is also needed to prevent chamber damage from vertically unstable SR beams. An AC quadrupole modulation system will be used for beam-based alignment and BPM calibration. Other beam diagnostics include upgraded tune and current monitors, a new SR monitor, and bunch phase and turn-turn position monitors. The timing system will be modified to enable injection from the 358.5 MHz booster into the 476.4 MHz ring. Machine and personnel protection systems will be expanded, and a new cable plant will be installed. Radiation shielding will be improved in some areas, and LCW and AC distribution systems will be refurbished.

5 ACKNOWLEDGMENTS

6 REFERENCES

[1] W. Davies-White, H. Wiedemann, "SPEAR Upgrade Program", SSRL internal report, Jan. 8, 1997.

[2] "SPEAR 3 Conceptual Design Report", 1998, in press.

[3] "SPEAR 3 Workshop: Making the Scientific Case", May 29-30, 1997, SLAC Pub SLAC-R-513.

[4] J. Corbett, C. Limborg, Y. Nosochkov, J. Safranek, A. Garren, "Design of the SPEAR 3 Magnet Lattice, 1998 EPAC, 574.

[5] J. Corbett, Y. Nosochkov, J. Safranek, "Dynamic Aperture Studies for SPEAR 3", these proceedings.

[6] C. Limborg, J. Sebek, "Collective Effects in SPEAR 3", these proceedings.

[7] N. Kurita, E. Daly, B. Scott, "Overview of the SPEAR 3 Vacuum System", these proceedings.

[8] G. Blokesch, M. Negrazus, K. Wille, Nucl. Inst. and Meth. in Phys. Res. A 338 (1994) 151-155.

[9] R. Rimmer, M. Allen, J. Saba, H. Schwarz, F. Belser, D. Berger, R. Franks, "Development a High-Power RF Cavity for the PEP-II B-Factory", Proc. of the 1995 PAC, 1729.

BM-2 chamber
3.54 m

Copper chamber

12 mm slot

34 x 84 mm
beam duct

CuNi insert
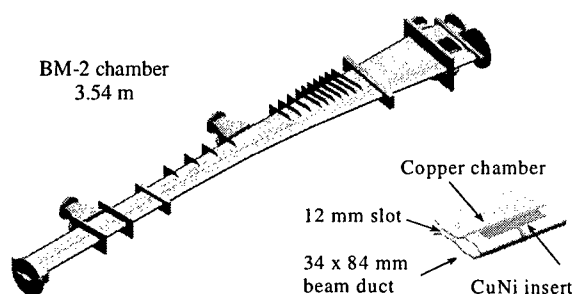
Figure 3. One of 3 girder chamber sections. Inset shows CuproNickel^{TM} insert to reduce eddy current attenuation of corrector AC fields if chamber is made of copper.

SHANGHAI SYNCHROTRON RADIATION FACILITY

S. Y. Chen, H. J. Xu, Z. T. Zhao

SSRF Project Team, Chinese Academy of Sciences, Shanghai, P. R. China

Abstract

The Shanghai Synchrotron Radiation Facility (SSRF) was proposed by the Chinese Academy of Sciences and the Shanghai Municipal Government in 1995. The estimated total budget is around 120M USD, and the operation is scheduled to begin by the end of 2004. Although the whole SSRF project is still awaiting final approval, its R&D has been approved already. The SSRF is a third generation light source designed to produce high brightness and flux soft X-ray and hard X-ray in the energy region of 0.1~40keV. It consists of a 300MeV linac, a 3.5GeV booster, a 3.5GeV storage ring and dozens of beam lines and experimental stations. In this paper, the main parameters and features of the SSRF are presented.

1 INTRODUCTION

In order to meet the growing demand for synchrotron radiation application in China, the Chinese Academy of Sciences (CAS) and the Shanghai Municipal Government (SMG) made a joint proposal for constructing an advanced third generation light source, namely, the Shanghai Synchrotron Radiation Facility (SSRF), in 1995. The SMG promised to contribute one third of the total project budget, and the CAS took the scientific and technical guarantee for the project. One year later the draft of the SSRF conceptual design was completed and positively reviewed by an international review committee in September of 1996. Then the R&D of the SSRF project was approved by the state in 1997, and the 80M Chinese Yuan budget for this R&D was allocated in 1998. For assuring the success of the project construction, the leading group of the SSRF was set up by the CAS and the SMG with the president of the CAS as its head and the executive deputy mayor of the SMG and a vice minister of the Ministry of Science and Technology of China as its deputy heads in September of 1998. Since then the R&D of the SSRF has been undertaken.

2 DESIGN OVERVIEW

2.1 Design Goal

The purpose to construct the SSRF is to establish a multidiscipline frontier research center and a high-tech R&D base in order to offer attractive research opportunities for a wide variety of fields in China.

The requirements of the CAS and the SMG on the construction of the SSRF are as follows. (1) The performance of the SSRF should be better than that of the present existing third generation light sources at the same energy region, and be at the forefront of its kind when it is completed at the beginning of the 21st century. (2) The research lifetime must be longer than 20~30 years after its establishment. (3) And its budget should be around 120M USD. They are quite ambitious.

Since the largest part of user community in China works in the X-ray region of spectrum 4-40keV and the second largest in the soft X-ray region of 0.1~4keV, the SSRF is designed to produce high brightness and flux X-ray in the energy region of 0.1~40keV.

2.2 Design Modification

In the initial design [1] of the SSRF, the nominal energy of the SSRF storage ring is 2.2GeV, so actually the SSRF would be a VUV and soft X-ray light source even its energy can be upgraded to 2.5GeV, it cannot fully meet the user demands. This is mainly due to the budget limitation. The emphasis of the former design is laid on reaching low emittance, therefore the brightness of the SSRF would be higher than that of currently operating VUV and soft X-ray third generation light sources. After examining other alternatives, the modified TBA lattice structure with the emittance of 3~4nm-rad and the circumference of 345m is chosen for the SSRF storage ring. In order to provide the capability of the hard X-ray with the energy extending to 60keV, several normal bending magnets can be replaced by superconducting dipoles. Furthermore two super long straight sections of 18m are preserved for the potential use in the future.

Considering seriously the suggestions [2] of the experts attending the 96' International Review Meeting on the Concept Design Report of the SSRF, and the sharp increase of the user demand for X-ray and hard X-ray, we have modified the SSRF design goal to greatly increase the brightness of the energy spectrum in hard X-ray region and make the SSRF cover much wider spectrum by increasing the design energy to 3.5GeV with adding a little investment, so that the SSRF has a better cost-effectiveness. In the new design, we sacrifice the performance of the SSRF in VUV and soft X-ray region and give up the original goal of providing the brightest beam in the photon energies below 3keV. To meet the design goal, several possible lattice structures including DBA [3] and modified TBA[4] types have been studied,

and are available for the SSRF. For simplicity we adopted the DBA lattice structure.

3 MACHINE FEATURES

The SSRF complex sketched in Fig.1 consists of three major parts, a full energy injector including a 300MeV linac and a 3.5GeV booster as well as the corresponding beam transport lines, a 3.5GeV storage ring and the synchrotron radiation experimental facilities.
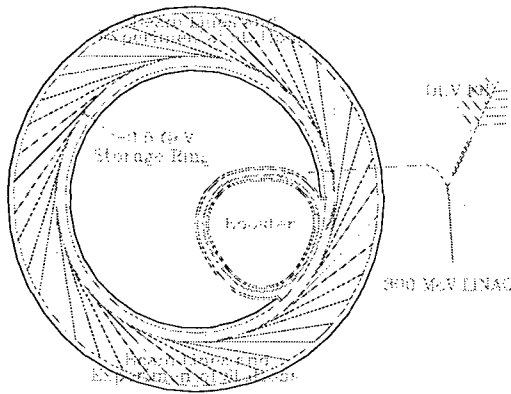
Fig.1 Layout of the SSRF

3.1 Lattice

The new lattice of the SSRF storage ring is a double-bend achromat structure. It is composed of 20 cells with 10 of 6.6 m and 10 of 4.6m long dispersion-free straight sections. The circumference of the storage ring is 384m. Each asymmetrical DBA cell contains 2 bending magnets, 10 focusing quadrupoles and 7 sextupoles. Its linear lattice functions are shown in Fig.2.
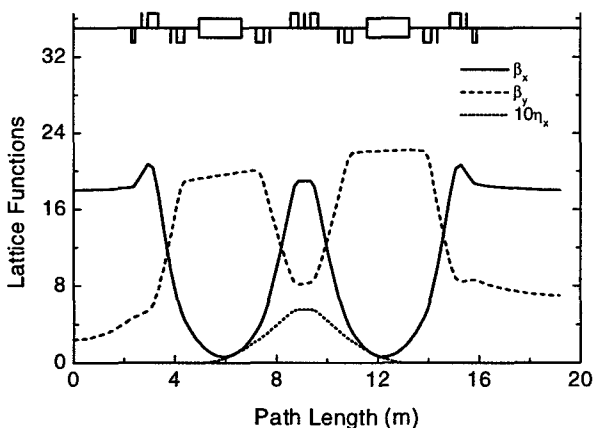
Fig.2 Lattice functions for one cell

There are altogether 4 families of sextupole, in which two of them located at the achromatic arc are used to correct chromaticities, and the other two families distributed in the non-dispersive region are used for

harmonic correction to improve the dynamic aperture as well as the energy acceptance. After tentative optimisation, the horizontal and vertical dynamic apertures off momentum (±3%) with multipole field errors at the injection point reach ±20 mm and ±18mm respectively, as shown in Fig.3. And the energy acceptance of the ring is larger than 3%.
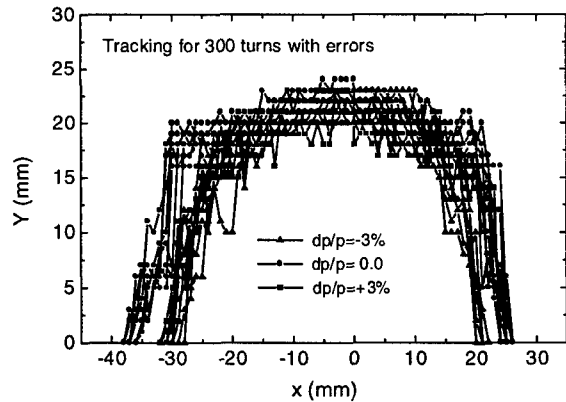
Fig. 3 Dynamic aperture at the injection point

Besides, the effects of magnetic imperfect, the closed orbit distortion and correction, the effects of insertion devices, the beam instabilities and the beam lifetime, the injection and etc. have been preliminarily studied, they also meet the design requirement. The storage ring optics with non-zero dispersion in the straight sections has been examined, giving a reduction factor of about 2 in the beam emittance. Now the lattice optimisation of the storage ring is still underway.

3.2 Main Parameters of the Storage Ring

Energy	3.5 GeV
Circumference	384 m
Natural Horizontal Emittance (rms)	12.1 nm·rad
Beam Current (multi-bunch)	200-300 mA
(single bunch)	>5 mA
Number of cells	20
Insertion Straight Sections	6.6m10,4.6m 1 0
Magnetic filed , normal dipole	1.104 T
Number of quadrupoles	200
Max. gradient for quads	18.5 T/m
Number of Sextupoles	140
Max. sextupole strength.	450 T/m^2
Betatron tunes, Q_x/Q_y	18.22/7.18
Natural Chromaticities ξ_x/ξ_y	-45.1/-20.8
Momentum compaction	7.1×10^{-4}
Harmonic number	640
Radio Frequency	499.65 MHz
RF Voltage	4.0 MV
Energy Loss per Turn	1.256 MeV
Bunch Length (rms) σ_s	4.87 mm
Beam Lifetime	>20 hrs

3.3 Photon Brightness and Flux

Fig.4 and Fig.5 show the brightness and flux of the SSRF under the current existing insertion devices. Comparing with the original design, after the modification, the high harmonics from undulators could provide X-ray beams of 7~20keV with a brightness of about 10^{17} or higher, 3 or more orders of magnitude higher than that from the super-conducing bending magnet in the original SSRF design. This significant increase in hard X-ray brightness is the most important feature of the SSRF. In addition, the larger emittance and the higher electron energy will greatly increase the beam lifetime and also the dynamic aperture of the storage ring. Another advantage of this design is that the 300MeV SSRF linac could be used meanwhile for the application research of the DUV FEL (Deep Ultra Violet Free Electron Laser).
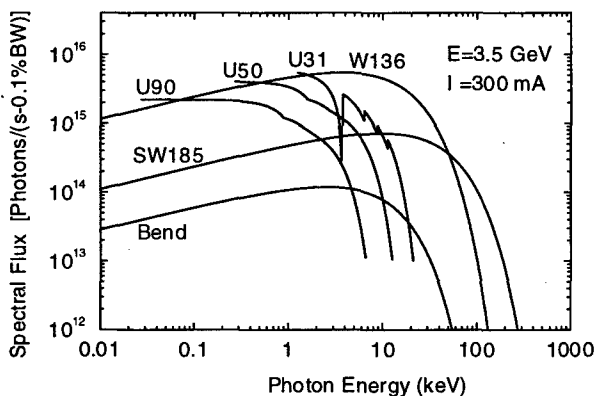
Fig. 4 Spectral Flux of SSRF
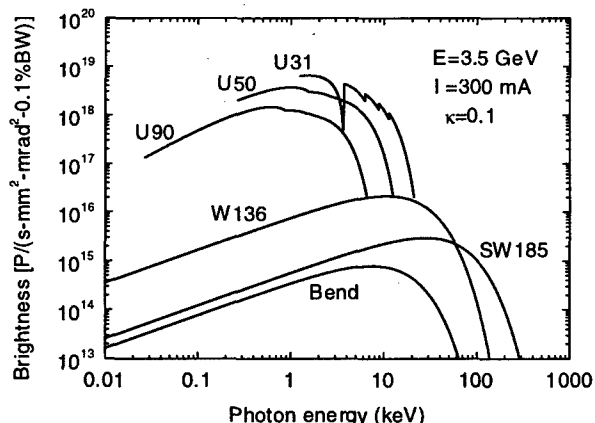
Fig. 5 Spectral Brightness of SSRF

In short, the new design might be considered the best in cost-effectiveness over a broad spectral range and the SSRF will be close to the best in the world over a spectral range extending from the VUV to the hard X-ray with a little more cost.

Moreover, 7 beam lines and experimental stations for the first phase construction were selected by the first SSRF Users' Meeting last December, they are for macromolecular crystallography, X-ray absorption fine structure spectroscopy, high resolution diffraction and scattering, microfocusing, medical application, soft X-ray coherent microscopy and LIGA.

4 COST ESTIMATE AND SCHEDULE

On the basis of the information acquired from domestic and foreign industries as well as some light source laboratories in the world, the preliminarily estimated cost of the SSRF is around 1 Billion Chinese Yuan (in the FY of 1998, excluding management cost and staff wages). Of course, the final estimated cost will be achieved when we complete the detailed design and the R&D of the SSRF.

To catch up with the development of synchrotron radiation application in the world, we shall strive to make the SSRF one of the advanced third generation synchrotron radiation facilities that will be operated at the beginning of the 21st century. The tentative project schedule has been proposed under the important prerequisite that the whole SSRF project should be approved before the middle of 2000 by the Chinese government. The proposed overall schedule of the SSRF project is to start the light source commissioning in April of 2004 and to run it for the users from the following October.

6 REFERENCES

[1] S. Y. Chen and H. J. Xu, "Current Status of the Proposed Shanghai Synchrotron Radiation Facility", Proc. of APAC'98, Tsukuba, (1998)

[2] H. Winick, et al, "Report of the Review Committee on the Conceptual Design Report (CDR) of the Shanghai Synchrotron Radiation Facility (SSRF)", Shanghai, (1996)

[3] R. Chasman and K. Green, "Preliminary Design of a Dedicated Synchrotron Radiation Facility", IEEE on Trans. Nucl. Sci., NS-22, 1765 (1975)

[4] A. Jackson, "A Comparison of Chasman Green and Triple Bend Achromat", Particle Accelerator, Vol.22, 111 (1987)

HIGH POWER FREE-ELECTRON LASERS[*]

S. Benson, TJNAF, Newport News, VA

Abstract

Though free-electron lasers have long had the potential for high average power, only recently has significant progress towards this goal been evident. This paper will summarize some of the issues that all high average power free-electron lasers must contend with and will show how researchers have addressed these problems as encountered in four different approaches.

Progress and problems in each of these programs will be summarized and the paths towards even higher power will be discussed.

1 INTRODUCTION

From the early days of free-electron lasers, it was generally believed that FELs were capable of high average power, if for no other reason than that high average power electron beams had been demonstrated. The Strategic Defense Initiative produced a huge effort aimed at producing high average power from a FEL but the initial efforts were predominantly aimed at developing the technologies involved in building a high power device rather than actually building one [1]. Recently several projects have been initiated using existing technologies to build a high average power free-electron laser (HAPFEL). This paper will discuss the problems such projects face and will describe four projects as examples of the approaches possible.

It is useful to start with the most basic ideas. The power from a free-electron laser is given by

$$P_{FEL} = E_{eb}I_{eb}\eta_{FEL}\eta_{opt} \qquad (1)$$

where E_{eb} is the electron beam energy, I_{eb} is the average electron beam current, η_{FEL} is the efficiency of conversion of electron beam energy to laser light, and η_{opt} is the output coupling efficiency of the optical cavity. The electron beam energy is bracketed by the resonance equation for FELs

$$\lambda = \frac{\lambda_W(1 + K^2)}{(1 + \beta)\beta\gamma^2} \qquad (2)$$

where λ_W is the wiggler wavelength, K is the wiggler parameter, β is the velocity of the electron divided by the speed of light and γ is the relativistic energy divided by the rest mass of the electron. The numerator can range from about 3 cm to 300 cm for an undulator capable of transporting a high-average-power electron beam. This brackets the energy for any given wavelength to a range of a factor of ten. One generally likes to operate at the highest energy one can afford in this range. The energy of a HAPFEL is therefore determined more by the desired cost and footprint rather than by any physics requirements.

The output coupling efficiency is normally rather close to unity. It is very unwise to design a high average power device with low efficiency since the power lost in the cavity will lead to problems with component failure. Since this efficiency is already high, the dominant knobs one has to increase the power are the average electron beam current and the FEL efficiency.

Increasing the electron beam current leads to many practical design problems such as providing the required acceleration and dumping the beam after the FEL. One approach to these problems is to recover as much of the energy of the electrons as possible. The higher the efficiency, the more difficult a task energy recovery becomes. When using energy recovery, the efficiency is limited to a few percent. If one can increase the efficiency by a large factor, the required beam current is reduced by the same factor for a given average power. The problem with this approach is that the requirement for electron beam brightness is much more stringent.

With all the previous comments in hand, two approaches to attaining high average power present themselves. The first is to produce a very high-average-current beam with moderate brightness, lase with moderate efficiency, and recover as much of the electron beam energy as possible. The second approach is to produce a very high brightness electron beam at moderate average current, extract as much power as possible, and dump the beam at full energy.

A third possible approach which has received a great deal of study is the use of a storage ring. Unfortunately the efficiency of storage ring FELs is limited by the so-called Renieri limit [2] which limits the laser power to a small fraction of the synchrotron light emission in the ring. Until this limit can be circumvented, storage ring FELs will not scale well to very high power.

Different energy ranges are more efficiently provided with different accelerator technologies. We therefore find that the mm-wave region is best served by DC or long pulse accelerating techniques such as Pelletrons, modulators, and Induction linacs. To reach the optical wavelength range it is more efficient to use RF acceleration. When energy recovery is used, the choice of superconducting RF is very attractive since the RF power required is dramatically reduced. The cost and complexity of SRF acceleration may not be as attractive for systems without energy recovery though it may still be appropriate due to the large aperture of the SRF cavities. The low shunt impedance of the SRF cavities reduces wake fields that cause emittance and energy spread growth.

With the previous comments as a guiding principle, I have organized this paper as follows: In section 2 I discuss some of the design issues in common with all. I then cover, in section 3, a pair of examples of low energy electron accelerators driving mm-wave FELs both with and without energy recovery. Finally, in section 4, I discuss two high-energy RF accelerators driving infrared FELs again with and without energy recovery.

2. GENERAL DESIGN ISSUES

Many of the challenges in building a high power FEL are common to all approaches. This section discusses some of these challenges.

The biggest design challenge facing those building high power FELs is to build an electron source with a combination of high average current and high brightness. Either feature is easy to produce but they are rarely available simultaneously. For high-energy RF accelerators this pushes one towards photocathode sources. DC and long pulse sources are well served by state-of-the-art thermionic guns.

Even with a high-extraction-efficiency FEL, the average current in a HAPFEL is quite high. Since the peak current is also high, the possibility of non-linear effects leading to halo formation arises. Halo created in the injector is often present as well. The beam loss in the transport system must be held as low as possible. It is important to remember that the electron beam in such a device will have on the order of 1 MW of power. A loss of even 0.1% can lead to serious problems unless the loss point is designed to handle the power. Energy recovery can exacerbate this problem since the energy spread after the FEL can be quite large and the energy aperture must be larger than this energy spread.

Even if losses are low in most of the system, the final beam dump is usually a tremendous design challenge. If the beam is dumped at high energy, activation of the dump and production of radionuclides is a problem that must be dealt with. At low energy, the current density must be sufficiently low to keep the power density on the dump below 1 kW/cm^2. Since the total power at the dump might be as large as 1 MW, the resulting size of the dump can be quite large.

FELs have very good optical mode quality and a very small mode volume. This means that the power density in the optical cavity can be enormous in a HAPFEL. The optical cavity must be designed so that the mode diffracts out to a reasonable power density before hitting any surface. This can lead to a large increase in the device footprint, especially at short wavelengths where the mode divergence is small.

Finally, it should be noted that the overall system cost for a given average power increases as the net efficiency of the FEL falls [3]. Thus, the net efficiency must be made reasonably high to keep the capital cost down.

3. LOW ENERGY MACHINES

FELs operating in the mm-wave region required electron beam energies in the range of 2–20 MeV. Electron beam brightness in the range can be quite high using DC acceleration as in a Pelletron or in a pulsed modulator or an induction linac. The very high peak current in the induction linac provides one with the option of high efficiency. The first approach discussed here is an induction linac used to drive a high-extraction-efficiency FEL. The example used is that of the ETA III induction linac driving a 2.1 mm FEL used for plasma heating experiments in the Alcator C tokamak [4]. The ETA III produced high current pulses with a 35 nsec, 2.5 kA, flattop at an energy of 6.3 MeV. The typical repetition rate was 1 Hz but the machine could be operated in a burst mode with up to 50 pulses being emitted at 2 kHz. In low repetition rate operation the laser put out up to 2 GW in a 15 nsec pulse. The peak efficiency was therefore over 12%. In burst mode, the efficiency dropped but approximately 6 kW in a 12 ms burst was achieved.

Though the peak power and efficiency in the ETA III device is quite impressive, it is important to note that the efficiency averaged over the 50 nsec FWHM pulse is not quite as impressive and the efficiency in burst mode was quite modest. Any attempt to scale this system to high average power will have to deal with the problem of the wasted beam during the turn-on and turn-off transients. Since this beam may not be well transported, it may lead to transport problems as well. In general, high average power lasers have been CW or long-pulse devices. Pulsed systems, though useful in their own right, do not scale well to high average power.

A second approach to achieving high-average-power mm-wave radiation is being used at the FOM Plasma Physics Institute in Rinhuizen, the Netherlands. The application, as with the ETA III FEL, is for plasma heating. It uses a DC accelerator with an energy up to 2 MV to accelerate a continuous electron beam along a straight beam path through the FEL and then decelerate the beam back to a depressed collector [5]. The design current is up to 12 Amperes. The power supply for the accelerator is only capable of providing 20 mA of current so the energy recovery must be greater than 99.8% for this device to operate with CW beam.

The laser has been operated in "inverted mode" to date. In this mode, the gun is placed in the high voltage dome and the beam is accelerated down to ground. It is then passed through the FEL and dumped. The current in this case is coming from the stored energy in the accelerator and the pulse length is limited to around 20 μs before the voltage has drooped too much. In this mode the laser has operated with power levels as high as 730 kW at 1.46–1.52 mm with an electron beam energy of 1.75–1.83 MeV. The laser lases for around 10 microseconds before the electron beam moves out of resonance

with the cavity mode. The efficiency of the FEL is approximately 5%, which is equal to the design value for full power operation.

The project is now installing the depressed collector and the mm-wave transport so that the machine can operate in energy recovery mode. Even when operated pulsed with ms pulses, the laser should be capable of kilojoule pulses. The FEL has a novel optical cavity that allows variable cavity output coupling and low losses while allowing the electron beam to pass through in a straight line. The power density on the mirrors in this cavity is extremely high and remains one of the largest risks of this project. The power may ultimately be limited by optical cavity distortion.

Note that there are many other efforts at producing high average power in the mm-wave range. The University of California at Santa Barbara [6], the University of Central Florida [7], Tel Aviv University [8], and KAERI in Korea [9] have programs producing machines similar to the FOM machine but with average power in the kilowatt range. The Naval Research Laboratory produced a pulsed modulator based device that produced up to 36 W of average power as well [10].

4 HIGH ENERGY MACHINES

4.1 Room temperature Linacs

An interesting approach using a room temperature linac with high-extraction-efficiency is the regenerative amplifier arrangement (RAFEL) [11]. The idea of this device is to use the simplest accelerator possible to produce a very high brightness electron beam. This is then sent through a high gain wiggler with two plane focussing. The first part of the wiggler is untapered to produce high gain. The second part is tapered to enhance the extraction efficiency. The outer edge of the output of this laser is scraped off using an annular mirror and recirculated back through the wiggler using another annular mirror. Since the gain is very high, the output is only weakly dependent on the recycled light. Since the exit mirror only sees the edge of the output distribution, it is not exposed to the high intensities in the center of the cavity. The output coupling efficiency is extremely high since only 8% of the light is actually picked off to be sent back into the optical cavity. The electron beam is separated from the optical mode using a magnet after the annular mirror and dumped.

Results to date from this device are impressive. With 4.5 nC, 16 ps long electron pulses at 16.7 MeV with a normalized emittance of 7 π mm-mrad and an energy spread of 0.5% FWHM, the laser output is 1.9 mJ per micropulse [10]. The macropulse energy for a 16 μsec macropulse is 2.1 J at 1 Hz. When the macropulse repetition rate is increased, the average power increases to 13 W at 10 Hz. For 1 Hz operation, the efficiency is 2.5%. The design efficiency is 5% for 6 nC bunches.

The biggest challenge facing the designer of RAFEL type lasers is increasing the duty cycle while maintaining the electron beam brightness. The present device is limited to around 30 μA of average beam current. A high power device will need average current exceeding 1 mA. The drive laser is the main limitation in the present system. A high power system may have to use a photocathode with a good efficiency in the visible. When the electron beam is raised above 20 MeV the issue of the beam dump must be addressed. Dumping a high power electron beam at high energy produces massive quantities of radionuclides. This is a major design challenge. In a very high power device the beam may have to be decelerated just to reduce the radiation.

There have been many proposals to use a high efficiency FEL to attain high average power but the Los Alamos device is the first to make much progress in showing that such devices may be practical. Design studies show that such a device may be scalable to the 100 kW power level.

4.2 SRF Linacs

The IR Demo FEL at Jefferson Lab was constructed in the period from July 1996 through July 1998 [12]. The accelerator is shown in figure 1. The beam is produced in a DC photocathode gun at a nominal voltage of 350 kV. It is then bunched in a room temperature buncher cavity and accelerated up to 9.5 MeV in two high performance superconducting cavities. The beam is then sent into a 38 MeV cryomodule using an achromatic chicane and accelerated up to the operating energy. For most of the results reported here the final kinetic energy was 38 MeV. The beam is then bent around the output coupler of the laser cavity and matched into a 40 period wiggler with a period of 2.7 cm and a wiggler parameter K of 0.98. The exhaust beam is then bent around the high reflector and transport back to the entrance of the cryomodule in two Bates style achromatic bends [13]. These bends have a design acceptance of greater than 6%.
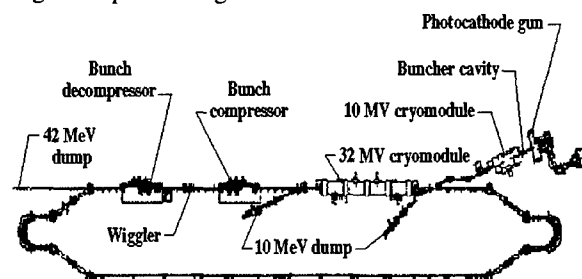
Figure 1. Schematic of IR Demo: the dimensions of the recirculation loop are roughly 49m x 6m.

When operated in a "straight-ahead" mode so that the beam is dumped at full energy, the average current is limited to 1.1 mA by the available RF power. In this configuration the laser emitted up to 311 W [11]. When the beam is recirculated very little RF power is required and the current is limited to 5 mA by the injector. The recir-

culator has been operated at current up to 4 mA with no lasing and 3.8 mA while lasing. When optimized, the laser emitted 710 W with a current of 3.6 mA on March 11, 1999. This is the highest average power yet recorded from a FEL.

Several features of this laser should be noted. First, the power required in the full cryomodule is essentially independent of the current up to 3.5 mA as shown in figure 2 [14]. This is a verification that recirculation is effective in reducing the required RF power. The loaded cavity Q was chosen to minimized the RF power for a level of microphonics much higher than actually seen so the required power might be lowered below that required now.
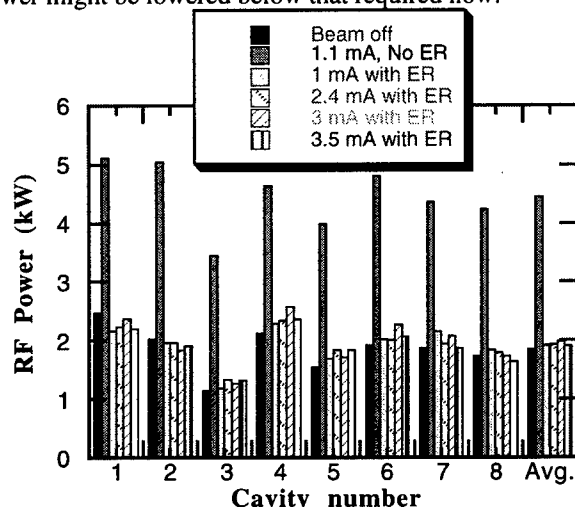
Figure 2. Required RF power for each of the 8 cavities of the full cryomodule and their average as a function of the current. The 1.1 mA values are without energy recovery. All values are with lasing.

The losses in the transport at full energy are quite low. This is very evident in radiation surveys taken after running at high current. When running in "straight-ahead" mode at 1.1 mA the radiation near the dump is over 100 mrem/hr even several hours after the beam is shut off. After running for hours with over 3 mA, the highest radiation level in the vault shortly after shutting off the beam was only 0.5 mrem/hr. This level was near an insertable dump used for tuning up the beam. The only loss point that could be found from these surveys is in the center of the cryomodule where the dose was 0.2 mrem/hr 30 cm from the module. Losses at the entrance of the wiggler with full current in the machine are less than 1 nA.

The power and extraction efficiency seem to be in good agreement with simple theoretical estimates as shown in figure 3 [15]. The errors in the theory (about ±20%) are actually much larger than the differences between the theory and the experiment. The efficiency for a continuous beam should be approximately $1/4N$ where N is the number of wiggler periods. For a pulsed device the theoretical normalized efficiency is 70% of this value. This is close to what we see. The efficiency is also not dependent on the current. We have found that higher efficiency can be

achieved by operating at a longer cavity length but that the efficiency is then dependent on the current. We do not understand this at this time. The IR Demo has had few problems arise in its commissioning. The most serious problem has been the availability of the gun, which is now around 35%. High voltage arcs during operation cause sufficient damage that several weeks are required to repair the gun after an arc. Recently the quantum efficiency of the photocathode has been poor as well. This has limited the photocathode to the 4 mA run to date. Finally, the pressure in the 10 MeV dump region grows rapidly for average current higher than 3 mA.
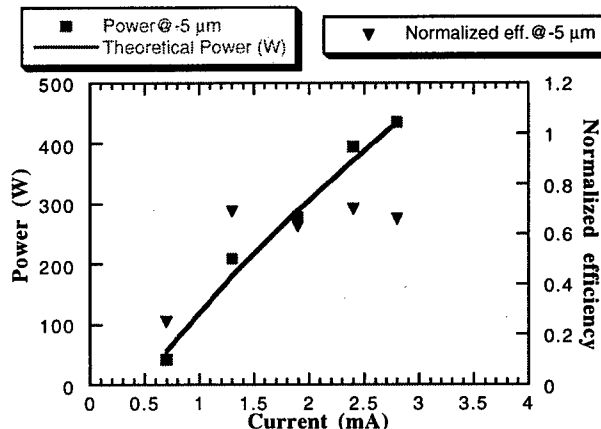
Figure 3. Power at a cavity detuning of −5 μm from the synchronous length and the efficiency divided by $4N$. The theoretical model assumes constant bunch length and emittance and energy spread proportional to the square root of the charge per bunch.

Many potential problems did not arise. No RF instabilities have been seen in the system. Calculations showed that this should be the case but the model could not use the exact physical model of the FEL gain medium. The laser has been very easy to start and diagnostics have allowed good optimization before lasing is attempted. The quality of the magnets has been excellent and the energy acceptance of the Bates bends has exceeded its specification.

Recent work has centered on lasing at 3 μm using a beam energy of 47 MeV. With only a few days operation we have succeeded in recirculating up to 3 mA of beam with no lasing. When high-power 3 μm mirrors are installed, lasing at over one kilowatt should be straightforward.

Several other groups have proposed or are building HAPFELs with energy recovery. Some do not use SRF cavities. A group from the INP in Novosibirsk has proposed a recirculating microtron with 100 mA of beam current and has built the injector for this device [16]. A group at JAERI has operated a device with SRF cavities but without energy recovery and achieved pulsed operation at 100 W [17]. Future plans include energy recovery to increase the average power. A group at Lawrence Berkeley Lab has proposed using PEP B Factory cavities to operate

at very high average power in the near IR for power beaming [18]. All these devices have moderate efficiency and, at least in the future, energy recovery.

5 CONCLUSIONS

Clearly FELs are capable of high average power. The most promising devices to date use energy recovery to enhance the overall efficiency of the device. Since even a low peak current device can achieve reasonably high efficiency in the mm-wave region, there seems to be no clear benefit to using pulsed devices in that wavelength range. The FELs using DC accelerators seem to be extremely promising sources of very high mm-wave power. The high brightness available from pulsed photocathode RF guns make them attractive as sources for high average power FELs in the optical range with large extraction efficiency but the duty cycle must be increased by several orders of magnitude with no degradation of the beam quality. This is a major challenge. The lack of energy recovery is also a problem due to radiation hazards. The concept of recirculation and energy recovery has been proven at Jefferson Lab. The main challenge in that type of device is scaling up the energy and current to reach even higher power levels.

6 ACKNOWLEDGEMENTS

7 REFERENCES

[1] "Star Wars and the FEL", Roger Warren, unpublished.
[2] A. Renieri, Nuovo Cimento 53B (1979) 160.
[3] "A Cost Estimation Model For High Power FELs", G. R. Neil, Proc. 1995 Part. Accel. Conf. (Dallas TX, 1995) 137.
[4] S. L. Allen et al., "Generation of High Power 140 GHz Microwaves with an FEL for the MTX Experiment", Proc. 1993 Part. Accel. Conf. (Washington D.C., 1993) 1551, and C. J. Lasnier et al., "Burst Mode FEL with the ETA III Induction Linac", Proc. 1993 Part. Accel. Conf. (Washington D.C., 1993) 1554.
[5] "The Fusion-FEM: 730 kW at 200 GHz", W.H. Urbanus, To appear in Nucl. Inst. And Meth. A.
[6] Gerry Ramian, personal communication
[7] L. Elias et al. Nucl. Inst. and Meth. A304 (1991) 219.
[8] A. Abramovich et al., Nucl. Inst. and Meth. A407 (1998) 16.
[9] B. C. Lee et al., Nucl. Inst. and Meth. A375 (1996) 28.
[10] D. E. Pershing, R. D. Seeley, R. H. Jackson, and H. P. Freund, Nucl. Inst. and Meth. A355 (19951) 104.
[11] "First Lasing of the Regenerative Amplifier FEL", D.C.Nguyen, R.L. Sheffield, C.M. Fortgang, J.C. Goldstein, J.M. Kinross-Wright, N.A. Ebrahim, To appear in Nucl. Inst. And Meth. A.
[12] C. L. Bohn, "Recirculating Accelerator Driver for a High-Power FEL: A Design Overview", Proc. 1997 Part. Accel. Conf, pp. 909-911 (1998).
[13] J. Flanz, G. Franklin, S. Kowalski and C. P. Sargent, MIT-Bates Laboratory, Recirculator Status Reports, 1980 (unpublished); described in R. Rand, "Recirculating Electron Accelerators" (Harwood, New York, 1984) p. 107–109 and 155.
[14] L. Merminga et al. "First results on energy recovery in the Jefferson Lab IR FEL" these proceedings.
[15] S. Benson, "A Spreadsheet for Calculating the Performance of a Free-electron Laser", TJNAF TN-94-065.
[16] N. A. Vinokurov et al., Nucl. Inst. and Meth. A375 (1996) 403, "2-MeV CW Electron Accelerator for High-Power Free-Electron Lasers", B. C. Lee, Y.g U. Jeong, S. O. Cho, S. K. Kim, J. Lee, and G. N. Kulipanov, To appear in Nucl. Inst. And Meth. A.
[17] E.J.Minehara et al., "A 0.1 kW Operation of the JAERI Superconducting RF Linac based FEL" To appear in Nucl. Inst. And Meth. A.
[18] "FEL Designs for Power Beaming" A. Zholents, Presented at Photonics West, San José CA 1999. Proc. 3614.

A MEASUREMENT OF HIGH GAIN SASE FEL INDUCED ELECTRON BEAM MICRO-BUNCHING USING COHERENT TRANSITION RADIATION*

A. Tremaine#, S. Anderson, P. Frigola, M. Hogan, A. Murokh, C. Pellegrini, J.Rosenzweig
University of California, Los Angeles,
405 Hilgard Ave., Los Angeles, CA., 90095

D.Nguyen, R.Sheffield
Los Alamos National Laboratory,
Los Alamos, NM, 87545, USA

Abstract

Coherent transition radiation (CTR) was used to study the longitudinal modulations of an electron beam exiting the UCLA/LANL high gain SASE FEL. The induced longitudinal micro-bunching of the electron beam at the exit of the undulator was measured with a frequency domain technique using the CTR emitted when this beam strikes a thin conducting foil. Formalisms for both CTR and SASE theories are related using the simulation code GINGER in which the SASE FEL gain of the output radiation and the micro-bunching of the electron beam are given. Experimental results from the CTR measurement will show the limit of standard transition radiation (TR) theory is being approached and new analysis is needed.

1 INTRODUCTION

Diagnostics measuring very short periodic electron beam modulations will be necessary for future experiments in which the modulating wavelength will be several microns and less. Up to the present, time domain measurements such as the streak camera and interfermetric CTR [1] have reliably measured the longitudinal structure of electron beams to a resolution of several hundred femtoseconds. However, as advanced accelerating techniques [2] and FELS [3,4] are becoming more common, a dependable means of measurement for these very short longitudinal electron beam modulations are needed. Using the CTR frequency domain technique described here, a higher resolution than the time domain measurements can be achieved.

A SASE FEL was used to induce the longitudinal electron beam modulation and as this beam strikes a thin conducting foil, the emitted CTR will give information about the electron beam spatial distribution. For the SASE FEL process, this electron beam micro-bunching is directly related to the gain of the SASE radiation and using CTR, we are able to reconstruct the beam distribution at the undulator exit. The results presented here agree well with the predicted performance of the SASE FEL given by simulation. Since we will be

studying forward emitted CTR, scattering effects in the foil will be shown to cause a significant degradation in the emitted signal.

2 BACKGROUND

This section reviews the theory of transition radiation (TR) needed to understand the experimental measurements and also to point out the assumptions made in the standard model that may not be entirely accurate for this and future experiments.

The emitted coherent radiation energy spectrum from a multi-particle electron beam striking a metallic foil is given by

$$\frac{d^2U}{d\Omega d\omega} \approx N^2 |f(\omega)|^2 \frac{d^2U}{d\Omega d\omega}\bigg|_{1\,e^-} \tag{1}$$

where N is the number of electrons in the bunch, Ω is the solid angle, ω is the frequency of radiation, and

$$f(\omega) = \int \exp\left(\frac{i\omega \vec{r} \cdot \hat{n}}{c}\right) S(\vec{r}) d^3 r \tag{2}$$

is the Fourier transform of the beam particle distribution, $S(r)$. Immediately from Eq. 1, one sees the emitted CTR spectrum has the same Fourier spectrum as the electron beam distribution and any modulations in the electron beam will be seen in the emitted CTR spectrum.

The single electron energy spectrum for transition radiation (TR) is given by the familiar relation,

$$\frac{d^2U}{d\Omega d\omega}\bigg|_{1\,e^-} = \frac{e^2}{4\pi^2 c} \frac{\sin^2\theta}{(1-\beta\cos\theta)^2} . \tag{3}$$

217

Eq. 3 is derived by modeling single electron TR as a collision between the electron with its image charge at the metal/vacuum boundary and using the Lienard-Weichert fields for moving charges. In addition, the frequencies of emitted radiation is assumed much smaller than the characteristic time for the collision to take place,

$$t_{coll} \ll t_{rad\,per} \tag{4}$$

and the assumption that $\omega \to 0$ in the Lienard-Weichert fields is used. However, it will be shown below this assumption's limit is being approached in this and future experiments and modifications to existing standard TR modeling need to be made.

The electron beam distribution exiting a SASE FEL is given by [5,6]

$$S(\vec{r}) = \frac{\exp\left(-\dfrac{r^2}{2\sigma_r^2}\right)}{2\pi\sigma_r^2} \frac{\exp\left(-\dfrac{z^2}{2\sigma_z^2}\right)}{\sqrt{2\pi}\sigma_z} \sum_n \left[1 + b_n \cos(nk_r z)\right] \tag{5}$$

where Gaussian distributions are assumed in the radial and longitudinal dimensions (r, z) and the longitudinal micro-bunching profile superimposed on the longitudinal distribution is given by a co-sinusoidal term with the harmonic wavenumber, $k_r = 2\pi / \lambda_r$, where λ_r is the longitudinal electron beam micro-bunching wavelength equal to the fundamental SASE radiation wavelength. Higher harmonic, n, wavelengths are driven by the SASE FEL process and are included in Eq. 4, but only the fundamental harmonic ($n = 1$) induced micro-bunching could be measured in this experiment.

Integrating Eq. 2 about the solid angle, Ω, gives a line spectrum

$$\frac{dU}{dk} = \frac{N^2 b_n^2 e^2}{4\pi} \left(\frac{\gamma}{k_r \sigma_r}\right)^4 \exp\left[-(k - nk_r)^2 \sigma_z^2\right]. \tag{6}$$

Notice, there is a peak in the emitted CTR line spectrum at the micro-bunching frequency as expected from Eq. 2. Each peak is very narrow compared to the separation with the neighboring harmonic Gaussian if $\sigma_r \gg \lambda_r$. The total energy of the emitted CTR is found integrating Eq. 5 to be

$$U_{CTR} = \frac{(Nb_1 e)^2}{4\sqrt{\pi}\sigma_z} \left(\frac{\gamma}{k_r \sigma_r}\right)^4. \tag{7}$$

It can be seen from Eq. 7 that the CTR energy depends heavily on having a highly focused electron beam at the foil since $U_{CTR} \propto 1/\sigma_r^4$.

It should be noted that Eq. 6 was found integrating over the solid angle, but in the next section we will see the angular acceptance of the optical beam was only $\theta_{acc} = 15 mrad$. Also, the beam must propagate through the foil to emit forward CTR (at the back surface of the foil) and degradation of signal due to scattering effects in the foil needs to be included. Both of these effects will be accounted for in the theoretical analysis of this experiment.

3 EXPERIMENTAL SETUP

The CTR/SASE experiments were performed at the Advanced FEL (AFEL) at Los Alamos National Laboratory in which the experimental setup has been described elsewhere [7], but is reviewed briefly here. Important experimental parameters are given in Table 1.

Table 1: Electron beam and SASE FEL parameters.

Beam Energy	E	17.5 MeV
Charge/bunch	Q	1.2 nC
Bunch Length (FWHM)	τ	9.2 ps
Wiggler period	λ_u	2 cm
On axis field	B_0	7.4 kG
FEL Wavelength	λ_r	13 µm
RMS beam size	σ_r	180 µm

The AFEL photo-injector uses a 10.5 cell L-band standing wave accelerator running at 1300MHz. A modelocked (108MHz) diode pumped Nd:YLF is compressed using a fiber/diffraction grating pair and then amplified with a pair of flashlamp pumped Yd:YLF rods. The emitted pulse train has 350 individual pulses separated by 9.23ns each with a FWHM of 9.2 ps. When the laser pulse train illuminates the Cs_2Te cathode, an electron train with nearly the same parameters as the laser train is created and accelerated down the beamline with each electron bunch having a charge of 1.2nC. Solenoids are placed near the cathode for emittance compensation and before the undulator to match the electron beam to the proper SASE FEL conditions.

The 2m undulator was built from a collaboration between the Kurchatov Institute and UCLA [8] and has a magnetic period $\lambda_u = 2.06 cm$, on axis field $B_0 = 7.4 kG$,

and a normalized undulator field $K \approx 1$. An insertable $6\mu m$ radiating foil was placed 1 cm behind the last undulator period. When inserted, the foil reflects all the SASE radiation (skin depth <50 nm) and the only light to continue down the optical beamline to the calibrated HgCdTe detector is the forward emitted CTR. When the radiating foil is retracted, only the SASE radiation will propagate to the detector. Since the SASE and CTR are at the same wavelength (see Eq. 6) and have the same source points, the end of the undulator, the collecting optics need not be changed from the two measurements.

The HgCdTe detector was placed about 3.5 m from the source point which limited the angular collection of the optical beamline to just $\theta_{acc} = 15mrad$ and Eq. 7 is not entirely correct. To correct for this, numerical integrations of Eq. 1 are done out to θ_{acc}. Also, θ_{acc} forces collection of the coherent transition radiation which is emitted at $\theta_{coh} = (\sqrt{2}\sigma_r k_r)^{-1} \approx 8mrad$ and very little collection of the incoherent light emitted at $\theta_{incoh} \approx 1/\gamma = 28mrad$. Included in the numerical integration is the effect of electron beam scattering within the foil. The forward emitted CTR is derived from the electron beam propagating through the foil and is emitted when the beam travels from metal to vacuum at the foil back surface. Since the scattering angle is found to be $\theta_{scatt} \approx 8mrad$, we find the transverse size of the electron beam (σ_r) will increase and the forward emitted CTR signal is degraded (Eq. 1) by almost 40% compared to a signal assuming a foil thickness of $0\mu m$.

4 MEASUREMENTS VS. THEORY

In order to accurately predict the expected emitted CTR, it can be seen from Eq. 7 the bunching factor, b, needs to be estimated. The bunching is predicted for these conditions by the 3D FEL simulation code GINGER. For a range of parameters corresponding to experimental uncertainties, the bunching is found to be $b_1 = .017$ and an estimated gain of 10^5 was achieved as reported in References 5 and 8 for this system.

An estimation for the absolute energy of the forward emitted CTR can now be calculated. Taking into consideration foil scattering effects on the electron beam, angular acceptance, θ_{acc}, the micro-bunching amplitude above and the parameters in Table 1, an energy of 3.1 pJ is predicted at the detector by numerical integration of Eq. 1. It should be mentioned that scattering degradation and θ_{acc} each reduces the total amount of expected CTR at the detector by about 40% and not including either will cause a significant overestimation of the signal. The energy measured at the detector was 2.7 pJ, agreeing well with the predicted number given above.

Next, a Jerrell Ash monochromator was placed before the detector and line spectrum measurements were taken. Because of the high attenuation of this optic, it was found the monochromator bandwidth had to be broadened in order to pass a reasonable CTR signal to the detector and an intrinsic resolution of $.177\mu m$ is estimated for the modified monochromator setting. First, the SASE radiation was scanned with the bandwidth broadened monochromator and results of this measurement are shown in Fig.1. A centroid at $12.8\mu m$ is seen in the SASE spectrum and as mentioned before, this is the modulation wavelength of the induced electron beam longitudinal micro-bunching, λ_r. Next, the screen was inserted and the emitted CTR spectrum was scanned and the results are also shown in Fig. 1. As expected, the CTR spectrum is centered around nearly the same wavelength as the SASE spectrum and is Gaussian in shape agreeing with Eq. 6. It should be mentioned the CTR has been normalized to make it the same scale as the SASE spectrum.
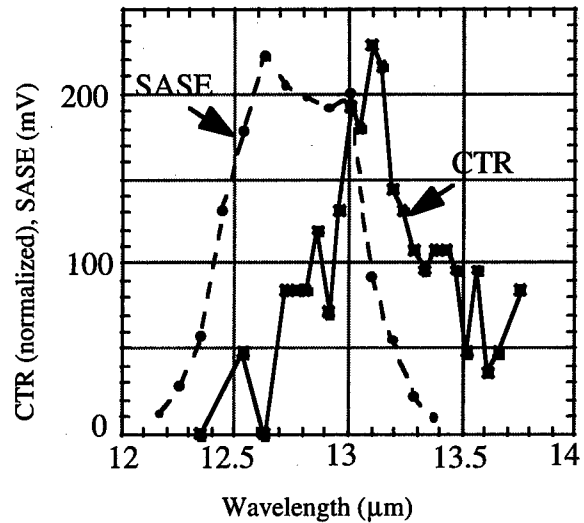
Figure 1: CTR and SASE signals as a function of wavelength with CTR scaled to SASE amplitude.

5 DISCUSSION

Because there is good agreement between the predictions and measurements presented here, the formalism developed above is assumed accurate and the electron beam distribution given by Eq. 5 is correct and no higher transverse modes are present. We have also demonstrated the narrow angular spectrum expected for coherent radiation by choosing an appropriate acceptance angle of the optical beam line to allow collection of the CTR and insignificant collection of incoherent TR. These conditions imply the electron beam micro-bunching is uniform transversely across the beam.

A slight frequency shift was observed in the CTR spectrum center shown in Fig. 1. Looking at the transition radiation model traditionally used, limits of its

validity here are suspect. The criterion for using Eq. 3 for the TR spectrum is given by Eq. 4. We see in this experiment the period of emitted radiation is $t = 4.3*10^{-14} s$ and the assumption that this is much greater than a collision time (for the electron/image charge collision model) is questionable. If the condition in Eq. 4 is not applicable for the TR collision model, the more general spectrum for TR from the Lienard-Wiechert fields is found to be

$$\frac{d^2U}{d\Omega d\omega} = \frac{e^2\omega^2}{4\pi^2 c}\left|\int_{-\infty}^{\infty} \hat{n} \times (\hat{n} \times \vec{\beta})\exp\left[i\omega\left(t - \frac{\hat{n}\cdot\vec{r}(t)}{c}\right)\right]dt\right|$$

(8)

where $\hat{n}$ is the unit vector from the interaction to the observation point, β is the velocity of the electron or image charge and $\vec{r}(t)$ is the trajectory of the particles in the collision. Not only do the initial velocities need to be known, but the physics of the particle trajectories during the collision must be calculated. It is immediately seen the spectrum in Eq. 8 contains additional phase information not present in the standard TR spectrum given by Eq. 3 and could account for the observed frequency shift of the CTR spectrum shown in Fig. 1. As the frequencies of emitted TR increase for future experiments, the traditional spectrum from Eq. 3 will have to be replaced by the more general TR spectrum given by Eq. 8.

6 CONCLUSION

The experiment and technique described here was shown to reliably measure longitudinal beam modulations to a few microns and less. Since this experiment was performed on a SASE FEL, this measurement verified the crucial role of micro-bunching in the SASE FEL gain process. Simulations were used and the results agreed well with the measurements described above, thus serving as an independent check on the code predictions.

7 REFERENCES

[1] U. Happek et al., Phys. Rev. Lett. 67, 2962 (1991).

[2] J. Rosenzweig et al., Phys. Rev. Lett. 74, 2467 (1995).

[3] R. Bonifacio et al., Opt. Commun. 50, 373 (1984).

[4] J. Rosenzweig, G. Travish, and A. Tremaine, Nucl. Instrum. Methods Phys. Res., Sect. A 365, 255 (1995).

[5] A. Tremaine et al., Phys. Rev. Lett. 81, 5816 (1998).

[6] D.C. Nguyen et al., "A High-Power compact Regenerative Amplifier FEL", PAC Conference, Vancouver, B.C., Canada, 1997.

[7] N. Osmanov et al., Nucl. Inst. Meth. Phys. Res. A 407, 423 (1998).

[8] M. Hogan et al., Phys. Rev. Lett. 81, 4867 (1998).

THE DEEP-UV OPERATION
OF THE OK-4/DUKE STORAGE RING FEL .

V.N. Litvinenko, S.H. Park, I.V. Pinayev, Y. Wu, M. Emamian, N. Hower, P. Morcombe,
O. Oakeley, G. Swift, P. Wang, FEL Laboratory, Physics Department, Duke University, Durham,
NC

Abstract

In this paper we present the result of the deep-UV lasing
with the OK-4/Duke storage ring FEL. The OK-4 FEL
was initially commissioned in the near-UV at Duke Free
Electron Laboratory in November, 1996 followed by a
year-long shutdown. After re-establishing the storage ring
operation in early 1998, the OK-4 FEL lasing was
demonstrated in the wavelength range of 217 to 256 nm in
1998. A number of lasing modes with electron energies
ranging from 300 to 750 MeV have been established to
accommodate application research. Starting September,
1998, the coherent deep-UV radiation is used for
applications in cornea surgery, cell biology, surface
physics, and nuclear physics. In this paper we report the
results of the deep-UV lasing with the OK-4/Duke storage
ring FEL as well as our plans to advance towards the
VUV.

1 INTRODUCTION

The 1.1 GeV Duke storage ring was commissioned in
November, 1994 [2] and later was used for number of FEL
experiments. The development of the OK-4/Duke storage
ring FEL started in April 1992 when the Duke FEL
Laboratory and Budker Institute of Nuclear Physics
(Novosibirsk, Russia) signed a Memorandum of
Understanding on collaborative research in development of
the XUV FELs [3]. The OK-4 FEL was previously
employed for the visible and the UV lasing at VEPP-3
storage ring [4]. It was transferred to the Duke FEL
laboratory (DFELL) in May of 1995 and was
commissioned in November, 1996, by demonstrating
lasing in the near UV and the visible [5] and production of
nearly monochromatic γ-rays via Compton back-scattering
[6]. At the middle of December, 1996 the operations of the
Duke storage ring has been stopped and next operations of
the OK-4 FEL was possible only in 1998. In April, 1998
we demonstrated lasing in the deep-UV range with
tunability from 226 nm to 256 nm and also tested the
operation of newly build gain modulator [7]. After three
months shut-down for construction of initial stage of new
Keck Life Science building , we reestablished operation of
the OK-4 FEL and lased at shorter wavelength down to
217 nm. The set of mirrors used for this lasing turned out
not to be radiation resistive and mirrors degraded within
two weeks to unusable condition. In September, 1998 we

re-installed mirrors with central wavelength of 245 nm, re-
established lasing and used these set-up for user program
till the February, 1999 [8]. During these six months of
operation we delivered OK-4 FEL beams to our user on
regular basis for experiments in cornea surgery, cell
biology, photo-emission electron microscopy [9] and γ-
ray nuclear physics (10-40 MeV) [1].
At present, we operate the OK-4 FEL in the visible/near
UV ranges (345- 730 nm) to generate low energies (2 - 20
MeV) monochromatic γ-rays via Compton back-scattering
[1].

2 OK-4/ DUKE STORAGE RING FEL

The layout of the Duke storage ring with the OK-4 FEL,
and the 270 MeV linac-injector are shown on Fig.1. Most
of the technical parameters of the storage ring and the OK-
4 FEL has been presented in our previous publications
[10, 8]. The recent developments of the OK-4/Duke
storage ring FEL involved installation and commissioning
closed orbit measuring system comprised of 34 units of
Bergoz BPM electronics [11], the new timing system, the
gain modulator [7]. We have also purchased the
Hamamatsu streak camera with 2 ps resolution which is
used for both storage ring and the OK-4 FEL diagnostics.
These systems enhanced diagnostics capability of the OK-
4/Duke storage ring system and the use of closed orbit
measuring system ended previously used DFELL "blind-
folded technique" of the UV FEL alignment. We have
improved the performance of the linac-injector by raising
its energy to 270 MeV and by installing the new nitrogen
laser with higher power and low jitter (less than 1 nsec) to
drive photo-cathode for single bunch injection. At present,
the system is capable of continuos injection with 0.5
mA/shot rate in the desirable RF bucket with no spills.
Maximum stored current in a single bunch is limited to 5
- 15 mA. Above the threshold value, electron beam
develops vertical instability and reduces its intensity by
about a half. This threshold value does not exhibit strong
dependence on the global parameters such as chromaticity
or betatron tunes but depends on the beam orbit and
HOMs in the RF cavity. The nature of the effect limiting
the current per bunch is not obvious and we study it in
order to improve this parameter in the future. A typical set
of Duke storage ring parameters used for described
experiments is listed in the Table I.

DUKE FEL STORAGE RING
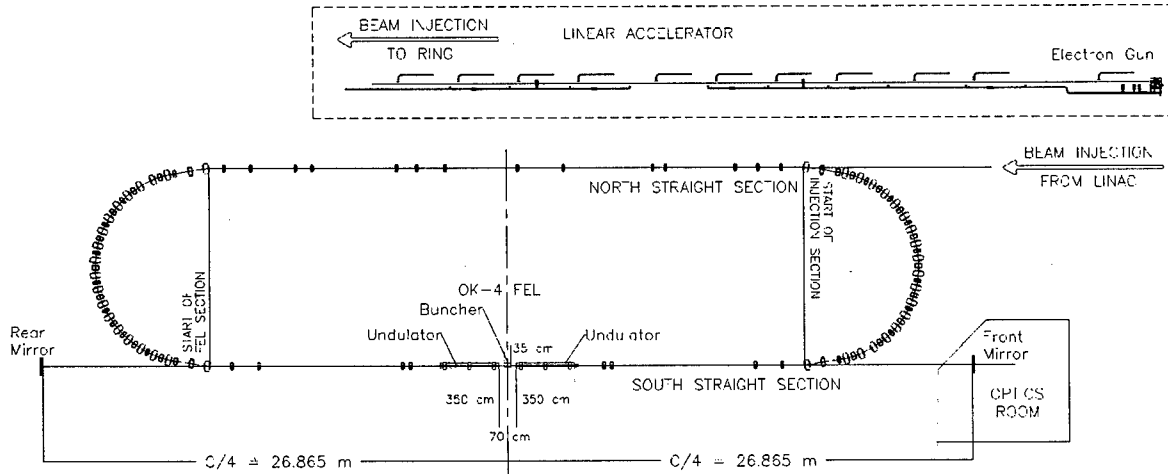
Figure 1. Layout of the Duke/OK-4 storage ring FEL.

Table 1. Typical parameters used for the deep-UV lasing

Electron Energy [GeV]	0.3-0.75
RF voltage (178 MHz), kV	200-550
Number of electron bunches	1 - 3
Beam current [mA], per bunch	3 - 8
Broad band impedance , Zn/n [Ohm]	3.25±0.25
Typical lifetime with laser on [hours]	1-3

The only improvement in the OK-4 FEL system was the increase of currents in both power supplies for the electromagnetic wigglers (to 2.7 kA and maximum K_w to 4.6) and in the buncher (to 1.5 kA). These up-grades allowed us to operate at higher energies of electron beam (up to 750 MeV) and to generate higher average power.
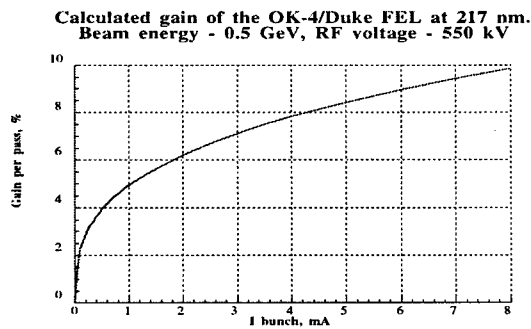
Fig.2. Typical calculated dependence of the OK-4/Duke FEL gain on the electron current per bunch. We used broad-band impedance of $Z_n/n=3.25$ Ohm for this calculations.

The 53.73 m long optical cavity of the OK-4 FEL comprises of two mirrors with 26.46 m radii and has Rayleigh range only 3 m. It makes is very susceptible to vibrations and angular errors. The design of the optical cavity and a its sophisticated feed-back and control system are described elsewhere [5, 12].

The present vacuum chambers of Duke storage ring have very large longitudinal impedance (see Table 1) which causes microwave instability to start at sub-mA currents

per bunch. Well-developed and saturated microwave instability determines the energy spread and bunch-lengthening of the beam at most of operating parameters listed in Table. 1, and therefore determines the maximum gain attainable with the OK-4 FEL. Fig. 2 shows dependence of the maximum gain in the OK-4/Duke FEL for deep-UV with typical cubic root dependence on current per bunch. Our direct measurements of the maximum gain are in good agreement with our predictions.

3 LASING IN THE DEEP-UV

The deep-UV lasing with the OK-4/Duke storage ring FEL has been demonstrated in April and August of 1998 using a number of set-ups and energies. Generally, lasing was easier to achieve and was more stable when we operate storage ring at higher energies (i.e. from 500 to 750 MeV). We contribute this effect to better stability of electron beam and power supplies.

We used two sets of multilayer dielectric mirrors custom manufactured by Lumonix Optics Group (Canada). The reflectivity bands of these mirrors as well as typical tunability ranges attained during initial lasing runs are shown on Fig.3.

Mirrors with central wavelength of 225 nm were not radiation resistive and we did not use them for user applications. Starting September, 1998 we used the 245 nm mirrors to provide the OK-4 FEL laser beams to our users on regular scheduled basis for six months in both CW and pulsed mode. We out-coupled maximum of 100 mW of average laser power per mirror into TEMoo mode using 700 MeV electron beam with 16 mA average current in two bunches. Giant pulses with 50-200 microsecond duration were generated using the gain modulator [7], at a maximum reprate of 30 Hz with maximum 0.25-0.4 mJ per macropulse and a peak out-coupled power of about 0.3 MW. In addition to the full transverse coherence (TEMoo mode) of the OK-4 FEL radiation we demonstrated full

longitudinal coherence by generating the Fourier limited Gaussian wavepackets with RMS duration close to 2 ps and RMS linewidth close to 0.003%.
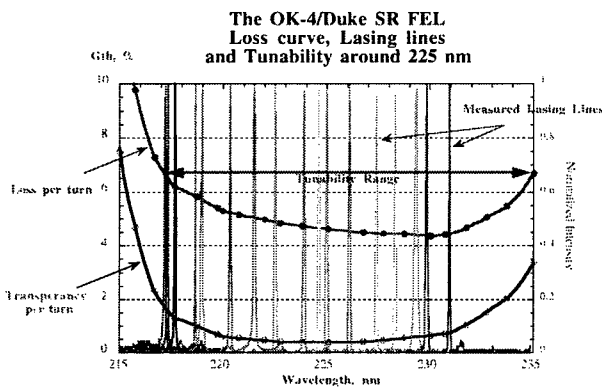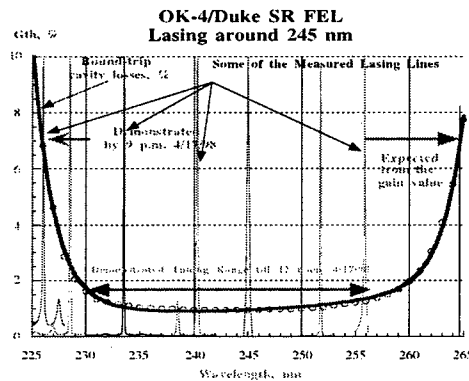
Fig.3 Tunability of the OK-4/Duke FEL operating at 500 MeV around 245 nm (April 3, 1998: 1.98 mA/bunch, 500 MeV, 200 kV RF) and around 225 nm (August 11, 1998: 1.5 mA/bunch, 500 kV RF). The thick-solid curve shows measured round trip losses and thin curves show samples of measured spectra. The stop-bands define the level of the FEL gain. From the above graph we concluded that the OK-4 FEL has the gain at least 6.9% per pass @ 226 nm and 6.5% per pass @ 217 nm with the above beam parameters.

4 CONCLUSIONS

The OK-4/Duke storage ring FEL has demonstrated reliable lasing as well as generated usable laser beams in the deep-UV range of spectrum. The OK-4 FEL demonstrated average spectral brightness of $(2-4) \cdot 10^{20}$ and peak spectral brightness of $3 \cdot 10^{26}$ ph/sec/mm^2/mrad^2/($10^3 \cdot$BW) in the deep-UV spectral range. The transparency of used mirrors was too low for the optimized out-coupling. At the central wavelength of 245

nm, the mirror transparency of 0.035% and initial loss of 0.47% provide an outcoupling efficiency less than 8%. We ordered a new set of mirrors with transparency of 0.5-0.75% at the central wavelength for better extraction efficiency. These modifications as well as extension of the OK-4 FEL operation below 200 nm will enhance capability and strength of our user program. The UV and γ-ray beams from the OK-4 FEL will be soon delivered into newly built Keck Life Science Laboratory housing the FEL users. The exploration of the shorter wavelength range with the OK-4/Duke storage ring FEL will continue in parallel with the user applications. We are in the process of design and construction of the 22 m long OK-5 FEL comprising four electromagnetic helical wigglers with switchable polarization. The OK-5 FEL will have gain in excess of 100% per pass and will allow us to lase in the VUV range.

5 ACKNOWLEDGMENTS

6. REFERENCES

[1] S.H.Park et al., "Performance of the Duke storage ring γ-ray source", Presented at these Particle Accelerator Conference
[2] V.N.Litvinenko et al., Proc. of PAC'95, 1995, p. 213.
[3] V.N.Litvinenko, J.M.J.Madey, N.A.Vinokurov, Proc. of PAC' 93, 1993, p.1442
[4] V.N.Litvinenko, "The optical klystron on VEPP-3 storage ring - lasing in the visible and the ultraviolet", Thesis, Novosibirsk, 1989; G.N.Kulipanov et al., NIM A296 (1990) 1;
[5] V.N.Litvinenko et al., NIM, A 407 (1998) 8 V.N.Litvinenko et al., Proc. of PAC'97, 1997, P.883
[6] V.N.Litvinenko et al., Phys.Rev. Lett., V.78, N.4, June 1997, p.4569
[7] I.V.Pinayev et al., "Critical Systems for High Peak Power Storage Ring FEL", these proceedings.
[8] Y. Wu et al., NIM B 144 (1998) 90
[9] H.Ade et al., Surface Review and Letters, Vol. 5, No. 6 (1998) 1257
[10] Y.Wu, V.N.Litvinenko, B.Burnham, S.H.Park and J.M.J.Madey, IEEE Transaction on Nuclear Science, Vol. 44, No. 5, 1997, p.1753
V.N.Litvinenko et al., "The Duke XUV FEL Storage Ring Facility", Proc. of the first APAC Conference, March, 1998, Tsukuba, Japan.
V.N.Litvinenko et al., NIM A375 (1996) 46-52
[11] P.Wang et al., "Beam Position Monitors for Duke FEL Storage Ring", these proceedings.
[12] I.V.Pinayev et al., AIP Proc., CP451 (1998) 545

QUANTUM ASPECTS OF BEAM PHYSICS*

Pisin Chen[†], Stanford Linear Accelerator Center, Stanford University, Stanford, CA 94309

Abstract

The continued demand for higher beam energies, luminosities, and brightness, induces increasing number of beam phenomena that invlove quantum effects. In this paper we review the various quantum aspects of beam physics, with emphasis on their recent advances. These include quantum effects in beam dynamics, electron-photon interaction, beam phenomena under strong fields, fundamental physics under violent acceleration, and quantum methodology in beam physics. We conclude with a future outlook of this very exciting new field by the name *quantum beam physics*.

1 WHERE IS $\hbar$ IN BEAM PHYSICS?

It is common knowledge that quantum effects are pronounced in physical systems where the particles involved exihibit the wave nature, or the (radiation) waves involved exhibit the particle nature. In accelerators the de Broglie wavelength of a high energy beam particle is

$$\lambda_{db} = \frac{\hbar}{p_\perp} \lesssim \frac{\hbar}{\gamma mc} \frac{p}{p_\perp} = \lambda_c \sqrt{\frac{\beta}{\gamma \epsilon_n}}, \quad (1)$$

where β and ϵ_n are the β-function and the normalized emittance, respectively. This value is generally much smaller than the typical apertures of the cavities and magnets in the accelerator. In addition, the synchrotron radiation induced by the magnets is typically low-energy and long wavelength, and the number of photons per volume of the wavelength is much larger than unity. Therefore the conventional beam dynamics is essentially classical physics to the leading order.

The ever-increasing demand for higher beam energy, luminosity and brightness in accelerators pushes for ever higher acceleration gradients, smaller apertures, and tighter beam phase space, and quantum effects in beam physics become increasingly important.

2 QUANTUM EFFECTS IN BEAM DYNAMICS

2.1 Ultimate Limit of Phase Space

The basic assumptions in the standard treatment of synchrotron radiation reaction were that the photon emission occurs instantly and the recoil of the particle is equal and opposite to the momentum of the emitted photon. As the

photon emission is random, its reaction causes random excitations in the beam phase space. It was found[1], however, that these assumptions are violated in a continuous focusing channel. The radiation formation length can in principle be comparable to the betatron oscillation length, and the focusing channel serves as a third party participating in the overall energy-momentum conservation. As a result, the radiation reaction does not cause any excitation of the transverse momentum, but an *absolute damping* of the emittance. This points to a theoretical minimum action, limited only by the zero-point fluctuations due to the uncertainty principle, i.e., $J_{min} = \hbar/2$, or

$$\epsilon_{n,min} = J_{min}/mc = \lambda_c/2 \sim 10^{-11} \text{cm}. \quad (2)$$

The above result can be genralized to combined focusing-bending systems where the radiation formation length (ρ/γ) is comparable to the average betatron wavelength (due to a very strong focusing)[2]. Pure bending and pure focusing are the two limiting regimes of the general formalism.

2.2 Classical vs. Quantum Tracking

In conventional treatments in particle tracking each point in phase space is assumed to have a perfect resolution. But due to the uncertainty principle, the phase space cannot have infinite resolution. Heifets and Yan[3] show that in the stochastic regions in phase space where classical trajectories tend to diverge exponentially, trackings of particles could be sensitive to such qauntum granularities.

2.3 Coherence and Bose-Einstein Condensate of Particle Beams

We are interested in better understanding, and hopefully eventually attaining a coldest possible particle beam that Nature would allow. To this end a comparison with photon beams should be helpful. Ordinary lights emit different frquency photons at random. It is well-known that laser photons, on the other hand, are monochromatic and coherent. The evolution of the laser spot size is governed by

$$a^2(s) = \frac{\lambda}{\pi} Z_R \left(1 + \frac{s^2}{Z_R^2}\right), \quad (3)$$

where Z_R is the Raleigh length.

An ultimate, coherent particle beam analogous to a laser would have a minimum emittance associated with its de Broglie wavelength. Then we would have a coherent beam that propagates as

$$\sigma^2(s) = \frac{\lambda_c}{2\pi\gamma} \beta^* \left(1 + \frac{s^2}{\beta^{*2}}\right). \quad (4)$$

Would such coherent particle beam necessarily imply certain kind of condensation? Recent progresses on Bose-Einstein condensate (BEC) and the *atom laser*[4, 5] inspire us to wonder if particle beams in accelerator environments can in principle also form condensates. Although particle beams are typically made of fermions, this possibility may not necessarily be ruled out. Afterall, fermions such as He^3 do exhibit superfluidity at low temperatures.

3 ELECTRON-PHOTON INTERACTION IN BEAM PHYSICS

There emerges a new class of beam phenomena which involve quantum mechanics. This is mainly through the applications of lasers in various beam production, cooling, and monitoring schemes.

3.1 Compton Backscattering

Compton scattering between a high energy electron and a (much lower energy) photon, e.g., that in a laser, will induce a dramatic exchange of energies between the photon and the electron. As a result the final state photon will emerge with much higher energy in the lab frame. This mechanism is by now widely applied in beam physics. In the early 1980s a photon-photon collider concept was introduced[6], in which the high energy photon beams are to be produced through the Compton backscattering process. More recently, studies were made[7] in producing intense X-rays by the same mechanism. Turning the attention to the final-state electron, Telnov[8] suggested that Compton backscattering can also be used to reduce the electron beam energy with little increase in its divergence, and thus an effective reduction in the normalized emittance. Another creative concept, proposed by Shintake[9], is to monitor sub-micron beams by intercepting them with a pre-established laser interference pattern.

3.2 Laser Cooling of Stored Beams

Lasers are also invoked to cool stored beams. As an extension to the celebrated idea of stochastic cooling, Michailichenko and Zolotorev[10] suggested the use of laser that would largely expand the bandwidth for the probe. Extending Telnov's idea, Huang and Ruth[11] proposed repeated Compton-scattering cooling of a stored electron beam. Using the *dispersive* cooling mechanism the coolings of ion beam longitudinal and transverse temperatures are found to be highly efficient[12, 13]. In the extreme limit, one expects that crystalline structure be developed in ion beams[14, 15].

3.3 Quantum Effects in Free Electron Laser

The quantum correction to the classical FEL gain formula becomes important when the photon energy is comparable

to, or larger than, the gain bandwidth[16]. Such a correction is small when the FEL gain is small, i.e.,

$$\frac{\hbar\omega_s}{E_e/N_u} \approx \frac{\hbar\omega_s}{\Delta E_e} \ll 1, \tag{5}$$

where $\hbar\omega_s$ is the FEL photon energy, E_e and electron energy, and N_u is number of undulator sections.

However, in the high-gain SASE FEL[17], the recoil effect can in principle become severe. It was found[18, 16], that quantum corrections to SASE noise can be kept small if the emission is non-degenerate:

$$(\gamma\Delta x\Delta\phi)^2(\Delta z\Delta\gamma) \ll N_e(\pi\lambda_c)^3, \tag{6}$$

where N_e is the number of electrons in the bunch.

4 BEAM PHENOMENA UNDER STRONG FIELDS

For an initial state electron with momentum p_μ traverses an external electromagnetic field, $F_{\mu\nu}$, there is a dimensionless, Lorentz invariant parameter which characterizes the nonlinear QED phenomema:

$$\Upsilon = \frac{|p_\mu F^{\mu\nu} p^\lambda F_{\lambda\nu}|^{1/2}}{mF_c}, \tag{7}$$

where $F_c \equiv m^2c^3/e\hbar \approx 4.4 \times 10^{13}$Gauss $= 1.8 \times 10^{18}$V/m is the Schwinger critical field strength. The physics involved is essentially classical if $\Upsilon \ll 1$. Quantum effects become dominant when $\Upsilon \gtrsim 1$. It happens that several beam phenomena fall under this condition.

4.1 Beam-Beam Interaction in Linear Colliders

During beam-beam interaction in linear colliders (LCs), particles in one beam interaction with the extremely intense collective EM fields of the oncoming beam. This triggers intense radiation of hard photons by the name *beamstrahlung* [19], characterized by the *beamstrahlung parameter* based on the *mean field* of the beam[20]:

$$\Upsilon = \gamma\frac{\langle E + B\rangle}{F_c} \approx \frac{5}{6}\frac{r_e\lambda_c\gamma N_e}{\sigma_z(\sigma_x + \sigma_y)}. \tag{8}$$

At $\Upsilon \sim 1$, severe beamstrahlung ($\sim 10 - 30\%$ averaged energy loss) is expected.

It was then discovered[21] that when $\Upsilon \gtrsim 1$, copious e^+e^- pairs will also be produced through the coherent interaction between the beamstrahlung photons and the collective fields of the oncoming beam. One of the pair particles always carries the same sign of charge as that of the oncoming beam, and will thus be deflected unbound, causing potentially severe particle detector backgrounds. Another background[22, 23, 24] is the quantum chromodynamic (QCD) *minijets*. As photon can manifest itself from time to time as a quark-antiquark pair, two beamstrahlung photons can interact hadronically through their

quark-gluon contents. Since the $\gamma\gamma$ cross section rises as the center-of-mass energy increases, this background is expected to become more severe in future generations of LCs.

All these backgrounds are directly influenced by the number of beamstrahlung photons emitted per electron throughout the collision[25],

$$n_\gamma \approx 2.54 \left(\frac{\alpha \sigma_z}{\lambda_c \gamma} \right) \frac{\Upsilon}{(1 + \Upsilon^{2/3})^{1/2}}. \qquad (9)$$

It is interesting to note that n_γ as a function of Υ peaks at $\Upsilon \sim 10$, and diminishes not only in small but also in large Υ limits, thanks to the quantum nature of hard photon emissions[25]. While the current LC design efforts focus on constraining $\Upsilon \lesssim 1$, it is hardly avoidable that far future LCs would necessarily be operated in the deep quantum regime. Nevertheless, it is conforting that the beamstrahlung backgrounds would not be worsen[3].

4.2 Relativistic Heavy Ion Collisions

For low energy heavy-ion collisions near the Coulomb barrier, quasi-bound molecular states are formed with binding energies dive into the negative energy continuum, resulting in a resonance which subsequently decays into an $e^+ e^-$ pair[26]. In the collision between two relativistic heavy ions, a different nonlinear QED effect, analogous to beamstrahlung coherent pair creation, should in principle occur[27], and has indeed been observed experimentally[28]. In the near future, ion energies above 100 GeV/nucleon will be available in the Relativistic Heavy Ion Collider (RHIC) at Brookhaven and the Large Hadron Collider (LHC) at CERN. These should provide opportunities to study nonlinear QED with effective coupling constant $Z\alpha \sim 1$.

4.3 Crystal Channeling of Relativistic Beams

Another physical environment where high energy beams encounter strong fields is crystal channeling[29, 30], where the confining (or focusing) field is as large as $10^{12} V/m$. Such strong fields are useful in beam handling and production. For example, a bent crystal is able to redirect proton beams in a short distance[31]. For channeling electrons or positron at energies 100 GeV and beyond, there will be copious coherent $e^+ e^-$ pairs produced. Because of the same channeling effect, the outcoming positron emittance should be much reduced. This can be invoked for a novel positron source.

4.4 Electron Interaction with Ultra-Intense Laser

If a laser is very intense, there is a finite probability that multiple photons can involve in one Compton scattering process. Such multiphoton QED processes are characterized by an additional Lorentz invariant parameter:

$$a_0 = \frac{eE_0}{m\omega_0 c} = \frac{eE_0 \lambda_c}{\hbar \omega_0}, \qquad (10)$$

where E_0 is the amplitude and ω_0 is the frequency of the laser.

The multiphoton Compton scattering tends to degrade the spectrum and the polarization of the high energy backscattered photons. It thus imposes a contraint on the various applications of the Compton backscattering mentioned above[3]. On the other hand, these multiphoton QED processes are fundamentally interesting for its own right. Indeed, experimentally they were never observed until recent years. The SLAC experiment E144[32] was dedicated particularly for that purpose, and has provided important data on the phenomena.

4.5 Spontaneous and Stimulated Breakdowns of the Vacuum

One issue in nonlinear QED that remains unclear regards the nature of the breakdown of the QED vacuum. In an attempt to clerify the issue, Chen and Pellegrini[3] borrow the terms "spontaneous" and "stimulated" to distinguish two different types of vacuum breakdowns. The stimulated breakdown, examplified by the coherent beamstrahlung pair creation process [21] and the multiphoton pair production process[32], requires an initial state particle that interacts with the external EM field.

On the other hand, the QED vacuum can also breakdown by a pure classical EM field without any initial state particle. The penetration of the vacuum-fluctuated pairs through the potential barrier is spontaneous in this case. The Lorentz invariant parameters involved are[33]

$$\begin{cases} \mathcal{F}^2 = \frac{1}{2} F_{\mu\nu} F^{\mu\nu} = \vec{B}^2 - \vec{E}^2, \\ \mathcal{G}^2 = \frac{1}{4} F_{\mu\nu} F^{*\mu\nu} = \vec{E} \cdot \vec{B}, \end{cases} \qquad (11)$$

where $F^*_{\mu\nu}$ is the dual field-strength tensor. Therefore in the case of a cross field with $|E| = |B|$ (or a plane wave), both $\mathcal{F}$ and $\mathcal{G}$ vanish, and this nonlinear effect would never occur. This is in sharp contrast with the stimulated process under the same EM field. It occurs that the proposed Linear Coherent Light Source (LCLS) (a free electron laser) at SLAC should have the right intensity for a test on the spontaneous process in the near future[3].

5 FUNDAMENTAL PHYSICS UNDER VIOLENT ACCELERATION

When a laser is ultra-intense, i.e., $a_0 = eE/mc\omega_0 \gg 1$, an electron under the direct influence of the laser can be accelerated and decelerated intermittantly during every laser cycle. Since it occurs within a laser cycle, the acceleration gradient can be as high as[34]:

$$G_l \sim 10 \text{TeV/m} \sim 10^{25} g_\oplus. \qquad (12)$$

While such intermittant acceleration is not useful for bringing electrons to ultra-high energy, it has been recently suggested [34] that this may be used for studying fundamental physics related to General Relativity, based on the Equivalence Principle.

5.1 The Hawking-Unruh Effect

Bell and Leinaas (BL)[35] first suggested that the well-known phenomenon of the equilibrium spin polarization in electron storage rings may be interpreted as a manifestation of the Unruh effect.

A uniformly accelerated object sees the vacuum fluctuations as a thermal bath, with a temperature given by[36]

$$kT = \frac{\hbar a}{2\pi c},\qquad(13)$$

where a is the object's proper acceleration. Historically this temperature was deduced as an extension of the seminal discovery by Hawking[37] on the blackbody radiation of black holes.

The spin of a circularly accelerated electron serves as a detector where its populations at the two spin levels would follow the Boltzmann distributions. Barber and Mane[38] showed that the BL formulation is equivalent to that of Derbenev-Kondratenko, and the known result of synchrotron radiation power can be reporduced using the Unruh picture. BL also observed that the resultant temperature is higher than that predicted for the linear acceleration. Most recently, Unruh[3] reinvestigated into this issue, and confirmed the BL findings. He explains that the seemingly higher effective temperature in the case of circular acceleration is not due to a supposed nonthermal nature of the heat bath, but rather due to the time-dependence of the spin-orbit coupling.

To avoid the complications caused by the spin-orbit coupling, Chen and Tajima (CT)[34] investigated the Hawking-Unruh effect under linear, albeit time-varying, acceleration. They proposed that by using an ultra-intense laser with, the sought-after signal should be above the Larmor radiation background. This Hawking-Unruh radiation has also been studied by McDonald earlier[39].

6 QUANTUM METHODOLOGY IN BEAM PHYSICS

There are abundant applications of the theoretical formulations initially developed for quantum mechanics and quantum field theory in beam physics. Some of these efforts do deal with the quantum effects in beam physics. Some others, however, aim at applying the quantum formulations to solve beam physics problems that are essentially classical.

6.1 Quantum Approach to Beam Optics

Jagannathan and co-workers[40] have developed a fully quantum mechanical formalism (Dirac-Pauli equation) for charged particle beam optics. While the leading order recovers the conventional beam optics, the higher orders describe effects such as spin-orbit interaction. Such activity also has practical implications. For example, Pusterla et al.[3] show that the Stern-Gerlach force has been studied under this formalism for a potential application to produce polarized beams.

6.2 Schroedinger Equation for Phase Space Dynamics

When mutual interactions among beam particles are included, two different approaches have been developed. The standard treatment relies on the Fokker-Planck equation for describing the time evolution of the beam density, while the *thermal wave model* more recently introduced[41], is based on a mathematical coarse-graining of the Vlasov equation, which leads to a quantum-like Schroedinger equation, with the normalized emittance playing the role of the Planck constant. Pestroni et al.[3] show that the stochastic dynamics of the Nelson type[42] provides a physical foundation to the quantum-like models that invoke Schroedinger equation.

Rosenzweig demonstrates[3] that the formal similarity of the linear Fokker-Planck equation to the Schroedinger equation for the simple-harmonic oscillator also helps to elucidate certain beam phenomena such as the stochastic cooling of the beam longitudinal momentum spectrum.

6.3 Wigner Function and Beam Distribution

When the analogy between the Wigner function and the Liouville function is invoked, the unitary trasnformation in quantum mechanics is recognized as the counter-part of the symplectic map in classical beam dynamics. Dragt and Hibib show[3] that while Wigner and Liouville functions do transform in an identical way under linear symplectic maps, in general they do not transform identically under nonlinear symplectic maps. Instead there are "quantum corrections" whose $\hbar \to 0$ limit may be very complicated.

Another challenge has been that the Wigner function can in principle be negative, while the classical distribution function has to be positive definite. By invoking a novel *tomography* technique, Fedele and Man'ko[3] are able to develop a *marginal distribution* for the classical particle beam transport, that contains all the information of the Wigner function.

6.4 Supersymmetry in Beam Dynamics

Using the formalism of stochastic quantization in quantum field theory, Bjorken and Chen[43] recently demonstrated that the longitudinal phase space (classical) dynamics in proton storage rings, under the influence of the nonlinear RF potential and its random noise, exhibits the property of *supersymmetry*! Its physical implications are currently under further investigations.

7 FUTURE OUTLOOK

The major issues, as well as the future challenge, in *quantum beam physics* can be summarized as follows:

• What is the fundamental limitation on phase space?
• Can high energy charged particle beams ever be condensed?

- Do we fully understand all aspects of physics under strong fields?
- What highest acceleration gradient can we ever attain, and what can we do with it in the laboratory studies of fundamental physics?
- What are the uses of quantum formulations in beam physics?

There are undoubtedly other important QM effects than we can poorly envision here. But even with this rather limited scope, it is hopefully evident that this new subject, *quantum beam physics*, will only become more prominent in the next century.

8 REFERENCES

[1] Z. Huang, P. Chen, and R. D. Ruth, *Phys. Rev. Lett.* **74**, 1759 (1995).

[2] Z. Huang, *Radiative Cooling of Relativistic Electron Beams*, PhD Thesis, Stanford University (1998).

[3] In *Quantum Aspects of Beam Physics (QABP98)*, ed. P. Chen (World Scientific, 1998).

[4] D. Kleppner, *Phys. Today*, Aug., p. 11 (1996).

[5] W. Ketterle, in *McGrow-Hill 1999 Yearbook of Science and Technology*, in press.

[6] I. Ginzburg, Kotkin, V. Serbo, and V. M. Telnov, *Nucl. Instr. Meth.* **205**, 47 (1983).

[7] P. Eisenberger and S. Suckewer, *Science* **274**, 201 (1996); W. P. Leemans et al., *Phys. Rev. Lett.* **77**, 4182 (1996).

[8] V. M. Telnov, *Phys. Rev. Lett.* **78**, 4757 (1997); erratum ibid. **80**, 976 (1998).

[9] T. Shintake, *Nucl. Instr. Meth.* **A311**, 453 (1992).

[10] A. Mikhailichenko and M. Zolotorev, *Phys. Rev. Lett.* **71**, 4146 (1993).

[11] Z. Huang and R. D. Ruth, *Phys. Rev. Lett.* **80**, 2318 (1998).

[12] J. Hangst *et al.*, *Phys. Rev. Lett.* **74**, 4432 (1995).

[13] D. Habs and R. Grimm, *Ann. Rev. Nucl. Part. Sci.* **45**. 391 (1995).

[14] See *Crystalline Beams and Related Issues*, ed. D. M. Maletic and A. G. Ruggiero (World Scientific, 1996).

[15] J. Wei, H. Okamoto, A. M. Sessler, *Phys. Rev. Lett.* **80**, 2606 (1998).

[16] K-j. Kim, in *QABP98*, Ref.[3].

[17] R. Bonifacio, C. Pellegrini, and L. M. Narducci, *Opt. Comm* **50**, 373 (1984).

[18] A. Michailichenko, in *Advanced Accelerator Concepts*, eds. S. Chattopadyay, J. McCullough, and P. Dahl, AIP Conf. Proc. No. 398 (1996);

[19] R. Blankenbecler and S. D. Drell, *Phys. Rev. D* **36**, 277 (1987); M. Bell and J. S. Bell, *Part. Accel.* **20**, 301 (1988); P. Chen and K. Yokoya, *Phys. Rev. Lett.* **61**, 1101 (1988); M. Jacob and T. T. Wu, *Nucl. Phys. B* **308**, 373 (1988); V. Baier, V. Katkov, and Strakhovenko, *Nucl. Phys. B* **328**, 387 (1989).

[20] P. Chen and R. J. Noble, SLAC-PUB-4050, 1986.

[21] P. Chen, in *High Energy Physics in the 1990s– Snowmass*, ed. S. Jenson (World Scientific, 1988); P. Chen and V. I. Telnov, *Phys. Rev. Lett.*, **63**, 1796 (1989).

[22] M. Drees and R. Godbole, *Phys. Rev. Lett.* **67**, 1189 (1991).

[23] J. R. Forshaw and J. K. Storrow, *Phys. Rev. D* **46**, 4955 (1992).

[24] P. Chen, T. Barklow, and M. Peskin, *Phys. Rev. D* **49**, 3209 (1994).

[25] K. Yokoya and P. Chen, in *Frontiers of Particle Beams: Intensity Limitations*, eds. M. Dienes, M. Month, and S. Turner, *Lecture Notes in Phys.* **400** (Springer-Verlag, 1990); P. Chen *Phys. Rev. D* **46**, 1186 (1992).

[26] W. Greiner, B. Mueller, J. Rafelski, *Quantum Electrodynamics of Strong Fields*, (Springer, 1985).

[27] B. Segev and J. C. Wells, *Phys. Rev. A* **57**, 1849 (1998).

[28] C. R. Vane, et al., *Phys. Rev. Lett.* **69**, 1911 (1992); *Phys. Rev. A* **50**, 2313 (1994); *Phys. Rev. A* **56**, 3682 (1997).

[29] J. Lindhard, *Mat. Fys. Medd. Dan. Vidensk. Selsk.* **34**, No. 14 (1965); A. H. Sørensen and E. Uggerhøj, *Nucl. Sci. Appl.* **3**, 147 (1989).

[30] V. N. Baier, V. M. Katkov, and V. M. Strakhovenko, *Nucl. Inst. Meth. B* **69**, 258 (1992).

[31] See *Channeling and Other Coherent Crystal Effects at Relativistic Energies*, eds. H. Andersen, R. Carrigan, and E. Uggerhøj, *Nucl. Inst. Meth. B*, NIMBEU, **119** (1996).

[32] C. Bula et al., *Phys. Rev. Lett.* **76**, 3116 (1996); D. Burke et al., *Phys. Rev. Lett.* **79**, 1626 (1997).

[33] J. Schwinger, *Phys. Rev.* **82**, 664 (1951); **93**, 615 (1954).

[34] P. Chen and T. Tajima, SLAC-PUB-7543, March, 1998.

[35] J. S. Bell and J. Leinaas, *Nulc. Phys. B* **212**, 131 (1983); *Nucl. Phys. B* **284**, 488 (1987).

[36] W. G. Unruh, *Phys. Rev. D* **14**, 870 (1976).

[37] S. W. Hawking, *Nature* **248**, 30 (1974); *Comm. Math. Phys.* **43**, 199 (1975).

[38] D. P. Barber and S. R. Mane, *Phys. Rev. A* **37**, 456 (1988).

[39] K. McDonald, in *Laser Acceleration of Particles*, ed. C. Jashi and T. Katsouleas, AIP Conf. Proc. No. 130 (1985); and in *QABP98*.

[40] R. Jagannathan, R. Simon, E. C. G. Sudarshan, and N. Mukunda, *Phys. Lett. A* **134**, 457 (1989); S. A. Khan and R. Jagannathan, *Phys. Rev. E* **51**, 2510 (1995).

[41] R. Fedele and G. Miele, *Il Nuovo Cimento* **D13**, 1527 (1991).

[42] E. Nelson, *Quantum Fluctuations* (Princeton Univ. Press, 1985).

[43] J. D. Bjorken and P. Chen, SLAC-PUB-8093, 1999.

PRODUCING AND MEASURING SMALL ELECTRON BUNCHES *

X.J. Wang

Brookhaven Accelerator Test Facility, National Synchrotron Light Source

Brookhaven National Laboratory

Upton, NY 11973,USA

Abstract

Significant progress has been made in the last few years in ultra-short and high-brightness electron beam production and measurements. For many applications, such as laser and high-frequency RF (W-band) accelerators, and high-gain harmonic generation free electron laser, electron beams with bunch length and transverse emittance smaller than optical wavelength are required. The status of such small electron beam production around the world will be briefly reviewed. The experimental results of small electron beam production using photocathode RF gun with magnetic bunch compression system, and emittance growth in the compressor will be discussed. We will also discuss various techniques for characterizing such small electron beam, specially RF kicker cavity for photocathode RF gun based linac, and using coherent radiation for bunch length measurement. The analysis of the kilo-Ampere 10 fs electron beam generation at the ATF will be presented .

1 INTRODUCTION

One of the fundamental phenomena during the interaction between the charge particle bunches and electromagnetic fields is the distribution of the charge particle beam will be modified by the electromagnetic fields, which in turn will affect the field properties. The basic task for accelerator science is to learn how to produce and control the charge particle beam. We have taken granted for a long time the fact, magnets are commonly used to confine and modified the transverse profile of the charge particle beam. The challenge in controlling the longitudinal distribution (bunching or debunching) of the particle beam is that, the speed of the charge particle becomes more difficult to manipulate as the beam energy increase due to the relativistic effect. We are also limited in manipulating the electron bunches in low energy because of the space charge effect. The common phrase in our daily life, such as "time is flying" reflects the simple fact that, we have great difficulty in catching the fast objects, such as the electron bunches, and measuring its bunch distribution. These difficult subjects, the status of producing and

measuring small electron bunches will be discussed in this report.

Generally speaking, smallness in producing and measuring the electron bunches longitudinal distribution is relative to two physical parameters. One is the wavelength of the acceleration fields employed to accelerate the electron bunches, small electron bunches implies that, the phase spread of the electron bunch is a small fraction of 2π. For a S-band (2856 Mhz) linac, electron bunch length smaller than 10 ps is needed. For a typical plasma based laser accelerator schemes, the wavelength of the plasma wave is on the order of 100μm, so electron beam on the order of 10 μm (30 fs) is needed in order to preserve the beam quality [1]. For Inverse Cerenkov, and Inverse Free Electron Laser (IFEL) accelerators using CO_2 laser, the bunch length on the order of 1 μm is preferred [2].

The second natural scale in measuring the small electron bunches is the transition time. Many dynamic process, such as phase transition and biological mutation occurs under room temperature on the time scale τ,

$$\tau \approx \eta/kT \approx 100 \ fs \qquad (1)$$

In the following section, the status of the small bunches production and measurement is briefly reviewed. We will discuss the experimental results of short bunch production from photocathode RF gun based linac, and discuss RF kicker cavity for measuring small beam for FEL applications. We will present an initial analysis of producing kA 10 fs electron bunch at the Brookhaven Accelerator Test Facility (ATF).

2 STATUS OF SMALL BUNCHES GENERATION AND MEASUREMT

Short electron bunches production and measurement can be treated as two different aspects of the same problem. Significant progress were made in both fronts in the last decade[3]. One of the most important feature in this development is the mutual promotion between the production and measurement techniques in short bunch research. This is best exemplified by the development in using coherent radiation for bunch length measurement as electron bunches getting shorter. We will briefly review the small bunches production and measurement techniques for sub-picosecond electron bunches, and discuss emittance growth caused by the CSCF and CSR.

2.1 Short Bunches Production

The shorter electron bunches can be produced in many ways, conceptually it can be classify into three categories and their combination. The three commonly used techniques in producing small electron bunches are:

Direct production: Using photocathode RF gun [4], plasma bases laser accelerator techniques(LILAC) [5-6], electron bunch from pico-second to femto-second can be produced directly. The primary issue in direct production in high brightness short electron bunches is the space charge effect, which varies as $1/\gamma 3$. To produce sub-picosecond short electron bunches directly with reasonable charge ($>10^7$ electrons) require high acceleration gradient to minimise the space charge effect. The coupling between the longitudinal and transverse space also plays critical role in direct producing sub-picosecond electron bunches due to the divergence of the electron beam.

Selection: Taking advantage of electron beam longitudinal position dependency on the transverse position (dispersion), short bunches as part of a long electron bunch can be selected. This ideas was implemented at the BNL ATF to generate sub-picosecond slice beam, and to study the photocathode RF gun emittance compensation process[7]. Another example is the femto-second X-ray production at ALS [8], where small portion of the electron beam was first energy modulated by a femto-seconds laser, and energy modulated electron beam was selected in the dispersion region to produce femto-second X-ray.

Compression: For low energy electron beam, both ballistic[9] and α-magnet[10] compressions were used to produce sub-picosecond electron bunches. In ballistic compression, faster (higher energy) electrons trail the slower electron, so both ends of the electron bunches move toward the centre of the bunch, which could be used to counter balance the bunch lengthening by space charge effect.

To overcome space charge effects, the most popular scheme to produce small electron bunches is magnetic compressor at higher energy. It takes advantage of the relativistic effect $\Delta v/v = (1/\gamma^2) \Delta p/p$. Magnetic compressor is designed in such way that, the electrons path length inside the compressor is proportional to their energy. Electrons locate at the head of the bunch posses higher energy, travel longer path and falling behind. While electrons at tail catch up since they travel in shorter distance. So magnetic compressor must consist two parts. The electron bunches must be first energy modulated to produce the desired energy distribution, and energy modulated electron bunch is compressed when it passes through the magnetic system.

A typical chicane magnetic compressor consists of four equal strength dipole magnets. Using transport notation, the bunch length compression property is described by R_{56} [11],

$$R_{56} = \int (\frac{1}{\gamma^2} - \frac{D(s)}{R}) ds \approx -\int \frac{D(s)}{R} ds$$

$$= 2\theta_B^2 (\Delta L + \frac{2}{3} L_B) \qquad (2)$$

Where θ_B is the bending angle of the dipole magnets, and ΔL is the separation between the magnets, and L_B is the path length of the dipole magnet. The major advantage of 4-magnet chicane compressor is that, due to the symmetry of the arrangement, all higher order geometric effects are cancelled. The minimum bunch length produced by the compressor is determined by the ratio of the initial energy spread to the amplitude of the energy modulation.

Using a BNL ATF photocathode RF gun injection system and chicane magnetic compressor, University of Tokyo has successfully compressed a 13 ps, 250 pC charge electron bunch to less than 240 fs (FWHM) [12](Fig.1).

Non-linear and wake field in the chicane magnet compressor were extensively studied [13], the second order chromatic bunch lengthening is proportional to the first order term R_{56}, this limits on the correlated energy spread, and hence the final bunch length.
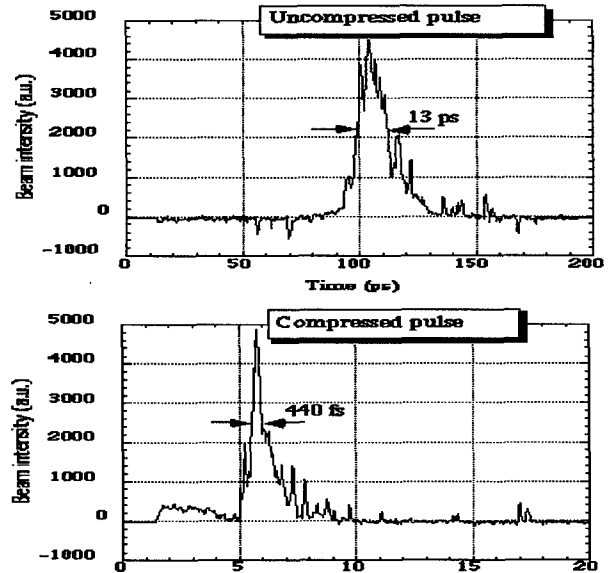
Figure 1: 250pC charge electron bunch is compressed to less than 240 fs after 370 fs streak camera resolution is considered.

Preserve the beam emittance is critical in any bunch compressor. Two energy independent effects could significantly increase the electron bunch transverse emittance for small electron bunches. One is so called Centrifugal Space Charge Force (CSCF), which is short range and caused by the curved trajectory of the electron bunches. The emittance growth by CSCF is [14],

$$\Delta\varepsilon^{CSCF} = 0.38N\alpha^2 \frac{I_p}{I_A}\ln(\frac{h}{4\sigma_x})\frac{2\sigma^2_x}{3\sigma_z} \qquad (3)$$

where N is the total number of the bending magnets, α is the bending angle, I_A is the Alfven current, I_p is the peak current, h is the dipole magnet chamber height, σ_z is the bunch length, and σ_x is the bending plane beam spot size. The other is Coherent Synchrotron Radiation (CSR), which is long range, and can radiate significant amount of power. The emittance growth for CSR is [14],

$$\Delta\varepsilon^{CSR} = 0.5N\alpha^2\frac{I_p}{I_A}\sigma_x(\frac{R}{\sigma_z})^{1/3} \qquad (4)$$

where R is the bending radius of the dipole magnet. Using ATF 20 deg. double bend achromatic transport system, we have measured emittance growth due to CSCF and CSR for a 250 pC charge[15]. Fig. 2 shows measured bunch length, and emittance growth as function of the electron beam spot size at the dipole. It agreed with the theoretical prediction, similar measurement for chicane magnet compressor was done recently at CERN[16].

2.2 Small bunches measurement

The other aspect of the small bunch physics is the techniques for measuring the bunch length. As electron bunches getting shorter, it demands new techniques to handle the new issues arise. Such as transverse form factor effect on coherent radiation from micro-bunched electron beam. There are many reviews on the bunch length measurement techniques recently [17,18]. We will concentrate on time domain and coherent radiation techniques in the rest of the section.

Streak camera is a single-shot time domain technique. The state of art streak camera is represented by FCS-200 streak camera manufactured by Hammmasu, it has demonstrated a 370 fs (FWHM) resolution (Fig.1). Using streak camera for electron beam bunch length measurement involves production and imaging the optical radiation the streak camera. Many effects could introduce significant error in sub-picosecond measurement, such as dispersion of the optics; bandwidth of the filter [19] and the finite size of the source. Transition radiation is the choice for very short bunch length measurement because of its promptness. For short electron bunch length measurement, the synchronisation between the streak camera and accelerator RF system could significantly enhance the experiment. Space charge effect in the streak camera tube limit the dynamic range of the measurement.
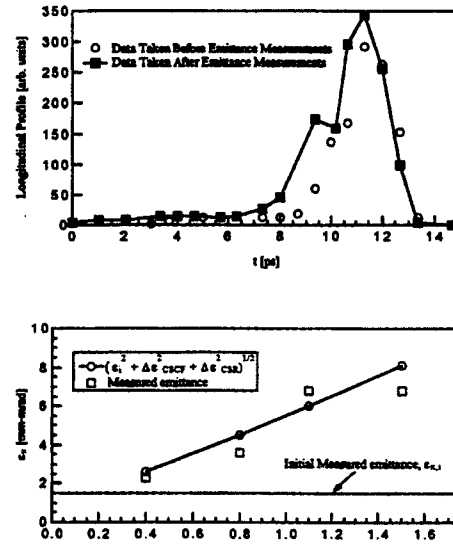
Figure 2: Emittance growth measurement for a 250 pC charge bunch. Top is the bunch length measurement, bottom is the compression between the measurement and theory.

$$\frac{\Delta p_y}{p_z} \approx k\Delta z$$

$$\frac{\Delta p_z}{p_z} \approx ky \qquad (5)$$

$$k = \frac{2\pi}{\lambda}\frac{A}{\gamma}\sqrt{PQ} \qquad (6)$$

RF cavity operating in the TM_{110} mode(kicker cavity) is another time domain measurement device (Fig.3). It has been used in many laboratories for low energy beams. When electron bunches pass through the zero phase crossing, the amplitude of the kick effect can be described by [20],

Where Δz is the electron position inside the electron bunch, k is the kicker constant,
where A is constant related to the cavity dimension, λ is the RF wavelength, P is the RF power, and Q is the quality factor of the cavity, and γ is the relativistic factor.

For SASE X-ray FEL and linear collider applications, electron bunch compression usual occurs at hundreds MeV or a few GeV. It seems RF kicker cavity has little application for high energy short bunches measurement.

Carefully examine Eq.(6), using shorter wavelength RF power source (λ), or using superconducting RF cavity (high Q, such as B-factory crab cavity), femto-seconds resolution can be realised by the RF kicker cavity with a high resolution beam profile monitor. Good resolution of the RF kicker cavity come from two important sources. One is the space charge effect which is negligible at high energy, second is small geometric emittance of the electron beam. RF kicker cavity enjoys many advantages over streak camera. It can be self calibrated, single shot to produce longitudinal profile of the electron bunches. It can be used for non-destructive timing jitter measurement of the electron bunches combining with beam position monitor, and can measure the longitudinal phase space of the electron beam in the dispersive beam line[20].

electron beam bunch length. The spectrum of the coherent radiation can be obtained by Fourier transform the interfrogram. The bunch length information from coherent radiation can be extracted using Kramers-Kronig relation [22]. Good agreement was observed between streak camera measurement and coherent radiation technique at University of Tokyo [12](Fig.4).

Interfrometric technique has demonstrated many advantages, such as simplicity, cost effective and no fundamental limit in its resolution. Recently, holographic Fourier spectroscopy technique was suggested [20] for single-shot measurement, and to eliminate mechanical constrain. The detector bandwidth and calibration of the measurement are two main challenges as electron bunch length getting shorter for coherent radiation technique.

Figure 3: Schematic of the RF kicker cavity.

As electron beam bunch length getting shorter, the shielding effect from beam pipe is reduced, so coherent radiation from small electron bunches getting stronger. The total radiation power generated by a bunch of N charge particles can be expressed as,

$$I^{tot}(\omega) = I(\omega)[N + N(N-1)F(\omega)] \qquad (7)$$

Where I(ω) is the single electron radiation power and,

$$F(\omega) = \int S(r) \, e^{-2\pi\omega r} \, dr = F_L(\omega)F_T(\omega) \qquad (8)$$

F(ω) is the Fourier transform of three-dimension beam distribution S(r), which can be further divided into transverse form factor $F_T(\omega)$ and longitudinal form factor $F_L(\omega)$. The first part of Eq(1) is the incoherent radiation and second part is coherent radiation. It is coherent radiation contains the bunch length information. Longitudinal form factor is none negligible only when radiation wavelength is comparable with the bunch length. After initial experimental observations of coherent radiation in Tohoku University of Japan and Cornell University [21,22], Fourier spectrometer using Michelson interferometer was successfully used at Stanford University [10] to measured hundred femto-second long electron pulse train. This techniques can be treated both in time domain and frequency domain, the width of the interferogram is the auto-correlation of the coherent radiation, which can be used directly to estimated the

Figure 4: Reconstructed bunch distribution by the interferometry (solid curve) and the result by the streak camera (dashed curve).

4 EXTREME SMALL ELECTRON BUNCH PRODUCTION AT THE ATF

Photocathode RF gun not only can optimise the transverse emittance of the electron beam, it is also capable of control the longitudinal emittance of the electron beam. It is later that determine the final bunch length can be achieved in the compressor. The longitudinal emittance of the photoelectron beam can be expressed by:

$$\varepsilon_\varphi = \sqrt{<\phi^2><(\frac{\Delta p}{p})^2> - <\phi\frac{\Delta p}{p}>^2}$$

$$\approx \frac{1}{2}\sigma_\phi^{\,3}\cos(\phi_0) \qquad (9)$$

where σ_ϕ is the longitudinal phase spread of the photoelectron beam at the RF gun exit, ϕ_0 is the photoelectron launch phase. Above equation shows that, photoelectron beam longitudinal emittance strongly depends on its bunch length at the RF gun exit. Fig.5 is the experimental results of the photoelectron beam bunch length as function of the RF gun phase produced by the 10 ps (FWHM) laser pulse. By optimising the RF gun phase, we were able to produce a 200 fs (FWHM) (330 fs full width) electron bunch with 40 pc charge, the normalise emittance measured was 0.5 mm-mrad. Combining with a magnetic compressors consist of undulator and chicane magnet, we can further reduce the electron bunch length. We will present a preliminary analysis how to produce a kilo-Ampere 10 fs long electron bunch at the ATF.

Two recent developments at the ATF made it possible producing such short electron bunches, one the the linac energy upgrade to more than 70 MeV [23], and other is the install undulator and chicane magnets for HGHG experiment [24]. The 10 fs long electron bunch will be produced in three stages. From Fig.5, we can produce a 20 pC charge, 30 MeV, 100 fs (FWHM) long electron bunch by reducing the RF gun operating phase. With recent ATF linac energy upgrade, first section of the ATF two sections of travelling linac will be able to produce 30 MeV electron bunch. The second section will be phased in such way that, 0.5 to 1% correlated energy spread introduce to the 100 fs long electron beam. This electron beam then was compressed first by the modulator undulator of the ATF HGHG experiment , whose R_{56} is about 10 μm/%. The under compressed beam is further compressed by the HGHG dispersion magnet with R_{56} equals to 35 μm/%.
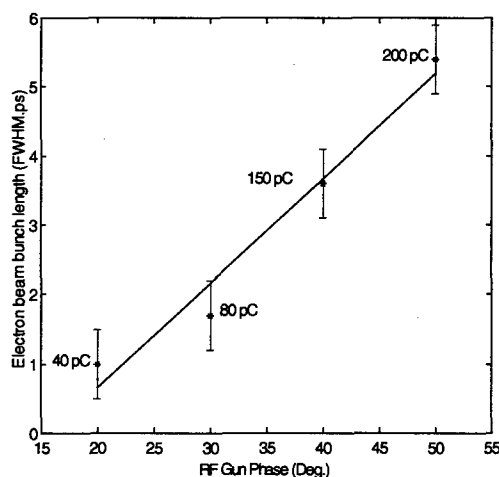
Figure 5: Photo-electron bunch length dependency on the RF gun phase.

The limiting factor of the final bunch length will be the electron beam divergence and space charge induced bunch lengthening. The bunch lengthening caused by the beam divergence can be calculated by:

$$\Delta\lambda = \frac{1}{2}\int (x'^2 + y'^2)ds \qquad (10)$$

To minimise the bunch lengthening, care must be taken to design the beam transport line. The space charge effect can be estimated by[25]:

$$\Delta\lambda = \frac{2Qcz^2}{I_A\gamma^4 RL} \qquad (11)$$

where γ is relativistic energy, Q is the charge, R and L are transverse and longitudinal size of the beam, and z is the beam transport distance. Because of strong dependence on the beam energy γ, this effect is less than a few femto-seconds for a 30 MeV beam.

5 REFERENCES

[1] T.C. Chiou and T. Katsouleas, Phys. Rev. Lett. **81**, 3411 (1998).

[2] W.D. Kimura *et al*, To be published in the Proc. Of 8th AAC workshop, Baltimore, Maryland (1998).

[3] Proceeding of Micro Bunches Workshop, AIP Conference Proceeding 367, edited by E.B. Blum, M. Dienes and J.B. Murphy (1995).

[4] L. Serafini et at, Nucl. Inst. Methods A **387**, 305-314(1997).

[5] D. Umstadter *at al*, Phys. Rev. Lett. **76**, 1285 (1995).

[6] E. Esarey *at al*, Phys. Rev. Lett. **79**, 2682 (1998).

[7] X. Qiu *et al*, Phys. Rev. Lett. **76**, 3723 (1996).

[8] A.A. Zholents *et al*, Phys. Rev. Lett. **76**, 912 (1996).

[9] X. J. Wang *et al*, Phys. Rev. E **54**, R3121 (1996).

[10] P. Kung *at al*, Phys. Rev. Lett. **73**, 967 (1994).

[11] T.O. Raubenheimer *et al*, Proc. Of 1993 PAC, p.635-637 (1993).

[12] M. Uesaka *et al*, To be published in the Proc. Of 8th AAC workshop, Baltimore, Maryland (1998).

[13] B.E. Carlsten, Nucl. Inst. Methods A **380**, 505-516 (1996).

[14] B.E. Carlsten *et al*, Phys. Rev. E **51**, 1453 (1995).

[15] X.J. Wang and D. Kehne, BNL-64646 (1997).

[16] H.H. Braun *et al*, submitted to Phys. Rev. Lett. , SLAC-PUB-7758 (1999).

[17] A.H. Lumplin, FEL Chanllenges II, San Jose, Jan., 1999.

[18] D.X. Wang, Proc. Of PAC97, (1997).

[19] M. Uesaka *et al*, Nucl. Inst. Methods A **406**, 371-379(1998).

[20] K.T. McDonald and D.P. Russell, Lecture Note in 343 published by Springer-Verlag, p.122-132(1988).

[21] T. Nakazato *et al*, Phys. Rev. Lett. **63**, 1245 (1989).

[22] R. Lai and A.J. Sievers, Nucl. Inst. Methods A **397**, 221-231(1997).

[23] X.J. Wang *et al*, these proceeding.

[24] L.H. Yu *et al*, these proceeding.

[25] T.C. Katsouleas *et al* , IEEE Transactions on Plasma Science **24**, 443(1996).

THE MARYLAND ELECTRON RING FOR INVESTIGATING SPACE-CHARGE DOMINATED BEAMS IN A CIRCULAR FODO SYSTEM*

M. Reiser[†], P.G. O'Shea, R.A. Kishek, S. Bernal, P. Chin, S. Guharay, Y. Li, M. Venturini,
J.G. Wang, V. Yun, W. Zhang, Y. Zou, M. Pruessner, Univ. of Maryland, College Park, MD,
T. Godlove, D. Kehne, P. Haldemann, FM Technologies, Inc.,
R. York, D. Lawton, L. G. Vorobiev, Michigan State University,
I. Haber, NRL, Washington, DC, and H. Nishimura, LBNL, Berkeley, CA

Abstract

The University of Maryland Electron Ring (UMER), currently under construction, has been designed to study the physics of space-charge dominated beams at extremely large values of the betatron tune shift which exceed those of existing strong-focusing synchrotrons and rings by more than an order of magnitude. In this paper, the unique design features of this research facility, the new beam physics to be investigated, and recent experimental results in the injector prototype as well as simulation studies will be reviewed.

1 INTRODUCTION

The University of Maryland Electron Ring (UMER), currently under construction, has been designed to study the physics of space-charge dominated beams with extremely large tune shift far beyond the operating regime of existing synchrotrons and storage rings. The project is being developed with the collaboration of FM Technologies, Inc., Michigan State University, NRL and LBNL.

Unique design features of the facility include a strong-focusing lattice with printed-circuit quadrupoles and dipoles, compensation of the earth magnetic field with specially designed Helmholtz coils, single-turn injection and extraction with the use of pulsed Panofsky quads and dipoles. Three induction gaps provide fast-rising electric fields to prevent erosion of the bunch ends due to space-charge forces as well as acceleration from 10 keV to 50 keV over 100 turns in a future extension of the UMER operation. The operating regime can be changed from the extreme end of space-charge domination and large tune depression towards the low currents and small tune shifts of existing rings. UMER is a compact, low-cost university facility which will be dedicated entirely to physics research. It will provide a unique testbed for comparing and validating computer simulation codes and theory with experimental results.

2 BEAM PHYSICS

The relative importance of space charge in the behavior of charged particle beams propagating through transport sys-

tems can be understood from the smooth matched-beam envelope equation [1]

$$k_0^2 a - \frac{K}{a} - \frac{\epsilon^2}{a^3} = 0. \tag{1}$$

Here, a is the effective beam radius, k_0 the wavenumber of the betatron oscillation without space charge, $K = (I/I_0)(1/\beta^3\gamma^3)$ the generalized perveance, $I_0 \approx (1/30)(mc^2/q) = 17$ kA for electrons, and ϵ the effective unnormalized emittance. Equation (1) represents the balance between the focusing force (first term), the space charge (second term), and the emittance (third term). The betatron wavenumber with space charge can be defined as

$$k = k_0(1 - K/k_0^2 a^2)^{1/2}. \tag{2}$$

The ratio k/k_0 is known as the "tune depression". In circular machines it can be written in terms of the number of betatron oscillations per revolution with (ν) and without (ν_0) space charge, as ν/ν_0, using the relations $k_0 = \nu_0/R$, $k = \nu/R$, where R is the mean ring radius. By introducing the dimensionless intensity parameter

$$\chi = \frac{K}{k_0^2 a^2}, \tag{3}$$

one can express the tune depression in the form

$$\frac{k}{k_0} = \frac{\nu}{\nu_0} = (1 - \chi)^{1/2}. \tag{4}$$

When space charge is a dominant effect in the beam physics, deviations from the equilibrium state and temperature anisotropies lead to rapid relaxation via plasma waves and instabilities (see Ch. 6 in Ref. 1). For these processes, the plasma frequency ω_p, or the corresponding plasma oscillation wavenumber $k_p = \omega_p/v$ (where v is the particle velocity) play an important role. The ratio k_p/k_0, or, in circular machines, the ratio of the number of plasma oscillations per revolution (ν_p) and ν_0, i.e. ν_p/ν_0, can be expressed in terms of the intensity parameter χ as

$$\frac{k_p}{k_0} = \frac{\nu_p}{\nu_0} = (2\chi)^{1/2}. \tag{5}$$

The plot of ν/ν_0 and ν_p/ν_0 versus χ, shown in Fig. 1, provides a convenient roadmap for characterizing the relative importance of space charge and emittance (or temperature) in the beam physics. When space charge is negligible

($\chi = 0$), we have $\nu/\nu_0 = 1$ and $\nu_p/\nu_0 = 0$; hence, the beam radius a is entirely determined by the emittance, and from Eq. (1) it is given by $a = (\epsilon/k_0)^{1/2}$. At the other extreme end of the parameter regime, where $\chi = 1.0$, the beam is laminar, the emittance is zero ($\epsilon = 0$), the beam radius is given by $a = K^{1/2}/k_0$, $\nu = 0$, and $\nu_p = \sqrt{2}\nu_0$. For $\chi = 0.5$, the space-charge and emittance terms in the envelope equation are equal, and $\nu/\nu_0 = \sqrt{0.5}$, while $\nu_p/\nu_0 = 1.0$, or $\nu_p = \sqrt{2}\nu$. Thus, for the range $0 \le \chi \le 0.5$, we can say that the beam radius (hence the beam physics) is emittance-dominated, while for $0.5 < \chi \le 1.0$ the beam radius (physics) is space-charge dominated.

Since K decreases rapidly with increasing energy, space-charge effects are most important at nonrelativistic energies near the particle sources and in the injector linacs for high-energy accelerators. High-energy synchrotrons and storage rings, on the other hand, operate in the emittance-dominated regime. To avoid dangerous resonance traversal, the intensity parameter is limited so that the tune shift values $\Delta\nu = \nu_0 - \nu$ are typically between 0.25 and 0.50. The corresponding values for the tune depression depend on ν_0. For high energy rings (AGS, Tevatron, etc.) they are in the range $0.97 < \nu/\nu_0 < 0.92$, $0.05 < \chi < 0.15$, which is marked in Fig. 1. The largest tune shift of $\Delta\nu = 1.9$ was achieved in a rapid-bunching experiment at the AGS (where $\nu_0 = 8.84$) by the late A. Maschke and collaborators in 1977 [2]. The corresponding tune depression of $\nu/\nu_0 = 0.79$ at $\chi = 0.376$ is also indicated in Fig. 1.

UMER is designed to explore the intensity regime far beyond Maschke's milestone, namely, in the extreme region of a highly space-charge dominated beam where no experiments exist at the present time. Initial operation is aimed at a high beam intensity where $\nu/\nu_0 = 0.25$. In future experiments, the intensity parameter χ will be decreased and the working point will be moved along the ν/ν_0, and ν_p/ν_0 curves towards Maschke's limit, and even further as indicated in Fig. 1. This is accomplished by decreasing the beam current from 100 mA to 25 mA or less in our specially designed variable perveance electron gun [3] and/or by increasing the beam energy via acceleration in the ring from 10 keV to 50 keV over about 100 turns.

The unknown territory in the extreme space-charge dominated regime will be very challenging and should provide a wealth of new phenomena. The UMER facility will allow us to investigate emittance growth due to conversion of free energy, halo formation, and equipartitioning in a circular machine. So far these effects have only been studied in linear transport lines. In addition, UMER will permit experimental investigations of longitudinal-transverse coupling and beam profile changes due to dispersion, the behavior of bunch ends, resonance traversal, the longitudinal resistive wall instability, and other effects in the space-charge dominated regime that is currently inaccessible. The results will provide a better understanding of the role of space charge in bending systems and circular machines and should be of great value for the design of
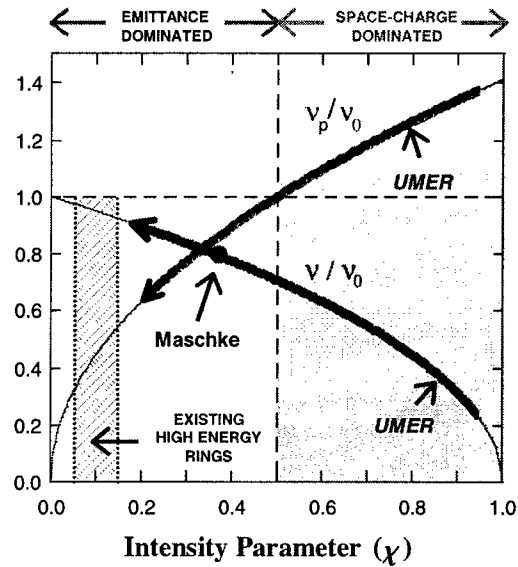
Figure 1: Beam physics regimes: Betatron and plasma oscillations vs. intensity parameter χ.

future rapid cycling, high-intensity rings.

3 DESIGN FEATURES

A schematic layout of UMER is shown in Fig. 2. The focusing lattice consists of 36 FODO periods of length 0.32 m and the ring circumference is 11.52 m. Each FODO section contains two printed quadrupole magnets and one printed dipole. The zero-current phase advance per peiod is $\sigma_0 = 76^o$, corresponding to a tune of $\nu_0 \approx 7.6$. The maximum tune depression due to space charge is expected to be between 0.2 and 0.3, depending on the emittance.

There are 15 diagnostic parts containing capacitive BPMs [4] and phosphor screens; three induction modules provide fast-rising "ear fields" to prevent expansion of the bunch ends [5] and acceleration in a future extension of ring operation. The electron bunch is injected into the ring at a repetition rate of 60 Hz or less from the injector system [3] with the help of two pulsed Panofsky quads [6] and a pulsed dipole. The bunch can be extracted within the first turn or after any number of turns with a system that duplicates the features of the injector line except that the electron gun is replaced by a large diagnostic chamber with phosphor screen, emittance meter and energy analyzer. Completion of the ring and of the first revolution of the beam is expected in late 2001 or early 2002. More details on the ring design can be found in other papers presented at this conference, and on our website: www.ipr.umd.edu/ebte/ring.

4 PROTOTYPE EXPERIMENTS AND THEORETICAL STUDIES

A test facility was built to investigate the performance of the printed-circuit quads and study beam transport through

235
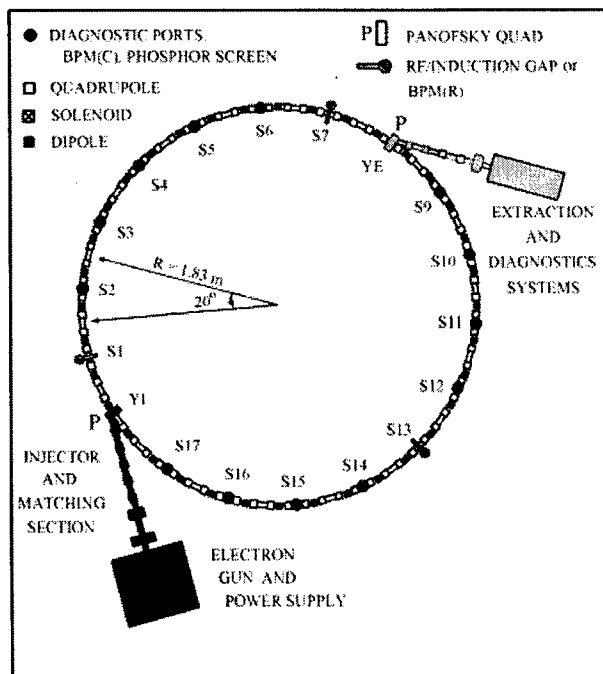
Figure 2: UMER layout.

the injector and a 20° prototype sector of the ring. The experimental results were compared with simulation studies using the WARP code [8]. Agreement was excellent and gave us confidence in the extensive simulation work on beam propagation through the ring itself [9]. A new theoretical model of space-charge dominated beams in a circular lattice was used to derive a set of coupled rms envelope equations for studying rms beam behavior in rings and bending lines and for the design of combined betatron and dispersion matching for beam injection into a ring [10].

A major discovery in the prototype injector experiments was the observation of transverse space-charge waves propagating from the outer edge of the beam inward toward the center [11]. In simulation studies with the WARP code these waves were reproduced and followed over distances extending far beyond the injector length. The electron beam is passing through an aperture at the anode to reduce the beam current. The aperture cuts off the radial tails of the particle distribution, and the resulting perturbation relaxes toward equilibrium as the radial waves propagate inward and the amplitude is attenuated.

Experimental tests of the prototype 20° bending section with the electron beam from the injector showed excellent performance with no beam quality deterioration or particle losses.

5 SUMMARY

UMER will occupy a new extreme of space-charge dominated beam physics by offering a unique opportunity to study beams of unprecedented intensity and tune depression with strong focusing and dispersion, involving physics relevant to colliders, heavy ion inertial fusion, high inten-

sity rings, etc. Preparatory test experiments have already shown exciting new transverse wave phenomena. Injector experiments are planned for the summer of 1999 and experiments will begin in the fall with the first ring segments. A staged program of experiments leading to single turn operation will be completed by 2001.

6 REFERENCES

[1] M. Reiser, *Theory and Design of Charged Particle Beams* (New York: John Wiley & Sons, 1994).

[2] G. Danly, E. Gill, J. Keane, and A. W. Maschke, "Preliminary Results of 100 MeV Bunching Experiment," Rep. BNL 50643, March 1, 1977.

[3] D. Kehne, et al., "The 10 keV injector for the University of Maryland Electron Ring Project," WEA36, this conference.

[4] Y. Zou, et al., "Development of a prototype capacitive BPM," WEA96, this conference.

[5] Y. Li et al., "Calculation of particle motion at the head and tail of a bunch for the University of Maryland Electron Ring," TUP76, this conference.

[6] Y. Li et al., "Design, simulation and test of Panofsky quadrupole," THP169, this conference.

[7] W. W. Zhang, "Magnetic field measurement of printed circuit quadrupoles and dipoles," THP170, this conference.

[8] S. Bernal et al., "Transport of a space-charge dominated electron beam in a short-quadrupole channel," Phys. Rev. ST Accel. Beams, **4**, 044202 (1998).

[9] R. Kishek, "PIC code simulations of collective effects in the space-charge dominated beam of the University of Maryland Electron Ring," TUP118, this conference.

[10] M. Venturini et al., "rms envelope equations in the presence of space charge and dispersion," Phys. Rev. Lett. **81**, 96 (1998); M. Venturini et al., "The problem of dispersion matching in space charge dominated beams," THP134, this conference.

[11] S. Bernal et al., "Observations and simulations of transverse density waves in a collimated space-charge dominated electron beam," to appear in Phys. Rev. Lett. (See also TUP115, this conference.)

Prototype "Electron Lens" Set-up for the Tevatron Beam-Beam Compensation

C.Crawford, F.Niell, G.Saewert, J.Santucci, A.Sery, A.Shemyakin*, V.Shiltsev, D.Wildman, FNAL

A.Aleksandrov, L.Arapov, G.Kuznetsov, P.Logachov, A.Sharapa, B.Skarbo, B.Sukhina, Budker INP

Abstract

A prototype "electron lens" for the Tevatron beam-beam compensation project is commissioned at Fermilab. We describe the set-up, report results of the first tests of the electron beam, and discuss future plans.

1 SCOPE

Compensation of beam-beam effects in the Tevatron with electron beams is a promising technique to improve the collider performance [1]. The method implies that an antiproton beam propagates through a countertraveling low-energy high-current electron beam ("electron lens"). An impact of the negative electron space charge can reduce betatron tune spread within antiproton bunch and a bunch-to-bunch tune spread – the effects due to collision with intensive proton beam which limit beam lifetime and luminosity.

An experimental R&D program on beam-beam compensation was started at FNAL Beam Division early in 1998. The "electron lens" prototype has been designed, fabricated, assembled in the Linac Lab and commissioned in December 1998. The goal of the set-up is to study feasibility and properties of the electron beam required for the beam-beam compensation. Currently, these studies are under way.

Table 1 shows the Tevatron "electron lens" (TEL) design parameters and parameters of the prototype set-up operation to date.

Parameter	units	TEL	Prototype
Effective length,	m	2.0	1.96
Electron current,max,	A	2.2	3.05
Electron energy, max	kV	5-10	6.4
CW modulation time,	μs	0.4(0.13)	0.5
Solenoid field,	kG	50	4
Beam deviousness,rms	mm	0.1	0.07
Configuration		2 bends	straight
Beam shape control		yes	yes

2 "ELECTRON LENS" PROTOTYPE

Major components and systems of the "electron lens" prototype are: electron gun, electron collector, modulator, power supplies, magnetic system, vacuum system, control system. The set-up (in present configuration) is shown in Fig.1. Electrons are thermally emitted from a cathode of the gun and extracted toward the positive potential of an anode U_a. Then they propagate through some 2 m long beam pipe which is under potential U_p (usually, $U_p \approx U_a$). Finally, electron beam is absorbed in a high efficiency collector at a smaller potential $U_c \leq U_a$. Some of the electrons can be

lost and absorbed on the vacuum pipe walls or at other aperture limits, i.e., not in the designated place of the collector. Strong longitudinal magnetic fields (of the order of few kG all along the set-up) helps to keep these losses low.
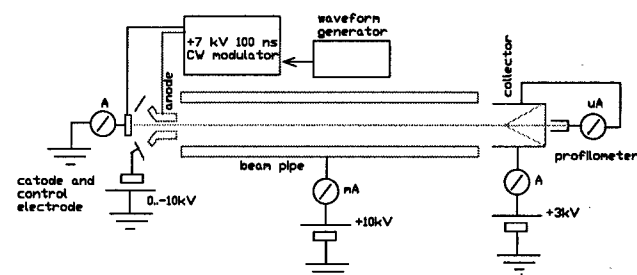
Figure 1: Electrical scheme of the "electron lens" prototype.

The high perveance electron gun is made in accordance with a novel approach proposed in [2] based on use of a convex cathode. The gun is immersed in 0.7-2 kG longitudinal magnetic field. It has a uniform current density profile, low transverse beam temperature and high perveance (these conditions can not be met in a standard Pierce geometry with a planar cathode). Fig.2 shows the gun construction.
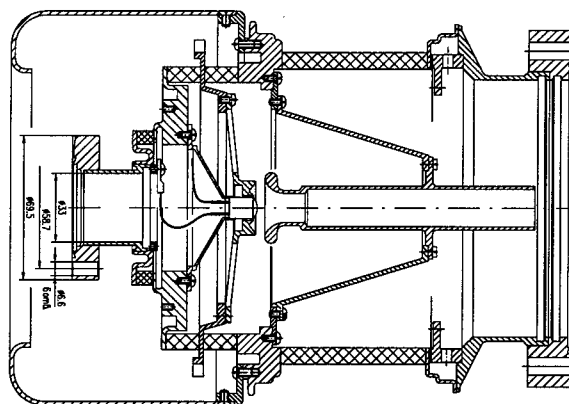
Figure 2: Electron gun of the "electron lens"

A 10 mm diameter 45° convex cathode is made of tungsten impregnated with emitting oxides (made by HeatWave Co., CA; see details in [3]). Fig.3 shows the maximum electron current J_e vs voltage between the anode and the cathode of the gun U_a. The maximum current is limited by negative space charge of the electron cloud near the cathode and follows Child's law $J_e = \mathcal{P}U_a^{3/2}$. Numerical simulations of the gun yielded *the perveance* $\mathcal{P} = 4.9 \cdot 10^{-6}\, A/V^{3/2}$, while a fit of the measured current at the Fig.3 gives somewhat larger perveance of $\mathcal{P} = 5.85 \cdot 10^{-6}\, A/V^{3/2}$.
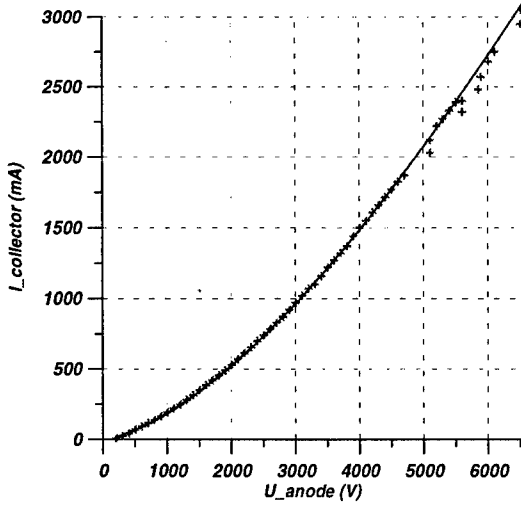
Figure 3: Current in the collector vs anode voltage. Smooth line represents a fit accordingly to Child's law with microperveance of $\mu P = 5.85$.

A possible explanation of excessive perveance (and current) can be imperfect alignment of the cathode and a control electrode. The latter is a specially shaped ring (simulated by computer) placed around the cathode which can vary the electron beam profile depending on its potential relative to the cathode. If the control electrode is grounded as well as the cathode $U_{ce} = 0$, then the electron beam current profile has a smoothed rectangular shape. If U_{ce} is *negative* and more than 3.5 times the *positive* anode potential, $-U_{ce} \geq 3.5 \cdot U_a$, then no current comes from the cathode (full emission suppression). At the intermediate cases, the negative control electrode potential $0 < -U_{ce} < 3.5 \cdot U_a$ suppresses the emission from the areas of the cathode which are close to the electrode, the total current is reduced and the profile becomes "bell-shape-like". Fig.4 demonstrates an example of such a shape when the total current is reduced on about 30% from 0.22 A (at $U_{ce} = 0$) to 0.16 A (other parameters: $B_{gun} = 2$ kG, $B_{coll} = 0.5$ kG, main solenoid field 2 kG, $U_a = 1.9$ kV, U_{coll}=2.5 kV, U_{pipe}=2.5 kV).

The electron beam current profile measurements are possible using a profile analyzer installed in the collector. The collector is able to absorb about 5-10 kW of electron beam power on its water cooled walls. There are no additional electrodes in the collector for repelling secondary electrons (low energy electrons born after the incoming electrons hit the collector walls) and reflected part of the primary beam. To lower the outcoming stream of electrons, the collector is designed to work in a magnetic field quickly decreasing from about 2 kG at the collector entrance to almost zero at its backplate. Good collector efficiency allowed us to achieve very small relative losses of electrons - typically of the order of $5 \cdot 10^{-4}$ (minimum 10^{-4}). The losses were of extreme concern at the stage of commissioning because a) they caused intensive outgassing from the vacuum pipe wall, b) there was a fear of excessive heat release at the anode (if the electron current goes onto it), c) beam pipe potential was kept by a high voltage power supply with maximum current of 2.5 mA and that sets a limit on maximum allowable losses. Routinely, positive potential at the collec-

tor is 1.5-2 times less than the anode potential and that is enough to keep the losses low.
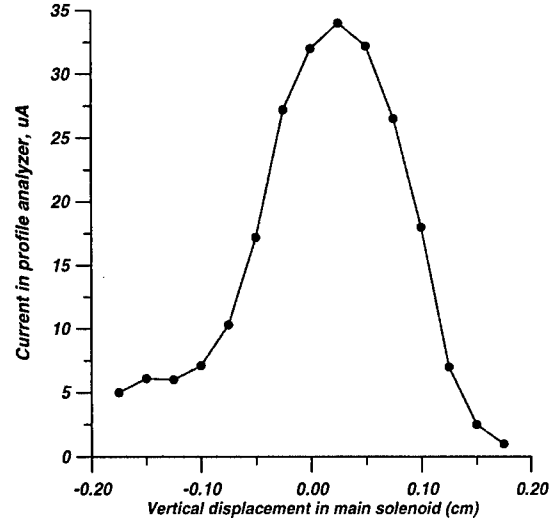
Figure 4: Vertical beam scan: analyzer current vs beam deflection in main solenoid.

The backplate of the collector has a tiny hole 0.2 mm in diameter and an additional Faraday cup behind it to measure the current which goes through the hole. This current is a measure of the electron beam current density. Using dipole correctors we are able to move the electron beam across the hole and measure the current profile like one presented in Fig.4. Usually a magnetic field B_{coll} of a few hundreds Gauss helps to increase the current density (as the adiabatic invariant in the magnetic field is $Ba^2 = const$, a is electron beam size) and, thus, the current coming through the hole, to easily detectable level of dozens of μA.

The magnetic system of the "electron lens" prototype consists of three solenoid magnets, 17 dipole correctors and independent power supplies. Two solenoid magnets (50 cm long and 28 cm inner diameter) produce longitudinal magnetic fields in the gun and collector (4 kG maximum with 2.7 kA of the coil current, typical values are 1 kG in the gun and 0 in the collector). The main solenoid (1.96 m long, 20 cm inner diameter) provides 4 kG with 10 kA of the coil current. One of the goals of the prototype is to get a straight electron beam in the main solenoid with a deviation less than 0.1 mm rms. Because low temperature electrons in a strong magnetic field just follow the magnetic field lines, we paid special attention to the magnetic field quality. The ways to keep the field distortions low are a) precise coil fabrication and winding, b) special measures to distribute evenly the return current in 8 rods of the main solenoid, c) dipole corrector coils to compensate the field imperfections on axis of the main solenoid, d) a magnetic shield over the magnets. With these steps we have achieved the field errors $\delta B_\perp / B_\parallel$ of about 10^{-4} in the main solenoid, about 10^{-3} in the central region of the gun and collector solenoids, and about 0.01 in the gap between the main and gun solenoid magnets. Most of imperfections take place either near the ends of the magnets, or in the middle of the main solenoid, where two of its sections are connected together (see details

238

in [4]). The resulting deviousness of the magnetic field lines (and, therefore, the electron beam) is about 0.05 mm rms in each transverse plane, or about 0.07 mm total. The vacuum pipe, gun and collector were installed into the solenoids only after the measurements and correction of the magnetic field were completed.
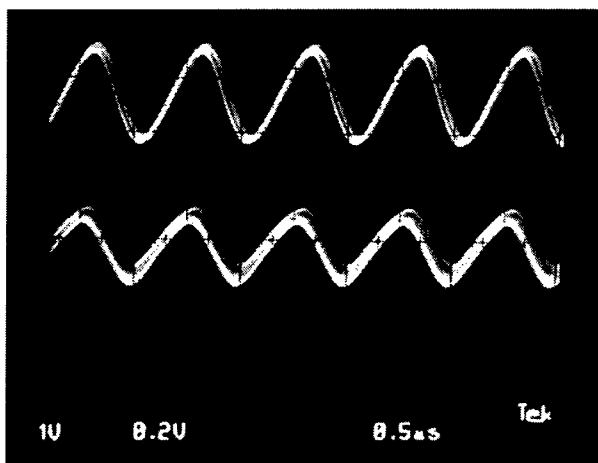
Figure 5: Current modulation in the "electron lens" prototype with frequency 1 MHz. Upper line - current in the collector 0.2 A/div (0.43 A peak-to-peak), lower line - anode voltage 1 kV/div (1.5 kV peak-to-peak).

A linear "electron lens" will be used to compensate bunch-to-bunch tune spread in the Tevatron antiproton beam. The minimum bunch spacing in the Tevatron, that is 396 ns in the Run II and 132 ns in the TEV33 upgrade of the collider. A straightforward way to get needed CW modulation of the current is to vary the anode voltage $U_a(t)$. The anode is modulated using a grid driven, 25 kW tetrode (EIMAC 4CW25000B) in series with a 5 kOhm resistor connected between the tetrode's plate and the 10 kV, 1.5A DC plate power supply. The anode is attached directly to the plate of the tetrode resulting in the 70 pF anode capacitance being added in parallel with the 25 pF tube output capacitance. The tetrode is operated in a grounded cathode configuration with the grid being driven by a 150 W solid-state amplifier. A 60 Hz de-rippling circuit is connected in series with the DC grid bias to remove any unwanted 60 Hz modulation due to the AC filament supply. Fig.5 shows 500 ns modulation of the anode voltage (1.5 kV peak-to-peak, 3 kV maximum)- see lower line, and the total electron current (0.43 A peak-to-peak, 0.7 A maximum) - see upper line. Future upgrades to the modulator include lowering the plate series resistance and obtaining a higher current DC plate supply. These two upgrades will allow a greater degree of anode modulation at higher frequencies. A new all solid-state modulator, utilizing MOSFET technology, is also under development [5].

The "electron lens" control system utilizes Internet Rack Monitors (IRMs) for all of its settings, read backs, control and status. The IRM is a general purpose intelligent data acquisition system based on the VME chassis and the Motorola MVME-162 processor. It contains the processor, network connection and the analog and digital I/O in the same chassis. The IRM's capabilities are expandable via two VME slots. As its name suggests, this device is a node on the world-wide Internet. Experimenters can access the IRM via any terminal with permission and the right interfacing software (LabVIEW, FNAL's "Local Station", etc.) A local database within each IRM allows it to function as a stand-alone control system for the equipment it controls.

High vacuum during routine operation is provided by a diode ion pump with 50 l/s rate. A turbomolecular pump with liquid nitrogen trap is used for rough pumping and during baking. A T-crossing located in a gap between the main solenoid and the gun solenoid provides a connection of the main pipe with the vacuum pumps. The entire vacuum system was assembled and baked at 250-300° C over few days. The main concern during the system commissioning was outgassing of the internal surfaces of the collector and the vacuum pipe due to currents of primary and secondary electrons. The beam current was increased step by step, keeping the vacuum below 10^{-6} Torr (in order to to reduce the cathode emission capability) and the electron current to the pipe less than 2.5 mA. Continuous increase of the produced electron charge in the system resulted in steady vacuum improvement. Finally, we achieved the design goal of 2 A on December 23, 1998. A month later, after installation of an additional collector power supply, we got more than 3 A of electron current. At the present time, the vacuum without the electron beam is about $2 \cdot 10^{-9}$ Torr, while 1 A current leads to pressure of $(3 - 5) \cdot 10^{-8}$ Torr. The set-up operation has become easy and very reliable. It takes about ten minutes (mostly to heat the cathode) to get a high current electron beam.

Our future plans at the "electron lens" prototype include studies of the collector efficiency vs the set-up parameters, electron beam profile measurements with a thin wire in main solenoid; and installation of diagnostic tools to control the amount of ions and secondary electrons in the system. A new (smaller size) electron gun and collector are under consideration.

3 REFERENCES

[1] V.Shiltsev, et.al, "Compensation of Beam-Beam Effects in the Tevatron with Electron Beams", FNAL-Pub-98/260 (1998); see also these Proceedings.

[2] A.Sharapa, et.al, NIM A, **406** (1998), p.169.

[3] J.L.Cronin, Microwave Journal, Sept. 1979, p. 57.

[4] C.Crawford, et.al, these Proceedings.

[5] F.Niell, "Electron Gun Beam Extraction with MOSFETS ", this Proceedings.

ACCELERATOR PHYSICS CHALLENGES IN FUTURE LINEAR COLLIDERS*

T.O. Raubenheimer[†]

Stanford Linear Accelerator Center, Stanford University, Stanford, CA, 94309

Abstract

At the present time, there are a number of future linear collider designs with a center-of-mass energy of 500 GeV or more that have luminosities in excess of $10^{34}\,\mathrm{cm}^{-2}\,\mathrm{s}^{-1}$. Many of these designs are very advanced, however, to attain the high luminosity, the colliders require very small beam emittances, strong focusing, and very good stability. In this paper, some of the outstanding issues related to the small spot sizes are discussed. Although the different designs are based very different rf technologies, many of these problems are common to all designs.

1 INTRODUCTION

Over the last decade, a number of linear collider designs have been developed to reach center-of-mass (cms) energies of 500 GeV or more [1]. These designs are the "next-generation" linear colliders and they incorporate extensively from the Stanford Linear Collider (SLC) which began operation in 1988. At present, there are four designs that are actively being pursued: TESLA [2], JLC-X [3], NLC [4], and CLIC [5]. The TESLA design is based on low frequency super-conducting rf technology while the others are normal-conducting designs. The JLC-X and the NLC designs are very similar; both utilize X-band (11.424 GHz) rf and are based on the same rf technology with identical beam parameters—for this reason, we will refer to the two designs as a single JLC/NLC design. Finally, the CLIC design is based on 30 GHz rf to allow higher acceleration gradients and the possibility of multi-TeV operation. Representative parameters for the designs are listed in Table 1.

All of the designs need to attain high luminosities:

$$\mathcal{L} = f_{rep}\frac{n_b N^2}{4\pi\sigma_x^\star\sigma_y^\star}H_D \qquad (1)$$

where f_{rep} is the collider repetition rate, $\sigma_x^\star/\sigma_y^\star$ are the rms beam sizes at the interaction point (IP), N is the bunch charge, n_b is the number of bunches per rf pulse, and H_D is the luminosity enhancement which arises when the opposite charged bunches focus each other, increasing the beam densities. Unlike circular colliders, f_{rep} tends to be low and thus the luminosity must be attained through the bunch charge and spot sizes. Fortunately, the beam-beam tune shift is not a severe limitation and thus the beam sizes can be reduced. Typical beam sizes, listed in Table 1, are roughly a factor of 1000 smaller than in the LEP2 or PEP-II storage rings.

Table 1: Representative parameters of future linear collider designs.

	TESLA	JLC/NLC	CLIC
Energy [TeV]	0.8	1	3
Lum. [10^{34}/cm^2/s]	5.0	1.3	10
Rf freq. [GHz]	1.3	11.4	30
Rep. Rate [Hz]	3	120	75
N [10^{10}]	1.4	0.95	0.4
Bunch Spacing [ns]	189	2.8	0.67
Ave. Current [A]	0.012	0.6	1.0
Pulse len. [μs]	850	0.27	0.10
$\gamma\epsilon_x^\star/\gamma\epsilon_y^\star$ [mm-mrad]	8/0.01	4.5/0.10	0.6/0.01
$\sigma_x^\star/\sigma_y^\star$ [nm]	391/2	234/3.9	40/0.6

Thus, there are two classes of problems in a linear collider: those related to accelerating the beam, which depends on the rf technology, and issues associated with the very small spot sizes at the IP. To attain the small spot sizes, the colliders must operate with very small beam emittances, strong focusing, and very good stability. All of these designs are very advanced and have dealt with many or most of the technical issues, however, in the following, we will discuss some of the issues which are not yet adequately resolved related to producing and operating with the small spot sizes. In particular, we will discuss the topic of stability in the main linacs and damping rings, which is essential for tuning and operation of the collider, and then discuss the problem of beam collimation, which is difficult due to the very high beam densities and beam powers. These issues will be presented in reference to the JLC/NLC design although similar problems exist in the other designs.

2 DESIGN HIGHLIGHTS

Before discussing the issues in greater detail, it is worth discussing some of the principal features of the different collider designs [6]. All of the colliders consist of a polarized electron source and a positron source, damping rings to decrease the source emittances, bunch compressors to shorten the bunch lengths, main linacs to accelerate the beams to the full energy, collimation sections to remove tail particles that could contribute to backgrounds in the detectors, and final focus systems that demagnify the beams to the very small spot sizes at the IP. A schematic of the NLC design is illustrated in Fig. 1.

The TESLA design can achieve good rf efficiency at low beam currents and can operate with long pulse lengths because of the high-Q super-conducting rf cavities. At the low rf frequency, the wakefields, which dilute the beam emittances, are relatively weak and thus the dynamics in
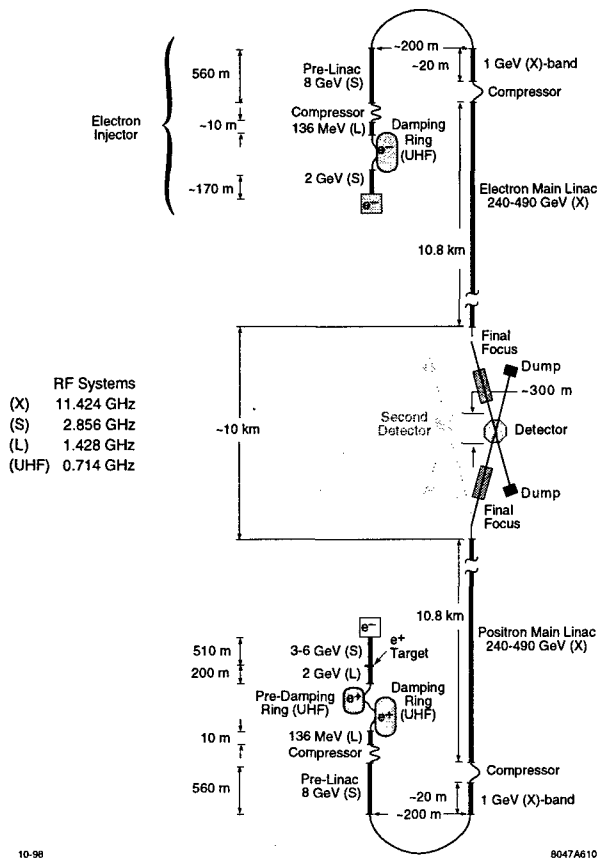
Figure 1: Schematic of the NLC from Ref. [4]

the linac is straightforward. In addition, because of the long bunch train, TESLA can use intra-train feedback to correct the effect of high frequency ground motion or other sources of train-to-train jitter. However, the long bunch train also has some liabilities: a novel damping ring with a 15 km circumference is required to store all of the bunches at once and one cannot design a conventional positron source that could produce the required bunch train.

The JLC/NLC design operates at an rf frequency which is four times that of the SLC linac. This allows for a higher loaded acceleration gradient of roughly 60 MV/m but it also implies stronger wakefields which were a significant limitation in the SLC operation. To deal with this problem, the JLC/NLC beam parameters have been chosen such that the effect of the wakefields on the beam dynamics is actually about four times less than in the SLC. Regardless, the design must rely on beam-based alignment techniques to attain the needed alignment tolerances. Furthermore, the shorter bunch train makes intra-train feedback a more difficult proposition and thus stability is very important. In addition, the higher rf frequency makes the rf sources significantly more difficult than in the SLC although research over the last decade has produced rf systems that meet the requirements.

Finally, the CLIC design operates at 30 GHz to allow for even higher acceleration gradients. However, at this frequency conventional rf sources are believed to be substantially more difficult and thus the CLIC design is based

on a Two-Beam Accelerator (TBA) concept where the rf power is extracted from a drive beam, traveling adjacent to the primary beam, and transfered to the primary beam accelerator structures; although not as well tested as the more conventional rf systems, the TBA scheme extends to multi-TeV operation in a straightforward manner. At the higher rf frequency, the wakefields are still stronger (scaling as f_{rf}^3) than in the JLC/NLC design. However, for properly scaled beam parameters, the alignment tolerances only decrease inversely with the rf frequency [7] and thus the tolerances are comparable to those in the JLC/NLC design.

3 MAIN LINACS

In this section, we will discuss three issues which are related to stability in the main linacs: the Beam Break-Up (BBU) instability, diagnostic and magnetic field stability which is important for the beam-based alignment techniques, and beam-based feedback systems.

3.1 Higher-Order Modes & Beam Break-Up

In all designs, the main linacs operate with long trains of bunches to improve the rf efficiency. However, with the long bunch trains, the transverse wakefield must be carefully controlled to prevent the BBU instability. Beam break-up will amplify any incoming jitter and could easily make the linac inoperable.

In the NLC design, the 1.8-meter accelerator structures are constructed from 206 cavities, each of which is designed to have a different dipole mode frequency. This detuning causes a rapid decoherence of the long-range wakefield. In addition, as can be seen in Fig. 2, the transverse wakefield is weakly damped, to prevent the modes from re-cohering at a later time, by coupling the cavities to four manifolds that parallel the cavities [8]. However, in the present structure design it is difficult to couple the last few cavities at the end of the structure to the manifold and this results in a few modes that are not sufficiently damped, causing to a severe BBU instability [9]. Once it was identified, a number of methods have been found to solve this problem, however, it illustrates the sensitivity of the beam dynamics to the cavity design; a similar problem has been identified in the TESLA cavities [10].
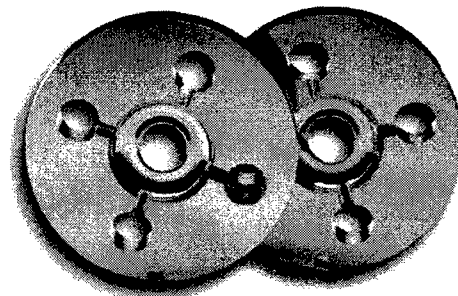
Figure 2: Photograph of two NLC Rounded Damped-Detuned Structure (RDDS) cavities.

241

3.2 Beam-Based Alignment

In the NLC and CLIC designs, the tolerances are sufficiently tight that the accelerator structures and focusing quadrupoles must be aligned using beam-based alignment techniques. The procedure envisioned for the NLC is similar to the technique used to align the Final Focus Test Beam (FFTB) facility at SLAC, namely:

1. Determine the position of the quadrupole magnetic center with respect to the Beam Position Monitor (BPM) mounted in the magnet by shunting the magnet and observing the downstream deflection

2. Move the quadrupoles to steer the beam through the magnetic center of the magnets

3. Align the accelerator structures to the trajectory using information derived from power measurements on the structure damping manifold [11]

The last two steps are iterated as component positions shift over time; more detail on the NLC scheme can be found in Ref. [12] and similar techniques are thought to be used in the CLIC facility [13, 14].

To facilitate the alignment, both the quadrupoles and the girders supporting the accelerator structures are mounted on remote movers. These techniques rely heavily on the diagnostic performance and on the accuracy of the mover systems. The NLC will use components similar to those developed for the FFTB, i.e. stripline BPMs with 1 μm resolution and movers with a 100 nm step. Depending of the time-scale of the misalignments, this alignment procedure would probably be implemented as a slow-feedback loop. However, there are still questions regarding the reproducibility of the magnetic center and the stability of the BPM electrical center over time. If the magnetic field center shifts significantly during the shunting procedure due to mechanical deformation of the magnet, thermal changes, or variations in the pole permeability, the alignment performance will be degraded [15]; experiments are underway at SLAC to measure the stability of the magnetic center. Similarly, if the electrical center of the BPMs shifts relative to the magnet center, the more time intensive 1st step must be repeated.

3.3 Beam-Based Feedback

In future linear colliders, both train-to-train and intra-train beam-based feedback will be used to significantly ease tolerances that would be otherwise difficult to attain. Pulse-to-pulse beam-based feedback has been used extensively at the SLC to improve the operation of the collider. However, there were a number of difficulties using the feedbacks and the system gain was usually greatly reduced. Because of the importance of feedback in a future linear collider, we need to understand the performance limitations of the SLC systems.

The biggest limitations are believed to arise from the wakefields in the SLC linac at high current; actually, during low current tests in 1996, the feedback systems performed
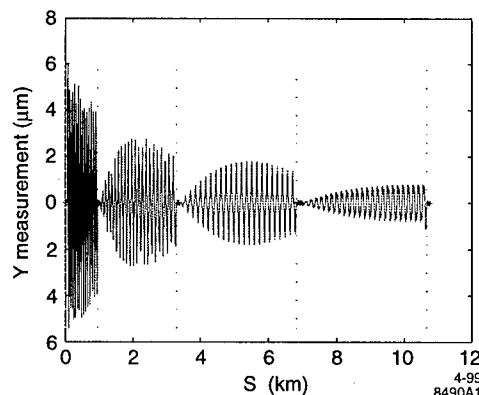
Figure 3: Simulation of SLC-style feedback in NLC linac; the dotted lines indicate the feedback locations.

as expected. The wakefields have two primary effects [16]: they make the transport nonlinear along the linac length and they cause correlations along the beam that are not simply corrected by correcting the centroid as illustrated in Fig. 3. The former effect can be corrected by having the upstream feedback loops communicate with all downstream loops rather than the simpler linear cascade used in the SLC. The second limitation can be remedied by increasing the number of BPMs used by the feedback loops and minimizing the measured trajectory in an rms sense. Both of the these solutions require significant increases in the feedback processing rate and communication bandwidth.

Different limitations arise with the intra-train feedbacks. In particular, intra-train feedback will be very useful to relieve the tight jitter tolerances on the final focusing magnets. However, the system is complicated by the nonlinearity of the beam-beam deflection and the difficulty of separating angular separations from position offsets; an example of such a system is described in Ref. [17].

4 DAMPING RINGS

The damping rings for these colliders must produce very low emittance beams and they have all of the problems of the 3rd generation synchrotron radiation sources, i.e. strong focusing optics with small dynamic aperture, heavily loaded rf systems, small impedance budgets, etc. For example, the NLC damping rings operate with an average beam current of roughly 1 A and need to produce beams with emittances of $\epsilon_{x,y}$ = 0.8 nm-rad and 8 pm-rad [18].

In all the designs, the rings always operate in a transient regime where beams are injected and extracted at the collider repetition rate. This makes stability difficult but a very stable extracted beam phase space is extremely important for the operation of the rest of the collider; jitter of the beam will lead to emittance dilution and will make beam-based tuning techniques extremely difficult. We will mention a few of the more difficult issues below.

4.1 Injection/Extraction Kickers

As stated, the rings operate with bunch trains injected and extracted at the collider repetition rate. In the JLC/NLC and CLIC rings, the full bunch train must be injected or extracted at once; these rings damp multiple trains of bunches at the same time and the trains are separated by a gap for the kicker to rise or fall (65 ns in the NLC rings). In the TESLA ring, the bunches are separated by roughly 10 ns and are extracted at a rate of one every few hundred nanoseconds to produce the TESLA bunch train. To avoid emittance dilution, the beams are injected and extracted on axis. This requires a large kick—typically the order of a few milliradians.

The required stability on the kicker is determined by the extracted horizontal emittance. In the NLC design, it is $\Delta\theta/\theta \lesssim 4 \times 10^{-4}$; this tolerance can be eased using a double kicker system [4] but is still a tight constraint for a pulsed device.

4.2 Instabilities

Another source of pulse-to-pulse or intra-train jitter are instabilities. First, to control the multi-bunch instabilities, the damping rings must use damped rf cavities and care must be taken in the design of all the vacuum components to avoid high-Q resonances. Furthermore, the rings require bunch-by-bunch feedback systems similar to those employed at the recently commissioned Φ-factory and the B-factories. The feedback gain requirements are determined by the chamber impedance, the expected injection errors, and the need to damp all transients by the time of extraction, however, one must be careful not to set the gain so high that noise from the feedback pickups or processing is amplified to point of being a significant source of jitter.

Second, to control the single bunch instabilities, the vacuum chamber must be designed to have a very low broadband impedance. For these rings, the longitudinal microwave instability usually has the lowest single bunch threshold. This microwave instability is frequently considered a 'benign' instability, however, bursting manifestations, like the 'sawtooth' instability observed in the SLC damping rings [19], are a limitation because of the sensitivity of the downstream systems to jitter sources. In the SLC, a 3% variation of the longitudinal distribution in the ring was clearly observable in the linacs [20]. Unfortunately, with further scrutiny, it appears that bursting modes of instability are prevalent in storage rings.

Finally, because of the low beam emittances and high densities, novel instabilities such as the fast beam-ion instability [21] or electron cloud instabilities [22] are potential limitations. At this time, there is insufficient experience with these effects to fully understand their implications however it is expected that they will impose severe constraints on the vacuum system design.

4.3 Transients

Other collective effects are directly related to the transient nature of the damping ring operation. Because beams are being injected and extracted at the collider repetition rate, one must be sure that all injection transients damp to levels small compared to the extracted beams by the time of extraction. This is complicated because most rings damp multiple bunch trains at once and the long-range wakefields can couple an oscillation from the most recently injected bunch train to drive a damped train to large amplitude even if the ring is 'stable' [23].

Another form of transient arises because of the gap between bunch trains which exists for the injection/extraction kickers in the NLC and CLIC rings and is created during the slow injection or extraction process in the TESLA ring. Here, the gap causes transient loading in the rf cavities which leads to a variation in rf phase along the bunch train; a similar effect in the transverse will cause a variation in position along the train.

4.4 Vibration and Slow Drifts

The final topic for the damping rings that we will mention is the effect of vibration or drifts. Fortunately, because of the high revolution rate, the effect of component vibration and drift on the trajectory can be treated using feedback in a manner similar to that used by the synchrotron light storage rings. However, it is also important to control the vertical equilibrium emittance which in the NLC rings is roughly 0.7% of the horizontal. This means controlling the coupling and the vertical dispersion which are more difficult to directly stabilize using feedback because the measurement is more complex; it is presently thought that accurate control of the trajectory will be sufficient although this needs verification.

In addition, the beam energy needs to be held fixed to a fraction of the natural energy spread. This arises because the bunch length is compressed by rotating the longitudinal phase space by roughly 90°. Thus, energy fluctuations from the ring turn into phase errors in the linacs which will cause energy errors at the IP and will shift the IP position.

To avoid shifts in the beam energy, the nominal-energy path length must be controlled. The path length can be varied due to orbit changes where the dispersion is non-zero or changes in the ring circumference. In the NLC damping rings, the variation of the circumference must be less than 18 μm to keep the beam energy changes to less than 0.01%. The observed changes in operating synchrotron radiation sources are over an order-of-magnitude larger; a method of controlling the path length is described in Ref. [24].

5 BEAM COLLIMATION AND MACHINE PROTECTION

Finally, the last problem we will mention is beam collimation and machine protection; this is a problem faced by all the linear collider designs. The collimation is needed because transverse particle tails get populated due to the transverse wakefields, beam-gas, beam-photon, and intrabeam scattering processes, and energy errors combined with chromatic effects. These large amplitude particles can generate backgrounds in the detector if they impact at small

apertures in the final telescope or generate synchrotron radiation in the quadrupoles which impacts further downstream. In the NLC final focus design, the later effect limits the effective aperture to roughly $12\sigma_x \times 45\sigma_y$.

While $12\sigma_x \times 45\sigma_y$ may sound like large amplitude, the nominal linac beam sizes are $10 \times 1\,\mu m$. Thus, without increasing the beta functions significantly, the collimation would have to be performed at the $50 \sim 100\,\mu m$ level. Unfortunately, the wakefields from these narrow gaps are very severe and could cause unacceptable emittance dilution or jitter amplification [25]. In addition, the very dense beams could destroy the collimators.

There are two primary ways in which the beams can damage the collimators: dE/dx heating when the beam passes through the collimators and ohmic heating by the image currents when a beam passes close to the collimator surface. The collimator could be damaged if the sudden thermal shock due to the beam causes stresses that exceed the tensile strength of the material. For Cu, this is expected to arise for $\Delta T \sim 200\,°C$, while for Ti or W, the limit is closer to $\Delta T \sim 800\,°C$. For comparison, the expected temperature rise in a thin Cu iris due to impact by the full bunch train at the end of the NLC linac is $\Delta T \sim 8\times10^5\,°C$.

The solution proposed in Ref. [4] is to increase the nominal beam size so that a spoiler system could withstand the passage of a full bunch train. This solution also acts as a partial component of the Machine Protection System (MPS) [26] which has a difficult task since the nominal beams can destroy the beamline components. However, this solution is also quite lengthy and uses very strong optics with large nonlinearities to generate the needed beta functions. The resulting tolerances and energy bandwidth are actually tighter than that in the final focus.

Our present concept is to reduce the passive survival constraint on the collimation system to only ensure survival for off-energy beams, a frequent occurrence in a linac, and use sacrificial devices to collimation the betatron phase space because large betatron errors without a corresponding energy error are infrequent. Further study on the material limitations, the collimator wakefields, and the optical solutions is still needed.

6 CONCLUSIONS

In this paper, we have discussed some of the remaining challenges in the designs of the next-generation linear colliders. These designs are all very advanced and have dealt with most of the technical problems. However, there are still a number of unresolved issues related to operation with the very small beams needed to achieve the high luminosities that are specified. These problems should be addressed over the next couple of years.

7 REFERENCES

[1] *International Linear Collider Technical Review Report*, G.A. Loew ed., SLAC Report–471 (1996).

[2] *Conceptual Design of a 500 GeV e+/e- Linear Collider with Integrated X-ray Facility*, R. Brinkmann ed., DESY 97–48 (1997).

[3] *JLC Design Study*, N. Toge ed., KEK Report 97–1 (1997).

[4] *Zeroth-Order Design Report for the Next Linear Collider*, T.O. Raubenheimer ed., SLAC–Report–474 (1996); updated parameters can be found on the Accelerator Physics web pages at http://www-project.slac.stanford.edu/lc/nlc-tech.htlm.

[5] R. Bossart, et al., "The CLIC Study of a multi-TeV Linear Collider," these proceedings.

[6] Also see: R. Brinkmann, "Technology and Challenges of Linear Colliders," these proceedings.

[7] J.P. Delahaye, et al., "Scaling Laws for e+/e- Linear Colliders," Nucl. Instr. Meth., **A421**:369 (1998).

[8] J. Wang, et al., "Accelerator Structure R&D for Linear Colliders," these proceedings.

[9] R. Jones, et al., "Emittance Dilution due to Long-Range Wakefields for RDDS in the NLC," these proceedings.

[10] F. Marhauser, et al., "Trapped Modes in TESLA Cavities," these proceedings.

[11] C. Aldophsen, et al., "Wakefield and Beam Centering Measurements of a DDS X-Band Accelerator Structure," these proceedings.

[12] P. Tenenbaum, "Simulation Studies of Main Linac Steering in the NLC," these proceedings.

[13] T.O. Raubenheimer, D. Schulte, "The Ballistic Alignment Method," these proceedings.

[14] T. D'Amico, G. Guignard, "Multi-Step Lining-Up: A New Correction Method for CLIC," these proceedings.

[15] P. Tenenbaum, "Resolution and Systematics in Beam-Based Alignment of a Long Periodic Beam Line," LCC–Note–006, on web pages at [4].

[16] L. Hendrickson, et al., "Feedback Systems for Linear Colliders," these proceedings.

[17] I. Reyzl, "Fast Feedback Systems for Orbit Correction in the TESLA Linear Collider," these proceedings.

[18] J. Corlett, et al., "The NLC Damping Ring Complex," these proceedings.

[19] P. Krejcik, et al., "High Intensity Bunch Length Instability in the SLC Damping Rings," *Proc. 1993 Part. Acc. Conf.*, Washington DC (1993), p. 3240.

[20] B. Podobedov, R. Siemann, "Sawtooth Instability in the SLC damping Rings," *Proc. 1997 Part. Acc. Conf.*, Vancouver, CN (1997), p. 1629.

[21] T.O. Raubenheimer, F. Zimmermann, "A Fast Beam-Ion Instability," Phys. Rev., **E52**:5487 (1995).

[22] K. Harkay, "Theory and Measurements of the Electron Cloud Effect," these proceedings.

[23] K. Thompson, et al., "Transverse coupled bunch instabilities in damping rings of high-energy linear colliders," Phys. Rev., **D43**:3049 (1991).

[24] P. Emma, T.O. Raubenheimer, "Circumference Control in Damping Rings using Chicanes," these proceedings.

[25] P. Tenenbaum, et al., "An Aperatus for the Direct Measurement of Collimator Transverse Wakefields," these proceedings.

[26] C. Adolphsen, et al., "The NLC Machine Protection System," these proceedings.

EXPERIENCE WITH SUPERCONDUCTING CAVITY OPERATION IN THE TESLA TEST FACILITY

M. Pekeler for the TESLA Collaboration*

Deutsches Elektronen-Synchrotron DESY, D–22603 Hamburg, Germany

Abstract

A description of the TESLA Test Facility, which has been set up at DESY by the TESLA Collaboration, will be given. Measurements of the superconducting 9-cell cavities in vertical and horizontal test cryostats will be presented, as well as the experience with the first two accelerator modules in the TTF linac. Future cavity R&D efforts will be described.

1 INTRODUCTION

A linear e^+e^- collider with a center-of-mass energy of ≥ 500 GeV would be an ideal machine to search for further fundamental constituents of matter and their interactions and to address the problem of mass generation in the Standard Model. Among the different designs (NLC, JLC, VLEPP, CLIC & TESLA), TESLA is the only one using superconducting cavities and a low radio frequency of 1.3 GHz. The high conversion efficiency from primary to beam power and the small emittance dilution makes the superconducting version an ideal choice for high luminosity operation [1]. The TESLA 500 GeV collider design is based on nine-cell cavities with a gradient of 25 MV/m at a quality factor Q of more than $5 \cdot 10^9$ [2]. An important feature is the integrated X ray Free Electron Laser (FEL) working on the Self-Amplified Spontaneous Emission (SASE) principle. This FEL will produce a photon beam at Angstrom wavelengths with peak brilliance exceeding that of third generation synchrotron radiation sources by 10 orders of magnitude.

2 THE TESLA TEST FACILITY

In 1992 the TESLA Collaboration decided to set up the TESLA Test Facility (TTF) [3] at DESY comprising the complete infrastructure for the treatment, assembly and test of 9-cell superconducting cavities and a superconducting linac for a fully integrated systems test with beam. The

aim was to achieve gradients of 15 MV/m in a first step and to gradually approach the 25 MV/m design gradient of the linear collider.

2.1 The TTF linac

The original proposal was to built a 500 MeV superconducting linac as a test bed for the cavities and RF systems foreseen for TESLA, but during the last years the design of the TTF Linac was extended to include from the beginning the important option of a Free Electron Laser in the Vacuum Ultraviolet regime [4]. Two injectors have been in use, a 250 keV thermionic gun [5] producing an average current of 8 mA at low bunch charge, and a 4 MeV laser-driven RF photoinjector [6] with the same average current, but a high bunch charge of 8 nC corresponding to the TESLA specifications. The electrons are captured by a superconducting nine-cell cavity (see figure 1) providing an energy gain of 13 MeV. In 1997 the first stage of the linac was successfully commissioned with the thermionic injector and one cryomodule containing eight 9-cell cavities with an average gradient of 15 MV/m [7]. The second cryomodule was installed in summer 1998. All cavities exceeded a gradient of 20 MV/m in the vertical test, four reached even the TESLA goal of 25 MV/m. The cavities of the third module which is presently being assembled will all operate at 25 MV/m.

Together with the installation of module 2, the thermionic gun was replaced by the photoinjector and a bunch compressor was installed between the two modules. The undulator magnet together with module 3 will be mounted this summer. The proof-of-principle experiment for the SASE type FEL is planned for the fall. In Phase II the TTF linac will be equipped with 5 more cryomodules, a second bunch compressor and a three times longer undulator. The completion of a VUV FEL user facility is planned for the fall of 2001.

2.2 The TTF infrastructure

The TTF infrastructure for cavity preparation and test [8] was completed in 1995 and is composed of a complex of clean rooms (from class 10 000 to class 10), a chemical etching facility and an ultra-clean water supply. A UHV furnace is available to improve the thermal conductivity of the cavity via heat-treatment at 1400 °C in the presence of titanium gettering. The last step of cavity preparation is a high pressure (100 bar) rinsing with ultra pure water.

*TESLA Collaboration: **Armenia:** Yerevan Pysics Institute, **P.R. China:** IHEP Beijing, Tsinghua Univ. Beijing, **Finland:** Inst. of Physics Helsinki, **France:** CEA/DSM Saclay, IN2P3 Orsay, **Germany:** Max-Born-Inst. Berlin, DESY Hamburg and Zeuthen, Univ. Wuppertal, Univ. Hamburg, Univ. Frankfurt, GKSS Geesthacht, FZ Karlsruhe, TU Darmstadt, TU Berlin, TU Dresden, RWTH Aachen, Univ. Rostock, **Italy:** INFN Frascati, INFN Legnaro, INFN Milano, INFN Roma, Univ. Roma II, **Poland:** Polish Acad. of Sciences, Univ. Warsaw, INP Cracow, Univ. of Mining & Metallurgy, Polish Atomic Energy Agency, Soltan Inst. for Nuclear Studies, **Russia:** JINR Dubna, IHEP Protvino, INP Novosibirsk, INR Troitsk, **USA:** Argonne National Lab., Cornell Univ., FNAL, UCLA

Original TTF Linac (Design Report 1995)

1997: Commissioning of injector 1 and module 1

TTF Linac Phase I

1998: Commissioning of RF gun, module 2 and bunch compressor 1
1999: Installation of undulator and module 3, SASE FEL proof of principle

TTF Linac Phase II

2001: Installation of more modules, bunch compressor 2 and long undulator for 1-2 GeV SASE FEL
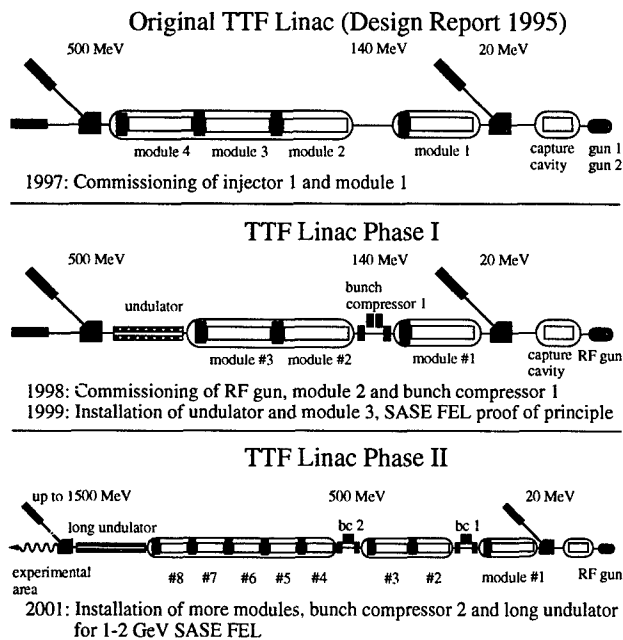
Figure 1: Development stages of the TTF linac design.

Effective length	1036 mm
Aperture diameter	70 mm
Coupling cell to cell	1.98 %
$E_{\text{peak}}/E_{\text{acc}}$	2.0
$B_{\text{peak}}/E_{\text{acc}}$	4.2 mT/(MV/m)
R/Q per cavity	1036 Ω
$\Delta f / \Delta L$	315 kHz/mm
Cavity bandwidth ($Q_{\text{ext}} = 3 \cdot 10^6$)	433 Hz

Figure 2: Cross section and some design parameters of the 1.3 GHz TTF 9-cell cavity

All cavities are tested in superfluid helium of 2 K in a vertical bath cryostat. The possibility exists to apply high peak power processing [9] as well as temperature mapping of the outer cavity surface [10]. Cavities having passed the vertical test are welded into their helium tank. The fully assembled cavity can be tested in a horizontal cryostat in pulsed power mode (500 μs rise time, 800 μs flat-top time at a 10 Hz repetition rate). The performance of the main power coupler, the higher-order-mode couplers and the cold tuning mechanism is checked here before the cavity is installed into the cryomodule.

The cavities can be tested also after installation in the linac. As in the horizontal cryostat, the quality factor Q is determined by measuring the dynamic heat-load. The cryoplant of the TTF permits a heat-load measurement at 2 K with a resolution of 0.05 W (as a reference, a cavity operated at 25 MV/m and $Q = 5 \cdot 10^9$ gives a heat dissipation of 1.8 W with the TTF pulsed mode).

3 CAVITY PREPARATION AND TESTS

A cross section of the TTF nine-cell cavity is shown in figure 2. The cavities are fabricated from RRR 300 niobium by electron-beam welding of half cells that are deep-drawn from niobium sheet metal. Up to now 55 cavities have been ordered at 4 European companies. The first series of 28 cavities were ordered in 1994, the second series of 27 in 1997. So far, 41 cavities have been tested in the vertical and 18 cavities in the horizontal cryostat.

The presently used cavity preparation at DESY consists of the following steps:

- Removal of a damage layer from the inner cavity surface by 80 μm Buffered Chemical Polishing (BCP)

using a mixture of HF (48 %), HNO_3 (65 %) and H_3PO_4 (85 %) in the ratio 1:1:2. This is followed by rinsing with ultrapure water until the resistivity of the water is higher than 18 MΩcm.

- Removal of 30 μm from the outer surface by BCP.
- A 2 hours heat-treatment at 800 °C for hydrogen degasing and recrystallisation.
- A 4 hours heat-treatment at 1400 °C with titanium getter for improvement of the thermal conductivity and homogenization of the niobium.
- Removal of the titanium layer by 80 μm inner and 30 μm outer BCP.
- Tuning to correct frequency and field flatness.
- Final 20 μm removal from the inner surface by BCP.
- High pressure rinsing with 100 bar ultrapure water.
- Drying by laminar flow in class 10 cleanroom, assembly of all flanges, leak-check.
- 2 times high pressure water rinsing, drying by laminar flow and assembly of input antenna.

3.1 Vertical test results

The vertical test results are listed in table 1. Several cavities of the first series reached gradients up to 29 MV/m, but the distribution of achieved gradients is very wide. In cavities with low performance defects in the welds or in the bulk niobium were found [11].

To avoid such defects, the welding technique was improved and all niobium sheets used for the second series were eddy current scanned [12] to eliminate foreign material inclusions. Almost all cavities of the second production reached gradients above 20 MV/m (see table 1). Two cavities (S34 and Z49) suffered from field emission and will be retested soon after a new high pressure water rinse. Cavity C43 shows a quench at a repaired equator weld where a hole was blown during electron beam welding. The ma-

Table 1: Performance of TTF cavities in vertical tests.
+: limited by available cw RF power (no quench observed).

cavity	E_{acc} MV/m	Q_0 10^9	status / comment
first production			
P1	29.1+	6	prototype cavity
P2	16.3	22	prototype cavity
D1	24.7	17	linac operation (module 1)
D2	21.9	4	module 1
D3	25.6	29	module 1
D4	13.5	16	module 1
D5	8.6	24	material defect
D6	13.6	12	material defect
S7	13.8	8	module 1 / weld defects
S8	12.5	12	module 1 / weld defects
S9	11.4	11	weld defects
S10	14.2	16	module 1 / weld defects
S11	13.5	13	module 1 / weld defects
S12	12.6	13	used at FNAL / weld defects
A14	6.4	11	quench at repaired weld
A15	23.0+	4	module 2
A16	20.8	6	field emission
C19	22.1	2	linac (capture cavity)
C21	29.3+	8	module 2
C22	20.2	21	module 2 / weld defect
C23	25.3+	8	module 2
C24	19.7+	5	module 2
C25	28.4+	9	module 2
C26	21.4+	4	module 2
C27	26.7+	8	module 2
second production			
S28	25.3+	6	module 3
S29	26.7+	6	module 3
S30	28.4+	7	module 3
S31	28.1	4	
S32	26.5+	7	module 3
S33	23.9	7	
S34	14.4+	2	field emission
D37	20.3	5	
D38	19.5	3	
D39	25.2+	7	module 3
D40	22.8+	5	module 3
D41	23.3+	5	module 3
D42	24.6	7	module 3
C43	12.9	20	quench at repaired weld
C44	25.5+	6	
Z49	18.0+	2	field emission

jority of the cavities reached their excellent performance already in the first vertical test. It is only occassionally necessary to repeat preparation steps.

The average gradient of all cavities is 20.5 MV/m. Neglecting cavities with identified material or fabrication errors gives an average gradient of 23.1 MV/m.

Figure 3 shows the time development of the best vertical test results. Since 1997 fabrication and material defects have been almost eliminated. Practically all of the new cavities reach gradients between 20 and 30 MV/m with an average of 25 MV/m.
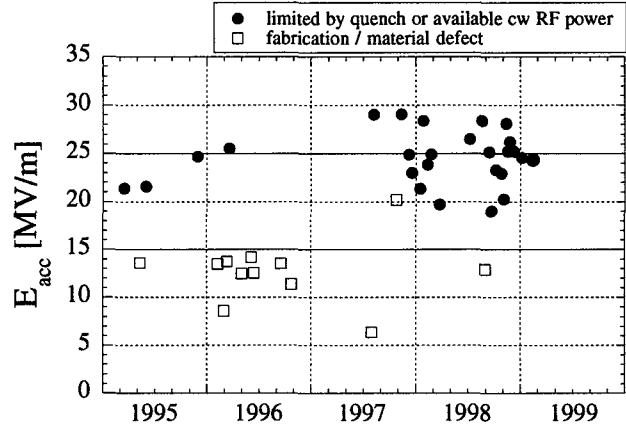
Figure 3: Time development of maximum gradient achieved in TTF 9-cell cavities.

3.2 Horizontal tests

After the successful vertical test, the helium vessel is welded to the conical head plates of the cavity (see figure 2). A 20 μm removal from the inner surface and a careful high pressure rinse follows. The last preparation step is the delicate assembly of the main power coupler.

The average gradient obtained in the 18 cavities tested in the horizontal cryostat was 22.5 MV/m and does not differ from the average value these cavities reached during the vertical tests (22.3 MV/m). The best horizontal test result was 33 MV/m with $Q = 4 \cdot 10^9$. Most of the good cavities are limited by RF breakdown in the main power coupler. Four of the eight cavities selected for module 3 were tested in the horizontal cryostat and all exceeded 25 MV/m with quality factors above $5 \cdot 10^9$.

4 OPERATION OF CAVITIES IN THE TTF LINAC

The two modules installed in the TTF linac are supplied with RF power by one 5 MW klystron. In the future it is foreseen to supply 32 cavities by one 10 MW klystron (as in the TESLA design). The cavities are not controlled individually but only the sum of the electric field vectors of all cavities is regulated by a digital RF control system. In addition to the feedback control which suppresses stochastic errors, an adaptive feedforward is applied to correct for repetitive perturbations, induced by beam loading and dynamic Lorentz force detuning [13]. The remaining errors from noise and other sources are small and require only a low gain in the feedback loop. An amplitude stability of
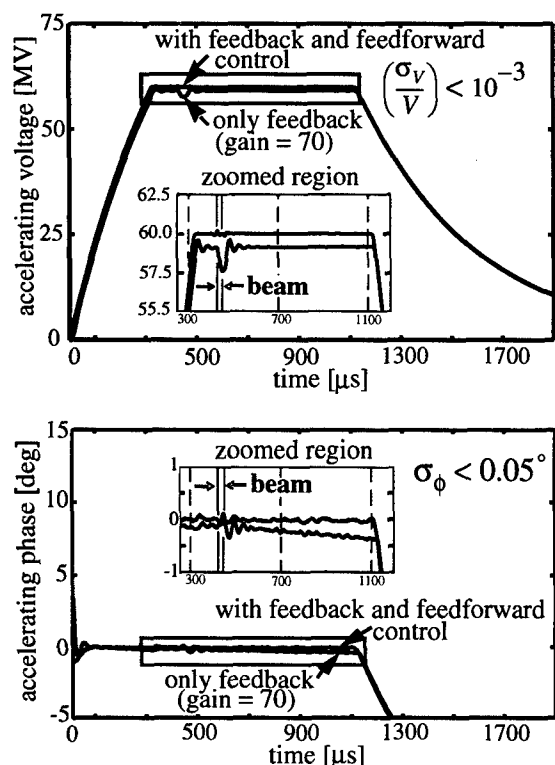
Figure 4: RF control system performance without and with adaptive feedforward. The beam pulse had a length of 30 μs.

$< 10^{-3}$ and a phase stability of $< 0.05°$ was achieved for the vector sum (see figure 4).

The cavities installed in module 1 reached an average gradient of 15 MV/m, two of them were already close to or above the TESLA specs (25 MV/m with $Q > 5 \cdot 10^9$) [7].

After the installation of module 2, there was only limited time for main coupler conditioning. No measurements of individual cavities were possible but an integral check of the whole module, with all cavities operating at the same gradient. With the full TTF pulse (10 Hz, 500/800 μs rise/flat-top time) 20 MV/m could be reached. The gradient could not be increased further because of coupler breakdowns. Heavy field emission was detected in one of the cavities. It was decided to apply in-situ high peak power processing (HPP) prior the second test and fields up to 29 MV/m were reached in this cavity. After the HPP the heat load of module 2 with all cavities operating at 20 MV/m was 6.5 W, corresponding to an average quality factor of $Q = 6 \cdot 10^9$. By detuning the cavity in which still some field emission was present the cryogenic load reduced to 2.9 W giving at 20 MV/m a Q of $1.3 \cdot 10^{10}$ of the remaining 7 cavities.

5   FUTURE CAVITY R&D

From the good test results of TTF cavities after mid 1997 one can conclude that the TESLA goal of 25 MV/m in 9-

cell resonators has been established with the present fabrication and preparation methods. However for a possible energy upgrade of TESLA there is a strong motivation to push the cavities closer to the physical limit of 50 MV/m which is determined by the critical magnetic field of the superconductor niobium.

There are three main effects which prevent us from reaching gradients well beyond 25 MV/m: thermal breakdown at material defects, field emission and Q-drop at high fields.

Occasionally we observe quenches at about 25 MV/m. New vertical tests with temperature mapping of the outer cavity surface are necessary in order to find out, if the delicate equator welds or very small foreign material inclusions are responsible for the thermal breakdown. In addition the eddy current scanning apparatus [12] was improved significantly for a better diagnostic of polluted niobium sheets with tiny defects.

With the present preparation techniques, field emission may be observed at gradients above 20 MV/m. Efforts are undertaken to further reduce field emission by improvement of the high pressure rinsing system and a better in-situ particle control during the assembly in the cleanroom.

A new type of field limitation, first observed in single cell cavities at Saclay, and recently also seen at DESY, is the decrease of the quality factor at fields around 25 MV/m without any evidence for field emission (see figure 5). In a collaboration between Saclay and KEK it was shown that electropolishing of the surface reduces this Q-drop and enhances the high-field capability compared to a buffered chemical polished surface [14]. An R&D effort has been launched in collaboration with CERN, KEK, Saclay and an industrial company to apply electropolishing to the 9-cell TESLA structures.
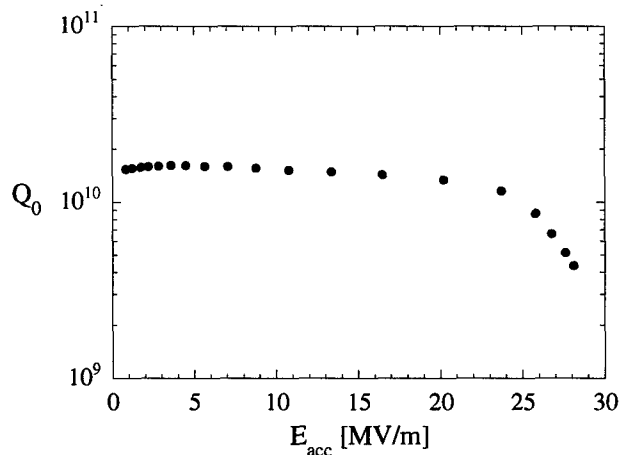
Figure 5: Observation of Q-drop at high gradient without any evidence of field emission in a TTF 9-cell cavity.

New cavity fabrication methods [15] like spinning or hydroforming [16] are under development and have the potential of reducing the costs. First test results on prototype cavities are promising (figure 6). A spun five-cell 1.5 GHz
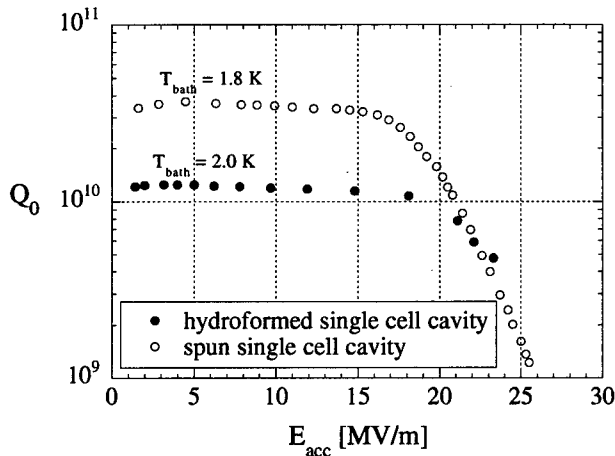
Figure 6: Vertical test results of prototype 1.3 GHz single cell cavities manufactured by hydroforming and a spinning technique.

cavity measured at CEBAF reached even 30 MV/m [17].

A new way of cavity reinforcement is plasma jet spraying of copper or other metals onto a niobium cavity [18]. The stiffening rings (see figure 2), presently used to counteract the Lorentz forces in pulsed operation, can probably be eliminated and additional stiffening at the equator can be achieved using this method.

In the superstructure concept [19] several multi-cell cavities are coupled to each other by a shorter and larger diameter beam pipe. Only one main input coupler is foreseen for such a group of cavities. This year a design for a 4 × 7-cell superstructure will be completed and 7-cell 1.3 GHz superstructure cavities will be ordered. The number of main couplers can be reduced to 1/3 as compared to the present TESLA design and the filling factor, the ratio of the linac active length to the total length, is increased from 0.66 to 0.76. We hope to test a superstructure with beam in 2001, in order to study beamloading and wakefield effects.

6 CONCLUSIONS

The results obtained so far in the framework of TTF are very encouraging and the technical possibility to built TESLA is becoming reality. In particular the cavities are now routinely reaching the TESLA requirements of 25 MV/m at $Q > 5 \cdot 10^9$. No degradation of cavity performance is found between vertical test, horizontal test and after installation in the linac.

7 ACKNOWLEDGEMENTS

8 REFERENCES

[1] R. Brinkmann, Low Frequency Linear Colliders, Proceedings EPAC 94, London, England, 1994.

[2] R. Brinkmann, G. Materlik, J. Rossbach, A. Wagner (Eds.), Conceptual Design of a 500 GeV e^+e^- Linear Collider with Integrated X-Ray Laser Facility, DESY 1997-048 and ECFA 1997-182.

[3] Proposal for a TESLA Test Facility, DESY Report TESLA 93-01.
D. A. Edwards (Ed.), TESLA Test Facility Linac - Design Report, DESY Report TESLA 95-01.

[4] J. Rossbach (Ed.), A VUV FEL at the TESLA Test Facility - Conceptual Design Report, DESY Rep. TESLA-FEL 95-03.

[5] T. Garvey et al., First Beam Test of the TTF Injector, Proceedings PAC 97, Vancouver, Canada, 1997.

[6] E. Colby et. al., Experimental Testing of the TTF RF Photoinjector, Proceedings PAC 97, Vancouver, Canada, 1997.
S. Schreiber, Experiments with the RF gun based Injector for the TESLA Test Facility Linac, this conference.

[7] A. Gössel et al., Vertical and Horizontal Test Results in Comparison with Performance in the TTF Linac, 8th Workshop on RF Superconductivity, Abano Terme, Italy, 1997.

[8] S. Wolff, The Infrastructure for the TESLA Test Facility, Proceedings PAC 95, Dallas, USA, 1995.

[9] C. Crawford et al., High Gradients in Linear Collider Superconducting Accelerator Cavities by High Pulsed Power to Suppress Field Emission, Part. Acc. 49, pp. 1-13, 1995.

[10] Q. S. Shu et al., An Advanced Rotating T-R Mapping & its Diagnoses of the TESLA 9-cell Superconducting Cavities, Proceedings PAC 95, Dallas, USA, 1995.

[11] M. Pekeler, Test Results on the Superconducting 9-cell 1.3 GHz Cavities for the TESLA Test Facility Linac, Proceedings EPAC 98, Stockholm, Sweden, 1998.

[12] W. Singer et al., Diagnostics of Defects in High Pure Niobium, 8th Workshop on RF Superconductivity, Abano Terme, Italy, 1997.

[13] A. Gamp et al., Experience with the Control of the Vector Sum at the TESLA Test Facility, Proceedings EPAC 98, Stockholm, Sweden, 1998.

[14] E Kako et al., Improvement of Cavity Performance by Electropolishing in the 1.3 GHz Nb Superconducting Cavities, this conference.

[15] V. Palmieri, New Technologies in Superconducting Cavity Fabrication, Proceedings Applied Superconductivity Conference, Palm Desert, USA, 1998.

[16] H. Kaiser et. al, Hydroforming of Seamless Niobium Cavity of TESLA Shape, Proc. HEACC 98, Dubna, Russia, 1998.

[17] P. Kneisel and V. Palmieri, Development of Seamless Niobium Cavities for Accelerator Application, this conference.

[18] S. Bousson et al., A New Fabrication and Stiffening Method of SRF Cavities, Proc. EPAC 98, Stockholm, Sweden, 1998.

[19] J. Sekutowicz et al., Superconducting Superstructure for the TESLA Collider, Proceedings EPAC 98, Stockholm, Sweden, 1998 and DESY Report TESLA 98-08.

The CLIC STUDY of a MULTI-TeV e± LINEAR COLLIDER

Jean-Pierre Delahaye for the CLIC study team:
R. Bossart, H.H. Braun, G. Carron, W. Coosemans, R. Corsini, T.E. d'Amico, J.C. Godot,
G. Guignard, J. Hagel. S. Hutchins, E. Jensen, M. Luong, A. Millich, P. Pearce, J.P. Potier,
A.J. Riche, L. Rinolfi, D. Schulte, G. Suberlucq, L. Thorndahl, M. Valentini, I.Wilson,
W. Wuensch, CERN, T. Raubenheimer, R. Ruth, SLAC, I. Syratchev, BINP.

ABSTRACT

The progress of the Compact LInear Collider (CLIC) study of a multi-TeV (0.5 - 5 TeV) high-luminosity (5×10^{33} to 1.5×10^{35} cm^{-2} sec^{-1}) e± linear collider based on Two-Beam Acceleration (TBA) is presented. The length and, in consequence, the cost of the overall complex is reduced by the use of high accelerating fields (150 MV/m), which are generated by specially damped 30 GHz normal-conducting accelerating structures. The large amount of RF power (400 MW/m) required to generate these high fields is provided by a novel RF power generating scheme which is potentially both cost and power efficient. After summarising the progress made in the developments of 30 GHz components and the performance obtained in the present phase of the CLIC Test Facility (CTF2), the design of a new test facility (CTF3), which will demonstrate the feasibility of the RF power generating scheme, is described.

1 INTRODUCTION

The Compact Linear Collider (CLIC) [1] has been optimised for a 3 TeV e± colliding beam energy to meet post-LHC physics requirements [2]. It covers a centre-of-mass energy range for e± collisions of 0.5 – 5 TeV and can be built in stages without major modifications. An overall layout of the complex is shown in Fig.1. In order to limit the overall length, beam acceleration is performed by using normal conducting travelling wave accelerating structures operating at high frequency (30 GHz) and developing fields of 100 to 200 MV/m. The RF power to feed the accelerating structures is extracted by transfer structures from high-intensity/low-energy drive beams running parallel to the main beam (Fig. 2). A single tunnel, housing both linacs and the various beam transfer lines without any modulators or klystrons, results in a simple, cost effective and easily extendable arrangement.
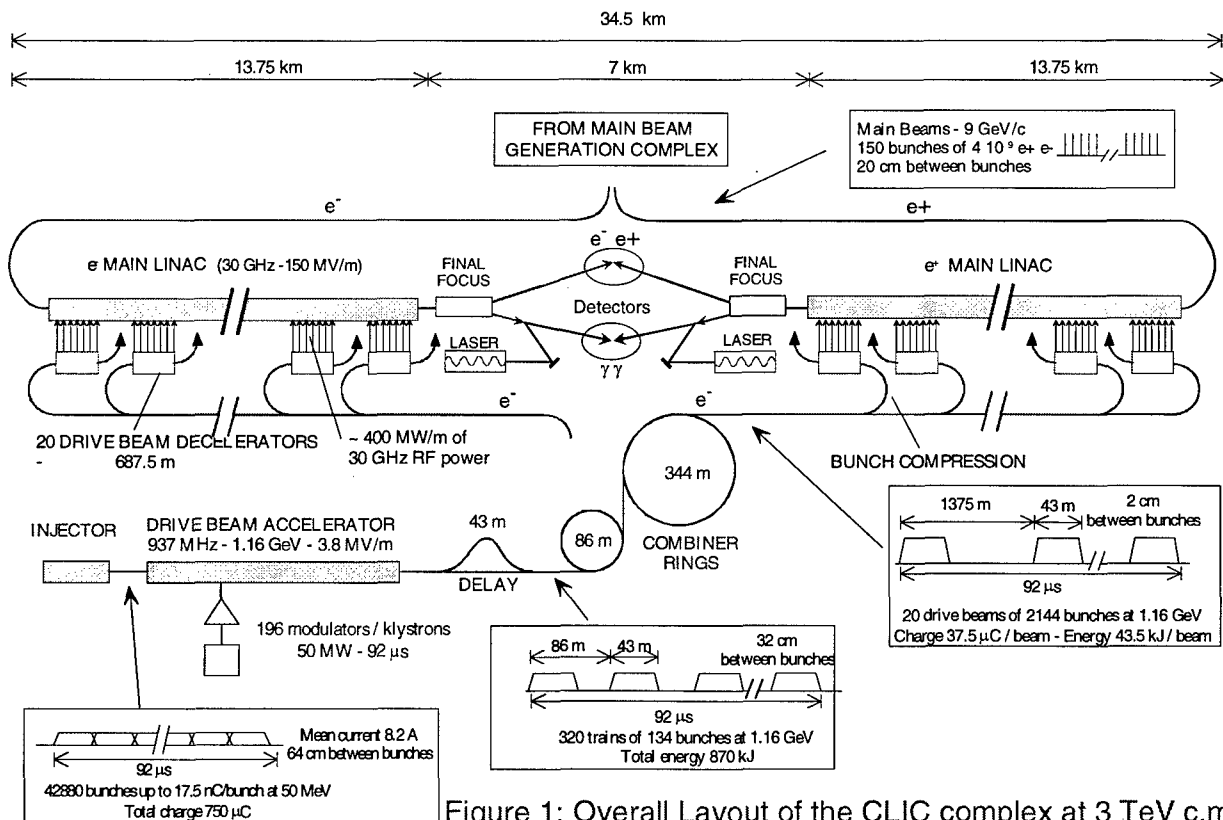
Figure 1: Overall Layout of the CLIC complex at 3 TeV c.m.

Drive Beam Decelerator

223 cm

Main Linac Accelerator
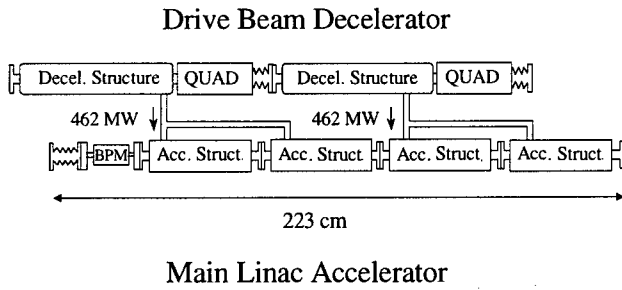
Figure 2: One main beam and drive beam module.

2 MAIN BEAM - LINAC PARAMETERS

The main beam and linac parameters are listed in Table 1 for various collision energies. They are deduced from general scaling laws [3] covering more than a decade in frequency. These laws agree with optimised linear collider designs [4] and show that the beam blow-up is independent of frequency for equivalent beam trajectory correction. To preserve the vertical emittance ε_{nv} at high frequency requires small charge per bunch N, short bunches, strong focusing and large accelerating gradient. A high RF to beam transfer efficiency results from multibunch operation with a close bunch spacing. Above 1 TeV, the vertical beam emittance is decreased and a high beam-strahlung regime retained, to limit the power consumption. Thanks to the short bunches however, the luminosity spectrum does not deteriorate significantly with the energy [5] and the increase of the number of emitted gammas is limited (Table 1). Hence, the effects of the 30 GHz transverse wakefields W_T can be kept moderate by choosing N to be 4×10^9 and σ_z at the limit of the momentum acceptance of the final focus. The overall blow-up $\Delta\varepsilon_{ny}$ remains below ≈ 100 % at all energies [6]. The required luminosities impose a reduction in the injected ε_{ny} from 5×10^{-8} rad.m at 0.5 TeV to 0.5×10^{-8} rad.m at 5 TeV. The focusing optics, scaled as (energy)$^{0.5}$, is generated by a FODO lattice made up of sectors with equi-spaced quadrupoles and matching insertions between sectors. The RF cavities and quadrupoles are pre-aligned to 10 and 50 μm respectively using a stretched-wire positioning system. Limiting $\Delta\varepsilon_{ny}$ relies in part on the use of bumps which are created locally at 5 to10 positions along the linac by mis-aligning a few upstream cavities. The measurement of the misalignments of the beam position monitors (BPMs), is crucial for emittance control [7]. A section of 12 quadrupoles is switched off, and with the beam centred in the two end BPMs of this section, the relative mis-alignments of the other monitors are measured with an accuracy of 0.1 μm. The beam trajectory and ground motion effects are then corrected by a 1 to 1 method. BNS damping is achieved by running off-crest of the RF-wave by 6° to 10°. For the sake of multi-bunch beam stability, each cell of the 150-cell structure [8] is damped by its own set of four radial waveguides giving a Q of 16 for the lowest dipole mode. A simple linear taper of the

Beam param. at I.P.	0.5 TeV	1 TeV	3 TeV	5 TeV
Luminosity (10^{34}cm^{-1}s^{-1})	0.5	1.1	10.6	14.9
Mean energy loss (%)	3.6	9.2	32	40
Photons /electrons	0.8	1.1	2.2	2.6
Rep. Rate (Hz)	200	150	75	50
$10^9 e^\pm$ / bunch	4	4	4	4
Bunches / pulse	150	150	150	150
Bunch spacing (cm)	20	20	20	20
H/V ε_n (10^{-8}rad.m)	188/10	148/7	60/1	58/1
Beam size (H/V) (nm)	196/4.	123/2.7	40/0.6	27/0.45
Bunch length σ_z (μm)	50	50	30	25
Accel.gradient (MV/m)	100	100	150	200
Two linac length (km)	7	14	27.5	35
Accelerating Sections	10802	21604	43736	54802
Power / section (MW)	116	116	231	386
RF to beam effic. (%)	35.5	35.5	26.6	19.4
AC to beam effic. (%)	14.2	14.2	10.6	7.8
AC power (MW)	68	102	206	310

Table 1: Main beam and linac parameters

iris dimension provides a detuning frequency spread of 2 GHz (5.4%). Transverse wakefield calculations in this structure with non-perfect loads show a short-range level of about 1000 V/(pC·mm·m) decreasing to less than 1 % at the second bunch and a long time level below 0.1 %.

3 THE RF POWER SOURCE

The RF power for each 687.5 m section of the main linac is provided by a secondary low-energy high-intensity electron beam which runs parallel to the main linac [9]. The power is generated by deceleration of this beam through energy-extracting RF structures in the so-called "Drive Beam Decelerator". For the 3 TeV c.m. collider there are 20 drive beams per linac. Each drive beam has an energy of 1.16 GeV and consists of 2144 bunches with a spacing of 2 cm and a maximum charge per bunch of 17.5 nC. These 20 drive beams, spaced at intervals of 1.375 km, are produced as one long pulse by one single drive beam generator. By sending this drive beam train towards the on-coming main beam, different time slices of the pulse can be used to power separate sections of the main linac (Fig. 1). All the bunches (for 20 drive beams) are first generated and accelerated with a spacing of 64 cm as one 92 μs long continuous train in a normal-conducting fully-loaded 937 MHz linac with an RF/beam efficiency $\approx$ 97%. After acceleration the continuous beam is split up into trains of bunches using the combined action of a delay line and a grouping of bunches in odd and even RF buckets. These trains are then combined in two stages by interleaving four bunches in odd and even RF buckets. These trains are successive bunch trains over four turns in each of two subsequent isochronous rings yielding a final bunch repetition frequency and corresponding beam energy compression by a factor 32. The energy-extracting structures consist of 4 periodically-loaded rectangular

waveguides coupled to a circular beam pipe [10]. Each structure provides 462 MW of 30 GHz RF power, enough to feed two accelerating structures. For stability in the drive beam decelerator, these structures are damped to reduce long-range transverse wakefield effects. The overall wall plug to RF power production efficiency is of the order of 40%.

4 TEST FACILITIES

The first CLIC Test Facility (CTF1) operated from 1990 to 1995 and demonstrated the feasibility of two-beam power generation. It produced 76 MW of 30 GHz RF power and generated on-axis gradients in the 30 GHz structures of 125 MV/m. A new test facility (CTF2) [11] equipped with 30 GHz modules made with RF components as similar as possible to the one envisaged for CLIC and including a few μm precision active alignment system, is being commissioned. The nominal configuration is as follows: The 48-bunch 640 nC drive beam train is generated by a laser-driven S-band RF gun with a Cs_2Te photocathode. It is accelerated to 62 MeV by two travelling-wave sections operating at two slightly different frequencies to provide beam loading compensation along the train. After bunch compression in a magnetic chicane, the bunch train passes through four power extracting structures, each producing enough power to drive two 30 GHz accelerating sections with 40 MW, 16 ns long pulses. The two bunches of the probe beam, also generated by an RF gun, are pre-accelerated to 50 MeV at S-band before being injected into the 30 GHz accelerating linac. The installation is now complete. The drive beam RF gun has produced a single bunch charge of 112 nC and a maximum charge of 755 nC in 48 bunches. 50 MW of 30 GHz RF power have been produced so far using a 450 nC drive beam. This resulted in a 30 MeV energy gain of the 0.7 nC probe beam. The highest accelerating gradient obtained is 70 MV/m with all the power generated by one structure feeding one accelerating structure.

A new facility (CTF3) is under study (Fig.3), which would test all major parts of the CLIC RF power scheme. To reduce costs, it is based on the use of the ten 3 GHz 40 MW klystrons and modulators from the LEP injector Linac. The drive beam is generated by two thermionic guns and is accelerated to 180 MeV by 20 short fully-loaded structures operating at 7.4 MV/m with an RF to beam efficiency of 96%. The beam pulse is 1.4 μs long with a current of 4 A. The bunches are initially spaced by 20 cm (two 3 GHz buckets) but after two stages of frequency multiplication they have a final spacing of 2 cm. This bunch train is then decelerated by seven power extracting structures in the drive beam decelerator. Each structure provides 512 MW. The main beam is accelerated to 1.1 GeV by fourteen 30 GHz accelerating structures operating at a gradient of 150 MV/m.
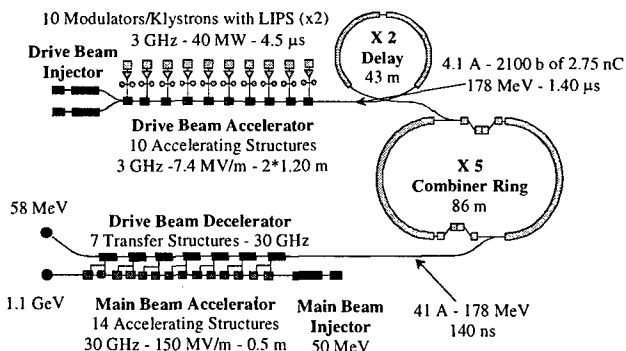
Figure 3: CTF3 schematic layout

5 CONCLUSION

The CLIC Two-Beam scheme is the ideal technology for extending the energy reach of a future high-luminosity linear collider in the multi-TeV range. The high operating frequency (30 GHz) allows the use of high accelerating gradients (100-200 MV/m) which shorten the linacs (27.5 km for 3 TeV) and reduce the cost. The effects of the high transverse wakefields have been compensated by a judicial choice of bunch length, charge and focusing strength such that the emittance blow-up is made independent of frequency for equivalent beam trajectory correction techniques. The upgrading in the multi-TeV range of the beam delivery from the linac to the detector still has to be studied. The two-beam RF power source based on a fully-loaded normal-conducting low-frequency linac and frequency multiplication in combiner rings is an efficient, cost effective and flexible way of producing 30 GHz power. The feasibility of Two-Beam power production has been demonstrated in the CLIC Test Facilities (CTF1 and CTF2). A third test facility is being studied to demonstrate the drive beam generation and frequency multiplication schemes.

REFERENCES

[1] J.P.Delahaye and 30 co-authors, Proc. EPAC'98, Stockholm,Sweden and CERN/PS 98-09, 1998.

[2] J. Ellis, E. Keil, G. Rolandi, CERN-EP/98-03, 1998.

[3] J.P.Delahaye and 3 co-authors,CERN/PS/97-51,1997.

[4] Int. Linear Collider Technical Review Committee Report, ed. G. Loew, SLAC-R-95-471, 1995.

[5] J.P.Delahaye and 6 co-authors, Proc. PAC'97, Vancouver, B.C., Canada, and CERN/PS 97-23, 1997.

[6] D. Schulte, Proc. EPAC'98, Stockholm,Sweden and CERN/PS 98-09, 1998 and G. Guignard, J. Hagel, CLIC Note 348 and Proc. PAC'97, Vancouver, Canada, 1997.

[7] D.Schulte and T.Raubenheimer, this conference.

[8] M.Dehler, CLIC note 358, 1998; M. Dehler and 5 co-authors, Proc. PAC'97, Vancouver, B.C., Canada, 1997.

[9] H.H. Braun and 14 co-authors, Proc. EPAC'98, Stockholm, Sweden and CERN Yellow report, 1999.

[10] G.Carron, A.Millich, L.Thondahl, Proc. ICAP'98 Monterey, CA, USA and CERN/PS 98-012 (1998).

[11] The CLIC study group, CERN/PS 96-14, 1996.

THE NEXT LINEAR COLLIDER MACHINE PROTECTION SYSTEM *

C. Adolphsen, J. Frisch, R.K. Jobe, D. McCormick, W.R. Nelson, T.O. Raubenheimer, S. Rokni,
M.C. Ross#, P. Tenenbaum, D.R. Walz,

Stanford Linear Accelerator Center, Stanford, CA, 94309.

Abstract

The Next Linear Collider (NLC) electron and positron beams are capable of damaging the linac accelerating structure and beamline vacuum chambers during an individual aberrant accelerator pulse. Machine protection system (MPS) considerations, outlined in this paper for the 1 TeV NLC design, have an impact on the engineering and design of most machine components downstream of the damping ring injector complex. The MPS consists of two functional levels. The first level provides a benign, single bunch, low intensity, high emittance pilot beam that will be used for commissioning and also whenever the integrity or the settings of the downstream components are in doubt. This level also provides for the smooth transition back and forth between high power operation and the benign diagnostic pilot bunch operation. The pilot bunch parameters in the main linac are estimated on the basis of the expected stress in the accelerator structure copper. Beam tests have been done at the SLAC linac to examine the behavior of the copper at the damage stress threshold. Typical pilot beam parameters (compared with nominal) are: 10 times reduced intensity, 10 times increased horizontal emittance and 1000 times increased vertical emittance, resulting in a reduction in charge density of 10^5. The second level is the primary protection against a single aberrant pulse. Its goal is to reduce the possibility that a substantial transverse field changes the trajectory of the high power beam from one pulse to the next. All devices that could produce such a field are 1) monitored by a fast response network and where possible have 2) deliberately slowed response times. A 'maximum allowable interpulse difference' is evaluated for each such device as well as the beam trajectory monitors in each interpulse period.

1 INTRODUCTION

The purpose of the MPS[1] is to provide machine components with a reasonable level of protection from damage caused by the beam. Because of its high charge (150 nCb) and very small cross-sectional area (7 x 1 μm), a single full intensity NLC [2] pulse can badly damage any physical object, including the main linac copper disk-loaded waveguide structure, if allowed to strike it directly. The MPS must provide the tools to 1) allow the beam power to be raised to the nominal following an

interruption and the tools to 2) sustain nominal power operation. This paper describes the determination of the pilot bunch parameters, the pulse sequence transition to full power, and the monitoring needed to sustain full power operation.

2 PILOT BEAM

It is obvious that NLC operation cannot be initiated with high power pulses; the first pulse to traverse the linac must be one without the capability to damage the structure. Indeed, following any time interval large enough to allow a substantial change in the beam trajectory or component alignment (~ a fraction of a second), the pilot beam must be used to prove the integrity of the system before allowing high power operation to resume. This means that high intensity, low repetition rate is not allowed.
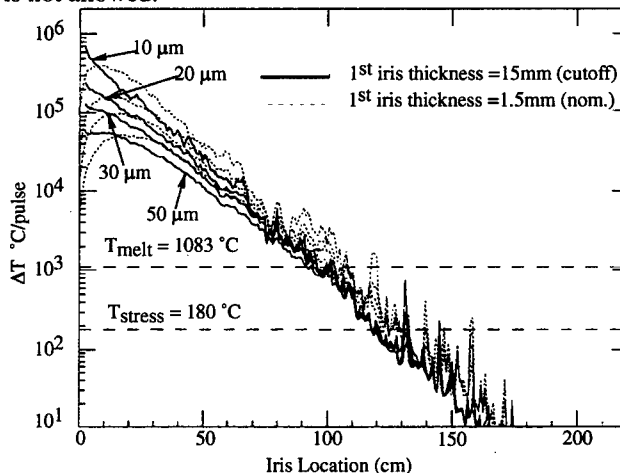
Figure 1: Predicted [3] maximum temperature rise in the irises of the NLC X-band accelerating structure as a function of distance for the nominal 10^{12} particles/pulse at 500 GeV. The horizontal dashed lines indicate the melting point and the expected thermal stress limit in fully annealed copper.

2.1 Single Pulse Structure Damage

We expect that the threshold charge density for structure damage is well below the point at which the material actually melts. Substantial crystalline grain growth and possible fracture should be observed at the point where the

deposited heat causes local stresses beyond the tensile limit. This is expected to occur a threshold ΔT of 180 °C.
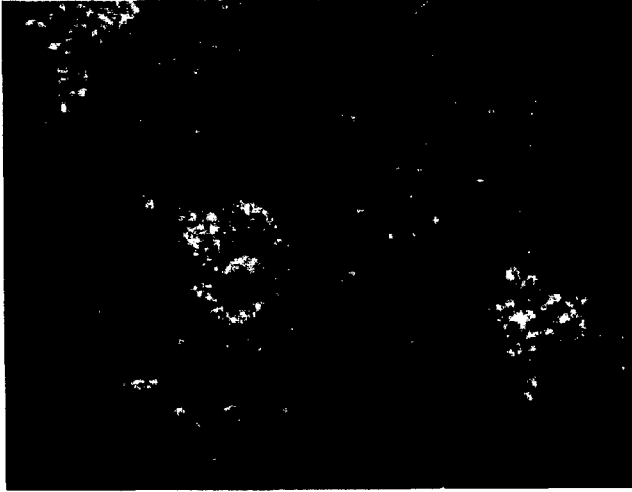
Figure 2: An optical microscope picture (500x) of the back side of the 1.4 mm thick copper iris sample following a single hit by a 10^{10}, $\sigma_{x,y}$ =15μm round beam, $\Delta T \sim$ 1000 °C. A small melted spot, about 10 μm wide, is easily seen.

Figure 1 shows the estimated maximum temperature rise in the structure following a hit from a misdirected beam. The peak temperature is expected either at the rear surface of the structure cut-off iris (located at either end) or several disks following the disk first hit by the beam. In Table 1, proposed pilot beam parameters, (steps numbered 1, 1.1 and 1.2), have been set so as to limit the maximum accelerator disk temperature rise to 180° C, 0.036 pCb/μm² at 500 GeV. Pilot beam step 1 shows the limiting intensity at an emittance $\varepsilon_x(=\varepsilon_y) \sim 10\varepsilon_x$ nominal, step 1.1 shows the limiting intensity with the NLC damping rings operating on the coupling resonance ($v_x=v_y$) and step 1.2 shows the limiting emittance at nominal *NLC* bunch intensities, (in this case, $\varepsilon_{x,y}>$ injector emittance of 7e-5 m-rad).

2.2 Beam Test Results

In order to validate both the calculations shown in Figure 1 and our estimate of the impact on the structure material, we have done a beam test in the Final Focus Test Beam [4] at SLAC, where small, high charge density pulses can be focused onto a target sample. In the test, a sample similar to a single disk-loaded waveguide iris was subjected to single pulses of a 28.5 GeV e- beam. The intensity and size of the beam were varied over the ranges of interest. At present, we are in the process of examining the damage observed on the back side of the sample. Figure 2 shows a typical melted spot from a single beam pulse as seen using an optical microscope.

3 TRANSITION TO FULL POWER

Once the pilot beam operation is satisfactory, the NLC MPS will allow the production of a high power beam. Table 1 shows the progression of steps that occur in the transition from 1) pilot, to 2) nominal single bunch intensity, to 3) nominal emittance and finally to 4) the nominal number of bunches $n_b=95$. During the pilot bunch operation and the transition, the emittance is increased by introducing a vertical dispersion or coupling bump in the main damping ring; the intensity is reduced at the source.

The MPS includes subsystems that make sure that the performance of the high power beam is close enough to that of the pilot beam throughout and also following transitions in either direction. Care must be taken to feedforward to those devices whose equilibrium performance (e.g. temperature) depends on the beam power, such as the highly loaded accelerating structures.

Also, during the sequence, care must be taken to allow time for beam-based feedback systems to properly close. This is required not so much because of the need to control single aberrant pulses but because of the requirement to limit fractional losses of the beam in given locations. This 'average power' limiting MPS is commonly used in high power linacs [5]. Reference

Table 1: Linac MPS Transition Sequence from pilot beam to nominal full power operation. Only step 4 has $n_b>1$. The peak charge density ρ is computed using $2\pi\sigma_x\sigma_y$ as the peak density. The beam sizes, σ_x and σ_y are estimated using the linac quadrupole magnet spacing and the optical phase advance to estimate the geometric mean ($\sqrt{\beta_x\beta_y}$). Step 4.1 shows parameters associated with the n_b =190, 1.4 ns inter-bunch time operation.

Step #	I /pulse e±/pulse	$\gamma\varepsilon_{x,y}$ (m-rad)	$\sigma_x \sigma_y$ begin (μm²)	$\sigma_{x,y}$ begin (μm)	ρ begin pCb/μm²	$\sigma_x \sigma_y$ end (μm²)	$\sigma_{x,y}$ end (μm)	ρ end pCb/μm²	ΔT max (°C)
1	1.1E+09	3.0E-05	13,000	110	.0022	780	28	.036	180
1.1	0.70E+08	1.5E-06	650	26	.0022	39	6.2	.036	180
1.2	1.0E+10	2.7E-04	117,500	340	.0022	7016	84	.036	180
2	1.0E+10	3.0E-05	13,000	110	.019	780	28	.36	1800
		$\gamma\varepsilon_x \gamma\varepsilon_y$							
3	1.0E+10	3.0E-06 x 3.0E-08	31.3 x 4.4	1.4	11.0	7.7x 1.1	23	1.1E+05	
4	9.0E+11	3.0E-06 x 3.0E-08	31.3 x 4.4	120	11.0	7.7x 1.1	2100	1E+07	
4.1	1.4E+12	3.0E-06 x 3.0E-08	31.3 x 4.4	190	11.0	7.7x 1.1	3325	1.6E+07	

[6] outlines a predictor system using a long ion chamber sensor.

4 MAXIMUM ALLOWABLE INTERPULSE DIFFERENCE

The maximum allowable interpulse difference (MAID) can be defined along the beamline and is determined by the structure and dynamics of the downstream system. It is the responsibility of the MAID system to guarantee that subsequent beam pulses all lie within an elliptical region centered near the present pulse. The MAID MPS primarily uses position monitor readings and device controller monitoring. Similar MPS are used at high current synchrotron light sources.

Since the NLC has a linear geometry, it is not possible to abort a pulse following its extraction from the damping ring. The trajectory of the previous pulse is compared to the MAID threshold and used to generate a permit for ring extraction. Typical linac MAID trajectory thresholds are 300 μm x by 100 μm y.

Table 2 lists some critical devices that must be checked before ring extraction because they may change substantially during the interpulse interval. A fault in the klystron / modulator pair primarily results in a small reduction in energy rather than a strong transverse kick, so the permit is based on a multiplicity count that allows several of them to fault on a given pulse. The minimum practical time for the polling to occur is about 100μs before ring extraction. The devices listed in Table 2 must be engineered such that the chance that failure not signalled by the fast polling network is very small.

Table 2: Examples of main linac devices which are checked just before damping ring extraction. The Response/ Sensor indicates steps taken in the design to reduce the risk of this failure.

Device	Problem	Response/ Sensor
Klystron/ Modulator	Internal interlock trip	Compare with allowed multiplicity
Magnet	Cable/magnet failure	Monitor voltage/ current
Mover	Runaway	Designed to be slow
Timing	Distribution failure	Designed to be redundant
Control system	Loss of connection	Redundancy

In order to limit the list as much as possible, we have segmented the NLC into three sections using high power collimation that prevents the passage of a pulse with excursions large enough to strike the downstream section. The segmentation separates the linac, with its small number of different kinds of components, from the upstream damping ring and first bunch compressor and from the downstream beam delivery.

High power collimation of such small beams at 500 GeV and higher energies remains to be designed. The performance of the collimators will determine the MAID limits in the linac and set MPS parameters in that segment of the NLC.

5 CONCLUSIONS

The NLC MPS affects the design of most components ranging from beamline vacuum chambers to high power devices and their controls. An integrated system is needed to provide smooth operation with a minimum of false alarms. The proposed MPS builds on experience at SLAC and other large, high intensity machines to achieve this, although this is the first application of the pilot beam with an intensity and emittance transition sequence.

6 ACKNOWLEDGEMENTS

7 REFERENCES

[1] M. Ross, "Machine Protection Schemes for SLC", Proc. *PAC91*, 1502 (1991).

[2] NLC ZDR Design Group, "Zeroth-Order Design Report for the Next Linear Collider", SLAC Report 474, (1996). Updated parameters can be found on the NLC Accelerator Physics Web pages at http://www-project.slac.stanford.edu/lc/nlc-tech.html.

[3] W.R.Nelson, H.Hirayama and D.W.O. Rogers, "The EGS4 Code System", SLAC Report 265, (1985).

4] V.A. Alexandrof *et al*, "Results of Final Focus Test Beam," Proc. *PAC95*, 2742 (1995).

[5] S. Clark *et al*, "Smart Machine Protection System", Proc. *ICALEPS91*, 420 (1991).

[6] M.C. Ross and D. McCormick, "A Coaxial Cable Beam Loss Monitor Ion Chamber System for High Power Multibunch Beams", Proc. *LINAC98*, (1998).

VERTICAL EMITTANCE IN THE KEK ACCELERATOR TEST FACILITY

T. Hirose, T. Okugi*, Y. Takayama, Tokyo Metro. Univ., Hachioji, Tokyo, Japan
H. Hayano, S. Kamada, K. Kubo, T. Naito, J. Urakawa, KEK, Tsukuba, Ibaraki Japan
S. Kashiwagi[†], The Graduate Univ. for Advanced Studies, Tsukuba, Ibaraki, Japan
M. Takano, Toho Univ., Funabashi, Chiba, Japan
M. Minty, J. Turner, M. Woodley, F. Zimmermann[‡], SLAC, Stanford, CA, USA

Abstract

We applied three methods in order to measure the vertical emittance of KEK-ATF. The first is a SR interferometer[1, 2], the second method is the emittance measurement by using wire scanners at the beam extraction line. The last method is emittance estimation by measuring an intensity dependence of a momentum spread, which is caused by the intra-beam scattering. The measured vertical emittance for KEK-ATF is 0.02–0.06 nm, which is a few times larger than the design target of KEK-ATF.

1 INTRODUCTION

The horizontal emittance damped in the KEK-ATF damping ring was precisely measured by using the wire scanners at the beam extraction line. The measured horizontal emittance was 1.37±0.03 nm[3] at the bunch population of 3–5×10^9, which agreed well with the design value. On the other hand, the design target of the vertical emittance is 0.01 nm, which corresponds to 1% of the horizontal emittance. Due to the vertical dispersion, a betatron coupling and other effects, it is hard to construct a damping ring with this extremely small vertical emittance. Furthermore, it is difficult to measure the vertical emittance itself due to the corresponding small vertical beam size both in the damping ring and at the extraction line. Due to these effects, we have currently not being able to measure the target value of the vertical emittance.

2 EMITTANCE EXPECTATION

2.1 Vertical Dispersion

Alignment errors of magnet devices generate an additional dispersion and a betatron coupling in a ring accelerator. The vertical dispersion, as a consequence, generates an additional vertical emittance component, which is generally larger than an ideal theoretical emittance. In order to produce a beam with extremely low vertical emittance, it is essential to reduce the vertical dispersion in the arc section of the accelerator. The relation between the dispersion and the emittance were simulated with the SAD code[4, 5]. The emittance has linear dependence with the square of the
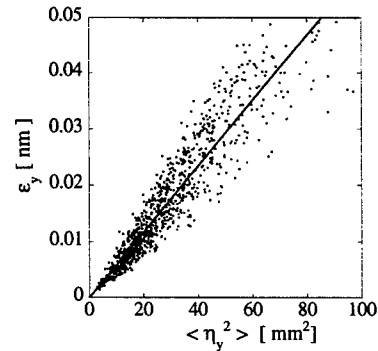
Figure 1: Simulation results for the vertical emittance of KEK-ATF damping ring as a function of the square of the vertical dispersion averaged over BPMs in the arc section.

vertical dispersion at the BPMs by

$$\varepsilon_y \, [\mathrm{nm}] \approx 0.0006 \left\langle \eta_{y,\mathrm{BPM}}^2 \, [\mathrm{mm}^2] \right\rangle_{\mathrm{arc}} , \qquad (1)$$

where the bracket means averaged over the arc section (see Figure 1). Furthermore, it was found from the simulation that the betatron coupling source does not create large vertical emittance enhancement for a KEK-ATF alignment accuracy[6]. Since the root mean square of the vertical dispersion was 4–9 mm, the vertical emittance is expected to be 0.010–0.049 nm through 1998 November–1999 March beam operation period.

2.2 Beam-gas Scattering

There are two scattering effects for increasing the vertical emittance. One is beam-gas scattering and the other is intra-beam scattering. Both effects are prominent for a beam with low emittance and low energy, such as the KEK-ATF beam. The effect of beam-gas scattering on beam emittance was examined by deriving the beam distribution function for linear collider damping rings[7]. For reasonable vacuum pressures, the beam-gas scattering does not have a large effect on the core of the beam, but only a few particles are scattered to significant amplitudes. Figure 2 shows the effect of the beam-gas scattering on the vertical emittance for the KEK-ATF damping ring. Figure 2(a) shows the beam distribution function with the vertical emittance of 0.01 nm at several CO_2 partial pressure. Figure 2(b) shows the corresponding vertical emittance as

---

* Address will be changed to "KEK, Japan" from 1999 April.
† Address will be changed to "Waseda Univ., Japan" from 1999 April.
‡ Present address is "CERN, Switzerland".
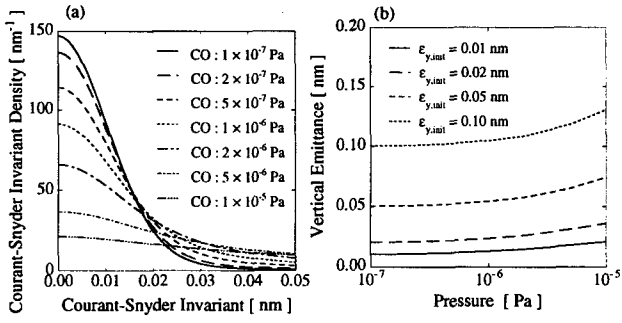
Figure 2: Effect of the beam-gas scattering. (a) Beam distribution function for the KEK-ATF beam with vertical emittance of 0.01 nm. (b) Corresponding vertical emittance.

a function of CO_2 partial pressure. Since the vacuum pressure of the KEK-ATF damping ring is less than 10^{-6} Pa, the emittance enhancement by the beam-gas scattering is evaluated to be less than a few 10% of the emittance of the unscattered beam.

2.3 Intra-beam Scattering

Intra-beam scattering is an effect of a small scattering within the bunch, which are not sufficient to produce particle losses, but which nevertheless disturb the particle statistical distribution (noise source)[8, 9]. A spontaneous momentum deviation induces an energy oscillation around the nominal energy defined by the synchrotron radiation.

Since the bunch volume in the KEK-ATF damping ring is extremely small, it is expected that the effect of the intra-beam scattering has a strong influence on the momentum spread enhancement, as the consequence, on the vertical emittance enhancement. The effect of the intra-beam scattering on the momentum spread and the vertical emittance can be calculated by using a self-consistent equation for the KEK-ATF damping ring beam as shown in Figure 3. Since the intra-beam scattering is roughly proportional to the beam charge density, the enhancements are significant for higher beam intensities.

3 EMITTANCE MEASUREMENT

3.1 SR Interferometer

The SR interferometer is the beam size monitor by using the spatial coherence (visibility)[1, 2]. This monitor has some advantages compared with other methods, because we do not have to pay attention to the field depth and the deflection limit of the SR light. Furthermore, since the validity for the application of the van Cittert-Zernike theorem to the beam in the KEK-ATF bending magnet field was confirmed[2], the SR interferometer is used as one of the most important emittance measurement tools in the KEK-ATF damping ring, especially as an online beam size monitor. The measured vertical beam size was 11–13 μm, which
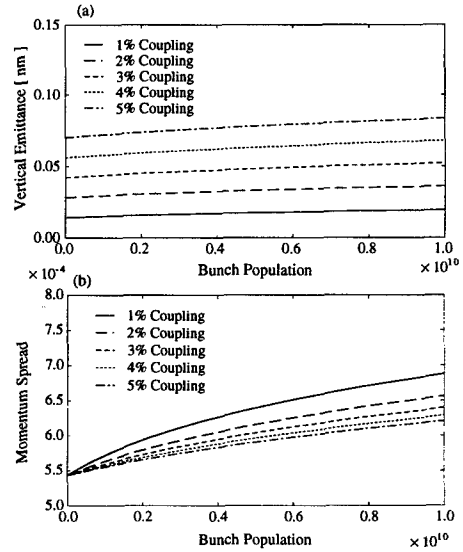
Figure 3: Calculation of the intra-beam scattering effect. (a) Effect on the vertical emittance. (b) Effect on the momentum spread.

corresponds to the vertical emittance of $\sim$0.05 nm through the 1998 November–1999 March beam operation.

3.2 Wire Scanner

In order to diagnose the beam properties, such as beam emittance, the damped beam is extracted to a beam extraction line in KEK-ATF. The beam optics of the KEK-ATF extraction line was designed to measure the vertical emittance by five wire scanners. Therefore, the beta function at each wire scanner was designed to be more than 5 m in order to make a large vertical beam size. Also, the phase advance between each wire scanner should be more than 10° in order to measure with each individual monitor. A typical emittance result of the wire scanner is shown in Figure 4. In Figure 4(a), The circle represents the beam distribution in Floquet phase space. Five lines show the measured beam size boundaries converted to the same phase space. Figure 4(b) shows the measured beam size and expected beam
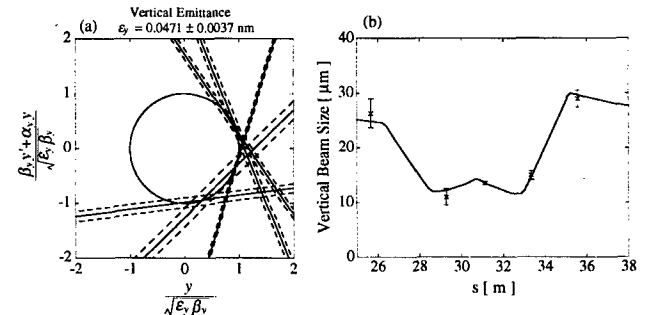
Figure 4: Typical emittance evaluation by wire scanner. (a) the measured beam size boundary at Floquet phase space, (b) measured beam size and expected beam size at beam diagnostic section.
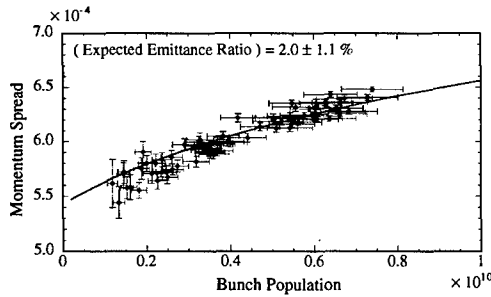
Figure 5: The intensity dependence of the momentum spread on the intra-beam scattering. Circles show the measured momentum spread and curve shows the calculated intensity dependence for the beam with the emittance ratio of 2.0%.

Table 1: Summary of the vertical emittance in KEK-ATF.

	Vertical Emittance	Charge
Calculation	0.010–0.049 nm	0
	0.020–0.059 nm	5×10^9
Measurement		
SR Interferometer	~ 0.05 nm	3–5×10^9
Wire Scanner	0.04–0.06 nm	3–5×10^9
Momentum Spread	0.027 ± 0.015 nm	3–5×10^9

size at the beam diagnostic section. The corresponding emittance value is 0.04–0.06 nm at the bunch population of 3–5×10^9 through the beam operation period.

3.3 Intra-beam Scattering

We applied one more vertical emittance estimation by using the intensity dependence of the momentum spread on the intra-beam scattering. This intensity dependence of the momentum spread was observed regularly during beam operation. The effect of the intra-beam scattering on a momentum spread enhancement was evaluated in Section 2.3. If we assume that the emittance ratio $\varepsilon_y/\varepsilon_x$ is constant, the measured beam intensity dependence of the momentum spread corresponds to an emittance ratio of $\varepsilon_y/\varepsilon_x$= $2.0 \pm 1.1\%$ (see Figure 5). Since the horizontal emittance is 1.37 ± 0.03 nm at the bunch population of 3–5×10^9[3], the emittance ratio measured above corresponds to a vertical emittance of 0.027 ± 0.015 nm at this beam intensity.

4 DISCUSSION

The measured vertical emittance for each measurement was listed in Table 1. Each measured emittance was not far from the expectation value estimated from the observed vertical dispersion at the BPMs in the arc section of the KEK-ATF damping ring, however, it shows a slightly larger than the emittance expectation.

The results by SR interferometer and wire scanner were within the range of 0.04–0.06 nm at the bunch population of 3–5×10^9, and they were not reduced to less than 0.04 nm through the entire beam operation period, even when the apparent vertical dispersion was well suppressed in the arc section.

On the other hand, the vertical emittance evaluated by using the intensity dependence of the momentum spread is 0.027 ± 0.015 nm at the same beam intensity, which was consistent with the expectation value of the vertical emittance, but smaller than the value found by the other methods. This difference has not been clarified yet. The difference might come from systematic errors of these measurement methods or come from the effect of the betatron coupling (beam tilt).

5 SUMMARY

The evaluated emittance is 2–6 times larger than the target vertical emittance of the KEK-ATF. One source of the large emittance was concluded as the vertical dispersion. We must reduce the vertical dispersion to less than 4 mm at the BPMs in the arc section of the damping ring in order to achieve the vertical emittance of 0.01 nm. Furthermore, we need clarify the discrepancy between the emittance measurement and the emittance evaluation from the vertical dispersion measurement.

6 ACKNOWLEDGEMENT

7 REFERENCES

[1] T. Mitsuhashi and T. Naito, *Proc. of 6th European Particle Accelerator Conference*, (1998) 1565.

[2] Y. Takayama et al., "Application Limit of SR Interferometer for Emittance Measurement", in this conference.

[3] T. Okugi et al., *Phys. Rev. ST-AB*, **2** (1999) 022801.

[4] K. Kubo et al., "OPTICS DIAGNOSTICS AND TUNING FOR LOW EMITTANCE BEAM IN KEK-ATF DAMPING RING", in this conference.

[5] hppt://www-acc-theory.kek.jp/SAD/sad.html.

[6] M. Takano et al., *Proc. of 5th Int. Workshop on Accelerator Alignment*, KEK Preprint 97-190 (1997).

[7] T. Raubenheimer, *KEK Report* 92-7 (1992).

[8] J. Le Duff, CERN 95-06 (1995) 573.

[9] A. Piwinski, *Proc. of 9th Int. Conf. on High Energy Accelerators*, (1974) 405.

[10] T. Naito et al., "EMITTANCE MEASUREMENT AT KEK-ATF DAMPING RING", in this conference.

FURTHER DEVELOPMENTS IN DYNAMIC FOCUSING*

J.Irwin, D.Helm, K.Thompson, SLAC, Stanford, CA, D.Schulte, CERN, Geneva, Switzerland

Abstract

Dynamic focusing has been proposed[1] as a way to eliminate a conventional collimation and final focus system in linear colliders, and is a scheme that is more readily extended to colliders at several TeV center-of-mass energy. In this paper we examine several outstanding issues, in particular, the optimization of the lens and main beam parameters. Simulations of the lens-lens, lens-main, and main-main beam collisions using a modified version of the GUINEAPIG beam-beam code are in progress.

1 INTRODUCTION

Dynamic focusing has been discussed in earlier conference papers[1, 2, 3]. We continue with what we hope is a more insightful discussion of the equations controlling the lens-beam parameters, accompanied by the first particle tracking simulations. The GUINEAPIG code[4] has been modified to support very unequal bunch lengths (necessary for the lens-main collison). A full simulation begins at the entry to the lens-lens collision after the particle distribution has been shaped by the octupole modules[3], followed by simulation of the lens-lens collision, the lens-main collision and the main-main collisions. The dependence of the system on both the main-beam and lens-beam bunch length are of special interest. The main-beam bunch length can be varied to achieve maximum luminosity in the main-main collision, while the lens-beam bunch length should be made as long as possible in order to minimize the synchrotron radiation[5] of the main beam in the lens-main collision.

2 THE PINCH EQUATION

The central equation in the determination of lens-beam parameters is the pinch equation[6]. For a diverging lens beam, assuming for simplicity that the main beam has a uniform longitudinal distribution, this equation has the form

$$
\frac{1}{60}\left(\frac{\sigma_{z,M}}{f_Q}\frac{\ell^*}{\beta^*}\right)^2 = \frac{<s^2>}{\beta^{*2}} = \left(\frac{\sigma_f^2 - \sigma_0^2}{\sigma_0^2}\right) \quad . \quad (1)
$$

where s is the displacment of the focal point, β^* is the main-beam beta function at the IP, ℓ^* is the distance between the lens-main collision and the IP, $\sigma_{z,M}$ is the main-beam bunch length, $\sigma_0 = \sqrt{\epsilon_M \beta^*}$, σ_f is the final rms size of the main beam at the IP taking into account beam enlargement from the pinch effect, and f_Q is the focal length experienced by the lens beam as it passes through

the main beam. The ratio ℓ^*/β^* equals the demagnification $\xi = \sigma_M/\sigma_0$, where σ_M is the size of the main beam at the lens-main collision. Introducing the formula for the focal length f_Q, and noting the presence of factors which occur in the definition of the main-beam disruption at the IP, we may write Eq. 1 as

$$
D_0\frac{\gamma_M}{\gamma_Q} = \sqrt{60\left(\frac{\sigma_f^2}{\sigma_0^2} - 1\right)} \cdot \xi \quad (2)
$$

where D_0 is the disruption parameter based on a beam size σ_0 at the IP. Since the actual beam size is σ_f, it is the disruption parameter based on this beam size which is relevant to determining the luminosity enhancement. Therefore it is better to write this equation as

$$
D_f\frac{\gamma_M}{\gamma_Q} = c_p\xi \quad \text{where} \quad c_p \equiv \sqrt{60\frac{\sigma_0^4}{\sigma_f^4}\left(\frac{\sigma_f^2}{\sigma_0^2} - 1\right)} \quad (3)
$$

As the main-beam bunch length is increased, the pinch aberration will cause the ratio σ_f/σ_0 to grow. c_p has a maximum of $c_p = \sqrt{15} = 3.87$ at $\sigma_f/\sigma_0 = \sqrt{2}$, and a value $c_p = \sqrt{40/3} = 3.65$ at $\sigma_f/\sigma_0 = \sqrt{1.5}$. Since it is a major advantage to have a large γ-ratio and a large disruption, it will be advantageous to operate with a main-beam bunch length that gives an apparent 50% luminosity loss due to the lens pinch aberration, since this loss is more than compensated by the enhancement achievable from the larger disruption parameter. Simulations are underway to see how this plays out when there is no assumption on the longitudinal uniformity of the lens beam. A sensible set of parameters satisfying Eq. 3 are $D_f = 1.2$ (giving a round-beam enhancement $H \approx 4$), a γ ratio of about 100, and a demagnification of 33.

3 THE POWER-RATIO EQUATION

We have previously shown[3] that

$$
\frac{\ell^*}{f_Q} = \frac{P_M}{P_0} = \frac{\gamma_M N_M}{\gamma_Q N_{Q0}} \quad \text{where} \quad N_{Q0} = \frac{\gamma \epsilon_M}{r_e}\xi \quad . \quad (4)
$$

The charge in the uniform disk of the lens beam is $(\sigma_Q/\sigma_M)^2 N_{Q0} \approx 3N_{Q0}$, where the ratio $(\sigma_Q/\sigma_M)^2$ is chosen so that only about 10% of the main beam tail is not properly focused. Using the γ-ratio as determined by Eq. 3, Eq. 4 becomes

$$
\frac{\ell^*}{f_Q} = c_p\frac{\sigma_f^2}{\sigma_0^2}\frac{Fr_e}{\gamma_M}\frac{\beta^*}{D_F H} \quad . \quad (5)
$$

F, which has the dimension of a flux, is basically a ratio of luminosity to beam power, coming from the luminosity

equation:

$$\frac{N_M H}{\sigma_f^2} = 4\pi L \frac{E_B}{P_B} \equiv F \quad . \tag{6}$$

Assuming beam power is allowed to increase as the square root of the energy, F/γ_M is increasing as energy to the 3/2, while all other parameters in Eq. 5 tend to remain constant. Hence it is difficult to hold ℓ^*/f_Q constant at energies of 5 TeV c.m. and above. However the product $D_f H$ and β^* can change some.

Eq. 5 may also be regarded as an equation for f_Q:

$$f_Q = \frac{1}{c_p} \frac{\sigma_0^2}{\sigma_f^2} \frac{\gamma_M}{F r_e} D_f H \xi \quad . \tag{7}$$

To maintain a diverging lens-beam geometry, we require $\beta_Q^* \le 3 f_Q$, so f_Q cannot be allowed to get too small.

4 THE LENS-LENS COLLISION

As previously noted, the lens-lens collision can be used for self-alignment[3]. In that case

$$\frac{\ell^*}{f_Q} = 2\sqrt{2\frac{\gamma_M}{\gamma_Q} + 2} \quad . \tag{8}$$

For a γ ratio of 100, we find $\ell^*/f_Q = 30.2$. Table 1 gives parameters (not yet fully optimized) for c.m. energies from 0.5 TeV to 3 TeV with $\ell^*/f_Q \approx 30$. In all cases, $\sigma_Q^2 = R_Q^2/2$, demagnification $\sigma_M/\sigma_0 = \ell^*/\beta^* \approx 35$, $\beta^*/f_Q = 0.67$, $(\sigma_f/\sigma_0)^2 = 1.5$, $(\sigma_Q/\sigma_M)^2 = 3$, $N_Q/N_{QD} = 1.2$, $f_Q = \sigma_{z,Q}$, $A \equiv \sigma_{z,M}/\beta^* = 0.18$, $D_f = 1.27$, and an analytic estimate of luminosity enhancement factor $H_D=3.67$. The main beam power $P_B = 80$ MW for 1 TeV c.m. and scales as $\sqrt{E}$, but the luminosity L departs somewhat from E^2 scaling.

5 THE DEMAGNIFICATION PARAMETER

For c.m. energies larger than 5 TeV, Eq. 7 indicates a larger demagnification and a larger disruption are desirable. From the chromatic condition

$$\left(\frac{\sigma^*}{\sigma_1}\right)^2 = \left(\frac{\ell^*}{\ell_1}\right)^2 + \frac{\ell^*}{\ell_1}\left(\frac{\ell^*}{\ell^1}\xi^2 - 2\right)\bar{\delta}^2 + \bar{\delta}^4 \tag{9}$$

and for $\ell^*/\ell_1 = 400$, the demagnification ξ can be as large as 30 and one can still have a 2% bandwidth. However, the tolerances on the lens beam quality become more stringent for larger demagnification.

6 LENS-BEAM CURRENT

The lens-beam parameters in Table 1 appear reasonable enough. However the round main-beam parameters have a small bunch charge and imply a train with many bunches. To maintain the efficiency of the main linac it is necessary to maintain a beam current (during the pulse) of about 0.5

Table 1: Parameters

c.m. energy [TeV]	1/2	1	1 1/2	3
γ_M	5.E5	1.E6	1.5E6	3.0E6
γ_Q	5.E3	9.9E3	1.5E4	3.E4
$\sigma_{z,M}$ [μm]	182	129	70.2	82.8
$\sigma_{z,Q}$ [μm]	1170	824	449	529
$(\gamma\epsilon)_M$ [μm]	.543	.221	.103	.0733
$(\gamma\epsilon)_Q$ [μm]	2.88	1.17	.544	.389
N_M [10^{10}]	.204	.0829	.0385	.0276
N_Q [10^{10}]	2.44	.989	.460	.329
ℓ^* [cm]	3.54	2.50	1.36	1.61
δ_B[%]	2.3	5.3	10.4	13.8
Υ_{avg}	0.06	0.19	0.59	1.10
n_B (rep rate 120 Hz)	565	983	1727	1708
L [10^{34}cm^{-2}sec^{-1}]	0.5	1.0	2.25	2.70
Lens-main collision:				
β_Q^*[mm] (waist in front)	.781	.552	.301	.354
σ_M [nm]	1160	440	181	117
σ_Q [nm]	2010	762	313	203
Main-main collision:				
σ_f [nm]	40.6	15.4	6.32	4.10
σ_0 [nm]	33.2	12.6	5.16	3.35
β^* [mm]	1.01	.716	.389	.459

Amps. Remarkably this optimum does not depend much on the fundamental frequency of the accelerating structures. For the main-beam bunch charge at 1 TeV the required spacing equals the C-band wavelength. Furthermore, since

$$N_{QT} = \frac{N_{QT}}{N_{QD}} \frac{\sigma_Q^2}{\sigma_M^2} N_{Q0} \approx 3.6 N_{Q0} \quad , \tag{10}$$

we have

$$\frac{N_{QT}}{N_M} = \frac{\gamma_M}{\gamma_Q} \frac{P_Q}{P_M} = \frac{\gamma_M}{\gamma_Q} \frac{N_{QT}}{N_{Q0}} \frac{P_{Q0}}{P_M} \approx 12 \quad . \tag{11}$$

This implies the lens-beam current would be about 6 Amps. This is a large current for a ring (the PEP LER is designed for 2 Amps) and implies a major perturbation to the rf system as the 84-meter bunch train passes. We have not decided on the best way to overcome this problem. One solution is to have a lower current in the damping ring and use a combiner ring to compress the bunch train much as in the two-beam accelerator drive beam complex. And since the beam is only in the combiner ring for a few revolutions, that ring is simple and need not have an rf system.

7 LENS-BEAM PROPERTIES

We have described two physical configurations of the lens beam beamlines: i) injection from a damping ring into a jitter-correction and beam-shaping loop into the IP region[2], and ii) injection from a damping ring into a linac followed by a jitter-correction and beam-shaping loop[3]. If one desires a lens-beam system that extends to 3 TeV

c.m., the pure damping ring solution becomes very difficult. For this reason, and because of a need for bunch compression, we presently favor the linac solution.

The lens beam must have the following systems and properties:

- an energy about 1/100th of the main beam energy,
- an emittance given by

$$(\gamma\epsilon)_Q \leq \frac{1}{4}\frac{\beta_Q^*}{2f_Q}\frac{\sigma_Q^2}{\sigma_M^2}N_M r_e \quad , \qquad (12)$$

which is about 1 μm-r at 1 TeV c.m. and does not get too much smaller,

- a final bunch length of about $\sigma_{z,Q} = 0.5$ mm,
- number of electrons per bunch $\leq 10^{10}$,
- a current entering the IP of about 6 Amps,
- bunch-to-bunch jitter at the IP of less than 1%,
- a β_Q^* that would be about 2 mm in the absence of a lens-lens collision and that is about 0.5 mm with the lens-lens collision,
- a transverse distribution approximating a uniform disk at the lens-main collision,
- recapture of positrons and reinjection into a damping ring with a transverse emittance that can be redamped to the design emittance in a few damping times.

To meet these requirements this system probably contains

- two damping rings at about 2 GeV,
- bunch compression systems upon extraction from the damping ring,
- combiner rings following the bunch compression, probably containing jitter damping systems,
- an efficient S-band or C-band linac for acceleration to final lens-beam energy,
- loops after the linac each containing octupole modules for beam shaping, and perhaps feed-forward jitter controls,
- chromatically-corrected incoming final-focus systems for an incoming β_Q^* of about 2 mm,
- crab cavities at the entrance to the detector region,
- recapture loops after the IP,
- a linear wiggler for reducing at least positrons to the damping ring energy,
- a reinjection loop into the damping rings.

This is not a simple beam system, and perhaps it will not represent a cost savings compared to the conventional system. However, a centralized campus for main damping rings and low-energy linacs would allow the lens-beam linac to double as a main-beam pre-linac (to 10 GeV), and the returning lens-beam electrons could be used to create positrons. Major cost reductions and improved operability should follow from the round beam parameters with their lower charge, the wider focusing bandwidth (2%) that reduces energy compensation tolerances, the absence of a collimation system, and absence of final focusing elements

in the detector. The system scales to energies of 3 TeV c.m. and perhaps higher, and is self-aligning at 3 TeV c.m. and below.

8 DISCUSSION AND CONCLUSIONS

Simulations of the entire series of beam manipulations, from shaping of the lens beam by octupoles, through the lens-lens collision, lens-main collisions, and main-main collisions are in progress. In Figure 1 we show an example of a main beam distribution, after GUINEAPIG simulation of the lens-main collision and then transport by $\ell^* = 25$ mm to the main-main interaction point. The full simulations have yet to be completed; of particular importance will be to demonstrate in detail that it is possible to get sufficiently uniform lenses at both the lens-lens and lens-main collisions. With the caveat that such simulations bear out our expectations, dynamic focusing appears to be a promising alternative to conventional final-focus and collimation systems. We note also that a first experiment[7] has shown that the crab cavity phases can be measured with the required precision of 0.01 degrees at X-band.
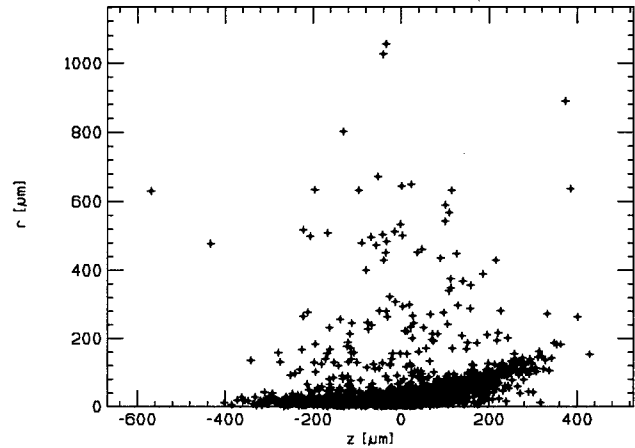
Figure 1: Main beam distribution after lens-main collision and transport by $\ell^* = 25$ mm to main-main collision.

9 REFERENCES

[1] J.Irwin, Proceedings IEEE Particle Accelerator Conference (PAC97), Vancouver, B.C., 12-16 May 1997.

[2] J.Irwin, 8th Workshop on Advanced Accelerator Concepts (AAC98), Baltimore, Maryland, 5-11 July 1998.

[3] J.Irwin, 19th International Linear Accelerator Conference (LINAC98), Chicago, 23-28 Aug 1998.

[4] D.Schulte, Ph.D. thesis (1996), TESLA-97-08.

[5] K. Oide, Phys.Rev.Lett., 61, 1713 (10 October 1988).

[6] Ref 2. Eq. 1 for pinch. There was a factor of 2 error in the original equation which is corrected here.

[7] S.Tantawi, private communication.

RADIATIVE COOLING OF RELATIVISTIC ELECTRON BEAMS*

Zhirong Huang, APS/ANL, Argonne, IL 60439

Ronald D. Ruth, SLAC, Stanford, CA 94309

Abstract

Radiative cooling is a natural and effective method of phase-space cooling for stored electron beams. In electron storage rings the average effects of synchrotron radiation from the bending magnets cause the beam emittances in all three degrees of freedom to damp towards equilibria, determined by the fluctuating nature of quantum emissions. In this paper, we show that the radiation damping in a focusing system is fundamentally different from that in a bending system. Quantum excitation to the transverse dimensions is absent in a straight, continuous focusing channel, and is exponentially suppressed in a focusing-dominated ring. Thus, the transverse normalized emittances in such systems can in principle be damped to the Compton wavelength of the electron, limited only by the Heisenberg Uncertainty Principle. In addition, we investigate methods of rapid damping such as radiative laser cooling. We propose a laser-electron storage ring (LESR) where the electron beam in a compact storage ring repetitively interacts with an intense laser pulse stored in an optical resonator. The laser-electron interaction gives rise to fast cooling of electron beams and can be used to overcome the space-charge effects encountered in a medium-energy circular machine. Applications to the designs of ultra-low-emittance damping rings and compact x-ray sources are also explored.

1 INTRODUCTION

Modern high-energy particle accelerators and synchrotron light sources demand smaller and smaller beam emittances in order to achieve greater luminosity or higher brightness. In electron synchrotrons and storage rings, radiative cooling is a natural and effective way to obtain low-emittance beams. Radiation damping in the longitudinal phase space occurs because higher energy electrons in a bunch lose more energy than lower energy electrons. Furthermore, the fact that electrons on average lose momenta in all three degrees of freedom to the radiation will contribute to the damping in the transverse phase space. Thus, both the longitudinal and the transverse damping rates are proportional to the energy damping rate, which is the ratio of the average radiation power P_γ to the electron energy $E = \gamma mc^2$:

$$\Gamma_b = \frac{\langle P_\gamma \rangle}{E} = \frac{2}{3} c r_e \gamma^3 \left\langle \frac{1}{\rho^2} \right\rangle_s, \qquad (1)$$

where $r_e = 2.82 \times 10^{-15}$ m is the classical electron radius, ρ is the radius of the bending magnets, and the index s indicates averaging around the ring. In fact, the damping

rates of the transverse and the longitudinal emittances are related through the Robinson theorem [1]:

$$\frac{d\varepsilon_i}{dt} = -\mathcal{J}_i \Gamma_b \varepsilon_i \quad \text{with} \quad \sum_i \mathcal{J}_i = 4, \qquad (2)$$

where $i = x, y, s$ denotes horizontal, vertical, and longitudinal directions, respectively.

Nevertheless, particle motion does not contract to a point in phase space because synchrotron radiation occurs in quanta of discrete energies. Each time a photon is emitted the energy of the electron makes a small discontinuous jump. This quantum "noise" suddenly changes the off-energy orbit of the horizontal betatron oscillation and the instantaneous angle of the vertical betatron motion. The cumulative effect of many such disturbances introduces diffusion into oscillation modes. The amplitude of oscillation will grow until quantum excitation is, on average, balanced by the damping of the oscillations. In a smooth and separated-function storage ring, the equilibrium-normalized transverse emittances can be written as [2]

$$\varepsilon_x^n = \gamma \varepsilon_x \sim \lambda_c \frac{\beta_x^3}{(\rho/\gamma)^3} \sim \lambda_c \frac{\gamma^3}{\nu_x^3},$$

$$\varepsilon_y^n = \gamma \varepsilon_y \sim \lambda_c \frac{\beta_y}{(\rho/\gamma)} \sim \lambda_c \frac{\gamma}{\nu_y}, \qquad (3)$$

where $\lambda_c = \hbar/mc = 3.86 \times 10^{-13}$m is the Compton wavelength of the electron, β_x, β_y and ν_x, ν_y are the average beta functions and the tunes of the machine. In the longitudinal direction, the equilibrium energy spread is [2]

$$\sigma_\delta \sim \gamma \sqrt{\frac{\lambda_c}{2\rho}}. \qquad (4)$$

While the normalized longitudinal emittance $\varepsilon_s^n \equiv \gamma \sigma_\delta \sigma_s$ can be changed by adjusting the bunch length σ_s through the rf systems, the equilibrium-normalized transverse emittances (sometimes called the natural emittances) are more or less fixed for a given lattice. Equation (3) indicates that lower emittances can be obtained by going to a lower energy and higher tune machine whenever possible. In practice, the tunes are much smaller than γ and the quantities $\frac{\beta_{x,y}}{(\rho/\gamma)}$ are always much larger than 1, resulting emittances many orders of magnitude larger than the Compton wavelength, and the horizontal emittance is much larger than the vertical.

The above consideration suggests that a smaller equilibrium emittance could be obtainable by reducing the rate of quantum excitation and/or increasing the rate of radiation damping. If one considers an ideal limit $\rho \to \infty$ with γ

and $\beta_{x,y}$ fixed, then the equilibrium emittance would vanish according to Eq. (3). In Section 2 we show that quantum excitation to the transverse oscillations is absent in this straight focusing channel and is exponentially suppressed in a focusing-dominated damping ring. The normalized transverse emittances in such systems do not vanish but are limited by the Compton wavelength. In Section 3 we study a fast damping mechanism by employing a high peak or a high average power laser in an optical resonator to cool an electron bunch in a compact storage ring. This laser-electron storage ring (LESR) can be configured either for the production of low-emittance electron beams or as a high-intensity x-ray source.

2 SUPPRESSION OF QUANTUM EXCITATION

In deriving Eq. (3), the photon emissions are considered to be instantaneous and modeled as statistical noise [2]. Such a quasiclassical picture of quantum excitation is valid as long as the time associated with the emission of radiation quanta is short compared with the periods of the classical modes of oscillation in all three degrees of freedoms. The typical radiation formation length is on the order of ρ/γ and is much smaller than the betatron oscillation wavelengths $\beta_{x,y}$ in normal storage rings. However, as the strength of the transverse focusing increases or as the bending field gradually decreases, the radiation formation length and the betatron oscillation wavelengths may become comparable. The validity of the quasiclassical approximation along with Eq. (3) is suspect. In Refs. [3, 4], two such cases were investigated and an interesting regime for ultra-low emittance generation was found. The basic results are summarized here.

2.1 A straight focusing channel

Let us consider an ideal focusing channel: a continuous focusing force $(-K_x x)$ in the x direction and a free, relativistic longitudinal z motion. The Hamiltonian is then

$$H = \sqrt{m_e^2 c^4 + p_z^2 c^2 + p_x^2 c^2} + \frac{K_x x^2}{2}$$
$$\approx E_z + J_x \omega_x, \qquad (5)$$

where $E_z \equiv \sqrt{m_e^2 c^4 + p_z^2 c^2}$ is the longitudinal energy, $\omega_x = \sqrt{K_x c^2 / E_z}$ is the transverse oscillation frequency, and J_x is the transverse action. It is obvious that both p_z and J_x are constants of motion because their conjugate coordinates are absent in the Hamiltonian. The transverse action, averaged over the beam distribution, is related to the normalized transverse emittance by

$$\varepsilon_x^n = \frac{\langle J_x \rangle_{\text{beam}}}{mc}. \qquad (6)$$

In the event of a photon emission, the total energy and the total longitudinal momentum between the electron and
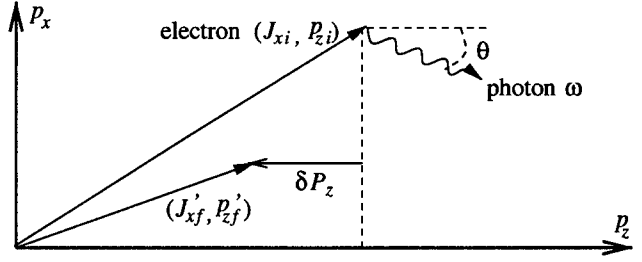
Figure 1: The initial and the final states of the electron in a focusing channel after a random photon emission.

the photon are conserved. Suppose a photon of energy $\hbar\omega$ is emitted with an angle θ relative to the longitudinal direction (Fig. 1), then the change of electron energy and longitudinal momentum are given by

$$\delta E = -\hbar\omega, \qquad \delta p_z c = -\hbar\omega \cos\theta. \qquad (7)$$

From Eq. (5), we obtain the change of the transverse action

$$\delta J_x = -\frac{\hbar\omega}{\omega_x}\left(1 - \beta\cos\theta + \frac{\theta_p^2}{4}\right) < 0, \qquad (8)$$

where $\beta = p_z c / E_z$ is the average velocity, and $\theta_p^2 = 2J_x \omega_x / E_z$ is the pitch angle of the electron. Thus, the transverse action (as well as the transverse emittance) always decreases in spite of random photon direction of emissions. Electron does not recoil directly against the photon because of the existence of the transverse focusing environment.

The lack of quantum excitation in a focusing channel leads to a classical point in the transverse phase space for the electron. In quantum mechanics, this ground state is described by a Gaussian wave packet that has the minimum action set by the Heisenberg uncertainly principle:

$$J_x = \delta x \delta p_x \geq \frac{\hbar}{2}. \qquad (9)$$

A beam of N electrons occupying different longitudinal phase space or spin states can all be damped to their transverse ground states, reaching the fundamental emittance

$$\varepsilon_0^n = \frac{\hbar/2}{mc} = \frac{\lambda_c}{2} = 1.93 \times 10^{-13}\text{m}. \qquad (10)$$

The channeling radiation damping rate can be obtained most easily by going to the longitudinal comoving frame of the channeled electron when the transverse oscillation amplitude is small $(\gamma\theta_p \ll 1)$. The longitudinal translational invariance guarantees that the electron sees a one-dimensional (transverse) harmonic potential with the focusing strength $K_x^\star = \gamma K_x$ in this frame (denoted by a star). The electron gives away transverse energy $E_x^\star = \langle K_x^\star x^2 \rangle$ through dipole radiation with a rate

$$\frac{1}{E_x^\star}\frac{dE_x^\star}{dt^\star} = \frac{1}{\langle K_x^\star x^2 \rangle}\frac{2}{3}\frac{r_e}{mc}\langle (K_x^\star x)^2 \rangle = \frac{2}{3}\frac{r_e}{mc}K_x^\star. \qquad (11)$$

When transforming back to the lab frame, we obtain an energy-independent damping rate for the focusing channel

$$(\Gamma_c)_x = \frac{2}{3}\frac{r_e}{mc}K_x. \tag{12}$$

A more detailed analysis of channeling radiation damping when the oscillation amplitude is large and when the focusing strength is periodic (such as in a FODO lattice) can be found in Ref. [5]. As an example, suppose the quadrupole field gradient is about $g = 100$ T/m, corresponding to a focusing strength $K_x \simeq 30$ GeV/m^2. The damping constant $\Gamma_c \sim 30$ s^{-1}, which is a negligible effect for linear accelerators. However, the focusing strength for a typical crystal channel is $K_x \sim 10^{11}$ GeV/m^2, resulting in $\Gamma_c \sim 10$ ns^{-1} and the damping distance on the order of meters. Of course, a crystal channel is far from ideal, and the multiple Coulomb scattering is the primary excitation mechanism competing against the radiation damping.

2.2 A focusing-dominated damping ring

However, it is not necessary to have a straight channel. In a bent focusing system where the radiation formation length is comparable to the betatron oscillation wavelength, the quasiclassical picture of the instantaneous radiation is insufficient to describe the radiation reaction. By using a quantum mechanical perturbation approach, we have analyzed a continuous focusing and bending combined system, and obtain the rate of change for the transverse emittances [5]

$$\frac{d\varepsilon_x^n}{dt} = -\Gamma_b\left[(\chi_x^2 - 1)\left(\varepsilon_x^n - \frac{\lambda_c}{2}\right) - \lambda_c\frac{F_x(\chi_x)}{96\chi_x^3}e^{-2\sqrt{3}\chi_x}\right],$$

$$\frac{d\varepsilon_y^n}{dt} = -\Gamma_b\left[(\chi_y^2 + 1)\left(\varepsilon_y^n - \frac{\lambda_c}{2}\right) - \lambda_c\frac{F_y(\chi_y)}{96\chi_y}e^{-2\sqrt{3}\chi_y}\right], \tag{13}$$

where $\chi_x = \frac{\rho/\gamma}{\beta_x}$ and $\chi_y = \frac{\rho/\gamma}{\beta_y}$, and

$$F_x(\chi_x) = 55\sqrt{3} + 330\chi_x + 262\sqrt{3}\chi_x^2 + 300\chi_x^3 + 48\sqrt{3}\chi_x^4,$$
$$F_y(\chi_y) = 13\sqrt{3} + 30\chi_y + 12\sqrt{3}\chi_y^2. \tag{14}$$

Equation (13) describes the general results of radiation damping (the first term) and quantum excitation (the second term) to the transverse emittances in this combined-function system. The relative amount of damping and excitation in each transverse plane is determined from a single dimensionless parameter $\chi_{x,y}$, which is the measure of the radiation formation length in units of the average beta function. For separated-function systems, it is expected that the average effect of the bending magnets in the horizontal plane is damping ($\mathcal{J}_x = 1$) instead of anti-damping ($\mathcal{J}_x = -1$). In the limit of $\chi_{x,y} \ll 1$ or $\rho/\gamma \ll \beta_{x,y}$, setting these rates equal to zero reproduces the equilibrium transverse emittances of storage rings (i.e., Eq. (3)). In the opposite limit where $\chi_{x,y} \gg 1$, or $\rho \rightarrow \infty$, we have
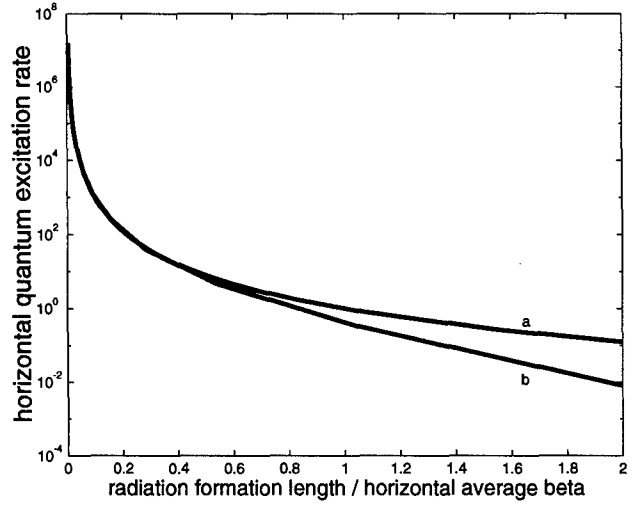
Figure 2: Horizontal quantum excitation rate in units of $\Gamma_b\lambda_c$, predicted by (a) the quasi-classical model, and (b) the quantum mechanical perturbation approach.

$\Gamma_b\chi_{x,y}^2 = (\Gamma_c)_{x,y}$ from Eq. (12), and the quantum excitation term vanishes, the basic results for a straight focusing channel.

In the intermediate regime where the radiation formation length is on the order of the average beta function ($\rho/\gamma \sim \beta_{x,y}$ or $\chi_{x,y} \sim 1$), the transverse damping comes from both the bending and the focusing fields. The rates of quantum excitation in both transverse dimensions are exponentially suppressed according to Eq. (13) and start to depart from the results based on the quasiclassical approach (see Fig. 2). Thus, the fundamental emittance can be approached very closely in such a focusing-dominated system. The reason for the suppression of quantum excitation can be interpreted as follows: The transverse energy levels of the electron are well separated as a result of the strong focusing forces. Radiative transition to higher transverse levels becomes impossible for the electron with almost all photon emissions, and hence the quantum excitation is suppressed by the focusing environment.

In the same regime, the average radiation power comes predominately from the bending field rather than from the focusing field, and the longitudinal damping rate remains the same as the storage ring limit. In addition, since the synchrotron oscillation period is always much longer than the betatron ones, the radiation formation length is always much smaller than the synchrotron oscillation wavelength. Thus, the instantaneous picture of quantum emission is still valid in the longitudinal phase space and Eq. (4) still holds. The total phase-space volume of an N-electron beam is limited by the Fermi statistics, i.e.,

$$\varepsilon_x^n\varepsilon_y^n\varepsilon_s^n \geq \frac{N}{2}\left(\frac{\lambda_c}{2}\right)^3. \tag{15}$$

When $\varepsilon_{x,y}^n \sim \lambda_c/2$, we have $\varepsilon_s^n \geq N\lambda_c/4$. For $N \sim 10^{10}$, this gives a limit of about 1 mm for ε_s^n, which is quite rea-

sonable because the end use of the beam does not require ultra-short bunches with ultra-small energy spread.

A focusing-dominated damping ring can be designed with many repetitive FODO cells. As indicated from Eqs. (3) and (13), it is favorable to use high-gradient focusing quads and low-energy electron beams. For instance, suppose that permanent-magnet quads have a field gradient 4 Tesla/cm, and that the electron energy is 25 MeV. We can have a ring with an average radius of about 2 m, an average beta function of 4 cm in both transverse planes, and a cell length of 2 cm with 60-degree phase advance. In principle, the equilibrium-normalized transverse emittances can reach the Compton wavelength while the energy spread is on the order of 10^{-5}. The damping time is inevitably long, about 30 s in all three degrees of freedom. Thus, the intensity of the ultra-cold beam is limited by the collective effects such as space charge and wakefields. It is conceivable to operate this ring below the transition energy $\gamma_t \approx \nu_x$, so that a six-dimensional phase space equilibrium may exist due to the effect of intrabeam scattering [6]. These effects have yet to be studied in this new regime.

3 RADIATIVE LASER COOLING

In this section, we investigate another route to low-emittance generation: a fast radiative cooling method. Traditionally, the increase of the damping rate in a storage ring is achieved through the insertion wigglers [7]. The effect of these damping wigglers is to generate a lot more radiation while keeping quantum excitation in check. This can be done by placing the wigglers in the dispersion-free region of the storage ring. Recently, Telnov pointed out [8] that with a sufficiently intense laser pulse, a high-energy electron beam can be cooled significantly during a single collision with the laser pulse. The electrons radiate energy in the form of scattered photons, and hence the term "radiative laser cooling." Later, we proposed [9] a compact laser-electron storage ring (LESR) where radiative laser cooling is used to overcome the space-charge effects encountered in a medium-energy circular machine for electron beam cooling or x-ray generation.

The basic idea of a laser-electron storage ring is shown in Fig. 3. An electron beam is injected into a storage ring and at the same time an intense laser pulse is built up inside a high-finesse optical resonator. The laser light path is chosen to match exactly the time it takes for the electron to circulate once around the ring so that a focused electron beam repeatedly encounters the short light pulse at the focus of the resonator each turn. Normally, in the absence of the laser the electron beam would damp at the rate determined by the time it takes to radiate its complete energy in the bending magnets in the ring. In the LESR, the laser pulse acts like an extremely strong damping undulator, and the fast radiative laser cooling leads to a very low-emittance beam for very moderate electron energy (around 100 MeV). As the beam circulates around the ring, the lost energy is restored by an rf accelerating system, as in a nor-
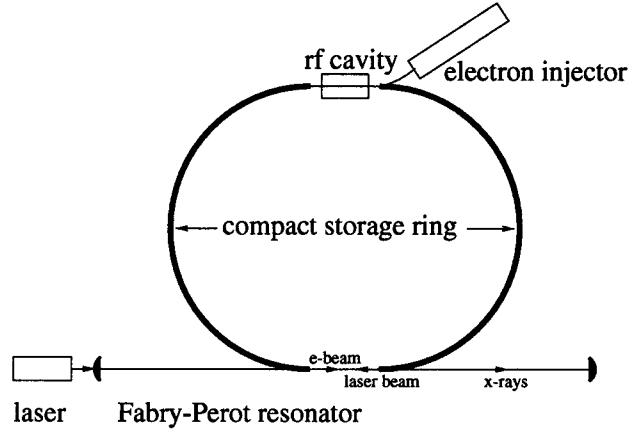
Figure 3: The schematic diagram of a laser-electron storage ring.

mal storage ring. This cooling effect can also be utilized as a stabilization mechanism to maintain a dense bunch of electrons for the generation of intense x-rays.

For electrons no more than a few hundred MeV, the normal radiation damping and quantum excitation from the bending magnets is negligible compared with those from the laser field. The laser field can be regarded as an undulator with an equivalent period one half of the laser wavelength λ_L, and an equivalent bending field given by

$$B_u = \frac{2}{c}\sqrt{2Z_0 I}, \tag{16}$$

where I is the laser intensity, and $Z_0 = (c\epsilon_0)^{-1} = 377$ Ω. The radiation damping rate can then be calculated from Eq. (1). Writing in terms of the laser flash energy E_L and the Rayleigh range Z_R, we have [9]

$$\Gamma_L = \frac{E_L[\text{J}]E[\text{MeV}]}{1.6 \times 10^5 \lambda_L[\mu\text{m}]Z_R[\text{mm}]}\frac{1}{T_0}, \tag{17}$$

where T_0 is the revolution period. The damping partition numbers are

$$\mathcal{J}_x = \mathcal{J}_y = 1, \quad \mathcal{J}_s = 2. \tag{18}$$

The laser-electron interaction also gives rise to quantum excitation of the transverse emittances the same way as in a bending magnet. It can be shown [9] that the minimum-normalized transverse emittances are

$$(\varepsilon_{x,y}^n)_{\min} = \frac{3\pi}{5}\frac{\lambda_c}{\lambda_L}\beta_{x,y}^*, \tag{19}$$

where $\beta_{x,y}^*$ are the beta functions at the interaction region. The minimum energy spread is determined by the rms fluctuation of the scattered photons and is given by [5]

$$(\sigma_\delta)_{\min} = \sqrt{\frac{7\pi}{5}\frac{\lambda_c}{\lambda_L}\gamma}. \tag{20}$$

In addition to quantum excitation, intrabeam scattering [6] provides an intensity-dependent diffusion in the phase

Table 1: Two laser-electron storage ring configurations

LESR mode	transient	steady state
Laser and resonator para.		
wavelength [μm]	1	1
flash energy in resonator	2 J	20 mJ
Rayleigh range [mm]	5	8
focal spot size [μm]	20	25
Electron storage ring para.		
energy [MeV]	100	8
number of electrons	1×10^{10}	1×10^{10}
average ring radius [m]	1	0.5
horizontal/vertical tune	~10	~10
energy loss per turn	25 keV	1 eV
trans. damping time	84 μs	84 ms
equil. energy spread	1.8%	2.3%
rf frequency [MHz]	2856	1428
rf peak voltage	1 MV	60 kV
momentum acceptance	10%	23%
rms bunch length [mm]	5.8	6.6
norm. long. emit. [mm]	21	2.4
norm. trans. emit. [m]	1×10^{-7}	6×10^{-6}
X-ray parameter		
wavelength	6.25 pm	1 nm
photon energy [keV]	200	1.24
photon flux [sec^{-1}]	2×10^{20}	8×10^{14}

space of the electron beam. The equilibrium emittances and energy spread can be obtained by balancing the rate of radiative laser cooling against the combined rate of intrabeam scattering and quantum excitation.

Two configurations will be discussed to demonstrate some LESR design considerations for various applications. One is a transient mode device that is capable of producing very low emittance electron beams. The other is a steady-state operation for the generation of intense soft x-rays. Table 1 lists some typical parameters. In both configurations we assume that the two half circles of storage rings consist of identical FODO cells and that the Fabry-Perot resonators are made of mirrors with total reflectivity $R = 99.99\%$. To simplify the intrabeam scattering calculations, we consider a round beam for both cases.

In the transient mode, a 200-GW peak power, 10-ps-long laser pulse is built up inside the resonator. Suppose that a 100-MeV electron beam is injected into this ring with both normalized transverse emittances initially at 1×10^{-5} m. The laser pulse scatters off the electron bunch each round trip with little change of intensity because of negligible laser depletion and internal loss. From Table 1, 1×10^{10} electrons are cooled rapidly to the equilibrium-normalized transverse emittances 1×10^{-7} m. At the same time, very bright, energetic x-rays are also produced. After the extraction of the cold electron beam, a new laser pulse can be built up, and a new electron beam can be injected to repeat the process. The normalized transverse emittances

achieved in the LESR are much smaller than those of the SLC damping ring, and are also well below present rf gun technology. The relatively large energy spread can also be made much smaller by adiabatic acceleration.

For the steady-state configuration, in order to sustain the energy level of the laser pulse in the Fabry-Perot resonator, a 200-W average power, mode-locked Nd:YAG laser is resonantly coupled to the resonator. From Table 1, when the accumulated laser pulse scatters off an 8-MeV electron bunch in the resonator, the interaction not only gives rise to soft x-rays with wavelength around 1 nm, but also provides a cooling and stabilization mechanism to maintain the intense compact bunch (1×10^{10} electrons) so that all electrons participate in each laser pulse collision. As a result of the radiative laser cooling, an average flux of 8×10^{14} x-ray photons per second is generated. The intensity and the compactness of this x-ray source may be suitable for x-ray lithography.

4 CONCLUSION

In summary, we have found two new approaches to generate very low-emittance electron beams. One is the suppression of quantum excitation through focusing environment. This approach can in principle reach the fundamental beam emittance with probably a rather limited intensity. The other is the radiative laser cooling in a laser-electron storage ring, which provides rapid damping for a dense electron beam. Generation of low-emittance electron beams is an interesting subject in its own right, and the two methods discussed here may have potential applications in linear colliders, novel accelerators, or light sources.

5 ACKNOWLEDGMENTS

6 REFERENCES

[1] K. Robinson, Phys. Rev. **111**, 373 (1958).

[2] M. Sands, SLAC Report No. 121, (1970).

[3] Z. Huang, P. Chen and R.D. Ruth, Phys. Rev. Lett. **74**, 1759 (1995).

[4] Z. Huang and R. D. Ruth, Phys. Rev. Lett. **80**, 2318 (1998).

[5] Z. Huang, Ph. D. dissertation, Stanford University, SLAC-R-527, (1998).

[6] A. Piwinski, in the Proceedings of the 4th Advanced Accelerator Physics Course, CERN Accelerator School, 226 (1991).

[7] H. Wiedemann, Nucl. Instr. Meth. A **250**, 24 (1988).

[8] V. Telnov, Phys. Rev. Lett. **78**, 4757 (1997).

[9] Z. Huang and R. D. Ruth, Phys. Rev. Lett. **80**, 976 (1998).

SASE BASED 4TH GENERATION LIGHT SOURCES AND THE LCLS PROJECT

M. Cornacchia[#], Stanford Linear Accelerator Center, P.O. Box 4349, Stanford, CA 94309

Abstract

Advances in the physics and technology of photoinjectors, linear accelerators, insertion devices and free-electron lasers make it now possible to generate coherent radiation in the x-ray region by means of the Self-Amplified-Spontaneous-Emission (SASE) process. This radiation has much higher brightness, shorter pulses and coherence than present 3rd generation sources. The status of the physics and technology involved in a radiation source based on SASE is reviewed, together with an overview of the main activities in this field around the world. The design status of a 1.5 Å SASE-FEL at SLAC, called the Linac Coherent Light Source (LCLS), is described.

1 INTRODUCTION

To the author's knowledge, the discourse on the next generation of light sources, what "next generation" might mean in terms of radiation properties, and on what electron source might best achieve them, started in earnest in 1992 at the first Workshop on 4th Generation Light Sources[1]. It was suggested then[2] that progress in electron sources and linear accelerators was making it possible to design and build an x-ray FEL based on Self-Amplified-Spontaneous-Emission. In 1996, a second workshop was held in Grenoble[3]. It was pointed out then[4] that the scientific opportunities in the future would require:

- Shorter light pulses (in the femtosecond regime)
- Transverse and temporal coherence
- Improvements in brightness by many orders of magnitude

At the same workshop the upper limits of performance of 3rd generation sources were reviewed [5]. It appeared that the types of improvement that would lead to a new generation of light sources were difficult to achieve in a storage ring in the x-ray region. It was shown again [6] that a linear accelerator had the potential to provide the electron source capable of producing coherent light of extremely high brightness, fully transversely coherent and delivered in sub-picosecond pulses. More recently, the Basic Energy Sciences Advisory Committee of the US Department of Energy recognized the importance of x-ray free electron lasers with its report of the "Panel on Future, Coherent Light Sources"[7]. The report states that " Given currently available knowledge and limited funding resources, the hard x-ray region (8-20 keV or higher) is identified as the mos exciting potential area for innovative science. DOE should pursue the development of coherent light source technology in the hard X-ray region as a priority. This technology will most likely take the form of a linac-based free-electron laser device using self-amplified spontaneous emission or some form of seeded stimulated emission..."

2 PRINCIPLE OF OPERATION

At present, the SASE process is the most promising approach to reaching x-ray wavelengths with a free-electron laser. In the Self-Amplified-Spontaneous-Emission process the spontaneous radiation is amplified in the single pass of an electron beam through an undulator, and no mirrors are required. This is an essential requirement for x-ray FELs, since the reflectivity of mirrors decreases at wavelengths lower than ~2000 Å and optical resonators become impractical at short wavelengths. The FEL radiation is also easily tunable by changing the electron beam energy.

The physics of SASE [8] imposes four main conditions on the electron beam quality [9]:

a) For the electron beam transverse emittances, $\varepsilon \approx \lambda/4\pi$ and λ is the FEL radiation wavelength.

b) For the energy spread, $\sigma_E/E < \rho$, where ρ is the

$$\text{FEL parameter} = \left[K\Omega_p f_b \Big/ (4\gamma\omega_u) \right]^{2/3},$$

$\omega_u = 2\pi c/\lambda_u$ is the frequency associated to the undulator periodicity and $K = eB_u\lambda_u \Big/ (2\pi mc^2)$ (cgs units). $\Omega_p = \left(4\pi r_e c^2 n_e \Big/ \gamma \right)^{1/2}$ is the beam plasma frequency, n_e is the electron density, r_e is the classical electron radius and f_B is the Bessel function factor. B_u is the undulator peak magnetic field, mc^2 the electron's rest energy.

c) For the undulator length, $N_u\lambda_u \approx 10L_g$, where L_g is the field gain length, $L_g \approx \lambda_u \Big/ (2\pi\sqrt{3}\rho)$.

[#] E-mail: cornacchia@ssrl.slac.stanford.edu

d) The radiation gain length must be shorter than the radiation Raleigh range, $L_g < L_R$, where

$$L_R = \frac{\pi w_0^2}{\lambda}$$ and w_0 is the radiation beam radius.

The condition indicates that the emittance of the electron beam scales like the wavelength, and therefore the condition becomes more demanding as the wavelength decreases. In the x-ray region (1.5 Å) the emittance must be of the order of 0.01π nm-rad in both planes. This is much smaller than anything achieved, or even achievable, in storage rings. Radio-frequency photoinjectors [10] on the other hands, have reached the stage where such emittances are obtainable. Once a bright electron beam is created, it must be preserved through the beam manipulation and acceleration phases in the linear accelerator. It is essential that transverse and longitudinal wakefields[11] and other effects (like the emission of coherent synchrotron radiation [12] in a bending section) do not appreciably reduce the electron beam brightness

Conditions c) and d) set a limit for the shortest length of the undulator that allows the FEL radiation to reach saturation. It is important that the device operates at saturation in order to minimize the fluctuations of the radiation output intensity.

3 THE EXPERIMENTAL EVIDENCE OF SASE AMPLIFICATION

The results of several experiments in recent years are providing confidence that the theory and the computations give a reliable description of the physics of SASE. The first experimental results on SASE were obtained in the microwave region[13], with gains of the order of 10^6-10^7. Over the last couple of years, experiments in the infrared and visible region obtained gains of one to two orders of magnitude[14] and, more recently, a gain of 3×10^5 was obtained at 12 μm[15]. In this experiment the gain length and output power fluctuations were measured, giving results in very good agreement with theory and simulations.

Although these results are encouraging and provide already, together with the theory and the simulations, a solid basis for the SASE-FEL design, no experiment has yet reached the saturation regime, where the LCLS and other future facilities will operate. For this reason, more experiments are planned to further study the SASE-FEL physics at saturation and shorter wavelengths. An overview of these plans is given in the next section.

4 OVERVIEW OF SASE-FEL PLANNED EXPERIMENTS AND FACILITIES

A BNL-LANL-LLNL-SLAC-UCLA group is preparing a 0.6-0.8 μm experiment (VISA, Visible Infrared Sase Amplifier) that will use the high brightness electron beam of the Accelerator Test Facility at NSLS/BNL in 1999. A

4 m long undulator with distributed strong focusing has been built for this purpose. VISA will reach saturation and it will study the radiation time structure and angular distribution. Still at NSLS/BNL, the Source Development Laboratory plans to start late in 1999 a SASE demonstration experiment at 0.3 μm with its 210 MeV linac and photoinjector.

The ANL program makes use of the APS Injector Linac and the Low Energy Undulator Test Line (LEUTL). The initial plan is to start at 0.53 μm with a 218 MeV beam in 1999. This will show some gain, although not yet saturation. More undulators will be added in 1999 allowing the experiment to reach saturation. The time averaged brightness of this facility will be 10^{20} ph/(s mm^2 mr^2 0.1%) and the peak brightness 10^{28}.

At DESY, construction is underway for a 420 Å SASE-FEL that will use the TESLA Test Facility (TTF) superconducting linac (390 MeV), with first operation expected in 1999[16]. In phase 2[17], scheduled around 2003, the wavelength will reach down to 60 Å with an electron beam of 1 GeV. This phase is already approved. Ultimately, when the Linear Collider is built, the 25 GeV beam will be able to emit FEL radiation at 1 Å in a long undulator. Table 1 offers the brightness and flux (in the usual units) at the various stages.

Table 1

Projected performance of DESY FEL.

	Phase I	Phase II	X-ray FEL
Brightness	4.3×10^{28}	2.2×10^{30}	9.7×10^{33}
Flux	1.0×10^{26}	1.0×10^{26}	3.3×10^{25}

A SLAC-ANL-LANL-LLNL-UCLA collaboration is proposing to build a SASE-based free-electron laser operating in the wavelength range of 1.5-15 Å. This facility, LCLS (Linac Coherent Light Source) is to be based at SLAC and makes use of the last 1/3 of the SLAC Linac.

An overview of the design and performances is the subject of the rest of this report.

5 THE LINAC COHERENT LIGHT SOURCE

5.1 General layout

Fig. 2 shows the layout of the proposed facility. The hexagonal shape at the end of the linac is the PEP-II B Factory electron-positron collider that uses the first 2 km of the Linear Accelerator as the injector. The last 1 km of the linac will be used by the LCLS.

A new injector consisting of a gun and a short linac will be used to inject an electron beam into the last kilometer of the SLAC linac. With the addition of two stages of magnetic bunch compression, the electron beam exits the linac with an energy of 14.3 GeV, a peak current of 3,400 A, and a normalized emittance of 1.5π mm-mrad. A transfer line takes the beam and matches it to the entrance

The LCLS
(Linac Coherent Light Source)
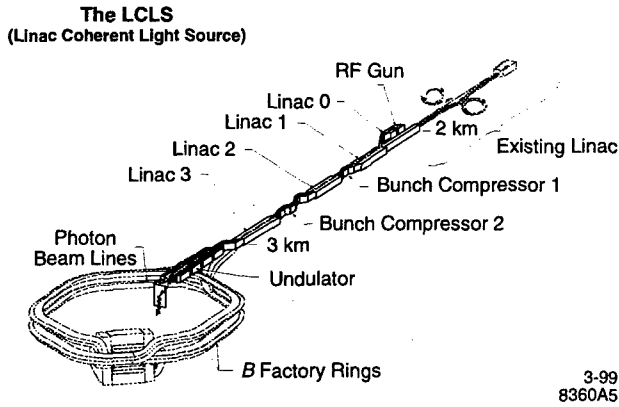
Figure 1. Layout of the Linac Coherent Light Source.

of the undulator. The 100 m long undulator will be installed in the tunnel that presently houses the Final Focus Test Beam (FFTB). After exiting the undulator, the electron beam is deflected onto a beam dump, while the photon beam enters the experimental areas.

5.2 Performance characteristics

The main parameters are shown in Table 2.

Table 2. Main LCLS parameters

Parameters	Value	Units
Electron Beam Energy	14.35	GeV
Emittance	1.5	π mm-mrad
Peak current	3,400	A
Energy spread (uncorrelated)	0.006	%, rms
Energy spread (correlated)	0.10	%, rms
Bunch length	67	fsec, rms
Undulator period	3	cm
Number of undulator periods	3,328	
Undulator magnetic length	99.8	m
Undulator field	1.32	Tesla
Undulator gap	6	mm
Undulator parameter, K	3.7	
FEL parameter, ρ	4.7×10^{-4}	
Field gain length	11.7	m
Repetition rate	120	Hz
Saturation peak power	9	GW
Peak brightness	1.2×10^{32} – 1.2×10^{33}	Photons/(s mm^2 mrad^2 0.1% bandwidth)
Average brightness	4.2×10^{21} – 4.2×10^{22}	Photons/(s mm^2 mrad^2 0.1% bandwidth)

Fig. 3 shows the average and peak brightness as a function of the photon energy for the LCLS and other

operating facilities. It indicates that the peak brightness of the LCLS would be about ten orders of magnitude greater than currently achieved in 3rd generation sources.
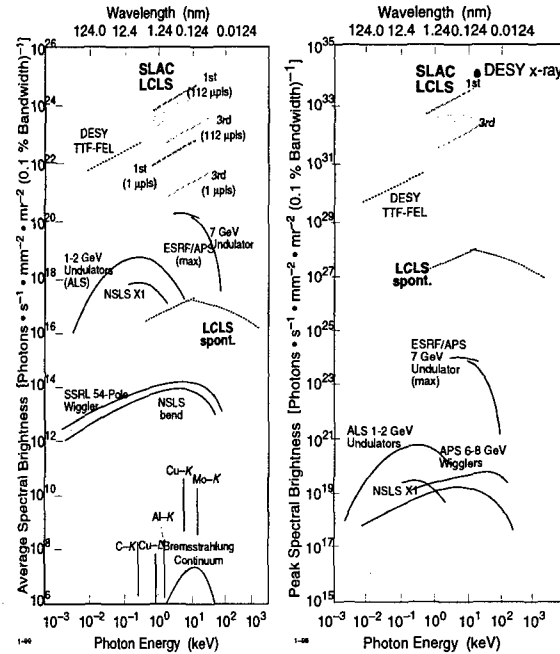
Figure 2. Average and peak brightness calculated for the LCLS and for other facilities, planned or under construction.

The sub-picosecond pulse length is two orders of magnitude shorter than can be achieved in a synchrotron. The FEL radiation has full transverse coherence. Longitudinally, the radiation is delivered in wave-trains[18]. The wave-trains are uncorrelated from each other. The longitudinal coherence is defined by the relative bandwidth of the wave-train, which, at saturation, is approximately $1/N_u \sim \rho = 4.7 \times 10^{-4}$.

5.3 Components performance and R&D issues

In this section we review the main components of the LCLS and discuss their specifications.

5.3.1 The photoinjector

The rf photoinjector is required to produce bunches of ~ 1 nC charge and 10 ps long with a normalized rms transverse emittance (horizontal and vertical) of ~ 1 π mm-mrad. The design was developed by a BNL-SLAC-UCLA collaboration[19]. A performance (1.2 π mm-mrad with 0.8 nC) close to the design specification was measured at the Accelerator Test Facility[20]. The simulation code PARMELA predicts that the design emittance can be reached by appropriate transverse and longitudinal laser pulse shaping [21]. The research on laser pulse shaping is being conducted at the Gun Test Facility at SLAC.

5.3.2 Acceleration and compression

For operation at 1.5 Å an electron peak current of 3,400 A with a transverse emittance of 1.5 π at 14.3 GeV is required. With these parameters the length of the
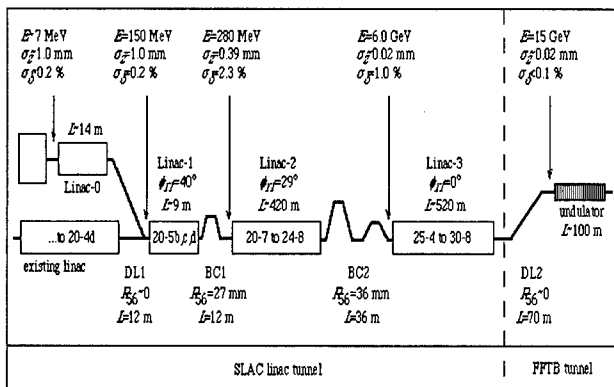
Figure 3. Layout of acceleration and compression systems

undulator that will give lasing with a comfortable margin for field errors and misalignments is ~ 112 m, which fits comfortably in the FFTB SLAC tunnel[22]. Since the photo-injector can produce 1 nC in 3 a ps long bunch, corresponding to a peak current of 100 A, the bunch has to be compressed 30 times to reach the peak current of 3,400 A required for lasing. The layout of the compression and acceleration is shown in Fig. 3.

The energy of the first compressor is 280 MeV, the lower limit being set by the need to minimize space charge effects at low energy, while the upper limit is set by the desire to compress the bunch early in the linac to ease transverse wake-fields. In the first compressor the bunch shrinks from 1 mm to 390 μm rms. After the second compressor the bunch length is only 20 μm. The energy of the second compressor, 6 GeV, is set by the conflicting requirements of longitudinal emittance dilution due to synchrotron radiation effects and longitudinal wake-fields. The second compressor (BC2) is asymmetric, with the last two dipoles having a weaker field to avoid the emittance blow up induced by the coherent synchrotron radiation emitted in the bends where the bunch is shortest [12]. Since the energy spread introduced by the coherent synchrotron radiation is correlated along the bunch, its effect on the transverse emittance is minimized by introducing a double chicane and optical symmetry to cancel the longitudinal-to-transverse coupling. With this scheme the simulations indicate that the emittance blow up due to coherent synchrotron radiation is of the order of 3-5 %.

5.3.3 The undulator

From the end of acceleration a transfer line transports the beam to the undulator.
After reviewing several possible magnet designs, a planar Halbach hybrid type was adopted, with a period of 30 cm

and a fixed 6 mm magnetic gap. The poles are made of vanadium permendur, and the magnets that drive them will be made of NdFeB.

The undulator was optimized in terms of its focusing lattice and strength. The eletron optics consists of FODO cells, with a cell length of 4.32 m. Focusing is obtained by placing permanent magnet quadrupoles in the interruptions of the undulator sections. Each interruption is 23.5 cm long, and also includes beam position monitors and vacuum ports. It was found, theoretically [23] and through computer studies, that such interruptions are harmless to the FEL process.

The corrections to the electron orbit are obtained by a small lateral displacement of the quadrupoles; the total movement is 0.5 mm with a resolution of 1 μm. The electron beam trajectory is required to be straight to within 5 μm over a field gain length (11.7 m) to achieve adequate overlap between the electron and photon beams. The excellent resolution of monitors of choice (microwave type detectors), better than 1 μm, is not sufficient to satisfy the requirements for absolute orbit correction, since this requires the knowledge of the absolute position of the monitors with the same order of accuracy as the electron beam straightness. This absolute accuracy is not achievable with present mechanical alignment techniques. Fortunately, a beam based alignment method, already in use at the SLC and FFTB, offers a solution to this problem. The technique uses BPM readings as a function of large, deliberate variations in the electron energy. The measurements are analyzed and then converted to (a) quadrupole magnet transverse position corrections, (b) BPM offset corrections and (3) adjustments of the incoming beam position and angle at the undulator entrance. A detailed description of the method can be found in the LCLS Design Report [24]. The simulations that have been performed to verify the method include all conceivable errors of the BPMs and quadrupoles, and show that the absolute position of the trajectory can be made to be straight to within 5 μm with only two iterations.

5.3.4 The x-ray optics and experimental area

The coherent output of the LCLS features peak output powers in the 10 GW range, average powers of the order of 1 W, spectral bandwidth of the order of 0.1%, full transverse coherence and pulse lengths of approximately 300 fs. The total peak power of the spontaneous radiation is 80 GW, thus largely exceeding the power of the coherent FEL output. The peak on-axis power density of the spontaneous radiation is 10^{13} W/cm^2 (at 1.5 Å), approximately one hundred times smaller than that of the coherent line, which, due to its full transverse coherence can, in principle, be focused to an approximate limit of 10^{25} W/cm^2. In the present concept the Experimental Hall will consist, initially, of one crystal and one mirror beamline.

6 ACKNOWLEDGMENTS

7 REFERENCES

[1] Workshop on Fourth Generation Light Sources, Feb. 24-27, 1992, M. Cornacchia and H. Winick Chairmen, SSRL report 92/02.

[2] Ibid., C. Pellegrini, "A 4 to 0.1 Å FEL Based on the SLAC Linac".

[3] 10th ICFA Beam Dynamics Workshop on 4th Generation Light Sources, Grenoble, Jan. 22-25, 1996.

[4] Ibid., I. Lindau, "Conclusions of Working Group on Scientific Opportunities for 4th Generation Light Sources VUV/Soft X-rays", p. 25.

[5] Ibid., M. Cornacchia, "Conclusions of Working Group on Lattice and Stability Aspects", pp. 41-48

[6] bid., C. Pellegrini, "Conclusions of Working Group on Linac Sources", pp. 57-66.

[7] Report of the Panel on Future, Coherent Light Sources, February 1999.

[8] R. Bonifacio, C. Pellegrini, and L. Narducci, Optics Comm. **50**, 373 (1984); K.-J. Kim, Nucl. Instr. and Meth. **A250**, 396 (1986); J.-M. Wang and L.-H. Yu, Nuclear Instruments and Methods **A250**, 484 (1986); G. T. Moore, Nuclear Instruments and Methods **A239**, 19 (1985); E. T. Scharlemann, A. M. Sessler, and J. S. Wurtele, Phys. Rev. Lett. **54**, 1925 (1985); M. Xie and D.A.G. Deacon, Nuclear Instruments and Methods **A250**, 426 (1986). K.-J. Kim, Phys. Rev. Lett. **57**, 1871 (1986); L.-H. Yu, S. Krinsky and R. Gluckstern, Phys. Rev. Lett. **64**, 3011 (1990).

[9] J.B. Murphy and C. Pellegrini, "Introduction to the Physics of the Free-Electron Laser", in *Laser Handbook*, Vol. 6, pp.9-70, W.B. Colson, C. Pellegrini and R. Renieri eds., North-Holland, 1990.

[10] R.L. Sheffield, "Photocathode rf guns" in *Physics of Particle Accelerators, AIP*, Vol. 184, pp.1500-1531, M. Month and M. Dienes, eds. (1992)

[11] See, for instance, K. Bane, "Wakefield effects in a Linear Collider", *AIP Conf. Proc.* Vol. 153, p.971 (1987).

[12] B.E.Carlsen and T.O. Raubenheimer, *Phys. Rev. E* **51**: 1453 (1995); Ya. S. Darbenev et al., "Microbunch Radiative Head-Tail Interaction", *DESY Report*, Sep. 1995.

[13] T. Orzechowski et al., *Phys. Rev. Lett.* **54**, 889 (1985); D. Kirkpatrick, *Nucl. Instr. And Meth.* **A285**, 43 (1989); J. Gardelle, J. Labrouch and J.L. Rullier, *Phys. Rev. Lett.* **76**, 4532 (1996).

[14] R. Prazieres et al., *Phys. Rev. Lett.* **54**, 889 (1985); M. Hogan et al. *Phys. Rev. Lett.* **80**, 289 (1998); M. Babzien et al, *Proc. Of the 19th International Free Electron Laser Conference*, pp. V-267-270, North-Holland, 1998. D.C. Nguyen et al., *Phys. Rev. Lett.*, **81**, 4 (1998).

[15] M. Hogan et al., *Phys. Rev Lett.*

[16] W. Brefeld et al. *Nucl. Inst. And Meth. In Phys. Res.* **A 393** 269.

[17] J. Rossbach, *Nucl. Inst. And Meth. In Phys. Res.* **A 375** 119-124.

[18] R. Bonifacio et al., *Phys. Rev. Lett. 73*, p. 70 (1994).

[19] D.T. Palmer et al., SPIE 2522, 514 (1995)

[20] M. Babzien et al. *Phys. Rev. E*, **57**, 5 (1998).

[21] J.F. Schmerge et al.,"Photocathode rf gun emittance measurements using variable length laser pulses", Presented at SPIE Photonics West, LASE 99 - Free-Electron Laser Challenges II, San Jose, CA January 26-27, 1999, Proceedings of SPIE Vol.3614

[22] The magnetic length of the undulator is 99.8 m. The physical length, that includes the separations between segments, is 111.8 m.

[23] K.-J. Kim, "Undulator Interruption in High-Gain Free-Electron Lasers", LBNL report No. F6, August 1997.

[24] LCLS Design Study Report, SLAC Publication R-521 and UC-414, p. 8-43.

[25] For the complete list of collaborators, see the LCLS Design Report, SLAC-R-521, p.i.

THE HIGH LUMINOSITY PERFORMANCE OF CESR WITH THE NEW GENERATION SUPERCONDUCTING CAVITY *

S. Belomestnykh [#], Laboratory of Nuclear Studies, Cornell University, Ithaca, NY 14853, U.S.A.

Abstract

With the installation of the first SRF cavity in September of 1997, the upgrade of the CESR RF system has begun [1]. This cavity belongs to the new generation of so-called HOM damped cavities designed for high current storage rings [2]. The upgrade is proceeding by replacing one by one old copper cavities with superconducting ones during short machine shutdowns.

CESR continues to demonstrate spectacular performance. It operates with 36 bunches in 9 trains of 4 bunches in each beam with total beam current up to 550 mA at the start of fills for high energy physics. In the course of last year both peak luminosity and integrated luminosity per day increased by 67% and are equal now to 8.0×10^{32} cm^{-2}s^{-1}, and 40.2 pb^{-1}/day. The latter number corresponds roughly to 43 thousands of B mesons per day. The first superconducting cavity has been in operation in CESR since October of 1997. The cavity operates at accelerating gradients up to 7 MV/m and delivers to the beam maximum RF power of 220 kW through the ceramic window, the record value for superconducting cavities. We found that pulsed power processing without beam is extremely helpful in improving RF window performance. The maximum HOM power extracted from the beam by one cavity is 5.7 kW.

Four single-cell HOM damped cavities will eventually support a total beam current of 1 A. Because of the very low impedance of superconducting cavity module, we calculate the longitudinal instability threshold from cavity HOMs to be in excess of 1 A. The second cavity was installed in CESR during October'98 shutdown. The third cavity is already installed in CESR, and its commissioning will start immediately after this conference. The fourth cryomodule is being assembled and is schedule for installation in summer of 1999.

1 INTRODUCTION

Prior to the installation of the first SRF cavity, since November of 1994, CESR operated in the Phase II configuration with nine two-bunch trains and ±2.1 mrad crossing angle [3]. The maximum total current in two colliding beams was 350 mA, peak luminosity up to 4.4×10^{32} cm^{-2}s^{-1}, and maximum integrated luminosity of 23.6 pb^{-1}/day. Total current was limited by a longitudinal coupled bunch instability caused by higher-order modes in the 5-cell copper RF accelerating cavities [4, 5].

Table 1: CESR Phase III Parameters.

Beam energy	5.289 GeV
Number SRF cavities	4
Total RF voltage	7.2 - 12 MV
Natural bunch length	13 mm
Number of bunch trains	9
Number of bunched per train	5
Bunch spacing	14 ns
Total beam current in two beams	1 A
Crossing angle	2.7 mrad
Vertical tune shift parameter	0.04
Luminosity	1.7×10^{33} cm^{-2}s^{-1}

Phase III of the CESR luminosity upgrade involves replacement of the final focus quadrupoles and interaction region vacuum chambers, and installation of the new superconducting RF system [6]. The CESR III design parameters are shown in Table 1. To achieve the desired luminosity of 1.7×10^{33} cm^{-2}s^{-1}, 1 Ampere beam current must be stored in multibunch beams in CESR. Due to such a high beam currents, input couplers, windows, and HOM loads of accelerating cavities must be capable to deal with very high RF power. The big number of bunches puts severe restriction on the Q factors and R/Qs of HOMs in order to avoid multibunch instabilities. Apart from this, even fundamental mode can cause problems if its R/Q is too high [7, 8, 9]. Minimizing the number of cavities in the ring helps reducing total impedance of RF system as well. These challenges to CESR RF system are similar to challenges to RF systems of other high current machines and were reviewed at previous conferences [10, 11, 7, 12, 2]. Several superconducting (SC) and normal conducting (NC) cavity designs have been developed to meet new requirements of high power and low impedance. A storage ring RF system based on SC cavities has lower impedance than its NC counterpart because of i) the higher achievable accelerating gradient decreases the number of cells needed, ii) low R/Q of the fundamental mode, iii) simple and effective method of HOM damping. These factors and a long experience with superconducting RF (SRF) at Cornell determined the cavity choice for the CESR Upgrade.

2 CESR RF SYSTEM UPGRADE

Table 2 contains the major design parameters of the CESR Phase III RF system [13]. The system consists of

four single cell superconducting niobium cavities [14] in their individual cryostats. The cavities are located in the CESR East (cavities E1 and E2) and West (cavities W1 and W2) RF straight sections. Two cavities are fed by RF power from one klystron via magic T. The HOM power absorbed by ferrite loads is expected to be 13.7 kW per cavity. With installation of all four SRF cavities the bunch length in CESR can be reduced to 13 mm. RF power of 325 kW will be delivered to the beam through each input coupler and RF window. New refrigeration and cryogen distribution system is installed to provide liquid helium to RF cavities, interaction point superconducting quadrupole lenses and superconducting solenoid of detector CLEO. As part of the Phase III of the CESR Luminosity Upgrade Program, other components of RF system are being upgraded as well. 800 kW klystrons will replace old 600 kW ones. Two new 2 MW SLAC-type high voltage klystron power supplies are installed.

Table 2: Parameters of the CESR III RF system.

Frequency	499.765 MHz
Accelerating field	6 - 10 MV/m
Effective cell length	0.3 m
Number of cavities	4
Total RF voltage	7.2 - 12 MV
Cryomodule length	2.86 m
R/Q (R=V²/P)	89 ohm
Q_0 at operating field (4.5 K)	$>10^9$
Q_{ext} of RF coupler	2×10^5
Cryostat static heat losses	30 W
Cryostat liquid He volume	520 liters
Loss factor of a module with one taper at $\sigma_z = 13$ mm	0.48 V/pC
Power delivered to 1 A beam through the RF window	325 kW

3 CRYOMODULE

A novel superconducting cavity geometry [14] was initially proposed for the Cornell B-factory project. Later on this cavity became a part of the Phase III of the CESR luminosity upgrade program. Initial R&D efforts [15, 16, 17, 18] were followed by the development and tests of the cryomodule-prototype and its elements [19]. A successful beam test in 1994 [20] allowed us to design new, MARK II, cryostat to meet rather tight requirements of the CESR tunnel [21].

A drawing of the cryomodule is presented in Figure 1. A 500 MHz niobium cavity is placed inside the helium vessel. Bell-shaped cavity geometry with wide openings of 24 cm diameter beam tubes makes R/Q of the HOMs small in comparison with a conventional cavity geometry (Figure 2) and allows monopole HOMs to propagate toward a ferrite absorbers. The Q factors of most higher-order modes are of the order of 100.

Because the first two dipole modes have resonant frequencies below cut-off of the 24 cm diameter round beam tube (RBT), beam tube on one side has flutes which lower the cut-off frequency. As a result, these dipole HOMs can now propagate via fluted beam tube (FBT) to the FBT side load.
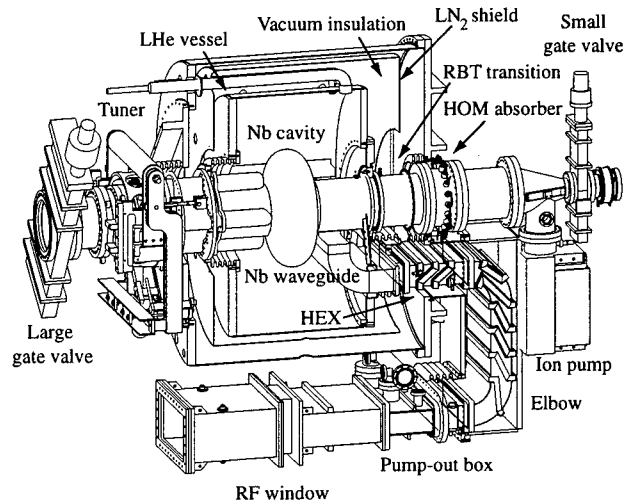
Figure 1. The CESR B-cell cryomodule.

Turning to the cryostat, the helium vessel inside surface is covered with copper foil to make its temperature more even during cool down. The He vessel is suspended inside the cryostat on four invar rods. The space between the He vessel and cryostat walls serves as vacuum insulation. Also, it contains liquid nitrogen cooled radiation shield, 60 layers of mylar super insulation, and magnetic shielding. Within vacuum envelope of the cryostat are thermal transition pieces on the RBT and FBT beam pipes and the waveguide designed to keep radiation and conduction heat loads of the liquid He bath at low level. The beam line transition pieces are of the same cross section as the ends of the niobium cavity. They are made of 1 mm thick stainless steel with 3.8 μm copper coating to reduce RF losses due to beam current. The waveguide thermal transition incorporates a gaseous helium heat exchanger (HEX) to help carry away the heat generated in the walls by the high RF power. This stainless steel unit is plated inside with 25 μm of copper. The next portion of the waveguide, the 180° waveguide U, is cooled by liquid nitrogen.

The ceramic RF window is connected to the waveguide inside the cryostat via the short section furnished with two 60 l/s ion pumps. The window is capable to transfer RF power up to 500 kW in travelling mode [22].

In both directions along the beam line outside the cryostat are the ferrite-lined higher-order mode loads [23, 24]. They serve to absorb the beam induced HOM power.

R/Q, Ohm
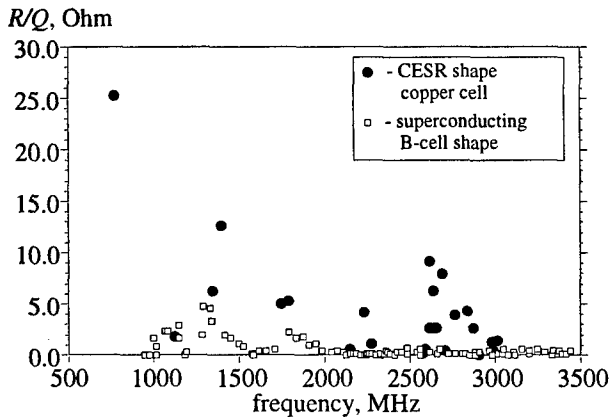
Figure 2. Comparison of HOM *R/Q*s of the conventional copper cavity and superconducting B-cell cavity.

The cryomodules are designed for installation alone or in a pair. Standard installation in CESR is in pairs. RBT end of the module is connected to the CESR beam pipe. It is equipped with a taper from 24 cm diameter of the cavity beam pipes to a smaller size cross section of adjacent CESR vacuum chamber. A small gate valve serves to separate cavity vacuum from machine vacuum whenever it is necessary. Two cryomodules in a pair are connected to each other by FBT ends with 24 cm diameter straight vacuum pipe. Vacuum volumes of two cryomodules can be separated by large diameter gate valves. In case of one cavity installation a taper is connected to the FBT end of the cryomodule next to the large gate valve.

4 SRF CAVITY INSTALLATION AND COMMISSIONING RESULTS

The first SRF cavity was installed in CESR in September of 1997 in E2 location. Using a NC and a SC cavity as a pair makes operation somewhat complicated. To maintain the same RF field as the copper cavity, the SRF cavity requires much less incident power without beam present [25]. For example, to get accelerating voltage of 1.5 MV, one needs to provide forward power of approximately 100 kW to the NRF cavity, but only about 30 kW to the SRF cavity with nearly all of it reflected. The numbers converge with increasing beam current, but even at 0.6 A total beam current we get forward power of 250 kW for the NRF cavity versus 210 kW for the SRF cavity. In order to keep voltages reasonably even, it was proposed [25] to use a waveguide 4 dB hybrid instead of magic T as an RF power splitter. In the 4 dB splitter configuration the SRF cavity was operated at a field of 6.3 MV/m or voltage of 1.9 MV.

At first, multipacting and arcing in the RF coupler region limited the CESR beam current and delivered by the SRF cavity beam power at about 100 kW. After exploring several RF processing techniques, we found that the best results are achieved when processing

without beam by pulsed power on or close to cavity resonance. By pulse processing, the beam power could gradually be raised to 140 kW and total beam current to 350 mA. At this power level we observed for a first time dependence of the RF power on the cavity field: transmitted power is higher when there is bigger standing wave component. Computer simulations [26] confirmed that travelling to standing wave mixing ratio affects multipacting bands.

Also, we observed fast vacuum events caused by releasing cryopumped hydrogen due to RF heating of the HEX surface, and following arc. Analysis of residual gas evolution [27] during cavity warm up showed that after about 2 months of operation without warming the cavity up, cold surfaces accumulated several equivalent monolayers of hydrogen. Eventually it was found that baking RF window ceramics to >150°C and periodic warm ups cures this effect.
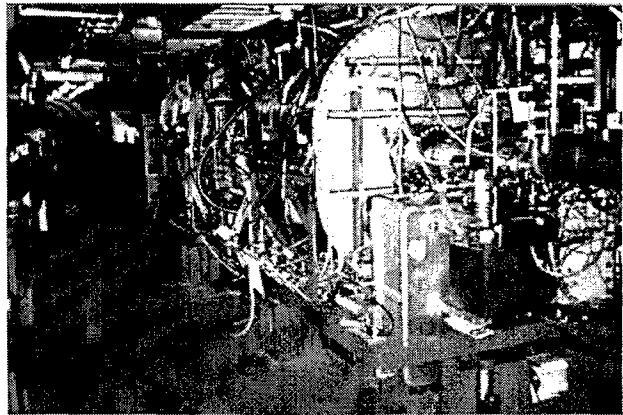
Figure 3. Photo of E1 and E2 cryomodules in the CESR tunnel.

To explore the ability of E2 SRF cavity to deliver higher RF powers to beam, we switched from a 4 dB hybrid back to a magic T 3 dB waveguide configuration after the next cavity warm up. This allowed us to load the SRF cavity stronger with beam and reached 212 kW in travelling wave and to operate at the field level of 7 MV/m.

A low frequency vibration from the neighbouring NRF cavity cooling water pump caused microphonics effect in the E2 cavity. Added stiffeners reduced this effect to a tolerable level. This effect disappeared when the NRF cavity was replaced with the second superconducting cavity.

Operating experience obtained with the first SRF cavity allowed us to introduce several changes in cryomodule design and preparation procedure [1]. As we will see in the next section, as we addressed these problems, CESR continued to set new peak and integrated luminosity records.

5 CESR PERFORMANCE AND LIMITATIONS

With installation of the first SRF cavity we were able to raise beam current steadily. Initial beam current limitation due to RF window multipacting was overcome using pulse processing. As it was mentioned earlier, the major limitation of the total beam current prior to installation of the E2 cavity was the longitudinal coupled bunch instability. The instability current threshold measurements [4] and computer calculations [28] showed that this threshold depends on the bunch spacing within the bunch train. The CESR standard filling patterns allow the bunches within each train to be spaced in increments of 14 ns, up to maximum of 5 bunches per train. Initially CESR was operating in 9×2 mode with 28 ns spacing. After learning that 42 ns spacing had a higher current threshold, the routine operation of CESR was changed to this bunch spacing. Nevertheless, this was not enough as the single beam threshold current was only about 230 mA. A longitudinal multibunch feedback system has been implemented [29] based on a digital signal processing to produce bunch by bunch beam stabilization.

In spite of installation of a low impedance SC cavity, the total HOM impedance of the ring was still dominated by remaining NC cavities and changes of the beam current thresholds were small [30]. Moreover, the current threshold at 42 ns spacing became lower. The instability growth rate calculations showed that as long as there is even one NC cavity in the ring, one should not expect a dramatic change in the current threshold. Therefore, it has become crucial to have detail information about current threshold for all possible bunch train patterns and choose the bunch pattern appropriately. That is why CESR operation has been switched from 9×2 to 9×3 configuration, and later to 9×4 bunch train configuration. Latest measurements of instability thresholds and HOM spectra of horizontal separators indicate that there could be other sources of a narrow band impedance apart from RF cavities [31]. This impedance might limit the threshold current after complete installation of the new SRF system and it is important to have reliable longitudinal feedback system in place.

During the running period with one SRF cavity the maximum extracted HOM power was about 5.7 kW at 510 mA total current in two beams of nine three-bunch trains each (obtained during machine studies experiment).

E1 superconducting cavity was installed in the machine in October of 1999. Shortly after its commissioning we were able to reach and exceed 200 kW power delivered to beam by one cavity [1]. Operating with two SRF cavities proved to be easier and more stable than with one SRF and one NRF cavity in the same pair.
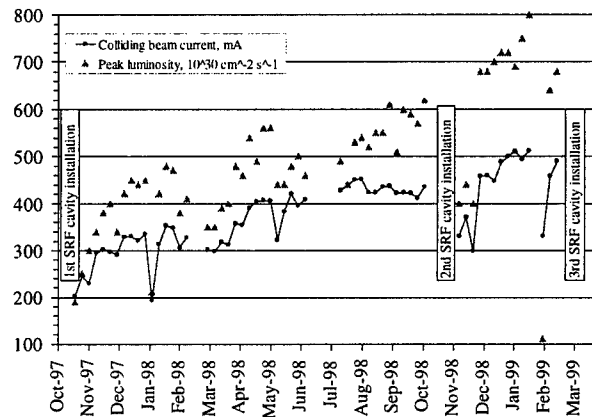
Figure 4. CESR peak luminosity and colliding beam current performance since the beginning of RF system upgrade.

The ability of SRF cavities to deliver high beam power and continuing efforts to improve performance of the longitudinal feedback system helped to increase total beam current to 550 mA at the beginning of the HEP fills and peak luminosity to 8×10^{32} cm^{-2}s^{-1}. Figure 4 illustrates change of the beam current brought into collision and peak luminosity week by week since the beginning of the CESR RF system upgrade. Another important factor in achieving record peak luminosity is ability to reach high beam-beam tune shift parameter (ξ_v). In last several weeks of operation CESR was running with ξ_v up to 0.049. This can be attributed in part to improved alignment of magnetic elements [32]. More details about CESR performance and upgrade status can be found in [33]. Table 3 lists highest parameters achieved by CESR II.

6 SUMMARY

Today CESR is the highest luminosity collider running at 8×10^{32} cm^{-2}s^{-1} with an upgrade in progress to double the luminosity. Two SC cavities have been successfully commissioned and are in operation. The SRF cavities provided reliable operation with high beam currents up to 550 mA and allowed CESR to establish several peak and integrated luminosity records.

The ultimate measure of CESR performance is an integrated luminosity delivered to CLEO detector. February of 1999 was the last month when CESR II was running for HEP experiments as CLEO has begun its upgrade to CLEO III. The history of monthly integrated luminosity delivered by CESR since the beginning of its Phase II upgrade is shown in Figure 5. The total luminosity delivered by the collider is 18.07 fb^{-1}.

The next one and a half month long run of CESR will be dedicated exclusively to experiments on synchrotron radiation facility CHESS and machine studies with three SC cavities. The third cryomodule is installed in CESR in place of remaining two NC cavities and it is being

275
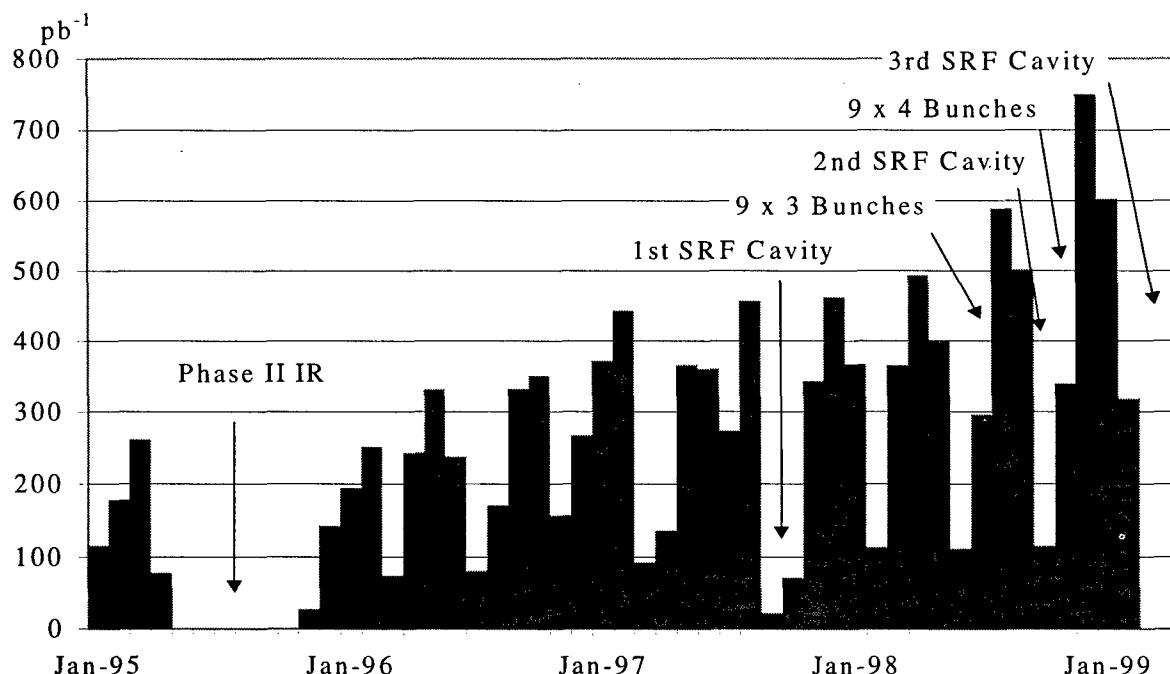
Figure 5. CESR integrated luminosity per month.

commissioned now. Three SC cavities will provide enough RF voltage and power to support two beams. The fourth cryomodule is being assembled and is scheduled for installation during long CLEO III / CESR III shutdown in summer'99. Installation of all four SRF cavities will reduce the ring impedance and provide a stable operation at high beam currents up to 1 ampere.

Table 3: Highest parameters achieved during CESR Phase II HEP performance.

Peak luminosity	8×10^{32} cm^{-2}s^{-1}
Integrated luminosity per day	40.2 pb^{-1}
Integrated luminosity per month	750 pb^{-1}
Integrated luminosity per year	4442 pb^{-1}
Total current	550 mA
Beam-beam parameter, ξ_v	0.050

7 ACKNOWLEDGEMENTS

8 REFERENCES

[1] S. Belomestnykh, et al., MOP135, *these proceedings*.

[2] H. Padamsee, *Proc. 6th EPAC*, Stockholm, 1998.

[3] D. L. Rubin, *Proc. 1997 Part. Accel. Conf.*, Vol. 1, p. 372.

[4] M. Billing, *Proc. 1997 Part. Accel. Conf.*, Vol. 2, p. 2317.

[5] A. Temnykh, et al., *Proc. 1997 Part. Accel. Conf.*, Vol. 2, p. 1718.

[6] D. L. Rubin, *Proc. 6th EPAC*, Stockholm, 1998.

[7] K. Akai, *Proc. 5th European Part. Accel. Conf.*, Vol. 1, p. 205.

[8] S. Belomestnykh, Cornell LNS Report SRF970314-01 (1997).

[9] D. Fromowitz, Cornell LNS Report CON97-10.

[10] J. Kirchgessner, *Part. Accel.*, 46(1), p. 151 (1994).

[11] J. Kirchgessner, *Proc. 1995 Part. Accel. Conf.*, Vol. 3, p. 1469.

[12] R. Boni, *Proc. 5th European Part. Accel. Conf.*, Vol. 1, p. 182.

[13] S. Belomestnykh, et al., *Proc. 5th EPAC*, Vol. 3, p. 2100.

[14] H. Padamsee, et al., *Part. Accel.*, 40, p. 17 (1992).

[15] D. Moffat, et al., *Proc. 1993 Part. Accel. Conf.*, Vol. 2, p. 763.

[16] D. Moffat, et al., *Proc. 1993 Part. Accel. Conf.*, Vol. 2, p. 977.

[17] D. Metzger, et al., *Proc. 1993 Part. Accel. Conf.*, Vol. 2, p. 1399.

[18] E. Nordberg, et al., *Proc. 1993 Part. Accel. Conf.*, Vol. 2, p. 995.

[19] H. Padamsee, et al., *Proc. 4th EPAC*, Vol. 3, p. 2048.

[20] H. Padamsee, et al., *Proc. of the 1995 PAC*, Vol. 3, p. 1515.

[21] J. Kirchgessner, et al., *Proc. 7th SRF Workshop*, Vol. 1, p. 35.

[22] E. Chojnacki, et al., *Part. Accel.*, 61, p. [309]/45 (1998).

[23] S. Belomestnykh, et al., *Proc. 1995 PAC*, Vol. 5, p. 3394.

[24] E. Chojnacki, W. J. Alton, MOP77, *these proceedings*.

[25] S. Belomestnykh, et al., Cornell LNS Report SRF961217-04.

[26] R. L. Geng and H. Padamsee, THAL5, *these proceedings*.

[27] R. L. Geng and H. Padamsee, MOP136, *these proceedings*.

[28] S. Belomestnykh, unpublished.

[29] J. Sikora, et al., TUA19, *these proceedings*.

[30] M. G. Billing and S. Belomestnykh, TUA18, *these proceedings*.

[31] A. Temnykh, private communication.

[32] R. Holtzapple and D. Rice, THP7, *these proceedings*.

[33] S. B. Peck, D. L. Rubin, WEAR3, *these proceedings*.

DAΦNE OPERATING EXPERIENCE

S. Guiducci, for the DAΦNE Commissioning Team[1], LNF-INFN, Frascati, Italy

Abstract

Commissioning of the DAΦNE Φ-factory without experimental apparatus ended last November, when the construction of KLOE detector was complete. KLOE is presently being installed and operation with beam will resume next April for physics runs. We report in the following the DAΦNE performance achieved during the first phase of operation for single beam and colliding beams.

1 INTRODUCTION

The first commissioning phase of DAΦNE was concluded for the installation of the KLOE [1] detector (Fig. 1). The main results obtained in ~ 6 months of beam time are presented in the following.
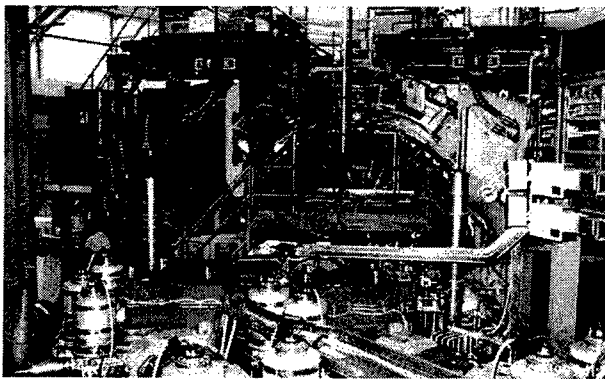
Figure 1: The KLOE detector during installation.

The strategy of the commissioning phase aimed at tuning the machine for collisions and optimizing the single bunch luminosity before KLOE's installation. This should guarantee that, after correcting the perturbation introduced by the KLOE solenoidal magnet, the machine is ready for two beams operation.

Single beam commissioning of the two rings, in single bunch mode, is completed: electron and positron currents larger than twice the design value (110 mA reached, 44 mA design) have been stored without instabilities and

machine parameters have been measured and found in good agreement with the predictions of theoretical models. In particular, a machine coupling much smaller than the design value has been obtained.

Multibunch feedback systems have been put into operation and currents of 0.54 A of electrons and 0.56 A of positrons have been stored, only limited by vacuum.

A maximum single bunch luminosity of 1.6×10^{30} cm^{-2} s^{-1} has been so far obtained, while in multibunch collision, less extensively tested, a luminosity value of ~ 10^{31} cm^{-2} s^{-1} in 13+13 bunches configuration has been achieved.

2 GENERAL DESCRIPTION

The main DAΦNE [2] design parameters are summarized in Table 1, while the magnetic layout is shown in Fig. 2.

Table 1: DAΦNE Design Parameters

Energy [GeV]	0.51
Trajectory length [m]	97.69
RF frequency [MHz]	368.26
Harmonic number	120
Damping time, τ_E/τ_x [ms]	17.8/36.0
Bunch length [cm]	3
Emittance, $\varepsilon_x/\varepsilon_y$ [mm·mrad]	1/0.01
Beta function, β_x^*/β_y^* [m]	4.5/0.045
Particles/bunch [10^{10}]	8.9
Single bunch luminosity [cm^{-2}s^{-1}]	4.4×10^{30}

High current, multibunch and flat beam approach has been adopted for DAΦNE, similar to PEPII [3] and KEKB[4]. Electron and positron beams, stored in two separate rings, travel in the same vacuum chamber in the Interaction Regions (IR) and collide in two Interaction Points (IP). Crossing at a horizontal angle of 25 mrad minimizes the effect of parasitic collisions and allows to store many bunches, increasing the luminosity by a factor equal to the number of bunches.

DAΦNE's design allows a maximum number of 120 bunches and all the critical subsystems (injector, RF, vacuum system, diagnostics) are dimensioned to cope with a stored current of ~ 5 A.

The Phase I luminosity target is 10^{32} cm^{-2} s^{-1} with 30 bunches and the main effort of the next machine shifts will be devoted to improve by a factor two single bunch luminosity and beam current in a reliable way.

[1] DAΦNE Commissioning Team: M.E. Biagini, C. Biscari, R. Boni, M. Boscolo, V. Chimenti, A. Clozza, G. Delle Monache, S. De Simone, G. Di Pirro, A. Drago, A. Gallo, A. Ghigo, S. Guiducci, F. Marcellini, C. Marchetti, M.R. Masullo, G. Mazzitelli, C. Milardi, L Pellegrino, M.A. Preger, R. Ricci, C. Sanelli, F. Sannibale, M. Serio, F. Sgamma, A. Stecchi, A. Stella C. Vaccarezza, M. Vescovi, G. Vignola, M. Zobov.

Once this target is obtained, in parallel with physics runs, the accent will be put to progressively tune the machine systems for higher currents and increase the number of bunches. To operate with 120 bunches further investment on the longitudinal feedback and additional work on the cures of the parasitic crossings effects will be needed.
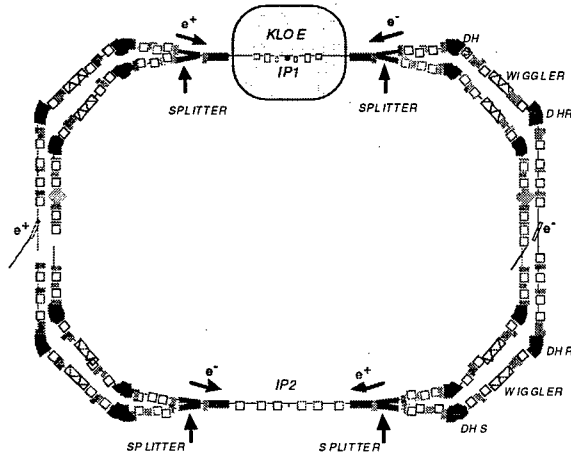
Figure 2: Main Rings magnetic layout (March 99).

3 SINGLE BEAM PERFORMANCE

3.1 Main Rings Optics

For commissioning purposes two temporary interaction regions (day-one IR), consisting of seven normal conducting quadrupoles, have been used to tune the optical functions. The first order transfer matrix and the β functions at the IP are the same for the day-one IR and the KLOE one, in order to match the same optical functions in the arcs, while the optical functions inside the IR and the quadrupole layouts are different.

The β functions along the ring have been measured in each quadrupole and used for lattice modeling. This model takes into account the fringing fields of dipoles and quadrupoles (non negligible because of the short lengths and large apertures of the magnetic elements), all the focusing effects in the wigglers and the off-axis trajectory in the IR quadrupoles.

The closed orbit before correction was inside the ring aperture in both rings. The sources of closed orbit are alignment errors, compensation of the trajectory in the wigglers and, since the two rings are very close, the stray fields from high field elements of the other ring. After closed orbit correction a coupling of the order of $\kappa \sim .002$ has been obtained, much smaller than the design value ($\kappa = .01$), also when sextupoles are turned on.

Coupling has been estimated from the synchrotron light monitor and by the closest tune approach distance. Another sensitive measurement of the relative variation of the coupling is the beam lifetime which is essentially determined by the Touschek effect and therefore it is inversely proportional to the beam density and, for small coupling, it is nearly proportional to square root of the coupling. The minimum achieved coupling, well below the synchrotron light monitor resolution, has been tuned by measuring the beam lifetime as a function of the strength of a skew quadrupole.

The horizontal emittance measured by the synchrotron light monitor (see Fig. 3) is in good agreement with the design value for both rings.
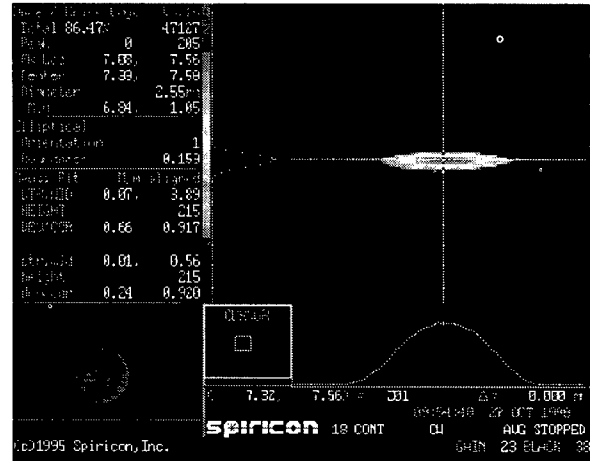
Figure 3: Beam image from the synchrotron light monitor at design coupling $\kappa = .01$.

The chromaticity has been measured and corrected using the same sextupole strengths in both rings and the behavior of the tunes versus the relative energy deviation, shown in Fig. 4 for the positrons, is the same for both rings. The sextupole strengths have been tuned in order to improve the energy acceptance of the ring and therefore the beam lifetime. Indeed the beam lifetime depends on the physical and dynamic aperture for the betatron and synchrotron oscillations.

The design value of the energy acceptance has been reached by powering only the eight sextupoles located in the arcs arranged in four families [5].
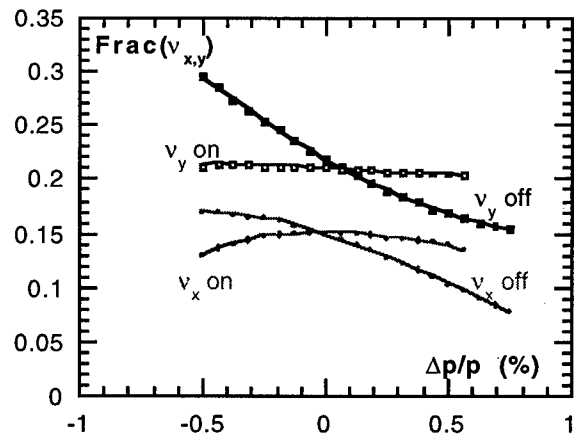
Figure 4: Betatron tunes versus relative energy deviation with sextupoles on and off for e^+ ring.

3.2 Principal subsystems

Special RF cavities, with low impedance parasitic high order mode (HOM) content, have been developed to allow stable high current-multibunch operation [6]. The cavities, one per ring, are normal conducting copper single cells, with a system of HOM damping waveguides which couple out and dissipate the HOM energy induced by the beam on external 50 Ω loads. The HOM shunt impedance has been reduced by up to three orders of magnitude. No evidence of arcing or multipacting effects due to the loading waveguides has been observed and the performance of the damped cavities under high beam loading is quite satisfactory.

A longitudinal bunch-by-bunch feedback system [7], implemented in collaboration with the SLAC/LBL PEP II group, is operational in both rings. It consists of a time domain system employing digital techniques. A damping time faster than ~ 200 μsec has been demonstrated in the positron ring with 30 bunches.

The specially designed arc vacuum chambers [8] and the Ti sublimation pumps have been very effective and the static gas pressure in the arcs was in the 10^{-10} Torr range. At the moment no baking of the arc chambers is needed and further improvement of the vacuum is expected by beam conditioning of the vacuum chamber, very effective due to the high emission of synchrotron radiation. The vacuum in the *day-one* IRs was very poor since they were not baked, in view of replacing them with the final ones. The bad IR vacuum, specially under high beam loading, was a limit for high current operation.

During the winter shutdown some operations to substantially improve the vacuum of the rings straight sections have been performed. Two special designed NEG pumps capable of a pumping speed for CO of 2000l/s have been installed in the KLOE IR, the distributed ion pumps inside the splitter magnets have been activated and the straight sections vacuum chambers adjacent to the IRs have been baked out.

3.3 Beam Dynamics

The maximum current stored in single bunch mode, 110 mA in both rings, largely exceeds the design value of 44 mA. The bunch length has been measured as a function of bunch current in the positron ring and found in very good agreement with numerical simulations based on machine impedance estimates [9]. According to these data the normalized coupling impedance |Z/n| is below 0.6 Ω. The transverse impedance is very low, as confirmed by the high threshold of the head-tail instability without sextupoles (13 mA in a single bunch).

Ion trapping effects have been observed in the electron ring, due to the poor vacuum of the commissioning IRs, even in single bunch mode above 20÷30 mA. Clearing electrodes [10] have been successfully tested. Although only partially powered, they helped in reducing the tune spread and shift due to the ions in the electron beam. In multibunch operation different filling configurations with a gap have been tested.

3.4 Multibunch operation

In the multibunch mode (all 120 bunches filled) 0.3 A in the positron beam and 0.23 A in the electron one have been stored without feedback. With the longitudinal feedback system on, up to 0.54 A of electrons have been stored in 25 bunches with a spacing of four RF buckets and an ion clearing gap of 5 consecutive bunches. With the positron beam 0.56 A have been stored in 30 uniformly spaced bunches. The uniformity of the stored current in the different bunches is quite satisfactory for both beams. These currents correspond to half the design value for 30 bunches and seem limited by vacuum and ion trapping.

4 COLLIDING BEAMS

Maximum beam overlap is the preliminary condition to obtain high luminosity in a two rings collider. For this purpose a careful adjustment of the longitudinal timing and of the orbits at the IP has been performed.

The longitudinal overlap of collisions at the nominal IP has been optimized by monitoring the distance between the combined signals of the two beams on two sets of symmetric BPMs on each side of the IP. The RF phase of one of the two beams is shifted to bring them into collision at the low-β point. Fine tuning is performed by looking for the maximum counting rate of the luminosity monitor at high currents.

The vertical distance between the two beams at the IP has to be small with respect to a vertical beam size $\sigma_y = 20\ \mu$m. The position in the IR is measured for each single beam in the same seven BPMs, canceling therefore any monitor offset. A BPM at the IP, installed for this purpose in the *day-one* IR, has been helpful during the initial set-up of orbit and timing for collisions. Averaging over 100 readings, a measurement of the beam position in the IR with an rms deviation better than 10 μm is obtained. Closed orbit bumps in the IR with four correctors are used to adjust angle and displacement at the IP to equalize the orbit of the two beams in the vertical plane and set the crossing angle at the design value $\theta = 25$ mrad. Fine tuning of the vertical orbit is performed by changing the position at the IP in steps of 5 μm and looking for maximum luminosity monitor signal. Tuning the horizontal position and vertical angle is not necessary because the orbits are set with more than enough precision with respect to the beam size ($\sigma_x = 2.1$ mm) and to the angles inside the beam ($\sigma'_y = 0.47$ mrad).

The minimum of the vertical beta function β_y^* has to be the same for the two rings and to coincide with the crossing point. As the IP is not a symmetry point of the

machine, symmetric beta functions with the same β_y^* at the IP for both rings have been obtained by iterating the measurement and tune of β functions in the IR.

The beams were brought into collision in one IP only, while kept vertically separated in the other one. A vertical orbit bump separated the beam centers by $\Delta y = 4$ mm corresponding to nearly $2\sigma_x$ and $200\ \sigma_y$.

After the initial operation on the working point (5.11, 5.07) it was decided to run on the one (5.15, 5.21) farther from integers and sextupolar resonances. On this point the machine is less sensitive to closed orbit distortion, the dynamic aperture is larger and the lifetime longer.

Beam-beam simulations [11] predict for this working point, with a single interaction point, a luminosity of 2.2 10^{30}cm^{-2}s^{-1} with a beam-beam tune shift parameter $\xi_{x,y}$ of 0.03 and good lifetime. A brick-wall plot of the relative luminosity predicted by simulations in the tune diagram around 5.15, 5.21 is shown in Fig. 5.
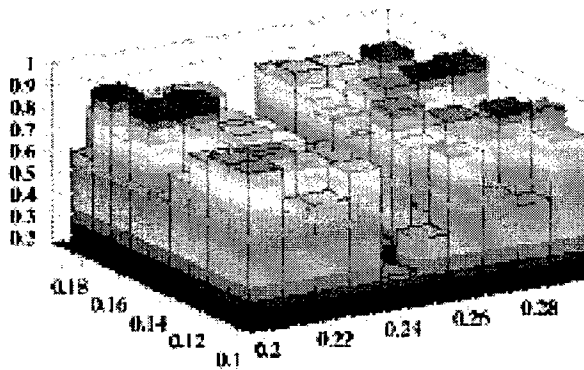
Figure 5: Relative luminosity predicted by simulations in the tune diagram.

During injection in collision mode the intensity of the injected beam saturated below the current of the already stored beam. The longitudinal and transverse oscillations of the bunch at injection cause crossings out of the nominal IP during a time comparable with the radiation damping one and produce particle losses. At present injection with the vertical separation bump is not very effective because the correctors are not synchronized and produce orbit distortions while turning off the separation.

To overcome this limitation a 'RF fast phase jump' procedure was implemented [6]. Injection is made on non interacting buckets and then the RF phase of one beam is rapidly shifted towards the collision phase. If the phase shift is performed with a fast ramp (~ 600 μsec) the bunch follows the RF phase. This procedure proved to work also in multibunch mode, shifting by two buckets 400 mA in 30 bunches without any beam loss.

During the November shifts, when the highest luminosity has been obtained, the positron beam has been injected two buckets apart from the colliding one and then brought in collision by means of the RF fast phase jump. This procedure has been also useful for luminosity

tune-up, comparing beam sizes and lifetimes in and out of collision; moreover it makes gas background subtraction for the luminosity monitor easier and more accurate.

The single bunch luminosity measurements are shown in Fig. 6 as a function of the product of the electron and positron currents; the line represents the luminosity calculated with the design parameters for the same currents.
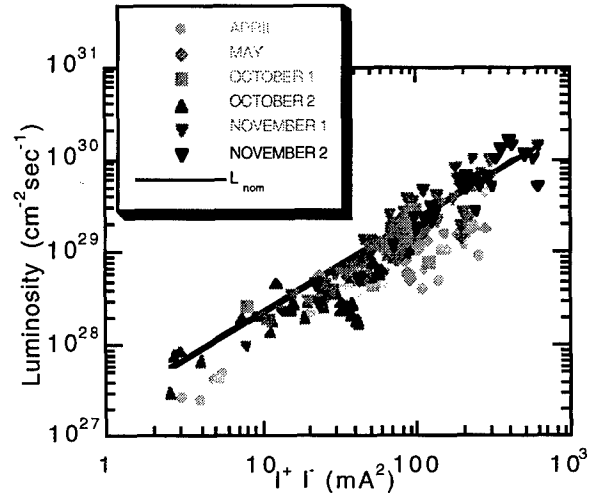
Figure 6: Luminosity versus the product of the e$^+$ and e$^-$ currents.

After careful tuning of the collision parameters the measured luminosity is in good agreement with predictions, showing that a good beam overlap and a vertical beam size as low as the design value have been achieved. Due to the excellent result obtained for the minimum coupling, when the current in the interacting bunches is less than design, it is possible to improve the luminosity by squeezing the vertical beam size. The maximum single bunch luminosity (1.6 10^{30} cm^{-2} s^{-1}) has been obtained with I$^+$ = 19 mA, I$^-$ = 21 mA (assuming equal tune shifts for the two beams this corresponds to ξ_y ~ .03). This is in good agreement with the predictions of beam-beam simulations with one IP on this working point. A tune scan around the working point has been performed, showing a qualitative behavior in agreement with the simulations [12].

Only two days were dedicated to multibunch luminosity measurements. Using the RF fast phase jump procedure a luminosity of the order of 10^{31} cm^{-2} s^{-1} has been obtained with 13+13 bunches.

A short time has also been dedicated to luminosity measurements with two interaction points. In this case there is a luminosity degradation (~ 40%) in agreement with simulations. Since the lattice is asymmetric with respect to the IP, the beam experiences different phase advances going from IP1 to IP2 and back. The beam-beam behavior depends on the machine tunes but also on the phase advance difference between the two IPs.

In the future, luminosity measurements with two IPs will be done on the optimum value of the phase advance difference predicted by the simulations.

5 KLOE IR

The KLOE detector consists of a cylindrical drift chamber surrounded by a lead-scintillating fiber electromagnetic calorimeter and immersed in the .6 T magnetic field of a 2.5m radius superconducting solenoid.

In order to leave the maximum free solid angle around the IP, SmC permanent magnets low-β quadrupoles, built by Aster Enterprises, have been adopted. They are confined inside a 9° cone around the IP and the solid angle available for the detector is 99%. There are three of these quadrupoles on each side of the IP, supported by the detector.

The high integrated field of the KLOE solenoid (2.4 Tm) is a strong perturbation for the low energy DAΦNE beam (510 MeV). It rotates the beam by ~ 45° in the transverse plane and it is the main source of machine coupling. A compensation scheme, the Rotating Frame Method [13], has been adopted to cancel this coupling. This scheme requires two compensating solenoid in a position symmetric to the main solenoid and a rotation of the low-β quadrupoles.

The three quadrupoles are carefully aligned and rigidly connected as shown in Fig. 7. After installation each triplet can be rigidly moved with 5 degrees of freedom (displacement and tilt in the x and y plane and rotation around the axis) by means of a cam system.
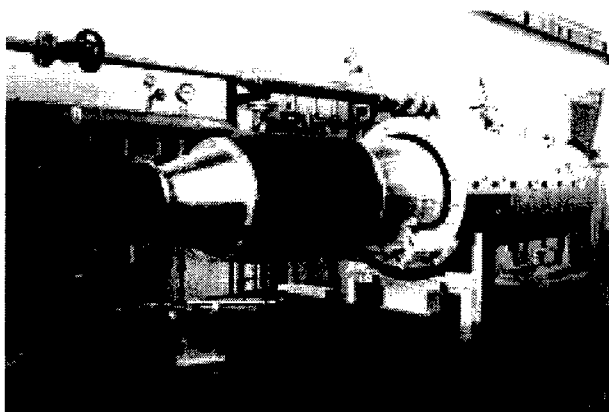
Figure 7: One of the KLOE low-β triplets on the alignment bench.

The beam pipe around the IP has to be as transparent as possible for the outcoming particles. In order to avoid K_S^0 regeneration, it is required that the K_S^0 decay before hitting the pipe. In order to have a large enough fiducial volume for the K_S^0, the cylindrical pipe around the IP is welded to a 500 μm thick sphere with a 10 cm radius. A 50 μm thick Be cylindrical shield is welded inside the sphere to provide RF continuity of the beam pipe.

The chamber, built by BrushWellman is made with a Be-Al alloy (AlBeMet, 68% Be, 32% Al). The chamber, before the insertion in the KLOE detector, is shown in Fig. 8.
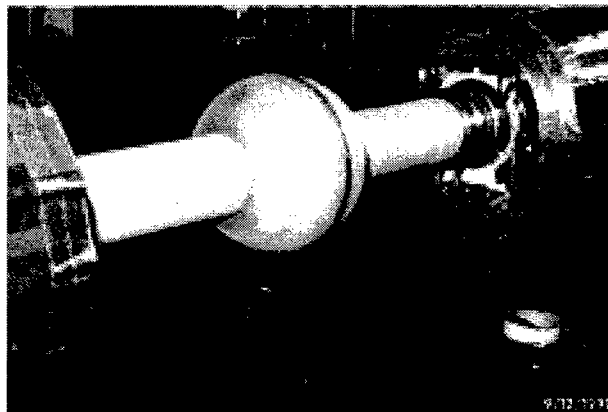
Figure 8: The KLOE vacuum chamber.

6 CONCLUSIONS

The performances of the DAΦNE Φ-Factory in single beam mode and the results of colliding beams have been described.

At present the shutdown for the installation of KLOE is concluded. The cool down of the KLOE solenoid is in progress, energization is expected in few days and operation with beam will resume right after.

7 ACKNOWLEDGMENTS

8 REFERENCES

[1] The KLOE collaboration, KLOE a general purpose detector for DAΦNE, LNF-92/019(IR), April 1992.

[2] G. Vignola, and DAΦNE Project Team, DAΦNE, The Frascati F-factory, Proc. of PAC '93, Washington.

[3] J.T. Seeman, Commissioning Results of B-Factories, these Proceedings.

[4] K. Oide, The KEKB Commissioning Team, Commissioning of the KEKB B-Factory, these Proceedings.

[5] M.E. Biagini et al., Chromaticity Correction in DAΦNE, DAΦNE Technical Note BM-4, March 1999.

[6] R. Boni et. al., Operational Experience with the DAΦNE Radio-frequency Systems, these Proceedings.

[7] M. Serio et. al., Multibunch Instabilities and Cures, Proceedings of EPAC '96, Sitges, June '96.

[8] V. Chimenti et al., An UHV Vacuum System for DAΦNE, Proceedings of EPAC'96, Sitges, June '96

[9] C. Biscari et al., Single and Multibunch Beam Dynamics, these Proceedings.

[10] C. Vaccarezza, Ion Trapping Effects and Clearing in the DAΦNE Main Electron Ring, DAΦNE Note G-38, March '96.

[11] M. Zobov et al., Beam-Beam Interactions at the Working Point (5.15; 5.21), DAΦNE Technical Note G-51, March 1999.

[12] M.E. Biagini et. al., Optimization of Beam-beam Performance, these Proceedings.

[13] M. Bassetti et. al., The Design of the DAΦNE Interaction Region, Proc. of PAC '93, Washington.

OPERATIONAL STATUS AND FUTURE UPGRADES OF BEPC

Y. Z. Wu for the BEPC team

Institute of High Energy Physics, P.O. Box 918, Beijing 100039, China

Abstract

In this paper the operational status of Beijing Electron-Positron Collider(BEPC) in recent years is described. The luminosity upgrades have been performed in recent years. By lowering the vertical β function at interaction point the peak luminosity is nearly doubled. The single interaction point in BEPC is also studied experimentally. The results show that beam-beam tune shifts decrease significantly compare to the two IP's operation. The overall performance of dedicated synchrotron radiation operation is improved by installing new insertion device and optimising the beam lifetime. The future upgrades of BEPC are briefly introduced. The design studies of a new τ-charm factory has been carried out continuously. On the other hand the further upgrade potential based on existing machine is being exploited.

1 INTRODUCTION

Beijing Electron-Positron Collider(BEPC) has been in operation for 10 years, working for high energy physics experiments as well as synchrotron radiation research in dedicated or parasitic mode. The running time is about 5500 hours/year, in which roughly 40% for particle physics, 30% for dedicated synchrotron radiation and 30% for others(machine study, etc.).

Beijing Electron Positron Collider

1.2. 1st. I.R. expert. hall
3. Power station of ring mag. and computer center
4. RF station   5. 2nd I.R. expert. hall
6. Tunnel of storage ring   7. Tunnel of trans. line
8. Tunnel of Linac   9. Klystron gallery
10. Nuclear phy. expert. hall   11. Power sta. of trans. line
12. East hall for S.R. expert.   13. West hall for S.R. expert.
14. Computer center
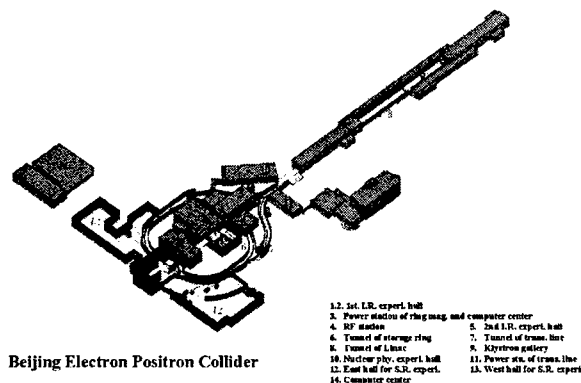
Figure 1: The schematic of BEPC

BEPC as a collider mainly works in the τ-charm energy region for physics experiments. Since 1989 BES(Beijing Electromagnetic Spectrometer) detector has accumulated

- 10 million J/ψ events
- 3.7 million ψ' events
- 22.3 pb^{-1} integrated luminosity at D_s, etc.

BEPC also serves as the unique x-ray synchrotron light source in China known as Beijing Synchrotron Radiation Facility(BSRF). There are eight beamlines(five from 2 wiggler magnets, three from bending magnets) and 12 experimental stations. More than four hundreds users have been utilizing BSRF as the tools in different scientific research programs.

In the past several years the upgrade program is carried out mainly aiming at increasing the luminosity of BEPC. Major items include:

- linac energy upgrade(from 1.3 GeV to 1.55 GeV)
- improvements for control and beam diagnostic system
- luminosity upgrade for BEPC collider ring
- BES and BSRF upgrades

Up to now the basic goals of above upgrades have been achieved. The overall efficiency (in terms of integrated hadron events/day) of BES physics run is doubled. The performance of dedicated synchrotron radiation operation is also substantially improved.

2 OPERATIONAL STATUS

2.1 BEPC present operation parameters

The BEPC facility has been decribed in detail in several documents[1,2,3]. The accelerator facility is located in IHEP, Beijing. A 200 meter long linac provides electron and positron beams with the energy up to 1.55 GeV. The storage ring with a circumference of 240.4 m is capable of operating up to 2.8 GeV. However, because of the strong interest in J/ψ physics in recent years, since 1996 performance has been optimized at 1.55GeV beam energy mainly. In the spring of 1999 the physics experiment is measuring R value. The R value scan experiment works at the beam energy region from 1.0GeV to 2.5GeV. This is a somewhat difficult task for machine because sometimes it works at lower energy than the design. The beam energy of dedicated synchrotron radiation operation is 2.2 GeV since 1990 to provide soft x-ray and VUV photon beams. It is hoped that the operating energy is to be increased to

2.5 GeV or higher. A list of the principal operating characteristics of BEPC may be found in Table 1.

	Colliding beam mode	Dedicated S.R. mode
Beam energy(GeV)	1.0 ~ 2.8	2.2
Inj. Energy(GeV)	1.0~1.55	1.3
Bunch/beam	1	50~80
Emittance(nm.rad)	400(1.55GeV)	79
Tunes	5.81/6.78	8.72/4.80
β-functions at IP	1.2/0.05	18/18
RF frequency(MHz)	199.536	199.536
Total current(mA)	45 (1.55GeV)	80 ~ 100
Beam lifetime(hour)	5 ~ 10	~ 20

Table 1: Principle parameters for current BEPC operation

2.2 Operation with lower-β lattice

For the luminosity upgrades, the original proposal was to install a mini-β insertion(compact permanent quadrupole magnets)[4]. But later it was found that the bunch length of BEPC storage ring is significantly longer than the proposed vertical β-function at IP(3.6cm) [5] even an attempt was made to reduce the coupling impedance by shielding most of bellows and removing 2 kickers. Therefore the proposed mini-β lattice was modified by relocation of the insertion quadrupoles 35cm closer to the interaction points. The current distance from IP to the first quadrupole is 2.15 m. This allows the operation with lower vertical β function, say, 5cm instead of 8.5 cm at interaction points.

Since 1996 the extensive machine studies with lower β configuration have been performed mainly at 1.55 GeV beam energy which the physics program required in recent years. The peak luminosity has reached $4.9 \times 10^{30} \text{cm}^{-2} \text{s}^{-1}$. See Figure 1. The maximum vertical beam-beam parameter is about 0.033. The hadronic event rate at J/ψ energy seen by BES detector in routine operation is increased by a factor over 2.
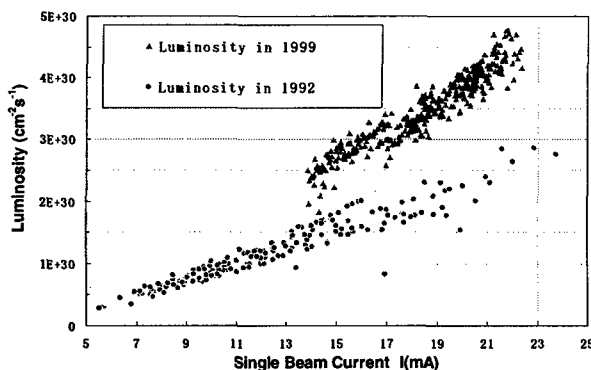
Figure 1: Luminosity increase with lower β optics

2.3 Single Interaction Point Experiments

BES is the only detector for particle physics experiment on BEPC since its operation started in 1989. The idea that beams collide only at the south IP where the BES detector is located to enhance luminosity has been investigated since 1991.[5]   The basic scheme is to separate the electron and positron beams at north IP by 1 pair of vertical electrostatic separator. The early experiments did not give any positive results. The major reason is that the phase advance between separators is not exact 180°. The vertical orbit distortion created by north separators leak out to the active IP. In the fall of 1995 with adding 4 new power supplies for the insertion quadrupoles near north IP, a new lattice with eliminating one low-β insertion was designed. The new configuration ensures the exact 180° phase advance between two north separators. The horizontal and vertical β-functions at north IP become 4.62 m and 0.65 m respectively. The tunes of the ring, ν_x=6.12, above the integer, ν_y=6.62, above the half integer, are quite different from those of normal double-IP operation.

The single IP experiments are carried out since 1996 during machine studies. Up to now the best performance occurred with low-β configuration in which the vertical β-function at south IP is 7 cm. The beam-beam tune shift per revolution decrease significantly comparing with that in two IP's operation. The maximum beam current and beam-beam parameter have been increased, which results a higher luminosity than that with same β-function of two IP's operation. More experiments are going to be done to explore the potential with lower vertical β-function at south IP.
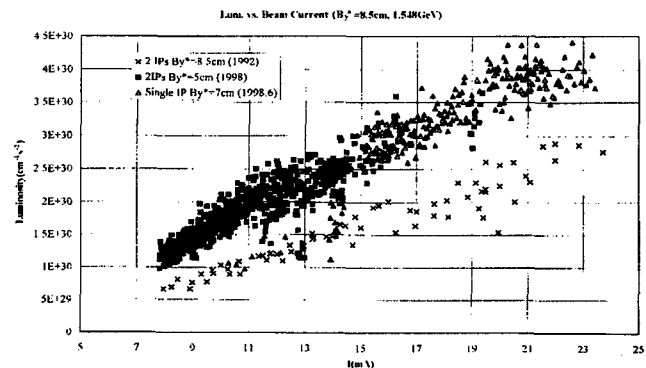
Figure 2: Luminosity increase with single IP

2.4 Dedicated Synchrotron Radiation Operation

BEPC is designed to serve as a research facility for both elementary particle physics and synchrotron radiation

experiments. A low emittance configuration has been brought into routine dedicated synchrotron radiation operation mode since 1990. The operating beam energy of this mode is 2.2 GeV with natural horizontal emittance of 76 nm.rad, one order of magnitude smaller than that of collision mode for particle physics (660 nm.rad at 2.015 GeV). Recently a new lattice configuration aiming at operating machine at 2.5 GeV by adjusting the focusing strengths of a few quadrupoles has been made. The natural horizontal emittance increases to 79 nm.rad at 2.2 GeV.

During the shutdown in 1996, a five-period permanent wiggler magnet was installed in the storage ring of BEPC in order to provide the higher performance photon beams. The period length is 30 cm and the peak magnetic field is 1.5 Tesla. The gap is adjustable from 3.9 cm to 22 cm. Two new beamlines extracted from this wiggler magnet have been built. The higher flux photon beams provided by this new wiggler have attracted more users in various research fields from different universities and institutes. The beam current intensity in dedicated synchrotron operation is 80~100 mA. The beam lifetime, which is dominated mainly by the Touschek effect, is increased to over 20 hours by filling 50-80 unequal bunches. The operation at higher beam energy, i.e., 2.5 GeV is commissioned successfully. The parasitic operation mode with new wiggler in particle physics run is being tested.

3 FUTURE UPGRADES

The rich physics in τ-charm energy region and the achievements in BEPC have been encouraging us to make continuous efforts in the further developments of collider facility.

The brightest option is to build a new research facility dedicated to the same energy region as BEPC but with highly superior performance as to luminosity (specifically 10^{33}cm^{-2}s^{-1}) and incorporating additional parameters, such as the possibility of polarized circulating beams or specialised optics providing highly mono-chromatic beams, called τ-charm Factory. The feasibility study has been going on since 1994[7,8,9]. If this project is approved the existing BEPC storage ring will become a fully dedicated synchrotron radiation facility. A study to upgrade it to the higher energy(3.0GeV) and lower emittance(< 20 nm.rad) is carried out[10].

On the other hand the possibility of continual improving the performance of BEPC is investigated. The major scheme of this improvement is multi-bunch operation by adopting pretzel scheme like CESR[11]. Figure 4 shows the schematic of this scheme on BEPC. Both horizontal and vertical pretzel schemes have been preliminarily exploited[12,13]. It seems that both separation schemes can meet the design requirements. The number of bunch, determined by the integer part of tunes of ring, can be 6 or 7. The expected luminosity gain factor is 4 ~5.

Besides the theoretical studies, some selected experiments
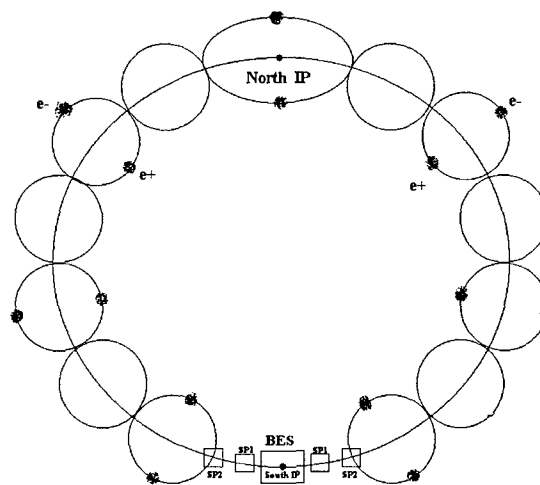
Figure 4: Pretzel Scheme with 7 bunches on BEPC

are performed during machine study time to investigate some key issues in future projects, such as multi-bunch instabilities especially the Photon-Electron Instability [14], horizontal and vertical pretzel orbits experiments with single beam, etc.

4 SUMMARY

BEPC is now operating with a nearly doubled luminosity after the upgrades in recent years. The plans are underway to greatly improve the luminosity in the future.

5 ACKNOWLEDGMENTS

This article is a brief review of the work done by many dedicated people in the accelerator and technical sector at IHEP. More detailed contributions on specific items can be found elsewhere in these proceedings.

6 REFERENCES

[1] S. X. Fang, S.Y. Chen, Proc. 14th Int. Conf. On High Energy acc., 51(1989)

[2] Y. Z. Wu, PAC'91, San Francisco, 180(1991)

[3] C. Zhang, HEACC'92, Hamburg, 84(1992)

[4] Y. Z. Wu, BEPC Luminosity Upgrades Workshop, 184(1991)

[5] Z. Y. Guo et al., BEPC Performance Workshop'96, (1996)

[6] X. A. Luo et al., this proceeding(1999)

[7] Beijing Tau-charm Factory Feasibility Study Report(1996)

[8] N. Huang, et al., PAC'97, Vancouver (1997)

[9] D. Wang, Y. Z. Wu, ICFA Workshop on Beam Dynamics issues for e+e- Factories, Frascati, 397(1997)

[10] J.Q. Guo, L.M. Chen, IHEP/AC/AP/99-03(1999)

[11] D. Rice, PAC'93, San Francisco, 1978(1991)

[12] L.F. Wang, C. Zhang, PAC'97, Vancouver(1997)

[13] Q. Qin, BEPC Performance Workshop'98, 76(1998)

[14] Z.Y. Guo, et al., this proceeding(1999)

CESR PERFORMANCE and UPGRADE STATUS*

S. B. Peck, D. L. Rubin† for the CESR Operations Group
Laboratory of Nuclear Studies, Cornell University, Ithaca, NY 14853, USA

1 INTRODUCTION

The CESR electron-positron collider operates with nine trains of closely spaced bunches stored in each beam. During the Fall of 1998 the number of bunches in each of the trains was increased from three to four and the spacing of the bunches reduced from 28ns to 14ns. A beam current of 550mA was supported by two single cell superconducting cavities and two 5-cell copper cavities. We measured a peak luminosity of $8.3 \times 10^{32}\,\mathrm{cm}^{-2}\mathrm{s}^{-1}$ and a beam-beam tune shift parameter of $\xi_v = 0.05$.

The replacement of the remaining room temperature cavities with superconducting RF cavities in the next several months will provide the capability to store a total beam current of 1A. Because of the very low impedance of the superconducting RF, we anticipate the longitudinal instability threshold to be in excess of 1A. And with an accelerating gradient of 10MV/m, the bunch length in CESR can be decreased from the present value of 19mm to 13mm so that we can exploit a corresponding decrease in β^*. The interaction region optics will be replaced in 2000 with a hybrid of permanent magnet quadrupole and superconducting quadrupoles. Magnet gradients and apertures are consistent with a vertical β of as small as 7mm.

2 BUNCH TRAINS AND CROSSING ANGLE

In CESR the counterrotating beams share a common vacuum chamber. Electrostatic separators are used to differentially displace the orbits of the electron and positron beams so that there are collisions of the multiple bunch beams only at the single interaction point. The beam trajectories intersect at the interaction point with a small horizontal crossing angle. The 'pretzeled' orbits are indicated in Figure 1.

The length of each train is limited by the pretzel scenario to be about 60% of a betatron half wavelength. The existing optics are compatible with a train length of 56ns. CESR has operated with trains of three bunches, spaced 28ns apart, and most recently with four bunch trains, spaced 14ns apart. We have recently discovered that, with the addition of a pair of quadrupoles, the lattice optics can be modified to improve the separation efficiency, and the length of the train increased to 70ns. The quadrupoles will be installed this summer.

The long range beam-beam tune shift due to a near miss is, $\Delta Q_{h,v} \propto \frac{I_b \beta_{h,v}}{x^2}$. The minimum spacing of bunches within the train is determined by this effective transverse
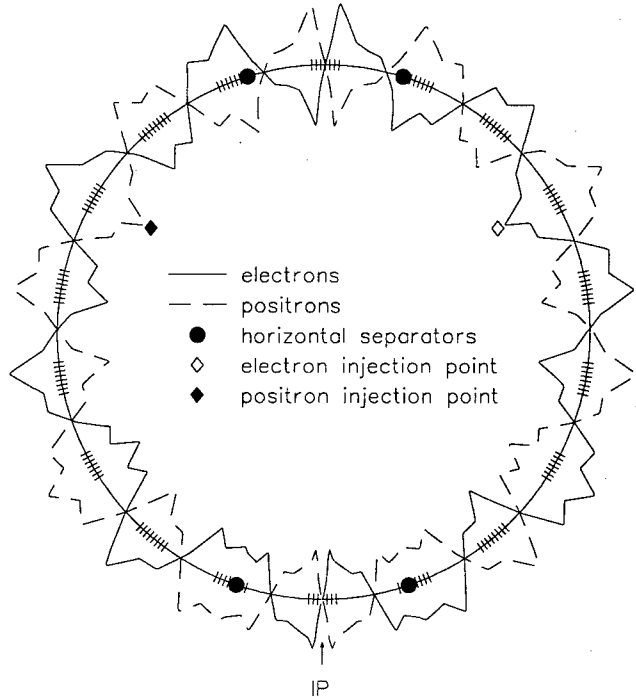
Figure 1: Pretzeled orbits. The maximum horizontal displacement of the beams from the center of the vacuum chamber is about 20mm. The tic marks indicate the parasitic crossing points of electron and positron bunches corresponding to 9 trains with 4 bunches/train. The bunches within each train are 14ns apart.

separation of the bunches at the parasitic crossing nearest the interaction point. In order to accomodate more closely spaced bunches the interaction region quadrupole will be replaced with high gradient superconducting magnets. With stronger focusing quads, it is possible to reduce the β-function at the IP without a dramatic increase in β nearby, permitting closer spacing and/or higher bunch currents. Schematics of the interaction region optics are shown in Figure 2. The existing configuration is designated Phase II and the upgraded configuration Phase III.

With the modification to the optics in the arcs, the train length and the number of bunches in each train can be increased to six. If we find that the new interaction region optics allow a decrease in bunch spacing, the number of bunches per train could be further increased to as many as twelve. Bunch lengthening effects tend to scale with bunch current and higher order mode dissipation in RF cavities, transitions, sliding joints etc. with the square of the bunch current. The flexibility to increase the number of bunches and decrease the bunch charge may prove valuable in optimizing luminosity.
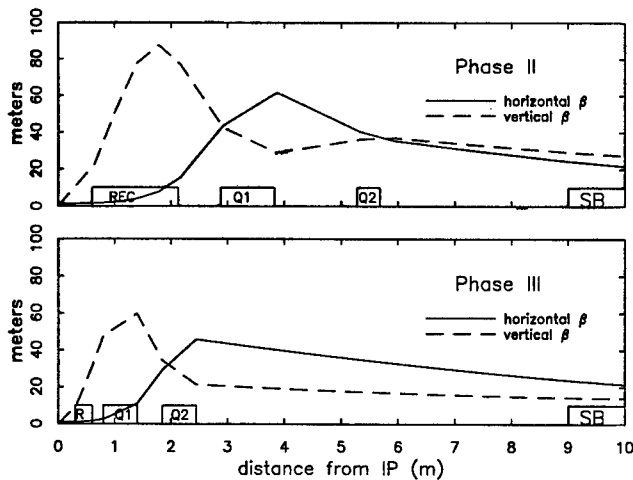
Figure 2: Upper plot shows optical functions in Phase II IR. With superconducting quadrupoles (Q1 and Q2) in Phase III, $\beta_v^* \sim 10mm$ and β_v at the parasitic crossing 7ns(2.1m) from the IP is $30m$.

3 LONGITUDINAL INSTABILITY

A longitudinal coupled bunch instability is excited by high Q parasitic modes in the normal conducting multicell RF accelerating cavities[1]. In addition, a longitudinal coupled bunch mode is excited by interaction of the beam with the cavity fundamental[2]. With the replacement of the room temperature 5-cell cavities with single cell superconducting cavities, the total impedance at the fundamental will decrease by a factor of fifteen and all of the high Q parasitic modes will be eliminated.

Implementation of a longitudinal feedback system allowed an increase in current well beyond the instability threshold[3]. The system consists of a receiver, a digital filter processor, power amplifier, and kicker. A horizontal stripline kicker couples to the longitudinal motion of the beam. There is finite dispersion in the lattice at the location of the kicker. A differential pulse on the two plates of the stripline generates a horizontal kick that drives the beam longitudinally by modulating the path length of the beam. A broadband analog power amplifier drives the kicker differentially.

The instability excited by the cavity fundamental is damped by modulation of the RF cavity drive.

4 SUPERCONDUCTING RF

A single cell, superconducting RF cavity system has been developed to support the high current multiple bunch beams in CESR[4]. The accelerating mode resonates at 500MHz. The impedance in the fundamental of the single cell cavity is 1/15 of the 5-cell copper cavity that it replaces. Due to the open geometry of the cell and large beam tube, the R/Q of the higher order modes is small. Furthermore, all of the higher order modes propagate along the 24cm diameter beam tube to ferrite absorbers that line that same

beam tube outside the cryostat. The Q values of higher order modes are less than ~ 100.

RF power is transmitted into the cavity through a waveguide input coupler and a planar ceramic waveguide window. The cavities are designed to operate at a gradient of up to 10MV/m while transmitting 325kW to the beam. Four cavities will support a 1A beam with a bunch length of 13mm.

The second superconducting cavity was installed in CESR in October 1998. Within a month of installation the new single cell cavity was delivering 220kW to a 550mA stored beam. In February 1999, the remaining multicell cavities were removed from the ring and a third SRF cavity installed. The principle objective of the April 1999 commissioning run, is to determine the threshold for longitudinal multibunch instabilities, in a machine with exclusively single cell superconducting cavities. The fourth SRF cavity will be installed in CESR in August 1999.

5 BEAM-BEAM PERFORMANCE

The zero current vertical beam size is a result of residual transverse coupling and it may evolve a current dependence due to the existence of synchro-betatron sidebands of the horizontal and vertical difference resonance. Displacement of the orbit from the midplane of the sextupoles is an important source of coupling. The coupling introduced by the experimental solenoid is compensated by rotations of the interaction region quadrupoles. The crossing angle configuration results in an equal but opposite horizontal displacement of the beams in the rotated quadrupoles which effects an equal but opposite vertical kick on the electron and positron beams. Errors in the solenoid compensation can yield differential vertical displacement of the beams at the IP and through the arcs.

In CESR there is no straightforward mechanism for independently adjusting the vertical orbits of the two beams. Vertical separators located about the crossing point diametrically opposite the interaction region provide some leverage. But any such remote adjustment of the vertical orbit at the IP necessarily involves an intervening orbit ripple that extends through the machine arcs and in particular through the sextupoles. During the most recent running cycle, diagnostic instrumentation and software has enabled us to systematically correct the solenoid compensation so that collisions can be maintained without distorting the vertical orbit in the machine arcs [5].

The displacement of the trajectories of the counterrotating beams in the distributed sextupoles results in distortion of the lattice functions. The effective focal length of a sextupole is proportional to the beam displacement, and since electrons and positrons are displaced in opposite directions, the distortion is different for the two beams. We have found that beam-beam performance is especially sensitive to details of the sextupole distribution, (all of the CESR sextupoles are powered independently) and have developed analytic algorithms for creating the distribution. In partic-

286

ular, sextupoles are chosen that will minimize dependence of β-functions on pretzel amplitude, energy offset, and horizontal betatron amplitude, and of coupling parameters on vertical betatron amplitude. Of course it is not possible to simultaneously eliminate all of the dependencies. A compromise is guided by simulations and experiments.
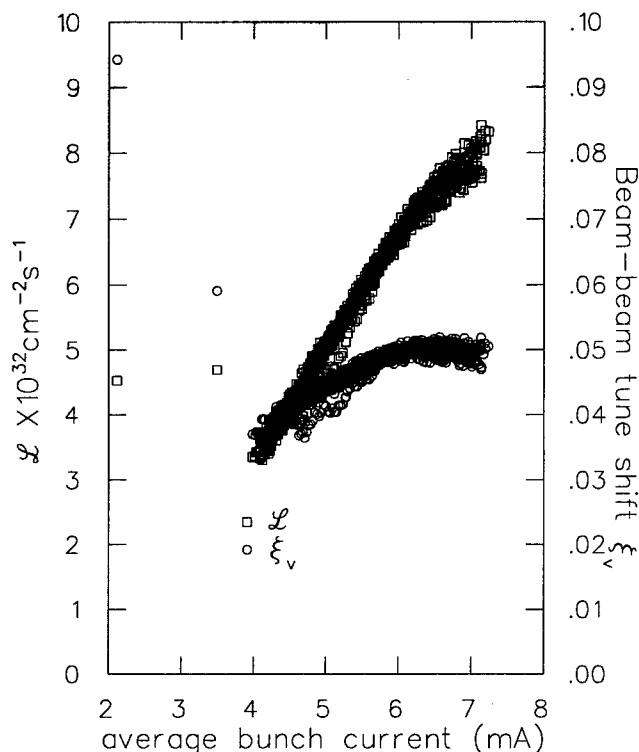
Figure 3: Luminosity and beam-beam tune shift parameter vs bunch current.
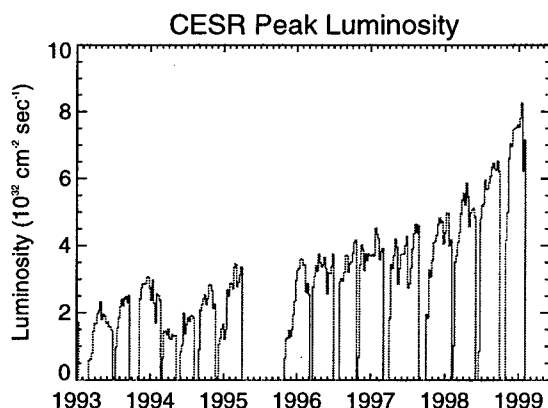
Figure 4: Peak luminosity during the course of the upgrade

The measured current dependence of luminosity and beam-beam tune shift parameter is shown in Figure 3. The peak luminosity, indicated in Figure 4, and daily integrated luminosity have continued to rise with increasing beam current and beam-beam tune shift parameter. The maximum total beam current brought to collision is 530mA.

The parameters describing the CESR configuration (CESR Phase II) and performance in early 1999 are summarized in Table 1. For the 1998 calender year CESR integrated $4442pb^{-1}$. In December, 1998 CESR delivered $750pb^{-1}$ to the CLEO detector.

6 PHASE III

The CESR Phase III design parameters are summarized in Table 1. With four superconducting RF cavities, CESR will have the capability to store 500mA/beam in nine trains of as many as 5-12 bunches. After the installation of the superconducting IR quadrupoles [6] in 2000, the practical minimum β_v^* will be limited by the natural bunch length to 13mm. A beam-beam tune shift parameter of $\xi_v \sim 0.04$, and 500mA/beam yields a luminosity $\sim 1.7 \times 10^{33} \, \mathrm{cm}^{-2}\mathrm{s}^{-1}$. CESR operates at present with a tune shift parameter of $\xi_v = 0.05$, 260mA/beam and $\beta_v^* = 18$mm. If we can preserve the high tune shift with the increased beam current and reduced β^*, the luminosity will exceed $2 \times 10^{33} \, \mathrm{cm}^{-2}\mathrm{s}^{-1}$.

Table 1: CESR Parameters

	January 1999	Phase III 2000
beam energy[GeV]	5.289	5.289
5-cell copper cavities	2	0
single cell SRF cavities	2	4
RF accelerating voltage[MV]	6.0	7-12
β_v^*[mm]	18	13
natural bunch length[mm]	19	13
number of bunch trains	9	9
number of bunches/train	4	5-10
bunch spacing [ns]	14	6-14
peak colliding beam current [A]	0.550	1
crossing angle [mrad]	2.3	2.7
vert tune shift param	0.05	0.04
luminosity[$\times 10^{32} \mathrm{cm}^{-2}\mathrm{s}^{-1}$]	8.3	> 17

7 REFERENCES

[1] Billing,M., et al., Observations of Longitudinal Coupled Bunch Instability in CESR, these proceedings.

[2] Fromowitz,D., CON 97-10, August 1997.

[3] J.Sikora et al., Longitudinal Feedback at CESR, these proceedings.

[4] Belomestnykh, S., The High Luminosity Performance of CESR with the New Generation Superconducting Cavity, these proceedings.

[5] D. Sagan, D. Rubin, and S. Greenwald "Betatron Phase Measurements in CESR" Proc. 1996 European Part. Acc. Conf., pg. 1335 (1996)

[6] S. Henderson, et al. CESR Phase III Interaction Region, these proceedings

COMMISSIONING OF THE KEKB B–FACTORY

K. Akai, N. Akasaka, A. Enomoto, J. Flanagan, H. Fukuma, Y. Funakoshi, K. Furukawa, J. Haba,
S. Hiramatsu, K. Hosoyama, N. Huang*, T. Ieiri, N. Iida, T. Kamitani, S. Kato, M. Kikuchi,
E. Kikutani, H. Koiso, S.–I. Kurokawa, M. Masuzawa, S. Michizono, T. Mimashi, T. Nakamura,
Y. Ogawa, K. Ohmi, Y. Ohnishi, S. Ohsawa, N. Ohuchi, K. Oide, D. Pestrikov†, K. Satoh,
M. Suetake, Y. Suetsugu, T. Suwada, M. Tawada, M. Tejima, M. Tobiyama, N. Yamamoto,
M. Yoshida, S. Yoshimoto, M. Yoshioka, KEK, Oho, Tsukuba, Ibaraki 305-0801, Japan,
T. Browder, Univ. of Hawaii, 2505 Correa Road, Honolulu, HI 96822, U.S.A.

Abstract

The commissioning of the KEKB B–Factory storage rings started on Dec. 1, 1998. The two rings both achieved a stored current of over 0.5 A after operating for four months. The two beams were successfully collided several times. The commissioning stopped on Apr. 19, taking a 5-week break to install the Belle detector.

1 BRIEF HISTORY OF THE COMMISSIONING

The KEKB B–Factory[1] consists of two storage rings, the LER (3.5 GeV, e^+) and the HER (8 GeV, e^-), and the injector Linac/beam-transport (BT) system. The Linac was upgraded from the injector for TRISTAN, and was commissioned starting in June 1997, including part of the BT line. The injector complex was ready before the start of commissioning of the rings.[2]

Figure 1 shows the growth of the stored currents in the two rings through the period of commissioning. The first storage of the HER and LER were on Dec. 13 and Jan. 14, respectively. The initial rise of the intensity was quite good in both rings. This figure also shows several breaks, the scheduled one (for new-year holidays) and the unscheduled shutdowns. The total length of breaks were more than one month. So far both rings have achieved stored currents more than 0.5 A, which corresponds to 20% (50%) of the design goal of the LER (HER). The maximum current of the HER is limited by the rf power available from the number of cavities currently installed. On the other hand, LER's maximum current seems to be limited by the vertical beam blow-up due to a muti-bunch instability, as shown later.

Two major unscheduled shutdowns were experienced during this period. One was an accident related to a false fire alarm at the end of January, which had nothing to do with the beam operation. Another break at the end of February was the melt-down of a vacuum chamber in the HER near the interaction point (IP) due to synchrotron radiation. The synchrotron radiation produced in the outgoing superconducting quadrupole (QCS) hit the chamber as a result of radiation background tuning with a large-angle bump orbit. The chamber was replaced in 3 weeks with a new heat-resistant design.

---

* visiting from IHEP, China.
† visiting from BINP, Russia.

288
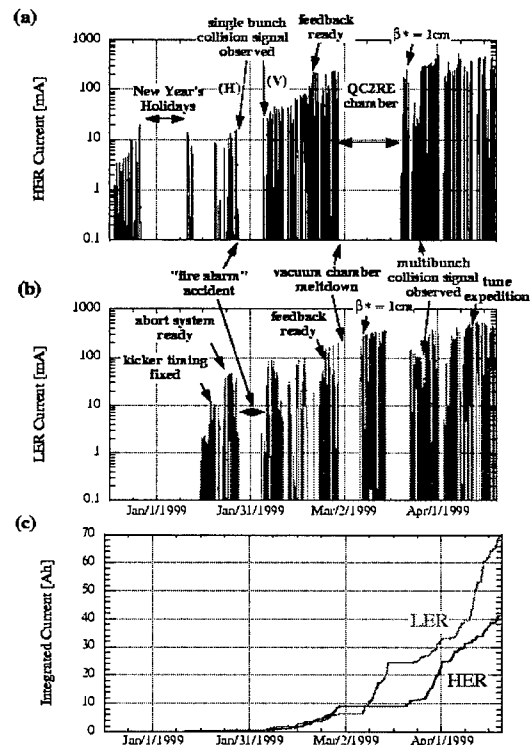
Figure 1: The stored beam currents, in log scale, during the commissioning are shown in HER (a) and LER (b). Several significant events are also shown. The integrated beam current is shown in (c).

Table 1: e^+ Linac/Beam Transport

Item	Design	Achieved	
Energy	3.5	4	GeV
Charge@e^+ target	10	10	nC
Charge@end of Linac	0.64	0.6	nC
Charge@end of BT	0.64	0.4	nC
Repetition	50	50	Hz
Emittance	0.25	0.4	μm

2 PERFORMANCE

Tables 1–4 list the main machine parameters achieved during this period, in comparison with the design values.

Table 2: LER

Item	Design	Achieved	
Energy	3.5	3.5	GeV
Beam current	2.6	0.54	A
Bunch current	0.52	2.3	mA
Bunches	5000	1024	
β_x^*/β_y^*	33/1	100/1.0	cm
ν_x/ν_y	45.35/44.41	45.27/44.18	
Rf voltage	8	4.8	MV
ν_z@4 MV	0.0118	0.0110	
Injection efficiency	100	80	%
Lifetime@0 A	14	>8	hour

Table 4: HER

Item	Design	Achieved	
Energy	8	8	GeV
Beam current	1.1	0.51	A
Bunch current	0.22	4	mA
Bunches	5000	800	
β_x^*/β_y^*	33/1	100/1.1	cm
ν_x/ν_y	44.53/42.20	44.65/42.1	
Rf voltage	20	9	MV
ν_z@8 MV	0.0119	0.0114	
σ_z@0 mA	5.6	5.6	mm
Injection efficiency	100	80	%
Lifetime@0 A	45	>8	hour

Table 3: e⁻ Linac/Beam Transport

Item	Design	Achieved	
Energy	8	8.5	GeV
Charge@end of Linac	1.2	1.2	nC
Charge@end of BT	1.2	1	nC
Repetition	50	50	Hz
Emittance	<0.1	0.06	μm

2.1 Lattice

The commissioning started with a $\beta_y^* = 2$ cm lattice, and later switched to $\beta_y^* = 1$ cm at the time shown in Fig. 1. No degradation in injection efficiency, maximum current, or lifetime was observed in either ring with the $\beta_y^* = 1$ cm optics. As for β_x^*, only 100 cm has been tried so far for either ring.

The ring lattices have been understood for the basic parameters such as tunes, β-functions, dispersions, etc.[3] The betatron tunes have been searched to optimize the injection efficiency, maximum current, beam profile, and the noise in the pilot detector at the IP, BEAST. So far the two rings have been operated at different betatron tunes, since they have been optimized independently. They will be adjusted if necessary for the beam-beam effect. Those tunes are also different from the design tunes which were optimized by beam-beam simulation. The simulation suggests a point, $(0.52, 0.08)$, which is very close to the integer or half-integer resonances. It has, however, been difficult to access such a location with the current size of the betatron stop bands (~ 0.05).

One of the discrepancies in the lattice between the model and the measurements is the differences of the betatron tunes as shown in Tables 2 and 4. They are bigger in the LER, and the calibration of the superconducting quadrupoles at the IP, which are common to both LER and HER, relative to the iron quadrupoles is under investigation. The super- and normal conducting magnetic measurements were done independently.[4] An analysis using single kicks of the corrector dipoles all around the ring was done.[5] It shows a mismatch of the β-functions in both rings of 20–50%, while the measured β^*s are sufficiently close to the model. It is speculated that the mismatch of the betas should bring an error in chromaticities, which currently differ from the model by a factor of 2–5. The higher order chromaticity is also somewhat different from that of the model.

Though such differences are seen, the measured transverse dynamic aperture is at least larger than the physical aperture. The longitudinal acceptance of the LER is about $\pm 1.5\%$ which is smaller than the model ($\pm 2.5\%$). This can be a source of injection background in the LER, which is a few times higher than that in the HER.

The x-y couplings of the rings are roughly corrected by vertical bump orbits at strong sextupoles, looking at the effect of a single kick in one plane on the orbit in the other plane.

So far no problem has been seen related to the alignment of the rings. The circumferences of the rings are different from the design by about 5 mm, and their relative difference was only 0.3 mm. The offset of HER's circumference was corrected by choosing the rf frequency (including the Linac), then the LER's was adjusted to the HER's using chicanes. In the initial stage of commissioning, a turn-by-turn beam position/phase monitor (TBTM) played an important role in detecting the path length via phase oscillation.

2.2 Orbit Fluctuation

One of the biggest issues, unanticipated at the design stage, is fluctuations of the closed orbit. Two kinds of fluctuation, both in the vertical direction, have been observed so far. The first one is a slow drift. The vertical closed orbits of the rings drift randomly by typically 1 mm/hour at the IP quads, or 0.2 mm/hour in the arc section. The drifts in the two rings are highly correlated and the magnitudes are roughly equal. Orbit analysis locates the source at the quadrupoles at the IP, but it was hard to distinguish whether one or all of them are responsible. Also, a correlation with the ambient temperature around the IP is observed (fig. 2). The amount of drift translates into an offset at the IP of 5 μm/hour, whereas the design beam size is 1.4 μm. The
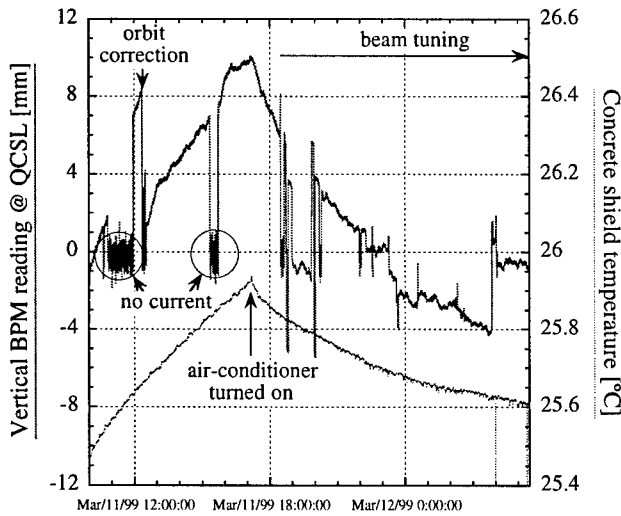
Figure 2: The change of orbit (upper trace) and the temperature of the concrete shield structure (lower) at the IP. These data were taken on Mar. 11 for about 20 hours, after switching off the air-conditioner in Tsukuba hall around the IP. The air-conditioner was turned on in the middle. Though orbit correction was applied several times during this period, a clear correlation between the orbit and the tempereture is seen.

drift is also large enough to increase the background and degrade the injection efficiency. To cure the drift a continuous closed-orbit correction system has been applied to both rings to maintain the orbit at the beam-position monitors(BPMs), and has been so far found effective.

The second kind of orbit fluctuation is a vertical vibration of the orbit at about 14 Hz. The amplitude of the vibration is about 100 μm_{pp} in the arc, and continues with constant amplitude for hours or days. Sometimes it stops for hours and then restarts. Both rings have similar vibrations, but they are not synchronized and their frequencies are slightly different. Orbit analysis points to a source around the IP, but it has not yet been identified. This vibration can make the two beams miss each other vertically by a few sigma. A collision feedback responding rapidly enough will be necessary.

2.3 High Intensity

The LER is equipped with 12 ARES copper cavities, and the HER 6 ARES and 4 superconducting cavities. So far the number of rf cavities installed in the rings is enough to store about half of the design intensity. The HER has already reached this limit. Both rf systems have been working quite well and the down time due to rf has been quite small.

At the initial stage of commissioning, the baking of the vacuum chamber is the most important task in any electron-positron storage ring. Figure 3 shows how the photo-desorption coefficient has improved as the integrated current has increased. These curves basically fit the expec-
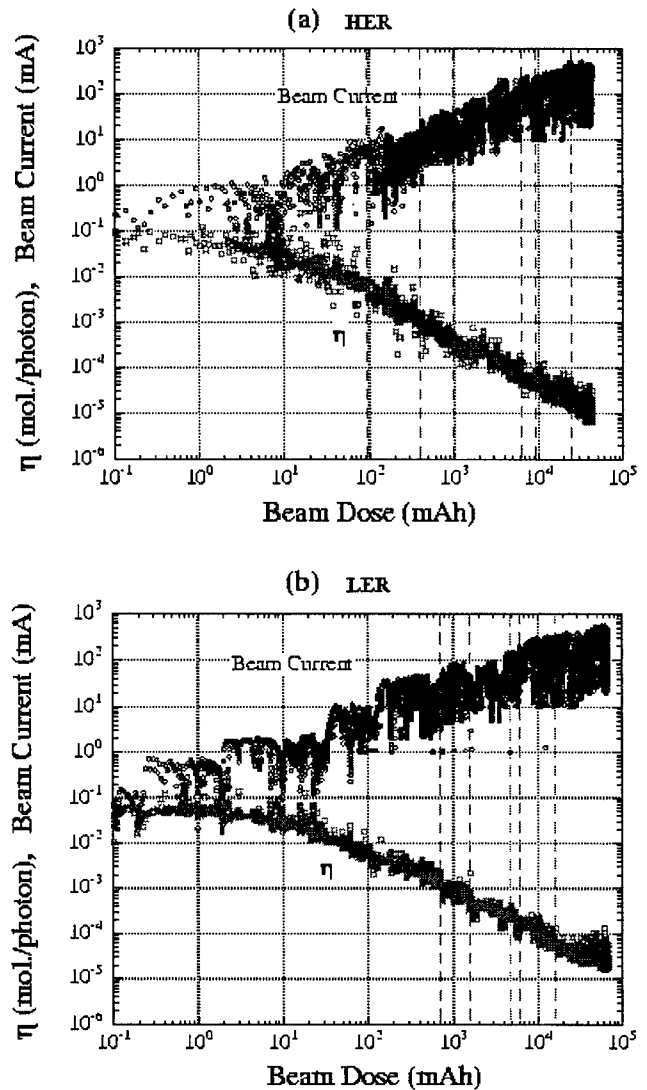
Figure 3: The photo-desorption coefficient (lower trace) and the beam current (upper trace) versus the integrated beam current for HER (a) and LER (b). The vertical dashed lines indicate the timings of the conditioning of the NEG strip modules.

tation very well, so the baking of the chambers has been successful so far.

The beam lifetime is so far determined by the vacuum pressure. The lifetime extrapolated to zero current is longer than 8 hours. It matches the design numbers shown in Table 2 and 4 to within the accuracy of the extrapolation. The lifetime of the LER is decreased at high current when the vertical masks are closed. This is due to a blow-up of the vertical size caused by a mutibunch instability, described below.

An abrupt decay of the lifetime has been observed in the HER below 200 mA. A possible explanation is dust-trapping. Spikes in the background have also been reported by the BEAST, which are correlated to the presumed dust events. An interesting phenomenon noticed in the BEAST was a "micro-dust event" which looks similar to a larger

dust event but is too small to be evidenced in the lifetime. These dust events decrease at higher current.

2.4 Instabilities

Single bunch currents can be stored much at higher than the design value with sufficient margin. No disastrous instability or bunch-lengthening has been seen.

The LER and HER have been operated in multi-bunch mode mostly with 10 ns bunch spacing. Both rings have a bunch gap of about 10% for the rise of the abort kicker. Usually the HER has 4–7 more gaps (i.e., bunch-trains) for clearing ions.
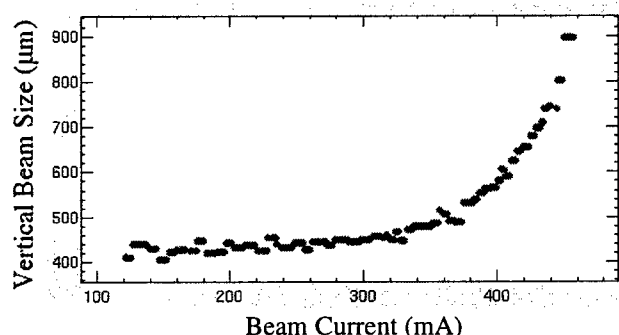
Figure 4: The vertical beam size of the LER measured by the synchrotron radiation interferometer as a function of the beam current. The bunch-by-bunch feedback was turned off.

Several multi-bunch instabilities have been observed in both rings, but none of them has an identified source yet. The LER sees an excitation of longitudinal oscillation, with its strength depending on the *betatron* tunes. With a particular choice of betatron tunes, the LER accumulated 440 mA without bunch-by-bunch transverse feedback.[6] At bad tunes, the oscillation starts at about 10 mA, but at the best tune, only at 350 mA or higher. At bad tunes, vertical oscillation was observed simultaneously, so the bunch-by-bunch feedback was effective in such cases. The threshold depends on the vertical closed orbit, vertical dispersion, and vertical chromaticity. It is unknown what the relation is between the longitudinal and the vertical instabilities.

An important phenomenon in the LER is a blow-up of the vertical beam size at $I \geq 350$ mA (Fig. 4), observed by the synchrotron light monitor,[7] using both direct imaging and interferometry. The observed vertical size, translated to emittance assuming the design β_y, reaches $\varepsilon_y/\varepsilon_x \gtrsim 1$ at $I = 500$ mA. Though the beam size increases as the current, no vertical oscillation was seen. Among suspected sources of the blow-up are vertical dispersion and synchrotron oscillations, but these are not yet confirmed. This vertical blow-up eventually limits the stored current by hitting the vertical masks in the arc. No pure-transverse instability has been seen in LER up to 500 mA.

In the HER, there is a strong vertical instability over 100 mA. The bunch-by-bunch feedback is very effective

for this instability. Without the feedback, usually the tails of the bunch-trains are lost. Dependences on the tunes, orbit, synchrotron motion, bunch fill pattern, etc., are under investigation.

2.5 Injection

The injector linac has already achieved its design performance, at least for the short term.[2] There remain a number of issues related to long-term stability and repeatability. A difficult problem is switching the same linac between four modes (KEKB e$^-$, KEKB e$^+$, PF, PF-AR) which need different settings of rf, magnets, and even different guns. Further improvement in the injector is necessary.

3 COLLISION

Table 5: Parameters of the multi-bunch collision in Mar. 1999. Beam sizes are obtained from the beam-beam scan in Fig. 5, assuming equal sizes for both beams.

	LER	HER	
Current	65	13	mA
Bunches	200	200	
σ_x/σ_y	197/4.0		μm
Lifetime	200	40	min.
Estimated luminosity	1.7×10^{31}		cm^{-2}s^{-1}

(a) horizontal scan
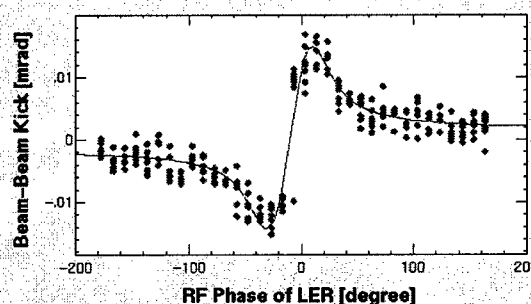
(b) vertical scan
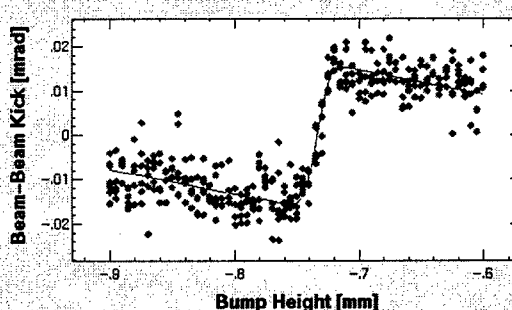
Figure 5: The beam-beam deflection in (a) horizontal and (b) vertical planes, during the multi-bunch collision in Mar. 1999. Lines are fitted curves for Gaussian bunches.

Collision of the two beams has been tried three times,[8] once per month since February. In February the first collision was done with single bunches, and horizontal and vertical beam-beam deflections were clearly observed. The horizontal deflection was detected by changing the RF phase of the LER, looking at BPM readings of the HER. Due to the finite crossing angle at the IP, the change in RF phase shifts the longitudinal collision point and the horizontal separation of the two beams. The measured horizontal offset between the beams is cancelled by use of horizontal dipole correctors. The vertical deflection was measured by scanning a vertical bump orbit in one ring, looking at the BPM signals of the other ring. It was interesting that there was a vertical offset between the two beam of 0.73 mm at the IP.

In March, a multi-bunch collision was tried with the parameters shown in Table 5. The resultant deflection curves are shown in Fig. 5. There was also a successful single-bunch collision, and the vertical offset remained the same after 50 days from the previous single-bunch collision. There was also a correlation between the beam-beam deflection and Bhabha events in the BEAST detectors. Unfortunately the orbit drift was not cured then, so it was hard to obtain a real luminosity for substantial duration.

In April there was a third trial of the collision to establish conditions with high current. This time, the orbit vibration in the LER at about 14 Hz strongly disturbed the vertical deflection signal. The vibration had disappeared fortuitously during the collisions in February and March. Also the lifetime of the LER was shortened during the vertical scan when the two beams became closer than about 30 μm. It is not known whether this loss of lifetime is related to the vibration or not. Another suspected cause of the loss of lifetime is the blowup of the vertical beam size at high current.

Optimization of the collision conditions such as tunes, orbits, beam sizes, etc. will be necessary after the roll-in of Belle.

4 DETECTOR BACKGROUND

The beam background at a detector is always a serious problem for a good and clean experiment. In an experiment with a high current collider like KEKB, it is one of the biggest concerns in two respects: radiation damage of the detector material; and high occupancy of the detector signal due to beam background.

To monitor the beam back ground during commissioning, the BEAST detector was installed around the IP chamber. It consists of 24 PIN diodes, 53 propotional counters, 10 CsI counters, 72 BGO counters and other dosimeters such as MOSFETs. Background optimization has been made by tuning the masks in the arc and at the IP, injection orbit and phase, matching wih the transport line, and so on. By a series of optimizations, the background at injection, which was the dominant source of background at the early stage of commissioning, is now comparable with the

background due to stored current. The background during storage mode is almost decided by the vacuum level inside the beam pipe and, therefore, has been gradually improved.

For the HER beam, the background measured now is nearly propotional to the beam current and not quadratic. This implies that background reduction due to vacuum improvement is reaching its limit. By energy spectral measurement of background, SR can be excluded as the dominant source of the current background. The dependence of dose on radial distance from beam indicates a somewhat uniformly distributed background component, which may be generated away from the IP. One candidate source is a hot spot down stream of the IP where several beam loss monitors exhibit large activity. Further investigations are necessary to identify and extinguish it. The LER on the other hand still exhibits a quadratic dependence of background on beam current and, therofere, the background is decreasing along with vacuum improvement. Together with the fine tuning of several parameters mentioned above, LER background in storage mode has also been reduced much and is better than the one in HER.

Although the current level of background is still higher than expected at the design stage of the BELLE detector, it becomes just possible to operate the BELLE detector in this background environment with a reasonable life time due to radiation damage. Further improvement is expected by the installation of additional arc masks for both the LER and the HER and reinforcement of shielding in front of the detector.

5 REFERENCES

[1] KEKB B–Factory Design Report, KEK–Report–95–7, (1995).

[2] Y. Ogawa et al, in these proceedings.

[3] H. Koiso et al, in these proceedings.

[4] For the iron magnets, see M. Masuzawa and K. Egawa et al, in these proceedings.

[5] Y. Ohnishi et al, in these proceedings.

[6] E. Kikutani and M. Tobiyama et al, in these proceedings.

[7] J. Flanagan and T. Mitsuhashi et al, in these proceedings.

[8] Y. Funakoshi et al, in these proceedings.

COMMISSIONING OF THE PEP-II LOW-ENERGY RING*

M. S. Zisman[†], Lawrence Berkeley National Laboratory, Berkeley, CA 94720 and T. M. Himel, Stanford Linear Accelerator Center, Stanford, CA 94939, for the PEP-II LER Commissioning Team

Abstract*[†]

The newly constructed PEP-II Low-Energy Ring (LER) is designed to store up to 3 A of 3.1 GeV positrons. It was built as a collaboration between SLAC, LBNL, and LLNL [1]. The ring was completely installed and under vacuum on July 10, 1998. First stored beam was obtained on July 16, and first evidence for electron-positron collisions between LER and HER (High-Energy Ring) beams was observed on July 23, marking the formal completion of the PEP-II project. To date, three commissioning runs have occurred, the first in July 1998 (3 weeks), the second during October–December 1998 (7 weeks), and the most recent during January–February 1999 (5 weeks). During these runs various problems were uncovered and corrected, and the stored beam current has increased from 1 mA to 1160 mA. In this paper, the final LER configuration is described and results of the commissioning runs are presented. The LER is making steady progress toward its operating current of 2.16 A.

1. INTRODUCTION

The PEP-II LER is being commissioned by a team of physicists from SLAC and LBNL. Table 1 gives the main LER parameters. The ring (see Fig. 1) is sixfold symmetric, with six FODO arcs (having 90° phase advance per cell in both planes) of 255 m connected by six straight sections of 110 m. Ring areas are designated according to the clock, with straight sections having even numbers (Regions 12, 2, 4, 6, 8, 10) and arcs odd numbers; beam direction is counter-clockwise. Optical elements are mirror symmetric about an axis between the centers of Region 8 and Region 2.

Functional units of the ring are contained in the straight sections, as indicated in Fig. 1. Except in Region 2, the

Table 1. PEP-II LER main parameters.

Energy [GeV]	3.1
Circumference [m]	2200
Emittance, y/x [nm-rad]	1.5/49
Beta function at IP, y/x [cm]	1.5/50
Beam-beam tune shift	0.03
RF frequency [MHz]	476
RF voltage [MV]	3.2
Bunch length, rms [mm]	12
No. of bunches	1658
Total current [A]	2.16
Energy loss per turn [MeV]	0.65
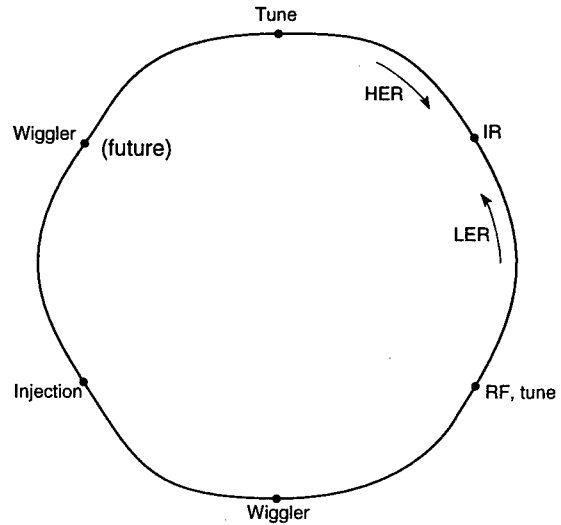
Fig. 1. Functional layout of the LER.

LER is 89 cm above the HER; in the IR the LER beam is transported downward to the plane of the HER and then restored to its normal elevation at the downstream end. A description of the lattice is found in Ref. [2].

To reach high currents with stable beam, bunch-by-bunch feedback systems operating in the time domain are employed to combat longitudinal [3] and transverse [4] instabilities. Diagnostics devices use designs common to the HER [5].

2. JULY 1998 RUN

The LER was fully under vacuum (with a few significant leaks) on July 10, 1998; injection activities commenced immediately thereafter. Considerable time was spent beforehand to check out power supplies and polarities of more than 900 magnets, with the result that only one magnet wiring error was discovered with the beam. In view of the limited commissioning time available before detector installation, and the limited optics adjustment range available from the permanent magnet IR quadrupoles, the nominal collision lattice was used from the outset.

To minimize radiation dose to the "background" detectors at the interaction point (IP), a dipole string immediately upstream of the IP was initially turned off and the DC injection bump magnets were tuned for on-axis injection (incoming orbit 45 mm above the LER median plane). Two hours after the beam first arrived at the injection point it had reached the upstream side of Region 2, nearly 1.1 km downstream. Over the next few days the beam was tuned through the complicated IR and

steered to get multiple turns. A 1 mA beam was stored on July 16, as observed with a beam position monitor (BPM) button attached to an oscilloscope and a DC current transformer (DCCT).

The main goals for this initial run were to store 50 mA of positrons, to begin characterizing the lattice and beam orbit, to commission the pulsed magnets (injection and abort kickers), and to commission key diagnostics devices, such as the BPM and beam loss monitor (BLM) systems [5] and the DCCT. By the end of the run, the total beam current had reached 53 mA and the single-bunch current had reached 5 mA (the latter being about four times higher than the design value).

Agreement between the model and measured beta functions was reasonable; differences at the IR quadrupoles were about 50%. The measured natural chromaticity of the ring was about 10% higher than expected in both planes. We ascribe this to the orbit offset in the strong LER sextupoles. (In Region 2, orbit deviations at the sextupoles were initially 15 mm, though the rms orbit in the arcs was below 5 mm. This was ultimately traced to a 3.6% error in the polynomial for the "long bends" in Region 2.)

After storing the beam and correcting the orbit, it was observed that the orbit was not centered. Vertically, it was high by about 1 mm and radially it was offset toward ring center by about the same amount. The first offset was attributed to field from circulating currents in the cable tray above the ring (later verified by post-run measurements). The second offset was ascribed to an error of 4 mm in the 2200 m circumference.

The main difficulty during this run was poor lifetime—only 3 minutes—even at low beam current. The lifetime was insensitive to steering and tunes, and was shown to be unrelated to RF acceptance. Because of the high pressure in a few locations, vacuum was hard to eliminate as the cause of the poor lifetime. However, a few "suspicious" orbit bumps were found to be necessary in Arc 11, and the BLMs nearby had elevated count rates. After the run ended, a visual inspection of the Arc 11 chamber interior showed a folded-over RF gasket that occluded much of the beam aperture. Due to poor lifetime scrubbing was minimal; only 0.5 A-hr was accumulated during the run.

3. OCTOBER 1998 RUN

During the shutdown, considerable work was done to improve the ring vacuum. Major leaks were found and repaired, though a few small ones remained. For this run, the goals were to store a beam current of 250 mA and to reach a lifetime of 1 hour at 150 mA. Other important goals included correcting the rms orbit below 1 mm and commissioning the newly installed synchrotron light monitor along with the longitudinal and transverse feedback systems.

Comparison between HER and LER orbits showed that both rings were too large by about the same amount and a 1 kHz reduction in the RF system master oscillator frequency was made to center the orbit. (To keep the rings phase-locked to the SLAC linac, a corresponding –6 kHz adjustment was made to the linac frequency.) Subsequently, the LER rms orbit was corrected to less than 1 mm in both planes. (The vertical orbit was corrected, despite the cable tray current, with an algorithm that does not minimize corrector strengths.) Later, it became apparent that the LER (and HER) showed mm-scale orbit motion near the IP resulting from thermal motion of the magnet supports along with thermal flexing of various IR beam pipes, which causes slight magnet motion. (At high beam currents, various HER IR thermocouples show significant, though not extreme, temperature increases. This is due to two effects: synchrotron radiation fans from upstream HER dipoles striking uncooled stainless steel portions of the HER vacuum chamber, and strong LER synchrotron radiation fans from the B1 separation dipoles near the IP illuminating the upstream HER beam pipes.) The orbit change in each ring is correctable with a single corrector near the IP and we implemented orbit feedback loops to control the motion. This behavior should improve when *BABAR* comes on line due to changes in the vacuum chambers (bellows added to provide a "frangible link") and better thermal stabilization with the detector present.

To improve the beam quality for collisions, we decoupled the ring with the global skew quadrupoles. Once the beam was well centered in the sextupoles, it was routinely possible to reach a closest tune approach of ≤0.001. Dispersion steering was also done, reducing the residual vertical dispersion in the arcs to about 10 mm.

Both the longitudinal and transverse feedback systems were made operational during this run. The beam was longitudinally stable up to about 300 mA but did show evidence for some "mode-0" oscillation amplitude, driven by the RF system. (The so-called woofer link between the longitudinal feedback and RF systems had not yet been implemented.) The transverse feedback system also showed no evidence for strong coupled-bunch motion aside from the resistive-wall instability. The newly installed LER synchrotron radiation monitor proved very useful in diagnosing beam instabilities as the current was increased, but its mirror is distorted sufficiently to prevent a good determination of the vertical beam size.

During the run, the beam lifetime measured at low current (≈1 mA) reached 100 minutes; a beam lifetime of 63 minutes at 150 mA was also reached. By the end of the run in December, a beam of 415 mA was stored, and scrubbing of the vacuum chamber reached 20 A-hr.

4. JANUARY 1999 RUN

This period marked the final commissioning period before *BABAR* comes on line. The main goal was to reach a high beam current, 1100 mA, with beam stability sufficient for

luminosity-producing collisions. (Maximum beam current was limited by the interim Q2 vacuum chambers; these are now being replaced to permit full-current operation.) As seen in Fig. 2, the beam current increased steadily during the run; a stored positron beam current above 1 A was reached on February 12. At the end of the run, 1160 mA was stored in the LER, making it presently the world's highest current positron ring. The integrated current has reached 153 A-hr. Unfortunately, there was an accidental vent in one arc (not beam related) one week prior to the end of the run. After resuming operation, the lifetime recovered to its earlier value (1 hour at 700 mA) but did not further improve. During collision tests, a 680 mA LER beam colliding with a 350 mA HER beam produced a measured luminosity of 5.2×10^{32} cm^{-2} s^{-1}.

The woofer link from the longitudinal feedback system to the RF system was commissioned and it reduced the mode-0 motion to below 0.01°. This was important in reaching the highest beam currents. Evidence was seen for true longitudinal coupled-bunch motion at high currents; the growing modes are mainly consistent with expectations based on meas ' RF cavity modes.

At high currents, we find that the pressure readings of the vacuum pumps increase markedly (see Fig. 3). The observed effect is sensitive to the fill pattern, with a larger number of bunches showing less increase. All pumps exhibit such behavior, with the straight sections being worse. The increase is clearly a real pressure rise, as the beam lifetime decreases and the background detectors in Region 2 show a corresponding increase and the same bunch pattern dependence. We believe the pressure rise is due to a pressure-bump phenomenon in which secondary electrons (or possibly ions) desorb gas locally from the chamber walls. There is evidence that scrubbing alleviates the effect, since the arcs show less pressure rise than the straight sections, and the upstream part of a straight section (which is illuminated by synchrotron radiation) is better than the downstream part that has no scrubbing.

5. SCHEDULE AND PLANS

The next run will be from May–August 1999. For the LER, the main goals will be to continue scrubbing, to
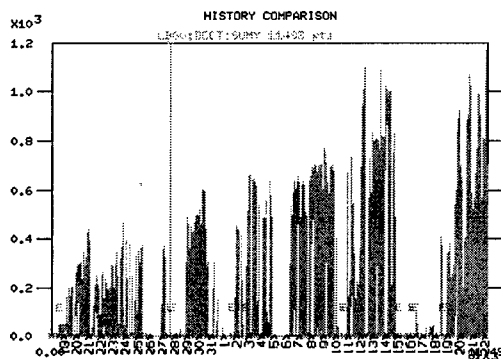
Fig. 2. LER beam current vs. time during run.
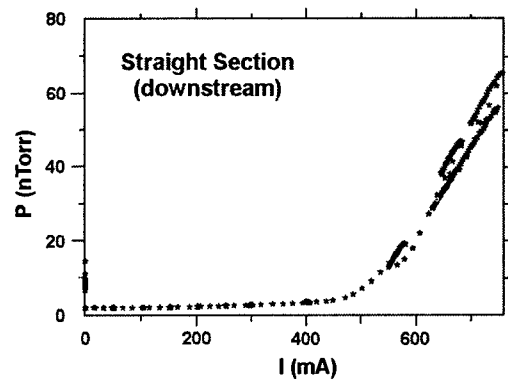
Fig. 3. Pressure in straight section vs. beam current.

reduce detector backgrounds (with improved injected beam quality, with collimators, and possibly with a solenoidal field to suppress the anomalous pressure rise), and to continue optimizing the luminosity. During this run we hope to reach a luminosity of 1×10^{33} cm^{-2} s^{-1}.

6. SUMMARY

LER commissioning is well under way, following in the footsteps of the very successful HER program. Thus far, there have been few surprises. We see no large instabilities, no major misalignments or aperture restrictions, and component heating is modest. Scrubbing is proceeding well, though we have a recurring problem with small leaks at the arc chamber flange joints.

7. ACKNOWLEDGMENTS

LER performance thus far is a testimony to the care with which ring components were fabricated and installed. The engineering and technical staffs of PEP-II deserve the credit for this. Equally important to rapid commissioning are the skill and effort of our colleagues on the LER Commissioning Team; successes reported here are theirs.

8. REFERENCES

[1] PEP-II Conceptual Design Report, ed. M. Zisman, LBL-PUB-5379, SLAC-418, CALT-68-1869, UCRL-ID-114055, UC-IIRPA-93-01, June 1993.

[2] Y. Cai et al., "Low Energy Ring Lattice of the PEP-II Asymmetric B Factory, Proc. of 1995 Particle Accel. Conf., p. 576.

[3] J. Fox et al., "Observation, Control, and Modal Analysis of Longitudinal Coupled-Bunch Instabilities in the ALS via a Digital Feedback System," Proc. of 1996 Beam Instrumentation Workshop, Argonne, IL, May 1996, p. .

[4] W. Barry et al., "Design of the PEP-II Transverse Coupled-Bunch Feedback System," Proc. of 1995 Particle Accel. Conf., p. 2681.

[5] A. S. Fisher, "Instrumentation and Diagnostics for PEP-II," Proceedings of the Beam Instrumentation Workshop, Stanford, CA, May 1998, AIP Conference Proceedings 451, p. 95.

BEAM-BEAM COLLISIONS AT THE PEP-II *B* FACTORY[*]

M. Sullivan[#], Y. Cai, M. Donald, S. Ecklund, T. Fieguth, C. Field, A.S. Fisher, L. Henderson,
T. Himel, P. Krejcik, G. Mazaheri, M. Minty, I. Reichel, J. Seeman, U. Wienands,
Stanford Linear Accelerator Center, Stanford University, Stanford, CA 94309
J. Corlett, M. Zisman, Lawrence Berkeley National Laboratory, Berkeley, CA 94720
W. Kozanecki, DAPNIA-SPP, CEA-Saclay, F91191 GIF-SUR-YVETTE, France
M. Placidi, A. Hofmann, CERN, CH-1211 Geneva 23, Switzerland

Abstract

We describe first beam collisions at the PEP-II *B* Factory, a collaboration of SLAC, LBNL, and LLNL. The beams are brought close to each other in the transverse (x,y) and longitudinal (timing) directions through the use of two shared beam position monitors located 0.72 m from either side of the interaction point (IP). Transverse beam-beam deflection scans and the use of a zero-angle luminosity detector allow us to center the collisions. Beam collisions were also seen by exciting one beam at its tune frequency and observing a response in the other beam at the same frequency. Shifts in betatron tunes have also been measured. To date, the peak measured luminosity attained is $5.2\pm1\times10^{32}$ cm^{-2} s^{-1} with 786 bunches in each beam and with beam currents of 354 mA for the high-energy beam (HEB) and 680 mA for the low-energy beam (LEB).

1 PEP-II

PEP-II [1], an asymmetric-energy two-storage-ring accelerator, is designed to allow the study of the decay channels of the Upsilon (4S) resonance from a boosted center-of-mass system. The boost permits the separation in time of the decay of the matter and anti-matter B mesons the 4S produces thereby allowing one to look for asymmetries in the decay-time distributions of these mesons and hence a violation of CP conservation.

The high-energy ring (HER) was completed first and a beam was stored in the ring in June of 1997. The low-energy ring (LER) and the final interaction region beam pipes and magnets were finished and installed in July of 1998 with beam stored in the LER shortly thereafter. Table 1 lists some of the PEP-II design parameters.

The PEP-II interaction region, shown in figure 1, employs two strong horizontal bending magnets (B1) located ±21 cm from the IP to bring the beams into a head-on collision. On either side of the IP, the beams also pass through a shared quadrupole (QD1) which is centered on the HEB. This design places the LEB off-axis in this shared defocusing quad which further horizontally separates the two beams prior to the beams entering separate

Table 1. PEP-II IP design parameters.

	HER	LER
Energy (GeV)	8.9732	3.1186
Current (A)	0.75	2.15
β_x^* (m)	0.50	
β_y^* (m)	0.015	
σ_x (μm)	155	
σ_y (μm)	4.7	
Σ_x (μm)= $\sigma_x \sqrt{2}$	220	
Σ_y (μm)= $\sigma_y \sqrt{2}$	6.6	
ξ_x and ξ_y	0.03	
Revolution freq. (kHz)	136.311	
Bunch spacing (m)	1.26	
Number of bunches	1658	
Bunch luminosity (cm^{-2}s^{-1})	1.8×10^{30}	
Total luminosity (cm^{-2}s^{-1})	3×10^{33}	

vacuum chambers. The next three magnets on either side of the IP are septum quadrupole magnets where one of the beams travels through a field-free region while the other is focused either horizontally or vertically. The first of these magnets (QF2) is a focusing magnet for the LEB and completes the final focus doublet for the LEB. The next two magnets (QD4 and QF5) are the final focus doublet for the HEB with the shared QD1 magnet supplying additional vertical focusing [2].
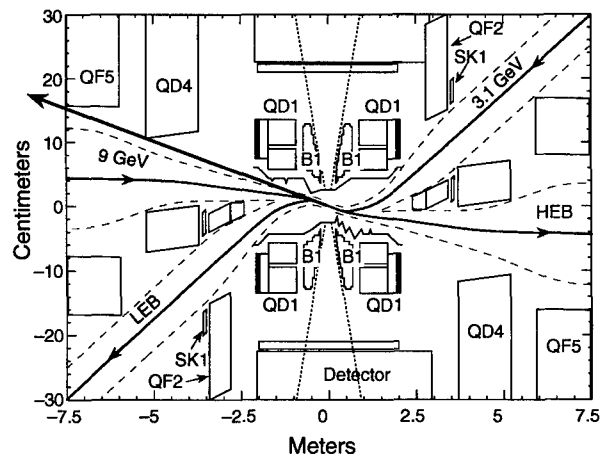
Figure 1. Layout of the interaction region. Note the expanded transverse scale. The large thick arrow leaving the IP denotes the direction of the radiative Bhabha photons used for measuring luminosity.

[#]email: Sullivan@SLAC.Stanford.edu

Luminosity is measured by detecting radiative Bhabha photons emitted by incoming positrons. The photon travels along the collision axis and exits the beam pipe of the incoming HEB at about 9 m from the IP. The photon is detected in a Pb-shielded fused-silica Cherenkov detector[3,4]. Figure 1 shows the direction of the radiated photons observed by the luminosity detector. Photons emitted by beam-gas bremsstrahlung produce a background for the luminosity detector. However, the strong B1 bending magnets close to the IP restrict this background to beam-gas events generated within ±30 cm of the IP.

2 COLLISION RUNS

Several blocks of time during each running period were dedicated to collision studies.

2.1 July 1998, First evidence for collisions

Our first collisions were attempted on July 23rd and 25th. The low LER beam lifetime (1-2 min.) required constant injection of positrons into the LER. We saw evidence of collisions by scanning one beam through the other transversely and observing beam loss in the LER, indicating that the LEB was being disrupted by the HEB. The LEB lifetime degraded as the beams started to pass through each other, then it recovered when the horizontal scan centered the beams and degraded again while the beams were moving out of collision. We also observed a hint of a collision signature in beam-beam deflection scans. In another test, we transversely excited the HER at one of the tune frequencies and saw the signal transferred to the LER frequency spectrum. We saw no signal in the luminosity detector at this time, however, later analysis indicated that the collision axis was not pointed at the detector.

2.2 Fall 1998 run, November-December

During the fall there were a total of five collision runs each lasting about two days.

On Nov. 10, the first collision run of the fall, we observed a luminosity signal in the detector and saw definite beam-beam deflections. Σ_x and Σ_y, defined as follows:

$$\Sigma_x \equiv \sqrt{\sigma^2_{x-} + \sigma^2_{x+}} \text{ and } \Sigma_y \equiv \sqrt{\sigma^2_{y-} + \sigma^2_{y+}},$$

were both measured by scanning one beam through the other and recording the luminosity signal. Most of the time Σ_x was measured to be close to the design value of 220 μm. However, Σ_y started out high at 40 μm. Throughout the fall running Σ_y was successfully made smaller by improving the optics and decreasing the vertical dispersion in each ring. By the end of the fall run Σ_y was consistently in the range of 11-14 μm.

At the start of each collision run, the collisions were tuned up with a single bunch in each beam. Then, multibunch collisions were tried, first 11 on 11, then 36×36

(60 m spacing), 87×87 (22.7 m spacing) and finally 261×261 (7.56 m spacing). In all multibunch cases, the luminosity scaled with the number of bunches. The highest luminosity for the fall was 8.9×10^{31} cm^{-2}s^{-1}.

Much of the time during collisions was spent studying luminosity and beam size as a function of bunch currents. It appears that when the HEB bunch current gets near or above 0.5 mA the LEB lifetime drops significantly and the beam size "blows up" particularly in x. This corresponds to a subsequent roll-off in luminosity as the HEB current is increased past the 0.5 mA per bunch value. We have tried raising the LER bunch current to find a value that upsets the HER, but instead have found that for high LER bunch currents (up to 3 mA) the LER lifetime seems to fall off at lower (about 0.4 mA) HER bunch currents.

Most of one entire collision run (about 5 shifts) was devoted to exploring various tune-plane working points. Each ring was separately moved from the design value to a new working point to see if this improved the luminosity per bunch. No immediate improvement was seen.

A feedback loop designed to keep the beams in collision by optimizing the luminosity signal was also commissioned in December.

The measured luminosity and the luminosity calculated from the beam currents and from two different methods for finding the transverse beam sizes (transverse luminosity scans and beam-beam deflections) yielded consistent results as long as the e$^-$ current was below 0.5 mA/bunch.

2.3 Winter 1999 run, January-February

There were two main collision runs in the winter: Feb. 4-8 and Feb. 19-22. The first run investigated a new working point for the LER that was below the diagonal in the tune plane. This new point proved to be a significantly better place for the LER; it produced the luminosity record of 5.2×10^{32} cm^{-2} s^{-1} with 680 mA of e$^+$ and 354 mA of e$^-$ in 786 bunches and with a Σ_y of 12 μm.

The last collision run concentrated on lowering Σ_y by systematically reducing the vertical dispersion and coupling in each ring and by vertically aligning the beams at the IP. The result was a record minimum Σ_y of 8.6 μm with a consistent value between 9-11 μm. Figure 2 shows a typical vertical beam scan.

The design fill pattern (1656 bunches) has parasitic crossings (PCs) at ±0.63 m from the IP. In order to study Pcs, fill patterns with PCs (1656×1656 and 1048×1048) were tried. The 1048 fill pattern has every third bunch of the design pattern empty generating a series of mini-gaps around the entire ring. PC effects are not strong. More time is needed to determine if PCs influence the performance of the machine.

3 SOME RESULTS

Here we list some of the results from the collision runs. In most cases we would store a relatively high LEB current
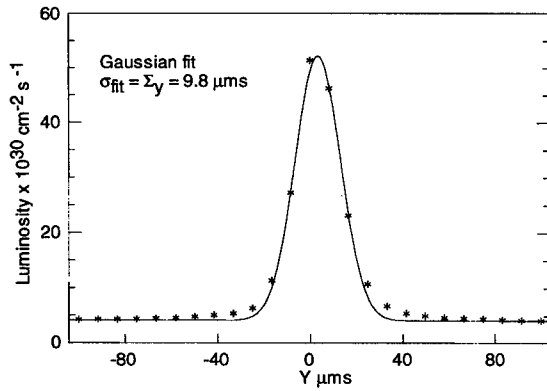
Figure 2. Plot of a typical vertical beam scan. The σ is the fitted Gaussian sigma. The background level is quite low for all measured values of luminosity.

and then start with a low HEB current and record Σ_x, Σ_y and luminosity as a function of increasing HEB current. Figure 3 is a plot of the measured luminosity as a function of increasing HER current and figure 4 shows a plot of the measured Σ_y values throughout the month of Feb. Table 2 compares some of the present accelerator achievements with the design values.
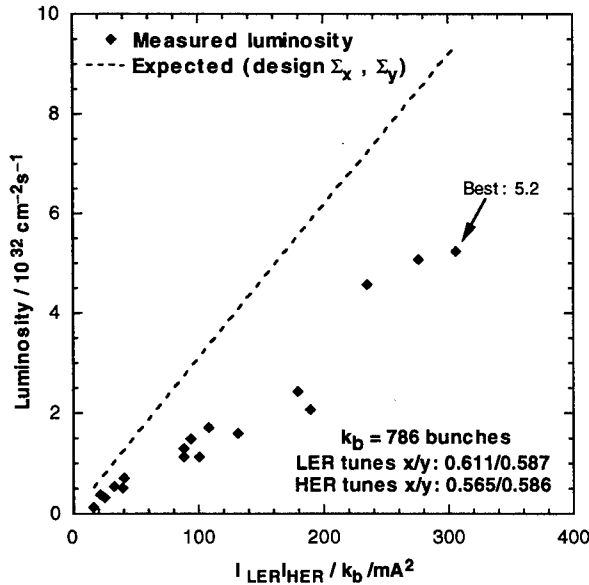
Figure 3. Plot of the measured luminosity as a function of the HER beam current, the LER current being held constant. The dashed line is the expected value for the luminosity based on the design Σs.

Table 2.

Present achievements compared with design values. The coherent beam-beam parameter (Ξ) we define as $\xi/2$.

	Design	Achieved
Σ_x (μm)	220	200-250
Σ_y (μm)	6.6	8.6
Ξ_x (e^+,e^-)	0.015, 0.015	0.0075, 0.017
Ξ_y (e^+,e^-)	0.015, 0.015	0.009, 0.014
L (cm^{-2}s^{-1})	3×10^{33}	5×10^{32}
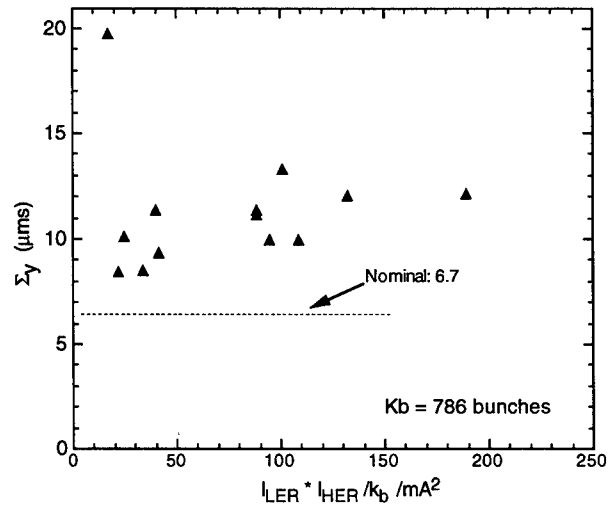
Figure 4. Plot of measured Σ_y values in Feb. for the fill pattern of 786 bunches/beam (2.52 m spacing).

4 SUMMARY

A total of about 20 days have been spent studying collisions at PEP-II. Over a period of 72 hrs in February, PEP-II had an average luminosity of 2×10^{32} cm^{-2}s^{-1}. The luminosity achieved is in agreement with calculations based on the beam currents and the measured Σs at the IP. Lowering Σ_y, matching the spot sizes of the two beams at the IP and increasing the beam currents should lead to the design luminosity.

Presently, PEP-II is off for the BaBar detector installation. Startup is scheduled for the first part of May. Initially, in order to keep detector backgrounds low, beam currents will be limited to 500 mA. However, even with this limitation, PEP-II should be able to achieve a luminosity of at least 1-3 $\times$ 10^{32} cm^{-2}s^{-1} on a regular basis.

5 ACKNOWLEDGMENTS

6 REFERENCES

[1] "PEP-II an Asymmetric B Factory", Conceptual Design Report, CALT-68-1869, LBL-PUB-5379, SLAC-418, UCRL-ID-114055, UC-IIRPA-93-01, June 1993.

[2] M. Sullivan, et.al. "Interaction Region Design at the PEP-II B Factory", pg. 460, EPAC 1996, June 1996

[3] W. R. Nelson, S. Ecklund, R. C. Field, "EGS4 Calculations for a PEP-II Luminosity Monitor", SLAC-PUB-7621, Aug. 1997

[4] V. Telnov, private communication.

HIGH ENERGY OPERATION OF LEP2

S. Myers (for the LEP2 team), CERN, Geneva, Switzerland

Abstract

The LEP collider was operated during 1998 for the first time at a beam energy of 94.5GeV. The 272 superconducting (sc) cavities were operated at an average gradient of more than 6MV/m. The high current in short bunches caused severe higher order mode heating of components. Nevertheless the machine proved very reliable with excellent performance. The maximum integrated luminosity over a 24 hour period exceeded 3.5pb^{-1} and the vertical beam-beam shift parameter reached more than .075 in three of the interaction regions with a record of .08 in the fourth. The present and future performance and limitations of the machine are reviewed as well as some of the crucial technical systems. During 1999 attempts will be made to increase the beam energy to around 100GeV with the help of an additional 16 sc cavities and by operating at gradients around 7MV/m.

Figure 1: Integrated Luminosity during 1998

1 INTRODUCTION

The CERN Large Electron Positron (LEP) collider is a 26.6km circumference e$^+$e$^-$ storage ring which has, until the end of 1995, operated with 4 to 12 bunches per beam in an energy range of 20 to 50GeV [1].

The first superconducting cavities for the LEP2 upgrade were installed in 1993. The complete installation of 256 Niobium film cavities and 16 sheet Niobium was completed early in 1998. By using up all remaining spare components and purchasing some missing parts a further 16 cavities have been produced and installed in the LEP tunnel in early 1999 [2],[3]. It is foreseen to operate LEP2 at the highest energies compatible with high integrated luminosity during 1999, and in 2000 to operate at the highest possible energy. Operation of LEP2 will be halted towards the end of 2000 to allow the preparation of the tunnel for the installation and operation of the LHC collider.

2 HIGHLIGHTS OF 1998

The integrated luminosity for 1998 (as compared with the four previous years) is shown in Fig 1. Clearly 1998 was highly successful, producing more than a factor of 2.5 higher than any previous year.

1998 was the first year which allowed operation of LEP2 for physics at high energies over a long uninterrupted period (around 120 days). The initial physics operation was performed with a new optics configuration with 102°/90° phase advance per cell in the horizontal/vertical plane. This optics was designed to produce higher specific luminosity due to the inherently smaller horizontal emittance and a

higher single bunch threshold for the transverse mode coupling instability due to the reduction in the effective transverse impedance produced by stronger focusing in the vertical plane. High tune optics also provide higher beam energy for the same RF voltage due to the reduction in the "overvoltage factor" brought about by the higher γ_t. In addition, at very high energies the natural emittance remains below the maximum value of 45nm allowed in LEP for reasons of background and collimation. A detailed description of the advantages of this optics will be presented at this conference [4].

The main disadvantage with this optics is associated with the low energy running that is required for calibration of the detectors on the Z^0 peak. The inherent low emittance causes the beam beam limit to be reached at moderately low bunch intensities and therefore reduces the peak luminosity and lengthens the time needed to reach the required integrated luminosity of 2.5pb^{-1}.

The strategy for defining the maximum energy of LEP is as follows. The all-out maximum voltage available is derived from the sum of

- the Niobium film sc cavities at their design value of 6MV/m (256 in total in1998)
- the sheet Niobium cavities at 5MV/m (16 in total)
- and the room temperature copper cavities.

From this all-out maximum, the "operational" voltage is evaluated by subtracting 4% (for sick cavities) along with a further 160MV, which is the voltage reduction which would result from the failure of 2 klystrons each of which feed 8 cavities (at 6MV/m). Knowing this operational voltage, the details of the optics, the value of the damping partition number, and assuming a quantum lifetime of 15 hours allows evaluation of the maximum beam energy. During

physics, the cavities are operated at their all-out maximum (sometimes minus 4%) thereby permitting the simultaneous failure of 2 klystrons without incurring total beam loss. The peak energy value was set to 94.5 GeV for 1998 and was maintained at this value throughout the year. A single beam was accelerated to a maximum energy of 96.5 GeV during a test run.

After initial conditioning and commissioning, the RF system behaved with remarkable reliability at (and sometimes above) its design gradient and with a total beam current of 6 mA. The beam current was limited to this value by Higher Order Mode heating of the cavity control antennae (see later) and for normal operation the cavity conditions were optimized for this intensity value. Although the total current was limited, record peak luminosities of 1.0×10^{32} $cm^{-2}s^{-1}$ were reached due to the very small emittance ratio of 1% achieved (refer to Fig 3). The maximum integrated luminosity reached in a floating 24 hour period was $3.5pb^{-1}$ and $3.2pb^{-1}$ for a calendar day (see Fig 2).

On the beam dynamics front, the vertical beam-beam tune shift (ξ_y), as measured from the average of the luminosities in the four detectors, reached values $\sim .075$ (see Fig 3) with a peak of $\sim.080$ in one of the collision points. Even at these elevated values there was little sign of saturation with ξ_y increasing almost in direct proportion to the bunch current. Nevertheless such very high values of ξ_y can only be achieved and maintained by very careful fine tuning of the lattice parameters (tunes, betatron coupling, global dispersion, local dispersion at the interaction points and the RF stations, etc.). This fine tuning is performed continuously during the physics data taking and successful manipulations are retained for future fills ("golden settings").

3 PERFORMANCE LIMITATIONS IN 1998

3.1 Energy Calibration

In LEP the accuracy of the measurement of the beam energy is of crucial importance for the precision of the physics. For LEP1 the beam energy is measured around the Z^0 equivalent energy by transverse resonant depolarization [5]. For LEP2 it is likely that the polarization level at high energies will be too small to be measured. Hence the beam energy at W± must be estimated by extrapolation from beam energy measurement using resonant depolarization at lower energies [6]. The extrapolation is performed by the use of 16 NMR probes situated in a number of LEP dipoles, and the total bending field as measured by the flux loop. Clearly the accuracy of the extrapolation depends on the energy range over which the precise depolarisation measurements can be performed. In 1998, for the first time, successful calibrations were performed at four different energies in the range 41 to 61 GeV/beam and in the same machine run. A second similar calibration was performed later in the year. Following this extension of the range, the re-
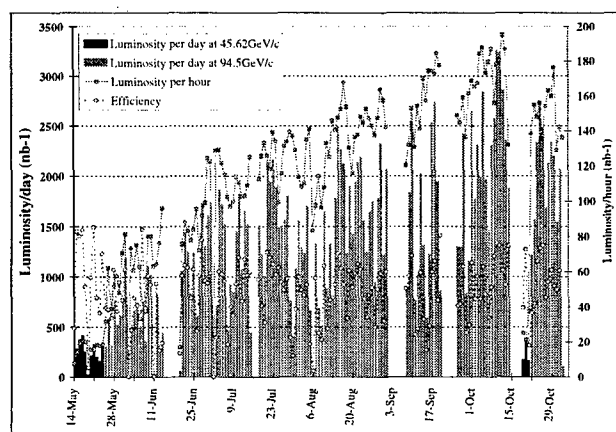
Figure 2: Daily and Hourly Luminosity during 1998
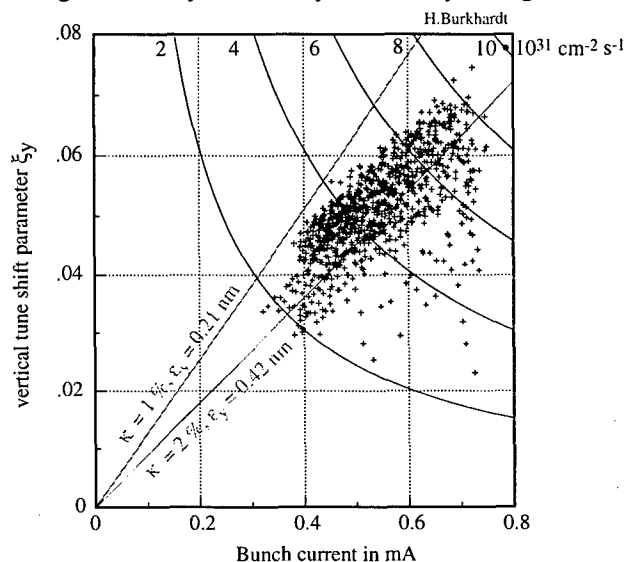
Figure 3: Vertical Beam-beam strength parameter (ξ_y) as a function of bunch current.

maining systematic error of around ±20MeV comes from discrepancies between the NMR and the flux loop. In order to reduce these errors to around ±10MeV it is planned in 1999 to attempt resonant depolarisation at even higher energies. In addition a new spectrometer device [7] will be made available in 1999 as an additional cross-check.

Other techniques for energy calibration based on the energy loss per turn and the relationship between the synchrotron tune and the RF voltage were also tried [8] for the first time in 1998. These tests produced some promising results and will be pursued in 1999.

3.2 Limitation due to cryogenic power

In 1998, LEP2 was reliably operated with 4 cryogenic stations each having a maximum cooling capacity of around 12kW. After subtracting the static losses associated with each of these stations the remaining "dynamic" power for cooling the cavities and any beam losses is $\sim6.2kW$. The required power for cooling of the cavities is

$$P_{cav} \propto \frac{Gradient^2}{Q_{cav}} \qquad (1)$$

where Q_{cav} is the cavity quality factor which decreases with increasing gradient.

The second contribution to the cryogenic power is due to higher order mode losses and can be characterised by

$$P_{cm} = ZI_{tot}^2 = \frac{R_m(\sigma_s)}{n_b k_b} I_{tot}^2 \qquad (2)$$

where $n_b k_b$ is the total number of bunches in both beams and $R_m(\sigma_s)$ is the bunch length dependent impedance related to the HOM loss factor.

Measurements of the increase in the cryogenic power as a function of beam current allowed (in 1997) R_m to be evaluated as 16MΩ [9].

Use of equations (1) and (2) with the known maximum dynamic power and the measured value for R_m allows evaluation of the maximum permissible current as a function of the cavity gradient (beam energy). This procedure indicated a total current of around 6.7mA at an average gradient of 6MV/m which corresponds to a beam energy of 94.5 GeV.

3.3 Heating and Damage to Cavity Antennae Cables

During the winter shutdown 1997/1998 it was discovered that many of the cables attached to the cavity electromagnetic field probes were electrically damaged and some were severely burnt and open circuited. These cables transmit the signals used to control the field and phase of the cavities. The damage always occurred at a location where the cables had been routed through the cavity superinsulation. Subsequent studies showed that the spurious cavity (produced by the housing inside which the antennae were lodged) was responsible for significantly enhancing the coupling of the high frequency beam power to the antennae.

Later investigation also showed that the heating of the cables explained the beam-related cryogenic losses as measured via equation (2).

In order to reduce the risk of overheating a large number of cables during the 1998 run it was decided that the cable temperature should be limited. It was however impossible to obtain an accurate measurement of the temperature in situ and in the presence of beam. For this reason a power/temperature calibration test was done in the laboratory [10] in order to evaluate the power at which the cable temperature reached the upper limit of its specifications. Following this calibration the power induced in the cables as measured in the tunnel was limited to 8W which corresponded to the maximum temperature permissible. Throughout the 1998 run every effort was made to increase the beam intensity without exceeding the 8W limit. This involved the maximization of the bunch length throughout the ramp by the use of wiggler magnets and Q_s

variations. The maximum beam intensity was ultimately limited to around 6mA.

Towards the end of the 1998 run, the limit was increased to 8.5W and the rate of loss of cables increased dramatically. Hence for the last few weeks the intensity was more severely constrained in order to survive with a full complement of cavities to the scheduled end of the run.

4 FUTURE PERFORMANCE AND LIMITATIONS

4.1 Higher Order Mode Heating

Replacement of RF Antennae Cables By the end of the 1998 run, even with the total beam current limited to 6mA, more than 30 cavity antennae cables had been burned. In September 1998 an in situ test was scheduled to replace the existing antennae cables on a single RF module (4 cavities) by thicker ones which were not routed through the superinsulation. Following the success of this test a crash programme was launched to replace every single antennae cable in LEP during the winter shutdown. This programme was successfully completed by mid February 1999. Consequently the level of the intensity limitation due to antennae cable heating will in the future be significantly higher than other intensity limitations.

A comparison of the power losses in the module equipped with the new cables showed that the beam related heat losses were reduced by nearly a factor of two (in equation (2), R_m was reduced to around 8MΩ). This results from the better heat conducting properties of the newly installed cables.

4.2 Cryogenics Upgrade

It has been shown in section 3 that, with the existing 12kW LEP2 cryogenic installation, the beam energy in LEP cannot be significantly increased beyond the 1998 values. In order to allow an increase in the operational energies it was decided in 1997 to upgrade the four cryogenic installations. The most economic way to perform these upgrades was to plan an early installation of part of the cryogenics system needed for the LHC magnets. In this way each of the four cryo plants could be upgraded to around 18kW thereby leaving around 12kW "dynamic" power: giving almost a factor of two increase.

4.3 RF Gradients

The over-riding limitation to the beam energy comes from the available total RF voltage which is simply the product of the active length of the cavities and the average gradient. During the 1998/1999 shutdown an additional 16 Niobium film sc cavities were installed in the LEP tunnel bringing the total to 272 with an additional 16 sc cavities made from Niobium sheet.

The required average gradient of the installed sc cavities is plotted as a function of the beam energy in Fig 4. It is
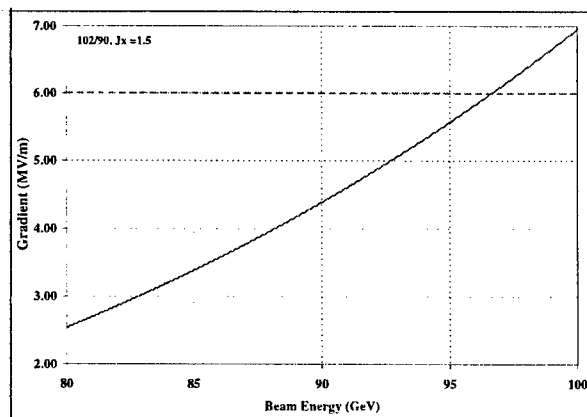
Figure 4: Required gradient in the 272 NbCu cavities as a function of the beam energy ($102°/90°$ optics and $J_x = 1.5$)

Figure 5: Measured radiation as a function of the gradient.

clear that the design gradients of 6MV/m must be increased to 7MV/m in order to reach a beam energy of 100GeV. The three main difficulties with increasing the cavity gradients are:

1. electron emission,
2. dispersion in the gradients about the average value,
3. mechanical oscillations driven by the electromagnetic pressure (ponderomotive oscillations).

Electron emission in the cavities. Early in 1997 after conditioning and processing the sc cavities up to their design value of 6MV/m, it was found that the radiation levels in some cavities remained high ($\leq$20krads/hour) when operating at 6MV/m. Early in 1998, in order to reduce the radiation levels (at the nearby vacuum valves) to below around 10krads/hour, the cavities were conditioned by a mixture of pulsed and continuous processing at gradients between 6.5 and 7MV/m. Fig 5 shows that this operation was successful in that at average gradients of 6MV/m the levels are all below 10krads/hour. However further augmentation of the gradients produced a large increase in the radiation (refer to to points at or above 7MV/m in Fig 5. Consequently, in order to operate around 7MV/m with reduced radiation, it will be necessary to condition the cavities with a mixture of pulsed and continuous processing at fields between 7.5 and 8MV/m. Such high fields will be risky for the whole RF system, particularly the couplers and the cavities themselves.

Helium processing is used less frequently because of the time constraint and the inherent danger for the main couplers. Nevertheless Helium processing has and will continue to be used to recuperate "sick cavities".

Dispersion in cavity gradients. When an RF unit (8 cavities fed by one klystron) is operating at an average gradient per cavity of 6MV/m, the spread in the gradients is typically more than $\pm$1MV/m. Consequently some of the cavities in a unit are already being operated at 7MV/m. It
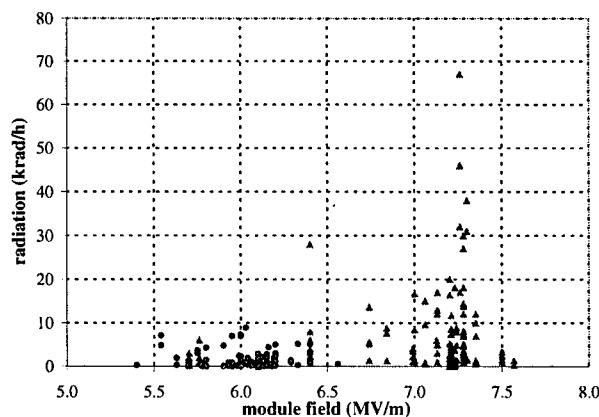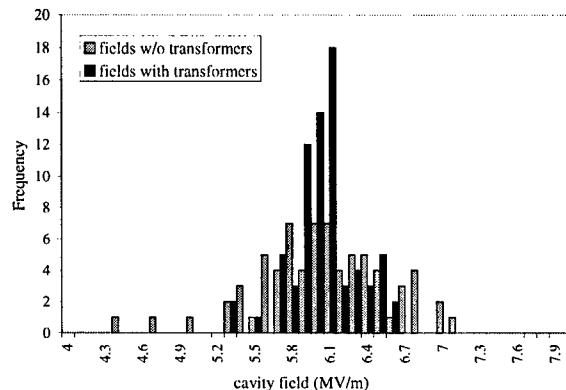
Figure 6: Dispersion in cavity gradients.

is clear that an average of 7MV/m will be more easily obtained if the spread of gradients in the modules is significantly reduced.

The spread in the gradients results from waveguide differences, asymmetries in the power splitting and most importantly differences in the external Q values. The latter can be improved by installing transformers in the waveguides. Fig 6 shows (for measurements made in a test sector) the spread in gradients for modules before and after being equipped with such transformers. Following these results an aggressive programme is on-going to equip the maximum number of cavities with such transformers.

Ponderomotive Oscillations Early operation of the LEP2 cavities showed that, at high beam currents and high gradients, the cavities oscillated mechanically at around 100Hz which resulted in large gradient oscillations at the same frequency. The cause of these oscillations was later identified [11] as an instability driven by the combination of volume changes in the cavities, caused by the electromagnetic forces and the fact that the cavities are driven off-tune. The growth rate of the instability was shown to be proportional to the product of the gradient squared and the beam current. These oscillations have, until the end of 1998 been controlled by variation of the tuning of the cav-

Active Damping System

Unit 873_2,   Vc=10.2 MV,   Ib=5.2 mA
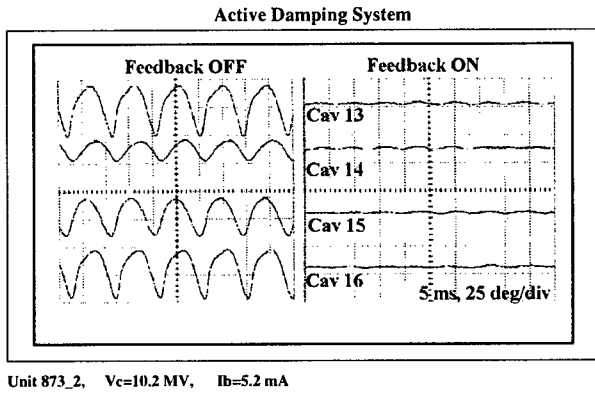
Figure 7: Influence of the system for damping ponderomotive oscillations
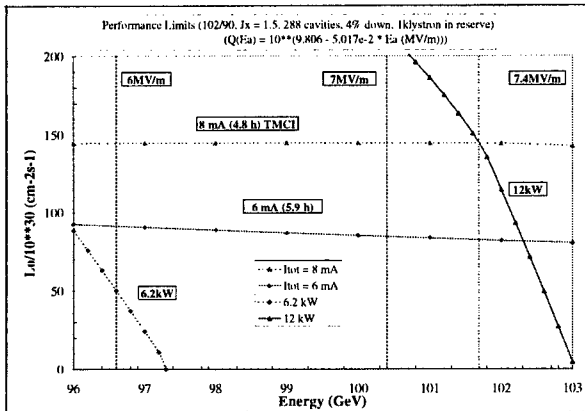
Figure 8: Luminosity and Energy Limitations

ities. During 1998 an automatic programme was used to find the optimum setting for each individual cavity. Unfortunately these settings are energy (gradient) and beam current dependent. During 1998 a new tuning/damping system was developed which feeds back on the cavity tuners from signals derived from the phase and amplitude of the cavity field. Fig 7 shows the damping of oscillations with this new system. A progressive installation of the new damping system will be carried out during 1999.

5   PERFORMANCE IN 1999 AND 2000

The addition of 16 sc cavities, the replacement of the antennae cables and the upgrade of the cryogenics plants significantly increases the potential for LEP2. Fig 8 shows the performance limits in the luminosity against energy plane [12] [13]. The conditions used for this plot are those pertinent for 1999 and 2000, consequently they are not directly comparable with the previously stated limits for 1998.

Examination of this plot indicates that the most crucial limit to performance is given by the RF gradients. It is evident that, provided the gradients can be raised to values of 7MV/m in a technically reliable way, the high luminosity physics will be possible at energies in the 100GeV/beam range.

6   CONCLUSIONS

The performance of the LEP collider was significantly improved for the 1998 run with higher energies and a very high integrated luminosity. The recent various technical upgrades combined with the detailed work carried out to allow higher RF gradients may allow operation at energies in the 100GeV range with high luminosities.

7   ACKNOWLEDGEMENTS

8   REFERENCES

[1] S. Myers; "LEP Status and Plans", Proc. of the US Particle Accelerator Conference and the 16th Int. Conf. on High Energy Accelerators, Dallas USA. (1995).

[2] K. Hübner; "LEP Present and Future Performance and Limitations", Proc. of the Sixth European Particle Conference (EPAC98), held in Stockholm, Sweden from 22 June until 26 June 1998, also CERN-SL-98-043-DI.

[3] S. Myers; "LEP2; Present and Future Performance and Limitations", Proc. of the 1997 US Particle Accelerator Conference (PAC'97), held in Vancouver, BC, Canada, from 12 May until 16 May 1997 . Publ. in Proceedings also CERN-SL-97-022-DI.

[4] M. Meddahi et al. "Experience with a low emittance optics in LEP", paper presented to this conference.

[5] R. Assmann et al., "Calibration of centre-of-mass energies at LEP1 for precise measurements of Z properties", Eur. Phys. J. C6, 187-223 (1999) also CERN-SL/98-012.

[6] A. Blondel et al., "Evaluation of the LEP centre-of-mass energy above the W-pair production threshold", CERN-EP-/98-191 also CERN-SL/98-073, December 1998. Submitted for publication in Eur. Phys. J. C.

[7] B. Dehning, "The LEP Spectrometer", Proc. of the 1999 Workshop on LEP-SPS (Chamonix IX) held in Chamonix, France in January 1999.

[8] A-S. Müller, "Energy Calibration for the price of a Fig", Proc. of the 1999 Workshop on LEP-SPS (Chamonix IX) held in Chamonix, France in January 1999.

[9] Lep2000 Working Group, "LEP 2000 Status Report", CERN SL-98-011 DI, March 1998.

[10] G. Cavallari, private communication May 1998.

[11] D.Boussard, P. Brown, and J. Tückmantel, "Electroacoustic oscillations in the LEP SC. cavities" Proc. 5th European Particle Accelerator Conference, EPAC '96 held in Sitges, Barcelona, Spain on 10 to 14 Jun 1996, also CERN-SL-96-017-RF.

[12] D. Brandt and S. Myers; "LEP Performance Limits revisited", CERN-SL-98-074-DI.

[13] D. Brandt, K. Hübner, and S. Myers; "On LEP Performance Limits in 1999 and 2000", (CERN-SL-98-005-DI).

EXPERIENCE WITH A LOW EMITTANCE OPTICS IN LEP

D. Brandt, W. Herr*, M. Lamont, M. Meddahi, A. Verdier and L. Vos
CERN, Geneva, Switzerland

Abstract

Since start-up in 1998, LEP has operated with a low emittance lattice with a phase advance of 102° in the horizontal and 90° in the vertical planes. This optics provides a horizontal detuning with amplitude which is small enough to avoid a reduced dynamic aperture in the horizontal plane, a problem experienced in other low emittance lattices. The optics is designed to operate at the highest LEP energies up to and above 100 GeV, as well as at 45.6 GeV (still required to provide Z^0s for the calibration of the experiments' detectors). The experience gained with this low emittance lattice after one year of operation is presented and its future potential is discussed.

1 PREVIOUS EXPERIENCE WITH LOW EMITTANCE OPTICS

In order to obtain the highest luminosity with LEP at its highest energies the smallest possible beam emittances are required. Besides providing smaller horizontal emittance, higher horizontal phase advance (μ_x) in the arc FODO cells has the additional advantage of a smaller momentum compaction thereby increasing the maximum energy attainable with a given RF voltage. A considerable amount of work has been done over the past years to find the best possible lattice and various optics with $90° \leq \mu_x \leq 135°$ have been tested ([1] to [5]). The vertical phase advance per cell used was either $\mu_y = 60°$ or $90°$ to make it possible to correct the vertical non-linear chromaticity associated with the low-β insertions [6]. The choice of μ_x resulted from an optimisation of the horizontal detuning with amplitude, as the non-linear horizontal chromaticity is much less important than the vertical.

The first lattice developed and tested had 135° per cell in the horizontal and 60° in the vertical plane (in short 135°/60°). However in preliminary tests no circulating beam could be established; the problems associated with this lattice were studied extensively [7]. It was found impossible to correct both the third order resonance and the derivative of the horizontal tune with respect to the horizontal amplitude. The horizontal detuning for this lattice was -1.6×10^5 m^{-1}.

In 1994, a 108°/60° lattice was developed. The horizontal detuning was 2.26×10^4 m^{-1}. This is a factor of seven smaller than the horizontal detuning of the 135°/60° lattice. After successful tests the 108° lattice was recommended

for operation in 1996 [2]. In parallel, a 108°/90° optics was developed which had a smaller cross detuning term (horizontal detuning with respect to vertical amplitude and vice versa) than the 108°/60° optics, resulting in a larger horizontal dynamic aperture. Both optics still had a strong horizontal detuning and it was demonstrated that this detuning can bring particles onto non-linear resonances, in particular $3Q_x$ [7]. As a consequence, operation with $\mu_x = 108°$ optics was hampered by the presence of strong tails, even with a single beam in the machine [8].

The objective was therefore to find an optics with a reduced horizontal detuning. In reducing μ_x from 108° to 102°, the horizontal detuning decreases by more than a factor of two. The cross detuning of the 102°/90° lattice is smaller than that of the 1997 operational lattice (90°/60°) by a factor 2.

Although $\mu_x = 102° = 17\pi/30$ is not a simple fraction of π, the excitation term of the systematic 3rd order resonance is smaller than for the 90°/60° lattice [9].

Measurements with the 102°/90° were first performed in 1997 with a detuned optics ($\beta_y^* = 27$ cm) for which chromatic errors were corrected by using only one sextupole family in each plane. After encouraging results, a test under physics conditions was performed with a squeezed optics ($\beta_y^* = 5$ cm). This necessitated a re-cabling of the vertical sextupole families from three to two families (90° in the vertical plane instead of 60° previously used). In the horizontal plane, with a $\beta_x^* = 2$ m, one horizontal sextupole family was enough to correct for the non-linear horizontal chromaticity. A successful test was made where the performance with colliding beams was in good agreement with expectation [10].

For 1998, the possibility of reducing β_x^* from 2.0 m to 1.25 m was exploited, increasing the operational flexibility. In this case, the horizontal non-linear chromaticity was corrected by grouping the horizontally focusing sextupoles into several families. The grouping of the families was optimised so that the correction of the horizontal non-linear chromaticity reduces the horizontal detuning without increasing either the vertical or the cross detuning terms. Beside this, two sextupoles per octant are powered independently to allow a further reduction of the horizontal detuning down to a value 20 times smaller than that of the 108° optics. The 102°/90° optics developed for 1998 allows a variation of the horizontal detuning between 0.11 to 1.4×10^4 m^{-1}.

2 EXPERIENCE IN 1998

The high energy running at LEP in 1998 was performed exclusively with the 102°/90° optics and at a beam energy of 94.5 GeV.

2.1 Optics - observations

Horizontal emittance and J_x At 100 GeV, operating on central orbit, the 90°/60° lattice has a horizontal emittance of 56 nm, while the 102°/90° has an emittance of 44 nm. This means that all other parameters equal, the 102°/90° has the potential to provide a luminosity 1.3 times larger than that of 90°/60°. It also gives almost 0.6 GeV more centre of mass energy for the same RF voltage.

One way to further reduce the emittance is to increase the horizontal damping partition number (J_x) through a RF frequency shift. For the 90°/60°, the variation of J_x with the momentum shift ($\partial J_x/\partial \Delta p/p$) was 312 and is 305 for the 102°/90°. In 1998, the 102°/90° was operated with a RF frequency shift of +120 Hz, i.e a J_x of 1.67 and therefore a horizontal emittance of around 23.6 nm at 94.5 GeV.

Transverse tails Transverse beam tails have been measured with the 102° optics under physics data taking conditions [11]. The horizontal tails measured at high energies were normally acceptable. However, non-Gaussian tails have been observed during so-called background storms [14].

Ramp & Squeeze The recent years of LEP operation have seen a combined ramp and squeeze in which the vertical squeeze was made during the ramp from 42 to 44 GeV. This year, with the wigglers on, some lifetime problems were observed between 50 and 60 GeV. A possible cause was an insufficient momentum acceptance of the squeezed 102°/90° optics. With a σ_E/E=0.18 % in the incriminated energy region, the criteria of $8\sigma_E/E$ absolute momentum deviation to guarantee the linear stability is marginal with the squeezed optics but entirely fulfilled with the unsqueezed optics. To avoid this the squeeze was implemented after the wigglers have been switched off at high energy; the lifetime problem was cured. The long range beam-beam effects at the IPs remained acceptably small, despite the increased β_y^* [12].

Minimum β_x^* and β_y^* Background considerations due to the aperture in the horizontally focusing quadrupoles near the experiments limit the minimum β_x^*. For J_x =1, the limit is 1.21 m at 100 GeV, which is close to the operational value (1.25 m) [13]. It was shown [14] that the background storms observed during physics fills and cured by small horizontal tune changes, are less severe for larger β_x^*, another argument against a further reduction of this value.

Beam-beam effects demand that β_y^* should be larger than $2\sigma_l$ to avoid affecting the luminosity [15]. For σ_l = 10 mm, the limit on β_y^* is 2 cm, compared to the present value of 4 cm.

A further reduction might be tested to evaluate its operational feasibility. However an attempt to match the physics optics for β_y^* = 3.5 cm showed that β_y values were increasing at the collimators near the experiments and that the necessary sextupole strength was severely increased. Beside limiting this 3.5 cm optics to 95 GeV, the large sextupole strength enhances excitation of non-linear resonances and increases the tune dependence with amplitude. Both effects reduce the dynamic aperture [5]. With the 3.5 cm optics, the non-linear chromaticity correction showed a reduced aperture in momentum $\Delta p/p = \pm 0.013$ (originally $\pm$ 0.015) and it was demonstrated that a further reduction of the β_y^* would lead to marginal momentum aperture [16]. In conclusion, β_x^* of 1.25 m and β_y^* of 4 cm are very close to the limit for the horizontal and vertical squeeze and will most likely be the standard values for future operation.

2.2 Experience at 45.6 GeV

After the new 102°/90° optics was successfully commissioned, the calibration of the LEP detectors on the Z_0 peak at 45.6 GeV, needed every year, was performed with this lattice at relatively low intensities (to minimise beam-beam effects linked to the low emittance). Previous experience with low emittance lattices at 45.6 GeV (108° optics) showed that performance was limited by the presence of tails. The 102° optics, with its reduced detuning, did not suffer from the same problems. Physics was performed with trains of 8+8 bunches and the intensity was limited to 250 μA per bunch, in order to keep an acceptable horizontal beam-beam parameter. The luminosity and the vertical beam-beam parameter were exactly as expected. The vertical beam-beam parameter was 0.02-0.025 and the emittance ratio between 1 and 1.5 %. The 102° optics is the only low emittance LEP lattice which proved to work at low as well as high energies.

2.3 Experience at 94.5 GeV

At high energy, three different physics periods can be differentiated, depending on the value of the beta functions at the interaction points. During the first period (up to fill 5140, Fig.1), β_x^* = 1.5 m and β_y^* = 5 cm were used and both ξ_y and the peak luminosity were increasing as the total current was increased. For the second period (fills 5140-5262), β_x^* was decreased to 1.25 m while β_y^* remained unchanged. Both ξ_y and the peak luminosity were still increasing without any further increase of the total current. Finally, from fill 5263 onwards, β_y^* was reduced to 4 cm while β_x^* remained unchanged. The result was a decrease of ξ_y and an increase of the luminosity compared to the second period, with a similar total current.

In order to quantify these changes and to check whether the effects of the horizontal and vertical squeeze were as expected, we compare one representative fill in each of the three physics periods (see table 1).

For the horizontal squeeze, for the same bunch intensity, squeezing the horizontal beta value from 1.5 m to
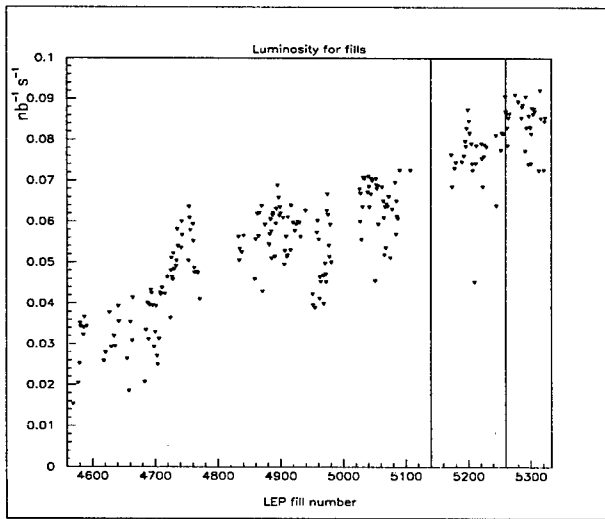
Figure 1: Luminosity as a function of fill number

β^*_x m	β^*_y cm	ξ_y	ξ_x	Lum. $\times 10^{31}$	I/bunch μA	Δf_{rf} Hz
1.50	5	0.062	0.042	7.3	750	0
1.25	5	0.076	0.042	9.0	750	120
1.25	4	0.061	0.042	9.5	750	120

Table 1: Three fills during the different running periods

1.25 m and increasing the RF frequency shift from 100 Hz to 120 Hz, is expected to give 20 % increase in both the ξ_y and peak luminosity. The expectations were effectively met. For the same bunch intensity, and a vertical squeeze from 5 cm to 4 cm, one expects 11 % decrease in ξ_y and 11 % increase in luminosity. The expectations were met in ξ_y and were very close in luminosity [13].

High beam-beam parameters were regularly achieved and did not show any sign of saturation with increasing current. This is extensively treated in [17].

3 FUTURE PERFORMANCE

All magnets and power converters allow the 102°/90° optics to operate up to 103 GeV. In 1999, the performance limitations will depend on the maximum possible intensity and on the highest reliable accelerating gradient [18]. For 2000, the cryogenics cooling power will also be a limitation for energies above 100 GeV. Performance estimates for 1999 foresee an integrated luminosity of 1.5 pb^{-1}/day for 6 mA total current. With 8 mA, 2 pb^{-1}/day are expected. However it should be emphasised that for high intensity and high energy the global efficiency is likely to be reduced. A word of caution has to be added regarding the available aperture: it remains to be demonstrated that a horizontal emittance of 47.3 nm at 103 GeV can be accommodated in the machine. Also, the available momentum aperture, which is limited by the non-linear vertical chromaticity correction, was shown to be marginal above

100 GeV [16]. Optimisation of the phases of the experimental interaction regions and/or vertical phase advance in the arcs can be made in order to improve the non-linear chromaticity correction.

4 CONCLUSIONS

In 1997, a low emittance optics with a phase advance of 102° per cell in the horizontal and 90° in the vertical planes was developed and commissioned. This optics has significantly smaller detuning with amplitude than previously tested low emittance lattices with larger horizontal phase advance. As a consequence it has less operational problems. In 1998, it was used for the whole year in operation and the performance was excellent. The 102°/90° optics gives a slightly higher energy for a given total RF voltage and has a potentially higher performance at the highest energy achievable at LEP. It is the first low emittance lattice which proved to work for both low and high energies.

5 REFERENCES

[1] D. Brandt et al., Proc. 3rd Eur. Part. Acc. Conf., Berlin 1992.

[2] Y. Alexahin et al, Proc. Part. Acc. Conf., Dallas 1995.

[3] Y. Alexahin et al, Proc. 5th Eur. Part. Acc. Conf., Sitges 1996.

[4] D. Brandt et al., Proc. Part. Acc. Conf., Vancouver 1997.

[5] D. Brandt et al; Proc. 6th Eur. Part. Acc. Conf., Stockholm 1998.

[6] A. Verdier, Proc. Part. Acc. Conf., Dallas 1995.

[7] Y. Alexahin, CERN SL/95-110 (AP), 1995.

[8] H. Burkhardt, Proc. 8th LEP performance workshop, CERN SL/98-06.

[9] A. Verdier, Proc. 7th LEP performance workshop, CERN-SL/97-06.

[10] M. Meddahi; Proc. 8th LEP performance workshop, CERN SL/98-06.

[11] K. Affholderbach et al; SL-Note-98-073 (MD).

[12] D. Brandt and M. Lamont, SL-Note-98-070(MD).

[13] M. Meddahi; Proc. 9th LEP performance workshop. CERN-SL/99-07.

[14] G. von Holtey; Proc. 9th LEP performance workshop. CERN-SL/99-07.

[15] S. Myers; Inst. and Meth. 211 (1983) 263-282, North Holland Publishing Company.

[16] A. Verdier; Proc. 9th LEP performance workshop. CERN-SL/99-07.

[17] D. Brandt et al.; Is LEP beam-beam limited at its highest energy?; These Proceedings.

[18] D. Brandt, S. Myers, CERN SL/98-074 (DI).

EXPERIMENTAL EVIDENCE FOR BEAM-BEAM DISRUPTION AT THE SLC*

T. Barklow, G. Bower, F.J. Decker, C. Field, L.J. Hendrickson, T. Markiewicz,
D.J. McCormick, M. Minty, N. Phinney#, P. Raimondi+, M.C. Ross, K.A. Thompson,
T. Usher, M.D. Woodley, F. Zimmermann+, SLAC, Stanford, CA

Abstract

A significant luminosity enhancement from beam-beam disruption was observed for the first time during the 1997-98 run of the SLAC Linear Collider (SLC). Disruption, or pinch effect, is due to the decrease in effective beam size during collisions as each beam is focused by the field of the other beam. With beam intensities of 4.0 10^{10} per bunch, bunch lengths of 1.1 mm, and horizontal and vertical beam sizes of $\sigma_x = 1.5$ μm and $\sigma_y = 0.65$ μm, the luminosity increase from disruption was more than 100%. Measured data rates as recorded by the SLD detector were in agreement with the theoretically calculated disruption enhancement.

1 INTRODUCTION

The beam-beam interaction has been studied extensively both for electron-positron storage rings and for linear colliders. During the collisions, each beam is focused by the collective electromagnetic fields of the other oppositely charged beam. In storage rings, this additional focusing causes the beam-beam tune shift which must be controlled so that the beams do not become unstable. For a linear collider, if the focal length is on the order of or less than the bunch length, the effective beam size shrinks during the collisions, increasing the luminosity. In principle, since the beams are discarded after colliding, one tries to maximize the beam-beam interaction and produce the largest luminosity enhancement.

The practical limit on the disruption value achieved may be set by the increase in outgoing emittance and the beamstrahlung radiation. The larger emittance of the disrupted beam may be difficult to capture and extract cleanly, causing backgrounds in the detector or problems with critical downstream diagnostics. For high energy colliders, the beamstrahlung radiation becomes significant and the particles which have radiated collide at lower energy than nominal. This smearing of the collision energy can degrade the quality of physics experiments. An additional practical problem is that the disruption severely distorts standard techniques for measuring the beam size at the interaction point such as beam-beam deflection

scans, making it difficult to properly characterize the beams. To extract the correct beam size, the effects of disruption must be included in the analysis.

2 THEORETICAL FRAMEWORK

The phenomenon of disruption was studied for round beams ($\sigma_x/\sigma_y = 1$) by Hollebeek in 1980 [1] and for flat beams ($\sigma_x/\sigma_y \gg 1$) by Chen [2] and others. The strength of the effect is characterized by the disruption parameter, $D_{x,y}$, for each plane which is the inverse focal length in units of the bunch length, σ_z.

$$D_{x,y} = \frac{2Nr_e\sigma_z}{\gamma\sigma_{x,y}(\sigma_x+\sigma_y)} \qquad (1)$$

where $\sigma_{x,y,z}$ are the horizontal, vertical and longitudinal beam sizes, N is the bunch population and r_e is the classical electron radius. The luminosity enhancement factor, H_D, is the increase in luminosity due to the change in beam size. For typical machine parameters, the beam-beam interaction is non-linear and cannot be calculated analytically. Simulations must be used to model the behavior using programs such as ABEL [3] or more recently, Guinea Pig [4]. Chen and Yokoya [5] derived a parameterization of H_D for the case of round beams which is given by the equation

$$H_D = 1 + D^{1/4}\left(\frac{D^3}{1+D^3}\right)\left\{\ln\left(\sqrt{D}+1\right)+2\ln(0.8/A)\right\} \qquad (2)$$

where D is the same for both planes and $A = \sigma_z/\beta^*$, the ratio of the bunch length to the β function at the collision point. For SLC operation, the horizontal beam size is only a factor of two to three larger than the vertical beam size and is closer to a round beam than to the extreme flat beam limit. Chen [6] proposed that for such "quasiflat" beams, the luminosity enhancement scales as

$$H_D = H_{D_x}^{1/2} H_{D_y}^{f(R)} \qquad (3)$$

where

$$f(R) = \frac{1+2R^3}{6R^3}$$

with $R = \sigma_x/\sigma_y$ and where both H_{D_x} and H_{D_y} are approximated by the round beam parameterization given

in equation (2). This formula has been used to predict the expected disruption enhancement at the SLC.

3 SLC HISTORY

Prior to the 1994-95 SLC run, the beam intensity was limited to less than $3*10^{10}$ particles per bunch by the onset of a microwave bunch lengthening instability in the damping rings. The instability was caused by the interaction of the beam with sharp transitions in the vacuum chamber diameter. For 1994, new low impedance vacuum chambers with smooth transitions were installed in both rings. There was also a major upgrade to the optics of the final focus to reduce contributions to the beam size from 3rd order aberrations caused by the interleaved horizontal and vertical sextupoles in the SLC chromatic correction sections. These two upgrades combined with other improvements to the beam stability and tuning finally brought the SLC beam parameters into the regime where disruption could contribute to the luminosity. The predicted disruption enhancement was about 20%. The parameters achieved in 1994-95 are listed in Table 1 along with those for 1996 and for the 1997-98 run.

For the short 1996 run, there were no major upgrades to the machine but the beam intensity was increased slightly and better emittance control resulted in smaller horizontal beam sizes. The predicted disruption enhancement was about 30%. In both runs, only a small excess of luminosity was seen beyond what would be predicted for undisrupted beams, 5-10%. At least two factors contributed to the discrepancy between predicted and observed luminosity enhancement. An analysis of the final optimization procedures at the interaction point (IP) indicated that the resolution was inadequate for micron size beams. Mistuning was estimated to degrade the luminosity by up to 30% [7]. After the 1996 run, it was also found that the bunch length had been much shorter than desireable for maximal disruption.

The primary evidence for disruption seen in this period was a distortion of the deflection angles during the beam-beam deflection scans used to measure the beam size at the IP. If the fit to the deflection data assumed that the beams remained rigid throughout the collision, the vertical beam size would be overestimated by up to 25% [8]. A new fit had to be developed which took into account the change in beam size described by equation (3).

4 1997-98 SLC RUN

In the 1997-98 run, the SLC luminosity increased by more than a factor of three [9]. More than 350,000 Z^0 events were recorded by the SLD detector, nearly double the total sample from all previous runs. A major contribution to this performance came from a significant disruption enhancement, typically 50-100%, meaning that about half of the luminosity was due to disruption. The improvement was due almost entirely to changes in tuning procedures

and reconfiguration of existing hardware with no major upgrade projects. Improved alignment and emittance tuning techniques throughout the accelerator resulted in minimal emittance growth from the damping rings to the final focus. In particular, a revised strategy for wakefield cancellation using precision beam size measurements at the entrance of the final focus improved emittance optimization. The final focus lattice was modified to provide stronger demagnification near the interaction point and to remove residual higher-order aberrations. Beam sizes as small as 1.5 by 0.65 microns were achieved at full beam intensity of $4*10^{10}$ particles per pulse. These parameters are shown in Table 1.

Table 1: Beam parameters at the SLC interaction point

		1994 / 95	1996	1997 / 98
$N^{+/-}$	(10^{10})	3.5	3.7	4.0
$\Sigma_{x/y}$	(μm)	3.7 1.2	3.2 1.2	2.1 0.9
σ_z	(mm)	1.0	1.0	1.1
θ^*	(μrad)	350 270	350 270	450 250
H_D		1.2	1.3	2.1
L	$(10^{30}/cm^2/sec)$	0.75	1.0	2.8

To eliminate the tuning problems encountered in previous runs, a novel 'dithering' feedback was implemented to perform the final beam optimization at the IP [10]. Five corrections must be routinely applied to each beam which include centering of the x and y beam waist positions, zeroing of the dispersion η_x and η_y, and minimizing an $x-y$ coupling term. The feedback optimized a direct measure of the luminosity as a function of small changes in each parameter. By averaging over thousands of beam pulses, it was possible to improve the resolution by a factor of 10. Care was also taken to optimize the longitudinal beam profile and bunch length in the linac using dedicated machine experiments [11].

5 MEASUREMENT OF H_D

The value of H_D can be measured by comparing the luminosity as recorded by SLD to that which would be predicted for rigid beams without disruption given the observed SLC beam parameters. To improve statistics, the SLD luminosity was calculated from the number of Z^0 and Bhabha scattering events recorded in each half hour interval. The Bhabha cross section is 3.65 times the Z^0 production cross section at the mass of the Z^0. In any finite interval, some fraction of the beam pulses are not available for luminosity either because of machine protection or diagnostic tuning procedures. To compensate for the variable rate of these missing pulses, the raw Bhabha plus Z^0 event count must be scaled up to an

equivalent 120 Hz rate, by dividing by the fraction of pulses with both beams in collision at the IP. The SLD fast data acquisition recorded beam intensities as well as signals from beamstrahlung and luminosity counters for every pulse at 120 Hz. This data could then be used to accurately count pulses with beams in collision.

The calculation of SLC luminosity without disruption was based on the beam intensity for each pulse from the SLD 120 Hz data stream. The transverse beam overlap size was measured at least hourly with beam-beam deflection scans, where the fit to the deflection angle versus position data included a correction for the beam size change during collision. To improve the quality of these scans, the incoming beam trajectories are measured on each pulse and the fitted position of the beams at the IP is used to correct for pulse-to-pulse jitter. These trajectory measurements are also used to calculate the RMS jitter for the two beams in both planes and provide an estimate of the luminosity loss due to pulse-to-pulse motion. This correction factor, typically about 6%, is applied to the calculated SLC luminosity. Figure 1 shows the measured disruption enhancement factor, H_D, for different values of the SLD luminosity. H_D is the ratio of actual SLD luminosity to that predicted from the observed SLC beam parameters without disruption, as described above.

disruption enhancement agrees extremely well with the theoretical value as shown in Figure 2 by the close agreement between actual SLD event rates and those calculated including the theoretical estimate of disruption.
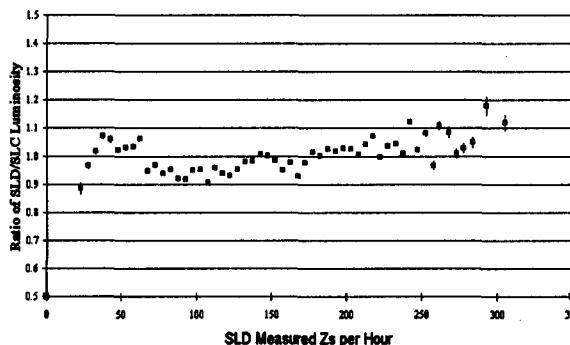
Figure 2: Ratio of measured SLD luminosity to calculated SLC luminosity including the theoretical estimate of disruption.

7 CONCLUSIONS

A significant luminosity enhancement from beam-beam disruption was observed for the first time at the SLC during the 1997-98 run, with peak values in excess of 100%. The measured disruption was in agreement with theoretical predictions over a wide range of machine parameters. The improved SLC performance which led to this result was due to the hard work and dedication of many people, including the operations and maintenance staff and physicists from Accelerator Research and SLD. Their efforts are gratefully acknowledged by the authors.

Figure 1: Measured disruption enhancement factor, H_D, plotted versus SLD measured Zs per hour.

6 COMPARISON WITH THEORY

The theoretical prediction for H_D was calculated from the measured beam parameters using Chen's formalism for quasiflat beams as given in section 2. The beam intensity was measured by toroids at the entrance to each final focus. The transverse beam size was taken from the most recent beam-beam deflection scans. The bunch length was measured infrequently and then continuously monitored for stability with microwave bunch length monitors in the linac and final focus [12]. The longitudinal distribution of events recorded by the SLD provided a cross check of the overlap of the two bunch lengths. The measured

8 REFERENCES

[1] R. Hollebeek, "Disruption Limits for Linear Colliders", Nucl. Instrum. Meth. **184**, 333 (1981).

[2] P. Chen, "An Introduction to Beamstrahlung and Disruption", Frontiers. of Particle Beams **296**, (1988).

[3] K. Yokoya, KEK Report 85-9 (1985).

[4] D. Schulte, "Beam-beam Simulations with GUINEA-PIG", CERN-PS-99-014.

[5] P. Chen and K. Yokoya, "Disruption Effects From The Interaction Of Round E+ E- Beams", Phys.Rev.**D38**, 987 (1988).

[6] P. Chen, "Disruption Effects from the Collision of Quasiflat Beams," PAC 93, Washington, DC, (1993).

[7] P. Emma, et al., "Limitations of Interaction Point Spot Size Tuning at the SLC," PAC 97, Vancouver, Canada, (1997).

[8] P. Raimondi, et al., "Disruption Effects on the Beam Size Measurement", PAC95, Dallas, Texas, (1995).

[9] P. Raimondi, et al., "Recent Luminosity Improvements at the SLC," EPAC 98, Stockholm, Sweden, (1998).

[10] L. Hendrickson, et al., "Luminosity Optimization Feedback in the SLC," ICALEPCS 97, Beijing, China, (1997).

[11] F.J. Decker, et al., "Longitudinal Phase Space Setup for the SLC Beams," PAC 97, Vancouver, Canada, (1997).

[12] F. Zimmermann, et al., "An RF Bunch Length Monitor for the SLC Final Focus," PAC 97, Vancouver, Canada, (1997).

MUON COLLIDERS: STATUS OF R&D AND FUTURE PLANS

Kirk T. McDonald,* *Princeton U., Princeton, NJ 08544*, for the Muon Collider Collaboration[†]

Abstract

The case for a future high-energy collider based on muon beams is reviewed briefly.

1 THE Y2K PROBLEM FOR PARTICLE PHYSICS

- Can elementary particle physics prosper for a 2nd century with laboratory experiments based on innovative particle sources?

- Can a full range of new phenomena be investigated?

    - Neutrino mass $\Rightarrow$ a 2nd 3×3 mixing matrix.

    - Precision studies of Higgs bosons.

    - A rich supersymmetric sector (with manifestations of higher dimensions).

    - ... And more ...

- Will our investment in future accelerators result in more cost-effective technology, capable of extension to 10's of TeV of constituent CoM energy?

Many of us believe that a **Muon Collider** [1, 2, 3, 4, 5, 6] is the best answer to the above.

2 WHAT IS A MUON COLLIDER?

An accelerator complex in which

- Muons (both μ^+ and μ^-) are collected from pion decay following a pN interaction.

- Muon phase volume is reduced by 10^6 by ionization cooling [7, 8].

- The cooled muons are accelerated and then stored in a ring [9, 10].

- $\mu^+\mu^-$ collisions are observed over the useful muon life of ≈ 1000 turns at any energy.

- Intense neutrino beams and spallation neutron beams are available as byproducts.

Muons decay: $\mu \rightarrow e\nu \quad \Rightarrow$

- Cool muons quickly (stochastic cooling won't do).

- Detector backgrounds at LHC level.

- Potential personnel hazard from ν interactions.

Table 1: Baseline parameters for muon colliders at 3 TeV, 400 GeV (top factory) and 100 GeV (light Higgs factory).

CoM energy (TeV)	3	0.4	0.1
p energy (GeV)	16	16	16
p's/bunch	2.5e13	2.5e13	5e13
Bunches/fill	4	4	2
Rep. rate (Hz)	15	15	15
p power (MW)	4	4	4
μ/bunch	2e12	2e12	4e12
μ power (MW)	28	4	1
Wall power (MW)	204	120	81
Collider circum. (m)	6000	1000	350
Ave. bending field (T)	5.2	4.7	3
Depth (m)	500	100	10
Rms $\Delta P/P$ (%)	0.16	0.14	0.003-0.12
6d ϵ_6 $(\pi m)^3$	1.7e−10	1.7e−10	1.7e−10
Rms ϵ_n (π mm-mrad)	50	50	85- 290
β^*, σ_z (cm)	0.3	2.6	4.1-14.1
σ_r spot (μm)	3.2	26	86-294
σ_θ IP (mrad)	1.1	1.0	2.1
Tune shift	0.044	0.044	0.051-0.022
n_{turns} (effective)	785	700	450
Luminosity (cm^{-2}s^{-1})	7e34	1e33	1e31-1.2e32
Higgs/year			2-4e3

Higgs/year assumes a cross section $\sigma = 5 \times 10^4$ fb; a Higgs width $\Gamma = 2.7$ MeV; 1 year $= 10^7$ s.
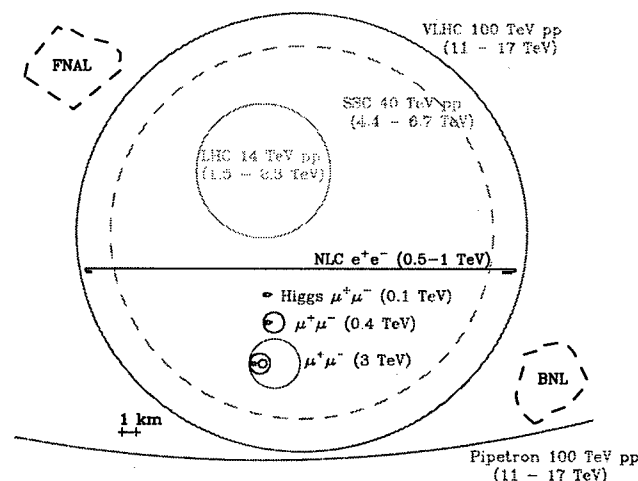
Figure 1: Comparison of footprints of various future colliders.

3 THE CASE FOR A MUON COLLIDER

- More affordable than an e^+e^- collider at the TeV (LHC) scale.
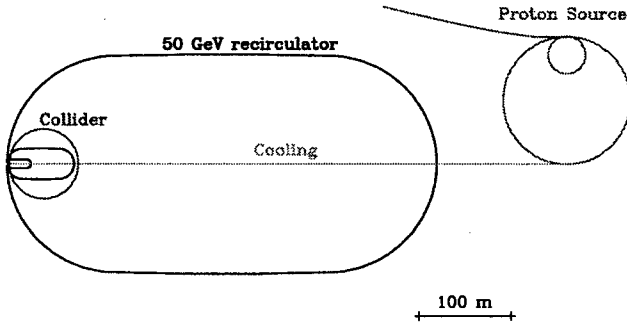
Figure 2: A First Muon Collider to study light-Higgs production.

- More affordable than either a hadron or an e^+e^- collider for (effective) energies beyond the LHC.

- Precision initial state superior even to e^+e^-.

  - Muon polarization $\approx 25\%$, $\Rightarrow$ can determine E_{beam} to 10^{-5} via $g-2$ spin precession [11].
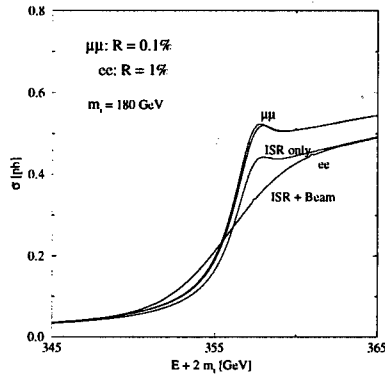
Figure 3: The effect of beam energy resolution at the $t\bar{t}$ threshold.

- Initial machine could produce light Higgs via s-channel [5]:

  - Higgs coupling to μ is $(m_\mu/m_e)^2 \approx 40,000\times$ that to e.

  - Beam energy resolution at a muon collider $< 10^{-5}$, $\Rightarrow$ can measure Higgs width directly.

  - Add rings to 3 TeV later.

- Neutrino beams from μ decay about 10^4 hotter than present.

  - Possible initial scenario in a low-energy muon storage ring [12].

  - Study CP violation via CP conjugate initial states:

$$\begin{cases} \mu^+ \rightarrow e^+\bar{\nu}_\mu\nu_e \\ \mu^- \rightarrow e^-\nu_\mu\bar{\nu}_e \end{cases}$$

4 TECHNICAL CHALLENGES

[*References in this section are to papers contributed to PAC'99.*]

- Proton Driver, 16-GeV, 15 Hz, 4MW, 1-ns bunch [19].

- Targetry and Capture [28, 32, 35, 49, 51, 53].

- Muon Cooling [14, 15, 16, 21, 24, 25, 27, 29, 33, 34, 36, 42, 48, 50, 52, 54, 55, 56].

- Acceleration [13, 31, 44, 57].
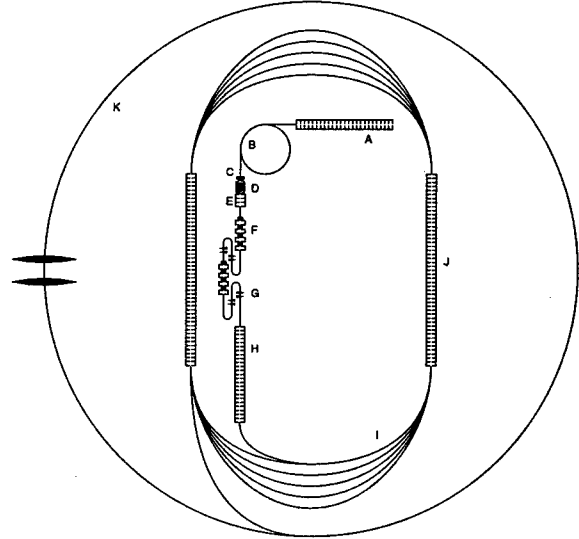
Figure 4: Muon collider components: A. Proton linac; B. Proton driver; C. Proton target; D. Capture solenoid; E. Phase rotation channel; F. Transverse cooling; G. Longitudinal cooling; H. Accelerating linac; I. Arcs of recirculator; J. Accelerating linac; L. Collider ring.

- Storage rings [17, 18, 37, 38, 39, 40, 41, 43, 47].
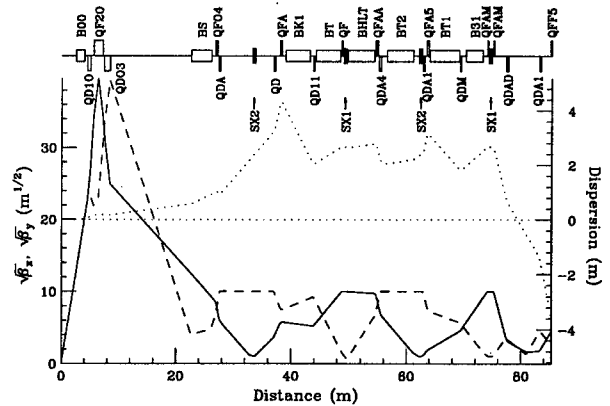
Figure 5: Collider ring lattice near the interaction point.

- Interaction region and detector design.

- Neutrino beams [22, 26, 30, 45, 46].

311
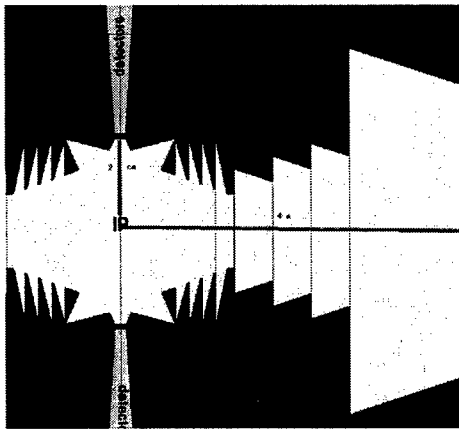
Figure 6: Tungsten masks around the interaction region.
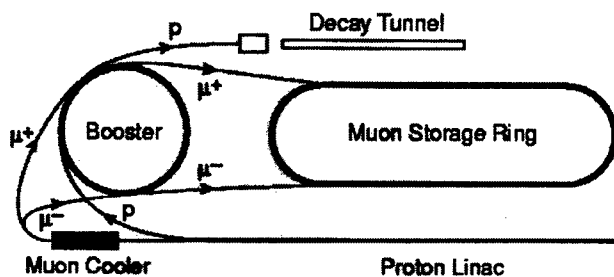
Figure 7: Sketch of an accelerator complex to produce neutrino beams via a muon storage ring.

5 MUON COLLIDER R&D PROGRAM

5.1 Targetry and Capture at a Muon Collider Source
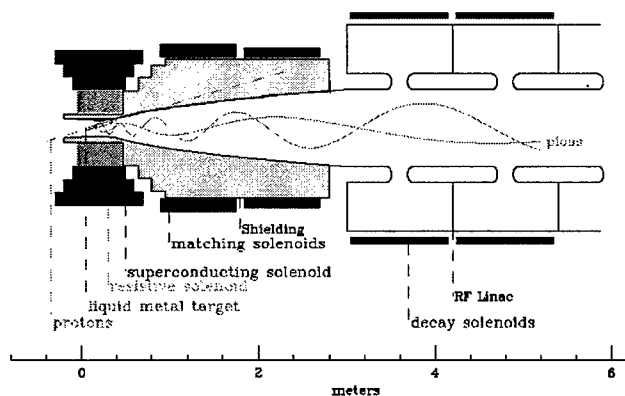
Figure 8: Baseline targetry scenario using a liquid metal jet inside a 20-T magnet.

To achieve useful physics luminosity, a muon collider must produce about 10^{14} μ/sec.

- $\Rightarrow$ $> 10^{15}$ proton/sec onto a high-Z target $-$ 4 MW beam power.

- Capture pions of $P_\perp \lesssim 200$ MeV/c in a 20-T solenoid magnet.

- Transfer the pions into a 1.25-T-solenoid decay channel.

- Compress π/μ bunch energy with rf cavities and deliver to muon cooling channel.

Targetry Issues:

- 1-ns beam pulse $\Rightarrow$ shock heating of target.

- Eddy currents arise as metal jet enters the capture magnet.
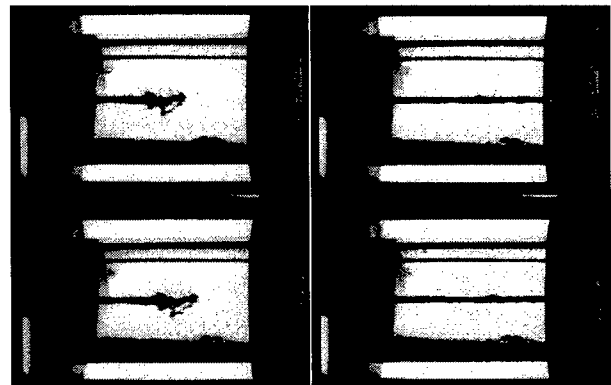
High-speed photographs of mercury jet target for CERN-PS-AA (laboratory tests)
4,000 frames per second, Jet speed: 20 ms-1, diameter: 3 mm. Reynold's Number:>100,000
A. Poncet

Figure 9: Hg jet studied at CERN, but not in beam or magnetic field.

- Targetry area also contains beam dump.

Targetry R&D Goals:

- Long Term: Provide a facility to test key components of the front-end of a muon collider in realistic beam conditions.

- Near Term (1-2 years): Explore viability of a liquid metal jet target in intense, short proton pulses and (separately) in strong magnetic fields. (Change target technology if encounter severe difficulties.)

- Mid Term (3-4 years): Add 20-T magnet to BNL AGS beam tests; Test 70-MHz rf cavity (+ 1.25-T magnet) downstream of target; Characterize pion yield.

5.2 Ionization Cooling

The Theory:

- Ionization: takes momentum away.

- RF acceleration: puts momentum back along z axis.
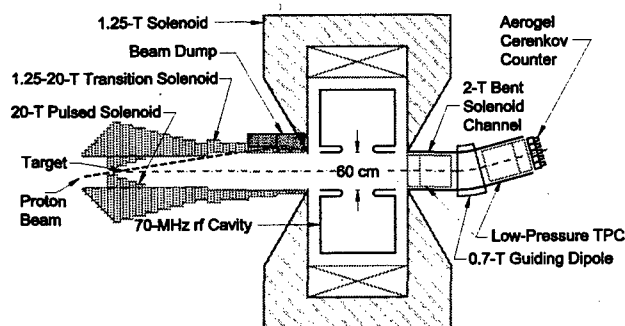
Figure 10: The proposed facility for targetry R&D at BNL [58, 59].

Particles are slowed along their path (dE/dx)

Particles are accelerated longitudinally
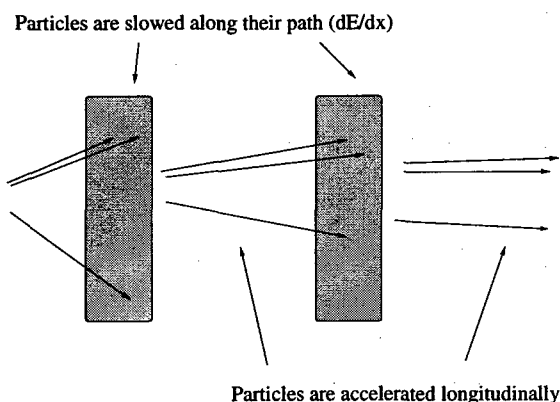
Figure 11: The concept of transverse ionization cooling.

- ⇒ Transverse "cooling"; O'Neill [7] (1956).

- This won't work for electrons or protons.

- So use muons: Balbekov [8], Budker [9], Skrinsky [10], late 1960's.

The Details are Delicate:

- Use channel of LH_2 absorbers, rf cavities and alternating solenoids (to avoid buildup of angular momentum).
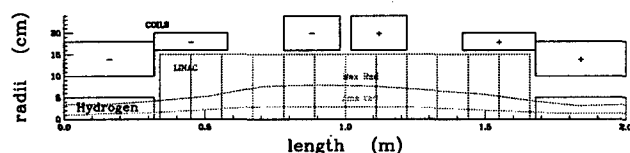
Figure 12: One cell of the cooling channel.

- But, the energy spread rises due to "straggling".

- ⇒ Must exchange longitudinal and transverse emittance frequently to avoid beam loss due to bunch spreading.

- Can reduce energy spread by a wedge absorber at a momentum dispersion point:
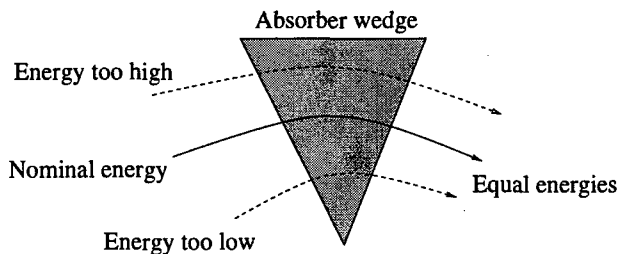
Figure 13: Longitudinal/transverse emittance exchange in a wedge absorber.

Cooling Demonstration Experiment:

- Test basic cooling components:

  - Alternating solenoid lattice, RF cavities, LH_2 absorber.

  - Lithium lens (for final cooling).

  - Dispersion + wedge absorbers to exchange longitudinal and transverse phase space.

- Track individual muons; simulate a bunch in software.
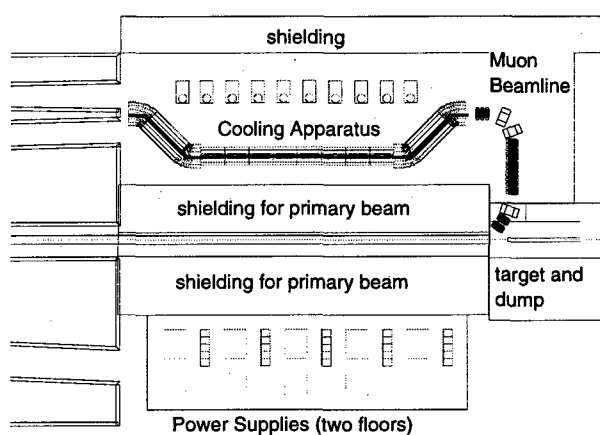
Figure 14: Possible site for the muon cooling experiment in the Fermilab Meson Hall [60, 61].
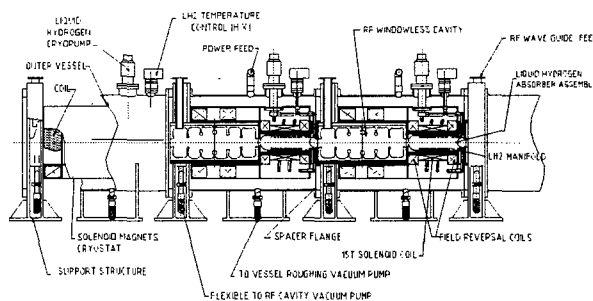
Figure 15: Side view of three cells of a cooling channel, incorporating LH_2 absorbers, 15-T alternating solenoid magnets, and high-gradient 800-MHz rf cavities.
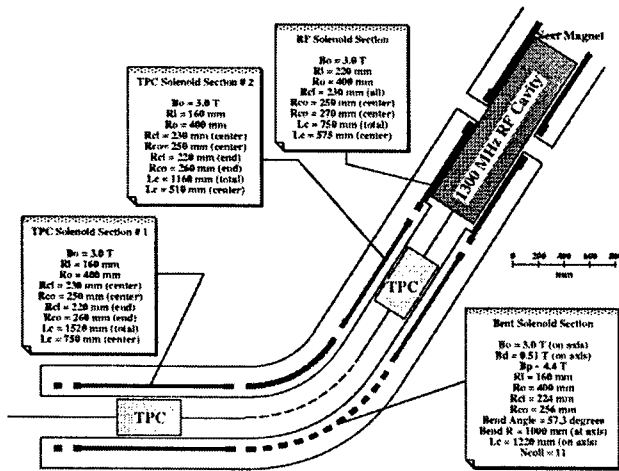
Figure 16: Emittance diagnostics via a bent solenoid spectrometer.

6 REFERENCES

[1] http://www.cap.bnl.gov/mumu/status_report.html

[2] http://www.cap.bnl.gov/mumu/book.html

[3] AIP Conf. Proc. **352** (1995).

[4] AIP Conf. Proc. **372** (1996).

[5] AIP Conf. Proc. **435** (1998).

[6] AIP Conf. Proc. **441** (1998).

[7] G.K. O'Neill, Phys. Rev. **102**, 1418 (1956).

[8] Yu.M. Ado and V.I. Balbekov, Sov. Atomic Energy **31**, 731 (1971).

[9] G.I. Budker, see AIP Conf. Proc. **352**, 4 (1996).

[10] A.N. Skrinsky, see AIP Conf. Proc. **352**, 6 (1996).

[11] http://xxx.lanl.gov/ps/hep-ex/9801004

[12] http://nicewww.cern.ch/~autin/MuonsAtCERN/Neutrino.htm

[13] http://ftp.pac99.bnl.gov/Papers/Wpac/MOP86.pdf

[14] http://ftp.pac99.bnl.gov/Papers/Wpac/MOP98.pdf

[15] http://ftp.pac99.bnl.gov/Papers/Wpac/TUA147.pdf

[16] http://ftp.pac99.bnl.gov/Papers/Wpac/TUP101.pdf

[17] http://ftp.pac99.bnl.gov/Papers/Wpac/TUP129.pdf

[18] http://ftp.pac99.bnl.gov/Papers/Wpac/TUP154.pdf

[19] http://ftp.pac99.bnl.gov/Papers/Wpac/WEA163.pdf

[20] http://ftp.pac99.bnl.gov/Papers/Wpac/WEBR4.pdf

[21] http://ftp.pac99.bnl.gov/Papers/Wpac/WEBR5.pdf

[22] http://ftp.pac99.bnl.gov/Papers/Wpac/WEBR6.pdf

[23] http://ftp.pac99.bnl.gov/Papers/Wpac/WEP118.pdf

[24] http://ftp.pac99.bnl.gov/Papers/Wpac/THA130.pdf

[25] http://ftp.pac99.bnl.gov/Papers/Wpac/THP31.pdf

[26] http://ftp.pac99.bnl.gov/Papers/Wpac/THP32.pdf

[27] http://ftp.pac99.bnl.gov/Papers/Wpac/THP33.pdf

[28] http://ftp.pac99.bnl.gov/Papers/Wpac/THP34.pdf

[29] http://ftp.pac99.bnl.gov/Papers/Wpac/THP35.pdf

[30] http://ftp.pac99.bnl.gov/Papers/Wpac/THP36.pdf

[31] http://ftp.pac99.bnl.gov/Papers/Wpac/THP37.pdf

[32] http://ftp.pac99.bnl.gov/Papers/Wpac/THP38.pdf

[33] http://ftp.pac99.bnl.gov/Papers/Wpac/THP39.pdf

[34] http://ftp.pac99.bnl.gov/Papers/Wpac/THP40.pdf

[35] http://ftp.pac99.bnl.gov/Papers/Wpac/THP41.pdf

[36] http://ftp.pac99.bnl.gov/Papers/Wpac/THP42.pdf

[37] http://ftp.pac99.bnl.gov/Papers/Wpac/THP44.pdf

[38] http://ftp.pac99.bnl.gov/Papers/Wpac/THP44.pdf

[39] http://ftp.pac99.bnl.gov/Papers/Wpac/THP45.pdf

[40] http://ftp.pac99.bnl.gov/Papers/Wpac/THP46.pdf

[41] http://ftp.pac99.bnl.gov/Papers/Wpac/THP47.pdf

[42] http://ftp.pac99.bnl.gov/Papers/Wpac/THP48.pdf

[43] http://ftp.pac99.bnl.gov/Papers/Wpac/THP49.pdf

[44] http://ftp.pac99.bnl.gov/Papers/Wpac/THP50.pdf

[45] http://ftp.pac99.bnl.gov/Papers/Wpac/THP51.pdf

[46] http://ftp.pac99.bnl.gov/Papers/Wpac/THP52.pdf

[47] http://ftp.pac99.bnl.gov/Papers/Wpac/THP53.pdf

[48] http://ftp.pac99.bnl.gov/Papers/Wpac/THP54.pdf

[49] http://ftp.pac99.bnl.gov/Papers/Wpac/THP55.pdf

[50] http://ftp.pac99.bnl.gov/Papers/Wpac/THP56.pdf

[51] http://ftp.pac99.bnl.gov/Papers/Wpac/THP57.pdf

[52] http://ftp.pac99.bnl.gov/Papers/Wpac/THP58.pdf

[53] http://ftp.pac99.bnl.gov/Papers/Wpac/THP59.pdf

[54] http://ftp.pac99.bnl.gov/Papers/Wpac/THP60.pdf

[55] http://ftp.pac99.bnl.gov/Papers/Wpac/THP83.pdf

[56] http://ftp.pac99.bnl.gov/Papers/Wpac/THP85.pdf

[57] http://ftp.pac99.bnl.gov/Papers/Wpac/THP86.pdf

[58] http://puhep1.princeton.edu/mumu/target/targetprop.ps

[59] http://puhep1.princeton.edu/mumu/target/

[60] http://www.fnal.gov/projects/muon_collider/

[61] http://www.fnal.gov/projects/muon_collider/cool/cool.html

POSSIBILITY OF USING A RING ACCELERATOR FOR IONIZATION COOLING OF MUONS*

V.I.Balbekov, FNAL, Batavia, IL

Abstract

A possibility of using a racetrack-like ring accelerator as the first stage of a cooler for muon collider is considered. The ring cooler includes bending magnets with field index 0.5, bent solenoids, and straight sections with accelerating cavities and solenoids. LiH rods placed in straight sections are used for transverse cooling whereas wedge absorbers in bending parts provide transverse-longitudinal emittance exchange. Results of analytical calculations and Monte Carlo simulations with scattering and straggling are presented, and problem of suppression of nonlinear and chromatic effects is discussed.

1 INTRODUCTION

This report examines the possibility of using a racetrack-like ring accelerator in the cooling stage of muon collider (Fig.1). The main merit of such a cooler is lower projected cost because the same accelerating and focusing system is used repeatedly (about 20 turns in a typical scenario) [1].
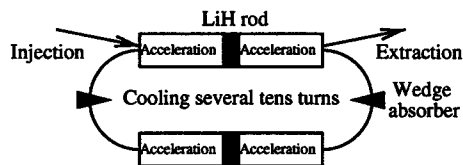
Figure 1: Schematic of a ring cooler.

'Usual' ring accelerator could provide the cooling which is schematically shown on Fig.2, left. Boundary of a beam on phase plane $(X - X')$ is a phase trajectory depending on β - function and conserving the shape if compression by a cooling exist. But X' size is restricted by multiple Coulomb scattering typically 300 mrad on 3σ - level. Initial size cannot be significantly more because of aperture restriction, so a deep cooling is impossible in such a scheme. To provide it, it is necessary to get independent motion in $X-$ and $X'-$ directions on phase plane as shown on Fig.1, right. It means that transfer matrix is $\pm I$; another words, *betatron frequency of the ring cooler must be integer or half-integer*.

It refers to synchrotron motion, too, but it is very difficult to get synchrotron frequency 0.5 at low RF. But the considered version of a ring cooler is focused on initial stage of cooling when bunch length is several meters [2, 3], and using of high RF is impossible. Hence *such a cooler must operate at transition energy* which formally corresponds to synchrotron frequency 0. Bunchers are needed only for longitudinal compression of the bunch.
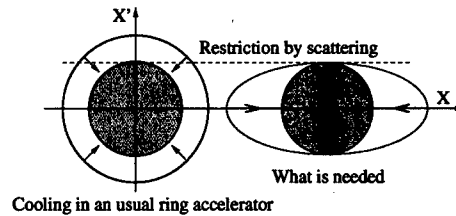
Figure 2: The cooling dynamics in 'usual' and 'resonant' ring cooler.

2 SCHEMATIC AND PARAMETERS OF THE COOLER

Schematic of the cooler is shown on Fig.3. LiH rods 0.31 m long are placed inside solenoids 2.32 m long. Each solenoid is divided on 2 non equal parts with opposite direction of field: (1) $L = 1.142$ m, $B = 3.207$ T, (2) $L = 1.178$ m, $B = -2.646$ T, and each part provides betatron phase advance $\pi/2$. The main destination of these solenoids is to focus very divergent beam going out the rods to parts of straight section with cavities. Four 0.5 m solenoids are used to focus the beam in these parts. Each solenoid with adjacent drift spaces provides phase advance $\pi/2$. Field of the solenoid depends on its position and lies in the range 1.95 -2.36 T.

Bent solenoids of radius 0.75 m are placed inside combine function magnets with field index 0.5. This complex provides the same focusing as central solenoid and recreates the beam size and angle divergence. Front and back bent solenoids have opposite and slightly different fields 2.105 T and -2.035 T because energy loss in center of wedge absorber is 10.7 MeV. Dipole fields are 1.489 and 1.439 T. Such a combination is very suitable for emittance exchange section because has simple transfer matrix -I and easy controlled and quite sufficient for emittance exchange dispersion function (Fig.4). It gives rather small nonlinear and chromatic distortions. A bending system without solenoid
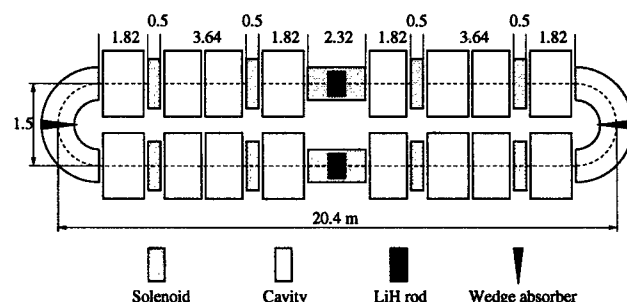
Figure 3: Schematic of a ring cooler with solenoids.

was considered in previous version of a ring cooler [1]. In that case beam size in the bending part was essentially more resulting strong nonlinear distortions. Drawback of new system is less dispersion function resulting decrease of momentum compaction factor and growth of transition energy which is operating energy of the ring cooler. Other parameters of the cooler are listed in Table 1.
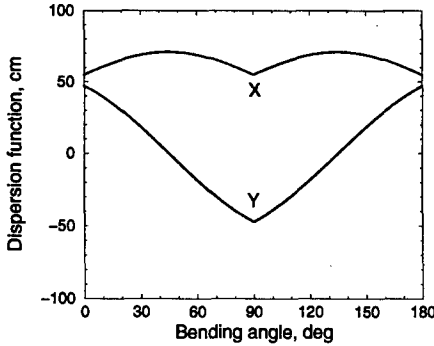
Figure 4: Dispersion function in bending part of the ring.

Table 1: Main parameters of the cooler

Muon momentum, MeV/c	297 - 360
Circumference, m	42.47
Revolution frequency	6.167 MHz
Energy gain, MeV/turn	120
Muon decay, %/turn	2

3 LINEAR SIMULATION

Results of simulation in linear approximation without chromaticity are presented in this section to estimate ultimate capabilities of the cooler. Gaussian distribution with parameters: $\sigma_x = \sigma_y = 7.5$ cm, $\sigma_{p_x} = \sigma_{p_y} = 23$ MeV/c, $\sigma_z = 150$ cm, $\sigma_E = 11$ MeV was taken for consideration. The parameters are chosen to get constant angle and energy spread during the cooling what is really obtained.

Dependence of normalized r.m.s. emittance and transmission on number of periods is shown on Fig.5 (1 turn = 2 periods). 6-dimensional emittance decreases 2400 times by 30 turns and do not reach equilibrium yet. Transmission is is about 55% in agreement with muon decay.

Fig.6-7 give distributions of injected (left) and cooled beams on transverse and longitudinal phase plane.

4 TRANSVERSE NONLINEARITY AND CHROMATICITY

The beam envelopes between the rod and the wedge absorber are shown schematically on Fig.8 before and after the cooling. In both cases there is strong modulation responsible for chromatic distortions accompanied by parametric
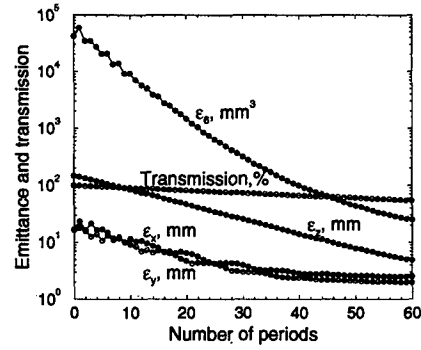
Figure 5: Dependence of emittance and transmission on number of periods.
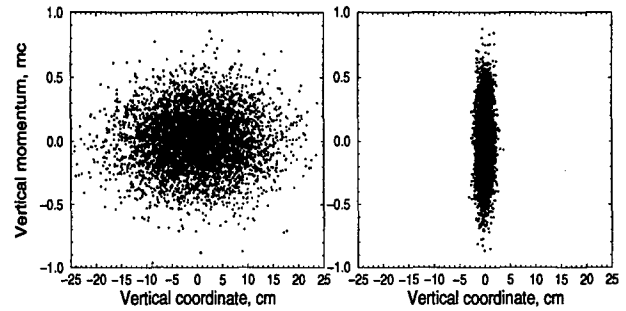
Figure 6: Initial and final transverse distributions.
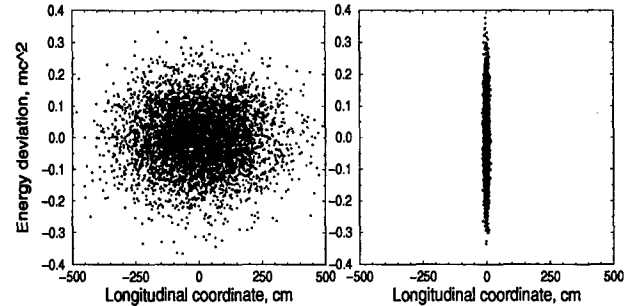
Figure 7: Initial and final transverse distributions.

resonance. The latest changes amplitude of betatron oscillations depending on them phases. Parameters of the cooler are chosen to decrease the amplitude of non-equilibrium particles going out the rod with large angle and relatively small transverse coordinate what is typical for the end of the cooling. In this case, chromatic distortions are demonstrated by Fig.9. Chromaticity is rather large still and nonlinear dispersion is observed, too. It causes transverse emittance blow up by factor 1.6 - 1.7 (see Table 2 in next section, too).

Fig.9 demonstrates transverse nonlinear effects by 1 period for equilibrium particles. Initial phase ellipses are canonical corresponding to transverse emittance on the levels 1,2,3 σ. These distortions are tolerable, but it is necessary to remember that effect substantially enhanced for

non-equilibrium particles. They give an additional emittance blow up on 10 - 15%.
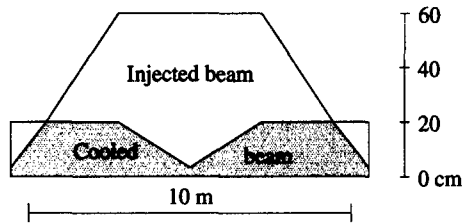
Figure 8: Beam envelop between the rod and the wedge absorber (1/4 of a turn, schematically).
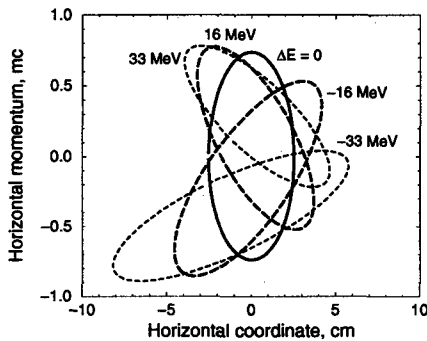
Figure 9: Phase ellipse after 1 period at different energy deviation. Initial ellipse is canonical, $\sigma_E = 11$ Mev.
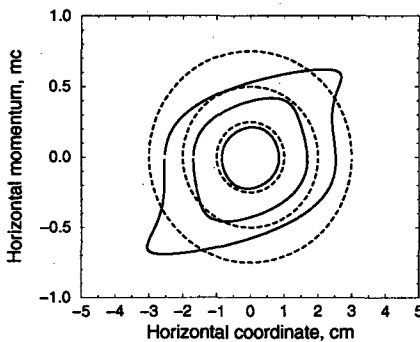
Figure 10: Nonlinear distortions by 1 period. Dashed lines – phase ellipses in the beginning (1,2,3 σ - levels), solid lines – in the end.

5 LONGITUDINAL NONLINEARITY

All demonstrated results are obtained with accelerating field of harmonic number $h = 1$, and almost the same turns out at $h = 2$. But dependence of a trajectory length on amplitude of betatron oscillations was not taken into account yet. With it, there is significant blow up of longitudinal emittance and additional particles loss which really stop the cooling about after 16 turns. Final distributions are shown on Fig.11. It is seen that time-amplitude dependence shifts all the distribution right (average flying time increases), and
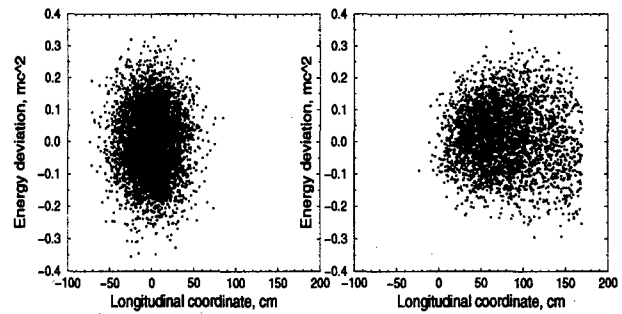
Figure 11: Longitudinal phase plane after 16 turns: linear (left) and nonlinear approximations.

a tail appears which is partially cut on the plot. After 16 turns the core of the bunch continues to compress but r.m.s. size does not change because the tail grows and the distribution becomes non Gaussian. Resulting emittances and transmission are presented in Table 2.

Table 2: Effect of different factors on the cooling (16 turns)

	ε_{tr}, cm	ε_z, cm	ε_6, cm^3	Trans.
Injected beam	1.76	14.7	45.7	1.00
Linear apx.	0.34	2.2	0.26	0.73
+chromaticity	0.50	2.4	0.60	0.62
+trans. nonlin.	0.61	2.7	1.00	0.57
+long. nonlin.	0.55	3.8	1.15	0.50

6 CONCLUSION

The low-frequency ring cooler appears capable of satisfactory cooling a muon beam both in transverse and longitudinal directions. The achievable emittance suggests its use as a precooler in a muon collider complex especially for effective bunch shortening which is necessary in any scenario. The most serious problems are:

● Chromatic effects are very strong yet. Probably, a combined system with solenoids, quads and sextupole correctors should be developed to reduce it.

● Time-amplitude correlations are the most limiting factor for the longitudinal cooling. It is possible, special form of absorbers can help to suppress it.

● Development of low-frequency high gradient accelerating system is necessary in any case.

7 REFERENCES

[1] V.I. Balbekov and A. Van Ginneken, Ring Cooler for Muon Collider. AIP Conf. Proc. 441, 310 (1997)

[2] R. Palmer, Progress on $\mu^+\mu^-$ Collider. Proc. PAC 97 (Vancouver, Canada, 1997), p.286.

[3] D. Neuffer and A. Van Ginneken, Muon Collection Channel. Fermilab Pub-98/296 (1998).

POTENTIAL HAZARDS FROM NEUTRINO RADIATION AT MUON COLLIDERS

Bruce J. King, Brookhaven National Laboratory [1]

Abstract

High energy muon colliders, such as the TeV-scale conceptual designs now being considered, are found to produce enough high energy neutrinos to constitute a potentially serious off-site radiation hazard in the neighbourhood of the accelerator site. A general characterization of this radiation hazard is given, followed by an order-of-magnitude calculation for the off-site annual radiation dose and a discussion of accelerator design and site selection strategies to minimize the radiation hazard.

1 INTRODUCTION

Current conceptual designs for muon colliders [1] envisage large currents of opposing positively and negatively charged muons circulating in a collider ring until decay into neutrinos and electrons:

$$
\begin{aligned}
\mu^- &\rightarrow \nu_\mu + \overline{\nu_e} + e^-, \\
\mu^+ &\rightarrow \overline{\nu_\mu} + \nu_e + e^+.
\end{aligned}
\tag{1}
$$

This will produce an intense disk of neutrinos emanating out in the plane of the collider ring. The vertical angular divergence of the neutrino disk can be characterized by the spread in the relative angle between the neutrino and muon directions and, from relativistic kinematics, the neutrinos in the forward hemisphere in the muon rest frame are boosted, in the laboratory frame, into a narrow cone with an opening half-angle,

$$
\theta_\nu \simeq \sin\theta_\nu = 1/\gamma = \frac{m_\mu c^2}{E_\mu} \simeq \frac{10^{-4}}{E_\mu[\text{TeV}]},
\tag{2}
$$

with γ the relativistic boost factor of the muon, E_μ the muon energy and m_μ the muon rest mass.

The vertical angular spread of the neutrino disk could, in principle, also receive contributions from the angular spread of the muon beam. However, for reasonable magnet lattice designs this will usually produce negligible additional divergence everywhere around the collider ring except at the final focus regions around collider experiments.

The potential radiation hazard comes from the showers of ionizing particles produced in interactions of neutrinos in the soil and other objects bathed by the disk. The tiny interaction cross-section for neutrinos is greatly compensated by the huge number of high energy neutrinos produced at muon colliders.

2 QUANTITATIVE DERIVATION OF RADIATION DOSE

A quantitative expression for the radiation dose received by a person from the decay of N_μ muons of each sign, at tangential distance L from an idealized perfectly circular muon collider ring and in the plane of the ring is given by:

$$
D^{ave} = \frac{N_\mu}{L^2} \int_0^{2\pi} \frac{d\theta}{2\pi} \cdot \frac{1}{4\pi} \frac{d\Omega'}{d\Omega}(\theta) \times
$$
$$
\sum_{\nu type, i=1,4} \int_0^1 dx f^i(x) \sigma^i(E_\nu) d^i(E_\nu),
\tag{3}
$$

where E_ν is a function of both integration variables, x and θ and the variables and form of the expression are explained in the following paragraphs.

In principle, neutrinos can be emitted in all directions relative to the muon trajectory at decay so the angle between the muon beam and the neutrino direction, θ, is formally integrated over all muon directions around ring, However, equation 1 shows that most of the contribution to the radiation dose will come from neutrinos oriented within of order $1/\gamma$ or less from the muon beam direction, so the size of the collider ring can be ignored. Clearly, a fraction $\frac{d\theta}{2\pi}$ of the muons will decay in the angular increment $d\theta$ and, for the reasonable assumption that the muon beams are unpolarized on average, the neutrino decays will be isotropic in muon rest frame and the fraction of neutrino decays per unit solid angle in the laboratory rest frame is is $\frac{1}{4\pi} \frac{d\Omega'}{d\Omega}(\theta)$, where primed coordinates denote the muon rest frame and unprimed coordinates the laboratory rest frame.

A biological target in the radiation disk is tangent to the collider ring in two places and so will receive neutrinos from the decays of both positive and negative muons. Therefore, the neutrino type index, i, runs over all 4 neutrino types – $\overline{\nu_e}$, ν_μ, $\overline{\nu_\mu}$ and ν_e.

The energy probability distribution in the muon rest frame for the production of neutrino type i is $dx \cdot f_x^i$, with x defined as the fraction of the maximum neutrino energy in the muon rest frame: $E_\nu' = \frac{x.m_\mu c^2}{2}$. The explicit form for f is known to be: $f = 6.x^2 - 4.x^3$ for unpolarized muon-type neutrinos or anti-neutrinos and $f = 12.x^2 - 12.x^3$ for unpolarized electron-type neutrinos or anti-neutrinos. Boosting to the laboratory frame gives

$$
E_\nu(x, \cos\theta') = x \cdot \frac{E_\mu}{2} (1 + \beta\cos\theta').
\tag{4}
$$

The cross-section per nucleon, $\sigma^i(E_\nu)$, is expressed, for now, in the same units of length as L and $d^i(E_\nu)$ is the average radiation dose from a neutrino of type i and energy E_ν interacting in each nucleon of a biological target, assuming

the equilibrium approximation and expressed in the same units as D^{ave}.

Most of the ionization energy dose deposited in a person will come from interactions in the soil and other objects in the person's vicinity rather than from the more direct process of neutrinos interacting inside a person. At TeV energy scales, much less than one percent of the energy flux from the daughters of such interactions will be absorbed in the relatively small amount of matter contained in a person, with the rest passing beyond the person.

Equation 3 implicitly assumes the simplifying "equilibrium approximation" that the ionization energy absorbed by a person is equal to the energy of the showers initiated by interactions in that person.

It seems reasonable to assume that the equilibrium approximation should give either a reasonable estimate or a conservative overestimate of the radiation dose absorbed by a person for most of the innumerable possible distributions of matter. From conservation of energy, it would clearly be a good approximation for the reference case of a homogeneous medium of any density sufficient that the radial extent of the hadronic and electromagnetic showers initiated by neutrino interactions is small compared to the height of the neutrino radiation disk. In realistic geometries, some of the shower energy will typically leak out to beyond the extent of the neutrino disk through low density regions of air etc., presumably decreasing the radiation dose to below the equilibrium estimate.

The radiation dose in units of Sieverts (Sv) is numerically almost equal to the energy deposition in a biological target in units of J/kg for the energetic hadronic and electromagnetic showers from neutrino interactions.

Equation 3 may be converted into a quantitative prediction for the radiation dose:

$$D^{ave}[Sv] = 3.7 \times 10^{-23} \times \frac{N_\mu \times (E_\mu[TeV])^3}{(L[km])^2}. \quad (5)$$

using straightforward calculations [2] that take into account the nearly-linear dependence on energy of the neutrino cross-section.

The radiation intensity would be expected to vary greatly around the neutrino disk, depending on the detailed design of the collider ring magnet lattice, so the value of D_{ave} by itself is not sufficient to assess the radiation hazard for any particular collider design. For example, it is clear from the derivation of equation 5 that the radiation contribution tangent to the collider ring at a dipole bending magnet will be proportional to the beam's bending radius at the magnet, which is inversely proportional to the magnetic field strength.

For even bigger variations, tangents to the collider ring at anywhere other than a dipole magnet the muon currents will travel in straight line trajectories and the neutrinos will line up as local radiation "hot spots" in the radiation disk – cones of more intense radiation with characteristic opening half-angles of $\theta_\nu = 1/\gamma$.

The contribution from straight sections is given by an equation analagous to equation 3:

$$D^{ss} = \frac{f^{ss} \times N_\mu}{L^2} \times \frac{\gamma^2}{\pi} \times$$

$$\sum_{\nu type, i=1,2} \int_0^1 dx f^i(x) \sigma^i(E_\nu) d^i(E_\nu), \quad (6)$$

where f^{ss} is the length of the straight section as a fraction of the collider circumference

$$f^{ss} = L/C \quad (7)$$

and the factor γ^2/π is the fraction of neutrinos decaying in the forward direction per unit solid angle after being boosted from isotropic decays in the muon rest frame into the laboratory frame.

The summation in equation 6 is now only over the 2 neutrino types produced by the sign of muon travelling in the considered direction, i.e., either $\overline{\nu_e}$ and ν_μ for μ^- decays or $\overline{\nu_\mu}$ and ν_e for μ^+ decays (equation 1), where the summed contributions for μ^+ and μ^- are very nearly equal, so it is reasonable to use the average contribution.

Following a similar derivation to that for equation 5 the numerical value for the dose is:

$$D^{ss}[Sv] = 1.1 \times 10^{-18} \times \frac{f^{ss} \times N_\mu \times (E_\mu[TeV])^4}{(L[km])^2}. \quad (8)$$

The radiation cones from the final focus regions around collider experiments are important exceptions to equation 8, since the muon beam itself will have an angular divergence in these regions that may be large enough to spread out the neutrino beam by at least an order of magnitude in both x and y.

More detailed calculations to check and refine these calculations, using Monte Carlo-based particle tracking computer simulations, are in progress.

On comparing equations 5 and 8 it is easily seen that the length of straight section to produce an extra contribution equal to the planar average dose, l_{equiv}, is approximately:

$$l_{equiv}[meters] \simeq 0.034 \times \frac{C[km]}{E_\mu[TeV]} \simeq \frac{0.71}{B_{ave}[T]}, \quad (9)$$

where the final expression uses the relation between muon energy, ring circumference and and average bending magnetic field in units of Tesla:

$$C[km] = \frac{2\pi \cdot E_\mu[TeV]}{0.3 \cdot B_{ave}[T]}, \quad (10)$$

valid for a circular ring.

Two mitigating factors come into play at many-TeV energies to reduce the radiation rise with energy to well below the predictions of equations 5 and 8:

1. the neutrino cross section begins to rise significantly less rapidly than linearly with neutrino energy

319

2. the radiation disk (or cone) becomes so narrow that the "equilibrium approximation" is no longer accurate because much of the induced shower of charged particles leaks out transversely beyond the extent of the radiation disk. (See [2] for details.)

3 STRATEGIES TO MINIMIZE OFF-SITE RADIATION DOSES

Because of the strong dependence on muon energy, the radiation levels rapidly become a serious design constraint for colliders at the TeV scale and above. For illustration, the average annual radiation doses [2] in the plane of the collider ring are 3×10^{-5}, 9×10^{-4}, 9×10^{-4}, 0.66 and 6.7 mSv/year for some example muon collider parameter sets [3] at respective energies of 0.1, 1, 4, 10 and 100 TeV. (The 4 TeV parameter set assumes a muon current that is more than an order of magnitude smaller than the others.) For comparison, the U.S. federal off-site radiation limit is 10^{-3} Sv/year, which is of the same order of magnitude as the typical background radiation from natural causes (i.e. 0.4 to 4×10^{-3} Sv/yr [2]) and it is assumed that acceptable radiation levels must be considerably lower than these values.

As a desirable design strategy for all energies, it is clear that great care must be taken to minimize or eliminate long straight sections in the collider ring. For example, the magnet lattice could consist partly or entirely of dual function magnets, where the beam focusing and bend are accomplished in the same magnets. Optionally, it might be convenient to retain one or two long straight sections by constructing radiation enclosures around where their radiation hot spots exit the ground.

Perhaps the most direct way of decreasing the radiation levels is to greatly decrease the muon current. This can be done either by sacrificing luminosity (as in the 4 TeV parameter set of table 2) or, more attractively, by increasing the luminosity per given current through better muon cooling or other technological advances.

Further, one might consider placing the accelerator deep underground so the radiation disk won't reach the surface for some distance. For the example of a very flat region of the Earth the exit distance to the surface L_{exit} will be related to the collider depth, D, and the Earth's radius, $R_E = 6.4 \times 10^6$m, by $L_{exit} = (2 \times D \times R_E)^{1/2}$, where the three parameters are in consistent units of length, e.g., meters. This implies that the radiation dose at exit falls inversely with collider depth, and the value of R_E determines that exit distances of order 10 km are easily achievable, but achieving an L_{exit} of order 100 km is already starting to require a prohibitively large depth. (See [2] for explicit formulae and further discussion.)

Further speculative options that have been discussed include (i) tilting the ring to take best advantage of the local topography, (ii) placing the collider ring on a hill so the radiation disk passes harmlessly above the surroundings and, even more speculatively, (iii) spreading out and diluting the neutrino radiation disk by continuously sweeping the muon beam orbit in a vertical plane using dipole corrector magnets.

Even when the preceding strategies have been used, the strong rise in neutrino energy probably dictates that muon colliders at CoM energies of beyond a few TeV will probably have to be constructed at isolated sites where the public would not be exposed to the neutrino radiation disk at all. This would definitely be required for the 10 TeV and 100 TeV parameter sets of table 2. Because of the additional costs this would involve, these will presumably be "second generation" machines, arriving after the technology of muon colliders has been established in one or more smaller and less expensive machines built at existing HEP laboratories.

4 CONCLUSIONS

In conclusion, some order-of-magnitude calculations have been presented which show that the neutrino-induced radiation hazard might be a very serious problem for high energy muon colliders. The neutrino radiation problem appears to impose severe constraints on the site selection for a muon collider complex and on the layout of the complex.

It is speculated that the highest energy muon (and hadron) colliders and their associated neutrino radiation disks may be required to be enclosed within a huge new world HEP laboratory somewhere where there is a large area of cheap, sparsely populated land.

5 ACKNOWLEDGEMENTS

6 REFERENCES

[1] The Muon Collider Collaboration, "Status of Muon Collider Research and Development and Future Plans", to be submitted to Phys. Rev. E.

[2] A longer version of this paper that contains more explicit derivations of the quantitative results in this paper and more detail on the radiation doses for example muon collider parameters is available at http://pubweb.bnl.gov/people/bking/.

[3] B.J. King, "Discussion on Muon Collider Parameters at Center of Mass Energies from 0.1 TeV to 100 TeV", 19 June, 1998, Submitted to Proc. Sixth European Particle Accelerator Conference (EPAC'98), Stockholm, Sweden, 22-26 June, 1998. Available at http://pubweb.bnl.gov/people/bking/.

THE LASER DRIVEN ELECTRON ACCELERATOR EXPERIMENT AT STANFORD UNIVERSITY

R.L. Byer, T.Plettner[†], Y.C. Huang[‡], Ginzton Laboratories, Stanford University

E. Colby, R.L. Siemann, J.E. Spencer, H. Wiedemann, C. Barnes, SLAC

T.I. Smith, R.L. Swent, HEPL, Stanford University

Abstract

This experiment seeks to demonstrate laser driven particle acceleration in a dielectric loaded vacuum structure. Evidence for particle acceleration will be inferred from the change in the observed energy spread of the electron bunch. Under optimum conditions we expect an increase by a factor bigger than 3. However, the energy profile as a function of several controllable beam parameters provides the most distinctive signature.

1 INTRODUCTION

The main motivation for considering an eventual accelerator built from a dielectric material and powered by a laser beam is the increase of the damage threshold of the structure for ultra short laser pulses [1], [2], and hence the achievable gradient of the cell by about an order of magnitude. The principle of acceleration from a pair of linearly crossed laser beams has been studied extensively in the past [3], and dielectric structures capable of 1 GeV/m average gradient have been proposed [4], [5]. This is much lower than the peak gradient observed in plasma accelerators. However the main advantage of the crossed laser beam acceleration scheme is the absence of any material in the path of the particle beam. This allows, at least in principle, for the preservation of a low emittance and low energy spread of the particle beam and hence for indefinite cascading. Finally, a cleverly designed dielectric accelerator structure could allow for recycling of the laser beam, and therefore a very energy efficient system.

2 THE EXPERIMENT

The electron beam and laser beam parameters employed in this experiment are summarised in Table 1. There are two important issues that determine the design and the kind of results expected in the experiment. One is the enormous mismatch in the repetition rate of the laser beam and the electron micro bunch train. Only one in ten thousand micro bunches may overlap with the laser pulse. In order to avoid the background from unusable micro bunches a fast kicker located in the main line deflects only

the desired micro bunch into a separate beam line where the experiment is located. The other important issue is the time duration of the e-beam pulse, which covers several optical cycles of the laser pulse. Therefore instead of observing an overall shift in the energy a change in the energy spread of the beam is expected. A high-resolution spectrometer magnet located downstream from the test laser accelerator cell measures the energy spread of the electron beam.

Table 1: Electron and laser beam parameters

	Wavelength	800 nm
Ti:Sa amplified laser	Pulse duration	0.1 - 30 psec
	Repetition rate	10 Hz
	Energy per pulse	0.055 mJ
	FWHM spot size	130 μm
SCA electron beam	Energy	32 MeV
	Micropulse period	85 nsec
	Macropulse period	0.1 sec
	Bunch length	2 psec
	FWHM energy spread	16 keV
	Electrons per bunch	10^7
	Invariant emittance	8π mm-mrad

The expected effect is of the order of tens of keV, therefore the key for the success of this experiment is the very low energy spread attainable at the SCA-FEL facility.

2.1 The accelerator cell

The accelerator cell consists of high reflector coated dielectric optics which are arranged such that the electron beam enters and leaves the cell through a vertical slit formed by these optics. The optics are mounted on motorised translation stages so that the size of the slits can be changed. A wide slit allows the electron beam to traverse the cell with no loss but truncates the laser field and severely reduces the energy gain. With a 5 μm slit and a 1 psec laser pulse the energy spread of the electron beam is expected to increase by a factor of more than 3, whereas a 100 μm slit has virtually no effect. So far we have succeeded in sending the electron beam through a 50-60 μm slit with usable intensity, but have not been able to close the slits below 30 μm and still observe the beam. The detailed geometry of the accelerator cell has been

described in detail in previous papers [6]. A simplified diagram of the accelerator cell is given in Fig. 1.
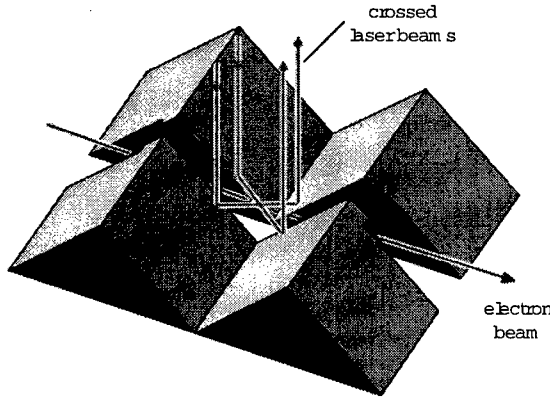
Figure 1: The accelerator cell.

2.2 Timing of the laser and the electron beam

The two beams have to be timed to within 1 psec in order to achieve good temporal overlap. Two monitors are employed; one coarse timing monitor that can detect the timing difference of the two beams to within 1 nsec, and a fine timing monitor capable of measuring timing changes between the beams with a 1 psec resolution. The coarse timing monitor is a silicon photodiode detector placed at the straight ahead port of the spectrometer that is capable of observing both beams. The fine timing system compares the timing between the modelocked laser, whose amplified pulse is sent to the accelerator, with the
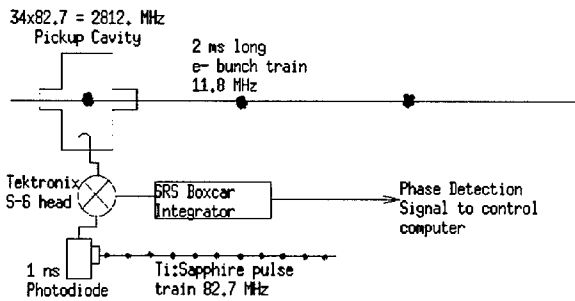
phase of the electron beam, as depicted in Fig. 2.

Figure 2: Block diagram for the fine timing detection

2.3 Characterisation of the e-beam

Both the fluctuations in the mean energy of the beam and its spread have been measured. The energy spread shows rather small fluctuations, however a considerable jitter in the mean energy is readily observed and has shown both short and long term oscillations. The beam has also been diagnosed near the accelerator cell and was found to show considerable jitter in the position of the beam centroid. Table 2 summarises a consistent set of beam

measurements taken during a recent, parasitic run. During non-parasitic operation we have obtained a mean energy spread of 16 keV (FWHM) or 0.05%. Work is continuing on characterising and improving the e-beam quality.

Table 2: Some parasitic e-beam parameters in LEAP

Beam Energy	Energy spread FWHM	37 keV
	r.m.s mean energy jitter	16 keV
	r.m.s. energy spread jitter	15 keV
Near the accelerator cell	horizontal position jitter	10 μm
	vertical position jitter	54 μm
	FWHM horizontal spot size	70 μm
	FWHM vertical spot size	113 μm
	Horizontal spot size jitter	20%
	Vertical spot size jitter	20%

3 CALCULATIONS

3.1 Expected laser induced effects

The laser beam is expected to cause a broadening in the energy spread instead of inducing an overall shift in energy. Our calculations have shown that only a very limited range of combinations of the experimental parameters can lead to a readily observable effect. The parameters that have the largest effect are the slit width, the laser pulse duration, the electron beam pulse duration and its natural energy spread.

The first step in the numerical evaluation of the laser induced energy spread profile is a diffraction calculation that finds the longitudinal electric field along the axis of propagation of the electron. The acceleration effect from two crossed gaussian beams interacting with the electron beam over a finite distance has been calculated before [7]. In order for the particle beam to enter and leave the cell an aperture of some kind has to be provided and hence partial truncation of the laser beams entering the accelerator cell and a leakage field behind the accelerator are expected. The diffraction calculation method employed here is a generalisation of a 2-D plane wave decomposition method used to find the electric field of cylindrical laser beams [8]. The expression for the longitudinal electric field at a point behind the input plane given in equation (1) of ref. [8] becomes

$$E_z(x, y, z) = -e^{-i\omega t} \cdot \int_{-\frac{\pi}{2}}^{\frac{\pi}{2}} \int_{-\frac{\pi}{2}}^{\frac{\pi}{2}} (a(\alpha, \beta) \cdot \sin(\alpha) \cdot$$

$$e^{ikx \cdot \sin \alpha + iky \cdot \sin \beta} \cdot e^{ikz\sqrt{1 - \sin^2 \alpha - \sin^2 \beta}}) \cdot d\alpha \cdot d\beta$$

where E_z is the longitudinal field , $a(\alpha, \beta)$ the plane wave spectrum of the input laser field and α and β are the horizontal and vertical tilt angles of the plane wave with respect to the propagation axis z. The present calculation

assumes that $|a(\alpha,\beta)|$ is significant only for small angles $|\alpha|,|\beta| \ll 1$. The effect of the slits on the electric field is very clear on Fig. 3.
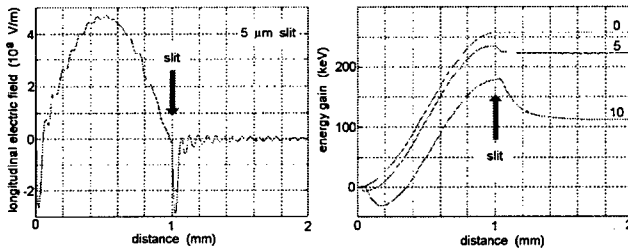
Figure 3: The longitudinal electric field and potential

The position of the exit slit is indicated with an arrow. The simulations assume a laser beam pulse of 100 fsec, having a beam waist of 65 µm located at the centre of the cell with a peak intensity of 1.7 J/cm². The finite gamma due to the relatively low energy of the electron beam (32 MeV) is taken into account. From Fig. 3 it can be concluded that a 10 µm slit reduces the maximum attainable energy gain by one half.

3.2 Cell length optimisation

The optimum cell length depends on the slippage distance between the electron and the laser beam, which is a function of the energy of the of the electron beam and the angle of crossing of the laser beams. For an electron with an energy of 32 MeV beam (γ=63) and a laser beam at 23.44 mrad crossing angle the slippage distance is 1.2 mm. The energy of the beam at the SCA-FEL facility ranges between 28 and 35 MeV, which sets the optimum cell length between 700 and 800 microns, as indicated in Fig. 4.
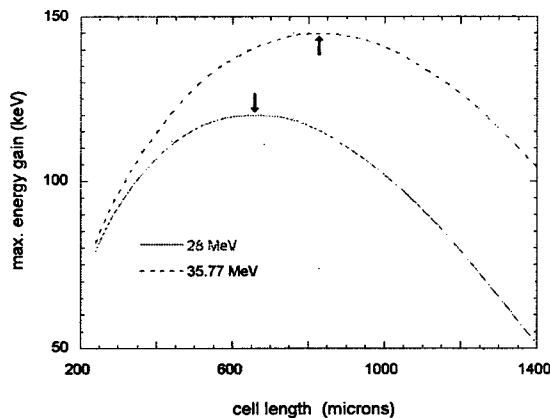
Figure 4: Dependence of the energy gain on cell length

The electron bunch length is longer than the wavelength of the laser beam by more than three orders of magnitude. Instead of experiencing a uniform energy gain due to a

particular phase of the laser field the electron beam gets spread out in energy. The resulting signature in the energy spread is a function of the initial energy spread of the beam, the maximum attainable energy gain, relative pulse durations of the laser and the electron beam and the spatial overlap of the two beams.

3.3 Calculation of the energy distribution

After determining the maximum energy gain from the electric field calculations the numerical simulation constructs a histogram $H(E)$ of the density of electrons versus energy gain for a given laser field strength ε. The initial energy spread $S(E)$ is small compared to the total energy, hence it is assumed that over this small energy range the maximum gain is constant. The resulting energy spread $S'(E,\varepsilon)$ is

$$S'(E,\varepsilon) = \int S(E-E') \cdot H(E',\varepsilon) dE'$$

Let $N(t)$ and $\varepsilon(t)$ be the electron beam and the laser beam profile in time. The resulting energy spread $S''(E)$ becomes

$$S''(E,\varepsilon) = \int S'(E,\varepsilon(t)) \cdot N(t) dt$$

Figure 5 shows the expected energy spread signatures for 5µm, 10 µm and 20 µm slits. The central peak in each case is the natural energy spread, assumed to be at its narrowest. The simulation assumes a 5 psec laser pulse. The acceleration and deceleration peaks clearly visible in the 5 µm slit case are completely absent in the 20 µm slit case. Further, an overall narrowing of the laser-induced energy spread can be observed as the slit is increased.
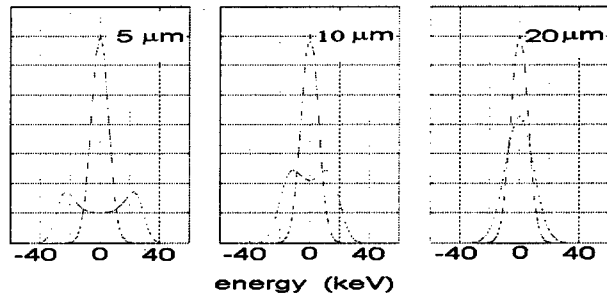
Figure 5: Energy spread signature at various slit values

Temporal overlap between the two beams also determines the energy spread signature. The pulse length of the laser available to the experiment can be set between 0.1 psec and 30 psec. A 0.1 psec laser pulse has the highest peak field but very poor overlap with the 2 psec electron bunch and therefore a small effect on the energy spread of the electron beam. A 10 psec laser pulse illuminates the

electron bunch almost uniformly but has a peak electric field ten times weaker than a 0.1 psec pulse. As Fig. 6 indicates, the optimum laser pulse duration is about 1 psec, close to the electron bunch duration.
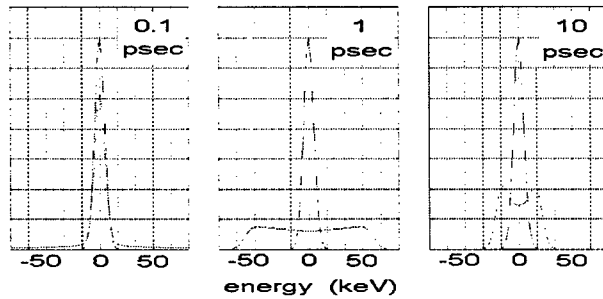
Figure 6: The effect of various laser pulse durations

3.4 Losses from diffraction radiation

Slits of the order of few μm in width could cause considerable energy losses on the beam due to radiative effects. An estimate of the radiation from a single electron traversing the slit was performed using a plane wave decomposition method of the field created by the particle in the slit area [9]. The energy radiated by single 32 MeV electron traversing a 1μm infinite slit with perfect conducting boundaries was estimated to be 2×10^{-3} eV. For a bunch with 10^8 electrons radiating coherently the energy lost would be 200 keV per electron. The characteristic wavelength of the radiation from the slit is

$$\lambda \le \frac{\text{slit width}}{\gamma} = \frac{1\ \mu\text{m}}{63} \sim 16\ \text{nm}$$

which corresponds to a photon energy of ~77 eV. The electron beam is not optically bunched in this experiment, but is a pulse of $\sim 10^6$ electrons spread over 2 mm. This corresponds to 1.3 electrons in one radian of a wave cycle. The radiation from the aperture is not coherent and hence the energy loss is negligible.

4 CONCLUSIONS

The numerical simulations show that in order to observe laser driven acceleration the slits of the accelerator cell may not be wider than 10 μm. At present we have not succeeded in achieving satisfactory transmission of the electron beam through the cell with its slits closed beyond 50 μm. Since the charge density of the beam is very low, no coherent radiation effects and hence no significant energy losses are expected to occur, in spite of the very narrow slit settings that the experiment requires. To obtain a better transmission through the cell improvements on the beam optics can be made. Further, a more sensitive detector can be placed at the spectrometer screen, so that even with a low transmission through the cell the experiment can be carried out. Once this obstacle is overcome we will be able to perform time scans of the laser beam and look for evidence of laser driven particle acceleration from the dielectric cell.

5 REFERENCES

[1] G. Mourou, et al, "Laser induced breakdown by impact ionization in SiO2 with pulse widths from 7 ns to 150 fs," Appl. Phys. Lett, June, 1994.

[2] B.C. Stuart, M.D. Feit, A.M. Rubenick, B.W. Shore, and M.D. Perry, Phys. Rev. Lett. 74 (12) 2248 (1995).

[3] C.M. Haarland, "Laser Electron Acceleration in Vacuum", Opt. Comm. 114, 280 (1995).

[4] Y.C. Huang, D. Zheng, W.M. Tulloch, R.L. Byer, "Proposed structure for a crossed-laser beam, GeV per meter gradient, vacuum electron linear accelerator", Appl. Phys. Lett. 68 (6) 753 (1996).

[5] Y.C. Huang, R.L. Byer, "A proposed high-gradient laser-driven electron accelerator using crossed cylindrical focusing" Appl. Phys. Lett. 69 (15) 2175 (1996).

[6] T. Plettner et al, Conference paper, AAC (1998).

[7] P. Sprangle, E. Esarey, J. Krall, A. Ting, Opt. Comm. 124, 69 (1996).

[8] J.A. Edinghofer and R.H. Pantell, "Energy exchange between free electrons and light in vacuum", J. Appl. Phys. 50(10) 6120 (1979).

[9] M.L. Ter-Mikaelian, "High-Energy Processes in Condensed Media, No 29, Interscience Tracts on Pysics and Astronomy, pp 377-384

CHANNEL GUIDING FOR LASER WAKEFIELD ACCELERATORS*

<u>W.P. Leemans</u>,[†] P. Volfbeyn, L. Archambault, P. Catravas, S. Dimaggio, and E. Esarey

Lawrence Berkeley National Laboratory, University of California, Berkeley CA 94720

Abstract

Experimental investigations of laser guiding in plasma channels at LBNL are reported. Intense ($> 2 \times 10^{17}$ W/cm^2), short (60 fs) laser pulses have been injected and guided in slab or cylindrical channels. The channels are produced in H_2 gas, delivered by a high pressure gasjet, with the dual-pulse Ignitor-Heater technique [1]. Using cylindrical focusing optics, a first ultrashort (< 100 fs) laser pulse (Ignitor), is brought to a line focus to ionize the gas jet. A second 160 ps long laser pulse (Heater) is subsequently used to heat the existing spark via inverse Bremsstrahlung. The hydrodynamic shock expansion creates a channel. The channel profile is diagnosed with time resolved longitudinal interferometry. The effects of laser beam size and divergence mismatch at the channel entrance and leakage of the laser energy out of the channel are studied in 1D and 2D.

1 INTRODUCTION

Optical guiding of intense laser pulses in plasma channels [2] is beneficial to a variety of applications, including plasma-based accelerators [3]. The distance over which a laser beam propagates in vacuum is limited by the diffraction or Rayleigh length $Z_R = \pi r_0^2/\lambda$, where r_0 is the laser spot radius at focus of a Gausssian laser mode with an intensity profile $I \propto \exp(-2r^2/r_0^2)$, $\lambda = 2\pi c/\omega_0$ is the laser wavelength, and ω_0 is the laser frequency. For example, in the laser wakefield accelerator [3], plasma wave excitation requires laser intensities on the order of 10^{18} W/cm^2, which implies μm-scale spot sizes for TW-level laser powers ($Z_R \simeq 300$ μm for $r_0 = 10$ μm and $\lambda = 1$ μm). Hence, high electron energy gains require guiding over long acceleration distances (many Z_R).

Plasma channels have been proposed as a means of guiding laser pulses [2,4,6-8]. The index of refraction in a plasma of density n is approximately $\eta_R \simeq 1 - \omega_p^2/2\omega_0^2$, where $\omega_p = (4\pi n e^2/m_e)^{1/2}$ is the electron plasma frequency. As in an optical fiber, a plasma channel can provide optical guiding if the index of refraction peaks on axis, $\partial\eta_R/\partial r < 0$, which can be achieved with a plasma density profile that has a local minimum on axis, $\partial n/\partial r > 0$. Specifically, a channel with a radially parabolic density profile of the form $n(r) = n_0 + \Delta n r^2/r_0^2$ can guide a Gaussian laser pulse with a constant spot size r_0 provided the channel depth Δn satisfies $\Delta n = \Delta n_c$, where $\Delta n_c = 1/\pi r_e r_0^2$ is the critical channel depth [4] and $r_e =$

$e^2/m_e c^2$ is the classical electron radius, i.e., $\Delta n_c[\text{cm}^{-3}] \simeq 1.13 \times 10^{20}/r_0^2[\mu\text{m}]$.

Plasma channels have been created in the laboratory by a variety of methods: (i) Passing a long laser pulse through an optic to create a line focus in a gas, which ionizes and heats the gas, creating a radially expanding hydrodynamic shock [1,5-11], (ii) using a slow capillary discharge to control the plasma profile [12], and (iii) using the ponderomotive force of an intense, relativistically self-guided laser pulse in a plasma, which creates a channel in its wake [13-21].

To guide highly intense laser pulses, plasmas channels must be produced in deeply ionized gases, where the density profile cannot be changed by the guided pulse through further ionization. An increase in density on-axis would lead to ionization-induced refraction [22] and hence negate the guiding. Reaching sufficient depth of ionization is most easily satisfied through the use of low atomic number, Z, gases. In laser created channels, the use of low Z-gases (e.g., hydrogen or helium) requires that the channel producing laser pulse satisfy two conditions: (1) be sufficiently intense to create free electrons through barrier suppression ionization [23] (typically $> 2 \times 10^{14}$ W/cm^2) and (2) be energetic and long (several 100 mJ's/pulse in > 100 ps) but relatively low intensity ($< 1 \times 10^{13}$ W/cm^2) to efficiently heat the plasma through inverse Bremsstrahlung heating. Short intense pulses are indeed inefficient at heating plasmas since the collision frequency is reduced for large quiver velocities [24].

To meet these two conditions, we have developed a novel technique which, rather than utilizing a single laser pulse for ionization and heating, makes use of two laser pulses [1]. A sub-ps low energy but intense ($> 2 \times 10^{14}$ W/cm^2) "Ignitor" pulse is first used to create the initial spark, followed by a long (tens to hundreds of ps), energetic (> 100 mJ) "Heater" pulse. Using the Ignitor-Heater method, the total laser energy required to generate a channel with length L_{ch} is greatly reduced compared to a single pulse. As a practical example, to achieve $> 2 \times 10^{14}$ W/cm^2 in a 100 ps long pulse, focused to a spot size of 5 μm $\times$5 mm (L_{ch}=5 mm) would require 5 J laser energy compared to 5 mJ for a 100 fs pulse.

The geometrical shape of the plasma channel cross-section is strongly affected by the initial transverse shape of the hot plasma volume. With the Ignitor-Heater method, control of the initial spark shape is possible by appropriate choice of the propagation geometry of the two pulses. As will be shown, slab-like channels were produced by allowing the Ignitor and Heater beams to copropagate and cylindrically symmetric channels were created by propagating the two beams orthogonally to each other thereby limiting

the hot plasma region to the intersection volume of the two beams.

In practice, the transverse extent and peak plasma density of the channel are finite. Hence, tunneling of the laser radiation through the channel wall becomes an important loss factor [6]. Similarly to glass fibers, coupling a laser beam into a plasma fiber is subject to losses from mode mismatch and reflections at the entrance of the fiber. While the mode mismatch losses in the two cases are very similar, the nature of the entrance reflection is more complicated in a plasma channel. A gas jet must be used in an evacuated chamber to avoid ionization induced refraction [22] that would occur in a statically filled experimental chamber. This paper addresses guiding loss mechanisms and beam propagation issues, both in transversely elongated (slab) channels and in cylindrically symmetric (round) channels.

2 CHANNEL PRODUCTION

The experiments were performed using the multi-TW Ti:Al$_2$O$_3$ laser ($\lambda \simeq 820$ nm) at the l'OASIS laboratory of the Center for Beam Physics at Lawrence Berkeley National Laboratory [1,10]. To implement the Ignitor-Heater method, two laser pulses were combined in a line-focus by means of cylindrical optics onto a gas jet (Fig. 1). A short (typically 60-75 fs), 20-40 mJ intense Ignitor pulse was focused to a ~ 5 μm $\times$ 5 mm area by reflecting off a cylindrical reflector, resulting in an intensity of $\sim 5 \times 10^{14}$ W/cm^2. The cylindrical reflector was a plano-concave ($R = 38$ mm) cylindrical lens, coated with a dielectric high reflection coating for 45° angle of incidence. The use of a reflective optic was required to avoid undesirable nonlinear effects that would prevent obtaining a well focused, near diffraction limited beam spot. The Heater pulse (~ 270 mJ, 160 ps long) was focused with an F/5 refractive cylindrical lens (focal length $f_l = 50$ mm) at the exact location of the Ignitor focus. In addition to the ease of the optical setup, stemming from the fact that the channel forming beams propagate perpendicularly to the guided pulse, the use of two independent cylindrical optics provided precise independent adjustment of the angles of incidence and positions of the line foci.
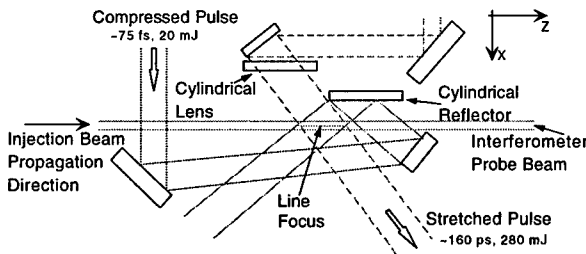
Figure 1: Experimental Setup.

A Mach-Zehnder type interferometer with a measured spatial resolution of 4 μm was built to measure line integrated plasma density. This interferometer measures the relative spatial phase shift between two blue (410 nm) $\sim$

50 fs pulses, one propagating through plasma (down the channel axis, perpendicular to the Ignitor-Heater pulses) and one through air (see Fig. 1). These pulses were produced by frequency doubling and were synchronized with the high power beams used in the plasma production. The evolution of the transverse plasma density profile was measured with a temporal resolution determined by the duration of the blue pulse.

The Ignitor-Heater scheme was first implemented with both pulses propagating in the same plane through a nitrogen- or hydrogen-backed gas jet. In this geometry, heat is deposited there where the Ignitor pulse intensity exceeds the ionization threshold. Figure 2 (a) shows interferograms taken with the interferometer pulse delayed by 560 ps and by 1 ns with respect to the Heater pulse in N$_2$ at 1000 psi. ¿From the inferred plasma density line-outs of Fig. 2 (b), it is seen that a plasma density depression is created only in the vertical direction. These slab channels provide one-dimensional (1D) guiding. The x-size of the channels roughly corresponds to the Rayleigh range of the Ignitor pulse. Figure 3 shows, as obtained from interferograms (e.g., Fig. 2), the evolution of (a) maximum density n_{max}, (b) distance between density peaks $2x_{ch}$, and (c) $\Delta n_{ch} = n_{max} - n_0$ of the channels, where n_0 is the on-axis density, versus time T after spark ignition in N$_2$ at 1000 psi. As expected from 1D hydrodynamic shock theory [13], $x_{ch} \sim T^{2/3}$ and, once plasma production ceases, $n_{max} \sim T^{-2/3}$ (these fits are shown in Fig. 3).
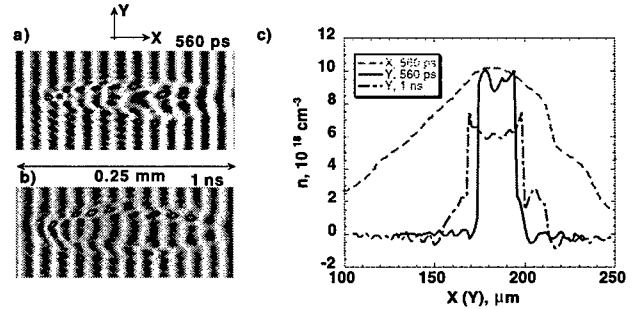
Figure 2: Channel interferograms at (a) 560 ps and (b) 1 ns after the heater pulse in N$_2$ at 1000 psi, both Ignitor and Heater pulses propagate along the x-axis, interferometer beam travels along the z-axis, the gasjet plume is much wider than the x-extent of the channel; (b) inferred plasma density lineouts: $n(x)$ (dashed curve) and $n(y)$ (solid curve) at 560 ps; and $n(y)$ (dot-dash curve) at 1 ns.

To create cylindrically symmetric channels, the Ignitor and Heater beams were made to propagate orthogonally to each other (and to the guided beam). This 90° geometry limited the transverse extent of the initial heat deposition volume to the small intersection volume of the two beams (typically 5 μm $\times$ 5 μm). Fig. 4 (a) and (b) show the geometry for producing slab-like and cylindrically symmetric plasma channels, respectively.

To demonstrate the change in channel shape, shadow-

a)

b)

c)
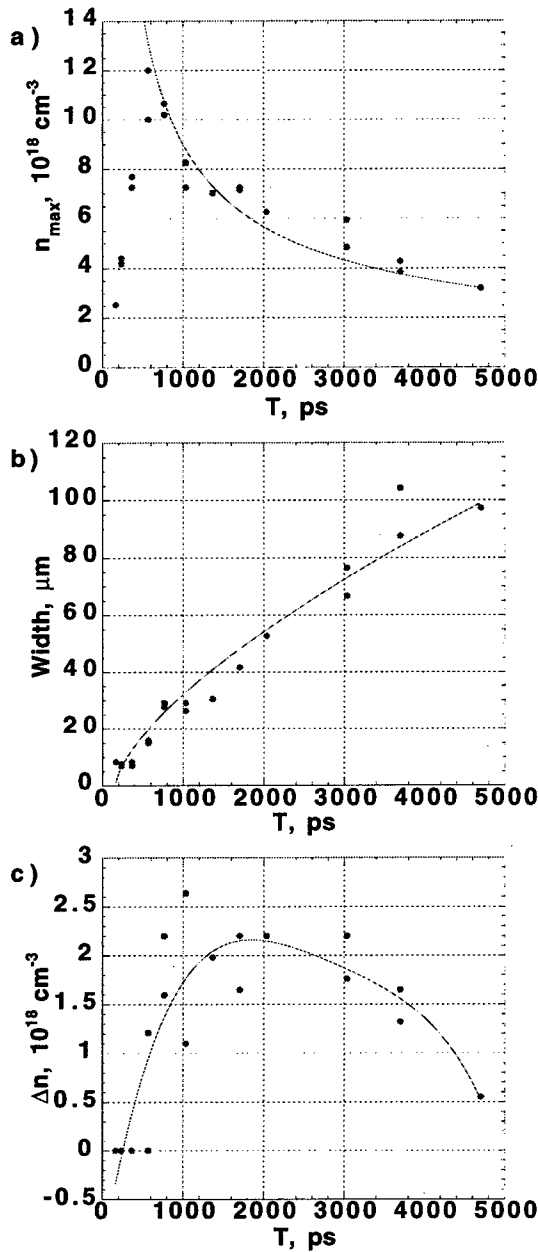
Figure 3: Channel evolution versus time T after spark ignition in N_2 at 1000 psi: (a) Maximum density n_{max} (points are data; curve is a $T^{-2/3}$ fit), (b) distance between n_{max} peaks (points are data; curve is a $T^{2/3}$ fit), and (c) $\Delta n_{ch} = n_{max} - n_0$ (points are data; curve is fourth order polynomial fit).

grams were used, Figs. 4 (c) and (d). A shadowgram is obtained by taking an image of the probe interferometric beam (with the reference beam blocked) at the exit of the channel. Refraction in the channel walls expels the blue light, thus casting a shadow on the image of the probe beam. The part of the probe beam that falls inside of the channel walls was observed to be guided. Figures 4 (c) and (d) clearly demonstrate the effect of the geometry change: the 1D elongated channels of the in-plane configuration,

Fig. 4 (c), are contrasted by the round 90° configuration channels, Fig. 4 (d).
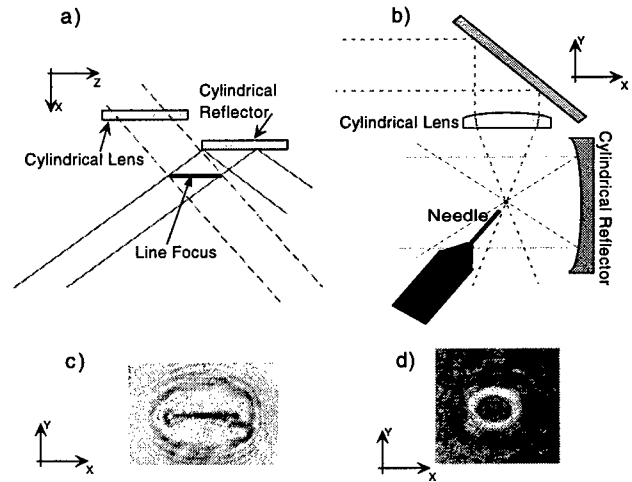
Figure 4: a) In-plane laser beam combining and b) 90° beam configurations; with c) and d) the corresponding channel shadowgrams in the x, y plane.

3 GUIDING

Laser pulses (injection pulses) were focused near the entrance of slab-like and cylindrical channels using an off-axis parabola. To diagnose the guiding, the laser beam was imaged onto a charged-coupled device (CCD) camera using a 1 inch diameter MgF_2 lens of focal length of $f_l = 68.3$ mm at 800 nm. The CCD camera was mounted on an optical rail allowing a change in position of the object plane with a range of 50 cm. The resolution and magnification of the imaging system was calibrated for different CCD camera locations.

Figure 5 shows images of a laser pulse (75 fs, 20-40 mJ, with a minimum focal spot size of ~ 5 μm in vacuum, i.e., $\sim 5 \times 10^{17}$ W/cm^2) injected into the slab-like channels for a) propagating through vacuum (gas jet turned off), b) after undergoing ionization induced refraction [22] in the gas jet plume without the Heater pulse being present, hence no channel formed, and c) guided by the channel, for a gas jet backed with nitrogen at 1000 psi. Vertical line-outs of these images, shown in Fig. 5 d), clearly demonstrate the changes induced by the plasma channel on the guided laser pulse. The guided spot size near the end of the channel was ~ 8 μm $\times 50$ μm. The reduction in vertical beam size by ~ 8 times provided by the channel is consistent with a laser beam of $Z_R \sim 0.1$ mm propagating a distance of ~ 0.8 mm (the half-width of the jet).

As seen in Fig. 2, for the in-plane Ignitor and Heater pulse configuration, plasma channels were created in an elongated, elliptical shape. In turn, the guided beam images (Fig. 5 (c)) had a similar elongated shape.

As the gas jet was moved further away from the laser focus, larger portions of the injected laser energy did not

a) b) c)

d)
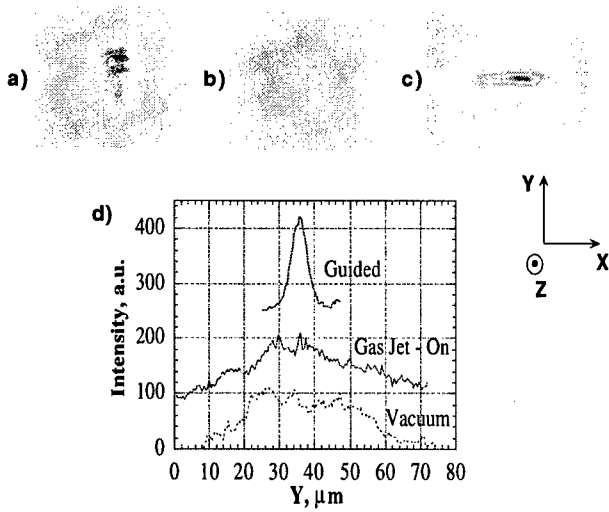
Figure 5: Transverse laser beam images for the beam propagating (a) in vacuum, (b) through the gas jet plume with only the Ignitor pulse, and (c) in a slab-like nitrogen plasma channel. The plane imaged onto the CCD camera was located at the channel exit. The gas jet backing pressure was 1000 psi.

couple into the channel. To obtain a quantitative measurement for the guiding properties of these channels, the image intensity integral of the CCD images was used as a measure of the laser energy. This allowed a comparison of the amount of the laser energy guided by the channel to the total intensity integral of the CCD image (full beam energy, E_{full}). The intensity integral of the isolated central lobe of the images was taken to be the guided energy.

The ratio of the guided energy, E_g, to the total image intensity integral, E_{full} is shown in Fig. 6. As expected, the fraction of the laser beam that is coupled into the channel becomes larger as the injection pulse focus is moved closer to the jet's edge than when the gas jet is moved further away from the laser focus position in vacuum. It should be noted that the F-numbers of the off-axis parabola and the imaging MgF_2 lens are rather close and the collection angle is limited. Nevertheless, the leakage of the fundamental mode of the plasma channel is fully collected.

As the laser waist is moved closer to the channel entrance, the laser spot size becomes comparable with the channel size and most of the power is coupled to the modes of the channel. The ratio of E_g to the E_{full} approaches $\sim 55\%$. This number is in good agreement with analytical results [1], where the leakage fraction was estimated to be $\sim 50\%$.

To demonstrate the dependence of the number of guided modes on the channel depth, shadowgrams of the round channels (90° geometry in H_2) were taken with variable time delay with respect to the arrival time of the Heater pulse. As the shock wave propagates further out, leaving a deeper plasma density depression on the channel axis, the guided part of the probe beam couples to higher and higher order modes of the channel. Figure 7 presents the results of
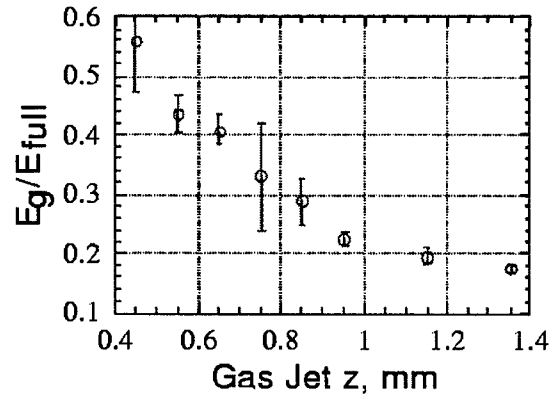
Figure 6: Ratio of energy in the guided central lobe,, E_g, to that of the full beam, E_{full}, plotted versus the gas jet position, z, where $z = 0$ corresponds to the injection pulse focus being in the center of the gas jet plume (half-width of the gas jet plume is $\sim 0.8 - 1$ mm).

such a time delay scan taken with a channel created in hydrogen. The increase in the number of lobes in the guided part of the blue pulse for longer probe pulse delays demonstrates the dependence of the number of guided modes on the channel depth and width. Similar measurements were previously reported for channels created in high Z gases [6,7].
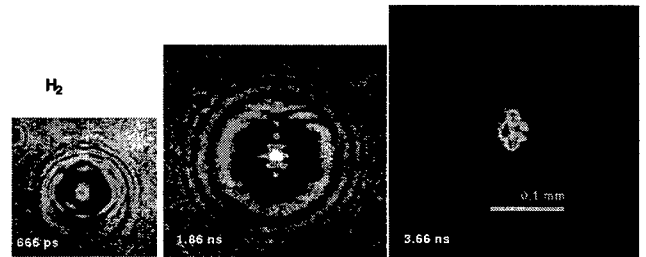
Figure 7: Shadowgrams of round channels created in hydrogen at three different time delays after the heating: 666 ps (left), 1.86 ns (center), and 3.66 ns (right).

Beam images of laser pulses (20 mJ in 60 fs) in vacuum and injected in round channels, produced in a H_2 gasjet, are shown in Fig. 8 (a) and (b) respectively. Lineprofiles are shown Fig.8(c). The injected spot size was measured to be about 10 μm resulting in an injected intensity of $\sim 2 \times 10^{17}$ W/cm^2. The channeling efficiency was measured to be typically $> 70\%$. Optimization of channeling efficiency and detailed measurements of mode matching and wakefield excitation for higher intensity pulses ($\sim 10^{18}$ W/cm^2) in these channels are underway.

4 DISCUSSION

To overcome the laser diffraction length limit, a novel method of plasma channel production for laser guiding, the Ignitor-Heater technique, was proposed and tested experimentally. With this technique, plasma channels can be cre-
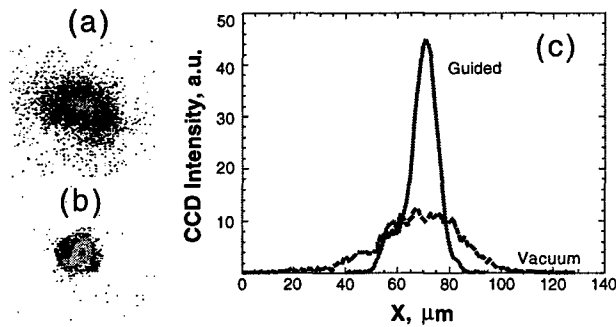
Figure 8: Transverse laser beam images for the beam propagating (a) in vacuum, (b) in a cylindrical hydrogen plasma channel, and (c) the corresponding lineprofiles. The plane imaged onto the CCD camera was located at the channel exit. The gas jet backing pressure was 1000 psi.

ated in hydrogen and deeply ionized nitrogen without high atomic number additives, thereby allowing high intensity laser pulse guiding. To avoid ionization induced refraction of the guided laser pulse, channels were formed in the plume of a pulsed gas jet. It should also be noted that the Ignitor-Heater scheme employs cylindrical optics that are out of the path of the accelerator beam (for plasma-based accelerator applications) and, potentially, may allow the recycling of the laser beams. The channel formation process was fully characterized with time resolved 2D longitudinal interferometry diagnostic using a sub-ps probe pulse. The shape of the initial spark was proven to affect the shape of the plasma channel. By using in-plane or orthogonal beam combining configurations, elongated, or slab channels, with 1D guiding properties and cylindrically symmetric, round, channels with guiding in both transverse dimensions were created in both nitrogen and hydrogen.

Laser pulses at high intensity ($\sim 2 - 5 \times 10^{17}$ W/cm^2) were injected in nitrogen slab channels and in hydrogen cylindrical channels and observed to be guided over $\sim$ 5 − 10 Rayleigh lengths, limited by the gasjet length. Leakage and transmission measurements for the slab channels were found to agree well with the theoretical predictions. Similar measurements in cylindrical channels are underway.

Single mode and multimode laser propagation in round channels was observed as a function of time delay of the probe pulse injection after the spark heating. The modal content is found to be in good qualitative agreement with predictions from a 2D leakage theory [1].

An optical diagnostic is currently being designed to diagnose the spatial density profile of the channel, and to measure the laser excited wakefields in the channel [25]. Efforts are also directed towards the development of long scalelength high pressure gasjets ($\sim 1 - 2cm$), resulting in a substantial increase in guiding distance. Such gasjets could also have applications in the field of high harmonic generation [26] and x-ray lasers [27].

5 ACKNOWLEDGMENTS

6 REFERENCES

[1] P. Volfbeyn and W.P. Leemans, in Proc. 6th European Part. Accl. Conf., Ed. by S. Myers et al., (Inst. of Phys., Philadelphia, 1998), p. 265; P. Volfbeyn, MIT Ph.D. Thesis, LBNL Report 41892 (1998); P. Volfbeyn, E. Esarey and W.P. Leemans, Phys. Plasmas, May (1999).

[2] For a review see, E. Esarey et al., IEEE J. Quantum Electron. 33, 1879 (1997).

[3] T. Tajima and J.M. Dawson, Phys. Rev. Lett. 43, 267 (1979); For a review see, E. Esarey et al., IEEE Trans. Plasma Sci. 24, 252 (1996);

[4] P. Sprangle and E. Esarey, Phys. Fluids B 4, 2241 (1992); P. Sprangle et al., Phys. Rev. Lett. 69, 2200 (1992). W.P. Leemans et al., IEEE Trans. Plasma Sci. 24, 331 (1996).

[5] L.C. Johnson and T.K. Chu, Phys. Rev. Lett. 32, 517 (1974).

[6] C.G. Durfee III and H. M. Milchberg, Phys. Rev. Lett. 71, 2409 (1993); H.M. Milchberg et al., Phys. Plasmas 3, 2149 (1996).

[7] T.R. Clark and H.M. Milchberg, Phys. Rev. Lett. 78, 2373 (1997); T.R. Clark and H.M. Milchberg, Phys. Rev. Lett. 81, 357 (1998).

[8] V. Malka et al., Phys. Rev. Lett. 79, 2979 (1997).

[9] T. Ditmire et al., Opt. Lett. 23, 322 (1998).

[10] W.P. Leemans et al., Phys. Plasmas, 5, 1615 (1998).

[11] E. Gaul et al., Advanced Accelerator Concepts, Edited by W. Lawson, AIP Conf. Proc. (AIP, NY, in press).

[12] Y. Ehrlich et al., Phys. Rev. Lett. 77, 4186 (1996); Y. Ehrlich et al., J. Opt. Soc. Am. B 15, 2416 (1998).

[13] K. Krushelnick et al., Phys. Rev. Lett. 78, 4047 (1997); A. Ting et al., Phys. Plasmas 4, 1889 (1997),

[14] S.Y. Chen et al., Phys. Rev. Lett. 80, 2610 (1998).

[15] A.B. Borisov et al., J. Opt. Soc. Am. B 11, 1941 (1994).

[16] P. Gibbon et al., IEEE Trans. Plasma Sci. 24, 343 (1996).

[17] A. Chiron et al., Phys. Plasmas 3, 1373 (1996).

[18] P.E. Young and P.R. Bolton, Phys. Rev. Lett. 77, 4556 (1996).

[19] M. Borghesi et al., Phys. Rev. Lett. 78, 879 (1997).

[20] J. Fuchs et al., Phys. Rev. Lett. 80, 1658 (1998).

[21] C.E. Clayton et al., Phys. Rev. Lett. 81, 100 (1998).

[22] W.P. Leemans et al., Phys. Rev. A 46, 1091 (1992).

[23] S. Augst et al., Phys. Rev. Lett. 63, 2212 (1989).

[24] C.D. Decker et al., Phys. Plasmas 1, 4043 (1994); G. Shvets and N.J. Fisch, Phys. Plasmas 4, 428 (1997).

[25]] P. Volfbeyn and W.P. Leemans, these Proceedings.

[26] C.G. Durfee et al., Opt. Lett. 22, 1565 (1997).

[27] N.H. Burnett and P.B. Corkum, J. Opt. Soc. Am. B 6, 1195 (1989); D.C. Eder et al., Phys. Plasmas 1, 1744 (1994).

PROGRESS TOWARD E-157: A 1 GeV PLASMA WAKEFIELD ACCELERATOR[*]

R. Assmann[+], P. Chen, F.-J. Decker, R. Iverson, M. J. Hogan, S. Rokni, R.H. Siemann, D. Walz, D. Whittum, SLAC, Stanford, CA

P. Catravas, S. Chattopadhyay, E. Esarey, W.P. Leemans, P. Volfbeyn, LBNL, Berkeley, CA

C. Clayton, R. Hemker, C. Joshi, K. Marsh, W. B. Mori, S. Wang, UCLA, Los Angeles, CA

T. Katsouleas[#], S. Lee, P. Muggli, USC, Los Angeles, CA

Abstract

A plasma based wakefield acceleration (PWFA) experiment, scheduled to run this summer, will accelerate parts of a 28.5 GeV bunch from the SLAC linac by up to 1 GeV over a length of 1 meter. A single 28.5 GeV bunch will both induce the wakefields in the one meter long plasma and witness the resulting acceleration fields. The experiment will explore and further develop the techniques that are needed to apply high-gradient PWFA to large scale accelerators. This paper summarizes the goals of the first round of experiments as well as the status of the individual components: construction and diagnosis of the homogeneous lithium oven plasma source and associated ionization laser, commissioning of the electron beam, simulated performance of the electron beam energy measurement, and first PIC simulations of the full meter long experiment.

1 INTRODUCTION

In the experiment known as E-157 [1], a 28.5 GeV electron bunch is used to both excite and witness a large amplitude wake in a meter long plasma cell. The experiment has a rich physics agenda which includes demonstrating high-gradient plasma acceleration over meter scales, measuring large amplitude wakes of order GeV/m in the blowout regime of plasma acceleration [2], and studying beam propagation issues such as betatron oscillations important for future 1-10 GeV stages based on the PWFA mechanism. To accomplish these objectives requires special attention to all three of the key experimental components: the beam, the plasma and the beam diagnostics (see Fig. 1). The construction of each component is well underway in preparation for the scheduled experimental run this summer. This paper describes progress on each of the three experimental components plus recent advances in simulating the experiment over a full meter with parallel PIC simulations.
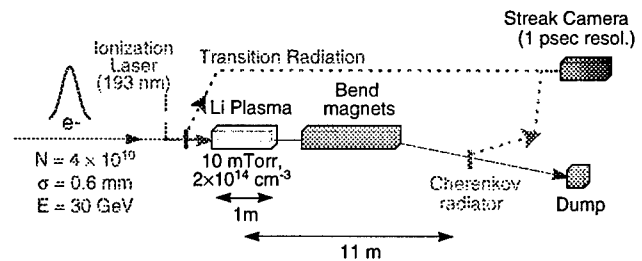
Figure 1: Layout of E-157.

2 EXPERIMENTAL COMPONENTS

In this section each of the three main experimental components is described: the beam diagnostics, the plasma source and the beam. For more detail on each, see the accompanying individual papers [3, 4, 7-9] in these proceedings.

2.1 Beam Diagnostics

Energy change(-+-) and absolute energy spread(-x) of 1ps slices along the bunch
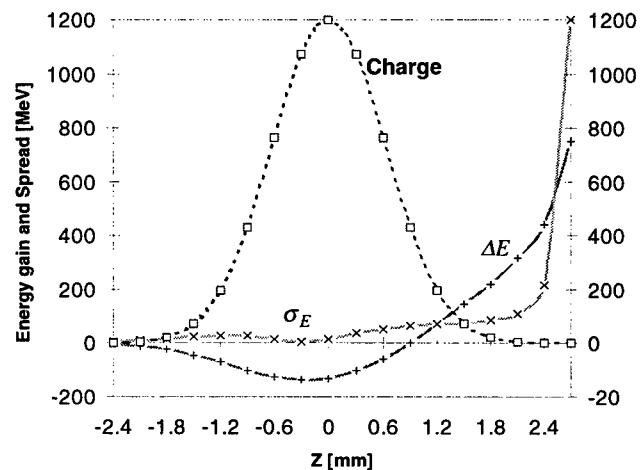
Figure 2: Simulated time resolved measurements.

As shown in Fig. 2, the electrons in the tail of the drive bunch experience the accelerating field of the plasma wake and gain an energy of about half a GeV over the meter long plasma. Since only the electrons in the tail experience the highest energy gains, their measurement requires time resolved diagnostics on fast time scales (~1ps) and at the highest sensitivities (<10^7 electrons Below we describe the strategies we have developed for accomplishing this.

Upstream of the plasma, OTR is used to diagnose the properties of the incident beam. The ability of OTR to provide the required resolution in spot size and divergence at 28.5 GeV has been experimentally verified. Results from a quadrupole scan are shown in Figure 3, in which 50 micron waists in both axes were resolved using near field OTR images. Beam divergences of 100 μrad have been measured using the two-foil far field interference pattern for a foil separation of 0.5 meter [4]. Use of a streak camera to study the time evolution of the beam spot size and divergence is planned, building on experiments at lower beam energies [5,6].
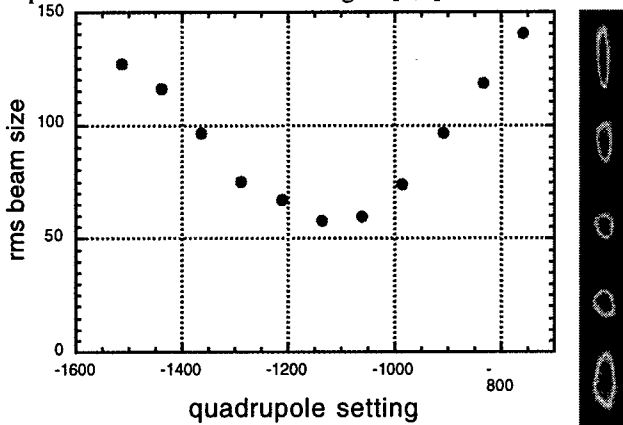
Figure 3: Quadrupole scan (left) in electron beam spot size measured with OTR (images on right) at 28.5 GeV.

After the plasma (Fig. 1), the electron beam is dispersed in energy by a series of deflecting magnets. Eleven meters downstream, the dispersion D in the vertical plane is about 3 mm/GeV. At this location the
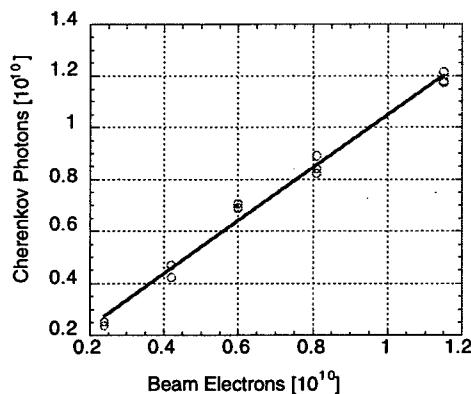
Figure 4: Photon yield vs. number of electrons.

beam is sent through a low index of refraction transparent material to generate Cherenkov radiation (CR) in the visible wavelength range. The CR and OTR radiators can be imaged onto a CCD camera to produce a time integrated image of the beam, or onto the slit of a streak camera (slit in the energy dispersion plane) to produce an energy versus time spectrum of the beam.

For the Cerenkov material we chose to use silica aerogel, approximately 3mm thick. This material has an index of refraction of 1.009 and overcomes difficulties associated with lower index materials such as air (requiring a thick target and introducing depth of focus issues for imaging) or higher index materials such as glass (having a large Cerenkov angle making it difficult to collect and transport all of the light). However, the new material posed uncertainties concerning its photon yield and survivability. To address these, preliminary tests were performed. [Fig. 4] The photon yield is approximately one photon per electron. Calibration of photon yield assumed 50% quantum efficiency of the CCD and neglects any losses through collection optics. This is more than an order of magnitude higher than that from OTR and enables measurement of charge down to the level of 100fC. In addition the aerogel showed no signs of deterioration over the two week testing period.

2.2 Plasma Source

The requirements on the plasma represent a significant advance over what has been achieved previously: one meter length, minimum transverse size of 1 mm, density of $2\text{-}4\times10^{14}$ cm^{-3} uniform to within 10% with a density times length-squared product tuned to within 2% [10]. In addition the plasma must be either fully ionized or sufficiently low Z that beam impact ionization does not cause a significant plasma density increase.

The plasma parameters necessary for the experiment have been achieved in a short version of a Li heat-pipe oven [3]. The neutral density was $n_0 = 2\times10^{14}$ cm^{-3} over a length of $L=25$ cm. The product n_0L was measured by the hook method, and by uv and white light absorption. The length of the vapor column was inferred from longitudinal temperature profile measurements. The Li vapor was ionized by a uv ArF laser pulse through a single photon absorption process. The plasma density was measured by uv absorption and by CO_2 laser and visible laser interferometry. As expected the plasma density varied linearly with the incident fluence, and reached a maximum value of $\approx3\times10^{14}$ cm^{-3}, corresponding to a fractional ionization of 15%. The time for the plasma density to drop by a factor of two from its maximum value was 12 μs. In the experiment the plasma density will be adjusted on a shot-to-shot basis by changing the delay between the ionizing laser pulse and the electron beam. The length of the vapor/plasma column can be changed over a longer time scale by adjusting the heating power delivered to the source.

Based on these results, a 1-meter long source has been built and is being tested [9]. Similar neutral and plasma density values are expected from this longer source.

2.3 Beam Production

To achieve the goal of high-gradient acceleration (GeV/m) in the blow-out regime places specific requirements on the drive beam. It must have significant charge $(N = 4 \cdot 10^{10})$, short bunch length $(\sigma_z \leq 0.63$ mm), modest spot size of 25-50 μm and be aligned to within 10 μm [10].

An SLC-like beam with an emittance of 5 in x and 0.3 $\cdot 10^{-5}$ m-rad in y seems ideal. The bunch length is a critical factor for plasma acceleration (the wake amplitude scales as charge over bunch length-squared). For E-157 the bunch length has to be reduced from the typical 1.2 mm for minimum energy spread (0.15%) to 0.6 mm or even 0.4 mm. These shorter bunches generate not only a plasma wakefield, but also a strong longitudinal wakefield in the conventional accelerator giving the beam a large double-horned energy distribution of up to 4 % between horns.

A test run in the winter of 98/99 [7] checked the compatibility with PEP-II, where an additional 10 Hz beam was sent to the plasma experiment area. The bunch length was measured with a 36 GHz cavity and optimised to about 0.55 mm at 29.5 MeV compressor amplitude. Figure 5 shows the inverted cavity signal after normalizing it to a toroid reading (stars:*) and scaling it to the expected curve (solid line, for an $R_{56} = 0.7$ m). By reducing the R_{56} to 0.6 m or 0.5 m and raising the compressor strength a shorter bunch is possible.

The transverse beam emittances and stability were after initial difficulties reduced below the required values, but the charge was still only 2.2 $\cdot 10^{10}$ particles.
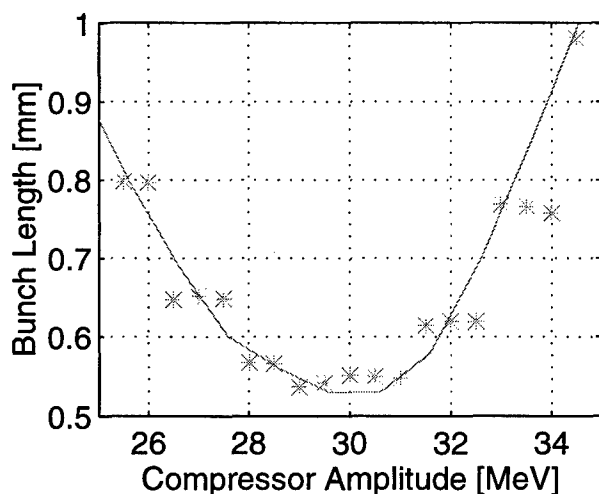
Figure 5: Linac bunch length versus compressor strength.

3 SIMULATIONS

Detailed PIC modeling of plasma wakefield generation has been performed in 2-D [1]. Recently the models have been implemented in a massively parallel object-oriented

code on the T3E at NERSC. The parallel implementation had enabled production runs to model the full meter long experiment in two days. The results [8] show the betatron oscillations of the beam at the predicted frequency. The beam undergoes three betatron oscillations reaching sub-micron spot sizes within the plasma (plasma lensing); however, the wake remains stable throughout. Fig. 6 shows the shape of the plasma wake (E_z) near the peak accelerating field $(E_z$ vs. r and z). Note the flattened profile in front of the peak that is characteristic of the blowout regime [2]. The width of the accelerating structure narrows to approximately 50 microns in the last ps before the peak. The height of the peak is approximately 1 GV/m.
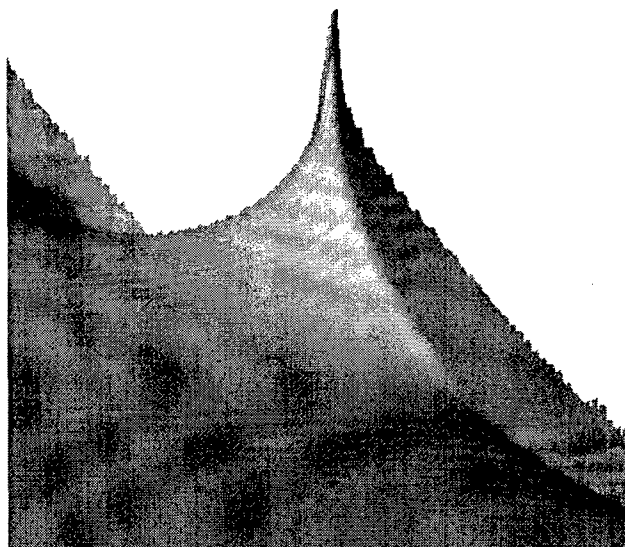
Figure 6: Accelerating wake E_z versus z and r. Wake is moving to the right.

4 REFERENCES

[1] R. Assmann et al., SLAC proposal for "One Gev Beam Acceleration in a One Meter Long Plasma Cell," http://www/slac.stanford.edu/grp/arb/e157/archive/pwfa_slacpub.pdf

[2] J. Rosenzweig et al., Phys. Rev. A, 44, R6189 (1991).

[3] P. Muggli et al., "Photo-ionized Plasma Source for Second Generation Plasma Based Accelerators," these proceedings, paper FRA 115.

[4] P. Catravas and W. Leemans, "Optical Transition Radiation based diagnosis at multi-GeV energies," these proceedings, paper WEA 100.

[5] W.P. Leemans et. al., "X-ray based subpicosecond electron bunch characterization using 90 degrees Thomson scattering," Phys. Rev. Lett., 77(20), 4182-5, 1996.

[6] M. Hogan et al.

[7] F.-J. Decker et al., "Short High Charge Bunches in the SLAC Linac for Plasma Experiments," these proceedings FRA 114.

[8] R. Hemker et al., "Development of Parallel 3D codes for Modeling Plasma Based Accelerators," these proceedings, FRA 124.

[9] S. DiMaggio et al., "Development of 1-meter long Lithium heat pipe oven and Excimer M2 reduction for plasma accelerator applications," these proceedings, paper FRA 138

[10] T. Katsouleas et al., ARDB Tech. Note 3/15/99, "On the Tolerance to Tail Misalignment in E-157;" T. Katsouleas et al., ARDB Tech. Note 3/5/99, "On the Tolerance to Beam Ionization in E-157."

STATE-OF-THE-ART DEVELOPMENTS IN ACCELERATOR CONTROLS AT THE APS *

Frank Lenkszus[#]

Argonne National Laboratory, 9700 South Cass Avenue, Argonne, IL 60439 U.S.A.

Abstract

The performance requirements of the Advanced Photon Source (APS) challenge the control system in a number of areas. This paper will review a few applications of advanced technology in the control and monitoring of the APS. The application of digital signal processors (DSPs) and techniques will be discussed, both from the perspective of a large distributed multiprocessor system and from that of embedded systems. In particular, two embedded applications will be highlighted, a beam position monitor processor and a DSP-based power supply controller. Fast data distribution is often a requirement. The application of a high-speed network based on reflective memory will also be discussed in the context of the APS global orbit feedback system. Timing systems provide opportunities to apply technologies such as high-speed logic and fiber optics. Examples of the use of these technologies will also be included. Finally, every modern accelerator control system of any size requires networking. Features of the APS accelerator controls network will be discussed.

1 INTRODUCTION

It is not without some measure of trepidation that the author attempts to address a topic such as "state-of–the-art" developments in accelerator controls at the APS. Such a term tends to inspire anticipation of revelations of completely new and previously unknown applications of technology. Such revelations are a rarity, and this paper does not aspire to such a lofty level. Rather, the author views this as an opportunity to introduce the reader to a sampling of what are hoped to be interesting applications at the APS of currently available technology.

The applications discussed cover three broad areas: digital signal processing and processors, networks, and fast logic.

2 FAST ORBIT FEEDBACK SYSTEM

The APS fast orbit feedback system has been in routine operation with users since June of 1997. Reference [1] contains an extensive description of the details of this system.

2.1 Overview

The fast orbit feedback system consists of 21 VME crates, (1 master and 20 slaves), distributed around the 1104-m-circumference storage ring. Each crate contains a 68040-based processor running EPICS control software. This processor serves as an interface to the control system and two DSP cards, a Pentek [2] 4284 and a Pentek 4283. The 4284 uses the TI C40 DSP chip and computes vertical orbit corrections, while the 4283 uses the TI C30 chip and computes horizontal corrections. A reflective memory network (discussed later in this paper) is used to distribute data and control information between VME nodes.

Each VME slave node has a direct digital data feed of BPM position data from the rf BPM system [3]. In addition, position data is received from beamline x-ray BPMs and narrow-band rf BPMs [4] straddling each insertion device via VME interface cards located in each node. As this paper is written, these BPMs have not been integrated into the fast orbit feedback system. However, the position data from the x-ray BPMs and the narrow-band rf BPMs is available to the control system through the EPICS processor.

Since the last report [1], the feedback system sampling rate has been increased to 1.67 kHz. Orbit corrections are synchronously computed and corrector values written at the sampling rate. The correction algorithm corrects global orbit errors in an rms sense using 160 BPMs and 38 "fast" correctors in each plane. A high-pass digital filter rolls off frequency response below 100 mHz. Low frequency orbit correction to DC and local steering is handled by a workstation-based program [5] running at 0.5 Hz.

2.2 Performance

Table 1 summarizes performance. Quoted orbit motion is from the latest available data with 1% x-y coupling.

Table 1: Fast Orbit Feedback Performance

	Horizontal (rms)		Vertical (rms)	
	F/B off	F/B on	F/B off	F/B on
Required Orbit stability (with 10% coupling)	17.5 μm		4.5 μm	
Motion 0.016-30 Hz	18.4 μm	3.4 μm	3.1 μm	1.4 μm
Motion 0.25-800 Hz	20.8 μm	13.5 μm	8.0 μm	7.0 μm
β at ID source points	17 m		3 m	

2.3 Future Development

Future upgrade plans include integrating the narrow-band rf BPMs and the x-ray BPMs into the fast orbit correction algorithm. In addition, the Pentek boards allow the addition of daughter card DSPs. We plan to add daughter cards to each DSP card. The additional DSP power will allow implementation of more sophisticated regulators and local control at each storage ring insertion device. Presently we do not plan to increase the total number of BPMs used in the correction algorithm. The time to read in the error vectors over VME consumes a significant part of each sample interval. Decreasing this time would require replacing the 4283 DSP boards, which would be a significant expense.

3 REFLECTIVE MEMORY

Reflective memory is a commercially available technology that is a critical component of the fast orbit feedback system. It may even be considered an enabling technology. It is available from at least two vendors that the author is aware of, VMIC [6] and Systran [7].

3.1 Description

Reflective memory may be defined as a network of replicated, shared memory. A reflective memory card is located in each node participating in the network. The card appears as random-access memory (RAM) to the node's system bus. Any processor on the system bus (in our case VME) can write or read the reflective memory. The reflective memories are connected head to tail in a ring. When a value is written to a location, that value and its RAM address are transmitted around the ring. Each reflective memory deposits the value into the same address in its RAM. The originating node strips the message from the ring when it is received. Through this mechanism, the RAM image is replicated in each reflective memory participating in the ring. Thus, after a message transit time, each node sees an identical, replicated image of RAM. Figures 1 and 2 illustrate the process.

The VMIC VMIVME-5588DMA, which is used in the fast orbit feedback system, sends and receives data over a 1.2-Gbaud serial fiber optic ring. The actual specified data transmission rate is 29.5 Mbytes/s. A maximum of 256 nodes is allowed; the fast orbit feedback system has 21 nodes. When multimode fiber is used, nodes may be located up to 1 km apart (10 km node spacing is specified with single mode fiber). Memory sizes up to 16 Mbytes are available.

A very attractive feature of reflective memory networks is that they do not require processor involvement in network initialization or management. They are treated as RAM. To communicate values to all nodes in the ring, the values are merely written to reflective memory. The reflective memory hardware
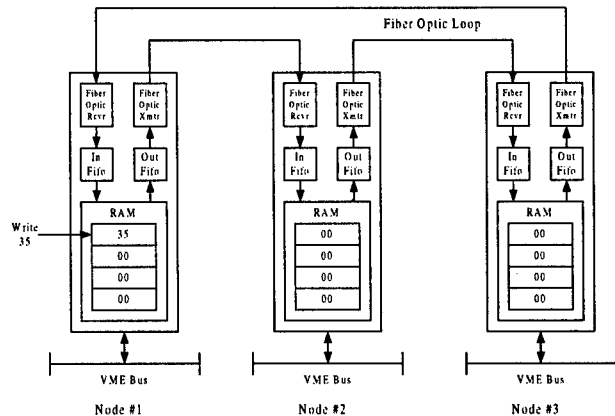
Figure 1: Write to a reflective memory.
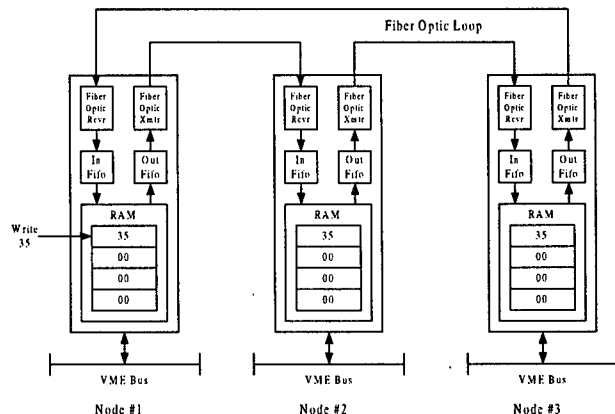
Figure 2: Replication of reflective memory contents.

handles the actual transfer. In addition, the reflective memory network is deterministic as long as the network bandwidth limits are observed. Error detection is provided and corrupted messages are discarded.

3.2 Application

The reflective memory is used to communicate data and control information between the nodes of the fast orbit feedback system. At every feedback 1.67-MHz clock tick, each DSP reads BPM data from sectors within its span of control, computes error values, and deposits the result into assigned locations within an error vector located in reflective memory. In addition, each DSP sets a flag in a "done" vector in reflective memory. All DSPs monitor the done vector. When the done vector is complete, all DSPs read the complete error vector and compute corrector error values.

The reflective memory is also used to communicate control information from the master node to the slaves. Parameters such as filter coefficients and controls such as loop on/off are deposited in specific locations in reflective memory by the master node. Slave nodes read new values upon command.

Each DSP deposits into reflective memory additional information such as position data and corrector error

334

values. The DSPs in the master node can access this data through a 40-channel digital scope feature. This has proven to be a powerful diagnostic tool for determining causes of unwanted beam motion and beam loss.

Reflective memory is an interesting alternative for data communication in any distributed control application.

4 POWER SUPPLY CONTROLLER

The APS has initiated the development of a new power supply controller for the storage ring power supplies. The storage ring uses 1400 power converters, one for each magnet (other than the main dipole bus). The present system uses an analog regulator with control and monitoring performed by a single G64-based 68000 processor per converter cabinet. Each cabinet contains up to eight power converters. BitBus is used to subnet the 68000s to the control system. While this system has served the APS well, its limited power both in computing resources and network performance has limited the tasks that can be accomplished.

A new controller based on DSPs and Ethernet is under development. A single SHARC [8] DSP is used.

4.1 Goals

Primary goals of the new design are:
1. Provide glitch detection to aid the analysis of beam loss events.
2. Provide 18-bit settability for power converters (specifically required for the correctors to meet long-term APS orbit stability goals).

Additional expected benefits are:
1. Fast data collection and anomaly detection (detect noisy converters).
2. Improved power converter dynamic stability.
3. Reduced likelihood of power converter glitches due to replacement of the analog regulator with a digital implementation.
4. Improved reliability and maintainability through a reduction in the number of cables and connectors.

4.2 Implementation

Figure 3 shows the block diagram of the regulator design. A SHARC DSP will implement the digital regulator. The power circuit input voltage and the magnet current are digitized by a pair of 16-bit ADCs. An 18-bit pulse width modulator (PWM) drives the power circuit insulated gate bipolar transistor (IGBT) switches. On-board flash memory stores code and parameters. Communications to a control system processor is via an on-board Ethernet interface.

The control algorithm is implemented in the SHARC. An external 20-kHz clock triggers the PWM and initiates a DSP control cycle. Sets of regulators will be driven by different phases of the 20 kHz to distribute the load presented to the raw supply. Snapshot waveform storage of voltage or current samples will be stored in the SHARC internal RAM and will be accessible to the control system through the network interface. Performance measures such as mean absolute deviation (MAD) and variance will be computed at the 20-kHz rate. Output current glitch detection will be based on MAD exceeding a specified threshold. A continuous circular buffer of measured current will be maintained. Glitch detection will stop the circular buffer a specified number of samples after the glitch. Through this mechanism, the output current both pre- and post-glitch will be recorded.

Glitch detection will be an important new feature in that it will help determine which of the many converters caused a beam dump.

4.3 Status

A VME-based prototype is nearing completion and should be under test at the time of this publication. VME was chosen as the prototype platform because of its modularity. Each major function—DSP, ADC, PWM, network, etc.—is implemented on a separate VME card. This allows replacement of a function without replicating the entire circuit. The final design is expected to be a single board to maximize reliability and minimize cost.
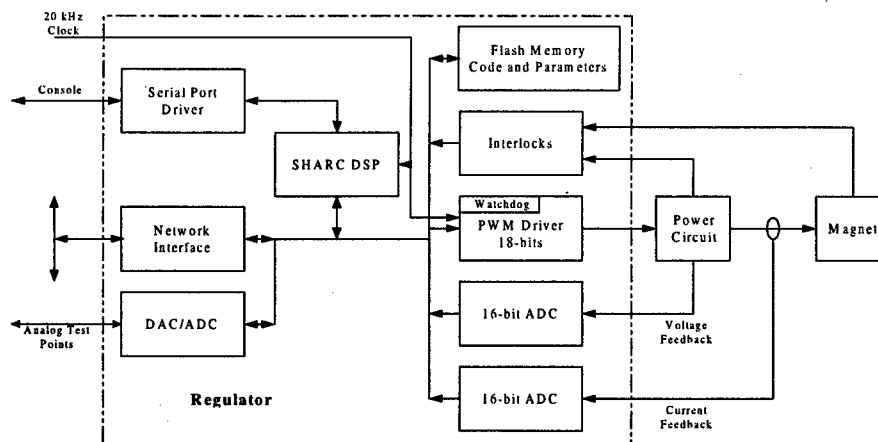
Figure 3: DSP-based power supply regulator.

5 BUNCH CURRENT MONITOR

A bunch current monitor capable of simultaneously measuring the current in every bunch in the ring has been in operation for nearly one year. Figure 4 shows a block diagram. The sum signal from a storage ring strip line is digitized by a high speed 8-bit ADC manufactured by Celerity Systems [9]. The digitizer is driven by an external clock and an external trigger. The storage ring rf, 352 MHz, is used as an external clock input. The storage ring revolution clock is used as an external trigger. Once the digitizer is triggered, it digitizes the input signal at the 352-MHz rate. Digitized values are stored in a 64-kbyte FIFO and read out to VME. Using the storage ring clock as the digitizer's clock input ensures that the digitization process is synchronous with the bunch train.
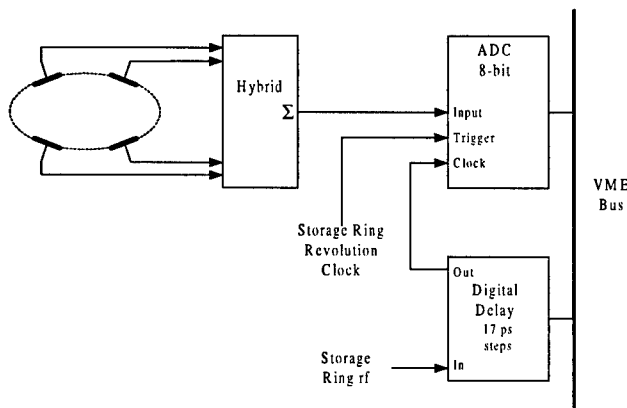
Figure 4: Bunch current monitor.

The storage ring rf is passed through a programmable digital delay with a resolution of 17 ps per step. This delay allows the digitizer to be timed to the input bunch train. Up to 48 consecutive turns of data may be digitized in one pass. The 48 turns of data are averaged to reduce the measurement's variance.

The digitizer has a peculiarity due to its design. It exhibits up to an 8-channel uncertainty between the trigger input and the location in the FIFO of the digitized value corresponding to the trigger time; i.e., the position of the beginning of the bunch train within the record has up to an 8-channel uncertainty. All our storage ring fill patterns place charge in bucket zero. The software searches for the first non-zero value over a limited range of the digitized record to find bunch zero. All further processing is then relative to the position determined to be bunch zero. At normal operating levels, the raw resolution of the digitizer is about 0.037 mA/bit. With averaging of 48 turns, the rms error is less than 0.010 mA.

The bunch current monitor plays a crucial role in storage ring top-up mode. In top-up mode, additional charge is injected into the storage ring at short time intervals (2 minutes) to counteract beam decay due to lifetime. The bunch current monitor output is used to determine which bunch(es) have the least charge. Those bunches are then targeted for injection.

6 BPM PROCESSOR

The existing rf BPM system [3] uses a module known as a memory scanner that applies a boxcar filter to BPM data collected from the BPM digitizers. It is believed that BPM data quality can be enhanced by applying DSP techniques to improve AC performance of the filter. A drop-in replacement is being designed at this time.

The new memory scanner will be a VXI module with six SHARC DSPs connected as a multiprocessor cluster [10]. The SHARC has features that facilitate multiprocessor configurations. BPM x, y and sum values from nine BPM digitizers (one sector's worth) will be available to the module via the VXI local bus. The digitizers alternate between x and y digitizations on every other turn. The incoming data rate will be 2.4 Msamples per second (nine 'x' or nine 'y' values times 270 kHz revolution rate). The board will provide three basic functions:

1. Low pass filtering through multistage decimation filters.
2. BPM beam history storage.
3. Fast Fourier transform (FFT)-based calculations

A 300-Hz low pass filter will provide BPM data to the fast orbit feedback system. Filters with cutoff frequencies in the few Hertz range will provide BPM data to the control system. Other cutoff frequencies may also be implemented depending on future requirements. The beam history function will use an 8-Mbyte RAM to store temporal BPM data as fast as turn by turn. Allocation of RAM to the BPM data sources will be configurable under software control. FFT based calculations, such as power spectral density, will be supported onboard.

One of the six DSPs will be the master, and the remaining five DSPs will serve as compute engines. The master will control slave operation; manage the beam history RAM; and manage the interfaces to the VXI bus, VXI local bus, and the fast orbit feedback system. Presently it is felt that three of the DSPs will be sufficient to perform all low pass filtering requirements. The remaining two slave DSPs will be available for FFT and statistical data computations.

7 TIMING

7.1 Fast Logic

Several digital logic modules have been designed at the APS that operate synchronously at the storage ring rf of 352 MHz [11]. We recently designed a digital divider based on the ECLinPS [12] family of emitter coupled logic (ECL). This circuit divides the 2.865-GHz linac rf by 24 to produce a 119-MHz signal that is used as a reference for a laser driving a photocathode electron gun

and as a sweep input to a streak camera. The circuit is housed on a small daughter card that is mounted on a VME base board. VME is used merely as a convenience, i.e., there are no programmable functions.

7.2 Low-Cost 352-MHz Distribution

Bunch clock generators [13] are in the process of being installed on multiple beamlines. These modules provide beamlines with timing pulses coincident with stored bunches. Each module requires a 352-MHz storage ring rf reference. In the few installations completed to date, single-mode fiber with single-mode fiber optic transmitters and receivers have been used to distribute the 352-MHz reference.

Single-mode fiber optic transmitters and receivers are costly. It was felt that not all beamlines would demand the low jitter performance achieved with the single-mode components. Thus, we devised a lower cost scheme, shown in Figure 5, that permits the use of inexpensive multimode fiber optic components to distribute the 352-MHz to those beamlines that can tolerate a somewhat higher jitter. The method divides down the 352 MHz to a frequency that can be easily handled by the multimode components. In our case we digitally divide the 352 MHz by 8 and transmit the resulting 44 MHz. At each receiving beamline, the 44 MHz is fed into a phase-locked loop that multiplies the 44 MHz by 8 to reconstruct a 352-MHz reference.
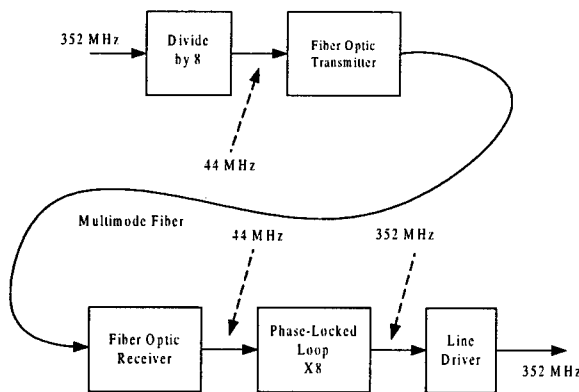
Figure 5: 352-MHz distribution over multimode fiber.

We chose a part manufactured by Micro Networks [14]. With this scheme, we achieve peak-to-peak jitter of 50 ps (rms of 7 ps) over 625 m of multimode fiber. One system has been in use for about six months. We are in the process of installing additional systems.

8 NETWORK

The APS controls network has previously been described [15]. At that time, the network was based on hubs, FDDI, and 10-Mbit fiber Ethernet. We are now in the midst of a major network upgrade. Existing FDDI links will be replaced with 1-Gbit Ethernet. The central enterprise FDDI hub will be replaced with a Gbit Ethernet switch featuring better than a 30-Gbit/s backplane fabric. The existing remote hubs, which are combination repeaters and blocking switches, will be replaced with fully switched 10/100 Ethernet switches with backplane fabrics in excess of 20 Gbits/s. The remote hubs will connect to the central switch via dual 1-Gbit Ethernet uplinks. Redundancy will be maintained from the IOCs up through the central switch and file servers. The servers and operator interface workstations will attach to the central switch through either Gbit or fast Ethernet.

All our existing IOCs use 10BaseFX. We will, however, be upgrading selected IOC processors to PowerPC-based units with 100BaseTX. Dual redundant 100BaseFX transceivers will connect these processors to two independent remote switches.

This upgrade will significantly increase total network bandwidth and eliminate over subscription at the remote hubs.

9 ACKNOWLEDGEMENTS

10 REFERENCES

[1] J. Carwardine, F. Lenkszus, "Real-Time Feedback at the APS," BIW98, AIP Conf. Proc. No. 451, pp. 125-144 (1998).

[2] Pentek, Inc., Upper Saddle River, NJ; http://www.pentek.com

[3] F. Lenkszus et al., "Beam Position Monitor Data Acquisition System for the Advanced Photon Source," Proceedings of the 1993 Particle Accelerator Conference, Washington DC, May 1993, pp. 1814-1816 (1993).

[4] O. Singh et al., "Commissioning Results of the Narrow-band Beam Position Monitor System Upgrade in the APS Storage Ring," these proceedings.

[5] L. Emery, M. Borland, "Advances in Orbit Drift Correction in the Advanced Photon Source Ring," Proceedings of the 1997 Particle Accelerator Conference, Vancouver, BC, Canada, pp. 742-744 (1998).

[6] VMIC, Inc., Huntsville, Al 35803; http://www.vmic.com

[7] Systran Corp., Dayton, Oh. 45432; http://www.systran.com

[8] Analog Devices, Norwood, MA, 02062; http://www.analog.com

[9] Celerity Systems, Inc., San Jose, CA. 95117; http://www.csidaq.com

[10] R. Merl, Advanced Photon Source, private communication.

[11] F. Lenkszus and R. Laird, "The Advanced Photon Source Injection Timing System," Proceedings ICALEPCS'95, Chicago, IL, pp. 567-571 (1996).

[12] Motorola Semiconductor Products Sector (SPS), Austin, TX; http://motorola.com/sps/

[13] F. Lenkszus and R. Laird, "A Bunch Clock for the Advanced Photon Source," Proceedings of the 1997 Particle Accelerator Conference, Vancouver, BC, Canada, pp. 2490-2492 (1998).

[14] Micro Networks, Worcester, MA 01606; http://www.mnc.com

[15] W. McDowell and K. Sidorowicz, "An Accelerator Controls Network Designed for Reliability and Flexibility," Proc. of ICALEPCS'97, Beijing, China, pp. 302-304 (1998).

FEEDBACK SYSTEMS FOR LINEAR COLLIDERS*

L. Hendrickson#, P. Grossberg, T. Himel, M. Minty, N. Phinney, P. Raimondi,
T. Raubenheimer, H. Shoaee, P. Tenenbaum, SLAC, Stanford, CA

Abstract

Feedback systems are essential for stable operation of a linear collider, providing a cost-effective method for relaxing tight tolerances. In the Stanford Linear Collider (SLC), feedback controls beam parameters such as trajectory, energy, and intensity throughout the accelerator. A novel dithering optimization system which adjusts final focus parameters to maximize luminosity contributed to achieving record performance in the 1997-98 run. Performance limitations of the steering feedback have been investigated, and improvements have been made.

For the Next Linear Collider (NLC), extensive feedback systems are planned as an integral part of the design. Feedback requirements for JLC (the Japanese Linear Collider) are essentially identical to NLC; some of the TESLA requirements are similar but there are significant differences. For NLC, algorithms which incorporate improvements upon the SLC implementation are being prototyped. Specialized systems for the damping rings, RF and interaction point will operate at high bandwidth and fast response. To correct for the motion of individual bunches within a train, both feedforward and feedback systems are planned. SLC experience has shown that feedback systems are an invaluable operational tool for decoupling systems, allowing precision tuning, and providing pulse-to-pulse diagnostics. Feedback systems for the NLC will incorporate the key SLC features and the benefits of advancing technologies.

1 OPERATIONAL ISSUES

Linear colliders have severe operational challenges, and feedback systems are an essential tool. Feedback systems distributed throughout the machine allow less-invasive tuning procedures, so that when upstream parameters are modified, downstream feedback stabilizes the beam, allowing routine operation to continue. Feedback is also invaluable in facilitating quick startup after outages. A robust design ensures that the feedback is not confused when the beam returns after an outage, and that control devices are not moved in the absence of beam. Feedback is a useful element in higher-order tuning applications. In the SLC linac, the emittance tuning packages move feedback setpoints to create an oscillation in the linac which is closed by a downstream feedback. In the

final focus, the built-in averaging capabilities of the optimization feedback enable it to be used as a high-resolution measurement device for complex tuning procedures. A variety of diagnostics are provided for beam jitter, fit quality and other information, and the feedback system is also used to take a snapshot of data for diagnosing machine trips.

2 SLC FEEDBACK

The SLC feedback system provides a valuable base of experience for future systems. A generalized, database driven beam based system [1] was implemented starting in 1990. The system was expanded to control a variety of beam parameters in every major region of the machine. At the end of the 1998 run, there were 50 control loops for the SLC alone, and another 25 to support other programs such as the PEPII B factory, Final Focus Test Beam and fixed target experiments. In general the data is available to the feedback at the pulsed rate of 120 Hz, although many loops run more slowly due to CPU limitations and other considerations.

2.1 Basic Feedback Systems

In the injector, feedback controls a variety of intensity-related parameters associated with the polarized electron gun, including laser voltages and kicker timing. A higher order system controls the asymmetry between the intensity of left and right polarized beam averaging several thousand pulses.

Steering feedback systems are found throughout the machine, reading beam position monitors (BPMs) and moving correctors. Several performance limitations with these systems are discussed in a later section. A cascade system was developed to minimize overcorrection associated with multiple feedback loops in a beamline which all control the same parameters [2].

The energy of the SLC is controlled in a variety of locations, typically by reading BPMs in a high-dispersion region and moving phase shifters or controlling klystron amplitudes. A hardware based feedforward system coordinates with the beam based feedback to compensate for the energy change due to intensity fluctuations. The intensity is measured while the beam is in the damping ring and communicated to the energy feedback system in the linac for correction on the same pulse.

At the interaction point, a specialized feedback keeps the beams in collision using the beam-beam deflection measured from the BPMs. The beam-beam separation is determined by normalizing the deflection to compensate

338

for intensity fluctuations, and fast pulsed correctors allow full 120 Hz control.

2.2 Feedback Architecture and Calculations

The SLC feedback system is generalized and database driven so that feedback loops can often be added without additional software. The feedback is designed to use the components (CPU, BPMs, correctors, etc.) of the existing control system and dedicated hardware is not required except where speed is essential. A fast point-to-point network has been developed to communicate between different microprocessors, supporting feedback loops with elements from more than one region. The feedback calculations use matrices which are generated offline and stored in an online database. The matrix design is based on the state space formalism of digital control theory, using Kalman filters and Linear Quadratic Gaussian regulators [3]. The noise model includes a combination of white noise and low frequency noise, with the goal of achieving a robust system with good step response.

2.3 Specialized Frequency Control

The SLC is a 120 Hz pulsed machine, with a slight difference in even and odd pulses (timeslots) due to the AC power sources, causing 60 Hz energy or trajectory oscillations. A feedback system stabilizes the energy difference between the two timeslots using specialized logic that calculates and controls the average and difference of odd and even pulses, resulting in excellent damping at and near the Nyquist frequency.

A 59 Hz oscillation in the beam position was caused by pump vibrations in the linac, and the downsampled 20 Hz loops resulted in aliasing to 1 Hz. The rate of some linac feedback systems was modified to minimize this aliasing. To damp the 59 Hz, feedback with the timeslot control algorithm was implemented at the end of the linac and at the interaction point. Performance tests showed that the 59 Hz oscillation was damped by a factor of 5.

2.4 Optimization Feedback

Optimization feedback has been implemented for the SLC which uses automated subtolerance excitation techniques in order to determine an optimal setting for a nonlinear system. The first optimization feedback controlled energy spread by varying phase offsets [4]. The phase offset was moved up and down by a small amount, averaging over many pulses and then the slope of a parabola was calculated to determine the optimal setting. This application was found useful at first but the minimum control bit size available in the hardware was too invasive for routine operation, and this automated procedure was eventually discontinued. A similar system was developed to minimize the linac jitter by optimizing the damping ring extraction kicker timing. This system worked well in principle, but was used intermittently and never remained in routine operation.

In the final focus of the SLC, five orthogonal parameters for each of the two beams are routinely tuned to maximize the luminosity. Originally, a scan method was employed, where a linear combination of devices was moved through a series of settings, the beam size was measured at each point, and a parabola was fitted to the square of the beam size to determine the optimal setting. The beam size was measured using beam-beam deflection scans. With smaller beam sizes, the measurement resolution became a significant issue [5], leading to an estimated 20-40% luminosity loss due to mistuning. Furthermore, the tuning procedures required a significant amount of operator time and attention, and the results were dependent upon individual judgement, resulting in variable luminosity. At higher luminosity, monitors became available to return a statistically significant signal which is proportional to the luminosity on a pulse to pulse basis. These monitors use beamstrahlung radiation from the beam-beam interaction and also wide angle radiated Bhabha scattering events.

A fully automated feedback system [6] was developed to dither each linear combination of devices through three settings, averaging the luminosity signal over many pulses. Figure 1 shows the dithering process in operation; as the dither knob is moved, the luminosity monitors show a response. Under most conditions, the Bhabha monitor could have excessive luminosity-related backgrounds, and the beamstrahlung detector provided better results. The offset of a parabola was calculated to determine the optimal point. A scheduling process determined which of the ten parameters was to be optimized at a given time, based upon user-selected scheduling and tolerances. The dithering process required only a few percent luminosity degradation, while improving the resolution by a factor of 5 to 10. Overall this resulted in a significant net luminosity increase, while allowing the operations staff to concentrate on other tuning.
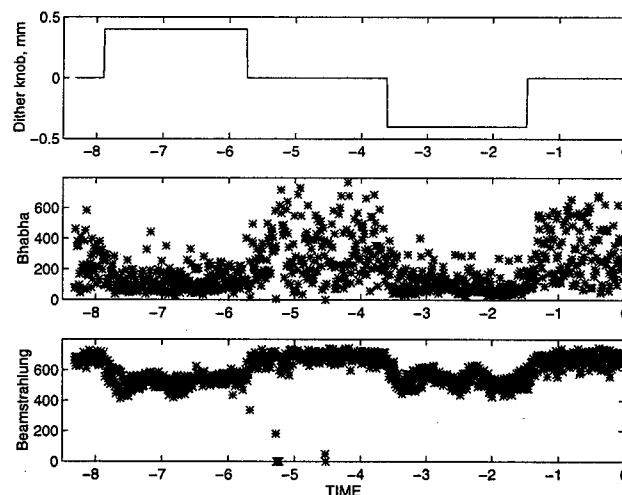
Fig 1: Dithering Process for Luminosity Optimization Feedback
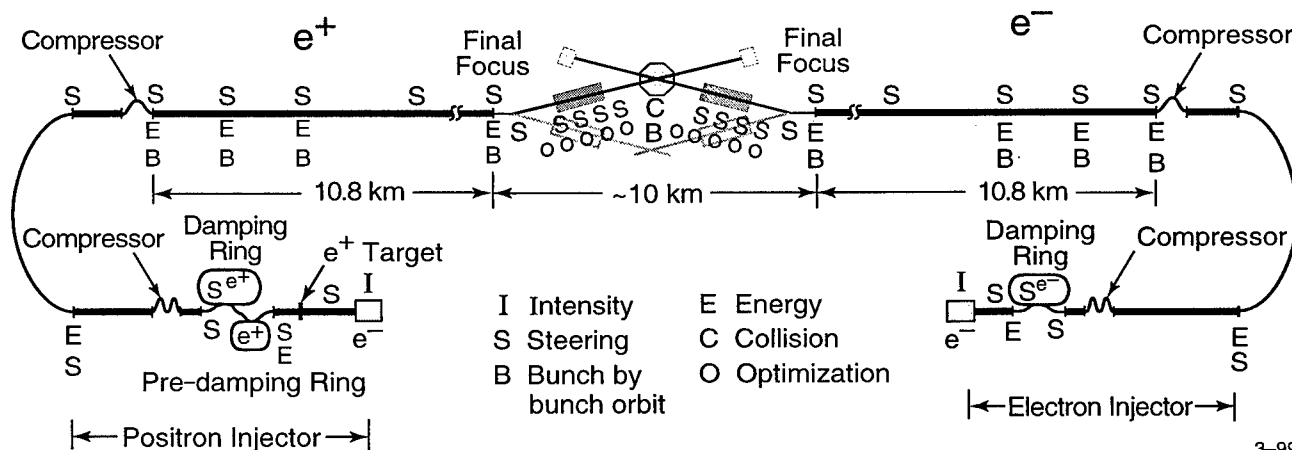
Fig 2: NLC Schematic with Feedback Loops Shown

3 NLC FEEDBACK

The NLC requires several new types of feedback systems in addition to the capabilities developed for the SLC. The control system must provide the CPU and network bandwidth to support flexible feedback communications at the full machine rate. Performance improvements are also needed to remedy problems found at the SLC. Figure 2 shows locations where feedback systems are planned.

3.1 Bunch-to-bunch Feedback

The NLC will have a pulse train of 95 bunches. In addition to controlling beam parameters for the mean of the bunches in the train, feedback systems are required to correct the differences of intensity, energy and position along the train. Because the interbunch spacing is only 2.8 nanoseconds, most of these loops are not designed to respond in an interbunch period, but would typically run at the pulse rate of 120 Hz, correcting the shape of the train on a later pulse. Specialized beam position monitors must return information on each bunch of the train, and pulsed actuators are required to have enough bandwidth to adjust the individual bunches.

An ultrafast feedback is being studied to bring the beams into collision for subsequent bunches of the pulse train [7]. Separate dedicated hardware based systems would control the horizontal and vertical planes. The relative beam offset would be measured by an outgoing beam position monitor near the interaction point, and the control actuator would be a weak, fast kicker controlling the incoming position of the other beam. This configuration minimizes delays for signal travel as both measurement and control are in the same location. A pilot bunch which is sent through undeflected, without the opposing beam, would provide a reference for deflection calculations. The measured deflection of the first colliding bunches can then be used to calculate a correction for the remainder of the train. The gain factor to convert

deflection angle to position would be set by an interface with a slower software based feedback. Preliminary estimates indicate that the feedback may be able to produce a control response within about 10 ns.

3.2 Damping Rings

For the NLC damping rings, longitudinal and transverse feedback systems will take advantage of architecture and algorithms from storage rings such as PEPII, APS, PSI, etc. Some of these will be dedicated high-bandwidth systems, but beam based global or local orbit feedback systems are also anticipated.

3.3 Additional Capabilities

Several other unusual feedback systems are planned for the NLC. To stabilize vibration of the final quadrupoles near the IP, a hybrid system may be used to span both low and high frequencies. An accelerometer based system measuring vibration data at 5 KHz may provide high frequency response while a beam based feedback running at 120 Hz covers low frequencies. Another feedback system must synchronize the phases of the two final focus crab cavities. Additional systems will stabilize the relative phase of the beam with respect to the RF, and control the effective fiber length for the timing system. Finally, a variety of RF-related feedback systems are planned.

3.4 Control System Issues

The NLC feedback system will be well integrated with the rest of the control system. Feedback will share measurements with users, so that requested measurements do not interrupt the feedback system. Sufficient CPU and networking are planned, so that feedback can generally run at the full beam rate and latency is minimized. The standard timing budget will result in a control response within two 120 Hz interpulse periods after a perturbation is seen. One pulse is allowed for digitization of the BPMs, network traffic and feedback computations. A second

340

pulse is required to ramp power supplies and affect the beam. New BPMs are designed for high resolution, good stability and wide dynamic range.

Coordination with the main control system is essential to maximize effectiveness. Diagnostics should include fast time plots, where users can view beam parameters on a pulse to pulse basis, as well as longer-term history plots, RMS calculations and FFTs. Feedback data should be accessible to and integrated with other applications. Applications should be able to automatically turn on and off feedback loops, change setpoints and obtain control values. A variety of measurement devices and actuator types should be supported in order to allow for easy expansion. Other applications must recognise when a device is under feedback control to avoid contention. Finally, flexible networking systems must accommodate unplanned future extensions.

4 PERFORMANCE ISSUES

Performance limitations have been a significant area of concern with the SLC feedback system, and one of the goals for the NLC is to insure that these issues are adequately understood and addressed. Experiments using the SLC have been able to identify and characterize a variety of problems.

4.1 Cascade

In both the SLC and NLC, the linac is a long, straight beamline with several orbit feedback systems in sequence. Overcompensation and ringing will occur if multiple systems respond to the same disturbance. For the SLC linac, a cascade system communicates processed beam information from each feedback to the next downstream loop. The transport matrices between loops are calculated adaptively to eliminate sensitivity to optics drifts. The system was initially successful, allowing feedback to run at high gain factors with good system response. However, this algorithm assumes that the beam transport is independent of the source of a perturbation.

With higher intensity operation, wakefields and chromatic effects make the beam transport nonlinear and oscillations propagate differently depending on their point of origin. When a bunch passes off-axis through the accelerating structures, the asymmetric fields induced by the head of the bunch kick the later particles, producing a tilted distribution which remains after the centroid is corrected. In order to correctly model the beam transport, each feedback must receive information from all of the upstream loops to identify the source of the disturbance and avoid overcorrection. An improved algorithm has been successfully tested in simulation.

4.2 Simulation Environment

In order to evaluate feedback designs and analyze performance issues, a Matlab simulation environment was created [8]. The LIAR beam transport code [9] is called as a subroutine, realistically simulating wakefields, ground motion effects such as ATL, and other errors including alignment and field strength. The state space matrix design program was converted from MatrixX to Matlab to allow for easier simulations and evaluation of alternative algorithms.

4.3 Configuration for Wakefield Effects

The configuration of feedback for the NLC linac was modelled using the Matlab simulation environment. The original proposal was based on a typical SLC setup, where linac feedback loops use a minimal number of correctors immediately followed by 8-10 BPMs. Due to wakefield effects, this configuration resulted in a large orbit RMS and significant emittance growth. Figure 3 shows the vertical beam position along the linac after a perturbation has been introduced at the beginning of the linac and the feedback has converged. Each feedback perfectly flattens the orbit at the feedback BPMs, but large orbit excursions are seen between the feedback locations.
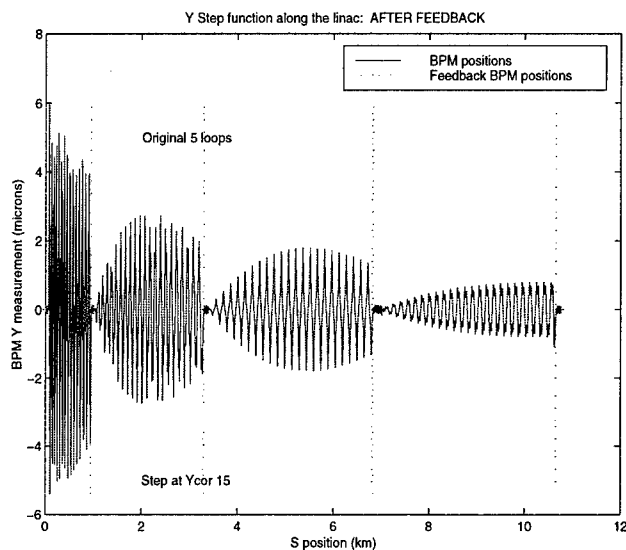
Fig 3: Linac Orbit with Original Feedback Configuration
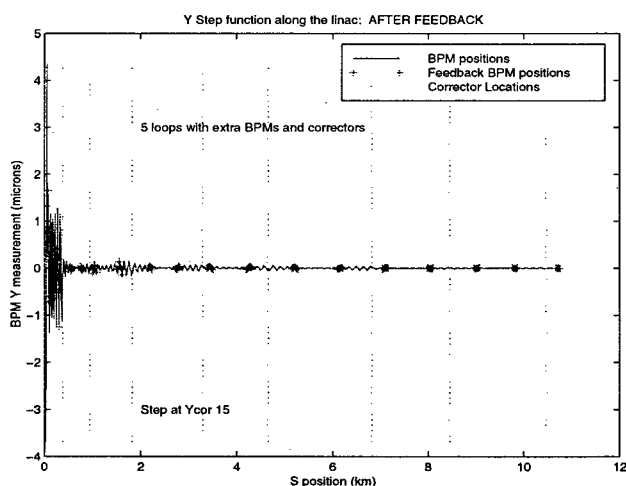
Fig 4: Linac Orbit with Improved Feedback Configuration

Several alternative configurations were evaluated with respect to orbit RMS, emittance growth, bunch shape at the end of the linac, and ATL ground motion response. Better performance was achieved by adding more beam position monitors and correctors than were originally proposed. When these additional devices are spread over long distances in a single feedback, the wakefield compensation can be further improved. However, there are practical limitations to the span of a single feedback due to imperfections in the model. For a global feedback controlling the entire linac, these errors can be significant and degrade performance. More work is needed to evaluate beam transport variation with klystron phase offsets and other errors. In the presently preferred configuration, the linac is divided among five feedback systems, each including four sets of BPMs and two sets of correctors. Figure 4 shows the resulting beam trajectory for this system, after it has responded to the same disturbance shown in figure 3.

4.4 Other Performance Issues

Measurements of SLC corrector response determined that the speeds of many devices were much slower than in the feedback design model. The model assumes a delay of two 120 Hz pulses for the actuators to respond but in many locations, the measured response is a ramp of 9 or more pulses. Simulations indicate this would have only a moderate effect on feedback performance if it were the only flaw. However, when combined with other imperfections, the slow correctors can have a significant performance impact.

In some areas of the SLC, the beam transport is poorly modeled. Sometimes this can be fixed by identifying and correcting accelerator errors such as klystron mis-phasing. Otherwise a calibration procedure is used to measure the beam transport and incorporate it into the feedback design.

Hardware problems such as broken correctors and erratic BPMs also degrade the feedback performance if they are not detected. Due to limited CPU and networking and a suboptimal cascade scheme, many feedback loops run slower than the full 120 Hz pulse rate, and most run with decreased feedback gain factors. This results in a system response which amplifies beam noise around 1 Hz. At the SLC, the large number of feedback loops, the many sources of imperfections, and inadequate diagnostic tools result in degraded feedback performance.

For NLC, plans are underway to ensure that these issues are adequately addressed. Additional SLC beam testing and simulations are planned. More work is needed to analyze calibration or adaption schemes for the beam transport model. In order to diagnose remaining problems a feedback performance watchdog is needed. An excellent algorithm for this could come from model-independent analysis techniques [10], which are capable of identifying the locations of broken BPMs, correctors and misbehaving feedback loops.

5 TESLA FEEDBACK

The TESLA Linear Collider has some significant differences from NLC. The linac uses superconducting RF where the wakefield effects are minimal, simplifying the feedback requirements. The interbunch spacing is 377 ns, compared with 2.8 ns in the NLC. This allows for orbit feedback systems to more easily correct on subsequent bunches of the train. Plans for these systems are described more fully in reference [11].

6 CONCLUSIONS

Linear colliders present significant challenges for controls, due to tight tolerances and stability requirements, and complex tuning procedures. Extensive feedback systems are an essential tool for operation. Much work remains to be done for future colliders to insure that the benefits of these feedback systems are fully realized, while addressing the performance issues associated with a large number of systems.

7 ACKNOWLEDGEMENTS

8 REFERENCES

[1] L. Hendrickson, et al., "Generalized Fast Feedback System in the SLC," ICALEPCS, Tsukuba, Japan, SLAC-PUB-5683 (1991).

[2] T. Himel, et al., "Adaptive Cascaded Beam-Based Feedback at the SLC," PAC, Washington, D.C., SLAC-PUB-6125 (1993).

[3] T. Himel, et al., "Use of Digital Control Theory State Space Formalism for Feedback at SLC," PAC, San Francisco, CA, SLAC-PUB-5470 (1991).

[4] M. Ross, et al., "Precise System Stabilization at SLC Using Dither Techniques," PAC, Washington, D.C., SLAC-PUB-6102 (1993).

[5] P. Emma, et al., "Limitations of Interaction-Point Spot-Size Tuning at the SLC," PAC, Vancouver, Canada, SLAC-PUB-7509 (1997).

[6] L. Hendrickson,et al., "Luminosity Optimization Feedback in the SLC," ICALEPCS,Beijing,China, SLAC-PUB-8027 (1999).

[7] M. Breidenbach, private communication (1999).

[8] P. Tenenbaum, et al., "Use of Simulation Programs for the Modelling of the Next Linear Collider," Proceedings of this conference (1999).

[9] R. Assmann, et al., "The Computer program LIAR for the simulation and modeling of high performance linacs," PAC, Vancouver, Canada (1997).

[10] J. Irwin, et al., "Model-Independent Beam Dynamics Analysis," Proceedings of this conference (1999).

[11] I. Reyzl, et al., "Fast Feedback Systems for Orbit Correction in the TESLA Linear Collider," Proceedings of this conference (1999).

KEKB CONTROL SYSTEM: THE PRESENT AND THE FUTURE

A. Akiyama, S. Araki, J-I. Odagiri, T. Katoh, T. Kawamoto,
I. Komada, K. Kudo, T. T. Nakamura, T. Naito, N. Yamamoto*,
KEK, Tsukuba, JAPAN
M. Kaji, Mitsubishi Electric Co., Ltd., JAPAN
T. Kitabayashi, K. Yoshii,
Mitsubishi Electric System & Service Engineering Co., Ltd., JAPAN
N. Koizumi, Mitsubishi Space Software Co., Ltd. JAPAN
M. Takagi, S. Yoshida, Kanto Information Service, JAPAN

Abstract

Achievements of KEKB control system during the commissioning of KEKB accelerators will be reported. The KEKB control system is the first major application of EPICS toolkit in JAPAN. We added some software components on the top of EPICS toolkit. One of these is the system to automate generation of the EPICS database configuration files using ORACLE database management system. Although it costs us a lot of effort to develop, this kind of configuration management system is essential for a large accelerator like KEKB. Another component is an implementation of EPICS CA(Channel Access) interface in the script languages. SAD, a modeling program with a scripting language capability, and Python, an object oriented scripting language are currently supported in the KEKB control system. These scripting languages are used to develop high level applications, such as an orbit correction program with graphical user interface using Tk library. Combination of these scripting languages and EPICS CA provides flexibility in the control system. KEKB control system also includes some new hardware components, including Arcnet based magnet power supply controllers and VME single board computers based on Motrolla's PowerPC750 CPU. The performance of these components will also be reported. The problems and (possible) solutions found during the KEKB commissioning will also be discussed.

1 OVERVIEW OF KEKB CONTROL SYSTEM

Commissioning of KEKB[1], an asymmetric electron-positron collider for B-meson physics, has started on December 1st, 1998 after 5 years of construction. The control system for KEKB accelerators[2] also started its operation shortly before December 1st. Although some applications in the control system had limited functionality, basic operation of the equipment could be performed using KEKB control system.

Network: The KEKB control system includes 26 local control rooms along 3km circumference ring accelerators and a central control room. These control rooms are linked

System Overview
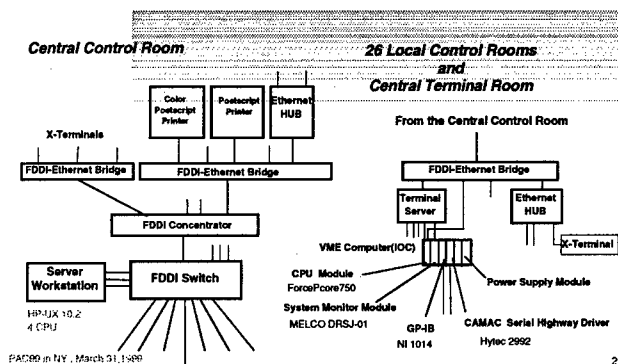
Figure 1: Schematic view of the KEKB control system

Table 1: VME single board computers used in the KEKB control system

CPU Type	Number of CPU
Force PowerCore6750	78
Force PowerCore6603	13
Force CPU40	9

with switched FDDI network [See Figure 1.] In each local control rooms, a VME single board computer, called Input/Output Controller or IOC in EPICS terminology, connected to the KEKB control system network through FDDI-Ethernet bridge. A console port of IOC and a serial port on a system monitor board in each VME subrack are connected to a terminal server and remotely accessible.

IOC: We use VME single-board computers equipped with Motrolla PowerPC 750 (Force PowerCore 6750) as IOCs. We also use some VME single board computers with PowerPC603e and MC68040. 100 IOCs in total are used in the KEKB control system currently.

Fieldbus interfaces: We use several fieldbuses, CAMAC, GP-IB, Arcnet, Modbus+, MXI and the serial line, in the KEKB control system. IOC controls devices on these fieldbuses using a fieldbus interface board in a VME subrack. We developed drivers for Arcnet and Modbus+ inter-

Table 2: Parameters of the Host computer for KEKB control system

CPU	HP PA-RISC	Alpha
# of CPUs	4(@120MHz)	4(@440MHz) & 6(@330MHz)
memory	2GB	1GB
Network	FDDI	FDDI
Storage	20GB RAID	50GB RAID

System OverView (cont'd)

Figure 2: Software components in the KEKB control system

Table 3: Some system parameters shows working condition of a host computer in the KEKB control system

Load average:	4-5	(4	CPU	configuration)
Users:	150			
Processes:	900			
Memory:	AVAIL	USED	FREE	USED
Usage(KB):	1,635,272	275,920	1,359,352	17%

Figure 3: KEKB control system currently has two starts points, KEKB task launcher(right) and KEKBOPERA-TION.adl(left).

faces. EPICS drivers are used for other fieldbuses.

Host computers: Mitsubishi ME/RK-460 computer(HP-UX 10.20) equipped with four CPUs is used as the host computer in the KEKB accelerator control system. The host computer also serves a development environment for VxWorks which is the operating system of IOCs. X-terminals are used as an operator interface in the KEKB accelerator control system.

A cluster of Alpha servers is used as a servers for accelerator modeling/simulation. These servers also have network interfaces to KEKB control network and runs some KEKB control system applications.

Software: Software in the KEKB control system is constructed using the framework of EPICS. PL/SQL programs generates parameter files to generate EPICS database files combined with template databases. MEDM, a GUI tool in EPICS, is used to build a simple user interface. Other applications which has GUI are developed using ether SAD or Python. SAD is an accelerator modeling/simulation program developed at KEK. User of SAD can control the program using SAD script, which has a syntax similar to the syntax in Mathematica[11]

Python is an object oriented interpreter language developed by G. von Rossum [9, 10] Both languages have interfaces to EPICS-CA and Tk widgets and used to build an application which may not fit in MEDM.

2 SYSTEM PERFORMANCE

The Basic unit of information in EPICS is a record. Distributed EPICS runtime database on IOCs keeps 208,716 records in it. Average number of records on an IOC is 2,319. Software and Database on IOC occupy 5MB of memory on average.

In the KKEB control system network, 2000 packets are transfered every second on average.

Table 3 shows some system parameters in working conditions. When we started commissioning of KEKB in last December, the host computer just had two CPUs. "rup" value reached more than 10 and it resulted slow response of the system.

Fieldbus interfaces: 2517 magnet power supplies have Arcnet interface controller board developed at KEK. These interface board are connected to one of 176 Arcnet network segments. 12 IOCs are are used to control magnet power supplies. One IOC controllers up to 200 power supplies and receives a status packet information to IOCs every 5 seconds. Occasional Arcnet network reconfiguration does not harm operation of magnet power supplies.

Software: Figure 3 shows a main screen of KEKB control system. A user or an operator can choose a control application from this screen. More than 120 programs in SAD or Python and 50 MEDM screens are registered to the main control.

3 PROBLEMS

Slow response: When we just started the operation KEKB control system we found some problems in the control system. Most noticeable is slow response of GUI written in script languages. Tuning of Unix system parameters on Unix host and improved situation. Finally we increased number of CPUs on the host computer from 2 to 4. It drastically improved the situation.

Software collision: Each software components is developed and tested separately and integrated onto a IOC later. This approach works for most of cases but caused incompatibility problems in some cases. In some cases, we took a simple solution, introducing new IOCS and run these applications in separate IOCs.

Console port monitoring: To analyze cause of IOC crashes or suspended vxWorks tasks, we need to correct some data when it occurs. A console port of each IOCs is connected to a port of a terminal servers. A xterm window for each console port is opened on the console for IOC monitoring. It allows us to store messages printed on the console to the file on the host computer and to analyze it later. We also developed simple application to find these information easily.

4 FUTURE

Here we list up possible upgrade plans for KEKB control system. Some of them can be installed soon.

EPICS core software upgrade: Currently we use the release 3.13beta11 of EPICS core software. We should move to the latest release 3.13.1 as soon as possible. Merging of local changes into 3.13.1 is underway. The release 3.13.1 will be used in the KEKB operation after we test drivers and device support routines in the release 3.13.1 environment. This has to be done as soon as possible.

Arcnet upgrade: The current daisy chain configuration of Arcnet will be partly replaced by the star configuration using Arcnet HUB. This change will reduce the chance of network reconfiguration and increase reliability of Arcnet communication.

Dual host computers: Although we use 3 Unix servers for KEKB operation, ORACLE runs only on one of them. Dual server configuration of ORACLE servers is essential for the stable operation of KEKB control system.

network upgrade plan: Because of scalable architecture, it is possible to increase system POWER gradually in principle. However, network bandwidth at the network interfaces on host servers can be a bottleneck of the system in (near) future.

When we designed KEKB control system, FDDI was a mature technology and seemed to have a future upgrade path. ATM was a growing network technology at that time but still is not a standard network technology. 100Base-T and Giga-bit Ethernet technology are gaining the position of de facto standard for future network technology. We have to find smooth way to change network infrastructure .

5 CONCLUSION

The KEKB control system has been operational since last December. It is the first large scale implementation of EPICS in JAPAN.

We found that the use of interpreter in an accelerator control system is quite useful. For the accelerator like KEKB, flexibility of the control application is as important as its stability, especially in its commissioning phase.

6 REFERENCES

[1] "KEKB B-Factory Design Report", KEK Report 95-7, August 1995

[2] T. Katoh et al., "Present Status of the KEKB Control System", ICALEPCS '97, Beijing, China, November 3-7, 1997

[3] W. McDowell et al.:"EPICS Home Page", "http://epics.aps.anl.gov/asd/controls/epics/EpicsDocumentation/EpicsGeneral/"

[4] L. Dalesio et al. "Distributed Software Development in the EPICS Collaboration,", Proc. ICALEPCS95, Chicago, USA, 1995; L. Dalesio et al.: The Experimental Physics and Industrial Control System Architecture: Past, Present, and Future, Proc. ICALEPCS, Berlin, Germany, 1993, pp 179-184.

[5] A. Akiyama et al., "KEKB Power Supply Interface Controller Module", ICALEPCS '97, Beijing, China, November 3-7, 1997

[6] 'SAD home page' at "http://www-acc-theory.kek.jp/SAD/sad.html"

[7] M. Kaji et al., "RELATIONAL DATABASE SYSTEM IN THE KEKB ACCELERATOR CONTROL SYSTEM", Proc. of the first Asian particle accelerator conference(APAC98), Tsukuba, JAPAN, 1998.

[8] J. Odagiri et al., "Performance Evaluation of EPICS on PowerPC ", ICALEPCS '97, Beijing, China, November 3-7, 1997

[9] M. Lutz, "Programming Python", O'Reilly & Associates, Inc. USA, 1996

[10] 'Python Home Page', "http://www.python.org/"

[11] S. Wolfram, "Mathematica: A system for Doing mathematics by Computer", 2nd ed. Addison-Wesley Publishing Company, Inc. USA, 1991

FIRST EXPERIENCE WITH CONTROL AND OPERATIONAL MODELS FOR VACUUM EQUIPMENT IN THE AD DECELERATOR

P. M. Strubin, N. N. Trofimov, CERN, 1211 Geneva 23, Switzerland

Abstract

Control and Operational models for Vacuum Equipment have been studied at CERN for several years [1]. A prototype implementation was tried out on ion gauges in LEP followed by a full-scale implementation for all vacuum equipment to be controlled in the newly built AD ring.

In order to meet the tight time schedule, the existing hardware and software infrastructure of the PS complex has been used. The model server was built on top of this infrastructure. This has introduced some restrictions with respect to a full implementation of the models, but made the server available for all vacuum equipment already installed in the various accelerators which are connected to this control system.

In order to test the server, a simplified man-machine interface has been created. This interface presents the available acquisition and control values in a very homogeneous way to the operator, making the advantage of the chosen model approach evident. It also makes additional diagnostic information, previously unavailable, accessible to the vacuum operators.

1 INTRODUCTION

Our Group is operating the vacuum systems of all accelerators in CERN since 1990. During this period, a significant effort was made to reduce the diversity in both hardware and software. For instance, the vacuum operators are offered a unified Man Machine Interface for the PS complex and the SPS and LEP accelerators. Nevertheless, despite the uniform operator interface, there still exists three different versions of the MMI because of the varying ways to access the equipment. For the same reason, alarm and data logging programs are different for each environment.

The objective of the work presented here was to try out a systematic approach using operational and control models of the vacuum equipment.

2 MODELS

The operational model may be considered as a kind of user requirement document, which specifies generic control procedures and related "control knobs and meters" for rather broad "families" of vacuum devices (e.g. ion pumps), without mentioning how the controls are, or shall be, physically implemented.

For each family, the model describes the functionality of the device in the vacuum system and the services which shall be provided for the users (vacuum technicians or accelerator operators) in order to monitor and control the operation of the device. This includes, in particular, the description of various physical variables in the device which can be observed and modified by the users, the states that the device can take during operation and the commands that it can accept to modify its state. In principle, formal modeling techniques (state diagrams, "use cases", etc.) can be used for definition of the operational model, but in our case it is basically a narrative description.

Although the operational model does not directly imply any particular implementation, its aim is to provide a control system designer with a set of guidelines for software development, as well as a thorough definition of the internal system interfaces - most notably the definition of the Application Programming Interface (API). At the API level, we speak about the control model which defines the application programmer's view of the vacuum equipment.

The control model defines in a formal way the procedures and data required for the application programs to implement the equipment control facilities described by the operational model. We apply object-oriented approach to define the control model: the vacuum equipment is organized in device classes; each class defines a control interface for a certain category of the vacuum devices. Devices of the same class have the same set of properties; a property typically corresponds to a physical variable in the operational model.

Several classes of properties have been defined to represent different kinds of the physical variables: analogue measurements, discrete command channels, boolean error indicators, etc. Each property has a value and, depending on its class, a number of other characteristics, such as units of measurement, time stamp, minimum and maximum values, resolution, etc.

Status	OK
Timestamp	Tue Mar 23 10:41:45 1999
Min	1e-12
Max	1e-6
Units	mbar
Resolution	1e-13
Format	2.1e
Access	Read-Only

Table 1: Characteristics of property "pressure"

346

As an example, table 1 shows the characteristics of property "pressure". The values shown are applicable to an ionisation gauge. The values for the "Min", "Max" and "Resolution" characteristics would be different for a cold cathode gauge, but the same characteristics would exist.

3 IMPLEMENTATION

In order to meet the tight time schedule of the AD project, the existing hardware and software infrastructure of the PS complex has been used. The implementation follows the three tier architecture shown in Figure 1, where the model server acts as an intermediary between the standard PS equipment access software and the model based applications.
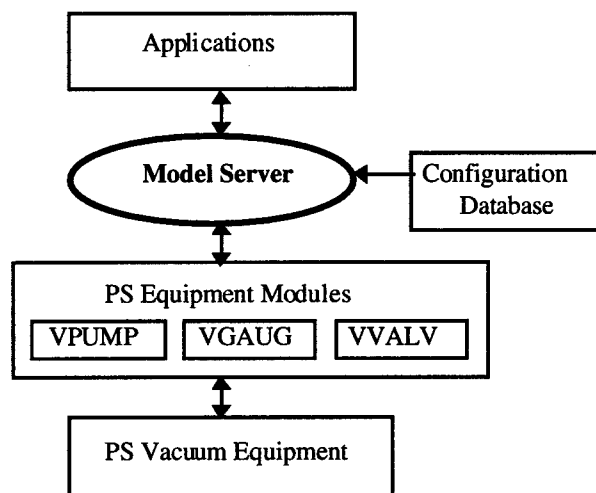
Figure 1: Implementation of the control models in the PS Control environment

Equipment access in the PS control system is organised through Equipment Modules; each Equipment Module is a collection of procedures and data allowing to drive certain type of equipment. The model server transforms the system specific view of the vacuum equipment provided by the PS vacuum Equipment Modules (VPUMP, VGAUG, VVALV [2]) into the model defined representation. In some cases, the model properties directly correspond to the Equipment Module data, but more often a dedicated procedure is required in the server to obtain "raw" equipment data and present it in the form defined by the model.

The server software is in a large part data driven. At start up the server reads a formalized control model description (devices, device classes, properties, characteristics) from the configuration database. The database also describes the equipment interface topology: where and how each individual device which is connected to the control system. This

information is merely imported from the existing PS controls database.

3.1 Problems and constraints

Decision to use the existing controls infrastructure with minimum modifications has allowed us to speed up the development and to connect all vacuum equipment already installed in the various accelerators of the PS complex to the model server. But, at the same time, it introduced some restrictions with respect to a full implementation of the models.

Some features could not be implemented due to hardware and software limitations in the low level equipment controls. For example, only a limited subset of properties defined in the Ionisation-Gauge class is available because of the limitation on the number of parameters that can be passed in the internal software protocol frame [3].

Since equipment access via the Equipment Modules has to be preserved for existing applications, commands can be issued to the equipment bypassing the model server. It is not always possible to trace such commands in the server. As a result one can see, for example, an open valve with last registered command "close", but all other properties indicating normal operation.

The model server does not read values from the vacuum equipment directly; rather, it is using cached data from the Equipment Module data tables. Information in the data tables is updated approximately every 30 to 40 seconds - this cannot be done faster due to performance limitations in the low level equipment network and leads to a further limitation of the model server. In general, the update rate is sufficient for relatively slow changing measurement variables, but sometimes it is not fast enough to monitor status values. For example, when a sublimation pump goes for 30 seconds to the "sublimating" state, this very important event, from the operational point of view, can be missed between two consecutive updates.

However, despite the problems imposed by the implementation constraints, equipment representation provided by the model server essentially conforms to the operational models for all main categories of the PS vacuum equipment (pumps, gauges, valves).

3 USER INTERFACE

The graphical user interface program developed for the AD vacuum control basically performs direct visualisation of the model data. It also provides virtual knobs which allow the users to change the value of device properties and to send commands to the equipment. There are many possible ways of graphical representation of the control model - standardization at this level was not our goal at first instance. Rather, we tried to follow the same "non

revolutionary" approach as in implementation in general and be as close as possible to the conventions and customary style of equipment control adopted in the PS complex [4].

Following these rules, we represent the vacuum equipment in a spreadsheet style tabular format. Devices are grouped in "working sets" which are represented as tables: a row per device and a column for a device variable (property). Property values are displayed in the table cells; clicking on a cell displays detailed information on a property (all its characteristics) or activates a control tool that allows to change the value of the property.

The main working set view is complemented by the detailed status display which shows the current state of all error indicators associated with the working set and a chronologically ordered list of all errors encountered since the program start-up.

The user interface application is based on a relatively small set of the software components (C++, Motif) which are combined and configured at run time using descriptive information on devices and their interfaces available on the model server. Given a device name, one can obtain a list of all properties supported for the device and for each property a full description of its characteristics. This run time interface discovery feature allows the application to easily adjust to changes in the equipment interface. For example, when a new device class is added to the model, it automatically becomes supported by the user interface application - as soon as the class description is entered into the configuration database.

4 OPERATOR'S EXPERIENCE

Although a number of compromises had to be done to adapt to the existing control system architecture, the advantages for the vacuum operators are numerous.

The first one is a coherent presentation of the data available from various types of equipment. Every value is systematically assigned a time stamp and status to allow for correct interpretation of the validity of the data. This allows to correctly handle and display values which have been taken right before a device changed state (e.g., a gauge was switched off) without loosing this last value.

A second advantage is the systematic way of signaling errors and warnings. Whereas it was common practice to encode an analogue value (e.g., a pressure value) to give some hints on problems (like returning -1.0 for under-range), the new approach defines a specific error-indicator property with an associated characteristic setting the severity (warning, fault, etc.). Another useful characteristic of these indicators is the availability of an associated plain text message which allows to clearly display the meaning of the error, like "Equipment error: offset too large". The systematic use of higher level indicators for such problems as communication errors,

allows for quicker diagnostics than device specific "error bits" commonly used in present systems.

A final advantage from the user's point of view is that all properties for all devices can be documented in a database with adequate access tools. It makes it therefore easy to implement on line help features, for instance to guide the operators in diagnostic and repair activities.

5 CONCLUSIONS

We could successfully implement a model server for the vacuum equipment of the new AD decelerator on top of the existing controls infrastructure of the PS complex. It has been running for the commissionning of the decelerator and showed a number of useful features, both for the operators and for the application programmer.

However, the full power of the proposed approach can only be obtained in a new project or in a major reconstruction of an existing system. In this case, the models should serve as a conceptual skeleton for the system design from the equipment interface hardware up to the user interface level.

The operational model may serve as a core requirement document for selection, customization and integration of the industrial components, as well as for in-house developments. Internal system protocols and interfaces should be tailored to the needs of implementing the control model in a complete, consistent and efficient way.

6 ACKNOWLEDGMENTS

7 REFERENCES

[1] P.M.Strubin, N.N.Trofimov, 'Control and Operational Models for Vacuum Equipment', IEEE Particle Accelerator Conference, Vancouver, 1997.

[2] A. Rosenstedt, Control System Software for the Vacuum System, CERN PS, July 1992

[3] G. Benincasa at al., Final Report on the Uniform Equipment access at CERN, CERN/PS 93-16

[4] 'Workstations as Consoles', CERN PS/CO/Note 93-26

A TRANSIENT TOLERANT AUTOMATED CONTROL SYSTEM FOR THE LEDA 75kV INJECTOR*

M. Thuot, L. R. Dalesio, M. Harrington, D. Hodgkins, D. Kerstiens, B. Quintana, J. D. Sherman, M. Stettler, D. Warren, and T. Zaugg, LANL, Los Alamos, NM

A. Arvin, S. Bolt and M. Richards, SRS, Aiken, SC

Abstract

The Low-Energy Demonstration Accelerator (LEDA) injector [1] is designed to inject 75-keV, 110-mA, proton beams into the LEDA RFQ [2]. The injector operation has been automated to provide long term, high availability operation using the Experimental Physics and Industrial Control System (EPICS) [3]. Automated recovery from spark-downs demands reliable spark detection and sequence execution by the injector controller. Reliable computer control in the high-energy transient environment required transient suppression and isolation of hundreds of analog and binary data lines connecting the EPICS computer controller to the injector and it's power supplies and diagnostics. A transient suppression design based on measured and modeled spark transient parameters provides robust injector operation. This paper describes the control system hardware and software design, implementation and operational performance.

1 INTRODUCTION

Accelerator Production of Tritium (APT) applications of high power accelerators requires high beam availability. To maximize beam-on time, rapid recovery from routine events, like injector spark- down, is needed. Reliable recovery from injector spark-down can be provided through computer based automated sequencing. For reliable operation, the data in computers must be protected from being corrupted by the severe EMI transients produced during the spark-down. Coupling between the high voltage power supply (HVPS) and the computer control system is a primary cause of the disruption or damage to computers/logic that occasionally occurs during injector high voltage spark-down. The HVPS circuitry, the method of connecting to the injector, and the physical layout of the injector determines significant EMI coupling parameters such as stored energy, peak current, discharge frequency, di/dt and dv/dt. Computer interface designs, based on circuit models that generate values for these parameters, can effectively suppress the transients and provide reliable operation in a harsh EMI environment.

2 MODELING THE SPARK DISCHARGE AND HVPS CIRCUIT

To estimate the peak current, di/dt, dv/dt and the frequency content of the spark transient, a spark-down circuit model of the LEDA injector and the HVPS was constructed. (See Figure 1). The values of the HVPS components in the model were set to the actual circuit values. The inductance of two of the major loops involved in the discharge of the injector control the natural frequency of the discharge current. These two loops are a large loop formed by the RG218 coaxial HV cable connecting the HVPS to the injector, and a much smaller loop formed by the source and the wave-guide above the grounded source table. The inductance of these conductors was calculated using the formula, from Ott [4], for the inductance of a conductor above a ground plane. These calculated inductance values were compared to actual circuit values by comparing the natural frequency of the calculated spark transients with oscilloscope traces taken during actual spark-down transients on the CW injector.

The HV coaxial cable that connects the HVPS to the injector was modeled as a transmission line. The model of the discharge circuit produced waveform records through SPICE analysis performed by a commercial software package, Electronic Workbench® running on a PC. Electronic Workbench represents the circuit as a schematic rather than a SPICE node list, which simplifies the modification of circuit values and connections.
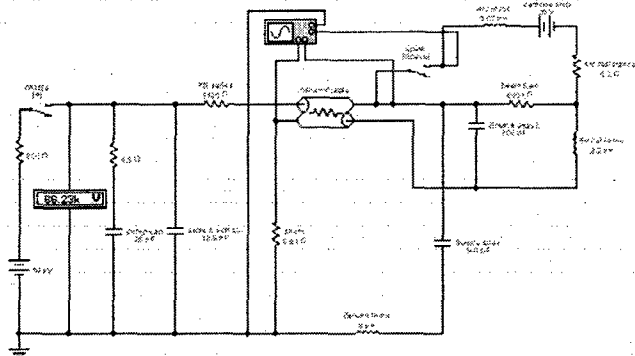
Figure 1. LEDA injector and HVPS transient analysis circuit model in Electronic Workbench®.

2.1 Results of the spark-down transient analysis

The waveforms from the SPICE model of the injector and HVPS were analyzed to extract the peak current (300 to 1200 A), the transient current natural frequencies (2 to 6 MHz) and the maximum di/dt (~1E+10 A/s) and dv/dt (~2E+12 V/s). These parameters quantify the level of the source of the electromagnetic interference (EMI) the control system interface must suppress. If these levels or coupling from this source exceed the transient suppression capability of the control system interface, then they represent a threat to the proper operation of the control system.

The coupling between sparks in the HVPS and the control system follows several paths, each with some coupling constant that primarily depends on the natural frequency of discharge circuit. Capacitive coupling from the HVPS' high dv/dt through the high impedance electric field is relatively easy to shield. Proper grounding of the metal enclosures surrounding the HVPS and of the shields on signal cables will eliminate almost all of the dv/dt driven interference. The only area of the injector system where this EMI source may dominate is if unshielded cables or transducers are exposed to the high voltage circuits. The effect of this, sometimes unavoidable, coupling can be minimized by shielding the exposed cables and transducers and/or shunting their stray capacitance with an RC low pass filter.

The most likely path of EMI into the control system is di/dt (Φ) coupling through the transient low impedance (magnetic) field. This low impedance field is much more difficult to shield. Coupling paths will exist through any mutual inductance between the HVPS discharge circuits and the control system. To control low impedance coupling, the best defense is the reduction of the inductance of all source and signal loops. This source of EMI may be suppressed on signal cables by installing isolators that break the low impedance loop formed by the signal cable conductors and thus convert the Φ induced voltage into a common mode voltage on the isolators. This defense is usually effective, but it can fail if the frequency and/or amplitude of the source of the EMI is extreme, thus driving noise current through the isolators. If the isolators are preceded by a passive low pass filter, the effect of extreme di/dt is mitigated. Our design employs this arrangement with the low pass filters followed by isolators built into the wiring terminal barrier strips.

3 GROUNDING

Proper grounding will reduce the coupling of the spark induced transients into the data acquisition system. There are three grounding systems of particular interest: the AC power system, the HVPS system and the signal cable/data acquisition system. After analysis of the transients estimated the transient frequencies, an elegant solution to the issue of AC power conducted interference was indicated. The thickness of common construction materials used in electrical power distribution systems is much greater than a skin depth at the transient frequencies. This fact allows the use of conduits and junction boxes for barrier shields and permits effective safety and transient current grounds to be easily made. A three phase shielded isolation transformer is employed to isolate the three phase ac power to the HVPS thereby limiting the coupling of spark transients to the AC power lines. The secondary wiring of this transformer is enclosed in rigid conduit to prevent coupling to the data acquisition environment. Another shielded three-phase transformer provides three isolated single phase 115v power sources for "clean" power for the computer and ADCs, "semi-clean" power for the vacuum controls and "dirty" power for the injector auxiliary power supplies.

The HVPS is grounded for safety and the injector is also grounded by the beam line. To avoid a large ground loop with high transient currents, the HVPS cable must be shielded and the shield must be grounded at both ends. This arrangement insures the HVPS transient discharge current (primarily) flows back along the cable shield since the coaxial cable/shield is in "cutoff" [4]. Measurements made on the CW LEDA injector demonstrated a greater than four times reduction in ground displacement voltage at the injector after grounding the high voltage cable shield at both ends. The concurrent advantage is that the inductance of the primary transient discharge loop, a major source of Φ coupling, is greatly minimized.

The few hundred signal cables are wired from the injector transducers with shielded twisted pair cable with the cable shields connected to a system ground point at the low pass filters. This arrangement helps convert normal mode transients into common mode transients due to the distributed capacitance of the cable shield. The low pass filters effectively attenuate the high frequency common mode transients. The shielded twisted pair cables transferring the signals from the low-pass filter circuits to the signal isolators have the shields grounded at the isolator end, again to help convert any remaining normal mode transients to common mode since the isolators attenuate only common mode transients.

4 TWO STAGE SIGNAL FILTERING AND ISOLATION

The analog isolation board and low-pass filter board were designed from the transient parameter analysis data to protect the control computer and data acquisition electronics from spark-down transients. The passive low-pass (1 to 100 kHz, -3 db) filter board is an RC network, built into a terminal barrier strip, placed in the field wiring junction box close to the injector to shunt the brunt of the spark down energy. This filter is used for all analog and binary input and output channels.

The analog and binary isolation boards are located near the computer and ADCs to provide common mode

attenuation and to isolate signal ground loops. The analog isolator also provides isolated power, 1, 2, 5, 10 signal gain and a 100 ma. current driver output if needed. Assembly and wiring costs are both reduced by packaging/mounting the isolators on Phoenix Contact rails in the trunk wiring junction box. (see figure 2) The isolators provide 1500 Vrms isolation a with a -3 db frequency of 6 to 60 kHz, depending on component selection.
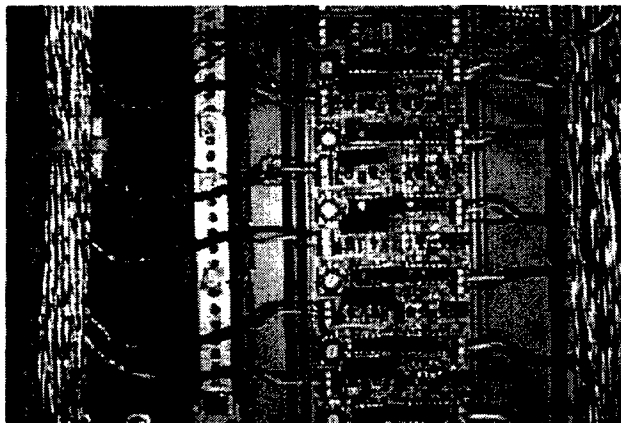
Figure 2: Junction Box Rail mounted Analog Isolators

This two stage transient suppression system has been in use for about four months and has demonstrated its effectiveness. The fourth spark the injector system experienced, shortly after the wiring, filters and isolators had been installed, interrupted computer operation. An inspection revealed that several ground wires on the filter boards were misconnected, bypassing the filters. Once corrected, there has not been any loss of data or computer interrupts during more than 200 spark-downs.

5 EPICS CONTROL AND AUTOMATION

EPICS is a toolkit for building network distributed process control and data acquisition systems. EPICS (originated at Los Alamos) is now developed jointly by a collaboration of >100 institutions, including accelerators, light sources, telescopes, detector collaborations, universities, etc.[5]. EPICS provides control and monitoring of the LEDA injector. Logic in the EPICS run-time database enforces proper operation of the injector to provide equipment protection, as outlined in the LEDA injector standard operating procedure. This logic controls the order in which devices may be turned on when starting up the injector. Logic is used to check the injector status to determine if a controlled device may be safely operated. This status consists of both discrete status, including the PSS (Personnel Safety System) and cooling water flow, and analog read-back/thresholds which determine whether or not the injector is in a state that is proper for operations initiated by the injector operator or

by an automatic sequence. Control thresholds are available to the operator to modify as needed for running beam in varying conditions. For example, the HVPS thresholds are different when conditioning the injector than when operating.

To provide automatic shutdown and recovery from injector sparks, sequence logic was implemented in an EPICS database. The spark detection is based upon the voltage read-back of the FuG HVPS and is executed at a rate of 10 Hz. When this voltage drops below a specified threshold, the ion source microwave power is disabled. The operator may adjust the spark detection threshold as necessary, depending on injector operating conditions. In the automatic spark recovery mode, the disabling of microwave power is followed by a few seconds delay which allows the system to stabilize. Then the magnetron power is reset to the set-point recorded before the spark. The automated recovery from spark down will be repeated, if necessary, up to 3 times within a 30-second time frame. If a fourth spark occurs within the 30-second time frame, the automatic recovery sequence is disabled by logic until an operator intervenes, preventing a series of continuing sparks from causing damage.

The automatic shutdown and recovery has functioned well for the past four months of operation under most conditions. There are, however, conditions when the injector insulators are degraded and the injector experiences a rapid series of external sparks. The 10 Hz software detection in this case is not sufficient, so we have implemented fast hardware logic to provide adequate spark detection and shutdown under these conditions.

6 CONCLUSIONS

Reliable computer automation of processes operating in a high-energy transient environment can be assured by employing proper grounding and transient suppressing computer interfaces. Modelling the transient sources leads to computer interface designs that are effective in transmitting control signals while attenuating transients. By employing a cost-effective two stage transient suppression system, reliable EPICS based automation of the LEDA injector has been demonstrated.

7 REFERENCES

[1] Status Report on a dc 130-mA, 75-keV Proton Injector, J.D. Sherman et al., Rev. Sci. Instrum. 69 (1998) 1003-8.

[2] CW RFQ Fabrication and Engineering, D. Schrage, et al., Proc. LINAC98 (Chicago, 24-28 Aug. 1998) (in press).

[3] The Success and the Future of EPICS, M. Thuot, et al., Proc. LINAC96 (Geneva, 26-30 Aug. 1996).

[4] H. W. Ott, Noise Reduction Techniques in Electronic Systems, Wiley-Interscience 1976.

[5] http://www.atdiv.lanl.gov/aot8/epics/epicshm.htm

CONTROLLING EPICS FROM A WEB BROWSER[*]

K. Evans, Jr.[+]

Argonne National Laboratory, Argonne, IL

Abstract

An alternative to using a large graphical display manager like MEDM [1,2] to interface to a control system, is to use individual control objects, such as text boxes, meters, etc., running in a browser. This paper presents three implementations of this concept, one using ActiveX controls, one with Java applets, and another with Microsoft Agent [3]. The ActiveX controls have performance nearing that of MEDM, but they only work on Windows platforms. The Java applets require a server to get around Web security restrictions and are not as fast, but they have the advantage of working on most platforms and with both of the leading Web browsers. The agent works on Windows platforms with and without a browser and allows voice recognition and speech synthesis, making it somewhat more innovative than MEDM.

1 INTRODUCTION

The concepts described in this paper fall into two groups: (1) the browser objects: ActiveX controls and Java applets, and (2) the agent application. We will speak of the browser objects first and leave the agent application for the end. We will only consider the use of these controls in EPICS [4].

There are advantages to using a Web browser rather than a large program like MEDM to access a control system, particularly if the control system is small or you have special needs. The browser replaces MEDM's EXECUTE mode, and your favorite HTML editor replaces MEDM's EDIT mode. Only the objects need to be provided. The rest is done for you by large and presumably competent groups of programmers and designers working for well-known companies.

In place of the somewhat fixed objects that are available in a program like MEDM, the browser objects can be about anything that a person wants. They are relatively small and are largely self-contained. The ease with which they can be modified solves the extensibility limitations with the large graphical control-system interfaces, such as MEDM. Once the boilerplate code that makes these controls work with the control system and the browser is written, the specific functionality of whether they are, say, a meter or a text entry is relatively simple and easily changed.

In addition to being easily changed, the objects can communicate with each other and to other browser objects via their methods and properties in ways that MEDM-type objects do not.

2 HTML FOR BROWSER OBJECTS

It is important to keep in mind that these browser objects are, indeed, objects in the sense of object-oriented design. That is, they have properties and methods, and they respond to events. How they do this is typically encapsulated in the object and is often of no concern to the person who uses them. When such an object is used in a Web page, it is manipulated via these properties, methods, and events.

The types of objects we are describing are incorporated into a browser page in much the same way as the images we see all the time. Figure 1 shows typical HTML for images, applets, and controls. The PARAMs, which are the basic difference from an image, specify the object's properties.

```
Image
<IMAGE
  WIDTH=540 HEIGHT=80 ALIGN=center HSPACE=5
  VSPACE=0 NAME="image1">
</IMAGE>
```

```
Applet
<APPLET
  CODE="CaGetJ.class"
  WIDTH=540 HEIGHT=80 ALIGN=center HSPACE=5
  VSPACE=0 NAME="cagetj1">
    <PARAM NAME="Monitor" VALUE="False">
    <PARAM NAME="ShowName" VALUE="True">
    <PARAM NAME="Name" VALUE="evans:calc">
    <PARAM NAME="Address" VALUE="localhost">
    <PARAM NAME="fontSize" VALUE="28">
    <PARAM NAME="fgColor" VALUE="#000000">
    <PARAM NAME="bgColor" VALUE="16777215">
</APPLET>
```

```
ActiveX Control
<OBJECT
  CLASSID="clsid:0925E806-BA7A-11D0-99E9-
  020AFF2AC47"
  CODEBASE="CaGetX.ocx"
  WIDTH=540 HEIGHT=80 ALIGN=center HSPACE=5
  VSPACE=0 NAME="cagetx1">
    <PARAM NAME="Monitor" VALUE="False">
    <PARAM NAME="ShowName" VALUE="True">
    <PARAM NAME="Name" VALUE="evans:calc">
    <PARAM NAME="BackColor" VALUE="16777215">
    <PARAM NAME="MonitorTime" VALUE="100">
</OBJECT>
```

Figure 1: HTML for three kinds of browser object.

[+] Email:evans@aps.anl.gov

Figure 2 shows a browser object that we have implemented both as an ActiveX control and as a Java applet. It is a text area that includes the name of the process variable and its value as an alphanumeric string. It has properties such as its foreground and background colors, the
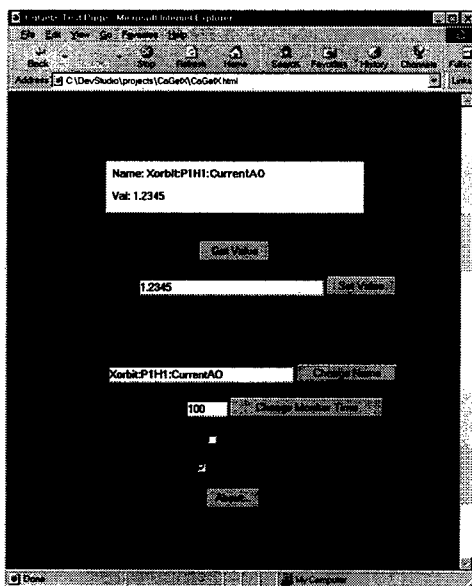
Figure 2: An ActiveX control in a Web page. The Java implementation looks just the same.

process variable name and value, whether the name shows, and whether it is monitoring. It has methods such as GetValue, PutValue, and AboutBox. It does not, but could, respond to events. Other objects, such as check boxes, in the browser page may access our object's methods and properties. For example, the text entry for the name and the push button next to it allow you to change the process variable name (and connect to the new name). The Monitor check box allows you to set it to monitor or not. This interaction between objects is something that cannot be done in MEDM. Further, you can put other sorts of browser things, like links, in the page, so there is no need for MEDM's Related Display object.

2 ACTIVEX CONTROLS

ActiveX controls are primarily useful in Windows. They work with Internet Explorer [5] but do not work with Netscape [6]. ActiveX controls are written in a language, such as C, that makes platform-dependent code and which is not safe. That is, the control can contain code that, for instance, deletes files on your computer. Internet Explorer allows you to specify whether you want to run such controls at all, have it ask before running them, or always run them without asking. The default is to not run them, but it is easily changed. These "unsafe" controls are more relevant to an Intranet than the Internet. Just like MEDM, which is also written in C and can delete files on your computer, you must trust them.

Since our controls must interact with EPICS Channel Access, which is written in C, they are written in C. Since C is a strong and well-developed language and is optimized for a particular platform, this makes them fast and efficient. Figure 2 shows a Web page handling 100 of our controls, set to have the name not show and attached to process variables that are updating at 10 Hz. The browser displaying this page is running on a 200-MHz PC that is connected over an ISDN line through a PV Gateway. The performance approaches that of MEDM. Note that the menu controls labeled "Change"
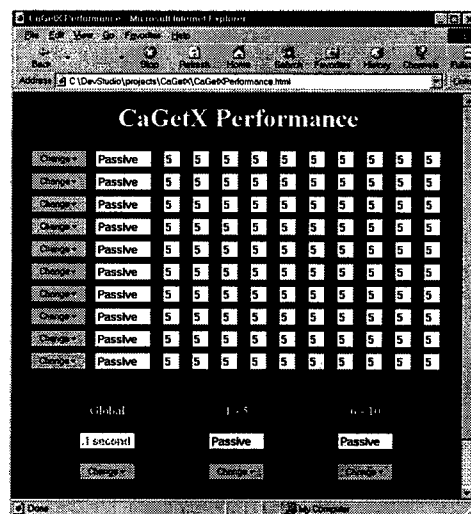
Figure 3: A Web page with 100 ActiveX controls, each updating at 10 Hz.

are ActiveX controls that come with Internet Explorer. They change the scan rate for various blocks of the page by communicating with the ActiveX controls that access the appropriate SCAN process variables (the ones mostly displaying Passive, which are overridden by the global control with the red foreground.).

3 JAVA APPLETS

One of the primary benefits of Java is that it is platform independent. Java applets work in most browsers and on most platforms, while ActiveX controls work on Windows and require Internet Explorer. It is difficult to use them on UNIX. We have made a Java applet that looks like and has the same functionality as the ActiveX one. It has the same methods and properties and works the same way. The Web page looks essentially the same.

One problem that arises is that Java security is different than ActiveX security. Java applets running in a browser have a "sandbox" in which they must operate. One of the rules is that they may not access files or sockets on your machine. This makes them safe. They are allowed to access files and sockets on the server machine, the one that served the Web page and the applet. (What the server lets its applets do is their problem and is not a security issue for you.)

A second problem is that EPICS Channel Access is written in C, not Java. Java does provide a means, JNI, for using native languages, such as C, with Java. The result is not "Pure Java," and it is not platform independent. Moreover, one of the sandbox rules is that applets cannot run JNI code on your machine. We are stuck with the facts that we must use JNI in order to use Channel Access and that we cannot use it in the applet.

Consequently, we need to serve the applet from an HTTP server and provide a Channel-Access server to talk to the control system. The arrangement is shown in Fig. 4. For ActiveX, the controls can live on the workstation

CAGetX Network Diagram   **CAJava Network Diagram**
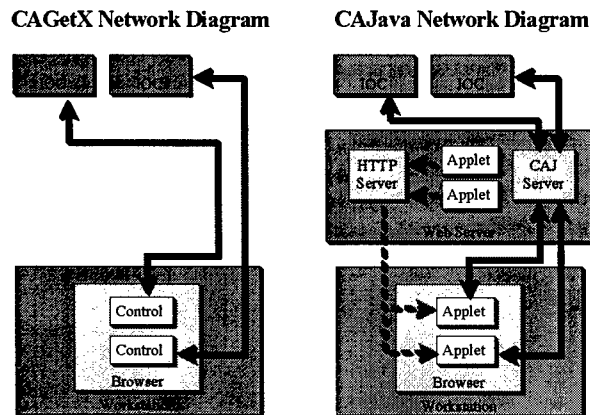
Figure 4: Diagrams showing how the ActiveX controls and Java applets each interact with the network. Owing to security considerations for Java, the Java interaction is more complicated.

and talk directly to the EPICS input/output controller (IOC). For Java, they must live on the HTTP server and talk through sockets to the Channel-Access server on the same machine as the HTTP server. The Channel-Access server then talks to the IOC. On the positive side, Java is strong in network capabilities, and it is relatively easy to write the Channel-Access server in Java and to have the applet communicate with it.

To the user in his browser, the two controls appear to operate the same – up to a point. The performance of Java is slower than that of C, and, to date, we have not found it possible to make a high-performance page, such as the one in Fig. 3, work well for Java. Less ambitious pages work fine. The primary advantage of Java is that the applets can be used in Netscape and consequently on UNIX.

It should be noted that there are means to overcome the security restrictions for Java applets in a browser. Also, you can run ActiveX controls in UNIX and in Netscape. What we have described are the restrictions when doing things the normal way.

4 AGENT APPLICATIONS

Microsoft Agent is a set of software services that supports the presentation of software agents as animated, interac-

tive personalities. It is a glorification of the Office Assistant found in Microsoft Office [7]. It will work either from a browser page or as an application. Like with the browser, most of the programming has been done for you. You just have to implement the little bit you need. Among the capabilities provided for you are voice recognition and speech synthesis. Figure 5 shows the agent, in the form of a genie, getting the value of a process variable from the control system. To get him to do this, you would say something like "Genie, get me a process variable," then enter the name in a dialog box he gives you. He
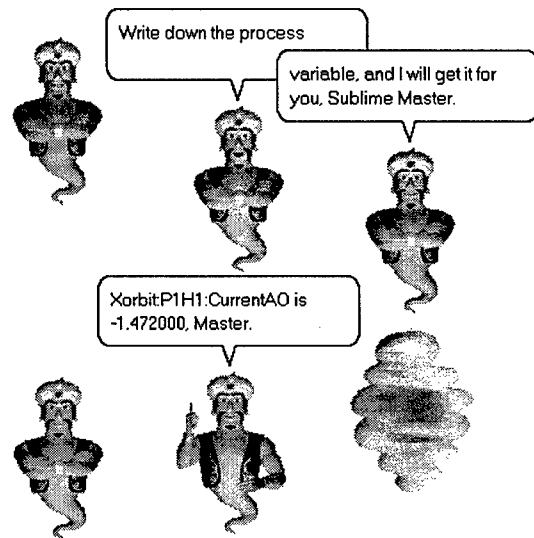
Figure 5: Agent getting a process variable.

speaks the words in the balloons as well as displaying them. (The dialog box is used because he is not yet up to recognizing the abstruse types of names typically used for process variables, though he does pretty well at pronouncing them.) We are truly at the point where we can demonstrably and feasibly converse with the control system and say things like, "Accelerator, correct the orbit," or "Telescope, move twenty degrees to the East," as fictionally happened some time ago with Hal in *2001* and happens regularly on *Star Trek*.

REFERENCES

[1] http://www.aps.anl.gov/asd/controls/epics/EpicsDocumentation/ExtensionsManuals/MEDM/MEDM.html.
[2] Paper MOP37, this conference.
[3] http://www.microsoft.com/msagent/default.asp.
[4] http://www.aps.anl.gov/asd/controls/epics/EpicsDocumentation has extensive information on all parts of EPICS.
[5] Internet Explorer is a product of Microsoft Corporation, Redmond, WA.
[6] Netscape is a product of Netscape Communications Corporation, Mountain View, CA.
[7] Microsoft Office is a product of Microsoft Corporation, Redmond, WA.

PLANS FOR A COLLABORATIVELY DEVELOPED DISTRIBUTED CONTROL SYSTEM FOR THE SPALLATION NEUTRON SOURCE[*]

W. R. DeVan, ORNL, Oak Ridge, TN; D. P. Gurd[#], LANL, Los Alamos, NM
J. Hammonds, ANL, Chicago, IL; S. A. Lewis, LBNL, Berkeley, CA
J. D. Smith, BNL, Upton, NY

Abstract

The Spallation Neutron Source (SNS) is an accelerator-based pulsed neutron source to be built in Oak Ridge, Tennessee [1]. The facility has five major sections - a "front end" consisting of a 65 kev H ion source followed by a 2.5 MeV RFQ; a 1 GeV linac; a storage ring; a 1MW spallation neutron target (upgradeable to 2 MW); the conventional facilities to support these machines and a suite of neutron scattering instruments to exploit them. These components will be designed and implemented by five collaborating institutions: Lawrence Berkeley National Laboratory (Front End), Los Alamos National Laboratory (Linac); Brookhaven National Laboratory (Storage Ring); Argonne National Laboratory (Instruments); and Oak Ridge National Laboratory (Neutron Source and Conventional Facilities). It is proposed to implement a fully integrated control system for all aspects of this complex. The system will be developed collaboratively, with some degree of local autonomy for distributed systems, but centralized accountability. Technical integration will be based upon the widely-used EPICS control system toolkit, and a complete set of hardware and software standards. The scope of the integrated control system includes site-wide timing and synchronization, networking and machine protection. This paper discusses the technical and organisational issues of planning a large control system to be developed collaboratively at five different institutions, the approaches being taken to address those issues, as well as some of the particular technical challenges for the SNS control system.

1 INTRODUCTION – WHAT IS SNS?

The Spallation Neutron Source (SNS) will be a 1 MW (upgradeable to 2 MW and eventually 4MW) accelerator-based facility that produces pulsed beams of neutrons by bombarding a liquid mercury target with intense beams of 1 GeV protons. It is being designed primarily to meet the needs of the neutron scattering community, with operations expected to begin in 2005. Some reference design parameters are given in Table 1.

(At the time of this conference, the original concept – a 1GeV linac followed by an accumulator ring – is under review. Alternative concepts, including less than full energy injection into a rapid cycling synchrotron, and/or starting at 2MW with a solid target, are under consideration. This paper assumes the original concept. Should a change take place the control system requirements and configuration would be unchanged except for details, and the issues of collaborative management discussed in this paper unaffected. The collaborative nature of the project and its siting at Oak Ridge are not under review.)

Table 1 – Design Parameters

REFERENCE DESIGN PARAMETER	INITIAL (1.0MW)	UPGRADE (2.0MW)
Pulse repetition rate	60 Hz	
Peak ion source H-current	35 mA	70 mA
Linac length	493 m	
Linac duty factor	6.2%	
Linac final beam energy	1.0 GeV	
Accumulator ring circumf.	220.7 m	
Ring orbit rotation time	841 ns	
Pulse length at ring injection	546 ns	
Kicker gap at ring injection	295 ns	
Ring filling fraction	65%	
Number of injected turns	1225	
Ring filling time	1.02 ms	
Protons per pulse on target	1.04×10^{14}	2.08×10^{14}
Protons per second on target	6.3×10^{15}	1.25×10^{16}
Time avg. beam current	1.0 mA	2.0 mA
Beam power on target	1.0 MW	2.0 MW

The SNS is a truly collaborative project, with the participating laboratories taking lead roles and responsibilities for specific sections of the complete facility. Laboratories were chosen on the basis of their expertise in particular technology areas. The lead laboratory for a given section is responsible for assembling all necessary resources to accomplish not only

the design but also the fabrication, testing, installation, and commissioning of its part of the SNS at the Oak Ridge site. Specific roles and responsibilities are as follows:

- ORNL is responsible for overall project management and co-ordination; for conventional facilities and construction; for maintaining and operating the SNS once completed; and for managing future upgrades.
- LBNL is responsible for the front end systems, including ion source and RFQ.
- LANL is responsible for the linac systems and has co-ordination responsibility for the controls design.
- BNL is responsible for the accumulator ring and associated transport lines.
- ORNL is responsible for the primary target system.
- ORNL and ANL are jointly responsible for the experimental systems (instruments, beamlines, choppers, etc.).

"Collaboration" is indeed the watchword of the SNS Project. This is true especially for the controls team, which is itself spread among the five collaborating laboratories. Even more than usual attention to organisation, integration and standardisation are required in this collaborative environment, and these are discussed in the sections that follow.

SNS is not the first collaborative effort of this nature. It is common in high energy physics for both the data acquisition and the detector "slow-controls" software to be developed collaboratively. In these cases the collaborators are generally more numerous and more geographically distributed. The difficulties are exacerbated, and yet these enterprises are generally successful. In data acquisition systems, however, a centralised team generally develops the real-time software. The peer relationship of the SNS control system collaborators is perhaps also an innovation.

2 ORGANIZATION

To facilitate the imposition of standards and overall system integration, the SNS has opted to unify the entire controls effort under one "level two" WBS element (Figure 1). This uncommon organization is a change from the original concept, in which the controls effort was distributed throughout the WBS structure, and was adopted at least in part in response to the recommendation of review committees.

The organization is a compromise, and was agreed to only after discussion among team leaders from all of the collaborating institutions. Potential disadvantages include:

- "Loss of ownership" of controls requirements by sub-project managers ("Not my problem");

- Difficulty in integration of controls activities into sub-project schedules;
- Disconnect between requirements changes effecting controls and resulting cost escalation of the controls element ("scope creep"); and
- A very complicated cost and schedule variance reporting system which must integrate the different systems in place at each collaborating laboratory.

Notwithstanding this impressive list of negatives, the integrated organization was preferred because of anticipated benefits in ease of integration and standards imposition, and the potential for resulting cost savings, during both construction and operation.

An attempt to mitigate the potential problems itemised above was made by organising the integrated controls effort to reflect the organization of the project as a whole, with a third level WBS element for each of the major distributed and subsystem-specific control systems. These distributed parts of the control system include I/O hardware, local databases, interlocks, automation and engineering screens, and subproject-specific high-level (physics) applications. The schedules for the distributed parts are integrated with the corresponding sub-project schedules, assuring requirements and schedule integration. Work at this level will be done at the collaborating laboratory, although common tasks, such as some device drivers, will be assigned wherever the appropriate resource is available.

"Global Systems" apply across the project. They include the network, timing system, equipment protection system and main control room, and are treated together as another level 3 WBS element. Work on these systems will be allocated among the collaborators. For example, the control system communication network will be implemented by the Oak Ridge members of the controls team.

All of the controls activity is co-ordinated by an "Integrated Controls Working Group," (ICWG) which includes each of the level 3 task leaders. This group meets weekly by telephone and regularly together, as well as using computer-based collaboration tools.

Money is allocated to the Level 2 controls task leader, and then, after consultation with the working group, sub-allocated among the laboratories according to agreed work packages. Some part of the controls allocation is withheld at Oak Ridge, which greatly facilitates reallocation as required. An intriguing and initially unappreciated benefit of this approach is flexibility to make purchases through the laboratory that can make the best deal, without moving money between laboratories and incurring additional taxes.
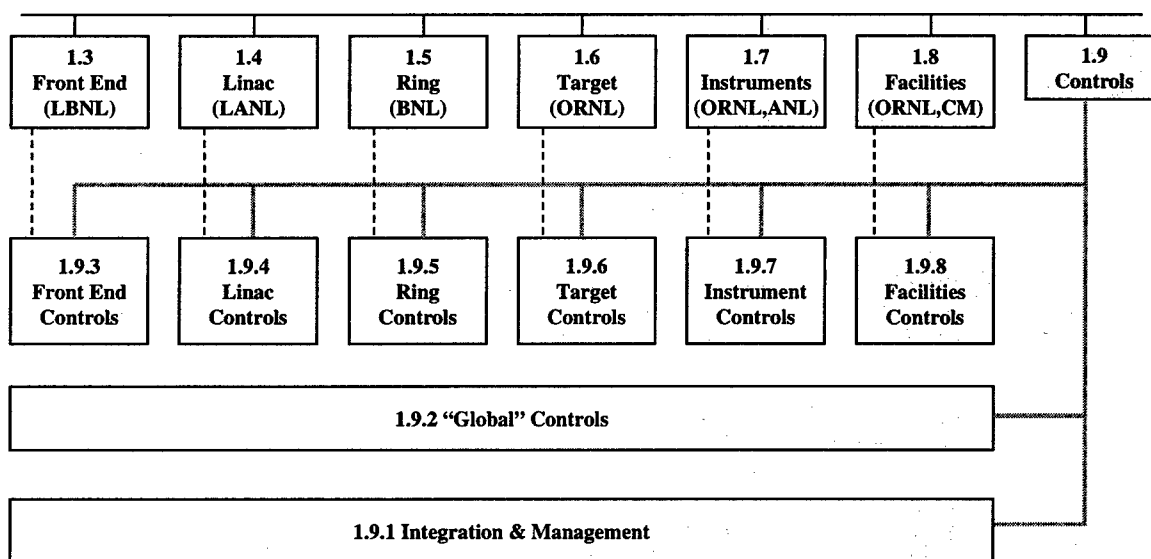
Figure 1. SNS Work Breakdown Structure Showing Controls WBS Level 3 Elements

3 INTEGRATION

3.1 Integration

The SNS control system will be completely integrated. That is, a single infrastructure and set of standards will be applied to all aspects of the facility. This approach is not entirely obvious. It is not the usual practice in accelerator laboratories to include target, experimental instruments or conventional facilities (power systems, plant cooling systems, HVAC, etc) in the accelerator control system infrastructure. It has, however, been a common experience that signals from these non-accelerator systems are found to be needed in the control room for purposes of correlation, and that ad-hoc integration is performed after operation begins. We plan to integrate these systems from the outset. EPICS (see section 4.1below) will serve as the integrating layer, making the specifics of local control systems transparent. Except for the imposition of standards, local process systems need not be conceptually different from familiar practice.

3.2 Interface

The "default" interface to the control system is defined to be at the input to a crate-based system (Figure 2). The transducer or measuring instrument itself belongs to the system it is in, as does the cabling from the instrument to the I/O module front panel. Standards will be established for the signals presented to these modules. This interface definition can be modified by negotiation on a case-by-case basis. Exceptions already established are in the beam instrumentation and low-level RF systems, where sophisticated and custom I/O modules will be developed

and packaged in specialised form-factors such as VXI. The interface is then at the crate backplane.

Notwithstanding the existence of this default interface, a series of detailed interface definition documents will be developed to delineate between subsystem and global functions, and to assure a seamless interface between parts of the control system executed by different institutions.
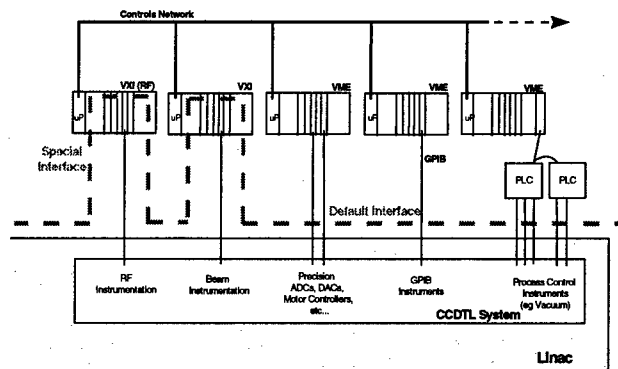
Figure 2 – Interface to SNS Control System

3.3 Project Database

SNS intends to follow the recent successful examples at BESSY and KEKB of a comprehensive project-wide relational database from which (among other things) the EPICS distributed database can be automatically produced. Oracle will be used for this purpose. Following the BESSY example, project engineers will be responsible for maintaining the data for their own subsystems.

The database will be based upon a consistent, hierarchical, plant-wide naming convention that has been in place for over a year. From the point of view of the operators or of the control system, the naming convention

provides standard names for devices and signals. These names should also be used for all aspects of the project, such as models, mechanical drawings, equipment databases, cable plant databases, etc.

As now defined, the complete formal signal names may in some cases exceed the present string length limitation in EPICS. Because we do not believe that a software limitation should constrain names developed for operational convenience, this constraint will be removed from EPICS.

3.4 Application Development Environment

The SNS controls team has installed and is now operating a distributed Concurrent Version System (CVS) at Oak Ridge. This system assures a uniform software development environment for all five laboratories, as well as release control through the overlapping phases of software development, integration and operation.

Running on that system will be an Application Development Environment (ADE) developed together with the controls groups at the APS at Argonne and BESSY in Berlin, and benefiting from experience at TJNAF in Virginia. The ADE defines the file structures and procedures for software development and integration for all of the SNS laboratories. APS will adopt the same environment.

4 STANDARDS

4.1 EPICS

The recognised need for an open system standard, and the general acceptance and track record of EPICS in the accelerator community (and beyond [2]), resulted in an early and easy agreement to use the EPICS toolkit [3] as the basis for the SNS control system. This decision was reached with strong support from project management, review committees and all participating laboratories, including those having little or no EPICS experience. It represents an important first step in the attainment of an integrated control system, and was reached early enough to allow time to prepare standards and examine remaining integration issues.

Because neither ORNL nor BNL had experience with EPICS, an early activity was to do on site training at these laboratories. Local test stations were then set up, and at this time there are active groups implementing EPICS applications at all five collaborating laboratories.

4.2 Software Standards

The selection of EPICS is far from a complete definition of required software. Within the EPICS toolkit there are a number of choices to be made, and EPICS in any case does not include any of the high-level applications required for accelerator commissioning and operation. In the interest of uniform software development across the

collaboration, the ICWG has undertaken to make a number of these choices before the end of the year, although in many cases it is neither necessary nor desirable to do so prematurely.

- Operator Interface. There are two EPICS tools for screen development and display – MEDM and EDD/DM. MEDM comes in two flavors – European and American. The community is developing new tools, based, for example, on JAVA. Commercial tools are also available. SNS is currently experimenting with both flavors of MEDM and with JAVA. A common approach will be selected.

- Archiver. Several EPICS Archivers have been developed. A new archiver is currently under operational test for LEDA. If satisfactory, this will form the basis of the SNS data archiver.

- Alarm Manager. This is a case where the EPICS community all uses the same tool. SNS will do the same.

- Database Configuration. Several tools are available for building the EPICS active distributed configuration database. As mentioned already, SNS expects to follow the model of both BESSY and KEKB, using the graphical tool "Capfast" to design database templates, and then to populate and instantiate the database from an Oracle-based project-wide configuration database.

- Applications. EPICS has been interfaced to a number of commercial mathematical packages, such as Mathematica, MatLab, PVWave and IDL. SDDS, a specialised package for accelerator physics, is in use at the APS. SAD, a combined physics modelling and mathematical package, is being used with EPICS to commission KEKB. SNS will use a subset of these tools, and is also experimenting with the "Unified Accelerator Library" now in use at RHIC.

- Client and Development Systems. Developments to date have been done under Solaris, however the collaboration anticipates adopting LINUX in the near future.

4.3 Hardware Standards

In addition to an attempt to use common software, SNS will try to standardise hardware choices in the distributed systems to the extent that that is reasonable. Given the duration of the project, we recognise that time-phased standards may in some cases be more cost effective. Candidates for standardisation include: distributed processors, preferred I/O modules, fieldbuses, interface standards, PLCs, isolation standards and a uniform device and signal naming standard.

- I/O Controllers (IOCs). Most implementations of EPICS use VME or VXI crates to house I/O processors and modules. LEDA has experimented successfully with PC-based IOCs, which are much cheaper to field. Newer backplane systems are now

available. SNS expects to use a traditional approach, although PC-based IOCs are also likely.

- **I/O Processors.** It is probably unwise to settle on one processor at this time – the market changes rapidly. Early IOCs will use the PowerPC, already applied in the EPICS community. We are using these in test stand applications at BNL.
- **PLCs.** Because of the inclusion of conventional facilities, there will be many PLC-based systems interfaced to EPICS. Although we recognise that compromises are inevitable, SNS intends to identify preferred PLC manufacturers, models, programming languages and interface mechanisms. Tests are taking place at BNL, LBNL, and ORNL.
- **Fieldbuses.** A number of multidrop systems have been used with EPICS for interfacing power supplies, vacuum equipment, etc. These include Canbus (BESSY), Bitnet (APS), Arcnet (KEKB) and others. SNS is currently evaluating these and other possibilities (DeviceNet, ControlNet, G3, etc) for appropriate applications. SNS will attempt to standardise on all vacuum and power supply equipment (pumps, gauges, etc) which will facilitate the controls task. The LBNL front end test stand is experimenting with some of these.

5 GLOBAL SYSTEMS

Work on the "global systems" will be distributed among the collaborating laboratories, based upon expertise and available resources.

5.1 Timing System

The most interesting and time-critical technical issue facing the SNS controls team has to do with timing and synchronization. The entire accelerator chain, including accelerating structures, choppers and bunchers, injection and extraction kickers and data acquisition systems must be synchronized with each other and with a large number of independently-phased neutron choppers. These choppers, a key element in all of the neutron scattering experiments, are rapidly rotating (thousands of rpm) slotted flywheels, which are used to select neutrons of a specific energy from the spectrum emitted by the target. Where there is a single chopper, protons can be extracted based upon a signal from that chopper. Where there are several choppers, the question becomes: "who is the boss?". The solution to this issue affects both the rf low-level and power systems, as well as the timing and synchronization system.

This system will be modelled upon systems with similar requirements at RHIC, PSR, ISIS or the IPNS.

5.2 Equipment Protection Systems

Equipment Protection systems include:

- a hardware-based "fast protect" system which turns off the injector and dumps any beam in the machine within 10usecs of sensing an anomalous condition (typically high radiation);
- a hardware-based "beam pulse enable system" which permits injection pulse-by-pulse provided that all systems, including kickers, are ready; and
- A software-based "run permit" system which compares the accelerator state with the operator-selected running mode before permitting beam injection.

These systems are all independent of the personnel safety systems, which are both physically and organisationally separate from the control system.

5.3 Network

A preliminary SNS control system network design is based upon 100 Mbit switched Ethernet with a Gigabit switched Ethernet backbone.

5.4 Control Room

All systems – accelerators, target and conventional facilities --will be operated and monitored from a single control room, although there will be local control rooms available for commissioning and troubleshooting. It is anticipated that the main control room will be modelled after the APS main control room, which features a functional round console arrangement.

6 CONCLUSIONS

A collaboration of five national laboratories is proposing to construct a 1 MW (upgradable) accelerator-based pulsed spallation neutron source (SNS) in Oak Ridge, Tennessee. To facilitate integration and standardization, the control system is treated as a peer to the other major project subsystems (linac, ring, target etc). The control system will be integrated over the entire facility, including the conventional facilities, and will be based upon the widely used EPICS toolkit.

7 REFERENCES

1. Alonso, these proceedings
2. In the past year, for example, a number of new facilities have come on line using EPICS. These include, among others: LEDA – the Low Energy Demonstration Accelerator at Los Alamos, NM; NSTX – the National Sperical Toroid Experiment at Princeton, NJ; ISAC – a radioactive beam facility at TRIUMF, Vancouver, Canada; The Swiss Light Source (SLS) Test Stand at the Paul Scherrer Institute in Villigen, Switzerland; and the Gemini North Observatory on Mauna Kea, Hawaii.
3. http://epics.aps.anl.gov/asd/controls/epics/EpicsDocumentation/WWWPages/EpicsFrames.html

An Advanced Electromagnetic Eigenmode Solver
for Vacuum Electronics Devices - CTLSS *

S.J. Cooke, B.Levush, NRL, DC;
A.A. Mondelli, J.J. Petillo, D.P. Chernin, C. Kostas, M. Czarnaski, SAIC, McLean, VA;
E. Nelson, LANL, NM; T.M. Antonsen, Jr., U. Maryland, MD.

Abstract

The Cold-Test and Large-Signal Simulation code (CTLSS), a design tool for vacuum electronics devices, is presented. The prototype tool is a three-dimensional, frequency-domain cold-test code that operates on a rectangular structured grid. It uses a generalisation [1] of the Jacobi-Davidson algorithm [2] that has proven effective in solving for eigenmodes in problems having sharp-edged structures with materials having large dielectric constants and loss tangents as high as 100%. We present the CTLSS algorithm and code features that are useful for vacuum electronics design. Analysis of both closed cavities and periodic slow-wave structures are given. Tests indicate that the CTLSS algorithm can determine mode frequencies to well below 0.1% accuracy for all modes computed. A new formulation has been implemented to compute the complex axial wavenumber, k_z, in a periodic waveguide, as the eigenvalue for a specified real frequency, and test results will be presented. This code is being extended to include an unstructured mesh for the conformal representation of structures using high order elements [3].

1 INTRODUCTION

CTLSS provides fully 3-dimensional eigenmode analysis of complex electromagnetic structures, in particular where strongly absorbing dielectric materials are present. This requirement arises in the design of some vacuum electronic components and devices, and in wider fields where control of mode structure and attenuation in waveguides and cavities is important. Our implementation of the Jacobi-Davidson algorithm for determining the eigenfrequencies underlies the ability to handle lossy systems, and previous tests [1, 4] have indicated that material losses as large as $\tan \delta = 1$ are permissible. We summarise here the algorithms used by CTLSS, and describe recent developments.

2 ELECTROMAGNETIC MODEL

We use the following field eigenvalue equation, derived directly from Maxwell's equations for oscillatory fields,

$$\left\{ \operatorname{curl} \mu^{-1} \operatorname{curl} - \omega_n^2 \, \epsilon \right\} \vec{E}_n = 0 \qquad (1)$$

The solutions of this equation includes infinitely-degenerate, zero-frequency solutions having electric field

eigenvectors that may be expressed as the gradient of an arbitrary scalar field. These solutions have proved problematic historically, and care must be taken to ensure that they remain completely decoupled from the desired solutions. The discretisation process that we use is derived so as to ensure that the corresponding eigenvalues of the discretised problem remain exactly zero.

2.1 Structured grid cold-test model

The present implementation of CTLSS uses a structured orthogonal grid to optimise the matrix computation, since it is the time spent computing the action of the operator on a field vector that dominates the computation. We use the method of contour-path integration to discretise the continuum field equations in local cell-coordinates, for which it corresponds to the Yee formulation. This method permits us to use non-uniform grids in arbitrary orthogonal coordinate systems to best match the geometry being modelled.

2.2 Non-Hermitian matrices

When all materials are lossless, the matrices that result are Hermitian for any phase advance of a periodic system, and therefore the eigenfrequencies are real-valued and the eigenfields are orthogonal. However, if absorbing materials exist in the computational domain, represented by complex values of the material constants, ϵ and μ, then the matrix equations are non-Hermitian. The eigenvectors are not orthogonal and the eigenfrequencies are complex-valued. For the particular cases of 0° or 180° phase advance, or if the system is a closed cavity, the matrices are complex-symmetric. However, if arbitrary phase-advance boundary conditions are specified, then the matrices have no explicit symmetry. In any case, methods of solution that can handle non-Hermitian systems are necessary. We have adapted the Jacobi-Davidson algorithm to solve for the eigenfrequency solutions of problems of this type.

3 JACOBI-DAVIDSON ALGORITHM

In outline, the Jacobi-Davidson method is an iterative subspace method, in which the large matrix problem to be solved is projected onto smaller subspaces to obtain estimated eigensolutions at each iteration. The subspaces are extended by applying an orthogonal correction procedure to selected eigensolution estimates. The correction vectors are used to *extend* the subspaces, to promote an improved
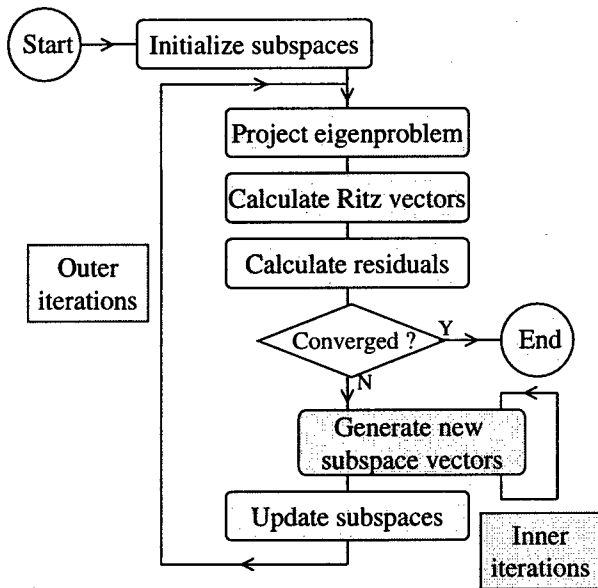
Figure 1: Jacobi-Davidson algorithm

Figure 2: Helix-waveguide dispersion and coupling impedance data, compared with experimental data and with calculations using the ARGUS code

solution estimate at the next iteration.. Typically, this procedure is restarted after some fixed number of iterations to limit the maximum subspace size that must be stored. After a number of iterations, the subspace is contracted to include only a few of the solution estimates that lie closest to the desired eigensolutions, and the process of subspace expansion recommences. In place of this approach, we employ a strategy in which eigenvectors associated with the eigenvalue estimates furthest from a target eigenvalue are removed from the subspaces at each iteration and replaced with the update vectors derived from the closest estimates. This maximises the retention of information in the subspace that can contribute to the convergence of the algorithm.

We may choose a target frequency in the centre of our frequency band of interest, and are therefore not limited to finding the lowest frequency eigensolutions. This enables us to exclude all of the zero-frequency eigensolutions from the computation, and also to find just a few selected solutions from within a complex spectrum.

Figure 1 summarises the iterative procedure implemented by the Jacobi-Davidson algorithm. The large eigenproblem is projected onto a pair of subspaces (represented by small sets of orthogonal vectors), and the resulting reduced eigenproblem is solved for eigenvalue and eigenvector estimates. The Ritz vectors are these vectors projected back into the full solution space, and the residual error vectors characterise the deviation of the Ritz vectors from true solutions of the full eigenproblem. The vector subspace corrections are derived from the residuals associated with solutions closest to a target frequency, using an orthogonal correction step [2]. This step requires an approximate solution of a linear system of equations, and may be implemented as a few iterations of an iterative procedure, for which we use the quasi-minimal residual (QMR)
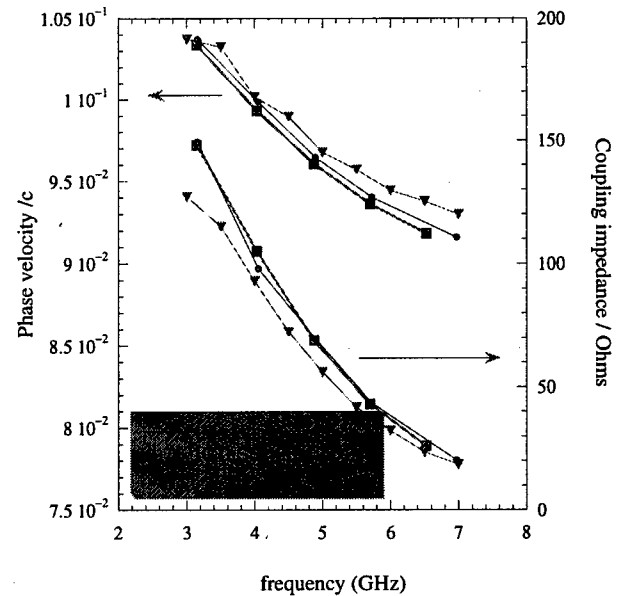
method [5]. The correction vectors then replace the unwanted Ritz vectors in the subspaces, and the procedure is repeated until convergence is obtained.

For systems that are not Hermitian, the left and right eigenvectors corresponding to an eigenvalue will in general not be equal, and separate subspaces should in principle be maintained and updated. For complex-symmetric matrices, the left-hand subspace may be taken as the complex conjugate of the right-hand subspace, and the symmetry is maintined throughout the calculation to reduce the associated memory requirement. For fully non-symmetric matrices, it is still possible for this type of problem to use a single subspace, but it is necessary to use a non-symmetric iterative solver for the linear system. The transpose-free variant of the QMR routine (TFQMR) was found to be ideal for this purpose.

Figure 2 shows the results of a calculation modelling a single period of a helix-waveguide structure in which a helical wire is supported by dielectric vanes inside a cylindrical waveguide to create a slow-wave structure. The calculation using CTLSS of the dispersion of the phase velocity, ω/k_z, of this system is shown in comparison with experimental values, provided by Northrop-Grumman, and with a similar calculation using the ARGUS code. The second set of curves shows the coupling impedance parameter derived from the lowest frequency eigenfield solution.

4 DRIVEN FREQUENCY ALGORITHM

An alternative formulation has been implemented to determine the eigenmodes of a waveguide. Instead of finding the eigenfrequencies for known values of k_z, it is useful when losses are present to find instead the complex valued $k_z(\omega)$

at given real frequencies.

In this method, we excite the waveguide with a trial source current $\vec{J}(\omega, k_z) \propto \exp(ik_z z)$ representing the charged particle beam with a fixed interaction frequency and spatial variation. We can solve directly for the electric field distribution in the waveguide by discretising the equation

$$\left\{ \operatorname{curl} \mu^{-1} \operatorname{curl} - \omega^2 \, \epsilon \right\} \vec{E} = i\omega \vec{J} \qquad (2)$$

and using QMR to solve for the field $\vec{E}$. From this solution, we define an impedance function in terms of the fields, for total beam current I,

$$Z(\omega, k_z) = \frac{1}{I^2} \int dx^3 \, \vec{J}^* \cdot \vec{E} \qquad (3)$$

This function has a pole when k_z approaches the resonance eigenvalue, k_z^*, according to

$$Z(\omega, k_z) = \frac{N}{k_z - k_z^*} + C + O(k_z - k_z^*) \qquad (4)$$

A search over k_z for the roots of Z^{-1} therefore provides the eigenwavevector solution. In addition, the coupling impedance may be derived from the value of N, while the value of the constant C characterises the coupling to the space-charge field. These parameters may be determined by evaluating Z close to the resonance, and passed to a large-signal code for a full non-linear analysis of the particle/wave interaction. This method offers an alternative means of solving the eigenwave problem that could offer a speed advantage over the standard matrix eigenmode analysis for this type of problem.

Figure 3 shows the function Z^{-1} evaluated for a range of phase-advance angles across each period, $\theta = k_z L$. It is clear that the function is smoothly varying, and therefore amenable to automated root-finding. The lower graph shows dispersion data $\omega(k_z)$ calculated using the Jacobi-Davidson method. The roots of Z^{-1} above correspond to the propagating modes at the frequencies chosen.

5 LARGE-SIGNAL MODEL

The 3-D eigensolver module of CTLSS has been linked to the non-linear parametric simulation code CHRISTINE [6]. Using a 1-dimensional parametric model ideal for rapid design optimisation, this code calculates the non-linear interaction between a travelling electromagnetic wave and a beam of electrons that is the basis for wave amplification in a class of vacuum electronic devices. From the optimum 1-D solution, a trial structure is generated automatically for full 3-D analysis using CTLSS that may be adjusted to obtain the realistic travelling wave dispersion and coupling impedance characteristics closest to the design values. These values may be fed back to the non-linear code to predict the actual device efficiency and complete an cycle of the design procedure. This methodology provides a means to predict the true non-linear characteristics of a complex 3-dimensional device. This application of the CTLSS code is presently being tested.
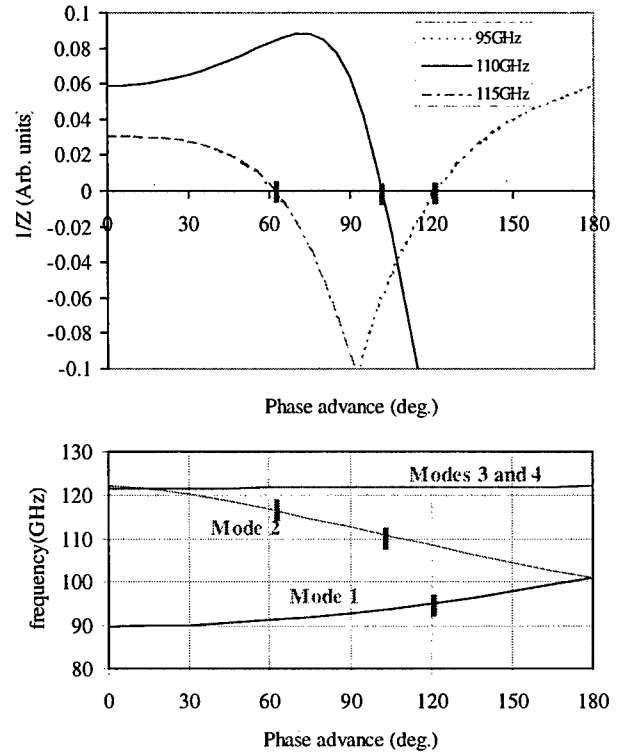
Figure 3: Correspondence between the eigenmode dispersion solution and the poles of the driven frequency impedance function for a coupled-cavity waveguide

6 CONCLUSION

The CTLSS code has been demonstrated as a useful design tool in the simulation of complex electromagnetic structures for applications in particle beam devices.

7 REFERENCES

[1] S.J. Cooke and B. Levush, "Eigenmodes of Microwave Cavities Containing High-Loss Dielectric Materials" Proc. 1997 Part. Accel. Conf. (Vancouver, BC, 1997).

[2] G.L.G. Sleijpen and H.A. van der Vorst, , "A Jacobi-Davidson Iteration Method for Linear Eigenvalue Problems," SIAM J. Matrix Anal. 17, 401-425 (1996).

[3] E.M. Nelson, AIP Conf. Proceedings 391: Computational Accelerator Physics, p77 (1996)

[4] S.J. Cooke and B. Levush, "Eigenmode solution of 2-D and 3-D electromagnetic cavities containing absorbing materials using the Jacobi-Davidson algorithm." Submitted to J. Comput. Phys.

[5] R. W. Freund and N.M. Nachtigal, "An implementation of the QMR method based on coupled 2-term recurrences," SIAM J. Sci. Comput., vol. 15, no. 2, pp. 313–337, 1994.

[6] T.M. Antonsen, Jr. and B. Levush, "CHRISTINE: A Multi-frequency Parametric Simulation Code for Traveling Wave Tube Amplifiers," NRL Memo Report NRL/FR/6840–97–9845 (1997).

COMPUTATION OF NONLINEAR ONE-TURN MAPS FROM MEASUREMENT WITH MODEL-INDEPENDENT ANALYSIS *

Chun-xi Wang, John Irwin, Yiton T. Yan
Stanford Linear Accelerator Center, ms 26, P.O. Box 4349, Stanford, CA 94309

Abstract

It is desirable to determine the nonlinear transformation maps, especially the one-turn map, of a storage ring from measured BPM data for nonlinear analysis in order to improve the machine performance. However, the accuracy of detecting the weak signals from nonlinear effects is often limited by the available BPM resolution. With the recent development of Model-Independent Analysis methods, which can significantly reduce BPM random noise via statistical analysis, it is possible to more accurately determine the nonlinear maps from measured data by using a large number of BPMs. Computational techniques and some simulation results for PEP-II will be presented.

1 INTRODUCTION

Although the map approach is very successful in single particle beam dynamics studies and dominates modern beam optics design tools, it is rarely used for beam diagnosis and control. In order to diagnose and improve beam dynamics in a ring, various techniques are used to measure the global properties such as chromaticity and tune-shift-with-amplitude, which can also be extracted from a nonlinear one-turn map if measured. In reference [1] we argued the possibility to measure a nonlinear one-turn map with good accuracy, provided that the BPM resolution is sufficiently high. However, the required resolution is often not available.

Recently we developed Model-Independent Analysis (MIA) methods to study beam dynamics[2, 3]. One important achievement of MIA is the capability to significantly reduce random noise of individual BPM readings via statistical analysis of an ensemble of BPM readings of a large number of pulses at a large number of BPMs. Therefore MIA can facilitate/accomodate nonlinear map measurements. This paper will explore this possibility. We will first discuss how to apply MIA to nonlinear map measurements in general, then present some simulation results for the PEP-II high energy ring.

2 MAP COEFFICIENTS AS PHYSICAL BASIS OF MIA

The single particle beam dynamics can be represented by the transformation map $\mathcal{M}_{a\to b}$ that maps any initial phase space point X^a at location a to a phase space point X^b at location b. Using a Taylor map representation, $\mathcal{M}_{a\to b}$ may

be written as

$$X_k^b = C_k^b + R_{kl}^{a\to b} X_l^a + T_{klm}^{a\to b} X_l^a X_m^a + \qquad (1)$$
$$U_{klmp}^{a\to b} X_l^a X_m^a X_p^a + V_{klmpq}^{a\to b} X_l^a X_m^a X_p^a X_q^a + \cdots$$

where the summation convention on the repeated indices is assumed. X_k is the k-th component of a phase space vector. C_k^b is the zero-order term of the k-th component and should vanish if the closed orbit is chosen as a reference. $R^{a\to b}$, $T^{a\to b}$, $U^{a\to b}$, and $V^{a\to b}$ are the usual TRANSPORT notations for the 1st, 2nd, 3rd, and 4th order map coefficients.

Now consider BPM readings for P pulses/turns at M locations b_1, b_2, $\cdots$, b_M in a ring, obviously we can cast the BPM-reading matrix B for the horizontal plane into a physical base decomposition via Eq.(1),[2, 3]

$$B = QF^T \qquad (2)$$

where F consists of all coefficients in the x components of the maps as the physical basis (see Fig.2) and Q contains the corresponding initial conditions, such as

$$F = \begin{bmatrix} C_1^{b_1} & R_{11}^{a\to b_1} & R_{12}^{a\to b_1} & \cdots & T_{111}^{a\to b_1} & \cdots \\ C_1^{b_2} & R_{11}^{a\to b_2} & R_{12}^{a\to b_2} & \cdots & T_{111}^{a\to b_2} & \cdots \\ \vdots & \vdots & \vdots & & \vdots & \\ C_1^{b_M} & R_{11}^{a\to b_M} & R_{12}^{a\to b_M} & \cdots & T_{111}^{a\to b_M} & \cdots \end{bmatrix}$$

and

$$Q = \begin{bmatrix} 1 & x_1^a & p_{x_1}^a & \cdots & (x_1^a)^2 & \cdots \\ 1 & x_2^a & p_{x_2}^a & \cdots & (x_2^a)^2 & \cdots \\ \vdots & \vdots & \vdots & & \vdots & \\ 1 & x_P^a & p_{x_P}^a & \cdots & (x_P^a)^2 & \cdots \end{bmatrix}.$$

Now the constant terms C_1^b's may contain BPM offsets also. The best way to take out such terms is to use the measured closed orbit as the reference and use the difference orbits to construct B. It is better not to use the average orbit as the reference because the high order terms may not average to zero and yield significant errors, when the beam is excited to large amplitudes, which is necessary in order to measure the high order map coefficients. On the other hand, it is possible to get a very accurate closed orbit in a ring by averaging over a large number of turns of the unperturbed beam.

Similarly one can construct a physical base decomposition for the vertical BPM readings with the y components of the maps. However, to get the x' and y' components of the maps, such information at each BPM is required. Note that the Q matrix is the same for all components. In

fact, one can stack the BPM readings for both planes into one matrix and extend the physical base decomposition to cover both planes. However, the benefits of doing so are still not clear.

One particularly interesting nonlinear map is the one-turn map of a ring. To accommodate this into Eq.(2), F should contain the one-turn map coefficients and B should contain the measured phase-space variables one-turn after the initial values used in Q. Reference [1] has a concrete example. Note that in this case, F does not contain any BPM patterns as in the usual MIA application. However, the Q matrix is still the same.

Standard least-squares fitting can be used to solve Eq.(2) for the map coefficients. The difficulty is to get a sufficiently accurate B and Q.

3 PHASE-SPACE MEASUREMENT AND SVD NOISE REDUCTION

To measure the weak nonlinearity in phase-space dynamics of a ring, the background has to be sufficiently clean. MIA provides a nice way to check this requirement. First obtain a BPM-reading matrix $B_{P \times M}$ by recording a large number (e.g. $P = 5000$) of turn-by-turn data at all available BPMs (e.g. $M = 150$) with the stored beam unperturbed. Then check the singular value spectrum of B. Ideally it should contain only the BPM noise floor since all physical motions should be well damped. Very noisy BPMs can be easily identified at this stage. Any other significant modes indicate systematic BPM errors and/or physical sources exciting the beam. Such problems need to be fixed in order to pursue nonlinear map measurements. We assume the singular value spectrum is clean. We will take the average orbit as the reference orbit and identify the noise level for later use.

Now measure another BPM-reading matrix with large (e.g. 8σ) betatron oscillations excited by fast kickers for example. Subtract the mentioned reference orbit from each measured orbit in order to get rid of BPM offsets and define the expansion points of the measured maps. At this stage, two MIA procedures can be employed to improve the phase-space dynamics measurement: SVD noise reduction and degrees-of-freedom analysis.

To reduce the random noise, compute a Singular Value Decomposition (SVD) as $B = USV^T$, identify the noise floor or use the noise level mentioned above, set the corresponding noise singular values to zeroes, and then re-multiply these matrices to construct a noise-cut matrix $\underline{B}$. This simple procedure can reduce the BPM random noise by a factor of $\sqrt{\frac{d}{M}}$, where d is the number of remaining singular values above the noise floor. Depending on the situation, such noise reduction could be rather significant, especially when the BPM resolution is poor and one is struggling to measure a few leading nonlinear coefficients.

The degrees-of-freedom analysis could help to locate the best linear section in the ring for phase-space variable mea-

surements. Then two BPMs in each plane are used to determine the initial conditions using the noise-cut data. In principle, one can use the orthogonal linear modes as the phase-space variables. However, it is probably better to use the model of the mentioned linear section to define the phase-space variables from orbit measurements. Note that even if the linear machine model might not be sufficiently accurate, it will not affect the sensitivity of nonlinear map measurement.

4 SIMULATION FOR PEP-II

Simulations for PEP-II high energy ring have been carried out to investigate the feasibility of nonlinear map measurements. 5000 turn data at all BPMs (147 for each plane) were generated by tracking 200 turns of 25 randomly chosen x and y initial conditions (no energy change) within 10σ ranges. In addition, various levels of random noise were added in order to test the sensitivity of map measurements and the effects of noise reduction described in section 3. BPM resolutions are randomly selected from the specified ranges.

Fig.1 shows the singular value spectra of the simulated system. Linear coupling and nonlinear modes are orders of magnitude weaker than the two dominant betatron modes—the reason nonlinear map measurements is challenging. The main frame shows the tail part of the x spectra in detail. Note that the noise floor is about 10 μm, much lower than the individual BPM resolutions—a statistical benefit. Otherwise, all the nonlinear signals would be below the 100 μm noise level. The arrow indicates where to cut off the noise floor.

Table 1 shows the rms errors of dynamical variable measurements for various BPM resolutions and the effects of noise-cut. Despite noticeable fluctuations, the accuracy of phase-space measurements is significantly improved, which makes nonlinear map measurements feasible with-
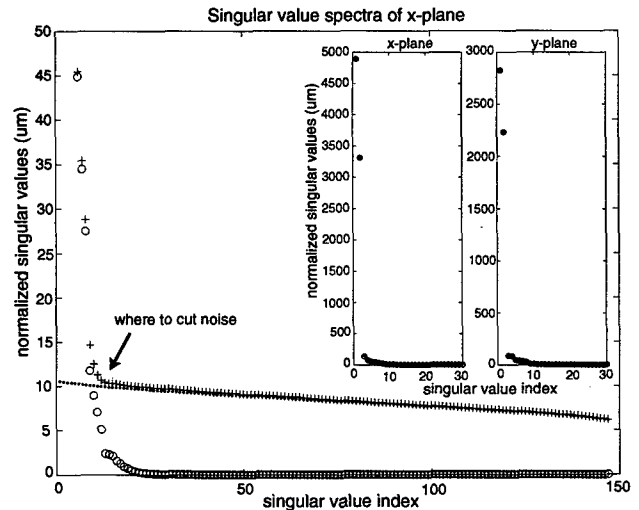
Figure 1: Singular value spectra of simulated data with "o" for signal only, "·" for $100 \pm 20\mu m$ BPM noise only, and "+" for both. Insertions show the full vertical scale.

Table 1: rms errors of phase-space variable measurements

BPM reso-	without noise-cut				with noise-cut			
lutions (μm)	$x(\mu m)$	$x'(\mu r)$	y	y'	x	x'	y	y'
100±20	102	7.1	156	14.	36.	2.6	25.	2.1
80±16	74.	6.4	126	11.	17.	2.1	24.	2.0
60±12	55.	4.9	103	9.3	12.	2.4	20.	1.8
40±8	30.	2.3	56.	5.1	8.2	1.2	14.	1.3
20±4	20.	1.7	30.	3.4	10.	1.1	11.	1.3

out stringent BPM resolution requirements.

Fig.2 plots the linear and a few nonlinear map coefficients along all the BPMs. They are normalized to the 10σ of phase-space variables, thus reflect the strength of each nonlinear term near the border of dynamical aperture.The apparent non-sinusoidal patterns in R_{11} and R_{12} are due to the uneven BPM locations. The peaks in the 2nd order coefficients are due to the main sextupoles around the interaction point at the center. Such spatial patterns form the physical bases for the BPM readings. Simulation re-
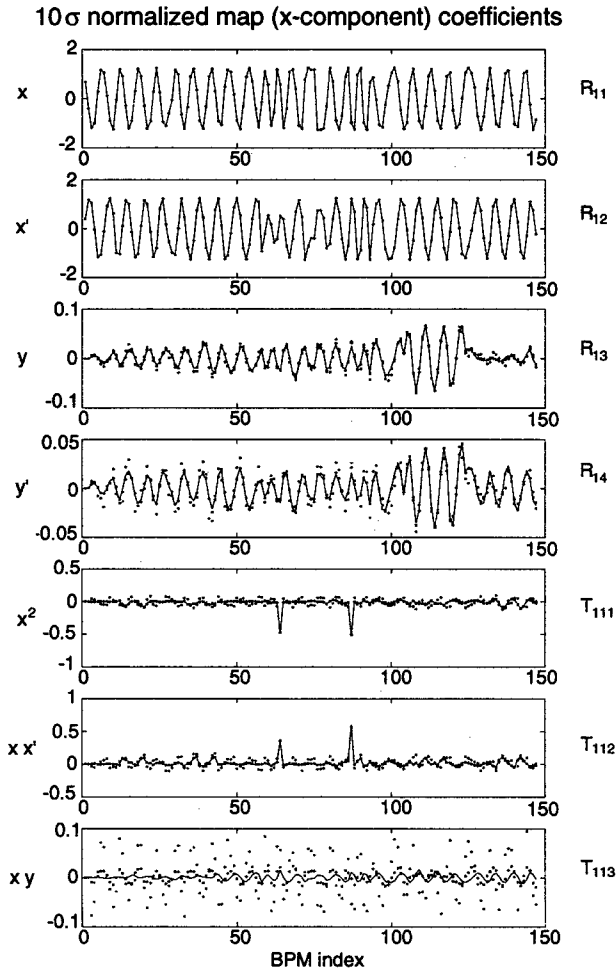
Figure 2: Map coefficients as physical basis. Only a few terms are shown. Solid lines are the exact values and dots are the simulated measurements. The lighter/darker dots are with/without noise-cut. (The on-line version shows the dots in different colors.)

Figure 3: 10σ normalized one-turn map coefficients up to the 3rd order (x-component). "o" and "•" are for $100 \pm 20\mu m$ BPM noise, with and without noise-cut respectively.
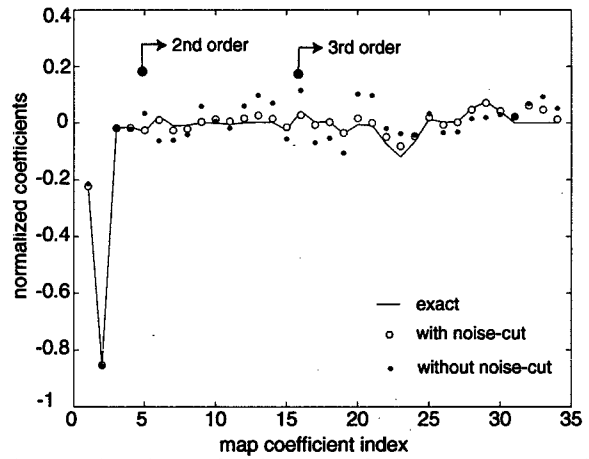
sults are also shown for the case of 100 μm BPM resolutions, with and without noise-cut, on top of the exact solid curves. Although the main features can be obtained even without noise-cut, the accuracy is significantly improved by the noise-cut, which is crucial (after all, everyone knows where the sextupoles are). Note that the linear coupling terms R_{13} and R_{14} can be obtained rather accurately. Such information can be used to calculate the global linear coupling coefficient and furthermore help to localize the coupling sources. The errors in T_{113} are due to the weakness of this nonlinear coupling term.

Fig.3 plots the results of simulated one-turn map measurement with 100 μm BPM resolution. Again the effect of the noise-cut is obvious. The accuracy is sufficient to reveal useful nonlinearity information. For example, a few percent error of the main sextupole strength should be detectable according to the simulations. More effective methods are under investigation.

5 CONCLUSION

Measurements of nonlinear (especially low order) maps in a ring become feasible with MIA methods, provided that systematic BPM errors are tolerable. Nonlinear map measurements can yield localized as well as global (one-turn map) nonlinearity information in a ring, which is valuable to beam dynamics study and machine improvement.

6 REFERENCES

[1] Chun-xi Wang and John Irwin, "Possibility to measure the Poincare section map of a circular accelerator", SLAC-PUB-7547

[2] J. Irwin, C.X. Wang, Y.T.Yan, K.L.F. Bane, Y. Cai, F.-J. Decker, M.G. Minty, G.V. Stupakov, and F. Zimmermann, Phys. Rev. Lett. vol.82 no.8 p.1684 (1999)

[3] Chun-xi Wang, John Irwin, Karl Bane, Yunhai Cai, Michiko Minty, Franz J. Decker, Yiton T. Yan,"Model-Independent Analysis of beam dynamics in accelerators", to be published.

PARALLEL OBJECT-ORIENTED DESIGN IN FORTRAN FOR BEAM DYNAMICS SIMULATIONS*

J. Qiang[†],R. D. Ryne, S. Habib, LANL, Los Alamos, NM

Abstract

In this paper we describe an object-oriented software design approach, using Fortran 90 (F90) and the Message Passing Interface (MPI), for modeling the transport of intense charged particle beams. The object-oriented approach improves the maintainability, resuability, and extensibility of the software, while the use of explicit message passing provides the freedom necessary to achieve high performance. Furthermore, an approach to object-oriented design based on Fortran will help those physicists familiar with procedure-oriented programming to make the transition to object-oriented design. In this paper we will describe the implementation of this approach and our success in developing two-dimensional and three-dimensional parallel beam dynamics codes that achieve high performance with only a small overhead associated with the object-oriented design.

1 INTRODUCTION

Object-oriented design is being widely applied in computer software engineering to implement complex codes which possess good maintainability, reusability, and extensibility. This technique also enables the encapsulation of detailed communication syntax in parallel computing, thereby reducing the extent of difficulty of parallel programming using MPI. In the parallel computing environment, such efforts have mostly been directed to the design of object-oriented frameworks using explicit message passing and C++ [1]. However, in the the accelerator physics community, Fortran still remains a popular language for demanding numerical simulations. Most popular used accelerator codes were programmed using Fortran based on procedure-oriented software design. It will be beneficial to the accelerator community to be able to to take advantage the object-oriented software design using Fortran language.

In this paper, we present an effort to implement object-oriented software design using F90 with MPI in the simulation of charged particle transport in accelerators. The paper is organized as follows: The physical system is described in Section 2, the implementation of object-oriented software design is presented in Section 3, parallel domain decomposition is discussed in Section 4, and performance tests are described in Section 5. We conclude by presenting an application to the simulation of high intensity beam transport through a superconducting linac.

2 PHYSICAL SYSTEM

The physical system addressed in this paper consists of an intense charged particle beam and a linear accelerating system. The accelerating system contains three types of beam line elements: drift spaces, quadrupole magnets and rf gaps. The forces acting on the beam particles are due to externally applied fields and the inter-particle Coulomb field. The dynamics of particles is governed by the Poisson-Vlasov system of equations. In accelerator simulations, it is a usual practice to take z to be the independent variable rather than the time t. The Vlasov equation is written as:

$$\frac{\partial f}{\partial z} + [H, f] = 0 \tag{1}$$

and the Poisson equation is

$$\nabla^2 \phi = -\rho/\epsilon \tag{2}$$

where f is the particle distribution function in phase space, $[,]$ is the Poisson bracket, H is the Hamiltonian of system with z as the independent variable, ϕ is the space charge potential from the Coulomb interaction, ρ is the charge density associated with the distribution function, and ϵ is the dielectric constant in vacuum. This system of equations is solved using a particle-in-cell method.

3 OBJECT-ORIENTED SOFTWARE DESIGN IN FORTRAN 90 FOR ACCELERATOR SIMULATION

In this study, parallel object-oriented software design is implemented using F90 and MPI. Object-oriented design is an approach encompassing the process of object-oriented decomposition [2]. In an objected-oriented design, after analysis of the (complex) physical system, the system is first decomposed into simpler physical modules. Next, objects are identified inside each module. Then, classes are abstracted from these objects. Each class has interfaces to communicate with the outside environment. Then relationships are built up among different classes and objects. These classes and objects are implemented in a concrete language representation. The implemented classes and objects are tested separately and then put into the physical modules. Each module is tested separately before it is assembled into the whole program. Finally, the whole program is tested to meet the requirements of problem.

Our implementation of the object-oriented software design methodology to beam dynamics studies in accelerators results in the decomposition of the physical system into five modules. The first module handles the particle

information consisting of the *Beam, BeamBC,* and the *Distribution* classes. The second module handles information regarding quantities defined on the field grid containing *Field* and *FieldBC* classes. The third module handles the external focusing and accelerating elements containing the *BeamLineElem* base class and its derived classes, the drift tube class, the quadrupole classes, and the rf gap class. The fourth module handles the computational domain geometry containing the *Geometry* class. The last module provides auxiliary and low level classes to handle explicit communication and input-output containing the *Pgrid2d, Communication, Utility, InOut* and *Timer* classes. The class diagram of the object-oriented model for a beam dynamics system is presented in Fig. 1.
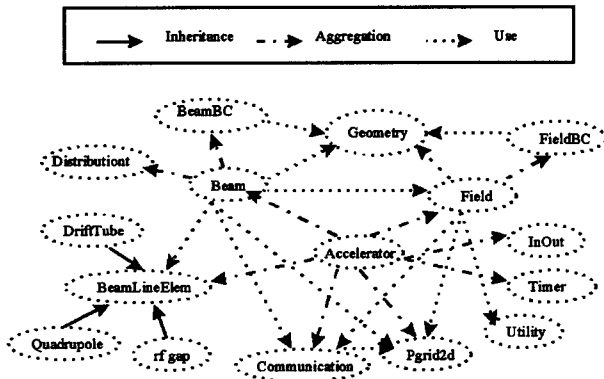
Figure 1: Class diagram of the accelerator beam dynamics system

The detailed method of writing objected-oriented programs using F90 was discussed by Decyk et al.[3]. In the following, we will give an example of using run-time polymorphism to implement the beam line elements in our simulation. In the beam dynamics simulation with F90, we define a base class *BeamLineElem*, and three derived classes for the drift, quadrupole magnet, and rf gap beam line elements. The scaled down sketch of this class is below:

```
module BeamLineElemclass
  use DriftTubeclass
  use Quadrupoleclass
  use Rfclass
  type BeamLineElem
    private
    type (DriftTube), pointer :: pdrift
    type (Quadrupole), pointer :: pquad
    type (Rf), pointer :: prf
  end type BeamLineElem
  interface assign_BeamLineElem
    module procedure assign_quad,&
        assign_rf,assign_drift
  end interface
contains
  function assign_drift(pdrift) &
```

```
        result(ppdrift)
  function assign_quadf(pquad) &
        result(ppquad)
  function assign_rf(prf) result(pprf)
  subroutine update_BeamLineElem(this,&
        z0,z1)
end module BeamLineElemclass
```

Since there is no direct support of inheritance in F90, we define a derived type in the *BeamLineElem* base class which contains three pointers to the derived classes as private data members. An overloaded function *assign_BeamLineElem* which includes three assignment functions is used to initialize the base *BeamLineElem* class object with different derived class object addresses. In each assignment function, only one pointer is initialized and the other two pointers are set to null. In the public function *update_BeamLineElem* of the base class, updating operations from derived classes are selected according to the different actual object association of pointers in the base class data member. The polymorphism is achieved by calling this subroutine with a constructed base *BeamLineElem* object in the application.

4 PARALLEL NUMERICAL ALGORITHM

In the following, we will describe the parallel numerical algorithm used in this study. A domain-decomposition approach is employed in the algorithm. For example, in the three-dimensional beam dynamics simulation, the physical computational domain is defined as a 3-dimensional rectangular box with range $x_{min} \leq x \leq x_{max}$, $y_{min} \leq y \leq y_{max}$, and $z_{min} \leq z \leq z_{max}$. This domain is decomposed on the $y - z$ plane into a number of small rectangular blocks. These blocks are mapped to a logical two-dimensional Cartesian processor grid. Each processor contains one rectangular block domain. The range of each block on a single processor is defined as $x_{min} \leq x \leq x_{max}$, $y_{lcmin} \leq y \leq y_{lcmax}$, and $z_{lcmin} \leq z \leq z_{lcmax}$. Here, the subscript *lcmin* and *lcmax* specify local minimum and local maximum, respectively, of computation domain. The particles with spatial positions within the local computational boundary are assigned to the processor containing that part of physical domain.

The explicit communication in the parallel computation is encapsulated in the communication class. A particle manager function is defined to move the particles from one computation domain to another computation domain. A field manager function is defined to resize the grid number which is needed in solving Poisson's equation with open boundary condition. The grid exchange functions are defined to get the grid information from neighboring processors.

For the particles local to the computational domain, a symplectic integration scheme is employed to advance the particles[4]. The charge density is obtained using a cloud-

in-cell charge deposition scheme. The potential in Poisson's equation is obtained using Hockey's algorithm for open boundary condition[5]. The electrical field is calculated using a central finite difference scheme and interpolated onto the particles.

5 PERFORMANCE TEST

The performance of the object-oriented F90/MPI parallel codes was tested on both SGI/Cray T3E-900 and SGI Origin 2000. As a test of the overhead in object-oriented F90, which might be due to the use of pointers and dynamically allocated arrays, we give a comparison of the time costs on SGI/Cray T3E between the object-oriented code and the conventional procedure-based code in Fig. 2. We
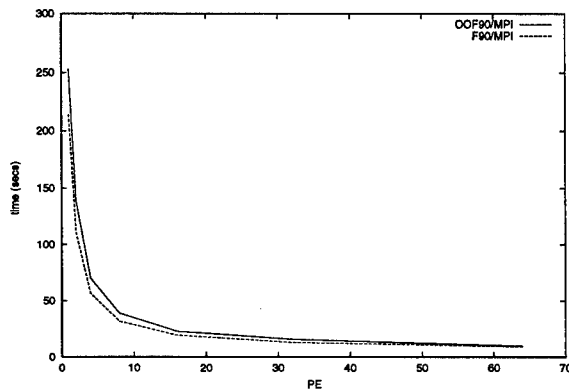
Figure 2: Time costs of object-oriented and procedure based F90/MPI codes as a function of PEs on T3E

note that even on a small number of processors, the overhead from object-oriented code is about 10%. This overhead decreases with increasing number of processors. As an example, in Fig. 3 we also give the time costs of the three-dimensional object-oriented F90/MPI code on Cray T3E and SGI Origin as a function of the number of processors. Good scalability is achieved on both machines.
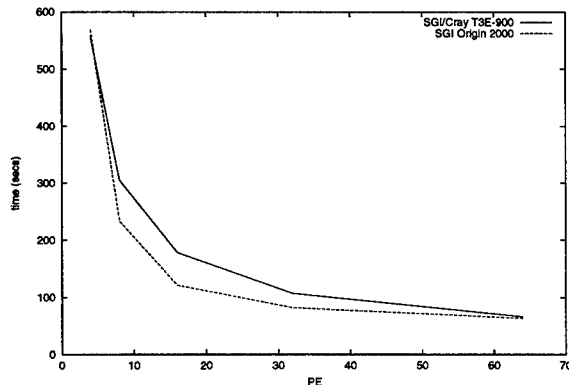
Figure 3: Time costs of 3-dimensional object-oriented F90/MPI code as a function of PEs on T3E and SGI Origin

6 APPLICATION

As an application, we simulate the beam transport through three super-conducting sections in a design of the APT linac[6]. Fig. 4 gives the transverse maximum amplitudes as a function of kinetic energy. These maximum amp-
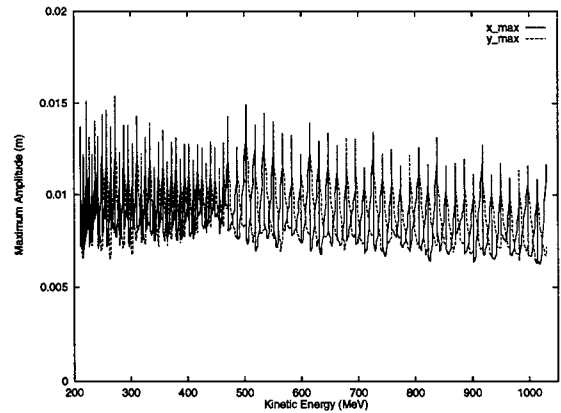
Figure 4: Transverse maximum amplitudes x and y of beam as a function of kinetic energy

litudes set the lower bound of the minimum aperture that can be achieved in the design.

7 CONCLUSIONS

In this paper we have described parallel object-oriented design in Fortran for beam dynamics simulations. As previously stated, our implementation with F90/MPI encapsulates the details of communication in low level auxiliary classes. This also provides the benefits of better maintainability, reusability and extensibility of software with small performance overhead.

8 ACKNOWLEDGMENTS

9 REFERENCES

[1] G. Wilson, L. Paul, (ed.), Parallel Programming Using C++, MIT Press, Cambridge (1996).

[2] G. Booch, Object-Oriented Analysis and Design with Applications, Benjamin/Cummings, Menlo Park, CA, (1994).

[3] V. K. Decyk, C. D. Norton, and B. K. Szymanski, Computer Physics Communications 115, p.9 (1998).

[4] R. D. Ryne and S. Habib, "High Performance Computing for Beam Physics Applications", LA-UR-94-2904 (1994).

[5] R. W. Hockney and J. W. Eastwood, Computer Simulation Using Particles, Adam Hilger, New York, (1988).

[6] T. P. Wangler, private communication (1998).

OBJECT ORIENTED C++ SOFTWARE COMPONENTS FOR ACCELERATOR DESIGN*

D. L. Bruhwiler,# J. R. Cary,+ and S. G. Shasharina, Tech-X Corporation, Boulder, CO

Abstract

Object oriented programming techniques make it possible for accelerator designers to independently develop C++ software components that can work together. As an example of this approach, we discuss some of the software components being developed at Tech-X Corporation, including: TxSTD, a library of standard utilities [1]; TxID, a library of data-holding and nonlinear dynamics classes [2]; TxAC, an accelerator modeling class library [3]; an X/Motif library used in the MAPA application [4] for interactive visualisation of dynamical systems such as particle accelerators; TxAN, a library of analysis and simulation classes relevant to dynamical systems; and the LION++ nonlinear optimization library [5].

1 OBJECT-ORIENTED PROGRAMMING

The computer software industry has been rapidly moving towards the use of object oriented programming (OOP) [Ref.'s 6-10]. OOP provides a superior mechanism for rapid development and testing, as well as ease of maintenance and extensibility for large scientific codes.

OOP consists of designing classes, where a class is a format for holding and interacting with data. An object is a particular instance of a class, just as 3.1 is a particular instance of a real number. Each object has its own data, while all objects of a given class share the same functions (called methods). A program is constructed by first defining the classes. The program instantiates objects corresponding to the classes and, by calling the public methods of these objects, manipulates or displays the data. The public methods of a class define its interface.

The three defining properties of OOP are *encapsulation*, *inheritance* and *polymorphism*. *Encapsulation* refers to the fact that objects are accessed only through a public interface, while their internal data and implementations remain hidden. This feature ensures that the code is safe from unwanted modifications. *Inheritance* allows the programmer to define new classes that inherit most of their coding from existing classes, only modifying or adding data and methods as needed. This allows for flexibility to increase the capability of an application in ways not foreseen by the original programmers, without rewriting the code. *Polymorphism* allows different classes to support the same interface but fulfill requests differently at run time. This makes *extensibility* possible – a new class that implements a new algorithm can inherit from an existing class and be used in its place.

C++ is the best available OOP language for scientific applications. The "expression template" technique [11-13] allows C++ code to perform as well as optimized Fortran77 in vector loop comparisons. Furthermore, the use of "generic programming" and "template meta-programming" methods has yielded C++ linear algebra solvers that are faster than Fortran77. [14] The base of numerical libraries for C++ is rapidly increasing, [15] and, because C++ is a superset of the well-established C language, it has access to a great wealth of legacy C code.

2 PUTTING THE PIECES TOGETHER

Leo Michelotti developed the first C++ class library for modeling beam dynamics in an accelerator [16] and deserves credit for introducing the accelerator physics community to the benefits of C++ and object oriented programming. Other C++ codes are now under development, including MAD-9 [17], LEGO [18], Teapot++ and MAPA [4,19]. Unfortunately, these codes are independently developed, and the C++ libraries used in one code cannot be used in the others.

The goal of the CLASSIC project [20] was to standardize the structure and interface of a C++ accelerator dynamics library in order to promote the sharing and reuse of code among the various developers. We propose an alternative approach – the use of template based "traits" mechanisms [21-23] – to make C++ accelerator class libraries interoperable and, hence, true software components. First, we briefly describe the class libraries under development at Tech-X Corporation, then we elaborate further on the use of traits.

3 ACCELERATOR DYNAMICS LIBRARY

The Tech-X accelerator dynamics library TxAC, now at the first alpha release, has been used to successfully model the Advanced Light Source, finding correct values for tunes and dynamic apertures. TxAC includes an SIF parser (Standard Interchange Format, the MAD-8 input language [24]) that can create an accelerator model (beamlines, elements, and properties of the charged particle) with full support for mathematical formulas. TxAC comes with a number of built-in element types (e.g. quadrupoles, dipoles, thin RF cavities) which use analytical models for the electric and magnetic fields. Each element type knows how to calculate the phase

---

Email: bruhwile@txcorp.com
+ Also, University of Colorado Physics Department, Boulder, CO

space map for particles passing through it, so the code can be used for tracking, and it allows the user to specify whether tracking should use 2, 4, or 6 dimensions. [19] TxAC also includes a beamline class, allowing the user to define an arbitrarily deep hierarchy of beamlines within beamlines -- critical for describing large rings, which may consist of only a dozen or so unique elements that are repeated in various combinations for a total of hundreds or thousands. Synchrotron radiation effects are optional.

The TxAC class hierarchy is shown in Fig. 1. A new element type can derive from the most appropriate part of this hierarchy and thus obtain most of the needed features. New features can then be added in the derived C++ class, which must also provide the code that implements tracking through the element. Once a new element class has been defined, it need only be registered with a name in the TxacElements file and, upon recompilation, the new element type will be supported by the parser and the graphical user interface (GUI).
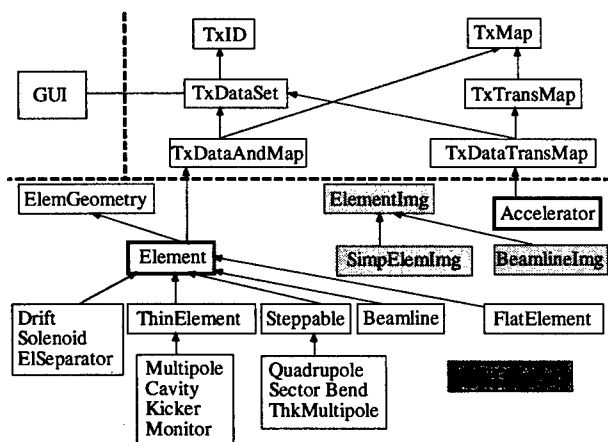
Figure 1: Schematic showing TxID object hierarchy (upper right), the TxAC object hierarchy (bottom) and one example of interface with the X/Motif graphical user interface (upper left).

4 ACCELERATOR ANALYSIS LIBRARY

The accelerator analysis library TxAN uses TxAC to calculate matched Twiss parameters (or the linear and 2nd-order dispersion) for any closed orbit or to propagate specified initial values element by element through a beamline. TxAN can also calculate the position and orientation of all beamline elements in a global Cartesian coordinate system, or use Monte Carlo methods to propagate the RMS moments of a particle distribution. The classes of TxAN inherit from the data holding classes of TxID and define a new data holding class for storing the analysis results. Developers can define a new C++ class for accelerator simulation, inheriting appropriately from the TxAN hierarchy. The data resulting from the new simulation is stored in the plot data class,

while any parameters relevant to the simulation are stored in the TxDataSet class of TxID. The X/Motif GUI can extract data from these classes, thus allowing the user interactive control over the simulation with immediate rendering of the resulting data.

5 GRAPHICAL USER INTERFACE

The X/Motif GUI supports on-line tracking and renders the resulting surface-of-section (SOS) plots. Initial conditions for the next particle can be specified simply by clicking in the windows. These SOS plots can be resized interactively, and the phase space variables can be paired up in any order. Fixed points can also be found.

The GUI also allows one to browse the local file system for an appropriate input file, and then to save changes in the same file or in a new file. The GUI can plot a schematic layout of the accelerator, warning the user if, for example, a ring does not close on itself.

The GUI provides appropriate windows for interactively changing any relevant parameters for the accelerator, for individual elements or for the analyses. For each type of analysis, the GUI provides a menu item allowing the user to activate the simulation, and then renders line plots of the resulting data. Developers can define new element classes or analysis classes through inheritance, and these new types will be directly supported by the GUI after compiling the new classes and relinking the application.

6 LION++ OPTIMIZATION LIBRARY

LION++ [5] is a suite of flexible and extensible C++ software components for numerical computing. Still being actively developed, the present release features TxOptSlv, a library for the optimization of nonlinear user-specified functions, and TxBase, a library of unary functors and other general utilities. LION++ takes full advantage of sophisticated templating techniques and object oriented design in order to provide users with maximum flexibility in the choice of argument typé and return type for the merit function that needs to be optimized and in the configuration of options for the built-in algorithms.

Three multidimensional algorithms have been implemented, including nonlinear *simplex* and *Powell*, which do not need the gradient of the function, and one due to *Fletcher, Reeves, Polak and Rebiere* (FRPR), which does require access to the gradient. The Powell and FRPR algorithms require access to 1-D line optimization algorithms. Three 1-D algorithms have been implemented, including *golden section* and *Brent*, which do not need the function derivative, and a *modified secant* algorithm, which does require access to the derivative.

At present, all of the optimization algorithms are unconstrained although we are currently implementing algorithms that constrain the arguments in various ways. We

are also now implementing the Levenberg-Marquardt algorithm, which is effective for nonlinear least squares fitting and, more generally, for simultaneous optimization of many nonlinear functions. LION++ is readily extensible so developers can implement their favorite algorithms or create a thin interface to other C and C++ algorithms, all with the same convenient user interface.

7 THE TRAITS MECHANISM

"Traits" are defined through a template class or struct. For example, Fig. 2 shows the definition of two traits for a 1-D array class: the type of the argument held by the array and a public method Resize() that will change the length of the array. It is assumed that the 1-D array supports the [] operator for accessing the elements. The TxArrayWrap class in Fig. 2 wraps a simple C-style pointer, which does not have built-in resizing capability.

In LION++, the argument list for multidimensional functions is declared to be of type VecType, and all optimization classes are templated over VecType. Users must instantiate a templated optimization object, where the template parameter specifies the argument type of the function to be optimized. Thus, LION++ is "container-free" as defined in Ref. [23].
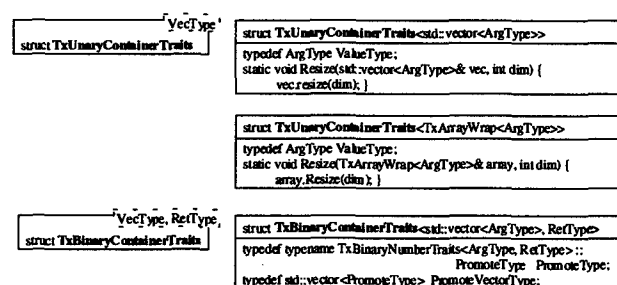
Figure 2: Unary (above) and binary (below) traits for containers (user-defined 1-D arrays).

The method for tracking in an accelerator library (called Advance() in TxAC) could be templated over the type of the class that is to be tracked. Then the traits mechanism could be used to allow this class to be any of: a) a single particle of precision float, double, etc.; b) a 1-D array of particles, with the array type completely arbitrary; c) a generalized user-defined particle class; or d) any C++ differential algebra (DA) library. Thus, the traits mechanism immediately allows for some interchange of software components between different C++ code developers (particle classes and DA libraries).

Taking this idea a step further, one could template the controlling class of the accelerator dynamics library (called Accelerator in TxAC) over the element type. In this case, the "traits" would include methods for reading and writing the physical data associated with an element, tracking a particle (or array, or DA vector) through an element, etc. With this approach, the developer of one class library could use the element classes from another

accelerator class library, allowing for direct model inter-comparisons.

There are two prices to be paid for this approach. The first is that such heavy use of templates can lead to very long compilation times. The second is that the use of traits requires the use of rather awkward syntax in the source code for the accelerator class library.

8 CONCLUSIONS

A "container free" approach to the development of C++ class libraries for the modeling and design of accelerators is an elegant and relatively straightforward way to make the many existing class libraries interoperable. This approach places some burdens on the library developer, but it avoids the difficulty of trying to convince developers that they should base their code on some standard class library design.

The authors thank Julian Cummings for discussions regarding the use of traits and John Verboncoeur for discussions regarding object-oriented programming.

9 REFERENCES

[1] TxSTD page, URL http://www.techxhome.com/freestuff/txstd
[2] TxID page, URL http://www.techxhome.com/freestuff/txid
[3] TxAC page, URL http://www.techxhome.com/freestuff/txac
[4] MAPA page, URL http://www.techxhome.com/products/mapa
[5] LION++ page, URL http://www.techxhome.com/products/lion
[6] G. Booch, "Object Oriented Development," *IEEE Transactions on Software Engineering* 12, 211 (1986).
[7] B. Stroustrup, *The C++ Programming Language*, Third Ed. (Addison-Wesley, Reading, Massachusetts, 1998).
[8] S. B. Lippman and J. Lajoie, *C++ Primer*, Third Ed. (Addison-Wesley, Reading, Massachusetts, 1998).
[9] E. Gamma, R. Helm et. al, *Design Patterns* (Addison-Wesley, Reading, Massachusetts, 1995).
[10] A. Elins, *Principles of Object Oriented Software Development* (Addison-Wesley, Reading, Massachusetts, 1994).
[11] A. D. Robison, "C++ Gets Faster for Scientific Computing", *Computers in Physics* 10, 458 (1996).
[12] T. Veldhuizen, "Expression Templates," *C++ Report* 7 (1995).
[13] S. Haney, "Beating the Abstraction Penalty in C++ Using Expression Templates", *Computers in Physics* 10, 552 (1996).
[14] The Matrix Template Library (MTL) home page at URL http://www.lsc.nd.edu/research/mtl/
[15] URL http://monet.uwaterloo.ca/blitz/oon.html#libraries
[16] L. Michelotti, "MXYZPTLK and Beamline: C++ Objects for Beam Physics," AIP Conf. Proc. 255 (Corpus Christi, 1992).
[17] MAD-9 web site, URL http://wwwslap.cern.ch/~fci/mad/mad9
[18] Y. Cai, M. Donald, J. Irwin, Y. Yan, "Lego: A Modular Accelerator Designer Code,"SLAC-7642, August 1997.
[19] D. L. Bruhwiler, J. R. Cary and S. G. Shasharina., Proc. Sixth European Particle Accelerator Conf., (Stockholm, June, 1998).
[20] CLASSIC web site, URL http://wwwslap.cern.ch/classic
[21] N. C. Meyers, "Traits: a New and Useful Template Technique," *C++ Report* 7 (1995); URL http://www.cantrip.org/traits.html
[22] T. Veldhuizen, "Using C++ Trait Classes for Scientific Computing;" URL http://monet.uwaterloo.ca/~tveldhui/papers/traits.html
[23] G. Furnish, "Container-Free Numerical Algorithms in C++," *Computers in Physics* 12 (3) (May, 1998).
[24] MAD-8 web site, URL http://wwwslap.cern.ch/~fci/mad/mad8

THE LHC DYNAMIC APERTURE

J.-P. Koutchouk, *for the LHC Team,*
CERN, Geneva, Switzerland

Abstract

In 1996, the expected field errors in the dipoles and quadrupoles yielded a long-term dynamic aperture of some 8σ at injection. The target was set to 12σ to account for the limitations of our model (imperfections and dynamics). From scaling laws and tracking, a specification for the field imperfections yielding the target dynamic aperture was deduced. The gap between specification and expected errors is being bridged by *i)* an improvement of the dipole field quality, *ii)* a balance between geometric and persistent current errors, *iii)* additional correction circuits (a_3, b_4). With the goal in view, the emphasis has now turned to the sensitivity of the dynamic aperture to the optical parameters. The distortion of the dynamics at the lower amplitudes effectively reached by the particles is minimized by optimizing the distribution of the betatron phase advance. At collision energy, the dynamic aperture is limited by the field imperfections of the low-β triplets, enhanced by the crossing angle. With correction of the most important aberrations, the dynamic aperture reaches the target set to 10σ.

1 INTRODUCTION

With the approval of LHC in 1994, the studies of dynamic aperture (D.A.) became more strictly targeted towards establishing the requirements of the magnetic field quality. For that purpose, the largest stable amplitude was selected as the most reliable indicator of stability. The computing power was increased significantly [1] to a level where it is not a serious limit anymore. The correctness of the model of the imperfections and the understanding of the stability limit became essential as compared to tracking issues. We describe in this paper the methods selected for LHC, the results obtained and the consequences for the machine design (field quality, correction systems and optics).

2 DEFINITION OF THE DYNAMIC APERTURE

In the following, the D.A. is defined as the radius of the largest circle inscribed inside the domain of initial conditions in (x, y) space observed to be stable after 10^5 turns, i.e about 10 seconds of LHC time. The reduction of the 6D hyper-volume to a circle is practically necessary for tracking and justified by the observed irrelevance of the initial angles [2] and by the choice of a maximum relative momentum deviation which maximizes the chromatic perturbations. Testing the connexity of this area is practically limited by the mesh size $(\sigma/30)$. Thanks to the ever increasing power of computers, 60 possible instances of multipoles distributions are tracked. The D.A. is approached

from below. The average is used as a relative indicator, e.g. to compare correction systems. The **minimum** is retained as the absolute D.A. of LHC (95% confidence level) and expressed in units of the unperturbed rms beam size. Out of the thousands of cases analysed, no evidence was found of abnormally small D.A.'s inside the stability domain.

3 SOURCES OF NON-LINEARITIES

The combination of all available results over the last few years, though not always strictly comparable, gives the relative importance of the non-linear perturbations (Table 1). These results assume the baseline multipole correction scheme which includes b_3 and b_5 coils at the end of each dipole. Unlike in low emittance electron machines,

Non-linearity	Injection	Collision
Chromatic sextupoles	28	≈ 70
Multipoles in Dipoles	6.5	> 27
Multipoles in Lattice Quads	≈ 12	> 27
Multipoles in Low-β Quads.	> 23	6.5
Long-range Beam-beam Kicks	6.5	6

Table 1: Computed D.A.s versus non-linear sources in LHC V2 and V4

the sextupolar non-linearities can be neglected (lower beam momentum spread). At injection, the multipoles in the dipoles dominate. At collision energy, the effect of the low-β quadrupole imperfections becomes overwhelming due to the very large β-function and the crossing angle. In both cases, the beam separation on either side of the crossing points sets the maximum D.A.

4 REQUIREMENT FOR THE DYNAMIC APERTURE

4.1 Actual Dynamic Aperture

To protect efficiently the s.c. magnets from quenching (a loss of only 100 ppm of the full beam intensity is sufficient), the collimation system reduces the useful aperture to 6 σ, where we require the motion to be stable over long times. This figure can be compared to the 4.5 σ D.A. found in HERA [3] to allow good performance of the machine, in the absence of constraints from collimators. The SPS Experiment [4] suggests, on the other hand, that a D.A. of 8 σ could be insufficient to ensure a long lifetime in presence of large tune modulation. These few data seem to confirm that a target of 6 σ is reasonable, given the larger sensitivity of LHC to modulation.

4.2 Computed Dynamic Aperture

Table 2 summarizes our assumptions on the predictability of the D.A. from the tracking results. Items (1) and (3) are related to the sensitivity to initial conditions. To reduce complexity, the linear imperfections (2) are usually not included in the D.A. calculation. When this is done and after correction, the D.A. is reduced by about 5%. The variation of the multipole errors occurring during the snap-back (5) are approximately taken into account by selecting the worst case for each multipole and then assuming a static situation. Items (1), (3), (4) and (6) are related to the limits in computer power. The initial conditions are mostly chosen on the diagonal in the x, y plane. Tracking is mostly carried out to 10^5 turns although the injection plateau is expected to last about 400 times longer. Relevant studies of ripple require tracking beyond 10^5 turns. Longer tracking with a more complete exploration of initial conditions and ripple are carried out exceptionally to evaluate the impact on the D.A.. Fits of the survival plots [5] show a moderate reduction of the D.A. from 10^5 to 10^7 turns. Finally, the safety

Table 2: *Relation between long-term and computed D.A.'s.*

Source or Uncertainty	Impact	D.A. in σ
Target D.A. at 10^5 turns		12.0
(1) Finite mesh size	-5%	
(2) Linear Imperfections	-5%	
(3) Amplitude ratio x_i/y_i	-5%	
(4) Extrapolation to $4\,10^7$ turns	-7%	9.6
(5) Time-dependent multipoles	-10%	
(6) Ripple	-10%	7.8
(7) safety margin	-20%	6.2
Long term D.A.		6.2

margin (7) is estimated from the SPS D.A. Experiment [4] and from Fermilab/E778 [6] to be 20%. This is probably an optimistic view of the predictability of the D.A.: in HERA, the D.A. was predicted [7] [8] using the **measured** field imperfections, without or with the decay of persistent currents; compared to the measured D.A., the discrepancies are in a range of 10% to 100%.

In order to cope with these uncertainties, the impacts are combined linearly and the target for the computed D.A. is fixed to 12σ at injection. Such an approach in a highly non-linear domain is not un-controversial: the large target D.A. might create artificial requirements on the higher-order multipoles. This was not found to be the case for LHC.

The 12σ target is significantly more ambitious than the D.A.'s recorded a few years ago (see table 1). It is now reached with improvements discussed below. At collision energy, the limitations are only in the low-β quadrupoles and thus better defined. We have suppressed the safety margin and set the target to $10\,\sigma$.

5 EFFECT OF THE MAIN DIPOLES

5.1 The Most Significant Imperfections

The multipole expansion of the main dipole field is listed in Table 3. Expressed in relative field error at 12σ, the

Order	Normal			Skew		
	S	U	R	S	U	R
3 (sext.)	-9.7	1.38	1.47	-.08	.87	.48
4 (oct.)	.23	.34	.51	-	.14	.51
5 (dec.)	.89	.44	.43	.007	.42	.34
6	-.01	.06	.09	-	.06	.17
7	-.16	.05	.22	.017	-	.08
8	-	-	.04	-	-	.08
9	.36	.03	.07	-.006	-	.11
10	-	-	-	-	-	.01
11	.57	-	-	.002	-	-

Table 3: Table 9901: Multipole expansion b_n, a_n (Systematic, Uncertainty, Random) of the dipole field at injection energy at the reference radius of 17mm in units of 10^{-4}.

field error is one order of magnitude above that of the SPS or LEP but only slightly worse after a perfect correction of b_3 and b_5. The errors can be systematic (finite number of blocks in the coil, 2-in-1 design), uncertain, i.e. predictable in a range (production bias) or random from dipole to dipole. The uncertainties are large compared to the bias of the random components. In the model of the imperfections, we assume eight production lines with different uncertainties; the dipoles in one arc come from the **same** line.

The computation of the D.A. for either all random errors combined **R** or for individual systematic multipole errors (Figure 1) shows that the LHC D.A. is dominated by systematic effects. The effect of b_3 is almost perfectly suppressed by the sextupolar coils in the dipole ends. The effect of b_5 is sufficiently though not completely corrected by the decapole coils in the dipole ends. b_4 is the next limitation. The D.A.'s due to the other multipoles are rather balanced. To avoid a D.A. which would be too sensitive to optics parameters, we require both the effect of individual multipoles and their combined effect to be small enough.
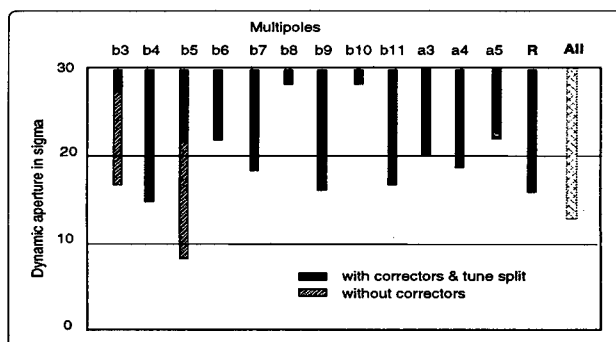
Figure 1: D.A. per source for error table 9901

5.2 The Consequences on the Beam Dynamics

Figure 2 shows the D.A. as a function of Q_x. The nominal fractional betatron tunes are .28 and .31 between 3rd and 4th-order resonances. This position is favourable to avoid high-order resonances in collision mode and was used at the Sp$\bar{p}$S and HERA. The D.A.'s in this report are computed for this working point. A second point between 4th and 5th-order resonances is explored occasionally in case the 3rd-order resonances would be too strong or in case tuning the two rings differently would be an advantage.
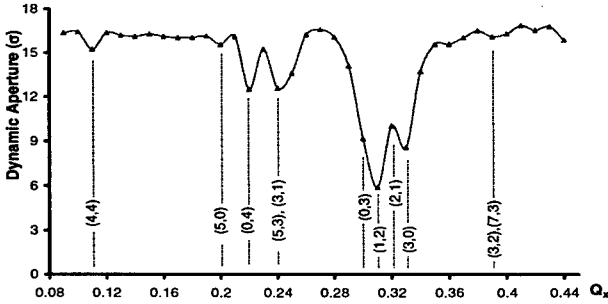
Figure 2: Average short-term D.A. versus tunes ($Q_y = Q_x + .03$) for the target error table [9](no linear errors)

The chromaticity due to the persistent currents is about 400 units. It is corrected in each dipole with b_3-coils powered in series per arc. A break-down of the correctors in one arc causes a 8% loss of D.A. together with an increase of the excitation of 3rd order resonances [10], justifying a distributed correction scheme.

The effect of b_5 causes mostly an amplitude detuning larger than 0.01 at 4σ and $\Delta p/p = 1.5\sigma_e$. The correction is efficient but not sufficiently local to allow b_5 to increase too much above its design value: the distance between the dipole center and end (where the b_5 coil is mounted) is significant at this order. On the other hand, corrector break-downs in several arcs are tolerable [10], confirming that the main effect is indeed a detuning.
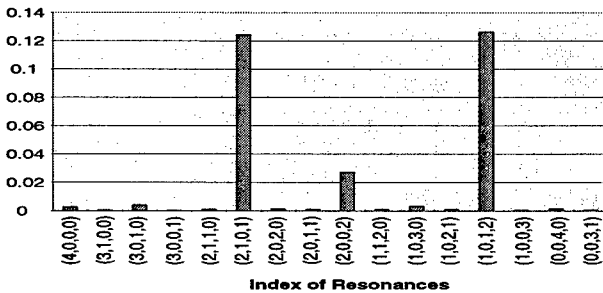
Figure 3: Driving terms of 4th order resonances, from [11]

The amplitude detuning for on-momentum particles is mostly due to the uncertain b_4 in the dipoles and partly to a second-order in lattice sextupole perturbation; in some cases, a second order in the uncertain a_4 appears as well. A significant correlation [12] is found between b_4, amplitude

detuning (of up to 0.01 at 8σ) and D.A. A full recovery of the loss of D.A. (about 1.5σ) is obtained by correcting the detuning with b_4 correctors in the dipole ends distributed in 50% of the arcs [13].

a_4 excites the 'sub-resonance' $Q_x - Q_y = p$. Figure 3 shows that its driving terms (2101, 1012) are by far the largest fourth-order terms; on the frequency map [14] (Figure 4), large amplitude particles appear attracted by the resonance. Its correction by a_4 coils in 50% of the arc dipoles
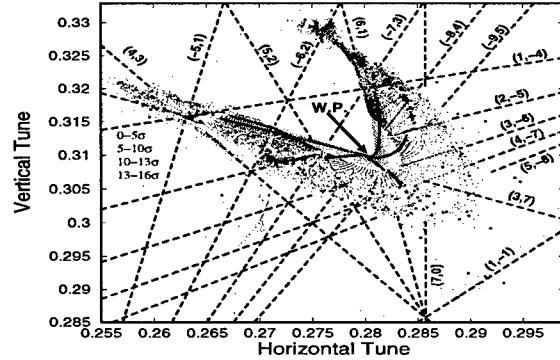
Figure 4: Frequency map showing the attraction by the 4th-order resonance (1,-1) of large amplitude particles.

allows full recovery of the loss of D.A.(about 1.5σ). The higher-order detuning which is resonant with $Q_x - Q_y = p$ is decreased by the same token [13].

a_3 causes a smearing in phase space, a loss of D.A. of about 0.5σ and a large second-order chromaticity. The mechanism is a momentum dependent betatron coupling [15] which modulates the tunes at twice the synchrotron frequency. The modulation depth of 0.01 or more depends on the working point. A resonant correction with skew sextupoles cures these effects.

The LHC D.A. appears to depend mostly on first-order amplitude detunings and resonances driven by field uncertainties. This is different from the former SSC and LHC observations where the detunings were associated with systematic errors, the resonances to random higher-order terms and the D.A. to the interplay of higher-order resonances. This simpler phenomenology stems from a better knowledge of the sources of field errors. It opens possibilities for optimal lattice design as long as the hypotheses on the errors are confirmed.

5.3 The Target Table for Imperfections

Using the scaling law of D.A. for individual multipoles and combining them according to an empirical conjecture [16], we could construct rather rapidly a 'Target Table'(Table 4) for field imperfections which yields the target D.A. of 12σ, starting from the error table 9607 which yielded 8 to 9σ. Tracking globally confirmed the prediction. This approach allowed the dipole designers to include the constraint of field quality at the design stage rather than after

Order	Normal	Skew
3	1	0.05
4	.02	1 (.28)
5	0.5(0.37)	.9
7	.6(0.15)	-
9	1	-
11	1 (0.38)	-

Table 4: Ratio of multipoles in the Target Error Table over those of the realistic Tables 9901 (or 9607).

and speeded up the improvements.

5.4 Improvements of the Dipole Field Quality

The change from a 5-block to a 6-block coil design [17] permitted a better compensation of persistent currents at injection. The allowed field errors are close to target (Table 4). The uncertainty on a_4 is reduced by alternating the orientation of the dipole collared coils assemblies.

5.5 Multipole Corrector Schemes

The multipoles a_3 and b_4 were however found irreducible, thus requiring new correction schemes.

We foresee for LHC version 6 a non local resonant correction of the resonance $Q_x - Q_y = p$ driven by a_3. The required integrated strength of the skew sextupoles is comparable to that of all lattice sextupoles at injection. An elegant implementation [18] involves tilting 4 lattice sextupoles per arc, chosen such as to minimize geometric aberrations.

The correction of the amplitude detuning will be carried out by octupole windings lodged into the decapolar corrector of the dipoles. Tracking shows indeed [13] that reducing the amplitude detunings to 0.001 at 8σ provides more robust D.A.'s which can be expected to be less sensitive to tune drifts during operation. The Landau damping octupoles, close to the quadrupoles, cannot reduce simultaneously the three terms of the detuning. With a cell phase advance close to 90°, they may produce other aberrations. We take advantage of the fact that the b_4/b_5 correctors correct mainly detuning terms to equip the dipoles in every second cell only. This upgrade of the correction system is almost cost neutral and provides the required efficiency.

5.6 Optimized Optics

Up to version 4, the integer LHC betatron tunes were identical. A tune split was introduced in LHC version 5 when the linear coupling was identified to be exceptionally strong [19]. It is caused by the systematic part of a_2, and the feed-downs of the b_3 corrections coils due to alignment tolerances. This was achieved by breaking the optics antisymmetry with a more flexible hardware [20]. The tune split was adjusted to 4 units (2 in the arcs, 2 arising naturally in the dispersion suppressors) to weaken sufficiently the perturbation arising from the systematic and uncertain parts of a_2 (Figure 5). It increased the D.A. of version 5 by

about 1σ. The optimal tune split for coupling cancellation is 1 per arc. The LHC quadrupole gradients are specified to allow this potentially interesting possibility (used in [21]).
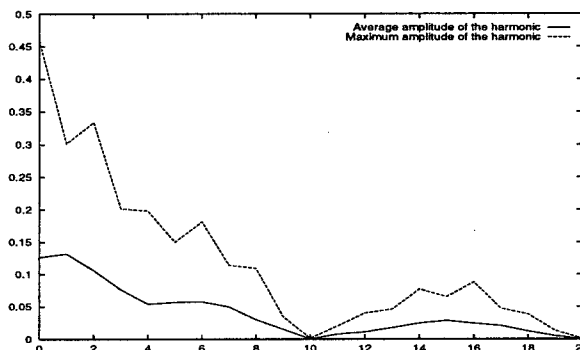
Figure 5: Azimuthal harmonics of a field uncertainty averaged over 1000 seeds

With the present understanding of the consequences of a_3 and a_4 (section 5.2) and the identification of a hidden super-periodicity in $\mu_x - \mu_y$ leading to a possibly constructive build-up of $Q_x - Q_y = p$, the tune split is now increased from 4 to 5 in version 6. The D.A. increases again by about 1σ (Table 5). It is close to target with realistic errors (Figure 1). The onset of chaos is observed at 9 to 10σ.

Besides this pragmatic use of the tune split, first-order perturbation theory [22] was used to compute the largest amplitude allowed in presence of a realistic mechanical aperture at 10σ. In this 4D approach, the normal and skew octupolar imperfections were found to perturb most the dynamics. On Figure 6, the variation of the integer tunes allows a minimization of the perturbation (the size of the ellipse is a measure of the aperture loss). The new tunes of
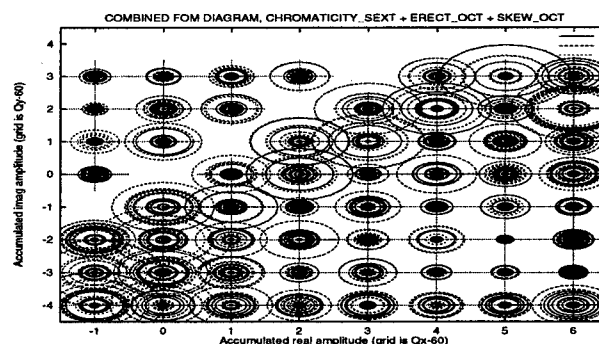
Figure 6: Distortion versus integer tunes (origin is 60/60)

LHC version 6 are 64.28/59.31, i.e. one of the best combinations.

Pushing further the idea of minimizing the driving terms of first-order resonances, it was shown that a tune split of 1 per arc complemented by a condition on the horizontal cell phase advance cancels the contribution of each arc to al-

most all first-order resonances [21], provided the field multipoles are constant in each arc. Tracking not only confirms that the D.A. is increased (Table 5), but shows that this is still true if b_4 is increased significantly [23].

Tunes	Aver. D.A.
63/59 (LHC V5)	12.0
64/59 (LHC V6)	13.4
65/58 (LHC V6)	13.8
68/59 (LHC V6)	14.5

Table 5: D.A. versus tunes (Target Error Table + expected a_4/b_4 from 9712)

6 EFFECT OF THE BEAM-BEAM KICKS

To meet the D.A. requirement, the beam separation in the section common to the two beams was increased to 10σ [24] at injection and 7σ in collision [25]. The corresponding crossing angle is $\pm150\mu$rad at 7 TeV.

7 EFFECT OF THE QUADRUPOLES

At injection, the b_6 due to persistent currents in the lattice quadrupoles (Table 1) contributed to the limitation of the D.A.. This effect was partly compensated by changing the coil geometry, leaving a negligible residue.

At 7 TeV, the field errors in the low-β quadrupoles limit severely the D.A. (Table 1). In the first design, the main effect [26] was that of a too large $b_{10} \approx 0.5$ units, enhanced by the large β-function (4.7km) and the off-axis orbit (±5mm). Since then the field quality was much improved in the US/LHC design [27]. The aberrations are further minimized by choosing the magnet orientation, by body-end compensation and by adding non-linear correctors ($n = 3, 4, 6$). The present performance fully satisfies the requirements with a D.A. of 10σ and an amplitude detuning small compared to the beam-beam detuning [27]. The KEK quadrupole field quality is still being improved.

Case	DA(σ_{xy})	Min. DA	$\Delta\nu$ (10^{-3})
no correction	10.7 ± 1.7	8	1.9 ± 1.1
with correction	13.3 ± 1.6	10	1.0 ± 0.7

Table 6: D.A. with and without correctors at 7 TeV

8 METHODS

The model of the LHC machine and the tracking methods are detailed in [28] [24]. Basically, element by element tracking is performed using thin lenses. The power of the computer cluster has been increased by a factor of 2.5 since 1997. The computation of a D.A. takes 2 days of CPU and much more in preparation and analysis. Fast tracking with symplectified maps was not operational for the design of LHC but could become interesting for optimization.

Modern tools such as map analysis by resonant and non-resonant normal forms and frequency analysis of the betatron motion are used to compute global quantities. The classical resonance theory has remained so far the only approach to design multipolar correction circuits or optimized optics. It retains indeed the azimuthal dependence of the imperfections and corrections and has yielded satisfactory results for LHC. The frequency map analysis seems a useful qualitative help in understanding the dynamics, e.g. to judge on the respective efficiency of correction schemes.

The real issue in improving our knowledge of the D.A., as formally noted by Ritson [29] lies first in the ability to describe in a realistic way the machine with realistic imperfections, achievable corrections, time-dependent effects,...

9 CONCLUSION

The target D.A. of 12σ at injection and 10σ at 7 TeV is now reached. It may be viewed either as ensuring a realistic D.A. of 6σ with a safety factor of 2 or as a guaranty that the onset of chaos occurs beyond the amplitudes practically allowed by the collimation system. The improvement of the field quality of the dipoles and low-β quadrupoles, the addition of correcting circuits and the tune split all contributed to the improvement. The dominant role played by first-order resonances and detuning terms opens the possibility of handling the consequences of unexpected systematic multipole imperfections by optimizing the optics.

10 REFERENCES

[1] E. McIntosh et al., Part. Acc. Vol. 54(2-4),p. 223 (1996).

[2] F. Schmidt, LHC Project Note 30, 1996.

[3] F. Willeke, private communication.

[4] W. Fischer et al., CERN SL/95-96(AP) 1995

[5] M. Giovannozzi et al., Part. Acc.56:195-225(1997).

[6] Chao et al., Phys.Rev.Lett. 61,2752-2755(1988).

[7] F. Zimmermann, Part.Accel.49:67-104,1995.

[8] O. Brüning et al., DESY-HERA 95-05, 1995

[9] L. Jin, F. Schmidt, LHC Project Note 182 (1999).

[10] F. Schmidt, G. Xu, LHC Project Note 96 (1997).

[11] Y. Cai, J.P. Koutchouk, LHC Project Note75, 1996.

[12] M. Böge et al., PAC 1997.

[13] L. Jin et al., LHC Project report 253 (1998).

[14] I. Papaphilippou, this conference.

[15] J.P. Koutchouk, LHC Project Note 113(1997).

[16] V. Ziemann, Part.Accel.55:141-150,1996.

[17] S. Ramberger, S. Russenschuck, EPAC 98,Sweden.

[18] S. Fartoukh, LHC Project Report 278(1999).

[19] J.P. Koutchouk, Part.Accel.55:183-191,1996.

[20] J.P. Koutchouk, PAC97.

[21] A. Verdier, this conference.

[22] R. Talman, LHC Project Reports 197 and 233 (1998).

[23] F. Schmidt, A. Verdier, this conference.

[24] J.P. Koutchouk et al., PAC97.

[25] W. Chou, D. Ritson, PAC97.

[26] A. Faus-Golfe & A. Verdier, EPAC96, 1996.

[27] J. Wei et al., EPAC98.

[28] M. Böge, F. Schmidt, PAC 1997.

[29] D. Ritson, Part.Accel.54:93-105,1996

EFFICIENT DIFFERENTIAL ALGEBRA COMPUTATIONS[*]

John R. Cary, Tech-X Corporation, Boulder, CO and University of Colorado, Boulder, CO

Svetlana G. Shasharina, Tech-X Corporation, Boulder, CO

Abstract

Numerical Differential Algebra (DA) is a powerful tool for studying non-linear motion in accelerators, beam and optics devices. Implementation of DA is the easiest in an object oriented programming language, especially C++. In addition to standard object oriented features, C++ allows for operator overloading and static polymorphism via templates. In this paper we discuss (1) use of templates for polymorphic use of the code, so it can treat both dynamical variables and DA maps, (2) methods of optimisation for speed needed for efficient use DA in accelerator physics and other applications.

1 DIFFERENTIAL ALGEBRA IN LAYMAN'S TERMS

Dynamical systems – accelerators, beam and optics devices – can be represented by a mapping of initial conditions (depending on parameters a) to final values variables $z_f = M(z_i, a)$. Calculation of this map constitutes a very complicated task, since the motion of the particles is generally highly non-linear. The fields and parameters of the system are usually known to a certain order in a Taylor expansion in a deviation from some reference in the dynamical space. That is why it makes sense to limit the accuracy of map calculations to the same order and treat all functions of calculation as truncated Taylor series. First order derivatives of the map are known as transfer matrix. Nonzero higher order derivatives of the map represent aberrations, while derivatives with respect to parameters are sensitivities.

Coefficients of the truncated expansion can be used as DA representation of functions and, in fact, constitute a vector space. One can show that this space is a differential algebra so that it has arithmetic operations, inversion, roots and derivation [1]. DA representations of components of identity function, z_i (i=0,...,d, with d being the dimension) form algebra generators, vectors with all but one component equal zero. The nonzero component, 1, corresponds to first order derivative with respect to z_i. For example, the zeroth generator will have components {0,1,0,....,0} (with the first position reserved for the constant term). Note, that the order of coefficients in vector representation is a matter of choice, although lexicographical order is most popular (see [2]).

The whole realm of DA applications is very rich and powerful. The most commonly used application is calculation of non-linear maps for solving equations of motion in a range of initial conditions. Since the map is a solution of equations of motion and is equal identity at t=0, it can be found by propagating of identity map through the system. Identity map can be considered a d-dimensional vector of generators. Hence is the recipe for generating maps: one has to replace all functions in the integration algorithm with their DA representations and propagate the identity map. The resulting "matrix" will give the system map to the desired order. Once the map is found, there is no need to integrate trajectories with different conditions: one can calculate the final state by substituting monomials corresponding to initial condition into the map. This procedure is much faster than integration, so it can be used for multiparticle calculations and long-term stability studies.

2 C++TEMPLATES AND GENERATION OF MAPS

In this section we show how the recipe for generating maps discussed above can be elegantly implemented in C++. First we need to discuss C++ templates mechanism. Then we give an example of its application to generating a simple map.

2.1 C++ Templates and Static Polymorphism

Templates is a powerful tool for providing polymorphism used extensively in generic programming (see [3]). A typical example of a template function is Swap() function performing sequence of actions not dependent on type of the arguments:

```
template <class T> function Swap(T& a, T& b) {
  T temp(a);
  a = b;
  b = temp;
}
```

The type of the template parameters is passed to compiler at compile time when compiler substitutes the actual type into the templated code (template instantiation) and uses templated code as if it is not templated but indeed has the needed type inserted. This polymorphism is called static polymorphism since the choice of the type happens at compile, not run time. Thus, the Swap() function become

377

"untemplated" as soon as some concrete type is used for its arguments:

```
int main() {
  SomeType x (2);
  SomeType y(3);
  Swap(x, y);
}
```

If class `SomeType` declares copy constructor and assignment operator private, the main program will not compile. This gives a typical example of template programming: most of templates are built with some assumptions (template constraints) for the template parameters. Note that C++ allows developers to create free template functions, template classes and template member functions in non-template classes.

2.2 Templates, Traits and Map Generation

Now we are ready to explain how we can generate maps, provided that we know how to integrate usual dynamic variables. Imagine that we have class `System` which has a template function `Advance()` for calculation of final value the vector describing the dynamical variables in 6-dimensional space. For simplicity, we will use a function propagating through a simple drift. The argument will be encapsulated in a vector container whose choice depends on a user:

```
void template <class VecType>
System::Advance(VecType& z) {
  double pz   = CalcPz(p);
  double lenOverPz = length/pz;
    p[4]+=lenOverPz*
    (InvReferenceBeta()+p[5]) +
    length*(1+Eta()*Delta_S)*
    InvReferenceBeta();
    p[2]+=p[3]*lenOverPz;
    p[0]+=p[1]*lenOverPz;
  }
```

`VecType` can be any of multiple containers for double vectors (std::vector<double>, valaray<double> etc.). Now we want to generalise this function so that it can treat not only double vectors, but also maps.

To make the receipe described in the previous section work, we have to overload `operator[](int)` in DAMap class so that it returns a corresponding DA vector. In addition, we assume that DA maps and vectors are implemented as template classes with type of coefficients being the template parameters, so that we can describe real or complex DA's used for normal form analysis. We also found advantageous to have dimension and order as template parameters, but for simplicity will omit them here. Thus, schematically the DAMap class will have the following structure:

```
template <class U> class DAMap {
    DAVector<U>* data;
  public:
    const DAVector<U>& operator[](int i) const
```

```
    {return data[i];}
    DAVector<U>& operator[](int i)
      {return data[I];}
    //etc.
};
```

Now, lets go back to generalisation of the `Advance()` function. Instead of `VecType` we now imagine more general template parameter which can include not only vectors, but also maps, since we made sure that `DAMap::operator[](int)` is defined. The first question coming to mind is what should we put instead of type declaration "`double`"? Evidently, this type should be the same as a type of variable returned by `operator []` `(int)`. In case of a double vector, it should be `double`, in case of a DA map, this should be a DA vector! If we want to use one generalised `Advance()` function for both dynamic vectors and DA maps, how do we code this information so it works for both?

The solution is in using traits (see [4]). Traits are special classes, which provide mechanism to associate certain functions, values or types with particular classes and access them in a uniform way. For example, we often need to know what is the type of data is contained by the vector? In case of `std::vector<T>` it will be `T`. In case of `DAMap<U>`, it should be a `DAVector<U>`, since any map is just a vector of DA vectors. Similarly, we might want to know a size of the vector, which will be function `size()` for `std::vector<T>` and `DAMap<U>::Dimension()` for DA maps. This information can be encapsulated in the following traits classes. First we define a general template class which, being unspecialised, does not have anything:

```
template <class U> struct UnaryTraits {};
```

Now we can partially specialise it for vectors and maps:

```
template <class U>
UnaryTraits <std::vector<U> > {
//Define the type of data
  typedef U ValueType;

//Get size of the vector
  static int GetSize(const std::vector<U>& u) {
    return u.size()}
};
```

```
template <class U>
  UnaryTraits <DAMap<U> > {
  //Define the type of data
    typedef DAVector<U> ValueType;

  //Get size of the vector
    static int GetSize(const DAMap<U>& u) {
      return u.Dimension();}
};
```

With traits defined, we can rewrite our `Advance()` function in such a way that it will treat both vectors of

378

dynamic variables and DA maps by accessing the correct ValueType:

```
void template <class AnyType>
System::Advance(VecType& z) {
  typedef typename
    UnaryTraits<AnyType>::ValueType ValueType;
  ValueType pz   = CalcPz(p);
  ValueType lenOverPz = length/pz;
    p[4]+=lenOverPz*
    (InvReferenceBeta()+p[5]) +
    length*(1+Eta()*Delta_S)*
    InvReferenceBeta();
    p[2]+=p[3]*lenOverPz;
    p[0]+=p[1]*lenOverPz;
}
```

Note that function `CalcPz()` should be rewritten and become a template function to return the appropriate value:

```
template<class T> T System::CalcPz(T& p) {
  T result;
  //calculate result
  return result;
}
```

In the main program, one has to decide which quantity to propagate and use the `Advance()` function:

```
int main() {
//Create the system:
  System sys();
//Set system's parameters (not shown)
//Create a 6-dimensional double:
    std::vector<double> x(6);
//Set x to some intial conditions(not shown)
//Propagate x through the system
    sys.Advance(x);

//Create a default 6-dimensional map
//of the 4 order
    DAMap<double> map(6,4);
//Set this map to identity (not shown)
//Find the map of the system:
  sys.Advance(map);

//Vector x now has been propagated once,
//now do it the second time using the map
//(syntax arbitrary):
  x.Map(map);
//etc.
  return 0;
}
```

Thus, use of template functions and trait mechanism allows for true reuse of the code, so that the same function is used to integrate dynamic variables and generate non-linear maps.

3 OPTIMIZATION FOR NUMERICAL EFFICIENCY

3.1 C++ and Performance

As many scientist like to complain, C++ can be inefficient for numerical for number crunching. There are many reasons for that, one of which is that it is very easy to write a bad C++ code. Another, objective, reason, sometimes called a burden of abstraction, is that ordinarily overloaded operators are defined in such a way that they create a temporary out of binary operation whenever more operations are present in the expression. For example, adding 3 vectors together, a = x + y + z; will create temp1 = (y + z) with one looping over indices performed. Then it will calculate temp2 = x + temp and assign a to temp2. One can easily see that we can get rid of at least one temporary and one loop if we just loop through all 3 vectors together. In our previous work (see [5]), we have shown how to overcome this burden: by using of expression templates (ET). ET makes addition/subtraction and multiplication/division by a scalar as fast as hand-coded C and speeds up these operations by an order of magnitude!

Another common technique, reference counting, allows safe copying via pointers, which saves enormous time, whenever assignment or copying in and out of functions is performed (see [5]).

Unfortunately, these methods do not contribute much to efficiency of multiplication of DA vectors. Typically, DA calculations deal with 6-dimensional maps in 1 to 12 orders. This implies very long vectors and situations when to obtain a product of 2 vectors, compiler has to perform half-a-million elementary multiplications between double numbers is not uncommon. This poses a task of speeding up multiplication and operations using it (powers). Note that solution to this problem almost does not depend on the choice of programming language.

We discovered several techniques useful for optimisation of multiplication. One is optimisation of multiplication tables, as we described in [5]. For the sake of completeness, we will remind how it is done in the next section. Then we will comment on effects of programming style on efficiency.

3.2 Optimisation of Multiplication Tables

Once the order of monomials in DA vectors is set, one can obtain the multiplication table by looping through the index of the first factor (external loop) with the internal loop running through the index of the second factor. For each pair there is an integer that corresponds to the index of the product to which this pair contributes. For example, lets multiply two second order 2-dimensional DA vectors:

c = a*b;
a=a0+a1*x+a2*y+a3*x*x+a4*x*y+a5*y*y=

{a0, a1, a2, a3, a4, a5}};
b=b0+b1*x+b2*y+b3*x*x+b4*x*y+b5*y*y=
{b0, b1, b2, b3, b4, b5};
c ={c0,c1,c2, c3, c4, c5}.

The multiplication table can be easily found by multiplication of polynomials):

ip	if1	if2
0	0	0
1	0	1
2	0	2
3	0	3
4	0	4
5	0	5
1	1	0
3	1	1
4	1	2
2	2	0
4	2	1
5	2	2
3	3	0
4	4	0
5	5	0

To obtain the product c with this table, one has to go through the table and perform 3 lookups for each step:

```
for(int i=0; i<table.length(); ++i)
    c[table[i][ip]]+=a[table[i][if1]*b[table[i][if2];
```

Such naïve approach leads to pretty slow multiplication. One can improve the speed by reorganising the table in the following way. First, let us split it into symmetric and asymmetric parts. Symmetric table has if1 = if2 with these indices being simply incremented in the table, while the product index is still to be looked up. Then, in the asymmetric part, we leave only lines where the first factor is smaller than the second (this leads to getting almost a factor of 2 of speedup). For our example, we obtain the following symmetric table:

ip	if1	if2
3	1	1
5	2	2

and 2 asymmetric tables:

ip	if1	if2
1	0	1
2	0	2
3	0	3
4	0	4
5	0	5

ip	if1	if2
4	1	2

One can see that to obtain the product, one has to loop through the symmetric table adding a[if1](b[if1], where if1 does not have to be looked up. Then one goes through all asymmetric tables, adding a[if1]*b[if2]+a[if2]*b[if1]. The number of lookups can be reduced even more, if one notices that each asymmetric table has the first index equal to the number of the table i (starting from 0), while the second index can be found by incrementing an integer initially equal to (i+1). As a result, there will be only one look up for each row of the table, instead of 3.

3.3 Programming Style

When we compared different approaches to DA implementation, we discovered that general programming style makes a big difference in performance. One should try to avoid lookups, dereferencing, if-statements. Thus, we discovered that pointer arithmetic is faster than operating with dereferenced arrays, so that the following code:

```
double* xPtr = x[0];
double* xEndPtr = x[5];
double* yPtr = y[0];
double* aPtr = a[0];
while (xPtr<xEndPtr) {
  *a = *x + *y;
  a++; x++, y++;
}
```

is faster than:

```
for(int i=0;i<a.size;++i)
  a[i] = x[i] + y[i]
```

We used pointer arithmetic in the numerical implementation of multiplication combined with optimisation of multiplication tables, as described above, to obtain pretty good results. Our multiplication is 5-8 (depending on platform and compiler) faster than other C++ codes. This is shown on Fig. 1.

Figure 1: DA multiplication time for DA versus the number of primitive multiplications of real numbers.

4 FUTURE DIRECTIONS FOR OPTIMISATION

4.1 Optimisation for Cache

In our studies of multiplication, we noticed that CPU time taken by one multiplication of DA vectors grows linearly with the number of elementary scalar multiplications up to a point where it changes its slope (see Fig. 1). Such behaviour is a typical manifestation of cache problems.

Cache is a small fast memory holding recently accessed data, designed to speed up subsequent access to the same data. All data requested by the program is fetched into cache and stays there until it is flushed by new data. Cache operates on presumption of spatial and temporal locality: it expects that the data requested by the program will be used soon again, as well as data close to the requested. Hence, data is cached in memory lines, which are typically larger then the specifically requested data. The access for main memory is much slower than accesses to cache. Thus, when the size of the data needed to perform a multiply reaches a certain size, the calculation slows down, because of accesses to main memory rather than cache. This fact was noticed by computer scientists optimising multiplication of matrices. A special technique "blocking" (sometimes also called "tiling") has been developed (see [6]). It divides matrices into blocks with sizes optimised for particular cache size, so that the operations are able to reuse data staying in cache. We can not directly take this idea since we deal with the multiplication table and different objects. But we will reorganise the multiplication tables into subtables, so that the indices of each subtable stay close to each other within some blocking size. The optimal size will depend on the platform. The idea to efficiently utilise the memory hierarchy is natural, because while the speed of processors has been increased rapidly, it has not accompanied by a similar increase in the memory speed.

4.2 Optimisation of low-order DA's

In the case when the order of the DA is low (1 or 2), the multiplication table looks particularly simple. We will provide a special version of the library for such cases, which will be used in automatic differentiation. Templating over order permits the definition of special cases.

4.3 Optimisation of powers

These operations will not be implemented in terms of multiplication operator, but rather on a lower level (similar to multiplication), because explicit use of the symmetry of the factors in the product will be advantageous for speed. Thus, instead of $x^8 = x*x*x*x*x*x*x*x$ one should make compiler do $(x^4)*(x^4)$.

5 CONCLUSIONS

We have developed a prototype of C++ library for Differential Algebra, which has a potential to become the most efficient C++ library. It has expression templates for efficient addition/subtraction and multiplication/division by a scalar. It has reference counting for safe and rapid copying, whose speed does not depend on the length of vectors. Implementation of multiplication uses optimised multiplication tables and is free of parasite operations. The resulting speed of our classes is 5-8 times faster than other C++ libraries. The classes are polymorphic, so that we can have DAVector<double>, DAVector<complex> for normal form analysis, or even DAVector<DAVector<complex> for determining parameter dependence of dynamics parameters. In addition, our classes are templated on dimension and order (we did not discuss this in the paper), which allows for aggressive compile time optimisation and adds to efficiency. We hope that in the nearest future we can further develop the library by testing our ideas of optimisation for cache. We will have to add elementary functions and all needed operators in DA vector class, create the map library including normal forms, symplectification and Lie factorisation.

6 REFERENCES

[1] M. Berz, "Differential Algebraic Description of Beam Dynamics to very High Order," Particle Accelerators, 24, 109 (1989).

[2] A. Dragt and M. Venturini, "Design of Optimal Truncated Power Series Algebra. Routines: II. Computing Sums and Ordinary and Lie Polynomials Using Monomial Indexing and Linked Lists," University of Maryland, Sept. 1996 (Draft).

[3] M. Nelson, C++ Programmer Guide to the Standard Template Library (IDG Books Worldwide, Foster City, CA, 1995).

[4] G.Furnish, "Container-Free Numerical algorithms in C++," Computers in Physics, v.12, No 3, 258(1998).

[5] John R. Cary and S. G. Shasharina, "Efficient C++ Library for Differential Algebra," Proceeding of European Particle Accelerator Conference, Stockholm 1998.

[6] M. S. Lam, E. E. Rothberg and M. E. Wolf, "The Cache Performance and Optimisation of Blocked Algorithms," Proceedings of the Fourth International Conference on Architectural Support for Programming Languages and Operating Systems, April, 1991.

NONLINEAR LONGITUDINAL DYNAMICS STUDIES AT THE ALS*

J. M. Byrd[†], W-H Cheng, S. DeSantis, D. Li, LBNL, G. Stupakov, F. Zimmermann, SLAC

Abstract

We present a summary of results for a variety of studies of nonlinear longitudinal dynamics in the Advanced Light Source, an electron storage ring. These include observation of decoherence at injection, decay of an injected beam, forced synchrotron oscillations and diffusion from one bunch to the next. All of the measurements were made using a dual–scan streak camera which allowed the real-time observation of the longitudinal distribution of the electron beam.

Introduction Synchrotron oscillations are inherently nonlinear, mostly because of the sinusoidal radiofrequency (RF) voltage used to longitudinally focus the beam. When the bunch length is small compared to the RF wavelength, the RF voltage over the length of the bunch can be considered as linear, minimizing nonlinear effects. In electron storage rings, this is almost always the case. However, as the performance demands on electron rings grow, it becomes increasingly important to understand several of the subtle effects caused by the nonlinearities. These effects are also fascinating unto themselves and their study constitutes a contribution to the physics of beams. This paper presents a summary of results of experimental studies of several nonlinear effects in longitudinal beam dynamics in the Advanced Light Source (ALS), an electron storage ring optimized for producing high brightness synchrotron radiation. Machine parameters relevant to our experiments are listed in Table 1. Due to space considerations, only a qualitative description of the results are presented here. More theoretical and experimental details can be found elsewhere[2, 5, 6].

Section II describes the streak camera used for all of the results in this paper. Section III presents a study of injection transients with and without beam capture. Section IV presents measurements of diffusion from one bunch to another. Section V describes measurements of forced nonlinear synchrotron oscillations. Section VI summarizes the paper.

Dual scan streak camera To make a detailed study of the longitudinal beam dynamics, we used a streak camera (SC) to observe the evolution of the longitudinal bunch distribution. A schematic diagram of the Hamamatsu C5680 SC is shown in Figure 1. The SC converts the time structure of a pulse of synchrotron radiation at optical wavelengths from a bend magnet into vertical deflection at the CCD camera. In our experiments, the vertical deflection plates are driven

Parameter	Description	Value
E	Beam energy	1.5 GeV
C	Circumference	196.8 m
f_{rf}	RF frequency	499.664 MHz
V_{rf}	RF voltage	1.1 MV
h	Harmonic number	328
α	Momentum compaction	1.6×10^{-3}
Q_s	Synchrotron tune	0.0075
λ_{rad}	Long. rad. damping rate	5×10^{-5}
σ_ℓ	RMS natural bunch length	4.5 mm
σ_ϵ	RMS $\delta E/E$	7.1×10^{-4}

Table 1: Nominal ALS longitudinal parameters.

Figure 1: Schematic diagram of the streak camera in synchroscan mode with dual sweep. A: photocathode, B: accel. mesh, C: vert. deflection electrode, D: horz. defl. electrode, E: microchannel plate F: phosphor screen, G: CCD camera.

by a 125 MHz sinusoidal voltage synchronized to the RF frequency. In addition, there is an optional slow horizontal deflection which allows observation of the longitudinal profile as a function of time. The time scale of the horizontal sweep can be adjusted to observe several turns or thousands of turns and can be triggered to coincide with an event such as injection. For sweep times longer than several hundred turns, individual turns can no longer be resolved and so the longitudinal profile appears as a continuous line across the image.

The synchroscan principle is illustrated in Fig. 2 which shows the 125 MHz vertical deflecting voltage with respect to the arrival times of 4 storage ring bunches. Only deflections within the marked bands appear on the microchannel, allowing an effective means of gating a particular bunch. The phase of the deflecting voltage can be adjusted to place the arrival of a single bunch on the center of the screen.

Injection transients Optimizing the beam injection into electron rings is important for increasing the filling rate and reducing radiation backgrounds. Understanding the injec-

Figure 2: Vertical deflecting voltage shown with respect to the arrival times of 4 storage ring bunches. Only deflections within the marked bands are observed.

Figure 3: Illustration of quadrupole bunch oscillations at injection for bunch mismatched to the storage ring RF bucket.

tion process and subsequent transient is particularly important in damping rings for linear colliders and also for continuous injection (i.e. top–up.) This section describes measurements of the longitudinal beam distribution following injection in the ALS.

When an electron bunch is injected into the storage ring, it's length and energy spread will either grow or damp to the natural bunch length and energy spread of the storage ring over several radiation damping times[1]. In the ALS, the injected bunch length is about five times the natural bunch length and the injected energy spread is close to the natural energy spread. If this mismatched bunch is injected into the center of an RF bucket, it rotates in the bucket at the synchrotron frequency, modulating the bunch length as shown schematically in Fig. 3. However, the nonlinearity of the RF voltage creates a dependence of synchrotron frequency on amplitude, causing the bunch head and tail to advance slower in phase than the bunch center, causing a filamentation of the bunch distribution as shown in the results of a computer simulation in Fig. 4.

Shown in Fig. 5a is a SC image of beam 0.3 msec following injection into an empty storage ring. The vertical axis represents the longitudinal bunch length in units of time and the horizontal axis is time. The bunch length is modulated at half the synchrotron period of 87 μsec due to the rotation of the mismatched bunch shape as shown in Fig. 3.

Figure 4: Phase space distribution 4560 turns following injection for ALS injected beam conditions illustrating phase space filamentation.

Figure 5: a) Measured SC image 0.3 msec following injection showing modulation of the bunch length. b) SC image 2.4 msec later showing filamentation of the large amplitude particles. c) A computer simulated image found from tracking.

Fig. 5b shows the SC image 2.4 msec later. The bunch filamentation is evidenced by the tails forming on the bunch distribution. This compares very well with a simulated SC image as shown in Fig. 5c, where each vertical slice is the projection of the phase space distribution as shown in Fig. 4 onto the phase axis.

It is also interesting to examine the decay of an injected beam without RF capture (i.e. no RF voltage). As the beam loses energy, its orbit spirals inwards and it eventually is lost. The ring orbit period also decreases according to the relation

$$\frac{\Delta T}{T_0} = \alpha \delta_{tot} \tag{1}$$

where α is the momentum compaction, and δ_{tot} is the total frequency energy lost. Assuming the energy loss per turn is constant and α is independent of energy, the path difference

Figure 6: Transient of a decaying, uncaptured electron beam at injection. The calculated drift for parameters given in Table 1 is shown as a white line.

Figure 7: Phase space orbits including radiation damping. The RF buckets are no longer closed, with attractors for following buckets lying above each bucket.

is given by

$$\delta_{tot} = \frac{f_0^2 \delta_{turn}}{2} t^2 \qquad (2)$$

If the energy loss/turn is known, this may be another technique for measuring the momentum compaction.

Fig. 6 shows a SC image at injection with the storage ring RF turned off. As the uncaptured beam decays, it arrives earlier on each turn w.r.t the synchroscan voltage shown in Fig. 2, creating an increasing vertical deflection on the SC. Also shown is the calculated decrease in orbit period using parameters given in Table 1. We are currently analysing the evolution of the bunch shape.

Bunch-bunch diffusion Ignoring radiation damping, which acts as a frictional damping to the synchrotron oscillations, synchrotron oscillations within the RF bucket are stable. Electrons with synchrotron orbits outside of the RF bucket slowly lose energy and eventually are lost. Generally, this approximation is good because radiation damping times in electron storage rings are typically small compared with synchrotron periods. However, radiation damping provides a mechanism by which electrons with synchrotron orbits outside the RF bucket have a small probability of being recaptured into a subsequent RF

bucket. Given an electron bunch stored in a ring, electrons can be ejected from the RF bucket by processes such as large–angle intrabeam (Touschek) scattering or quantum excitation. We refer to the recapture of a fraction of the ejected electrons as a diffusion process. This section presents a brief description and measurements of this diffusion process at the ALS. More details are given elsewhere[2]. Similar studies have been done at UVSOR and the Photon Factory[3].

Although the diffusion process is interesting from the point of view of accelerator physics, it can also be important for operation of a synchrotron light source. For example, one operational mode at several facilities requires large single light pulses separated by at least several hundred nanoseconds to accommodate the time–of–flight techniques used by experimenters. In this mode at the ALS, the ring is filled with two electron bunches separated by 328 nsec. The storage ring injection process typically fills several unwanted parasite bunches which are removed prior to an experiment using a common RF knockout technique. However, the diffusion process can create additional parasite bunches over time, possibly contaminating the experiment.

The effect of the radiation damping on longitudinal phase space is illustrated in Fig. 7. The RF bucket is no longer a closed area but rather a basin of attraction for electrons within the boundaries shown. For a given bucket, the attractors of subsequent buckets lie above the bucket. Electrons ejected from the bucket have a small probability of landing on an attractor and damping to a subsequent bucket. The diffusion rate can be calculated as the product of the the probablity of exciting an electron to an amplitude and the width and position of the attractor. Note the the process is not symmetric in that only particles ejected with too much energy can be recaptured. Also note that other particle loss mechanisms are ignored.

Our experiment consisted of filling a single bunch to a level of several milliamps and recording its current and that of the following parasite bunch as a function of time. The relative current in the parasite bunch was measured using the SC simply as a means of gating the synchrotron light signal such that it could be measured independently from the main bunch.

Measurement of the diffusion into the parasite bunch relative to the initial charge in main as a function of time is shown in Figure 8. The two cases are for RF voltages of 1.1 and 0.78 MV with corresponding synchrotron tunes of 7.7e-3 and 6.4e-3. Diffusion is faster for lower RF voltages since the attractors are closer to the bunch.

One technique for eliminating the diffusion is to adjust the momentum acceptance of the lattice to be approximately equal to the RF acceptance such that any particle ejected from the bucket is lost. This already occurs in the ALS in some conditions, albeit unintentionally. Studies[4] indicate that the ring momentum acceptance decreases below the RF acceptance when the wiggler is in its fully closed position. We no longer observed the diffusion in

Figure 8: Measured charge in the parasite bunch relative to the main bunch for 2 different RF voltages. The solid lines for each data set are the calculated diffusion using the measured Touschek lifetime for each RF voltage.

Figure 9: Measured response curve for a modulation frequency swept upwards and downwards through the resonance.

this condition.

Forced oscillations The subject of forced, or driven, synchrotron oscillations has many applications in the physics of beams[5]. Forced synchrotron oscillations occur when the beam is driven by modulations of the bending fields or voltage or phase modulations in the RF system. Both of these effects can have significant impact on operation, particularly in efforts to achieve very short electron bunches. This section presents highlights from our studies of phase modulation of synchrotron oscillations. More details are given elsewhere[6].

Synchrotron oscillations are very similar to those of a pendulum, which has a response curve as shown in Fig. 9. When the frequency of the driving force is below the bifurcation frequency, the response has two stable points as also shown in a Poincarè map of the phase space in a frame rotating at the driving frequency. The beam can be distributed

between the two islands. If the excitation frequency is swept through the bifurcation point, the actual distribution depends on the initial beam distribution as well as the beam current. Our experiments consisted of mapping the fixed points of the system as a function of modulation amplitude and frequency. We also studied the diffusion process from one island to another and related it to the Touschek scattering process.

An example SC image at a condition where the phase modulation frequency is just below the bifurcation frequency is shown in Fig. 11. As the modulation frequency is swept upwards above the bifurcation frequency, the smaller amplitude island disappears as can be seen from the response curve in Fig. 9. The measured fixed points of the system for a upward and downward sweep of the modulation frequency are shown in Fig. 9. The hysteresis typical of such as system is also evident in the difference between the direction of the swept frequency.

To measure the interisland diffusion rates, we filled a single bunch with current and used the SC to measure the longitudinal profile as a function of time after initiating the phase modulation at a fixed frequency. The modulation frequency was always below the bifurcation frequency, ensuring the presence of two stable islands. For each beam current, we measured the diffusion as a function of modulation frequency in order to vary the island size and separation.

We extracted the initial diffusion rate by comparing the relative rate of increase of the peak signal in the island A (outer island) compared to the island B (central island.) A plot of the diffusion rates as a function of modulation frequency for several beam currents is shown in Figure 12. Calculations of the diffusion rate with Touschek scattering as the diffusion mechanism and the separatrix of island B as the momentum acceptance show approximate agreement with the measurements.

We have also studied the structure of higher resonances

Figure 10: Poincarè map of the phase space in a frame rotating with the modulation frequency when exciting below the below bifurcation frequency.

Figure 11: SC Image of the longitudinal profile when the modulation frequency is just below the bifurcation frequency. The beam populates both stable phase space islands.

Figure 12: Measured and predicted diffusion rates as a function of modulation frequency for three bunch currents.

at multiples of the synchrotron frequency. At twice the synchrotron frequency, two or three phase space islands are expected to form, depending on the modulation frequency. An example is shown in Fig. 13, which shows the bunch split into two islands. The calculated phase space structure is also shown. At three times the synchrotron frequency three or four islands can form. An example of this resonance is also shown in Fig. 13.

Figure 13: Measured SC image showing formation of two and three islands for excitation near 2^*f_s and 3^*f_s. The calculated phase space structure is also shown.

Conclusions The nonlinearity of synchrotron oscillations creates several interesting and subtle effects in electron storage rings. These experiments also demonstrate that the dual–scan SC is an invaluable tool for understanding longitudinal beam dynamics in electron storage rings.

The author would like to thank Dr. Albert Hofman and Prof. S. Y. Lee for many useful discussions on longitudinal dynamics and Dr. Alex Lumpkin, Jim Hinkson, and Mike Chin for helping set up and understand the streak camera.

1 REFERENCES

[1] H. Mosshammer, Phys. Rev. E **48**, 1390, (1993). H. Mosshammer, Nucl. Inst. Methods A **323**, 553, (1992). H. Mosshammer, Phys. Rev. E **48**, 2140, (1993).

[2] J. M. Byrd, G. Stupakov, *Proc. of the 1998 Conf. on Quantum Aspects of Beam Physics*, ed. P. Chen (1998).

[3] T. Kasuga, H. Yonehara, M. Hasumoto, and T. Kinoshita, *Jpn. J. Appl. Phys.* **28** (1989) 541. M. Tobiyama, A. Higuchi, T. Mitsuhashi, T. Kasuga, S. Sakanaka, *Proc. of the 1995 Part. Accel. Conf.* (1995) 3300.

[4] W. Decking, D. Robin, Proc. of the 16th Advanced Beam Dynamics Workshop, Arcidosso, (1998).

[5] M. Ellison, et. al., Phys. Rev. Lett. **70**, 591, (1993). H. Huang, et. al., Phys. Rev. E **48**, 4678, 1993. G. Tsironis, S. Peggs, T. Chen, 1990 EPAC, p1753. J. Ellison, H.-J. Shih, M. Kummer, Phys. Rev. E **49**, 2484, (1994). D. Li et al., Phys. Rev. E **48**, 1638, (1993). D. Li et al., Nucl. Instr. Methods A 361, p. 205–223 (1995).

[6] J. M. Byrd, W.H. Cheng, F. Zimmermann, Phys. Rev. E **57**, 4706, (1998).

Beam Manipulation with an RF dipole[†]

Mei Bai

BNL, Upton, NY 11973, U.S.A

Abstract

Coherent betatron motion adiabatically excited by an RF dipole has been successfully employed to overcome strong intrinsic spin depolarization resonances in the AGS, while a solenoid partial snake has been used to correct imperfection spin resonances. The experimental results showed that a full spin flip was obtained in passing through an intrinsic spin resonance when all the beam particles were forced to oscillate coherently at a large amplitude without diluting the beam emittance. With this method, we have successfully accelerated polarized beam up to 23.5 GeV/c. A new type of second order spin resonances was also discovered. As a non-destructive manipulation, this method can also be used for nonlinear beam dynamics studies and beam diagnosis such as measuring phase advance and betatron amplitude function.

1 INTRODUCTION

For various purposes, one often needs to excite a coherent oscillation in an accelerator. However, the free coherent oscillation excited by a short pulsed dipole kicker can quickly decohere and cause beam emittance growth due to the tune spread arising from the chromatic and other effects. Alternatively, coherent oscillation can also be excited by driving beam with an RF dipole which provides a magnetic field oscillating at a frequency close to the beam free betatron oscillation frequency. If the excitation is made adiabatically by slowly energizing the RF dipole field, it can be well controlled and also keep beam emittance preserved. This nice feature is very useful for many applications which desire a non destructive beam manipulation. This method has been successfully applied in the Brookhaven National Laboratory AGS polarized proton acceleration experiment to maintain the beam polarization through strong intrinsic spin resonances. This paper discusses the application of RF dipole in spin manipulation as well as in beam diagnosis and non-linear beam dynamics studies.

As a driven oscillator, the beam coherent oscillation is determined by the RF dipole field strength and its frequency. Consider a particle driven by an RF dipole where the betatron amplitude function is β_z. Here, z is used to denote the vertical coordinate. The same discussion also applies to the horizontal plane. The RF dipole field ΔB oscillates as

$$\Delta B = \Delta B_{\mathrm{m}} \cos \nu_m \phi(s), \qquad (1)$$

where ΔB_{m} is the oscillating amplitude of the RF dipole field, ν_{m} is the modulation tune defined as the ratio of the RF dipole oscillating frequency to the accelerator's revolution frequency, and $\phi(s)$ is azimuthal angle along the accelerator. In an accelerator with linear magnetic fields, the particle's equation of motion becomes

$$z'' + K_z(s)z = -\frac{\Delta B_{\mathrm{m}}(s)}{B\rho} \cos \nu_{\mathrm{m}}\phi(s), \qquad (2)$$

where the prime is the derivative with respect to the longitudinal coordinate s and k_z is the focusing strength. Its Hamiltonian is

$$H = \frac{1}{2}z'^2 + \frac{1}{2}K_z z^2 + \frac{\Delta B_{\mathrm{m}}}{B\rho} z \cos \nu_{\mathrm{m}}\phi. \qquad (3)$$

At resonance $\nu_{\mathrm{m}} = n \pm \nu_z$, the resonance term dominates the Hamiltonian. Here, n is an integer. Expressing the Hamiltonian in terms of action J and its conjugate variable ψ, the new Hamiltonian $H(J,\psi)$ becomes

$$H(J,\psi) \approx \nu_z J + \frac{1}{2}\sqrt{2J}|C_{\mathrm{res}}| \cos(\psi - n\phi + \nu_{\mathrm{m}}\phi), \quad (4)$$

where $|C_{\mathrm{res}}| = \frac{\Delta B \ell}{2\pi B\rho} \sqrt{\beta_z}$. Transferring this Hamiltonian into the resonant frame which rotates with the RF dipole driving frequency, we have

$$H(J,\psi) \approx \delta J + \frac{1}{2}\sqrt{2J}|C_{\mathrm{res}}| \cos \psi, \qquad (5)$$

where the resonance proximity parameter $\delta = \nu_z - (n - \nu_{\mathrm{m}})$ is the distance of the external excitation to the resonance. In general, this is a very small number.

The stable fixed point in Eq. (5) is

$$J_{\mathrm{SFP}} = \frac{1}{2}\left(\frac{C_{\mathrm{res}}}{2\delta}\right)^2, \qquad (6)$$

Hence, the amplitude of the excited oscillation Z_{coh} is

$$Z_{\mathrm{coh}} = \sqrt{2\beta_z J} = \frac{\Delta B_{\mathrm{m}}\ell}{4\pi(B\rho)|\delta|} \beta_z, \qquad (7)$$

where $B\rho$ is the momentum per charge. This shows that for an accelerator with linear magnetic fields, the RF dipole has to be slightly off resonance to maintain the beam stability. Eq. (7) can also be illustrated by the particle's phase space motion in the resonant frame [1].

This method was successfully tested at the Brookhaven AGS with Au^{+77} beam during the heavy ion physics run [1]. The experiment demonstrated that a large coherent oscillation can be adiabatically induced by slowly ramping the RF dipole field oscillation amplitude. Duration time of the excited oscillation is determined by the length of the RF dipole field pulse. Beam emittance was preserved after the

Figure 1: Measured transverse rms beam size versus time in an AGS acceleration cycle (top) and corresponding turn-by-turn beam position monitor data in the AGS cycle (bottom). The beam profiles are displayed in an mountain-range fashion.

manipulation. The top part of Fig. 1 is a typical example of the beam profile measurement and the corresponding beam coherent oscillation measured by a turn-by-turn beam position monitor . It clearly shows the beam emittance before and after the excitation remained constant. The beam profile was measured with the AGS IPM (Ionization Profile Measurement) system. The seemed bigger emittance during the excitation is because every IPM measurement takes 3 ms which is about 900 revolutions around the accelerator, and is the combination of the coherent motion and the actual beam size, i.e.

$$\sigma_{mea} = \sigma_0 \sqrt{1 + \frac{Z_{\text{coh}}}{2\sigma_0}}, \qquad (8)$$

where σ_{mea} and σ_0 are the measured beam size and actual beam size.

For an accelerator with non-linear magnetic fields, the RF dipole driven oscillation becomes more complicated and the simple relation of Eq. (7) is no longer valid. The most common non-linearity in an accelerator is detuning effect arising from the octupole magnetic fields and the second order effect of sextupoles. In the presence of those higher order multipole magnetic fields, the beam betatron oscillation tune is no longer independent of the size of the betatron oscillation. Assuming the coupling effect between the two transverse planes is negligible, the detuning effect then adds an additional term to the Hamiltonian in Eq. (9).

$$H(J, \psi) \approx \delta J + \frac{1}{2}\alpha_{zz}J^2 + \frac{1}{2}\sqrt{2J}|C_r es|\cos\psi \qquad (9)$$

where α_{zz} is the detuning coefficient. Fig. 2 shows the corresponding Poincare when the RF dipole modulation tune is above a certain bifurcation tune.

Figure 2: The Poincarer surface of section in the resonant frame which rotates with the RF dipole modulation frequency. w_1 and w_2 are the two stable fixed points. w_3 is the unstable fixed point.

2 APPLICATIONS OF BEAM MANIPULATION WITH AN RF DIPOLE

2.1 Overcoming intrinsic spin resonance

Intrinsic spin resonance is one of the common spin depolarization mechanisms in circular accelerators. It is driven by the quadrupole focusing magnetic fields due to the vertical betatron oscillation. For a perfect synchrotron with only the vertical magnetic guiding fields, the spin vector precesses about the vertical axis $G\gamma$ times per revolution, where $G = (g-2)/2 = 1.7928474$ is the proton anomalous magnetic g-factor, and γ is the relativistic Lorentz factor. $G\gamma$ is called the spin tune. Under the influence of the quadrupole focusing fields, the spin motion is perturbed. The perturbation is normally small. However, when the frequency at which the spin vector is perturbed coincides with the spin precession frequency, the spin vector is kicked away from the vertical direction constructively and a spin resonance occurs. Thus, the intrinsic spin resonance condition is $G\gamma = kP \pm \nu_z$, where k is an integer, P is the superperiods and ν_z is the vertical betatron tune [3, 4]. The other common spin depolarization mechanism is imperfection spin resonance which locates at $G\gamma = kP$ [3, 4].

The polarization after a beam crossing an isolated spin resonance is given by the Frossiart-Stora formula[5]

$$P_f = \left(2e^{-\pi|\epsilon_K|^2/2\alpha} - 1\right) P_i \qquad (10)$$

where P_i is the beam polarization before crossing the spin resonance. ϵ_K is the resonance strength, α is resonance crossing rate given by

$$\alpha = \frac{d(G\gamma - kP \mp m\nu_z)}{d\theta}, \qquad (11)$$

and θ is the orbiting angle in the synchrotron.

For an intrinsic spin resonance, the strength is proportional to the betatron oscillation amplitude. Normally in a

beam, particles close to the core of the beam oscillate less than particles around the edge. Thus, the final polarization is an ensemble average of the Frossiart-Stora formula over the betatron amplitude of the beam particles. Using the Gaussian beam distribution model, the final polarization becomes

$$P_f = \left(\frac{1 - \pi |\epsilon_{rms}|^2/\alpha}{1 + \pi |\epsilon_{rms}|^2/\alpha} \right) P_i \,, \tag{12}$$

where ϵ_{rms} is the spin resonance strength for a particle with an rms emittance. For a given intrinsic spin resonance, no polarization will be lost if the resonance is crossed very fast, i.e. $\frac{\pi |\epsilon_{rms}|^2}{\alpha} \ll 1$. Although the fast-crossing resonance can be achieved by jumping the betatron tune with fast quadrupoles [6], it is a non-adiabatic manipulation and can cause beam emittance growth. On the other hand, the beam polarization can be preserved by crossing the resonance slowly so that the spin vector can be adiabatically flipped ($P_f = -P_i$). However, for strong spin resonance, this method is limited.

Alternatively, a full spin flip can also be obtained under the normal acceleration rate by enhancing the resonance strength. For intrinsic spin resonances, the effective resonance strength in Eq. (12) can be greatly strengthened in the presence of a large amplitude coherent oscillation which can be adiabatically excited by an RF dipole. Since the betatron coordinate can be expressed as the linear combination of the vertical betatron motion and the coherent betatron motion [?], the particles experience not only the intrinsic spin resonance, but also a coherent spin resonance at the driving frequency. The resulting polarization, in the limiting case that the driving frequency coincides with the free oscillation frequency, is given by [2]

$$\langle \frac{P_f}{P_i} \rangle = \frac{2}{1 + \pi |\epsilon_{rms}|^2/\alpha} \tag{13}$$

$$\exp \left\{ -\frac{(Z_{coh}^2 \hat{\beta}_z / 2\beta_z \sigma_z^2)(\pi |\epsilon_{rms}|^2/\alpha)}{1 + \pi |\epsilon_{rms}|^2/\alpha} \right\} - 1,$$

and in the case that the two resonances are well separated, by

$$\langle \frac{P_f}{P_i} \rangle = \frac{1 - \pi |\epsilon_{rms}|^2/\alpha}{1 + \pi |\epsilon_{rms}|^2/\alpha} \tag{14}$$

$$\left(2 \exp \left\{ -\frac{Z_{coh}^2 \hat{\beta}_z}{\beta_z \sigma_z^2} \frac{\pi |\epsilon_{rms}|^2}{2\alpha} \right\} - 1 \right).$$

Here $\hat{\beta}_z$ is the maximum vertical betatron function in the accelerator, and σ_z is the rms beam size. Any case in between can produce rich interference patterns and the beam polarization is determined by both the relative strengths and phase of the two resonances [10].

Experimental results

This method has been successfully tested in the AGS polarized proton acceleration experiments [9] for attaining a full spin flip at intrinsic spin resonances. Acceleration of polarized protons in the AGS up to 25 GeV/c encounters 7 intrinsic spin resonances at $0 + \nu_z, 12 + \nu_z, 24 - \nu_z, 36 - \nu_z, 24 + \nu_z, 48 - \nu_z$ and $36 + \nu_z$. Among them, $0 + \nu_z$, $12 + \nu_z$ and $36 \pm \nu_z$ are strong ones. The beam polarization losses at the other three spin resonances are negligible under the AGS normal acceleration speed. The imperfection spin resonances during the polarized proton acceleration were corrected by the AGS 5% partial snake [7, 8].

Figure 3 shows the measured polarization at three intrinsic resonances vs the coherent oscillation amplitude which is proportional to the RF dipole strength. The data at spin resonance $12 + \nu_z$ (in the middle plot) demonstrates that the spin was fully flipped at large coherent oscillations when the measured polarization saturated. The same result is also indicated from the data at $0 + \nu_z$ (in the bottom plot) and $36 - \nu_z$ (in the top plot) with the smallest resonance proximity parameter δ. The systematic error of the beam polarization was estimated to be 10%, and the statistical error was about ± 3 %. The lines shown on the figure correspond to results obtained from numerical spin simulations of two spin resonances model.

Since the spin resonance at $12 + \nu_z$ was relatively weak, the measured polarization depended smoothly on the dipole field strength shown in the middle plot of Fig. 3. On the other hand, since the intrinsic spin resonances at $0 + \nu_z$ and $36 - \nu_z$ were strong enough to partially flip the spin, they strongly interfered with the coherent spin resonance induced by the RF dipole. A significant interference pattern is shown in the top and the bottom plots of Fig. 3, where the degree of spin flip also depends on the relative phase. In agreement with the numerical simulation, the upper and lower plots of Fig. 3 show complicated interference patterns when the tune separation is large. Nevertheless, a full spin flip can eventually be obtained when the strength of the RF-induced spin resonance becomes strong.

2.2 Measure betatron amplitude function

Both the betatron amplitude function and phase advance are very important parameters for accelerators [?, ?, ?]. The coherent oscillation adiabatically excited by an RF dipole can be maintained for thousands of revolutions around the accelerator is very useful for measuring these two parameters in the machine. Especially, since this is a non-destructive method, it can also be used as a routine diagnostic tool for machine operation.

Assuming there are two beam position monitors (BPMs) which can measure the turn-by-turn betatron oscillation in the accelerator as shown Fig. 4, the coordinates at BPM2 are related with the coordinates at BPM1 through the transfer matrix between the two BPMs.

Therefore, x_1' can then be expressed by the positions at the two BPMs, i.e.

$$x_1' = \frac{x_2}{\sqrt{\beta_1 \beta_2} \sin \psi_{21}} - \frac{\cot \psi_{21} + \alpha_1}{\beta_1} x_1. \tag{15}$$

389

Figure 3: The measured proton polarization vs the coherent betatron oscillation amplitude (in mm) for different tune separations at spin depolarizing resonances $0 + \nu_z$ (bottom plot), $12 + \nu_z$ (middle plot), and $36 - \nu_z$ (upper plot) respectively. The error bars show only the statistical errors. The resonance strength of the coherent spin resonance due to the RF dipole is promotional to the coherent betatron amplitude. The lines are the results of multiparticle spin simulations based on the two nearby spin resonances model.

Figure 4: the schematic drawing of using an RF dipole and two BPMs to measure the linear optics.

where β_i and α_i, i=1,2, are the twiss parameters at BPM1 and BPM2, respectively. ψ_{21} is the phase advance between the two BPMs. Since

$$x_1^2 + (\beta_1 x_1' + \alpha_1 x_1)^2 = 2\beta_1 J, \tag{16}$$

x_1 and x_2 satisfy the elliptical equation

$$x_1^2 + (\sqrt{\frac{\beta_1}{\beta_2}} \frac{x_2}{\sin \psi_{21}} - \cot \psi_{21} x_1)^2 = 2\beta_1 J. \tag{17}$$

Hence, the ratio of the betatron functions $\sqrt{\frac{\beta_1}{\beta_2}}$, the phase advance between the two BPMs ψ_{21} and $\beta_1 J$ can be obtained by fitting the turn-by-turn data recorded at the two BPMs.

In the same spirit, this method can also be applied for the non-linear beam dynamics diagnosis and studies in accelerators [11]. Beside manipulating beam motion, an RF dipole can also be used as a spin flipper to change the spin vector by 180° degrees[12]. For this application, the RF dipole introduces an artificial spin resonance at its oscillating frequency. By slowly ramping its frequency through the spin precession frequency, a full spin flip can be obtained (See Eq. (10)).

Unlike the strength of the spin resonance due to the large amplitude coherent oscillation by operating an RF dipole close to the vertical betatron tune which is proportional to the amplitude of the oscillation (see Eq. (3.37)), the resonance strength of a spin flipper is independent of the lattice parameters and fully determined by the magnetic field strength of the spin flipper. Based on the Thomas-BMT equation, the resonance strength is given by

$$\epsilon_K = \frac{1 + G\gamma}{4\pi} \frac{\Delta B \Delta L}{B\rho}, \tag{18}$$

where $\Delta B \Delta L$ is the integrated field strength of the spin flipper. To achieve more than 99% spin flip, the spin resonance strength ϵ_K of the spin flipper should be greater than $1.84\sqrt{\alpha}$.

3 CONCLUSION

It was demonstrated that a sustained coherent oscillation with large amplitude can be adiabatically excited by an RF dipole while the beam emittance is preserved. This method has been successfully applied in the AGS polarized proton acceleration to overcome strong intrinsic spin depolarizing resonances. As a non-destructive method, it can also find other applications in beam diagnostics and dynamics studies, spin manipulations and etc.

4 ACKNOWLEDGMENT

5 REFERENCES

[1] M. Bai et al., Phys. Rev. E56, 5 (1997).

[2] M. Bai, S. Y. Lee, H. Huamg, T. Roser and M. Syphers, AGS Tech Note.

[3] E.D. Courant and R. Ruth, BNL report, BNL-51270 (1980).

[4] See e.g., S.Y. Lee, *Spin Dynamics and Snakes in Synchrotrons*, (World Scientific Pub. Co., Singapore, 1997)

[5] M. Froissart, and R. Stora, Nucl. Inst. Meth. **7**, 297 (1960).

[6] B.B. Blinov, *et al.*, Phys. Rev. Lett. **73**, 1621 (1994).

[7] T. Roser, in *High-Energy Spin Physics-1988, Proceedings of the 8th International Symposium on High-Energy Spin Physics*, Minneapolis, 1988, edited by K. J. Heller, AIP Conf. Proc. No. 187 (AIP, New York, 1989), P.1442.

[8] H. Huang *et al.*, Phys. Rev. Lett. **73**, 2982 (1994); Ph.D. Thesis, Indiana Unversity (1995), unpublished;

[9] M. Bai *et al.*, *Overcoming Intrinsic Spin Resonances with an rf Dipole* Phys. Rev. Lett. **80**, 4673 (1998).

[10] S. Tepikian, S.Y. Lee, E.D. Courant, Particle Accelerators **20**, 1 (1986).

[11] S. Peggs, "*Nonlinear Diagnostics Using AC Dipoles*", Particle Accelerator Conference 1999, New York.

[12] A. Chao and M. Tigner, *Handbook of Accelerator Physics and Engineering*, to be published.

SIBERIAN SNAKE EXPERIMENTS AT THE IUCF COOLER RING *

<u>V.A. Anferov</u>[†], B.B. Blinov, D.A. Crandell, Ya.S. Derbenev, T. Kageya, S.V. Koutin, A.D. Krisch,
R.A. Phelps, W. Lorenzon, L.G. Ratner, D.W. Sivers, K.V. Sourkont, V.K. Wong, S.S. Youssof,
Univ. of Michigan, Ann Arbor, MI
C.M. Chu, S.Y. Lee, T. Rinckel, P. Schwandt, F. Sperisen, B. von Przewoski, IUCF, Bloomington, IN
V.N. Grishin, P.A. Semenov, IHEP, Protvino, Russia
H. Sato, HEARO, Tsukuba, Japan

Abstract

Recent polarized proton beam experiments in the IUCF
Cooler Ring found an evidence for a second-order snake
depolarizing resonance, when the vertical betatron tune
was inadvertently set near a quarter-integer. We have also
studied the possibility of spin-flipping the beam polariza-
tion in the presence of a full Siberian snake using an rf
solenoid. By varying the rf solenoid's ramp time and fre-
quency range, we reached a spin-flip efficiency of about
97%.

1 SECOND-ORDER SNAKE DEPOLARIZING RESONANCE

One must overcome many spin depolarizing resonances to
accelerate a polarized proton beam to high energy. Ear-
lier IUCF experiments [1] suggest that the Siberian snake
technique [2] could universally overcome all intrinsic and
imperfection depolarizing resonances even at high energy.
However, another type of depolarizing resonances called
"snake" resonances could occur at certain values of the ver-
tical betatron tune even in the presence of a full Siberian
snake in a ring. Using a 104 MeV stored polarized proton
beam and a full Siberian snake, we recently found evidence
for a second-order "snake" depolarizing resonance.

In any circular accelerator or storage ring, each proton's
spin precesses around the vertical fields of the ring's dipole
magnets. The spin tune ν_s, which is the number of spin
precessions during one turn around the ring, is proportional
to the proton's energy

$$\nu_s = G\gamma , \tag{1}$$

where γ is the Lorentz energy factor and $G = 1.792847$
is the proton's anomalous magnetic moment. The beam
can be depolarized when the spin precession frequency is
synchronized with some horizontal magnetic field, which
can be caused either by the ring's imperfections or by the
vertical betatron oscillations. These spin perturbations are
called imperfection and intrinsic depolarizing resonances,
respectively; they occur when the spin tune is equal to an
integer or to a harmonic of the betatron tune ν_y:

$$\nu_s = G\gamma = n \pm k\nu_y, \tag{2}$$

where n and k are integers.

A full Siberian snake makes the spin tune energy inde-
pendent at a half-integer; thus, it should overcome all im-
perfection and first-order intrinsic depolarizing resonances.
However, in a ring with its betatron tune near a quarter in-
teger, the snake can cause a second-order depolarizing res-
onance whenever

$$\nu_s = n \pm 2\nu_y, \tag{3}$$

where n is an integer. Such a snake resonance [3] could
depolarize a high-energy polarized beam.

We recently studied a second-order snake resonance us-
ing a 104.1 MeV polarized proton beam with a full Siberian
snake in the IUCF Cooler Ring. The experimental appa-
ratus, as shown in Fig. 1, included the snake's supercon-
ducting solenoid and eight correction quadrupoles, the po-
larimeter, the rf dipole, and the rf solenoid. The electron
cooling section consists of the main solenoid, two toroidal
magnets, two correction solenoids (CSA and CSB), and a
set of vertical steerers to compensate for the orbit perturba-
tion in the toroidal magnets.

It was shown earlier [4] that the electron cooling section
produces an additional spin rotation which shifts the spin
tune even in the presence of a full Siberian snake. By vary-
ing the current in the correction solenoids (CSA and CSB)

Figure 1: The IUCF Cooler Ring with the Siberian snake,
the rf solenoid, the rf dipole, the polarimeter, and the
CSA/CSB correction solenoids.

Figure 2: The measured radial polarization P_r is plotted against the field integral in the correction solenoids (CSA and CSB) for different ν_y values. The dashed curves are hand-drawn lines to guide the eye.

one can effectively vary the spin tune at a rate of about $0.00036 \, A^{-1}$. We used this technique as a sensitive tool to study weak second-order snake depolarizing resonance.

When the vertical betatron tune was inadvertently set at 4.763, we found the broad partial depolarization region, shown in Fig. 2a. The data suggested proximity to a second-order snake resonance because ν_y was near a quarter-integer. To test this hypothesis, we then changed ν_y to 4.756, and observed the much stronger depolarization dip, shown in Fig. 2b. Finally, we moved ν_y away from the quarter-integer to 4.781. As expected, the beam polarization returned to its full value, as shown in Fig. 2c. Our future plans include further studies of higher-order snake resonances.

2 SPIN-FLIPPING IN THE PRESENCE OF A FULL SIBERIAN SNAKE

Spin-polarized beam experiments in storage rings such as the IUCF Cooler Ring, HERA [5], RHIC [6] and possibly Fermilab [7], require frequent reversals of the beam polarization direction to reduce the systematic errors in the measured asymmetry. An rf solenoid was used earlier to spin-

flip a vertically polarized proton beam stored in a ring with no Siberian snake [8]. Since any very high energy ring will need full Siberian snakes to maintain the proton beam polarization, it is important to develop spin-flipping capability in the presence of a full snake. Using an rf solenoid, we made the first spin-flipping demonstration of a stored polarized proton beam with an efficiency of $91\pm1\%$ [9]. We then tried to improve the spin-flipping efficiency by eliminating possible synchrotron sidebands and by using a weak rf dipole.

Even with a full Siberian snake in a ring, an rf magnetic field from either an rf solenoid or an rf dipole can induce an rf depolarizing resonance; this resonance is sometimes called a snake resonance, because it only exists at its frequency in the presence of a Siberian snake. Such resonances can be used to flip the spin direction of the ring's stored polarized protons.

The frequency f_r, at which an rf magnet can induce a depolarizing resonance, is given by

$$f_r = f_c(k \pm \nu_s), \qquad (4)$$

where f_c is the proton's circulation frequency, and k is an integer. Slowly sweeping the rf magnet's frequency through f_r can flip the spin. The Froissart-Stora equation [10] gives the ratio of P_f, the polarization after crossing the resonance, to the initial polarization P_i,

$$P_f = P_i \left(2 \exp\left[\frac{-(\pi w)^2}{4\Delta f / \Delta t} \right] - 1 \right), \qquad (5)$$

where w is the resonance width in Hz, and $\Delta f / \Delta t$ is the resonance crossing rate with Δf being the frequency range during the ramp time Δt.

With a nearly full Siberian snake in the ring, the spin tune ν_s is very close, but is not exactly equal, to 0.5. Thus, there

Figure 3: The measured radial proton polarization at 104.1 MeV is plotted against the frequency of the rf solenoid and of the rf dipole. The rf solenoid's data ($\bullet$) are fitted with a third-order Lorentzian (solid curve). The rf dipole's data ($\times$) are fitted with a first-order Lorentzian (dashed curve).

should be two closely spaced rf depolarizing resonances around $1.5f_c = 2.2574$ MHz. We excited these rf depolarizing resonances by operating the rf solenoid and the rf dipole near 2.25 MHz. The rf solenoid's amplitude was set at 6 kV, which corresponds to an $\int B \cdot d\ell = 1.6$ T·mm; the single turn horizontal kicker was operated as an rf dipole at 23 V giving $\int B \cdot d\ell$ about 0.03 T·mm. The measured radial polarization is plotted against the rf solenoid and rf dipole frequency in Fig. 3. For the rf solenoid's induced resonance, the resonance frequency and width were found to be $f_1 = 2,275,410 \pm 43$ Hz and $w_1 = 2,270 \pm 90$ Hz. For the rf dipole's induced resonance, they were $f_2 = 2,275,530 \pm 10$ Hz and $w_2 = 540 \pm 30$ Hz.

We then studied spin-flipping with a nearly full Siberian snake by crossing the rf induced snake resonance; we linearly ramped the frequency, of the rf solenoid or the rf dipole, through a frequency range Δf which included the resonance frequency f_r at various ramp times Δt. The radial beam polarization measured after each ramp is plotted in Fig. 4. Clearly the spin-flip efficiency is much better with the rf solenoid than with the rf dipole. By comparing the measured polarization of $58.2 \pm 2.1\%$ at $\Delta t = 0$ with the average polarization of $-20 \pm 2\%$ at long dipole ramp times, we found a $30 \pm 4\%$ dipole spin-flip efficiency.

To better estimate the solenoid's spin-flip efficiency, we measured the beam polarization after many spin-flips. We varied the number of spin-flips, while keeping the ramp time, frequency range and the rf voltage fixed; the data are shown in Fig. 5. We fit the data using the equation

$$P = P_i \cdot \epsilon^n, \tag{6}$$

where P_i is the initial polarization, ϵ is the spin-flip efficiency, and n is the number of spin-flips. The best fit to the spin-flip efficiency is $97 \pm 1\%$. We plan to study further this spin-flipping technique for both a nearly full and an exactly 100% Siberian snake.

3 REFERENCES

[1] A.D. Krisch *et al.*, Phys. Rev. Lett. **63**, 1137 (1989); J.E. Goodwin *et al.*, Phys. Rev. Lett. **64**, 2779 (1990).

[2] Ya.S. Derbenev and A.M. Kondratenko, Sov. Phys. Dokl. **20**, 562 (1978).

[3] S.Y. Lee and S. Tepikian, Phys. Rev. Lett. **56**, 1635 (1986).

[4] R.E. Pollock, Nucl. Instr. Meth. **300**, 210 (1991).

[5] SPIN Collaboration and DESY Polarization Team, *Acceleration of polarized protons to 820 GeV at HERA*, University of Michigan Report UM-HE 96-20 (1996).

[6] Y. Makdisi, Proc. 11th International Symposium on High Energy Spin Physics, Bloomington 1994, AIP Conf. Proc. **343**, 75 (1995).

[7] SPIN Collaboration, *Acceleration of polarized protons to 120 GeV and 1 TeV at Fermilab*, University of Michigan Report UM-HE 95-09 (1995).

[8] D. D. Caussyn *et al.*, Phys. Rev. Lett. **73**, 2857 (1994).

[9] B.B. Blinov *et al.*, Phys. Rev. Lett. **81**, 2906 (1998).

[10] M. Froissart and R. Stora, Nucl. Instr. Meth. **7**, 297 (1960).

Figure 4: The measured radial proton polarization at 104.1 MeV is plotted against the ramp time Δt of the rf dipole (a) and the rf solenoid (b). The frequency ranges Δf were 3 kHz for the rf dipole, and 12 kHz for the rf solenoid. The curve is a fit to the data using Eq. (5).

Figure 5: The measured radial proton polarization at 104.1 MeV is plotted against the number of spin-flips. The rf solenoid's ramp time Δt is 60 msec, and its frequency range Δf is 3.5 kHz. The curve is a fit using Eq.(6).

TUNE-SHIFT WITH AMPLITUDE DUE TO NONLINEAR KINEMATIC EFFECT*

W. Wan, FNAL, Batavia, IL

Abstract

Tracking studies of the Muon Collider 50 on 50 GeV collider ring [1] show that the on-momentum dynamic aperture is limited to around 10σ even with the chromaticity sextupoles turned off. Numerical results from the normal form algorithm show that the tune-shift with amplitude is surprisingly large. Both analytical and numerical results are presented to show that nonlinear kinematic effect originated from the large angles of particles in the interaction region is responsible for the large tune-shift which in turn limits the dynamic aperture. A comparative study of the LHC collider ring is also presented to demonstrate the difference between the two machines.

Figure 1: Dynamic aperture of the 50 on 50 GeV collider ring, with sextupoles (a) on and (b) off. Tracking was done using the code COSY INFINITY [14]

1 INTRODUCTION

Nonlinear effects have been studied in detail throughout the history of alternating gradient accelerators. Among the different approaches [2], the canonical perturbation theory developed and introduced to the accelerator community by Moser [3] has become the *de facto* standard method to treat resonances analytically (for early reviews, see references [4, 5, 6]). Over the years, calculations of first [6], second [4, 5, 8] and, at least in one instance [7], third order perturbations were carried out. Among all the works mentioned above, one common assumption is paraxial approximation, which assumes that $p_{x,y}/p_0 \ll 1$ and keeps only quadratic terms of $p_{x,y}/p_0$ in the Hamiltonian. Until recently paraxial approximation, together with the canonical perturbation theory, has proven itself rather effective to describe single particle dynamics of high energy accelerators. One of the most important prediction of paraxial approximation is that, free of nonlinear field, the motion of a particle is purely linear, which entails that stability, once established, is global.

With the advance of the idea of muon colliders [1, 9], new constraints are placed on the collider rings due to the finite muon life time. In order to reach the desired luminosity, β^* and circumference have to be as small as possible. To remove detector background from muon decays and subsequent showers, the inner triplet of the low-β insertion has to be kept at a distance to the interaction point (IP). For example, the β^* and the distance from the IP to the inner triplet of the 50 on 50 GeV muon collider are 4 cm and 4.5 m, respectively. As a comparison, those of the Large Hadron Collider are 0.5 m and 23 m. In this report, numerical results are presented to demonstrate that paraxial approximation breaks down in the case of the 50 on 50 GeV muon collider ring. A first-order perturbation theory beyond paraxial approximation is developed to explain the simulation results and

establish algebraic relations between tune-shift with amplitude and the parameters mentioned above. Suggestion of a possible correction scheme is made in Section 4.

2 NUMERICAL EVIDENCE

It is well known that an accelerator free of errors can have a very large dynamic aperture for on-momentum particles. The reason is that the only nonlinear elements present, i. e. the chromaticity sextupoles, start to contribute to the tune-shift with amplitude only through the second-order perturbation, although they drive third-order resonances directly through first-order perturbation. Therefore, the tunes of the particles can be far away from major resonances at very large amplitude, when, for most purposes, the center tunes are so chosen. Taking again the Large Hadron Collider as an example, the dynamic aperture of its ideal collision lattice is well above 30 σ. Hence it was rather unexpected to learn that the dynamic aperture of the on-momentum particles is always below 10 σ, independent of the actual layout of the machine [10]. Furthermore, this is qualitatively true even when the sextupoles are turned off (see Fig. 1). Similar behavior was observed by the author using rather different arcs and Ohnuma [12] using a Runge-Kutta integrator for the inner triplet and a linear matrix for the rest of the ring. This study shows definitively that the limit of dynamic aperture lies in the interaction region.

An other indicator of the strength of nonlinearity is the tune-shift with amplitude. Fig. 2 depicts the tune-shift with amplitude obtained from DA normal form calculations. It is rather clear that even the lowest order contribution to the tune shift is very large, to the extent that it is hard to be-

	LHC	MC
L (m)	46	9
β^* (m)	0.5	0.04
$L\gamma^{*2}$ (1/m)	184	5625
ϵ_{rms} (π mm mrad)	0.168	0.0005
$\Delta\nu_x$ (10σ)	2.7e-7	0.0028

Figure 2: Tune footprint of the 50 on 50 GeV collider ring obtained from DA normal form calculations using the third-order one-turn map. Left plot: The lower left corner of the diagram represent the center tunes; the upper right corner represent the tunes of the particle with $x, y = 5\sigma$, $p_x, p_y = 0$; the lower right corner represent the tunes of the particle with $x = 5\sigma$, $y, p_x, p_y = 0$. Right: Same as the left one except that the maximum displacement is 10σ.

Table 1: Tune shifts are calculated assuming $x = 10\sigma$ and the other coordinates equal 0.

lieve that it actually reflects reality. In fact, it appears from the numerical results that the Taylor serieses of the tunes as functions of normal coordinates are divergent, which shows how strongly paraxial approximation has been violated.

3 FIRST-ORDER PERTURBATION THEORY

Since there is no nonlinear field in the interaction region, the only source of nonlinearity is the high-order terms in $P_s = \sqrt{P^2 - P_x^2 - P_y^2}$, which demonstrates that for the 50 on 50 collider ring paraxial approximation is no longer valid. To move beyond paraxial approximation, we go back to the exact Hamiltonian, which is, following the notation in [11],

$$H = -p_s = -\frac{e}{c}A_s - \left(1 + \frac{x}{\rho}\right)\sqrt{(P^2 - P_x^2 - P_y^2)}, \quad (1)$$

where p_s and A_s are the longitudinal momentum and the vector potential, respectively. Note that Eq. (1) is exact only when there is not electric field present and fringe field is neglected. Since only the interaction region is of our interest, $\rho \to 0$. Furthermore, P is set to P_0, for only on-momentum particles are considered. Finally, after normalizing P_x, P_y and H by P_0 and expanding P_x and P_y to the fourth power, the Hamiltonian becomes

$$H = \frac{1}{2}P_x^2 + \frac{1}{2}P_y^2 - \frac{1}{2}K_1(s)x^2 + \frac{1}{2}K_1(s)y^2 + \frac{1}{8}\left(P_x^2 + P_y^2\right)^2. \quad (2)$$

To develop a canonical perturbation theory, it is more convenient to use action-angle variables, which transform the Hamiltonian to

$$H_1 = \frac{J_x}{\beta_x} + \frac{J_y}{\beta_y} - \frac{1}{2}\left[\frac{J_x}{\beta_x}(\sin\theta_x + \alpha_x\cos\theta_x)^2 + \frac{J_y}{\beta_y}(\sin\theta_y + \alpha_y\cos\theta_y)^2\right]^2. \quad (3)$$

After straightforward derivation, the angle independent part

of the Hamiltonian is obtained, which is

$$H_{10} = \frac{J_x}{\beta_x} + \frac{J_y}{\beta_y} + \frac{1}{2}\left(\frac{3}{8}\gamma_x^2 J_x^2 + \frac{1}{2}\gamma_x\gamma_y J_x J_y + \frac{3}{8}\gamma_y^2 J_y^2\right). \quad (4)$$

As a result, the tunes are

$$\nu_x(\vec{J}) = \nu_{x0} + \frac{1}{2\pi}\int_0^C \left(\frac{3}{8}\gamma_x^2 J_x + \frac{1}{4}\gamma_y^2 J_y\right), \quad (5)$$

$$\nu_y(\vec{J}) = \nu_{y0} + \frac{1}{2\pi}\int_0^C \left(\frac{1}{4}\gamma_x^2 J_x + \frac{3}{8}\gamma_y^2 J_y\right), \quad (6)$$

where C is the circumference of the machine.

Since γ is inversely proportional to β, the drift space between the inner triplets may contribute significantly to the tune-shift with amplitude. Although numerical results show that it constitutes a small fraction of the total tune footprint, it can be used as a parameter to roughly estimate the validity of paraxial approximation. Since γ remains constant throughout a drift space, the tune-shift with amplitude given by Eq. (6) is greatly simplified, which are

$$\Delta\nu_x = \frac{1}{2\pi}\left(\frac{3}{8}\gamma_x^2 J_x + \frac{1}{4}\gamma_y^2 J_y\right)L, \quad (7)$$

$$\Delta\nu_y = \frac{1}{2\pi}\left(\frac{1}{4}\gamma_x^2 J_x + \frac{3}{8}\gamma_y^2 J_y\right)L, \quad (8)$$

where L is the length of the drift. Table 3 illustrates the drastic contrast between the Large Hadron Collider and the 50 on 50 GeV muon collider. Note that the tune shift of the muon collider listed here is comparable to the beam-beam tune shift of the Large Hadron Collider. [14]

4 CONCLUSION

Numerical simulations show that paraxial approximation is not valid for the 50 on 50 GeV muon collider. First-order canonical perturbation theory is developed taking into account the next to leading order terms in P_x and P_y. With respect to the correction of the first-order tune shift, octupole pairs can be placed at high β locations with 45° phase separation, same polarity and strengths adjusted properly to cancel the tune-shift without driving resonances. It is most desirable to place the pair at locations where β_x/β_y are equal, because all resonances driven by octupoles can be completely suppressed. Otherwise only partial suppression can be achieved.

5 ACKNOWLEDGEMENTS

6 REFERENCES

[1] Charles M. Ankenbrandt, et. al., BNL-65-623, Fermilab-PUB-98/179, LBNL-41935, (submitted to Phys. Rev. ST Accel. Beams).

[2] See Section 1 of Ref. [5] and references therein.

[3] J. Moser, Nachr. Akad. Wiss. Göttingen, IIa, Nr. **6** 87 (1955).

[4] R. Hagedorn, CERN 57-1 (1957).

[5] A. Schoch, CERN 57-21 (1958).

[6] G. Guignard, CERN 78-11 (1978).

[7] F. Willeke, FN-422 (1985).

[8] Z. Parsa, S. Tepikian and E. Courant, Part. Accel. **22**, 205 (1985).

[9] C. Johnstone, W. Wan and A. Garren, this proceedings.

[10] See Section VII of Ref. [1] .

[11] R. Ruth, in "Physics of High Energy Particle Accelerators", edited by M. Month, P. F. Dahl and M. Dienes, AIP Conf. Proc. No. 127 (AIP, Woodbury, N. Y., 1985).

[12] S. Ohnuma, private communication

[13] M. Berz, Technical Report MSUCL-977, Michigan State University, (1995).

[14] N. Gelfand, C . Johnstone, T. Sen and W. Wan, this proceedings.

RESONANCE FREE LATTICES FOR A.G. MACHINES

A. Verdier

CERN SL Division

Abstract

A part of an alternating gradient circular machine composed of a number of identical cells N_c will not contribute to the excitation of most of the non-linear resonances to first order in multipole strength, if the two phase advances per cell take the values $2\pi k_1/N_c$ and $2\pi k_2/N_c$. k_1 and k_2 are any integers and $k_1 \neq k_2$. This property is demonstrated here. Its application to synchrotron light sources and colliders is discussed.

1 INTRODUCTION

The problem of non-linear resonances has been considered from the beginning in the design of AG machines [1]. The first synchrotrons had a high periodicity to avoid systematic resonances and this principle is still used widely. For a collider this is not possible because of the small number of insertions. In this case, the choice of a proper phase advance per cell in the arcs makes it possible to avoid most of the systematic non-linear resonances, thanks to the cancellation of their driving term per super-period.

It is shown here how to design these parts of a machine which are constituted of identical cells, so that they do not contribute to most of the non-linear resonances. Firstly some results of the resonance theory are recalled. The resonance driving term is computed for an ensemble of identical cells and the condition for resonance cancellation is derived. Eventually some applications are given.

2 DRIVING TERM OF A NON-LINEAR RESONANCE

The theory of non-linear resonances is quite old [2]. Apart from the pioneer Moser [1] many authors contributed in the accelerator field. The formulae used here are extracted from [3]. More modern approaches based on normal form analysis lead to similar results (see for instance [4]).

We consider here only the response in amplitude of an harmonic oscillator driven by the non-linear field associated with the unperturbed linear oscillation, **to first order in multipole strength**. The change of frequency with amplitude is not taken into account.

On a resonance of order n defined by $n_x.Q_x + n_y.Q_y = integer$, with $|n_x| + |n_y| = n$, the driving term, which originates from the Fourier transform of the non-linear field created by the excursion of the linear motion in the multipole b_n, is proportional to the circumferential integral [3]

$$
\mathcal{I} = \left| \int_0^C b_n \beta_x^{\frac{n_x}{2}} \beta_y^{\frac{n_y}{2}} e^{i(n_x\mu_x + n_y\mu_y)} ds \right| \quad (1)
$$

The resonance order n is the same as the multipole index for the main resonance. It is equal to $n - 2m$, where m is an integer, for the sub-resonances of order $n - 2m$ associated with the same multipole. These sub-resonances have a similar driving term.

The integral $\mathcal{I}$ can be easily calculated for a sequence of identical cells. Indeed the optics functions β_x and β_y have identical values at homologous places inside each cell and the phase advances in the $(p+1)^{th}$ cell are given by : $\mu_{x,p+1}(s) = \mu_{x,0}(s) + p\mu_{x,c}$ and $\mu_{y,p+1}(s) = \mu_{y,0}(s) + p\mu_{y,c}$, if the longitudinal coordinate s has its origin at homologous places inside each cell. $\mu_{x,c}$ and $\mu_{y,c}$ are the phase advances per cell in both planes, i.e. constants. Thus, making a straightforward change of variable : $s \rightarrow s + p \times Lc$, where Lc is the cell length, the contribution of the $(p+1)^{th}$ cell to the integral $\mathcal{I}$ (1) defined by equation (1) can then be written as the product of an integral, which is the same for all cells, and a phase term depending only on the index p and the phase advances per cell :

$$
e^{ip(n_x\mu_{x,c} + n_y\mu_{y,c})} \int_{cell} \beta_x^{\frac{n_x}{2}} \beta_y^{\frac{n_y}{2}} e^{i(n_x\mu_{x,0} + n_y\mu_{y,0})} ds.
$$
$$
(2)
$$

The integral $\mathcal{I}$ is obtained eventually from the modulus of the sum of all the terms given by (2) associated with the different cells. They all contain the same integral which can be factorised and does not need to be evaluated for our purpose. The modulus of the sum of the phase terms can be referred to as the amplification factor of the resonance $\{n_x, n_y\}$ since it tells us by how much the driving term associated with a single cell has to be multiplied to obtain the driving term associated with the whole structure.

3 RESONANCE CANCELLATION

The driving term on resonance associated with the ensemble of N_c cells vanishes if the resonance amplification factor defined in the preceding section is zero, i.e. :

$$
\left| \sum_{p=0}^{N_c-1} e^{ip(n_x\mu_{x,c} + n_y\mu_{y,c})} \right| =
$$

$$
\sqrt{\frac{1 - \cos[N_c(n_x\mu_{x,c} + n_y\mu_{y,c})]}{1 - \cos(n_x\mu_{x,c} + n_y\mu_{y,c})}} = 0 \quad (3)
$$

This is achieved if :

$$N_c(n_x\mu_{x,c} + n_y\mu_{y,c}) = 2k\pi \qquad (4)$$

provided the denominator of equation (3) is non zero, i.e. :

$$n_x\mu_{x,c} + n_y\mu_{y,c} \neq 2k'\pi \qquad (5)$$

k and k' are any integers. In what follows, the letter k with or without indices will mean "any integer". The resonance amplification factor has a value oscillating between zero and about one for almost all values of the variable $n_x\mu_{x,c} + n_y\mu_{y,c}$ except those satisfying the equality in 5. In the latter case it is equal to N_c. Starting from this value, it decreases to zero when the variable is equal to $2\pi/N_c$ and takes the value $N_c/2$ for a value of $2\sqrt{3}/N_c$. This gives the range of the variable for which the resonance amplification factor takes large values.

Setting now the phase advances to the values :

$$\mu_{x,c}/2\pi = k_1/N_c, \quad \mu_{y,c}/2\pi = k_2/N_c, \qquad (6)$$

we see that the condition for the cancellation of resonances (4) is satisfied. Indeed, introducing these values into equation (4), we obtain :

$$N_c(n_x 2\pi k_1/N_c + n_y 2\pi k_2/N_c) = 2k\pi$$

which can be simplified into :

$$n_x k_1 + n_y k_2 = k$$

For any integer values of n_x, k_1, n_y, k_2, the value of the expression $n_x k_1 + n_y k_2$ is always an integer. This means that this equation is satisfied for any value of k_1 and k_2. This results in the following important property :

" **A part of a circular machine containing N_c identical cells will not contribute to the excitation of any non-linear resonance, except those defined by $n_x\mu_{x,c} + n_y\mu_{y,c} = 2k_3\pi$, if the phase advances per cell satisfy the two conditions :**

$N_c\mu_{x,c} = 2k_1\pi$ (**cancellation of one-D horizontal non-linear resonances**)

$N_c\mu_{y,c} = 2k_2\pi$ (**cancellation of one-D vertical non-linear resonances**)

k_1 k_2 **and k_3 being any integers.**"

The usefulness of this property lies in the fact that, for a given resonance order, there are much more resonances cancelled than excited. For certain orders all resonances are cancelled. Numerical examples are given below.

It is interesting to point out a useful by-product of this property. The linear coupling resonance defined by $n_x = 1, n_y = -1$ is cancelled provided $\mu_{x,c} - \mu_{y,c} \neq 2k'\pi$. Taking $k_2 = k_1 \pm 1$, it is sure that this condition is satisfied for FODO cells. Thus, for an ensemble of FODO cells, the linear coupling resonance is always cancelled when the above property holds. The demonstration of the cancellation of the linear coupling has been done in LEP [5]. The solution retained was $\mu_{y,c} = 60°$ and $\mu_{x,c} = 71.5°$. The value

of 60° of the vertical phase was needed for the non-linear chromaticity correction, it does not fulfil the above condition. The number of cells per arc of 31 imposes a value of the horizontal phase advance of $60° + k \times 11.613°$, the value retained for $\mu_{x,c}$ corresponds to $k = 1$.

4 NUMEROLOGY

We want to find good values of the three parameters : N_c, k_1, k_2, i.e. values which satisfy equation 5 for the largest number of resonances. In order to solve this equation, $\mu_{x,c}$ and $\mu_{y,c}$ are replaced by their values given by equation (6). This leads to the Diophantine equation :

$$n_x k_1 + n_y k_2 \neq k' N_c \qquad (7)$$

For instance for machines with strong systematic multipoles of low-order, it is extremely interesting to seek the smallest number of cells and the phase advances for which there are no second nor third order resonances. Thus equation (7) has to be solved for n_x and $n_y \in [1, 2, 3]$. The easiest procedure is in fact to list the resonances satisfying the equality in this equation after having fixed N_c, k_1 and k_2 in order to decide whether these numbers are acceptable.

At first it is clear that N_c must not be equal to one, two or three. As the addition of a multiple of N_c on either side of equation (7) do dot modify it, it is sufficient to examine values smaller than N_c. As equation 7 is symmetrical in k_1 and k_2 it is sufficient to examine the cases $k_1 > k_2$. To suppress the linear coupling, it is necessary that $k_1 \neq k_2$. To suppress the third order resonances, k_1 must be different from $2k_2$.

n_x	0	1	2	3	4	5	6
n_y	5	1	2	-2	-1	0	2
res. order	5	2	4	5	5	5	8

Table 1: Resonances satisfying the equality in equation 7 associated with $k_1=3$, $k_2=2$ and $N_c=5$. The resonance order is equal to $|n_x| + |n_y|$, it has been limited to 10.

For $N_c = 4$ there are only two couples $\{k_1, k_2\}$ to consider : $\{3,1\}$ and $\{3,2\}$. Both have systematic second order but no third orders. The fourth order are all systematic, which prevents the use of systematic octupole excitation to adjust the anharmonicity.

For $N_c=5$, there are five solutions with always at least one resonance of order smaller than 3 excited. There are two solutions without third order resonance $\{3,2\}$ and $\{4,1\}$. The list of systematic resonances associated with $\{3,2\}$ is given in table 1. This case is interesting for a machine with magnets containing no systematic do-decapole component both erect and skew.

The first value of N_c for which there is a solution without first second and third order is 8. The search was stopped here as the objective of this study was to find a solution for LHC with $N_c=25$. Before examining it, we consider the case of purely periodic machines for which it is worth clarifying the concept of systematic resonances.

399

5 PURE SUPER-PERIODIC MACHINES

This is the case of almost all accelerators or synchrotron light sources. For a number of super-periods equal to N_c, the resonance amplification factor can be written in terms of the tunes Q_x and Q_y :

$$\sqrt{\frac{1 - \cos 2\pi(n_x Q_x + n_y Q_y)}{1 - \cos[2\pi(n_x Q_x + n_y Q_y)/N_c]}} \quad (8)$$

It is clear that this expression is zero only on resonance. Away from the resonance, the factor becomes of the order of unity. Consequently a large value of N_c is interesting to gain more freedom to find tunes which maximise the denominator. Note that, if the anharmonicity can bring a tune on resonance which zeroes the expression (8) at a certain amplitude, the resonance will not appear in the phase-space plot. However the plots will be distorted because the resonance has a non zero effect except for a single value of the tune.

As an example the synchrotron light source ESRF was designed with 16 super-periods and the design tunes were Qx=32.2, Qy=11.2. For the values of Qx=32 and Qy=11, the amplification factor associated with the third order resonances is exactly zero. For the actual tune values, it is 1.54 for the resonance 3Qx and 1.09 for Qx+2Qy. This is why a sextupole arrangement with more than two families had to be found [6] to cancel these resonances. This situation will be encountered in any purely super-periodic machine.

6 MACHINES WITH INSERTIONS

This is the case to fully exploit the results of section 3. Insertions with an arbitrary phase advance make it possible to adjust the fractional part of the tunes independently of the phase advance of the arc cells.

A nice example is that of the SPEAR 3 upgrade project. It has a racetrack layout, i.e. two arcs jointed with straight sections, with 9 cells per arc and matching cells in the straight sections [7]. For N_c=9, two couples $\{k_1, k_2\}$ make the lattice free from all third order resonances : $\{5,4\}$ and $\{7,2\}$. The second order sum coupling resonance is systematic for both. In a study of this lattice by tracking trajectories and systematic tune scan [7], two sets of phase advances per cell giving the largest dynamic aperture were found. The first set is $\mu_{x,c} = 0.79 * 2\pi$ and $\mu_{y,c} = 0.25 * 2\pi$, i.e. close to the values corresponding to the couple $\{7,2\}$: $\mu_{x,c} = \frac{7}{9}2\pi$ and $\mu_{y,c} = \frac{2}{9}2\pi$. The second set is $\mu_{x,c} = 0.78 * 2\pi$ and $\mu_{y,c} = 0.42 * 2\pi$ again close to the couple $\{7,4\}$ which has only a skew third order systematic resonance.

For a superconducting storage ring, like LHC at CERN, there are systematic octupole components in the dipoles and fourth order resonances have to be avoided. LHC is composed of eight arcs with 23 FODO cells and one dispersion suppressor at each end. The latter break the periodicity of the cell's arrangement. Assimilating a dispersion suppressor with one cell, we have to deal with 25 cells per arc. Because of the design gradient of the arc quadrupoles and the restricted aperture, the possible couples $\{k_1, k_2\}$ are $\{7,6\}$ and $\{6,5\}$. Trajectories have been tracked with systematic a4, b4 and b5 producing separately a relative field error of $0.5.10^{-4}$ at 17mm from the dipole axis, for the couple $\{7,6\}$. The dynamic aperture is increased by more than 50% for a model arc made from 25 cells and insertions, compared with the nominal lattice with a phase advance per cell close to 90°. For the actual LHC with the dispersion suppressors, there is less improvement but the lattice is much less sensitive to systematic expected octupole errors [8]. This opens the possibility of powering the octupole spool pieces correctors which have the same periodicity as the cells, without killing the dynamic aperture, to adjust the anharmonicity for Landau damping.

7 CONCLUSION

The analysis done in this paper shows that paying attention to the phase advance per cell is extremely beneficial to storage rings with strong focusing or large multipole errors and no strong non-linear chromaticity due to low-β insertions.

It is shown that a high superperiodicity is not the best ingredient to avoid non-linear resonances. It is better to design a machine with a low superperiodicity and arc cells with a proper phase advance so that the effect of the arc non-linearities is minimised. This is one of the strategies followed for LHC in order to minimise the effect of systematic multipole components which have different values in each of the eight arcs. It has been shown that such a lattice is rather insensitive to a substantial increase of the systematic per arc octupole component. It is also insensitive to a possible dangerous systematic per arc skew sextupole component.

8 REFERENCES

[1] J. Moser, The resonance lines for the synchrotron. CERN Symposium 1956, vol 1, p 290-2.

[2] H. Poincaré, Nouvelles méthodes de la mécanique celeste. Gauthier-Villars, Paris,1892.

[3] G. Guignard, A general treatment of resonances in accelerators. CERN 78-11 (November 10, 1978).

[4] E. Todesco and F. Schmidt, Evaluating high order resonances using resonant normal forms. 5th European Part. Acc. Conf., Sitges, Spain, June 1996. Also CERN-SL-96-32 AP.

[5] J. P. Koutchouk, Observations on the 78/78 optics. Proc. of the second workshop on LEP performance, Chamonix, January 19-25, 1992 (J. Poole editor). CERN SL/92-29 (DI).

[6] A. Ropert, Sextupole correction scheme for the ESRF, second advanced ICFA beam dynamics workshop, Lugano, April 1988. CERN 88-04 (1988).

[7] Y. Nosochkov and J. Corbett, Dynamic aperture studies for SPEAR3. 16th ICFA beam dynamics workshop (Arcidosso Sept. 1998).

[8] F. Schmidt and A. Verdier, Optimisation of the LHC dynamic aperture via the phase advance of the arc cells (this conf.).

DISPERSION AND BETATRON FUNCTION CORRECTION IN THE ADVANCED PHOTON SOURCE STORAGE RING USING SINGULAR VALUE DECOMPOSITION*

L. Emery, ANL, Argonne, IL

Abstract

Magnet errors and off-center orbits through sextupoles perturb the dispersion and beta functions in a storage ring (SR), which affects machine performance. In a large ring such as the Advanced Photon Source (APS), the magnet errors are difficult to determine with beam-based methods. Also the non-zero orbit through sextupoles result from user requests for steering at light source points. For expediency, a singular value decomposition (SVD) matrix method analogous to orbit correction was adopted to make global corrections to these functions using strengths of several quadrupoles as correcting elements. The direct response matrix is calculated from the model of the perfect lattice. The inverse is calculated by SVD with a selected number of singular vectors. Resulting improvement in the lattice functions and machine performance will be presented.

1 INTRODUCTION

The lattice functions (β_x, β_y, η_x, and η_y) in the APS storage ring are perturbed from those of the ideal model because of possible quadrupole calibration errors and off-center orbits through the sextupoles. It is desirable to correct these lattice functions because they have some impact on machine performance such as injection efficiency, dynamic aperture, momentum aperture (for Touschek lifetime), tune adjustment, and orbit correction.

There exist beam-based methods that achieve the above goal by first determining an accurate model of the ring from a fit to experimental data, then making changes to the quadrupole magnet setpoints to compensate for the calibration errors (see for example [1]). The machine functions after correction agree well with the ideal.

The above method and similar methods are difficult to apply to the APS storage ring for several reasons. For one, the strong sextupoles in the APS ring can potentially produce a significant focusing magnetic field that confuses with the nearby quadrupoles. When the method has been applied to smaller rings as in [1], the sextupoles were eliminated from the fitting process by simply turning them off and making measurements with a stored beam with uncorrected chromaticity. The APS ring has such a large natural chromaticity that the beam cannot be stored when the sextupole magnets are turned off. If the sextupoles are left on, the focusing effect of the sextupoles could be included as a known quantity in the fitting by suppying the horizontal beam position through the sextupoles. However, deter-

mining accurate positions of the beam relative to sextupole magnetic centers is not a trivial measurement.

Another fitting method uses measurements of several trajectories through parts of the ring made linear by turning sextupoles off [2]. Since the APS ring can store beam with at least two of the 40 sectors with sextupoles turned off, this method initially held promise. However, the difficulty here is the confounding of the calibration factors of quadrupoles with the gain errors of the beam position monitors.

We decided to adopt a philosophy similar to orbit correction where we make corrections to the lattice functions directly without identifying the source of errors, even though it is clear what kinds of magnet errors produce lattice function perturbations. We measure the lattice function errors and determine corrections by applying a change in setpoints to a small set of magnets. This idea is particularly applicable to the APS storage ring since all quadrupoles are individually controlled. It is hoped that the goal of improving machine performance can be attained by reducing the lattice perturbation globally and not necessarily by making a complete correction at all points around the ring.

2 METHODOLOGY

Though one may guess that the correction of the lattice functions to be more complex than orbit correction, the process is mathematically analogous to orbit correction because the perturbations of the lattice functions are derived from similar differential equations with driving terms linear in some magnet error (for β the relevant quantity that obeys a linear differential equation is $(\Delta\beta/\beta)$ [3]). Any such formulation can be turned into a matrix correction algorithm for use in a control system operator interface.

As in orbit correction, the correction setup requires first calculating a response matrix in which each element corresponds to the response a measurement quantity makes to the action of a control quantity. For example, in the η_x correction the measurement quantity is the dispersion measured at the SR beam position monitors (BPMs) and the control quantities are quadrupoles in the dispersion matching section. The response matrix is then inverted using singular value decomposition, a standard matrix inversion algorithm that allows some flexibility in controlling the amount of correction and stability of correction. For instance, selecting only a small number of the largest singular values (SVs) reduces the ability to correct the short wavelength features, but tends to stabilize the correction in the presence of measurement errors or model inaccuracies.

The response matrix is constructed by combining the results of several calculations, each using a baseline model of

the ring plus a small change in one particular magnetic element representing the control quantity. The `elegant` [4] code was used to make the calculations. The output data (lattice functions) is written in the Self-Describing Data Sets (SDDS) file format [5, 6], which comes with a powerful postprocessing toolkit. For each lattice function to be corrected, Tcl/Tk scripts composed of postprocessing commands generate the response matrix, the inverse response matrix, and a magnet setpoint delta file to write to the accelerator control system.

The corrections were applied separately to the lattice functions in APS storage ring. Correcting all lattice functions simultaneously can be done in principle using an all-inclusive matrix. Correcting only β_y, say, could affect η_x since quadrupoles are control quantities for both lattice functions. Considering the main harmonic component of each lattice perturbation, it is hoped that correction interaction between the lattice functions is not significant. For the APS ring, where $\nu_x = 35.2$ and $\nu_y = 19.3$, the 35th harmonic of quadrupole correction dominates the η_x correction, the 70th harmonic dominates the β_x correction, and the 38th and 39th harmonics dominate β_y. Since η_y uniquely uses the skew quadrupoles, η_y remains corrected after any regular quadrupole change.

In addition, one can reduce the possible interaction by selecting quadrupoles at "good" locations as correctors for each lattice function. For instance, β_x should be corrected using quadrupoles where $\beta_x > \beta_y$ and $\eta_x = 0$.

A practical aspect is the time required for collecting measurement data. Since lattice functions are physically derived quantities, the correction could take a shift. Pre-existing Tcl/Tk applications are used to measure η and β and write results to a file. It takes about one minute to make dispersion function measurements at all SR BPMs (which number greater than 360). The β readback consists of a sequence of relatively accurate β measurement at quadrupole positions, each taking 5 to 7 minutes for both β_x and β_y. Therefore, to make several correction iterations practical, the β readback can only consist of a handful of β values spread uniformly around the ring. One must assume that the readbacks sample a smooth global perturbation consisting of a few harmonics such that reducing the perturbation at the measurement points with a few-SVs correcting matrix will reduce the perturbation at all points.

Another operational issue is the requirement of standardizing the quadrupole magnets after every correction before making another lattice function measurement.

3 RESULTS

The current unperturbed lattice functions for the APS sector are shown in Figure 1. The ten quadrupoles in the sector are designated A:Q1 through A:Q5, then B:Q5 to B:Q1. Figure 2 shows the perturbed η_x with a dominant harmonic at the integer tune of 35 appearing as a 5-period modulation due to the 40-fold symmetry of the lattice.

The dispersion correction uses all SR BPMs, and 40 A:Q5-B:Q5 quadrupole pairs as 40 individual correctors.

Figure 1: APS sector lattice functions

Figure 2: Original dispersion

Using all 40 SVs for the matrix inversion gave a stable correction probably due to the large ratio of number of readbacks to correctors. After several iterations, the η_x perturbation rms was reduced from 37 mm to 7 mm. The η_x at one location measured in each sector (Figure 3) clearly shows the reduction of the 35th harmonic component. The amplitude of quadrupole relative strength change was about $\pm 6 \times 10^{-3}$. After the correction the beam lifetime im-

Figure 3: Reduction in η_x error by matrix correction

proved from 28 hours to 37 hours for the standard user fill pattern, presumably due to an indirectly-caused increase in momentum aperture (not measured). The emittance in both planes did not change appreciably.

It is expected that correcting the vertical dispersion will reduce the vertical emittance and xy coupling of the stored

beam. Also, the injection losses from incoming particle motion growing in y will be reduced.

There are 19 skew quadrupoles distributed around the ring and available as correctors. (A 20th skew quadrupole was removed because of a redesign of a vacuum chamber.) Ten of the skew quadrupoles are located in the η_x matching section (near A:Q4), and the other nine are in a nominally dispersion-free section (near B:Q3). The SVD matrix inversion automatically eliminated the latter nine since they have no effect on η_y.

Given that there are about 360 dispersion measurement points and only nine independent correctors, the correction can be made with as many as nine SVs. Trying eight SVs for the matrix inversion produced large skew quadrupole setpoint changes, and caused a divergence in η_y and a noticeable tilt on the synchrotron light beam image. This is surprising given that the ratio in the number of readbacks and correctors is large. There may be significant error due to small xy coupling in the BPMs. Also the skew quadrupole-to-η_y response matrix may be sensitive to errors in the phase difference between the x and y motion. The corrections made with four SVs gave more reasonable results, which demonstrates the flexibility of SVD decomposition. Figure 4 shows the overall improvement of η_y. The minimum rms achieved was 2.4 mm, a threefold reduction in this case. According to lifetime measurements, the vertical emittance was reduced by approximately a factor of two, making the ratio to horizontal emittance about 0.3%.

Figure 5: β modulation at several A:Q1 quadrupoles

turned out to be insufficient in representing the overall perturbation. As a compromise, readings at 12 A:Q1s are taken, the A:Q1s being selected for their proximity to the small vertical apertures. The control quadrupoles selected are the 40 A:Q4s, which have $\beta_y > \beta_y$.

There was not much opportunity to test various numbers of SVs for β correction. Figure 6 shows the resulting β_y at 12 measurement points from using 8 SVs on the original 20 readbacks, then 8 SVs again with the same 12 readbacks. The modulation was reduced from 17% to 9%. The short wavelength modulation that remains appears to be outside the range of the global correction.

Figure 4: Reduction in η_y by matrix correction

The β_x perturbation of the ring was relatively small. Figure 5 shows the measured β_x and β_y at A:Q1s in every other sector around the ring. On this plot, a 70th harmonic in β_x perturbation should appear as a 10th harmonic, which is not evident. Thus no attempt was made to correct β_x.

A large β_y modulation is observed and is a suspected cause of injection losses at the small vertical apertures. Correcting the modulation in β_y will maximize the vertical acceptance of the 5-m-long small aperture vacuum chambers. The full β_y measurement takes a prohibitively long time to perform. Nevertheless an efficient set of measurement locations must be adopted. During initial tests, various small numbers of points (4 and 8) were used, which

Figure 6: β_y modulation after correction

4 REFERENCES

[1] J. Safranek, "Experimental Determination of storage ring optics using orbit response measurements," NIM A 388 (1997) p. 27-36.

[2] M. Borland, private communication.

[3] H. Wiedemann, "Particle Accelerators Physics I," Springer Verlag, p. 246 (1993).

[4] M. Borland, ANL, unpublished program.

[5] M. Borland, "A Self-Describing File Protocol for Simulation Integration and Shared Postprocessors," Proc. 1995 PAC, May 1-5, 1995, Dallas, Texas, pp. 2184-2186 (1996).

[6] M. Borland, "A Universal Postprocessing Toolkit for Accelerator Simulation and Data Analysis," Proc. 1998 ICAP Conference, Sept. 14-18, 1998, Monterey, California, to be published.

DA METHOD AND SYMPLECTIFICATION FOR FIELD MAP GENERATED MATRICES OF SIBERIAN SNAKE IN RHIC

M. Xiao [#], T. Katayama, CNS, U. of Tokyo/RIKEN, Japan

E. Forest, KEK, Japan

Abstract

The simulation of spin precession and orbital motion in Siberian Snakes in RHIC based on the calculated or measured numerical magnetic field has been done. DA (Differential Algebraic) approach was introduced to calculate the orbital map of full Siberian Snakes to second order in the phase space variables. The symplectification was done for the maps obtained by DA. The symplectified maps that satisfy exactly the symplectic conditions will be presented in this paper.

1 INTRODUCTION

During the acceleration of polarized proton beam in RHIC, it is necessary to preserve the spin orientation to a high degree. For this reason, we must include spin tracking and the effect of the proposed Siberian snakes in simulations. Spin precession of the proton depends on the ambient magnetic field and thus it is coupled with the orbital motion. The spin matrix, a rotation in spin space, provides the required rotation of the spin and the correct angle of the precession axis. The Siberian Snake was designed to turn the direction of spin by 180° with minimal effect on orbital motion.

The laws of physics require that the spin matrix be unitary and the orbit matrix be symplectic. In fact, the entire non-linear orbit map must be symplectic. In general it is not clear that an approximate solution for the spin matrix and the orbital map will produce unitary matrices for the spin and symplectic maps for the orbital part. The violation of the (unitary/symplectic) condition becomes unacceptable whenever the simulation code is used in an iterative mode, i.e., whenever several turns of a machine are tracked. A violation of the condition then leads to a growth or shrinkage of the phase space; occasionally it leads to more complex but still unphysical behavior. It is this issue that motivates the present paper.

The issue of symplectic integration has been addressed by several authors [1][2]. Grossly speaking, symplectic integrators can be divided into the explicit and implicit types. Most accelerator physics codes, of the "kick-code" variety, are explicit integrators. These codes are fast and conceptually simple because a variety of effects can be added to them in a more or less self-consistent way. Unfortunately, it seems very hard to produce explicit symplectic integrators for a non-ideal magnetic field, the complexity is compounded by the absence of an analytical representation for the magnetic field.

Therefore, we have opted here to keep using an ordinary integrator, from which we extract a map. This has a small advantage: because the integrator is not symplectic, any violation of the symplectic condition will be a reflection of the integration accuracy or of the non-Maxwellian aspects of the fields. In other words it gives us an idea of the absolute error before any symplectic "fudging" algorithm masks it.

The DA (Differential Algebra) approach [3][4] pioneered by Berz in beam physics permits the calculation of a truncated Taylor map of an arbitrary element to any order, and the Taylor coefficients of the resulting truncated map will be accurate to machine precision. However, since the magnetic field given numerically and interpolated by spline function is smooth in the first derivatives and continuous in the second derivatives, it is possible to introduce DA methods to calculate the map of the full snake to the second order in the phase space variables without refitting the fields.

In fact, the matrices calculated from a field map are not symplectic in general. This is a problem resulting not only from the method we used, but also from the deviation of the magnetic field from the Maxwellian property. The symplectification for the maps obtained by the DA approach will be introduced and symplectified maps that satisfy exactly the symplectic conditions will be presented in this paper.

2 6-D MAP OF ORBITAL MOTION BY DA APPROACH

The DA(Differential Algebra) approach is a technique to propagate the derivatives of a function $f(x_i)$ systematically through mathematical transformations on f by simply applying the familiar sum, product and chain rules of differentiation[4]. The derivatives of any complicated function, which may be obtained by successive mapping, can be calculated by extending any function f to a vector f called "DA-vectors". For map-tracking, all phase-space coordinates z_i become the DA

vectors z_i. The first element of z_i contains the current value of the coordinates z_i, and the subsequent elements contain the derivatives with respect to the initial values of z_i. The vectors z_i are initialized by setting the first element to the initial value of z_i, the element which contains the first derivative with respect to the ith initial coordinate is set to be unity, and all the other elements are zero. Each mathematical operation that involves phase-space variables is replaced by a vector operation. Then, a truncated Taylor map

$$\bar{z}_{final} = \sum_{j_1+j_2+\cdots+j_n \leq N} \bar{a}_{j_1,j_2,\cdots,j_n} \prod_i z_i^{j_i}$$

can be obtained. The LBNL version of the DA package written by Berz was introduced, and Program DA-SSSTRA was written to do the simulation. In order to make use of DA, the magnetic field was reconstructed again to the second order,

$$B_W(x,y,s) = b_W(x,y,s) + \frac{\partial b_W(x,y,s)}{\partial x} \cdot x$$

$$+ \frac{\partial b_W(x,y,s)}{\partial y} \cdot y + \frac{1}{2} \cdot \frac{\partial^2 b_W(x,y,s)}{\partial x^2} \cdot x^2$$

$$+ \frac{\partial^2 b_W(x,y,s)}{\partial x \partial y} \cdot xy + \frac{1}{2} \cdot \frac{\partial^2 b_W(x,y,s)}{\partial y^2} \cdot y^2 + \cdots$$

$$w = x, \quad y, \quad s$$

Where $b_W(x,y,s)$ as well as its first and second derivatives are expressed by spline interpolation functions [5] fitted from the numerical field data. Since the spline function is smooth in the first derivatives and continuous in the second derivatives, the truncated Taylor map to the second order can be obtained around any ray started from the entrance of the snake.

The magnetic field strength of Siberian Snake was optimized first in order to make the spin precession turn 180^0 and the spin matrix of the snake close to unitary as possible for the particle with the energy E=250GeV (storage mode)[5]. Then, six-dimensional map with the variables of $(x, p_x, y, p_y, -ct, p_t)$ [7] to the second order around any ray can be extracted automatically for the particles with the energy from E=25GeV to E=250GeV. Linear matrix M_T for the motion at E=250GeV around the central ray was listed in Table 1.

3 SYMPLECTIFICATION

3.1 Symplectic condition checking

A $2n \times 2n$ matrix, M, is said to be symplectic if $M^T \cdot J \cdot M = J$, where M^T is the transpose of M, and J is the matrix

$$M_T = \begin{bmatrix} 0.99987402 & 12.2799388 & 0.00007164 \\ -0.0002035 & 0.99987606 & -0.00000085 \\ -0.00002987 & 0.00014282 & 0.99947619 \\ -0.00001740 & -0.00013731 & -0.00008627 \\ 0. & 0.00000009 & 0. \\ 0. & 0. & 0. \end{bmatrix} \cdots$$

$$\cdots \begin{bmatrix} -0.00029680 & 0. & 0.00000018 \\ -0.00012853 & 0. & 0. \\ 12.2777225 & 0. & 0.00000012 \\ 0.99946440 & 0. & 0.00000003 \\ -0.00000006 & 1. & 0.00020931 \\ 0. & 0. & 1. \end{bmatrix}$$

Table 1. The matrix M_T obtained by DA before symplectified.

$$J = \begin{bmatrix} 0 & I \\ -I & 0 \end{bmatrix}$$

Here each entry in J is a $n \times n$ matrix, I denotes the $n \times n$ identity matrix, and all the other entries are zero. It follows that a symplectic matrix has a unit determinant.

The check of the symplecticity for maps of the snake was done, and the results show that it does not satisfy the symplectic conditions completely, although a deviation of the determinant of M_T from 1 is as small as 2.8199×10^{-14}. The maximum error among the matrix elements is -1.2853×10^{-5}. The Maxwellian property of the magnetic field around the central ray was checked and it was found that the maximum error is around 10^{-2}, the same order as the symplectic property of the orbital matrix.

3.2 Symplectification

The Dragt-Finn factorisation states that a map near the identity can be expressed as follow [1]:

$$M_K = \exp(\vec{F} \cdot \nabla) I_d$$

Where I_d is identity map. The Poisson bracket operator, $[f,g]$, is a special case of the general vector field operator

$$: f : \vec{g} = [f,g] = \nabla f^T \cdot J \cdot \nabla \vec{g} = -\underbrace{J\nabla f}_{\vec{F}} \nabla \vec{g},$$

Where $\vec{g}$ is an arbitrary vector function of phase space. Then,

$$f = \int_0^x J \cdot \vec{F} \cdot dx'$$

If $\vec{F}$ is symplectic, then this computation involves an integral of a curl free function. Thus, the function f is

unique. If $\vec{F}$ is slightly non-symplectic, then the function f is one of possible symplectifications of the vector field $\vec{F}$, and it will depend on the path of the integration.

We know that the map M (including second order) from the entrance to exit of the snake is nearly the map for a drift of the length equal to the full snake. Therefore, one needs to construct a new map M_K

$$M_k = D^{-1}(\frac{L}{2}) \cdot M \cdot D^{-1}(\frac{L}{2}),$$

Where $D(L/2)$ is a drift of half-length of the full snake. So the linear part of the M_K is a matrix near the identity.

In the program DA-SSSTRA, a possible symplectic matrix M_{K_sym} for M_K was computed by an iterative process as follows. First, we compute the vector $\vec{F}$ in such a way that

$$M_K = \exp(\vec{F} \cdot \nabla) I_d.$$

Later, we will find a Poisson bracket approximating this general vector field. We then compute

$$vectorm = \exp(-\vec{F}_j \cdot \nabla) \cdot M_K \cdot I_d$$

as a correction of $\vec{F}$ and check whether $vectorm$ is close enough to zero. If not, then we set

$$\vec{F}_{j+1} \Leftarrow \vec{F}_j + vectorm,$$

and repeat the iteration.

Notice that this computation does not separate the map to be symplectified into the first and second orders, so it can be used for the symplectification of arbitrary order.

Once, $:f:$ is obtained from $\vec{F}$, the resulting symplectified map is

$$M_{sym} = D^{-1}(\frac{L}{2}) \cdot M_{k\_sym} \cdot D^{-1}(\frac{L}{2})$$

$$= D^{-1}(\frac{L}{2}) \cdot \exp(: f :) I_d \cdot D^{-1}(\frac{L}{2})$$

The maps for the Siberian Snake generated by numerical magnetic field including second order were symplectified, and the symplectified linear matrix was listed in Table 2.

The symplectification results show that there is a little adjustment for every element of the linear map of the snake calculated by DA to be symplectic, but for the second order map, the elements corresponding to the cross terms such as $x_0 \cdot p_{xo}$ change significantly.

Further work is being done to put the symplectified map into the full lattice of RHIC for spin tracking. The accuracy will have to be gauged in an actual run.

$$
M_{T\_sym} = \begin{bmatrix}
0.99987402 & 12.27993880 & -0.00000235 \\
-0.0002035 & 0.99987606 & -0.00000912 \\
-0.00004410 & 0.00020831 & 0.99947619 \\
-0.00000913 & -0.00010970 & -0.00008626 \\
0. & 0.00000013 & -0.00000001 \\
0. & 0. & 0.
\end{bmatrix}
$$

$$
\cdots \begin{bmatrix}
-0.00036238 & 0. & 0.00000013 \\
-0.00015614 & 0. & 0. \\
12.27772254 & 0. & 0.00000000 \\
0.99946440 & 0. & 0.00000001 \\
-0.00000018 & 1. & 0.00020931 \\
0. & 0. & 1.
\end{bmatrix}
$$

Table 2. The matrix after symplectifed

4 REFERENCES

[1] A. J. Dragt, AIP Conference Proceedings, 1987.

[2] E. Forest, et al., KEK Report 92-14, September 1992

[3] M Berz, Particle Accelerators, Vol. 24, 1989.

[4] F.Willeke, Proceedings of the CAS (CERN Accelerator School) Fifth Advanced Accelerator Physics Course, CERN 95-06(1995), Greece 1993.

[5] M. Xiao, et al., Spin note AGS/RHIC/SN No. 078, September 10, 1998.

[6] I.Alekseev,et al, Design Manual , Polarized Proton Collider at RHIC, July, 1998 .

[7] F.C.Iselin,The MAD Program Physical Methods Manual. Geneva, Switzerland, January, 1994.

ELECTRON DYNAMICS IN THE HERA LUMINOSITY UPGRADE LATTICE OF THE YEAR 2000

G. Hoffstätter*, F. Willeke, DESY, Hamburg, Germany

Abstract

It is planned to upgrade the HERA luminosity to $7 \cdot 10^{31} \mathrm{cm}^{-2}\mathrm{s}^{-1}$, which is 4 times the original design luminosity. This is to be achieved by decreasing the proton beam size by moving quadrupoles closer to the interaction point and by increasing their strength. Similar measures decrease the electron beam size. However, to match the smaller proton beam size, the horizontal electron emittance additionally has to be decreased.

The electron emittance can be decreased either by stronger focusing in the arcs, or by changing the damping partition numbers. In the HERA case, however, both methods have to be applied simultaneously, since changing the damping partition numbers increases the longitudinal emittance, which can only be tolerated with the current RF parameters if the bucket is increased by a stronger focusing in the arcs. These two methods of decreasing the emittance have competing effects on long term stability. Stronger focusing usually leads to a greater reduction of the dynamic aperture than of the emittance; whereas a change of the damping partition numbers tends to increase the dynamic aperture relative to the emittance. Playing the two competing effects against each other, it is possible to decrease the electron emittance while keeping the relative dynamic aperture as well as the requirements on the RF system tolerable.

1 EMITTANCE REDUCTION

In the HERA luminosity upgrade the horizontal emittance of the electron beam has to be reduced from currently 41πnm to 22πnm [1, 2]. The horizontal emittance ε_x of an electron storage ring is given by

$$\varepsilon_x = \frac{C_q\gamma^2}{1-\mathcal{D}} \frac{< |G|^3 \frac{1}{\beta}[\eta^2 + (\beta\eta' + \alpha\eta)^2] >}{< G^2 >}, \quad (1)$$

$$\mathcal{D} = \frac{< \eta G(G^2 + 2K) >}{< G^2 >}, \quad (2)$$

with the curvature G of and the focusing strength K on the closed orbit. The parentheses $< \ldots >$ indicate an average around the ring and η is the periodic dispersion. The optic functions α and β are used and $C_q \approx 384$fm is a constant. On the design orbit of a separated function ring, which HERA is to a good approximation, $G \cdot K = 0$ around the ring.

Since the curvature in dipoles is fixed, there are two ways of reducing the emittance: changing $\mathcal{D}$ in the denominator by shifting the RF frequency and changing the numerator by focusing stronger in the FODO cells. An RF frequency

*Email: georg.hoffstaetter@desy.de

shift changes the energy of the electrons and makes the beam travel along a dispersive orbit, which has curvature in quadrupoles. The product $G \cdot K$ no longer vanishes in quadrupoles, and changes in $\mathcal{D}$ of the order of one can easily be obtained which largely changes the horizontal emittance. changed. However, the energy spread σ_δ of the electron bunch increases when ε_x is decreased by this method since it is determined by

$$\sigma_\delta^2 = \frac{C_q\gamma^2}{2+\mathcal{D}} \frac{< |G|^3 >}{< G^2 >}. \quad (3)$$

If one does not want to compromise on particle loss out of the RF bucket, the RF bucket height $\Delta E/E_0$ has to be increased accordingly. We do not want to increase the bucket size by increasing the cavity voltage, since we need all available power for the storage of the 56mA design current. Therefore we have to decrease the dispersion to take advantage of the fact that $\Delta E/E_0 \propto 1/\sqrt{< G\eta >}$. The dispersion η in the arcs of the ring is decreased when we increase the horizontal focusing from currently $60°$ per FODO cell. By doing so, an additional fact comes in very handy: stronger focusing reduces the emittance by reducing the numerator of equation 1.

2 DYNAMIC APERTURE

Initially it was tried to obtain the 22nm design emittance by stronger focusing alone [3]. This could be achieved by going to $90°$ horizontal phase advance per FODO cell. However, the stronger natural chromaticity required stronger sextupoles and these nonlinear fields reduced the dynamic aperture significantly. The dynamic aperture for on energy particles for the four slightly different electron optics used in HERA during 1997 and 1998 are shown in figure 1. These calculations were performed by tracking for 1000 turns with MAD. Tracking with the second order TRANSPORT formalism and with third and fourth order generating functions leads to equivalent results. The dynamic aperture was always in a band between the 23σ and the 31σ horizontal and vertical emittance. The vertical emittance was assumed to be $\varepsilon_x/2$, which has proved to be a useful assumption in the literature. The dynamic aperture for the lumi upgrade optics with $90°$ horizontal phase advance per FODO cell is reduced to approximately 15σ and is also shown in this figure.

Because of this disadvantage of unnecessary strong focusing we have analyzed the possibility of reducing the emittance partly by stronger focusing and partly by an RF frequency shift. Figure 2 shows the decrease of the equilibrium emittance with an RF frequency increase and with an increase of horizontal focusing. On the red line, the ratio

Figure 1: The boundaries or stable motion x and y are shown in units of beam sigmas. The dynamic apertures between 23σ and the 31σ were computed for the four electron optics used in HERA during 1997 and 1998. The curve around 15σ was computed for a lumi upgrade optics with $90°$ phase advance per FODO cell, which leads to the 22nm design emittance.

of relative bucket height to energy spread is constant. For a given phase advance we should therefore not increase the RF frequency further than indicated by the red line. However, we also do not want to shift it less, since this would imply unnecessary strong focusing. For the lumi upgrade lattice, the point on the red curve which leads to the 22nm design emittance is very close to $72°$ phase advance and an RF frequency increase of 200Hz in HERA's 500MHz system.

Without an RF frequency shift, the electron beam in the new $72°$ lattice has an emittance of 27πmm·mrad at 27.5GeV. The stronger focusing gives space for 200Hz increase in frequency which further reduces the emittance to 22πmm·mrad. The energy decrease going along with such a frequency shift is only -0.083% . The energy dependent dynamic aperture of this new lumi upgrade lattice is shown in figure 3.

3 CHROMATIC OPTICS CORRECTION

The on energy dynamic aperture of the presented lumi upgrade optics is as large as the current dynamic aperture. The reduction of the dynamic aperture with energy deviation can possibly be reduced by chromatic sextupole correction of the optics.

At present six independent families of sextupoles are used in the $60°$ lattice to reduce the sensitivity of the beta functions and dispersion on energy. There are two sextupoles in each FODO cell and every sixth sextupole in

Figure 2: The change of the horizontal emittance with focusing per FODO cell and with $\mathcal{D}$. On the read line the ratio of energy bucket size to energy spread of the beam is invariant; here the focusing is just strong enough to allow for the RF frequency shift. This red curve leads to a 22nm emittance at $72°$ focusing.

Figure 3: The boundaries of stable motion in x and y shown in units of beam sigmas for the $72°$ lumi upgrade optics with RF frequency shift for energy deviations (red: -0.25%, green: -0%, blue: 0.25%).

one octant belongs to the same family. In this interleaved sextupole arrangement the betatron phase advance between successive elements of one families is $180°$, and therefore the sextupoles of a family have a coherent effect on the chromatic beta beat. Each octant has 24 FODO structures with sextupoles and therefore 8 sextupoles for each family.

In a $72°$ optics the phase increases by $180°$ after every 5th FODO and we are therefore left with ten independent families. If two sextupoles are added to each octant, each family has 5 sextupoles per octant. Since there are

currently only wires and power supplies for six independent families, we have fitted only six independent sextupole field strength to minimize the chromatic beta and dispersion beats. One can freely choose which of the 5 families to keep dependent and which to optimize independently.

4 FEASIBILITY OF AN RF FREQUENCY SHIFT IN HERA

There is a leverage for decreasing the emittance by increasing the RF frequency only if the current operation RF frequency f_0 is not too far above the central frequency f_c, where $\mathcal{D}$ in equation 1 is approximately zero. Several experiments were therefore performed during the December 1998 machine studies to specify a possible shift of the current RF frequency away from f_c [4].

The current frequency f_0 of the RF system is known very accurately. The central frequency f_c, however, is defined by the length of the specific closed orbit which goes through the center of quadrupoles; and five methods were applied to measure this frequency. The results together with an estimate of the random errors of these methods are shown in table 1. They all show that the current frequency f_0 is not severely above f_c; more likely f_0 is even below f_c. The frequency can therefore safely be increased to reduce the horizontal emittance in the luminosity upgrade project.

Table 1: The distance of HERA's operation RF frequency from the central frequency

Measurement	$\Delta f_0 = f_0 - f_c$
Beam loss at damping poles	-163 ± 20 Hz
Extrapolation of damping rates	-250 ± 150 Hz
Horizontal center of sextupoles	$+130 \pm 25$ Hz
Vertical center of sextupoles	-70 ± 50 Hz
Emittance change with frequency	-175 ± 70 Hz

5 FEASIBILITY OF STRONGER FOCUSING IN HERA

To test the usability of a 72° electron optics in the upgraded HERA, a 72° optic was installed in the current ring, which leads to a simulated horizontal emittance of 34πnm. The dynamic aperture of this optics was measured and compared to measurements of the dynamic aperture for the current 60° optics.

The sextupoles in this new 72° luminosity optics and in the 72° injection optics were used in two families to correct the chromaticities. Since the current six family scheme is designed for a 60° optics, no chromatic correction of optical functions was performed in the 72° case.

With these new optics arrangements injection, accumulation, ramp, and installing the luminosity optics and tunes of Qx=52.148 and Qy=52.216 was unproblematic. The usual lifetime of around 15 hours at low currents (15mA)

could be achieved and the orbit could be corrected to a usual rms of 1.22mm horizontally and 0.98 vertically. For this condition the dynamic aperture was then measured and compared with old measurements for the current 60° luminosity optics.

5.1 Measurement of dynamic aperture

When the beam is kicked by an angle Θ, the central particles travel with a Courant Snyder invariant $\beta_k \Theta^2$, with the beta function β_k at the kicker. When the central particles are kicked to a Courant Snyder invariant which corresponds to the dynamic aperture DA, then approximately half of the beam distribution will be outside the dynamic aperture and half will be inside. The kick which leads to a loss of half the beam was measured at 27.5GeV; the absolute dynamic aperture (DA) and the DA relative to the computed emittances is depicted in table 2.

Table 2: Dynamic aperture for the 72° and the 60° optics in the current HERA. The dynamic apertures are comparable, but both are presumably small due to defect magnets, which have by now been repaired.

Optics	DA	DA_{rel}
72° luminosity	2.7πmm·mrad	8.5σ
72° ramp file	2.6πmm·mrad	8.1σ
60° luminosity # 1	2.6πmm·mrad	7.9σ
60° luminosity # 2	2.2πmm·mrad	7.2σ
60° luminosity # 3	2.3πmm·mrad	7.4σ
60° luminosity # 4	2.4πmm·mrad	7.6σ

On average the dynamic aperture was 7.5σ with the current 60° optics; with the 72° optics the average was 8.3σ. Since these studies, shortages to ground were found in three magnets. The repair of these shortages increased the injection efficiency strongly and most likely the dynamic aperture has also increased, future measurements will show by how much.

The fact that the dynamic aperture did not decrease when installing the new optics supports the applicability of a 72° optics in the luminosity upgrade.

6 REFERENCES

[1] Editor: U. Schneekloth, "The HERA Luminosity Upgrade", DESY-HERA 98-05 (1998)

[2] M. Seidel for the HERA upgrade group, "Luminosity Upgrade of HERA", these proceedings (1999)

[3] T. Sen, "Dynamic aperture in the luminosity upgrade HERA-e lattice", EPAC Proceedings, Stockholm and DESY M 98-06 (1998)

[4] M. Bieler et al., "HERA machine studies December 1998", DESY M 99 (1999)

INVESTIGATION OF THE MÖBIUS ACCELERATOR AT CESR *

S. Henderson[†], M. Billing, R. Holtzapple, R. Littauer, B. McDaniel, D. Rice, D. Rubin,
D. Sagan, R. Talman, and A. Temnykh, Cornell University, Ithaca, NY

Abstract

We present a status report on the investigation of the Möbius scheme for producing equal-emittance round beams at CESR [1]. An insert has been constructed with six 45° rotated quadrupoles which interchange horizontal and vertical betatron oscillations on each passage. We describe the single-beam dynamics and the limitations introduced by the chromaticity correcting sextupoles. We also report on our two-beam experience.

1 INTRODUCTION

The collision of round beams (rather than flat) shows promise for substantial increases in luminosity at colliding beam facilities. We reported previously [2] on an experimental investigation of round-beam e^+e^- collisions at the Cornell Electron Storage Ring (CESR), in which beam-beam tuneshift parameters, ξ, as large as 0.09 were achieved. In that study, the beams were made round at the interaction point (IP) by resonant coupling in a lattice having equal betatron functions at the IP ($\beta_x^\star = \beta_y^\star$). Transverse emittances were made equal by tuning the lattice to the coupling resonance ($Q_x - Q_y$ = integer) and powering weak skew quadrupoles. Since we were unable to produce competitive luminosity due to limitations of the existing IR quadrupoles (only rather large values of $\beta^\star$ were accessible), our studies focused on the beam-beam tuneshift ξ instead. Indeed, those results confirmed the expectation [3] of improved beam-beam performance from round-beam collisions.

The Möbius scheme, proposed by Talman, provides an alternative, potentially superior, way to obtain full emittance coupling [1]. A lattice insert is constructed which exchanges the horizontal and vertical betatron oscillations. When such an insert is added to an ordinary uncoupled accelerator lattice, horizontal betatron motion on one turn becomes vertical on the next turn and vice versa. It has been our hope that the Möbius scheme would provide a more robust method of producing round-beams, avoiding the operational difficulties that are associated with resonant coupling. We present a status report on our investigation of the Möbius scheme at CESR.

2 MÖBIUS LATTICE DESIGN

2.1 General Properties

An insert with the desired $x - y$ exchange property can be constructed by axially rotating a special bend-free sec-

tion of the lattice through 45°. If the insert has $\alpha_x = \alpha_y$, $\beta_x = \beta_y$ at the boundaries, and betatron phase advances that differ by π, then its 4×4 transport matrices before and after rotation will be

$$M_{erect} = \begin{pmatrix} T & 0 \\ 0 & -T \end{pmatrix} \quad (1)$$

and

$$M_{skew} = \begin{pmatrix} 0 & T \\ T & 0 \end{pmatrix} \quad (2)$$

where T is a 2×2 transport matrix. We will refer to the lattices before and after rotation of the Möbius insert as the *erect* and *Möbius* lattices, respectively.

The normal mode tunes of the Möbius lattice are denoted $Q_{1,-1}$ and are related to the erect-lattice tunes by

$$Q_1 = \frac{1}{2}(Q_x + Q_y) - \frac{1}{4}, \quad Q_{-1} = \frac{1}{2}(Q_x + Q_y) + \frac{1}{4} \quad (3)$$

Since the tunes are always separated by $\frac{1}{2}$, we have only one adjustable parameter for making tune adjustments. However, the separate values of Q_x and Q_y may affect lattice properties such as resonances (see below).

2.2 Möbius Insert Design

We have constructed a Möbius insert from existing CESR quadrupoles which are rotated by 45°. The insert includes 6 quadrupoles in the North IR straight straddling the symmetry point opposite the south IR (the collision point) where the CLEO detector is located. The machine layout and one example of insert optics are shown in Figure 1. The insert is taken to extend between the centers of vertical separators (VSW,VSE) on either side of the North IP. As described above, the insert satisfies the Möbius requirements of $\beta_x = \beta_y$ and $\alpha_x = \alpha_y$ at the boundaries and $\phi_x = \phi_y + \pi$ through the insert. The optics design maintained the existing position of all the CESR quadrupoles but required the installation of two additional quadrupoles which are not in use in ordinary CESR operation. Polarity reversal (relative to ordinary CESR operation) of one quadrupole on either side of the insert was required to properly match the insert optics to the CESR arcs.

The six quadrupoles which form the insert are mounted on individual rotators which allow manual rotation from erect to 45°. Precision angle adjustment is provided at the 0° and 45° positions. Upon rotation the quadrupole centers remain fixed to within 0.25 mm.

2.3 Möbius Lattice

Three Möbius lattices have been studied thus far, one of which is shown in Figure 2. Apart from the Möbius insert

Figure 1: Möbius insert layout and optics. Quadrupoles (Q), bends (B) and vertical separators (V) are shown. Arrows mark the insert boundaries.

Figure 2: Möbius lattice functions for one-half of the CESR ring. The collision point (the South IR) is at the left and the Möbius insert (the North IR) is at the right.

properties described above, the lattice has the following additional features. The dispersion vanishes in both the north and south interaction regions. The high-η point in the ring (~260 m) is located at the injection point to take advantage of off-energy injection into CESR, a feature which improves injection efficiency and reduces losses at the peak-β_x point in the IR. The IR optics match those of the round-beam collision studies ($\beta_x^\star = \beta_y^\star = 30$ cm, $\eta^\star = 0$). Three lattices (hereafter referred to as A,B,C) have been studied thus far. All have the features described above, but differ primarily in their operating points (Möbius tunes $Q_1 = 9.82$ (A), 10.32 (B) and 9.89 (C)).

3 EXPERIMENTAL

Generally, machine studies shifts began with the erect lattice. After recovery of injection conditions, the tunes were corrected and the closed orbit flattened by standard methods. The Möbius insert quadrupoles were then rotated and injection conditions recovered. Since the rotated quadrupole centers do not remain perfectly fixed, further orbit correction was required. This was accomplished with a merit-function minimization technique which took into account the closed-orbit response in both transverse planes to a single corrector. Typically, the corrected closed orbit had $x_{rms}, y_{rms} < 1$mm.

The initial lattice optics correction was performed in the erect lattice. Normal-mode betatron phase advance measurements in the Möbius lattice agreed with theoretical expectations.

4 RESULTS AND DISCUSSION

4.1 Single Beam Dynamics

We observed early in our investigation that a beam could be stored in the Möbius lattice rather easily, but that the tune plane was broken into narrow bands by resonances. The thrust of our efforts to date has been to understand the single-beam dynamics of the Möbius accelerator.

Tune scans were performed in the various lattices to determine the operating range in the tune plane. Figure 3 shows a tune scan of lattice B, together with the results of a tracking program. The experimental data are shown as dark bands and represent the regions in Q_1 in which a beam could be stored with long lifetime ($\tau > 90$ min). The tracking results show the maximum horizontal amplitude reached in 1000 turns for a particle launched at the IP with displacements $5\sigma_E$ and $5\sigma_x$ (the normal modes at the IP lie along $45°$ diagonals so that x displacement excites both normal modes). Regions with good lifetime correspond rather well to those predicted from the tracking results.

The tune plane is dominated by rather strong betatron and synchrobetatron resonances. Betatron resonances which are excited by field errors are as follows: dipole errors, $1/2n, n$; quadrupoles errors, $1/4n, 1/2n, 3/4n, n$; and sextupole errors, $1/6n, 1/3n, 1/2n, 2/3n, 5/6n, n$ where n is an integer. The "extra" lines are an inherent property of a strongly coupled lattice in which the normal mode tunes are separated by $\frac{1}{2}$; they arise from one of the normal mode tunes satisfying the usual resonance conditions, or from sum resonances such as $Q_1 + Q_{-1} = n$, $Q_1 + 2Q_{-1} = n$. In addition, synchrobetatron resonance lines are excited by dispersion in sextupoles [4]. A simple model shows that the following sidebands are excited: integer $\pm 1/2Q_s, \pm Q_s, \pm 2Q_s$; half-integer $\pm 1/2Q_s, \pm Q_s, \pm 2Q_s$; and quarter-integer $\pm 1/2Q_s$. Several of these lines are clearly seen in the tracking data shown in the Figure. Finally, a mismatch at the Möbius insert (e.g., $\beta_x \neq \beta_y$) creates regions of instability near $Q_1 = 1/4n, 1/2n, 3/4n, n$ [1].

411

There are two important features to emphasize. First, the density of "structural" resonance lines is doubled relative to an uncoupled machine. Second, the density of synchro-betatron resonace lines arising from the presence of sex-tupoles is also doubled, *although their spacing relative to integer and half integer lines is preserved.* The net result is decreased operating room in the tune plane. There is little that can be done in regards to the "structural" resonances, but the synchrobetatron resonances driven by dispersion at the sextupoles may be attacked by proper design of a sex-tupole distribution taking the dispersion into account [4].

A simple two-family sextupole distribution was used for chromaticity correction. In an attempt to minimize the third-order betatron resonance amplitude driven by sex-tupoles ($Q_1 = 10.33$), a sextupole distribution was de-signed by traditional methods [5] to minimize the reso-nance driving terms. Increased operating room was indeed observed in the proximity of the third-order resonance; however there was little effect on the synchrobetatron res-onances.

The region near $Q_1 = 10.38$ in Figure 3 looks more fa-vorable for operation than the design operating point. An-other lattice (C) was designed with operating point $Q_1 = 9.88$. The results of a measured tune scan and tracking sim-ulation are shown in Figure 4 for a two-family sextupole distribution. The experimental results show a wider region of stable operation than the previous lattice. A broad region from $Q_1 = 9.85$ to 9.89 is broken up by a very narrow res-onance which is not evident in the tracking results. Further-more, this quadrant of the tune plane (9.75-10.00) appears to be more favorable from the standpoint of both synchro-betatron excitation and third-order resonance excitation. In fact, we have verified with a simple model that, in general, the synchrobetatron amplitudes arising from dispersion in sextupoles are greater in the region $n < Q_1 < n + 1/2$ than in the region $n + 1/2 < Q_1 < n + 1$, although the mechanism for this distinction is not yet understood.

4.2 Two-beam Experience

We have also investigated some aspects of two-beam op-eration. In order to provide beam separation at the north IP, an electrostatic separator bump was constructed using a vertical separator adjacent to the Möbius insert and two horizontal separators on the other side of the insert. Sep-aration at the south IP during injection was provided by powering a single electrostatic separator. We were able to inject both beams to single bunch currents above those in normal HEP operation. We attempted to collide in lattice B but suffered from poor beam lifetimes, presumably due to the single-beam limitations described above. We have not attempted collisions in the other lattices.

5 SUMMARY

We have implemented a Möbius insert and designed lattices which allow exploration of the Möbius scheme at CESR. The single-beam dynamics are dominated by the presence

Figure 3: Tune scan results for lattice B. Dashed lines show betatron resonances and dotted lines show synchrobetatron sidebands. The dark bands are regions with good beam lifetime.

Figure 4: Tune scan results for lattice C.

of strong betatron and synchrobetatron resonances. The synchrobetatron resonances are due to dispersion in the chromaticity correcting sextupoles, and are expected to be ameliorated with a design of the sextupole distribution which takes dispersion into account. Despite these features, we observe a favorable operating point near $Q_1 = 9.88$ and will investigate collisions in this region.

6 REFERENCES

[1] R. Talman, Phys. Rev. Lett. 74 (1995) 1590.

[2] E. Young et. al., Proc. 1997 Part. Acc. Conf., p. 1542.

[3] S. Krishnagopal and R. Siemann, Proc. 1989 Part. Acc. Conf. (1989) 836.

[4] A. Piwinski, Accelerator Physics at the SSC, AIP Conf. Proc. 326 (1995) 202, A. Piwinski, DESY 93-189.

[5] H. Wiedemann, Particle Accelerator Physics II, Springer-Verlag, 1995, p.146.

HIGH FIELD-GRADIENT CAVITIES LOADED WITH MAGNETIC ALLOYS FOR SYNCHROTRONS

C. Ohmori*, E. Ezura, M. Fujieda, Y. Mori, R. Muramatsu, H. Nakayama,
Y. Sato, A. Takagi, M. Toda, T. Uesugi, M. Yamamoto, and M. Yoshii, KEK

M. Kanazawa and K. Noda, NIRS

Abstract

Very high field-gradient has become available by a new Magnetic Alloy (MA)-loaded cavity developed for high intensity proton synchrotrons. The available RF voltage per core is ten times larger than that of the ordinary ferrite core. The maximum voltage of 20 kV has been achieved by the High-Field Gradient Cavity(HGC) of 40 cm in length[1].

Because the intrinsic Q-value of the MA core is low, acceleration without any tuning system also becomes possible. The first beam acceleration test using the HGC has been performed successfully at the HIMAC(Heavy Ion Medical Accelerator in Chiba). Furthermore, the dual harmonic RF and barrier bucket experiments have been carried out.

Another advantage of the MA-loaded cavity is that it is easy to compensate the beam loading. The feed forward beam compensation was applied for both HGC on the test bench using electron beam and MA-loaded cavity installed in the AGS for the barrier bucket experiment. A new development for high-Q HGC using cut core configuration will be also reported.

1 INTRODUCTION

The field gradient of a RF cavity is one of the most important parameters to design a high intensity machine. In order to minimize the circumference of the synchrotron and to increase the repetition rate of acceleration cycle for the high beam current, high field gradient is required. In case of JHF(Japan Hadron Facility)[2], the total RF voltage of 420 kV is necessary for the 3 GeV Booster synchrotron. Some future upgrades including the energy up to 5-6 GeV and/or 50 Hz operation require about 800 kV. So far, the maximum field gradient in the frequency region of 2-3.4 MHz was about 15 kV/m for the ferrite-loaded cavity because of the characteristics of the ferrite core. The shunt impedance of ferrite core becomes very low at the magnetic flux density of few 100 Gauss because the saturation flux density(Bs) is small as shown in Fig. 1. If ordinary ferrite-loaded cavities are used for the JHF, the total length for them becomes about 60 m. It means that most of the long straight sections are occupied for the RF stations.

To achieve high field gradient, the characteristics of the magnetic core should be stable in high RF field. Recently, soft magnetic alloys (MA) with high permeability, such as FINEMET[3], Metglas[4] and other amorphous have been developed. Some of the cores have very high saturation

* E-mail: chihiro@insuty.tanashi.kek.jp

flux density of more than 10 kGauss, as shown in Fig. 1. On the other hand, the hysteresis loss in the ferrite core will be increased at the large RF amplitude. However, the loss in the MA core does not depend on the RF amplitude. The MA has conductivity and the RF power is lost mainly by the eddy current in the material. To reduce the eddy loss, the material is composed of the tape of 16 μm thickness which is insulated by a thin Silica layer.

Figure 1: The hysteresis curves of magnetic materials. B_s means the saturation magnetic flux density. The usable B_{RF} is much smaller than B_s.

The characteristics of the MA and ferrite cores have been measured by a test bench using a 1 kW transistor amplifier[3]. The results are shown in Fig. 2. To evaluate the characteristics of magnetic materials, the product of relative permeability(μ), quality factor of the material(Q) and frequency(f), so called $\mu Q f$-product has been used. The $\mu Q f$-product is given by $Rp = \mu_0 \times t \times ln(a/b) \times (\mu Q f)$, where R_p, t, a and b are shunt impedance, thickness, outer diameter and inner diameter, respectively. The $\mu Q f$-product depends on the magnetic flux density in a core, B_{RF}. It is given by $B_{RF} = \frac{V}{\omega S}$, where V and S are the voltage and cross section of the core, respectively. B_{RF} is the averaged value in the core and the flux density near the inside is larger than it. The MA core shows an excellent characteristics at very high magnetic flux density of 2 kGauss. The characteristics of a ferrite core are also

shown in the figure. Below 100 Gauss, ferrite core has larger μQf-product than the MA core. However, the MA has larger value at the large RF amplitude. Another measurement using 30 kW tetrode amplifier also shows a large MA core of 550 mm O.D. was stable at the magnetic flux density of 1.3 kGauss and 5.5 kV was obtained by the core which had the thickness of 2.5 cm.

Figure 2: Magnetic flux density dependence of magnetic materials. SY2 is a typical ferrite core and the magnetic flux density dependence was observed. FT3-small and -large are MA cores of 570mm O. D. and 70 mm O.D., respectively. The MA cores have a constant shunt impedance up to 2 kGauss.

The characteristics of MA core are summarized as followings;

(1) μQf-product of the MA core does not depend on the flux density. One of MA cores, FINEMET, has larger saturation flux density than other MA and can be used at the very high RF flux density of 2 kGauss.

(2) The intrinsic Q-value of the MA core is 0.6-1. It is suitable for the wide frequency sweep without tuning system, barrier bucket, and multi-harmonic RF acceleration.

(3) The permeability of the MA core is about 10 times higher than that of ferrite. Although the Q-value is low, the μQf-product is not small to use for RF cavity.

(4) The MA core has very high Curie temperature of $570^{o}C$. And the characteristics of the core remained constant at high temperature of $170^{o}C$.

(5)The Q-value of the core can be changed up to more than 10 by using the cut core technique(see section 5). The R/Q-value of the cavity is a variable without changing the shunt impedance.

(6) The core consists of thin MA tape which is coated by silica insulator. It is possible to make a large core of about 100 cm diameter.

2 HIGH-FIELD GRADIENT CAVITY(HGC)

2.1 High Field Gradient

A prototype of HGC has been developed as shown in Fig. 3. The cavity has one acceleration gap and consists of two sets of $\frac{1}{4}\lambda$ cell. Each cell composed of 3 MA cores and they are installed in a water tank to cool by water directly. The size of MA cores is 305mm I.D., 670mm O.D. and 26mm thickness. The impedance of the cavity is shown in Fig. 4. The impedance is very broad because of the characteristics of core. The cavity has been driven by a push-pull amplifier using two sets of 150 kW tetrode, 4CW150,000. The maximum voltage of 20 kV has been achieved for the pulse operation. The field gradient per cavity length was 50 kV/m. For the high duty operation, 15 kV has been obtained. The voltage and duty are limited by the capacities of the plate power supply and cooling water.

Figure 3: High field gradient cavity. The length of the cavity is 40 cm.

2.2 Fast Frequency Sweep

Because of the broadband impedance of the MA core, any delay effcts on the magnetic material, such as a magnetic-after effect of ferrite core, has not been observed. Very fast repetition of about 1 kHz for the frequency sweep has been achieved. Figure 5 shows the envelope of the gap voltage when the 1-5 MHz frequency sweep was performed in 1.1 ms.

3 BEAM TEST AT HIMAC

The HGC has been installed in the HIMAC for the beam test. The HIMAC is a heavy ion synchrotron for the cancer

Figure 4: Very broad impedance curve of the HGC. The resonance frequency was shifted when the high power amplifier was connected.

Figure 5: The envelope of the gap voltage while the fast frequency sweep was performed. Because of the characteristics of the drive amplifier, the RF voltages was low at 1 MHz.

therapy. The main parameters of the HIMAC are listed in Table 1.

Table 1: Main Parameters of HIMAC

Circumference	129.6 m
Injection Energy	6 MeV/u
Extraction Energy	800 MeV/u
RF frequency	1-8 MHz for Si
	1-5 MHz for He
Harmonic Number	4
Repetition	0.3 Hz
Ramping Time	1 s
Beam Intensity	1.4×10^{11} at Injection
Extraction	Slow Extraction

3.1 Beam Acceleration without Any Feedback Loop

Beam acceleration test has been performed for several ion beams, He, C, Ne and Si[5]. Because the HGC has a very broad impedance, it can be used for 1-8 MHz without the tuning system. The block diagram of the HGC accelerating system is shown in Fig. 6. The preprogrammed voltage control system was employed to obtain the constant RF voltage during acceleration. Without preprogramming, the RF voltage became rather low at the particular frequencies because of the gain characteristics of the driver amplifier. The RF voltage was gradually changed during the adiabatic capture process and beginning of the acceleration. The preprogramming controlled the gap voltage accurate enough to accelerate the beam without beam loss. The AGC(Auto Gain Control) loop was not necessary to control the gap voltage. The RF frequency pattern for the beam acceleration using another ferrite-loaded cavity is stored in the memory of a DDS system. The same RF frequency pattern was used for the beam acceleration using the HGC.

Figure 6: The Block Diagram of the HGC accelerating system.

3.2 Multi-harmonic Experiments

The HGC RF system is broadband and can generate the multi-harmonic frequencies on the gap simultaneously[6]. The dual harmonic RF was applied successfully. The fundamental RF frequency is divided by a splitter and doubled by a frequency doubler circuit. Both harmonic frequencies were combined after adjusting the phase by a phase shifter circuit. The amplitudes of both frequencies were controlled by PIN diode attenuators. The bunching factor of the beam was increased from 0.28 to 0.40 by the dual harmonic RF as shown in Fig. 7. The beam loss was reduced. The DDS system for the multi-harmonic RF is under development for the dual harmonic acceleration. Another multi-harmonic experiment to produce the saw-tooth RF on the gap has been performed[6].

415

Bunch Shape

Figure 7: The difference of the bunch shapes by applying the dual harmonics.

3.3 Bunch Compression By Barrier Voltages

The barrier RF experiment has been carried out for the bunch compression experiment[6]. The wideband RF system is suitable for the barrier bucket experiment[7, 8]. Two barrier RF voltages were excited by the single HGC. The shape of the barrier is under development. Figure 8 shows the gap voltage after the improvement. The overshoot has been disappeared.

Figure 8: The barrier RF voltage. The barrier voltage is 1.1 kV and the repetition of the barrier RF is 261 kHz.

4 BEAM LOADING

4.1 Beam Loading Compensation Test using Electron Beam

The beam loading is one of the most severe problems on the RF system for the high intensity accelerator. The HGC has low impedance and this is suitable for the stational beam loading because the relative loading parameter becomes small. However, R/Q-value is not ideal because of low

Q-value. The beam loading effects on the HGC has been tested by the electron beam[10]. The energy of the electron beam is 180 keV and it is modulated with the frequency of 3 MHz to simulate the circulating beam. The length of the pulse train is 5 μsec. The electron beam current was measured by a fast current transformer and faraday cup. The beam transmission rate was almost 90 %. The wake voltage was about 1.2 kV when the electron beam peak current was 8.6 A.

The wake voltage was compensated by the feed forward scheme as shown in Fig. 9. The electron beam current picked up by the CT was divided into 3 harmonics(3, 6, 9 MHz) by the filters, the gain and delay were adjusted, individually, and all harmonics were combined together. The combined signal was returned to the driver amplifier. These 3 harmonics were compensated, remarkably[11].

Figure 9: Set up of the compensation test system.

4.2 Feed Forward Beam Compensation at AGS

A MA-loaded cavity has been installed in the AGS for the barrier bucket experiments[8]. The feed forward technique was applied to compensate it and the voltage induced by the 8×10^{12} proton per bunch was reduced up to 1/9 successfully[7].

5 CORE IMPROVEMENTS

5.1 Cut Core

The Q-value of the MA core can be increased by use of a radial gap in the cut core configuration without having large deterioration of the $\mu Q f$-product. Figure 10 shows the Q-value of the MA core for the various radial gap height. By this improvement, R/Q-value of the cavity will be reduced remarkably. In the JHF-50 GeV main ring, the peak beam

416

current reaches more than 100 A because the bunching factor will be 0.05 at the top energy. The very low R/Q-value less than 100 Ω is suitable to handle the bucket distortion by such a high peak beam current. However, we should note that the beam loading for low-Q system can be easily compensated. Furthermore, it is pointed out that Q-value should avoid around H/2 where H is the harmonic number of the ring to reduce the transient beam loading effects[9]. There are two choices for the JHF RF, that is, high-Q HGC which is very strong for the beam loading and low-Q HGC which is suitable for beam gymnastics and for beam loading compensation.

Figure 10: The Q-value of the cut core vs. gap height.

5.2 Variable-Q HGC

In order to investigate the optimum Q-value of the HGC, a variable-Q HGC is now under development. For the cavity, large cut cores of 950 cm O.D. will be used. The cavity has two gaps and will be driven by a new high power amplifier which use two set of 600 kW tetrode, TH558. The beam loading effects including the transient process will be examined by the electron beam test bench. For the experiments, a new electron gun will be used to obtain the peak current of 30 A.

6 CONCLUSION

High-Field Gradient Cavity has been developed using a newly developed Magnetic Alloy and the field gradient of 50 kV/m becomes possible. In the core, the field gradient of 220 kV/m has been achieved. Q-value of the cavity can be changed from 0.6(intrinsic Q-value) to more than 10 by the cut core configuration. A low-Q HGC is suitable for the barrier bucket scheme, multi-harmonic acceleration and wide frequency sweep. It is also easy to compensate the beam loading on the cavity using the feed forward technique. The scheme was applied for the HGC at the electron beam test bench and for a MA-loaded cavity installed in the AGS for barrier bucket experiment. The voltage by the intense AGS beam becomes 1/9 by this method. High-

Q HGC is now under development and it will be suitable for high intensity accelerators because of its low R/Q-value and small shunt impedance.

8 REFERENCES

[1] Y. Mori et al., "A New Type of RF Cavity for High Intensity Proton Synchrotron Using High Permeability Magnetic Alloy", Proc. of EPAC98, p299-301.

[2] Y. Yamazaki et al., in this conference.

[3] T. Uesugi et al., "New magnetic material for proton synchrotron rf cavity", Proc. of Symp. on Acc. Sci. and Tech., Nishiharima, Japan 1997.

[4] I. Bolotin et al., "Ferromagnetic Cores Made from Amorphous Material for Broad-band accelerating System" Proc. of PAC95, p1833-1835.

[5] R. Muramatsu et al., in this conference.

[6] M. Yamamoto et al., in this conference.

[7] M. Fujieda et al., in this conference.

[8] M. Fujieda et al., "MA-Loaded Cavity for Barrier Bucket Experiment", Proc. of EPAC98, p1796-1798.

[9] M. Yamamoto et al., "Beam Loading Effects in JHF Synchrotrons", Proc. of APAC98, p399-402.

[10] Y. Hashimoto et al., "Beam Loading Experiment with Short Bunched Electron Beam for New Type of Accelerating RF System of High Intensity Proton Synchrotron", Proc. of EPAC98, p1770-1772.

[11] M. Yamamoto et al., in this conference.

DEVELOPMENT OF HIGH POWER GRIDDED TUBE CW RF SYSTEMS WITH EXCELLENT RELIABILITY AND MAINTAINABILITY

J. Cherix, M. Maerki, H.R. Fitze, H. Frei, P. K. Sigg*, PSI, Villigen, Switzerland

Abstract

In the course of expanding the PSI proton accelerator complex towards very high beam currents, the entire RF system (except cavities) was redesigned. Aside from the set beam intensity goal, higher reliability became a prime objective. Analysing problem areas and failure mechanisms led to a much improved overall system. New power amplifiers and coupling loops were designed, together with improved protection, spark detection and RF recovery systems. This paper shows and explains the recently obtained results in performance and discusses means for further improvements.

1 INTRODUCTION

As a first step in the upgrade of the 590 MeV(p) PSI accelerator complex, from initially 200 μA to 1.5 - 2 mA; the conventional injector cyclotron (72 MeV(p)), was replaced by a different design: a separated sector cyclotron [1]. This concept allows more energy gain per turn and therefore, lower beam losses at injection and extraction (< 0.02 %). An extracted beam current of 1.5mA @ 72 MeV(p) was first obtained in 1991 [2].

Extensive changes on the 590 MeV ring cyclotron RF system were required. Total beam power increased from 60 kW to 1 MW, calling for 250 kW beam power per cavity. To stay clear of the expected longitudinal space charge limit at these elevated beam currents, the cavity voltage was raised from 480 kV_{peak} to 730 kV_{peak}, thus increasing cavity losses from 120 kW to 300 kW.

Therefore, new power amplifiers were needed, each to deliver > 600 kW (CW) @ 50 MHz. To facilitate maintenance, and to reduce the number of activated components, these new final amplifiers were planned to be placed outside the cyclotron vault, even though this called for RF power lines of 20 to 45 m in length between amplifiers and cavities. The amplifiers were designed with ease of maintenance and high reliability in mind. The net result is a much shorter MDT (Mean Down Time) in case of amplifier or power tube failure.

Additionally, the flattop system (3rd harmonic RF) was completely redesigned, in order to obtain stable operation of the amplifiers and control system over a wide power range of 30 kW to 120 kW [3].

In all RF systems, the MTBF (Mean Time Before Failure) of the power coupling windows was inadequate at power levels above 200 kW. Analysis of the sparking phenomena on RF windows led to a better understanding of the voltage breakdown mechanisms [3]. This resulted in the design of new coupling windows, capable of handling RF power levels in excess of 600 kW, and life expectancies of 3 years or more.

2 BEAM INTERRUPTIONS

Next to beam quality, the *frequency of occurrence* and the *length of beam interruptions* during scheduled beam production time are **the** measures of accelerator performance.

2.1 Classes of Beam Interruptions

One way of defining classes of beam interruptions is acc-ording to the length of the 'beam-off time': three groups seem to be sufficient in the case of the PSI accelerators.

Table 1: Classification of beam interruptions (trips)

DURATION OF BEAM INTERRUPTION	CLASS
Short beam trips (duration ≤ 1 min)	1
Medium length beam trips; between 1 min to about 1 hr	2
Long interruptions, lasting > 1 hr (mostly component failures !)	3

Analysing the beam trip data base and consulting the accelerator log book (maintained by the cyclotron operating group) allows an assessment of the sub-systems involved. The following table lists the cyclotron sub-systems (both accelerators) and the classes of beam trips they contribute to most frequently.

Table 2: Cyclotron subsystems and beam trip classes

SUBSYSTEM	CLASS
Electrostatic beam deflection devices	1&3
Beam monitoring devices, interlocks	1
RF SYSTEMS	**1&2&3**
All other systems (magnets, power supplies, vacuum & cooling, controls)	3

---

*Email: peter.sigg@psi.ch

2.2 Beam Interruptions Caused by RF Systems

The presumption that RF systems do contribute heavily to the total unscheduled beam-off time is confirmed by the accelerator operating statistics. Take, for example, the year 1997, the last year before all new RF system components were installed, calibrated, and operational.

The RF systems of the ring cyclotron were to blame for ≈ 23 % of the accumulated (unscheduled) down time; all RF systems together (both accelerators) accounted for ≈ 34 %. This corresponds roughly to the percentages of previous years. In 1998 however, the ring cyclotron was responsible for a mere 0.2 % (with a bit of luck !); the share of all RF systems decreased to 14 %. The figures in table 3 - accumulated class 2 and 3 events - have to be attributed mostly to component failures.

Table 3: Cumulative beam down times (hrs), and their percentages of total scheduled beam time

Cumulative Beam Down Time	1997		1998	
	hrs	%	hrs	%
Ring Cyclotron RF	160	2.7	10	0.2
Inj. II Cyclotron RF	80	1.35	81	2.0
Total, RF	240	4.1	91	2.2
Total, all Systems	705	12.0	648	15.9
Sched. Beam Time	*5870*	*100*	*4080*	*100*

The reduction seen for the year 1998 reflects, for the first time, the full effect of the RF system improvement pro-gram, with one exception: *45 hrs* of the injector cyclotron down time had been caused by the need to convert the last of the old RF power coupling windows on a resona-tor to the new design after it had failed. In the future, we anticipate the beam-off time to be approx. *8 hrs* in the case that an RF- window has to be replaced; most of this time will now be used for the cyclotron vacuum pump-down.

2.3 Class 2 & 3 Beam Trips in RF systems

Class 2 beam interruptions triggered by RF system inter-locks are mainly caused by multipacting in cavities after a spark, combined with thermal effects affecting the cavity geometry, which, in turn, prevent the build-up of the acceleration voltage for up to ½ hrs. The latter effect is caused by the limited range of the cavity resonance tuning system and occurs in the case that the cavity voltage cannot be restored within ≈ 2 min. after a spark. The number of these events has now been drastically reduced (see Fig.1), mainly because of a new cavity tuning, power pulsing and turn-on concept [4], but also due to additional 'Aquadag' coating in some cavities that were not previously treated.

Beam interruptions of class 3 (component failures) are now the dominant contributors to the Cumulative Down Time (CDT), as well as the mean down time (MDT).

2.4 Short Beam Trips of Class 1 (Sparking !)

Trips of < 1 min. duration are quite frequent in RF systems and electrostatic beam deflection devices. They contribute very little to the cumulative down time (CDT); they are, however, mainly responsible for poor Mean Time To Failure (MTTF) performance of the cyclotrons, and become increasingly important in applications of accelerators which demand extremely stable beam conditions.

RF- triggered short beam trips are almost exclusively caused by sparking in cavities and around RF power coupling windows. Depending on the duration (and location) of a spark (or discharge), two different spark-handling procedures are employed:

- *Spark in cavity, of < 650 µs duration*; this is what we call a 'micro-spark' (µ- spark):
  → RF drive stays on;
  → **beam stays on.**
- *Spark in cavity, but of > 650 µs duration:*
  → **beam is turned off** after 650 µs, then:
  → after 3 ms: RF drive is turned off, followed by:
  → 'Auto Start' procedure: tuning, pulsing and ramping to full voltage, within 4 to 6 sec.

A special case is the following:

A spark at the coupling window (vacuum side) is detected by the electron (e⁻) detection probe:
  → RF drive is suppressed within 3µs, for 150 µs; then *turned back on to full power* immediately.

In the event that the beam is turned off, the time needed to turn on and ramp up the beam to full intensity dominates; taking about 45 sec.

2.5 New Data on Cavity Voltage Trips

In Nov. and Dec. 1998, we monitored the cavity voltage, and several related parameters with a fast, multi-channel digital oscilloscope connected to a computer for storage of **all** events (µs resolution) in cavity No. 4, for 40 days. This allowed us to get statistical data on the frequency of sparks: in a (well conditioned) cavity, on the RF coupling window, as well as on all other interlocks .

After analysing every event individually, it turned out that, of a **total** of **60** RF trips in 40 days, **20** were so-called (self-recovering) **µ- sparks** of < 650 µs duration, which did not even turn off the beam. This results in a *MTTF of ≈45 hrs* for µ-sparks, comparing very well with ≈ 10 min on the first days after a cavity has been exposed to air! Only **one** spark of longer than 650 µs (= **non-recovering spark**) was recorded. **25** events were caused by **external** non-RF interlocks (RF 'off' and 'on', including scheduled interruptions for maintenance, etc.). The remaining 15 events were due to faults in the RF system, 10 of them caused by a malfunctioning crowbar unit in the final amplifier HV supply (these events do not show up in Fig. 2, because they occurred during set-up -

and not operation - of the cyclotron). Obviously **absent** were sparks at the **coupling loop**, a fact confirmed by an independent event counter on the spark monitoring device. The remaining cavities, during that same period, accumulated 1, 0, 2 and 14 such events.

Since it is not clear now whether we were fortunate with the choice of this particular cavity for this monitoring project, nor if and how these results are dependent on conditioning and other influences, it is proposed to install such monitoring on all RF systems. The biggest disadvantage, aside from equipment cost, is the fact that event viewing and screening still has to be done manually; some automation might be needed in the future. Furthermore, such a database should also conform to the cyclotron operation database, which collects data with a sampling rate of ≈ 1 min., and the device interlock statistics, which only count events during scheduled beam time.

3 RELIABILITY OF RF SYSTEMS

A simple definition of *reliability* first: During the scheduled beam production time of an accelerator: we want a minimal number of beam trips and, *if* they occur, minimal time to restore beam again!

Or, using statistical terminology: *decrease* the frequency of fault occurrences in a cyclotron, that is: *lengthen* the MTTF; and *decrease* the time to repair, corresponding roughly to the MDT .

3.1 Increasing the Mean Time Before Failure (MTBF)

- Reduce the influence of sparks:
  Do *not turn off beam* during short, self-recovering μ- sparks in cavity (duration: ≤ 650 μs).
- Reduce the absolute number of sparks: This can be achieved by *conditioning* RF cavities. It is a very time-consuming process, and it has to be repeated after each breaking of the cyclotron vacuum. Controlled filling of the cyclotron with nitrogen makes a big difference in the conditioning time required, compared to the (uncontrolled) filling with (moist) air, as is the case when an RF window breaks during heavy sparking across the ceramic surface! Important goal:
  ⇒ **Avoid cracking windows altogether !**
  In the case of our aluminium cavities: by using 'Aquadag' coating inside and on metallic coupler surfaces, we reduce multipacting and facilitate conditioning dramatically.
- Reduce Component Failure Frequency (1/MTBF): Improve and refine the *protection circuitry*, especially of high power/high voltage components (RF amplifiers, HV- supplies), but also for RF windows.

Generally speaking: use high quality components if possible (with power tubes: choice is based on past experience). Employ reliability engineering methods and ample safety margins in design

That such measures can result in dramatic improvements in MTBF is best illustrated by the following figure (1), showing the cavity voltages for the four ring cyclotron acceleration cavities recorded during two typical 10-day intervals. Typical in this context means: comparable beam intensities (1.5 mA), no breakdown of non-RF systems, and no scheduled maintenance- or other beam-off periods planned during this time.

Figure 1: Ring cyclotron cavity voltages in kV_p for two typical 10-day beam production periods;
- Upper trace: 10 days in August 1997,
- Lower trace: 10 days in September 1998

3.2 Reducing the Mean Down Time (MDT)

As is the case for MTBF, only spotty statistical data is presently available on past and present MDT data for individual subsystems of the cyclotrons. Nevertheless, maintenance experience for individual components allowed us to pinpoint weak spots. Several measures were then taken to alleviate the most obvious ones, and to derive some rules to improve the replacement- and/or repair times of most critical systems:

- *Speed up cavity voltage recovery* in the case of sparks that do not extinguish for > 3 ms; because, in that case, the *amplifier protection circuits* will turn off the RF drive and the beam. *Resonance tuning, pulsing and ramping* procedures will now

re-establish full resonator voltage within 4..6 s, (compared to 2..25 min with the old system).

- **Reduce spark damage** to coupling windows:
  Redesign the RF-coupling windows, include *ionisation detection pick-ups* at the couplers. The protection system turns off the RF-drive for 150 µs immediately (within 3µs) after electrons of a spark at the window are detected. This way, the amount of material evaporated, and deposited on ceramic insulator surfaces with each spark is strongly reduced.
  ⇒ *Lifetime of all types of RF coupling windows is now > 3 years !* (better than most power tubes)

- **Reduce repair times:**
  Design quick *fault diagnostic tools*, provide test points to facilitate fault location; both on a system level *and* on device levels.
  Allow *fast exchange* of components by employing suitable mechanical design and fast connectors for RF-, electrical-, HV-, cooling water and air cooling hook-up.
  Provide *ready-to-operate replacement units* (hot spares), from power supplies to final amplifiers (tuned and calibrated) !
  Specify all units to use a strictly *modular design* (or: convert to modular design). At PSI, this has been done for amplifiers, coupling windows, power supplies, amplitude-, phase-, and frequency control systems and RF-interlock devices.

- **Identify components with limited lifetime**;
  include them in *preventive maintenance* schedules, and design them for ease of replacement and minimal adjustment work (starting with components like: RF power tubes, RF coupling windows, etc)

Again, there is some data available to compare the effect of the measures mentioned above to the time before they were all operational. However, since many features were introduced in the course of several years, data on the contribution of individual measures would be difficult to extract reliably. Also, since this is an ongoing process, and the first steps were certainly the most effective, it is unlikely that such spectacular improvements can be demonstrated in the future. (Fig. 2)

This figure confirms the message of Fig. 1 (significant reduction of *number* of beam trips), but also clearly shows the second effect of the improvement program: the reduction in the cumulative down time (CDT). It is inter-esting to notice that the only significant data point in the lower diagram (marked by *) can attributed to one single problem: a cooling water safety interlock switch of a replacement amplifier being set too close to the limit. It took 13 beam trips to locate and solve the problem.

Figure 2: Ring cyclotron cavity drop-out distribution, during scheduled beam time; compiled for 3 months (Sept. to Nov.) in 1997 (upper chart), and the same time period in 1998 (lower chart).

4 RF POWER EQUIPMENT

4.1 Amplifier Design Considerations

The power amplifier chain of a PSI ring cyclotron RF system consists of 4 stages, of 1 kW, 10 kW 100 kW and 800 kW nominal output power (CW). All tubes are power tetrodes of metal-ceramic design. The 1 and 10 kW amplifiers are forced-air cooled, while the 100 & 800 kW amplifiers each use the same tube type, and are water cooled.

In case of a tube failure, the air cooled tubes are replaced directly, within about 1 hour (to full power operation); while in the case of a 100 or 800 kW stage failure, the entire amplifier is exchanged. Total time to operation in this case takes about 2 hrs., and requires at least two qualified persons from the RF group.

This is only possible because all amplifiers are designed and built with very tight mechanical specifications, allowing quick 'plug-in' connection of HV-, RF-, power- and control signals; as well as air- and water cooling hook-up, as can be seen in figure. 3.

Further contributing to the reliability of the amplifiers were external measures to reduce any tendency for parasitic oscillations. They are mostly caused by load changes

Figure 3: Connector Side of 850 kW Final Amplifier
(cover removed)

and output mismatch for higher harmonics, and do occur despite careful internal circuit design, generous cooling, etc. In the past, damage by parasitics was also caused by unreliable (water cooled) power absorbers, employed in some grid input circuits and on transmission line higher order mode absorbers. Any fixed frequency RF amplifier connected to a narrow-band and/or variable load works best if the line length between amplifier and load is adjusted to integer multiples of $\lambda/2$. At higher harmonic- and parasitic frequencies, multiple reflections due to mismatch will occur on such a line, possibly resulting in parasitic oscillations in the amplifier. This effect can be countered by inserting directional 3 dB couplers between amplifiers, with integral band-stop filters for the fundamental frequency inserted between incident- and reflected power ports and 50 Ω power absorbers. These absorbers dampen signals over a wide frequency range on the transmission line (outside the fundamental frequency band) by ≤ 6 dB, and prove to be very effective in providing stable amplifier operating conditions and preventing damage due to uncontrolled parasitic oscillations.

4.2 Tube Lifetime

Average tube lifetime differs little between small and large tubes. Despite the start of the high power operation ($I_{BEAM} = 1.5$ mA) some 3 years ago, tube replacement data still indicate an average tube life time of 18'000 hrs (corresponding to ≈ 3 years of cyclotron operation).

Unfortunately, the 800 kW tube (RS 2074 HF) showed very large fluctuations in life time for a while, varying between 1000 hrs. and 27'000 hrs.,('record holder': > 60'000 hrs !) and failing for different reasons as well; from breaking of the filament to shorts between control-grid and cathode. In any case: the sample sizes for the different tube types are just too small to get a reliable statistical data base. Normally, tubes 'die' slowly of low cathode emission, thus giving ample lead time to plan a replacement during regular maintenance periods (bi-weekly), provided they are monitored regularly. Life time of cathodes is dependent on limiting the turn-on current pulse (to ≈ 150 %) and constant filament power; we employ passive power control systems to achieve this goal.

Manufactures of power grid tubes have improved reliability through better understanding of the chemical and physical processes inside the tubes, employing new materials and new, computerised manufacturing methods, allowing very tight internal tolerances. Standard lifetimes are now quoted to be > 15'000 hrs, corresponding well to our own observations. [5]

5 OUTLOOK, CONCLUSIONS

Improved statistical data, allowing us to better correlate sparking with all other activities in the cyclotron and across all cavities, will hopefully help to increase our comprehension of the underlying phenomena of sparking. (Compare sub-section 2.5) Additional studies might be needed in this field, but the goal will be worthwhile: to improve accelerator reliability and availability further, eventually preventing sparking in cavities during accelerator operation completely !

Another reason for the high reliability of our RF systems may be found in an organisational - rather than a technical - aspect: we do not employ separate groups for development and for maintenance of the RF systems. Whoever designed equipment will remain responsible for it during operation, and will therefore be much more inclined to improve or redesign, instead of just repair; thus assuring a continuous improvement of all systems.

At present, we are developing a new cavity with higher acceleration voltage (1 MV_p) for our ring cyclotron. In the future, such cavities will allow us to further decrease the turn number in the cyclotron, raise the space charge limit, and to produce extracted beam currents in excess of 2 mA @ 590 MeV(p). [6]

[1] U. Schryber et al., 9th Intl. Conf. on Cyclotrons and Applications, Caen (1981); p. 43.

[2] T. Stammbach, 13th Intl. Conf. on Cyclotrons and Applications, Vancouver (1992); p. 28.

[3] P. Sigg et al., 14th Intl. Conf. on Cyclotrons and Applications, Cape Town (1995); p. 161.

[4] P. Sigg et al., PSI Scientific Report 1998, Vol. VI (GFA), to be published.

[5] B. Gellert, W. Rohrbach, IEEE Trans. on Dielectric & Electrical Insulation, Vol. 2, No. 2, April 1995

[6] HR. Fitze et al., 'Development of a New High Power Cavity for the PSI Ring Cyclotron', this conference

A COMPARISON BETWEEN PULSE COMPRESSION OPTIONS FOR NLC[*]

S. G. Tantawi[#$], R. D. Ruth, P. B. Wilson, SLAC, Stanford, CA

Abstract

We present a comparison, between options for pulse compression systems that provide rf power to the main linac of the Next Linear Collider (NLC). The parameters which are compared are efficiency, number of components and length of rf storage lines. Based on these parameters we produce a cost model for each system as a function of compression ratio, number of rf sources per unit system, and storage line parameters. The systems considered are Delay Line Distribution Systems (DLDS), Binary Pulse Compression (BPC), and Resonant Delay Lines (SLED-II). For all these systems we consider possible improvements through the use of several modes, active switches, and circulators.

1 INTRODUCTION

During the past few years high power rf pulse compression systems have developed considerably. These systems provide a method for enhancing the peak power capability of high power rf sources while matching the long pulse of that source to the shorter filling time of the accelerator structure. In particular, future linear colliders, such as the proposed NLC[1] require peak rf powers that cannot be generated by current state-of-the-art microwave tubes. The SLED pulse compression system [2] was implemented to increase the gradient of the two-mile linac at the Stanford Linear Accelerator Center (SLAC). One drawback of SLED is that it produces an exponentially decaying pulse. To produce a flat pulse and to improve the efficiency, the Binary Pulse Compression (BPC) system [3] was invented. The BPC system has the advantage of 100% intrinsic efficiency and a flat output pulse. Also, if one accepts some efficiency degradation, it can be driven by a single power source [4]. However, The implementation of the BPC [5] requires a large assembly of over-moded waveguides, making it expensive and extremely large in size. The SLED II pulse compression system is a variation of SLED that gives a flat output pulse [6]. The SLED II intrinsic efficiency is better than SLED, but not as good as BPC. However, from the compactness point of view, SLED II is far superior to BPC. Several attempts have been made to improve its efficiency by turning it into a system using active switching [7]. However, the intrinsic efficiency of the

active SLED-II system is still lower than that of the BPC. The DLDS [8] is a similar system to BPC, but by sending the rf upstream twords the gun it utilzes the return delay of the electron beam to reduce the length of the over-moded waveguide assembly. However it still uses more over-moded waveguide than that required by SLED-II. To further enhance the DLDS a variation on that system, the Multi-moded DLDS (MDLDS) [9] was introduced, which further reduces the length of the waveguide system by multiplexing several low-loss rf modes in the same waveguide. The system has an intrinsic efficiency of 100%, and the total over-moded waveguide length has been reduced considerably.

We present a comparison, based on cost, for all various compression schemes that are available for the Next Linear Collider. In this comparison we do not describe the systems involved at any level of detail. The reader is referred to the cited references for details. However, it is our purpose to give an accurate formulation for the system efficiency, number of components, and length of delay lines or storage lines for each of these schemes as a function of compression ratio (the ratio of the source rf pulse width to the compressed pulse width). This will provide the basis for cost comparison. We will also extrapolate on the potential to expand and/or improve systems through the usage of

a. Multi-moded structures,
b. Active switching,
c. Circulators.

2 COST MODEL

Basically, the rf sources available now or in the near future will produce a pulse T of about 1.5 μs. The NLC accelerator structure needs a pulse of 380 ns. Hence, a pulse compression system which compresses the source rf pulse by a factor $C_r=4$ is required. The factor of 4 is the minimum required compression ratio. If rf sources can be improved to provide longer pulse lengths at the same peak power, one might utilize a bigger ratio.

To achieve this pulse compression a storage system is employed to store the rf power until it is needed. Different portions of the rf pulse T are stored for different amount of times. The initial portion of the rf pulse is stored for a time period t_m, the maximum amount of storage time for any part of T. The maximum value for t_m is

$$t_m^{max} = \tau(C_r - 1) \qquad (1)$$

where $\tau = \dfrac{T}{C_r}$ is the accelerator structure pulse width,

and C_r is the compression ratio. The value given in by Eq.(1) is typical for most systems with the exception of

DLDS, which stores the energy for only half the time. The realization of the storage system is usually achieved using low-loss waveguide delay lines. These lines are usually guides that propagate the rf signal at nearly the speed of light. The maximum length required for these guides, per compression system, is

$$l^{max} = t_m v_g \frac{C_r}{2},$$ (2)

where v_g is the group velocity of the wave in the delay line. The total number of rf pulse compression systems required for the accelerator system is given by

$$N_c = \frac{N_a P_a}{P_k n_k C_r \eta_c},$$ (3)

where N_a is the total number of accelerator structure in the linac, P_k is the klystron (or the rf power source) peak power, P_a is the accelerator structure required peak power, n_k is the number of klystrons combined in one pulse compression system, and η_c is the efficiency of the pulse compression system. Thus the total length of waveguide storage line for the entire linac is given by

$$L = l^{max} N_c R_l = \frac{1}{n_k \eta_c} \frac{N_a P_a}{P_k} \frac{t_m v_g}{2} R_l.$$ (4)

where R_l is a length reduction factor which varies from one system to another and in general is also a function of the compression ratio. The total number of klystrons in the system is given by,

$$N_k = \frac{1}{C_r \eta_c} \frac{N_a P_a}{P_k}.$$ (5)

The cost of the rf system is divided into three different parts: cost of the klystron tube, the klystron power source and modulator, and the rf pulse compression and transportation system. The cost of the klystron tubes is given by

$$S^k = N_k A_k = \frac{1}{C_r \eta_c} \frac{N_a P_a}{P_k} A_{k0} \left(\frac{C_r}{C_{r0}} \right)^{a_k},$$ (6)

where A_{k0} is the cost per klystron at a compression ratio C_{r0}. The exponent a_k is a number that depends on the details of manufacturing klystrons. For our present discussion we will assume that this number is 0.4 and C_{r0} =4 [10].

The cost of *conventional* modulators is also dependent on the compression ratio. If the klystron pulse width is increased the stored energy in modulator is increased and hence its cost. A fraction k_m^s of the modulator cost is due to its energy storage elements [11]. The rest of the fractional cost, $1 - k_m^s$, is due to the rest of the system, in particular the switching elements. Hence, a suitable model for the modulator cost is

$$S^m = N_k A_{m0} \left(1 + k_m^s \left(\frac{C_r}{C_{r0}} - 1 \right) \right) = \frac{1}{\eta_c} \frac{N_a P_a}{P_k} \left(\frac{1 - k_m^s}{C_r} + \frac{k_m^s}{C_{r0}} \right) A_{m0},$$ (7)

where A_{m0} is the cost of the modulator per klystron at a compression ratio C_{r0}.

The cost of the rf pulse compression and power transmission is divided into two parts: a part that is dependent on the storage line length L and diameter D, and a part that is dependent on the number of components per pulse compression system n_c. The storage line cost is divided into two parts: the cost of the vacuum system, which is a very weak function of diameter, and the cost of the pipes, which is directly proportional to the diameter. The cost model is, then, given by

$$S^c = \left(A_l^v + A_l^p D \right) L + N_c A_c n_c = \frac{N_a P_a}{n_k P_k \eta_c} \left(v_g \frac{(C_r - 1)}{2} R_l \left(A_l^v + A_l^p D \right) + \frac{1}{C_r} A_c n_c \right)$$ (8)

where A_l^v is the cost of vacuum system per unit length, A_l^p is the cost of waveguide pipe per unit length and diameter, and A_c is the cost per component. The total cost of the rf system normalized to the cost of one klystron A_{k0} is given by

$$S_r(C_r, D, n_k, R_l; k_m, k_l^p, k_l^v, k_c, k_m^s) =$$

$$\frac{P_a}{P_k \eta_c} \left(\frac{1}{C_r} \left(\frac{C_r}{C_{r0}} \right)^{a_k} + k_m \left(\frac{1 - k_m^s}{C_r} + \frac{k_m^s}{C_{r0}} \right) + \frac{k_c}{n_k} \left(\frac{(C_r - 1)}{2} R_l \left(k_l^v + k_l^p D \right) + \frac{n_c}{C_r} \right) \right).$$ (9)

The parameters K_m, K_l^v, K_c, K_l^r are the normalized cost factors and are given by

$$k_m = \frac{A_{m0}}{A_{k0}}, k_c = \frac{A_c}{A_{k0}}, k_l^v = \frac{A_l^v v_g}{A_c}, \text{ and } k_l^p = \frac{A_l^p v_g}{A_c} \text{ cm-1}$$ (10)

The cost of the modulators and components are normalized to the cost of a klystron at a compression ratio C_{r0}. However, the cost of the delay line is normalized to the cost of a component. This is done because of the nature of the information available for the cost estimates at this time [12].

In the following we will compare all available pulse compression techniques based on the above-described criteria. To make the comparison more specific for the proposed NLC design we will make the following assumptions:

a. The operating frequency of the system is 11.424 GHz
b. The duration of the accelerator rf pulse is 380 ns.
c. The basic waveguide delay system uses the TE_{01} mode.
d. The next higher order modes that can be used are the two polarizations of the TE_{12}, and the two polarizations of the TE_{22} mode. Hence in calculating the efficiency of the compression system, the theoretical attenuation as a function of diameter for these modes is considered.
e. The efficiency of transmission from the klystrons to the pulse compression system and from the pulse

compression system to the accelerator structure is about 90%. Hence the total efficiency of the rf system is, $\eta_c = 0.9\eta_t\eta_i$; where η_i is the intrinsic efficiency of the system, and η_t is the efficiency of the delay lines. The maximum possible value is achieved with the DLDS using the TE_{01} mode in all waveguides.

f. The number of accelerator structures N_a is 9936 for 1 TeV collider, and the power needed per accelerator structure P_a is 170 MW.

g. Based on [12], we will assume that the ratios $k_c = 0.012$, $k_m = 0.5$, $k_l^v = 36$, $k_l^p = 1.4 \, \text{cm}^{-1}$, $k_m^s = 1/3$, $C_{r0} = 4$

h. The maximum amount of energy per rf pulse E^{max} that can be handled by rf components limits the maximum number of klystrons, n_k, that can be combined to provide power to a single pulse compression system; i.e., $n_k \le E^{max}/(P_kC_r\tau)$.

Fig. 1 Comparison between different pulse compression schemes. The relative cost is normalized to the cost of a single moded DLDS at a compression ratio of 4.

i. Because components vary in their complexity we will give different weights to them. Hence in counting the number of components n_c for each system, we will assume that some complex components are the equivalent of several simple components.

Fig. 1 shows the relative cost for several systems vs compression ratio. For each of these systems we calculated a general expression for the number of components, for the length reduction factor, and for the efficiency as a function of compression ratio.

3 CONCLUSION

For most systems there is a considerable cost reduction as one goes to higher compression ratios. This implies the need for rf power sources that are capable of longer pulse width.

The development of high power circulators, multi-moded technology and active super-high-power switches will result in a considerable cost reduction for the NLC

4 REFERENCES

[1] The NLC Design Group "Zeroth-Order Design Report for the Next Linear Collider," SLAC-Report-474, May 1996.

[2] Z. D. Farkas et. al., "SLED: A Method of Doubling SLAC's Energy," Proc. of the 9th Int Conf. on High Energy Accelerators, 1976, p. 576.

[3] Z. D. Farkas, "Binary Peak Power Multiplier and its Application to Linear Accelerator Design," IEEE Trans. MTT-34, 1986.

[4] P. E. Latham, "The Use of a Single source to Drive a Binary Peak Power Multiplier," Linear Accelerator Conference, Williamsburg, Virginia, 1988, CEBAF-R-89-001, pp. 623-624.

[5] Z. D. Farkas, et . al., "Two-Klystron Binary Pulse Compression at SLAC," Proc. of the IEEE Particle Accelerator Conference, Wasington DC, May 1993, p. 1208.

[6] P. B. Wilson, Z. D. Farkas, and R. D. Ruth, "SLED II: A New Method of RF Pulse Compression," Linear Accl. Conf., Albuquerque, NM, September 1990; SLAC-PUB-5330.

[7] S.G.Tantawi, et al. "Active High-Power RF Pulse Compression Using Optically Switched Resonant Delay lines" IEEE TRANSACTIONS ON MICROWAVE THEORY AND TECHNIQUES IEEE, Aug. 1997. vol.45, no.8, pt.2, p. 1486-92

[8] H. Mizuno, Y. Otake, "A New Rf Power Distribution System For X Band Linac Equivalent To An Rf Pulse Compression Scheme Of Factor 2**N," 17th International Linac Conference (LINAC94), Tsukuba, Japan, Aug 21 - 26, 1994, KEK-PREPRINT-94-112, Oct 1994. 3pp.

[9] S.G. Tantawi, et al. " A Multi-Moded RF Delay Line Distribution System for the Next Linear Collider," to be published in the proc. of the Eighth Workshop on Advanced Accelerator Concepts, Baltimore, MD, USA 6-11 Jul 1998.

[10] Robert M. Phillips, private communications.

[11] Richard Cassel, private communications.

[12] Michael L. Neubauer, private communications.

A PROOF-OF-PRINCIPLE POWER CONVERTER FOR THE SPALLATION NEUTRON SOURCE RF SYSTEM*

W.A. Reass[#], J.D. Doss, M.G. Fresquez, D.A. Miera, J.S. Mirabal, P.J. Tallerico

Los Alamos National Laboratory,

P.O. Box 1663, MS H-827, Los Alamos, NM 87545

Abstract

The power converter for the SNS RF system is a fast pulsed power supply that transforms 7 kV, 3-phase ac input power into 120 kV pulses with an amplitude of 80 A, a flat-top pulse length of 1.1 ms, and a repetition rate of 60 Hz. The power converter accomplishes this transformation by rectifying the input power to 8 kV dc. This is followed by a high-frequency (20 kHz) switched mode dc-to-dc converter that has rise and fall times below 0.1 ms. (The required peak power for a pair of 2.5 MW/805 MHz klystrons is almost 10 MW, and the average power is 750 kW). Since the peak and average power requirements are a significant advance of the state-of-the art for switched-mode power supplies, it is prudent to design and build a scale version of the circuit. This proof-of-principle version of the circuit is a 1/100th voltage model that operates with an input of 100 V and produces an output of 1200 V. The critical components of the converter are the IGBT switches and the high voltage transformer. The design of the low-power converter involved a novel high voltage transformer and the same switches that will be used in the high power converter. Simulations have been performed and data that shows agreement between the computer simulation and the scale model will be presented.

1 INTRODUCTION

The simplified block diagram of the (full-scale) IGBT converter-modulator is shown in Figure 1. This system topology offers a number of engineering advantages as compared to other long pulse modulator designs. The converter-modulator derives it's plus and minus buss voltages from a standard substation open frame cast-core transformer. The transformers and the associated support and personnel safety equipment is placed along the length of the LINAC, as placement requires, in utility sheds. This semi-remote equipment is "dumb"; it does not require control I/O or monitoring equipment. A utility umbilical cable connects to the converter-modulator assembly and the AC feed is locally switched and rectified in a utility cabinet, part of the converter-modulator assembly. A step-start network is required to minimize turn-on transients from the resonance of the capacitor bank, substation transformer leakage, and line harmonic filter networks. The rectifier stacks provide a buss voltage of + 4 kV and – 4 kV. The energy storage networks utilize self-clearing metalized hazy polypropylene capacitors. With these capacitors, soft degradation can be monitored

and capacitors can be replaced during a normal maintenance cycle, if needed. Switching is provided by a series string of 8 IGBT's for each plus and minus rail (for each phase). For three phase switching, 48 devices (3 x 16) are required. We have chosen 1700 volt devices because their superior switch current ratings and significantly lower (switching) loss as compared to higher voltage devices. With our chosen snubber networks, and relatively low string voltage, IGBT timing skews of 250 nS can easily be tolerated and yet maintain transient voltages within device ratings. A unique boost-transformer has been designed for the polyphase voltage step-up at 20 kHz. This transformer, whose core configuration is shown in Figure 2 is called a polyphase "Y". This transformer core design helps to provide a low leakage inductance, good balance between phases (core flux paths are all equal to one another), and minimal cost. Special magnetic alloys are expensive; this design uses half the core material as compared to 3 individual "C" cores. Transformer secondary shunt-peaking is desirable to tune out leakage inductance and maximize output voltage. Various shunt-peaking capacitor types may be used, but mica is a good low loss dielectric system for this voltage and frequency. Rectification is provided by series strings of ion-implanted diodes with 1400 volt, 75 Amp, and ~50 nS reverse recovery ratings. The output filter network is optimized to adequately filter the 120 kHz rectification pulses, yet have little stored energy. At the end of each klystron video pulse, the stored energy must be dissipated, in addition, in a klystron arc-down condition, excessive stored energy would be detrimental to the klystron. In series with each klystron, dI/dT limiting networks reduce the rate of energy deposition to help ensure continued klystron reliability.

2 COMPUTER MODELING

The system design topology has been thoroughly scrutinized with computer modeling to determine system performance, component sensitivities, circuit efficiency, and fault tolerance. Due to the repetitive pulse loading of the utility grid, line harmonic and power factor issues are a concern. Fortunately, a simple circuit with power factor correction capacitors and line filter chokes can provide almost unity power factor and line harmonics that are within IEEE specifications at full power operation.

Unfortunately, the resulting line impedance resonates with the transformer leakage inductance and capacitor filter network during start-up, resulting in over-voltage of the

capacitor bank. This problem can be alleviated by the use of a resistive step-start system. The step-start system must be cycled during any brownout or interruption of utility service, i.e. from a lighting strike or other anomaly. IGBT performance can be more reliably assured by the choice of appropriate snubber networks to help equalize dynamic voltage division. With our chosen parameters, the snubber loss for each IGBT is about 90 watts with ideal timing of the IGBT transistors. With a 250 nS timing skew, the peak transient voltage across the IGBT reaches about 1450 volts, well within the devices 1700 volt ratings, as shown in Figure 3. Continuous operation with this timing skew (250 nS) results in about 180 watts being dissipated in the snubber network resistor. The transformer design for this system also requires careful consideration. Transformer magnetizing and leakage inductance play a critical role in system performance. Fortunately, some leeway is provided by the use of shunt-peaking capacitors in the transformer secondary. The effect on the klystron output voltage, with steps of shunt-peaking capacitance, is shown in Figure 4. This results in changes of IGBT switch current. High values of shunt-peaking capacitance over-compensate the circuit and reduce voltage output and increase IGBT switching current. The circuit model is run with the IGBT's operating with a full 180-degree conduction angle. In the actual system operation, pulse width modulation will be utilized to regulate and flattop the klystron cathode voltage pulse. A detail of the cathode voltage pulse with full 180-degree conduction is shown in Figure 5. At all times the cathode voltage is above the required 120 kV. A reduced conduction angle will provide the appropriate output voltage. In addition, other computer modeling has shown that the turn-on overshoot can be totally removed by reducing the conduction angle of the IGBT's first few pulses. A klystron cathode voltage waveform at reduced voltage, due to reduced IGBT conduction angle is shown in Figure 6. What is interesting about this result is that there is no increase in the apparent output ripple. (The output fundamental is still 120 kHz, but there are significantly higher Fourier frequency components, which the output filter network smoothes more effectively). A critical parameter for any klystron modulator system is the energy deposited in the klystron during a fault condition. Our IGBT configuration is a very benign system; the total fault energy deposited in a klystron is about 8 joules, only in the event the converter is not interrupted during its' 1.1ms switching cycle. This result is shown in Figure 7. In addition, the peak fault current in the klystron is less than 200 Amps, with low dI/dT's.

3 SCALE MODEL RESULTS:

The scale model converter worked as designed with results that compare well to the computer model, the first time it was turned on. In addition, some results required further computer analysis to help analyze what we observed. It was counter-intuitive to us that at reduced output voltage and conduction angle, output ripple would not increase. The full output voltage from the scale model converter is shown in Figure 8 and compares well with Figure 5. With reduced conduction angle, the output voltage is shown in Figure 9, and it also compares well with Figure 6. Fortunately, the most fun comes from analyzing and optimizing the system performance in our test set-up. We have been able to determine the effect on IGBT timing offsets and examine the resultant output ripple, which also has agreed with our computer analysis.

4 CONCLUSION:

The IGBT converter-modulator full-scale design is nearly complete. The concept and performance of the novel design topologies have been proven with the scale model version. Comparison with the computer predicted results furthers our resolution that this circuit topology will prove eminently successful. In addition, control electronic designs have been tested and evaluated that can directly operate our full power version. It is clear to us that this type of converter-modulator offers many significant advantages over other system designs and techniques. Among these advantages are that no crowbar system is required; a single point network I/O; a small inexpensive and dumb substation; and a low voltage energy store with self-clearing capacitors. Other advantages are the reliability of a completely solid-state system, minimal oil requirements, a small footprint less than competing designs, and safety advantages over H.V. anode modulation systems.

Figure 1: Simplified Block Diagram of 20KHz IGBT Converter-Modulator

Cast-Core Substation Transformer
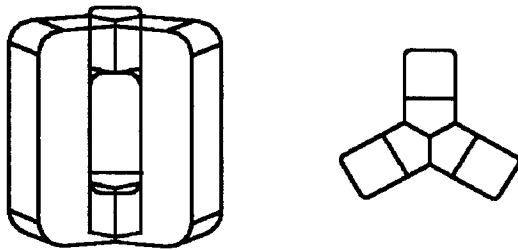
Step-Start

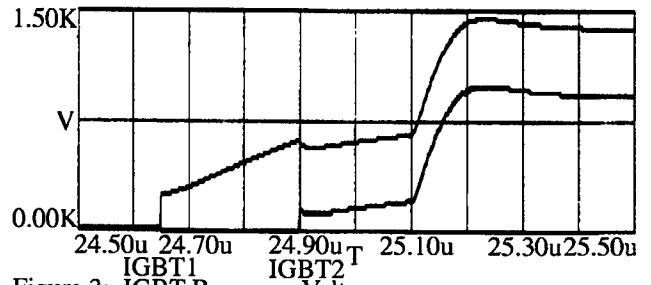Polyphase Conversion

Figure 2: Polyphase Y Transformer

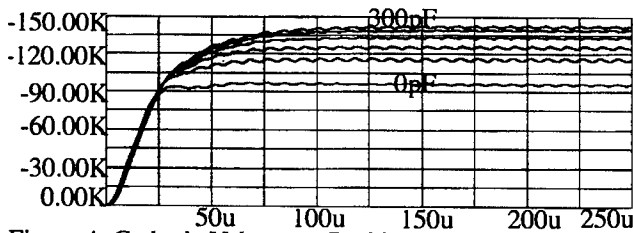Figure 3: IGBT Recovery Voltage

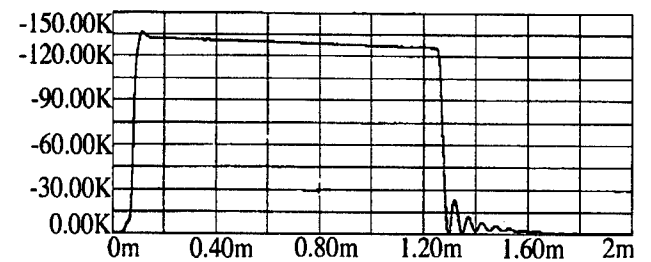Figure 4: Cathode Voltage vs Peaking Capacitance

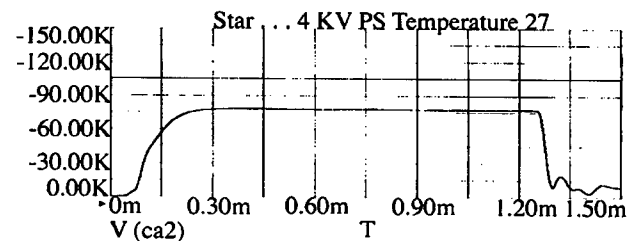Figure 5: Computer Model Cathode Voltage

Figure 6: Computer Model at Reduced Output.

Figure 7: Klystron Fault Energy

Figure 8: Scale Model Output Voltage

Figure 9: Scale Model at Reduced Output.

EXPLORING MULTIPACTING CHARACTERISTICS OF A RECTANGULAR WAVEGUIDE*

R.L. Geng[†‡], H.S. Padamsee, Laboratory of Nuclear Studies, Cornell University, Ithaca, NY 14853

Abstract

Multipacting (MP) characteristics of the rectangular waveguide used for CESR-III Superconducting RF (SRF) system were investigated by using a newly developed 3-D computer code. MP bands were identified for different operating modes, such as standing wave (SW) mode, traveling wave (TW) mode and the so called mixed wave mode (TW mixed with SW). A comparison between the simulation results and the experimental observations for the installed CESR-III SRF systems was made. Measures to suppress multipactor were explored. Our simulation results suggested that an external DC magnetic field of a few Gauss of amplitude in the wave propagation direction would be very effective in disturbing the trajectories. Further work will include disk-type windows in the waveguide couplers.

1 INTRODUCTION

Multipacting (MP) is a resonant electronic process that may happen when a system is subjected to RF fields and vacuum[1]. When MP occurs, a large number of electrons are generated, consuming the RF power in the system and resulting in vacuum degradation or discharge and metal sputtering.

The Multipacting phenomena for various systems have been studied intensively in the past few decades[2][3][4]. Scaling laws were established based on theoretical studies for simple geometries and have been successfully used for guiding designs. More recently, numerical simulations were performed to study MP in more complex RF structures for accelerators[5][6][7].

Waveguide input couplers are used for the PEP-II normal conducting RF system[8] and CESR-III SRF system[9]. These waveguides are expected to work in regimes which have not been encountered before, namely multi-hundred kW power levels and few hundred MHz frequencies. It is of interest to understand the MP characteristics and the influences of MP on the high power performance of these couplers. Basically two questions need to be answered: 1) are there any possibilities that MP may occur? 2) if there are possibilities what measures are available to stop the multipactor? To answer these questions, simple scaling laws are not enough and simulation codes are needed, because these couplers work not only in pure TW/SW modes, but also in a more complex mode, namely mixed wave mode. Also, it is highly desired to investigate MP in the ceramic window regions of these couplers. In this case no scaling law is handy and a numerical code is indispensable.

2 THE CODE

The simulation code essentially consists of two core parts, one for computing electron trajectories and the other for searching and analyzing MP. The leap-frog algorithm was used in the trajectory computing part and electron motions were described with relativistic dynamic equations. Note that the space-charge effect was not taken into account. For simplicity, it was assumed that the electron was emitted at an energy of 2 eV, with velocity perpendicular to the emission surface.

Denoting the wide and narrow dimensions of the reduced height waveguide in the CESR SRF system as a (0.433 m) and b (0.102 m), the electro-magnetic fields of the dominant mode (TE_{10}) can be generally described in a (x, y, z) coordinate system as follows,

$$\begin{cases} E_y = E_0 \sin(X)[\cos(\omega t - kz) + \rho \cos(\omega t + kz)], \\ B_x = \frac{-k}{\omega} E_0 \sin(X)[\cos(\omega t - kz) - \rho \cos(\omega t + kz)], \\ B_z = \frac{-\pi}{\omega a} E_0 \cos(X)[\sin(\omega t - kz) + \rho \sin(\omega t + kz)], \end{cases} \tag{1}$$

where E_0 is the maximum electric field of the forward wave, $X = \pi x/a$, $\omega = 2\pi f$ (f=500 MHz) is the angular frequency of the field, $k = \sqrt{\omega^2 \mu \epsilon - (\frac{\pi}{a})^2}$ is the propagation constant, t is time, and ρ is the voltage reflection coefficient. E_0 is related to the forward RF power (P_f) like this, $P_f = \frac{E_0^2 abk}{4\omega\mu}$. ρ can be derived from the forward and reflected (P_r) powers, $\rho = \sqrt{\frac{P_r}{P_f}}$. Note that the fields are pure TW if $\rho = 0$, pure SW if $\rho = \pm 1$, and mixed wave otherwise.

It is well known that MP characteristics depend strongly on the surface characteristics. In our simulation the secondary emission coefficient (SEC) of a "wet prepared" niobium[5] was used. For improving the computation efficiency the SEC (δ) is formulated[10] as follows,

$$\delta(u) = \delta_m \frac{1 - exp[-A(u/u_m)^B]}{C(u/u_m)^D}, \tag{2}$$

here u in eV is the impacting energy of the primary electron and $\delta_m = 1.6$ is the maximum SEC corresponding to an impacting energy of u_m=200 eV. The curved fitted $ABCD$ parameters are $A = 1.55$, $B = 0.9$, $C = 0.79$, and $D = 0.35$.

The very useful concepts of *counter function* and *enhanced counter function* were adopted in the MP searching and analyzing part. A complete description of these concepts can be found in Ref.[7]. Basically, the counter function is a measure of the number of survived primary electrons after several (e.g. 10 or 20) impacts, and the enhanced counter function is a measure of total number of electrons, including primaries and secondaries, after the same number

of impacts. In the following sections, we will show *relative enhanced counter function*, e_n where n is the number of impacts, as a function of the forward power. An e_n which is larger than unity is a good indication of the existance of an MP band.

3 MP BANDS FOR DIFFERENT WORKING MODES

Due to symmetry, it is enough to consider a waveguide section with a length of a quarter guided wavelength. After a survey launching over the whole inner surface of such a section, it was found that only electrons launched from the peak electric site may develop into MP. So in the following discussions, electrons are launched from only the peak electric site(s).

The relative enhanced counter functions for 10 and 20 impacts for the SW mode and TW mode are shown in Fig. 1 - Fig. 4 respectively. Among all the MP bands, only a

Figure 1: The relative enhanced counter function e_{10} for the SW mode. The $e_{10} = 1$ line is indicated.

Figure 2: The relative enhanced counter function e_{20} for the SW mode. The $e_{20}=1$ line is indicated.

few are robust enough to sustain 20, even more, impacts. All others are mild and can sustain only 10 impacts. The mild bands may appear when the surface's SEC is high but are expected to be easily processed. Robust bands could

Figure 3: The relative enhanced counter function e_{10} for the TW mode. The $e_{10}=1$ line is indicated.

Figure 4: The relative enhanced counter function e_{20} for the TW mode. The $e_{20}=1$ line is indicated.

constitute hard barriers. Further trajectory computations revealed that all those MP's are two-point MP. Electrons travel back and forth and impact with the bottom and top walls. For the SW mode, impacts are limited to two points on the bottom and top walls; while for the TW case, impacting points drift along the wave propagation direction. The MP order, number of half RF cycles elapsed between succeeding impacts, is also labeled in the plot of e_{20}.

Fig. 5 and Fig. 6 show the relative enhanced counter functions for 10 and 20 impacts for mixed waves with 1% and 4% reflected power mixed. Two main features manifest themselves as a result of trajectory disturbance due to wave mixing: 1) compared to the pure TW case (Fig. 3 and Fig. 4), the MP band at 90 kW is enhanced; 2) with more reflected power mixed, most MP bands are shifted up to higher power levels with lower intensities. These effects were experimentally confirmed during the machine studies of the first SRF cavity for CESR luminosity upgrade. A barrier was encountered at about 90 kW forward power. When the cavity was run at a 6.3 MV/m gradient, the forward power limit due to RF trip was 125 kW; while at 7 MV/m, the forward power limit was pushed to 135 kW. An extra 10 kW forward power was gained as a result of more reflected power mixed.
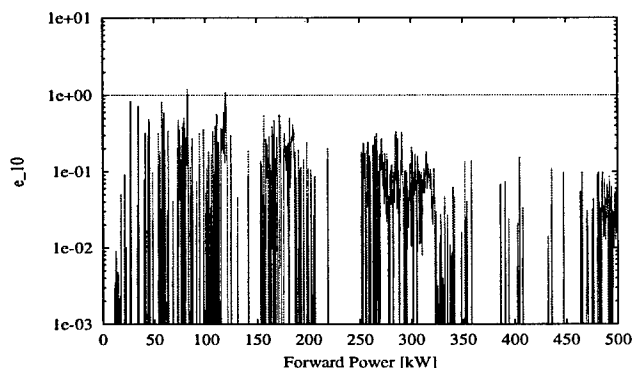
Figure 5: The relative enhanced counter function e_{10} for mixed wave modes. The $e_{10} = 1$ line is indicated.

Figure 6: The relative enhanced counter function e_{20} for mixed wave modes. The $e_{20} = 1$ line is indicated.

4 SUPPRESSING MP WITH PERTURBATION MAGNETIC FIELDS

It is well known that MP can be avoided by applying suitable perturbation DC electric or magnetic fields. In case of a rectangular waveguide, a magnetic perturbation seems more natural for this purpose. Fig.7 shows the relative enhanced counter functions for 20 impacts with 3 Gauss magnetic perturbation fields applied along x and z direction for the TW mode. It is shown that with a 3 Gauss perturbation field along x direction, the MP is enhanced, both in intensity and in bandwidth; while with a 3 Gauss field along z, all the MP bands bellow 500 kW are virtually eliminated. For the SW case, it is also justified that a perturbation magnetic field along z direction is effective in suppressing MP.

5 CONCLUSIONS AND OUTLOOK

Below 500 kW forward power, there are a couple of clearly defined MP bands in the reduced height waveguide in the CESR-III SRF system. For the TW mode these bands are quite likely dangerous. For the SW mode, only the bands below 150 kW forward power seem harmful. Mixing a forward wave with some portion of a reflected wave will push the multipactor to higher power levels and MP intensities

Figure 7: The relative enhanced counter functions e_{20} for the TW mode with perturbation magnetic fields (note that the data for $B_z = 3$ Gauss are too small, $\sim 10^{-10}$, to be shown). The $e_{20}=1$ line is indicated.

will decrease. A perturbation magnetic field along x direction makes the MP enhanced; while a perturbation magnetic field along z direction eliminates virtually all the MP bands bellow 500 kW forward power.

Currently we are studying MP in the ceramic window region in the waveguide. Due to the structure complexity in that region, the field distributions needed by the MP computation can only be obtained with a numerical code. A practical problem arises when computing MP with numerical fields due to space discretization. In order to work out a way to incorporate discretized fields into MP computations, the waveguide investigated above was studied again with MAFIA[11] field distributions. The main MP features were well repeated with a 3 mm mesh size, which gives us confidence to go on to complex structures like ceramic regions.

Finally, we would like to mention that the algorithm used in this paper was checked against analytical results for a parallel-plate and proved to be reliable.

6 REFERENCES

[1] H. Padamsee, J. Knobloch, and T. Hays, *RF superconductivity for accelerators*, John Wiley & Sons, Inc. 1998.

[2] E.W.B. Gill and A. von Engel, *Proc. R. Soc. London* A192, 446(1948).

[3] A.J. Hatch and H.B. Williams, *Phys. Rev.* 112(3), 681(1958).

[4] A. Woode and J. Petit, *ESA Journal* 14(4), 467(1990).

[5] H. Padamsee and A. Joshi, *J. Appl. Phys.* 50(2), 1112(1979).

[6] S. Yamaguchi et. al., *IEEE Trans. on Nucl. Sci.* 39(2), 278(1992).

[7] E. Somersalo et. al., *Particle Accelerators* 59, 107(1998).

[8] M. Neubauer et. al., *Proc. 1995 Part. Accel. Conf.* p.1803.

[9] E. Chojnacki et. al., *Proc. of the 8th Workshop on RF Superconductivity, Abano Terme, Italy*, 1997.

[10] G.E. Dionne, *J. Appl. Phys.* 46, 3347(1975).

[11] http://www.cst.de/

IMPROVEMENT OF CAVITY PERFORMANCE BY ELECTRO-POLISHING IN THE 1.3 GHZ NB SUPERCONDUCTING CAVITIES

E. Kako, S. Noguchi, M. Ono, K. Saito, T. Shishido, B. Aune*,
J.P. Charrier*, M. Juillard* and H. Safa*

KEK ; 1-1, Oho, Tsukuba, Ibaraki, 305-0801 JAPAN
CEA-Saclay ; Gif-sur-Yvette, 91191 FRANCE

Abstract

A steep drop of the cavity quality factor (Q_0) at high electric field has been observed frequently in chemically-polished and high-pressure-rinsed Saclay cavities, even in the absence of field emission. Three single-cell cavities from Saclay were tested at KEK following electropolishing and high pressure rinsing. This treatment eliminated the steep Q_0 drop, the quench field increased to an accelerating gradient of more than 30 MV/m with a quality factor above 2×10^{10}. No dependence of the quench field on the niobium RRR was observed between RRR = 200 and 320 in electropolished cavities.

1 INTRODUCTION

In superconducting cavities, the cavity performance strongly depends on surface preparation techniques. To obtain a smooth and clean surface, the cavity interior is finished by chemical polishing (CP) or electropolishing (EP). The high pressure rinsing (HPR) that follows has been proven effective to remove dust particles and chemical residues. A clean environment during assembly and careful handling are essential for suppression of field emission. By following these preparation steps, high accelerating gradients (Eacc) of 30~40 MV/m has been achieved without field emission in many cavities at KEK. In the latest investigation at KEK, it was noted that the cavities prepared by EP performed better than CP cavities [1]. To confirm this observation, extensive tests of both CP and EP cavities has been carried out in collaboration between KEK and CEA-Saclay. Baseline tests were carried out at Saclay, making use of various diagnostic systems developed at Saclay. Then, the cavities were sent to KEK for further tests to study systematically the effect of surface treatment on cavity behavior. The following treatments were carried out: 1) only HPR, 2) CP and HPR, 3) EP and HPR. The effect of "parking" the cavity at 100K for two hours was also investigated to check for the hydrogen Q_0-disease.

2 EXPERIMENTS AT SACLAY

Three 1.3 GHz Saclay cavities (listed in Table 1) were chosen for this study. These cavities were manufactured at Cerca (France). The initial CP was performed with a 20°C acid mixture of $HF:HNO_3:H_3PO_4$ = 1:1:2 in volume for a total removal of about 150µm at a rate of about 1 µm per minute. After HPR at 90 bar for 40 minutes, the cavities were dried in a dust-free air flow for three hours. These cavities were initially tested with no heat-treatment (HT). The location of a quench and the residual resistivity ratio (RRR) of the cavity were measured with a rotating temperature and RRR mapping system [2]. The obtained quench field and average RRR are shown in Table 1. One method to push up the quench field is purification of the niobium by Ti-gettering during HT to improve the thermal conductivity [3]. High temperature HT [4] was carried out on the cavities S-1 and S-2. The RRR was improved after HT, and the quench field increased to 25 MV/m. However, a steep drop of the Q_0 was observed above 18 MV/m, as seen in Figure 1. The same phenomenon had also been observed in KEK cavities tested at Saclay [5]. Neither x-rays nor field-emission electrons were observed at these higher fields. Similarly, thermometry measurement at 25 MV/m could not detect any field-emission sites. Each cavity in Figure 1 was limited by a quench around the equator seam of electron beam welding (EBW).

Table 1: Properties of the Saclay cavities

cavity	niobium sheets supplier	RRR*	no HT, CP150µm Eacc,max	ave.RRR
S-1	T-Denkai	200	20.9 MV/m	190
S-2	Heraeus	260	20.9 MV/m	160
S-3	Heraeus	280	15.1 MV/m	230

RRR* ; specification by the company.

Figure 1: Test results at Saclay

3 EXPERIMENTS AT KEK

The same cavities were tested three times each at KEK. For the initial test, only HPR at 85 bar for 60 minutes was performed. A second test was preceded by CP with a 25°C acid mixture of HF:HNO$_3$:H$_3$PO$_4$ = 1:1:1, yielding a

removal rate of 12 μm per minute (about ten times faster than that at Saclay). Finally, prior to the third test, EP was carried out with a horizontal, rotating electropolishing device [6]. An acid mixture of H$_2$SO$_4$: HF = 10:1 was used, and the removal rate of 12 μm per minute (about ten times faster than that at removal rate was 0.5 μm per minute at 30°C. In each case, HPR preceded the final cavity assembly. The wet cavity was pumped out and baked at 85°C for twenty hours. Then, the cavity was installed in the test stand, and no active pumping was performed during the cavity test. Figure 2 shows the KEK test results. In all cases, a quench (without field emission) was the ultimate field limitation, similar to the Saclay results. However, the quench field clearly increased after EP. The effect of 50μm EP with cavity S-3 was especially pronounced, pushing the quench field up from 17 MV/m to 33 MV/m. Moreover, in each test after EP, a steep Qo drop at high field was not observed, and changed to a standard slope. The quench field and the residual surface resistance (Rres) after each treatment are summarized in Figure 3. Both the quench field and the Rres had deteriorated in the first test at KEK (after HPR), presumably due to surface contamination during transport (e.g., exposure to the air). However, the cavity performance was recovered by CP. EP then augmented the quench field to above 30 MV/m. On the other hand, the Rres remained unchanged by EP. The relatively high surface resistance of the S-3 cavity may be due to the small grain size (this cavity was never heat-treated).

Figure 2: Test results at KEK

Figure 3: Summary of the quench field and the Rres

4 DISCUSSIONS

4.1 Degradation due to CP after EP

Additional EP of 70 μm was performed on cavity S-3, improving the quench field to 37 MV/m. A subsequent surface removal by CP clearly degraded the cavity performance again, as shown in Figure 4. A similar effect has been reported in reference [7]. Additional CP lowered the quench field even more and the steep decline of the Qo at high field appeared again. It is assumed that a chemical reaction between niobium and the acid during CP produces a bad superconductor, especially at the grain boundaries around the equator seam, where many impurities might concentrate due to recrystalization by EBW.

4.2 Quench field

High RRR niobium with its large thermal conductivity is needed to thermally stabilize surface defects that might otherwise cause a quench at a high gradient. The correlation between the quench field and the average RRR in eight cavities tested at Saclay is plotted in Figure 5. The results with the CP cavities in Figure 5 are consistent with above mention. After EP, however, no dependence of

quench field on RRR was observed. This demonstrates that the origin of a quench may differ in CP and EP cavities.

4.3 Qo-disease

The cavities were parked at 100K for two hours to investigate possible hydrogen problem of the niobium (Qo-disease). The obtained Rres results in three cavities are listed in Table 2. It is well-known that HT above 700°C for hydrogen degassing is effective to avoid the Qo-disease. It is noteworthy that no Qo-disease was observed in the S-3 cavity (no HT), even after 120μm EP. This result shows an omission of 700°C HT after EP.

Table 2: The Rres following a 100K "park" for two hours

cavity	surface treatment	initial*	100K,2h	ΔRres
S-1	1300°C HT, CP140μm	5.5	10.5	+5.0 nΩ
S-2	1000°C HT, CP130μm	7.7	8.0	+0.3 nΩ
S-3	no HT, CP200μm	6.1	5.9	-0.2 nΩ
	, +EP120μm	5.6	5.3	-0.3 nΩ

initial*; fast cool-down within 1 hour from 300K to 4.2K

5 SUMMARY

a. The 50 μm EP eliminated the steep Qo drop at high field in CP cavities and pushed up the quench field to more than 30 MV/m.
b. No dependence of the quench field on RRR was seen between RRR = 200 and 320 in cavities that were electropolished.
c. There was no difference in the Rres between CP and EP cavities.
d. CP after EP gradually reduced the quench field and caused the Qo drop at high field to appear again.
e. No Qo-disease was observed after parking the cavity at 100K for two hours, even in the no HT cavity after EP.

Figure 4: Cavity degradation due to CP after EP

Figure 5: Quench field vs. RRR

6 REFERENCES

[1] K. Saito, et al., "Superiority of Electropolishing over Chemical Polishing on High Gradients ", Proc. of the 8th Workshop on RF Superconductivity, Abano Terme (Padova), Italy (1997), to be published.
[2] M. Bolore, et al., "A New Inductive Method for Measuring the RRR-value of Niobium", Proc. of the 7th Workshop on RF Superconductivity, CEA-Saclay, Gif-sur-Yvette, France (1995), p541-545.
[3] P. Kneisel, "Use of the Titanium Solid State Gettering Process for the Improvement of the Performance of Superconducting RF Cavities ", J. of Less Common Metals, 139 (1988) p179-188.
[4] H. Safa, et al., "Nb Purification by Ti Gettering", ibid. [2], p649-652.
[5] E. Kako, et al., "Cavity Performance in the 1.3 GHz Saclay/KEK Nb Cavities", ibid. [1].
[6] K. Saito, et. al., "R & D of Superconducting Cavities at KEK", Proc. of the 4th Workshop on RF Super-conductivity, KEK, Tsukuba, Japan (1989), p635-694.
[7] E. Kako, et al., "Characteristics of the Results of Measurement on 1.3 GHz High Gradient Superconducting Cavities", ibid. [2], p425-429.

Architecture and Performance of the PEP-II Low-Level RF System*

P. Corredoura[†]

Stanford Linear Accelerator Center, Stanford, Ca 94309, USA

Abstract

Heavy beam loading in the PEP-II B Factory along with large ring circumferences places unique requirements upon the low-level RF (LLRF) system. RF feedback loops must reduce the impedance observed by the beam while ignoring the cavity transients caused by the ion clearing gap. Special attention must be placed on the cavity tuner loops to allow matching the ion clearing gap transients in the high energy ring and the low energy ring. A wideband fiber optic connection to the longitudinal feedback system allows a RF station to operate as a powerful "sub-woofer" to damp residual low order coupled bunch motion.

This paper describes the design and performance of the VXI based, EPICS controlled, PEP-II low-level RF system(s). Baseband in-phase and quadrature (IQ) signal processing using both analog and modern digital techniques are used throughout the system. A family of digital down converters provide extremely accurate measurements of many RF signals throughout the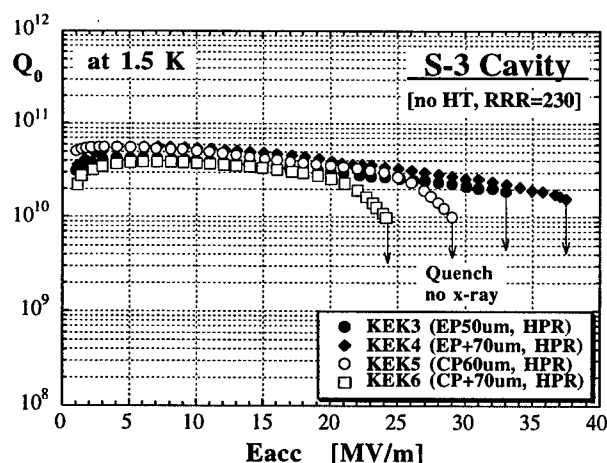 system. Each system incorporates a built-in network analyzer and arbitrary RF function generator which interface with Matlab to provide a wide range of functions ranging from automated config-uration of each feedback loop to cavity FM processing. EPICS based sequences make the entire system a turn-key operation requiring minimal operator intervention. In the event of a fault, fast history buffers throughout the system write selected RF signals to disk files which can be viewed later to help diagnose problems. Actual data from commis-sioning runs of PEP-II is presented.

1. INTRODUCTION

Both the high energy ring (HER) and the low energy ring (LER) of the PEP-II B factory are longitudinally unstable due to interaction between the beam and the fundamental mode of the RF cavities. Growth rate from the accelerating mode is determined by the difference of the total real impedance observed by the beam at the synchrotron side-bands corresponding to the mode in question (equation 1).

I_0 = average DC beam current
η = momentum compaction
β = particle velocity factor
ν_s = synchrotron tune
E = particle energy
e = electron charge
f_{rf} = RF frequency
R_{cb} = total real($Z_{upper} - Z_{lower}$)

$$\frac{1}{\tau} = \left(\frac{I_0 \eta f_{rf}}{2 \nu_s \beta^2 \frac{E}{e}} \right) R_{cb}$$

Equation 1. Growth rate for fundamental cavity mode [1]

Fig. 1. Cavity impedance, beam revolution harmonics, synchrotron sidebands - mode numbers labeled

For storage rings with large circumference, like PEP-II, several revolution harmonics interact strongly with the accelerating mode of the RF cavities. The cavity detuning required to store the high beam currents create a worst case scenario where the peak cavity impedance actually crosses the first revolution harmonic (figure 1). Evaluating equation 1 for these conditions produces longitudinal growth rates less than one revolution period. This drove the system design to include several RF feedback loops to reduce the impedance observed by the beam (figure 2) [1].

The direct RF feedback loop is a simple proportional controller operating on the complex RF vector using the cavities as the bandwidth limiting element(s). The gain of this loop is limited by the system delay and was the driv-ing force for the procurement of wide band (short delay) klystrons. With the 150 ns group delay klystrons we achieved <500 ns total loop group delay and apply 15 dB of direct loop gain. The measured impedance reduction is shown (figure 3). Notice the peak impedance is reduced as expected but the driving impedance for other modes has actually increased. This effect is caused by the loop delay.

To further reduce the growth rates digital comb filters operate in parallel to the direct loop to apply additional gain at the synchrotron sidebands of the low-order revolu-tion harmonics. Since the combs only have gain over a narrow bandwidth near each synchrotron sideband, they are not limited by the group delay and can contribute an additional 20 dB of impedance reduction. To allow maxi-mum comb gain the variation in group delay beyond the direct loop bandwidth is compensated for with a group delay equalizer filter. The equalized comb correction is digitally delayed to be applied on the next beam revolu-tion. The effect of the comb loop on the cavity impedance is also plotted (figure 3).

Fig. 2. Block diagram of RF feedback loops used in the PEP-II low-level RF system. Multi-cavities not shown.

At the design current the beam induced cavity voltage vector is larger than the klystron vector. To prevent the RF feedback loops from saturating while trying to fight the cavity transients caused by the 370 ns ion clearing gap, a dedicated module performs a learning algorithm and generates IQ references which track the gap transient.

To provide a safety margin of longitudinal control each RF station may be modulated with a band-limited version of the longitudinal feedback system "kick" signal. A fiber optic serial link allows each RF station to operate as a powerful "sub-woofer" for the wideband (but power limited) longitudinal multi-bunch [8] feedback system (LFB).

Fig. 3. Measured real cavity impedance with no feedback, direct RF feedback and also equalized comb feedback.

2. RF FEEDBACK DETAILS

All RF feedbacks loops use baseband In-phase and Quadrature (IQ) techniques which permit the use of the VXI local bus lines to pass information between modules. This significantly reduces the cable plant, lowers cost and improves reliability. IQ signals are the real and imaginary components of a complex vector and are the equivalent to

defining a vector in terms of its X and Y cartesian coordinates as opposed to the polar coordinates, amplitude and phase (figure 4). The IQ signals are bipolar, uniquely mapping a vector anywhere in the four quadrant system. All the information contained in the modulation of the original RF vector is preserved in the IQ signals. A signal with frequency above the carrier frequency will map to a vector rotating counter clockwise on the complex IQ plane. Signals lower than the carrier frequency become negative frequencies which rotate clockwise. Another advantage of IQ techniques is the electronics for the I and Q channels are identical. This is not true for amplitude and phase based RF control systems.

$$I = A\cos\theta$$
$$Q = A\sin\theta$$
$$A = \sqrt{I^2 + Q^2}$$
$$\phi = \mathrm{atan2}(Q, I)$$

Fig. 4. Diagram of IQ vs. phase/amplitude mapping

To provide adjustable gain and phase shifts of IQ vectors a baseband IQ modulator is used. This circuit is an analog representation of a scaled rotation matrix. An input vector can be scaled and rotated by any amount determined by the four multiplier weights (equation 2). Also note that any phase procession can be made without step discontinuities (unlike RF phase shifters).

$$\begin{bmatrix} I_{out} \\ Q_{out} \end{bmatrix} = A \begin{bmatrix} \cos\theta & -\sin\theta \\ \sin\theta & \cos\theta \end{bmatrix} \begin{bmatrix} I_{in} \\ Q_{in} \end{bmatrix}$$

Equation 2. Matrix Form of an Baseband IQ Modulator

Constructing a baseband analog IQ modulator requires four 4-quadrant multipliers and two summing amplifiers to perform the matrix mathematics (figure 5) [2]. Digital to analog converters (DACs) are used to produce the multiplier weights. Note that if the sign for the -sinθ term is handled as part of the summing circuit, only two weight values are required. We choose to use an individual DAC channel for each modulator weight to allow the multiplier offsets to be corrected for as part of each DAC weight.

The PEP-II Baseband IQ modulators use four AD834 [13] multipliers and two EL2073 [14] wideband op-amps to achieve <5ns group delay, > 40 MHz full power bandwidth and >50 dB dynamic range. A total of 7 baseband IQ modulators were used in the system requiring 28 DAC channels. Additional channels were used to null analog offsets. A total of 56 "slow" DAC channels were used. AD7805 8 channel, 12-bit DACs [13] were used to achieve the density and resolution required.

Fig. 5. Block Diagram of one IQ Baseband Modulator

RF signals from each of the cavity probes (4 in HER, and 2 in LER) are converted to analog IQ baseband signals using high level (+13 dBm) IQ demodulators [11]. The mixer outputs are AC coupled into 50 ohms, providing a good match and lowpass filtered (Fc = 225 MHz) to remove any RF. Video amplifiers provide sufficient gain (17 dB) to produce 1 volt maximum IQ signals for 0 dBm RF inputs. This level is fixed by the input specification for the AD834 multipliers [13] used in the IQ baseband modulators throughout the system.

Each demodulated cavity probe signal passes through a programmable combining network consisting of four IQ baseband modulators and two summing amplifiers. By setting the proper DAC values for each modulator, the resulting IQ signals represent the total accelerating RF vector for the station. Another baseband modulator operating on the vector sum allows adjusting the gain and phase of the direct RF feedback loop (figure 2). This modulator is also used to maintain loop phase as the cavities detune.

The output of the direct loop modulator is compared to the station IQ reference by a pair of difference amplifiers, producing IQ error signals which are then amplified 15dB. The error signals are used by the "gap loop" DSP to generate the station IQ references which may vary on a one-turn time frame to track any shape of ion clearing gap transient [3]. The adaption rate is set for 100 ms. When converged the IQ error signals (klystron drive) are constant.

Since the signals are all baseband, applying additional compensation to the direct loop is a simple way to achieve superior performance. Lead-lag compensation is used to provide increased phase margin when the cavities are detuned for full beam current. This decreases the closed loop translation of imaginary to real cavity impedance, further reducing the peak driving impedances by 25%. Integral compensation provides large gains at frequencies close to the RF carrier. With a 30 kHz bandwidth integrator, large modulation caused by the switching aspect of the klystron high voltage power supply ripple is rejected.

As beam is injected, the klystron output is increased by raising the cathode voltage. The resulting phase shift is corrected for by a DSP based "ripple" loop observing the IQ error signals and the klystron output [7]. Correction is applied to another baseband modulator at a 23 kHz rate. A slow (2 Hz) EPICS loop writes a set point in the ripple

loop to maintain constant gain through the forward path of the direct RF feedback loop as the klystron output rises.
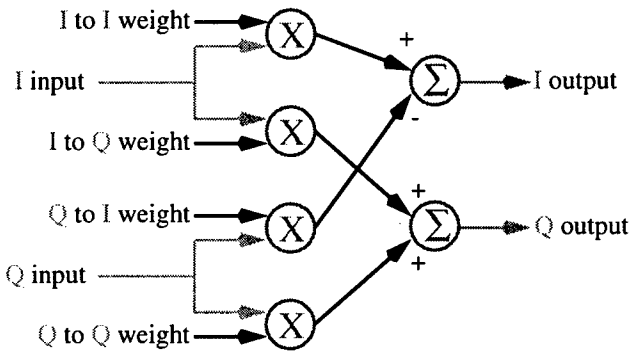
The error signals are limited with diode clamping circuits to prevent over-driving the solid state drive amplifier or klystron during transients. Finally the IQ drive signals are converted to currents and up-converted by an IQ RF modulator [11]. This high level modulator uses a +23 dBm LO and can produce enough power (+8dBm) to directly drive the 120 W klystron drive amplifier.

The comb filters AC couple to the direct loop just after the direct loop modulator so the cavity frequency offset tracking applies to both loops. The IQ signals are digitized and filtered in second order IIR digital filters (equation 3). The comb filter response peaks at synchrotron sidebands and has a zero at the revolution harmonics [1].

$$\frac{G(Z^0 - Z^{-72})}{1 - 2K\cos(2\pi v_s)Z^{-72} + K^2 Z^{-144}}$$

G = forward gain
Z^{-72} = 1 turn
v_s = synchrotron tune
K = reverse gain

Equation 3. Dual peak comb filter transfer function

The digital output from each comb filter is next filtered by 32 tap FIR filters. These filters perform both group delay equalization and bandwidth limiting. The equalizer is designed for the worst-case of full cavity detuning and keeps phase linear to <10 degrees over a 4 MHz bandwidth (figure 6). Filter gain roll-off begins at 1.1 MHz.

Fig. 6. Measured response without/with equalization

After the equalizer filters a partial turn delay is added to make the total delay for the comb path exactly one turn. Shift registers running at four times the comb sample rate provide vernier delay adjustment in 25 ns steps. Once adjusted, the phase response repeats at every revolution harmonic. The IQ digital outputs are then converted to analog voltages and summed to the direct loop output.

The final RF feedback loop is the "sub-woofer". A band limited (4 MHz) kick signal from the LFB system is sent over dedicated 10 bit fiber optic links running at 10 MHz. The data is group delay equalized and delayed (just as the comb filters) before modulating the station IQ reference phase. High loop gains (30 dB) and very strong damping is achieved for the low-order (|n|<10) longitudinal modes.

3. HARDWARE DETAILS

The PEP-II LLRF system [2] is based on 6 types of custom VXI modules, an off-the-shelf slot 0 controller/processor and an Allen Bradley (AB) VME scanner (figure 7). The processor is a National Instruments 68030 running the VxWorks real-time operating system which is supported by EPICS [5]. The AB scanner supports a serial communication link with the Allen Bradley hardware used for slow interlocks (temperatures, water flows, power supply monitoring), control of cavity tuner stepper motors and control of the klystron high voltage power supply (HVPS).

The clock/RF distribution module generates a 471.1 MHz LO and several digital system clocks. Special attention is paid to resynchronizing the PLL divider counters with a turn clock fiducial so the digital IQ detectors restore phases after a system reboot. The arc/interlock module detects window arcs, VXI faults and handshakes with the HVPS triggers and beam abort system [4].

Fig. 7. PEP-II LLRF system VXI crate topology (HER)

The RF Processing module (RFP) contains hardware to down convert the cavity probe signals, implement the direct and ripple loops, interface with the gap and comb modules and generate the low-level klystron drive. In addition a built-in 10 MHz baseband arbitrary IQ function generator/recorder forms a very inexpensive programmable network analyzer capable of performing a wide range of functions (figure 8). This feature has proven to be extremely useful if not essential. It provides the ability to automatically configure and remotely monitor the system through Matlab application scripts calling EPICS [9]. The network analyzer can be placed in continuous mode to catch RF faults or inject dynamic IQ reference signals from files to FM process the cavities.

Fig. 8. Block diagram of the baseband network/spectrum analyzer. Maximum resolution for FFT's is 18 Hz/bin.

Fig. 9. Block diagram of IQ digital down conversion

The IQA detector modules are 8 channel RF receivers using a digital down conversion technique for precise narrow-band measurements (figure 9) [6]. Each RF input is mixed with the LO to produce 4.9 MHz IF. A single ADC samples all eight IF's in a sequence which measures I,Q,-I,-Q for each channel. The -I and -Q samples are inverted to cancel out any mixer offsets. Programmable decimating digital filters (DDF) lowpass each IQ sample and provide 16 bit outputs [12]. This detection technique provide phase accuracy of <0.1 degree over a 50 dB dynamic range. All IQ measurements are transmitted to the EPICS database at a 2 Hz rate for station RF displays and the "slow" feedback loops (cavity tuners, cathode voltage control and direct loop gain tracking). Channel one of IQA module #1 measures the klystron output and interfaces to a serial link to support the ripple loop.

Linear diode detectors in the IQA (amplitude) modules are used for wide-band amplitude detection required for hardwired RF interlocks. A single 10 MHz ADC records any of the wideband outputs into a 512K circular buffer which is frozen and written to a file after a system fault (figure 10). Similar transient recorders exist in the comb filters, RFP and the gap module which provide a method to "see" faults which occur when no one is watching.

Fig. 10. Automatically recorded cavity reflected power transient caused by aborting a 500 mA beam in the HER

4. COUPLER DIRECTIVITY CORRECTION

The shape of the beam phase transient caused by the 5% ion clearing gap must be matched in the two rings to keep the collisions centered in the BaBar detector. Errors in cavity tuning can alter the shape of the transients and lower luminosity. The high power couplers before each cavity were found to have 20 dB of directivity, insufficient for the stringent cavity tuning requirements. A Matlab script using the built-in network analyzer, programmable tuner controls and RF measurements from the IQA modules was written. It determines the complex directivity of each coupler and generate a correction matrix (equation 4) which is written into the EPICS based tuner control loop.

$$\begin{bmatrix} forwardRF \\ reflectedRF \end{bmatrix} = \begin{bmatrix} 1 & Dreflected \\ Dforward & 1 \end{bmatrix}^{-1} \begin{bmatrix} forwardmeasured \\ reflectedmeasured \end{bmatrix}$$

Equation 4. Matrix formula to correct coupler directivity

The procedure operates the klystron at constant power and phase while taking nine measurements as the cavities are tuned over a +/-100 kHz range. The network analyzer measures the exact resonant frequency at each point while the IQA module provides the complex forward, reflected and probe vectors. The data are fit to a model, directivities extracted and the correction matrixes in IQ format are written to the EPICS tuner database. Phase errors were reduced to <1 degree (figure 11). This is an excellent example of the flexibility and performance of a modular LLRF system topology with instrumentation built-in.

Fig. 11. Raw and directivity corrected forward RF vector

5. BEAM PHASE DETECTOR

The LER RF stations have only two klystrons/cavity so each LER RFP module has two unused analog IQ detector channels driving 12 bit ADC's and 512 K memories. We connected two unused channels to HER and LER BPM's through a pair of high Q 476 MHz bandpass filters to form online beam phase detectors for each ring. Data from the detectors are synchronized to the turn clock, allowing gap transients to be compared. A Matlab script called by EPICS provides modal analysis at the touch of a button (figure 12). Motion is 0-mode <0.5 degrees attributed to the master oscillator which has since been improved [10].
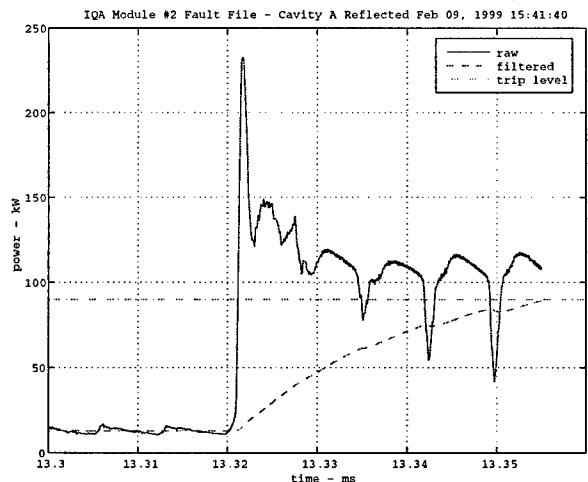

Fig. 12. Longitudinal modes in the LER with 350 mA beam measured with on-line beam phase detector

6. CONCLUSION

To date the HER and LER have stored >750 mA and >1100 mA respectively, limited by heating in temporary vacuum chambers. All RF feedback loops perform as designed to damp longitudinal coupled bunch modes strongly driven by the accelerating mode of the RF cavities. The PEP-II RF system has proven to be reliable, flexible and easy to operate. The use of EPICS state sequences has reduced the operation of the complex system to an on/off button for the users. Development of the EPICS summoned Matlab scripts has formed an expert system, allowing the very complicated configuration and testing tasks to be completed quickly by non-expert users.

I would like to thank everyone who worked on this project, especially Flemming Pedersen of CERN who conveyed his expertise of RF feedback to us early in the project. I would also like to express appreciation to the PEP-II management for giving us carte blanche to build a system which incorporates many new techniques.

7. REFERENCES

[1] F. Pedersen, "RF Cavity Feedback", SLAC-400, November 1992.
[2] P. Corredoura et al, "Low Level System Design for the PEP-II B Factory", PAC 95.
[3] W. Ross, R. Claus, L. Sapozhnikov, "Gap Voltage Feed-Forward Module for the PEP-II Low-Level RF System", PAC 97.
[4] R. Tighe, "Arc Detection and Interlock Module for the PEP-II Low Level RF System", PAC 97.
[5] S. Allison, R. Claus, "Operator Interface for the PEP-II Low Level RF Control System", PAC 97
[6] C. Ziomek, P. Corredoura "Digital I/Q Demodulator", PAC 95.
[7] P. Corredoura "Development of Digital Control for the PEP-II Klystrons", SLAC PEP-II Tech Note #60, 1994.
[8] J. Fox et al, "Bunch-by-Bunch Longitudinal Feedback System for PEP-II", EPAC 94
[9] P. Corredoura et al, "Commissioning Experience with the PEP-II Low-Level RF System", PAC 97.
[10] R. Tighe, "A Sampled Master Oscillator for the PEP-II B Factory", PAC 99 (this conference).
[11] Pulsar Microwave Corporation, Clifton, NJ 07012
[12] Harris Semiconductor HSP43220, Melbourne, FL 32919
[13] Analog Devices, Norwood, MA 02062
[14] Elantec Semiconductor, Milpitas, CA 95035

THE SUPERCONDUCTING CAVITY SYSTEM FOR KEKB

T. Tajima[1], K. Akai, E. Ezura, T. Furuya, K. Hosoyama, S. Mitsunobu
KEK, Tsukuba, Ibaraki, 305-0801, Japan

Abstract

The superconducting cavity (SCC) for KEKB is 508 MHz single-cell cavity that has large beam pipes (22 cm and 30 cm i.d.) so that higher-order modes propagate out of the cavity and be absorbed by a lossy material. The input coupler is the TRISTAN-type coaxial one with some modifications such that dc bias voltage can be applied to avoid multipactoring during beam operation, fins to efficiently cool the outer conductor and a heater to remove condensed gases. The higher-order mode absorber is made of ferrite directly sinter-bonded on the inner surface of the copper pipe using a technique called Hot Isostatic Press (HIP). One prototype cavity was tested up to 0.57 A at TRISTAN Accumulation Ring (AR) in 1996. Then, four cavities were constructed for KEKB. One of the cavities achieved an accelerating field of 19 MV/m at a test in a vertical cryostat; this field is the world record at this frequency to our knowledge. No degradation of the field after assembly into horizontal cryostats was observed up to the available power of 300 kW that corresponds to ~12 MV/m. These four cavities were installed in KEKB tunnel and are expected to supply 6 MV in total voltage to the 1.1 A electron beam in high energy ring (HER). Since beam commissioning started in Dec. 1998, the system has been supplying 6 MV and working very smoothly without any trouble. The maximum current has been ~ 240 mA and power delivered to beam per cavity is ~200 kW up to the end of Feb., 1999.

Table 1: Parameters of SCC module

Frequency	508.887 MHz
Gap length	243 mm
R/Q	93 Ω
Geometrical factor	251 Ω
Esp / Eacc	1.84
Hsp/Eacc	40.3 Gauss/(MV/m)
Loaded Q	6-8 x 10^4
Cryostat LHe volume	290 liter

Figure 1: Superconducting cavity module for KEKB

1 INTRODUCTION

Based on the successful beam tests at TRISTAN Accumulation Ring (AR) in 1996 [1-4], we started construction of four superconducting cavity modules for KEKB HER from the beginning of 1997. This paper describes its construction, performance of the cavities and some of the first data on the beam operation.

2 CONSTRUCTION

Table 1 gives the parameters of the cavity module. Figure 1 shows the whole module. It has two 300 liter/s ion pumps connected to the end cones and the diameter of the end gate valves is 15 cm. Figure 2 is a picture of the four modules installed in the Nikko D11 tunnel of KEKB. Each module was installed between two quadrupole magnets. We named the cavities RA, RB, RC and RD after the names of Klystrons from left to right in the tunnel.

Figure 2: A picture of four SCC modules in Nikko-D11 tunnel

---

[1] Email: tsuyoshi.tajima@kek.jp

2.1 Fabrication of Cavities

The cavities are made of 2.5 mm thick niobium with RRR being ~200. Cavity cells were spun from sheet material and electron beam welded. The procedure of surface treatment was as follows: 1) electropolishing 80 μm, 2) degassing at 700°C for 1.5 hours and 3) electropolishing 15 μm and rinsing with 3-4 ppm ozonized water.

2.2 Assembly with Cryostat, etc.

After cavity-alone tests in a vertical cryostat, cavities were chipped-off at flange valves and transported to a class 100 clean room, vented with filtered nitrogen gas and assembled with extension pipes made of stainless steel at both ends. Then, they were assembled with cryostats, and finally end cones that had been pre-assembled with dampers and gate valves were mounted at both ends.

3 PERFORMANCE OF THE CAVITIES

Figure 3 shows unloaded quality factor, Q_0, of the four cavities as a function of accelerating field. In the figures, open circles are the results of cavity themselves measured in a vertical cryostat. Open squares are the results of bench tests after fully equipped with horizontal cryostat and other parts before installation in the tunnel. Solid triangles and solid circles are the results measured in the tunnel on Nov. 27, 1998, before first operation and on Jan. 13, 1999, before second operation.

Although the designed voltage for operation is 1.5 MV or 6 MV/m per cavity, we set our target at 10 MV/m and $Q_0 \geq 1 \times 10^9$ to have enough margin for stable operation and in case of the operation with fewer modules. Cavity RA could not reach this target due to a defect on the equator. After the defect was ground off, the cavity showed nearly 10 MV/m. Cavity RB surpassed our record on vertical tests (15 MV/m) [5], reaching 19 MV/m. Using the numbers given in Table 1, one can obtain surface peak field of 35 MV/m and magnetic field of 750 Gauss. To our knowledge, this is the highest value ever reached with 500 MHz range cavities at 4.2 K. Cavity RC degraded during first vertical test due possibly to some damage created by discharge.

As to the results after full assembly and installation, the remarkable point is that very little degradation from cavity-alone tests occurred compared to the results of TRISTAN cavities [6]. Note that the highest fields are not marked in Fig. 3 since it is difficult to measure Q_0. Cavity RA got even better in Q_0 for some reason. As for cavity RB, we did not try to go much higher because the field is more than enough for operation and due to available power.

Figure 3: Unloaded Q vs. accelerating field of all the cavities. O.P. stands for operation point.

4 BEAM OPERATION

4.1 Conditioning

Before cooling down the cavities, we condition the input coupler up to 300 kW with perfect reflection condition, and up to 200 kW with dc bias voltages applied on the

inner conductor up to ± 2 kV. Normally, it takes one day with one operator for each module.

After the LHe vessel is filled up to 90 %, we try to raise coupler power up to 300 kW in off-resonance condition, and raise the cavity voltage, Vc, up to about 3 MV that corresponds to 12 MV/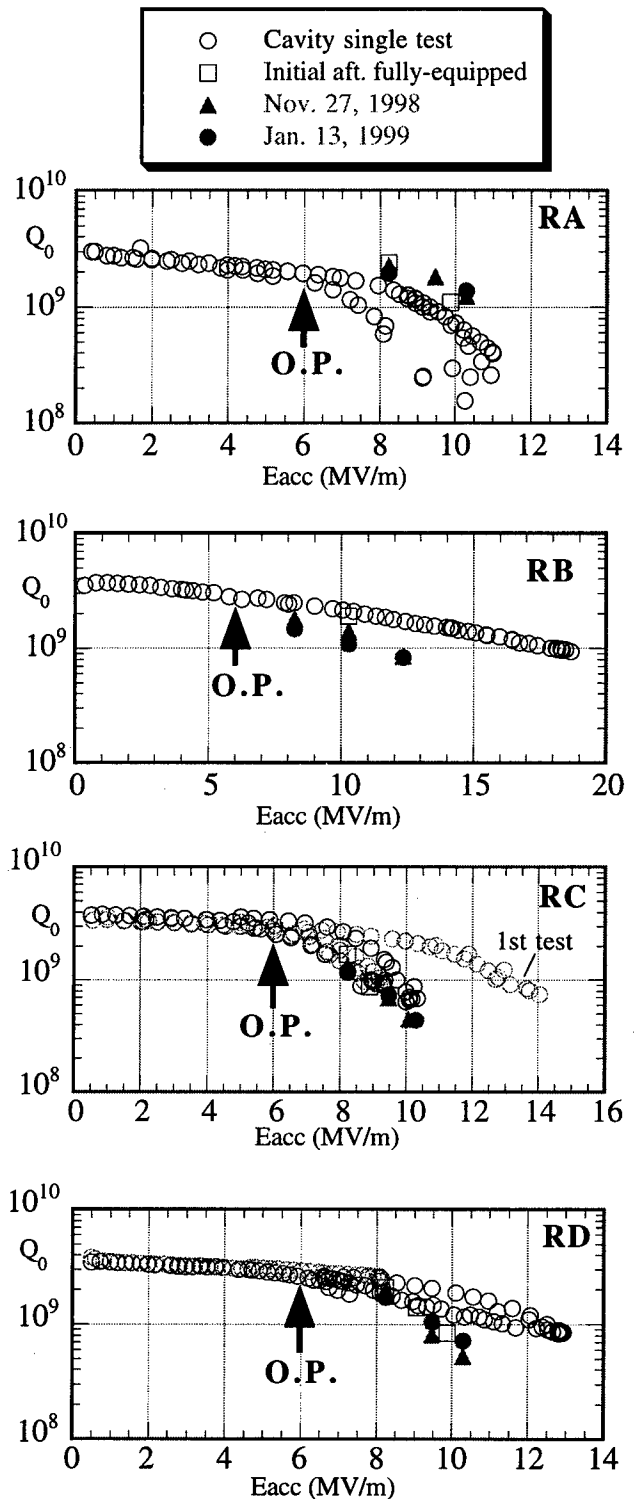m or till breakdown occurs. Then, we shift phase of cavity up to ± 30° so that the field profile in the coupler changes to condition the less conditioned parts of the coupler. When we see some degradation on the attainable field, we apply pulsed power conditioning. It takes only a few hours at most to recover. This also takes about one day.

Finally, we measure Q_0 at certain cavity voltages, e.g. at 2.0, 2.5 MV, with LHe consumption rate. This takes about 6 hours, depending on how many data we want to take.

Table 2 summarizes the present status of the modules.

Table 2 : Present performance of the modules
Mar. 18-19, 1999

Cavity	RA	RB	RC	RD
Q_0 @ 2MV (x10^9)	2.1	2.0	1.3	1.4
Eacc,max (MV/m)	12.3	13.0	10.7	11.3
Static loss (W)	31	77[1]	32	32

[1]Due to insufficient insulation vacuum caused by leak

4.2 Vacuum

Figure 4 shows the time evolution of pressure in the cavities and at the adjacent beam ducts. Considering the importance of making the amount of gas flowing into the cavity as small as possible for stable operation, we installed five 400 liter/s NEG pumps and one 300 liter/s ion pump on the duct between each module. The effective pumping speed at the neighboring ducts is ~77 liter/s·m [7]. As one can see in Fig. 4, the base pressure of the ducts is normally 0.6 to 0.7 nTorr at present. It is certain that this good vacuum is contributing to the stable operation.

Figure 5 shows the pressure increase with current. The pressure goes up linearly with current. Cavity RD is showing relatively higher pressure as seen in Fig. 5 for some reason, although the slope is same as others. The extrapolated pressure at 1.1 A is 5.7-6.8 nTorr. Compared with the last test in TRISTAN AR where the pressure went up to ~10 nTorr with 400 mA, this looks promising. However, taking into account that the beam loss will be much higher with shorter bunch length and pressure might increase non-linearly, we should keep watching it very carefully and it will be important to find appropriate indicators on the condition of trips in terms of pressure or amount of gas condensed on the cold surface, although it is of course desirable if there will be few trips in the future as it is now.

Figure 4 : Typical trend of pressure during beam operation

Figure 5 : Pressure at SCC versus beam current.

4.3 HOM Dampers

HOM dampers are made of ferrite [8] and tested up to 5 kW and 7 kW for SBP and LBP, respectively, with a 508 MHz coaxial line, then baked at 150°C for about one month to reduce outgassing rate. The expected rate after baking is less than 1.5×10^{-11} Torr·liter/s·cm^2 at room temperature, which corresponds to a total outgassing rate of the dampers being 5.2×10^{-8} Torr·liter/s.

The damper has 3/8" or 1/2" o.d. copper cooling pipe press-inserted on the outer layer made of oxygen free copper. Each cavity module has its own cooling unit for dampers and its capacity is 11.6 kW at 20°C. The normal operating condition is 5 liters/min at 23°C. The expected total power to be absorbed at 1.1 A with 5000 bunches is about 5 kW.

Figure 6 shows the power calculated from the difference of inlet and outlet water temperature and the flow rate as a function of beam current. This data was taken when the beam is coasting in order to minimize the inaccuracy due to delay of thermal response compared to the change of current. The fluctuation of the signal is caused by the fluctuation of inlet temperature to regulate the temperature. It relatively widens at lower temperature due to small temperature difference between inlet and outlet water. If one takes the lower envelope of each curve, he can obtain correct values since power should not be negative at zero current. All the data are shifted so that the power becomes zero with no current.

This data was taken with 8 trains of 40 bunches. The bunch separation was 5 RF buckets. If the loss factor is constant, i.e. bunch length does not change, and the number of bunches is unchanged during the coasting, power should increase quadratically with current as shown in the formula below. One can see this dependence in Fig. 6.

Figure 7 shows the loss factor, k, calculated with the following formula and the measured power, P_{loss}, together with a prediction drawn by a solid line.

$$k \, [V/pC] = \frac{P_{loss} \, [kW] \cdot N_b \cdot f_r \, [kHz]}{\left\{ I_b \, [mA] \right\}^2} \quad (1)$$

where N_b and f_r are the number of bunches and the revolution frequency, respectively. The error bar of the measured value corresponds to the distribution of all the four modules. As seen in Fig. 7, the measured data were slightly lower than the calculation at bunch length of 6 mm. Whether it will stay lower than the calculation or will go higher than that is not clear yet, although the results of a beam test carried out at TRISTAN showed that it tends to become higher than calculation with shorter bunches [9].

Figure 6 : Power absorbed at the dampers S and L versus beam current. Data of 4 modules are put in the same figure. Lower envelopes of the curves give correct values. Fluctuation is due to the temperature of inlet water being regulated.

Figure 7 : Loss factor versus bunch length. The solid line is the sum of ABCI calculation for the cavity structure with cones without absorber and analytic calculation [10] for the absorber. Error bar denotes the difference between modules.

4.4 Cryogenic System

We are reusing the cryogenic system constructed for TRISTAN [11] except that new transfer lines were developed to reduce heat loss and to add more flexibility in connecting with cavity modules. The system has been running smoothly, thanks to the skilled operators.

4.5 RF System

Based on the successful test at the TRISTAN AR [4], direct RF feedback has been implemented [12] and used, contributing to stable operation.

4.6 Trips

So far, up to the end of Feb., 1999, there have been only two trips since the commissioning started in Dec. 1998. These trips were caused by breakdown of a cavity but we could not identify the cause because it did not repeat. In our past experiences, trips are strongly related to the condensed gases on the input coupler or cavity near the coupler. Therefore, we will be watching the behavior of pressures at the cavity and at the adjacent beam ducts.

5 SCHEDULE FOR NEXT MODULES

We are planning to install another four modules to increase voltage and beam current to achieve 1.1 A. Table 3 shows a tentative schedule for the construction of the next four cavity modules. In our present plan, four cavities will be installed in the tunnel in August, 2000.

Table 3 : Schedule for the next 4 modules

Activity Name	2000							
	1	2	3	4	5	6	7	8
Manufacture of 4 cavities and cryostats	◼◆							
Bench tests with vertical cryostat		◇▬▬◇						
Full assembly with other parts				◇▬▬▬◇				
Bench tests with horizontal cryostat				◇▬▬▬◇				
Installation in the tunnel								◈◇
LHe transfer line install.								◈◼

6 SUMMARY

We finished construction and installation of four superconducting cavity modules for KEKB-HER by the fall of 1998. Since the beam commissioning started in Dec. 1998, all the modules have been operated at 1.5 MV(6 MV/m) each or 6 MV in total. Up to the end of Feb., 1999, maximum current is about 240 mA and maximum power delivered to beam is about 200 kW per cavity.

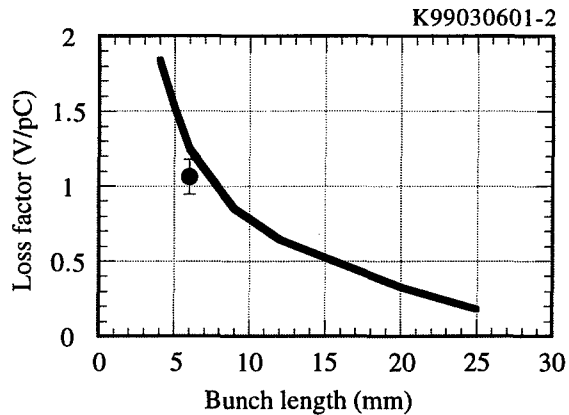The system has been running very smoothly with very few trips so far. As beam current gets higher and bunch length gets shorter, some dedicated studies such as beam related loss and HOM searches will be planned.

7 ACKNOWLEDGMENT

The authors are indebted to K.Kanazawa, Y.Suetsugu and their co-workers for design and installation of adjacent vacuum ducts and components, H.Nakanishi for waveguide architecture, S.Isagawa, S.Yoshimoto and their co-workers for maintaining Klystrons, K.Hara, A.Kabe, Y.Kojima, Y.Morita, H.Nakai and their co-workers for constructing cryogenic system and its maintenance. They also would like to thank Y.Kijima, T.Murai, S.Takagi and their co-workers of Mitsubishi Electric Company for their devotion to the construction. Finally, they are grateful to Professors S.Kurokawa, K.Takata, Y.Yamazaki and M. Kihara for their continuous encouragement.

8 REFERENCES

[1] T. Furuya et al.; Proc. PAC97, Vancouver, B.C., Canada, May 12-16, 1997. p. 3087
[2] T.Tajima et al.; ibid p. 3092
[3] S. Mitsunobu et al.; ibid p. 2908
[4] K.Akai et al.; 11th symposium on Accelerator Tachnology and Science, Hyogo, Japan, Oct. 21-23, 1997. KEK Preprint 97-137.
[5] T.Tajima et al.; 5th Workshop on RF Superconductivity, DESY, Hamburg, Germany, August 19-24,1991. KEK Preprint 91-193
[6] S.Noguchi et al.; EPAC '94 London, UK ; 27 Jun - 1 Jul 1994. KEK Preprint 94-43.
[7] Y.Suetsugu: private communication.
[8] T.Tajima et al.; Proc. PAC95 p. 1620
[9] T.Tajima et al.; KEK Report 96-7 (1996).
[10] Code for analytic calculation was written by N.Akasaka.
[11] K.Hosoyama et al.; Proc. 4th Workshop on RF Superconductivity, KEK, Tsukuba, Japan, Aug. 14-18, 1989, p. 755, KEK Report 89-21.
[12] K.Akai et al.; EPAC98, Stockholm, June 22-26, 1998. KEK Preprint 98-82.

ADVANCED HIGH-POWER MICROWAVE VACUUM ELECTRON DEVICE DEVELOPMENT

H. P. Bohlen, CPI Inc., Palo Alto, CA

Abstract

The microwave[1] power requirements of particle accelerators have been growing almost exponentially during the last three decades. As a result, economic necessities have been driving the development of microwave vacuum electron devices into three directions:

- Maximizing the power handling capability of any single device;
- Maximizing its overall efficiency;
- Minimizing its manufacturing costs.

This process has sparked a research into a multitude of new devices, as for instance magnicons, relativistic klystrons, super-reltrons and others. The field, however, is still dominated by the classic single-beam klystron, in both its super-power continuous wave and pulsed versions. Power capability and inherent reliability still make it the prime candidate for the majority of currently planned accelerators. Development efforts are therefore directed into further improving its efficiency, but mainly into reducing its costs. Distributed-beam devices, such as the multi-beam klystron (MBK) and the higher-order mode inductive-output tube (HOM-IOT) share a number of properties with the single-beam klystron, but offer the added advantages provided by lower beam voltage.

1 HISTORY

It is always difficult to define when a technological era actually began; thus the author simply claims that the first accelerator projects that required an extraordinary amount of average microwave power were LAMPF at Los Alamos National Laboratory in the early seventies, and a few years later PEP at SLAC and PETRA at DESY. Their demand triggered the development of super-power klystrons especially designed for accelerator use. They are listed in Table 1.

Compared to today's devices these klystrons were not at all optimized regarding performance. Lacking modern software tools, the designers had to approach the target specification through cumbersome cut-and-try procedures. As a result, electron beam focusing usually needed much individual adjustment. The power handling capability of these devices was in many cases stressed to its limits. Conversion efficiency values were with difficulty approaching the 60 % mark. On reaching this mark, beam focusing and operational stability of the CW klystrons became a concern; spurious noise oscillations due to backstreaming electrons created unwanted signals close to the operating frequency. Finally, these devices were expensive. Steps were taken early on to introduce some Design for Manufacturing (DFM), but priority was clearly on the basic issue of making the klystrons work at those unusual power levels. However, after careful adjustment, their life expectancy was usually good, and thus they helped the early high-energy accelerators reach their goals.

Table 1: Early super-power klystrons

Type	Frequency	Power / Pulse width	Source / Accelerator
VA-862A	805 MHz	1.25 MW 1 ms	Varian LAMPF
	353 MHz	350 kW CW	SLAC PEP
YK 1300	500 MHz	600 kW CW	VALVO PETRA

The YK 1300 (Figure 1) is a typical example of those early accelerator klystrons. It not only achieved high efficiency, but also employed features like modular cavity design and air-cooled solenoids for beam focusing, and thus became one of the trendsetters for those devices that represent today's state of the art.
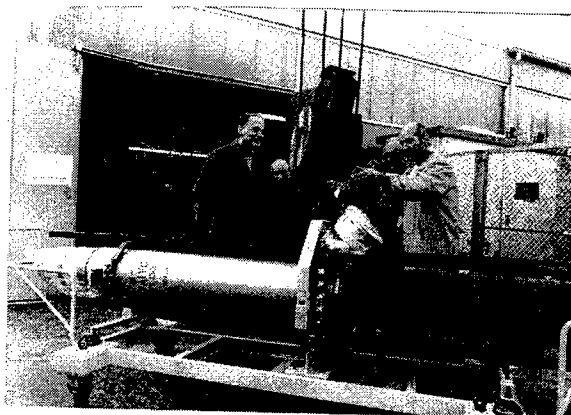

Fig.1: Arrival of the first YK 1300 at DESY (1977)[2]

---

[1] For the purpose of this paper "microwave" shall apply to frequencies higher than 300 MHz.

[2] Courtesy of Philips Semiconductors

2 STATE OF THE ART

Three distinct categories of klystrons are in use in particle accelerators:

- short-pulse devices, the pulse width varying from several hundred nanoseconds to about 6 microseconds (usually in S-band and higher);
- long-pulse devices with pulse widths around 1 to 10 milliseconds (usually in P- and L-band);
- continuous wave devices (usually in P-band).

2.1 Short-pulse klystrons (μs pulses)

The author believes that the state of the art in this category is best described by characterizing two distinct groups. The first group consists of a class of klystrons similar to those that have originally been developed for the linac of LEP at CERN, but found their application in a number of other linacs, too. Required were klystrons, produced by industry, at 3 GHz with a peak output power of 35 MW and 16 kW average at 4.5 μs pulse width. Two devices were developed and built in competition by TTE and Philips/VALVO. It turned out that both solutions, though different in approach, fully met the specification. Designed in the early eighties, they still represent the state of the art in this class as far as **standard production** types are concerned. A comparable device, though at a lower power level, is produced by Toshiba for the linac at KEK. Not developed by industry, but certainly representing part of the state of the art in large scale production in this class is the 5045 klystron (60 MW peak, 60 kW average power, 3.5 :s pulse width), developed by SLAC in the early eighties.

Table 2: Examples of **standard production** short-pulse klystrons

Type	Frequency	Power / Pulse width	Source
YK 1600	2998 MHz	35 MW 4.5 :s	VALVO (now: EEV)
TH 2094 TH 2100	2998 MHz	35 MW 4.5 :s	TTE
5045	2998 MHz	60 MW 3.5 :s	SLAC

The other group in this class has set its targets even higher. All types in this group have to be considered as **prototype production** or **under development**. The most advanced ones seem to be:

- the klystron developed by SLAC for the SBLC linear collider project at DESY, recently reproduced with some design-for-manufacturing changes by CPI (VKS-8333A, Figure 2). This again

is a 3 GHz device, with a peak output power of 150 MW and 27 kW average at a pulse length of 3 μs.

Figure 2: 150 MW short-pulse klystron VKS-8333

Table 3: Examples of **prototype and development** short-pulse klystrons

Type	Frequency / Focusing	Power / Pulse width	Source
	2998 MHz EM	150 MW 3 :s	SLAC
VKS-8333	2998 MHz EM	150 MW 3 :s	CPI
TH 2153	2998 MHz EM	150 MW 1.2 :s	TTE
XL 4	11.4 GHz EM	75 MW 1.2 :s	SLAC
	11.4 GHz PPM	50 MW 1.5 :s	SLAC
E3717	11.4 GHz EM	100 MW 0.5 :s	Toshiba

- an 11.4 GHz klystron, under development in SLAC, for the Next Linear Collider. It has reached 75 MW at 1.2 :s in an electro-magnet, and 50 MW with periodic permanent magnet (PPM) focusing. Presently work concentrates on increasing the power under PPM focusing conditions to 75 MW.

TTE has developed a 3 GHz / 150 MW klystron (TH 2153) for shorter pulses (1.2 :s). Toshiba has 11.4 GHz klystrons under development. Table 3 attempts to summarize the situation.

2.2 Long-pulse klystrons (ms pulses)

There has been little demand for new long-pulse devices in accelerators for quite a period of time, but that has changed drastically in recent years. Projects like TESLA at DESY and SNS at LANL require modern long-pulse klystrons. LANL, requesting 2.5 MW peak / 250 kW average power with 1.7 ms pulse width at 805 MHz, has decided to use single-beam devices. In response, two development projects are on their way, one at CPI and the other one at Litton. DESY requires 10 MW with 1.5 ms pulse width at 1.3 GHz, and a multi-beam klystron (MBK) to cover this specification is in a state of advanced development at TTE. This MBK features 7 beams, thus reducing the beam voltage to 115 kV, rather than the 220 to 230 kV a single-beam klystron would have needed in this application. The device is shown in Figure 3, and Table 4 summarizes the status.
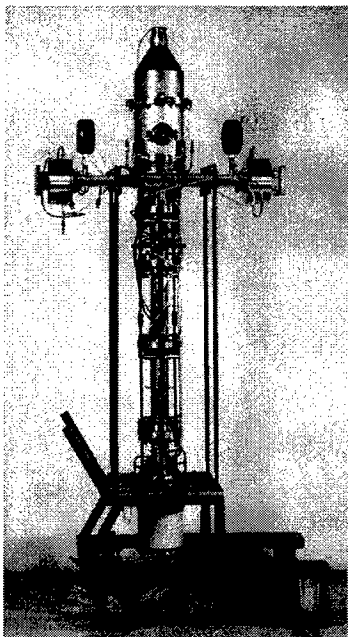
Table 4: Examples of long-pulse klystrons under development

Type	Frequency	Power / Pulse width	Source
VKP-8290	805 MHz	2.5 MW 1.7 ms	CPI
	805 MHz	2.5 MW 1.7 ms	Litton
MBK	1.3 GHz	10 MW 1.5 ms	TTE

2.3 CW klystrons

The bulk of activities after the early work for PEP and PETRA has certainly taken place in this category, be it at the accelerator sites, the development laboratories, or on the manufacturing floor. Several frequencies were (and still are) the points of emphasis in this application:
- 352/350 MHz (CERN, LANL)
- ~500 MHz (DESY, Cornell, Daresbury, KEK, ESLS)
- 700 MHz (LANL)
- 2.45 GHz (MAMI)

The state of the art is possibly best described by highlighting some of the devices in these areas. Some typical examples are the 350 MHz / 1.3 MW "work horses", independently designed and built by VALVO, TTE and EEV. Their excellent stability at high efficiency is shared by a few other "newcomers": the 500 MHz / 800 kW VKP-7958A and the 700 MHz / 1 MW VKP-7952 (Figure 4). Table 5 tries to provide a survey.

Figure 4: 1 MW CW klystron VKP-7952

Figure 3: 10 MW long-pulse MBK[3]

[3] Courtesy of Thomson Tubes Electroniques

Table 5: State-of-the-art CW accelerator klystrons (There are numerous other klystrons available, most of them designed for specific applications. The manufacturers should be consulted in all requirement cases).

Type	Frequency	Power	Source
TH 2089B	352 MHz	1.3 MW	TTE
K3513G	352 MHz	1.3 MW	EEV
B-Factory Klystron	476 MHz	1.2 MW	SLAC/ CPI
VKP-7958	500 MHz	800 kW	CPI
E3732	509 MHz	1.2 MW	Toshiba
K3510L	700 MHz	1 MW	EEV
VKP-7952	700 MHz	1 MW	CPI

Compared to the early devices, these modern CW klystrons are considerably improved in three areas.

- **Efficiency**: Most types listed in Table 5 provide efficiency values well beyond 65 %. 67 to 68 % are typical.
- **Beam focusing**: The only individual adjustment needed is typically that of the current through a low power bucking coil.
- **Operational stability**: The early klystron generations were plagued by instabilities in the output signal (spurious oscillation noise) once they reached efficiency levels around 65 %. Numerous investigations and corrections brought some relief, not always in a reliable manner [1]. The majority of the klystrons listed in Table 5 employ means to render the backward flow of electrons, inevitable at high efficiency levels, ineffective.

Lifetime results have to rely on the previous generation of klystrons; they are deemed acceptable. CERN reports that the average lifetime of the first 16 LEP klystrons has reached about 20,000 hours (4 failed during the first 4,000 hours, 5 are still alive after more than 35,000 hours). DESY experienced a similar result with YK 1301 / YK 1304, the predecessors of VKP-7958. Out of 50 klystrons put into service in HERA, 8 died prematurely below 5,000 hours while 7 continue to operate beyond 35,000 hours. Here the average age of 23 living klystrons has reached 23,200 hours.

However, there are still problems to solve.
- **Manufacturing costs**: Efforts in DFM (Design for Manufacturing) are continuing, but some technological break-through is still needed in order to bring the cost of the devices down to a level that permits building the large accelerator structures that are targeted.
- **Beam voltage**: The tendency to concentrate more and more power in single devices has lead to ever increasing beam voltages. This is expensive. It causes not only higher costs for the devices

themselves, but also for many things in their periphery: power supplies and modulators, high-voltage insulation, X-ray shielding, buildings (size), environmental protection measures.

3 FUTURE TRENDS

3.1 Improved manufacturability

Cost reduction will have high priority for any high-power vacuum electron device for accelerator application in the future. Design for Manufacturing considerations will not only comprise the use of pre-fabricated materials (like stainless steel tubes for cavity walls, copper pipes for waveguides, threaded rods for support, etc.) like in the past. Attention will also be given to the use of improved manufacturing processes like high-temperature exhaust (to reduce conditioning time) and software-controlled conditioning and test procedures. In addition, large-scale production will be applied where possible.

3.2 Distributed-beam devices

Another point of emphasis will be the development of devices that employ low beam voltage, without compromising but rather enhancing power capability. One category of these devices is the multi-beam klystron (MBK). Beam voltage reductions by a factor in the order of 2 are obtainable this way. So far, MBKs have only been designed for relatively low average power levels, but there is no particular upper threshold in this regard. The example already mentioned in Paragraph 2.2 uses basic-mode cavities.

A further step in the direction of achieving high average power is the transition from basic-mode to higher-order mode (HOM) cavities. The advantage, compared to basic-mode operation, is that the electron beams are no longer in competition with each other for the restricted space in the center of the cavity. Interaction with the outer lobes of an HOM field provides considerably more interaction space, thereby permitting large electron beam cross-sections and correspondingly low space charge density, a vital precondition for high efficiency.

An HOM-IOT (Higher-Order Mode Inductive-Output Tube) is presently under development at CPI. The project is sponsored by Los Alamos National Laboratory (LANL). The specification requires 1 MW CW output power at 700 MHz. The expected results of this development, compared to a klystron having the same specification, are listed in Table 5.

Table 5:
Comparison between HOM-IOT (expected results) and klystron, both operated at 1MW CW / 700 MHz

Device	HOM-IOT	Klystron
Effective efficiency[4]	73 %	60 %
Relative consumption	82 %	100 %
Assembly volume (appr.)	30 cbf	200 cbf
Assembly weight (approx.)	1,000 lbs	5,000 lbs
DC beam voltage	45 kV	90 kV
Gain	25 dB	46 dB

The essentially annular electron beam in this device consists of 25 beamlets, arranged in 5 groups at 5 each. Specific cathode emission density and specific power density in output cavity and collector represent only fractions of the comparable values in the klystron. The drawback, on the other hand, is the HOM-IOT's lower gain.

Figure 5: 1 MW CW HOM-IOT (prototype)

Presently the prototype device is ready for exhaust; test results are expected during summer of 1999.

In a way, the electron beam inside the HOM-IOT can be considered a sheet beam in annular arrangement. Thus the sheet-beam klystron [2], a possible approach to generate the power required for accelerators at very high

---

[4] For the purpose of amplitude regulation, the klystron has to be operated about 10 % below its power saturation point, while the HOM-IOT (like any IOT) does not saturate at the point of its highest efficiency.

frequencies, can be regarded a close relative of the HOM-IOT.

3.3 High efficiency via high voltage

Numerous developments for high-power microwave devices are staying with the high-voltage principle: magnicons [3], relativistic klystrons [4], super-reltrons and others. Sadly, the space available for this paper does not permit to describe the status they have reached so far.

4 ACKNOWLEDGEMENTS

Disclaimer

When writing this paper, care has been taken to describe the already restricted range of devices chosen completely enough to give the reader a useful account. Nevertheless, due to the limited size permitted for the paper, and certainly due to limitations in the authors knowledge and resources, the different classes of devices within this range are described through examples only; and perhaps not always by the most striking ones. The author, who has also taken the liberty of excluding devices with less than 10 kW average power from this report, apologizes for any flaws in this respect.

5 REFERENCES

[1] S. Isagawa, "Present Status of High Power CW Klystrons", CAST, Ako, 1997

[2] S. Solyga, W. Bruns, "Cavity Design for Planar MM-Wave Sheet Beam Klystron", EPAC 96, Sitges, 1996

[3] O. A. Nezhevenko et al., "Long Pulse 1.3 GHz Magnicon Amplifier", APS DPP Meeting, Pittsburgh, 1997

[4] A Sessler et al., "RF Power Source Development at The RTA Test Facility", EPAC 96, Sitges, 1996

RF SYSTEMS OF THE TRIUMF ISAC FACILITY

R. L. Poirier, P. Bricault, K. Fong, A. K. Mitra and H. W. Uzat
TRIUMF, Vancouver B. C. Canada
Y. V. Bylinsky, INR RAS, Moscow, Russia

Abstract

Five rf systems, each operating in cw mode, have so far been specified for the ISAC accelerator system; a pre-buncher, an RFQ, a MEBT re-buncher, five DTL cavities and three DTL bunchers. The pre-buncher was designed and built to operate at a frequency of 11.66 MHz plus three harmonics. So far it has operated successfully at full nominal voltage with fundamental plus the addition of two harmonics. Both the 8-meter long, 4-rod, split-ring type RFQ and the spiral two gap MEBT re-buncher were designed to operate at 35 MHz. The initial 2.8 meters of the RFQ (7 out of 19 rings) were installed in the 8 m long tank and have been successfully operated at full power with beam. Dark currents associated with field emission initially accounted for 40% extra power consumption at full voltage but could be eliminated with high power pulse conditioning. The remaining 12 rings are being installed to enable us to accelerate cw radioactive ion beams to 150 keV/u. A full scale model of the MEBT re-buncher was built and tested and the final structure is in the design stage. The DTL accelerator system consists of a series of multi-gap interdigital H-mode tanks and three gap split-ring buncher cavities both operating at 105 MHz. The first DTL cavity has been fabricated and is undergoing rf tests. The first DTL buncher was tested to twice the nominal operating power. All amplifiers for the above were designed and built in house. This paper will report on the performance achieved for these systems.

1 INTRODUCTION

A radioactive ion beam facility is being built at TRIUMF [1]. The accelerator complex of ISAC [2] consists of several different rf systems as shown in Fig. 1. Instead of a bunching section in the RFQ, the beam is pre-bunched at 11.66 MHz with a single gap, pseudo saw-tooth buncher. An 8 m long, 35 MHz, four vane split ring RFQ structure accelerates ions from 2 keV/u to 150 keV/u. The details of the bunch rotator and chopper have not been specified yet and will not be included in this paper. In the MEBT the beam is matched into the DTL with quadrupoles and a spiral two-gap 35 MHz re-buncher. The 105 MHz variable energy DTL post stripper [3] accelerates ions to a final energy between 0.15 MeV/u to 1.5 MeV/u.

2 LEBT PRE-BUNCHER

The pre-buncher [4] consists of two circular electrodes spaced 8 mm apart forming a single gap with a beam

aperture of 7-mm in radius. The fundamental frequency of 11.66 MHz and the first three harmonics are individually phase and amplitude controlled, and combined at signal level. The signal is amplified by an 800 W broadband amplifier that drives the two plates in push-pull mode with a peak voltage of about 200 V (400 V between plates). The capacitive plates are externally loaded with a resistor to make the system broadband. The amplifier is a 2 stage, transformer coupled wide band solid state amplifier. Because of a reduced gain at the higher frequencies, the initial testing was done with only two harmonics. Optimization of amplitude and phase of each harmonic results in an almost saw-tooth modulation on the beam velocity. The Pre-buncher system operated very reliably at full power for the first beam tests with the RFQ [5].
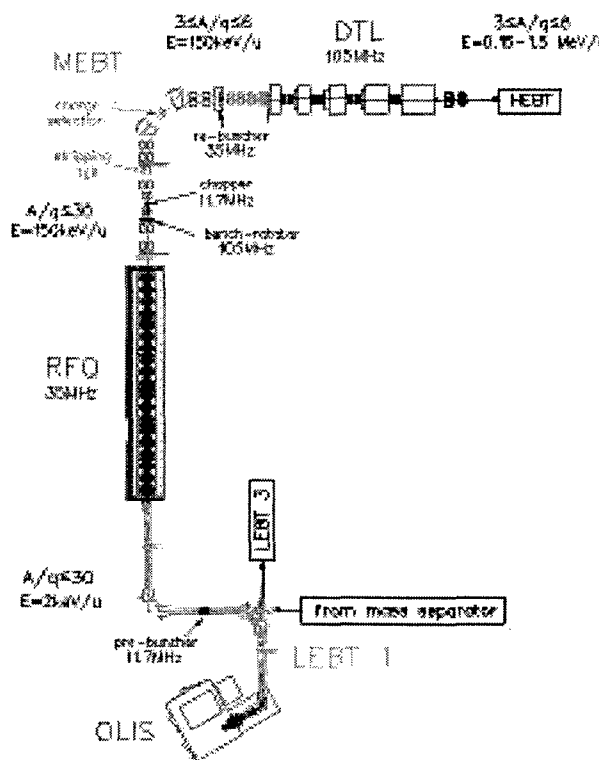

Figure 1. The ISAC Linear Accelerator

3 RFQ SYSTEM

The ISAC RFQ is an 8-meter long, 4-rod split-ring structure operating at 35 MHz in cw mode. An initial 2.8m section [6] of the accelerator (7 of 19 rings) was installed and aligned in the 8m, square cross-section, vacuum tank (Fig. 2) to allow RF and beam tests to be

carried out. The stringent, +/- 0.08 mm, quadrature positioning tolerance of the four rod electrodes was achieved [7] and a relative field variation along the 2.8 meter of the RFQ was measured to be +/- 1%, using the standard bead pull method.
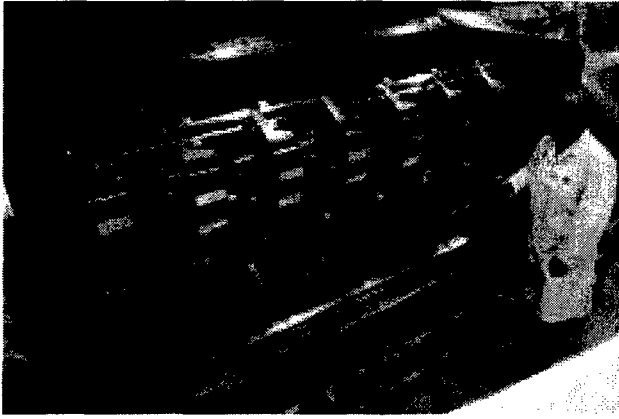

Figure 2. Seven ring assemblies installed and aligned ready for tests.

At signal level 57% of Q-value and a frequency within 2.8% of MAFIA simulations were achieved. Following a three day bake out at 60°C a base pressure of 1.4*10-7 torr was reached and 76 kV (2kV above design value) was achieved on the electrodes within four hours at the anticipated power level of 30 kW with an increase in pressure to 4.0 *10-7 torr. We were able to maintain this condition for two hours before our first major amplifier overload occurred. Subsequently, we were never able to achieve the above voltage for the same power. The rf power increased by as much as 40% for the same voltage level of 76 kV due to dark currents associated with field emission along the electrodes. The dark currents were essentially eliminated by one hour of high power pulse conditioning. The RFQ operated continuously for 15 hours at nominal voltage plus various runs for 5 and 10 hours before being interrupted by an amplifier trip. These amplifier trips were later found to be caused by a failing component in the grid bias power supply. Automatic recovery from a high VSWR has now been incorporated in the RF controls to cut the RF drive rather than trip the amplifier. Based on the RFQ prototype results, an amplifier was designed and built in house for a power output of 150kW. As a result of improved shunt impedance and reduced operating voltage, the 19 rings will only require 85 kW of RF power and the amplifier has been successfully tested into a resistive load to this power level.

The remaining 12 rings are now being installed and aligned to enable us to accelerate cw radioactive ion beams to 150 keV/u.

4 RF CONTROLS

The feedback control system for the ISAC pre-buncher regulates a 11 MHz signal and up to its third harmonic in both amplitude and phase to synthesis a special waveform for beam bunching. The RFQ control system uses a phase locked loop frequency source to generate a 35 MHz signal and also uses In-phase and Quadrature phase for amplitude and phase regulations. The system has a self-excited mode of operation that uses the RFQ cavity itself as the frequency-tuning element and allows the RFQ cavity to run without tuning control. The RFQ and the prebuncher, while operating at different harmonics, are phase locked together via a frequency distribution unit by generating these different harmonics with different phase shifts between them. The above control systems have been commissioned, enabling the prebuncher and the RFQ to operate coherently.

5 MEBT RE-BUNCHER

The MEBT rebuncher [8] will operate cw at 35 MHz with a gap voltage of 30 kV. Two designs for the 35 MHz rebuncher, a folded $\lambda/4$ and a spiral were evaluated on the basis of cost, size, rf and mechanical properties. A full-scale prototype of the spiral with water-cooling was constructed to measure the mechanical vibrations as well as rf parameters. The tests reveal that the vibrations are much lower than the allowable limits. MAFIA simulations have been done on the spiral to check the validity of the rf measurements of the prototype. From the computed and measured values of the shunt impedance, it is estimated that 1 kW of rf power will be adequate to produce a gap voltage of 100 kV.

6 DTL IH TANKS AND BUNCHERS

6.1 IH Tank

The first IH tank [9] with the stems and ridges installed and aligned are shown in Fig. 3. The ridges are mechanically fastened to the tank wall and therefore the fabrication tolerance on the flatness and surface finish of the bottom of the ridges and the mounting surfaces on the tank wall are very stringent in order to insure a good electrical contact.

The frequency was measured to be 3.5% higher and the Q to be 20% lower than the values from MAFIA simulations. A bead pull measurement shows the field variation across the gaps to be in close agreement with MAFIA simulations, causing only a +/- 0.1% phase error of the beam at the gap. Full power of 3.6 kW and drift tube gap voltage of 87.5 kV was achieved following 36 hours of low level multipacting conditioning. Stable operation for 100 hours was achieved.
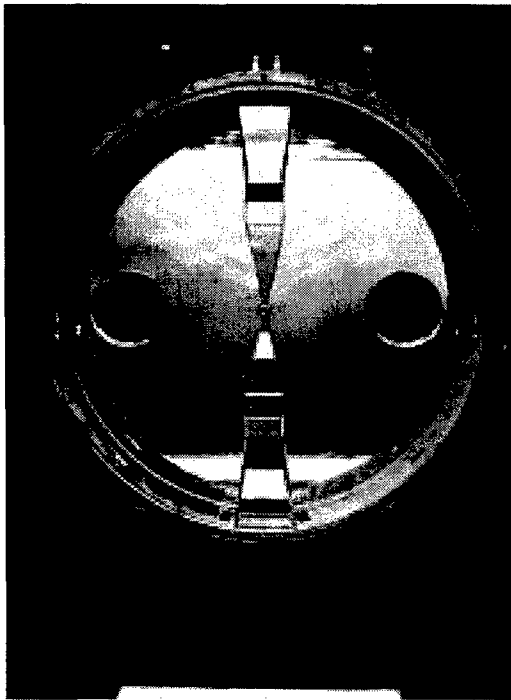
Figure 3. First DTL tank with ridges and stems installed and aligned.

6.2 Triple-Gap Bunchers

Shown in Fig. 4 is the first DTL buncher [10] that was developed at INR and tested at TRIUMF. It is a triple gap split ring rf structure operating at 105 MHz with 56 kV gap voltage. At signal level 74% of Q-value and frequency within 0.6% of MAFIA simulations were achieved.
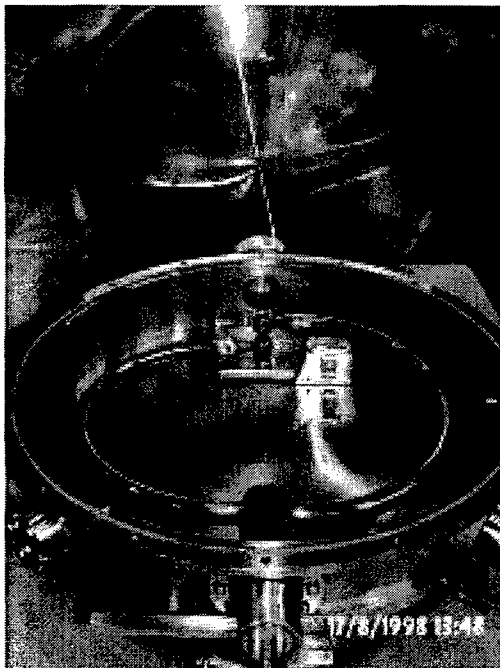

Figure 4. First DTL Buncher developed and manufactured at INR, Russia.

With a cooling water flow of 20 l/min, the mechanical vibrations were measured to be in the order of 1 micron. The first of 9 RF power amplifiers for the DTL linac was completed and successfully tested into a resistive load at a power level of 22 kW. This amplifier was used to test the INR buncher to 16 kW (2X nominal power) with stable operation. The remaining power amplifiers for the DTL are in the process of being assembled. Movement of the drift tubes due to the rf thermal load of the ring was measured using a telescope on targets installed inside the drift tubes. With a cooling water flow of 17 l/min per arm of spiral, the centers of the drift tubes were displaced by 0.25 mm when full rf power was applied. By reversing the water flow to cool the hottest ring area first, the displacement was reduced to 0.125 mm.

7 CONCLUSION

The commissioning of the Pre-buncher, RFQ and associated rf control systems enabled us to reach our goal of accelerating beam from the first seven rings of the RFQ [11]. Our goal now is to accelerate beam from the full compliment of 19 RFQ rings by the end of the year. It is hoped that the MEBT Re-buncher will also be commissioned by the end of the year followed by the commissioning of the first DTL section in the spring of 2000.

8 REFERENCES

[1] Paul Schmor, et al, "The High Intensity Radioactive Beam Facility at TRIUMF," EPAC97, Stockholm, Sweden.

[2] R. Laxdal et al, "Status of the ISAC Accelerator for Radioactive Beams", LINAC98, Chicago, USA

[3] R. E. Laxdal et al, " A Separated Function Drift Tube Linac for the ISAC Project at TRIUMF", PAC97, Vancouver, B. C.

[4] K. Fong, et al, " Sawtooth Wave Generator for Pre-buncher Cavity in ISAC", PAC97, Vancouver, B. C.

[5] R. Laxdal et al, "First Beam Test with the ISAC RFQ", LINAC98,

[6] R. L. Poirier, et al, "RF Tests on the Initial 2.8m Section of the 8m Long ISAC RFQ at TRIUMF", LINAC98, Chicago, USA.

[7] G. Stanford, et al, "Mechanical Design, Construction and Alignment of the ISAC RFQ Accelerator at TRIUMF", LINAC98 Chicago, USA

[8] A. K. Mitra, et al, " A 35 MHz Spiral Re- buncher Cavity for the TRIUMF ISAC Facility", This Conf.

[9] P. Bricault et alTank1 of the ISAC-DTL Linac", This Conference.

[10] Y. V. Bylinsky, et al, "High Power Test of the ISAC Triple Gap Buncher Operating in CW Mode", This Conf.

[11] R. Laxdal et al, " Beam Test Results with the ISAC 35 MHz RFQ", This conference.

SNS LINAC RF SYSTEM OVERVIEW*

M. Lynch, W. Reass, P. Tallerico, LANL, Los Alamos, NM

Abstract

The Spallation Neutron Source (SNS) being built at Oak Ridge National Lab (ORNL) in Tennessee requires a linac with an output energy of 1 GeV and an average current during the pulse of approximately 18 mA (including the effects of chopping). The average beam power for the initial baseline is 1 MW (1 mA average at 1 GeV). The linac is followed by an accumulator ring and target/instrument facility [1]. The RF system for the 1 MW linac requires 52 each 805 MHz klystrons and 3 each 402.5 MHz klystrons. The 805 MHz klystrons are configured in pairs to drive one resonant structure. This uses the installed RF very efficiently and in addition is convenient for the upgrade to 4 MW which must be considered in the design. The RF must have the correct amplitude and phase in order to ensure complete acceleration along the linac and to minimize beam loss. Due to the configuration proposed for SNS, the LLRF controls must equalize each pair of klystrons to ensure proper operation. The high voltage system for the klystrons will be based on Insulated Gate Bipolar Transistor (IGBT) technology to provide the best possible operation at the least cost.
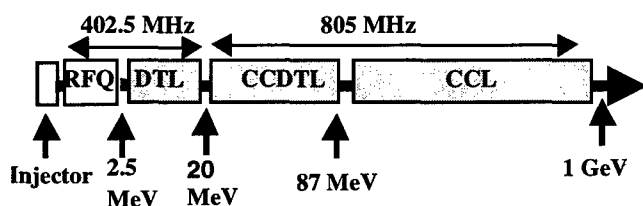
1 SYSTEM OVERVIEW

Figure 1: SNS Linac Block Diagram

The Linac is shown schematically in Figure 1. The RFQ (1 klystron) and Drift Tube Linac (DTL) (2 klystrons) operate at 402.5 MHz. The remainder of the Linac, which includes the Coupled Cavity Drift Tube Linac (CCDTL) and Coupled Cavity Linac (CCL) operates at 805 MHz. A total of 52 klystrons are needed for the 805 MHz portion of the Linac. An additional 805 MHz klystron is required for a bunch rotator located after the Linac, just before the ring injection point. The preliminary design activities started this year (FY-99), and the entire facility scheduled for completion in FY-05 with initial operation in FY-06.

Pertinent parameters for the Linac and RF systems are given in Table 1. In the definition of the system, an upgrade path is included that will ultimately provide 4 MW of average beam power. This is to be done through a combination of increased current from the front end (factor of 2) and the addition of a second front end which will be funneled into the CCDTL with the first front end (factor of 2). The Linac design has been done in an elegant and cost effective fashion [2,3] that accomplishes this upgrade by adding 1 klystron to each 2-klystron accelerator module. No additional structure power is needed for the upgrade, and only the additional beam loading must be provided by the additional RF power.

Table 1: Parameters of SNS Linac

H- Energy	1000 MeV
Beam Current	27.7 mA, peak
	1.04 mA avg.
Beam Power	1.04 MW, avg.
Pulse Width, (RF)	1.17 ms
Pulse Width, (beam)	1.04 ms
Repetition Rate	60 Hz
RF Duty Factor	7.02%
805 MHz power during pulse	97 MW
Total RF power during pulse	99 MW
Klystrons, 805 MHz, 2.5 MW pk.	53
Klystrons, 402.5 MHz, 1.25 MW pk.	3

1.1 Accelerator Module

A block diagram of one 805 MHz accelerator module is shown in Figure 2. Two klystrons are needed for each module, and they each drive the accelerator through a single RF/vacuum window and drive port. Each klystron is specified to deliver 2.5 MW peak at full saturated output. No circulators are planned for the initial installation. That should not present a problem as will be shown later, but circulators will most likely be required when the upgrade to 4 MW occurs.

The klystron specification includes the primary parameters of peak power, duty factor, pulse width, and gain. In addition we have specifications for phase and amplitude linearity, VSWR tolerance, heater hum limitations, and finally a specification that the tube must pass an extensive heat run (24 hours at full duty and 110% of nominal peak power). Table 2 lists many of the pertinent klystron parameters.
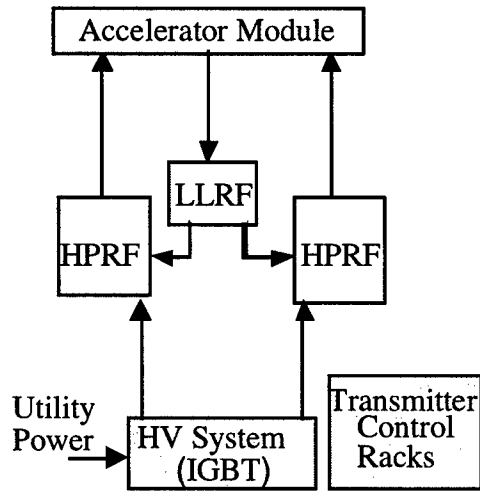
Figure 2: Layout of one Accelerator/RF Module

Two prototype 805 MHz klystrons have been ordered, one each from CPI and Litton. They are scheduled for delivery in June of this year. Both klystrons are modern designs with 5 fundamental and one-second harmonic cavitiy. Both klystrons are approximately 10 feet long.

Table 2: 805 MHz Klystron Specifications

Peak Power	2.5 MW
Repetition Rate	60 Hz
Duty Factor	10%
Gain at Saturation	≥45 dB
Efficiency at Saturation	≥55%
Gain Variation*	<1%
Phase Variation*	<0.5 degree
Allowable Load VSWR	1.5:1
Gain Variation due to Heater AC power phase	≤0.5 dB

*over range from 0.6 MW to 2.0 MW output

They are specified with a minimum efficiency of 55% at full output power and a minimum gain of 45 dB. [4] They have been ordered with a modulating anode to allow maximum flexibility in system design, detailed monitoring of performance, and to simplify testing at LANL in an existing modulator/HV system. The order for prototypes includes an option for a cathode-pulsed tube. The final klystrons for SNS will likely be cathode-pulsed klystrons. The HV system being designed for SNS is based on IGBT technology and will allow the use of cathode-pulsed tubes.

The waveguide layout for SNS is based on a similar layout done at LANSCE. This system has operated for over 25 years without circulators by carefully adjusting the waveguide length between the klystron output iris and the accelerator input iris. The length is adjusted to ensure

that reflections from the accelerator due to loss of beam appear at the klystron as a low impedance.

Table 3: Expected Mismatch for SNS RF Module

Module 25, Output Energy=969 MeV		
Avg. Beam Power	1 MW	4 MW
Cavity Power	3.107 MW	3.107 MW
Beam Power	0.755 MW	3.020 MW
Total Power	3.863 MW	6.13 MW
Beam Loading	19.60%	49.30%
VSWR without Beam	1.27:1	2.10:1

Table 3 shows calculations for the mismatch for a typical accelerator module in the 1 MW case and the 4 MW case. We are specifying that the klystrons must be able to operate into a 1.5:1 mismatch at any phase, so the 1 MW case should not present a problem due to the low effective beam loading (less than 20%). In the 4 MW case the beam loading is much higher (approximately 50%). Loss of beam in the 4 MW case presents a much worse mismatch to the klystron (2.12:1). For this reason we believe circulators will be required when the upgrade is installed.
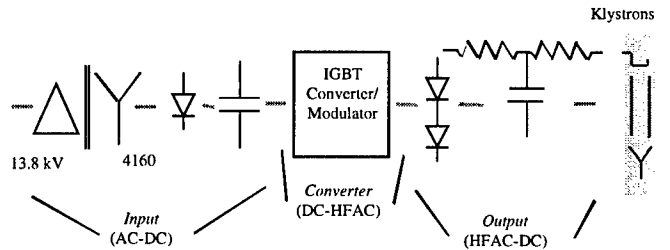
1.2 IGBT High Voltage System

Figure 3: Block Diagram of IGBT-based HV System

We are developing a high voltage system based on IGBT's. [5] The design is shown in block diagram form in Figure 3. Each IGBT Converter-Modulator system will provide the power for 2 klystrons. There are a few features of particular interest. The first is that the system replaces both the HV components (HV supply and capacitor bank) as well as the modulating components (HV modulator or PFN). The IGBT section operates at low voltage (4160 V), and the circuit is a three-phase circuit with each half of each phase switching at 20 kHz. The IGBT's must be stacked to accommodate peak voltage potentials, so the total number of IGBT's needed for the 0.75 MW average system is 48. The output HV transformer is followed by 3-phase rectification and a small amount of filtering. Since the transformer is not required to operate for the full pulse width (1 ms), it can be made very compact. The output ripple frequency is 120 kHz and is expected to be <1%. Ripple can be made smaller by adding more stored energy in the output section, but this would also add to the available fault energy. The current design requires no crowbar. Droop

454

over the 1 ms pulse is expected to be kept much less than 1% by pulse-width modulation of the IGBT's in the converter. In the case of a klystron arc the IGBT's are shut down. Backup protection comes from the saturation of the small high frequency HV transformer and ultimately from a fast vacuum interrupter on the input.

1.3 Low Level RF (LLRF) Controls

A block diagram of the LLRF system is shown in Figure 4. In addition to standard field control, the LLRF design must include the RF reference and distribution, resonance control of the accelerator cavities, and klystron control. Since each accelerator cavity is powered by 2 klystrons, the system must accommodate variations in the tube performance. A feedback loop is used around each klystron to equalize their performance. Field control of the accelerator will include feedback and, most likely, feedforward control.

Figure 4: Block Diagram of Feedback control System

We have specified the system to allow the accelerator physics designers a maximum of 2.0 MW per klystron at the accelerator. Since each module consists of 2 klystrons, this provides a maximum of 4.0 MW per module. The extra power (0.5 MW per klyston) is needed for many purposes. There are losses in the RF transport (estimated at 7% of the output from the klystron). These losses come from resistive losses in the waveguide and mismatch losses at flanges, bends, and other discontinuities. In addition there are coupling losses at the module due to imperfect beam amplitude and phase and coupling losses due to klystron inequalities (since there are two klystrons driving each module). Finally, excess power is needed for drive margin to allow the feedback/ feedforward system to operate effectively.

The drive margin is needed because of the saturation characteristics of the klystron. As a klystron is operated closer and closer to peak output the effective gain (Pout/Pin) approaches zero. This gain is a key element in the forward path of the control circuit. Hence, reduced klystron gain translates to reduced control loop gain. In a typical saturation curve, the klystron may have 3 dB less

gain at 75% output and 6 dB less gain at 90% output than it has at 50% output. Of course at saturation, the effective gain is zero. The effectiveness of the feedback control system is reduced more and more as the system operates closer to saturation. This system will likely need excellent control (±0.5% amplitude, ±0.5° phase), so the control margin is very important to maintain. We are adapting the model we are currently using for the Accelerator for Production of Tritium (APT) for the SNS application. [6] A sample result is shown in Figure 5. This modeling work will be used to estimate the amplitude and phase control limits in the presence of errors and noise, particularly from the beam and the klystron HV system. In addition, the modeling will be used as the basis for the control system design, determining whether feedforward is needed, etc.
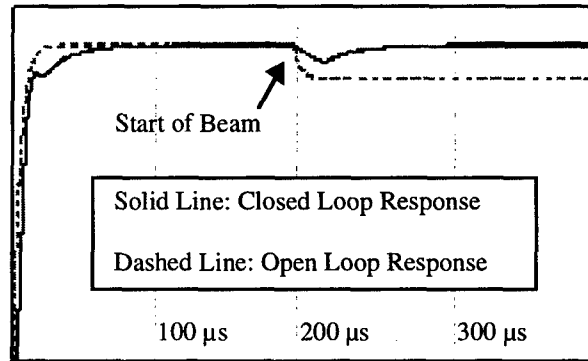

Figure 5: Modeling result of SNS RF transient response

2 SUMMARY

The SNS linac is an exciting program. To meet the program schedule and budget, we have been very selective in the technologies we are developing. The developments must be necessary to achieve the SNS operating parameters, or they must promise significant payback in cost or schedule. In addition, wherever possible, we are borrowing from developments we have achieved in other recent or existing programs.

3 REFERENCES

[1] J. Alonso, "The Spallation Neutron Source Project", Proceedings of PAC-99, New York, (1999)

[2] J. H. Billen, et al, "Linac RF Structures for the Spallation Neutron Source", Proceedings of PAC-99, New York, (1999)

[3] N.K. Bultman, et al, "Mechanical Engineering of the Linac for the Spallation Neutron Source", Proceedings of PAC-99, New York, (1999)

[4] T.A. Hargreaves, M.F Kirshner, et al, Litton Electron Devices, P.J. Tallerico W.A. Reass, LANL, "Development of a High Power Klystron for the Spallation Neutron Source", 26th IEEE International Conference on Plasma Science, Monterey, CA, June 21-24, 1999.

[5] W.A. Reass, P.J. Tallerico, J.D. Doss, "Proof-of-Principle Power Converter for the Spallation Neutron Source", Proceedings of PAC-99, New York, (1999)

[6] S.I. Kwon, Y.M. Wang, A. Regan, "SNS LLRF Control System Model Design", Proceedings of PAC-99, New York, (1999)

Applications of the 1000-turns Orbit Measurement System at LEP.

P. Castro*, DESY-Hamburg, Germany

Abstract

The software of the LEP beam orbit measurement system [1] allows the acquisition of the beam position for over 1000 consecutive turns. The acquisition can be synchronized to a deflection by a kicker in order to observe coherent betatron oscillations. In this paper we describe the use of this technique to study the dependence of head-tail damping on beam parameters and the tune dependence on the oscillation amplitude for various LEP optics [2]. Coherent oscillations can be represented in phase space to observe the effect of resonances and other non-linear behavior [4, 5]. Coherent oscillations can also be excited using a sinusoidal deflection in order to maintain the oscillation amplitude [6]. Thus, precise measurements of the phase advance are obtained by harmonic analysis of the signal at each pick-up. This technique has been used to measure the beam energy dependence of the phase advance due to chromaticity [7] and the bunch current dependence of the phase advance due to impedance [8]. Finally, we describe a method to obtain the betatron function from the measured phase advance and report about its accuracy and applications at LEP [9, 10].

1 INTRODUCTION

Measurements of the beam position turn-by-turn and their storage over many turns have many useful applications and have been relevant to LEP performance improvements [11]. The possibility of triggering these measurements on pre-programmed timing signals provide a valuable tool to study the trajectory of the beam at injection and during the energy ramp. This application is particularly helpful in order to establish a first circulating beam after a long shutdown. In superconducting proton machines like HERA, this feature is also used to store the beam orbit at the last turns before the beam is dumped in case of anomalous beam particle losses (in order to prevent further loss on superconducting magnets). In that way it is possible to diagnostic the cause of such losses.

In this report we present some of the recent applications of 1000-turns measurements involving the observation of beam coherent betatron oscillations at LEP. These measurements provide qualitative and quantitative measurements of linear and non-linear beam optics properties.

At LEP there are 504 pick-ups located around the circumference. On each turn and for every bunch the signals of the pick-ups are processed and stored in a memory buffer with a capacity to store up to 1024 turns. Beam coherent oscillations are excited using a fast bending mag-

net or kicker. A single transverse deflection can be applied to the beam in order to observe the damping of coherent oscillations. Studies of the amplitude decay of coherent oscillations were carried out to determine the contribution of head-tail damping and radiation damping and the horizontal detuning with amplitude at LEP [2]. The kicker can also introduce beam deflections on each turn with an amplitude that follows a sinusoidal curve at any given frequency. If the frequency of the continuous excitation is close to the betatron tune the beam will oscillate coherently and within a very short time an almost constant amplitude can be reached. A measurement of betatron phase advance between pick-ups can be obtained by harmonic analysis of these data. The measured phase advance between three pick-ups can be used to evaluate the optics parameters β and α at any azimuthal position around the storage ring [10].

2 MEASUREMENTS OF COHERENT DAMPING

The damping of coherent beam oscillations and the shift of its frequency can be observed using 1000-turns measurements. The measurement technique consists in triggering the 1000-turn acquisition a few turns before a single kick to the beam is applied. This permits to observe the start and damping of the coherent beam oscillations. An example of such measurement is shown in fig. 1.
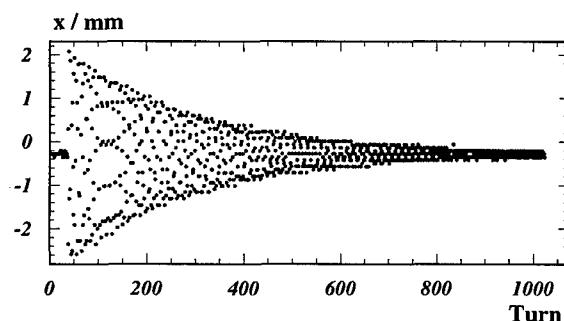

Figure 1: Measured center-of-charge position of a bunch versus turn number. A single kick was applied a few turns after the acquisition started.

A fit to the data using a damped oscillation with amplitude dependent frequency yields the coherent damping time τ. At LEP the coherent damping is a contribution of radiation and head-tail damping

$$\frac{1}{\tau} = \frac{1}{\tau_o} + \frac{1}{\tau_{\text{head-tail}}}$$

---

* Email: pcastro@mail.desy.de

At a given energy the head-tail damping is proportional to the chromaticity Q' and to the bunch current I_{bunch}. In general the head-tail damping is dominating and its contribution can be determined by measuring the coherent damping rate at bunches with different currents. The radiation damping rate can be extracted by an extrapolation to zero bunch current. A dedicated experiment was carried out at LEP [2] where the coherent damping rate was measured for various bunch currents and chromaticities at beam energies of 45.625 and 60.0 GeV. As an example, measured coherent damping rates as function of bunch current are plotted in fig. 2. With the radiation damping time, the horizontal damping partition number J_x is determined. The measured J_x agrees with results of direct measurements of the circumference using pick-ups and tide models [12]. This measurement plays an important role in the understanding of the LEP beam energy since the J_x shifts are accompanied by an energy shift.

Figure 2: Coherent damping rate versus bunch current measured at a beam energy of 45.625 GeV for several chromaticities.

3 TUNE SHIFT WITH AMPLITUDE

At LEP the fractional part of the horizontal betatron tune Q_x is about 0.28 and a large tune spread in the beam can drive some of the particles onto the third order resonance. A large detuning with amplitude (anharmonicity) limits therefore the amplitude range of stable particles, i.e. the aperture for the beam.

The detuning with amplitude can be extracted from 1000-turns measurements of damped betatron oscillations. The amplitude decay $A = A_o e^{-t/\tau}$ is obtained from a "global" fit to the damped oscillation. Taking subsamples of several turns we obtain the tune evolution as a function of the turn number. An example of the results of such fit is shown in fig. 3. At the second half (above 500 turns) the

oscillation amplitude is small and the results of the fit is less precise.

Figure 3: Detuning results as a function of turn number.

The horizontal detuning is a linear function of the Courant-Snyder invariant W defined as:

$$W = \frac{1+\alpha^2}{\beta}x^2 + 2\alpha xx' + \beta x'^2 \simeq \frac{A^2}{\beta}$$

where β is the value of the betatron function at the pick-up and $\alpha = -(1/2)(d\beta/ds)$. This linearity can be seen in fig. 4.
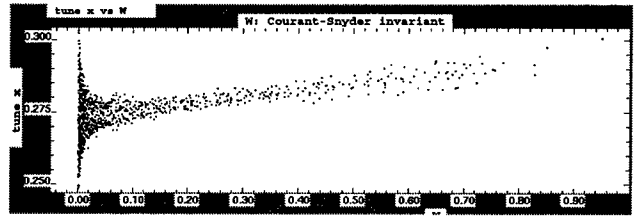

Figure 4: Detuning results as a function of the Courant-Snyder invariant W.

The detuning with amplitude $(\partial Q_x/\partial W)$ is obtained from a fit to the tune versus W. This procedure is applied to a large number of pick-ups to obtain a better statistics. Results of such measurements for three LEP physics optics are given in [2, 3] and confirms predictions of the LEP model.

4 PHASE SPACE REPRESENTATION

Coherent betatron oscillations in presence of resonances are studied in phase space diagrams. In these diagrams the beam is represented on each turn by a point with coordinates (x, x'), where x is the displacement and $x' = dx/ds$ is approx. the angle of the beam trajectory with respect to the design orbit (s is the longitudinal coordinate). The traditional way for representing the 1000-turns measurements in phase space consists in finding two pick-ups separated by a phase advance of 90°. When the phase advance is exactly 90° the signal at the second pick-ups is proportional to (dx/ds) at the first pick-up. However, beta-beating can introduce errors in the interpretation of the data.

The approach followed in [4, 5] consists in using the 1000-turns measurement of a single pick-up and rotating by 90° its Fourier transform to create a "virtual" pick-up. A betatron oscillation (even when it is damped) can be well described in terms of harmonic functions. Therefore, a

phase shift of 90° is equivalent to a differentiation operator. The procedure starts by performing a Fourier transformation to the 1000-turns data and obtaining an array of 1000 complex values (sine and cosine components of each frequency). Rotation by 90° means simply an exchange of values between real and imaginary parts and change of sign in the real (cosine) part. In order to reduce errors due to the discreteness (sampling) and finiteness (window) of data, a filter is introduced. The filter used is basically a linearly decreasing weight at frequencies below 0.12 and above 0.39 (in tune units). The 1000-turns of the virtual pick-up is obtained by a reverse Fourier transformation on the rotated and filtered complex array. A phase space representation is then obtained by plotting the positions of the virtual pick-up against the ones of the real pick-up, centering around the origin and normalizing by $1/\sqrt{\beta}$. An example of such a plot when kicking the beam with a tune slightly above 2/7 is shown in fig. 5. One observes in this figure the typical arms that are formed when the betatron tune is close to a resonance.

Figure 5: Coherent oscillation amplitude versus turn (left) and in phase space (right). The tune is slightly above 2/7. (Phase space not normalized by $1/\sqrt{\beta}$.)

The behavior of the coherent beam oscillations at LEP have been observed under several conditions (tunes, coupling) and at different beam energies. Effects like beam trapped in a 3rd order resonance and partially lost, crossing higher order resonances, coupling between horizontal and vertical motion, filamentation and other non-linearities have been reported in [4, 5].

5 BETATRON PHASE MEASUREMENTS

As already seen in section 2 the amplitude of coherent oscillations decreases rapidly within a few hundred turns mainly due to head-tail damping. In order to compensate this damping effect and maintain a coherent betatron oscillation with more or less constant amplitude we need to keep the transverse excitation. The kicker used at LEP can provide this excitation with a sinusoidal modulation of its field. If the frequency is close to the fractional part of the tune, coherent oscillations are excited and after a short time reach a constant amplitude. This amplitude depends on the

strength of the sinusoidal deflection and the proximity of the frequency to the tune. For a precise measurement of the phase of these oscillations, the beam must be excited to high amplitude to gain in signal to noise ratio. However, the presence of non-linear elements (like sextupoles, etc.) limits the valid amplitude range of this measurement.

The 1000-turns obtained during coherent oscillations of constant amplitude are then harmonically analyzed to give the amplitude and phase of the oscillation at each pick-up. The systematic error on the phase measurement is a function of the longitudinal size of the beam. At LEP, this systematic error is negligible because the bunch length is about 1 cm. The statistical error of the phase σ_ϕ is given by [9]

$$\sigma_\phi = \frac{1}{A} \sqrt{\frac{2}{N}} \, \sigma_x$$

where A is the amplitude of the oscillation, N the number of samples (or turns, in our case 1024) and σ_x is the statistical error of position measurements of the pick-up. For a typical oscillation amplitudes at LEP of around 2 mm and position resolution (turn-by-turn) of $\sigma_x \simeq 0.1$ mm the error of phase measurements is about 0.13°, i.e. the error on phase advance measurements is about 0.2°.

5.1 Applications of betatron phase measurements

Betatron phase measurements have been applied to check the chromaticity correction of the magnetic lattice of LEP [7] and the distribution of impedance of the vacuum chamber around the circumference of LEP [8]. The first was carried out by shifting the RF-frequency (which changes the length of the closed orbit and consequently the beam energy) and taking phase measurements at various beam energies. The results clearly show the negative chromaticity produced in the straight sections and its correction in the arcs. The agreement between experiment and calculation is very good and exclude strong localized sextupole errors.

The measurement of the impedance distribution was achieved by comparing phase measurements with bunch currents ranging from 50 to 450 μA. The results are in good agreement with the impedance model of LEP. These measurements clearly show the localized impedance contribution of copper cavities by a sudden phase shift around straight sections 2 and 6. In the rest of the machine the phase shift presents a rather constant slope due to the influence of bellows. As K. Cornelis put it once in the 95' CAS school: "It is indeed a very sophisticated way to find out the location of the accelerating cavities along the 26 km of LEP circumference".

6 BETATRON FUNCTION MEASUREMENTS

The measured phase advances between the pick-ups can be used to evaluate the optics parameters at any azimuthal position around the circumference [10, 9]. Taking a given

pick-up and the ones adjacent and using the three measured phase advances along with the theoretical phase advances coming from a tracking program such as MAD [13] one obtains the ratio of the real β value to the theoretical one:

$$\frac{\beta_2}{\beta_2^t} = \frac{\cot \phi_{12} + \cot \phi_{23}}{\cot \phi_{12}^t + \cot \phi_{23}^t}$$

where ^{t} denotes theoretical values, β_2 is the value of the betatron function at the 2nd pick-up, ϕ_{12} is the phase advance between 1st and 2nd pick-up and ϕ_{23} between 2nd and 3rd pick-up. Equivalent expressions are obtained for the 1st and 3rd pick-up. These expressions can also be written replacing the theoretical values by the second elements of the transfer matrices between the pick-ups. Thus,

$$\beta_2 = \frac{a_{12}b_{12}}{c_{12}}(\cot \phi_{12} + \cot \phi_{23}) = \frac{a_{12}b_{12}}{c_{12}} \frac{\sin \phi_{13}}{\sin \phi_{23} \sin \phi_{12}}$$

where a_{12}, b_{12} and c_{12} are the second element of A (transfer matrix between 1st and 2nd pick-up), of B (between 2nd and 3rd pick-up) and of $C = B \times A$, respectively.

When the transfer matrices between the three pick-ups are known, we obtain the relative phase advance $\phi(s) = \mu(s) - \mu(s_1)$ at any s between the three pick-ups:

$$\phi(s) = \arctan\left[\frac{a_{12}n_{12}(s)}{b_{12}m_{12}(s)} \cot \phi_{12} - \frac{c_{12}o_{12}(s)}{b_{12}m_{12}(s)} \cot \phi_{13}\right]$$

where $m_{12}(s)$, $n_{12}(s)$ and $o_{12}(s)$ are the second elements of the matrices $M(s)$, $N(s)$ and $O(s)$ defined in fig. 6.

Figure 6: Matrix notation used in the equations.

The value of β at s is given by

$$\beta(s) = \frac{b_{12} m_{12}^2(s)}{a_{12}c_{12}} \frac{\sin \phi_{12} \sin \phi_{13}}{\sin \phi_{23} \sin^2 \phi(s)}$$

If the theoretical values are known, then the ratio of the real β value to the theoretical one at s is

$$\frac{\beta(s)}{\beta^t(s)} = \frac{\beta_1}{\beta_1^t} \frac{\sin^2 \phi(s)}{\sin^2 \phi^t(s)}$$

An example of such measurements is shown in fig. 7. The values of the betatron function are obtained by "advancing" around the circumference from one central pick-up to the next.

6.1 Error analysis

If the transfer matrices are correct, i.e. the perturbation which is causing the beta-beating is outside the three chosen pick-ups, this procedure yields correct values only affected by the statistical error of the phase measurements.

Figure 7: Example of measured horizontal β (top) and beta-beating β/β^t (bottom) in the arcs

At LEP the perturbations arise in the insertion regions, so this procedure provides precise values of β in the arcs. In the arcs the systematic error in the measurement of β from relative errors of quadrupole gradients of about $5 \cdot 10^{-4}$ has been estimated to be about 0.2%.

The contribution of the statistical error of the phase measurement on the measured β depends on the phase advances between the three pick-ups. If the phase advance is around 60°, we have

$$\varepsilon_{\beta_2} = \sqrt{\frac{8}{3}}\,\sigma_\phi \simeq 1.63\,\sigma_\phi$$

assuming that the measurement errors of the phase are equal at the three pick-ups. For a $\sigma_\phi = 0.13°$, the relative error on the measured β is about 0.4%. The statistical error of β measurements is in the order of 0.5% in a range of phase advances from ~30° to ~75°. Outside this range, the error increases exponentially until the phase advance is 0 or 90°.

6.2 Applications of betatron function measurements

Betatron functions measurements show the mismatch of the betatron function with respect to the theoretical values (also called beta-beating or beta-wave). In terms of (β/β^t) this mismatch appears as an oscillation with a phase twice of the phase advance. An example of a vertical beta-beating measurement is shown in fig. 8. The beta-beating observed is of the order of 10% and up to 20% in some places. The curve is not drawn at places where the pick-up readings were not available during this measurement. In this figure we observe rapid changes of the beta-beating at the Interaction Points (IP) 2 and 4. The changes in the amplitude of the beta-beating observed at IP 2 and 4 indicate perturbations of the betatron function. As expected, beta-beating is introduced at the four low-β insertions (IP 2, 4, 6 and 8).

Phase advance measurements show also a similar mismatch as the betatron function. In fact, a "phase-beating" is also observed in the difference between measured and theoretical phase advance. The measured phase-beating plotted as a function of the theoretical phase advance in fig. 9
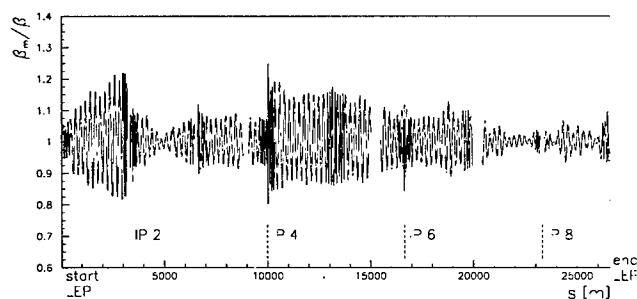
Figure 8: Measured vertical beta-beating.

corresponds to the same measurement of the beta-beating shown above in fig. 8. Phase advance changes at IP 2 and 4 indicate a local strong quadrupole gradient error.
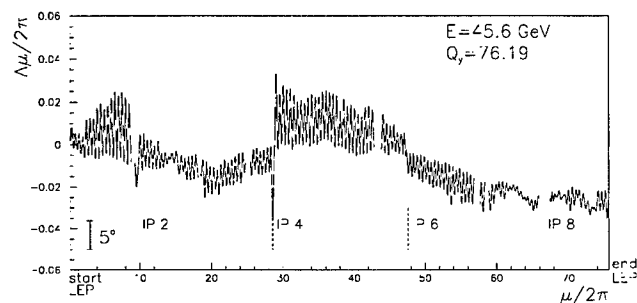

Figure 9: Measured vertical phase-beating.

Betatron function measurements have been extensively applied to calculate emittances from transverse beam profile measurements at LEP. Beta-beating introduces a systematic error on emittance measurements if only the theoretical betatron function is taken. Wire scanners at LEP, which are equipped with a high precision ruler, provide an accurate absolute measurement of the size of the beam profile. The measured values of the betatron function were applied in order to use the wire scanner emittance measurement as a reference to calibrate synchrotron light imaging monitors [15].

The strongest contribution to the beta-beating are quadrupole gradient errors. A smaller contribution has its origin in the beam energy changes around the circumference due to synchrotron radiation losses at the bending magnets. This energy loss is recovered in the RF cavities installed symmetrically around IPs 2 and 6. At 45.6 GeV the effect on the beta-beating is up to 6% and it is opposite for each type of particles. Measurements of the betatron function carried out with the electron and the positron beam were compared and its difference resulted in a $[\beta(e^-) - \beta(e^+)]/\beta$ with an amplitude of up to 12%. This is in very good agreement with the predictions [10].

In 1993 and 1994 the number of bunches per beam was increased to eight with the "pretzel" scheme [14]. In order to avoid beam encounters in the middle of the arcs, beams were separated in the horizontal plane and displaced up to about 4 mm from the design orbit. This separation introduces beta-beating, because of the large excursions of the beam off-center of the sextupole magnets which act on the

beam as an extra quadrupole gradient. Since the offset of the positron and the electron beam are just opposite, the beta-beating has also an opposite sign. Measurements of the betatron function were done with a single beam with and without the pretzel separation and confirmed the predictions for beta-beating of 20% and up to 30% due to the separation.

7 ACKNOWLEDGMENTS

8 REFERENCES

[1] G. Morpurgo, "The Software for the CERN LEP Orbit Measurement System", CERN-SL-91-41, (1991).

[2] A.-S. Müller and J. Wenninger, "Measurements of Coherent Damping and Tune Shifts with Amplitude at LEP", Proc. of the 6th EPAC, Stockholm, (1998).

[3] A.-S. Müller and J. Wenninger, "Measurements of Tune Shifts with Amplitude at LEP", poster THA129 at this conference.

[4] G. Morpurgo, "The BOM Turn Display: A Tool to Visualize the Transverse Phase-Space Topology at LEP", Proc. of the 6th EPAC, Stockholm, (1998), pp.1571-3, and CERN SL-98-045 (BI).

[5] G. Morpurgo, "Measurement and Visualization of the Transverse Phase-Space Topology at LEP", Proc. of the ICAP, Monterey, CA, (1998).

[6] J. Borer et al., "Harmonic Analysis of Coherent Bunch Oscillations in LEP", Proceedings of the 3rd EPAC, Berlin, (1992), pp. 1082-4.

[7] D. Brandt et al., "Measurement of Chromatic Effects in LEP", Proceedings of the 1995 PAC, Dallas, USA, 1995.

[8] D. Brandt et al., Measurement of Impedance Distributions and Instability Thresholds in LEP; Proc. of the 1995 PAC, Dallas, USA, 1995.

[9] J. Borer et al., "Betatron Function Measurement at LEP Using the BOM 1000 Turns Facility", Proc. of the 1993 PAC, Washington D.C., (1993), pp. 2103-5.

[10] P. Castro, "Luminosity and beta function measurement at the electron-positron collider ring LEP", Doctoral Thesis, CERN SL/96-70 (BI) (1996).

[11] S. Myers, "Performance Related Measurements on LEP", CERN-SL-99-002 DI, (1999).

[12] P. Melchior, "Tidal Interactions in the Earth Moon System", Communications, Serie B, No. 160, IUG General Assembly, Vienna, (1991).

[13] H. Grote and F.C. Iselin; "The MAD program", CERN/SL/90-13(AP), (1991).

[14] L. Bergström et al., "Report of the Working Group on High Luminosities at LEP", Editors E. Blucher, J. Jowett, F. Merrit, G. Mikenberg, J. Panman, F.M. Renard and D. Treille. CERN 91-02, (1991).

[15] R. Jung, "Precision emittance measurements in LEP with imaging telescopes, comparison with wire scanner and x-ray detector measurements", Proc. of the Workshop on Particle Dynamics in Accelerators, Tsukuba (Japan), (1994), and CERN-SL-95-63 (BI).

EXPERIMENTAL RESULTS FROM A MICROWAVE CAVITY BEAM POSITION MONITOR

V.Balakin, A. Bazhan, P. Lunev, N. Solyak, V. Vogel, P. Zhogolev, BINP,Protvino, Russia

A. Lisitsyn ,SSIE "Istok", Moscow, Russia

V. Yakimenko,BNL, Upton, NY.

Abstract

Future Linear Colliders have hard requirements for the beam transverse position stability in the accelerator. A beam Position Monitor (BPM) with the resolution better than 0.1 micron in the single bunch regime is needed to control the stability of the beam position along the linac. Proposed BPM is based on the measurement of the asymmetrical mode excited by single bunch in the cavity. Four stages of signal processing (space-,time-, frequency- and phase-filtering providing the required signal- to-noise ratio) are used to obtain extremely high resolution. The measurement set-up was designed by BINP and installed at ATF/BNL to test experimentally this concept. The set-up includes three two-coordinates BPM's at the frequency of 13.566 GHz, and reference intensity/phase cavity. BPM's were mounted on support table. The two-coordinates movers allow to move and align BPM's along the straight line, using the signals from the beam. The position of each monitor is controlled by the sensors with the accuracy 0.03 micron. The information from three monitors allows to exclude angle and position jitter of the beam and measure BPM resolution.. In the experiments the resolution of about 0.15 micron for 0.25 nC beam intensity was obtained, that is close to the value required.

1 INTRODUCTION

The first linear collider was proposed in 1978 as a way to a very high energies in electron-positron collisions[1]. Today a few projects of LC are under development [2]. For all the projects, the beam jitter should be less than 0.1 micron in the main linac and a few nanometres in final focus system (FFS), otherwise the luminosity will decrease. The simple and most effective microwave BPM is a circular cavity, excited in TM_{110}-mode by an off-axis beam. The cavity-type BPM has potentially a high resolution and can provide requirements for future colliders. By now, a few various designs of BPM's have been proposed and developed for a broad frequency range from 1.5 GHz (TESLA) up-to 33 GHz (CLIC) [4-10]. In this paper, our concept of signal processing for obtaining high resolution is presented [3], and the results of experimental studies of limitation in resolution are discussed.

The high frequency BPM has a submicron resolution. Today it seems impossible to find test beam with the required transverse stability to measure the resolution in BPM. Nevertheless it is possible to verify BPM even when the beam jitter is much high than the expected resolution[4]. Figure 1 explains how to verify the intrinsic BPM resolution using three BPMs irrespective of the

Figure 1. Set-up for determine intrinsic BPM resolution.

beam jitter. If all the BPM's are located close to each other, the beam trajectories are linear and the half-sum of beam off-sets in the first and last BPM's should be equal to that in the middle BPM. All measurement points should be in line (as shown in Fig.1). The dispersion points around this line yield the BPM resolution.

The measured amplitude of the transverse mode is proportional to the beam offset and bunch charge:

$$P = \frac{\omega^2}{2Q} S^2 M^2 \rho'(k\Delta x)^2 q^2 \qquad (1)$$

Where q is the beam charge, Q - loaded quality factor, ρ' - normalised transverse shunt impedance; M - beam transit time factor; $S = \exp(-\omega^2\sigma_z^2/2c^2)$ - space factor.

The phase of the oscillations depends on the direction of the beam offset. One of the main problems is a large amplitude of the fundamental mode and other symmetrical modes that are excited in the cavity by the beam irrespective of it's offset. These modes must be strongly dumped.

The thermal noise as well as a noise coming from electronics determine another limit of resolution. The upper limit of resolution can be achieved when the power of the signal (1) is equal to that of the thermal noise $P=4kT(\Delta f)$. Assuming $(\Delta f)=f/Q$ we obtain

$$(\Delta x)_{min} = \frac{\lambda}{2\pi \cdot q} \sqrt{\frac{4kT}{\omega \rho'_{ef}}} \qquad (2)$$

where λ means the wavelength, $\rho'_{ef}=\rho'M^2S^2$- normalized effective shunt impedance, T-temperature, k –Bolcman constant.

Estimation for 14 GHz BPM shows that the limitation coming from the thermal noise of electronics is of the order of a few nanometres.

2 CONCEPT OF SIGNAL PROCESSING

A more serious limitation appears from the symmetrical modes. For example, the dumping of E_{010} mode should be better than 140 dB for obtaining 1 nm resolution. The frequency filtration dumps this mode only by the factor

$$r = Q_{110}^2(1 - \frac{\omega_{010}^2}{\omega_{110}^2}) \qquad (3)$$

which is typically gives 60 dB. An extremely high resolution can be achieved by using a few stages of signal processing: "space-", "time-", frequency- and "phase-" filtering [3].

2.1 "Space filter"

Symmetrical and transverse modes have different field space distribution in the cavity and this fact can be used for filtering. Usually, in a BMP two pick-up antennas are used, whose signals are combined in a magic T. For symmetrical modes signals subtract, and for transverse ones add up. It gives typically a 20-30 dB additional dumping. The disadvantage of this method is effect of temperature on the amplitude difference and phase shift between the signals from antennas, especially if long cables are used. Another solution is to extract only the transverse mode signal from the cavity using a special geometry of output. In this case, the length of cable from antenna to RF circuit doesn't matter and the dumping of about 30-40 dB is available.

2.2 "Time filter"

The sharp front of the single bunch signal from the cavity provides wide spectrum from each resonant mode. It

Figure 2. Beam driven RF pulse (top) and spectrum (bottom) before (left) and after (right) RF-switch.

means that at the operating frequency we have a signal from symmetrical modes. The common mode rejection by frequency discrimination is defined by equation (3) and is

typically 60 dB. Within the rejection by "space filter" it gives approximately 100 dB. Further rejection 40 dB or more can be received by using a new method of "time filtration" proposed in [3]. The idea is to smooth sharp front of the signal, excited by bunch. For this purpose a special time "gate" (controlled RF switch) installed between cavity and the RF circuit. The gate is closed during sharp front and then open smoothly, as it shown in Figure 2. Additional attenuation of the signal from symmetrical mode depends on the switching time and can

Figure 3. Spectrum of RF signal with and without switch

be very high, limited mostly by switch isolation. Two experimentally measured spectra excited by a single bunch in the cavity are shown in Fig.3 (with an RF switch and without any) for demonstration of this method.

2.3 Frequency filter and phase detector

The signal is filtered at a frequency of transverse mode with pass-band in order to $\Delta f = f_{110}/Q_{110}$ to minimize the thermal noise. Phase detecting allow to measure sign of beam displacement. This part is shown in Fig.5.

This concept of signal processing has been realized in our design of BPM. The aim of the experiment was to obtain the maximum BPM resolution with a real beam jitter and to study possible limitations.

3 EXPERIMENTAL SET-UP

The experiment was performed at on the ATF/BNL linac, operating in a single bunch regime. Beam parameters were: U=45±1 MeV, q=0.25÷0.5 nC, the longitudinal beam size 5 - 10 ps and transverse jitter about 25 μm along the beam–line, where the set-up was installed. [11].

Figure 4 represents the setup of the experiment. Three prototypes of BPM cavities were manufactored for this experiment. Each BPM was placed on a high precision electromagnetic mover allowing to move the cavity in both directions (X and Y) in the range of ±1 mm with step equal 0,3 μm. This allowed to align and calibrate the BPM's. The position of the movers was controlled with

the accuracy 0.03 μm with respect to the support table. All magnetic elements were magnetically shielded to exclude the effects on the beam. All the three movers were placed on the support table and aligned using standard ATF procedure. To achieve an unrestricted motion of the BPMs, they were connected to the vacuum channel via bellows. Before the experiment started, all the movers had been calibrated.

The detection electronics allowed to take and process data pulse to pulse independently in horizontal and vertical positions in each BPM. Tests BPMs and detection electronics in the lab showed that the potential BPM

Figure 4. Experimental setup

resolution for ATF beam parameters should be less then 0.1 micron. Each BPM has two outputs for the horizontal and vertical signal coupled with detection electronics by 4m RF-cables because electronics was placed outside of the tunnel.

Before the test started the TM_{110}-mode resonant frequency of each BPM had been measured and tuned. For fine tuning thermal heating was used. Each BPM had individual heater with feedback temperature stabilization, which automatically kept the frequency at the desired value.

4 RF ELECTRONICS

Figure 5 represents the detection electronics used in the experiment for measurements in the horizontal (X) and vertical (Y) directions. These circuits comprise a RF-switch, a band-pass filter, a mixer, a phase detector, an intermediate frequency amplifier, and a video amplifier for each monitor. As the laboratory tests showed that the electronics had sensitivity of about $6*10^{-11}$ W and the dynamic range close to 65 dB [4].

Afterwards the signal wss transmitted from RF electronics to the analog-digital converter (ADC) located in CAMAC. The precision mover was controlled by CAMAC, too. The above circuit allowed to find the coordinates for each single bunch of the beam.

As a reference signal the signal from the reference cavity had been planned to be used. However, at the first

stage signal from ATF reference line at frequency f=2856 MHz was used that was multiplied by factor 5 for mixing down and divided by factor 4 for phase detecting

Figure 5. RF circuit.

The information about the beam intensity and phase (with respect to the reference line) of the beam was obtained from the reference cavity. The scheme of an RF circuit for this measurement is shown in Figure 6.

Figure 6. RF electronics for phase and amplitude control.

5 RESULTS

Before data taking began, the beam was placed as close to the centers of BPMs as possible using ATF equipment. For this procedure, in all measuring channels a crystal detector was used (see Fig.5 for the X channel). After that Y (or X)-channels in each BPM were connected to the circuits for phase measurements. Then all BPMs were moved off from the centre so as to provide a clear displacement signal for tuning of the detection circuit in phase measurements. For determination of sensitivity each BPM was moved in the range of ±35 μm with the step equal to 0.3 μm. Beam jitter had been excluded by

fitting the measured data. These sensitivities were used for calculating beam offset.

After wards, all the BPM's were moved to their fitted "zero" point for resolution measurements. The data obtained for the Y axis are shown in next Fig.7, where the beam off-set at the middle monitor is plotted as a function of the half-sum off-sets at the upstream and downstream monitors. The events with off-sets more than 10 µm in the X direction have been rejected (the coupling between modes of X and Y polarisation modes in the BPM cavity is about 40 dB). The resolution obtained in that run was 0.15µm for 0.25 nC bunch charge or 38 for 1nC normalised value.

Figure 7. Determination of the BPM resolution.

All tests were made with the 10 dB attenuation of the output signal of BPMs to escape saturation of electronics due to a high beam jitter.

6 DISCUSSION

An entire resonant BPM system has been tested at the ATF/BNL using real beam with the predetermined position, angle, intensity and energy jitter. Under these conditions the resolution of 0.15 µm for 0.25nC beam charge was obtained. Three independent BPMs were used to exclude position and angle jitter. For absolute BPMs calibration precision movers were applied. The resolution attained is not the limit for this type of BPM. Its value was determined by the experiment condition. Unfortunately beam jitter exceeded dynamic range of used in the test electronics. Therefore, the BPM output signal was attenuated.

The phase of laser pulse in RF gun was not absolutely stable with respect to accelerating RF signal, which was used as the reference signal for phase measurements. That is why the "beam phase" has jitter with respect to reference oscillations which explains for the additional jitter noise in the output signal in the phase detection electronics. This jitter could not be excluded using three BPMs.

The beam trajectory along the BPMs was not absolutely rectilinear of the effect of the magnetic field

has influence on moving charged particles. And even in a permanent magnetic field (e.g., the magnetic field of the Earth) trajectory deflection from the line is not abiding. It is determined by the beam energy. Therefor, in resolution determination the energy jitter in an accelerator yields erroneous reading when three BPMs are used.

We believe that resolution better than 38 nm for 1nC can be obtained in our design of BPM. This result is close to the result received in experiment [7], where the resolution near 25 nm was demonstrated for BPM at frequency 5712 MHz. This experiment was done on FFTB/SLAC with a 1 nC beam intensity and jitter on the order of 0.14 µm (200 times less than in our case). In this expeiment 'time-filtering" of signal didn't used.

7 CONCLUSION

Now it seems possible to have a BPM with the resolution better than 100 nm. The level of 1nm resolution takes more studying. For experimental tests, a very stable beam is needed.

8 ACKNOWLEDGEMENTS

We would like to thank the ATF staff for their help and hospitality during our stay in BNL. Our special thanks are due to R.Palmer, Ilan Ben-Zvi and X. J. Wang for making the experiment possible, as well as for smoothly coordination of our communication and joint activities.

9 REFERENCES

[1] V.Balakin, G.Budker, A.Skrinsky, "Feasibility of creating a superhigh energy colliding electron-positron beam facility", National Partical Accelerator Conference, 1978,Dubna, Russia, Trans.186, SLAC, 1978.

[2] International Linear Collider Technical Review Committee Report (TRC) 1995., SLAC 1995.

[3] V. Balakin " Concept BPM for VLEPP ", Proc. 3rd Intern. Workshop on Linear Colliders, v. 3, p. 155 (1991)

[4] V. Balakin, V. Vogel, N. Solyak "The Model of BPM for VLEPP ", Proc. 3rd Int. Workshop on Linear Colliders, v. 3, p. 188 (1991)

[5] W.Schnell "Common-mode rejection in resonant microwave position monitors for linear colliders" CERN-LEP-RF/88-41, CLIC Note 70.

[6] V. Balakin, A. Bazhan, P. Lunev et al., "Beam Position Monitor with nanometer resolution for Linear Collider", Proc. of the Fourth European Particle Accelerator Conference, v. 2, p. 1539 (1994).

[7] T.Slaton, G.Mazaheri,T. Shintake, "Development of nanometer resolution C-band radio frequency beam position monitors in the Final Focus Test Beam. Proc. of XIX International Linear Accelerator Conference (Linac98), Chicago, Illinois, August 23-28,1998.

[8] W.Schnell, J.P.H.Sladen,I.Wilson,W.Wuensch, "CLIC beam position monitor developments", CLIC-Note 170, 1992.

[9] J. P. H. Sladen, I. Wilson, W. Wuensch, "CLIC Beam Position Monitor Tests", CERN-LEP-RF (1996).

[10] R. Lorenz, K Yezza, "Test Results on Beam Position Monitor Prototype for the TTF", Proc. of the IV EPAC, v. 2, p. 1536 (1994).

[11] K Batchelor, M. Babzien, I Ben-Zvi et al,, "Operational experience on the Brookhaven National Laboratory Accelerator Test Facility", Proc. Fourth European Particle Accelerator Conference, v. 1, p. 736 (1994).

LHC BEAM INSTRUMENTATION

J.Bosser, C. Bovet, C. Fischer, R. Jung, H. Koziol, H. Schmickler, L. Vos

CERN, Geneva, Switzerland

Abstract

Six years before the scheduled commissioning of the LHC at CERN, the basic list of beam instruments has been established. This early date is needed due to the impact of the mechanical design of some detectors (mainly the beam position detectors) on the cryogenic part of the machine as well as for other projects due to the long R&D period (emittance measurements, tune and chromaticity diagnostics and control). This paper gives a detailed overview of the basic requirements and specifications of all beam instruments foreseen for transfer lines and main rings [1].

1 INTRODUCTION

Underneath the super-conducting dipoles around the LHC ring the annual radiation dose will be as low as 1 Gy. This is due to the extremely effective halo cleaning system necessary to prevent magnet quenches. For beam instrumentation this means that front-end electronics can be spread around the circumference, avoiding long and expensive cables.

Table 1. Summary list of LHC instruments [2]

Transfer lines between SPS and LHC (5 km)		Nb
Beam position monitors (using LEP buttons)		110
Beam current transformers		4
Beam loss monitors		20
Screens using optical transition radiation		20
LHC main ring		
Injection screens with optical transition radiation		16
Betatron matching, thin OTR foils	11 kHz	2
Beam position monitors	40 MHz	988
Beam loss monitors distributed	150 kHz	4000
BLM for halo cleaning (ACEM)	40 MHz	10
Beam current transformer systems		2
Wire scanners for beam size calibration		4
Synchrotron light telescopes	•40 MHz	4
Beam size detectors (R&D on the way)		4
Tune measurement systems using 4 kickers		2
Chromaticity (from head-tail phase shift)		2
Schottky pick-ups		4
On-line control systems of Q,Q' and closed orbit		6
Dump lines		
Screens		10
Beam current transformers		2

For distributed monitors like beam position (BPM) and beam loss (BLM) data collection will be done through some 240 acquisition crates located at 30 m from the monitors.

2 BEAM POSITION MEASUREMENT

Trajectory and closed orbit measurements are vital for commissioning and operation of accelerators. To achieve high luminosity, the azimuthal beam distribution becomes very complex, so that various phenomena (beam-beam forces, wake fields) strongly affect the orbits of individual bunches. Hence a system with high bandwidth capable of measuring the transverse position of each bunch is desirable. In LHC it is foreseen to install BPM's reading both planes at each lattice quadrupole which makes a total of 988 pick-ups spread over the two rings of 27 km circumference.

2.1 Mechanical design

Pick-ups will be made of four buttons yielding enough signal amplitude to measure the position of a pilot bunch of 5×10^9 protons. Most BPMs will be located near supra-conducting quadrupoles with local electronics mounted outside the cryostat and receiving beam signals through coaxial cables of 1.3 m length.

2.2 Signal treatment

In the context of the development of an orbit system for the LHC a high bandwidth was achieved by extending the principle of the narrow-band normaliser with phase detection to a wide-band time normaliser[3],[4]. The principle of this new circuit is shown in Fig. 1.

Figure 1. Principle of the wide-band normaliser

Results obtained in the laboratory on the first prototype prove that a linearity of 0.2% can be achieved over the full aperture, see Fig. 2. A bandwidth of more than 40 MHz and a dynamic range of 50 dB was achieved.

Figure 2. Position linearity with the wide-band normaliser

2.3 BPM performances

Absolute accuracy shown in Table 2 is mainly determined by alignment precision between the magnetic centre of the quadrupole and the electrical centre of the BPM. For the pilot bunch this is determining, while for nominal bunches the offset will be eliminated by using the K-modulation technique[5].

Table 2. BPM performances

Bunch type	Pilot		Nominal	
Mode	Traject.	Orbit	Traject.	Orbit
Absolute accuracy	1.5 mm	1 mm	150 µm	100 µm
Resolution	0.5 mm	0.2 mm	50 µm	5 µm

3 TRANSVERSE BEAM PROFILES

Keeping the highest possible transverse density through the whole injector chain up to the top energy in the LHC is one of the major goals to optimise luminosity. For that reason OTR screens (producing optical transition radiation) have been tested and will be provided in transfer lines. They are made of Ti or Al foils, a few µm thick and are viewed with high-resolution CCD cameras.

3.1 Injection matching

A new method has been introduced for betatron matching into a circular machine [6] which consists in using a thin detector to measure the beam size for several revolutions before dumping the beam. The detectors can be either secondary emission grids or OTR screens. When r.m.s beam size is beating by less than ±10%, which is easy to check, this means that the emittance blow-up by filamentation will be less than 1%.

3.2 Wire scanners

Wire scanners currently used in LEP will be very useful to measure beam profiles with great accuracy since the wire position can be measured to ±4 µm. Still they cannot be used with more than 200 nominal bunches for the wire to survive [7] and therefore cannot be used operationally, but will serve to calibrate the other types of monitors described in the next two paragraphs.

3.3 R&D on beam profile monitors

Three types of monitors using the residual gas in the machine vacuum are presently undergoing tests in the SPS with proton bunches separated by 25 ns:

- An ionisation profile monitor constructed at DESY will be tested with an additional magnetic field which should serve to collect electrons with minimum space charge blurring;

- Another monitor collects ions accelerated by the beam's electrostatic potential without any other external field. The velocity distribution of those ions escaping the vacuum chamber through a slit, is measured in a magnetic spectrometer and the beam size can be deduced from the velocity distribution;

- The third monitor observes the light emitted by residual gas molecules excited by the beam. Selecting a gas with fast decay allows to get a clean transverse beam profile and a local bump of nitrogen pressure of less than 10^{-6} torr is sufficient to collect enough photons in 20 ms.

A fourth monitor is also giving promising results: it consists of an ion-gun accelerating a beam of Xe^+ or Kr^+ to an energy of 2 keV which is sent at a right angle to the proton beam. The deflection angle of the ion beam is measured as a function of the ion beam position and the derivative of this function gives the proton beam profile. At top energy the r.m.s. beam size will be of some 400 µm and in order to perceive an emittance blow-up of a few percent the beam size should be measured to 1-2% relative accuracy. The best of the four preceding monitors will be retained for operational use.

3.4 Synchrotron radiation telescopes

The use of synchrotron radiation to measure transverse beam profiles has been analysed [8] and seems delicate at injection energy where a special short magnet is needed to produce enough power in the near infra-red region. This power will rise by 5 orders of magnitude during ramping, which is not easy to master at the detector level. This great dynamic range stems from the fact that useful photons belong to the higher part of the spectrum, well beyond the critical energy. Another possibility at injection energy would be to use the enhanced synchrotron radiation power produced in the fringe field of the same dipole. At top energy, in order to determine the beam sizes during physics, a UV telescope receiving light from a 3.5 T dipole could monitor permanently with a CCD camera the transverse beam density. Using a wavelength of 200 nm, the diffraction spot sizes will be of 300/130 µm for H/V-profiles respectively, to be deconvoluted from beam sizes of 890/480 µm.

For the detection of individual bunch emittances a photomultiplier with 16 anodes can acquire bunch sizes at a frequency of 40 MHz.

4 TUNE AND CHROMATICTY MEASUREMENTS

Tune, chromaticity and transverse coupling need to be controlled throughout critical phases of the machine cycle, in particular during ramping and beta-squeezing.

4.1 Use of the transverse feedback

Signals may be injected into the feedback loop, either white noise for broad-band spectral analysis, or a swept-frequency sine-wave. The latter allows the measurement of the beam transfer-function, i.e. the response in amplitude and phase.

4.2 Coherent oscillations created with a kicker

One would perhaps not include this method, needing special kickers, were it not for other possibilities that it provides:

- coupling is easily measured, using a single kick in one plane, and resonances can be studied, by "tickling" the beam.
- very importantly, kicking to oscillation amplitudes greater than the size of the beam, which is possible at injection energy, and using two pick-ups an odd multiple of quarter-betatron periods apart, allows to observe long-term evolution in transverse phase space, for study of the dynamic aperture. Therefore additional single-turn kickers with enough strength to displace the beams at 7 TeV by 8 σ will be installed.
- finally, the kicks can serve for the measurement of chromaticity, via the head-tail phase shift (next paragraph).

4.3 Head-tail chromaticity measurements

In addition to the classical methods of measuring chromaticty [9] a new method has been developed at CERN that allows the chromaticity to be calculated after several hundred turns from the turn-by-turn position data of a single bunch after transverse excitation.

This so-called head-tail chromaticity measurement [10] relies on the fact that for non-zero chromaticity a dephasing/re-phasing occurs between the head and tail betatron motion of a bunch with the synchrotron frequency. Immediately after the exciting kick, head and tail oscillate in phase. On subsequent turns, the head and tail de-phase due to chromaticity, reaching a maximum phase difference after half a synchrotron period. By measuring the turn-by-turn position data for two longitudinal positions in a bunch it is possible to extract the phase difference between the head and the tail oscillations and so to determine the chromaticity.

This technique has several advantages over other methods. Firstly, only a few hundred turns of data is required, which allows for short acquisition times. Secondly, unlike many other methods, no knowledge of the betatron tune is

required, and there is also very little dependence on energy for machines operating well above transition.

5 INTENSITY MEASUREMENTS

Beam transformers and many other beam diagnostics will be located where the beam separation is 0.4 m.

5.1 Beam current transformers

In order to obtain a bandwidth of the order of 1 GHz, current transformers of a single-turn variant or wall-current-monitor will be needed. Ferrite loading will extend the lower cut-off frequency.

Once injection is completed and the beams are circulating, the fast beam transformers will serve to determine the number of protons contained in each of the 2835 bunches, with 1% precision. For practical reasons, this will not be done on a single turn, which is acceptable as this information does not require continuous surveillance.

5.2 DC beam current transformers

These monitors are based on the principle of the magnetic amplifier, using a null-method, and will measure the intensity, or current, of the circulating beams.

DC beam transformers currently reach a resolution of 1 μA, corresponding to 5×10^8 protons in an LHC ring. The output drift is about 1 μA over 10 s, 2 μA over 1 day, and 3 μA over a week, but a significant improvement may be achieved before the LHC start-up. A resolution of 1 μA on the one hand, and a nominal beam intensity of 0.54 A on the other, means a dynamic range of 5×10^5, requiring an analogue to digital conversion of 21 bits.

6 ACKNOWLEDGEMENTS

7 REFERENCES

[1] J. Bosser et al., "LHC Design Report, chapter on Beam Instrumentation",LHC Project Report to be issued in 1999.

[2] C. Fischer, "A review of the LHC beam instrumentation", LHC Project Note 144, Apr. 1998.

[3] D. Cocq, "The wide-band normaliser – a new circuit to measure bunch position ...", NIM A 416 (1998) pp. 1-8.

[4] D. Cocq, H. Schmickler and G. Vismara, "A new wide-band time normaliser circuit ... ", HEACC, 1998.

[5] B. Dehning et al., "Dynamic beam based calibration of beam position monitors", EPAC'98, pp. 430-433.

[6] C. Bovet and R. Jung, "A new diagnostic for betatron phase space matching", LHC Project Report 3, Rev., 1996.

[7] J. Bosser and C. Bovet, "Wire scanners for the LHC" LHC Project Note 108, Rev., Oct. 1997.

[8] J. Bosser et al., "Preliminary studies on a profile monitor for the LHC using s.r.", LHC/Note 192, June 1992.

[9] H.Schmickler, "Diagnostics and control of the time evolution of beam parameters", DIPAC 1997, pp. 43-48.

[10] D.Cocq, R.Jones, H.Schmickler, "The measurement of chromaticity via head-tail phase shift", BIW 1998, pp. 281.

OBSERVATION OF BETHE-BLOCH IONIZATION USING THE BOOSTER ION PROFILE MONITOR

A.A. Hahn, J.R. Zagel, Fermi National Accelerator Laboratory, Batavia Il, 60510[*]

Abstract

The Booster Ion Profile Monitor (BIPM) was recently (April 1998) used in a test to study the feasibility of collecting the electrons instead of the more traditional ions. These electrons and ions are created by the ionization of the residual gas in the beam pipe by the proton beam. As a consistency check, the proton beam current is compared to the integrated area of the measured profile through the acceleration cycle. It was found necessary to include the effect of the proton beam energy upon ionization by means of the Bethe-Bloch equation in order to have satisfactory agreement.

1 INTRODUCTION

The Booster Ion Profile Monitor (BIPM) is one of a family of profile monitors[1,2] which are found throughout the FNAL Accelerator Complex. The BIPM[3] was the first operational IPM of the family. An IPM utilizes the ions or electrons from ionization of the residual gas by the particle beam. The density of ionization is proportional to the beam intensity distribution. An external transverse electric field drifts the ions or electrons towards a microchannel plate. The incoming charges are amplified in the microchannel plate and deposited on collectors (approximately thirty-two 1.5 mm width x 10 cm length strips in the Booster) which run parallel to the beam direction. The distribution of signal among the strips is representative of the transverse profile of the beam. These signals are further amplified and then digitized by the IPM electronics. The electronics can capture profiles on a turn by turn basis, which in the Booster amounts to 20000 turns of data.

Among the advantages of an IPM are that it is non-invasive and can capture turn-by-turn transverse beam profiles. One of the disadvantages is that the radial electric field from the charge distribution of the beam itself is comparable to that of the external field. This causes a spreading of the ion or electron cloud, and necessitates a "correction" to the measured profile distribution. This correction depends upon the beam density. A modest external magnetic field (400-3000 Gauss dependent upon beam density) can confine the electrons (but not the ions) and eliminate the need for a theoretical correction. An experiment to test this proposal was attempted in the Booster. The Booster was chosen because it was the only operational circular machine at the time (we are preparing for the startup of the new Main Injector and Run 2). Unfortunately, the correction is smallest in Booster

because the beam is transversely quite large. At the intensities (up to 2.5e12 protons) we were able to achieve in the study, the total correction effect was at most 10%. As will be seen, this is at or below the level of the hardware uncertainties of the current IPM system. The correction can range up to 300% in the case of the Tevatron IPM.

2 EXPERIMENT AND ANALYSIS

The Horizontal BIPM (H-BIPM) was fitted with an electromagnet whose field strength could be varied from 0 to 700 gauss. Two other electromagnets were utilized so that the total effect of the magnets would be a local 3 bump to the Booster beam orbit, thereby minimizing the impact on Booster operations. The external electric field could be reversed in order to collect ions or electrons on any particular Booster cycle.

The particular data described in this paper were actually acquired in the ion collection mode and with negligible magnetic field. As a control, we desired that the H-BIPM exhibit self-consistency. Whenever we record the turn-by-turn profile, we also simultaneously record the turn-by-turn measurement of "Charge 0". Charge 0 in the Booster represents the total charge in the circumference of the machine. To be consistent, the IPM should track this total charge through the acceleration cycle. The ionization of the residual gas is proportional to the beam current (velocity *Charge 0). The velocity of the Booster proton beam varies from about 0.713 c at injection (T = 400 MeV) to 0.9945 c at extraction (T = 8 GeV). Figure 1 shows plots of Charge 0 and the current. As seen by the IPM, the intensity of the ionization is the area of the beam profile. We extract the area from a 5 parameter gaussian fit,

$$y(x) = Ae^{-\frac{1}{2}\left(\frac{(x-\mu)}{\sigma}\right)^2} + B + Mx$$

where A = amplitude, μ = centroid, σ = sigma, and M and B parameterize a sloping background. The area of the gaussian is $\sqrt{2\pi}\sigma A$. The gaussian parameters, as well as $\beta\gamma$ (β=v/c, and γ=(1-β^2)$^{-1/2}$), the Lorentz quantities of the proton beam) are plotted in figure 2. The activity between turns 9000-12000 is due to the Booster going through transition. The results shown in this figure were derived from 1000 fits (equally spaced 20 turns apart) throughout the cycle. Each fit was made to the average of 20 turns of data to improve statistics. The results found by dividing the area by the beam current (with arbitrary normalization) are shown plotted in figure 3a against $\beta\gamma$.

Figure 1. The Booster charge and current through one acceleration cycle.

Figure 2. Plot of Sigma, Amplitude, Centroid from the fitting of 1000 turns spaced 20 turns apart through the Booster cycle, as well as $\beta\gamma$ vs. Booster Turn Number. Each Fit was to the sum of 20 individual turns. The activity between turns 9000 and 12000 ($5 < \beta\gamma < 7$) is due to the Booster going through transition.

From the injection point, $\beta\gamma \sim 1$ (turn 30) to $\beta\gamma = 2.7$ (turn 5000), the Area/I drops by about 60%. This is followed by a slow rise to extraction, $\beta\gamma = 9.5$ (turn 20000). In addition some instrumental effects were still observed, primarily coming from large transverse beam motion.

While calculating the ion production vs. gas density, it was realized that the Booster is running from below the minimum ionization energy (at injection) to above it at extraction. The slowly rising Area/I could be explained by the relativistic rise of -dE/dx and not a mundane instrumental effect. A subroutine was written to include the variation in ionization, using the Bethe-Bloch equation [4],

$$-dE/dx = Kz^2 \frac{Z}{A} \frac{1}{\beta^2} \left[\frac{1}{2} \ln\left(\frac{2m_e c^2 \beta^2 \gamma^2 T_{max}}{I^2} \right) - \beta^2 - \frac{\delta}{2} \right]$$

with Z = Atomic Number , A = Atomic Mass, δ = density effect, I = the mean ionization energy of the target medium, and z, β, γ, referring to the Atomic Number and Lorentz quantities of the ionizing particle. K= 0.307075

469

Figure 3: (a) The Area/I. Note the suppressed zero.
(b) The Area/(I*|dE/dx|) as calculated from the Bethe-Bloch equation.

MeV g^{-1} cm^2. The maximum possible kinetic energy which can be given to the electron is

$$T_{max} = \frac{2m_e c^2 \beta^2 \gamma^2}{1 + 2\gamma\, m_e/M + (m_e/M)^2}$$

with m$_e$ and M being the electron mass and the ionizing particle mass (the proton in the Booster case) respectively. The parameters (Z, A, I) chosen (2, 2, 38 eV) were those for Hydrogen gas (H$_2$) which represents 42% of the residual gas in the Booster. The density effect (δ) was ignored since it is chiefly applicable to liquids and solids, not gases. In any case since we do not know the absolute gain of the IPM, we are insensitive to the exact parameters (Z, A, I) of the medium. The results are shown in figure 3b. The agreement with the Bethe-Bloch equation is quite good. One can still see "glitches" which are correlated with the Booster Beam slewing across a wide region. Fortunately these remnant effects are at the 5% level, providing hope that they can be corrected once we have installed an overall gain measurement system (using a UV light shining on the microchannel plate).

However the H-BIPM seems to be working near the limit of its linear region. In another data set where the microchannel plate gain was only 10% higher, the system clearly showed saturation effects. The Area/(I*|dE/dx|) test is a useful method to demonstrate linearity, but it is clear that a more robust IPM will require an increase in its

dynamic range. This can be done either by raising the saturation level of the microchannel plate (by using a High Output microchannel plate with increased bias current) and/or increasing the sensitivity of the preamplifier electronics.

Finally, the H-BIPM did give reasonable profiles when run in the electron collection mode, however we cannot at this time(because of saturation effects in that data at the 10% level or more) conclusively prove that the electron mode is really better than the ion. The final results of that test will be reported in another paper.

3 REFERENCES

[1] Zagel, J.R., Chen, D., Crisp, J.L. "Fermilab Booster Ion Profile Monitor System Using LabVIEW",1994 Beam Instrumentation Workshop, AIP Conference Proceedings 333, pp 384-390.

[2] Zagel, J.R., Crisp, J.L., Hahn, A.A., Hurh, P.G., "Fermilab Main Ring Ion Profile Monitor System", Contribution to PAC97 Proceedings, Vancouver. B.C (1997).

[3] Graves, W.S., "Measurement of Transverse Emittance in the Fermilab Booster", PhD Thesis, University of Wisconsin-Madison, (1994)

[4] Review of Particle Physics, Phys.Rev D(54), (1996) p132

A p-Carbon CNI polarimeter for RHIC*

H.Huang[†], M. Bai, G. Bunce, Y. Makdisi, T. Roser, *BNL, Upton, NY*

K. Imai, M. Nakamura, J. Tojo, K. Yamamoto, L. Zhu,*Kyoto Univ., Japan*

B. Bassalleck, S. Eilerts, D.E. Fields, B. Lewis, B. Smith, T.L. Thomas, D. Wolfe,
Univ. of New Mexico, NM

Y. Goto, N. Hayoshi, M. Ishihara, K. Kurita, M. Okamura, N. Saito, A. Taketani,
RIKEN, Wako, Saitama, 351-01, Japan

D. Underwood, *ANL,Argonne,IL, USA*

J. Doskow, K. Kwiatkowski, B. Lozowski, H.O. Meyer, B. v. Przewoski, T. Rinckel,
Indiana Univ., Bloomington, IN 47405

S.B. Nurushev, M.N. Strikhanov, M.F. Runtzo, *IHEP, Protvino, Russia*

I.G. Alekseev, D.N. Svirida, *ITEP, Moscow, Russia*

A.Deshpande, V. Hughes, *Yale Univ., New Haven, CT*

Abstract

The RHIC spin program requires excellent polarimetry so that the knowledge of the beam polarization does not limit the errors on the experimental measurements. However, polarimetry of proton beams with energies higher than about 30GeV poses a difficult challenge. For polarization monitoring during operation, a fast and reliable polarimeter is required that produces a polarization measurement with a 10% relative error within a few minutes. The p-Carbon elastic scattering in the Coulomb-Nuclear-Scattering(CNI) region has a calculable and large analyzing power, but detecting the recoil carbon needs sophisticated detector system and a very thin target. Experiment has been planned in the AGS. This paper describes the experimental setup in the AGS.

1 INTRODUCTION

The collision of polarized proton beams at RHIC will provide qualitatively new and exciting physics. The RHIC spin project will collide 250 GeV polarized proton beams and will open up the unique physics opportunity of studying spin effects in hard processes [1]at high luminosities, including the measurement of the gluon polarization and the quark and anti-quark polarization by flavor. It will allow the study of the spin structure of the proton and also the verification of the well-documented expectations of spin effects in perturbative QCD and parity violation in W and Z production[2]. This work will involve the PHENIX and STAR detectors with longitudinal and transverse polarization at these intersections. In addition, pp2pp and BRAHMS detectors at the 2 o'clock intersection and the PHOBOS detector at the 10 o'clock intersection will have transversely polarized proton collisions.

The elastic p-Carbon scattering at Coulomb-nuclear interference (CNI) region was recently proposed as a possible

polarimeter for RHIC. It is quite attractive because measurement is compatible with the pion polarimeter and the detectors could be simple and inexpensive.

2 COULOMB-NUCLEAR INTERFERENCE

Small angle elastic scattering of hadrons in the CNI region has long been advocated for polarimetry. The predicted asymmetry is significant and largely independent of energy for energy above a few GeV. The prediction rests on hadronic spin flip being small, which is expected for high energies. Then the analyzing power can be reliably calculated and is about 3-5 %[3, 4] and a large cross section over the whole RHIC energy range from 23 GeV to 250 GeV is predicted. The analyzing power of p-p CNI was measured at 200GeV and was consistent with the theoretical values within the errors.

The CNI process has been proposed for RHIC polarimetry using a hydrogen jet target and in collider mode using the *pp2pp* experiment. Both would be *pp*CNI. It is also possible to use a carbon target, *pC*CNI, which is simpler and cheaper than a hydrogen jet, and can be installed in the individual rings, vs. requiring collision of both rings as for the *pp2pp* experiment. The analyzing power for *pC*CNI is similar to *pp*CNI and the cross section is high, giving a very large figure of merit NA^2. However, for *pC*CNI, the proton scattered forward is not easily detectable (it stays within the beam), and the energy of the recoil carbon nucleus is 100-600keV. The low energy carbon would stop in most targets. The *pC*CNI polarimeter becomes feasible with the development of very thin ribbon carbon targets at IUCF[5]. The slowness of the recoil carbon also makes detection difficult. However, the arrival time of the carbon can be set to be in between RHIC bunches, avoiding prompt background.

471

Figure 1: Coulomb-Nuclear interference analyzing power for pp and pC scattering at 250 GeV.

The analyzing power of CNI process is given by

$$A_N = \sqrt{\frac{8\pi Z\alpha}{m_p^2 \sigma_{tot}^{pA}}} \frac{y^{2/3}}{1+y^2}(\mu - 1 - 2\tau_A)$$

where μ is the anomalous magnetic moment of the proton (1.7928), m_p the proton mass, $y = \frac{\sigma_{tot}t}{8\pi Z\alpha}$, and $\tau_A = \frac{g}{\sqrt{\frac{-t}{m^2}}(g)}$ is the unknown contribution due to the hadronic spin-flip term g. The total cross section σ_{tot} is only weakly energy dependent over the relevant energy range. Fig. 1 shows the calculated analyzing power for a hydrogen target (Z = 1,σ_{tot}= 35 mb) and a carbon target (Z = 6,σ_{tot}= 330 mb [6]) as a function of (-t) at 250 GeV. The uncertainty of the hadronic spin flip amplitude has been estimated to be smaller than 10 % of the analyzing power from CNI [7]. Using a carbon ribbon target will result in the high luminosities required for fast polarization measurements. A ribbon target will also allow for measurements of the polarization profile of the circulating polarized proton beam. The sizable analyzing power, the large cross section and the advantages of a ribbon target makes this process suitable for a fast primary polarimeter for RHIC.

3 EXPERIMENTAL SETUP

3.1 Polarimeter Scheme

The range $-t = 0.003$ to $0.01\ GeV^2$ corresponds to carbon recoil energies of 0.09 - 1.00 MeV. It will be impossible to measure the forward-scattered proton at RHIC without drastically reducing the beam divergence at the target, which would severely reduce the scattering rate and cause unacceptable beam emittance growth. It will therefore be necessary to rely only on the measurement of the recoil carbon nucleus to identify elastic scattering.

Figure 2: Energy-angle correlation for the elastic and inelastic recoil carbon nucleus at 25 GeV.

Direct measurement of the 0.1 - 1 MeV recoil carbon nucleus is only possible for a very thin carbon target. A test at the IUCF Cooler has demonstrated the feasibility of detecting such low energy recoil carbon nuclei from a thin carbon target ribbon using a silicon surface-barrier detector. In addition, the time-of-flight should be measured to discriminate against target fragments. Tests of a micro-channel plate detector, which provides precise time-of-flight information, have recently taken place at Kyoto University. A more sophisticated test has been done in the AGS in March, 1999. The two detector schemes are combined for the AGS run in order to provide both the energy and TOF information for the recoil carbon, helping to resolve the elastic signal from the hadronic and inelastic. Fig. 2 shows the expected energy-angle correlation for the recoil carbon at 25 GeV. The horizontal band shows the expected angular straggling from the target ribbon. Also shown is the well-separated kinematic range for producing the first excited carbon state at 4.4 MeV.

3.2 Recoil Detectors and Target

We employ silicon strip detectors (SSD) and micro channel plates (MCP) for the detection of recoil carbon ions from the $\vec{p}+C$ elastic scattering. A vacuum chamber of 66cm diameter hosts the SSD and MCP detectors and target ladder. Two sets of SSDs and MCPs are mounted on left and right detector tables, respectively, which are perpendicular to the beam direction. The schematic layout of the one detector arm is shown in Fig. 3. The SSDs are used for measuring the recoil energy and time-of-flight while the MCPs will provide cross check of time-of-flight information.

Figure 3: Layout for one arm of the recoil detection system.

Each SSD has 12 1cm×2mm strips. In the AGS experiment, every two strips are combined as one channel. The six silicon channels on each side cover six-degree acceptance. This covers the inelastic channels, too, so we can measure their A_N as well. For this purpose, SSDs cover down to 86 degrees and that should cover the 4.44 MeV state (see Fig. 2). Moreover, SSDs begin with 92 degrees to avoid geometric biases.

The pre-amplifiers is installed in the vacuum and the signals then travel 300 feet to the DAQ electronics. Since the noise is significantly high around AGS ring, special efforts are taken to reduce the noise from rf. The bias voltage power supply for the SSD is in the ring next to the vacuum chamber. A copper cage covers pre-amplifiers and reduces pick-up noise significantly. The analog signals are also differentiated before digitized to eliminate rf noise. A refrigerator keeps temperature of the SSDs down to -30°C to reduce the leakage current.

The MCP is double-layered and has an effective area of 14mm diameter. The MCP is easy to handle like a photo multiplier due to its high gain especially against electronic noises. However, it is sensitive to the low energy electrons and X-rays. A thin carbon foil standing 10cm away from the target generates the electrons when hit by recoil carbon. The electrons are then accelerated by the accelerating grid and reflected to MCP by electrostatic mirror. A repeller is installed in front of the MCP to reflect electrons emitted from the target.

As a target we use carbon micro-ribbons of $5\mu g/cm^2$ thickness, with a width of $5\mu m$ and 2.5cm long. For the thinnest ribbons, there are 1.5×10^{14} C nuclei per cm length. The manufacturing process for such ribbons has been developed at IUCF [5], and is now routine. The ribbons are mounted perpendicular to the beam direction in free suspension between the ends of a fork. The fork can be moved into the beam in every AGS spill to a surveyed position, while the beam is shifted toward the target if necessary. This is to assure that the relative positions between detectors and target are fixed and no artificial asymmetry are introduced. Three targets can be mounted on the target

ladder. Since the event rate is hard to estimate, two targets with different thickness are installed. The last ladder interval is left empty to check background. A limit switch is used to calibrate the target position after some running period.

4 EXPERIMENT

50% polarized beam has been successfully accelerated to the RHIC injection energy in the AGS, which is sufficient to measure the analyzing power at this energy. Such a polarimeter has been installed in the AGS and the data taking run has finished in March 1999. The experiment uses bunched beam with harmonic number $h = 12$. The analyzing power in $\vec{p} + C$ elastic scattering at 21.7 GeV/c for the range of -t = 0.003 to 0.01 GeV^2 is measured with a 10% statistical accuracy. Only the recoil nuclei are detected.

When taking data, $\vec{p} + C$ CNI is measured over a half second flattop of bunched beam, followed by a 0.85 second measurement of the beam polarization with the AGS internal polarimeter using de-bunched beam. The purpose of the bunched beam is so that the recoil carbon nuclei arrive at the detector out of time with the prompt background from the target. Since the bunch length at 21.7GeV/c is about $25ns$, it is adequate to use SSD only to measure TOF.

The data analysis will give A_N for the RHIC injection energy. If this is a success, we plan to install the pC CNI polarimeter for the commissioning of RHIC in FY2000.

5 ACKNOWLEDGMENT

6 REFERENCES

[1] D. Underwood et al., Part. World. 3, 1(1992).

[2] Claude Bourrely, Jacques Soffer, Phys. Lett. B314, 132(1993).

[3] N.H. Buttimore et al., Phys. Rev. D18, 694 (1978).

[4] N.H. Buttimore, AIP Conf. Proc. 95, (AIP, New York, 1983), p.634.

[5] W.R. Lozowski and J.D. Hudson, Nucl. Instr. Meth. A303, 34 (1991).

[6] J.L. Rosen, AIP Conf. Proc. 26, (AIP, New York, 1975), p. 287.

[7] B. Kopeliovich, Workshop on Hadron Spin-flip at RHIC Energies, E. Leader and L. Trueman organizers, RIKEN BNL Research Center, 1997.

AN ULTRA LOW NOISE AC BEAM TRANSFORMER FOR DECELERATION AND DIAGNOSTICS OF LOW INTENSITY BEAMS.

C. Gonzalez and F. Pedersen[#], CERN, Geneva , Switzerland

Abstract

The design of a broad band ultra-low noise ferrite loaded AC beam transformer is presented. It is designed for use in the CERN Antiproton Decelerator [1] (AD), where beams of a few 10^7 charges must be decelerated from 3.5 GeV/c to 100 MeV/c. It is used in the RF beam-phase loop, and for intensity and bunch shape measurements during deceleration. When the beam is debunched for cooling on magnetic flat tops, the pick-up is used for measurements of intensity and momentum distribution by means of longitudinal Schottky scans. When used as Schottky pick-up, the signal to noise ratio should be better by about 40 dB than the existing stripline based longitudinal Schottky pick-up. The integrated design of pick-up and associated low-noise amplifier is presented. The achieved noise performance of a few $pA/\sqrt{Hz}$ from 1 to 3 MHz is obtained by attaching a low-noise, high-impedance silicon JFET (junction field effect transistor) amplifier to a high-Q resonant ferrite loaded cavity, and then eliminating the resonant response by low-noise RF feedback such that broad band response over almost 2 decades of frequency (0.3 - 15 MHz) is obtained. The longitudinal coupling impedance is close to 10 Ω in this frequency range, and the equivalent noise temperature of this resistance is about 0.4 °K mid-band although all components operate at ambient temperature. Finally the application of a similar design for single-pass bunch intensity measurements is discussed.

1 INTRODUCTION

The DC beam currents in the CERN AD (typically 0.2 to 15 μA with antiprotons) are too low to be measured with a DC beam transformer. Beam intensity is therefore measured by RF beam current measurements when the beam is bunched and longitudinal Schottky scans when the beam is debunched. The range of RF frequencies is 0.17 to 1.6 MHz, so to measure these quantities as well as bunch lengths an ultra-low noise AC beam transformer with a bandwidth from 0.1 to 15 MHz is required.

2 BEAM TRANSFORMER AND HEAD AMPLIFIER

The AC beam transformer consists of a ferrite loaded cavity with a ceramic gap in the beam pipe, a secondary winding of one additional turn (the cavity enclosure

---

[#] Email: Flemming.Pedersen@cern.ch

forms the first turn), and a low noise head amplifier with feedback connected to the secondary winding and mounted close to the cavity, Figure 1.

Figure 1. Ferrite loaded beam transformer and amplifier

A noise free amplifier cannot reduce noise already introduced by the pick-up itself, so the pick-up is made resonant with high Q to reduce this noise. The whole device is doubly shielded: an outer cavity (7 mm copper walls) surrounds the head amplifier and the inner cavity (also 7 mm copper), which contains the ferrite, the ceramic gap and the secondary winding and is assembled by e-beam welding to avoid RF contacts.

2.1 Transformer and Amplifier Noise Sources

It is easier and more transparent to characterise the noise properties of the amplifier [2] in terms of equivalent current and voltage noise sources and their dependence on frequency, device type and bias rather than noise figure which is often confusing.

Figure 2: Equivalent circuit and noise sources

The equivalent circuit for the resonant step-up transformer and its head amplifier is shown on Figure 2.

Here N is transformer step-up ratio, I_b the desired signal, V_{na} [$V/\sqrt{Hz}$] and I_{na} [$A/\sqrt{Hz}$] amplifier voltage and current noise, C_p and C_s primary and secondary capacities of the transformer, C_a amplifier input capacity, L_p primary inductance, and G amplifier gain. The Johnson noise I_{nth} of the shunt impedance R_p (~ 9 kΩ) is:

$$I_{nth} = \sqrt{4kT / R_p} \qquad (1)$$

where k [J/°K] is Boltzman's constant and T [°K] the absolute temperature.

The secondary circuit quantities can all be transformed to the primary circuit, Figure 3. Increasing N lowers voltage noise, but increases current noise and capacity.

Figure 3: Noise sources transformed to primary

The amplifier voltage noise V_{na}/N can be transformed into an equivalent current noise I_{vna} by the relation:

$$I_{vna} = V_{na} / (NZ_{pu}) \qquad (2)$$

where Z_{pu} is the primary pick-up impedance. If the 3 noise currents are uncorrelated (not quite true for I_a and V_{na}), they add as sum of the squares, and the total equivalent, input-noise current $I_{n,in}$ becomes:

$$I_{n,in} = \sqrt{I_{nth}^2 + (NI_a)^2 + (V_{na} / NZ_{pu})^2} \qquad (3)$$

There is an optimum value of N at a given frequency as amplifier current noise can be traded for voltage noise. If the amplifier noise is small, the total noise is dominated by the shunt impedance noise.

2.2 Amplifier Design

While bipolar transistors may have low voltage noise, the current noise at low frequencies $f \ll f_T$ is much larger than for FETs (field effect transistors) due to the electronic shot (Schottky) noise I_s:

$$I_s = \sqrt{2qI_{base}} \quad [\text{A}/\sqrt{\text{Hz}}] \qquad (4)$$

where q is the elementary charge and I_{base} the DC base bias current. A FET has an input voltage noise [3] closely related to the Johnson noise of the conducting channel:

$$V_n = \sqrt{8kT/3g_m} \quad [\text{V}/\sqrt{\text{Hz}}] \qquad (5)$$

where g_m is the transconductance [A/V], and an input current noise which is proportional to frequency:

$$I_n = \omega C_c V_n \ [\text{A}/\sqrt{\text{Hz}}] \qquad (6)$$

where C_c is the coupling capacitance, which is about 2/3 of the total gate to channel capacity C_{gs}. Due to the very low gate bias current, the Schottky noise can usually be neglected. It is always possible to lower the noise voltage by connecting several transistors in parallel (square root dependence), but this will of course increase the noise current in the same ratio. This is similar to the noise matching obtained with the step-up transformer discussed in the previous subsection. The noise quality (lowest current noise for a given voltage noise) is therefore given by the ratio g_m/C_{gs}, which is also the high

frequency figure of merit f_T. At frequencies below a certain corner frequency, all devices exhibit $1/f$ noise or flicker noise, where noise spectral densities higher than V_n given above (5) are observed.

The different types of FET transistors which may be considered [4] are: i) GaAs (Gallium Arsenide) MESFET: very high f_T (typically 15-25 GHz), but also high $1/f$ corner frequency: > 10 MHz typically, ii) Si (silicon) dual gate MOSFET: lower f_T (typically. 5 GHz), but somewhat better $1/f$ corner frequency: 1 - 5 MHz, iii) Si JFET: still lower f_T (typically 2 GHz), but much lower $1/f$ corner frequency: typically 10 Hz for Philips BF861C.

For the frequency range of interest (0.1 to 20 MHz), Si JFET's will be the best choice due to the low $1/f$ corner frequency. Although monolithic amplifiers with JFET inputs are available, none of them have sufficiently low voltage noise and propagation delay ($t_d \leq 5$ ns required for feedback stability) and an amplifier has therefore been designed with discrete SMD components.

Figure 4: Low noise wide band amplifier

The conceptual design (bias details omitted) of the low noise, wide bandwidth feedback amplifier with an overall gain of 300 and a propagation delay of 5 ns (bandwidth 75 MHz) is shown on Figure 4. The input stage with a gain of 11 consists of 16 parallel Si JFETs with each group of 4 forming a cascode with a bipolar transistor with high f_T (8 GHz). The JFETs are operating near their maximum current at 10 mA (for high g_m and low V_n) and the bipolar transistors near their optimum current of 40 mA. This results in a low input voltage noise (theory $0.22\,\text{nV}/\sqrt{\text{Hz}}$, achieved $0.28\,\text{nV}/\sqrt{\text{Hz}}$), and a very small propagation delay: < 1 ns.

The output stage is a current mode feedback op-amp with very high slew rate (2.5 kV/μs) and voltage swing (20 V_{pp}) capable of driving the low impedance feedback circuitry. The bipolar second stage provides the extra gain to prevent the rather noisy output stage from contributing to the noise. For this amplifier design, the equivalent, input-noise current sources are shown on Figure 5. The cavity shunt impedance noise (~1.5 pA/$\sqrt{\text{Hz}}$) dominates from 1.5 to 3.5 MHz, and corresponds to a noise temperature of 0.4 °K of a 10 Ω resistor. The longitudinal Schottky noise current densities for the AD are typically 4 to 500 pA/$\sqrt{\text{Hz}}$ around 1.6 MHz and lower at higher frequencies as the width of the Schottky bands are

proportional to the harmonic while the total power in each Schottky band is constant.

Figure 5: Equivalent, input-noise current sources (at gap)

2.3 Feedback Resistor and Circuits

Although the resonant high Q transformer with amplifier has a very good signal to noise ratio, the response is highly resonant ($Q \sim 120$, $f_r \sim 2$MHz) and the amplifier will saturate for very small currents near the resonance. The response can be made broad band if a current feedback resistor is introduced around the amplifier, Figure 6. This converts the amplifier input impedance into a low resistive impedance $R_{fb}/G \sim 40\ \Omega$, or $R_{fb}/(GN^2)$ $\sim 10\ \Omega$ referred to primary and the response becomes broad band with 3 dB frequencies of 0.3 and 15 MHz and a loop gain at resonance about 60 dB.

Figure 6: Equivalent circuit with current feedback

However, unless the feedback resistor and the gain are made very large ($R_{fb} > 0.4$ MΩ, G > 10'000), the noise of the feedback resistor will contribute significantly to (or even dominate) the noise. A large feedback resistor is difficult to implement at high frequencies, the amplifier will still saturate at very low currents, and large gain with short delay is difficult.

Figure 7: Low noise feedback 'resistor'

By passing the feedback signal through an integrator and injecting the feedback current through a small capacitor the equivalent feedback transfer function is still that of a resistor, Figure 7. For R_{int} small and $C_{int} \gg C_{fb}$, the effective noise temperature T_{noise} of the feedback

resistor is low: 15 °K for $R_{fb} = 12$ kΩ, or a current noise corresponding to a 240 kΩ resistor. The dynamic range is much increased (saturation for $I_b = 1.6$ mA) with only a very small increase in noise level.

2.4 Low Frequency Version

The low frequency response cut-off frequency (0.3 MHz) can be lowered by an appropriate integrating correcting network in the feedback amplifier, but the low frequency noise current is unchanged: limited by inductance $L_p = 6$ μH and noise voltage $V_n/N = 0.14$ nV/$\sqrt{\text{Hz}}$. To decrease the low frequency cut-off and at the same time lower the noise by 10 - 20 dB at 400 kHz and below, a low frequency cavity with higher inductance (4A15 ferrite, μ=1200, $L_p = 40$ μH) and with a step-up ratio of $N = 4$ (which halves the noise voltage to $V_n/N = 0.07$ nV/$\sqrt{\text{Hz}}$) has been built. It is installed in the AD ring adjacent to the high frequency device. Its response bandwidth is from 40 kHz to 3 MHz. The signals from the two devices are then combined to a single broadband signal with a crossover frequency (1 MHz) chosen for minimum noise.

3 LOW NOISE BEAM TRANSFORMER FOR BEAM TRANSFER LINE

To measure the charge of the extracted low intensity antiproton bunch (about 10^7 charges, length about 300 ns), an additional transformer (low frequency version) will be installed in the extraction line. The extracted charge is measured by integrating the current signal during $t_i = 1$ μs. A bandwidth of 3 kHz (18 kHz with response shaping) to 3 MHz is needed for less than 1% error due to the response limitations. The mean square error of the charge signal q due to noise is related to the (double-sided) power spectral density of the current noise $G_i(f)$ [A^2/Hz]:

$$\overline{q^2} = t_i^2 \int_0^\infty 2G_i(f) \frac{\sin^2(\omega t_i/2)}{(\omega t_i/2)^2} df \qquad (7)$$

which results in an expected RMS fluctuation of 1.9×10^4 charges (4 sigma is 7.6×10^4 charges).

4 REFERENCES

[1] S. Baird and 29 co-authors, "The Antiproton Decelerator: AD". Proc. 1997 Particle Accelerator Conference, Vancouver, Canada (1997)

[2] Y. Netzer, "The Design of Low-Noise Amplifiers", Proc. of the IEEE, Vol. 69, 728 (1981)

[3] A. van der Ziel, "Noise: Sources, Characteristics, Measurements" (Prentice Hall, Englewood Cliffs, NJ, 1970)

[4] F. Celani et al. "Behaviour and comparison of RF devices Si JFET, dual gate MOSFET and GaAs MESFET...", Proc. of the Symposium on Low Temperature Electronics and High Temperature Superconductors, Honolulu, HI, USA, p.476-88 (1987)

MEASURING EMITTANCE GROWTH DUE TO MAGNETIC BUNCHING OF AN ELECTRON BEAM USING THE SECOND MOMENT OF ITS IMAGE CHARGE

S. J. Russell[*] and B. E. Carlsten, Los Alamos National Laboratory

Abstract

Current thinking about the Next Linear Collider (NLC) places a great deal of importance on magnetic beam compression. However, theoretical work has predicted that a large emittance growth may occur during magnetic compression due to coherent synchrotron radiation and the non-inertial space-charge force[1]. Applications such as the NLC cannot tolerate such beam degradation. To verify this prediction we have measured the emittance of the Sub-Picosecond Accelerator electron beam as a function of compression in our magnetic chicane and compared the results to numerical simulation. These emittance measurements were carried out using a pair of quadrupole magnets and a beam position monitor.

1 INTRODUCTION

The Sub-Picosecond Accelerator facility (SPA) at Los Alamos National Laboratory is an 8 MeV, radio-frequency photoinjector operating at 1300 MHz[2]. The primary mission of SPA is to explore the uses and dynamics of bunched electron beams. State of the art in its field, SPA has compressed electron pulses containing 1 nC of charge to sub-picosecond lengths[3].

Beam compression on the SPA is accomplished with a magnetic chicane, illustrated in Fig. 1. To first order this series of dipole magnets is achromatic and has no net effect on the quality of the electron beam. However, recent work has identified two space-charge induced forces for beams in circular motion that are mostly independent of energy. In contrast, space-charge forces in straight-line motion scale inversely with the relativistic factor γ.

The first of these effects is considered a space-charge curvature effect and is known as the noninertial space-charge force, in which the energies of the particles are modified with little total loss by radiation. The second effect is known as the coherent synchrotron radiation force, in which the bunch radiates coherently. Both effects will lead to a redistribution of the energy of a bunch in circular motion within an achromatic bend. In turn, this redistribution can lead to an unacceptable increase in the beam's bend plane emittance that would be roughly independent of beam energy.

We have investigated this predicted emittance growth both numerically and experimentally. The experimental emittance values were obtained using Roger Miller's technique that measures the second moment of the beam image charge[4]. The current results of our investigations are presented here.

Figure 1: Motion of electron through magnetic chicane.

2 EXPERIMENT

Figure 2 is a schematic of the diagnostic section of the SPA beam line. The electron beam from the photoinjector enters from the left side of the diagram and is bunched by the chicane. The emittance is then measured utilizing the second two quadrupole magnets and the first beam position monitor (BPM)[4].

Figure 2: Schematic of experimental section of beam line.

---

[*] Email: srussell@lanl.gov

2.1 Beam Bunching

By correctly timing the arrival of the photoinjector drive laser pulse with respect to the rf fields in the accelerator, an energy versus phase correlation is generated across the beam bunch. Figure 3 shows an example from a PARMELA[5] simulation. Because the electrons at the front of the pulse have lower energy, they will travel a longer path through the chicane, Figure 1. If the angle of bend in the chicane, the energy versus phase correlation and initial length of the electron beam bunch are each chosen correctly, the beam bunch will be compressed to sub-picosecond lengths at the chicane exit.

Electron Energy vs. Position in Bunch

Figure 3: Energy versus electron position in beam bunch for efficient beam bunching from simulation.

2.2 Emittance Measurement

The emittance measurement technique used in these experiments was first suggested by Roger Miller et. al.[6] and later used to measure emittance on the SPA[4]. It employs two quadrupole magnets and a BPM. A cross section of the BPM is illustrated in Figure 4.

The normalized rms emittances are defined as

$$\varepsilon_{xn} \equiv \beta\gamma\sqrt{\langle x^2\rangle\langle x'^2\rangle - \langle xx'\rangle^2} , \tag{1}$$

and

$$\varepsilon_{yn} \equiv \beta\gamma\sqrt{\langle y^2\rangle\langle y'^2\rangle - \langle yy'\rangle^2} . \tag{2}$$

The angled brackets indicate an ensemble average over the beam's spatial distribution. To measure these quantities, the value of the vector

$$\vec{x} \equiv \begin{pmatrix} \langle x^2\rangle \\ \langle xx'\rangle \\ \langle x'^2\rangle \\ \langle y^2\rangle \\ \langle yy'\rangle \\ \langle y'^2\rangle \end{pmatrix}$$

must be determined at a single point in the beam line.

Figure 4: BPM schematic.

A BPM such as the one pictured in Figure 4 is capable of measuring not only the position of the beam center, $(\bar{x},\bar{y})$, but also the second moment of the beam image charge:

$$\langle x^2\rangle - \langle y^2\rangle + \bar{x}^2 - \bar{y}^2 = a^2 \frac{\alpha}{\sin 2\alpha} \frac{A_R + A_L - A_T - A_B}{A_R + A_L + A_T + A_B} .$$

A_R, A_L, A_T and A_B are the signal amplitudes of the right, left, top and bottom electrodes of the BPM. The accuracy of this measurement will be to order (beam size/BPM radius)^4[6].

It can be shown that

$$\langle x^2\rangle_f - \langle y^2\rangle_f = (R_{11})^2\langle x^2\rangle_i + 2R_{11}R_{12}\langle xx'\rangle_i + (R_{12})^2\langle x'^2\rangle_i$$
$$- (R_{33})^2\langle y^2\rangle_i - 2R_{33}R_{34}\langle yy'\rangle_i - (R_{34})^2\langle y'^2\rangle_i [6],$$

where the f subscript refers to the BPM location and the i subscript to a point upstream from the BPM. The constants R_{jk} are from the transfer matrix for the focusing channel between the upstream point and the BPM:

$$\bar{\bar{R}} = \begin{bmatrix} R_{11} & R_{12} & 0 & 0 \\ R_{21} & R_{22} & 0 & 0 \\ 0 & 0 & R_{33} & R_{34} \\ 0 & 0 & R_{43} & R_{44} \end{bmatrix} .$$

Changing this transfer matrix m times ($m \geq 6$), and measuring

$$\langle x^2\rangle_f - \langle y^2\rangle_f$$

for each change, results in a matrix equation that can be solved for $\bar{x}$ in the least squares sense. This estimates the rms beam parameters and, from (1) and (2), the normalized x and y emittances at the start of the focusing channel.

2.3 Experimental Apparatus

In Figure 2, the quadrupoles are identical. They are electromagnetic, have a pole length of 2.75 inches and a gap radius of one inch. The fields of these quadrupoles have been simulated and measured. From this it has been determined that their effective length is 86 mm and that, at a radius of 1 cm, the multipole components of the field are less than 1 percent of the quadrupole field. Attached to one pole of each magnet is a small Hall probe. The Hall probe voltages have been correlated to the gradients of the quadrupole fields. During beam operation, monitoring these voltages enables us to determine these gradients to within a percent.

The BPMs are dual axis, capacitive type probes that differentiate the beam image charge[7]. They were calibrated using a pulsed wire[8], [9].

The spectrometer is an electromagnetic dipole magnet that bends the beam 90°. Its edge angles are such that it focuses the beam on the screen shown in Figure 2. The spectrometer has been calibrated so that the average energy can be determined with two- percent accuracy.

The distance between the third quadrupole and the first BPM is 160 mm. The distance between the second and third quadrupoles is 850 mm. As stated before, these two quadrupoles and the first BPM are used to measure the emittance. This was accomplished by setting the two magnets to different field strengths and measuring the second moment of the beam with the BPM. These field strengths were carefully chosen to avoid unstable numerical conditions in the measurement[10].

A schematic of the data acquisition system used for capturing the signals from the BPM electrodes is shown in Figure 5. The signals from the four BPM electrodes travel down 50 Ohm, coaxial Heliax™ cables of equal length to 300 MHz, low-pass filters. From there they go to a Tektronix™ TDS 684C digitizing oscilloscope. The oscilloscope digitizes each of its four channels at five giga-samples per second with eight bit accuracy. It is set to be bandwidth limited to 250 MHz. The oscilloscope is linked to a PC running LabView© via GPIB.

The electron beam consists of a single beam bunch with a rep rate of 1 Hz. Upon capturing a beam shot, the 684C measures the peak-to-peak voltage of the BPM electrode signals and passes the information to the PC. The PC then calculates the beam intensity, position and second moment according to the BPM calibration. Typically when making emittance measurements, the parameters from 10 consecutive beam shots are averaged.

3 EXPERIMENTAL RESULTS

Two experiments were performed to investigate the predicated bend plane emittance growth. Each was done at a beam energy of 7.14 MeV and a nominal beam bunch charge of 1 nC. In the first the emittance was measured versus chicane bend angle with the phase of the electron beam set to approximately 20° with respect to the rf field zero. In the second the emittance is measured versus beam phase at a bend angle of 37°. In both experiments the maximum bunching was expected to occur at a phase of 20° and a chicane bend angle of 37°.

Figure 5: Schematic of data acquisition system.

It should be noted that during experiments the phase of the beam was not set with respect to the rf field zero. Instead the phase of the beam was first set so that the energy spread of the beam was a minimum. All other phase settings of the beam were then referenced to this point. This proved to be a much more practical, accurate, and reproducible reference point than the rf field zero. However, when comparing experimental results to numerical simulations of the SPA using PARMELA we needed to translate results to use the field zero to reference our phase. Since we have no good diagnostic for this, the experimental phases quoted here could be offset by several degrees.

At this time we do not have a bunch length diagnostic in place to measure the length of the electron beam

directly. Instead we rely on the observation of beam energy spread as described in [2]. That is, the energy spread of the beam will dip just before maximum beam bunching and increase dramatically when maximum beam bunching is achieved. Although this is a very good qualitative, online diagnostic for tuning the beam, the actual bunch length must be inferred from this measurement. This is less than satisfying. Presently we are working to implement more quantitative measurements of the beam bunch length[11].

3.1 Emittance Growth versus Bend Angle

Figure 6 shows a plot of the experiment measuring the emittance of the electron beam in the bend plane (x plane for the SPA) versus the chicane bend angle. Also pictured are the results of PARMELA simulations in which we attempted to duplicate the experimental conditions. The maximum beam bunching occurs at an angle of 37°. The peak current of the beam at this point is expected to be approximately 800 A, corresponding to a beam roughly 1.25 pico-seconds in length.

Normalized Emittance vs. Bend Angle

Figure 6: Normalized rms emittance in the bending plane versus chicane bending angle. Results of experiment and numerical calculation.

Although the shapes of the emittance curves are similar, we see a much greater increase in the emittance experimentally than theory predicts. Assuming that the emittance increase adds in quadrature to the initial emittance, simulation predicts an emittance growth of 24.6 mm mrad. Experimentally, however, we observe an increase of 46.9 mm mrad.

3.2 Emittance Growth versus Beam Phase

Figure 7 shows a plot of the experiment measuring the emittance of the electron beam in the bend plane versus the beam phase at a chicane angle of 37°. This experiment was performed to verify that the emittance growth in the previous experiment cannot be attributed to poor beam transport through the chicane.

Normalized Emittance vs. Beam Phase

Figure 7: Normalized rms emittance in the bending plane versus beam phase at a chicane bending angle of 37°

What is important about this data set is that the emittance remains fairly constant until the phase reaches the maximum bunching phase of 20°. Then it jumps to about 40 mm mrad, very close to what was observed in the previous experiment. This seems to confirm poor beam transport is not the cause of the observed emittance growth in the first experiment.

3.3 Discrepancy between Theory and Experiment

The disagreement between theory and experiment is significant. We have identified two likely explanations. The first is a possible error in the calibration of our charge diagnostic. If the charge was higher than 1 nC in these experiments, much of this discrepancy could be explained. The second possible explanation is a disagreement between the shape of the drive laser pulse in the experiment and the shape of the drive laser pulse assumed in the simulations. In the simulations, a Gaussian shape was used for the laser pulse. A recent, unrelated experiment has indicated that the real drive laser pulse is asymmetric with a long tail. We have not yet determined what effect, if any, this would have on our results.

4 CONCLUSION

We have successfully measured the emittance growth of an electron beam as it is bunched in a magnetic chicane due to the coherent synchrotron radiation and non-inertial space-charge force. However, there is a significant discrepancy between simulation and what was observed. We have identified two possible reasons for this discrepancy and hope to confirm or discredit each in the near future.

5 REFERENCES

[1] B. E. Carlsten, "Calculation of the Noninertial Space-Charge Force and the Coherent Synchrotron Radiation Force for Short Electron Bunches in Circular Motion Using the Retard Green's Function Technique," Phys. Rev. E **54**, 838 (1996).

[2] Bruce E. Carlsten *et. al.*, "Subpicosecond Compression Experiments at Los Alamos National Laboratory," *Proceedings of the Micro Bunches Workshop*, AIP Conf. Proc. 367, 21 (AIP, Upton, NY, 1995).

[3] B. E. Carlsten and S. J. Russell, "Subpicosecond compression of 0.1-1 nC electron bunches with a magnetic chicane at 8 MeV," *Phys. Rev. E* **53**, 2072 (1996).

[4] Steven J. Russell, "Emittance Measurements of the Sub-picosecond Accelerator Electron Beam Using Beam Position Monitors," Rev. of Sci. Instrum. **70**, 1362 (1999).

[5] L. M. Young, (private communication).

[6] R. H. Miller J. E. Clendenin, M. B. James, J. C. Sheppard, *Proceedings of the 12th International Conference on High Energy Accelerators*, 602 (Fermilab, 1983).

[7] J. D. Gilpatrick, J. F. Power, R. E. Meyer and C. R. Rose, *Proceedings of the 1993 Particle Accelerator Conference*, IEEE catalog No. 93CH3279-7, 2334 (IEEE, New York, 1993).

[8] J. F. Power, J. D. Gilpatrick, F. Neri and R. B. Shurter, *Proceedings of the 1992 Linear Accelerator Conference*, AECL catalog No. 10728, 362 (AECL Research, Chalk River, Ontario, Canada, 1992).

[9] S. J. Russell, J. D. Gilpatrick, J. F. Power and R. B. Shurter, *Proceedings of the 1995 Particle Accelerator Conference*, IEEE catalog No. 95CH35843, 2580 (IEEE, New York, 1996).

[10] S. J. Russell, "Unstable Matrix Equations and Their Relationship to Measuring the Emittance of an Electron Beam Using Beam Position Monitors," (Accepted for publication in *Nucl. Instrum. Phys. Res.* A).

[11] S. J. Russell, "Measuring the RMS length of Short Electron Pulses with an RF cavity and a Beam Position Monitor," *Proceedings of the 1997 Particle Accelerator Conference*, IEEE catalog No. 97CB36167, 2005 (IEEE, New York, 1998).

REVIEW OF BEAM DIAGNOSTICS FOR RADIOACTIVE BEAMS

Alberto Rovelli[#]

INFN Laboratori Nazionali del Sud, Catania, Italy

Abstract

Nuclear research with radioactive beams is the most recent challenge for both fundamental nuclear physics [1] and particles accelerators technologies research. Beam diagnostics is a typical component of any accelerators based facility, but for radioactive beams the technology to be used presents many analogies with that one used for standard nuclear detectors. The main reason of this peculiarity is the low, sometimes very low, intensity of the beams to be characterized but also the requirement for new kind of measurements like the unambiguous isotope identification. Another important request is the instrumentation for mass spectrometry setups where the fragments produced on the target have to be transported along a dedicated beam line as part of the detector itself. A big effort is in progress all over the word to develop new devices and techniques oriented to improve the performances of the standard beam instrumentation increasing the dynamic range in terms of energy and intensity sensitivity. Also the investigation on the use of new materials may represent a valid alternative for this improvement. In this review it will be presented the general guidelines, the problem evaluation, the requested features and the most significant ideas.

1 INTRODUCTION

The interest in low intensity beam diagnostics is due to the fact that a number of applications are based on the use of low intensity beams. A very important incentive for this activity came few years ago with the development of a new type of facility for the production of radioactive ion beams (RIB). The produced effort is mainly oriented to improve the performances of the conventional beam diagnostics in order to work properly also when the beam intensity is lower than 10^8 pps. The new challenge is very hard because the required sensitivity is in the range $10^5 \div 10^{11}$ pps, or even lower. The necessity to measure the beam characteristics all over such a wide intensity range and the variety of ions and energies involved forces the development of a complete set of beam instrumentation able to satisfy all the experimental requirements.

2 REQUIREMENTS

Several RIB facilities were proposed and realized, each one with its own characteristics [2]. For this reason it is possible to identify in the beam intensity the common problem, but the solution has to be found considering the specific procedures that are followed for the beam production, identification, acceleration and transport.

To fix the ideas, it is appropriate the effort to define an expected intensity and energy range. Starting from a general overview all around the projects it is possible to individuate the following ranges:

- beam intensity $10^5 \div 10^{11}$ pps
- beam energy $10^4 \div 10^7$ eV

The first problem is to individuate the right solution to develop a device able to work properly all over such wide ranges. The second one is the necessity to use the same device also when a high intensity stable beam has to be transported along the same line. Once fixed the operative ranges, it is necessary to fix also few general requirements related to the specific use of these devices. The typical parameters asked to characterize an ion beam are the current distribution, the position, the total current, the emittance and, sometime, also the time structure. A new request, typical for a RIB facility, is the unambiguous isotope identification. To perform all these measurements in a very efficient way this set of devices has to guarantee:

- the highest sensitivity to the lower current;
- the highest sensitivity to the lower energy;
- the highest reliability;
- the highest strength;
- the highest simplicity to use and to maintain it.

Furthermore, all these requirements have to fit the typical ones for standard beam diagnostics. It is evident that the ideal solution is not easy to achieve.

3 SOLUTIONS

There are two main guidelines that are followed approaching the low intensity beam diagnostics problem. The first one, based on the performances improvement of standard techniques, consists of a deep investigation and analysis of the typical limitations of the standard devices. The second one is based on the evaluation of using particle detection techniques very well proven for sensitivity and precision in nuclear physics research. The main problem is the difficulty to develop such a device able to cover the full range of operations. For this reason a realistic solution can be represented by two different sets of devices with an overlapping operative range.

[#] Email: rovelli@lns.infn.it

3.1 Standard techniques

The number of devices nowadays available for beam diagnostic is very big and they satisfy any kind of requirements. They are based on the secondary electrons emission (wire, grids, etc.), light emission (screen, fiber, etc.), gas ionization (residual, chamber, etc.), charge induction (pick-up, transformer, etc.) and many others. The typical advantage is the simplicity in their structure and use. The main limitation is the low signal-to-noise ratio. With the exception of the ionization chambers, extensively used also as nuclear physics detectors, all the others techniques have to be subjected to a deep revision in order to increase the general performances toward the lower limits.

Two main items drive this revision. The research for new materials: higher conversion and collection efficiency, lower noise and higher radiation hardness. The electronics improvement: lower electronic noise (cables, connectors, contacts, components), lower electromagnetic noise (shielding, grounding), higher signal first amplification, higher radiation hardness. The goal is to lead the minimum sensitivity down to $10^7 \div 10^5$ pps. In this way it will be possible to match the typical highest limit of the nuclear detectors.

3.2 Nuclear techniques

Typical instrumentation and techniques used in nuclear physics research can be also used for beam diagnostics if they are redesigned looking the peculiarity of this application. Typical solutions are based on:

- semiconductors;
- gas chambers;
- scintillators.

The main advantages of these devices are the sensitivity and the absolute measurements that can be performed after a suited calibration. The main limitation is the setup complexity from the point of view of its structure and use. Beam diagnostic measurements require a fast read-out of the information, on-line if possible, and at the same time well understandable by the operators. In this sense the main effort has to be devoted to:

- reduce the setup complexity;
- reduce the measuring time;
- increase the general hardness;
- increase the automated procedures.

3.3 The ideal solution

All these considerations allow the identification of the ideal solution. Starting from the general issue to improve the whole experimental setup it is possible to give a list of recommendations for such a device that has to be able to:

- measure different beam characteristics;
- cover a wide intensity and energy range;
- allow self calibration;
- minimize the interference with the beam;
- minimize maintenance operations and price;
- maximize reliability and versatility;
- perform charge/current collection;
- perform continuous/pulsed acquisition.

The achieved result will be as good as bigger will be the number of features satisfied. Two more general considerations have to be taken in account. Very important is the integration in the control system of the facility; this means that the operator in the console must operate the beam management with no regard to the beam intensity. Furthermore, the choice of the right device has to be done considering that the setup structure has to be strong enough to resist to quick intensity changes. If necessary, a suited interlock system (beam stop) has to be provided in order to protect the device in case of mistakes or faults.

4 SEMICONDUCTORS

The versatility of semiconductors, one of the most popular materials used to develop nuclear detectors, allows the realization of different configurations very useful also for beam diagnostics. In the end of this chapter it will be reported also some applications based on a particular material, the diamond. It is an insulator but it can be considered the most important alternative to the use of semiconductors.

4.1 Silicon based detectors

The reason of the wide use of the silicon as particles detector can be deduced from its main characteristics:

- the mean energy to produce a pair is 3.62 eV;
- well suited for different configurations;
- good timing performances;
- medium price.

Unfortunately its radiation hardness is very low. This aspect limits its use for beam diagnostics; in particular, it can be used only in single particle counting mode and, in any case, great care has to be devoted to protect it.

Silicon detectors can find useful applications for very low intensity beam diagnostics. Silicon micro-strips, for example, can be used as beam profile and position monitor. The sensitivity and the spatial resolution (higher than 100 μm over a 10×10 cm^2 area) are very high, but the electronics and the price are very expansive. Much more suited is the application for particle identification [3]. A thin Au target is used and a silicon telescope is positioned at a suited angle in order to match a suited scattering counting rate. The ΔE-E information allows the ion identification; the operative energy range depends on the silicon and dead layer thickness.

4.2 Germanium based detectors

This very sophisticated kind of detector is mainly used for high-resolution gamma ray spectroscopy. Its main characteristics are.

- the mean energy for a pair production is 2.96 eV;
- operating at 77 °K;
- very low radiation hardness;
- very complex experimental setup;
- very high price.

It is obvious, from this brief description, that such a detector has several limits for beam diagnostics application but, for a specific use, can be very useful. For example, it is a powerful tool for very rare radioisotopes identification [4]. The main advantage of this setup is that implanting the radio-isotope at very low energy it is possible their identification just after the production, allowing an efficient tune of the transport line avoiding any beam contamination.

4.3 Diamond based detectors

The operating principle of this isolating material is the same of the semiconductors one. Its main features are:
- the mean energy to produce a pair is ~ 13 eV;
- the collection length is 50 ÷ 100 μm;
- very good radiation and power hardness;
- very good timing performances;
- versatility for different configurations;
- high price.

Nevertheless the higher energy to produce a pair, an important advantage with respect the semiconductors is the high-energy gap that strongly reduces the noise. The strength of this material allows its use with high intensity as well as low intensity beams. The very short collection length, depending on the nature and density traps, determines very high performances in terms of spatial and time resolution. Can be used in pulses counting mode, for very low beam intensities, as well in current mode looking the continuous component of the signal produced by high intensity beams. An interesting application is the use of diamond film with 100 μm pitch micro-strips [5]; this setup allows the beam profile and position measurement.

The increasing interest on such a material is due to the advanced techniques nowadays available for the production of synthetic diamonds at realistic prices. The CVD (Chemical Vapor Deposition) technique allows the production of very thin diamond films of some centimeter size; the possibility to realize wide homogeneous layers with controlled impurity characteristics, justifies the big effort that is devoted to test new devices for beam diagnostics.

5 GAS BASED DETECTORS

Many kinds of detectors are based on the ionization produced by a charged particle crossing a gas volume. The gas can be used to fill a chamber with thin entrance and exit windows, or can be the residual gas itself contained along the beam pipes used to transport the beam.

5.1 Gas chamber based detectors

The most famous gas detector is the gas chamber; widely used as particle detector, it find many applications also for beam diagnostics. Its versatility, in terms of dimensions and shapes, allows the development of a variety of setups well suited for beam diagnostics applications. The signal is produced by the energy loss into the gas and its amplitude depends on the gas pressure and on the collecting electric field. The mean energy to produce a pair is about 30 eV, depending on the gas. The gas chambers have several very important features:
- very good radiation hardness;
- energy loss and charge multiplication effect;
- very good sensitivity;
- versatility for different configurations;
- medium price.

The most interesting configurations for beam diagnostics purposes are the wire chambers and the micro-strips chambers [6]. Both chambers were developed to improve the sensitivity of the previous ionization chambers. The electron avalanche due to the high intensity electric field close to the anode (the wire or the micro-strip) further amplifies the signal produced by the primary ionization. The main advantages of these setups are the sensitivity and the spatial resolution. Particular interest is devoted to the micro-strips chambers because the lithographic procedure to realize the strips on a suited substrate (typically glass) allows to obtain 100 ÷ 200 μm (the pitch) of spatial resolution. Also the chamber size can be reduced as well as the setup complexity.

Two very interesting devices were developed to measure the beam profile [7] and for particles identification [8]. Both are based on the use of a 5×5 cm² glass plate with 200 μm pitch of Au strips positioned parallel with respect the beam direction and the collection field perpendicular with respect the beam direction. To measure the horizontal or the vertical beam profile the strips are parallel with respect the beam direction; for particles identification are positioned perpendicular with respect the beam direction. The whole setup structure, very simple and light, can be easily inserted or removed, through a suited actuator, to intercept the beam.

5.2 Residual gas based detectors

The ionization produced by the beam interaction with the residual gas contained along the beam pipes can be used to measure several beam properties without any interference with the beam itself. Generally and especially with low intensity beams, the ionization events are very rare then it is necessary some signal amplification.

The typical setup foresees a charge collecting field perpendicular with respect the beam direction and an electron amplifier, generally a micro-channel-plate (MCP), to collect the charges.

The main advantage of this setup is that no interaction with the beam is required, for this reason it can be used without interference with the beam operations and there are no problems for the radiation damage, on condition that it is protected against the direct beam interaction. The MCP choice depends on the application; several model with different characteristics and performances are available.

In the MCP with electric readout the signal comes from the collecting electrode, the anode, is directly acquired and analyzed. This system, in different configurations, is very useful for both transversal and longitudinal beam profiles. To measure the vertical or the horizontal beam profile, as well as the beam position, the ions collecting electrode is coupled with a silicon micro-strips plate that collects the electrons coming from the previous amplification stage; the spatial resolution is very good $(0.3 \div 1 \text{ mm})$. A similar setup [9], but coupled with a 50 Ω anode is used to measure the longitudinal beam profile with a very good time resolution $(100 \div 200 \text{ ps})$.

The operating principle of the MCP with light readout is the same of the previous one; the only difference is that the electrons coming out from the last amplification stage are accelerated and sent on a scintillating screen. The light produced by the electrons hitting the scintillator can be acquired through a common CCD camera or directly through silicon strips.

A very simple setup to measure the horizontal or vertical beam profile is based on the use of a CCD camera that collects the light coming out from a quartz window [10]. The TV signal is acquired by a frame-grabber PC board. A simple program displays the acquired image together with the beam profile and position on-line information. Regarding the camera choice is better to use a camera with gain and shutter control to match the whole setup sensitivity. A most sophisticated setup, based on the use of a thin carbon foil allows the reconstruction at the same time of both the beam profiles in the transverse plane and with higher sensitivity.

6 SECONDARY ELECTRON EMISSION

SEM based devices probably are the most diffused ones for beam diagnostics. The ions hitting the outer layer of several materials produce an electron emission that is proportional to the released energy. Because only the electrons contained in the first microns can exit from the material, the emission is a typical surface effect that is proportional to the surface exposed to the beam.

Moving wires, grids and thin foils are commonly used to measure several beam properties. The limitation of their use for low intensity beam diagnostics is mainly due to the bad signal-to-noise ratio. To improve their performances it is possible to devote particular care to the material selection and to the electronic noise reduction; in any case it is very difficult to increase their sensitivity more than 10^7 pps. To do that, it is necessary to develop

most sophisticated apparatus based on such an amplification (MCP, channeltron, etc.) of the detected signal [11].

7 SCINTILLATORS

As the previous category, also the scintillating materials are very well known and used for beam diagnostics applications. The main advantage with respect the SEM based devices is that the wide choice of materials and light detectors allows to develop several apparatus well suited also for low intensity beam diagnostics.

The first important question concerns the material choice. It is not so easy to have a global view on the scintillating materials because of their very big number, continuously in progress with the fast improvement of the technology to produce them. A significant contribute comes out also from other sectors of the scientific research where scintillating materials are employed for completely different applications. Some criteria for their selection are:

- the mean energy to produce a photon;
- the decaying time constant;
- the photon wave length;
- the refraction index of the material;
- the efficiency of photon collection;
- the radiation hardness.

Many other properties [12] have to be considered: for examples, the mechanical features as well as the hygroscope one. Furthermore, also some amorphous materials like glasses, usually doped with rare earths elements (Tb, Gd, Ce, etc.), represent an alternative choice for radiation hardness and light emission efficiency. Also for the light detector there is a wide choice of devices. Rather than a long list of the available devices (photomultipliers tubes, photodiodes, avalanche photodiodes, hybrid photodiodes, etc.) it is better to do a brief overview of the most significant applications. Profile, total current and time measurements can be easily done using scintillating optical fibers and screens.

7.1 Beam profile and position monitor

The simplest setup to perform beam profile and position measurement is based on the use of a scintillating screen that intercepts the beam; the emitted light is collected through a quartz window by a CCD camera and analyzed by a frame-grabber PC board. The main limitation is the bad light collection efficiency that limits the application for low intensity beams. To improve the performances it is possible the use of more efficient scintillating screens (Cr doped alumina, rare earths plastic sheets, etc.) or collecting with the same camera the light emitted at different solid angles.

A most sensitive setup to measure the beam profile was developed for very low intensities $(10^4 \div 10^6$ pps) and energies (higher than 10^4 eV) [13]. It is based on the use of the CsI(Tl), a very performing material in terms of light

yield. A small brick of this material is positioned behind a moving slit and it is coupled with a compact photo-tube by means of a PMMA prism. The photo-tube is completely shielded by the slit itself with respect to the beam. The electronics allows both continuos and impulsive mode acquisition. The use of faster scintillators (CsI, BaF_2, etc.) increases the upper limit of the counting rate allowing absolute measurements also with normal intensities.

The scintillating fibers also offer an interesting choice for these applications. The advantage with respects the previous systems is that the efficiency in the light transmission is strongly improved. Plastics as well as glass fibers can be successful used. A very simple setup [14] is based on the same idea of the moving wires profile monitor. Sensitivity and spatial resolution depend on the fiber choice. Using glass fibers the radiation hardness is higher but the mechanical strength is lower. The light collection is performed through a compact photo-tube able to work also inside the beam pipe. A special I/V converter [15] was developed to get the continuous signal component as well as the impulsive one coming from the tube. This configuration allows to do beam measurements over the widest intensity range. Another important feature is that during the measurement it only partially intercepts the beam. The only limitations are the damage produced by the power released by the beam and the outer dead layer of the fiber (only the core is scintillating); this last problem limits its functionality at the lower energies.

7.2 Beam time structure and current monitor

For this kind of applications the best choice is the use of very fast organic scintillators. The high counting rate obtainable allows, if coupled with a suited photo-sensor, to get high time resolution and absolute current measurements over a wide intensity range.

To measure the phase and the phase width of pulsed beams a useful setup is based on the use of a fast plastic scintillator [16]. The PILOT-U sensor is coupled with a photo-tube through a long optical fiber; the whole setup is mounted on a radial probe to measure the beam time characteristics inside the cyclotron. The operating range is $10^3 \div 10^6$ pps. The same setup can be also coupled with a silicon detector to perform ΔE-E measurements but at lower rates (10^3 pps).

Total current absolute measurements can be performed using very fast scintillators after a suited calibration [17]. The short decay time of the polymeric plastic scintillators allows very high acquisition rates; they can be easily shaped in different geometry and are very cheap. The main drawback is their poor radiation hardness if used at low energies and high intensities.

8 SUMMARY AND PROSPECTS

It is not so easy to report a complete overview of the activities that are coming out developing low intensity beam diagnostics. The wide choice of materials, detectors and techniques involved produces an increasing quantity of experimental apparatus very different in terms of performances and operating ranges.

At the end of this very general overview it is possible to draw some conclusions regarding the state of art and the prospects of this activity. To satisfy all the requirements for the low intensity beam diagnostics the investigation on the use of particles detecting techniques has produced the most promising results. Gas chambers as well as scintillators based detectors represent the preferred solutions for their versatility, reliability and cost. For the next future, also the diamond based detectors will represent a good alternative. Few general statements come out from the gained experience and they can be considered as guidelines for the future setups improvements:

- necessity to reduce the setup complexity;
- necessity of integration with the control system;
- necessity to increase the dynamic range;
- necessity to improve the collaboration with the particle detecting, materials and electronics experts in order to develop new ideas, materials and electronics with better performances.

9 REFERENCES

[1] NuPECC Report, December 1997.

[2] J. D. Garret, *Nucl. Phys.* A 616 (1997) 3.
S. Kubono et al., *Nucl. Phys.* A 616 (1997) 11.
A. C. C. Villari, *Nucl. Phys.* A 616 (1997) 21.
D. Habs et al, *Nucl. Phys.* A 616 (1997) 29.
D. J. Morrissey, *Nucl. Phys.* A 616 (1997) 45.
I. Tanihata, *Nucl. Phys.* A 616 (1997) 56.
G. Ciavola et al, *Nucl. Phys.* A 616 (1997) 69.

[3] R. Pardo et al, presented at the RIB workshop, May 1997, Vancouver (Canada).

[4] B. Launé et al, presented at the RIB workshop, May 1997, Vancouver (Canada).

[5] H. Fenker et al., presented at *the IEEE Nucl. Sc. Symp.*, November 1995, S. Francisco (CA, USA).

[6] A.Oed, *NIM* A 263 (1988) 351.

[7] P. Finocchiaro et al., submitted to *NIM* A.

[8] S. Aiello et al., *NIM* A 400 (1997) 469

[9] J. P. Vignet et al, *AIP* 390 (1996) 223.

[10] A. Rovelli et al, *AIP* 390 (1996) 398.

[11] D. Shapira et al, presented at the RIB workshop, May 1997, Vancouver (Canada).

[12] G. F. Knoll, Radiation Detection and Measurement, 2nd edition.

[13] P. Finocchiaro et al., *IEEE Trans. on Nucl. Sc.*, Vol. 45, No. 3, June 1998.

[14] P. Finocchiaro et al., *NIM* A 385 (1997) 31.

[15] A. Amato et al., LNS Report 09-10-97.

[16] B. Launé et al, presented at the RIB workshop, May 1997, Vancouver (Canada).

[17] L. Rezzonico et al., presented at the RIB workshop, May 1997, Vancouver (Canada).

DEVELOPMENT OF DIFFRACTION RADIATION DIAGNOSTICS FOR NONINVASIVE BEAM SIZE, DIVERGENCE, AND EMITTANCE MEASUREMENTS[*]

W. D. Kimura,[#] STI Optronics, R. B. Fiorito, Catholic U. America, and D. W. Rule, NSWCCD

Abstract

The analysis and design for a nondestructive electron beam diagnostic that is based upon observing diffraction radiation (DR) is presented. DR is similar to transition radiation and is produced when the beam passes through an aperture or near an edge. Analysis of the DR permits a number of beam parameters to be determined, such as the beam's transverse size, longitudinal (temporal) distribution, divergence, emittance, and energy. Our analysis includes a procedure for separating out this information from the DR angular distribution pattern. This analysis then forms the basis for the design of a relatively simple and compact aperture or slit system that can be used to nondestructively measure these parameters in real time.

1 INTRODUCTION

Electron linear accelerators (linacs) are used in a wide variety of applications including scientific, medical, and industrial. New applications are emerging such as high-power self-amplified spontaneous emission (SASE) [1] free electron laser (FEL) devices and high-duty-cycle FELs for industrial processing [2]. These devices require electron beams (e-beams) with very high quality (i.e., low emittance), and accurate position and size control. The small beam size and high average power of these accelerators preclude the use of conventional interceptive diagnostics and make it very difficult to monitor the beam quality on line.

The ultimate goal of our program is to develop a suite of noninterceptive diffraction radiation (DR) diagnostics capable of measuring beam divergence, energy, position, transverse beam size, emittance and bunch length. These DR diagnostics will minimally perturb the beam, will respond rapidly to changes in the beam so that the beam can be tuned while its characteristics are being measured in real time, and will easily interface with automated computer-controlled data acquisition and feedback systems. Our approach features a compact design that is capable of simultaneously measuring multiple beam parameters at one position along the beamline.

2 REVIEW OF DR THEORY

DR is produced when an electron passes through an aperture or near an edge, e.g., a slit. It is closely related to transition radiation (TR) with similar behavior. However, the development of DR theory is still quite sparse compared with TR and even less experimental work on DR has been done [3].

Appreciable DR is generated when the condition $\gamma \lambda \geq a$ is satisfied, where γ = Lorentz factor, λ = DR wavelength/2π, and a = aperture radius. As illustrated in Fig. 1, a convenient geometry is to have the aperture inclined at 45° to the e-beam so that the backward DR light is directed orthogonal to the e-beam towards detectors.

Figure 1: DR emission geometry for 45° aperture.

For the case of a circular aperture the DR photon production is given by [4]

$$\frac{d^2 I_{DR}}{d\omega d\Omega} = \frac{d^2 I_{TR}}{d\omega d\Omega} B(N, \bar{k}, \ell, \sigma) G(q, a), \qquad (1)$$

where ω = frequency, Ω = solid angle, N = number of electrons, $k = 2\pi/\lambda$, σ = beam size, $q = k\sin\theta$, θ = observation angle, and a = aperture radius. The TR term goes as

$$\frac{d^2 I_{TR}}{d\omega d\Omega} \approx \frac{e^2}{\pi^2 c} \frac{\theta^2}{\left(\gamma^{-2} + \theta^2\right)^2}, \quad \gamma \gg 1, \qquad (2)$$

and the bunch form factor is given by

$$B(N,\bar{k},\ell,\sigma) = N + N(N-1)F(\bar{k},\ell,\sigma),$$

$$F(\bar{k},\ell,\sigma) = \left| \int S(\bar{r})e^{i\bar{k}\cdot\bar{r}}d\bar{r} \right|^2, \tag{3}$$

where $S(\bar{r})$ = beam distribution function. Note, when N > $N_c \equiv (1 - F)/F$, then coherent radiation dominates. Lastly, the geometrical factor for a circular aperture is

$$G(q,a) = J_0^2(ka\sin\theta) + (b/a)^2 J_1^2(ka\sin\theta), \tag{4}$$

where b is the offset from the center of the aperture and $J_{0,1}$ are Bessel functions. Thus, the aperture modifies the normal TR geometrical factor through the addition of a J_1^2 term.

An example of the amount of DR photons generated from a 2-mm dia. aperture is shown in Fig. 2 for conditions similar to the 6-GeV beam at the Thomas Jefferson National Accelerator Facility (TJNAF).

E = 6 GeV, a = 1 mm, 10% bandwidth, 10^5 e/bunch, θ=+/-100/γ, σ=200 µm, ℓ = 300 µm

Figure 2: Example of DR production from circular aperture.

The effect of coherence can be clearly seen where the photon number increases dramatically at wavelengths ≥ 300 µm, which corresponds to the bunch length ℓ.

3 DIAGNOSING WITH DR

The DR observables are: 1) near-field and far-field intensity, 2) polarization, 3) angular distribution in far-field, and 4) wavelength spectrum. Using these observables, the beam offset, size, divergence, and bunch length can be measured.

For example, the beam divergence and size can be separately determined for the circular aperture by observing the far-field angular distribution pattern using appropriate choices of aperture size and observation wavelength for a given beam energy [5]. We have recently shown that this can also be accomplished using a slit DR radiator by separately observing the perpendicular and parallel components of the far-field angular distribution pattern. As an example, for a slit the perpendicular polarization pattern is more sensitive to changes in beam size than the parallel polarization. This

is illustrated in Fig. 3 for a beam with size σ = 200 µm. As can be seen there are more DR photons at the center of the pattern for the perpendicular component than for the parallel component.

With the beam size and divergence it is possible to determine the beam emittance. This ability to separate the divergence and size information from the angular distribution pattern by using polarization is a new way of using DR as a diagnostic tool.

Perpendicular and Parallel DR for Slit
E = 6 GeV, a = 2 mm, λ =573 nm, y =200 µm, s = 0.1/γ

Figure 3: DR production from a 2-mm wide slit.

Our calculations have shown that a single slit DR diagnostic should be capable of resolving divergence angles ~0.1/γ and beam sizes ~50 µm. We are currently exploring ways to improve and extend the sensitivity of the measurements. For example, using double apertures can help further increase the sensitivity to beam divergence. In a dual-aperture interferometer, as depicted in Fig. 4, the backward and forward DR emission interfere with each other. For this to occur the distance between apertures must be greater than or equal to the forward coherence length $L_c = \gamma^2\lambda$.

Figure 4: Dual aperture DR interferometer.

This interference between the forward and backward DR causes an additional modulation on the angular distribution as shown in Fig. 5 for the case of $L = 6L_c$. Note, how divergence angles of ~0.05/γ can be resolved.

Another new development is using the near-field intensity distribution around the perimeter of the aperture to determine information about the beam position and profile. For example, as the beam moves away from the center towards one side of the aperture, increased DR emission will occur from that side and less from the side 180° away. An example of this is shown in

Fig. 6, which plots the DR intensity distribution around the perimeter for a 2-mm dia. aperture at offsets of $X_0 = 0$ and 200 µm from the center.

Figure 5: DR angular distribution pattern for dual apertures and beam divergence $s = 0$ and $s = 0.05/\gamma$.

Figure 6: Near-field DR intensity distribution for a Gaussian beam ($\sigma = 200$ µm) offset from the center by X_0.

Through this analysis we have found that for the same parameters used in Fig. 2 (i.e., TJNAF values), a 10-µm offset of the beam centroid will cause a normalized peak-to-peak difference (i.e., $\Delta I/I$) variation of the sinusoid curve shown in Fig. 6 of 7%. Since variations of a few percent should be discernible, this implies <10 µm offsets can be detected. Hence, this diagnostic has the capability of being a high resolution beam position monitor (BPM).

Similarly, if the beam is ellipsoidal in shape, the sinusoid curve in Fig. 6 will have a pair of peaks and valleys whose height and depth depends on the aspect ratio (σ_x/σ_y) of the ellipticity. Again, for the TJNAF conditions we find that an aspect ratio of $\sigma_x/\sigma_y = 0.9$ corresponds to an intensity contrast of $\Delta I/I \approx 5\%$. Thus, ~10% changes in aspect ratio should be discernible.

More details of the beam profile may be obtainable by applying the theory of moments [6] to the distribution of the near-field pattern.

As mentioned earlier, the bunch length can be directly measured by examining at what wavelength the coherent production of DR occurs as illustrated in Fig. 2.

4 DR DIAGNOSTIC SYSTEM

A DR diagnostic system is conceptually very simple in design and can be compact in size. An example of a general purpose DR diagnostic system is illustrated in Fig. 7. It has a moveable DR target, which might consist of a combination of apertures, slits, and/or single knife edges. This target is held at 45° with respect to the e-beam. A beamsplitter located below the beamline directs the DR light to a pair of high-sensitivity, low-noise CCD cameras. One camera images the near-field; the other images the far-field. Before the cameras are pairs of wheels containing polarizers and bandpass filters. The output from the cameras are sent to a PC for data reduction and analysis. Lead surrounds the cameras to minimize radiation-induced noise.

Figure 7: DR diagnostic system layout.

5 CONCLUSIONS

Our analysis has shown the viability of DR as a noninterceptive beam diagnostic tool and quantified its capabilities. We have also shown the radiative power loss caused by the aperture is minuscule (≈ 1 mW for a 6-GeV, 200 µA beam), the voltage stresses induced on the aperture edges by the self-fields of the electrons are small, and the wakefield effects on the beam for the TJNAF conditions are negligible.

6 REFERENCES

[1] Tenth Advanced ICFA Beam Dynamics Panel Workshop on 4th Generation Light Sources, Grenoble, France, Jan. 22-25, 1996.

[2] M.J. Kelley, H.F. Dylla, G.R. Neil, L.J. Brillson, D.P. Henkel, and H. Helvajian, SPIE **2703**, 15 (1996).

[3] See for example, Y. Shibata, et al., Phys. Rev. E **52**, 6787 (1995).

[4] D. W. Rule, R. B. Fiorito, W. D. Kimura, "Noninterceptive Beam Diagnostics Based on Diffraction Radiation," 7th Beam Instrumentation Workshop, Argonne, IL, May 6-9, 1996.

[5] R. B. Fiorito, D. W. Rule, and W. D. Kimura, "Noninvasive Beam Position, Size, Divergence, and Energy Diagnostics Using Diffraction Radiation," in Proceedings of 8th Workshop on Advanced Accelerator Concepts, Baltimore, MD, Jul. 5-11, 1998.

[6] M. R. Teague, J. Opt. Soc. Am. **70**, 920 (1980).

ELECTRO-OPTICAL DETECTION OF CHARGED PARTICLE BEAMS*

Y.K. Semertzidis[†], V. Castillo, R.C. Larsen, D.M. Lazarus, B. Magurno[‡], T. Srinivasan-Rao,
T. Tsang, V. Usack, Brookhaven National Lab.
L. Kowalski, Montclair State Univ.
D.E. Kraus, Univ. of Pittsburgh

Abstract

We have made the first observation of a charged particle
beam by means of its electro-optical effect on the propaga-
tion of laser light in a birefringent crystal at the Brookhaven
National Laboratory Accelerator Test Facility. Polarized
infrared light was coupled to a $LiNbO_3$ crystal through a
polarization maintaining fiber of 4 micron diameter.

An electron beam in 10 ps bunches of 1 mm diameter
was scanned across the crystal. The modulation of the laser
light during passage of the electron beam was observed us-
ing a photodiode with 45 GHz bandwidth. The fastest rise
time measured, 120 ps, was made in the single shot mode
and was limited by the bandwidth of the oscilloscope and
the associated electronics. Both polarization dependent and
polarization independent effects were observed. This tech-
nology holds promise of greatly improved spatial and tem-
poral resolution of charged particle beams.

1 INTRODUCTION

A collaborative effort has been initiated to develop an ultra-
fast charged particle detector based on the birefringence
induced in an optical fiber carrying polarized light due to
the electric field of a relativistic charged particle. An anal-
ysis of such a detector is described in [1]. The electro-
optical effect in amorphous optical media is known as the
Kerr effect [2] and is quadratic in the electric field E;
$\phi = 2\pi K E^2 d$, where ϕ is the ellipticity induced in the
polarized light, K is the Kerr coefficient and d is the length
of the electric field region experienced by the material.
In uniaxial crystals the induced ellipticity is linear in the
externally applied E-field and the effect is called Pock-
els effect [3]. The induced phase delay is then given by
$\phi = \pi(V/V_\pi)$ with V the applied voltage and V_π the volt-
age required for producing a phase shift equal to π rad. As
a first step towards realizing the single particle detector we
used an intense, short length, electron beam from the Ac-
celerator Test Facility (ATF) of Brookhaven National Lab
(BNL) and the Pockels effect to detect it by optical means.

2 SETUP AND SENSITIVITY

The experimental setup in Fig. 1 shows the laser (CW, from
Amoco Laser Company) with 20 mW of optical power in
the infra-red ($\lambda = 1.32\mu m$), polarized by the polarizer (P)

and coupled to the fiber (F) with the microscope objective
(L). The fiber is polarization maintaining with a core of
$4\mu m$ in diameter.

Figure 1: The experimental setup for detecting charged par-
ticle beams via optical means. The $LiNbO_3$ crystal was
located at the beam position indicated by E-field. The po-
sitions of the polarizer (P), lenses (L), analyzer (A) and
photodiode detector(D) are schematically indicated.

The fiber was coupled to a commercially available
$LiNbO_3$ crystal [4] as indicated in Fig. 1. The crystal pack-
age was modified to allow for the passage of a charged
beam without hitting the housing. The laser light was ex-
tracted from the fiber and its polarization state analyzed
with by means of a $\lambda/4$ plate and the analyzer (A). It was
then detected by the photodiode and pre-amplifier [5] the
output of which goes to a fast transient digitizer [6].

The transmitted light from the analyzer is equal to

$$I = I_0[\sigma^2 + (\alpha + \phi(t))^2] \approx I_0[\sigma^2 + \alpha^2 + 2\alpha\phi(t)], \quad (1)$$

with I_0 the light intensity before the analyzer, σ^2 the min-
imum possible ratio of (I/I_0) when α and ϕ are equal to
zero, ϕ the induced ellipticity, and α is an intentional mis-
alignment angle introduced to linearize and amplify the ef-
fect. As is apparent from Eq. 1, the time dependent part of
the light signal can be made positive or negative depending
on the sign of α relative to ϕ.

The ATF produced an electron beam of 45 MeV kinetic
energy, containing up to 1 nC in 10 ps bunches of 1 mm
in diameter and a repetition rate of 1.5 Hz. This charged
particle beam creates an electric (E) field at a distance r if
$r \gg$ than the dimensions of the beam bunch:

$$E = \gamma N_e \frac{q}{4\pi\epsilon_0 r^2} = \gamma N_e \times 5.8 \times 10^{-5} V/m, \quad (2)$$

with γ the relativistic Lorentz factor, N_e the number of
electrons in the beam, $q = 1.6 \times 10^{-19}C$ the electron

charge, ϵ_0 $=85 \times 10^{-12}$F/m the permittivity of free space, and r the distance from the material (in the example we used $r = 0.5$ cm). This electric field is present for

$$\Delta t = \frac{r}{\gamma u} = \frac{17}{\gamma}\text{ps}, \qquad (3)$$

with u the beam velocity.

The LiNbO$_3$ crystal used has V_π = V with an electrode separation of $15\,\mu$m and a length of l =5 cm. The integral then of $\int E\,d\,l = \int \frac{5V}{15 \times 10^{-6}\text{ m}} \, dl\theta\theta$ V is capable of producing π rad of phase shift or $\pi/\sqrt{2}$ rad maximum of ellipticity (the maximum ellipticity is induced when the laser polarization is at 45° with respect to the applied electric field direction). The same integral estimated for a particle beam located at the mid-plane orthogonal to the crystal at a distance $r = 0.5$ cm is

$$\int E\,d\,l = \frac{\gamma N_e q}{4\pi\epsilon_0 r}2(1 - \sin\theta_1) = \gamma N_e\,2.6 \times 10^{-7}\text{V}, \qquad (4)$$

with θ_1 the angle $A\hat{B}C$ where A is the location of the beam, B one end of the crystal in the long direction and C the center of the crystal. This produces an ellipticity of

$$\phi = \gamma N_e \times 0.1\text{mrad}, \qquad (5)$$

for $17/\gamma$ ps.

The signal to noise ratio (SNR) for a detection system which is photon statistics limited is given by

$$SNR = \phi\sqrt{\frac{PTq_p}{2\hbar\omega}}, \qquad (6)$$

with P the laser power, T the inverse of the detection system bandwidth, q_p the quantum efficiency of the photodiode, and $\omega\hbar$ the energy of the laser photon. As an example we will take an electron particle beam with $\gamma =1700$, $T = 1$ μs, $q_p = 0.8$, $P = 1$ μW (e.g. 1 mJ pulsed laser light for 10 ps) and $\hbar\omega = 0.9$ eV, then the required number of electrons in the beam for $SNR = 1$ is $N_e \sim 2$.

3 EXPERIMENTAL RESULTS

At the experimental setup we used a CW laser of 10 mW, and a detector with 100 ps time resolution. Then using the above Eqs. 3, 6 we estimated the number of particles needed in the electron beam to be $N_e = 1\,0$ for $SNR = 1$. Our beam of 1 nC corresponds to $N_e = \times 10^9$ which ensured its detection. The induced ellipticity (from Eq. 5) is $\phi = 1.0\,\gamma$ rad equivalent to $\phi = 0.2$ rad when the signal attenuation due to limited detector bandwidth is taken into account.

In Fig. 2 we show the polarization dependent signal (solid line) as observed with a single shot of the electron beam. Changing the sign of α (see Eq. 1) the signal also flips sign while retaining the same amplitude. The maximum modulation of the light intensity was about 9% of its DC level.

Figure 2: The polarization dependent signal (solid line). The electron beam was about $r = 0.5$ cm from the crystal. The polarization independent signal is also shown (dash line).

We have also observed a signal when the crystal intercepted the beam which is shown in Fig. 2 again in the single shot mode (dash line). We repeated this without the analyzer present and found it was independent of it. The difference from the polarization dependent signal is two-fold. First it does not flip sign under any polarization orientation, and second it has a much longer time decay constant.

We intend to improve the time resolution of the signal by increasing the laser light intensity and the oscilloscope bandwidth. Long term plans include the implementation of this sensitive method as a readout to a high rate single particle detector.

If r is reduced to $100\,\mu$m, the required N_e is reduced by a factor of 2, making possible ultra-fast single particle detection by optical means. The gain factor is only 2 because of the limited bandwidth of the assumed detector which attenuates the signal by the ratio of $\Delta t/T$.

We will also look into a new type of fiber which exhibits high polarizability [7] thus reducing the cost of the detector considerably.

4 REFERENCES

[1] Y.K. Semertzidis, XXVII International Conference on High Energy Physics gls0918 (1994).

[2] J. Kerr, Phi. Mag. 50, 337, 446 (1875).

[3] A. Yariv, Quantum Electronics, Wiley, New York, 1967, 3rd ed. 1989.

[4] Uniphase Telecommunications Products, 1289 Blue Hills Ave., Bloomfield, CT 06002.

[5] Type 1011 pre-amplifier from New Focus, Inc., 2630 Walsh Ave., Santa Clara, CA 95051. The conversion gain of the detector is 10 V/W, with a rise time of 9 ps.

[6] The oscilloscope used was from Hewlett Packard (HP SDC5000), of 7 GHz bandwidth.

[7] X.C. Long and S.R.J. Brueck, IEEE Photonic Technology Letters, vol 9, p.767, 1997.

MEASUREMENT OF SMALL BEAM SIZE BY THE USE OF SR INTERFEROMETER

S. HIRAMATSU, H. IWASAKI*, T. MITSUHASHI, T. NAITOH and Y. YAMAMOTO*
High Energy Accelerator Research Organisation, Oho, Tsukuba, Ibaraki, 305-0801 Japan
*SR center, Ritsumeikan University, 1916 Noji-cyo, Kusatsu, Shiga, 525-77 Japan

Abstract

The principle of measurement of the profile or size of small objects through the spatial coherency of the light is known as the van Citterut-Zernike theorem. Recently the SR interferometer (interferometer for synchrotron radiation) was developed to measure the spatial coherency of the visible region of the SR beam, and we demonstrated that this method is able to measure the beam profile and size. Since the small electron beam emits a SR beam which has a good spatial coherency, this method is suitable for measuring a small beam size. In this paper, the basic theory for the measurement of the profile or size of a small object by the spatial coherency of the light, a design of the SR interferometer, and the results of beam profile measurement are described. Two examples of the small beam size measurements are also described.

1. INTRODUCTION

The measurements of beam profile and size are two of the most fundamental diagnostics in an electron storage ring. The most conventional method to observe the beam profile is known as a beam profile monitor via imaging of the visible SR beam[1]. The resolution of this monitor is generally limited by diffraction phenomena. In the usual configuration of the profile monitor the RMS size of diffraction (1σ of the point spread function) is no smaller than 50 μm. In the last 10 years, research and development in electron storage rings (especially in the area of emittance reduction) has been very remarkable. We can realise sub-diffraction-limited beam sizes in electron storage rings. So the above-mentioned profile monitor via imaging of the visible SR beam becomes useless in precise quantitative measurements of the beam profile and size. In the visible optics, opticians use an interferometer as the standard method to measure the profile or size of very small objects. The principle of measurement of the profile of an object by means of spatial coherency was first proposed by H.Fizeau [2] and is now known as the Van Cittert-Zernike theorem [3]. It is well known that A. A. Michelson measured the angular dimension (extent) of a star with this method [4]. Recently we developed the SR interferometer (an interferometer for SR beams) to measure the spatial coherency of the visible region of an SR beam, and as one of the results of investigations on the spatial coherence of

e-mail: mitsuhas@mail.kek.jp

SR beams, we demonstrated that this method is applicable to measure the beam profile and size at the KEK Photon Factory [5]. Since the SR beam from a small electron beam has good spatial coherency, this method is suitable for measuring a small beam size. The characteristics of this method are: 1) we can measure beam sizes as small as 5μm with 1μm resolution in a non-destructive manner; 2) the profile is easy to measure using visible light (typically 500 nm); 3) the measurement time is a few seconds for size measurement and few tens of seconds for profile measurement. In this paper we describe the van Cittert-Zernike theorem, the design of the SR interferometer and examples of the profile and the beam size measurements

2. SPATIAL COHERENCE AND BEAM SIZE

According to van Citterut-Zernike's theorem, the profile of an object is given by the Fourier Transform of the complex degree of spatial coherence at longer wavelengths as in the visible light[3][6][8]. Let f denotes the beam profile as a function of position y, R denotes distance between source beam and the double slit, and γ denotes the complex degree of spatial coherence as a function of spatial frequency υ. Then γ is given by the Fourier transform of f as follows;

$$\gamma(\upsilon) = \int f(y)\exp(-2\pi i\upsilon \cdot y)dy, \quad \upsilon = \frac{2\pi D}{\lambda R}.$$

We can measure the beam profile and the beam size via spatial coherence measurement with the interferometer.

3. SR INTERFEROMETER

To measure the spatial coherence of SR beams, a wavefront-division type of two-beam interferometer using polarized quasi-monochromatic rays was designed as shown in Fig.1.

Fig.1 Outline of the SR interferometer.

In the vertical plane, the elliptical polarity of synchrotron radiation is opposite that in between the medium plane of the electron beam orbit. Therefore, there exists the π phase difference between the phases of the interferograms to correspond to the σ- and π-polarized components [12]. To eliminate the interferogram by π-polarized component, we mast apply a polarization filter. A typical interferogram observed with the SR interferometer is shown in Fig.2.

Fig. 2 A typical interferogram observed with the SR interferometer.

4 Convenient formulas for a Gaussian approximation of the beam profile

We often approximate the beam profile with a Gaussian shape. With this approximation, we can skip any phase measurement. The Fourier transform of even function (Gaussian) is simplified to a Fourier cosine transform. A spatial coherence is also given by a Gauss function. We can evaluate a RMS width of spatial coherence by using q least-squares analysis. The RMS beam size σ_{beam} is given by the RMS width of the spatial coherence curve σ_{γ} as follows:

$$\sigma_{beam} = \frac{\lambda \cdot R}{2 \cdot \pi \cdot \sigma_{\gamma}}$$

where R denotes the distance between the beam and the double slit. We can also estimate the RMS. beam size

$$\sigma_{beam} = \frac{\lambda \cdot F}{\pi \cdot D} \cdot \sqrt{\frac{1}{2} \cdot \ln\left(\frac{1}{\gamma}\right)}$$

from one data of visibility, which is measured at a fixed separation of double slit. The RMS beam size σ_{beam} is given by ,
where γ denotes the visibility, which is measured at a double slit separation of D.

5 . BEAM PROFILE MEASUREMENT

We can measure the beam profile by Fourier transform of the spatial coherence. Figure 3 shows the absolute value the complex degree of the spatial coherence ($|\gamma|$,visibility) was measured by changing the double slit separation from 5 mm to 15 mm at the Photon Factory[5].

Fig 3. Result of $|\gamma|$ at the Photon Factory

The result of beam profile by Fourier transform of the spatial coherence is shown Fig. 4.

Fig. 4 Beam profile by the Fourier transform of the spatial coherence at the Photon Factory

Another example of beam profile measurement was performed at the SR facility AURORA of Ritsumeikan university[6]. Figure 5 shows the result of the $|\gamma|$ which is measured for the large beam operation mode. In this operation mode, a fat beam is obtained by a RF kicker.

Fig. 6 Result of the $|\gamma|$ which is measured for the large beam operation mode

The result of beam profile by the Fourier transform of the $|\gamma|$ is Fig. 6. The trapezoidal profile of beam was observed due to the fat beam which is obtained by the use of RF kicker.

Fig. 6 The result of beam profile by the Fourier transform at the AURORA.

6. SMALL BEAM SIZE MEASUREMENT

As mentioned in section 3, to assume the Gaussian profile, we can evaluate the beam size in the small-beam based on the degree of spatial coherence. We introduce two examples of small beam size measurements in this section. One is the result of vertical beam size measurement at the AURORA[6] and other is the vertical and the horizontal beam size measurement the ATF damping ring at KEK[7]. Figure 7 shows the result of a least-squares fitting of the |γ| by a Gaussian profile at the AURORA. The obtained beam size from this fitting is 16.5 μm.

Fig. 7 Absolute value of the complex degree of spatial coherence in the vertical direction. Dotted line denotes measured |γ|, and solid line denotes the best-fit beam size of 16.5 ± 0.6μm.

Figures 8 show the result of a least-squares fitting of the |γ| by a Gaussian profile at the ATF damping ring for vertical direction.

Fig. 8. Absolute value of the complex degree of spatial coherence in the vertical direction at ATF damping ring. Dotted line denotes measured |γ|, and solid line denotes the best-fit beam size of 14.7 ± 0.6μm.

A least-squares fitting of the |γ| having a field depth effect for the horizontal direction is shown in Fig. 9. The obtained beam size from these fitting is 14.7 μm in the vertical and 39μm in the horizontal.

Fig. 9. Absolute value of the complex degree of spatial coherence in the horizontal plane at the ATF damping ring. The dotted line denotes measured |γ| and the solid line denotes the best-fit value of 39±1μm.

7. CONCLUSIONS

The SR interferometer was developed to measure the spatial coherency of the visible region of the SR beam, and we demonstrated that this method is able to measure the beam profile based on the van Cittert-Zernike theorem. Since the small electron beam emits a SR beam which has a good spatial coherency, this method is suitable for measuring a small beam size. We succeed to measure the small beam sizes of a 16.5μm at the AURORA, and 14.7μm at ATF damping ring with resolution less than 1μm. The measuring time is typically about 1sec for beam size measurement, is about 1 min for profile measurement with slit scanning.

8. ACKNOWLEDGMENTS

REFERENCES

[1] T. Mitsuhashi and M. Katoh, Proc. 5th European Particle Accelerator Conference, 1669, (1996), Sitges (Barcelona).
[2] H. Fizeau, C.R.Acd.Sci. Paris, 66, 934 (1868).
[3] P.H.van Cittert, Phisica, 1, 201(1934) and also see M. Born and E. Wolf, "Principles of Optics", chapter 10, P491, Pergamon press. (1980).
[4] A.A. Michelson, Astrophsyc.J51,257 (1920).
[5] T. Mitsuhashi, Proc of 1997 Particle Accelerator Conference, 766, (1997) ,Vancouver.
[6] T. Mitsuhashi, H. Iwasaki,Y. Yamamoto, T. Nakayama and D. Amano, Proc. 11th Symposium on Accelerator Science and Technology 441 (1997).
[7] T. Mitsuhashi and T. Naitoh, Proc.of 6th European Particle Accelerator Conference 1565,(1998), Stockholm.

OBSERVING BEAM MOTION USING INFRARED INTERFEROMETRY *

J. M. Byrd[†], M. Martin, W. McKinney

Lawrence Berkeley National Laboratory, One Cyclotron Road, Berkeley, California 94720

Abstract

Phase noise in the RF master oscillator driving synchrotron oscillations of the beam has been identified as one of the dominant sources of noise in the infrared beamline at the Advanced Light Source. We present measurements of the effect of the electron beam motion in a Fourier transform interferometer (FTIR) detector. This form of detector may be sensitive to very small beam motions.

Parameter	Description	Value
E	Beam energy	1.5–1.9 GeV
I	nominal current range	100–400 mA
$\epsilon_{x,y}$	x,y emittance @ 1.9 GeV	6,0.06 nm-rad
$\beta_{x,y}$	x,y beta functions	0.45,19.0 m
$\alpha_{x,y}$	x,y alpha functions	0.43,-7.7
η_x	dispersion function	4.18 cm
η'_x	dispersion slope	0.13

Table 1: ALS IR source parameters.

1 INTRODUCTION

Interest in infrared (IR) synchrotron radiation has grown dramatically in the past few years. However, measurements at the synchrotron IR source have proven to be very sensitive to both beam motion and mechanical motion of the endstation[1, 2, 3]. The beam motion can result from a combination of self-excited and driven motion, ranging in frequency from a few hertz to hundreds of kilohertz. IR beamline 1.4.3 at the Advanced Light Source (ALS) located at Lawrence Berkeley National Laboratory is no exception to these problems.

Over the past year, we have made an effort to identify and resolve noise issues in the beamline as well as understand the mechanisms for observing the noise. In particular, we have made an detailed study of beam motion excited by phase noise in the master oscillator (MO) of the RF system since this was determined to be one of the dominant noise sources. This has led us to the conclusion that the interferometer used in the endstation may serve as an excellent general diagnostic for observing very small beam motion. This paper summarizes our measurements to date and provides several hypotheses for the sensitivity to beam motion. Section 2 provides a description of the IR source, beamline, and interferometer. Section 3 presents measurements of the beam motion excited by MO phase noise.

2 MEASUREMENT SETUP

The ALS is a 1.5–1.9 GeV electron storage ring optimized for producing high brightness synchrotron radiation. The synchrotron light is collected from the 1.4 bending magnet with source parameters listed in Table 1.

The light passes through a 10mrad vertical and 40mrad horizontal opening, as schematically drawn in Figure 1.

This light is deflected vertically by 0.5 meter, then is refocused outside the shield wall by an ellipsoidal mirror, m2. A "switchyard" then contains a series of optics to collimate the IR beam and distribute the beam to one of three end stations.

Figure 1: Schematic layout of the ALS infrared beamline.

BL 1.4.3 directs the collimated synchrotron light into a Nicolet Magna 760 FTIR bench. The modulated light is then passed through a Nic-Plan IR microscope that can perform both transmission and reflection measurements. BL 1.4.2 uses the synchrotron light for the input of a Bruker IFS 66v/S vacuum FTIR spectrometer. This IFS 66v/S instrument has a wide spectral range, 50 cm-1 to 25,000 cm-1, and it has step-scan capabilities in addition to rapid-scan to enable fast timing measurements. BL 1.4.1 uses the UV part of the spectrum from the 1.4 front end to do photoluminescence and related studies up to 6eV.

r Spec   X: 0   Hz   Y: 1.29726 mV

Figure 2: Noise measured in the FTIR as a function of current. The highest peak was recorded at a current of 391 mA and the lowest at 158 mA. The frequency axis ranges from 0 to 23 kHz.

Figure 3: Transfer functions of the FTIR response from exciting the cavity phase at various beam currents.

3 MEASUREMENTS

To study the spectrum of noise in the FTIR, we fixed the moving mirror in the interferometer and recorded the output of the detector on a spectrum analyzer. An example of this measurement is shown in Fig. 2, which shows a noise peak at about 3.7 kHz which decreases in frequency and increases in amplitude with increasing beam current.

We recognized this as possibly being a form of synchrotron oscillations known as the Robinson mode that could be driven by broadband noise in the RF system. By measuring the noise at various points in the RF system, we determined that the dominant source was phase noise in the 500 MHz master oscillator. The details of beam motion driven by phase noise are discussed elsewhere[4].

In order to further demonstrate the effect of phase noise on the IR beamline, we deliberately excited the cavity by modulating the cavity phase with white noise and measured the response as a function of beam current as shown in Fig. 3a. Shown in Fig. 4a is a calculation of the expected response at the same beam currents, assuming that the motion results from energy oscillations of the beam at the source point.

To find the spectrum of beam motion driven by the MO

Figure 4: a) Calculated amplitude of the transfer function. This compares well with the measured values in Fig. 3. b) Calculated noise spectrum using the spectrum of MO phase noise and the calculated beam energy transfer function. This shows qualitative agreement with the measured noise in Fig. 2.

Figure 5: Three IR spectra showing the effects of the MO phase noise. The upper two traces were taken with the old MO, the bottom trace with the new MO.

phase noise, we computed the product of the MO phase noise determined from catalog values with the transfer function computed in Fig. 4a. This is shown in Fig. 4b. This has the same characteristic shape as the measured noise in Fig. 2. Replacement of the existing of the existing MO by a lower noise model reduced this motion by a factor of 5.

The net result of the reduction in phase noise can be observed in Fig 5, which shows several spectral scans taken before and after the MO phase noise was reduced.

Although we succesfully identified the source of the noise and reduced it, we still did not understand how the beam motion created a signal in the interferometer. To further study this, we measured the beam motion driven by the

noisy MO at very low beam current, where we could independently determine the amplitude of synchrotron oscillations and thus the amplitude of energy oscillations at the horizontally dispersive IR source point. Shown in Fig. 6 is a plot of the FTIR noise at low current for the old and new MO. We independently determined that the amplitude of beam energy oscillations was 2.8e-5 (relative to the nominal energy), corresponding the horizontal position and angle oscillations of 1.6 μm and 3.8 μrad, respectively.

Figure 6: Motion driven by MO phase noise at low beam current for two MO sources. The reduction is equal to the reduction in the phase noise.

Given such small beam motion with a signal/noise of about 40 indicated that the interferometer was sensitive to beam motion of about 40 nm! This suggests that the interferometer may be used as a beam motion detector with extremely high sensitivity. Following are two possible noise mechanisms which we are currently studying. Consider the schematic diagram of a Michelson interferometer as shown in Fig. 7. If the incoming light is not normal to the mirror (M2), there is a path length difference in between the two arms $L1$ and $L2$ of $\Delta L \theta^2$, where ΔL is the difference $L2 - L1$ and θ is the incident light angle. Angular variations of the incident light can occur from position variations of the light incident of the ellipsoidal focussing mirror or deviations from optical flatness of any of the subsequent mirrors. A second mechanism is nonflatness of the beam splitter. In this case, transverse motion of the incident light beam will result in a path length difference in the two arms.

4 CONCLUSIONS

Phase noise in the RF master oscillator has been identified as one of the dominant sources of noise in the ALS infrared beamline. The problem has been substantially reduced by replacing the MO with a lower noise source. Interferometric measurements of synchrotron radiation are very sensitive to beam motion and may be used as a sensitive beam diagnostic. The means by which the noise is observed at the ALS is still under investigation. We would like to thank H. Zyngier for many useful discussions.

Figure 7: Schematic diagram of a Michelson interferometer. Path length differences can arise from variations of the incident light angle or position variations combined with a nonflat beamsplitter.

5 REFERENCES

[1] A. R. Hight Walker, U. Arp, G. T. Fraser, T. B. Lucatorto, J. Wen, SPIE **3153**, 42, 1997.

[2] R. Biscardi, G. Ramirez, G. P. Williams, C. Zimba, Rev. Sci. Inst. **66**, 1856, 1995.

[3] G. Rakowsky, L. R. Highey, Rev. Sci. Inst. **66**, 1856, 1995.

[4] J. M. Byrd, *Effects of phase noise in heavily beam loaded storage rings*, these proceedings.

INITIAL PERFORMANCE OF THE IUCF COOLER INJECTOR SYNCHROTRON*

D.L Friesel,# M. Ball, B. Hamilton, Wm. Manwaring, and T. Sloan

IUCF, Bloomington, IN

Abstract

Construction of a compact 2.4 Tm Cooler Injector synchrotron (CIS) to injection intense polarised proton and deuteron beams into the IUCF 3.6 Tm electron cooled storage ring (Cooler) is complete. Beam commissioning began in 1997 with unpolarized H⁻ strip injection and progressed to the extraction of 210 MeV protons from CIS and the injection of 10^{10} protons at 200 MeV into the Cooler for experiment. With a circumference of 17.36 m, CIS is possibly the smallest and least expensive example of this accelerator type for protons, and may serve as a practical proton source for medical and other applications. This contribution discusses our design choices, the resulting technical and fabrication challenges, and their solutions. Emphasis is given to the CIS ring beam performance from 7 MeV H⁻ injection through Cooler 200 MeV proton injection and accumulation.

1 INTRODUCTION

A compact synchrotron to replace the Indiana k220 cyclotron as an injector of polarised protons and deuterons into the Cooler [1] was jointly funded by Indiana University ($1.5 M) and the NSF Academic Research Infrastructure Program ($2.0 M) in August of 1994. The primary goal was to inject over 10^{10} polarised particles/pulse into the Cooler to improve experimental luminosity for medium energy cooled beams on thin internal targets. Initial CIS design parameters were influenced by the relatively low intensities available from pulsed polarised ion sources (≈1 mA peak) and by the desire to avoid an intrinsic depolarising resonance in the Cooler for 186 MeV protons. A secondary goal was to simplify the Cooler injection process for polarised beams to reduce machine overhead and increase experimental duty factor. Finally, only limited space was available in the existing facility to house a new injector accelerator. These requirements dictated negative ion strip injection into a small synchrotron with single turn fast extraction and bucket-to-bucket kick injection into the Cooler. The injection and extraction energies (7 MeV H⁻ and 200 MeV P) were the minimum required to meet the intensity and resonance goals. The

Table I: CIS Booster Design Parameters

Polarised Source	25 keV H⁻	25keV d⁻
Linac Pre-accelerator	7 MeV H⁻	4 MeV d⁻
Strip Injection Foil	4.5μgm/cm² C	3.0μgm/c² C
Fast Extraction	220 MeV P	105 MeV d
Extracted Intensity	$\geq 10^{10}$ p/pulse	$\geq 5 \times 10^9$ d/p
Rep. Rate	1 to 5 Hz	1 to 5 Hz

resulting design parameters for CIS are listed in Table I. With a budget of $3.5 M, only the Linac, RF cavity, and ring magnetic, diagnostic and extraction system were designed and fabricated specifically for CIS. The majority of the remaining systems (temporary H⁻ source, injection and extraction beam lines, ring vacuum system, etc) were assembled from surplus equipment available either in-house or from other laboratories (FNAL, AGNL, etc).

2 CIS CONFIGURATION

A schematic of the present IUCF nuclear research accelerator facilities, consisting of the new CIS booster synchrotron and the electron cooler storage ring, is shown in Fig. 1. A 25 keV H⁻ beam is matched to the acceptance of a commercial 7 MeV H⁻ linac pre-accelerator consisting of a 3 MeV RFQ coupled to a 4 MeV DTL [2,3]. Both operate at 425MHz. The 7 MeV H⁻ beam is strip injected into the synchrotron, protons are accumulated, RF captured, accelerated to 210 MeV and single turn fast extracted for bucket-to-bucket transfer

Figure 1: Present IUCF Accelerator Research Facility

into the Cooler ring for accumulation, electron cooling and further acceleration.

2.1 Polarised Ion Source

A high intensity polarised negative ion source (≥ 1 mA H^-, d^- peak) with a colliding beam ionizer (CIPIOS) [4] was fabricated simultaneously with CIS, and was recently (3/99) installed in the CIS vault. Injection of polarised H^- beams from this new source, which is also capable of delivering polarised d^- ions, is scheduled to begin in June 1999. Deuteron beam pre-acceleration for CIS injection is done by replacing the 3 MeV H^- RFQ vanes with another set designed to accelerate q/A=1/2 ions to 4 MeV. The RFQ vacuum vessel and H^- vane assembly were fabricated with this replacement capability built in. The q/A=1/2 vane assembly is now being fabricated by AccSys Technology, Inc [5] with delivery scheduled for June 1999. Following initial installation and alignment of the new vanes (late 1999), switching from H^- to d^- operation will likely take 2 days. The CIS/Cooler H^- beam commissioning studies reported here were conducted using a surplus 0.5 mA (peak) unpolarized Duoplasotron source [6].

2.2 The CIS Lattice Design

A schematic of the CIS ring is shown in Fig. 2 and the lattice parameters are listed in Table II. CIS is a weak focusing synchrotron with optical properties determined by the ring dipole-straight length ratio and the dipole12° edge angles. A quadrupole was installed in each straight to correct for dipole edge angle fabrication errors and to study ring performance at transition by making large tune changes. The lattice, linac pre-accelerator and major accelerator system hardware designs were previously reported [7,8,9]. Each of the four 2.34m long straight sections are filled with apparatus required for H^-

Table II: Lattice Parameters for the CIS Ring

Circumference	17.364 m
Betatron Tunes; Qx, Qy	1.478, 0.72
Dipole Length	2.0 m
Dipole Edge Angle	12°
Dipole Bend radius	1.273 m
βx: Maximum	4.373 m
Minimum	0.996 m
βy: Maximum	3.786 m
Minimum	3.380 m
Dispersion: Maximum	1.759 m
Minimum	1.617 m
Chromaticity: Cx	-0.529
Cz	-0.156
Transition Energy	256 MeV

Figure 2: Plan view of the CIS 2.4 Tm Synchrotron Ring.

strip injection (1), single-turn kick extraction (2 & 3) and RF acceleration (4). Five vertical steering elements distributed around the ring and four main dipole trim coils are used for beam centering. Beam diagnostics consist of an x/y BPM pair placed at the entrance and exit of each dipole, a high bandwidth wall gap monitor, a ping tune kicker and a removable wire Harp to view circulating beam during injection [10].

2.3 Fabrication Challenges & Innovations

The energy and small circumference (1/5th Cooler) of CIS precipitated significant design and engineering challenges for the ring main dipoles and the fast extraction system. The ring design requires 90° laminated dipoles with a 1.273 m radius (37 cm sagitta) to ramp from 0.3 to 1.68 T at up to 5 Hz. 2-D and 3-D field calculations minimised multipole components in the C-shaped dipole [8], but a method to fabricate such small laminated 90° magnets was needed. The key to our design solution was the availability of 1.5mm thick modified 1006 sheet steel pre-coated with a B-stage epoxy resin (Remisol EB-540). A 4 to 6 micron thick layer of this resin, which serves as both the lamination insulation and bonding agent, is applied to each side of the sheet steel prior to stamping. The 90° magnet is fabricated from 5 wedge shaped and 2 end pack modules that are individually stacked, baked and precision machined to the required shape prior to mounting on a base plate assembly. The end pack pole ends are machined with a profile to minimise the magnet integrated sextupole component, which ensures a large dynamic aperture at fields up to 1.83 T. The magnet

499

Figure 3: 3 view of a CIS main Dipole Assembly.

DIPOLE PROPERTIES

Bend Angle:	90.0°
Bend Radius:	1.273 m
GAP:	58.0 mm
Edge Angle	12.0°
Field Max:	1.93 T
Field Gradient:	0.0 T/m
1/1000 dB/B opt	50 x 100 mm
Turns/Mag:	24
Dynn. Pwr/mag:	705 kW
Weight/Mag:	38,000 lbs

assembly is shown in Fig. 3 together with some measured field properties. The 1.5mm thick coated steel was also used to fabricate the remainder of the ring laminated magnets (2 rf cavity bias quads, 4 trim quads, and 5 ring vertical steering magnets). The steel was sheered to the required perimeter shape, stacked, and baked into blocks in-house and then sent out to be EDM machined to the desired pole tip shape, an economical solution for this small number of laminated magnets. The second challenge for this small ring is beam extraction. The orbit period for 200 MeV protons in CIS is 100 nsec. Hence, single turn kick extraction requires a fast kicker with $\leq$ 50nsec (10-90%) rise time to displace the beam across the 7mm thick septum of the Lambertson extraction dipole without loss [6]. A 1.3m long parallel plate, 50 Ω Blumlein kicker magnet [10] is installed in straight 2 (Fig. 2). A state-of-the-art pulse forming network and modulator were fabricated by Pulse Sciences, Inc. [11], which reliably delivers $\pm$ 55 kV, 300 nsec long pulses to the kicker with a rise time of about 35 nsec. 1.3m is the maximum space available anywhere in CIS, and the 55 kV plate voltage limit is imposed by reliability constraints on the pulse modulator thyratron tube, Application of $\pm$ 55 kV across the 4 cm kicker gap is calculated to displace a 200 MeV proton beam 20mm at the Lambertson septum entrance. This is enough for efficient extraction if the beam is bumped close to the septum prior to firing the kicker. The dipole trim coils are used to locally bump the beam away from the septum during acceleration and close to the septum for extraction. Kicker EMI during is negligible.

3 CIS BEAM COMMISSIONING

A 0.50 mA (peak) pulsed, 25 keV H beam from the duoplasmatron is focused at the entrance of the PL-7 linac. The H beam normalised emittance is 0.6 $\pi\mu$m,

smaller than the 1.0 μm acceptance of the RFQ. A double einsel lens focuses the beam (125mrad symmetric convergence cone) into the 2.5mm diameter RFQ entrance aperture. Beam transmission through the linac is nominally 80% and the normalised emittance and energy spread of the 7 MeV H beam are 1.0 $\pi\mu$m and 150 keV FWHM respectively, in good agreement with specifications.

The 425 MHz linac amplifiers have a 0.2% duty factor limit. The linac delivers a 200 μsec long, 300 μA (peak) 7 MeV H beam pulse at 4 Hz into a 9 m transfer beam line matched to the acceptance of CIS. Beam is strip injected on a 6mm x 25mm 4.5 μgm/cm^2 carbon foil. Two injection bumpers displace the circulating beam orbit 25mm onto the foil for coasting beam accumulation. The ring orbit period at injection is 0.48 μsec, hence the maximum theoretical peak intensity gain via strip accumulation is 400 (120 mA). Strip injection efficiency calculations [13] that account for phase space dilution effects of the foil predict an equilibrium gain of 120 (36 mA) after 200 μsec of accumulation. In practice, an intensity gain of 80 is routinely achieved after 175 μsec, corresponding to an initial coasting beam accumulation of 8 x 10^{10} protons. Part of the discrepancy between the calculated and measured gain is caused by the emittance growth of the circulating 7 MeV proton beam in the 0.1 μTorr average ring vacuum. Another source of beam loss at injection is the slow fall time (0.2 msec) of the bumper magnets after accumulation. Both effects can produce emittance growths nearly equal to that of the foil during injection. Vertical emittance growth during strip accumulation is the intensity limiting mechanism in CIS.

Optimal adiabatic capture of the accumulated beam requires a 2 msec ramp of the RF cavity to 250 V. The captured beam energy is 6.987 MeV. The fractional ring tunes are 0.48 horizontal and 0.72 vertical, in excellent agreement with the lattice predictions. The 1/e lifetime varies from 0.22 seconds to an equilibrium 1.72 seconds in the 200 msec immediately following capture. Beam acceleration is initiated within a few μsec of RF capture, by which time lifetime losses reduce the stored beam to $\leq$ 2 x 10^{10} protons. This intensity is also consistent with the calculated 7 MeV circulating beam space charge limit of 5 x 10^{10} protons, although this has yet to be identified as a CIS intensity limit. Work is continuing to improve the ring vacuum and to reduce the injection bumper fall time to increase stored beam intensity.

3.1 CIS Acceleration Performance

Proton beam ramping development began at 50 MeV in November 1997, progressed to 225 MeV by December 1997, and culminated with the acceleration of 1.1x10^{10} protons to 240 MeV in April 1998. The ramp time (seconds), and n (ramp power) is an integer variable

from 1 to 5 which is used to vary $dB\rho/dt$ from 1.0 Tm/s (n= 5) to 8 Tm/s (n=1) for a 0.5 sec up-ramp to 200 MeV. The software calculates both the main dipole current and RF cavity frequency as a function of $B\rho$ and creates a 96 vector ramp table for each. Beam acceleration is done open loop (no radial position feedback) via ramping the main dipole current and the accelerator cavity RF frequency. No other ring elements (dipole trims, quads, or steerers) are needed to achieve efficient, centered beam during ramping. 8 x/y BPM pairs and the high bandwidth Wall Gap Monitor (WGM) continuously monitor beam position and intensity around the ring during acceleration. The WGM also measures the circulating beam orbit period and bunching factor. Orbit centering errors are removed manually by making small modifications (≤0.4%) to the RF cavity frequency ramp vector tables. A software program was recently implemented to read the horizontal BPM positions during acceleration and adjust the RF frequency vector table automatically. Two iterations of this program are enough to center the beam to ±2 mm, a feature that reduces the setup time for new ramped energies to a matter of minutes.

To date, protons have been accelerated to energies from 50 to 240 MeV with ramp transmissions of 75% and flattop intensities over 1.1×10^{10} protons. All intensity losses occur during the first 200 msec of a 1-sec up-ramp and are also caused by gas scattering losses in the 0.1 μTorr ring vacuum. A beam phase feedback loop added to the RF acceleration system only marginally improves ramp transmission. The horizontal and vertical betatron tunes remain constant during acceleration at 1.485 ± 0.015 and 0.72 ± 0.015 respectively. The measured bunching factor varies from 3 at injection to about 5 at 225 MeV for RF accelerating voltages above 400 V. The 1/e lifetime of a 225 MeV proton beam in CIS is 573 sec.

The main dipole power supply has sufficient capacity to ramp protons to 250 MeV, although the magnets are already driven well into saturation (1.87 T) at 240 MeV. However, insufficient ac line capacity causes significant line "flicker" for ramps above 210 MeV at rep. rates faster than 1 Hz. While higher energy and faster rep. rate development is planned, 200 MeV at 1 Hz is an ideal beam for Cooler injection. A 0.8 Hz, 200 MeV proton ramp cycle consisting of a 0.5 sec up- and down-ramp, a 50 msec flattop for extraction and a 200 msec reset and fill period was developed for this purpose.

3.2 CIS Extraction Performance

The fast kicker and Lambertson septum extraction dipole present the smallest horizontal apertures, 4 cm and 5 cm respectively, to the CIS circulating beam. caused no intensity losses at injection when installed, but the Lambertson dipole requires a 7mm circulating beam local orbit bump away from the septum to

Figure 5: BPM scan for 0.5 ramp to 200 MeV protons.

maintain intensity during acceleration. This local bump is shown in Fig. 5, which is a BPM scan for a 0.5 sec ramp to 200 MeV. The kicker magnet is between dipoles 1 and 2, and the Lambertson entrance is just after the exit of dipole 2 (see Fig. 2). The beam positions at the entrance and exit of dipole 1 (top 2 traces) remain nearly centered during the ramp, while the positions in dipole 2 (bottom traces) are moved -7mm to the ring inside to prevent abrupt losses half way up the ramp. The Lambertson vacuum chamber apparently induces these losses, which were not observed prior to its installation. The local bump is inverted at the flattop just prior to extraction, when the beam exiting dipole 2 is bumped +17 mm to the septum edge. This can be seen in Fig. 5 beginning at 520 msec. Beam is extracted at 525 msec.

The Lambertson extraction channel horizontal width is 16mm. The diameter of a 10 πμm, 200 MeV proton beam is about 11mm, hence a careful alignment of the Lambertson dipole with the extraction orbit is required. Over 1×10^{10} protons have been extracted from CIS at 150, 200 and 210 MeV. Extraction efficiency is typically 75%, and has been as high as 86%. Fig. 6 is a display of the +55 kV extraction kicker pulse monitor (top), a WGM display of the last 4 orbits of the circulating beam at the flattop (middle), and a BPM

Figure 6: Kicker, WGM and BPM outputs for a 200 MeV extracted proton beam from CIS.

signal of the extracted beam in the Cooler transfer beam line (BL9A) for a 200 MeV proton beam. The horizontal scale is 100 nsec/Div. The rise time and width of the 55 kV kicker pulse are 35 and 300 nsec. The orbit period (WGM) of the 200 MeV flattop beam is 100 nsec, the FWHM bunch width is 21 nsec, and the bunch factor is 4.76. The BPM FWHM signal for the extracted beam is also 21 nsec, and measures 7×10^9 protons, 60% of the 1.1×10^{10} protons measured in CIS by the WGM. The extraction kicker for this run was at maximum voltage. In later runs, the kicker plate gap was reduced to 3.7 cm, and the extraction orbit bump was optimised to extract 1.1×10^{10} protons of 1.3×10^{10} at 200 MeV (85% extraction effic.) with a kicker voltage of ± 51 kV. While careful alignment of the extraction bump is required for this performance, experience has shown that the acceleration and extraction of beam from CIS is quite reproducable.

4 COOLER INJECTION

Approximately 9×10^9, 200 MeV protons/pulse at 0.8 Hz are routinely available from CIS for Cooler injection. A preliminary measurement of the normalised emittance in BL9A is about 18 $\pi\mu m$, and should be considered an upper limit. Transmission through BL9A to the Cooler injection system is $\geq$ 90%. The Cooler injection dipole apertures were recently modified to accept 10 $\pi\mu m$ emittance beams and the Cooler injection ferrite kicker magnet rise time was reduced from 200 ns to 70 ns to reduce losses at injection. The single pulse injection efficiency of CIS extracted beam into a Cooler stored orbit is 50%, corresponding to 4×10^9 injected per CIS cycle. Reducing the CIS extracted beam emittance by optimising strip injection parameters may increase Cooler injection efficiency, but has yet to be attempted.

Two methods of CIS beam accumulation in the Cooler have been demonstrated. The first and easiest is coasting beam cooled accumulation where CIS beam is injected and cooled with no Cooler RF cavity voltage. Fig. 7 is a low bandwidth PCT display of this type of accumulation for 200 MeV protons in which beam is accumulated to over 2.4 mA (8×10^9 protons) in 8 sec, or 6 pulses from CIS. The vertical scale is 0.5 mA/Div.

Figure 7: PCT display of 200 MeV proton accumulation

Beam also accumulates to nearly the same current via "sequential" cogging of 5 CIS pulses into the Cooler operating on the 5th harmonic. For this fill method, the timing of each extracted pulse from CIS is synched with the center of each Cooler RF bucket in sequence until all 5 buckets are filled. Beam centering and ramping was demonstrated in the Cooler using the new injection trajectory from CIS. The stored beam energy and 1/e lifetime in the Cooler are 201.57 MeV and 1100 sec. The momentum spread of the un-cooled beam injected into the Cooler is ± 0.2%, the Cooler design acceptance.

The present record of 3 mA accumulated in the Cooler with CIS injection is not yet limited by instabilities, but by the availability of development time. CIS/Cooler development competes with the polarised source installation work and Cooler experiment. Cooler experiments began with 200 MeV un-polarised protons from CIS in January 1999 with a significantly increased duty factor and stored beam intensity (1-2 mA average). The stability and reliability of Cooler stored beam is excellent, with intensities varying by less than 10% from cycle to cycle. Reproducibility is excellent throughout the system and turn-on and setup of the Cooler with CIS injection has been done in as little as 6 hours.

5 ACKNOWLEDGEMENTS

Most of the IUCF staff rendered significant technical contributions to the CIS/Cooler project during the last 4 years that made the performance reported here possible. These highly experienced and technically excellent people made this effort with a spirit of optimism and determination that was not justified by the pending future of the facility. It is this spirit and capability that is the essence of IUCF, and which made this an effective research facility for 24 years. My sincere thanks to these, my colleagues.

6 REFERENCES

[1]   R.E. Pollock, PAC'89, IEEE 89CH2699-0, 17 (1989)

[2]   D.L. Friesel et al, PAC'97, IEEE 97CH36167, 2811 (1997)

[3]   D.L. Friesel et al, Proc. Linac'98, Chicago, IL, Aug 23-28, 1998.

[4]   V. Derenchuk et al, AIP Conf. Proc. 421, 422 (1998).

[5]   R.W. Hamm, AccSys Technology, Inc, 11774 Quarry Lane, Pleasanton, CA, 94566

[6]   V. Derenchuk et al, PAC'97, IEEE 97CH36167, 2737 (1997).

[7]   X. Kang et al, PAC'97, IEEE 97CH36167, 264 (1997).

[8]   G.P. Berg et al, PAC'97, IEEE 97CH36167, 3303 (1997).

[9]   A. Pei et al, PAC'97, IEEE 97CH36167, 2968 (1997).

[10] M. Ball et al, Proc. 8th Beam Instrumentation Conf, Palo Alto, CA, May 4-7, 1998, to be published.

[11] J. Dinkel et al, PAC'93, IEEE 93CH3279-7, 1357 (1993)

[12] D. Morton, Titan Pulse Sciences, Inc, 600 McCormick St, San Leandro, CA, 94577

[13] K. Hedblom et al, PAC'95, IEEE 95CH35843, 1861 (1995).

OPERATION OF THE LOW-ENERGY DEMONSTRATION ACCELERATOR: THE PROTON INJECTOR FOR APT*

J. David Schneider", Los Alamos National Laboratory

Abstract

We report preliminary test results for a 6.7-MeV, 100-mA cw radio-frequency quadrupole. During the time this structure was in design, fabrication, assembly, tuning, and installation, we tested a 75-keV proton injector, 350-MHz high-power RF systems, EPICS controls, diagnostics, beam stop, and other hardware in preparation for the 670-kW beam test. Initial LEDA RFQ beam operation has commenced. This paper summarizes work in the past year, concentrating on RFQ assembly, tuning, installation, high-power conditioning and initial beam operation. We will include summaries of injector tests, 1.25-MeV RFQ-beam tests, beam-transport and beam-stop performance, and cavity resonance control. The technology being developed in this first section of the APT (accelerator production of tritium) linac is also appropriate for several other applications, including the transmutation of waste and medical isotope production.

1 LEDA DESCRIPTION

1.1 Purpose and Background

LEDA is designed to be a complete prototype[1] of the front end of the APT accelerator. Within LEDA, we plan to build, test, and characterize the injector, RFQ, first section of CCDTL, and all necessary interface components to help prove the feasibility of the APT 100-mA, cw linac. At this stage, the injector and RFQ (Fig 1) are functional and undergoing initial integrated beam testing.

Figure 1: Computer rendering of LEDA, showing injector and its electronics on left, RFQ inside frame, and short transport line and beam stop.

1.2 Injector

The unique LEDA injector[2] uses an ion source that is a slightly modified version of a simple and effective microwave-driven proton source developed at Chalk River Laboratory in Ontario. One unique feature of this source is that no electronics reside at high potential. Even the electromagnetic solenoids are at ground potential, separated from the source chamber by a specially designed polypropylene insulator. Microwave power is fed through an insulated waveguide break, allowing the 2-kW, 2.45-GHz power source to be at ground potential. Similarly, the hydrogen gas feed is through a small-diameter insulated tube kept at near atmospheric pressure to suppress breakdown.

The extractor is a 75-kV single-gap, shaped-surface configuration, with integral electron suppression. Both triode and tetrode versions have been tested[3]. The transport line[4] is about 2.7 m long, and includes two electromagnetic solenoids for focusing, and two pairs of dual-axis steerers. Variable and insertable ring collimators are used for additional beam-current control. Vacuum pumping and several diagnostic devices (mostly non-interceptive) are included in this transport line.

This injector configuration (Fig.2) has been tested[5] since 1992, demonstrating consistently excellent performance, including injection into a cw RFQ[6]. For example, this injector can provide more than 130 mA of ion current, with 90% proton fraction, at a rms normalized emittance of 0.19 π mm mrad. The LEDA injector sits on rail-mounted platforms to facilitate easy movement to the RFQ. Strict attention to layout and grounding guarantees that neither equipment damage nor computer upsets result from infrequent high-voltage sparkdowns[7].

Figure 2. Beamline hardware of the LEDA Injector.

1.3 Radio-Frequency Quadrupole

The LEDA RFQ must provide excellent performance under very demanding cw operation[8]. Output energy is 6.7 MeV, with proton injection at 75 keV. Total length is approximately 8 meters, comprised of eight sections to facilitate brazing. There are four 2-m-long resonant segments to facilitate RF tuning of this structure. After precise alignment during brazing and assembly, 128 static slug tuners are used to ensure proper field distribution and to reduce non-quadrupole fields to less than 2% of the primary field. During operation, structure resonance is maintained by precise automatic adjustment of the cooling water temperature[9]. Temperature control of the RFQ copper structure controls cavity dimensions and resonant frequency. Design peak fields for this cw RFQ are 1.8 Kilpatrick or 33 MV/m at 350 MHz.

All major pieces of the RFQ resonant structure are made of OFE copper. Some flanges are made of GlidCop™, a strengthened version of OFE, fortified with a suspension of aluminum oxide powder to increase hardness.

A major engineering challenge on this RFQ was to properly support this 8-m long, cylinder of annealed OFE copper. The weight (2360 kg) of the RFQ is supported by five struts, attached to the flanges separating the two-meter-long segments. The outer ends of these struts attach to a very study steel frame, that in turn is held above the floor by three kinematic mounts. A similar set of seven horizontal struts constrain the RFQ in transverse and longitudinal motion.

All other RFQ-related hardware, including windows, vacuum and water manifolds, and vacuum waveguide sections, are separately suspended from the outer steel frame, to avoid putting undue stress onto the RFQ copper.

Figure 3. Cross section of the LEDA RFQ, showing locations of the 24 water cooling channels in each of the eight sections.

Three of the eight RFQ sections have provisions for balanced RF power feeds, one into each quadrant of that section. Well-cooled, tapered, ridged vacuum waveguides carry this power to a coupling slot in the outer wall of the RFQ. Each coupling slot (Fig.4) is approximately 1.7 mm wide, by 8.9 cm long. A coaxial RF window is used

to separate atmospheric WR2300 waveguide from a half-height vacuum waveguide (Fig. 5).

Figure 4. Geometry of RF coupling iris, through which RF power enters the LEDA RFQ.

Figure 5. Depiction of the RF window assembly for feeding power into the RFQ.

All vacuum systems[10] used on LEDA are oil-free to minimize the chance of internal oil contamination on accelerating structures. Cryogenic pumps are used for the RFQ cavity, and non-evaporative getter (NEG) pumps maintain an a high-vacuum environment for the RF windows. Turbo-molecular pumps provide additional pumping for all structures.

1.4 RF Power

LEDA's RF power system[11] includes a number of both 350-MHz and 700-MHz cw transmitters. Three of the 350-MHz systems are dedicated for use on the RFQ. Although each 350-MHz RF klystron is rated for, and has demonstrated, 1.3 MW of supplied power, losses, mismatches, and control margin reduce the effective per-klystron RFQ-delivered power to just under 1.0 MW. Ohmic losses in the walls of the RFQ are approximately 1.2 MW, and absorbed beam power is about 0.67 MW. Two klystrons should thus provide all power needed for full-current operation, but this entails running the klystrons very near maximum levels. The third klystron was included to ensure that we have adequate operational power margin. We are now running 2 RF systems into the RFQ using the accelerating cavity as a power combiner. The third 350-MHz RF system is ready for use, but is not presently attached to the RFQ.

A nominal 1 MW of 350-MHz RF power from each klystron is carried through WR1500 waveguide about 40 meters from the klystron, to a magic-tee power splitter, and then split again. Power from each klystron[12] is split

equally into four feeds, each of which enters a quadrant of the RFQ. Commercial coaxial RF windows are used to separate the atmospheric waveguide from the stepped, ridged vacuum waveguide transitions that feed this power to the coupling irises on the RFQ outer wall. These commercial RF windows were tested[13] at sustained cw power levels of 1 MW, in preparation for use on the RFQ at less than 0.34 MW.

LEDA's specialized low-level RF (LLRF) system has a number of functions[14], including maintaining correct power and phase in the cavity fields. Controller boards for these functions use I & Q control[15] rather than direct amplitude and phase. A combination of digital and analog control loops is used to provide both long-term precision and fast response.

The LLRF system must maintain the RFQ cavity on resonance. This is done by sending a signal to the resonance-control cooling system (RCCS) that in turn makes adjustments to the cooling water temperature at the RFQ vane bases. Cooling water temperature is the only dynamically adjustable parameter for the RFQ. Protection against internal arcs and faults both in the RFQ cavity and in the several RF windows near the RFQ are additional functions provided by the LLRF system.

1.5 Beam Stop and Transport Line

The innovative beam stop is described previously[16] Key features of this design are its compactness, light-weight, integral neutron shielding, low radiation source term, simplicity, and ease of replacement or removal. Audio sensors on the cartridge should sense any unexpected water boiling well before thermal failure of the structure.

A smaller prototype was demonstrated with a 125-kW beam from the CRITS RFQ. A LEDA beam-stop replacement cartridge is under development now at General Atomics that includes an internal carbon liner to further reduce the prompt and residual radiation source term.

The high-energy beam transport (HEBT) line[17] is as simple and short (2.5 m) as feasible, includes five quadrupoles, two dual-axis beam steerers, vacuum pumping, and a number of beam diagnostic devices[18].

1.6 Facilities Upgrades

When LEDA assumed occupancy of an existing building at Los Alamos, that facility had only about 3 MW of ac power and cooling capacity. In order to operate up to six RF transmitters and other equipment, LEDA needs nearly 15 MW of power. We upgraded the raw ac power and distribution system and installed ten specialized cooling systems needed for all accelerating structures and related equipment.

This upgrade activity required as many as 85 crafts people working adjacent to a number of experimentalists. In this process, the LEDA project accumulated more than 220,000 construction man-hours with only a single minor lost-time accident.

1.7 Controls

The EPICS[19] system is used for all integrated controls on LEDA, although LabView is often used for off-line development of individual subsystems. In several instances, e.g. high-power RF and vacuum systems, a dedicated PLC (programmable logic controller) is used to facilitate local operation and to handle most interlocks. But, during integrated system operation from the control room, EPICS provides operator tools and links to nearly all read-back and control channels.

1.8 Safety and Protection Systems

The primary personnel safety system on LEDA is the personnel access control system (PACS), whose function is to ensure that personnel are excluded from the beam tunnel's potentially high radiation areas during beam operation. This LEDA safety system represents the best version of the PACS units used on LANSCE. All PACS wiring is in protected conduits, all switches are redundant and tamper-proof, all logic (in redundant, locked boxes) is via a dedicated PLC, and strict administrative controls are used for all installation, checkout, and routine use.

A backbone beam enable (BBE) hard-wired circuit is implemented in a fashion very similar to the PACS. This system ensures that beam operation is inhibited whenever hardware configurations are outside the safe operating boundary. One input example is the water level in a neutron shield tank surrounding the beam stop.

A hard-wired fast-protect system is used to interrupt beam current within a few micro-seconds in the event of a of a malfunction that indicate possible beam misbehavior.

A large fraction of the instrumented channels on LEDA are monitored by the beam run-permit system. This equipment-protection function is done in EPICS software, and may have response times approaching one second. However, its purpose is to ensure that beam delivery is permitted only when all critical systems are in proper operation and alignment.

Of course, many hard-wired interlocks are used extensively throughout LEDA. Adequate water flow in various electromagnets and valve positions are typical examples.

The LEDA Accelerator Readiness Assessment (ARA) process included a simultaneous review by an independent contractor team and a DOE team. This process, although demanding for a one-week period, worked extremely well. This readiness review was done the first week in December, 1998; only three working days after we were able to initiate RFQ conditioning with a single 1-MW klystron. Closeout of the ARA process was completed on March 12, two working days before our first RFQ-accelerated beam.

All our documentation and operational approval processes have been expedited by early and fruitful collaboration with all parties, especially with DOE, our sponsor for this work.

2 BEAM TESTING

2.1 RFQ Conditioning Notes

Initial conditioning[20] was done with a single klystron feeding into the four ports of segment B, with segment C ports blanked off, and waveguide terminations properly positioned outside segment D windows. All subsequent conditioning has been done with two phase-locked 1-MW klystrons, feeding into segments B and D.

At very low power levels (a few kW) we saw the expected initial multipacting in all window assemblies. However, some amount of multipacting persisted to higher-than-expected power levels. With four windows installed, we saw multipacting up to powers of about 400 kW. With eight windows, multipacting continued to about 800 kW. Thus we conclude that multipacting may be a problem up to about 100 kW on each window assembly. While this multipacting may assist in cleaning the coaxial metal surfaces, we saw typical vacuum outgassing while multipacting was present. Because of the 100 kW/window-assembly multipacting, we are planning a change in our configuration that requires fewer than 12 windows. If we stay with 12 windows, we could have multipacting up to the design operating level of 1.2 MW.

Another unexpected occurrence was localized melting at the edges of a few of the coupling irises. Each coupling iris is approximately 1.5 mm wide by 8.9 cm long. During the final tuning process, custom-sized holes (about 2 mm in diameter) were cut at the ends of each slot. After several hours of conditioning at full power levels, we discovered that the edges of some of these holes had melted, but only in the irises with the smaller diameter holes. Simulations with FEA codes indicated a wall-current enhancement factor of about 9 or 10 on these smaller holes. This was sufficient to raise a small amount of copper to above the melting temperature.

In most respects however, the conditioning went very well. We saw a few cavity shorts and vacuum bursts in the RFQ cavity. A "blanking box" detects high reflected power, and removes RF drive within a few μs, to ensure there is no surface damage from the arc. Conditioning maintained even after the RFQ was 'let up' to atmosphere with dry nitrogen, with subsequent re-conditioning requiring less than twenty minutes. Balancing the conditioning process for simultaneous conditioning of eight windows and the RFQ cavity required much care and learning. Progressive conditioning is a dynamic balance between peak power, duty factor, pulse length, a dc floor level of power, and proper frequency tracking. For successful conditioning, it is imperative to continuously monitor and maintain low pressures in all windows and the RFQ cavity.

2.2 Beam Commissioning

Initial beam operation was promising[21], in that we saw good transmission through the entire system on the very first beam pulse on March 16. Output beam energy was right on the design value of 6.7 MeV. RFQ transmission and output bunching have the expected behavior as the RF power is varied in the RFQ cavity.

Very limited beam testing during the past week has verified that the several diagnostic devices and systems work as expected. We have measured RFQ transmission, beam energy, acceptance of the injected beam, verified output beam steering and focusing, and confirmed that all sensors and protection systems are functional. Early beams used short pulses (<1 ms), low repetition rates (5—10 pps) and low currents (<30 mA) (Fig 6) to facilitate debug and tuneup with minimal risk of component damage.

Figure 6. A 1-ms, 27-mA beam pulse from the LEDA RFQ

Low-duty-factor beam-profile measurements are being checked with a two-dimensional wire scanner[22]. Later, video cameras and processing software will be used to measure profiles under cw conditions. These, and most other diagnostics[23] are mounted in the beam transport line immediately downstream of the RFQ.

Although our critical diagnostics gear[24] is functional, we do not have operating interfaces from all diagnostics into the central control system. Integration and checkout of these systems requires additional beam time. The damaged coupling irises place a limit on the average power we can sustain inside the RFQ, thus we need to run at less-than-ideal cavity power levels. Even though we cannot cw condition the cavity to the desired 120% of design power, our pulse conditioning has extended to at least 125% (1.5-MW) of design level.

During the past week, we have moved from initial beam operation at 5 pps, 500-μs, 8-mA to reliable operation at 10 pps, 2.5-ms, and 40-mA.

We expect that near-future RFQ commissioning will benefit from the successful experience[25] of testing the CRITS RFQ about one year earlier, where beam tests used the LEDA injector and demonstrated up to 100 mA of cw proton output beam. For those tests, the injector was operated at 50-keV, yet delivered as much as 130 mA of intput beam.

3 SCHEDULE

Design of the RFQ began in 1995, fabrication in 1996. Assembly was underway in early spring of 1998, and most of the remainder of 1998 was consumed by adding all utilities, support systems and completing final tuning[26]. First high-power conditioning began in late November, and initial beam was introduced in mid-March, 1999.

Beginning in late April, we expect to replace the RF coupling irises with more robust units, then increase our peak and average powers until we are able to sustain cw operation with 100 mA of proton beam current. At design power levels, the RFQ output beam will have a power of 670 kW.

The coming year will be spent in fully testing the RFQ with beam. Then, we will install a short section of coupled-cavity drift-tube linac (CCDTL) onto the end of the RFQ to permit a complete test of beam matching from the RFQ into the untested CCDTL structure.

Two complete 700-MHz RF systems, including three 1-MW klystrons, are in place in the LEDA facility, and are being used for testing components that will be used on the remainder of the LEDA and APT accelerators.

This low-energy beam testing on LEDA will be an important confirmation of the linac design[27] chosen for the APT and similar linacs[28].

4 LEDA PARTICIPANTS

Completion of the LEDA hardware involves teaming among several organizations. Some examples include:

- The injector was built using the ion source from Chalk River Labs.
- Initial RFQ beam tests were done with the cw CRITS RFQ, also from Chalk River.
- The vacuum system for the LEDA RFQ was designed, built, and installed by personnel from Lawrence Livermore National Laboratory (LLNL).
- A team from Allied Signal's Kansas City Plant provided the cooling and resonance-control system for the RFQ.
- Development of the beam stop and transport lines from the RFQ to beam stop was completed by teams from General Atomics.
- LANL is teamed with Burns & Roe, General Atomics, and Westinghouse Savannah River Company for the completion of the APT project.

A project of the size and complexity of LEDA can be successful only through the hard work and excellent collaboration of hundreds of people from many organizations. We extend our sincere thanks to all these teams who helped to make LEDA a success.

5 REFERENCE

[1] J. D. Schneider, "APT Accelerator Technology," Proceedings of the 1996 Linac Conf. MO202.

[2] J. Sherman, et al, " A DC Proton Injector for Use in High-Current CW linacs," p. 1424, Proceedings of EPAC98.

[3] T. Zaugg, et al, "Operation of a Microwave Proton Source in Pulsed Mode", LINAC98 Proceedings.

[4] H.V. Smith, et. al, "Comparison of Simulations with Measurements for the LEDA LEBT H⁺ Beam," these conference proceedings.

[5] J. Sherman, et al, "Development and Test Results of the Low-Energy Demonstration Accelerator (LEDA) Proton Injector on a 1.25-MeV cw Radio Frequency Quadrupole," Linac 98 Proceedings.

[6] J. Sherman, et al,"Half-Power Test of a CW Proton Injector Using a 1.25-MeV RFQ," these conference proceedings.

[7] M. Thuot, et al, "A Transient Tolerant Automated Control System for the LEDA 75-keV Injector," these proceedings.

[8] D. Schrage, et al, "CW RFQ Fabrication and Engineering", LINAC98 Proceedings.

[9] R. Floersch & G. Domer, "Resonance Control Cooling System for the APT/LEDA RFQ," Linac98.

[10] K. Kishiyama, et al, "Testing of Vacuum Pumps for APT/LEDA RFQ," Linac98 Proceedings.

[11] J. Bradley III, et al, "An Overview of the Low-energy Demonstration Accelerator (LEDA) Project RF Systems," PAC97

[12] W. T. Roybal, et al, "LEDA RF Distribution System Design and Component Test Results," LINAC98 Proceedings.

[13] K. Cummings, et al, "Results and Lessons Learned from Conditioning 1-MW CW 350-MHz Coaxial Vacuum Windows," Linac98 Proceedings.

[14] A. H. Regan, "LEDA LLRF Control System Characterization," LINAC98 Proceedings.

[15] A. H. Regan, et al., "APT LLRF Control System Functionality and Architecture," Proc. 1996 Linac Conf. MOP68.

[16] T. H. Van Hagan, D. W. Doll, "Design of an Ogive-Shaped Beamstop," LINAC98 Proceedings.

[17] W. P. Lysenko & J. D. Gilpatrick, "High-Energy Beam Transport Beamline for LEDA," Linac98 Proceedings.

[18] J. D. Gilpatrick, et al, "LEDA and APT Beam Diagnostics Instrumentation," PAC97 Proceedings.

[19] M. Thuot, et al, "The Success and Future of EPICS," Proc. 1996 Linac Conf.

[20] L. Young and L. Rybarcyk, "High-Power RF Conditioning of the LEDA RFQ", these conference proceedings.

[21] K. Johnson, "Commissioning of the Low-Energy Demonstration Accelerator (LEDA) Radio-Frequency Quadrupole," these conference proceedings.

[22] J. F. Ohara, et al, "Design and Development of the LEDA Slow-Wire Scanner Profile Measurement," Linac 98 Proceedings.

[23] J. D. Gilpatrick, et al, "LEDA and APT Beam Position Measurements System: Design and Initial Tests," Linac98 Proceedings.

[24] J.D. Gilpatrick, et al., "Low-Energy Demonstration Accelerator (LEDA) Beam Instrumentation: RFQ-Accelerated Beam Results," these proceedings.

[25] H. V. Smith, et al, "Comparison of Beam Simulations with Measurements for a 1.25-MeV Cw RFQ," Linac98 Proceedings.

[26] L. M. Young & L. Rybarcyk, "Tuning the LEDA RFQ 6.7-MeV Accelerator," Linac98 Proceedings.

[27] G. P. Lawrence, "High-Power Proton Linac for APT: Status of Design and Development," Linac98 Proceedings.

[28] P. W. Lisowski, "The Accelerator Production of Tritium Project", PAC97 Proceedings.

INITIAL COMMISSIONING OF THE ISAC RIB FACILITY

P.W. Schmor, TRIUMF, Vancouver, BC, Canada, V6T 2A3

Abstract

Construction began in 1995 on ISAC, a radioactive ion beam (RIB) and accelerator facility at TRIUMF that utilises the ISOL (on-line isotope separation) production method. ISAC includes: a new building, a beam line with adequate shielding to transport up to 100 uA of 500 MeV protons to two target/ion-source stations, remote handling facilities for the targets, a high-resolution mass-separator, linear accelerators and experimental facilities. The ISAC target/ion source station permits the production of nuclei far from stability over a large isotopic range with high luminosity. Ions from the target/ion-source can be transported at energies up to 60 keV through a low-resolution pre-separator magnet followed by a high-acceptance, high-resolution mass-separator magnet to a variety of low energy experimental stations. Alternatively, ions with q/A greater than or equal to 1/30 and an energy of 2 keV/amu can be bunched in the low energy beam transport line prior to a cw RFQ accelerator operating at 35 MHz. The 150 keV/amu beam from the RFQ is stripped and isotopes with a particular q/A greater than or equal to 1/6 are selected for acceleration in a DTL. The DTL is a separated function accelerator with five accelerating tanks and three split-ring bunchers operating cw at 105 MHz. The final energy will be variable from 0.15 to 1.5 MeV/amu. The accelerated beams will be used primarily for nuclear astrophysics studies. The beam commissioning of the proton beam line, target/ion source, mass separator and RFQ has started. The TRIUMF neutral atom trap (TRINAT) and a yield station began using the low energy ISAC beam in November 1998. The RFQ has accelerated stable ions up to 54 keV/amu. The first tank of the drift tube linac and the subsequent buncher have been commissioned at full rf power. Beam commissioning of the DTL is scheduled for the end of 1999. The full-energy RIB will become available for the DRAGON recoil spectrometer at the end of 2000. A new five-year plan that includes an upgrade of ISAC to permit acceleration of radioactive ions up to 6.5 MeV/amu for masses up to 150 amu has been presented for funding.

the target and primitive remote handling procedures for servicing irradiated components around the target have limited the proton beam intensity at TISOL to about 2 μA. TISOL will continue to be useful in the future as a facility to test new targets and ion sources for ISAC, albeit at lower currents. The design specifications for the ISAC-I RIB delivery system are listed in table 1.

Table 1: Design Parameters for ISAC I

ISOTOPE PRODUCTION SYSTEM		
Driver	Projectile	Protons
	Energy	470 – 510 MeV
	Intensity	# 100 μA
	Beam Size	# 1 cm^2
	Time Structure	cw
Target	Length	#_20 cm
	Power Deposited	# 20 kW
RADIOACTIVE ION BEAM SYSTEM		
Ion Source	Surface, ECR, Laser, FEBIAD, etc.	
	Max. Energy	# 60 keV
Mass Separator	Mass/δ(Mass)	# 10000
	Mass	# 240
	Vacuum	# 2x10^{-7} torr
ACCELERATOR SYSTEM		
Pre-Buncher	Fundamental Frequency	11.67 MHz
	Harmonics	3
RFQ	Input Energy	2 keV/amu
	Input charge/mass	∃ 1/30
	Output Energy	150 keV/amu
	Frequency	35 MHz
DTL	Charge/mass	∃ 1/6
	Output Energy	0.15 to 1.5 MeV/amu
	Frequency	105 MHz
	ΔE/E	< 0.1%

1 INTRODUCTION

There have been more than ten years of experience with radioactive ion beams at TRIUMF using the TISOL facility [1]. TISOL is a first generation ISOL type facility that has not only provided useful beams for scientific research but has also provided valuable information on targets, ion sources and remote handling requirements for a second generation facility. Although the proton beam line for TISOL is capable of 10 μA, inadequate shielding above

2 ISAC CIVIL CONSTRUCTION

The first major ISAC-I construction contract (for the relocation of site services) was awarded in May 1996 followed by the primary structure contract commencing in September 1996. In July 1997, TRIUMF personnel began occupying the experimental hall for installation of experimental apparatus. Figure 1 is a sketch of the building layout showing through cut out sections the main features

of ISAC-I. The main elements of the facility include the following; (a) a bored hole through the cyclotron vault wall and an underground tunnel to transport the high intensity proton beam from the cyclotron to the ISAC target stations, (b) a four story target service wing containing a chemistry laboratory, an assembly laboratory, a meeting room, service elevator, active sumps and two open areas for offices, (c) a heavily shielded target vault containing two target stations, shielding for two 50 kW beam dumps, two hot cells, a target storage pit, all of which can be accessed with a remotely controlled 20 ton rolling crane, (d) a penthouse above the target vault housing the HEPA filtered exhaust system, the building mechanical services and the heat exchanger, (e) a shielded room for a high resolution mass separator, (f) a grade level experimental hall for the accelerators and experimental stations with a 35 ton rolling crane, (g) a 250 kW diesel generator for emergency power, (h) two experimental counting rooms and (i) an accelerator control room.

Figure 1. A sketch of the ISAC-I facility showing the proton beam line, the target vault, the target service building, the mass separator vault, the TRINAT mezzanine (above the mass separator vault) and the accelerator/experimental hall.

3 ISAC TECHNICAL FACILITY

3.1 Proton Beam Line

A new beam line was built to take the proton beam from the cyclotron to the ISAC-I target. In May 1997, proton beams were extracted from the cyclotron into the front end of the beam line over the energy range 472 to 510 MeV. The entire beam line was completed to the ISAC-I beam dump by the spring 1998. This culminated with the timely completion of a major milestone, namely, beam to the ISAC beam dump in May 1998.

3.2 Target

The target hall vault has three main areas; a target area, a storage area and a hot cell area. The entire vault is serv-

iced by a 20 ton overhead crane that can be operated remotely from the target service building. In order to achieve efficient ISAC operation, it was necessary to shield the target area such that personnel could work in the target vault during beam operation. The required shielding was estimated assuming a 100 μA proton beam impinging on a high z target such as uranium. The shielding surrounds two, large, T-shaped, steel vacuum-tanks which each contain five removable modules. Two of the modules (an entrance module that contains proton beam diagnostics and an exit module that houses the proton beam dump) are required for the proton beam. The remaining three modules (a target module which holds the target, ion source and ion beam extraction electrodes and two exit modules which contain the ion beam optical elements and the ion beam diagnostics) are required for the RIB. These three modules have all of the ion optical elements placed inside of a primary vacuum vessel within the secondary vacuum space of the T-shaped tank. The dual vacuum system is designed to prevent radioactive contamination from migrating to either the outside walls of the modules or to the entrance and dump modules. The entrance and dump modules are located in the secondary vacuum of the large tank. Water-cooled windows are used where the proton beam enters and exits the target module. The volatile compounds that are pumped from the target tank are stored in tanks, monitored for activity and allowed to decay to acceptable levels prior to release to the atmosphere through HEPA filters. Although both target tanks were manufactured, initially only the west target tank and five modules are presently operational. The second tank is used to condition, store and leak check spare modules. The servicing philosophy of the components in the tanks is based on years of successful experience with the meson production targets. The services are manually disconnected from a module requiring servicing and then the overhead crane is used to pick up that module and transport it to either a storage vessel or to the hot cell where manipulators are used to remove and replace components. Details of the target station are found elsewhere in these proceedings [2].

Initially the beam current on target was only about one microampere. During this stage it was necessary to provide ohmic heating in order to achieve the required target temperature (about 1500° ± 100° C). These targets are similar to those presently used in TISOL. As the proton beam current (beam power) is increased it will eventually be necessary to cool the target.

3.3 Ion Source

The operational target and ion-source system requires frequent servicing to meet the experimental requests for isotopes. The first ion source to be approved for ISAC-I experiments is a surface ion source for alkali elements. A double-gap extraction system was designed and tested. The beam could be extracted over a wide range of masses

and energies without intensity or emittance degradation. As predicted by the simulations, it was unnecessary to adjust the electrode position each time a new mass or new ion energy was selected. The ion source and target have been designed to operate up to a maximum bias of 60 kV. The first experiment approved by the TRIUMF Experimental Evaluation Committee (EEC) required ^{37,38m}K beams. ISAC used a compressed CaO pellet target to produce the potassium isotopes. Other isotopes requiring different ion sources are required quickly. An electron-cyclotron-resonance (ECR) ion source has been very useful in ionising gaseous elements in TISOL. Development has started on a compact microwave ECR ion source. ECR ion sources produce ions with energy spreads of tens of eV. It is not possible to achieve a mass resolution (isobaric rejection) greater than 10,000, unless the energy spread is kept below about 2 eV. The initial experiments, requiring an ECR ion source, have not requested a high mass-resolution. Provision has been made so that the ISAC system can accommodate laser ion sources, FEBIAD ion sources and Cusp ion sources. These sources will have to be developed for ISAC as required by the scientific programs.

3.4 Mass Separator

The ISAC mass separator system includes a pre-separator magnet, three matching sections using electrostatic optics, an acceleration column, a mass analysing magnet and a deceleration column. The ion optics were calculated using the computer code GIOS which was modified to predict the effect of the acceleration columns. The pre-separator stage uses a >Y= shaped magnet that is designed to accept the RIB from either one of the two target stations. Its purpose is to select out most of the unwanted radioactive ions and to deposit this activity on slits that can be removed remotely to the hot cells for servicing. The mass separator-magnet was acquired from Chalk River in August 1997, following the closure of the TASCC laboratory. The separator is located on a high voltage platform that will eventually raised in potential up to 60 kV. By varying the potential of the mass separator it will be possible to scan and select a particular isotope without readjusting the magnetic field of the magnet. The system has been designed to provide a mass resolving power of 10,000 for an emittance of 30 π mm mrad. An outline drawing showing the configuration of the mass separator system is given in figure 2.

3.5 Low Energy Beam Transport

The ion beam from the mass separator can be transported either to the low energy experimental area or to the RFQ accelerator. At the same time, it is desirable to have an off-line ion source (OLIS) to provide a beam of stable isotopes to the same two areas, although its primary purpose is for commissioning the accelerators. A switchyard has been designed and built to meet these goals. All of the

optics in the low-energy-beam-transport (LEBT) is electrostatic. The line is made up of a number of similar modules. Spherical bends are used to achieve focusing in both transverse planes. The RFQ, having no bunching section, requires an external buncher in the LEBT. The section of the LEBT that connects the mass separator to the rest of the low energy beam line was assembled for the October 1998 beam commissioning to TRINAT. The LEBT from the OLIS to the RFQ was commissioned early in 1998. The installation of the OLIS began in July 1997 and the first ion beam was extracted in November of the same year. The LEBT and buncher were commissioned from OLIS to the entrance of the RFQ by March 1998.

Figure 2. Layout of the beam transport system at the target elevation from the target station through the mass separator system to the LEBT

3.6 Accelerators

Beams having a mass to charge ratio less than or equal to 30 are to be accelerated from the injection energy of 2 keV/amu up to a final energy of 1.5 MeV/amu. The accelerating system consists of a pre-buncher, a cw RFQ, a medium energy beam transport (MEBT) section, an electron stripper, a re-buncher, and a cw drift tube linac with three split ring bunchers [3],[4],[6],[7]. The pre-buncher provides a pseudo saw tooth velocity profile at a fundamental frequency of 11.67 MHz, thereby providing approximately 86 nS between beam bursts. Bunched beam from the pre-buncher fills every third bucket of the 35 MHz, cw, 8 m long RFQ. The beam out of the RFQ, at energy 0.15 Mev/amu, is first focused and stripped to

higher charge states. The beam is then magnetically bent to select only those isotopes having a mass to charge ratio less than or equal to 6 and then re-bunched in a 35 MHz spiral re-buncher prior to injection into the first tank of the DTL. The DTL must provide a bunched beam that can be continuously varied in energy from 0.15 to 1.5 MeV/amu. To achieve this a separated-function structure with five DTL tanks and three split-ring bunchers has been designed. As the DTL and buncher system operates cw at 105 MHz, only 1 in 9 rf buckets are used to accelerate beam.

Figure 3. Initial transmission of atomic and molecular nitrogen ion beams through the 7 ring RFQ with and without pre-buncher as a function of vane voltage.

In order to demonstrate that the RFQ would operate cw at 35 MHz, a 1 m long (3 rings) prototype was successfully tested without beam but at full power in November of 1996. The RFQ accelerator requires precise alignment to operate with the predicted acceptance. In order to demonstrate that the required alignment had indeed been achieved and that the numerical simulations were correct, a RFQ tank with only the first 7 of the eventual 19 rings was commissioned with beam in 1998 [8]. Beams of stable nitrogen isotopes were produced in the off line ion source and accelerated through the RFQ to a diagnostic station. The ion source provided both atomic (mass 14) and molecular (mass 28) ions. The beam transmission and acceptance of the RFQ were found to be in excellent agreement with predictions. In figure 3 the transmission through the RFQ is shown as a function of the two masses as a function of vane voltage.

A prototype 35 MHz spiral re-buncher was built in 1998 and has been tested at signal level [5]. The operational spiral buncher should be ready for installation by the end of 1999. The first tank of the DTL with electrodes

has been manufactured and tested at full power. The remaining four tanks will be sent out for manufacture in 1999 with the second tank ready for installation early in 2000. The first DTL split-ring buncher was built in collaboration with the Institute for Nuclear Research by the rf group at INR, Troitsk, Russia [6]. This buncher was delivered to TRIUMF in August 1998 and subsequently tested successfully at full power. This group is now constructing the remaining two bunchers. Detail design has started on the four magnetic triplets required to achieve transverse focusing between each DTL tank. Figure 4 locates the accelerator systems within the 30m wide by 64m long experimental hall.

Figure 4. The layout of the experimental/accelerator hall in ISAC-I shows the locations of the accelerators and the various experimental stations. The lifetime station is located to the right of the yield station.

3.7 ISAC Science Facilities

The initial experimental program at ISAC includes several experimental stations. Space in the experimental hall in ISAC has been allocated to accommodate these facilities. In particular, the experimental stations include; the TRIUMF Neutral Atom Trap (TRINAT), a Yield Station, the Low Temperature Nuclear Orientation system (LTNO), a General Purpose & Lifetime measurement station, the recoil mass spectrometer (DRAGON) facility and a ^{8}Li polarizer for the β-NMR station. The hall can accommodate additional stations. In particular, it is anticipated that the Canadian Penning Trap will move to ISAC when beams of interest become available. TRINAT is located below grade in a well-shielded mezzanine above the mass separator. The layout of the stations is given in figure 4.

TRINAT has been trapping radioactive atoms at the TISOL facility in a Zeeman optical trap. Detection of the decay products from these trapped atoms permits sensitive tests of the Standard Model. The trap was recently moved from TISOL to ISAC where the higher beam flux should yield increased sensitivity. In nuclear astrophysics, many of the reactions of interest involve proton or alpha captures. The ISAC nuclear astrophysical experiments will be carried out with reverse kinematics by bombarding a

high-pressure windowless gas-target with the accelerated radioactive ion beams. The reaction products are detected using a recoil mass fragment detector, DRAGON, designed to have a high detection-selectivity at the ISAC energies. The nuclear orientation facility (LTNO) has been shipped from ORNL to TRIUMF and has been reassembled in the low energy experimental area of ISAC. The initial scientific program for the LTNO will focus on nuclear structure in the mass range 80 to 100. In addition the facility will use nuclear magnetic resonance on oriented nuclei (NMRON) as a sensitive probe of condensed matter. The μSR group at TRIUMF is building a β-NMR facility that initially will be using a polarised ^{8}Li beam to enhance their condensed matter program at TRIUMF. The longer lifetime of the radioactive isotope, compared to that of the muon, makes it the preferred probe for relaxation studies in solids.

4 COMMISSIONING/OPERATION

A 1 μA proton beam has been transported from the cyclotron to the ISAC beam dump. It is expected that a target will be ready to permit a full power test at 100 μA by December 1999. A beam of stable isotopes was delivered to TRINAT in October 1998. In November the proton beam was used to produce a radioactive potassium beam from a CaO target for TRINAT and the ISAC lifetime station. Operation of the low energy beam will expand to the other low-energy experimental-stations as they become available in 1999. The off-line ion source allows the RFQ, MEBT, DTL and HEBT commissioning to take place at the same time as the radioactive beam is being delivered to the low energy experiments. The schedule anticipates that by the end of 2000 the accelerators will be operating and that the high-energy experiments will be ready for an accelerated radioactive ion beam.

5 FUTURE PLANS

The five-year funding cycle, which was used to build ISAC-I, began in June 1995 and ends in April 2000. A new proposal for the next five years was prepared for submission to the Canadian Government in November 1998. In response to TRIUMF=s request for input into the new five-year plan, the Canadian user community made a strong submission to have ISAC-I augmented up to an energy of 6.5 MeV/amu for masses less than or equal to 150. These submissions were used to produce some generalised facility specifications [9]. . Additionally, a request to provide slightly higher energies for the lighter masses is possible with this design. The proposed ISAC-II facility is shown in figure 5. The design would use a charge state booster in the LEBT before the RFQ and accelerate the isotopes in a new DTL to 400 keV/amu before further stripping the heavier masses to higher charge states for acceleration through a superconducting linac. A modest grade-level building expansion will be required to ac-commodate the additional accelerators and experimental stations. Construction of ISAC-II could be staged in order that the nuclear physics program can begin prior to facility completion. To achieve this early start to an experimental program, it is proposed to carry out the building construction concurrently with the assembly of small superconducting rf cavities. These cavities would then be initially installed, as they become available, downstream of the DTL1 in the ISAC-I experimental hall.

Figure 5. This proposed layout for ISAC-II shows how the accelerators and experimental stations might be added to ISAC-I.

6 REFERENCES

[1] J.M. D'Auria et al., Nuclear Instruments and Methods in Physics Research **B 126**, 7-11 (1997)

[2] P. Bricault et al., "A 500 MeV 100 micro Amp proton Target for ISAC Radioactive Ion Beam Facility", these proceedings, MODR4

[3] R.L. Poirier et al., "RF Systems of the ISAC Facility", these proceedings, THBL4

[4] M. Laverty et al., "Design and Testing of the TRIUMF ISAC RFQ Control System", these proceedings, MOP94

[5] A.K. Mitra, R.L. Poirier, "A 35 MHz Spiral Re-Buncher Cavity for the TRIUMF ISAC Facility", these proceedings, MOP75

[6] Y.V. Bylinsky et al., "High Power Test of the ISAC Triple Gap Buncher Operating in CW mode", these proceedings, MOP95

[7] P. Bricault et al., "Initial commissioning of the DTL Tank1 of the ISAC LINAC", these proceedings, FRA66

[8] R.E. Laxdal et al., "Final Beam Test Results with the ISAC 35 MHz RFQ", these proceedings, A08

[9] R.E Laxdal, R.A. Baartman, "Design Optimization of the proposed ISAC-2 Project at TRIUMF", these proceedings, FRA65

ACCELERATOR COMPLEX
FOR THE JOINT PROJECT OF KEK/JHF AND JAERI/NSP

Y. Yamazaki, M. Mizumoto, and JAERI/KEK Joint Accelerator Team

KEK, High Energy Accelerator Research Organization

1-1 Oho, Tsukuba-shi, Ibaraki-ken, 305-0801, Japan

JAERI, Japan Atomic Energy Research Institute

Tokai-mura, Naka-gun, Ibaraki-ken, 319-1195, Japan

Abstract

The JHF of KEK and the NSP of JAERI were joined to form one project in order to more effectively promote a wide range of scientific and engineering fields included in either of the projects. The Joint Project is divided into two phases. Phase I comprises a 400-MeV linac, a 3-GeV, 1-MW rapid-cycling synchrotron and a 50-GeV synchrotron. Phase II is the upgraded system, which includes a several-MW pulsed spallation neutron source. The high-energy linac of the Phase I will be a superconducting one, in order to develop one of the most crucial accelerator techniques for realizing an accelerator-driven nuclear waste transmutation system. The R&D results accomplished for the Joint Project are highlighted.

1 INTRODUCTION

High Energy Accelerator Research Organization (KEK) and Japan Atomic Energy Research Institute (JAERI) agreed with each other to bring the Japan Hadron Facility (JHF) Project [1-7] of KEK and the Neutron Science Project (NSP) [8-10] of JAERI into one joint project. Both projects have some common features which can be summarized by a single key word, that is, "high-power proton accelerators." The JHF project was from the beginning a joint one of the former KEK and the former Institute of Nuclear Study (INS) of University of Tokyo, which are joined together to form the present KEK in order to realize the JHF. These results evidently show how a wide variety of science and engineering fields are requiring high-power proton accelerators.

It was planned that the JHF comprises a 50-GeV synchrotron, a 3-GeV rapid-cycling synchrotron (RCS), and a 200-MeV linac [1-7]. The slowly extracted 50-GeV beam is used for both fundamental particle physics and nuclear physics, such as Kaon rare decay and hypernuclei spectroscopy. The fast-extracted one is used for a long-baseline tau-neutrino appearance experiment, by fully utilizing the SUPERKAMIOKANDE detector located 250 km from KEK. The 3-GeV beam is to be fast-extracted to three experimental areas: a pulsed spallation-neutron experimental area, a muon experimental area, and an exotic nuclei experimental area. In this way the JHF project would cover fundamental particle physics, nuclear physics, materials science, life science, and others. The project has been promoted by the related scientific communities as a first-priority project.

In contrast to the basic science nature of the JHF project, NSP has been oriented to engineering and industrial fields as well as basic science. It is aiming at higher proton beam power, based upon the high-intensity proton linac. Originally proposed for the accelerator-driven nuclear waste transmutation system(ADTS or ADS), that is, as one of the nuclear energy project OMEGA[11,12], the JAERI high-power proton project has gradually been shifted to science using a spallation neutron source. Since the ADS is also making use of spallation neutrons, this project is referred to as the "Neutron Science Project". The accelerator complex of the present NSP comprises a 1.5-GeV proton linac and storage rings (SR's). Since the ADS ultimately requires CW operation, the linac should be compatible with both CW operation and pulse operation. A superconducting (SC) linac is a natural choice for CW operation [13,14].

Both the JHF project and NSP include pulsed spallation neutron sources. The former one is of rather moderate power (0.6 MW), while the latter is ambitiously aiming at an extremely high power of up to 5 MW. The neutron-science community in Japan has assigned the former as the present, most urgent project, considering the latter as a future one. Meanwhile, JHF was slightly modified in order to assure a future upgrade to a 1-MW class machine. On the other hand, the 5-MW neutron source is very difficult to achieve, requiring intensive development. In this way, we consider it ideal to properly join the two projects from both the viewpoints of the usage and developments of high-power proton accelerators.

The Joint Project now covers both basic science and the engineering, that is, nuclear-energy applications. This is the natural result of the recent widening of the application fields of the high-power proton accelerators.

In the following section, we discuss the accelerator scheme of the Joint Project and our strategy for developing and realizing extremely high-power proton accelerators. Then, the research and development work will be presented, as has been done for the JHF and NSP, and will be elucidated from the new viewpoint of a Joint Project. In particular, we will show how the innovative results of the R&D have influenced us in order to formulate the above-mentioned strategy.

2 ACCELERATOR SCHEME OF JOINT PROJECT AND ITS USAGE

The accelerator complex of the Joint Project will be built at the Tokai site of JAERI, shown in Fig. 1. The project is divided into two phases. Phase I includes:
1) a 50-GeV main synchrotron with an average current of 15 μA and a repetition rate of 0.3 Hz,
2) a 3-GeV RCS with an average current of 333 μA and a repetition rate of 25 Hz, and
3) a 400-MeV proton linac with a peak current of 50 mA, a pulse length of 500 μs, and a repetition of 25 Hz.
Both the RCS and linac should be upgradable regarding their energy and intensity.

Fig. 1 Layout of the accelerator complex of the Joint Project. The facilities with parentheses are for the future upgrade.

The use of the 50-GeV synchrotron is exactly the same as in the JHF project. On the other hand, the 3-GeV, 1-MW beam will be provided to the pulsed spallation neutron experiment in the same way as both the JHF project and NSP. It will also be used for muon science, the production target for which is located upstream of the neutron source as well as that for exotic nuclei science.

A unique feature of the joint project is, from the user's view point, that the long-pulse, 400-MeV beam from the linac is transported to the ADS experimental area. From the accelerator viewpoint regarding ADS, the high-energy part of the 400-MeV linac will use SC accelerating cavities, which can be a prototype of the future CW accelerator for ADS use. The development work for the SC proton linac has been performed at JAERI [8-10] in collaboration with the SC linear collider group at KEK [15] as described in Sec. 3.3. In this way, the ADS technology will be steadily developed regarding both the target side and the accelerator side.

Phase II of the Joint Project is of course the upgrade of the Phase I. Another unique feature of the Joint Project is the high compatibility with various upgrade paths of the accelerator complex as follows. It is controversial which accelerator scheme is more realistic[13], the scheme of a full-energy linac with SR's or the RCS scheme, in order to achieve a several-MW pulsed neutron source. One of the major limiting factors on high-power proton accelerators is radioactivity arising from beam loss. In particular, beam loss is unavoidable, and most serious during the injection process to a ring, whether it is an SR or an RCS. Since the injection energy to the RCS is significantly lower than that to the SR, the radioactivity can be lowered by approximately the ratio of the former injection energy to the latter one. In addition, since the accelerated beam energy of the RCS can be higher than that of the SR, we can lower the beam current of the RCS more than that of the SR with the same power, that is, approximately the same neutron yield. In this two-folding way, we can allow a higher beam loss rate in the RCS scheme than that in the SR scheme, assuming the same neutron flux and the same allowable radioactivity (approximately a factor of 7.5 in the Phase I). It is true that the SR's are more advantageous than RCS regarding many features. For example, the high-power RF system required for a high-energy RCS is much more complicated than that for an SR. However, it should be noted that the recent innovative work done for the JHF-ring RF system [16-18] has significantly eased one of the major problems existing in the high-energy RCS, as detailed in Sec. 3.1. This kind of innovative work may change the pros and cons of competitive options. In any case, however, a beam study is indispensable in order to critically test which problems existing in the RCS scheme or the SR scheme are more serious.

The Phase-I machines will be fully utilized for this test. The several-GeV booster synchrotron is indispensable for the high-intensity several 10-GeV beams. This is one of the reasons why we are going to use the RCS for the Phase-I neutron source in contrast to the SNS project [19] and the ESS project [20]. If it turns out that the RCS scheme is more promising than the SR scheme, we will upgrade the Phase-I RCS to 6 GeV and will build one more 6-GeV RCS in order to provide a several-MW beam. In contrast, if the result is opposite, we will upgrade the linac to more than 1 GeV and will construct two or three SR's. Either path is possible, as seen from Fig. 1. The Phase-I linac will be constructed at a location where an energy upgrade is possible, if necessary. The upgrade paths conceived in the Joint Project are summarized in Table 1. The optimum may be in between the two extreme options.

Being logically independent of the pulsed spallation neutron science (not financially independent), further ADS development may require a higher linac energy. In that case, the linac energy will be upgraded in the same way as in the SR scheme for the neutron science. However, it should be here emphasized that the several-MW neutron source is too difficult to realize by any compromised scheme. It can only be realized for its own purpose.

514

Table 1. Upgrade Path of Linac and Rings

	RCS or SR			Linac (56 % chopping)				
Beam Power	Energy	Repetition	Number	Energy	Peak Current	Pulse Length	Repetition	Average Current
1.0 MW	3 GeV	25 Hz	1	400 MeV	50 mA	500 µs	25 Hz	333 µA
5.0 MW or	6 GeV	25 Hz	2	400 MeV	60 mA	500 µs	50 Hz	833 µA a)
5.0 MW	1 GeV	50 Hz	2 or 3	1 GeV	60 mA	3 ms	50 Hz	5 mA

a) The flat bottom of the RCS magnet power supply is lengthened.
The average current is obtained by a product of the peak current, the pulse length, the repetition, and the chopping rate of 56%.

Construction of the 60-MeV part of the linac was already started in KEK as the low-energy front of the 200-MeV linac [2,5,6] for the JHF project, which comprises a 3-MeV, 324-MHz RFQ linac, a 50-MeV, 324-MHz drift-tube linac (DTL), and a 200-MeV, 324-MHz Separated DTL (SDTL). The beam will be commissioned by the end of 2000. This part will be transported to the JAERI/Tokai site in order to fully use it for the Joint Project.

H⁻ ions with a peak current of 50 mA are accelerated up to 400 MeV by the linac. Then, the ions are injected to the 3-GeV RCS through a piece of charge-exchange foil. The large acceptance in the ring is transversely painted in order to maximally ease the space-charge effect. (The longitudinal painting will be done not intentionally, but partly by the sinusoidally varying magnetic fields.) The beam has already been chopped in the linac synchronously with 1.3-MHz RF acceleration in the RCS in order to longitudinally accept all beams from the linac. In this way, we can avoid the beam loss which is inherent in adiabatic capture. Two buckets are thus filled out for 500 µs.

The magnetic fields are to sinusoidally oscillate with a rapid cycle of 25 Hz. Each of the focusing quadrupoles, defocusing quadrupoles and bending magnets is to be driven through its own resonant network in order to maintain a greater number of adjustable knobs. The injection time is to be limited by the approximately flat bottom of the 25-Hz sinusoidal function. In each cycle the ring will accelerate $8 \cdot 10^{13}$ protons.

The two bunches thus accelerated are to be injected four times to the 50-GeV synchrotron, in which eight bunches are accelerated ($3.2 \cdot 10^{14}$ ppp). Two buckets are left empty in order to allow the rising of the fast-extraction kickers during the time thus opened. After the 0.12-s injection the beam energy is to be ramped up to 50 GeV for 1.9 s, and then the beam will be slowly extracted during a time of 0.7 s. The ramping cycle is to be completed in 3.42 s, including the falling time of 0.7 s.

3 R & D RESULTS FOR THE JOINT PROJECT

The R&D programs were formed for the JHF project and NSP in order to overcome various difficulties associated with their high-intensity character. The results so far accomplished are highlighted below.

3. 1 Accelerating cavities loaded with magnet alloy

It has been seen that the RCS for the joint project is characterized by a challengingly high energy and rapid cycling, even for Phase I. The rapid acceleration required for this option is very difficult to obtain by using the conventional ferrite-loaded cavities, in particular under the heavy beam loading. Although the ferrite material has been widely used for proton synchrotrons, because of its excellent permeability and tunability, it is still suffering from the following difficulties:

1) Since its saturation field is rather low, its µQf value, which is proportional to the shunt impedance, rapidly decreases as the operating magnetic field (thus, the field gradient) is increased. Together with its rather low Curie temperature (typically 100°C to 200°C), the highest-possible field gradient is limited to approximately 20 kV/m.

2) In order to tune a ferrite-loaded cavity by adjusting its permeability, it is necessary to supply the DC magnetic field on the ferrite through a bias circuit. The resulting complicated RF system viewed from the beams makes it difficult to analyze in order to overcome heavy beam-loading problems. Even worse, the response to the bias current is sometimes too slow for rapid cycling.

3) The high Q value, typically around a few ten, gives rise to coupled-bunch instabilities, which should be cured for high-current operation.

In particular, the problem 1) is most serious, as can be understood by attempting a lattice design for the high-energy RCS. Many long straight sections have to be prepared for the rapid acceleration, thus increasing the machine cost significantly.

Magnetic alloys (MA's), for example, FINEMET, appear to be very promising to simultaneously solve the above-mentioned problems [16-18]. The µQf value of MA's is almost constant throughout the wide range of the magnetic field valuesin contrast to that of ferrites. Together with its high Curie temperature (typically of 570°C) and easy-cooling taping structure, the former appears to be so promising for obtaining a high field gradient. Furthermore, in spite of its high µQf value, the

Q value is extremely low, typically around unity. Consequently, no tuning is necessary for the MA-loaded cavities.

In order to demonstrate the real usefulness of the MA-loaded cavities, they have been power-tested [16] and beam-tested by electron beams [16]. One of the prototypes was actually used for beam acceleration in the HIMAC synchrotron [16,17]. The other cavity loaded with water-cooled MA plates was powered up to 50 kV/m [16], which is several times as high as the conventional ferrite-loaded cavity. The tested field gradient was limited by the RF power rather than the MA performance.

The extremely low Q value of an MA-loaded cavity makes it ideal for the barrier-bucket application. Another prototype cavity was shipped, and installed to the BNL/AGS under the Japan/US high-energy physics collaboration program. The barrier bucket was generated in the AGS together with the BNL cavity [18]. The beam-loading compensation has been easily done by the one-turn feed-forward method[16], since the cavity is like a pure resistance rather than the resonant circuit.

On the basis of the above empirical test results, we decided to use MA-loaded cavities for both the RCS and 50-GeV synchrotron. It is noted that they can be used not only for acceleration, but also for barrier-bucket generation and for second-harmonic cavities. The latter two applications will greatly ease both the space-charge problem and longitudinal instability by improving the bunching factor.

3. 2 Low- and Medium-Energy Linac

These days it becomes common to use an RFQ with a rather high energy. This trend was initiated by the 3-MeV, 432-MHz RFQ linac [21], which was realized by inventing the π-mode stabilizing loop (PISL) [22]. This RFQ successfully accelerated a H beam of 13 mA peak [21].

In contrast to the medium duty of a few percent for the JHF, the very high duty of a few ten percent was a main challenge of the R&D program for the NSP. The 2-MeV, 200-MHz RFQ linac was tested for a proton peak current of 70 mA with a duty factor of 10% (a beam pulse length of 1 ms and a repetition of 100 Hz) [23]. A peak current of 100 mA was achieved at the duty factor of 1% (a beam pulse length of 1 ms and a repetition of 10 Hz). The first 9-cell of the DTL was power-tested up to the duty factor of 20% and 50% with the field gradients of 2 MV/m and 1.7 MV/m, respectively. The joint effort will realize highly stable RFQ and DTL with a high duty of 15% for the Phase II.

3. 3 High-Energy Linac

The SC cavities for the proton linac have been intensively developed by the JAERI/NSP group [10] in close collaboration with the SC linear collider group [15] in KEK. Among various accomplishments of this R&D program, it is emphasized that the world-highest accelerating field gradient of 8.8 MV/m (the maximum surface field of 44 MV/m) has been obtained for a $\beta = 0.5$ structure [10]. In particular, the electropolishing

technique [15] developed and mass-used for the KEK/TRISTAN was fully utilized for this accomplishment.

It is true that the pulse-mode operation of the SC cavities loses one of the most important advantages regarding energy savings [13]. However, the pulse length for the Joint Project is sufficiently long for making the SC and normal-conducting (NC) options competing. Then, the other advantages of the SC option are appreciated [13]: the higher field gradient, the higher stored energy and the larger bore radius. We consider that the reliability problem so far existing in the SC technology has been mostly solved by recent intensive efforts, including the above development. In particular, the recent development of the high-power input coupler for the SC cavities should be emphasized [24].

The most serious issue is how to overcome the problems associated with the pulse operation of the SC cavities, such as microphonic vibration problem and phase/amplitude control of the accelerating field. The extremely high accuracy required for the phase/amplitude control in the high-power proton linac in comparison with that for electron accelerators is very difficult to obtain for the pulse operation under the heavy beam loading.

The annular-ring coupled structure (ACS) first realized in KEK [25,26] was ready for normal-conducting back-up option. The ACS is characterized by the balanced performance: its shunt impedance and coupling are comparable to those of the widely-used side-coupled structure, while it has an axially symmetry which may be important regarding the minimization of halo formation [26].

3. 3 Other Accomplishments

In addition to the above accomplishments, the linac group has been developing the following items:

1) A volume-production type H ion source, which generates a peak current of 16 mA with a normalized 90% emittance of 0.5 π mm_mrad without cesium [21]. For the NSP linac a H ion peak current of 21 mA was obtained with a current density of 33 mA/cm^2 and a duty factor of 5% with Cesium seeded [27].

2) A newly optimized low-energy beam transport (LEBT) made of two solenoids [21]. The optimization work was based upon careful three-dimensional analyses of various LEBT schemes, while carefully taking into account the geometrical aberration. The beam experiment showed that a very strong space-charge neutralization effect maintained the high brightness throughout the LEBT.

3) Separated DTL (SDTL) [28] after around 50 MeV. Its idea is based upon the fact that quadrupole magnets (QM's) are not necessary in every drift tube (DT) after 50 MeV. By taking the QM's outside the DT's, that is, outside of the tank, we can optimize the geometrical shapes of the DT's in order to maximize the shunt impedance. The shunt impedance of SDTL is by 40 to 65 percent higher than that of a conventional DTL with the same frequency.

4) RF chopper after the 3-MeV RFQ. The chopping is one of the most difficult items to be developed. At present a

chopping system has been designed which is compatible with a beam loss of 1 percent in the linac [29].

The ring group has been developing the following items:
1) Transition-free lattice for the 50-GeV main synchrotron [3],
2) 50-GeV synchrotron magnet power supplies [2,3],
3) RCS magnet power supplies [2], and
4) ceramics vacuum chambers for the RCS.

The imaginary transition γ (γ_t), that is, negative-momentum compaction factor (α), should be realized in order to make the ring free of the transition. The imaginary γ_t is a unique feature of the lattice for the 50-GeV main ring. The synchrotron oscillation, the frequency of which is proportional to the square root of the slippage factor (η), loses stability at $\eta = 0$, resulting in beam loss. The beam energy and the value of γ which make η vanish are referred to as the transition energy and transition γ (γ_t), respectively. Since α is proportional to an orbit integral of the dispersion function divided by the bending radius (ρ), we can obtain a negative α if the dispersion function can be made negative at some of the bending magnets. Among various methods, we have chosen the missing-bend method rather than beta-function modulation, which is fairly harmful in any case.

The magnet power supplies of the 50-GeV synchrotron will use insulated gate bipolar transistors (IGBT), the gating time of which is so fast and flexible as to avoid a harmful reactive (wattles) power. This is also a long-waited device, but it is only recent that high-power devices (3.3 kV, 1200 A) have been successfully developed. Since the development is still continuing, we are expecting that the devices can be mass-used for our power supplies.

Three families of the magnets of the RCS respectively driven through three resonant networks need precise amplitude and phase controls in order to synchronously operate three systems. Two prototypes of the resonant networks have been fabricated and tested. They were successfully in phase within 1 mrad, which corresponds to 0.01 in the betatron tune difference.

The rapid cycle of 25 Hz of the RCS led us to use a ceramics chamber in order to avoid any harmful effect of the eddy current otherwise induced. The chamber, on the other hand, should RF-shield the beam current by means of copper strips or copper plating, or other. The R&D including the fabrication of the ceramics chamber is in progress.

4 CONCLUSION

The high-power proton accelerator project in Japan is strongly supported not only by the neutron-science community, but also by many scientific communities. In addition, the ADS is another engineering and industrial field to seriously develop. The Joint Project will effectively cover all of these requirements, thus making itself a very unique project, internationally supported by nuclear physicists and fundamental particle physicists.

On the other hand the user's request stimulated the development of the accelerator technology in such a way that the SC linac feasibility is seriously investigated for the ADS technology. Another example is the RCS, which plays both roles of a booster to the higher-energy synchrotron and a pulsed spallation neutron source. The request for the high-energy, high-intensity RCS stimulated the accelerator group to invent a new type of accelerating cavities. In this way, the Joint Project becomes unique also from the viewpoint of accelerator technology. It will present an accelerator test bench in order to determine which is more promising, RCS or SR, for higher power proton accelerators.

8 REFERENCES

[1] JHF Project Office, "Proposal for Japan Hadron Facility," KEK Report 97-3 (JHF-97-1).
[2] JHF Project Office, "JHF Accelerator Design Study Report" KEK Report 97-16 (JHF-97-10).
[3] Y. Mori, Proc. 1997 Part. Accel.Conf., 920 (1997).
[4] Y. Yamazaki, Proc. 1st Asian Part. Accel. Conf., 5A002-314 (1998).
[5] T. Kato, KEK Report 96-17 (1997).
[6] Y. Yamazaki and T. Kato, Proc. 1998 Linac Conf., TU4011 (1998).
[7] Y. Mori, Proc. 1st Asian Part. Accel. Conf., 5D001-375 (1998).
[8] M. Mizumoto et al., Proc. 1st Asian Part. Accel. Conf., 5A001-309 (1998).
[9] M. Mizumoto et al., "A High Intensity Proton Linac Development for the JAERI Neutron Science Project", Proc. 1998 Linac Conf., TU1004 (1998).
[10] N. Ouchi et al., "Development of Superconducting Cavities for High Intensity Proton Accelerator at JAERI", Proc. 1998 Applied Superconducting Conf. (1998).
[11] Y. Kaneko, "The Intense Proton Acclerator Program, " Proc. the 2nd International Symposium on Advanced Nuclear Energy Research, Mito, p. 25 (1990).
[12] M. Mizumoto, Proc. 1994 Linac Conf., 317 (1994)
[13] Y. Yamazaki, Proc. 1996 Linac Conf., 592 (1996).
[14] Y. Yamazaki, " Accelerator Development for the Japanese Hadron Project and Continuous-Beam, Superconducting Proton Linac", Proc. Workshop for JAERI Proton Technology Center Project, KEK Preprint 95-64 (1995) (in Japanese).
[15] E. Kako et al., "Improvement of Cavity Performance by Electropolishing in the 1.3 GHz Nb Superconducting Cavities", this conference, THAL6.
[16] C. Ohmori et al., "High Field-Gradient Cavities Loaded with Magnetic Alloys", this conference, THAL1.
[17] R. Muramatsu et al., "The First Beam Acceleration Test using High Gradient Cavity at HIMAC", this conference, MOP59.
[18] M. Fujieda et al., "Magnetic Alloy Loaded RF Cavity for Barrier Bucket Experiment at the AGS", this conference, MOP81.
[19] J. Alonso, "The Spallation Neutron Source Program", this conference, FRA01.
[20] K. Bongardt et al., Proc. 5th European Part. Accel. Conf., 158 (1996).
[21] A. Ueno et al., Proc. 1996 Linac Conf., 293 (1996).
[22] A. Ueno and Y. Yamazaki, Nucl. Instr. Meth. A300, 15 (1990).
[23] K. Hasegawa et al., "Development of a High Intensity RFQ at JAERI", Journal of Nuclear Science and Technology, 34, 622 (1997).
[24] S. Mitsunobu et al., "High Power Test of the Input Coupler for KEKB SC Cavity", Proc. 7th Workshop on RF Superconductivity, 735 (1995).
[25] T. Kageyama et al., Part. Accel. 32, 33(1990)
[26] T. Kageyama et al., Proc. 1992 Linac Conf., 456 (1992)
[27] H. Oguri et al., "Development of an Injector Section for the High Intensity Proton Accelerator at JAERI", Proc. 1998 European Part. Accel. Conf., (1998).
[28] T. Kato, KEK Report 92-10 (1992).
[29] T. Kato and S. Fu, "MEBT Design for the JHF 200-MeV Proton Linac", Proc. 1998 Linac Conf., MO4012 (1998).

COMMISSIONING OF THE LOS ALAMOS PSR INJECTION UPGRADE*

D. H. Fitzgerald, R. Garnett, K. Jones, R. J. Macek, F. Merrill, C. Pillai, M. A. Plum, and
O. R. Sander, LANL; A. Browman, Tech Source; D. Johnson, SAIC; and R. Kustom, ANL

Abstract

An upgrade has been completed and commissioned to the Los Alamos Proton Storage Ring (PSR) to allow direct injection of the H^- beam into the ring and to move the circulating beam off the stripper foil using an orbit bump system. The design benefits of the upgrade are matching the transverse phase space of the injected beam to the PSR acceptance and a factor-of-ten reduction of the foil hits by the circulating beam. Foil thickness is optimized to minimize the sum of circulating-beam losses and losses caused by excited H^0 states produced at injection. Design simulations predicted an overall reduction in losses by a factor of five. We discuss results of the commissioning and PSR performance in comparison to design projections and the goals of the upgrade project.

1 BEAM LOSSES IN PSR

Beam losses in PSR and the resulting radioactivation of ring components are the dominant factors limiting average beam current, a cause of equipment failure, and a major element in repair times. Prior to the upgrade, beam losses of 0.6-0.7% limited the average beam intensity in PSR to 70 μA. The primary upgrade goal was to increase the beam intensity to 100 μA while decreasing the fraction of beam lost by a factor of five. The beam loss reduction, in turn, supports the operational goals of >85% beam availability and operation for eight months per year.

There are two main causes of beam losses in PSR. First, nuclear and large-angle Coulomb scattering of the circulating beam in the injection stripping foil [1,2] led to beam losses of 0.3-0.5% prior to the upgrade. Second, a fraction of the injected beam interacts in the stripper foil and is converted to excited states of H^0. The excited H^0s are field stripped and fall outside the ring acceptance. [3] Before the upgrade, these "first-turn" losses were 0.2-0.3% of the injected beam.

2 DIRECT H^- INJECTION

Before the upgrade, beam was injected into PSR in a two-step, charge exchange process: H^- was stripped to H^0 in a strong dipole magnet and drifted into the ring through a channel in a dipole to a stripper foil where it was converted to H^+. Losses from foil scattering were large because the average proton traversed the foil 30-35% of the time, as determined from tracking simulations. In the horizontal plane, the stripper magnet introduced a three-fold emittance growth and the injected beam was significantly mismatched. The phase space for injected

and circulating beams at the stripper foil are shown in Figure 1. The neutral beam could not be manipulated to improve the match, so the beam filled the horizontal acceptance of the ring, leaving no room for a horizontal offset to reduce the number of foil traversals. In the vertical plane, the smaller emittance allowed some offset.

Figure 1. Injection phase space at the stripper foil for two-step H^0 injection prior to the upgrade.

In the upgrade, direct H^- injection was implemented to eliminate the horizontal emittance growth and allow optimization of the injected beam ellipses to minimize foil traversals. As can be seen in Figure 2, this substantially reduces the overlap of the circulating beam with the foil.

Figure 2. Injection phase space at the stripper foil for direct H^- injection.

To further reduce scattering losses, a vertical orbit bump was implemented to move the circulating beam off the foil during the injection cycle. These measures made possible a ten-fold reduction in the number of foil traversals. Part of this gain was traded off by increasing the foil thickness to reduce production of H^0 excited states. An optimization study using tracking simulations showed that total losses could be minimized by increasing the foil thickness from 220 to 400 μg/cm^2; the simulations predicted a reduction in total losses by a factor of five.

Table 1: Comparison of parameters for PSR before and after the upgrade

Parameter	Before Upgrade	After upgrade	
	Simulation [4]	Simulation [4]	Actual
Current (μA), protons per pulse @ 20 Hz	70, 2.2×10^{13}	100, 3.1×10^{13}	100, 3.1×10^{13}
Beam energy (MeV)	797	799	—
PSR accumulation time (μs)	625	825	825
Injected beam time spread (ns)	250	250	250
Input beam phase space: Transverse (π mm-mrad rms)	1.8×1.0	0.8	0.65 ± 0.15
Longitudinal (Δp/p rms)	0.063%	0.063%	—
Injected beam offset (mm, mrad) $(x_0,x_0') =$	0, 0	7.21, -1.96	5.4, -1.3
$(y_0,y_0') =$	8.0, 0.9	22.5, 3.10	16.9, 2.8
Closed orbit bump (mm, mrad) from $(y_0, y_0') =$	none	16.0, 2.2	12.0, 1.7
to $(y_0, y_0') =$		0.0, 0.0	0.0, 0.0
Stored beam 95% emit. (π mm-mrad) $\varepsilon_x =$	27	44	42 ± 12
$\varepsilon_y =$	39	57	76 ± 15
$\Delta p/p =$	±0.32%	±0.34%	$\pm(0.27 \pm 0.12)\%$
Tune (v_x, v_y)	3.172, 2.142	3.172, 2.142	3.19, 2.18
RF volts per turn, linear ramp	4-8 kV	6-10.5 kV	5.25-10.5
Harmonic number, frequency (MHz), [time] (ns)	1, 2.795, [358]	1, 2.795, [358]	1, 2.795, [358]
Foil thickness (μg/cm²)	220	400	450
Fraction of beam missing foil	7.4%	2.6%	total = 2-3%
H⁻ stripped to H⁰	1.3%	0.6%	
Foil hits per proton	307	35	—
Total beam losses	**0.57%**	**0.12%**	**0.25-0.30%**
Stored beam loss:	0.26%	0.05%	0.11-0.17%
Excited H⁰ loss:	0.26%	0.05%	0.11-0.17%
Extraction loss:	0.05%	0.01%	<0.01%

3 DESIGN AND IMPLEMENTATION

The upgrade design is described in detail elsewhere [5] so only a brief description is presented here. A comparison of parameters for the old and new injection schemes is presented in Table 1.

A skew section, rolled by approximately 27°, transports the beam from the H⁻ transfer line to PSR level, an elevation change of 3.35 m. Skew quadrupoles at the entrance and exit eliminate the X-Y coupling term from the transfer matrix. This coupling in the old skew section caused ~30% emittance growth. The new skew section is achromatic to prevent dispersion-related emittance growth and beam centroid motion caused by energy shifts.

Four quadrupoles downstream of the skew section are used to match the desired Courant-Snyder parameters at the injection stripper foil. Three dipoles then form a chicane to guide the beam around a ring main dipole and into a merging dipole in PSR. Quadrupoles in the chicane produce an achromat at injection. Four ferrite-based magnets in the ring produce a closed-orbit bump at the stripper foil that collapses to zero by the end of injection.

A small fraction of the beam emerges from the stripper foil as H⁻ and H⁰. These two waste beams have large offsets at the stripper foil and are diverging; the envelope of the two beams is 350 × 200 π mm-mr. Therefore, the ring dipole downstream of the stripper foil was replaced by two C-magnets to provide an adequate aperture for the waste beams. A dual-plane (X-Y) bending magnet directs the waste beams to the dump, and a quadrupole doublet merges and focuses the beams at the dump.

4 COMMISSIONING

The goals of the commissioning for the upgrade were to (a) confirm the correct installation and performance of the installed hardware, (b) characterize and optimize the beam optics tunes, and (c) establish an initial beam optics tune at a beam intensity of 100 μA with low losses. The results for the commissioning, successfully accomplished in the fall of 1998, are described in the ensuing subsections.

4.1 Hardware Performance

The installed hardware comprised 38 dc magnets, 4 time-varying bump magnets, 36 beam diagnostics instruments, a foil stripper system, 70 support and alignment stands, vacuum and water cooling systems, a cable installation, and controls hardware and software. Following extensive pre-beam checks, all hardware systems performed within design requirements. The only exception was the carbon foils produced with the mCADAD method, [6] which initially failed after rather short exposures to modest beam intensities. This was surprising because the maximum foil temperature was estimated to be approximately the same

(1700-1800 °K) at 100 μA after the upgrade as at 70 μA before the upgrade. Following these observations, the foil facility and production technique were modified, and the excellent dimensional stability and long life observed in the past for these foils appears to have been regained.

4.2 Beam Optics

The initial objective was to confirm that the design optics tune was established. The achromat at the downstream end of the skew section (upstream end of the matching section) was verified with an uncertainty of <0.1 cm/% by varying the beam momentum and observing beam motion at all BPMs in the beam line from the linear accelerator to the PSR stripper foil. The absence of X-Y coupling in the skew section was verified at approximately the 5% level by varying the upstream horizontal steering and observing beam motion in the horizontal and vertical planes downstream of the skew section.

We reconstruct rms beam ellipse parameters at injection from beam profiles measured at four locations upstream and downstream of the stripper foil. Uncertainties are typically ±10-15% for the emittance area and ±15-20% for α and β. Achieving a match to the desired beam ellipses at injection proved difficult using the design tune. The desire to separate control of transverse beam parameters and dispersion, coupled with the requirements for an achromatic beam and a small spot size (1.0 × 1.6 mm rms) at the foil, led to large beam spot sizes in the matching section (up to 18 mm rms). The magnifications inherent in this tune led to large uncertainties in projecting the ellipse parameters back to the entrance of the matching section, so the matching process did not converge. To remedy these problems, a compromise tune was adopted that reduced the maximum beam spot size in the matching section to 7 mm. As a consequence, 0.5 cm/% dispersion was introduced at injection, not an important consideration because this dispersion is an order of magnitude smaller than that of the circulating beam. More significantly, the

Figure 3. Design (a) and measured (b) beam ellipses at the stripper foil in the vertical plane for the (2σ) injected beam (dashed ellipse) and circulating beam (solid ellipse).

match at injection was compromised, particularly in the vertical plane. Shown in Fig. 3 are the injected and circulating beam ellipses at the stripper foil for the design (Fig. 3a) and achieved (Fig. 3b) injection parameters. For the injected beam, the value achieved for β_y was 2.0 m vs. the design value of 3.2 m. With this injected beam, only 75% of the design beam offset at injection could be achieved; as the offset was increased, the emittance area of the circulating beam exceeded design, and losses from beam scraping were observed. Similarly, in the horizontal plane, the value achieved for β_x was 1.8 m vs. the design value of 1.3 m, and the maximum offset without scraping was also about 75% of the design value.

4.3 Optimization of Beam Losses at 100 μ A

To reduce beam losses at high intensities, we conducted a multi-parameter search about design values for beam ellipses and offset at injection, stripper foil thickness, fraction of injected beam missing the foil, bump magnet amplitudes, PSR fractional tune, and the voltage, phase and ramp of the PSR buncher during injection. As can be seen in Table 1, the adopted operating parameters are all essentially equal to the design (simulation) values, with the exception of the injected beam ellipses and offsets.

During post-commissioning operations, early problems with stripper foils caused losses to be relatively high, and problems with cooling the moderator for the spallation neutron production target limited the beam current at times. However, during January operations, these initial problems were resolved, and 100 μA was delivered to the target with average losses of 0.25%, a reduction by a factor of 2.5-3.0 from pre-upgrade values for operation at 70 μA. This is approximately twice the value predicted for losses by tracking simulations. [4] However, the simulations do not include a complete treatment of space charge effects, and, therefore, somewhat underestimate the losses. Nevertheless, improving the match at injection may further reduce losses. As can be seen in Fig. 3, the overlap of the circulating beam with the stripper foil for the injection parameters achieved in the vertical plane is about twice that for the design case. Improving the match will require a higher-current power supply for the final quadrupole in the injection line; we anticipate this can be accomplished in a relatively short time.

5 REFERENCES

[1] R. Macek, et al., Proceedings of the European Particle Accelerator Conference (1988) 1252.

[2] R. J. Macek, et al., Proceedings of the 1993 Particle Accelerator Conference (1993) 3739.

[3] R. Hutson and R. Macek, Proceedings of the 1993 Particle Accelerator Conference (1993) 363.

[4] F. Neri, private communication.

[5] D. H. Fitzgerald, et al., Proceedings of the 1997 Particle Accelerator Conference (1997) 1012.

[6] M. J. Borden, et al., Proceedings of the 1997 Particle Accelerator Conference (1997) 187.

STATUS OF THE FERMILAB ELECTRON COOLING PROJECT

S. Nagaitsev[#], A. Burov, A.C. Crawford, T. Kroc, J. MacLachlan,
C.W. Schmidt, A. Shemyakin[+], and A. Warner, FNAL[*], Batavia, IL

Abstract

The first stage of the Fermilab Electron Cooling R&D program is now complete: technology necessary to generate hundreds of milliamps of electron beam current at MeV energies has been demonstrated. Conceptual design studies show that with an electron beam current of 200 mA and with a cooling section of 20 m electron cooling in the Fermilab Recycler ring can provide antiproton stacking rates suitable for the Tevatron upgrades beyond Run II luminosity goals. A prototype of such an electron cooling system is now being built at Fermilab as part of the continuing R&D program. This paper describes the electron cooling system design as well as the status of the Fermilab electron cooling R&D program.

1 INTRODUCTION

In 1995 Fermilab started an R&D program in electron cooling that has two principal objectives: (1) to determine the feasibility of electron cooling the 8.9 GeV/c momentum antiprotons; and (2) to develop and demonstrate the necessary technology. The ultimate goal is to realize a luminosity of 10^{33} cm^{-2}s^{-1} in the Tevatron collider by supplying a larger flux of antiprotons. The conceptual design studies [1] demonstrate that this can be accomplished by providing longitudinal emittance decrements in the Recycler of 200 eVs/h or higher. The primary technical problem is to generate a high-quality, monochromatic, dc, multi-MeV electron beam of 200 mA or greater. The technical goal set for a proof-of-principal demonstration using mostly existing equipment was to maintain a 200 mA beam for a period of one hour. The only technically feasible way to attain such high electron currents is through beam recirculation (energy recovery)[2]. This goal was achieved in 1998 by recirculating beam currents of 200 mA for periods of up to five hours without a single breakdown. Although the recirculation tests used a 1-1.5 MeV electron beam and the Fermilab electron cooling system requires a 4.3 MeV beam, the demonstration is relevant because the increased energy does not involve fundamental changes in technology. Currently, Fermilab is building a full-scale, 4.3 MeV electron beam facility to complete the experimental R&D program and to prepare installation of the cooler in the Recycler ring.

2 RECIRCULATION TEST

These tests were performed using a 2-MV Pelletron™ accelerator (Van de Graaff type) at National Electrostatics Corporation (NEC), Middleton, Wisconsin. It is the same accelerator as described in Ref. [3] and [4] with shorter acceleration and deceleration tubes, a new electron gun and collector [5], as well as a different beam line. Figure 1 shows the test beamline layout. Table 1 summarizes the important system parameters. This system employs the Pelletron accelerator with a maximum charging current of a few hundred microamps (typically 50 – 100 µA). The electron beam line consists of a 7.5 m long channel with discrete focusing elements (lenses and a 180° bending magnet) flanked by small aperture (2.54 cm ID) acceleration and deceleration tubes.

Figure 1: Recirculation system beamline layout.

Table 1: Recirculation System Parameters

Parameter	Symbol	Value	Units
Pelletron Voltage	U_o	1 - 1.5	MV
Max. Recirculated Beam Current	I_b	0.7	A
Typical Vacuum	p	$0.2\text{-}1\times10^{-7}$	Torr
Relative Losses	$\Delta I/I_b$	$0.5\text{-}2\times10^{-5}$	
Electron Gun			
Cathode Radius	R_c	1.7	mm
Gun Perveance	P	0.02-0.08	μPerv
Anode Voltage	U_A	≤ 50	kV
Control Voltage	U_C		
beam off		$-U_A/13$	
beam on		$-U_A/100$	
Electron Collector			
Collector Voltage	U_{COL}	≤ 5	kV
Relative Losses (30 keV bench test)		3×10^{-6}	

The conclusions from the recirculation tests can be summarized as follows:

1. An electron beam with current of hundreds of milliamperes and energy of 1-1.5 MeV was recirculated in a dc regime. At energy of 1.2 MeV a typical time between crashes is several hours for beam currents of 0.2 A; the maximum recirculated current is 0.7 A. The goal of the test (0.2 A during one hour) has been achieved.
2. Relative current losses from the collector do not exceed 5×10^{-6} for the beam current of up to 0.5 A.
3. The Pelletron-based recirculation scheme seems to be applicable for the multi-MeV range of beam energy since all of the limitations originate from the low energy part of the system.

3 ELECTRON BEAM TRANSPORT

The demonstration of the Pelletron-based electron beam recirculation provides the necessary basis for the next step of the electron cooling R&D program, electron beam transport. Figure 2 shows the schematic layout of the Recycler electron cooling system. This system is now being reproduced at Fermilab for the full-scale proof-of-principle test. Table 2 summarizes the important parameters of this test system. The principal goals for this system are: (1) to demonstrate the recirculation of a 4.3 MeV, 0.5 A electron beam for a period of one hour; (2) to verify that the electron beam quality in the cooling section meets the demands of the electron cooling; and (3) to design the system for the final installation in the Recycler.

Traditional electron cooling devices employ a continuous homogeneous longitudinal magnetic field in the kilogauss range for the beam transport through the cooling region. One of the main reasons is to suppress the transverse velocities arising from the electron beam space charge. In the Recycler system, the space charge effects

are much lower because of the higher beam energy. Thus, the longitudinal magnetic field value can be much smaller allowing for a non-traditional transport scheme. Also, the choice of a standard Pelletron accelerator prohibits us from immersing the electron beam line into a continuous magnetic field. Our transport scheme assumes a homogenous longitudinal magnetic field in the gun, collector, and in the cooling section, but a lumped focusing system in between.

Table 1: Electron Cooling System Parameters

Parameter	Value	Units
Electrostatic Accelerator		
Terminal Voltage	4.3	MV
Electron Beam Current	0.5	A
Terminal Voltage Ripple	500	V (FWHM)
Cathode Radius	2.5	mm
Gun Solenoid Field	≤ 400	G
Cooling Section		
Length	20	m
Solenoid Field	≤ 100	G
Vacuum Pressure	0.1	nTorr
Electron Beam Radius	6	mm
Electron Beam Divergence	≤ 80	μrad

The cooling rates are extremely sensitive to the angles between the electrons and the antiproton beam. Both coherent and incoherent angles must be smaller than 10^{-4} radians to avoid cooling degradation. To provide zero angular velocity inside the solenoid, the electrons must enter the solenoid with the correct radius and divergence, determined by the Busch theorem [6].

Figure 2: Schematic layout of the Recycler electron system.

The input beam line delivering the electrons to the cooling section has to conserve the rotational invariance. The most natural way to do that is to use axially symmetric optical elements: solenoidal lenses and bending magnets with a field index $n = \frac{1}{2}$. At the exit of the input beam line, the beam must be round with the required radius and zero radial angle. The effects of the chromaticity and nonlinearities must be smaller than the angle tolerances.

The output beam line should also conserve rotational invariance to provide beam collection in the collector without losses.

To simulate the beam transport, a computer code dealing with linear and nonlinear optics was developed. This code was cross-checked for low beam currents with a commercially available beam transport code OptiM 2.1 [7]. The preliminary results for the electron beam envelope using an axially-symmetric beam line are shown in Figure 3. All the requirements are satisfied with this transport line.

Figure 3: Electron beam envelope.

4 PROJECT STATUS

A 5 MV Pelletron accelerator has been ordered and will be installed at Fermilab in July of 2000 in a dedicated building. The initial recirculation tests will proceed with a short beamline similar to the one in Figure 1. Once the recirculation of a 0.5 A electron beam is demonstrated, the full scale beam line tests will begin. Under the most optimistic scenario the electron cooling system might be installed in the Recycler at the end of FY2001 (contingent upon the collider run schedule).

5 ACKNOWLEGDEMENTS

5 REFERENCES

[1] A. Burov, et al., "Design of Antiproton Electron Cooling in the Recycler", these proceedings.

[2] A.C. Crawford, S. Nagaitsev, A. Sharapa, and A. Shemyakin, "Successful MeV-range electron beam recirculation", in Proc. of EPAC-98 (Stockholm, Sweden, June 22-26, 1998).

[3] L.R. Elias and G. Ramian, IEEE Trans. Nucl. Sci. NS-32 No. 5 (1985), p. 1732.

[4] J.R. Adney, M.L. Sundquist, D.R. Anderson, D.J. Larson, and F.E. Mills, IEEE Proc. of 1989 Particle Accelerator Conf., pp. 348-350 (1989).

[5] A. Sharapa, A. Shemyakin, and S. Nagaitsev, Nucl. Instr. and Meth. A 417 (1998) 177.

[6] S. Nagaitsev et al., "Electron cooling for the Fermilab Recycler Ring", in Proc. of XVII Intl. Conf. On High Energy Accelerators (Dubna, Russia, Sep. 7-12, 1998).

[7] LDBS Co., 110 Bugle Ct., Yorktown, VA 23693 Phone: (757)867-7998, Fax: (757)867-6570

BEAM TESTS OF THE 12 MHz RFQ RIB INJECTOR FOR ATLAS

R.A. Kaye, K.W. Shepard, B.E. Clifft, M. Kedzie, ANL, Argonne, IL

Abstract

Beam tests of the ANL 12 MHz Radio-Frequency Quadrupole (RFQ), designed for use as the initial element of an injector system for radioactive beams into the existing ATLAS accelerators, are in progress. Recent high-voltage tests of the RFQ without beam achieved the design intervane voltage of 100 kV cw, enabling beam tests with A/q as large as 132 using beams from the ANL Physics Division 4 MV Dynamitron accelerator facility. Although the RFQ was designed for bunched beams, initial tests have been performed with unbunched beams. Experiments with stable, unbunched beams of singly-charged ^{132}Xe and ^{84}Kr measured the output beam energy distribution as a function of the RFQ operating voltage. The observed energies are in excellent agreement with numerical beam simulations.

1 INTRODUCTION

A prototype split-coaxial 12 MHz cw RFQ accelerator [1] has been constructed. The RFQ will form the initial element of a preaccelerator system [2,3] for injecting radioactive ion beams into the existing ATLAS accelerators at ANL. Early tests of the RFQ [4] have achieved stable operation at a cw intervane voltage of 102 kV with an rf input power of 17 kW. More recently, with further conditioning cw operation as high as 108 kV has been achieved, a voltage well above the design value of 100 kV.

Following these voltage tests, we have injected the RFQ with singly-charged ions of mass up to 132, the highest A/q beam the RFQ was designed to accelerate. The RFQ was designed to be injected with pre-bunched beams. Tests to date have been with injection of dc, unbunched beams. As shown below, much information can be obtained from accelerating an unbunched beam. For example, both experiment and numerical simulation show that about 15% of an injected dc beam is accelerated.

The following reports the results of energy measurements performed on RFQ-accelerated beams of unbunched ^{132}Xe and ^{84}Kr and compares the results to the predictions resulting from numerical simulation of the RFQ beam dynamics.

2 EXPERIMENTAL SETUP

Beam tests of the RFQ were performed at the ANL Physics Division 4 MV Dynamitron accelerator facility. At present, we inject unbunched beam into the RFQ and do not include transverse matching elements at the entrance and exit of the RFQ. A schematic overhead view

showing the Dynamitron injector, RFQ, and beam diagnostic system is shown in Fig. 1. A more comprehensive description of the system is given in previous work [5].

Beam energies were measured using a silicon (Si) charged-particle detector placed 1.4 m away from the RFQ exit. The energies were measured following either direct implantation, with the detector placed at $0°$ relative to the beam direction, or following elastic scattering from a very thin foil (23 μg/cm^2 Au with a 5.3 μg/cm^2 C backing). In the elastic scattering mode, the detector was placed at $10°$ relative to the beam direction. Energy calibrations were performed for beams of both ^{132}Xe and ^{84}Kr with energies determined by the Dynamitron terminal voltage, without the use of the RFQ, and were found to be linear throughout the energy range of interest.

Figure 1: Schematic overhead view of the RFQ beamline at the Dynamitron injector facility.

3 NUMERICAL SIMULATIONS

Numerical simulation of unbunched beams of A/q = 132 and 84 accelerated by the RFQ was performed using the ANL BeamTrak code. The ANL BeamTrak code fully tracks the position and velocity of each individual particle of a bunch through the entire RFQ structure.

An unbunched beam was simulated by considering a bunch 86 ns wide at the entrance of the RFQ, uniformly filling a complete rf period of the RFQ. An actual dc beam would consist of a superposition of a series of such bunches. A single 86 ns bunch is, however, completely representative of such a superposed ensemble.

In what follows, we show the results of simulation in terms of the coordinate and velocity distribution of the particles relative to the "bunch" centroid. Figure 2 shows the longitudinal phase space of a bunch of 500 A/q = 132 particles, representing a singly-charged ^{132}Xe beam. The bunch has an initial time width of 86 ns and

mean energy of 378 keV, and is then simulated travelling through the RFQ at an intervane voltage of 99 kV. The figure shows the bunch after exiting the RFQ and drifting until the leading edge intercepts the detector, located 1.4 m past the RFQ exit. Note that at this point in time, while most of the particles (each represented by a cross) have been unaccelerated or even partially decelerated, about 15% are accelerated. These accelerated particles form a bunch with an energy nearly 700 keV higher and a time lead of 800 ns relative to the centroid of the entire 500 particle segment of the original segment of dc beam. Note that since the centroid energy of the entire pseudo-bunch is 685 keV, the accelerated portion of the beam arrives at the detector at a total energy of 1368 keV. At this point in time, the original 86 ns wide bunch has spread out, and extends over nearly 1.6 μs.

Figure 2: Numerically simulated longitudinal phase space of 500 ^{132}Xe particles at the RFQ exit. The centroid energy of accelerated beam is 1368 keV.

An energy spectrum can be obtained from the simulated-beam longitudinal phase space by projecting the number of particles that fall within a specified range on the energy axis. Performing this projection and using an energy bin size of 50 keV results in the histogram displayed in Fig. 3, where the y-axis corresponds to the sum total of particles counted in each 50 keV bin, for the distribution shown in Fig. 2. Two distinct peaks can be observed in Fig. 3. The first, and most intense, is peaked near 300 keV. This peak has a high-energy "tail" with a smaller peak visible near 700 keV. The most distinct peak is well resolved from the first and is located near 1360 keV. This spectrum can be compared to the experimental spectrum generated from Si detector data (see Section 4.1).

Simulations have also been performed for a ^{84}Kr beam. In this case, the initial energy of the bunch is 241 keV in order to maintain the velocity profile defined by the RFQ vane modulations. The RFQ peak voltage, which scales with A/q, must be set at 65 kV for this beam. The simu-

lation results are qualitatively similar to the ^{132}Xe case. Both the longitudinal phase space and theoretical energy spectrum representing a bunch of 500 singly-charged ^{84}Kr particles at the RFQ exit indicated a clear peak near 860 keV, the accelerated portion of the beam, which was well separated and resolved from the remainder of the beam.

Figure 3: Energy spectrum of 500 ^{132}Xe particles at the RFQ exit projected from the simulated-beam longitudinal phase space of Fig. 2.

4 EXPERIMENTAL RESULTS

4.1 Beam tests with ^{132}Xe

Beam tests with ^{132}Xe were performed by injecting an unbunched 378 keV beam from the Dynamitron into the RFQ operating at voltages in the range of 80-99 kV. Ion energies were measured using the elastic scattering method described in Section 2. This method allows the detector to be shielded from the high background of x rays and electrons emitted by the RFQ.

Energy spectra of accelerated ^{132}Xe ions for RFQ operating voltages of 99 kV and 85 kV are shown in the top and bottom panels of Fig. 4, respectively. In each spectrum, two distinct peaks can be seen, in agreement with the simulations (see Fig. 3). The lowest-energy peak (displayed off-scale in Fig. 4) is mostly unaccelerated beam, although a portion of this peak (about 20%) is known to be a background of x rays and/or electrons which were also observed with the RFQ at these voltages, but with no injected beam. The precise position of the accelerated beam peak near 1400 keV is dependent on the RFQ operating voltage, and shifts from 1404 keV(top) to 1330 keV (bottom) with decreasing voltage. Centroid energies were determined by performing background-corrected Gaussian fits to the line shapes of each peak.

Figure 5: Experimental (filled circles) and theoretical (solid curve) accelerated ^{132}Xe beam energies as a function of RFQ voltage.

Figure 4: Experimental spectra of accelerated ^{132}Xe ions using an RFQ operating voltage of 99 kV (top) and 85 kV (bottom).

The energy of accelerated ^{132}Xe beam was measured for five different RFQ operating voltages, as seen in Fig. 5, which compares the results to the predictions from the numerical simulations described in Section 3. The beam energy gain remains nearly constant as the operating voltage is reduced below the design value of 100 kV, until 85 kV is reached, below which the beam energy drops sharply. This is due to the RFQ being designed for -30° synchronous phase. As the RFQ voltage is decreased, the accelerated particles slide back in phase to maintain velocity, until reaching 0° phase at which point they can no longer be fully accelerated. Measurements could not be extended below an RFQ voltage of 80 kV because the accelerated-beam peak then becomes indistinguishable from background.

4.2 Beam tests with ^{84}Kr

Similar beam tests were performed with ^{84}Kr by injecting an unbunched 241 keV beam from the Dynamitron into the RFQ operating at voltages in the range of 56-76 kV. Ion energies were measured with the detector placed directly at 0° relative to the beam direction, without the use of a scattering foil.

Both the theoretical and experimental energy spectra obtained for ^{84}Kr were qualitatively very similar to those obtained for ^{132}Xe. In this case, the accelerated beam component comprised about 20% of the total output beam, with its energy peaking at about 885 keV.

5 SUMMARY

Initial beam tests of the Argonne 12 MHz RFQ using ^{132}Xe and ^{84}Kr have been performed. The measured beam energies at the output of the RFQ are in excellent agreement with the results of numerical simulation. Future experiments will make use of the subnanosecond timing resolutions of Si detectors to measure the longitudinal emittance of accelerated beam.

6 ACKNOWLEDGMENTS

The authors gratefully acknowledge the technical assistance of C. Batson, P. Billquist, P. Strickhorn, M. Portillo, and J. Czernik. Helpful discussions with L. Bollinger, D. Henderson, R. Janssens, J. Nolen, R. Pardo, and A. Woosmaa are also greatly appreciated. This work is supported by the U.S. Department of Energy, Nuclear Physics Division, under Contract W-31-109-ENG-38.

7 REFERENCES

[1] K.W. Shepard and W.C. Sellyey, Proc. of the 1996 Linear Accelerator Conference, August 26-30, Geneva, Switzerland, CERN 96-07, 68 (1996).

[2] J.A. Nolen, Proc. of the 1995 IEEE Particle Accelerator Conference, May 1-5, Dallas, Texas, 95CH35843, 354 (1996).

[3] K.W. Shepard and J.W. Kim, Proc. of the 1995 IEEE Particle Accelerator Conference, May 1-5, Dallas, Texas, 95CH35843, 1128 (1996).

[4] K.W. Shepard, M. Kedzie, and R.A. Kaye, Proc. of the 1998 Linear Accelerator Conference, August 23-28, Chicago, Illinois (in press).

[5] R.A. Kaye, K.W. Shepard, B.E. Clifft, and M. Kedzie, Proc. of the Eighth International Conference on Heavy Ion Accelerator Technology, October 5-9, 1998, Chicago, Illinois (in press).

IMPROVED PERFORMANCE OF THE GSI HEAVY ION ACCELERATOR COMPLEX WITH COOLED SYNCHROTRON BEAMS

M. Steck, K. Blasche, H. Eickhoff, B. Franczak, B. Franzke, L. Groening, T. Winkler,
GSI Darmstadt, Germany

Abstract

Electron cooling at the injection energy of the heavy ion synchrotron SIS results in beam pulses of higher intensity and exceptional quality. The beam parameters after cooling have been measured and verify a reduction of the phase space volume by more than three orders of magnitude. Beam transfer of the cooled ion beam is much easier because of the reduced emittance. The time required to fill the storage ring ESR with highly charged ions has been reduced from minutes to seconds.

1 INTRODUCTION

An electron cooling system has recently been installed in the heavy ion synchrotron SIS [1]. It has been designed for fast accumulation of high intensity beams of highly charged ions at the injection energy [2]. The successful commissioning of the cooling device and the optimization of the accumulation procedure facilitate to increase the number of ions in a synchrotron pulse by more than one order of magnitude [3]. Even in view of the additional time required for the accumulation process a significant increase of the average beam intensity has been achieved, which will also be useful to provide beams of rare isotopes with increased intensity.

Although the accumulation process requires mainly an emittance reduction in the horizontal phase space plane, electron cooling provides a reduction of the 6-dimensional phase space volume. This has a beneficial effect on the general performance of the synchrotron and allows to deliver beams of unprecedented quality.

2 PROPERTIES OF THE COOLED HEAVY ION BEAM

The heavy ion beam after accumulation with cooling has lost any memory of its properties immediately after injection. The properties of the accumulated beam are determined by cooling and counteracting heating processes. Momentum spread and emittances are significantly reduced compared to the injected beam. The momentum spread of the coasting beam for moderate beam intensity can be directly determined from the width of the frequency distribution by Schottky noise analysis. Measurements for three ion species (Fig. 1) for identical electron beam parameters ($n_e = 5.5 \times 10^7 \mathrm{cm}^{-3}$) show an increase of the momentum spread with the particle number N proportional to $N^{0.37}$.

For larger particle numbers the determination of the momentum spread is doubtful due to collective effects in the noise signal. At small particle numbers the measured frequency spread is determined by the stability of power supplies or changes of the bending field caused by long lasting eddy current effects as the ring magnetic field is ramped to the injection level just before injection and accumulation.

Figure 1: Momentum spread of cooled heavy ion beams at the SIS injection energy.

The transverse emittance of the circulating ion beam could not be measured directly so far for lack of appropriate non-destructive diagnostics. An indirect determination of the horizontal beam emittance was obtained by variation of the bumper amplitude which is applied during multiturn injection. The minimum amplitude which does not result in beam accumulation indicates that beam injection starts in the center of the acceptance. Thus even the cooled circulating beam hits the electrostatic septum and is lost during the subsequent multiturn injection. The accumulation process starts when the bumper amplitude is further reduced.

By variation of the bumper amplitude in small steps (1 mm typically) it was confirmed that for increasing spacing between electrostatic septum and the outermost displacement of the closed orbit during injection an increasing number of ions can be accumulated. The emittance of the cooled beam grows with the number of accumulated ions. The ion beam intensity saturates when the injected current balances the beam loss in the tails of the cooled circulating beam during the closed orbit bump towards the septum. Assuming a Gaussian distribution of the horizontal emittance of the cooled beam the emittance can be evaluated from the

saturation current and the injected current. The horizontal beam emittance determined from this analysis increases almost linearly with the ion beam intensity (Fig. 2).

Figure 2: Horizontal emittance of the cooled beam evaluated from the saturation current in the synchrotron when the bumper amplitude was varied.

Usually the emittance of electron cooled highly charged ions is determined by an equilibrium between cooling and heating by intrabeam scattering. This equilibrium emittance however is expected to grow weaker than linearly with beam intensity [4]. Therefore the measured emittances might indicate an additional heating process. The dashed lines in Fig. 2 represent the emittance ϵ corresponding to a tune shift $\Delta Q = 0.1$ according to

$$\Delta Q = \frac{r_p}{2\pi\beta^2\gamma^3} \frac{q^2}{A} \frac{N}{\epsilon} \qquad (1)$$

for Ni^{26+} and Ar^{18+}, respectively. This tune shift is estimated for a coasting beam without any geometrical factor larger than unity and therefore represents the best case. Heating from betatron resonances might contribute to the observed equilibrium beam emittances. Moreover, imperfections in the closed orbit bumps can pretend an increased beam emittance, particularly for small particle numbers with correspondingly lower emittances. This means that the actual beam emittance is even smaller than estimated and resonance heating is stronger.

The beam quality after accumulation is dependent on the number of ions, but, in general, the cooled beams exhibit considerably better quality. The momentum spread of cooled beams is up to one order of magnitude reduced, compared to $\Delta p/p \simeq 1 \times 10^{-3}$ injected from the linac. The horizontal emittance which amounts to $\epsilon_x \simeq 150\ \pi$ mm mrad after multiturn injection is reduced by more than two orders of magnitude. The vertical emittance is $\epsilon_x \simeq 5 - 10\ \pi$ mm mrad without cooling. For electron cooled ion beams the vertical emittance is usually of similar value as the horizontal. Consequently the phase space volume is, dependent on the ion beam intensity, compressed by 3–6 orders of magnitude.

3 ACCELERATION AND BEAM EXTRACTION

During beam accumulation at the injection energy the rf amplitude is set to zero and only a few milliseconds before the acceleration starts the rf amplitude is raised adiabatically to 9 kV. If the electron velocity which determines the ion velocity is well matched (better than 10^{-3}) to the initial rf frequency (h=4) the capture into the buckets and subsequent acceleration can be performed without measurable particle losses. Due to the large bucket height it is not necessary to switch off the electron beam during rf capture and acceleration.

The accelerated ion beam can be extracted either by a slow resonant extraction or by fast kicker extraction. The parameters of the cooled beam have also been measured after acceleration. For a measurement of the momentum spread after acceleration the rf amplitude was decreased to zero adiabatically. Surprisingly measurements for a Zn^{28+} beam accelerated to 500 MeV/u showed a momentum spread $\Delta p/p \simeq 3 \times 10^{-4}$ independent of the beam intensity. The absence of the expected adiabatic shrinkage after acceleration indicates a mismatch of the ramps for frequency and magnetic field or the presence of unwanted noise or phase jumps on the rf system.

Figure 3: Normalized beam emittance measured with profile grids after extraction from the synchrotron.

For the transverse beam emittance a considerable improvement with cooled beam could be demonstrated. Beam profiles have been measured for Bi^{67+} after extraction (Fig. 3). Using the calculated β-functions at the profile grid the normalized emittances have been calculated. Even with ten times higher beam intensity the horizontal emittance of

the cooled beam after fast extraction is reduced by more than a factor 50 and the vertical emittance by more than a factor of 20. The values for the cooled beams are upper limits only as the measurement was limited by the resolution of the profile grid .

After slow extraction the normalized horizontal emittance is similar with and without cooling and amounts to about 3-4 π mm mrad. The normalized vertical emittance of the cooled beam is 2-3 π mm mrad compared to 12 π mm mrad without cooling. The emittance after slow extraction is spoiled by resonance heating and in the horizontal phase plane determined by the extraction channel. The main advantage for slow extraction is the increased intensity in a synchrotron pulse.

4 TRANSFER OF COOLED BEAMS TO THE STORAGE RING ESR

The high quality and intensity of the cooled synchrotron beams have considerably improved the conditions for filling of the storage ring ESR [1]. The small emittance allows beam transfer after fast extraction without significant losses. Even the additional increase of the beam emittance and the momentum spread after passage of a stripper which provides bare or few electron ions for storage in the ESR does not lead to additional beam losses.

Recently the possibility has been established to merge after acceleration the four synchrotron bunches which are generated for acceleration into one bunch by adiabatic debunching and rebunching at the first harmonic of the revolution frequency [5]. This single bunch is short enough to inject the whole contents of the synchrotron in one transfer to the ESR. The high intensity synchrotron bunch will also be advantageous for the production of radioactive nuclei in the fragment separator FRS from which $B\rho$ selected isotopes can be transferred to the storage ring ESR.

An additional option in the operation of the GSI accelerator complex is the reinjection of maximum charge state ions from the storage ring to the synchrotron. As the heaviest ions are not completely stripped at the usual injection energy (11.4 MeV/u) higher energies can be reached after stripping between the synchrotron and the storage ring and reinjection into the synchrotron with post-acceleration to the maximum energy for the bare charge state.

For the operation of such a reinjection cycle cooling and accumulation at the injection energy of the synchrotron could be favorably used. The time for accumulation (5 s) is short compared to the total cycle time (30 s) which allows to increase the average intensity available in the experimental area by nearly the gain factor for the accumulation process. The current transformer signal in synchrotron and storage ring for this reinjection mode demonstrate the high efficiency of beam transfer with cooled beam (Fig. 4). The reduction of the particle number after injection into the storage ring is caused by stripping to the bare charge state at the relatively low energy of 310 MeV/u. Before installation of the SIS electron cooling system the bare ions had

to be accumulated in the ESR over several minutes. This time consuming stacking procedure in the ESR has been abandoned and only a 12 s period is required to cool the bare ions with the ESR electron cooling system. Finally the bare gold ions are reinjected into the synchrotron, accelerated to the top energy of 1.5 GeV/u and extracted over a variable time interval.

Figure 4: Ion current in the synchrotron SIS and in the storage ring ESR during operation in the reinjection mode. The Au^{63+} ions were accumulated over 5 s in the SIS, accelerated to 310 MeV/u and fast extracted to the ESR after rebunching with h=1. Stripping between SIS and ESR produced Au^{79+} ions which were cooled in the ESR over 12 s, reinjected into the SIS, further accelerated to 1.5 GeV/u and finally slowly extracted over 5 s.

5 REFERENCES

[1] K. Blasche, B. Franzke, Proceedings of the 4th European Particle Accelerator Conference, London, 1994, edited by V. Suller and Ch. Petit-Jean-Genaz (World Scientific, Singapore, 1994) 133.

[2] M. Steck, K. Blasche, W. Bourgeois, B. Franzke, L. Groening, N.S. Dikansky, V.I. Kudelainen, V.V. Parkhomchuk, A.I. Sharapa, A.V. Shemyakin, B.M. Smirnov, Proceedings of the 5th European Particle Accelerator Conference, Sitges , 1996, (World Scientific, Singapore, 1996) 1185.

[3] K. Blasche, H. Eickhoff, B. Franczak, B. Franzke, L. Groening, M. Steck, T. Winkler, V.A. Dolgashev, V.V. Parkhomchuk, Proceedings of the 6th European Particle Accelerator Conference, Stockholm, 1998, (Institute of Physics Publishing, 1998) 550.

[4] M. Steck, K. Beckert, F. Bosch, H. Eickhoff, B. Franzke, O. Klepper, R. Moshammer, F. Nolden, P. Spädtke, T. Winkler, Proceedings of the 4th European Particle Accelerator Conference, London, 1994, edited by V. Suller and Ch. Petit-Jean-Genaz (World Scientific, Singapore, 1994) 1197.

[5] K. Blasche, O. Boine-Frankenheim, H. Eickhoff, M. Emmerling, B. Franczak, I. Hofmann, K. Kaspar, U. Ratzinger, P. Spiller, Proceedings of the 6th European Particle Accelerator Conference, Stockholm, 1998, (Institute of Physics Publishing, 1998) 1347.

EXPERIMENTS WITH THE TWO-BEAM FUNNELING RFQ*

H. Zimmermann, A. Bechtold, A. Firjahn-Andersch, H. Liebermann, A. Schempp,
J. Thibus, E. Winschuh,
*Institut für Angewandte Physik, Johann Wolfgang Goethe-Universität,
Robert-Mayer-Straße 2-4, D-60054 Frankfurt am Main, Germany*

Abstract

High intensity accelerator concepts for Heavy Ion Inertial Fusion (HIIF) injectors require small emittance, high current and high energy beams. The improvement of brightness in such a driver linac is done by several funneling stages at low energies, in which two identically bunched ion beams are combined into a single beam with twice the frequency, current and brightness. For the Heavy-Ion Driven Ignition Facility (HIDIF) we have proposed the use of a two-beam accelerator structure which provides two beams within one cavity and a single r.f. deflector structure which bends the two beams to one common axis. The progress of the experiment and first beam-test results will be presented.

1 INTRODUCTION

The beam currents of linacs are limited by space charge effects and the focusing and transport capability of the accelerator.

Funneling is doubling the beam current by the combination of two bunched beams preaccelerated at a frequency f_0 with an r.f. deflector to a common axis and injecting into another r.f. accelerator at frequency $2*f_0$.

By the use of the two-beam RFQ the two beams are brought very close together while they are still radially and longitudinally focused. Additional discrete elements like quadrupole-doublets and -triplets, debunchers and bending magnets, as they have been proposed in first funneling studies, are not necessary [1,2,3]. A short r.f. funneling deflector will be placed around the beam crossing position behind the RFQ. The layout of the proposed HIDIF-injector with two-beam RFQs in front of the first and second funneling sections is shown in figure 1 [4]. The HIDIF linac starts with 16 times 3 ion sources for three different ion species to allow so-called „telescoping" at the final focus [5]. With four funneling stages the frequency has been increased from 12.5 MHz to 200 MHz accordingly [6].

For studies of the new two-beam RFQ structure and the r.f. deflector, the first two-beam funneling experiments will be carried out with He^+-ions at low energies to facilitate ion source operation and beam diagnostics.

Figure 1: Layout of the 12.5...200MHz linac system for 400 mA of Bi^+.

Two small multicusp ion sources and electrostatic lenses, built by LBNL (Lawrence Berkeley National Laboratory) [7,8], are used. The ion sources and injection systems are attached directly on the front of the RFQ with an angle of 76 mrad, the angle of the beam axes of the two-beam RFQ.

Figure 2 shows a scheme of the experimental set-up of the two-beam funneling experiment.

Figure 2: Experimental set-up of the two-beam funneling experiment.

Two-beam RFQ	He^+	Bi^+
f_0 [MHz]	54	12,5
Voltage [kV]	10.5	180
R_p-value [kOhm·m]	80	250
Q_0-Value	1800	5000
T_{in} [keV]	4	209
T_{out} [MeV]	0.16	12.54
Angle between beam axes [mrad]	76	76

Table 1: Main parameter of the experiment with the He^+ and the design parameters of a first HIDIF funneling stage for Bi^+.

2 ION SOURCES AND INJECTION SYSTEMS

To investigate the synchronous operation, the beam of both ion sources and injection systems have been tested on an emittance measurement device by different parameters of the ion sources and injection system. The measured normalized 90% RMS-emittance is shown in fig. 3.

Figure 3: Normalized 90% RMS-emittance of the two injection systems at different beam currents.

3 THE TWO-BEAM RFQ

The two-beam RFQ consists of two sets of quadrupole electrodes, where the beams are bunched and accelerated with a phase shift of 180° between each bunch, driven by one resonant structure. With the use of identical RFQ electrode designs for both beam lines, the electrodes of one beam line are installed with a longitudinal shift of 2.55 cm (i.e. $\beta\lambda/2$ at final energy) to achieve the 180° phase shift between the beam bunches of each beam line. Figure 4 shows the with a fast faraday cup measured micro-bunch current of the two RFQs, which demonstrates the 180° phase shift between the beam bunches.

Figure 4: The measured micro-bunch current of the two RFQs demonstrate the 180° phase shift between the beam bunches. The scale is 5 ns/div. horizontally.

In Figure 5 the measured energy spectra behind the RFQ are shown. The final beam-energy of 166 keV is reached at an electrode voltage of 10 kV, which is the design voltage. Below 4 kV electrode voltage the He$^+$ beam is only transported and not accelerated. The energy is now the energy of the injection system of 4.15 keV.

Figure 5: Energy spectra behind the RFQs. With the design voltage of 10 kV the final beam-energy of 166 keV is reached.

At the beam crossing position behind the two-beam RFQ emittance measurements have been done. Figure 6 shows the two measured RMS-emittances. The normalized 90% RMS-emittance of the two beams are 0.107 and 0.114 mm mrad, the deviation is about 6 %.

Figure 6: Measured emittances 1m behind the RFQ at the place of beam crossing. The ellipses correspond to the 90% normalized RMS-emittances which are ε_{RMS}=0.107 and 0.114 mm mrad for each beam.

5 FUNNELING-DEFLECTOR

For bending the two beams to a common axis, a funneling-deflector is mounted directly behind RFQ. This device is like a plate capacitor with an electric field only in the

bending plane. The crosspoint of the two beams is situated right in the middle of the deflector. As the bunches leave the RFQ with a phase shift of 180° and with alternating angle (± 37.5 mrad), they are step by step deflected to angle zero, when the field is smaller in the case of wrong polarity. Figure 7 shows a simulation of the change in angle of the stable particle during the motion through the funneling-deflector. As the calculation shows, the optimum voltage for operation is about 3 kV. Figure 8 shows the scheme of the funneling-deflector.

Figure 9: E-field in the funneling-deflector over the length of two cells.

6 CONCLUSIONS

The beam test results of the two-beam RFQ and the theoretical investigations on the funneling section have shown that the chosen set-up should be able to bend the two beams to a common axis. Next step will be the experimental test of the funneling-deflector.

Figure 7: Motion of the stable-particle during bending in the funneling-deflector.

Figure 8: Picture of the funneling deflector. To reduce the E-field a drift tube is mounted between the plates each second cell.

To minimize the field in case of wrong polarity we decided to use drift tubes each second cell. The amplitude of the simulated E-field on the symmetrical axis of the deflector over the length of two cells is shown in Fig. 9.

REFERENCES

[1] K. Bongardt and D. Sanitz, Funneling of Heavy Ion Beams, Primary Report, Kernforschungszentrum Karlsruhe, 11 04 02P14C (September 1982)

[2] J.F. Stovall, F.W. Guy, R.H. Stokes and T.P. Wangler, Beam Funneling Studies at Los Alamos, Nucl. Instr, and Meth. A278 (1989) p143

[3] K.F. Johnson, O.R. Sander, G.O. Bolmer, J.D. Gilpatrick, F.W. Guy, J.H. Marquardt, K. Saadatmand, D. Dandoval and V. Yuan, A Beam Funnel Demonstration: Experiment and Simulation, Particle Accelerators, Vols. 37-38 (1992) p. 261

[4] A. Firjahn-Andersch, J. Madlung, A. Schempp, H. Zimmermann, A two-beam RFQ for ion beam funneling, Proc. (International) Particle Accelerator Conference 1997, p. 1081-1083

[5] M. Basco, M. Churazov, D. Koshkarev, Fusion Engineering and Design 32-33 (1996) p. 73.

[6] A. Schempp, The injector for the HIDIF driver linac, Nuclear Instruments and Methods in Physics Research A415 (1998) 209-217

[7] K.N. Leung, Multicusp Ion Sources, Rev. Sci. Instrum. 65(4) (1994) p. 1165.

[8] R. Keller in: The Physics and Technology of Ion Sources, Edited by I. G. Brown, Wiley-Interscience Publication, New York.

[9] A. Schempp, Design of Compact RFQs, Proc. Linear Accelerator Conference 1996, CERN 96-07, p. 53.

BEARS (BERKELEY EXPERIMENTS WITH ACCELERATED RADIOACTIVE SPECIES)*

J. Cerny III[+], F. Guo[+], R. Joosten[+], R.M. Larimer[+], C.M. Lyneis[+], M.A. McMahan[+#], E.B. Norman[+],
J. O'Neil[&], J. Powell[+], M. Rowe[+], H. VanBrocklin[&], D. Wutte[+], Z.Q. Xie[+], X.J. Xu[+], LBNL,
Berkeley, CA

P. Haustein, BNL, Upton, NY

Abstract

The BEARS project at Lawrence Berkeley National Laboratory is developing the capability for some proton-rich radioactive beams using a coupled-cyclotron method. Initial studies have focused on ^{11}C and ^{14}O and the first physics experiment is complete using ^{11}C in batch mode. Ionization efficiencies have been measured as high as 11% for ^{11}C^{+4}. The total efficiency for ionization and acceleration is approximately 1% and total beam intensities of $1*10^8$ have been observed. Upon completion of the transfer line, beam intensities of $2*10^8$ are expected for ^{11}C and $5*10^6$ for ^{14}O.

1 INTRODUCTION

There is at the present time extensive world-wide activity in the development and construction of radioactive ion beam (RIB) facilities of various types. The availability of beams of unstable nuclei offers exciting new opportunities for research into nuclear structure and nuclear astrophysics. Construction of the Isotope Separator On-Line (ISOL) is the next construction priority of the U.S. Nuclear Science Long Range Plan.

Much R&D must be done before ISOL can be realised, and completion of the project is years in the future. In the meantime, limited RIB capability can be achieved in a variety of ways. Berkeley Experiments with Accelerated Radioactive Species (BEARS) is an initiative to develop limited RIB capability at the Lawrence Berkeley National Laboratory (LBNL).

The basic concept for Phase I of the BEARS project involves coupling the Biomedical Isotope Facility (BIF) in Bldg. 56 at LBNL with the 88-Inch Cyclotron through a 300 meter transfer line, as shown in the site map of Figure 1. BIF [1] is a commercial 10 MeV fixed energy H_2^- cyclotron used for making isotopes for Positron Emission Tomography. It is well suited for making light neutron-deficient radioactive beams using gas targets. The 88-Inch Cyclotron facility, shown schematically in Figure 2, produces both heavy-ion and light-ion beams for nuclear physics studies. It's two Electron Cyclotron Resonance (ECR) ion sources, the LBL-ECR and the state-of-the-art Advanced ECR, the AECR-U, efficiently produce highly charged ions. As

will be shown, the combination of the efficiency of an ECR source with the mass resolution of a cyclotron creates a powerful secondary accelerator for radioactive ions.

Figure 1. Site map of transfer line between two cyclotrons

2 PRODUCTION AND TRANSPORT

The initial BEARS development has focused on the production of ^{11}C and ^{14}O, with half-lives of 20 minutes and 70 sec, respectively. Initial attempts were made to produce the species in solid targets and transport them on small aerosol clusters for direct injection into the ECR source. The method is broadly applicable to many isotopes; however, it failed to transport significant amounts of ^{11}C or ^{14}O. This was traced to the majority of the activity forming gaseous compounds and thus not attaching to the aerosol clusters. Much higher transportation efficiencies are obtained when the ^{11}C and ^{14}O is made in bombardments of protons on a N_2 gas target, in the reactions ^{14}N(p,^{4}He)^{11}C and ^{14}N(p,n)^{14}O, respectively. When a trace amount of O_2 is added to the target gas, the radioactive carbon is predominantly in _ the form of ^{11}CO$_2$. The CO$_2$ is swept out of the target with a He-jet and transported through a narrow capillary to one of the ECR sources.

Figure 2. The 88-Inch Cyclotron and its ECR ion sources.

. Once there, the radioactive CO_2 is trapped in liquid-N_2 and the helium support gas pumped away. This method allows simple, maximum-yield production at the BIF and is easily adapted to use in the AECR-U.

3 IONIZATION

The first development phase of the BEARS project took place solely at the 88-Inch Cyclotron, with protons from one ECR source accelerated to 10 MeV to mock up the BIF. The activity was transported to the second ECR source through a 300 m capillary where studies were made of the efficiencies and hold-up times for ionization and extraction of the radioactive ions. The best efficiency results were obtained using the AECR-U, a high performance source built in 1990 and upgraded in 1996. This ion source is well optimized for the production of highly charged ions, with a strong magnetic field configuration which can support the hotter plasma which is essential to the production of highly charged ions. [2] It is one of the few ECR sources that incorporate all of the advances in technology of ECR sources made in recent years – multiple-frequency plasma heating, good plasma chamber surface coating with high yield of cold secondary electrons and high magnetic mirror fields. [3] It has produced many record charge states and beam intensities.

Efficiencies for ionization of the radioactive species were obtained by measuring the activity at the cryogenic trap before emptying into the source, and

then the build up of activity on a Faraday cup after the 90 degree analyzing magnet at the exit of the source. Corrections were made for half-life and detector efficiencies. Ionization efficiencies using the LBL-ECR and AECR-U sources are shown in Table 1 for several charge states of ^{11}C and ^{14}O. Efficiencies as high as 11% were obtained for $^{11}C^{+4}$. There is room for improvement, however, as can be seen in the measured efficiencies of stable ^{12}C and ^{16}O charge states using a calibrated CO_2 leak. Here efficiencies of 23.4% were obtained for $^{12}C^{+4}$ and 33% for $^{16}O^{+6}$.

It is important for efficient RIB production that the time the radioactive species spends in the source, the "hold-up" time is short in comparison to its lifetime. Source hold-up times in the AECR-U have been measured for stable CO_2 and found to be of the order of 5-7 sec. When the decay of the activity is measured for ^{11}C and ^{14}O, two components are seen in the decay curve. The fast component is on the order of 20-30 sec for both species. The slow component is on the order of 360 sec for the ^{11}C. If one could shorten the hold-up times in the source to be nearer to that of stable carbon and oxygen, the ionization efficiencies should approach those of the stable species. This is particularly important for the 70 sec isotope ^{14}O, for which an order of magnitude improvement could be made. Once the transfer line is complete, these studies will be pursued.

Table 1: Ionization efficiencies and hold-up times for radioactive and stable CO_2 in AECR-U

Ion	ECR	AECR-U		Stable CO_2 Leak	
C	%	%	τ_{fast} (sec)	%	τ_{fast} (sec)
1+	1.1				
2+	0.7				
3+	0.4	4			
4+	0.9	11	24	23.4	5.6
5+	0.1	4		15.4	
6+		2			
O					
3+	0.4				
4+	0.4				
5+	0.4			12.5	
6+		3.6		33	7.1
7+		1.2	20-30	7.44	
8+		0.4			

4 ACCELERATION

In order to tune a low-intensity radioactive beam through the cyclotron, one tunes a stable beam close to the same charge to mass ratio (q/m). Table 2 lists the isotopic masses and the RF frequency at a typical energy for the two sets of analog beams: [^{11}C, ^{11}B and ^{22}Ne] and [^{14}O, ^{14}N, and ^{28}Si]. Also shown is the

Figure 3. Predicted ^{11}C intensities as a function of energy/nucleon. The solid curve is the maximum unstripped intensity using the most advantageous charge state at each energy using the ionization efficiencies of Table 3. The dashed curve is the intensity after stripping to +6.

frequency difference between the analog beam and its radioactive partner, a quantity that is directly related to the mass difference. The frequency resolution of the 88-Inch Cyclotron is approximately 2 kHz. Thus one can see that ^{11}C and ^{22}Ne can be easily separated by tuning the frequency, but ^{11}C and ^{11}B cannot be separated. Thus the ^{11}B, rather than being a convenient analog beam for tuning, becomes instead an annoying contaminant.

In the first tests to accelerate ^{11}C, the initial ^{11}B intensity was measured to be a factor of 100 less than that of the ^{11}C. However, in subsequent runs it was found that the ^{11}B intensity was very high, a factor of 1000 greater than that of the ^{11}C. Between the two runs, boron was run in the ion source and it remains a low level contaminant for months. Recent measurements have shown that the boron contamination has dropped off considerably. Another source of ^{11}B contamination naturally builds up during the course of an ^{11}C run, due to the decay of ^{11}C $\rightarrow$ ^{11}B inside the ion source.

Table 2: Analog Beams of ^{11}C and ^{14}O

Ion	Energy MeV	Mass (amu)	Frequency (MHz)	Δ Freq (kHz)
^{11}C^{+4}	125	11.011433	7.5222	-
^{11}B^{+4}	125	11.0093054	7.5236	1.4
^{22}Ne^{+4}	250	21.9913831	7.5327	10.5
^{14}O^{+6}	140	14.008595	7.0656	-
^{14}N^{+6}	140	14.003074	7.0684	2.7
^{28}Si^{+12}	280	27.976927	7.0756	10.0

The method developed to set up the cyclotron for a RIB run using ^{11}C and eliminate the ^{11}B background is a multi-step process:

i) Tune injection line, cyclotron and beam line using ^{22}Ne^{+8} at the same energy/nucleon

ii) Switch to ^{11}B^{+4} frequency and look for contamination; fine tune cyclotron and beam line

iii) Put a thin stripper foil in beam line before one of the final bending magnets

iv) Strip ^{11}B from +4 $\rightarrow$ +5 and retune line

v) Scale beam line magnets to ^{11}C^{+6}

vi) Put ^{11}C into ion source and fine tune source and beam line magnets for maximum intensity

Using this procedure, a first physics experiment was done using the ^{11}C beam, in spite of the fact that the transfer line to the BIF was not yet complete. The ^{11}C activity was carried from the BIF by truck, then cryotrapped and injected into the AECR-U, giving 30 minutes of beam every hour for several short runs. In the best case, a clean ^{11}C beam intensity of $1*10^8$ ions/sec was achieved for a short while, and $5*10^7$ ions/sec typically. It is expected that upon completion of the transfer line, beam intensities of $\approx 2*10^8$ ions/sec will be typical with an optimal choice of beam energies. Intensities for ^{14}O are expected to be $\approx 5*10^6$ ions/sec.

The above method relies on the fact that at these energies the probability to fully strip an ion in a thin foil is greater than 99%. At lower energies, the probability to fully strip the carbon ions will decrease. In addition, the transmission of the cyclotron decreases in certain regions of magnetic field and when running in higher harmonics. In Figure 3, these factors plus source ionization efficiencies are folded together to calculate a predicted ^{11}C beam intensity as a function of energy/nucleon. At energies near 1 MeV/nucleon, the region of interest for nuclear astrophysics intensities are significantly lower – approximately $5*10^6$ for unstripped beams and $5*10^5$ for clean ^{11}C^{+6} beams. Even at these intensities, the expected production of BEARS is comparable to that of other facilities such as HRIBF at Oak Ridge and CYCLONE at Louvain-la-Neuve. At energies applicable for nuclear structure and reaction studies, production from BEARS should rival the best of the Cyclone beams.

5 REFERENCES

[1] VanBrocklin, H.F. and O'Neil, J.P., in *Applications of Accelerators in Research and Industry*, ed by Duggan, J.L. and Morgan, I.L., New York: AIP Press, 1997, pp. 1329-1332

[2] Xie, Z.Q. and Lyneis, C.M., proceedings of the 13th Int'l Workshop on ECR Ion Sources, College Station, TX, Feb. 1997, p. 16

[3] Xie, Z.Q., Rev. Sci. Instrm. **69**. 625 (1998).

HIGH POWER COUPLER ISSUES IN NORMAL CONDUCTING AND SUPERCONDUCTING ACCELERATOR APPLICATIONS

H. Matsumoto, KEK, Tsukuba, 305, Japan

Abstract

The ceramic material (Al_2O_3) commonly used for the klystron output coupler in normal conducting, and for an input coupler to superconducting cavities is one of the most troublesome parts in accelerator applications. But the performance can be improved very much by starting with high purity (>99.9%) alumina powder of controlled grain-size (0.1~0.5-μm), and reducing the magnesium (Mg) sintering-binder to lower the dielectric loss to the order of 10^{-4} at S-band frequencies. It has been confirmed that the new ceramic can stand a peak S-band frequency rf power of up to 300 MW and 2.5 μsec pulse width.

1 INTRODUCTION

This study was carried out at KEK by the author and Dr. A. Miura, with the collaboration of Mr. W. R. Fowkes and Mr. R. S. Callin of SLAC.

The motivation of this study was to clarify the origin of discharge breakdowns of the alumina ceramic material in rf windows, and to demonstrate a breakthrough that allows use of rf windows for peak rf power exceeding 100 MW. Originally the breakdown mechanisms were not fully understood; but since light emission from the alumina ceramic disk was observed, multipactoring phenomenon was suspected [1]. Therefore many studies were done to study local heat build-up due to multipactoring [2], [3]. Considerable progress was made through efforts at SLAC [4], and Varian Co., Inc. A variety of surface-coating materials were tested as possible cures. Coating with TiN, which has a low secondary electron emission coefficient and good chemical stability, proved effective [5], [6]. However, more recently it was discovered at SLAC that even a TiN coated disk can be destroyed by discharge breakdown, most often when the rf power transmission exceeds 50 MW. In this power regime no clear correlation was found between light emission and breakdown. The problem was regarded mostly as a technical issue for the coating, and again many studies were undertaken [7], [8], [9]. From a literature survey and from examination of destroyed windows, we have come to suspect that high power breakdown of alumina disks may be due to phenomena taking place inside the alumina rather than (or besides) at its surface. The root cause of the problem might be voids within the alumina or structural defects due to binder materials used during the sintering process. Thus, the origins of destruction of the ceramic disk have to be separated into two regimes: one for the low peak rf power with cw or millisecond long pulses, and the other for high peak rf power with pulses on the order of several tens of microseconds.

In this paper I will describe the destruction breakdown mechanism of alumina ceramic in the rf window as

elucidated by simulation and experiment. Further, results of this study can be used to improve the ceramic material of input couplers for superconducting cavities.

2 ELECTRON MULTIPACTORING

We investigated the behavior of multipactor electrons on the rf window under various power transmission conditions. Then comparisons were made between the theoretical expectations and the actual experimental results on samples.

We used an rf window that would make it simple to study the electron multipactor and the discharge breakdown of ceramic disks. A de-mountable pill-box type rf window was developed to avoid the brazing that can cause discharge breakdown at the junction between the disk and the enclosure at high peak rf power. The window consists of an alumina disk in a pair of stainless steel enclosures that are copper plated (~20 μm) on their inner surfaces, as shown in Figure 1.

Figure 1: A cross-sectional view of the de-mountable type rf-window used in testing. The measured input VSWR is 1.05 or less at 2856 MHz $\pm$ 50 MHz.

Figure 2 shows the propagation modes in a typical pill-box type rf window as calculated by the MAFIA 3D-code. As can be seen in the figure, the propagation modes through the rf window are TE_{11}-like and TM_{11}-like. Therefore, there are two electric field patterns on the ceramic disk that are parallel and then perpendicular to the disk which appear alternately. The perpendicular electric field (Fig. 2-b) causes most discharge breakdowns of ceramic disks, such as pin-hole punctures and cracks. We have extended the original simulation code [10] in a few areas to suit our purposes.

Figure 3 shows a single-surface multipactoring electron orbit calculated during the simulation [11]. It shows that the free electron path is at most a few cm. Cathode luminescence of alumina is known to occur with incident electron energies below a few tens of keV. Thus the experimentally observed light emission from alumina windows is consistent with cathode luminescence due to bombardment of

multipactoring electrons.

(a) Side view of TE$_{11}$-like parallel electric field on the ceramic disk.

(b) Side view of the TM$_{11}$-like perpendicular electric field on the ceramic disk.

Figure 2: Propagating mode through the rf window. The arrows show the electric field direction.

Figure 3: Typical single-surface multipactoring with 4 MW rf power transmission through the window. (Y and Z are defined in Fig. 1). The curve is a projection of 3-dimensional electron trajectory onto the Y-Z plane. The free electron path in the X direction is Ø10 mm.

Figures 4-a1, -a2 and -a3 show the density distribution of electrons hitting the ceramic surface. Figures 4-b1, -b2 and -b3 show the light emission pattern observed during a high power test. The calculated multipactor region and the light emission pattern are in qualitatively good agreement.

(a1)

(b1)
Transmission rf power of 4 MW for 2.5 μsec.

(a2)

(b2)
Transmission rf power of 10 MW for 2.5 μsec.

(a3)

(b3)
Transmission rf power of 50 MW for 2.5 μsec.

Figure 4: Left shows the calculated distributions of multipactoring on the alumina ceramic disk surface. The gray scale darkness indicates the electron intensity in 5 steps, 0-100%. Right: shows the luminescence from the surface of the alumina ceramic disk in our experiment. None of the samples has any coating such as TiN.

According to the calculations, multipactoring is predicted to be basically non-existent at any transmission power above 50 MW, as shown in Figure 4-a3. Most likely this is because multipactoring depends on the $E\perp$, the strength of the electric field component perpendicular to the alumina surface. Our calculation shows that multipactoring is strongest when $E\perp$ is 100-450 kV/m. When the transmission power is above 50 MW, $E\perp$ exceeds 450 kV/m and a resonant condition favorable for multipactoring no longer obtains, because the electrons accelerated along $E\perp$ can reach the opposite copper surface and be absorbed during a half rf cycle. As seen in Figures 5 and 12 (lower traces), the multipactoring areas disappear in a high perpendicular electrical field ($E\perp$).

This leads us to conclude that when an alumina disk fails in a high power environment (transmission power >50 MW), it would be unreasonable to take multipactoring as the primary cause. Some other factors should be investigated as the root causes of breakdown of alumina disks at high rf power. Voids and impurities in the alumina are possibilities. However, even at high peak rf power levels, it was found that multipactor occurs during the rf pulse transient time (Fig. 5). Therefore, coating with TiN is necessary to maintain the best possible overall characteristics of alumina ceramic for rf windows.

From this, we may conclude that the TiN coating is very effective for low peak power and long pulse applications, such as for the input coupler to a superconducting cavity.

Figure 5 shows the typical time profile of the light emission from an alumina ceramic disk.

Figure 5: Upper trace: Time profile of rf power transmission through the rf window with alumina ceramic disk for sample 3. Lower trace: Signal from the photo-multiplier monitoring the light emission from the disk.

The light emission signal trace is synchronized with the transmission rf power profile. At the rising and falling edges

of the rf pulse, when the power transmission is close to 10 MW, light emission for a few hundred nano-seconds is clearly seen. Note that our sample did not have a TiN coating.

We understand that although the accelerating operational power was well above the multipactor regime, during the pulse transient time the disk momentarily experiences the power level where multipactoring is prominent. Therefore, for rf window disks in actual use, a TiN coating is required to reduce the charge on the alumina ceramic disk due to electron multipactoring during the pulse transient time.

3 ALUMINA CERAMIC MATERIAL IMPROVEMENT

3.1 High-Purity Fine Alumina Powder and HIP

Typical disks for windows have been made of 99.5% purity alumina ceramics, in which the 0.5% of impurities act to reduce the sintering temperature to around 1400-1500 °C. Sintering binders such as magnesium (Mg) comprise the major part of the impurities that keep the alumina grain size to around 10 to 20 μm after sintering. If the binder fraction is made smaller, the sintering temperature has to be increased up to 1600 °C, and this increases the prosity (void population). Thus, reduction of impurities and reduction of porosity are incompatible. Consistent with this, we found experimentally that high purity (99.9%) alumina disks do not perform much better in a high power environment [9]. Figure 6 shows photographs of typical alumina ceramic samples.

Figure 6: Photographs of alumina ceramics disks for rf windows. Voids within the alumina or structural defect are Black.

These problems have two possible solutions. The first is to use very fine alumina powder. If the powder size is smaller, the sintering temperature can be lowered while using only a small amount of binder. Recent progress in the alumina industry has resulted in high purity (99.9%) ultra fine alumina powders of 0.1-0.5 μm diameter, as shown in Fig. 7. Low temperature sintering of such fine powder reduces the void population.

Figure 7: Electron microscope photographs of alumina ceramic, made from ultra fine ($\emptyset$0.1-0.5 mm) and high purity (99.9%) alumina powder, showing the uniform grain size and the absence of large voids at grain boundaries.

The second solution is to apply Hot Isostatic Pressing (HIP), a thermo-mechanical process that applies gas pressure at high temperatures to attain high density [12]. The voids in alumina materials are removed ("squeezed out") in a high

temperature (1400 °C), high pressure (2000 kgf/cm^2) environment in an inert gas such as argon, as shown in Fig.8.

Figure 8: Schematic diagram of a HIP treatment set-up. The furnace is inside the pressure vessel, and it is set to keep the temperature well below the melting point of the material being processed.

This treatment can reduce the alumina ceramic porosity to a negligibly small 0.5%. The alumina grains are tightly packed. This also improves the mechanical strength. The improvements due to HIP treatment are summarized in Table 1 and the results, are shown in Fig. 9.

Table 1: Properties of the alumina ceramic disk before and after the HIP treatment.

	Before HIP	After HIP
Porosity (%) (volume/weight)	3.8	0.5
Fracture strength (kgf/cm^2)	29.8	36.1
Dielectric constant (at 2853 MHz)	9.4	9.7

(a) Before HIP   (b) After HIP

Figure 9: Electron microscope photographs of alumina ceramic before and after HIP treatment (1450 °C, 2000 kgf/cm^2, 2 hours): (a) shows voids at the alumina grain boundaries; (b) shows almost no voids in any area.

The light transparency of the alumina is also increased. Impurities or voids become easily identifiable, because they appear as dark clouds. This allows for easy visual inspection for rejection of undesirable alumina ceramic disks before use, as shown in Fig. 10.

(a) Clear   (b) Clouded

Figure 10: Comparison of clear and clouded alumina ceramic disks. The samples, of 3.5 mm thickness and 92 mm diameter, are held up to an incandescent light (100 W, 10 cm behind).

3.2 Sintering Binder and RF Loss

The rf loss of alumina ceramic disks is affected by the amount and composition of impurities. To function as an rf window the rf loss should be kept low of course. The rf loss due to binders has been found to depend strongly on the choice of binder materials [13]. For example, it is very sensitive to the presence of MgO. We have fabricated alumina ceramic disks of varying purity with and without MgO and measured their characteristics. Table 2 shows the results. With no contain MgO at all, a very low dielectric loss is achieved. Table 2 shows the results.

Table 2: Physical properties of high-purity alumina ceramic.

Alumina ceramic purity	99.5%	99.9%	99.9%
MgO content (%)	0.19	0.06	0
tan δ (× 10⁻⁴): (at 2853 MHz)	13.0	3.0	0.27 (at 10 GHz)
Thermal conductivity: (cal/cm·h·°C)	0.06	0.06	0.075

4 HIGH POWER TEST

4.1 Alumina Disk Samples

We used a Traveling Wave Resonator (TWR) to conduct high power tests of rf window alumina disks which were made with varying fractions of sintering binder (MgO). The parameters of the seven alumina ceramic disks are summarized in Table 3.

Samples 1 to 6 had been HIP-treated. No samples had TiN coating. Sample 1 had no visible imperfections (see Fig. 10-a), but sample 2 contained impurities that looked like a dark cloud (see Fig. 10-b). Samples 3 and 5 were made of 99.9% alumina with 0.06% MgO binder, and sample 4 of 99.9% alumina with no MgO binder. The test on sample 5 was done to study the reproducibility of the result of sample 3. Sample 6 had ten 0.5-mm-diameter holes through it. Sample 7 was made of the same material as samples 3 and 5 except for the porosity (0.8%), which was 1.6 times as large, because samples 3 and 5 had been HIP treated. Samples 6 and 7 were made to investigate the relation between micro discharge breakdown power and porosity size at the grain boundaries of alumina ceramic.

Table 3: Parameters of alumina disks tested in this experiment.

	Purity (%)	Prosity (%)	MgO (%)	Loss (10⁻⁴)	Visible impurity
#1	99.5	0.5	0.19	12	no
#2	99.5	0.5	0.19	12	yes
#3	99.9	0.5	0.06	3	no
#4	99.9	0.5	0.00	0.3	no
#5	99.9	0.5	0.06	3	no
#6	99.9	0.5	0.06	3	no (1)
#7	99.9	0.8 (2)	0.06	3	no

(1) This sample had ten 0.5 mm diameter holes through it. (2) No HIP treatment.

4.2 Experimental Results

Figure 11 summarizes the results of the experiment, showing the observed temperature rise at the window frame as a function of the average power for each sample.

Figure 11: Experimental results. No samples had any surface coating. Samples 1 to 6 had HIP treatment. Sample 7 was made from fine grain alumina powder (see Fig. 7).

Sample 1: During the operation, localized light emission from a single spot increased continuously. At a transmission power of 200 MW, a large discharge took place and the disk was destroyed. Electron microscopy showed numerous melted pin-holes with diameters of ~10 μm at the point where the light emission was seen, along with a few-cm-long crack. At a power transmission of 200 MW, multipactoring does not cover the entire window surface. Our interpretation is that a highly localized multipactor started at a defective spot on the surface, and the resultant electron collisions on the surface became the heat source causing the disk failure.

Sample 2: No localized discharge was seen during the test. Sample 2 did not experience a steep temperature rise, as did sample 1. At 25 Hz, when the power reached 113 MW, the alumina disk cracked and was destroyed. No trace of melting was seen on the surface. We interpret this failure as having been caused by heating due to the localized sintering binder (dark cloud).

Sample 3: The test was continued up to 280 MW at 25 Hz, then up to 200 MW at 50 Hz, and terminated at that point. The alumina disk showed no damage. The temperature rise was small and the operation very stable.

Figure 5 shows the light emission profile from sample 3 during the test. The light signal trace is synchronized with the input rf power. At the rising and falling edges of the rf pulse, when the power transmission approaches 10 MW, light emissions for a few hundred nano-seconds are clearly seen. Note that our samples do not have a TiN coating. Although the operational power was well above the multipactoring regime, during the pulse transient time the disk momentarily experienced power levels where multipactoring is prominent. Therefore, for rf window disks in practical use, TiN coating is required to reduce the charge up on the alumina ceramic disk due to the electrons multipactoring during the pulse transient time.

Figure 12 shows the time profile of X-ray emission from sample 4. The amount of X-ray emission was roughly proportional to the power transmission through

the window. This figure shows typical behavior of sample 4, when no discharge was taking place. As stated earlier, multipactoring is pronounced only during the pulse transient time, resulting in electrons with a relatively low energy (a few keV). Although they may also emit X-rays, the photon energies are too small to penetrate the window frame. Those soft X-rays are not observed by outside detectors.

Fig. 12: Time profiles of rf power, fluorescent light, and X-ray emission from sample 4 during stable operation.

Sample 4: No failure occurred. Sample 4 showed very stable performance with the lowest temperature rise even at the maximum power of 280 MW at 50 Hz.

Sample 5: No failure occurred at 300 MW at 50 Hz. Figure 9 shows that the temperature rise in sample 5 was very similar to that in sample 3. No melting spots or cracks were found on the disk.

Sample 6: Continuous discharging occurred at some pin holes we had made in the sample during rf operation above 50 MW transmission power. With a transmission power of 152 MW, a large discharge took place, and the disk was destroyed (cracked). Sample 6 showed the highest temperature rise among the samples tested.

Sample 7: No failure occurred at 280 MW and 50 Hz The temperature rise of sample 7 was 1.5 times as high as that of samples 3 and 5.

4.3 Discussions

What we have learned from these tests can be summarized as follows:

When there is a surface defect, it can initiate localized multipactoring. The surface temperature at the spot is increased. Then the secondary emission coefficient of the alumina is increased, and the thermal heat conductivity is decreased in proportion to the temperature rise. This process self-amplifies rapidly until the alumina disk is destroyed (sample 1). When there is an internal defect due to localized concentrations of sintering binders or voids, it can cause heat build-up at that spot and the thermal strain can cause cracking (sample 2). Clearly temperature rise depends on the degree of porosity of the alumina ceramic disk (sample 7). The high power performance of alumina disks can be dramatically improved by using HIP on high-purity alumina (samples 3, 4, and 5). By not adding MgO as the sintering binder for alumina, the dielectric rf loss is decreased and the rf heating is decreased. This also contributes to the stability of alumina disks in high power operation (sample 4).

5 CONCLUSIONS

A computer simulation of multipactoring electrons on the rf window disk surface was conducted for a theoretical study of the breakdown mechanism. Experiments using a TWR were carried out to study the high power behavior of window disks made of high purity alumina with HIP treatment, but without TiN coating. Over a wide range of transmission power, good agreement was found between the calculated distribution of multipactoring electrons hitting the alumina surface and the experimentally observed fluorescence pattern on the window. The simulation predicts that multipactoring will not take place at transmission powers above 50 MW. Observations in the TWR experiment confirmed this prediction. Even at this power level, however, multipactoring was found to occur during the rf pulse transient time. Therefore, coating with TiN is necessary to maintain the best possible overall characteristics of alumina disks for rf windows. At a power level above the multipactoring region, imperfections inside the alumina ceramic disk are the dominant source of breakdowns. As a cure, we have developed a technique based on the following combination:

1) use of high-purity ultra fine alumina powder, 2) avoidance of MgO sintering binder, and 3) HIP treatment.

This significantly improves the mechanical properties of alumina, and reduces the dielectric RF losses and the porosity. The high power performance of alumina disks fabricated this way is significantly superior to that of disks made in the traditional way. The optimization of alumina ceramic disk fabrication and testing for long-term performance of a large number of disks requires future work. Such studies will be continued in order to build a basis for the design of rf windows for future accelerators.

6 REFERENCES

[1] D. H. Preinst, IRE Trans. ED-8, 243 (July 1961).

[2] R. Hayes, Final Report, AD 256259, Eitel-McCullough Inc., San Carlos, June 1964.

[3] R. Nyaiesh, E. L. Garwin, F. K. King and R. E. Kirby, Proc. 32nd National Symp. of American Vacuum Society, Houston, November 1985.

[4] R. B. Neal, D. W. Dupen, H. A. Hogg and G. A. Loew, "The Stanford Two mail Accelerator", W. A. Benjamin Inc., 1968.

[5] Frank Kriensen, SLAC/AP-23, 1984.

[6] Y. Saito, S. Yamaguchi, S. Anami, S. Michizono, A. Kinbara and N. Matsuda, Proc. 14th Int. Sym. on Discharge and Electrical Insulation in Vacuum, September 1990.

[7] Y. Saito, N. Matsuda, S. Anami, A. Kinbara, G. Horikoshi and J. Tanaka, IEEE Trans. Electrical Insulation, 24 (6), p. 1029-1032, (1989).

[8] S. Michizono Y. Saito, S. Anami, A. Kinbara, et al., Proc. 16th Int. Symp. on Discharge and Electrical Insulation in Vacuum, 1992.

[9] A. Miura and H. Matsumoto, Proc. of Int. Conf. for High Energy Accelerators, 1992.

[10] S. Yamaguchi, Y. Saito, S. Anami and S. Michizono, IEEE Trans. Nucl. Sci. NS-39, (1992).

[11] A. Miura and H. Matsumoto, Proc. Int. Linear Accelerator Conf. Ottawa, 1992.

[12] A. Miura and H. Matsumoto, NIM A334 (1993) 341-352.

[13] W. R. Fowkes, R. S. Callin and M. Studzinski, Proc. IEEE Part. Accel. Conf., San Fransico, 1991.

SEAMLESS SUPERCONDUCTING RF CAVITIES

Vincenzo Palmieri

ISTITUTO NAZIONALE DI FISICA NUCLEARE
Laboratori Nazionali di Legnaro
Legnaro (PD), ITALY

Abstract

Electron beam welding is a well-established technique for superconducting cavity fabrication. Nevertheless it is not free from problems and its main drawback is cost. The paper reviews the most common techniques explored by who is running after the research of seamless cavity fabrication. In the end, it follows a brief overview of some unconventional forming techniques by the hidden potentialities.

1. INTRODUCTION

More than any other project, TESLA with the related proposal of 20.000 superconducting cavities has pointed out all the problems under a possible mass production.

Welds and all the related work of trimming, tolerance respect, alignment accuracy, etc. appear to consume great fractions of the production costs and to create more of the expected production difficulties. The main percentage of cavity failures indeed occur at the welds at the cavity equator, since this is the highest stress point and therefore the weakest point of the assembly.

However the standard technique used for fabricating nine-cell resonators works fine, but it suffers of the drawback to be absurdly expensive for that amount of pieces. At the end, as in many other fields, the machine feasibility is only determined by a mere cost problem!

The problem does not lie in the weld itself, since 20.000 pieces (at least 180.000 welds only for the resonator bodies) is a relatively small number for the production world. The real cost levitation is given by all the phases of piece preparation that are preliminary to the weld.

In such a framework the development of low fabrication cost alternative technologies becomes a need [1].

2. WHICH PROBLEMS UNDER ELECTRON BEAM WELDING

Electron Beam Welding (EBW) is the preferred technique for refractory metals. It consists into a high energy density fusion process that is accomplished by bombarding the joint to be welded with an intense strongly focused beam of electrons. The instantaneous conversion of electrons kinetic energy into thermal energy, as they impact and penetrate into the surface where they impinge, cause the weld-seam interface surfaces to melt and produce the weld-joint coalescence desired.

During EB welding, the thermal cycles produced by the rotation of the piece respect to the beam, cause physical state changes, metallurgical phase transformation, and transient thermal stress and metal movement. After welding is completed, the finished product may contain physical discontinuities, such as protrusions, material microprojections, craters, cracks or voids in the welds. These are mainly due to excessively rapid solidification, or altered microstructures due to the non uniform cooling or principally to residual stress and distortion due to plastic strains.

The perfect weld should be indistinguishable from the surrounding Niobium material. Instead, what one finds is the formation of three metallurgical zones upon completion of the thermal cycle: the Weld-Metal Zone (WMZ), the Heated-Affected Zone (HAZ), and the Base-Metal Zone (BMZ). The peak temperature and the subsequent cooling rates determine the HAZ structures, whereas the thermal gradients, the solidification rates, and the cooling rates at the liquid-solid pool boundary determine the WMZ structure. The size and flow direction of the melting pool determines the amount of dilution and weld penetration.

Two thermal states, quasi-stationary and transient, are associated with the welding process. During the welding, one assists to the formation of a transient thermal state in the weldment. At some point after weld initiation but before weld termination, the temperature distribution is stationary, or in thermal equilibrium. Hot cracking usually begins in the transient zone, because of non-equilibrium solidification of the base material. A crack that forms in the source-initiation stage may propagate along the weld if the solidification strains sufficiently multiply in the wake of the melting beam. Cracks generally appear in the weld craters and may propagate along the weld. The majority of the thermal expansion and shrinkage in the base Niobium occurs during the quasi-stationary thermal cycles. Residual stresses and weld distortion are the thermal stress and strain that remain in the weldment after completion of the thermal cycle. Moreover excessive grain growth in the weld HAZ and fusion zones can produce cracking during the weld.

Almost 20 years of EB practice have taught to limit defects formation probability by full penetrating welds and by means of a beam raster. The beam oscillation capability indeed allows wider welds, slower cooling rates and more uniform weld shapes without necessarily using beam defocusing. Also beam oscillations capability

reduces the need for accurate beam-to-seam alignment and makes precise joint tracking less crucial.

The parts to weld must be scrupulously assembled and point welding is performed in order to clamp the structure before the effective weld. The cost of joint preparation is higher than that encountered with other techniques, because the relatively small electron beam spot size requires a maniacal precision for the preparation of the joint gap and the accuracy of the alignment. In addition starting and stopping the weld are not operations that can be undervalued, since low uniformity and possible metal melt-through can occur at the end of the joints.

Before welding, the parts must be properly cleaned, since inadequate surface cleaning of the weld metal can cause weld flaws, a deterioration of superconducting properties of the weld, reducing also pumpdown times and gun operational stability. The Residual Resisitivity Ratio (RRR) of the weld critically depends on the grade of vacuum achieved in the chamber during the process, since this directly affects the interstitial impurity content in the weld.

3. BEFORE TO DECIDE FOR SEAMLESS CAVITIES, ARE WE SURE THAT EBW IS THE ONLY SUITABLE WELDING TECHNIQUE?

One of the advantages of EBW is the ability, with a lower total heat input, to make welds deeper and narrower than by other techniques.

The superiority of the EBW over other techniques lies in the fact that the kinetic energy of the electrons can be concentrated onto a small area on the workpiece. Power densities higher than those possible by any known continuous beam, including laser beams can be obtained. The high power density plus the extremely small intrinsic penetration of electrons in Niobium results in almost instantaneous local melting and vaporization of Niobium. That characteristic distinguishes EBW from other welding techniques in which the rate of melting is limited by thermal conduction.

On the other hand, EBW is expensive, both for manufacture time and for equipment. The capital cost of an EBW system can be close to $1 million. Note that the capital cost includes only the energy source, control system, fixturing, and material handling equipment. It does not include operating maintenance or inspection costs, which can vary widely depending on the amount of pieces to weld.

In the author's opinion a not detailed investigation has been done up to now about alternative techniques for welding Niobium. Laser Beam Welding for instance has unexplored resources and it could deserve interesting surprises whenever investigated for the application to Niobium.

In addition a less-known technique, but not for this less powerful, is the Ultrasonic Welding (USW). It consists in a quasi-solid state process that produces a weld by high frequency vibration shear forces at the interface between the two held under moderately high clamping forces. The resulting internal stresses result in elastoplastic deformations at the interface.

In particular the advantages of ultrasonic welding are that: i) permits to join materials independently of the respective thickness; ii) provides joints with good thermal and electrical conductivity; iii) it does not require terribly expensive tooling and particularly trained personnel.

4. SEAMLESS CAVITIES

You wont have to worry about anyone of the above mentioned problems about the obtained weld structure, when switching to seamless cavities.

Moreover, the fabrication time needed for fabricating a nine-cell resonator by the current EBW technology is of few weeks. The fabrication time of a seamless tube from a Niobium planar blank is around a few tens of minutes, while by seamless forming (either by hydroforming or by spinning) the same time becomes curtailed to only some hours.

The main research activity in this field is carried by several groups respectively in France (hydroforming and hot forming), Germany (hydroforming), Italy (spinning) and Japan (hydroforming and explosive forming).

As it will appear in the following, except the spinning that can start from a planar blank, all the below reported forming techniques require Niobium seamless tubes. Three techniques exist for producing such tubes: deepdrawing, flowturning and backward extrusion. Each one of these techniques work satisfactorily and can provide mechanically perfect tubes. The problem however lies in reducing contamination and trapped lubricant among grains during the application of plastic deformations.

4.1 Hydroforming

Tube hydroforming is a pressurized hydraulic forming process used to produce complex shapes as the cavity one in tubular components. Pressure can be applied by compressing a fluid, by pressing rubber, usually polyurethane, while the shape is determined by an external die. The drawback of hydroforming lays in the difficulty to achieve an expansion over 200% without intermediate annealings. In order to keep annealings to the minimum, the tube diameter has an intermediate size between the iris diameter and the equatorial one. The tube is initially swaged at the iris, then expanded under an additional axial compressive force. The effect of the tube shrinking during bulging results in a more uniform wall thickness of the cavity.

Hydroforming has been certainly the most investigated among the seamless cavities forming technologies. Copper cavities for Niobium sputtering were hydroformed at CERN by Hauviller, with only two intermediate annealings. Recently Kaiser at DESY has succeeded in hydroforming a Niobium tube jacketed in Steel liners. Antoine at Saclay has also hydroformed a monocell cavity starting from a seamless Niobium tube of low RRR. Both

grups have reached Q values over 1e+10 and accelerating fields around 20 MV/m. The results are very encouraging and they will certainly improve a lot after that enough good quality seamless tubes will be available. Hydroforming is also investigated by Saito at KEK, with the idea of applying it to Niobium clad Copper tubes.

4.2 Explosive Forming

Explosive forming is a high-velocity process in which the punch or diaphragm is related by an explosive charge. The tube is water filled and the explosives utilized are generally highly explosive chemicals, gaseous mixtures, or propellants. One of the most common explosive is Pentaerythritol tetranitrate (PETN) or Trinitrotoluene (TNT) and are placed into the tube center. Water is generally used as the energy transfer medium to insure a uniform transmission of energy and to muffle the sound of the explosive blast. After detonation a pressure pulse of high intensity is produced. A gas bubble is also produced which expands spherically and then collapses until it vents at the surface of the water. When the pressure pulse impinges against the workpiece, the metal is displayed onto the die with a velocity up to 100mt /sec). In order to ensure the proper die filling, it is important that air is evacuated from the die. This brings a little complication to the equipment, because this makes not easy the axial shortening of the tube during expansion, as it happens in hydroforming.

The main results on explosive forming have been obtained at KEK by Saito that succeeded in explosively forming a Copper three cells in only two steps, so only one intermediate annealing. In particular for explosive forming, the availability of good tubes is compulsory for the achievement of good results.

4.3 Hot forming

The formability at high temperature below the recristallization point, gives the possibility to increase formability of the material and to deform without riskof failures regardless of the pressure and load applied. Hot forming of Niobium 3 GHz two cell cavities has been proposed by Grandsire from LAL Orsay. The process is done in two steps, with 40 % of deformation in the first step, an annealing (900 °C, 2 hours), and another 90 % in a second step. The results are very promising, since once the proceedure is set up, large numbers of resonators can be produced in short time with high reliability. Obviously, the higher the forming temperature is, the higher formability is. This is an advandage but has the related drawback to need refractory material dies and Ultra High Vacuum.

4.4 Spinning

Spinning has been proposed by the Author, since it is a chipless production method of forming axially symmetrical hollow parts of almost any shape. It is a point deformation process by which a metal disc, or a cylindrical preformed hollow component is plastically deformed by axial or radial motions of a tool or rollers acting onto a workpiece clamped against a rotating chuck. It is a characteristic of this process that the movement of tools onto a rotating piece, acts upon a very localized area where plastic flow takes place. The chuck is made collapsible in order to be extracted from the interior, once the cavity is ready.

The parameters that more than other influence the forming process are the roller feed speed, the angular speed of the rotation chuck and the roller shape. Besides these fundamental importance is hold by the role of intermediate mandrels, that permit to spin a full nine-cell resonator from a planar blank without any intermediate annealing and with the actual rate of one-cell per hour.

Q values over 1e+10 and gradients up to 25 MV/m have been found by Pekeler at DESY, on the Niobium monocells spun at LNL. Niobium clad Copper has also no particular problems for spinning, since a monocell spun by the author at LNL and processed by Saito at KEK reached the 25 MV/m goal. Interesting results has also give the collaboration, with P. Kneisel of Jefferson Lab. Over seven cavities have been fabricated and characterized. The highest value of the field reached was 33 MV/m over 5e+09. Fivecells have been already produced and ninecell cavities, will not delay to come.

5. UNCONVENTIONAL METAL FORMING TECHNIQUES:

Besides the above mentioned techniques for seamless cavity forming, there are several unconventional ones, that even if at the moment are unexplored by our scientific community, are not less powerful than the previous.

5.1 Electromagnetic forming

Electomagnetic Forming (EMF) can be applied to a cavity by simultaneous radial compression and expansion of a seamless tube. EMF works by the magnetic induction effect. When a coil or a solenoid is place near a metallic conductor and pulsed via an energy store like a capacitor bank, a magnetic field is generated between the coil and the workpiece. If done quickly enough, the magnetic field is excluded from penetrating into the workpiece for a short time period. During this time, a pressure is generated on the workpiece that is proportional to the magnetic flux density squared. This "magnetic" pressure is what provides the forming energy. The energy is usually supplied to the workpiece in the form of kinetic energy. The magnetic pressure pulse accelerates the workpiece up to a certain velocity (such as 200-300 m/s). This kinetic energy drives the material into the die, causing forming on impact. The problem of coil extraction after cavity forming is a false problem, since the internal coil could be disassembled in sectors.

EMF produces a phenomenon called Hyperplasticity. Hyperplasticity results from inertial stabilization of material failure modes and permits dramatic increases in strain to failure. Hyperplastic formability, via EMF, of

structural aluminum alloys for instance can cause these alloys to have higher formability than drawing quality steels. One drawback of EMF instead lies in the different electrical conductivity of materials. Results obtained with Copper are not directly connected with what obtainable with Niobium.

5.2 Peen Forming:

Peen forming is a dieless forming process performed at room temperature. During the process, the surface of the workpiece is impacted by pressure from small, round steel shot. Every piece of shot impacting the surface acts as a tiny hammer, producing elastic stretching of the upper surface. The impact pressure of the peening shot causes local plastic deformation that manifests itself as a residual compressive stress. The surface force of the residual compressive stress combined with the stretching causes the material to develop a convex curvature on the peened side. Moreover it is well known that cracks do not propagate under compressive stresses. Peening forming is widely used in aeronautic industry for example for shaping aircraft wings. A possible application to cavities could be foreseen on a seamless tube of diameter equal to that of the cavity equator, rotating between headstock and tailstock of a lathe.

5.3 Laser Activated Stress Forming:

This technique is rather new and currently under research. Bellow-shaped components are easily formed.. The tube to be formed is stressed within 90% of its material yield point by a laser that induces temperature gradients activation. The piece rotates meanwhile laser irradiated and it is shortened under the application of an axial load.

5.4 Ultrasound Activated forming:

The ultrasonic-activated forming is a metalforming process that applies high-frequency vibrations to the workpiece through the tooling. The vibrations are usually greater than 15.000 cycles per second (cps) and are generally no more than a tenth of a millimeter in amplitude. Metalforming with the aids of ultrasonic energy dates back to the mid-1950s. Tests showed that when a wire was stressed in tension with ultrasonic activation, the yield strength of the material seemed to increase. It was also determined that this effect increased linearly with the increase in vibratory power and was independent of the frequency. This phenomenon was attributed to ultrasonically favored formation and movement of dislocations within the crystal lattice structure that assisted intercrystalline slip. The application of ultrasonic energy in the form of high-frequency vibrations during cold-forming operations reduces the forming force required, increases the deformation rate, decreases the total number of processing steps, and improves the quality of the finished product. Ultrasonic activation can be applied to both slow-speed and high-speed forming processes. In tube drawing operations, for

instance, either the draw die or the plug can be ultrasonically activated. Activating the die is generally preferred since the effect of the vibration is greatest, the number of passes can be greatly reduced.

6. CONCLUSIONS

Aim of this work was only to offer a panorama of the forming technologies that can be applied to the problem of seamless cavity fabrication. Some techniques seem more easy and low cost than others, however, there is a not simple answer to the question: "Which one will be chosen for TESLA cavities?". The times are not ripe for a right evaluation of the problem. Too much experimental work has still to be done before than one technique will prevail on the others.

7. ACKNOWLEDGMENTS

REFERENCES

V. Palmieri, Particle Accelerators, vol. 61, 1998, [pp. 479-519]/215-255.

MATERIALS RESEARCH RELATED TO W-BAND CAVITY CONSTRUCTION*

D. T. Palmer‡, M. Hill†‡, S. Schwartzkopf*, R. H. Siemann‡, and R. Witherspoon*

‡Stanford Linear Accelerator Center, Stanford University, Stanford CA 94309

†Harvard University, 42 Oxford Street, Cambridge MA 02138

* Ron Witherspoon, Inc., 430 Industrial Street, Campbell, CA 95008

Abstract

Low power rf measurements, S11, of electro-discharge machined (EDM) diffusion bonded mm-wave traveling wave rf cavities were not in satisfactory agreement with electromagnetic simulations. During subsequent mechanical inspection, the cell-to-cell iris were found to be distorted. This led to a series of systematic experiments to study the mechanical properties of oxygen free high conductivity Copper (OFHC) and Glidcop AL-15. Results of these studies which include cell-to-cell iris distortion, EDM machining accuracies, surface quality, and the results of different bonding techniques are presented.

The results of our mechanical studies are used to develop a set of mechanical design constraints for a second series of constant impedance W-Band structures that also used wire EDM and high temperature bonding for their manufacture.

1 INTRODUCTION

In this paper we shall present the results of mechanical studies as it relates to issues of mechanical fabrication of 90 GHz accelerating structures [1]. We shall present results from our material tests that indicate Glidcop AL-15, which is a dispersion strength material, is the material of choice when these materials must be exposed to temperature cycles greater than 1000°C. We present results that indicate that sinker EDM machining is capable of attaining the tolerances necessary to produce a tuned accelerator structure. Bonding studies are then presented. Finally, an overview of the available technology to mechanical inspect fabrication structures are presented.

These results have driven our efforts, to produce and test a W-band structures, away from bonded copper muffin tin structures to a novel rf zipper structure [2], that have no bond joints located in regions of large rf currents, produced from dispersion strengthened materials.

2 MATERIALS STUDIES

Visual inspection of the first 25 cell constant impedance(CI) traveling wave accelerating structure mechanical deformation of the cell to cell iris was observed, as seen in Figure 1. Two possible effects might have caused the iris deformation. The yield strength of the

Figure 1: Visual inspection of the cell to cell iris revealed distortion.

base material was exceeded during the diffusion bonding cycle or during the beam pipe EDM machining step.

To identify the cause of this distortion, we constructed a series of test structure made from OFHC copper and AL-15, using wire EDM milling technology. These sample cavities were put through identical thermal cycles that mimicked the diffusion bond process used to produce Figure 1.

Two subclasses of OFHC copper, annealed and work hardened, were investigated along with AL-15 as possible candidates for use as the base material for W-band structures.

Figure 2 shows a 30 μm iris distortion that was introduced in the the annealed OFHC copper after wire EDM milling of the test structure. It is thought that thermal induced crystal growth during the wire EDM milling process is responsible for this distortion.

A identical series of test were also conducted on AL-15 and work harden OFHC copper, see Figure 2. To within the optical resolution of our microscope no distortion was observed in either the AL-15 or work hardened copper due to the thermal cycle of the diffusion bonding process. But our metallurgy analysis of the 25 cell work hardened diffusion bonded OFHC structure indicated that the OFHC base material plastically deformed during the bonding process and therefore is not a candidate as an acceptable material for thermal bonding.

To summarize, annealed and work harden OFHC copper are unacceptable base materials for mm-wave accelerating structures which are fabricate by thermal bonding and EDM wire machining technologies. This is due to the deformation induced in the rf cavities during the wire milling and diffusion bonding processes. AL-15 is an acceptable material to fabricate, thermally bonded and wire EDM milled, mm-wave accelerating structures.

Seven Cell Test Structure Before Thermal Cycle

$\delta x = 30 \ \mu m$

OFHC   Glidcop

Work Hardend   AL-15   OFHC
Annealed

Figure 2: View of material test structures before and after thermal cycle.

Dimension (mm)	Mean (mm)	σ (mm)
1.000	0.99970	0.00232
0.250	0.24964	0.00200
2.000	1.99259	0.00136
2.400	2.39083	0.00170

Table 1: Optical inspection results of a series of 6 Sinker EDM 7 cell test structures.

3 ELECTRO-DISCHARGE MACHINING (EDM)

In this section we studied the surface finish attained by EDM machining techniques, wire milling and sinker EDM, using non-destructive inspection techniques.

During SEM analyses of the our first 25 cell structure zinc (Zn) was found to have contamination the structure. Clearly, this is a byproduct of the Brass coated EDM wire used during fabrication. It should be pointed out that there was limited flushing due to the constrained geometry of this structure. Our future design and step by step manufacturing process eliminates the problem of limited flushing action.

3.1 Wire EDM

Previous attenuation studies of EDM OFHC copper waveguide [3] measured an attenuation of -0.2 dB for Cu waveguide, manufactured using wire EDM technology. Since results in Section 2 indicate that the base material should be AL-15, we have extended the previous work to include the effect of different EDM wire base material used to fabricate structures out of AL-15.

In these studies, the surface finish of WR-10 waveguide, constructed out of AL-15, was investigated non-destructively, by measuring the attenuation of the rf power, in the frequency range of 85 to 95 GHz, as a function of EDM wire base material. Three 2 inches long W-band waveguides were wire EDM milled out of AL-15 using a Brass coated wire, trade name Cobra Cut A, pure Copper wire, and a Molybdenum wire.

Comparing the attenuation factor of pure copper, -0.13 dB, to that of AL-15, -0.29 dB. We find that Al-15 is satisfactory base material for accelerator structure in the mm-wavelength. No variation in the AL-15 attenuation factor was measured before or after cleaning.

3.2 Sinker EDM

Previous planer structure design at W-band have limited themselves to only utilized wire EDM. We have investigated the use of sinker EDM machining to produce the cavity structure. This technique would eliminate the need to bond the cavity structure in the region of large rf currents.

This test was conducted with a single electrode, produced by a precision wire EDM machine, with the negative of the 7 cell cavity structure we wanted to produce. In this manner we were able to transfer the precision of the wire EDM machine to the sinker EDM machine and the 7 cell test structure. Optical comparison techniques were utilized to inspect the surface finish of the cavity walls and bottom. The cavity walls and bottoms were found to have a RMS surface finish of 0.41 μm and 0.82 μm, respectively. Dimensional accuracy attained by the sinker EDM technique are tabulated in Table 1. In conclusion, we find that sinker the EDM machining technique can attain the dimensional tolerance required by mm-wave accelerating structures. Improvements in the surface finish are possible with the use of higher quality cathode material.

4 BONDING STUDIES

During the course of our studies into the cause of the iris distortion, see Figure 1, the iris to cavity bond was studied. Metallurgy analysis indicated that they was no significant epitaxy crystal growth in the iris region of the bonding surface. This is the region where large rf currents flow perpendicular to the bond joint. This has caused us to pursue a novel rf design [2] that does not necessitate any physical bond in the regions of large rf currents. But it should be noted that we are studying different bonding techniques, since the ability to bond metals together without physically distorting the structure allows for a larger range of rf structures to be envisaged and fabricated.

Therefore, we are investigating diffusion brazing with silver plated alloy, ultra thin alloy brazing, and also diffusion bonding of diamond fly cut surfaces. We shall discuss each of these process in the following subsections.

4.1 Diffusion Bonding

Initial diffusion bonding of W-band structures at SLAC utilizes hand lapping of all bonding surfaces, that are flat and parallel to 0.5 μm. A pressure of 20 psi was applied to the structure with a temperature plateau of 1020°C held for 1 hour. The metallurgy analysis indicated that they was no significant epitaxy crystal growth across the bonding surface and in some case no physical contact in the region of coupling iris where rf current flow.

The lack of bonding in the iris region could possible be

Machine	cell width (μm)	cell length (μm)
DMM 12-106	837.04 ± 0.43	2368.71 ± 0.90
M48	828.71 ± 0.50	2363.04 ± 0.81
Apex 200	828.43 ± 0.83	2361.54 ± 0.64

Table 2: 41 cell muffin tin structure baseline and optical inspection results.

due to the lose of surface flatness in the iris region due to preferential chemical etching used to clean the surfaces prior to bonding, or roll off in iris region induced during the lapping process.

Due to the success of diffusion bonding of diamond turned surfaces for X-band structure development [4] we are pursuing this technology with respect to W-band structures. To date, we have been able to utilize this technology with a W-band cavity plate without physically damaging precut irides. For this to be a viable technology for W-band structure, it must be applicable to AL-15.

4.2 Diffusion Brazing

To overcome the drawbacks of the solid-state diffusion bonding process in fabricating mm-wave accelerating structures, we began exploring an alternative bonding method called Liquid Interface Diffusion (LID) bonding. LID bonding is a metallurgical bonding technique commonly used in the aerospace industry for applications as diverse as the assembly of honeycomb structures and the assembly of jet turbines. In this technique, a low-melting point metal is inserted as an interlayer between the two metals to be bonded. The interlayer is chosen from among the metals that readily alloy with the metals to be bonded; for LID bonding of copper, the optimum low-melting alloy to use is silver. Upon heating, a liquid forms as the interlayer melts. As a result of liquid formation, a combination of wetting and capillary attraction insure that the mating surfaces are drawn closely together. By holding at the liquid-forming temperature, inter-diffusion between the interlayer and the higher-melting parent metal results in isothermal solidification of the bond line. When the bond-line is subsequently examined metallurgical, no evidence of a distinct low-melting phase can be observed. This is the principal difference between LID bonding and traditional brazing. Processing variables such as interlayer thickness, masking to limit deposition to only the interface to be bonded, and selection of joining temperatures and pressures are currently under investigation. A major advantage of LID is its significantly lower brazing temperature of 800°C versus that of 1020°C for conventional H^2 Brazing with Au-Cu alloys.

4.3 Ultra Thin Alloy Brazing

S-Band structure normally utilize 40 μm thick Au-Cu alloy to bond surfaces together. At higher frequency, the fil-

let produced by this technique would significantly detune a resonant structure. We have been able to bond copper surfaces together with 35-65 Au-Cu alloy that is 2.5 μm thick. No detuning fillet was observed. This same process is being studied with AL-15, as the base material of the structure.

5 MECHANICAL INSPECTION TECHNIQUES

Dimensional tolerance at W-band are on the order of 2.5 μm. Contact measurements are capable of attaining measurement tolerance of ±0.25 μm. It has been observed that contact measurement can cause significant damage to W-band structures constructed out of work hardened OFHC material [5]. Similar damage was observed on a Al-15 test fixture. We report, the results of our investigation into optical inspection techniques that would eliminate the surface damage induced by more invasive techniques.

To provide a calibrated baseline, SLAC's Leitz PMM 12-106 coordinate measuring machine was used to measure a 41 cell muffin tin structure. These results are accurate to within ±.25 μm.

The 41 cell muffin tin structure was then sent to Sandia National Laboratory and was inspected on a Moore M48 optical inspection machine. The 41 cell structure was also inspected on an Optical Gauging Products Apex 200 machine. The results of these inspection are listed in Table 2. The optical measurement technique under estimated the cell physical dimensions by 10 μm. This is due to the edge finding schemes getting confused by shadow effects at the wall edge. Whereas the contact method depends on physical force to find an edge of a cavity wall. It should be noted that during all optical inspection, the 41 cell structure was back lit with low intensity white light.

6 CONCLUSIONS

We find the Glidcop AL-15 is an acceptable base material for use in fabricating W-band accelerating structures. Problem with thermal bonding of planar structures must be overcome to increase the diversity of exotic structure that may be envisaged by accelerator physicists. We have bypassed this problem with a novel rf structure design that eliminates bonding metal surfaces together perpendicular to the rf current flow. Sinker EDM machining is capable of achieving the tolerances necessary to fabricate mm-wave structures. Optical inspection techniques under estimate the absolute dimensions due to lighting and edge effects.

7 REFERENCES

[1] P.J. Chou et al., PAC97, page 464

[2] Kroll et al., PAC99, FRA92

[3] M. Hill, ARDB Technical Note 126

[4] C. Pearson, Personal Communication

[5] P.J. Chou, ARDB Technical Note 115

COLLIMATOR SYSTEMS FOR THE SNS RING

H. Ludewig, N. Simos, J. Walker, P. Thieberger, A. Aronson, J. Wei, M. Todosow,

BNL, Upton, NY

Abstract

The requirements and performance goals for the collimators are to reduce the uncontrolled beam loss by 2×10^{-4}, absorb 2 kW of deposited heat, and minimize production and leakage of secondary radiation. In order to meet these requirements a self-shielding collimator configuration consisting of a layered structure was designed. The front layers (in the direction of the proton beam) are relatively transparent to the protons, and become progressively less transparent (blacker) with depth into the collimator. In addition, a high density (iron) shield is added around the outside. The protons will be stopped in the center of the collimator, and thus the bulk of the secondary particles are generated at this location. The conceptual design described, the method of analysis discussed, and preliminary performance parameters outlined.

1 INTRODUCTION

Collimators are used to remove halo or off-momentum particles from the main proton beam. In addition to removing halo particles collimators will also act as shielding for the remainder of the accelerator structures. Thus, collimators reduce uncontrolled losses around the ring and reduce activation of the accelerator components.

Requirements and performance goals for the collimator are summarized below:

1. Halo proton attenuation by a factor of 2×10^{-4},
2. Minimize production of secondary radiation, and its subsequent leakage, and
3. Remove heat (2 kW).

In order to meet these goals a self-shielding collimator configuration will be designed. An arrangement consisting of a layered structure will be considered. The initial layers (in the direction of the proton beam) are transparent to protons, and become progressively less transparent (blacker) with depth into the collimator. In addition, a high density (iron) shield will be added around this structure. The protons are stopped in the approximate center of the collimator, and thus the bulk of the secondary particles will also be generated there. Since these secondary particles are primarily produced isotropically their leakage path length will be maximized in this manner (high probability of capture or attenuation). In the case of neutrons a black layer is included at each end in order to further minimize their leakage in the direction of the beam. This design will therefore minimize the activation of surrounding accelerator components.

2 CONCEPTUAL DESIGN

The conceptual design, based on the above requirements and ring constraints, is shown on Figure 1. The protons travel from left to right, with the beam confined primarily to the inner diameter of the collimator. Halo particles are found between the collimator inner diameter and the beam tube inner diameter, and are assumed to pass into the collimator volume. On their way into the collimator the halo particles will first encounter the tapered transition surface between the collimator tube and the vacuum chamber. This surface has a wall thickness of 1 cm and is made of steel. The next 15 cm consist of a borated light-water volume. This region is relatively transparent to high energy protons, but lower energy neutrons would be thermalized in this region and be absorbed by the boron. The use of borated light water to thermalize and absorb neutrons is a common practice in the light water reactor industry.

All the zones to this point have the same composition in the radial direction. The following two zones have a radial variation at a radius of 20 cm. Within the 20 cm radius they consist of randomly packed spheres cooled by borated light water, and outside this radius they consist of solid iron plates. This arrangement is chosen to ease the assembly of the collimator, ensure heat removal, and minimize the cost. Randomly packed beds of particles are particularly efficient at heat transfer, since their area per unit volume is very large. Furthermore, the cost of small spheres of stainless steel is lower than machined discs of the same material. The void (coolant in this case) fraction of randomly packed spheres is approximately 35%, thus the solid fraction in these zones will be 65%. The 100 cm long particle bed zone will consist of 3 mm diameter stainless steel particles. The protons will lose the bulk of their energy in this zone, and since the production of neutrons per proton is modest for stainless steel, the secondary production of neutrons is relatively low. However, there is a probability of generating secondary protons in addition to the neutrons. Fortunately the yield of secondary protons is low compared to the neutron yield, due to the fact that the protons have to overcome the potential barrier before escaping the excited nucleus.

Finally, the back 15 cm of the collimator consists of the same borated light water used in the first 15 cm of the collimator. This volume will ensure that many of the remaining spallation neutrons are slowed down and captured. The collimator is encased in 45 cm of solid iron on all sides. The collimator thus has an overall radius of 75 cm and a total length of 222 cm (including the iron shield).

3 ANALYSIS AND RESULTS

The above collimator configuration was analyzed using the Monte Carlo codes LAHET [1], for particles above 20 MeV; and MCNP [2] for particles below 20 MeV. In addition, a suitably modified version of the ORIGEN [3] code was used to estimate the buildup of spallation products during machine operation, and their decay following shutdown. The proton beam is assumed to be traveling from left to right, parallel to the collimator tube. The source plane is situated at the transition piece. Radially the proton beam is assumed to have a Gaussian shape.

These results show that the backward (opposite to the direction of the proton beam) and forward (in the direction of the proton beam) proton currents in the halo zone of the beam (radius greater than 5 cm) decrease monotonically to the back end of the collimator. In addition, the leakage out of the front end of the collimator is also found to be vanishingly small. Within the collimator the proton current in the backward direction varies, with a maximum at the interface between the shield and the collimator containment vessel. The need for the thick iron shield is thus demonstrated. Thus, the proton leakage out of the back and front of the collimator meets the design goal set for it. Neutron currents (neutrons with energies above 20 MeV) were also determined. It was seen that in the forward direction the neutron current increases initially and then decreases monotonically to a low value at the outer surface. In the backwards direction the current peaks at the interface between the front shield and the collimator body.

The thick shield should minimize neutron leakage, which in turn will minimize the activation of the tunnel air. The only other activated material which can leave the collimator is the cooling water. Potentially ^7Be and ^3H are formed, and circulate in the coolant. For the above reason the cooling water will be cooled in a closed loop via an intermediate heat exchanger. The maximum heat load from a collimator is 2 kW. If a temperature rise of 5°C is assumed (T_{in}=30°C, and T_{out}=35°C) a flow rate of approximately $3x10^4$ m^3/s is required. This implies a moderate heat removal system for the design basis condition.

Estimates of the energy deposition in the collimator indicate the bulk of the power will be generated in the inner 20 cm of the front borated light water zone (9%), the front iron shield (10%), and the stainless steel particle bed (70%). All these zones need to be cooled by the cooling water system. The stainless steel particle bed zone is inside the collimator and is cooled by the borated water system. Preliminary estimates of the temperature indicate that they are well within the operating limits.

In addition to the estimates of energy deposition in bulk components, an estimate of the axial and radial variation of energy deposition was made in the collimator tube, and front shell. The energy deposition was found to be quite modest, with the maximum ($2.2x10^5$ W/m^3) occurring at the leading edge. The tube and containment shell are subject to the most challenging thermal environment, since they are cooled on one surface, and the coolant flow pattern in the leading edge corner can be ambiguous. Assuming a heat transfer coefficient of 100 W/m^2-°C on the surface and a coolant bulk temperature of 32°C the maximum temperature rise in the stainless steel collimator tube is approximately 12°C. The associated thermal stress is $9x10^6$ N/m^2. These values are well within the operating limits of the containment shell material. The cyclic nature of the beam appears to have very minimal impact on the thermal response of the shell. However, it should be pointed out that possible thermal fatigue effects from the cyclic beam off and on condition as well as from thermal-mechanical shock have not been addressed yet.

It was assumed that the machine has operated for 180 days at full power (1 MW, with 0.001 of the beam being captured in the collimator). Activation levels after 1 day, 7 days, and 30 days following shutdown were determined. It was found that the quadrupole magnets have an activation of 5 Curies. The primary activation products being ^{51}Cr, ^{54}Mn, ^{56}Mn, ^{55}Fe, ^{59}Fe, ^{65}Ni, ^{62}Cu, and ^{66}Cu. In the iron zones of the magnet structure the same activation products are important, except Cu and Ni. The magnets behind the collimator have a vanishingly small amount of radioactive buildup. The energy spectrum due to decay gamma rays was found to peak in the energy range between 0.85 MeV and 1.25 MeV. The activity of the solid components within the collimator is well shielded.

Furthermore, the question of scraping interactions, on the collimator walls of primary protons and the production of secondary particles is being investigated. A simulation of primary proton scrapping on the walls of a conical shaped collimator with an inner diameter of 10 cm at its entrance, for various included conical angles, and a length of 1 m, was carried out. The results indicate that for a scraping angle of 0.05° ~50 % of the particles re-emerge from the collimator, and 47 % are confined to a cone with an included angle of 30°. This fraction decreases

monotonically with increasing included collimator angle (~ 40% for 0.2°). The energy distribution of the emerging protons has a peak at the primary proton energy, but has a low energy tail which extends down to 100 MeV. The production of secondary electrons at SNS conditions has been estimated. First, based on a theory due to Sternglass [4, 5], and second scaled from experiments using the above theory [6]. The values of electron production per primary proton (e^-/p^+) vary from 200 to 25 for the above two estimates respectively. Currently, an experimental program is being carried out at BNL to study this phenomena. The objective of these experiments is to further quantify the processes involved, and more importantly to investigate possible methods of suppressing the production/capture of secondary electrons.

Finally, the possibility of incorporating a movable inner surface to the primary ring collimator is being investigated. A possible configuration is shown on Figure 2. The inner wall is constructed in halves which move in and out radially both vertically and horizontally, to vary the aperture. The pieces are made of copper with internal cooling loops. Initial estimates indicate that the energy deposition and neutron production is 10% - 15% higher than if a similar piece was made of stainless steel. However, due to its superior heat conduction, copper will be used in this application.

4 ACKNOWLEDGMENTS

5 REFERENCES

[1] R.E. Prael and H. Lichtenstein, "User Guide to LCS: The LAHET Code System," Los Alamos National Laboratory, Los Alamos, NM, LA-UR-89-3014 (1989).

[2] MCNP-A General Monte Carlo N-Particle Transport Code Version 4A, J.F. Breismeister, ed., Los Alamos National Laboratory, Los Alamos, NM, LA-12625-M (1993).

[3] A.G. Croff, "ORIGEN2 – A Revised and Updated Version of the Oak Ridge Isotope Generation and Depletion Code," Oak Ridge National Laboratory, Oak Ridge, TN, ORNL-5621 (1980).

[4] E.J. Sternglass, Phys. Rev. 108, #1,1 (1957).

[5] M. Plum, PSR-95-001, LANL, (1995).

[6] S.Y. Zhang, "Secondary Electron Emission at the SNS Storage Ring Collimator," SNS Tech Note #50 (1998).

Figure 1: Schematic of Beam Collimator

Figure 2: Moveable Beam Scrapers

ENGINEERING DESIGN OF A CONTINUOUS DUTY γ-PRODUCTION PROTON TARGET FOR THE CONTRABAND DETECTION SYSTEM*

J. Rathke, E. Peterson, Advanced Energy Systems, Inc. (AES), Medford, NY 11763

J. Klein, Northrop Grumman Corp., Bethpage, NY 11714

Abstract

A continuous duty γ-ray production proton target for use with the AES Contraband Detection System (CDS) has been designed, fabricated, and operated [1]. The active element of the target is a thin film of carbon-13 where production of the interrogating γ-rays occurs via a p-γ reaction. To inhibit production of "off-energy" γ-rays stemming from interactions with substrate material, the carbon is sputtered on a tantalum layer (high Z) which is brazed to the OFE copper target structure [2]. The water cooled target system is designed for continuous operation with a 10 ma, 1.76 MeV proton beam with peak power densities on the order of 39 kW/cm^2. To deal with this power density, the target is a disk which rotates at 600 RPM with the beam impingement at a radius of 15 cm. This paper discusses the engineering analysis, the design of the brazed disk assembly, and the design of the rotation mechanism and vacuum vessel.

1 INTRODUCTION

The CDS project is a collaboration between AES, Inc. and TRIUMF Technologies, Vancouver, Canada. AES is the prime contractor responsible for overall system engineering and facility integration while also being responsible for the ion injector, high energy beam transport, target system, and global controls. TRIUMF designed and fabricated the tandem accelerator system, the detector system, developed the threat algorithm's, and also provided the H⁻ ion source. The system installation began in Bethpage, NY in early 1997 and has been in operation since May, 1997. Since that time, the CDS has set world records for current through a tandem accelerator with extended operation at up to 2.2 mA. The CW production target was added to the system in mid-1998.

2 TARGET DESIGN & ANALYSIS

The requirements for the target system are given in Table 1. The design of this target system was approached through a combination of development testing and engineering analysis. The starting point for the design was a concept developed by TRIUMF utilizing a 12 inch diameter drum as the target. The rotation speed for that design was 600 RPM (10 Hz) which was carried forward

PARAMETER	VALUE
Beam Particle	Protons - H$^+$
Beam Energy	1.76 MeV
Beam Current	10 milliamps
Beam Power	17.6 kW
Spot Size (circular)	16 mm dia. (3σ)
Spot Profile	2-D gaussian (peak power density =~39kW/cm^2)
Duty Factor	100%
Cooling Water Flow	6.9 gpm (0.86 lbm/sec)
Pressure Drop	45 psi max. (65 psi system P)
Cooling Water Temp.	65° F

Table 1: Design Requirements

to this design. However, because of design complexity and difficulties associated with coating a consistent 1 μm of ^{13}C on the surface of the large drum, a solution utilizing a flat disk was developed. A cutaway view of the integrated system is shown in figure 1. The target is a φ14 inch water cooled disk that is sputter coated with ^{13}C.

Figure 1: Cutaway of CDS Target System

Development testing showed that for the ^{13}C coating to survive, it must be deposited on a surface that readily forms carbides and has a good combination of hydrogen solubility and diffusivity. These latter two properties inhibit the formation of hydrogen bubbles. In addition, the substrate also needs to be a high Z material to minimize the production of off-energy γ-rays that would increase the background noise in the detectors. Tantalum was chosen as the substrate and copper coupons with 0.010 inch thick Ta brazed to the surface were successfully tested under simulated CDS beam conditions using the AES pulsed proton beamline.

In parallel with the coating development, engineering analyses were conducted in an effort to understand the general conditions of stress, deflection, operating temperature, and pressure drop. The disk structure shown in figure 2 was developed and analysis began using the parameters from table 1. Results from these analyses

Figure 3: Steady State Temperatures @ 10mA, 1.76 MeV

Figure 2: Exploded View of Target Disk

Figure 4: Y-Deflections at Steady State

were evaluated looking for unexpected extremes of thermal stress or deflection. Because of the high rotation speed of the disk, the heat loads were applied as strips of uniform power density around the circumference of the target surface with a central peak value of 257 W/cm^2. Results for temperature, deflection, and stress are shown in figures 3, 4 and 5 respectively. The peak temperature of 181° F (201° F with fluid heat-up) is reasonable, and the deflections are below half the limit of 0.020 in. (10% of the detector pixel width). Von-Mises stresses of 17,800 psi are high for copper. However, these stresses are dominated by local thermal compressive stress and should result only in local yielding and strain hardening of the copper. Ultimately, cycling may lead to a thermal fatigue "mud-cracking" failure, although copper can generally be expected to perform well under conditions such as these. These results were judged adequate for the first prototype target where limitations on carbon coating lifetime are expected to be the limiting factor. Design changes such as the use of Glidcop (Al$_2$O$_3$ dispersion strengthened copper) will be considered for future designs.

Figure 5: Von-Mises Stresses at Steady State

Worthy of note here is that this scoping analysis was performed before development of the Ta foil substructure. This analysis assumed carbon deposited on a 20 μm layer of gold as the proton stopper. The use of Ta, although non-trivial, was evaluated qualitatively in view of the good performance of coupons in pulsed beam testing. 1-D analysis showed that despite the low conductivity of Ta (14% of Cu), the small thickness of 0.010 in. led to only about a 30° F increase in the steady state surface temperature. This, along with the significantly lower CTE of Ta relative to Cu (more closely matches carbon), led to the conclusion that this material system was appropriate for the first prototype target.

3 DETAILED DESIGN

Detailed design of the target system and specifically the target disk focused on the techniques for fabricating the water cooled disk with all of the necessary mix of materials and developing a drive system capable of operating for extended periods at 600 to 1000 RPM. A ground-rule at the start was that there be no rotating water seals inside the vacuum. This led directly to the requirement for a rotating high vacuum feedthru capable of these speeds. A two-inch, water cooled ferrofluidic type was chosen. The drive shaft comprises coaxial water tubes for feed and return flow riding on two high capacity bearings which prevent high loads from being transferred to the vacuum feedthru. Figure 6 shows the complete target system installed on the CDS while figure 7 presents an exploded view of the target and vacuum enclosure.

Figure 6: CDS CW Target Installation

Figure 7: Exploded View of Target System

The target disk itself is a built up brazed structure. Three braze heats in hydrogen atmosphere were required to fabricate the internally cooled structure. A 35/65 Au/Cu heat at 1900 F joined the flange to the hub followed by a PalCuSil-15 heat at 1680 F to join the hub to the back-plate. This heat was followed by machining of the 0.100" deep coolant passages in the back-plate. Because of the asymmetry of the passages, a pocket was

also machined to aid in dynamic balancing of the rotating part. This was followed by a CuSil hydrogen braze heat at 1460 F to join the face plate. The face plate was then machined with a groove to accept the 0.010" thick Ta wedges. These wedges were sized to be no bigger than the 2-inch diameter coupons that had been successfully fabricated and tested with beam. As discussed earlier, there is a factor of 2.6 mismatch in thermal expansion coefficient between Ta and Cu so the choice of wafer size was critical to achieving a successful braze.

The braze was performed using 0.003 inch thick InCuSil ABA braze alloy. Because of the high affinity of Ta for hydrogen, this braze was performed in high vacuum. The InCuSil ABA (active braze alloy) was chosen because of the relatively low liquidus (1319 F) and the highly aggressive wetting characteristics due to the addition of 1.25% Ti. This characteristic also required that the braze tooling be coated with yttrium oxide paint to prevent bonding.

This final brazing step was successfully completed with very little alloy wetting through to the top surface of the Ta. Final machining was performed to "true up" the assembly and clean the Ta in preparation for coating. Figure 8 shows the target disk after sputter coating with ^{13}C. The black spot on the copper was due to some contamination on the surface probably incurred during the final Ta cleaning process. No contamination was present on the Ta surface as evidenced by good performance in beam testing.

Figure 8: Target Disk After ^{13}C Sputter Coating

4 SUMMARY

The CW target was fabricated and has operated successfully at 1.4 mA producing a clean resonant γ-ray beam [3].

5 REFERENCES

[1] Sredniawski, et al; "A Contraband Detection System Proof-of-Principle Device Using Electrostatic Acceleration, "Proceedings of the XVIII International Linear Accelerator Conference, p. 444-446, 26-30 August, 1996; Geneva, Switzerland.

[2] Melnychuk, et al, "Development of a Thin Film 9.17 MeV Gamma Production Target for the Contraband Detection System", These Proceedings.

[3] Melnychuk, et al, "Operating Characteristics of a High Current Electrostatic Accelerator for a Contraband Detection System," These Proceedings.

DESIGN OF A HIGH POWER SYNCHROTRON RADIATION ABSORBER FOR HERA

M. Bieler*, E. Lohrmann, A. Meseck, G. Nawrath, M. Seidel, F. Willeke, DESY

Abstract

In the framework of the HERA Luminosity Upgrade Project it is foreseen to move the final focus quadrupole magnets of the proton machine 16 m closer to the interaction region. As the electrons must not be affected by these magnets, the beam pipes for electrons and protons have to be well separated at these magnets. This implies rather sharp bends with bending radii down to 360 m for the electron orbit in the interaction region. At an electron energy of 30 GeV and a beam current of 58 mA these bends cause a high level of synchrotron radiation. The synchrotron radiation will be guided through the interaction region and will be absorbed far downstream at low power densities. However, it is unavoidable to stop parts of the synchrotron radiation beam at high linear power densities of up to 2 kW/cm rather close to the interaction point where the electron and proton vacuum systems are separated. In order to protect the proton final focus magnet and the septum beam pipe from this synchrotron radiation, a high power synchrotron radiation absorber was designed. This absorber not only has to withstand the heat load of the synchrotron radiation, but it also has to be designed to minimize the backward scattering of the radiation, because these scattered photons might hit sensitive detector components in the interaction region.

This paper will first give an overview of the geometry of the interaction region with special emphasis on the synchrotron radiation. Then the geometrical and thermal requirements for the high power absorber will be described and finally the layout of the absorber will be presented.

1 THE UPGRADED HERA INTERACTION REGION

Fig 1 shows magnet positions, some detector components, the beam orbits and the synchrotron radiation fan for the upgraded HERA interaction region North (South will be nearly identical). In the interaction regions West and East, where the beams do not collide, the geometry of the machine will not be changed.

The straight orbit is the proton orbit, the curved orbit that for the electrons (or positrons). The electron final focus magnets (GJ,GI,GO, GG) are common magnets, acting on both beams. In order to compensate for the influence of the electron final focus magnets on the proton orbit for both possible polarities of the electron machine (electrons or positrons), different horizontal positions of the interaction point (IP) for electrons and positrons were chosen. The proton/positron IP will be shifted 8 mm towards the center

* Email: bieler@desy.de

Figure 1: Top view of the upgraded HERA interaction region North with magnet positions, some detector components, the orbits and the synchrotron radiation fan.

of HERA as compared to the proton/electron IP. This results in stronger bending radii for electrons compared to positrons. Therefore in this paper only electron data will be discussed.

Due to the high field strength of the proton final focus magnets (GM, GN), both beam pipes have to be well separated at the first GM magnet. The main difference between the present HERA optics and the Luminosity Upgrade optics is a decrease in spot sizes at the IP, achieved by a 16 m move of the proton final focus magnets towards the IP. A distance of 11m between the interaction point and the beam separation was chosen as a compromise between a small proton spot size in the IP and a tolerable level of synchrotron radiation created by the strong bend of the electrons. More details about the Luminosity Upgrade optics can be found in [1] [2].

2 SYNCHROTRON RADIATION IN THE INTERACTION REGION

All numbers given in this paper are calculated for the design current of 58 mA at the design energy of 30 GeV. Table 1 shows the magnets in the interaction region, their bending radii for electrons and the power and the critical energy of the emitted synchrotron radiation.

In order to keep the power density on the synchrotron radiation absorbers and the reflection back into the experimental area low, all absorbers are placed as far from the IP as possible. Between the IP and 11 m on the right side of the IP there are only emergency absorbers to protect the beam pipe in case of a mis-steered beam. If these absorbers

Magnet	Bend. Radius m	Power kW	Critical Energy keV
GJL9	2353	0.225	25
GIL7	1863	0.358	32
GOL2	390	13.933	154
GGR2	362	6.569	166
GIR4	402	7.683	149
GIR7	2362	0.223	25
GJR9	1414	0.622	42

Table 1: Magnets, bending radii, emitted power and critical energy.

are hit by the core of the synchrotron radiation fan, the electron beam will be dumped automatically.

On the right side at 11 m from the IP, right before the first GM half quadrupole, the beam pipes for electrons and protons are separated. Another beam pipe for the synchrotron radiation from the magnets GJ, GI and GO (left side of the IP) is added on the outer side of the proton beam pipe. In this beam pipe the main part of the synchrotron radiation from the IP is absorbed at low power densities in two absorbers at 19 m and 25 m from the IP.

At 11 m from the IP, where the beam pipe splits from one pipe into three, the sections between the beam pipes have to be protected by a high power synchrotron radiation absorber. Fig. 2 shows the cross section of the three beam pipes behind the absorber (looking away from the IP). The distance between the electron pipe and the proton pipe is given by the width of the mirror plates of the GM half quadrupoles, whereas the distance between the proton pipe and the synchrotron radiation pipe is given by the width of a NEG pump, pumping the proton pipe inside the GM magnets. In order to protect the proton pipe inside the GM magnets from synchrotron radiation, the aperture of the absorber is slightly smaller than the aperture of the beam pipe (3 mm on the outer side, 1 mm on the inner side).

Figure 2: Cross sections of the three beam pipes behind the 11 m synchrotron radiation absorber (looking away from the IP). Left to right synchrotron radiation pipe, pump channel, proton pipe, electron pipe and pump channel.

3 THE HIGH POWER ABSORBER

The synchrotron radiation absorber at 11 m consists of two parts, the outer part between the synchrotron radiation pipe and the proton pipe and the inner part between the proton pipe and the electron pipe. Table 2 shows the dimensions, positions, beam dimensions and synchrotron radiation power densities for both parts of the 11 m absorber.

Table 2: Synchrotron radiation power at 11 m

	Inner part	Outer part
Distance to IP	11 m	11 m
Absorber width (L)	2 cm	4 cm
Line power density	2 kW/cm	1.1 kW/cm
Total power	4 kW	4.4 kW
Beam height (σ)	0.8 mm	1.3 mm
Absorber area (L 2σ)	0.32 cm^2	1.04 cm^2
Power density (perpend.)	12.5 kW/cm^2	4.23 kW/cm^2
Power density (40 mrad)	0.5 kW/cm^2	0.17 kW/cm^2

The outer part of the absorber has to withstand a line power density of 1.1 kW/cm, the inner part 2.0 kW/cm. The height of the synchrotron radiation fan is σ=1.3 mm on the outer part and σ=0.8 mm on the inner part. With these numbers and the geometry of the absorber one ends up with power densities which would, at perpendicular incidence of the radiation, destroy the absorber. In order to reduce the heat load on the absorber surface, the surface area exposed to the synchrotron radiation has to be increased by tilting the absorber surface with respect to the incoming radiation. This also helps to minimize the number of photons backscattered from the absorber. These photons can be scattered into the detectors and give a major contribution to the detector background rate. The optimal solution is a vertical tilt of the absorber surface by 40 mrad with respect to the incoming radiation.

The longitudinal dimension of the absorber is limited to about 300 mm, given by the available space between the GJ and GM magnets.

Vertically the absorber has to cover an area 10 mm above and below the nominal beam position in order to take care for all possible tilts and offsets of the electron beam.

All these geometrical requirements can best be met by an inverse wedge shaped absorber as sketched in fig. 3.

Figure 3: Sketch of the shape of the 11 m synchrotron radiation absorber (synchrotron radiation coming from the left)

Calculations with the program EGS [3] show that the number of photons reflected back from the absorber to-

wards the IP (and the detector) can be reduced by a factor 2 by coating the copper body of the absorber with layers of gold (0.5 mm), silver (0.5 mm) and again copper (0.04 mm). However, if the final copper layer gets damaged, the reflection from the inner layers will be much higher than from an uncoated absorber. Therefore the absorbers will first be built uncoated.

Fig 4 shows a horizontal cut through the absorber. The synchrotron radiation fan will hit the tilted surfaces between the beam pipes. Below the three beam pipes five cooling water channels are sketched. The distance between the absorber surface and the water channels, the number and the size of the water channels have to be calculated to minimize the absorber surface temperature without boiling the cooling water.

Figure 4: Horizontal cut through the high power absorber.

In the horizontal plane perpendicular to the beam pipes there is a pumping channel with a flange for a vacuum pump attached to the electron pipe. At the position of this pumping channel the wedge of the absorber is still relatively open, so that the proton pipe is also pumped through this channel.

To estimate the temperature distribution in the absorber analytically, a simplified model was considered, where the cooling is done by a plain cooling surface at constant temperature. The difference in temperature T_c between the cooling surface and the surface of the absorber is given by

$$T_c(x) = \lim_{\Delta y \to 0} \frac{P}{L \cdot k} \frac{1}{4\sqrt{2\pi}^{3/2}}$$

$$\int_{-\infty}^{\infty} e^{-\xi^2/2\sigma^2} \ln \frac{(2y_0 - \Delta y)^2 + (x - \xi)^2}{\Delta y^2 + (x - \xi)^2} d\xi,$$

where P is the incident power, L the horizontal length of the absorber, k the thermal conductivity of the material (copper), σ the width (i.e.standard deviation) of the radiation fan, x the distance from the center of the radiation fan, and y_0 the distance between absorber surface and cooling plane. Assuming the following power and dimensions of: $P = 4\,\text{kW}$, $L = 2\,\text{cm}$, $\sigma = 0.8/0.04 = 20\,\text{mm}$ using a

40 mrad tilt angle, and $y_0 = 110\,\text{mm}$ (distance between the absorber and the cooling channel), the resulting temperature is: $T_c = 260, 280$ and $310°\text{C}$ for $\sigma = 2, 1.5$ and 1 cm. The heat transfer into the cooling water of a pipe is given by: $P = \frac{k_w \cdot N_m \cdot A}{D} \cdot \Delta T$, where $k_w = 0.6$ W/mK is the thermal conductivity of water, D and l the diameter and length of the pipe and $A = \pi D l$ its surface area. ΔT is the temperature difference between the cooling water and the wall, required to transfer heat with power P into the water.

For a pipe, the heat transfer coefficient (Nußelt number) is given by: $N_m = 0.032 Re^{0.8} P_r^{0.37} \left(\frac{D}{l}\right)^{0.054}$. The Reynolds number Re is $Re = \frac{vD}{\nu}$, where v is the velocity, ν the viscosity, and P_r Prandtl's number ($P_r = 7$).

In order to get a small temperature difference, Re has to be large, requiring a large flow velocity of the water.

The following numerical values have been chosen: $v = 3\,\text{m/s}$, $\nu = 10^{-6}\,\text{m}^2/\text{s}$, $D = 10\,\text{mm}$, $Re = 30,000$, $l = 2\,\text{cm}$ and $P = 4\,\text{kW}$. One has to stay below a power density of $100\,\text{W/cm}^2$, and therefore an area of at least $40\,\text{cm}^2$ for the cooling tubes is required. One could try 9 tubes arranged in two rows, with a distance of 20 mm between the centers of the tubes. Putting in numbers one gets $N_m = 0.032 \cdot 30000^{0.8} \cdot 2.05 \cdot 0.96 = 240$ and

$$\Delta T = \frac{P \cdot D}{k_w \cdot N_m \cdot A} = \frac{4000 \cdot 0.01}{0.6 \cdot 240 \cdot 40 \cdot 10^{-4}} = 69°\text{C}$$

Assuming a temperature of the cooling water of $30°\text{C}$, the temperature at the hottest spot of the absorber will be about $30 + 69 + 280 \approx 380°\text{C}$. The rise in water temperature will be comparatively small, about $1°\text{C}$.

For comparison numerical calculations have also been carried out with a finite element code. Here the surface temperature of the absorber is of the order of $350°\text{C}$ and the temperature on the surface of the cooling water pipes is well below $100°\text{C}$.

4 CONCLUSION

The HERA Luminosity Upgrade requires a high power synchrotron radiation absorber near the interaction region. The proposed design fulfills the geometric requirements, given by the surrounding magnets and vacuum chambers, minimizes the amount of back-scattered radiation and reduces the thermal load on the absorber surfaces.

5 REFERENCES

[1] U. Schneekloth (editor), "The HERA Luminosity Upgrade", DESY-HERA-98-05, (1998).

[2] M. Seidel , "Luminosity Upgrade of HERA", these proceedings.

[3] L. Suszycki, "Synchrotron Radiation at the HERA Upgrade", ZEUS Note 98-039, (1998).

COMMISSIONING OF RHIC VACUUM SYSTEMS*

H.C. Hseuh#, R. Davis, R.C. Lee, D. Pate, L. Smart, R. Todd, D. Weiss, D. Zigrosser

RHIC Project, BNL, Upton, NY 11973

Abstract

The Relativistic Heavy Ion Collider (RHIC) has two concentric rings 3.8km in circumference. There are three vacuum systems in RHIC; the insulating vacuum vessels housing the superconducting magnets, the cold beam tubes surrounded by the superconducting magnets, and the warm beam tube sections at the insertion regions and experimental regions. The vacuum requirements and the design of three vacuum systems are described. The experience gained during the commissioning of these vacuum systems is presented with emphasis on locating helium leaks in the long arc insulating vacuum system.

1 INTRODUCTION

RHIC [1] comprises two interweaving rings that intersect with each other at six experimental regions. RHIC will store and collide two counter-rotating ion beams with masses from proton to gold and energies up to 250 GeV/nucleon for periods greater than ten hours. Over 1700 superconducting magnets of various types and lengths, housed in the magnet cryostats and cooled by superfluid helium (He), are used to bend and focus the particle beams. There are three distinct vacuum systems in RHIC: (1) the room temperature (warm bore) beam vacuum regions which house the injection, acceleration, instrumentation and experimental regions; (2) the cold beam pipes (cold bore) encased by the superconducting magnets; and (3) the insulating vacuum vessels (cryostats).

Fig. 1 The Layout of Two RHIC Rings

The total length of cold bore and cryostats in these two rings is ~ 6.4 km, divided into 12 arc sections of 494m each and 24 short insertion sections. A schematic view of the collider is shown in Fig.1. The layout of the vacuum equipment for one-twelfth of the collider is shown in Fig. 2. Each 494m arc section consists of a continuous cryostat, housing 64 superconducting magnets with alternating dipole and corrector-quadrupole-sextupole (CQS). The lengths of the standard dipole and CQS are ~9.5m and ~4.5m, respectively. Major benefits of the long cryostats without vacuum barriers are economics, increased reliability and lower heat load, with increased pump down and leak checking difficulty as the main disadvantage. The 64 interconnected magnets form a continuous cold beam tube. The two adjacent insertion triplet magnet strings (Q3-Q2-Q1-D0) reside within a common cryostat due to their proximity. The large aperture DX magnet that bends and focuses both beams shares the same insulating volume with the triplets but has a warm beam tube connected to the experimental beam pipe and the DX-D0 chamber.

The required beam vacuum levels are derived from beam lifetime and detector background considerations. The warm bore design vacuum is $<5 \times 10^{-10}$ Torr (~$1.7 \times 10^{+7}$ molecules/cm^3) consisting of 90% H_2, 5% CO and 5% CH_4. The cold bore design vacuum is $<1 \times 10^{-11}$ Torr (~$2 \times 10^{+7}$ molecules/cm^3 after correcting for thermal transpiration) consisting of only H_2 and He since all other gases will condense on the 4K surface. Elastic and inelastic scattering from beam-residual gas interactions were considered when determining the vacuum requirements for the worst case in RHIC, i.e. Au at injection energy of 10 GeV/amu. The elastic scattering (multiple Coulomb scattering) causes the growth of the transverse emittance. Using the Fokker-Planck diffusion equation, the rate of growth is ~10^{-4} mm.mrad/hr [2] which is insignificant in comparison with the emittance growth due to intra-beam scattering.

The inelastic scattering includes electron capture and nuclear scattering, which cause immediate beam loss. The total electron capture cross section [3] consists of radiative, non-radiative and vacuum captures and is ~10^{-25} cm^2 for RHIC residual gas composition [2][4]. The energy independent nuclear scattering cross section is proportional to the geometrical cross section and is ~10^{-24} cm^2 for RHIC residual gas composition. The beam-gas lifetime dominated by the inelastic scattering will be several hundred hours for Au [4] at the design vacuum of $2 \times 10^{+7}$ molecules/cm^3 which is much longer than the overall beam lifetime of ten hours. Background noise to the detector due to beam-residual gas nuclear scattering at and near experimental regions puts the most stringent requirement on RHIC beam vacuum systems.

Fig. 2 The layout of Three Vacuum Systems in One-Twelfth of RHIC Rings

The probability of beam-gas interaction ±40m around the collision point will be ~1x10^{-4} interactions per bunch per crossing. The total beam-gas rate will be ~10^3 Hz which is comparable to the beam-beam rate [5] at the design luminosity of 10^{-26}cm^{-2} s^{-1}. Of course, only a small percentage of the beam-gas events fall into the interaction diamond and overlap with the beam-beam events.

To minimize the heat transfer from the ambient cryostat wall to the magnet cold mass and the He conduits through gas convection, insulating vacuum of 10^{-5} Torr inside the cryostat is necessary.

2 RHIC VACUUM SYSTEMS

2.1 Warm Bore Vacuum System

The warm bore regions occupy ~16% of the ring circumference and are divided into 52 vacuum sections with length ranging from 4m for rf cavities to 34m for a standard Q3-Q4 section. RF-shielded gate valves located at the ends of warm sections are used to isolate them from adjacent warm bore and cold bore sections. Most warm bore pipes are made of 127mm OD stainless steel and utilize conflat flanges. They are joined together with rf-shielded bellows and ion pump tees. The injection, rf cavity, extraction and instrumentation vacuum chambers have more complex geometry and include components with high outgassing materials such as ferrite and graphite. The DX-D0 chambers where both beams merge into DX magnets have long internal perforated shields to minimize beam impedance. The beam pipes inside the experimental detectors are made of 1mm thick beryllium for its transparency to energetic particles. The warm bore sections are pumped with large sputter ion pumps and titanium sublimation pumps. Inverted

magnetron cold cathode gauges (CCG) are used to monitor the warm bore vacuum. With the exception of the rf cavities, all warm bore sections including DX beam pipes are in-situ bakeable to 250°C.

2.2 Cold Bore Vacuum System

A series of interconnected magnets forms the RHIC cold bore, as shown in Fig. 3. Each magnet vessel comprises magnet coils and laminations built upon a seamless stainless steel tube that extends beyond the length of the magnet. Each magnet vessel was pressure tested to 20 atm. during manufacturing. The magnet vessel is then assembled along with four He conduits and an aluminum heat shield, insulated with blankets of multi-layer thermal insulation (MLI), and inserted in a carbon steel cryostat. Approximately 10% of the dipole magnets and all the CQS magnets were cold tested before installation. Once installed, the beam tubes with conflat flanges are connected with rf-shielded bellows to form a continuous cold bore.

There are 40 cold bore sections isolable from adjacent warm bore sections with rf-shielded gate valves. The cold bore pressure is expected to be immeasurably low if He leaks are absent. No welded, brazed or bolted vacuum joints serve as barriers between the beam vacuum and the contained superfluid He. Helium can leak into the cold bore from the He filled magnet vessels only through metallurgical flaws in the cold beam pipes. Sorption pumps containing activated charcoal are mounted to the pull through ports of the rf-shielded bellows at every fourth interconnect (~ 30m intervals) to pump He and H$_2$. The pumping speed of the sorption pump at the cold bore port is ~ 2.5 l/s. CCGs identical to those in the warm bore are used

Fig. 3 Vacuum Layout of RHIC Arc Section

to monitor the cold bore pressure. They are mounted on the ambient cryostat at ~30m intervals. A 1.5m long 1" diameter flexible conduit attached to cold bore port snakes through the MLI and the 55K heat shield, and is then connected to the CCG.

Prior to magnet cool down, the cold bore is usually roughed down to ~10^{-4} Torr with a turbomolecular pump station (TMP). After cooldown, the CCGs read mid-10^{-10} Torr pressure due to the localized outgassing of the gauge conduits. Changes in CCG pressure readings ΔP_w, are assumed to be contributed by He. With no net He flow between the cold bore and the CCG and factoring in thermal transpiration, then

$$\Delta P_w = S_{He} \times \{T_w / T_c\}^{0.5} \times P_c$$

with S_{He}: the CCG sensitivity correction for He (= 1/7)

  P_c: the cold bore He pressure

  T_w: the temperature at the CCG (~ 295K)

  T_c, the temperature of the cold bore (~ 4.5K)

then $P_c = $ ~0.8 x ΔP_w.

With background reading of 10^{-10} Torr at CCGs, pressure changes of 10^{-11} Torr level in the cold bore should be easily observable by the CCGs.

2.3 Cryostat Insulating Vacuum System

There are 28 insulating vacuum volumes: 12 long arcs, 12 triplets and 4 short cryostats between the ambient injection magnets. The volume of the long arc cryostat is ~150m³ and that of triplet-DX over 50m³. The insulating vacuum requirement is 10^{-5} Torr. At 4K, all gases except He will be effectively pumped by the magnet cold masses. Helium may originate from leaks in the magnet vessel welds or in the bellows where the superfluid He and the superconductor cables are piped from one magnet to the next. Helium may also come from the leaks in welds of the four He conduits running the full length of the cryostats. A side view of the cryostat magnets and interconnects is shown in Fig. 4.

Fig. 4 Magnet and Beam Tube Interconnecting Bellows

After installation and survey of each magnet, the superconductor cables are brazed together, insulated and tested followed by positioning and welding of the triple-ply

bellows. The four He conduits are then joined by welding. In all, there are 16 in-situ circumferential welds at each interconnect. Each of these welds must be verified at room temperature with sufficient sensitivity to ensure that it will not spoil insulating vacuum after cool down.

After completing a long string of interconnects, the He conduits are pumped down and the in-situ welded joints leak checked to a sensitivity of ~10^{-8} std.cc/sec He (all the leak rates referred from here on are equivalent leak rate at room temperature in standard cc per sec He). The triple-ply He bellows welds between magnets are leak checked by pressurizing the magnet vessel to ~2 atm He and sniffing around the weld zone. The sensitivity of this approach is ~10^{-4} std.cc/sec at best when sniffing is done carefully and the tunnel He background is low. Some earlier bellows welds were checked with vacuum-jacketed fixtures which gave far better sensitivity, however, they are not used due to the significant effort required to use the fixtures and the high success rate of the automatic welder. The cryostat clamshells surrounding the interconnect are then welded together to form the cryostat. The completed cryostat is roughed down to ~10^{-2} Torr by a mobile roots blower/mechanical pump station, before the pumping is transferred to a TMP.

Two major requirements in the design of the insulating vacuum system are: locating serious He leaks to within one interconnect; and instituting local pumping provisions on these leaks until repairs are made. A pump port and transverse conduit as shown in Fig. 5 are at each interconnect to meet these requirements. Transverse conduits are high conductance path at interconnects linking the three temperature regions (the 4K magnet, the 55K heat shield and the ambient wall). The He conductance of the conduit is 400 l/s, optimized using a voltage analogue to simulate actual conductance [6]. The 100mm pump ports are capped with manual valves allowing the addition of pumps without venting the cryostat. One TMP is mounted on the pump port located at the midpoint of each long cryostat. The combination of the transverse conduit and the

Fig. 5 Cross Sectional View of Arc Interconnect

TMP provides a He pumping speed of ~100 l/s. In the event of an internal helium leak, the TMP generates a He pressure gradient with sufficient resolution to locate the leak to within one interconnect. Additional TMPs are then added to the pump ports nearest the leaks to ensure that leaks of $<10^2$ std.cc/sec can be effectively pumped and adequate insulating vacuum maintained until repairs can be made.

3 COMMISSIONING EFFORT

The first sextant test (FST), the completion and testing of one-sixth of the ring, was carried out in January1997 with vacuum established, magnets cooled down and powered, and beam injected. Modifications were made to the design of some helium flex lines and to the assembly procedures when He leaks resulting from flux corroded flex lines and inappropriate use of ultrasonic welders were identified. The remaining sextants were commissioned in late 1998 and early 1999. This section summarizes the performance of the three vacuum systems during FST and recent commissioning effort, with emphasis on locating and repairing He leaks in the insulating vacuum systems which is by far the most difficult and time consuming efforts.

3.1 Commissioning the Warm Bore

Work on warm bore sections could only begin after the adjacent cryostats/cold bore sections were completed. After installation, alignment and assembly, a TMP backed by a dry mechanical pump was used to rough down the warm bore section. After leak checking, the sputter ion pumps were conditioned and energized. To this date, 44 of the 52 warm bore sections are complete with vacuum reaching 10^9 Torr in a few days comprising of mostly H_2, H_2O and CO. The remaining sections will be commissioned after the installation of the four experiment detectors and the termination of the ion pump and gauge cables. Three warm bore sections have been in-situ baked and reached pressure of ~1x10^{-10} Torr, comprising mostly H_2. Other warm sections will be baked and conditioned in the coming year.

3.2 Commissioning the Cold Bore

The cold bore sections were pumped down to pressures of 10^{-4} Torr or better by TMP and valved off. The pressure would slowly creep to mid 10^{-2} Torr over a few months, which is still adequate for cool down. After cool down, the CCGs at cold bore typically read 10^{-10} Torr range when the true pressure in the cold bore is $<10^{-11}$Torr. The usefulness of the CCGs in monitoring the cold bore He pressure, in the unlikely event of He leaks from magnet volume into the cold bore, was studied during FST [7]. Helium from a calibrated leak of 4x10^{-5} std.cc/sec was continuously introduced into the cold bore for 9 days while CCG readings were monitored and recorded. The CCG readings increased sharply when the He fronts reached the particular gauge locations, then leveled off. The cold bore He pressures derived from the changes in the CCG readings were compared and found to be in good agreement with those

calculated[7]. This result indicates that the CCGs are useful to detect cold bore pressure increases with sensitivity down to ~10^{-11} Torr. The study also validates the need and the effectiveness of the sorption pumps in slowing the He pressure front speed and in reducing the magnitude of the He pressure zone.

3.3 Commissioning the Insulating Vacuum

After the completion of installation and welding, the cryostat volume was pumped down by a mobile roots blower/mechanical pump station with pumping speeds of ~ 140 l/s and 30 l/s, respectively. Typical pump down curves for arc cryostats (with a volume of ~150 m^3) are shown in Fig. 6. The pressure decreased rapidly to ~1 Torr within one day then leveled off due to the gradual desorption of ~50 liters of water absorbed in the MLI [8]. Most insulating volumes have to be bled back to atmosphere pressure several times to repair cryostat vessel air leaks or internal He leaks. Without major air leaks, pressure of mid10^{-2} Torr is usually reached in a few days, which is needed to ensure adequate leak checking sensitivity. Once pressure of low 10^{-2} Torr was reached, the TMP was switched on to maintain the insulating vacuum until cool down.

Fig. 6 Pumpdown Curves of RHIC 494m Arc Cryostats
with 300CFM roots blower and 60 CFM mechanical pump

During FST, with insulating vacuum established, high He background levels were observed in the cryostats when the magnet vessels and He conduits were pressurized. A

Fig. 7 Helium Pressure Gradients at Interconnects in 494m Arc Cryostats

series of pressure tests were conducted to isolate the leaks to specific conduits by individually pressurizing each to 15 atm He while the others evacuated. After identifying which conduits leaked and quantifying the leak rates, the leak was traced to the offending interconnect by measuring the cryostat He pressure gradient generated by the TMP [9] as shown in Fig.7. The gradients across a typical CQS magnet were ~5% and across a dipole magnet ~10%. Two large leaks were found and repaired at specific interconnects in the arcs using the gradient method. After the repair, an additional 10^5 std.cc/sec leak, masked by the large leak, was found 200m away. A mobile TMP was positioned at the interconnect to pump He. After cool down, the leak rate increased to 1.5×10^2 std.cc/sec due to the increase in density and decrease in viscosity of superfluid He. The pressure at this interconnect was maintained at ~10^4 Torr range, considered the local upper limit for the insulating vacuum.

After FST, this interconnect was opened and the leak was located by sniffing while pressurizing the He conduit. This approach can only detect 10^5 std.cc/sec leaks, when parked on the leak. Bagging and accumulating helps identify 10^6 leaks, but provides little benefit for locating smaller leaks. For example, the 10^5 std.cc/sec leak was located by leaving the conduit under 5 atm. for overnight with the cryostat at atmospheric pressure. This yielded a slight increase above 5 ppm He background in air using a sniffer probe. A leak of ~10^6 std.cc/sec would require an impractical 10 days of accumulation to be observed with the sniffer probe.

Fig. 8 Helium Pressure Gradients in RHIC Triplet Cryostats

During the most recent commissioning effort, all He volumes were first pressurized to 3 atm. Ten He leaks of various sizes were observed at different insulating volumes. One dozen additional leaks showed up when the He pressure was increased to 15 atm. Leaks at 10^7-10^6 std.cc/sec levels were deemed too difficult to locate and vacuum could be safely maintained by mobile TMPs even when the leak rates increase by a few decades after cool down. The large ones (>10^3 std.cc/sec) were quickly located and repaired. Leaks of 10^5-10^4 std.cc/sec levels in the arcs were also located using He pressure gradient.

Locating 10^5-10^4 std.cc/sec range leaks in the triplet cryostats was more challenging due to the larger and more complicated cryostat vessel accommodating both strings of magnets, which reduces the effectiveness of the pressure gradient. Typical He pressure gradients inside the triplet cryostats are shown in Fig. 8. They do not point to the exact interconnect in some cases. Innovative approaches were developed to locate these leaks. Some leaks were located by differentiating the He arriving time at leak detectors mounted at each interconnect while pressurizing the He volumes. Others were located by differentiating the size of He signal when low pressure He was introduced into individual power lead at each interconnect. With the cryostat bled up to atmosphere, each interconnect was then probed with a sniffer through the pump port to confirm the measured He gradient data prior to cutting open the interconnect. With the interconnect open, the sniffer was then used to pin-point the leak location.

4 SUMMARY

The RHIC vacuum systems have been commissioned and are ready for collider operation. All three systems performed as expected. The designed vacuum of 5×10^{10} Torr in the warm sections can be reached without difficulty after bakeout. The combination of CCGs and sorption pumps is sufficient to monitor and pump He leaks in the cold bore and to achieve the designed vacuum of <10^{11} Torr. In the long arcs, the combination of transverse conduits and pumping ports proved effective to locate He leaks to within one interconnect and to pump on the leaks. In the DX-triplet cryostats, locating leaks has been more challenging due to the complex geometry and the high-conductance space which prevent the formation of He pressure gradients. Innovative approaches have been developed to locate these leaks

Overall, there were less than two dozen leaks found after the installation was complete. This excludes the damaged flex lines and bellows caused by misuse of ultra sonic welders prior to FST; and damaged triple-ply bellows which squirmed due to insufficiently supported interconnect pipes during commissioning. With approximately 25,000 in-situ He line welds and a total welded length of over 5 km, the welding and leak checking of insulating vacuum could be considered rather successful.

5. REFERENCES

[1] M.A.Harrison, 'Commissioning Results from RHIC', paper no MOAC2 of this conference.

[2] M.J. Rhoades-Brown and M.A. Harrison, RHIC Technical Note #106, BNL-47070, Dec. 1993.

[3] R. Anholt and U. Becker, Phys. Rev. A36, 4628 (1987).

[4] D. Trbojevic, Private Comm., Feb. 1993.

[5] S. White, Private Comm., Oct. 1991.

[6] R.J.Todd, D.J. Pate, K.M. Welch, BNL-49181, June 1993.

[7] H.C. Hseuh and E. Wallen, J. Vac. Sci. Technol., A16, 1145(1998).

[8] R.J. Todd, D.J. Pate, K.M. Welch, RHIC Tech. Note# AD/RHIC/RD-44, September, 1992.

[9] H.C. Hseuh, et. al, Proc. 14th Int'l Vac. Congress, Birmingham, UK, Sept. 1998 (in press).

THE AD VACUUM SYSTEM: CONSTRUCTION AND COMMISSIONING

M. Brouet, J. Hansen, H. Klette, P. M. Strubin, CERN, 1211 Geneva 23, Switzerland

Abstract

CERN has built a new experimental facility, called the Antiproton Decelerator (AD), by transforming two existing machines: the "Antiproton Collector" (AC) and the "Antiproton Accumulator" (AA). To achieve adequate beam performance once the antiproton beam is decelerated to its final value of 0.1 GeV/c, it was necessary to lower the average pressure by nearly two orders of magnitude. For this purpose, a large number of additional pumps were installed and a very careful preparation was applied to a variety of special machine equipment which, in its original construction, was not designed for ultra-high vacuum operation. An important improvement in the outgassing rates was achieved through an extended, mild bake-out of tanks and vacuum vessels containing large amounts of ferrite material and multi-layer thermal insulation.

This paper describes the necessary modifications of the vacuum system and in more detail the various steps taken to obtain the required pressure in the low 10^{-10} mbar range. It will also report on the unexpected difficulties which were encountered by re-using vacuum components that were not initially designed for bake-out.

1 INTRODUCTION

Following the decision to close the LEAR antiproton program, there was a strong request from the user community to continue certain experiments. The Antiproton Decelerator (AD) project was approved after a careful study of the feasibility of converting the existing Antiproton Collector (AC) into the new facility [1]. In addition, some parts of the LEAR ring, notably the electron cooling system, were recuperated and adapted for AD.

The decision to build this new facility with mostly existing equipment was justified by a lower cost and faster installation time. However, it required the Vacuum Group to apply a number of original solutions in order to meet the design pressure of $5\ 10^{-10}$ mbar. It also involved a number of unexpected difficulties, mainly when trying to apply mild bake-out to equipment which was not foreseen to be baked at all.

The first measure was obviously to increase the pumping speed wherever possible, in particular by the addition of about one hundred titanium sublimation pumps. The second measure was to minimize the outgasing rates of selected components, like injection and ejection kickers, RF cavities or stochastic cooling pickups and kickers. This was achieved by performing low temperature bake-out on these components. Finally, installing ion gauges, cold cathode gauges and gas analyzers, not previously available in AC, allowed for better diagnostic.

2 ASSESSING THE NEEDS

The goal of the improvement of the vacuum system was to reach an average pressure in the low 10^{-10} mbar, with residual gas mainly dominated by hydrogen [2]. The average pressure of the former AC was in the high 10^{-9} mbar range, with a significant amount of water vapor and carbon monoxide in addition to hydrogen. Calculations of the expected pressure profile were carried out in order to identify the most critical parts so as to concentrate the effort on them. Most effort was spent in order to achieve the lowest possible pressure in the regions where the antiproton beam has the highest vertical ß function. These regions are mainly where special equipment, like kickers and septa are installed.

3 INCREASING THE PUMPING SPEED

3.1 Bending sections

The pumping speed in the bending sections could be significantly increased by the addition of titanium sublimation pumps at each end of the vacuum chamber of every bending magnet. For this purpose, openings of 100 mm had to be drilled in the existing vacuum chamber and pumping ports were welded onto the chamber to support the pumps. In order to avoid a manpower-intensive dismounting of the vacuum chamber from the bending magnets, an original tool was developed with the help of an outside company which allowed drilling the holes in situ. A support rod was welded on the vacuum chamber at the center of the piece to be cut out to guide the circular saw. No lubricant was used during the drilling, to avoid any contamination of the vacuum chamber and the opening was de-burred with special care to avoid that metal chips were spread into the vacuum chamber. Welding the pumping ports onto the vacuum chamber and leak testing the welds was all done in situ. In total, 98 sublimation pumps have been added, increasing the total pumping speed for hydrogen by 78'000 l/s over 70% of the circumference.

3.2 Injection, ejection and stochastic cooling kickers

As there were no additional ports available on these kickers, a tee piece fitted on the entrance flange of the ion pumps was added in order to accommodate two titanium

sublimation pumps per tank. In addition, some ion pumps were exchanged to larger ones.

4 BAKE-OUT

As stated earlier, only parts of the decelerator, which presented excessively high degassing surfaces, were considered for baking. These include the RF cavities, the injection septum magnet, the injection and ejection kickers, the stochastic cooling pick-ups and kickers. However, because these components were not foreseen to be baked at all, temperatures had to be limited to a maximum of 150 °C, even below 100 °C for the RF cavities. To compensate for these low temperatures, the bake-out has been extended up to three weeks for some components.

Low-cost, low-temperature heating elements were used where adequate instead of the traditional heating tapes or heating jackets. These heating elements, with a specific heating capacity of 50 W/m can be cut to custom lengths, still allowing for direct mains (230 V) supply. As they are very flexible, they easily follow the sometime difficult shapes of the equipment to be baked. Heat-resistant tape is used to affix them on the surface of the vacuum vessel which is then covered with standard heat-insulating material.

The installed power of the heating elements was calculated to have a limited value, such as to make sure that under no circumstances would the temperature of the vacuum vessel exceed 150 °C. The price to pay for this is a longer rise time up to operating temperature. Also, in addition to the thermocouples required for regulation, a number of redundant thermocouples were installed and connected to a data acquisition system for monitoring and alarm purposes.

4.1 Bake-out of the RF Cavity

The RF cavity is a huge device of 2.2 meter in diameter and 2 meter in length, made of aluminium alloy. The flanges, however, are made out of stainless steel. The major worry was to minimize the temperature gradient at the aluminium-to-stainless-steel junctions, which are friction welded. The cavity is pumped by a 20'000 l/s cryopump, switched on after initial pumping with a mechanical pumping station (a set of roughing and turbomolecular pumps).

Initial tests were made in the laboratory by building a hut around the cavity with spare shielding blocks. A 16 kW air blower was used to provide the heating power, which was able to bring the temperature of the cavity to 60 °C after 2 days. The cavity was instrumented with thermocouples located in all critical areas and connected to a temperature scanner and logger. The measurements showed that the temperature differences between various parts of the cavity could be kept below 3 °C.

Starting from a pressure of about 10^{-4} mbar after initial pumping, the pressure rose into the 10^{-1} mbar range as soon as the temperature of the cavity reached 50 °C. From then on, the pressure continuously decreased and reached 10^{-4} mbar after 24 hours with an average temperature of the cavity of 60 °C. After cooldown, the pressure was 5 10^{-8} mbar with turbomolecular pumping only. This figure has to be compared with 4 10^{-7} mbar after 8 days of pumping without bake-out.

This first experiment proved that a considerable improvement in the degassing rate of the surface was achievable by applying a mild bake-out to this cavity. However, although quite easy to set up in the laboratory, the heating method was considered to be too space consuming for the accelerator environment. It was therefore decided to order tailor-made heating jackets from industry, with a limited power rating to ensure that under no circumstances would the temperature of any part of the cavity exceed 120 °C. An adequate programming of the temperature regulators insures that the required temperature gradients are satisfied. In addition, a computer monitoring extra temperature probes was programmed to stop the bake-out process should the temperature of one heating element rise above a predefined limit.

The spare cavity was equipped with the heating jackets and baked in the laboratory. Although the overall improvement was comparable to the first cavity, the pressure increase during the initial heating period was much smaller. The origin of this difference in behavior still remains to be studied.

The operational cavity has now been equipped with the jackets and the bake-out in the AD accelerator is foreseen for end of March 1999.

4.2 Bake-out of the Stochastic Cooling Pick-ups

The stochastic cooling pick-ups are operated at cryogenic temperatures of some 20 K. The active parts of the pick-up are thermally shielded from the vacuum vessel by multiple layers of superinsulation which act as a very large source of gas. Furthermore, the layers of superinsulation were seamed together at their extremities, which prevented the gas trapped between layers to be pumped. As a first step, the welds between layers of superinsulation were cut off in such a way as to allow for the gas to escape. Tests were then made to try and assess the required baking time to achieve the foreseen pressure decrease. When heating was only applied to the outer surface of the vacuum vessel, there was so little thermal transmission through the insulation layers to the inner structure of the pickup assembly that literally months of bake-out would have been required. Furthermore, the pickup electrodes being actively cooled under operation, heat was evacuated via the leads from the electrodes to the housing of the cold heads, the latter being dismantled during bake-out. To overcome this problem, the cold heads are replaced during bake-out by a copper block which is heated and hence transfers thermal power to the inner structure of the pickup assembly. To avoid too strong oxidation of the copper, the volume housing the copper block is pumped out. The atmospheric pressure applied is

also used to improve the thermal contact between the copper block and the leads to the pickup assembly. With this improvement, the temperature of the pickup electrodes reached 95 °C within 3 days as shown in Figure 1.

Figure 1: Evolution of temperature during bake-out of stochastic cooling pickup

5 ADDITIONAL VACUUM INSTRUMENTATION

The original Antiproton Collector was only equipped with the bare minimum of gauges, the pressure values being mostly evaluated from the current of the ion pumps. A total of 17 Bayard-Alpert gauges were installed all around the ring to allow for pressure measurement in the low 10^{-10} mbar range. These gauges, as well as the cold cathode gauges, are connected to the AD control system allowing for short- and long-term data logging.

Seven residual gas analyzers were mounted. In addition to allowing for a measurement of the quality of the achieved vacuum, these instruments proved very useful to diagnose a series of very nasty leaks on feedthroughs which were submitted to a pressure of 2 bar of SF_6 gas.

6 CONCLUSIONS AND FUTURE IMPROVEMENTS

The additional pumping speed obtained with the titanium sublimation pumps and the soft bake-out of the components with the highest degassing rates allowed to reach the required pressure without major modification of the existing equipment.

Figure 2 shows a comparison between the pressures measured in the former AC compared to pressures in AD, when available.

Figure 2: Pressure comparison between AC and AD

As a further step, it is foreseen to change the NEG cartridge used in the injection septum to a low-temperature one in such a way as to allow its use as both a heating element during bake-out and an active pump. Other studies have started to improve the venting of the vacuum system and to possibly work with a small overpressure of nitrogen during interventions.

7 REFERENCES

[1] The Antiproton Decelerator: AD, S. Baird et al., CERN, PAC 1997

[2] Upgrading The AC Vacuum System for the Antiproton Decelerator, M. Brouet and O. Gröbner, CERN Vacuum Technical Note 97-06, April 1997

DESIGN AND TEST OF A BEAM TRANSFORMER AS A CHOPPER

W. Chou*, FNAL, Batavia, Illinois, USA

Y. Mori, M. Muto, Y. Shirakabe, A. Takagi, KEK, Tanashi, Japan

Abstract

This paper introduces a new type of chopper, which is similar to a beam transformer first discussed by R. Wideroe[1]. It is based on the fact that the RFQ has a rather small energy window. A pulsed beam transformer that provides 10% energy modulation to the beam in front of an RFQ can effectively chop the beam. It has fast rise- and fall-time and a short physical length. A prototype, which consists of a cavity and a high voltage pulsed power supply, has been constructed and tested. Two types of magnetic materials were tried for making the core of the cavity – the Finemet and the ferrite Philips 4M2. While the former gave good performance, the latter failed the test. Results from the bench measurements and a plan for beam tests are briefly described. For details the readers are referred to Ref. [2].

1 INTRODUCTION

In a high intensity proton accelerator, a beam chopper is often necessary in order to reduce particle losses during injection from the linac to the first circular machine. A chopper can also serve other purposes such as to create a gap in a bunch train so that the extraction loss due to kicker rise-time can be eliminated.

There are various ways to chop the beam, *e.g.*, ion source chopping, transverse deflecting, *etc.* This paper introduces a new type of chopper, which is similar to a *beam transformer* first discussed by R. Wideroe.[1] It is based on the fact that the RFQ has a rather small energy window. Both simulations and measurements show that, a $\pm 10\%$ energy error in a beam before it enters the RFQ can effectively cut the transmission efficiency down to zero. For an RFQ with an injection energy of 50 keV, a 10% error is 5 keV. Therefore, a pulsed beam transformer that provides a 5 keV energy modulation to the beam in front of an RFQ can serve the purpose of a chopper. There are several advantages of this type of chopper.

1. Fast rise- and fall-time.
   As will be seen below in our bench test, a 40 ns rise-time has been achieved with a thyratron switch. It will be shortened to 10-20 ns when a solid state switch (*e.g.*, the HTS transistor) is used.

2. Short physical length and chopping at low energy.
   The beam transformer has a length of just about 10 cm. The chopped beam is at the RFQ injection energy (which is 50 keV at the JHF).

---

*Email: chou@fnal.gov

2 DESIGN

2.1 Components of a chopper

The chopper consists of a pulsed power supply and a cavity. The latter contains several magnetic cores and works as a transformer. When a voltage waveform is provided in the primary circuit, an acceleration voltage with the same waveform will be generated across the gap as the secondary. An ideal voltage waveform is a series of squares, each with steep rise and fall edges and a flat top. The height of the square is 5 kV (which could be higher or lower, depending on the design of the RFQ). The repetition rate (rep rate) of the squares are determined by the injection rf frequency. The spacing between two neighboring squares is equal to the chopped beam length.

It is necessary to use a bipolar waveform. A monopolar waveform will generate significant flyback voltage on an inductive load when the power supply is switched off, and also has a large dc component.

Take the JHF as an example. The bucket length of the JHF Booster at injection is 500 ns (2 MHz). Assume one-half of the beam will be chopped. The required voltage waveform is: +2.5 kV for 250 ns, –2.5kV for the next 250 ns in a period of 500 ns. When this voltage is transmitted to the beam through an accelerating gap, the beam energy will alternate between $E_{H^-} + 2.5$ keV and $E_{H^-} - 2.5$ keV, where E_{H^-} is the H^- ion source energy, which can be set to 47.5 keV. Thus, at the exit of the RFQ, a 250 ns gap will be created in the beam every 500 ns.

2.2 Magnetic core

The magnetic core is a critical part of the beam transformer. It must be able to stand high magnetic field B_{rf} and have high permeability μ. Two types of materials have been tested for making the core — the Finemet and the Philips 4M2 (which is a ferrite). Their magnetic parameters can be found in Ref. [3].

When a voltage waveform $v(t)$ is applied, the average field is $B_{ave} = \int v(t)dt/A$, in which A is the flux area of the core. Because the Finemet can be used at much higher B_{ave} (~ 5 kG or higher) than that for the 4M2 (~ 100 G), it makes the Finemet a preferred candidate.

The permeability of the Finemet and 4M2 has a strong dependence on the frequency. Assume the pulse has a period $\omega_0 T = 2\pi$ and a length of 2α as shown in Figure 1. The Fourier spectrum lines are $n\omega_0$, $n = 0, 1, 2, ...$ For the JHF, $T = 500$ ns, $\omega_0 = 2\pi \times 2$ MHz. Thus, the permeability value at 2 MHz gives a reasonable estimate. It is 2800 for the Finemet and 170 for the 4M2. This is another reason why the Finemet is a better material for a chopper.

Figure 1: A series of voltage pulses with square waveform.

2.3 Pulsed power supply

The power supply is a bipolar voltage source. It provides $\pm\frac{1}{2}V_0$ square pulses at a given rep rate (2 MHz for the JHF). The number of pulses in a burst is determined by the injection time. It is about 0.3 ms for the JHF, which corresponds to 600 pulses. The relative length of $+\frac{1}{2}V_0$ and $-\frac{1}{2}V_0$ should be a variable so that the chopping length can be adjusted to meet different needs at the injection.

The switch is the most important part of the power supply. It must be able to deliver high voltage (several kV), high current (several tens of amperes) at high rep rate (several MHz). It must also have short turn-on and turn-off time (a few tens of nanoseconds). There are some triodes and transistors that are commercially available and can serve the purpose, for example, the fast high voltage transistor switch HTS 81-09 from a German company Behlke. The peak power of the power supply is high (hundreds of kW). But the duty factor is low. For the JHF, the duty factor is below 1%.

3 MEASUREMENTS

A simple cavity was constructed as shown in Figure 2. It consists of a magnetic core, a copper shield, a one-turn coil (the primary circuit of the beam transformer) and a stainless steel beam pipe. The pipe has a 22-mm long ceramic gap (the secondary of the transformer).

A high voltage, low rep rate (3 Hz) kicker power supply was used in the experiment. This is a monopolar voltage source. It uses a thyratron as the fast switch and a pulse forming line (PFL) with a characteristic impedance 25 Ω. A dummy load of 25 Ω is added in parallel to the primary circuit for matching the PFL impedance.

Both the Finemet and 4M2 were tested. The dimensions of the Finemet core are: $OD = 58$ cm, $ID = 32$ cm, $d = 2.5$ cm. That of the 4M2 are 50 cm, 20 cm and 5 cm, respectively. The measured primary and secondary (i.e., the gap) voltages are shown in Figures 3-4.

- Finemet:

  It is seen that the gap voltage has a nearly square shape. The rise-time is about 40 ns, which is determined by the thyratron. The fall-time is a bit longer. The amplitude difference between the primary and secondary voltage is small, which indicates good coupling. The maximum gap voltage reaches about 7.5 kV. The cor-

Figure 2: A test cavity used in the measurements. It consists of a magnetic core, a metal shield, a one-turn coil and a stainless steel beam pipe with a ceramic gap.

responding primary voltage is about 8 kV. In this test, one achieved $B_{ave} = 4.9$ kG and $B_{max} = 6.7$ kG.

- 4M2:

  In Fig. 4, it is seen that there is a fast fall off in the voltage waveform after the switch is turned on. There are two reasons for this behavior: (1) The inductance of the 4M2 is smaller than the Finemet, the decay is faster. (2) The maximum B_{rf} of the 4M2 is rather low. At high voltage, the performance of the 4M2 is deteriorated. Moreover, when the switch is turned off, there is a voltage jump to the opposite side (flyback voltage).

Because the thyratron rep rate is low, a separate test using low voltage high rep rate power supplies (waveform generators) was performed. The measurements were done at 2 MHz and 7 MHz. The results are similar to that shown in Figs. 3-4 and can be found in Ref. [2].

4 PLAN FOR BEAM TESTS

A new power supply and a prototype chopper have been designed and are under construction. The power supply will use two HTS 81-09 transistors for a bipolar operation, as shown in Fig. 5. Each transistor can operate at 8 kV, 90 A at a burst frequency of 2.5 MHz. The pulse length can be varied from 200 ns to infinity.

Figure 5: A circuit diagram of a bipolar (push–pull) high voltage source using two HTS transistors as the switches.

Figure 3: The primary and secondary voltage waveform when a Finemet core is used. The rise-time is about 40 ns.

beam chopping experiment in the fall of 1999.

5 SUMMARY

It is feasible to construct a beam transformer to provide 5 kV (or higher) pulses with short rise- and fall-time and a flat top. When it is placed in front of an RFQ, it can be used as a beam chopper.

The Finemet has high B_{rf} and high μ. It is a good material for the magnetic core. The 4M2 gave poor performance in the tests because its B_{rf} and μ are too low.

A bipolar high voltage source with high current and fast switches is the preferred power supply.

There are several issues that have not yet been addressed, including: (1) The tolerable voltage variation on top of the waveform; (2) The effect of low energy (50 keV) H$^-$ particles bombarding the RFQ.

6 ACKNOWLEDGEMENTS

Figure 4: The primary and secondary voltage waveform when a 4M2 core is used.

The chopper will use three Finemet cores. The dimensions of each core are: $OD = 50$ cm, $ID = 16$ cm, $d = 2.5$ cm. The total inductance at 2 MHz is about 50 μH.

This chopper will be installed on the HIMAC linac for a

7 REFERENCES

[1] R. Wideroe, *Archiv fur Electrotechnik,* Vol. 21, p. 387 (1928).

[2] W. Chou *et al.,* KEK Report 98-10 (1998), and the references therein.

[3] T. Uesugi *et al.,* JHP-31, KEK (January 1997).

SOLID-STATE HIGH VOLTAGE, DC POWER DISTRIBUTION & CONTROL

Dr. Marcel P.J.Gaudreau P.E., Dr. Jeffrey A. Casey, Timothy J. Hawkey, Michael A. Kempkes,
J. Michael Mulvaney, Dr. Peter Ver Planck, Diversified Technologies, Inc.

1. ABSTRACT

Future high voltage, high power systems in the early stages of planning include U.S. large accelerator programs such as the Next Linear Collider (NLC), Spallation Neutron Source (SNS), and international systems at DESY, CERN and KEK. There are also many nuclear fusion and multi-megawatt sytems proposed for construction or upgrade. Each of these programs faces the challenge of distributing and controlling the high power required by tens to hundreds of RF amplifier tubes (e.g., klystrons) cost effectively.

In this paper, we present a new approach for distributing and modulating power based upon recent technological developments in high voltage, high power, solid state switching. DTI's development of fast, high voltage, opening and closing solid state switches enable, for the first time at high voltage, a nearly lossless "DC Transformer". With this DC transformer (i.e., down converter or buck regulator), it is now possible to distribute unregulated high voltage DC power in a large facility, and regulate and control it at the klystron. This approach is significantly more compact, less expensive, and more reliable than conventional methods of power distribution.

2. THE OPPORTUNITY

The early 20th century saw the triumph of Westinghouse's AC power distribution scheme over Edison's DC distribution approach because efficient AC power transformers were available, and DC transformers were not.

But, AC distribution is expensive, complex to manufacture and maintain, and inefficient. Typically, only 10% to 20% of the grid power provided to these systems is converted to RF power. The rest is converted to heat, which must then be removed via a complex plant infrastructure.

Recently, high power Insulated Gate Bipolar Transistors (IGBTs), capable of handling hundreds of kilowatts each, have become available. Along with the development of effective methods for combining these devices into very high power circuits, the opportunity for the replacement of traditional AC distribution technology with efficient DC voltage transformers has been created. We will describe this as DC Power Distribution and High Frequency Solid State Power Control.

3. THE ELEMENTS OF DC POWER DISTRIBUTION

The key to the next generation of power distribution and control systems is the availability of a fast, high voltage, solid state, opening and closing switch. Figure 1 shows a DTI PowerMod™ high voltage, solid state switch which operates at 125 kV, 400A, and up to 50 kHz in burst mode.

A high voltage pulse from the unit is shown in Figure 3.

Using DTI's high voltage solid state switching technology, the power distribution picture is dramatically simplified. Figure 2 illustrates the concept of transformed

Figure 1: DTI PowerMod™ 125 kV, 400A Solid State Switch with co-author Dr. Jeffrey A. Casey

three-phase DC power supplied to devices called "switching buck regulators". The route from source to klystron is described as follows:

- Three-phase high voltage power is taken from the power grid in an outdoor switchyard, and routed through SF_6 circuit breakers prior to going to the step-down transformer.

- The step-down transformer is a standard utility outdoor transformer (~ 50 MW). It transforms power from 230 kV AC to approximately 70kV AC (in the 100 kV DC example used here). This 70 kV AC power is then rectified to provide 100+kV unregulated DC power.

- The unregulated, 100+kV DC power is distributed throughout the facility using single pole, outdoor, pole-top

switchgear and fuses. This equipment replaces the 3-phase 13.8 kVAC switchgear used in the conventional approach, and has the advantage of being simple, inexpensive, and essentially maintenance free.

- Power is routed next to a solid state high voltage switch configured as a 'switching buck regulator'. The switch is composed of a patented, series stack of high power IGBTs. The IGBT switch is used to Pulse Width Modulate (PWM), or Pulse Frequency Modulate (PFM), this higher, unregulated voltage from the rectifier down to a diode stack and LC filter. The high speed variable PWM/PFM switching serves as the voltage regulator for the system, allowing control of the output voltage over a wide range (5-100kV) at constant power output. If the switching frequency is much higher

The entire buck regulator and series switch combination is essentially composed of two of the solid state modulators as shown in Figure 2. These units, approximately 60 ft^3 each, replace all of the equipment after the initial distribution transformer in the conventional approach.

4. Benefits of DC Distribution and Control

4.1 Simplicity

The DC power distribution and control approach eliminates the large, expensive transformers, series-pass tubes, and 13.8 kV switchgear required in the AC method. Further, DTI's high voltage switches are both opening and closing switches,

Figure 2: DC Power Distribution Scheme to a Klystron

than the AC frequency (i.e., 5-30 kHz vs. 60 Hz), the PWM can actively compensate for rectifier ripple, as well as provide very fast voltage regulation in pulsed operations.

The only magnetics required in this regulator is the series inductor, an air core assembly measuring approximately one cubic foot. It is inexpensive to build, because it consists of a single layer winding and no metal core.

DTI has conducted a buck regulator demonstration using a commercial DTI 3 MW peak power modulator. Pulses from the demonstration of a few milliseconds show a flat top current trace and confirm the suitability of the switch for this application.

- A second solid state high voltage IGBT switch serves both as a pulse modulator (where needed) and as a fast disconnect in the event of a klystron arc. This switch can detect an arc and open in less than 600 nanoseconds, thereby preventing damage to the klystron much more effectively than a crowbar. For pulsed systems, the speed of the switch allows pulse-to-pulse agility from 1 microsecond to DC, at pulse repetition rates up to and beyond 10 kHz.

eliminating the need for the specialized crowbar protection circuitry.

4.2 Efficiency

DC Distribution and Control eliminates 60 Hz SCR regulators and series-pass tube regulators / switch tubes, improving the efficiency and lowering the cost of power delivery. Primary 60 Hz SCR controllers have a bandwidth intrinsically limited to below the 360 Hz switching speed of the SCRs. On the other hand, a 20 kHz switch has nearly two orders of magnitude higher regulation speed capability. With high speed regulation, the series mod- regulator tube is not necessary, and as much as a 10 kV to 20 kV voltage drop out of 100 kV (200 kW – 400 kW at 2 MW) is no longer wasted. This is an immediate increase of 10%-20% in overall efficiency.

For a 100 kV series switch, the comparable voltage drop is 200V (4 kW, or 0.2%). The efficiency from the overall buck regulator / series switch combination is estimated at over 98%. In a 2 MW CW system, at $.05/kWH, each percent of inefficiency wastes approximately $10,000 per

year in electricity costs. Therefore, eliminating the voltage regulation tube alone saves $100K-$200K annually. This cost savings alone may justify the selection of solid state switching power supplies for future high power systems.

Finally, increased efficiency significantly reduces the need for cooling systems to support the power distribution and control system, further minimizing infrastructure and facilities costs.

4.3 Reliability

The conventional AC power distribution architecture offers several "single points of failure". When one of these points fails, the entire power supply chain for a klystron is brought down.

In contrast, the risk of system failure is much lower with

Figure 3: Nearly Ideal Pulse from PowerMod™ 100-150.80kV, 90A into Water Resistor

DC distribution and control. Each solid state switch consists of a number of IGBTs in series, typically derated by 30% or more. IGBTs, if they fail, fail shorted. This allows continued operation of the switch, even when individual elements fail. Any failed modules need only be replaced during routine periodic maintenance.

The modularity of solid state electronics enables this basic design to be delivered in virtually any voltage (up to 200 kV) and current (up to 2000A) combination without significant engineering or modifications to manufacturing processes.

Finally, the use of a second fast series switch brings an unprecedented level of flexibility to pulsed power systems. These switches can provide pulses between 1 microsecond and DC, in response to arbitrary pulse commands. They can also operate at 20 kHz and beyond.

4.4 Cost

The entire switch shown in Figure 1 can be built with commercially available components, and fabricated through conventional assembly techniques. No specialized machinery is required to assemble it, and no complex magnetics are used in construction. Even the largest assemblies can be moved easily with a manual pallet truck.

The largest cost components in this design are the semiconductors (IGBTs). Because of their widespread use in locomotive engines, subway cars, elevators, and a wide range of electrical motor drive and power supply systems, these devices are evolving at a rapid pace, especially in comparison with vacuum switch tubes. In the last decade, we have seen the switching speed and power handling capability of IGBTs increase by an order of magnitude (200 kVA to 4 MVA), at essentially constant prices. **This puts high power electronics, for the first time, on a favorable, long term cost reduction path. This is the equivalent of the computer industry's Moore's Law of continually higher performance per unit cost, but applied to power systems.**

Today, a 100 kV, 2MW buck regulator, with a series switch, can be built for approximately $500k USD. This cost will decline due to increased semiconductor performance and decreased manufacturing costs. In contrast, estimates for the equivalent conventional approach are $2- 3M USD, and show no trend towards cost reduction.

5. CONCLUSIONS

The emergence of high power, solid state electronics enables a new architecture for systems that deliver power to RF tubes such as klystrons- DC power distribution and control. The components to build and operate such a system are available today and have been successfully demonstrated by DTI.

The clear advantages of this architecture will lead to the use of DC distribution and control for future high power RF systems. For those responsible for the design and operation of these systems in the radar, accelerator, and fusion engineering communities, this will mean...

- Lower Capital Acquisition Cost
- Higher Levels of Tube Protection
- Higher Efficiency
- High Reliability
- Lower Lifecycle Cost

TECHNOLOGY DEVELOPMENT FOR THE ACCELERATOR PRODUCTION OF TRITIUM*

James L. Anderson[†]

Los Alamos National Laboratory

Los Alamos, NM 87544

Abstract

The Engineering Development and Demonstration (ED&D) program for the Accelerator Production of Tritium (APT) project provides critical data necessary for a plant built on schedule and within budget. The ED&D program is based on prioritized design data needs, and is driven by a formal systems-engineering approach. This paper describes the current role of the project for the U.S. defense program, the ED&D process, the functional areas where ED&D activities are underway, key ED&D activities, and how the technical data from the ED&D program are used.

1 INTRODUCTION

The APT Core Technology Plan (CTP) [1] delineates a program of ED&D activities that support design and construction of the APT facility. The goal of the ED&D programs is to provide critical data necessary for the APT to be built on schedule, based on a demonstrated technical foundation and avoiding costly over design.

1.1 APT Named Backup Tritium Supply Option

On December 22, 1998, Secretary of Energy Bill Richardson announced that the commercial light-water reactor program will be the primary tritium supply option for the United States. The Secretary designated the APT as the "backup" technology for tritium supply. As such, APT will prepare a preliminary design package for the plant, and will complete the essential technology development to support that design. A reduced ED&D program is still necessary. Details of the modified program scope and schedule are still being evaluated by the Project.

1.2 APT ED&D Program Driven by DDNs

The ED&D activities are driven by formal, articulated Design Data Needs (DDNs). The DDNs are identified by the APT design team and transmitted to the APT Technology Office, where they are evaluated and prioritized. The evaluation criteria include several factors:

- Can reasonable extrapolations be made from existing data?
- Is a new measurement needed?
- Is it possible to provide the data within budget and time constraints?

In some cases, the result of this evaluation is to require a more conservative plant design to compensate for the unavailability of supporting data. When appropriate, a test program is then undertaken to provide the necessary data. This formalized, systems-engineering approach to evaluating the DDNs has led to the establishment of an extensive engineering development program aimed at reducing technical, as well as cost and schedule, uncertainties.

2 THE ED&D PROCESS

2.1 The Systems Engineering Approach

A systems-engineering approach, illustrated in Figure 1, identifies and resolves cost, scope, and technical risk issues related to design requirements.

APT program objectives are translated into goals, requirements, and functions that must be met by the design. During the design process, DDNs are identified by the relevant design leaders whenever the existing database is insufficient to fully support a design. At that time, an assumption is made, then confirmed or modified, based on the outcome of the ED&D program. If the completed design meets performance goals and adequate performance is achieved, the design process is complete. If the outcome of the ED&D activity does not support assumptions made earlier that were required to proceed with the design, the design must be modified and new DDNs must be formulated and addressed.

2.2 ED&D Activity Areas

There are four major areas where ED&D activities are underway:

- *The Low Energy Demonstration Accelerator (LEDA):* to fabricate and operate a linac that produces a high quality, ~10-MeV, 100-mA, continuous-wave proton beam.
- *High-energy RF linac technology:* to develop and test component prototypes for normal conducting and superconducting high-energy linac structures (cavities, cryomodules, power couplers, etc.). Included are activities in development and

Figure 1. APT design approach

enhancement of RF power systems and high-energy beam transport components.

- *Target/Blanket (T/B) performance and Materials Studies*: including measurements of n/p and T/p; radiation damage effects from high-energy, high-flux proton and neutron irradiation; and radiation transport-code data development and/or enhancement.
- *Tritium Separation Facility (TSF) studies:* to determine tritium-processing and separation efficiencies under conditions expected in the APT plant.

2.3 Identified Key Activities

Key ED&D activities identified by the above process include:

- Demonstrate 100-mA proton beam at 100% duty cycle through the LEDA Radio Frequency Quadrupole (RFQ).
- Demonstrate 100-mA proton beam at 100% duty cycle through a Coupled Cavity Drift Tube Linac (CCDTL) section of LEDA to a final energy of ~10MeV.
- Determine proton/neutron irradiation effects on T/B materials.
- Develop and/or improve radiation transport codes and nuclear data libraries.

- Develop and confirm engineering design data for separating tritium from ^{3}He and hydrogen.
- Confirm five-cell $\beta=0.64$ superconducting cavity manufacturability and cavity performance; fabricate and test a cryomodule for the $\beta=0.64$ cavities.
- Confirm manufacturability and performance of the 210-kW coupler and RF window assembly for SC cavities.
- Determine performance, reliability, and failure modes of the new high-energy beam transport (HEBT) raster expander prototype.
- Determine performance and manufacturability of key RF distribution components, including waveguide switch, phase shifter, and waveguide valve.
- Determine performance and operability of beam diagnostics for measuring transverse intensity distribution in the linac and HEBT. Included are flying wire profile and gas fluorescence diagnostics.

3 ED&D PROGRAM RESULTS

The ED&D program provides technical data on the performance of all critical components of the APT facility.

3.1 Utilizing ED&D Program Data

ED&D data results will be compared with requirements given in the Preliminary Design Package (PDP) and the System Design Descriptions. These data will be utilized to establish confidence in the design, in the predicted plant availability, and to reduce cost when the data warrants design simplification. Thus, if at a later date the Department of Energy decides to build the APT plant, the facility will be built correctly the first time, on schedule, and without recourse to costly over-design. These results should also speed the commissioning process and ensure that full capacity production is attained on schedule.

3.2 Justifying the ED&D Program

The ED&D program is expected to provide the needed data within the projected schedule and resources. Specific schedules for delivery of data and descriptions of the needed data are contained in the DDNs. The total cost of the ED&D program is on the order of 10% of the project cost, and is considered a very good investment.

The ED&D will be judged a success when the data produced warrants design simplifications allowing reduction of design margins and cost. Present-day contingency estimates for the project greatly exceed 10% and it is expected that ED&D data will justify reduction of those contingencies by more than the cost of data production.

Even results that do not simplify the design or reduce cost are considered important and successful if they firmly establish performance, thus validating design and certifying cost within the existing contingencies.

Nevertheless, there is technical risk in some APT components that warrant careful attention. It is possible some results could be disappointing and may require design changes that increase cost moderately beyond the existing contingencies or cause moderate schedule slips.

4 CONCLUSION

With the Department of Energy's selection of the APT as the backup tritium supply option, the decision was made to carry the APT development to the stage that a PDP could be generated. To accomplish an adequate PDP, the technology development described in the CTP must be completed to support the preliminary design. While that means that not all of the identified ED&D activities will be completed, the essential technologies will be developed and tested to support the PDP. The CTP will be revised to reflect the changing scope required to support the PDP. The development of LEDA and the superconducting technologies continue to be major activities within the ED&D program. The current schedule calls for the ED&D activities to be completed by the end of Fiscal Year 2002.

5 REFERENCES

1. APT Core Technology Plan, Los Alamos National Laboratory Report, APT-CTP-002, August 2, 1997.

THE SPALLATION NEUTRON SOURCE PROJECT[*]

Jose R. Alonso[‡◊], for the SNS Team
Oak Ridge National Laboratory, SNS - 104 Union Valley Road
Oak Ridge, TN 37831-8218

Abstract

The SNS is a "joint-venture" project of five DOE National Laboratories, aimed at building the world's most powerful accelerator-based pulse spallation source. At its planned 2 MW operation, it will produce neutron fluxes at least a factor of ten greater than Rutherford Appleton Laboratory's ISIS, currently the world's leading spallation source. The current design of the SNS, shown in Figure 1, calls for 600 ns pulses of 1 GeV protons striking a liquid mercury target at a 60 Hz rate. Room-temperature and cryogenic moderators produce beams of slow neutrons suitable for materials research. Responsibility for system components is as follows: LBNL will provide the high-brightness H⁻ ion source, transport structures and a 2.5-MeV RFQ accelerator; Los Alamos will build linacs to bring the beam to the full energy of 1 GeV; Brookhaven will build the accumulator ring to compress the 1 ms linac pulse into the sharp pulse delivered to the target; ≈1200 turns will be injected, storing 2×10^{14} protons in the ring, which are extracted in a single turn; Oak Ridge will provide the mercury target systems and all conventional facilities; and Argonne and Oak Ridge are coordinating the design of at least 10 neutron-scattering instruments to be provided as the initial suite of experiment stations. The project is formally underway, having been approved and funded by DOE and the US Congress for a construction start in FY99. Neutron beams will be available for users in FY06.

FIGURE 1: Schematic layout of SNS

1 BEAM REQUIREMENTS

Neutron scattering requires low energy (< milli-electron volt) neutrons, to obtain De Broglie wavelengths commensurate with the size of the structures being studied.

Of critical importance is the ability to select or measure the wavelength of the neutrons impinging on and scattered from the sample. Accelerator-based sources of these neutrons offer advantages over reactors deriving from the ability to deliver sharp pulses (< 1 μs) of protons to a neutron-producing target. This leads to excellent timing of the neutrons arriving at the sample, as the neutron flight times are considerably greater than 1 μs, thus allowing for an easy determination of the neutron wavelength by a time-of-flight velocity measurement.

FIGURE 2: Neutron yield as a function of proton energy, for constant proton power deposition on target

Proton energies in the range of 1 to 3 GeV prove optimal for neutron production via spallation reactions in heavy-metal targets, and production rate is directly related to the power deposited on the target[1]. This is illustrated in Fig. 2, where, for instance the requirement of constant proton power means that for 2 MW on target, a 2 mA average beam current at 1 GeV will produce approximately the same neutron yield as would 1 mA of average beam current at 2 GeV.

The sharpness of the "start" signal of a time-of-flight measurement is dominated by the characteristics of the slow neutron pulse emerging from the moderators toward the measurement instruments. Neutrons are produced in the target at energies in the MeV (million-electron-volt) range through nuclear spallation reactions, but for neutron scattering applications the neutron energies must be reduced to the meV (milli-electron-volt) range. This is accomplished through multiple collisions in low-Z moderators, and the velocity distribution is ultimately determined by the temperature of the moderator. Moderators of water at room temperature and liquid methane or liquid hydrogen at cryogenic temperatures are most often used. Figure 3 shows calculated time-distribution widths of neutrons emerging from room-temperature moderators[2], assuming an instantaneous production pulse. The full-width at half-maximum (W) for energies below 10 meV is greater than 10 microseconds. Therefore, a proton pulse on target of length 1

FIGURE 3: Time widths W (FWHM) of neutrons emerging from a room-temperature water moderator, for (top-to-bottom) coupled, decoupled and decoupled-poisoned conditions.

microsecond or less will not appreciably increase the width of the effective start pulse for all but the highest-energy neutrons.

The desired velocity of the neutrons emerging from the face of the moderator is about 1000 meters per second or less. Because typical flight paths from moderator to instrument are 10 to 50 meters, the sensitive time range for neutron measurements will be from a few to a few tens of milliseconds. The requirement of resolving these pulses restricts the pulse-repetition rate for the accelerator to at most a few tens of Hertz. To maximize total power it is desirable to have the highest-possible repetition rate. However for slow neutrons one must deal with the "frame-overlap" problem (Fig. 4) in which slower neutrons from an earlier pulse could arrive at the same time as faster neutrons from a following pulse, thus confusing the interpretation of measurements.

FIGURE 4. Schematic showing arrival time of different neutron wavelengths at a detector located several tens of meters from the source of neutrons. Dotted line shows trajectory of a slow neutron that could be confused with a faster neutron from following pulse.

Optimization of neutron beam lines includes use of mechanical neutron choppers to define time windows in which neutrons are accepted into the line, and also careful selection of the repetition rate of beam on target. The most productive neutron-scattering facility should include at least two target stations receiving beam at different repetition rates to provide optimized neutron fluxes in different wavelength ranges.

2 SPECIFICATIONS FOR THE SNS

The current technical design calls for the linac to produce full-energy (1-GeV) beam at the required current level for

an average power of around 2 MW, in the form of 1 millisecond pulses at a 60-Hz rate. An accumulator ring (AR) will effect the current amplification needed to deliver to the target these pulses in the sub-microsecond time frame required. For a 60-Hz cycling rate, approximately 34 kJ per pulse is required; or, a peak-current of about 60 amperes for 600 nanosecond pulses. The current amplification required is about a factor of 1000, using conservatively achievable peak linac currents in the tens-of-milliampere range. The very high instantaneous power levels, close to 60 GW, cause concern about shock loads on the target. Use of liquid metal, specifically mercury, is viewed as the best way of mitigating this problem. Table 1 summarizes the basic parameters for this baseline design.

Table 1. SNS Baseline (AR) Design Parameters

Beam Species on Target	Protons
Proton Beam Energy	1 GeV
Average Beam Power	2 MW
Pulse Repetition Rate	60 Hz
Linac Pulse Length	1 ms
Turns Injected in Ring	1200
Particles Stored in Ring/pulse	2×10^{14}
Pulse Width on Target	600 ns
Instantaneous Current on Target	$\approx$60 A
Instantaneous Power on Target	$\approx$60 GW
Target Material	Flowing Mercury
Moderators, Ambient Temp	2 (water)
Moderators, Cryogenic	2 (Supercritical H_2)
Neutron Beamlines	18
Uncontrolled Beam Loss	< 1 watt/meter

An alternate technology approach is to use a lower-energy linac and a rapid-cycling synchrotron (RCS) to raise the beam to the GeV energy range. Linac energy would be between 300 and 500 MeV, the final RCS energy between 2 and 4 GeV. An example of such an approach can be seen in the IPNS-Upgrade Proposal[3]. Optimization studies performed two years for the SNS ago led to selection of the AR as the preferred technology. The somewhat higher cost ($\approx$15%) of this option was offset by the greater flexibility for power-upgrades and perceived lower technical risk. The new management team of the SNS project is considering re-opening the technology choice question, with the possibility of a baseline change. This paper will concentrate on the present AR baseline, and will describe the specific element design choices and progress towards solving physics and engineering issues associated with this technology option.

Note, the last line in Table 1 represents one of the biggest challenges in the design of the SNS. It represents a fractional uncontrolled beam loss of less than 1 x 10⁻⁴ over the whole length of the accelerator and transport lines. This very low loss is required to ensure that activation and residual-radiation levels in the tunnels are low enough to allow quick access and hands-on maintenance, and is driven by the very high reliability and availability specifications associated with the strong user-orientation of the SNS facility. Areas where unusable beam is diverted (so-called "controlled" beam-loss

points), such as collimators, scrapers and dumps, must be designed to collect these particles in a way that does not contribute to background levels in the tunnels where access is required. Normal loss mechanisms must receive particular attention to meet this specification. This implies very tight control over beam emittance, and emittance growth; designing for the largest-possible stay-clear apertures in linac, transport ,and ring structures; understanding of space-charge and halo effects in linac and ring; ensuring highest-possible vacuum in areas where H⁻ beam is transported to avoid stripping losses; extremely careful design of ring injection system and painting to ensure minimizing production of, and clean separation of H°*, and the minimum number of foil traversals of the circulating proton beam; understanding potential ring instabilities associated with the very high stored number of protons. In addition, operational issues of stability in power supplies, efficient tuning and feedback algorithms, quick turn-on and rapid tune-up procedures, high-quality diagnostics, and extremely high reliability of all components all add to the challenge of the SNS design.

Rising to these challenges, substantial progress has been made along all fronts of the systems design, this progress is highlighted in the following sections. Numerous papers in this conference cover details of all these systems, this paper summarizes principal features.

3 FRONT END

Figure 5 shows a schematic of LBNL's Front End systems[4] consisting of a volume-production H⁻ source coupled to the RFQ by a short (≈10 cm) electrostatic einzel-lens LEBT (Low-Energy Beam Transport), the RFQ itself accelerating the beam to 2.5 MeV, and the MEBT (Medium-Energy Beam Transport) that matches the RFQ beam to the following DTL, and houses the primary chopping system.

FIGURE 5: Schematic of Front End, showing ion source, LEBT, RFQ and MEBT.

The source, similar in concept to that delivered by the LBNL group for SSC[5], and which operated at currents over 100 mA (but 10^{-3} duty factor), is being engineered for currents ultimately up to 70 mA at a 6% duty factor. The trace shown in Figure 6 shows the current state of the R&D source, running with Cs, showing a very quiet, reproducible pulse of 43 mA at 12% duty factor. This is well above levels needed for 1-MW operation; and it is expected that this source, with some further development,

FIGURE 6: Trace from R&D #1 ion source

will reach the 70 mA needed for 2-MW operation[6]. The LEBT concept[7] is based on the successful model built by the same group for transport of positive ions, which demonstrated excellent beam-forming, transmission and emittance characteristics. The RFQ[8], operating at 402.5 MHz, is 3.8 meters long and is built in four roughly equal-length modules. Cold-model tests of this structure, using the pi-mode stabilizer concept developed by Ueno[9], demonstrates excellent field uniformity. A prototype full-power module of the RFQ is under fabrication.

Chopping is an essential part of the beam formation for the SNS. Generating longitudinal holes in the beam, of periodicity corresponding to the ring revolution frequency (1.19 MHz) and of approximately 250 ns length, is critical to minimize losses during the single-turn extraction from the accumulator ring. As this process requires removal of about 35% of the beam, it must be done where the beam energy is below the Coulomb barrier, so no activation will occur. Location of the main chopper is in the MEBT, where beam energy is 2.5 MeV. However, the amount of beam to be removed, and the very tight constraints on space available and small beam size represent an extremely high power density on the MEBT scraper, leading to difficult materials problems. To mitigate this, the beam will be pre-chopped in the LEBT, using the split einzel-lens electrodes to steer the unwanted beam onto slits at the RFQ entrance. Excellent progress is being made with this LEBT pre-chopper[10], good risetime (<20 ns) and extinction factors have been achieved, significantly easing the performance requirements from the MEBT chopper system. The desired risetime for the MEBT chopper should be in the few-nanosecond range, to minimize or better yet to eliminate any partially-chopped rf bunches that would be transported down the linac. At 402.5 MHz, these bunches come every 2.5 ns. A partially-chopped bunch will have its centroid substantially displaced from the central axis of the beam, thus potentially leading to large beam losses in the linac. To mitigate this, an "anti-chopper" is included in the second half of the MEBT, to balance the offset introduced by the first chopper for such partially-chopped bunches. Good progress with these chopper designs, both structure and pulsers, is being made by the LANL team responsible for this hardware.[11,12]

4 LINAC

FIGURE 7: Schematic (not to scale) of SNS linac configuration

Figure 7 shows LANL's configuration of the linacs that accelerate the beam from 2.5 MeV to 1 GeV[13,14]. The DTL (Drift-Tube Linac) operating at 402.5 MHz accelerates the beam to 20 MeV, a CCDTL (Coupled-Cavity Drift-Tube Linac) at 805 MHz accelerates the beam to 94 MeV, and CCL (Coupled-Cavity Linac) structures accelerate the beam to 1 GeV. Careful attention is paid to smooth FODO lattice transverse matching at all stages to prevent growth of beam halo. Periodicity is 8 $\beta\lambda$ (at 805 MHz) for the DTL and 12 $\beta\lambda$ for the CCDTL and CCL. CCDTL segments contain two 3/2 $\beta\lambda$ cells, while the CCL is divided into two parts, the first part, to 165 MeV, contains eight cells per segment; the higher energy part has 10 cells per segment. This arrangement allows ample room in the spaces between segments for the quadrupole, plus appropriate diagnostics, correctors and vacuum interfaces. Focusing in the DTL is accomplished with permanent magnet quadrupoles arranged in a FFDD configuration to more closely match the periodicity of the following structures. Very large apertures are provided to contain potential beam-radius or halo growth. The aperture to rms beam radius is over a factor of 10 at the higher energies.

RF power is provided by 66 2.5-MW klystrons, delivering a conservative 2.02 MV/m real-estate accelerating gradient[15]. $E_0 T$ in the cavities averages 2.7 MV/m. A novel pulsed HV power supply concept based on IGBT technology is being incorporated[16], which will significantly cut costs for the RF system by combining the HV supply, capacitor bank, crowbar system and modulator into a single pulsed supply.

Physics design is essentially complete, including error studies. Engineering design is commencing, plans for cold and hot models are progressing and these models will be ready by the summer of 1999.

5 RING AND TRANSPORT SYSTEMS

Brookhaven National Laboratory will provide the components shown in Figure 8: the HEBT (High-Energy Beam Transport) between the linac and the ring, the accumulator ring and the Ring-to-Target Beam Transport line, RTBT. The HEBT has a straight matching section, a 90° achromatic momentum analysis section, and a further matching section into the ring injection region. The 4-fold symmetric ring provides achromatic bends to the 4 zero-dispersion straights, for injection, collimation, RF and extraction. Horizontal and vertical tunes are 5.82 and 5.80. The RTBT line[17] takes the beam, extracted in a single turn by the kicker system, to the target. Beam is

shaped on the target as a 7 x 20 cm rectangle, of roughly uniform density, to prevent hot-spot power deposition in the window and target.

FIGURE 8: Schematic of accumulator ring and transport systems.

The collimation straight section contains the principal aperture restriction for the ring, in a location where little hands-on maintenance will be required. The collimators are designed[18] with graded low-Z and high-Z materials, so that protons penetrate deeply inside the 3-meter long structures before reacting, and neutrons are largely contained inside the structure. Calculations show that only one neutron emerges from the collimator for every 100 entering protons.

The injection region has been optimized to minimize beam losses[19]. By placing the stripping foil in the falling fringe-field of the combining dipole, halo in the ring due to Lorentz stripping of H°* is minimized. A tracking code developed at ORNL models the injection process, that accounts for space charge effects during stacking in the ring, and has been used in analyzing injection to minimize emittance and halo growth[20,21]. Note too that beam stacking in the ring is a dominant factor in the power density distribution on the target.

The ring RF is a dual harmonic system, with a peak amplitudes of 40 kV for first harmonic and 20 kV for second harmonic cavities. These voltage levels will ensure a high bunching factor, and good capture and retention of particles in the bucket. Cleanliness to better than 1 part in 10^4 of the 250 ns gap is necessary both for prevention of losses during the excitation of the extraction kicker, and to prevent buildup of electrons in the very deep potential well of the circulating beam. This has been identified as a potential cause of the observed instability in the Los Alamos PSR ring.

Extraction is performed via an 8-segment full-aperture fast kicker system, providing a vertical offset to the beam. A Lambertson magnet bends the beam into the RTBT channel. Beam shaping onto the target is performed with the last five quadrupoles in the line. However, beam distribution within the rectangular profile on the target is largely determined by the phase-space distribution of the beam just after injection has been completed in the ring, and so will be determined by the bump magnets controlling the stacking of beam into the ring.

FIGURE 9: Schematic of mercury target and moderator assemblies

6 TARGET

Figure 9 shows ORNL's mercury target, moderator and neutron beam-channel configuration. Mercury flows in from the lateral edges of the stainless vessel and around into the main body of the vessel. Flow rate is such that at full beam power temperature rise is only 30°C. Two room-temperature water moderators, below the target plane, and two super-critical hydrogen (20 K) moderators, above the target plane, deliver neutrons through the 18 beam ports to the experimental floor. Easy replacement of target and moderator assemblies is a design requirement, to assure minimum interruption of experimental programs for maintenance.

An ongoing R&D program is addressing important design issues. Experimental measurements and modeling codes are being used to examine materials effects, testing the impact of radiation in the presence of mercury on different containment materials, studying wetability, embrittlement and ductility. Hydrogen and helium formation is known in spallation processes to be significantly greater than experienced in reactor environments, and can have an adverse effect on target component lifetimes. Various mercury loops are also being built to study thermal hydraulics, flow of mercury through the target head geometry, as well as leaching of materials, such as nickel, from the containing 316 SS vessel. Shock effects and neutronics yields for mercury systems are being studied by an international collaboration[22] through accelerator tests and modeling. All these activities are beginning to yield good understanding of the proposed target design.

7 INSTRUMENTS

Neutron scattering instrumentation will be the heart of the SNS. As a dedicated user facility for the materials-sciences community, of paramount importance will be the ability to measure the detailed interaction of the neutrons produced with the samples brought by the experimenters. While an extensive body of instruments exists today at the various operating spallation sources, the challenge is that the fluxes from the SNS will be considerably higher than those for which the present-day instruments have been designed. It is expected that significant advances will be needed in neutron detectors, guides, neutron choppers and other elements of the instrumentation to make optimum use of the SNS beams. As a result, R&D efforts in all

these areas are being planned.

ANL has primary responsibility for instrument development, in collaboration with ORNL. Instruments will be built by SNS neutron scientists at ANL, ORNL and possibly other sites, with close contacts to the neutron-scattering community through appropriate oversight and advisory committees.

8 CONTROLS

EPICS has been selected as the basis for the controls systems for all elements of the SNS, including the conventional facilities. This system now has a proven track record, having been successfully implemented at CEBAF and APS as well as at numerous other smaller installations. Notable in this project is the need to tightly coordinate controls activities across all the laboratory boundaries. To this end a very active Global Controls Working Group has been formed, with LANL taking the lead, and with representatives from all the labs[23]. This group has been working through architectures, naming conventions, interface definitions and general implementation strategies. This Working Group is serving as a model for collaboration and interfacing in many other technical and managerial areas of the project.

9 SUMMARY

The present technical design has reached a sufficient level of maturity to have received endorsement from many internal and external review teams. As stated earlier, a new management team is currently undertaking assessments to decide whether to adopt this design as the project baseline, or to re-open different design options. The project, nonetheless, has received, for FY99, line-item authority and funding to begin Title I work, and is being held to the approved cost of $1.36B and scheduled completion date of December 2005. There are obviously very significant challenges ahead for the project.

[1] "Los Alamos Next-Generation Spallation Source," LA-UR-95-4300, Dec 1995, Vol 1, Figure 3-12, page 3-20
[2] NSNS Conceptual Design Report, Section 5, p. 5-97, NSNS-CDR-2,V1, ORNL, May 1997.
[3] IPNS-Upgrade Proposal, ANL-95/13, April 1995.
[4] R. Keller, MODR1 this conference
[5] K. Saadatmand et al, PAC93, IEEE 93CH3279-7, p. 2986.
[6] M. Leitner et al, WEA13 this conference
[7] D.W. Cheng et al, WEA34 this conference
[8] A. Ratti et al, MOP92 this conference
[9] A. Ueno et al, LINAC90, LANL Pub, LA-12004-C, P. 57
[10] J.W. Staples et al, WEA32, this conference.
[11] S.S. Kurennoy, J.F. Power, TUA139 this conference
[12] J.F. Power, S.S. Kurennoy, TUP7 this conference
[13] N.K. Bultman et al, FRA86 this conference
[14] T.S. Bhatia et al, LANL Preprint LA-UR-98-3595
[15] M. Lynch et al, THBL5 this conference
[16] W.A Reass et al, THAL4 this conference
[17] D. Raparia et al, TUA94 this conference
[18] J. Beebe-Wang et al, THP98 this conference
[19] J. Beebe-Wang, Y.Y. Lee, TUP113 this conference
[20] J.A. Holmes et al, TUAL1 this conference
[21] J.D. Galambos et al, THP81, THP82 this conference
[22] ASTE Collaboration (Jülich, PSI, JAERI, BNL, ORNL) J. Hastings (BNL) spokesman
[23] W.R.Devan, D.P.Gurd, J.P.Hammonds, S.A.Lewis, J.D.Smith, WEDL1 this conference

PROTON RADIOGRAPHY[*]

G. E. Hogan[#], K. J. Adams, K. R. Alrick, J. F. Amann, J. G. Boissevain, M. L. Crow, S. B. Cushing,
J. C. Eddleman, C. J. Espinoza, T. T. Fife, R. A. Gallegos, J. Gomez, T. J. Gorman, N. T. Gray,
V. H. Holmes, S. A. Jaramillo, N. S. P. King, J. N. Knudson, R. K. London, R. P. Lopez,
J. B. McClelland, F. E. Merrill, K. B. Morley, C. L. Morris, C. T. Mottershead, K. L. Mueller, Jr.,
F. A. Neri, D. M. Numkena, P. D. Pazuchanics, C. Pillai, R. E. Prael, C. M. Riedel, J. S. Sarracino,
A. Saunders, H. L. Stacy, B. E. Takala, H. A. Thiessen, H. E. Tucker, P. L. Walstrom, G. J. Yates,
H.-J. Ziock, J. D. Zumbro, LANL, Los Alamos, NM 87545
E. Ables, M. B. Aufderheide, P. D. Barnes Jr., R. M. Bionta, D. H. Fujino, E. P. Hartouni,
H.-S. Park, R. Soltz, D. M. Wright, LLNL, Livermore, CA 94550
S. Balzer, P. A. Flores, R. T. Thompson, Bechtel, Nevada, Los Alamos Operations, Los Alamos,
NM 87545
A. Pendzick, R. Prigl, J. Scaduto, E. T. Schwaner, BNL, Upton, NY 11973
J. M. O'Donnell, University of Minnesota, Minneapolis, MN 55455; current address: LANL

Abstract

With the nuclear weapons program moving to Science Based Stockpile Stewardship (SBSS), new diagnostic techniques are needed to replace weapons testing. Proton Radiography [1] is being developed within the SBSS program as one such tool. It is analogous to transmission X-ray radiography, but uses protons instead of photons. Proton Radiography has high penetrating power, high detection efficiency, small-scattered background, inherent multi-pulse capability, and large standoff distances between test objects and detectors. Multiple images on a single axis through progressively smaller angle-cutting apertures can provide material identification. Proton Radiography can make multi-axis, multi-frame radiographs: i.e., 3D radiographic movies. This approach to SBSS is being developed at the Los Alamos National Laboratory (LANL) and the Lawrence Livermore National Laboratory (LLNL). This new method of radiography, as well as radiography experiments performed at the LANSCE accelerator at LANL and at the Alternating Gradient Synchrotron (AGS) at Brookhaven National Laboratory, will be discussed in this paper.

1 INTRODUCTION

The SBSS program supports a weapons maintenance system based on detailed knowledge of the underlying physics as opposed to the performance based system of underground nuclear tests. An essential class of experiments in understanding the underlying physics of weapons is the hydrodynamic test (or hydrotest). The goal of these experiments is to understand how materials behave at the high temperatures and pressures generated by explosively driven pressure or shock waves. Obtaining high-quality data from such hydrotests is one of the main goals of SBSS.

Previously, weapons physics was addressed through a combination of weapons tests, hydrotests, and computer simulations. However, with the Comprehensive Test Ban Treaty, hydrotests and simulations are now the principle tools available for certifying weapons performance. Current simulations must be upgraded to include 3D effects from a) manufacturing defects, b) ageing, and c) safety tests. Hydrotests are needed to validate the simulations.

Multiple views are needed to handle 3D shapes (tomographic reconstruction) and multiple times (movies) to understand when perturbations become important and how they develop over time. This is the purpose of the proposed Advanced Hydrodynamic Facility (AHF), which is intended to provide hydrodynamic test data of sufficient precision to allow the certification of the weapons stockpile in the absence of underground testing. An AHF based on proton radiography can contribute to a full 3D understanding of the hydrodynamic problem within the SBSS program.

2 PRINCIPLES OF PROTON RADIOGRAPHY

In weapons X-ray radiography, a sharp image is formed because the X-rays start out at a small spot and travel in straight lines through the radiographed object to the X-ray film or detector, basically a variation on the pinhole camera. Images made in the same way with protons as with X-rays, using no lenses, would be blurred by the

multiple Coulomb scattering (MCS) of the protons from the charged nuclei of the object. In proton radiography, the effect of this blurring is mostly eliminated by passing the emergent proton beam through a series of magnetic lenses [2] that focus the proton beam to an image of the object at a distance of 20 to 100 meters away from the object itself. This approach is similar in principle to that used in ordinary visible-light cameras.

The three most important effects on the protons as they go through an object are absorption, multiple Coulomb scattering, and energy loss. First, some of the protons are absorbed by nuclear collisions. This is a simple exponential attenuation of the beam. Second, the protons are scattered into small angles by multiple Coulomb scattering. This not only produces image blurring, but it also changes the total attenuation as a detector may not see the full phase space of the scattered beam. Third, protons lose varying amounts of energy as they go through an object from both energy straggling and thickness variations in the object. This produces a spread in the momentum of the transmitted protons that blurs the final image due to chromatic aberrations in the lens.

The proton attenuation length in heavy metals is around a few hundred gm/cm^2, which makes proton radiography well matched to the AHF class of problems, and allows use of the minimum amount of beam (or dose) on the object. This reduces scattered background and multi-axis crosstalk. In addition, the penetrating power of protons and the fact that they are charged particles means that a single proton can pass through multiple thin detectors and be detected in all of them with high probability. This feature can be used to advantage to form multiple images when magnetic identity lenses and detector systems are placed in series downstream of the object.

3 LENS SYSTEM AND MATERIAL IDENTIFICATION

Protons that are not scattered or absorbed in the object emerge from the object with a reduced energy due to collision with atomic electrons and an energy spread due to both energy straggling and thickness variations in the object. This energy spread, together with chromatic aberrations in the lenses, causes image blurring. Chromatic aberrations in the magnetic lenses can be minimized by making the lens system as short as possible and by use of an illuminating beam with a special correlation between transverse position and angle. The lens is an inverting, unit-magnification lens. Thus, the relation between object position and image position is

$$x_{image} = -x_{object} + \text{aberration terms}$$

Including only the two aberration terms in the final position of the proton that depend in first order on the momentum variation, relationship is:

$$x_{image} = -x_{object} + (x\,|\,\theta\delta)\theta_{obj}\delta + (x\,|\,x\delta)x_{obj}\delta$$

where δ is the fractional momentum difference from the design momentum of the lens, x the lateral position of the proton at the object, and θ the angle with respect to the central axis of the lens. The items in parenthesis are aberration coefficients given by the lens design codes. Higher order terms are not shown. In the first aberration term, the momentum difference multiplies the angle at which the proton goes through the object. In the second term, the momentum difference multiplies the position of the proton at the object.

One can eliminate the position dependence of the second-order chromatic aberration by imposing the condition:

$$(x\,|\,\theta\delta)\theta_{object} = -(x\,|\,x\delta)x_{object}$$

on the incoming proton-beam phase space. With this special correlation, the only second-order chromatic blurring left in the image plane is due to the deviations from this angle due MCS.

This correlation also causes unscattered rays to come to a point focus at the center of the lens. Scattered protons are imaged away from the point with a distance proportional to the MCS angle. A collimator placed here can make cuts on this angle. Another effect of this correlation is to dramatically increase the field of view of the lens system.

Proton radiography offers the unique feature of material identification, in which regions in the test object made up of lighter atoms can be distinguished from regions made up of heavier atoms. Material identification is done by comparing two same-sized images of the same view that are formed at the same time by placing two identity lens and detector systems in series. An angle filter placed in the middle of the second lens system makes cuts on the MCS angle distribution of the protons that emerge from the object. Since nuclear attenuation has an $A^{2/3}$ dependence, whereas the r.m.s. MCS scattering angle varies as Z^2, the heavier atoms in the radiographed object contribute relatively more to the contrasts in the second image than in the first image.

A third lens upstream of the object allows an independent measurement of the intensity distribution of each proton pulse in the illuminating beam. This information can be used to correct for pulse-to-pulse variations in the beam position and shape. It also improves the statistical power of the measurement, as one knows the exact input density of protons at each point in image.

Scattering from the containment vessel that holds the object under test also affects the position resolution at the image plane and is not removed by the lens system. The containment vessel is needed for two reasons: first, to protect the equipment from several pounds of exploding HE; and second, to confine any hazardous material used in the experiment. The effect of this containment wall scattering scales inversely with the momentum of the proton beam and drives the final design energy of an AHF proton accelerator to the range of 50 GeV.

4 DETECTORS

The detection systems used in Proton Radiography are as important as the design of the beam. Ideally, what we want is a method to take good resolution pictures (< 1 mm FWHM) at a high frame rate (≥ 5 MHz). A common feature of these detectors is that they use the energy loss of protons through a detection medium to achieve almost 100% detection efficiency for individual protons. High efficiency minimizes the radiation dosage needed to achieve a given statistical accuracy. Because of the high instantaneous beam intensity (>10^4 protons per mm^2 in a 50 ns pulse), the detectors are all integrating devices rather than counting devices. We are working on a number of detection schemes that address these requirements.

4.1 Image Plates

Image plates are very similar to film. They are sheets of a metastable phosphorescent material that is directly exposed to the proton beam. As a proton passes through the plate, it excites metastable states in the plate material. The amount of material that is excited is proportional to the exposed proton flux. A laser scanner is used to measure this excitation. The chief practical difference with film is that the image plate is reusable. It produces very high-resolution images (~100 micron/pixel). It is also an order of magnitude more sensitive and very linear in its response to protons. Its chief advantage is that it produces very low cost, very high-resolution images. Our better than one line pair per millimeter resolution is limited by the beam optics, not the detector. Unfortunately, there is no practical way to make a movie with image plates. This is the detector of choice for static objects, such as a limited view tomographic reconstruction of a stable object.

4.2 Electronic Camera Systems

The present method for obtaining a sequence of images for dynamic experiments is to use a number of gateable, intensified CCD cameras [3]. One obtains an image by gating the CCD to turn on when the proton beam goes through a scintillating fiber optic array. The CCD camera is fiber-optically coupled to a fast gated (≥50ns) planar diode with a photocathode spectral response matched to the scintillator light output. We have used a variety of CCD arrays ranging in size from 512^2 to 2048^2 pixels. We have also used microchannel-based intensifiers in place of the planar diodes.

We get several pictures at different times by having several cameras pointed at the same scintillator with each camera gate timed to a different proton pulse. In our current tests, the pulses are usually spaced at one-microsecond intervals. The cameras view the scintillator via a series of mirrors. The scintillator is a close packed array of scintillating fibers (300micron core) aligned in the proton beam direction.

We have used up to eleven cameras at once. A prototype four-frame framing camera is currently under development. Available real estate for cameras restricts the number of frames per image plane. Optical coupling efficiency in the present lenses limits the statistics in the images obtained with this technique. Future possibilities include advanced CCD camera designs which permit multiple "on chip" frame storage. These designs would allow for very fast framing speeds and a large number of frames from a single camera. A solid state streak camera that uses 128 photodiodes and takes 512 frames at rates up to six million frames per second is being tested by LLNL.

4.3 Silicon Detectors

Another technology we are developing is direct detection using a solid state device with individual pixel readout. This work is being done with Lawrence Berkeley National Laboratory (LBNL). Conceptually, it is similar to putting a CCD directly in the beam. In this case the detector elements are much thinner and the readout scheme much faster. An 8 × 8 pixel prototype was been tried and has successfully taken a 1000 frame movie. The pixels were 1 mm^2. We hope to test a 100 × 100 pixel system next year. The main problem with this is that there is a systematic noise problem caused by nuclear interactions of the protons with the 3.5 µm thick silicon pixels. Thus the in-beam detector may not be useful, but the readout electronics being developed along with it will be tested in a lens to fiber array to silicon pixel coupling scheme.

4.4 Ion Chambers

A way around the nuclear interaction problem may be to use an ionization chamber with hydrogen gas instead of silicon as the detection media. Nuclear fragmentation is then not a problem. The ionization charge would be collected on a pixelated cathode plane. We will probably use the same high volume analog to digital conversion electronics being developed for the silicon detectors described above.

4.5 Cherenkov Detectors

When a charged particle travels through material, it loses energy in addition to being absorbed. We can detect this energy loss by measuring the Cherenkov radiation from protons. For 800-MeV protons, the index of refraction for the threshold of Cherenkov light production is 1.188. This index is not readily available from common materials. We fabricated the required material using high-density aerogel radiators. Once the light is produced, detection schemes are similar to the CCD camera system. This detector system is particularly useful for imaging very thin objects where the absorption of the beam is small. This is primarily being developed by LLNL [4]. This might allow low dose radiography of living objects.

4.6 Data Acquisition (DAQ) System

All of the various data streams are brought together into one DAQ program. The program is called PC DAQ [5] and it is a Windows® based general DAQ/Analysis/Monte Carlo shell developed as part of the Proton Radiography project. It integrates data from picture files, GPIB devices (scopes, pulsers, etc.), ActiveX servers, and CAMAC modules. In our latest round of measurements, it used or acquired data from 12 PC workstations. This program has been adopted as the principal DAQ system for several experiments outside of the Proton Radiography project. It is currently in use with experiments at Brookhaven National Laboratory (BNL) and LANSCE.

5 EXPERIMENTS

In 1996, we radiographed a test object known as the French Test Object (FTO) [6] with a 10-GeV proton beam at the AGS at BNL using a radiographic single-lens system. The object is made of spherical layers of different materials. It has a hollow cavity in the center, surrounded by layers of tungsten, copper, and finally foam. This experiment demonstrated proton radiography's spatial and density reconstruction capability.

Figure 1 shows two lineouts from image plate radiographs taken with different collimator cuts on the scattering angle. Each image integrated about 10^7 protons over several hours. Using the differences in the two line shapes, we have derived the separate nuclear and electromagnetic interaction lengths that go into the absorption equation. The derived values (Table 1) agree well with the published values.

Figure 1, Fits to the transmission data for the FTO. The upper two curves are the measured transmission vs. radius. The bottom curves are the residuals of the two fits.

skin [7]. An onion skin is a hemisphere about 2 inches in diameter with a detonator at the sphere center.

Figure 2 shows an analysis of an exploding onion skin. The picture is a reconstruction of the density of the material at 1.9 μs time after detonation. This image was obtained using image plates. The burn front in the HE is clearly visible. Comparable multiple images have been obtained with the electronic imaging system.

6 AHF ACCELERATOR

Construction of a proton radiography-based AHF would involve building a new proton accelerator similar in size, energy, and beam intensity to several other proton machines already built [8,9]. Our current studies center on a low-duty-factor 50 GeV synchrotron and 12 isochronous beamlines that converge on a test chamber to provide multiple simultaneous views.

The beam is extracted by a fast kicker and septum magnet. The beam distribution system is based on 4 levels of beam splitting using a combination of electrostatic,

Table 1, Fitted Results to the FTO Measurement

	Radius (cm)		Nuclear Attenuation (cm)		Radiation Length (cm)	
	Actual	Fit	Actual	Fit	Actual	Fit
Shell						
Air	1					
Tungsten	4.5	4.48	10.1	10.5	0.37	0.38
Copper	6.5	6.47	15.1	14.2	1.42	1.17
Foam	22.5		160		84	

Starting in 1997, we conducted Proton Radiography experiments using the 800-MeV primary beam at LANSCE. Using the accelerator's intense pulsed proton beam, we have been able to take movies (usually 7 pictures, with a current capability of up to 14) of explosively driven, dynamic systems. Because of the low energy of the beam, only relatively thin targets of a few tens of grams per cm^2 can be radiographed. Single pulse radiographs were typically taken using 2×10^9 protons within a 35-ns wide pulse. Dynamic shots of high explosive (HE) during detonation usually had pulses spaced at 1-microsecond intervals.

One of the capabilities that we demonstrated was that we could take radiographs of exploding HE and measure interesting characteristics of the HE. A simple system we studied was a small hemisphere of HE called an onion

Figure 2. Reconstructed density of an exploding onion skin 1.9 μs time after detonation. The scale on the right is grams per cm^3.

pulsed magnetic, and dc magnet elements. Each beamline is achromatic and isochronous. A single beam bunch extracted from the accelerator will be split 12 ways, and the protons from the bunch will arrive at the target at the same time on each axis. Four of the beam lines will have twice the nominal number of protons, as they will not have the fourth split. These four higher-intensity beam lines would be used for larger field-of-view lenses than the remaining eight.

Each of the beam lines would be outfitted with a lens system as discussed earlier with lens elements both before and after the target chamber. By using large diameter superconducting magnets, such as those in use for the spectrometers at the Thomas Jefferson Lab, it would be possible to have a field of view on each axis up to 50 cm across.

The proton synchrotron typically would have 5 MHz RF accelerating cavities, producing bunches of a few nanoseconds width at 200 ns intervals. With a harmonic number of 20, a motion picture of 20 frames and with a duration equal to the ring period (3-4 microseconds) would be produced if the beam were extracted on a single turn, as with a thyratron-type kicker modulator. A kicker modulator capable of single-pulse extraction in an arbitrary time format, with rise and fall times less than the nearly 200 ns free space between bunches, would make it possible to have nearly arbitrary pulse spacing at the target over times extending up to seconds. This is the mode of operation planned. For a single frame, approximately 1×10^{11} protons are required for 1% density measurements. To provide 20 frames, 2×10^{12} protons per accelerator cycle are required for each axis, with twice this for the axes that have large lenses. A total of 3.2×10^{13} protons per accelerator cycle is required for 12 axes (including four larger-intensity beamlines but excluding losses), a value approximately equal to that which has already been achieved in the Fermilab Main Ring.

A full AHF with up to 12 beam lines would be a costly undertaking. It is thus appropriate to consider staging strategies. A suitable initial step might be to construct a two-axis facility at 50 GeV, which could provide some 3-dimensional information from small-angle stereo views of the object under test. The number of beam lines could be increased later. PRISM-3D (Proton Radiography Intermediate Step Machine with some 3-Dimensional capability) is such a step towards a full future AHF. In this case, 4×10^{12} protons per pulse could be obtained by 800 MeV H⁻ injection from the existing 800 MeV LANSCE linac. In a future upgrade, a booster with an energy of a few GeV could be added to increase the protons per pulse to the level required for full AHF performance. There is a similar proposal from LLNL to build an all-new machine at the Nevada Test Site.

7 SUMMARY

In the three years since the start of serious work on exploring the potential of Proton Radiography, great progress has been made. We have demonstrated Proton Radiography at 800 MeV and 10 GeV. We have shown that we can do material identification. We have operated an 800-MeV dynamic radiographic facility, taking useful data characterizing HE properties. A number of detector projects have been initiated and have produced promising prototypes. The need for more advanced containment systems has been identified and is being addressed. Further experiments are planned to bring us closer to the proposed operating conditions of the AHF.

8 REFERENCES

[1] H.-J. Ziock, et al., "The Proton Radiography Concept," Proceeding of the Third International Symposium on Development and Application of Semiconductor Tracking Detectors (The Hiroshima Symposium) at Melbourne, December 9-12, 1997, to be published in Nucl. Instrum. Methods, LA-UR-98-1368.

[2] C.T. Mottershead and J. D. Zumbro, "Magnetic Optics for Proton Radiography", Proceedings of the 1997 Particle Accelerator Conference, Vancouver, B. C., Canada (to be published).

[3] G. J. Yates, et al., "An Intensified/Shuttered Cooled CCD Camera for Dynamic Proton Radiography," Conference on Digital Solid State Cameras: Designs and Applications, SPIE Proceedings Series Vol. 3302, pp. 140-151, January 28-29, 1998, San Jose, California.

[4] R. M. Bionta, H. S. Park et al., "An Energy-Loss Camera Based On Near-Threshold Cerenkov Radiation", Proceedings of American Nuclear Society Annual Meeting, Embedded Topical Meeting on Nuclear Applications of Accelerator Technology Proceedings , 97 (1997).

[5] For more information, contact the author at hogan_gary@lanl.gov.

[6] J. F. Amann, et al., "High-Energy Test of Proton Radiography Concepts (U)," 11th Biennial Nuclear Explosives Design Physics Conference (NEDPC'97), Livermore, California, October 20–24, 1997, Los Alamos National Laboratory document LA-UR-97-4721.

[7] K. B. Morley, et al., "Proof-of-Principle Demonstration of Proton Radiography on a Dynamic Object," 11th Biennial Nuclear Explosives Design Physics Conference (NEDPC'97), Livermore, California, October 20–24, 1997, Los Alamos National Laboratory document LA-CP-98-6.

[8] H. A. Thiessen, "Performance and Facility Issues for Proton Radiography," abstract submitted to the Beams 98 Conference, Haifa, Israel, June 7–12, 1998, Los Alamos National Laboratory document LA-UR-98-561.

[9] F. A. Neri, H. A. Thiessen, and P. L. Walstrom, "Synchrotrons and Beamlines for Proton Radiography", Proceedings of the 1997 Particle Accelerator Conference, Vancouver, B. C., Canada (to be published).

THE PLASMA WINDOW: A WINDOWLESS HIGH PRESSURE-VACUUM INTERFACE FOR VARIOUS ACCELERATOR APPLICATIONS*

A.I. Hershcovitch, E.D. Johnson, Brookhaven National Laboratory, Upton, NY 11973

R.C. Lanza, Massachusetts Institute of Technology, Cambridge, MA 02139

Abstract

The Plasma Window is a stabilized plasma arc used as an interface between accelerator vacuum and pressurized targets. There is no solid material introduced into the beam and thus it is also capable of transmitting particle beams and electromagnetic radiation with low loss and of sustaining high beam currents without damage. Measurements on a prototype system with a 3 mm diameter opening have shown that pressure differences of more than 2.5 atmospheres can be sustained with an input pressure of ~ 10-6 Torr. The system is capable of scaling to higher-pressure differences and larger apertures. Various plasma window applications for synchrotron light sources, high power lasers, internal targets, high current accelerators such as the HAWK, ATW, APT, DARHT, spallation sources, as well as for a number of commercial applications, will be discussed.

1 INTRODUCTION

Many industrial and scientific processes like ion material modification, electron beam melting and welding, as well as generation of high energy radiation are performed exclusively in vacuum nowadays, since electron guns, ion guns, their extractors and accelerators must be kept at a reasonably high vacuum. Consequently, there are numerous limitations, among which are low production rates due to required pumping time, limits on the size of target objects, and degradation of particle beams and radiation through foils or differentially pumped sections.

For transmission of high-energy synchrotron radiation thin beryllium windows are used (or SiN in a few cases). Attenuation and spatial structure non-uniformities, which attend the use of these conventional windows, represent a significant problem for various applications in synchrotron radiation research. Most of the problems are the result of window heating and degradation of the radiation. The target systems used for accelerator based neutron sources greatly limits the current, energy, and energy focus of the neutron beam. A pressurized windowless gas target system removes these limitations by removing all physical boundaries between the accelerator and the gas target. The gas target itself poses no limitations on the beam since it can be constantly cooled and replenished.

A novel apparatus, which utilized a short plasma arc, was successfully used to provide a vacuum-atmosphere interface as an alternative to differential pumping, and an electron beam was successfully propagated from vacuum to atmospheric pressure.[1,2]

Windowless gas targets, for neutron production, have been constructed using differentially pumped gas systems with a series of rotating valves. Although these systems have demonstrated the feasibility of such techniques, they are limited to use with pulsed accelerators with relatively low duty cycles, around 2.5%.[3]

Such a windowless gas target system can be formed by creating a plasma discharge between the high-pressure target chamber and the low-pressure vacuum chamber. The high temperature of the plasma discharge (12,000° K at the edges and 15,000° K at the center) causes the plasma to be over 40 times less dense than the target gas while being more viscous. These two properties combine to form an opaque plug. This plug allows the accelerated particles, or radiation to pass through while greatly reducing any flow between the high pressure and low pressure chambers. In the best results to date[4] of such a system, 40 psia were supported in the target chamber with 0.032 Torr in the first vacuum chamber.

The theory, experimental status, and possible applications of the Plasma Window will be discussed in this report.

2 PRINCIPLE OF OPERATION

Plasmas can be used for vacuum separation, interface with atmosphere, and as lenses. Ideally, maximizing the plasma temperature would optimize the first two applications, while maximizing the discharge current should broaden the use of the latter. For this Plasma Window, a "wall stabilized discharge" is used, i.e., a

stable plasma discharge is created down the center of a cooled tube. The temperature of the plasma ranges from 12,000° K at the edges to 15,000° K in the center. These temperatures are sufficiently low enough so that the plasma flow is dominated by intermolecular collisions (Knudsen number much less then one). This allows the plasma to be treated as a high temperature gas.

By treating the plasma as a high temperature gas, the ideal gas equation can be applied

$$P = \rho \cdot R \cdot T \qquad (1)$$

where P is the pressure, T is the temperature, ρ is the density, and R is the ideal gas constant.

Using this equation to compare the density of the plasma arc at 12,000° K to the density of the gas in the target chamber at 300° K, it is clear that the plasma is 40 times less dense while at the same pressure. This low density at high pressures is key in allowing the plasma to support large pressure differentials while still being transparent to the accelerated beam.

The pressure differential that the plasma arc will be able to support is determined by the flow rate of the plasma. This flow rate of an ideal gas through a small thin tube can be given by:

$$Q = \frac{\pi \cdot R^4}{8 \cdot \mu} \cdot \left(\frac{dp}{dx}\right) \qquad (2)$$

where Q is the flow rate, μ is the viscosity, R is the ideal gas constant, and dp/dx is the pressure difference in pipe. In order to minimize the flow through the pipe while maximizing the pressure differential, it is desirable to increase the viscosity as much as possible. Typical fluid mechanics shows that viscosity increases with temperature.

As the plasma gas is raised in temperature, the viscosity becomes directly proportional to the temperature at higher powers.[1,5] It is important to note that this plasma is in the absence of any applied magnetic field.

An added benefit gained from the use of the plasma window is a focusing effect on charged particle beams. As current flows in the plasma arc it creates a circular magnetic field around the center of the plasma which results in a field in the θ direction. With proper arc current orientation, charged particles passing through the plasma interact with the magnetic field and are subjected to an inward force given by

$$F = q \cdot \vec{v} \times \vec{B} \qquad (3)$$

where q is the charge of the particle, v is its velocity, and B is the induced magnetic field. More details on the theory of operation can be found in references 1 and 2.

3 EXPERIMENTAL RESULTS

Various plasma window experimental results can be found in references 1,2, and 4. The plasma window utilizes an arc discharge. The arc is a wall-stabilized type cascade arc discharge. The arc has been operated in argon and in helium.

3.1 Previous Experimental Results

The best results to date have been the following:

- Differential pumping: vacuum-atmosphere separation across a 2.36 mm diameter 4 cm long arc was achieved. With the arc open to atmosphere, pressure in a 4" pipe, on which plasma window was mounted, was 0.032 Torr. Gain over conventional differential pumping, by comparing pressures with plasma arc on versus plasma arc off, yielded a factor of 10^4 improvement. In that particular experiment[4] the vacuum system baseline pressure of 10^{-6} Torr was reached 20" from the plasma window (which was opened to atmosphere).

- High pressure gas cells were successfully maintained: 40 psia was separated from accelerator vacuum (for application to neutron generation); a 72 psia gas was separated from atmosphere, and a 5 mW He-Ne laser beam was passed through it (for gas laser applications).

- A 175 KeV electron beam was transmitted from vacuum through the plasma window to atmospheric pressure.

- Compatibility tests for transmission of electromagnetic radiation indicated that the plasma window does not generate electromagnetic interference, and that X-rays (away from resonance) are transtrmitted with negligible attenuation.

3.2 Possible Improvements

Testing of the Plasma Window system has not only proven the validity of the windowless vacuum-pressure interface, but has highlighted many areas for improvements.

Cooling of the chamber next to the plasma window in the most apparent area for improvement. Overheating of the system not only risks damaging equipment but also increases the rate of outgassing and thus increases the overall pressure in the system.

A dramatic decrease[1,2,4] in the flow from the first vacuum chamber to the second vacuum chamber can, in principle (based on density and temperature profiles of similar arcs), be gained by adding skimmers to the first chamber. These internally cooled curved blades will serve to deflect the gas streaming from the cool annulus of the plasma window, as well as any gas which is not directly on the beam line. Aperture size in the Plasma Window can be increased in order to accommodate

larger beam diameters. If gas flow through the Plasma Window is dominated by leak through the cool annulus, reasonable increases in window diameter will marginally increase the flow rate through the skimmer system.

4 APPLICATIONS

Several different types of accelerator systems can benefit from the utilization of the Plasma Window system.

4.1 Commercial Applications

Non-vacuum electron beam welding: With plasma windows, higher production rates, no limit on the size of target objects, and high quality electron beams in atmosphere.

Non-vacuum material modifications by ion implantation, and dry etching, or micro-fabrication: Presently performed only in vacuum, since ion beams at energies used in these applications are completely attenuated by foils and by long differentially pumped sections. Potentially very large yet unexplored market.

Electron beam melting: for manufacturing alloys is performed at a pressure of about 10^{-2} Torr. A major drawback of operating at this pressure range is the loss of elements with low vapor pressure. Consequently, it is desirable to raise the operating pressure to a higher level. Interested company.

Electron beam generation of photo-neutrons for the production of medical isotopes (e.g., Tc-99): A 40 MeV electron beam strikes a W target. Resultant radiation can dislodge a neutron (via a giant resonance) to create a new element. With a plasma window, the target can be in the air, sufficiently cooled to absorb an intense electron beam to generate photo-neutrons.

Windowless gas targets for fast neutron radiography to detect nitrogen (weapons) and carbon (diamonds), as well as for other forms of neutron tomography and therapy (BNCT).

Windows for high power lasers (especially high-pressure gas lasers).

4.2 Scientific Applications

Windowless beamlines for transmission of synchrotron radiation: Plasma windows offer many advantages over presently used beryllium windows: radiation passes through the window unaffected. A plasma window cannot be damaged by radiation. UV filter for rejection of 'high-order' light is of significant benefit to experiments like threshold photoionization spectroscopy, where contamination even at the 10^{-4} harmonic content can obscure the features of the spectrum of interest. X-ray microscopies, since it is free from the attenuation and spatial structure that attend the

use of conventional window materials (e.g. beryllium or SiN), i.e., no scratches.

Windowless gas targets for fast (fusion) neutron generation (neutron sources).

Radioactive waste transmutation (ATW): protons are accelerated to 2 GeV unto a heavy metal target in air. Resultant spallation neutrons reduce radioactive waste. Presently, windows limit proton output.

APT- tritium production by accelerator: Solid windows limit beam and tritium output.

Spallation Neutron Source (SNS): To replace various solid windows with cooling problem.

Windows for high power x-ray source (DARHT).

Internal (gas or plasma) targets, strippers, lenses in storage rings: A plasma stripper/lens or an internal gas target "sandwiched" between two plasma windows. Examples: BNCT based on recirculating proton beams and various internal targets (including spin polarized).

Fast acting valves in UHV beamlines. In case of vacuum breach, plasmas can be ignited faster than mechanical valves without damage to beamline (unlike, presently used, msec spring loaded shutters).

5 CONCLUSIONS

This examination of the Plasma Window has shown the viability of using a plasma arc to support a large pressure differential, which could be further improved. It operates steady state without maintenance for 2000 hours.

Through the use of the Plasma Window system, limitations on beam current, energy, energy focus and others have been removed. This allows the Plasma Window system to enhance a wide range of applications, which were not listed like using the HAWK intense electron beam to heat gas in hypersonic wind tunnels.

6 REFERENCES

1. Hershcovitch, Ady. "High-pressure arcs as vacuum-atmosphere interface and plasma lens for nonvacuum electron beam welding machines, electron beam melting, and nonvacuum ion material modification." *Journal of Applied Physics.* Vol. 78 (9), November, 1995

2. Hershcovitch, Ady. "A Plasma Window for Transmission of Particle Beams and Radiation from Vacuum to Atmosphere for Various Applications." Physics of Plasmas, vol.5, no.5, May 1998, pp.2130-6.

3. E.B. Iverson, R.C. Lanza, and L.M.Lidsky, "A Windowless Gas Target Neutron Source", 5th International Conference on Applications of Nuclear Techniques, Crete, 1996 in Proceedings of SPIE - the International Society for Optical Engineering, vol.2867, 1997, pp.513-16.

4. W. Gerber, R.C. Lanza, A. Hershcovitch, P. Stefan, C. Castle, E. Johnson, Invited Talk on AThe Plasma Porthole: a Windowless Vacuum-Pressure Interface With Various Accelerator Applications≡ at 15th International Conference on the Application of Accelerators, in Research and Industry CAARI'98, Denton, Texas, November 4-7, 1998; to be published in RSI.

5. Leontovich, Acad., *Reviews of Plasma Physics, Volume 1.* Consultants Bureau, New York, 1969.

OPERATING CHARACTERISTICS OF A HIGH CURRENT ELECTRO-STATIC ACCELERATOR FOR A CONTRABAND DETECTION SYSTEM

S.T. Melnychuk, E. Kamykowski, J. Sredniawski, T. Debiak, AES Inc., Medford NY; R. Ruegg, B. Milton, TRIUMF

Abstract

We will describe the operation of a tandem accelerator based Contraband Detection System (CDS) built jointly by Advanced Energy Systems (AES) and TRIUMF, which employs the Nuclear Resonance Absorption (NRA) technique for detecting the attenuation of 9.17 MeV gamma rays by ^{14}N. A key technology of the CDS device is a high current tandem accelerator designed to provide a 1.76 MeV, 10 mA proton beam to a high power thin film ^{13}C target. We will describe the operation of the accelerator and present data on the measured output current, emittance, and energy spread using the integrated ^{13}C target yield. This system has been used to generate images of explosive simulants which can be separated from non-nitrogenous background.

1 INTRODUCTION

The potential of GRA for detection of explosives has been cited in previous work [1,2]. Development of a high-current electrostatic accelerator for the Contraband Detection System (CDS) uses state-of-the-art technology that is beneficial to other applications like radiography or medical therapies. In this paper we will present some of

The ion injector uses a filament driven volume H- source with a 2 grid extraction system. Beam is matched to the tandem with a single solenoid magnet. A beam collimator consisting of four independent jaws is used to scrape beam halo and to limit the tandem input current while operating the ion source and extractor in "off-perveance" mode. A fast beam kicker dipole magnet is located after the LEBT solenoid in order to kick the tandem input beam into a water cooled beam stop in the event of an interlock trip generated either by a safety system, or the tandem sub-system.

The HEBT consists of 4 independently adjustable quadrupole magnets (aperture radius: 2.1 cm, pole tip length: 10 cm, gradient: 0.892 T/m/Amp) positioned in pairs on either side of a dipole magnet designed to bend the beam 80.66 deg onto the gamma production target, and several sets of adjustable collimators. The tandem output beam is transported either to a diagnostic station and beam dump or to the gamma production target. The HEBT is capable of producing a variety of elliptical beam spots on target.

The target consists of a ^{13}C thin film sputtered onto a Ta foil mounted onto a water cooled Cu structure. The target is designed to accommodate the full 17.6 kW beam load. Details of the target design are given in [3,4].

Figure 1. CDS Beamline.

the data on the current transmission of the accelerator, the radiation field around the machine during operation , measurements of the output beam emittance and energy spread, and show an example of an image generated by the CDS system.

2 ACCELERATOR DESIGN

The CDS accelerator system schematic is shown in fig. 1. The system consists of an H- injector and LEBT, the tandem accelerator, an HEBT section with a dipole bend magnet, a ^{13}C target, a diagnostic vessel and beam dump, and a gamma ray detection and imaging system.

The optical system was designed for matching a 40 kV, 10 mA H- beam to the tandem acceptance. End to end particle simulations of the beamline have been conducted [5] and show that almost no beam loss is expected despite significant space charge induced non-linearity. The physical apertures in the system are designed to be six times the rms radius of the matched beam.

Details of the tandem accelerator design have been presented in [6]. Figure 2 shows some of the accelerator details. The key features of the design consist of a compact power supply designed for 20 mA and 1MV

Figure 2. Tandem Accelerator Details.

output voltage, 2 acceleration tubes with a 10 cm aperture designed for 50 kV/inch acceleration gradient, a terminal housing a vapor stripper cell, cryo cold heads, a pair of triplet magnets for matching to the stripper, and all associated power supplies. The terminal equipment is fed by a 4 kW, 1:1 isolation transformer. The SF6 gas is used as the coolant for all the equipment by passing the gas through a heat exchanger. The accelerator vessel was designed conservatively so as not to exceed 177 kV/mm operating at 865 kV terminal voltage and 60 psig of SF6. To date we have not experienced any obvious breakdowns to the vessel walls from the terminal.

Initial tandem commissioning focussed on high voltage related troubleshooting issues. The HV power supply has proven to be very robust in terms of voltage holding capability and survivability of components during HV breakdowns. This power supply was tested at TRIUMF to 1 MV and 26 kW into a water load at 60 psig of SF6. Commissioning of the integrated structure shown in fig. 2 focussed on optimizing the voltage standoff and protection of power supplies in the terminal during HV sparks. This later issue was addressed by Faraday shielding wherever possible, use of low inductance ground straps to tie all terminal power supply cases to the terminal potential, and use of filters on all data, output and power lines for the power supplies. High voltage standoff development focussed on proper configuration of insulators spanning the gap from terminal voltage to ground.

All breakdown problems experienced during commissioning have been due to surface breakdowns along ungraded insulators. In order to inhibit the surface breakdowns it was necessary to electrically segment the insulators spanning the full terminal voltage, and tie the subsections to the high voltage power supply stack at equally spaced intervals to maintain a fixed gradient.

The grading scheme used has virtually eliminated the insulator breakdowns experienced early in the

commissioning phase. Initial voltage conditioning after handling components generally takes 1 to 4 hours. Subsequently the terminal can be ramped to operating voltage within a few minutes.

3 BEAM OPERATION

The accelerator has been operated with beam at terminal voltages from 600 to 900 kV. Fig. 3 shows the input and output current as a function of the ion source grid 1 voltage. The present experiments are geared toward optimizing the beam tune to minimize beam loss in the terminal, and minimize the radiation field at the operator station located approx. 5 m from the accelerator.

Figure 3. Tandem input and output current vs. Ion source grid 1 voltage at various beam energies. Solid : input; Open: output.

The highest beam current transported through the accelerator to the beam dump is approximately 2.2 mA at 775 kV terminal voltage. The transmission is optimized by variation of the tandem input beam parameters primarily via ion source arc current adjustment, ion source grid 1 voltage, LEBT collimator aperture setting, and via adjustment of the upstream terminal quadrupole triplet used for matching the beam to the stripper channel. Tandem output current measured with a DC beam toroid, and beam scrape-off measured as a temperature rise on a four quadrant collimator diagnostics located in the terminal provide the primary beam tune feedback.

Measurements of the x-rays generated from the tandem during beam operation at 775 kV terminal voltage show that the spectrum is peaked at 135 kV, and the shape is largely independent of the beam, i.e. we get roughly the same spectrum with beam on or beam off. Dose measurements at the containment vessel surface show a linear increase as a function of the input beam current with the dose at the tandem input side being 6 to 10 times greater than at the tandem exit. At 1.5 mA input current the contact dose at the tandem entrance is approximately 300 mR/hr, while the dose at the tandem exit is 40 mR/hr. This shows that the majority of

radiation is produced in the H- column which does not have magnetic electron /x-ray suppression.

Measurements of the beam emittance in the horiz.

Figure 4. Tandem output beam emittance, divergence and beam size vs. Output current.

plane show that the normalized rms emittance is 0.09 π-mm-mrad at 1.2 mA with an rms beam size of 2.9 mm, and a .94 mrad rms divergence. In the present configuration measurements in the bend plane of the magnet are not available. These data were taken with the emittance scanner located in the diagnostic station as shown in figure 1. The drift distance from the scanner to the center of the downstream quadrupole is 375.6 cm with quads set to 4.5 T/m.

Figure 5. 9.17 MeV gamma ray yield vs. Proton energy. (■) CDS accelerator 2 μm target. (●) VandeGraff, 0.25 μm target.

Figure 5 shows the yield curve for 9.17 MeV gamma rays obtained from a 2μm thick ^{13}C target measured on the CDS system compared with yield measurements from a 0.25 μm ^{13}C target done on a Van de Graff system .

The comparison of the two curves show that the thin target yield peak occurs at 1.746 MeV as expected and corresponds with the half maximum point of the 2μm target yield from the CDS accelerator. The 2μm thick target is sufficiently thick to generate gamma rays

through the entire CDS beam energy spread and shows that energy is properly calibrated and gives a FWHM CDS energy spread of 15 keV. This is well within the requirements for the CDS system.

Figure 3. Total Density Image

Figure 4. Nitrogen Density Image

Figure 6. Gamma ray image showing discrimination of nitrogenous explosive simulant from equal density non-nitrogenous phantom.

Using the gamma rays generated by this system we performed a basic imaging experiment designed to demonstrate the ability of the CDS system to discriminate nitrgenous and non-nitrogenous materials of equal density. . Figure 6 shows the gamma ray image obtained with an array of 7 segmented BGO detectors. The items imaged consisted of a cylinder of water and a volume of melamine used as an explosive simulant. The beam current on target was approximately 200 μA. Data was collected by first imaging the water cylinder and melamine in the resonant position, followed by displacing the detector array and phantoms out of the resonant cone and repeating the scan in the non-resonant position. The upper image in fig. 6 shows the non-resonant image proportional to total line density, and the lower image shows the nitrogen density image obtained by subtracting the resonant and non-resonant images. We can see that only the nitrogenous phantom remains visible.

4 REFERENCES

1. Gozani, T., "Nuclear Based Techniques for Cargo Inspection - A Review", *Proceedings of Contraband and Cargo Inspection Technology International Symposium*, pp. 9-19, October, 1992.

2. Vartsky, D., et al., "A Method for Detection of Explosives Based on Nuclear Resonance Absorption of Gamma Rays in 14N", *Nuclear Instruments & Methods in Physics Research, Section A 348*, pp. 688-691, 1994.

3. Melnychuk, S.T." Dev. Of a Thin Film 9.17 MeV Gamma Ray Production Target for the CDS". This Conf.

4. Rathke, J. R.,"Engineering Design of a Continuous Duty Gamma Production target for the CDS" This Conf.

5. Reusch, M. F. and Bruhwiler, D. Proc. Of the 18th Int. Linear Accel. Conf., 26-30 Aug. 1996, Geneva, Switz., v.1, p. 358.

6. Milton, B. F., "A High Current Tandem Accelerator for Gamma-Resonance Contraband Detection" 1997 Particle Accelerator Conference, Vancouver CA.

PORTABLE CW LINAC FOR COMMERCIAL APPLICATIONS

H.Deruyter*, R.Foose**, A.V.Mishin*, W.Sapp***, R.G.Schonberg**, D.Skowbo*

American Science & Engineering

Abstract

This paper continues our description of a new compact CW linac program started by Schonberg Research Corporation (SRC) under terms of a development contract. This work is now continued by High Energy Systems (HES) Division of AS&E. HES has been formed based on the acquisition of SRC by AS&E.

Since we published the design and the first experimental data on the 1 MeV CW linac [1], a complete test has been done as a continuation of the CW program. The accelerator is equipped with the local radiological shield and it can be operated on the manufacturing floor.

The linac can be used for a variety of commercial and scientific applications, which require high power electron beams such as NDT programs, sterilization of medical products, electron beam processing of composites and food irradiation.

In this paper, we will briefly describe the latest results and upgrades to the existing system.

1 UPGRADES TO SYSTEM DESIGN

The block diagram of the upgraded system is shown in Fig.1. We have replaced the 30 kW magnetron with a 30 kW klystron, driven by a 1 W solid-state source.

Figure 1: System block diagram

Electron beam is formed in the electron gun manufactured by Litton Industries (1). High voltage power supply (2) designed and built by HES provides 0 to 20 kV to the e-gun accelerating gap. From the electron gun, the electron

beam is injected into a 1.3 m long linac section (3), where it is accelerated to the designed energy of 1 MeV. Two solenoids have been added to the existing three (4). Each solenoid is powered by a separate Sorenson power supply (5). The existing system is now capable of providing adjustable magnetic field close to 1000G peak, depending on the relative location of the solenoids. A 30 kW klystron (7) has replaced the magnetron operating at 2450 MHz. Upgraded Spellman power supply (8) is used to operate the klystron. The multiple beam klystron operating voltage range is similar to that of the previously used magnetron. A permanent periodic magnetic (PPM) focusing system used on this klystron permitting us to eliminate the electromagnet, used for the CW magnetron. A three-port RF circulator manufactured by AFT(13) is used to protect the klystron from the reflected power. All the components associated with the set-up using the magnetron, such as cooling fans for the magnetron "dome" window and the anode, 1 kW phase-locking klystron with power supply, the second RF circulator were removed from the existing system. The other components, described in [1] are unchanged. The assembly drawing which shows the linac position with respect to the "flying spot" wheel support is shown in Fig.2.

Figure 2: Present linac incorporated into a "demo"system

Other components such as magnetron, circulator, etc. have not been shown in order not to overload the drawing.

---

* High Energy Systems Division of AS&E (Santa Clara, California)
*** Headquarters located in Billerica, Massachusetts
** Consultant

2 COMPONENTS DESIGN

We have described the design of the accelerator structure in our previous publication [1]. The original design of the accelerator guide is based on the concept of combining two different structures: Alvarez and on-axis or side-coupled structure. The cross section of the input coupler and Alvarez structure is shown on Fig. 3.

The concept permitted us to accelerate electron beam from low injection voltage of 12 ± 6 kV to 1 MeV in 1.3 m long accelerator guide shown on Fig.3 using power source of only 30 kW.

Figure 3: View of 1.3 m long accelerator guide.

Original calculations of beam dynamics and section geometry were made using a computer code AXIL. The preliminary results of these calculations were used for further more sophisticated beam dynamic simulation. The results of the computer simulation using codes Parmela and Beampath are shown in Fig.4 and 5. For the chosen geometry, a moderate field of 300-400 G is required to transport the electron beam through the structure.

The guide was tuned to the designed frequency of 2450 MHz. Separation of the neighboring resonances from the working resonance is close to 2 MHz (Fig.6).

The 30 kW, S-band, CW magnetron CWM-30S manufactured by California Tube Laboratory was originally used as a RF power source in the system .

We achieved fairly good results using this non-tuneable 30 kW CW magnetron, supplied by CTL. Phase-locking technique is described in the previous publication [1]. However, the fact that the magnetron is non-tuneable and the complexity of the phase-locking set-up generated the idea of using a 30 kW CW multiple beam klystron [8] with the characteristics very similar to the previously used CW magnetron. The new implemented technique permitted to substantially simplify the test set-up (Fig.8)

Figure 4: 30 kW multibeam CW klystron, circulator and cross-guide coupler assembled on a strongback.

The same Spellman MG48 power supply was used to drive the klystron, which has the similar loading characteristics and operates at anode voltage of 14 kV. The klystron is equipped with PPM focusing system, which eliminated the need for a solenoid. Two 12 kW inverter modules were added to the existing four to compensate for the lower efficiency factor. The automatic filament current runback for the klystron is not necessary, so it was disabled.

3 HIGH POWER TESTING

During the high power tests, we achieved maximum current of 4 mA at 1 MeV. Imaging tests have been successfully performed using the AS&E detectors. We are continuing commissioning of the accelerator.

The first tour of experiments has been completed. The next phase of the development is to improve the design of the accelerator to create a deliverable product.

4 REFERENCES

1. Portable Linac using CW magnetron as Power source Proceedings of EPAC 98

2. A.S.Alimov et al Compact Two Section CW Electron Linac With High Beam Power, Preprint INP MSU - 94 - 34/356, Moscow, 1994.

3. A.V.Mishin, R.G.Schonberg CW Particle Accelerator with Low Particle Injection Velocity, US Patent 5,744,919, 1998, priority 12/96.

4. American Science and Engineering Advertising Brochures.

5. ADMIT Corp. CW Klystron KIU-388DD, Advertising brochures.

APPLICATIONS AND PHYSICS OF THE TABLETOP STORAGE RING

H. Yamada*, Y. Kitazawa[1], I. Tohyama[1], N. Takeichi, T. Takayama[2], K. Ozaki, Y. Sakai, T. Kaneda, and K. Saka, Ritsumeikan, Shiga, A.I. Kleev, G.D.Bogomolov, V. Zavialov, Kapitza Inst., Moscow, H. Hama, M. Hosaka, J. Yamazaki, UVSOR, Okazaki, T. Koseki, H. Takaki, ISSP, Tokyo

Abstract

We are constructing the smallest electron storage ring for establishing hard/infrared/far-infrared beam facility. Physics subject to be studied are the study on a 2/3 resonance injection; the sub-pico second short electron bunch formation and the coherent synchrotron radiation; the photon storage ring (PhSR) lasing mechanism, the light pulse compression in the PhSR; the Compton back-scattering under strong magnetic field; and Characteristics of hard x-rays generated by a very thin wire target placed in the orbit.

1 HISTORY AND PRESENT STATUS

We are constructing the smallest electron storage ring for establishing hard x-ray as well as infrared/far-infrared beam facility [1-3]. This construction was initially motivated by an idea of the photon storage ring (PhSR)[4-7], which is a novel laser scheme originated by Yamada in 1989. The physics involved in the PhSR is similar to a free-electron laser, but an undulator is not used. Instead, one barrel shaped mirror provides the function of the undulator as well as an optical cavity in corroborating with a bunched electron beam circulating in an exact circular orbit. The hard x-ray generation scheme was later added to the project according to the Yamada's proposal in 1996 [8].

The storage ring was designed in 1993, funded by Ministry of Education in 1994, completed in 1997 (a 1 kW magnetron instead of klystron was used because of financial limit), and placed in the injector room of UVSOR Okazaki. We have performed 2/3 resonance injection by using a 15 MeV linac. We have observed circulating beams by a loss monitor. It was impossible to optimise injection and to store useful amount of current since the characteristic wavelength of synchrotron radiation is too long to monitor by fast response detector and another monitors was unavailable in the strong magnetic field of the ring.

A radiation safety room was built in 1996 at Ritsumeikan University, and the ring was moved from

Okazaki in 1998. A cw klystron was funded in 1997. Science and Technology Corp. of Japan funded a 21.5 MeV microtron in 1998. The microtron was built in collaboration with a team from P.L.Kapitza institute for physical problems, and succeeded in the commissioning last fall.

In order to adapt the resonance injection at 21.5 MeV, we have modified magnetic field distribution by adjusting pole shape with thin circular metal plates. Parameters of the smallest ring system are shown in Table 1.

FIG. 1. An overview of the tabletop electron storage ring system under construction installed in the 2 m deep and 3x7 m^2 wide pit.

2 CONFIGURATION OF THE SYSTEM

The smallest ring system is made of a 1.2 m out diameter and 1.5 m high normal conducting magnet and the circular microtron injector of 1.2 m out diameter as

FIG. 2. A schematic plane view of the facility is shown. A small experimental room is seen which can be utilised for x-ray beam applications. A double crystal monochrometer is placed inside the accelerator room

seen in Fig. 1. The ring is an exact circular type using one piece of weak focusing magnet. The magnet weigh is 8 ton in total to store electrons up to 50 MeV. The system is placed in a 7x 3 m² wide and 2 m deep pit as seen in Fig. 2 and is covered with 0.5 m thick concrete blocks. A small exposure room is attached. The x-ray as well as infrared/far-infrared beams can be extracted through a channel in the wall and through a double crystal monochrometer system (the crystal can be replaced to spherical mirrors for IR and FIR) placed inside the accelerator room to stop energetic γ rays.

3 APPLICATIONS AND PHYSICS PROBLEMS

Beam injection is scheduled from April 29. We are ready to study the following physics related to the smallest ring, and several beam application programs for initial demonstration.

Physics subject involved in the smallest electron storage ring are the following:
1. Experimental study on 2/3 resonance injection method.[2]
2. Beam instability problems appears in the lowest energy ring.[2]
3. Study on a forced cooling technique by laser and residual ions [9].
4. Sub-pico second short electron bunch formation [10].

Table 1 Main specifications of the system

Magnet	Weak focusing, normal conducting, Cylindrical
Pole gap	100 mm
Orbit radius	0.156 m
n-value	0.52
RF Cavity	Two set, re-entrant type
frequency	2.44 GHz
Harmonics	8
RF-voltage	50 kV
RF Source	Magnetron
Perturbator	Pair of one turn coils
pulse source	0.4 µs width, 6500 A peak current
Repitition rate	Max 100 Hz
Injector	21.5 MeV microtron
Critical wavelength	8.1 µm
Damping time	1.0 s

5. Coherent synchrotron radiation measurement.
6. Photon storage ring lasing mechanism [7]. Effect of the coherent radiation on the laser gain [6].
7. Light pulse compression in the photon storage ring and femt-second pulse formation [11].
8. Compton back-scattering under strong magnetic field [12].
9. Characteristics of hard x-ray beam generated by the very thin target placed in the orbit [8].

The 7-th subject is added according to the recent

theoretical study on the PhSR. The PhSR theory was earlier constructed on an assumption that a single mode electro-magnetic(EM) field (whispering garelly mode) appears in the circular optical cavity [7]. As a consequence the laser gain is calcuIted to the interaction between uniformly filed EM field and electron bunches. Recently we have improved the model and mathematical formalism [11]. We represent the mode in superposition of the multiple radial modes, and obtain the comprex wave numbers and each amplitude coefficient by solving eigen functions, which are determined by boundary conditions at optical cavity mirror surface and the envelop of circulating electron beam. If the bunched electron is not taken into account, the uniform EM field appears. We found that when the ratio between the mirror radius and the electron orbit radius sutisfyes the Yamada's resonance condition, the EM field becomes pulse mode. It will happen that the optical pulse width is narrower than the electron bunch width when the peak current is high and the mirror/orbit ratio is close to the resonance value as seen in FIG. 3.

In the next we discuss the primary beam applications, which are;
1. X-ray imaging using the phase-contrast method.
2. Medical treatment of arterioscleroses, cancer, lighiasis etc. by FIR beam [1].
3. A bio-molecular dynamics excited by FIR-rays [1].
4. Analysis of the water network structure effected by bio-molecules.

In our system the x-ray emission mechanism is not the synchrotron radiation but the bremsstrahlung from a thin wire target placed in the electron orbit [].

Regardless of magnetic or electric forces, the emission occurs due to acceleration of electrons. Characteristics of the photon emission are simply determined by the energy and momentum conservation lows. The bremsstrahlung should be emitted in the strongly forward direction in a $1/\gamma$ (the γ is the Lorentz factor) cone as same as the synchrotron radiation when the electron energy is relativistic. The high- energy x-ray can be generated more easily by the bremsstrahlung than by the synchrotron radiation, since the atomic Coulomb force is much stronger at the vicinity of nucleus than the magnetic field of bending magnet.

The characteristics of this x-ray source are quite different from that of synchrotron light sources in many regards. First of all, the beam lifetime is only minutes therefor we keep beam injection continuously. But because of the resonance injection, the beam in the central orbit will never be disturbed by the injection. Thus we will be able to keep the constant beam intensity. In the second, the x-ray spectral brightness is rather flat and is extended to the high energy up to the electron energy. The monochrometer is an essential need. We can select

any x-ray energy band according to an aim of exposure. In the third we can obtain source size as small as that of Spring-8, since that is determined by the target size as $10\mu m$ in our case. Beam position must be very stable since the source point is fixed. This is often the problem in the case of large synchrotrons due to sunshine and moon. The x-ray beam covers wide angle such as $1/\gamma = 0.01$ rad, since the electron energy is low. At 1 m distant from the source point the $10x10\ mm^2$ area can be exposed at a time. These all features are advantageous for the phase contrast x-ray imaging.

FIG. 3. Light pulse is compressed in the circular optical cavity, when the bunched beam exists. The dashed line represent the electron bunches, and the sold the optical pulse.

5 REFERENCES

[1] H. Yamada, J. Synchrotron Rad. (1998), 5, 1326-1331

[2] H. Yamada, Advances in Colloid and Interface Sci. 71-72, (1997) 371-392.

[3] H. Yamada et.al., Proc. 1st Asian Particle Accelerator Con. Tsukuba, KEK, Mar 6, 1998, www-proc.kek.jp/proc.html.

[4] H.Yamada, Japanese J. Appl. Phys. 28(9) (1989) L1665; H.Yamada, Nucl. Instrum. Methods in Phys. Res. A304 (1991) 700-702.

[5] H. Yamada, Nucl. Instrum. Methods in Phys. Res. B79, (1993) 762-766.

[6] H. Yamada, H. Tsutsui, K. Shimoda, and K. Mima, Nucl. Instrum. Methods. in Phys. Res. A331 (1993) 566-571

[7] Mima K., Shimoda K., and Yamada H., IEEE J. Quantum Electronics, 27, (1991) 2572-2577.

[8] H. Yamada, Jpn. J. Appl. Phys., 35 (1996) L182-L185.

[9] H. Yamada to be published.

[10] H. Yamada , AIP CONFERENCE PROC. 367, (1996) 165-180.

[11] A.I. Kleev and H. Yamada, Nucl. Instrum. Methods in Phys. Res

[12] I. Sakai and H. Yamada, Proceeding of 11st Conference on Accelerator Science and Technology, Himeji,Japan, 1998.

SCALPEL: PROJECTION ELECTRON BEAM LITHOGRAPHY[*]

L.R. Harriott[#], Bell Laboratories – Lucent Technologies, Murray Hill, New Jersey

INTRODUCTION

Much of the tremendous progress in integrated circuit technology and performance over the past 30 years has been fuelled by the progress in lithography. The ability to print increasingly smaller features has enabled higher speed transistors, higher packing densities and lower power dissipation in CMOS circuits. The productivity of the integrated circuit industry has been on a very steep performance curve, historically improving cost per function of integrated circuits by 30% per year over this period. Roughly half of this productivity improvement is attributable to continuos improvements in lithography technology. The remainder is made up of wafer and chip size increases and circuit design and process innovations.

Leading edge production lithography employs optical projection printing operating at the conventional Raleigh diffraction limit. Generally speaking, the smallest features that can be reliably printed are equal to the wavelength of the light being used. The wavelength of light used for production lithography has decreased historically on an exponential trend curve as illustrated in Figure 1. Light sources have evolved from Mercury arc lamps where they were filtered for the g-line (435 nm) and then I-line (365 nm). Recently, excimer lasers have been introduced as light sources. KrF excimer lasers produce light in the deep ultraviolet (deep uv or DUV) at a wavelength of 248 nm. This source is used currently to produce the most advanced circuits with minimum design rules of 250 nm. Actually, some manufacturers use 248 nm DUV to print transistor gate features as small as 160 nm with resolution enhancement technologies (RET) which allow, in some cases, printing of features somewhat below the conventional diffraction limit.

The issue with optical lithography, which has been characterized by some as a crisis, is also illustrated in Figure 1. Although the progress in optical lithography has been on an exponential improvement curve due to shrinking wavelengths, the slope of the productivity curve for integrated circuits is on a much steeper slope (commonly referred to as Moore's Law). In fact, the two curves intersect at about the KrF (248nm) node for optics and 250 nm node for circuits. This implies, that to make further progress, either new shorter wavelength printing (such as ArF at 193 nm or F_2 at 157 nm) systems must be

available sooner than the historical trend (very unlikely) or circuits must be printed below the diffraction limit (which is already beginning to happen). Resolution enhancement technologies or RET allow sub-diffraction printing by controlling the phase as well as amplitude of the light at the image plane in the printing system through the use of phase shifting masks and other "tricks". One other method uses pre-distorted amplitude patterns at the image plane to compensate for some diffraction effects (optical proximity effect correction or OPC). Further, control of the distribution and angle of light (off-axis illumination or OAI) at the illumination aperture can accentuate higher diffraction orders leading to improved performance. These methods are often used in combinations optimized for the particular pattern being printed.

Figure 1. Wavelength trend in optical lithography contrasted with the miniaturization trend in integrated circuits.[1]

The limit of the improvements offered by RET is the ability to print features at roughly half the wavelength of the light being used, shown as the theoretical limit in Figure 1. The use of these RET techniques can greatly increase the cost of wafer printing and history has shown that printing with shorter wavelengths has proven more economical than employing RET with current technology.

Figure 1 also shows that eventually, the IC productivity curve passes through the theoretical limit even for future optical printing systems. This occurs

somewhere before the 70 nm circuit generation (currently planned for production in 2009). The next generation of lithography technology beyond optical lithography (NGL) will likely be required for production of the 70 nm generation based on these physical limits. It is also possible that a NGL technology may be employed before to this if it is widely available and offers lower cost of ownership than optical lithography with RET extensions.

A complete technology for printing integrated circuits requires three main elements: the exposure tool, the mask technology, and the resist technology. In IC lithography, an image of the mask (usually reduced by 4 or 5 times) is projected onto the wafer substrate which has been coated with a photo-sensitive material (resist). The solubility of the resist is changed by exposure to light so that a pattern emerges upon development (much like a photograph). The remaining resist pattern is then used for subsequent process steps such as etching or implantation doping. Thus, any lithography technology must have fully developed exposure tool, mask, and resist technologies for it to be successful.

SCALPEL

One of the leading candidates for next generation lithography is SCALPEL® (SCattering with Angular Limitation Projection Electron-beam Lithography).2,3 SCALPEL is a reduction image projection technique which uses 100 keV electrons and scattering contrast. The use of electrons circumvents the limitation of diffraction in optical lithography. The principle is illustrated in Fig. 2.

Figure 2. SCALPEL principle.

The mask consists of a low atomic number membrane covered with a layer of a high atomic number material: the pattern is delineated in the latter. While the mask is almost completely electron-transparent at the energies used (100 keV), contrast is generated by utilizing the difference in electron scattering characteristics between the membrane and patterned materials. The membrane scatters electrons weakly and to small angles, while the pattern layer scatters them strongly and to high angles. An aperture in the back-focal (pupil) plane of the projection optics blocks the strongly scattered electrons, forming a high contrast aerial image at the wafer plane. The functions of contrast generation and energy absorption are thus separated between the mask and the aperture. This means that very little of the incident energy is actually absorbed by the mask, minimizing thermal instabilities in the mask.

Imaging Process

In the tool, a parallel beam of 100 keV electrons uniformly illuminates the mask. A reduction-projection optic, in a telecentric doublet arrangement, produces a 4:1 demagnified image of the mask at the wafer plane. Because the features being printed are much larger than the wavelength of the radiation used ($\lambda = 3.7$ pm), the full benefits of the reduction ratio are realized, especially in terms of the mask, because imaging is aberration limited, not diffraction limited. This is not the case for conventional optical lithography systems, which, while they are capable of printing very small features, are operating at the diffraction limit. In this non-linear regime, small errors in linewidth on the mask are printed with an effective reduction factor of less than 4:1, sometimes approaching 1:1. The illumination in the SCALPEL system is incoherent, so there are no interference effects. This, combined with the absence of diffraction effects and the high ultimate resolution (~ 35 nm), means that our current tool design will operate relatively linearly for feature sizes down to at least 70 nm, and that the results will be largely independent of the pattern printed. This means that equivalents to OPC (optical proximity-effect correction) are not required.

Writing Strategy

We have chosen to employ a small (1 mm x 1mm at the mask) electron optical field. This is consistent with our strutted mask design and step-and-scan writing strategy. The electron optical field is the same width as the patterned area between the mask struts. In order to achieve high throughput we must increase the effective height of the electron optical field by scanning the electron optical field electronically over an effective field. The effective field height is the same as the length of the patterned area between the mask cross-struts. Die exposure is accomplished by mechanically scanning the mask and wafer through the effective field. This is illustrated in figure 3.

Figure 3 Schematic diagram showing the SCALPEL step-and-scan writing strategy.

The SCALPEL step-and-scan approach confers advantages other than a simplified optical design. The die size that may be printed is not limited by the electron optics, but only by the available mask size and stage travel. This is different from optical step-and-scan systems where the optics must be large enough to illuminate a slit the width of the entire die. Another advantage, particularly in a mix-and-match environment, is that achieving good overlay is made easier. Since the image is effectively assembled from many small pieces, magnification errors or trapezoidal distortions errors can be amortized over a large number of stitching events. Control of the exact stage velocity ratio can be used to stretch or compress the image, and a novel electron optical device can be used to control the magnification and rotation of each individual illuminated area. The use of a small illumination area also allows us to place rigid struts approximately every millimeter to support the thin membrane of the mask, making a robust structure that has minimal susceptibility to pattern placement errors.

The device pattern is segmented on the mask in two dimensions by the struts and must be reassembled or stitched to form a continuous image on the wafer. It is essential to ensure that the critical dimension (CD) of any feature crossing a stitching boundary is maintained to within the tolerances specified by the error budget. The ease with which this may be accomplished is determined by how a feature divided between two stripes is joined. We will employ a seam blending approach to reduce the placement accuracy requirements for controlling feature dimensions across seam boundaries. The edge of each pattern stripe will contain a small overlap region (several microns) in which the pattern features are duplicated on adjacent stripes. These regions are illuminated with a tapered dose profile so that when they are printed, the net dose for these features will be uniform. This method reduces the feature placement requirement for a given critical dimension specification

by as much as a factor of five over what would be required if pattern edges were simply butted together.

Results

We have designed and constructed a proof of concept SCALPEL4 system which employs the step and scan writing strategy described above. Along with the exposure tool development, we have also developed the mask and imaging resist technology as a system. To date the masks are made from 100 mm Si wafers with SiN membranes and a patterned W/Cr scattering layer. The imaging resists used have largely been the same as those which have been developed for 248 nm and 193 nm deep UV optical lithography5. Figure 4 is a photograph of our SCALPEL

Figure 4 Photograph of SCALPEL exposure system.system at Bell Labs. It takes up roughly the same amount of space as an optical lithography tool.

Figure 5 shows a scanning electron micrograph of an 80 nm line in positive tone DUV photoresist. This isolated line pattern is part of a gate level transistor pattern.

Figure 5. Scanning electron micrograph of 80 nm isolated line gate structure in DUV resist.

Figure 6 shows another example of a pattern typical in integrated circuit designs, contact holes. This pattern is very difficult to reproduce in a diffraction

limited optical system due to its 2-dimensional nature. The image shows an array of 80 nm contacts imaged in a 750 nm thick photoresist film. Quantitative electron microscope measurements showed a depth of focus in excess of 20 microns for a 10% dimensional tolerance. This is nearly 100 times that afforded by today's optical lithography at much larger dimensions.

Figure 6 Scanning electron micrograph of an 80 nm contact hole pattern in 750 nm film of DUV photoresist.

SPACE CHARGE EFFECTS

The mutual repulsion of electrons or space charge effect in the beam tends to defocus the beam on average6. This average defocus can generally be corrected by adjusting the focusing lenses. However, the individual stochastic electron-electron interactions cause a blurring of the beam which is not correctable due to its random statistical nature. It is analogous to considering the average position of the electrons to be affected by space charge as well as the distribution about that average. One can re-adjust the average but cannot do anything about the distribution. As one might expect intuitively, the space charge effect is reduced for higher energies, shorter focusing columns and larger beam areas.

Various models and simulations have been employed to predict the effects of stochastic space charge blurring on lithographic image quality in a projection system such as SCALPEL. A primary concern in any lithography system is throughput. The number of wafers that can be printed per hour increases with increasing beam current. However, as the beam current is increased the image becomes blurred by the space charge effect and loses resolution. Thus in SCALPEL there is an inherent trade-off between wafer throughput and resolution. The models predict a somewhat sub-linear relationship between beam current and beam blur. The blur in the beam depends on the total beam current to a power somewhere between 1/2 and 2/3. For maximum throughput, systems such as SCALPEL should be operated in a regime where the performance is dominated by the space charge blur as opposed to aberrations.

Throughput models predict that throughputs of roughly 45, 200 mm diameter wafers per hour are possible on a SCALPEL system assuming a pattern density of 50 % or less (reasonable for critical gate and contact hole layers) and a resist sensitivity of 5-6 $\mu C/cm^2$. This is at least an order of magnitude larger than serial writing electron beam systems but still as much as 50% lower than that of a modern optical lithography system.

COST

The progress in the integrated circuit industry over the last 30 years has been driven by dramatic improvements in cost per function in circuits. For the next generation of lithography technology, whether it is based on optical or electron beams, must be cost effective in order to be consistent with the industry expectations. In estimating the cost of printing a lithographic pattern on a wafer, there are three main elements: 1) the cost of operating the exposure tool which is proportional to its price divided by its throughput, 2) the mask cost which is the price of the mask divided by the number of wafers to be printed with it, and 3) the cost of the resist materials and development of the image. The choice of the next generation lithography technology is likely to be made on this basis rather than on strictly on technical grounds since there are several alternatives that can achieve similar results but at different degrees of difficulty and cost.

In comparing SCALPEL to advanced optical lithography on the basis of estimated costs, the throughput of an optical tool may be as much as twice that of a SCALPEL tool but is likely to cost twice as much making the first term roughly equal. The resist and processing costs slightly favor SCALPEL since some complexities such as antireflective coatings under the resist are not needed. The most significant difference is in the mask costs. SCALPEL operates in a linear printing regime and therefore uses a true 4:1 representation of the circuit pattern on the mask. In sub-wavelength optical lithography, the masks must be much more complex to compensate for diffraction effects in printing. The mask cost will be the dominant factor in the overall costs and thus SCALPEL technology will have a significant advantage over optical lithography in the sub-wavelength regime.

SUMMARY

Even though virtually all integrated circuits over the past 30 years have been made using optical lithography, the limits of its usefulness are on the horizon. From the point of view of the physics of the image formation process, it is difficult to imagine practical processes operating at feature sizes at or near half the wavelength of the exposure system. The exposure wavelength trend has been to tend to ever smaller ultraviolet wavelengths but at a pace slower than the feature size trend for integrated circuits. Therefore, both the imaging mechanisms and industry timing indicate that a new disruptive lithography technology will be needed sometime after about 2003. We have developed SCALPEL electron beam lithography to the point where the basic functionality has been shown. Our efforts over the next few years will be to develop the exposure tool, mask and resist technology to the point of commercial introduction consistent with that timing. Ultimately, relative costs of lithography alternatives will determine the successor to current optical technology. The projections are that SCALPEL will operate at a significant cost advantage to sub-wavelength optical technology and other contenders for next generation lithography. Therefore, we feel that SCALPEL is likely to be the industry choice for 100 nm era circuits and beyond.7

ACKNOWLEDGEMENTS

REFERENCES

[1] Figure courtesy of Dr. Shinji Okazaki of Hitachi Ltd.

[2] J.M. Gibson and S.D. Berger, Appl. Phys. Lett., 57, 153 (1990).

[3] S.D. Berger, C. Biddick, M. Blakey, K. Bolan, S. Bowler, K. Brady, R.M. Camarda, W. Connelly, R. Farrow, J. Felker, L. Fetter, L.R. Harriott, H.A. Huggins, J.S. Kraus, J.A. Liddle, M. Mkrtchyan, A. Novembre, M. Peabody, T. Russell, W. Simpson, R. Tarascon, H. Wade, W. Waskiewicz, and P. Watson. Proc. SPIE 2322, 434 (1994), L.R. Harriott, S.D. Berger, C. Biddick, M. Blakey, S. Bowler, K. Brady, R. Camarda, W. Connelly, A. Crorken, J. Custy, R. DeMarco, R.C. Farrow, J.A. Felker, L. Fetter, L.C. Hopkins, H.A. Huggins, C.S. Knurek, J.S. Kraus, R. Freeman, J.A. Liddle, M.M. Mkrtchyan, A.E. Novembre, M.L. Peabody, R.G. Tarascon, H.H. Wade, W.K. Waskiewicz, G.P. Watson, K.S. Werder and D.L. Windt,., Microelectronic Engineering 35, 477, (1997)., W.K. Waskiewicz, C. Biddick, M. Blakey, K. Brady, R. Camarda, W. Connelly, A.H. Crorken, J. Custy, R. DeMarco, R.C. Farrow, J.A. Felker, L. Fetter, R. Freeman, L.R. Harriott, L.C. Hopkins, H.A. Huggins,R. J. Kasica, C.S. Knurek, J.S. Kraus, R. Freeman, J.A. Liddle, M.M. Mkrtchyan, A.E. Novembre, M.L. Peabody, L. Rutberg, H.H. Wade, G.P. Watson, K.S. Werder and D.L. Windt, Proc. SPIE 3048 (1997)., and L.R. Harriott, J. Vac. Sci. Technol B 15 (1997)

[4] L.R. Harriott, J. Vac. Sci. Technol B 15 (1997)

[5] A. E. Novembre, R.G. Tarascon, S.D. Berger, C.J. Biddick, M.I. Blakey, K.J. Bolan, L.A. Fetter, L.R. Harriott, H.A. Huggins, C.S. Knurek, J.A. Liddle, D.A. Mixon, and M. L. Peabody, J. Photopolymer Sci. & Technol., 9, 663, (1996).

[6] M.M. Mkrtchyan, J.A. Liddle, S.D. Berger, L.R. Harriott., A.M. Schwartz, and J.M. Gibson, J. Vac. Sci. Technol. B12, 3508 (1994). , L.R. Harriott, S.D. Berger, J.A. Liddle, G.P. Watson, and M.M. Mklrtchyan, J. Vac. Sci. Technol. B13, 2404 (1995).

[7] For further information, see our web site at http://www.lucent.com/SCALPEL .

PRESENT STATUS OF HIMAC AT NIRS

M.KANAZAWA, M.TORIKOSHI, S.YAMADA, Y.FUTAMI, K.KAWACHI, A.KITAGAWA,
M.KUMADA, T.MURAKAMI, M.MURAMATSU, K.NODA, Y.SATO, M.SHIMBO, M.SUDA,
E.TAKADA, M.ENDO, T.KANAI, H.KOYAMA-ITOU, N.MATSUFUJI, S.MINOHARA,
N.MIYAHARA, T.HOMMA, H.YAMASHITA, E.URAKABE, and F.SOGA.

National Institute of Radiological Sciences, Chiba, Japan

Abstract

Since 1994 clinical trials have been performed successfully with carbon beam. To improve the clinical result further, new irradiation systems are under development such as a 3D-irradiation system and a verification system of range with positron emitter. There are also improvements on the accelerator performances. One is the wide range of ion species; the others are concerned with the machine devices and new beam monitors to get good machine operation. In this report we present current status of HIMAC.

1 INTRODUCTION

Heavy ion therapy has both the advantage of high RBE (Relative Biological Effectiveness) and low OER (Oxygen Enhancement Ratio) with good dose concentration on the tumour. To verify its effectiveness in the cancer treatment, the HIMAC (Heavy Ion Medical Accelerator in Chiba) project[1] had started in 1987. In the treatment the carbon ion was selected because of its good dose distribution with high RBE value. Since June 1994, 557 patients were treated. In the first treatment in 1994 the head and neck tumours were treated, and now we are carrying out treatments on 9 tumour sites. The systematic clinical studies are made and suitable dose value is decided in each tumour site. Reports are published on the clinical results with the cases treated until August 1998[2][3].

In parallel with the clinical treatment in daytime, developments of new irradiation systems have been made during night and weekend. First is a synchronized irradiation with respiration, where newly developed extraction method was adopted[4]. Now the treatment with this technique is routinely used for the tumour site like lung and liver, whose movement due to respiration is not negligible. Second is 3-D irradiation system[5], which will be started in this year for the routine treatment. In this method the synchronized irradiation will also be combined, and the concentration of dose on the tumour can be improved. By this irradiation method the moving tumour site is also possible to be treated. Third is an irradiation system with positron emitter beam like ^{11}C. With this beam we can verify the range of the ion beam inside the patient body. For this, the secondary beam course has been constructed and its beam tests have also

been completed. Now we are constructing an irradiation system.

To supply the beam for various kinds of experiments, the injector linac system has been improved to accelerate different kinds of ions simultaneously. The accelerated beam are transported to medium experimental hall, upper and lower synchrotron rings, and the beam can be used in the different three experimental halls. Owing to this improvement the 53 groups of biological experiments and the 52 groups of physical ones were programmed during 1998 financial year by use of night and weekend machine time.

2 OPERATION AND ITS IMPROVEMENTS

In the daily operation, treatment is scheduled between 8:30 and 19:00 from Tuesday to Friday. Experiments are assigned from Monday night to Saturday night except the time for the treatment. Between treatment and experiment, it takes 90 minutes to change ion species, energies in two synchrotrons and to adjust corresponding transport lines. For the treatment in the horizontal irradiation system the beam energies of 290 and 400 MeV/u are used, and in the vertical one the beam energies of 290 and 350 MeV/u are used. Change of beam energy in each case is scheduled once a day. To switch the beam energy in the synchrotron and the transport line, 30 minutes are required. Additional 30 minutes are also necessary for range check in the irradiation system. Within this time beam centres are adjusted in all the treatment rooms, and the beam intensity is also adjusted. After that it is sufficient to only change the excitation of one switching magnet for the switch of the beam course from one treatment room to another. It is not necessary to check the beam centre again in the treatment room after switching the beam course. This reliability is highly important to treat many patients in the routine irradiation. To make this period short further, improvements on the control software's of accelerator [6] and monitors in the irradiation system are planed. One of these improvements is an automatic tuning system of the beam transport line[7]. Another improvement is the range check in the irradiation system when the beam energy is switched.

For the experiments three different ions can be used simultaneously in the three experimental halls, which are

accelerated in the injector linac, upper synchrotron and lower synchrotron[8]. Available ion species are increased with new ion sources of 18 GHz ECR[9] including proton and iron. Former is important for the R&D of the proton therapy whose facilities are now increasing. Latter is important to test the biological damage in the space ship.

To have better performance of synchrotron, we have made several improvements after commissioning. To obtain better spill structure of the slow extraction beam, power supplies of dipole and quadrupole magnets are improved in its control circuit to have low ripple currents. Strong ripples, which were existed in the beginning of the machine operation, are now suppressed satisfactory[10]. As a next step the spill control with feedback and feedforward systems[11] will be tested. To obtain higher beam intensity, sextupole magnets are installed to correct the vertical cromaticity. COD monitors and steering magnets are also installed to increase the beam intensity[12]. To obtain maximum beam intensity of 2×10^9 pps (particles per second) from the synchrotron in the case of carbon beam, the vertical COD correction is important. Further increase of the beam intensity will be required for the basic experiments. This is also strongly required in the secondary beam course. For this purpose the further machine study is important, and new following beam monitors are installed for the machine study.

a) A beam profile monitor with MCP in the synchrotron ring[13].

b) Tune monitor system with white noise generator and a real time spectrum analyzer. With this system we can measure the tune value in the acceleration period.

c) Quadrupole kicker and pick-up monitor to measure the incoherent tune shift.

3 NEW IRRADIATION SYSTEM IN THE SECONDARY BEAM COURSE

The secondary beam line for medical use has been constructed, and its beam test has showed the expected performances[14]. To use this course for medical use, the control should be easy, and the beam-tuning time should also be short. To realize these requirements, we have developed an automatic tuning system. To achieve high reproducibility of the course, the dipole magnetic fields are controlled with NMR. Owing to these developments, easy and quick handling of the secondary beam course has been achieved. The tuning of the secondary beam course becomes easy and requires only about 20 minutes for ^{11}C. The production rate of ^{11}C was 0.2% with 97% purity, which suggests a possibility to directly irradiate a small tumour volume. As a next stage, we have started to construct the irradiation system with a spot scanning method and the verification systems. To use secondary beam of low intensity, such as ^{11}C, the efficiency of the irradiation system should be much higher than that of the

existing system in HIMAC, where wobbler magnets are used with a scatterer. From this reason the spot scanning method is adopted. This irradiation system is also interesting from the viewpoint of better dose concentration on the cancer volume. In this beam scanning, the horizontal and vertical scanning magnets are used. The energy will be changed by the range-shifter placed just in front of the patient as shown in Figure 1. This method simplifies the operation of the accelerator, because it is not necessary to change the beam energy in the accelerator including the beam transport line. This is particularly suitable for the irradiation with secondary beam, because all parameters of the beam course including the thickness of the production target and achromatic degrader are optimized with the given beam energy to obtain high secondary beam intensity with good purity. Table 1 summarizes the irradiation system.

As a verification system, we are now considering a positron camera and also PET. As for the positron camera, a prototype is being tested with RI source and ^{11}C beam. A pair of large NaI block attached with 109 phototubes in each is used to achieve higher efficiency. With this camera the pencil beam, whose diameter is as small as 1mm, will be used to measure the correct range in the complex human body. To shorten the measurement time and to inject the beam at the several points successively, ^{10}C beam is also under consideration.

If we irradiate cancer volume with ^{11}C, the PET can be used to measure the irradiated volume. This possibility requires an increase in the efficiency, which is possible with modern 3D data acquisition PET such as Siemens HR+. With this PET we have tested the image quality of the positron emitter in the patient, which was produced in the irradiation devices and patient with ^{12}C beam. Using the ^{11}C beam we can improve the image quality with higher statistics by about one order.

Table 1: Parameters of irradiation system.

Expected ion species	^{12}C, ^{11}C, ^{10}C
Distance between the last quadrupole and the patient	6 m
Target volume	10^3 cm^3
Scan field with magnets (x and y)	10 cm
Range shifter (max.)	30g/cm^2
Range modulation	5mm with ridge filter
Beam intensity	$< 6 \times 10^6$ pps
Beam monitors	two intensity monitors (main and sub) one profile monitor(x,y)
Collimator	Multi-leaves aperture (x,y) ±75 mm step width 2.5 mm thickness (Fe) 140 mm
Patient setting	chair, bed

Figure 1: Irradiation system for the secondary beam course.

4 DEVELOPMENTS OF MACHINE COMPONENTS

Encouraged with nice results of heavy ion therapy, there are developments that have possibility to be used in the dedicated machine for therapy with carbon beam.

One is design study of an injector linac with IH type for carbon beam of C^{4+}. Characteristic point of this type is its high shunt impedance, and it is possible to make short injector linac. It has structure of APF (Alternative Phase Focusing) with input and output energies are 65 keV/u and 6 MeV/u in the tentative design. This low input energy can be obtained directly from ion source, and this make the injector linac system simple.

Others are compact acceleration cavities in the synchrotron that hasn't tuning system. In one type all pass network (APN) is used to obtain wide frequency range, where the acceleration cavity is one element in the APN circuit. In another type of the acceleration cavity, low Q material (Magnetic Alloy) is used in the cavity to obtain wide frequency range. Because of no tuning system in the wide frequency range, higher harmonics can be added in the acceleration voltage. This possibility is important to suppress the space charge effect, and is important for the small and low injection energy ring, that should be necessary for dedicated synchrotron. The beam test with one of these cavities is presented in this conference[15].

ACKNOWLEDGEMENTS

REFERENCES

[1] Y.Hirao, et al "Heavy Ion Synchrotron for Medical Use" Nucl. Phys. A538,541c(1992).

[2] "Report on the clinical trial with heavy ion therapy" NIRS-M-127 in Japanese

[3] H.TSUJII, et al., "The current status and perspective of heavy-ion therapy" ICRO/√GRO6, 709-721, 1998.

[4] K.Noda, et al., "Slow beam extraction by a transverse RF field with AM and FM" NIM A 374 269-277, 1996

[5] Y.Futami, et al. "Development of 3-Dimentional Irradiation System for Heavy-Ion Radiation Therapy" Proc. of 10th symp. Acc. Sci. and Tech., 442-444, 1995

[6] E.Takada et al., "Present Status of HIMAC Synchrotron Control System" Proc. of 10th symp. Acc. Sci. and Tech., 309-311, 1995

[7] M.Torikoshi, et al., "Development of Automatic Tuning for High Energy Beam lines at HIMAC" PAC99

[8] Y.Sato, et al., "Recent Developments At The NIRS-HIMAC Injector" Linac Conference 1998

[9] A.Kitagawa et al. "Development of 18 GHz NIRS electron cyclotron resonance ion source with high-voltage extraction configuration" Rev. Sci. Instrum 69, 2 1998

[10] M.Kumada, et al. "High Performance Active Filter for the Power Supply of the HIMAC Synchrotron Magnet", EPAC96, 2358-2360, 1996

[11] N.Araki et al. "A Beam Spill Controll System at HIMAC" Proc. of 10th symp. Acc. Sci. and Tech., 272-274, 1995

[12] M.Kanazawa et al. "COD Measurement and Correction in HIMAC Synchrotron" EPAC96 1710-1712, 1996

[13] S.Sato, et al. "Non-destructive Beam Profile Monitor at HIMAC" Proc. of 10th symp. Acc. Sci. and Tech., 266-268, 1995

[14] S.Kouda, et al "New Secondary Beam Course for Medical Use in HIMAC" PAC, 1997, to be published. M.Suda, et al. "Secondary beam tuning system at HIMAC" Proc. Of 10th symp. Acc. Sci. and Tech., 442-444, 1997

[15] M.Yamamoto, et al., "Multi-harmonic Acceleration With High Gradient MA Cavity at HIMAC" in this proceeding

ECONOMIC ASPECTS OF COLD FOOD PASTEURIZATION

S. L. Bogart, Photon-Electric Pasteurization Corporation (US)[*], N. G. Tolstun, NIIEFA Delta (RF)

Abstract

The economics of cold food pasteurization are governed by a number of factors, including: the type of ionizing radiation source (X-Ray, or Gamma), cost and power of the source, pasteurization dose, location of the pasteurization facility, facility capacity factor, and the annualized costs. Using a costing procedure developed by Morrison [1], calculations for typical sources, locations, etc., have been updated using facility cost estimates prepared by a major U.S. construction firm and scalings from the Morrison data.

The "owner's cost" per pound of product is a function of the facility scale, showing an asymptote at ~ 100 kT (220 million pounds) per year of product. Likewise, the owner's cost significantly depends on the annualization interest rate. A "stand-alone" location of the pasteurization facility has an effect on the cost of the process due to the need to transport product from the meat plant to the facility, the labor for unloading and loading the product at the facility, and the unshared G&A costs at the facility. This increases processing costs and "borrows" into the shelf-life value of the product. An "integrated" location of the pasteurization facility (at the meat plant) minimizes processing cost (inclusive of special labeling) and best fits the operating characteristics of a typical meat plant (2 shift, 5 day week).

1 INTRODUCTION

Food irradiation has been thoroughly demonstrated to significantly reduce food contamination by pathological organisms by five orders of magnitude or more and extend shelf-life. Irradiation may be performed by: electron-beams, radioisotope gamma decay, and X-rays. The first is the most efficient in terms of energetics but has serious limitations on product thickness, homogeneity (e.g., need for boneless product), and packaging. The second is the "standard" of the irradiation industry. The third has been made possible by recent advancements in electron-beam source power sizes, costs, and energies.

We analyze the radioisotope and X-ray options as we conclude that only these meet the current and future requirements of the food manufacturing industry – penetrating, uniform, and cost-effective irradiation of food products in final shipping boxes. Electron-beams are limited to product thickness of ~3 inches in comparison with tens of inches for X-rays and Gamma rays.

X-ray machines come in "unit sizes" as they are designed for a certain maximum power. Radioisotope machine power is a function of the inventory of radioactive material (e.g., Co-60) which can be adjusted in facility design to meet the specific throughput requirements of a food manufacturing facility. Thus, to meet the needs of a specific facility, an X-ray machine may operate at less than its rated power output. This fact affects economic comparisons unless care is taken to fit the current accelerator technologies with the market needs.

Finally, irradiation plant scale and capacity factor affect food irradiation economics. Morrison showed that economies of scale essentially vanish after a plant processes on the order of 200 million pounds per year. We restrict our analysis to plants for which economies of scale should not be in effect. We capture plant capacity factor with two scenarios – 3 and 2 shift per day operation. The former fully utilizes the capital equipment. The latter is better suited to most meat plants in the U.S.

2 THE MODEL

We use the costing formalism developed by Morrison in 1989 and updated in the recent "Proposed Rules" [2] published by the USDA for "Irradiation of Meat and Meat Products." For "sources," we use X-rays and Co-60 with cost estimates for the former from a survey in 1996 and for the latter, from Morrison. For the "balance of plant" (including shielding, machinery, related expenses, escalation, fees, etc.) we use a hybrid of costs – some scaled from Morrison and others from estimates of a US Engineering & Construction firm. While the model is complex due to this "hybridization," care has been taken to properly allocate costs and escalation expenses.

The source characteristics are presented in Table 1. We treat three sources – a low-cost/high-power accelerator, a high-cost/low-power accelerator, and Cobalt-60. As a special case, we also assess the effect of the high-cost accelerator operating at 7.5 MeV versus the current limit of 5.0 MeV. For Cobalt-60 irradiators, we "scale" the facility with the Cobalt loading required to meet the throughput and assign a nominal price for the source material at $1.20/Ci.

The case parameters presented in Table 2 correspond to the two highest through-put Morrison cases (208 and 416 million pounds per year for poultry). For an "integrated" plant (irradiation performed at the meat manufacturing facility), the lower of the two throughput cases (190 Tonne/shift) would meet the needs of ~ ½ of the ground meat production facilities in the U.S. For the higher

* - elbogart@aol.com

throughput level (380 Tonne/shift), there is no known plant in the U.S. requiring this production level at this time. Thus, such an integrated facility would be expected to irradiate other beef products as well. For poultry, the low throughput rate for the integrated plant would meet the needs of virtually all of the current U.S. manufacturing

facilities. The "stand-alone" plants have lower hourly throughput rates as they run three versus two shifts for the same annual production rates. On a shift basis, they are better sized for a large fraction of U.S. meat manufacturers.

Table 1 – Irradiation Source Parameters

Source Parameters	Low-Cost Accelerator	High-Cost Accelerator	Radioisotope Co-60
Unit Power (kW)	500	200	As Req.
Unit Cost (1000 $ or $/Ci)	2000	4000	1.2
Unit Cost/kW of E-beam (1000$/kW)	4	20	NA
Unit Cost/kW of X-ray/Gamma-ray (1000$/kW)	60	240	80
Net Utilization Efficiency	0.4	0.4	0.25-0.4
Unit Cost/kW of X-ray: 7.5 MeV (1000$/kW)		155	

Table 2 – Case Parameters

Sources	Balance of Plant		Notes
X-Ray	Based on Current A&E Costs Based on Product Throughput		Based on Accelerator Unit Sizes
Radioisotope (Gamma)	Scaled from 1989 Morrison Based on Product Throughput		Based on Product Throughput
Plant Type			
Stand Alone (Three 7 Hour. Shifts) Adders to Irradiation	Low Rate (Tonne/Shift) 130	High Rate (Tonne/Shift) 260	225 to 450 Million Pounds per year 0.2 Cents each for transportation and labeling
Integrated (Two 8 Hour Shifts) Adders to Irradiation	190	380	215 to 430 Million Pounds per year 0.2 Cents for labeling
Major Cost Variables			
Annualization Interest Rate (%)	5 to 15	5 to 15	All Cases
Dose (kGy)	2 to 3	2 to 3	Range for Selected Cases – 2.5 Nominal
Cost of Cobalt ($/Ci)	1.2 to 1.5	1.2 to 1.5	Range for Selected Costs – 1.2 Low

As noted in Table 2, the "source" scaling is based on integer accelerator sizes and continuous Cobalt-60 requirements. This means that, for Cobalt-60, the radiative power will exactly meet the selected processing rate requirements but, for the accelerators, the available radiative power will always exceed the required power for the selected processing rate – e.g., the capacity factor for the accelerator plant will be less than one for both integrated and stand-alone plants.

Costs for the X-ray plant "balance of plant" were developed from estimates prepared in 1998 by a U.S. architect & construction firm and are linearly scaled according to plant hourly throughput. For the Cobalt-60 plant, we used the 1988 Morrison estimates escalated to 1999 at 4 percent per year and, again, linearly scaled according to plant hourly throughput. For the plant processing rates analyzed, these linear scalings are justified as there were no economies of scale (capital cost) above Morrison's 208 million pound/year throughput.

Costs for transportation (stand-alone plant) and labeling (both plants) were taken from the USDA promulgation of the proposed meat irradiation rules – $0.002/lb each. We accept these estimates, but note that they will be product and process-specific. We also note that no costs were provided for the development and production of packaging materials that may be required for irradiation. We examine the parametric variation of unit costs ($/lb) as a function of "interest rate" used to calculate the annualized costs. Morrison assumed 5% which we felt was low in comparison with the food industries' required rate of return. An interest rate of 15%, the upper bound, still may be too low. Finally, our model includes the capability to assess the effect of dose and Cobalt costs, etc., on overall costs. We do not parametrically assess these effects, but use them to examine special cases.

3 RESULTS

Table 3 presents the parametric results for both capital investment and unit costs. For the former, it is evident that

the flat economies-of-scale prevail in the stand-alone plant and, to a lessor extent, in the integrated plant – the latter is due to a better fit of integer accelerators with plant requirements at higher throughput.

Table 3 – Parametric Analysis Results

Plant Type→	Stand Alone Plant (3 shift/day)			Integrated Plant (2 shift/day)		
	Low-cost Accelerator	High-cost Accelerator	Radioisotope Cobalt-60	Low-cost Accelerator	High-cost Accelerator	Radioisotope Cobalt-60
Costs↓	130 T/Shift			190 T/Shift		
Investment (Million $)	5.74	12.16	8.50	8.47	16.97	10.64
	Total Cost (Cents/lb)			Total Cost (Cents/lb)		
Annualization Rate – 5%	1.13	1.59	1.41	0.96	1.56	1.33
Annualization Rate – 10%	1.23	1.78	1.55	1.10	1.84	1.51
Annualization Rate – 15%	1.33	2.00	1.71	1.25	2.15	1.71
	260 T/Shift			380 T/Shift		
Investment (Million $)	11.48	24.31	17.00	14.67	29.33	21.27
	Total Cost (Cents/lb)			Total Cost (Cents/lb)		
Annualization Rate – 5%	1.03	1.48	1.30	0.81	1.33	1.26
Annualization Rate – 10%	1.12	1.67	1.44	0.93	1.57	1.44
Annualization Rate – 15%	1.22	1.89	1.60	1.06	1.84	1.64

In contrast with intuition, the stand-alone plant has poorer performance than the integrated plant. This is due to the relatively low annualized irradiation costs in comparison with the transportation cost "adder" for the stand-alone plant versus the lower annual costs for the integrated plant from reduced manpower.

The interest rate for annualizing costs is seen to have a significant effect for the higher cost plants. However, the overall unit costs for all cases are quite small and the extrema differ by only ~ 1.2 cent over the parametric range. The low-cost, high-power accelerator offers the minimum cost, followed by Cobalt-60, with the high-cost/low-power accelerator being the highest.

A calculation was made for the high-cost/low-power accelerator at 7.5 MeV for product throughputs that resulted in a nearly integer number of accelerators at an interest rate of 10% (midrange) to determine if this higher energy operation had a significant effect on unit costs. For the stand-alone plant, the unit costs were 1.54 and 1.41 cents/lb for processing rates of 104 and 208 Tonne/shift, respectively. For the integrated plant, the unit costs were 1.38, 1.25, and 1.19 cents/lb for processing rates of 119, 238, and 476 Tonne/shift, respectively. This resulted in costs that were competitive to Cobalt-60 for the stand-alone plant and less expensive than Cobalt-60 for the integrated plant (but still more costly than the low-cost/high-power accelerator).

A special case was run to assess the effect of a higher Net Utilization Efficiency (40%) for Cobalt-60, based on reports that near 40% had been demonstrated in existing plants. At a 10% interest rate, this reduced the costs of Cobalt-60 irradiation to 1.32 and 1.21 cents/lb for the stand-alone plant and 1.17 and 1.10 cents/lb for the integrated plant. These are significant improvements.

Last, a case was run to assess the effect of higher dose (3.5 kGy) for an interest rate of 10%. For the twelve cases at 10% in Table 3, the average increase in unit cost was less than 20% for the 40% increase in dose. This is due to the significance of the costs unrelated to the irradiation process – e.g., labeling and transportation.

4 CONCLUSIONS

Irradiation costs in general:

- Annualized irradiation unit costs are very low in comparison with product production costs. However, the cost differences between technologies can be $1-2 million/year;
- Packaging and transportation costs significantly add to irradiation costs. Other costs, such as oxygen control, may increase unit costs;
- Capital cost differences may be the major selection discriminator because of low unit costs;
- Integrated irradiators have lower unit costs because of lower transportation and manpower costs.

Irradiation costs for specific technologies:

- The least-cost technology is the low-cost accelerator, followed by Cobalt-60 then the high-cost accelerator;
- X-ray machine selection should be made to meet the processing requirements of meat production plants;
- Irradiation environment optimization should be performed for all irradiation technologies.

5 REFERENCES

[1] Morrison, R.M. "An Economic Analysis of Electron Accelerators and Cobalt-60 for Irradiating Food," USDA, TBN 1762, 1989.

[2] Proposed Rules, USDA, Food Safety and Inspection Service, RIN 0583-AC50, "Irradiation of Meat and Meat Products."

HALO FORMATION IN INTENSE BUNCHED BEAMS *

A.V. Fedotov† and R.L. Gluckstern
Physics Department, University of Maryland, College Park, MD 20742

Abstract

The latest designs for high current ion linacs (Accelerator for the Transmutation of Waste, Accelerator for the Production of Tritium, Heavy Ion Drivers, Spallation Neutron Source Injector) require minimal radioactivation by the beam striking the beam pipe. As a result, efforts are being made to understand and control the growth of beam halo. There is general agreement that halos develop as a result of the parametric resonance between the ion oscillations in the beam bunch and collective oscillations of the bunch itself induced by mismatch in the linac. Analytic studies for a 2-D KV beam were found to give excellent agreement with corresponding computer simulations, which were then extended to other 2-D beams. Recently, analytic and numerical studies were performed for 3-D beam bunches (6-D phase space distributions), focusing attention on the formation of longitudinal halos and the possibility of bunch growth or loss of longitudinal bunch stability, as well as coupling between the longitudinal and transverse halos.

1 INTRODUCTION

The need for high current in a variety of new accelerator applications has focused a great deal of attention on understanding the phenomenon of halo formation in ion beams, which can cause excessive radiation of the accelerator. This understanding requires both an analytical model which explains available observations as well as computer simulations to verify both the assumptions of the model and its predictions.

Analytic models have been developed to study halo development in both 2-D beams and 3-D beam bunches in a linac. These models suggest that the most likely explanation for the halos which have been observed and which are likely to be seen in future high current linacs involves the parametric resonance between the collective modes which describe "breathing" and the motion of individual ions. When these models are used in conjunction with multiparticle simulations involving millions of particles, which are now practical with supercomputers and parallel processing, one can have great confidence in the predictions for halo formation and emittance growth which are so crucial for the designs of high current acceleration of short beam bunches.

2 2-D MODEL

Early attention was devoted to the analytic study of 2-D round beams in a continuous focusing channel. In particular, the KV distribution [1], a hyperspherical shell in the 4-D phase space with the self-consistent [2] distribution

$$f(H) = N\delta(H_0 - H), \qquad (1)$$

where

$$H = \frac{mv^2}{2} + \frac{kr^2}{2} + e\Phi_{sc}(r), \qquad (2)$$

had the useful features of a uniform charge density within the beam, and uniform density in the x and y phase space projections. Here H_0 and N are constants, k is the constant external focusing gradient, and $e\Phi_{sc}(r)$ is the potential energy at r due to space charge.

Use of the equation for the beam envelope [3] permitted the analytic description of a "breathing" beam, in which the charge density oscillated between too tight and too loose a match to the external focusing force. These oscillations provided a periodic force to the ion motion, which was simple harmonic as long as the ions remained inside the beam. But for ions which traveled beyond the beam boundary, the oscillations were non-linear. In this case the ion's non-linear motion in the presence of a periodic force allowed it to be trapped in the parametric resonance, where the breathing frequency was twice the ion oscillation frequency. The analytic model thus predicted the formation of a "halo" [4] for certain combinations of mismatch and tune depression. The numerical simulations using the "particle-core" model confirmed the validity of the models, and pointed as well to the existence of chaotic motion as the tune depression became more severe [5]-[9].

Subsequent work focused on the possible mechanism for particles escaping from the beam into the region of non-linear oscillation [10]. In addition, numerical simulations were run for other, more physical, self-consistent stationary distributions of the form

$$f(r, v) = N(H_0 - H)^n, \qquad (3)$$

with $n = 0, 1$ [11]. These simulations exhibited the same halo structure and phase space patterns seen for the KV distribution, but with somewhat different quantitative dependence on mismatch and tune depression. The localization of the halo radius to approximately the same value predicted by the KV distribution gave the linac designers confidence that a beam pipe wall could be placed far enough from the beam to avoid intercepting the halo particles.

3 3-D MODEL

Attention then shifted to short 3-D beam bunches of ellispoidal shape with $c/a = $ length/width ratio in the range 2-4 [12, 13]. We continued our effort to study the self-consistent phase space stationary distributions of the form

$$f(\boldsymbol{r}, \boldsymbol{v}) = N(H_0 - H)^n, \qquad (4)$$

but this time, for $n = -1/2$, the differential equation for the charge density was linear and could be solved analytically [13]. In addition, for $c/a > 2$, the "breathing" modes could be approximately separated into transverse and longitudinal modes, each of which was capable of generating a halo. Thus the picture was of a beam bunch which, when mismatched accordingly, generated either a transverse or a longitudinal halo, or both. The signature of the longitudinal halo was the same as that of the transverse halo (a "peanut diagram" in the phase space projection). The transverse and longitudinal mismatch and tune depression parameter space was extensively explored with numerical simulations [13]. But a new concern surfaced: Would the longitudinal halo permit the loss of ions from the rf bucket? Unfortunately, the bucket "walls" cannot be moved far away without increasing the length and cost of the linac. Details about effects of non-linear RF fields can be found in [14].

Other issues involving halo formation were looked at, including equipartitioned distributions which were rms matched but not self-consistent [15]. These involved a rapid initial phase space redistribution, leading to a relatively small change in the parameters and extent of the halo formation due to the mismatch. In addition, they also point to the presence of a transverse-longitudinal coupling which allows either kind of halo to develop from either a transverse or longitudinal mismatch [15].

4 STATIONARY 6-D PHASE SPACE DISTRIBUTION

4.1 Analytic approximation to a spheroidal bunch

We take for the azimuthally symmetric 6-D phase space distribution

$$f(\boldsymbol{x}, \boldsymbol{p}) = N(H_0 - H)^{-1/2}, \qquad (5)$$

where

$$H = k_x r^2/2 + k_z z^2/2 + e\Phi_{sc}(\boldsymbol{x}) + mv^2/2. \qquad (6)$$

Here $\boldsymbol{p} = m\boldsymbol{v}$, $r^2 = x^2 + y^2$, and k_x, k_z are the smoothed transverse and longitudinal restoring force gradients. The quantity $\Phi_{sc}(\boldsymbol{x})$ is the electrostatic potential due to the space charge of the bunch. The distribution is normalized such that

$$\int d\boldsymbol{x} \int d\boldsymbol{p} f(\boldsymbol{x}, \boldsymbol{p}) = 1. \qquad (7)$$

The charge distribution corresponding to Eq. (5) is

$$\begin{aligned} \rho(\boldsymbol{x}) &= Q \int d\boldsymbol{p} f(\boldsymbol{x}, \boldsymbol{p}) \\ &= NQm^3 \int d\boldsymbol{v} \left[G(\boldsymbol{x}) - \frac{mv^2}{2} \right]^{-1/2}, \quad (8) \end{aligned}$$

where

$$G(\boldsymbol{x}) \equiv H_0 - \frac{k_x r^2}{2} - \frac{k_z z^2}{2} - e\Phi_{sc}(\boldsymbol{x}). \qquad (9)$$

Performing the integral over $d\boldsymbol{v} \equiv v^2 dv d\Omega_v$ in Eq. (8) leads to

$$\rho(\boldsymbol{x}) = QG(\boldsymbol{x}) / \int d\boldsymbol{x} G(\boldsymbol{x}), \qquad (10)$$

where the normalization constant satisfies

$$2\sqrt{2}\pi^2 Nm^{3/2} \int d\boldsymbol{x} G(\boldsymbol{x}) = 1. \qquad (11)$$

From Eq. (9) and Poisson's equation, we write

$$\nabla^2 G(\boldsymbol{x}) = -k_s - e\nabla^2 \Phi_{sc} = -k_s + (e/\epsilon_0)\rho(\boldsymbol{x}), \quad (12)$$

where

$$k_s = 2k_x + k_z. \qquad (13)$$

Using Eq. (10), we obtain the partial differential equation for $G(\boldsymbol{x})$

$$\nabla^2 G(\boldsymbol{x}) = -k_s + \kappa^2 G(\boldsymbol{x}), \qquad (14)$$

where

$$\kappa^2 = (eQ/\epsilon_0) / \int d\boldsymbol{x} G(\boldsymbol{x}). \qquad (15)$$

The solution of Eq. (14) for an axisymmetric, spheroidal shaped bunch can most easily be written in the spherical coordinates R, θ for which

$$z = R\cos\theta, \ r = R\sin\theta, \qquad (16)$$

as

$$G(\boldsymbol{x}) = (k_s/\kappa^2)g(\boldsymbol{x}), \qquad (17)$$

where

$$g(\boldsymbol{x}) = 1 + \sum_{\ell=0}^{\infty} \alpha_\ell P_{2\ell}(\cos\theta) i_{2\ell}(\kappa R). \qquad (18)$$

Here $P_{2\ell}(\cos\theta)$ are the even (fore-aft symmetric) Legendre polynomials and $i_{2\ell}(\kappa R)$ are the spherical Bessel functions (regular at $\kappa R = 0$) of imaginary argument.

Since $g(\boldsymbol{x})$ is proportional to the charge density, the edge of the bunch is defined as the border $g(\boldsymbol{x}) = 0$, closest to the origin. We therefore choose the α_ℓ's so that the surface of the bunch reproduces, as closely as possible, the ellipsoidal surface.

We also note that $m\langle\dot{x}^2\rangle = m\langle\dot{y}^2\rangle = m\langle\dot{z}^2\rangle = m\langle v^2\rangle/3$ because H depends only on v^2 and $\boldsymbol{x}$. Thus our choice of a stationary distribution of the form $f(H)$ *automatically* corresponds to equipartition (equal average kinetic energy in the three spatial directions).

4.2 Numerical implementation

We have developed a 3-D particle-in-cell (PIC) code HALO3D to test the analytic model described above, and to explore halo formation [13]. The single-particle equations of motion are integrated using a symplectic, split-operator technique [16]. The space charge calculation uses area weighting ("Cloud-in-Cell") and implements open boundary conditions with the Hockney convolution algorithm [17]. The code runs on parallel computers, and in particular, the space charge calculation has been optimized for parallel platforms using the Ferrell-Bertschinger method [18]. Some details about the code can be found in [19].

We initially populate the 6-D phase space according to Eq. (5), and then mismatch the x, y, z coordinates by factors $\mu_x = \mu_y = 1 + \delta a/a$, $\mu_z = 1 + \delta c/c$ and the corresponding momenta by $1/\mu_x = 1/\mu_y, 1/\mu_z$, with a, c being the minor and major semiaxes of our spheroidal bunch, respectively.

4.3 Longitudinal halo

We performed a systematic study for different c/a and mismatch factors in the range of interest [20], by looking at the halo extent at the time when the beam comes to a roughly saturated state after the development of a halo. Our new result is the dependence of the halo extent on tune depression. One sees a significant increase in halo extent for severe tune depressions. In addition the halo extent clearly depends on the mismatch parameter. The approximately linear dependence of the halo extent on the mismatch factor μ indicates that a serious effort should be made to match the beam to the channel as accurately as possible.

Simulation results [13] show that the halo intensity (roughly defined as the fraction of particles outside the core in phase space) depends primarily on the mismatch. Severe mismatches lead to several percent of the particles in the halo, which is clearly outside acceptable limits. No significant dependence of halo intensity on the tune depression is seen. Also, for tune depression $\eta_z \leq 0.4$ the clear peanut diagram in the longitudinal phase space now has a chaotic behavior.

One more important feature is how fast the halo develops. We first make the observation that for comparable mismatches the longitudinal halo develops much faster than the transverse halo when the mismatches and/or tune depressions are not severe. Such behavior simply occurs because for fixed charge we have $\eta_z < \eta_x$ for elongated equipartitioned bunches. For severe mismatches and/or tune depressions both the longitudinal and transverse halos develop very quickly. Of particular interest is the clear dependence of halo onset on tune depression. Specifically, for more severe tune depression the halo starts to develop earlier. More details can be found in [13].

4.4 Transverse halo

The transverse halo closely duplicates all the features observed for non-linear stationary distributions in 2-D simulations [11]. The agreement between 2-D and 3-D simulations is very good. The only two differences seen are related to the onset/rate of halo development. In the recent 3-D simulations there is a clear dependence on the tune depression which was not the case in the corresponding 2-D simulations [11]. The second difference is that the transverse halo in the 3-D simulations develops significantly faster than in 2-D for comparable mismatches and tune depressions. More details can be found in [13].

4.5 Coupling effects

In performing 3-D simulations we encounter halo formation in a beam bunch, where we clearly see coupling between the longitudinal and transverse motion. It was already noted [13] that due to the coupling between r and z, a transverse or longitudinal halo is observed even for a very small mismatch (less than 10%) as long as there is a significant mismatch in the other plane. Further numerical investigation [15] of this question showed that the effect of coupling becomes extremely important for nearly spherical bunches ($c/a \leq 2$) which is typical of the parameter range of interest for the APT design [20]. For example, for the short bunch with $c/a = 2$, with only a longitudinal initial mismatch ($\mu_z = 1.5$, $\mu_x = \mu_y = 1.0$), one finds particles at large amplitude in both the longitudinal and transverse directions [15].

5 NON-STATIONARY 6-D PHASE SPACE DISTRIBUTION

After we established the parameters which lead to halo formation in 3-D beam bunches for the self-consistent 6-D phase space stationary distribution [13], we explored rms matched distributions which are *not* self-consistent, to determine the extent to which the relatively rapid redistribution of the 6-D phase space contributes to the formation of halos [15].

5.1 Stability of the matched distribution

We have shown that an rms matched 3-D beam can produce transverse and/or longitudinal halos for a wide range of space charge intensity even when it is initially perfectly matched. Of course, from a practical point of view such halos are not important because the halo extent is very small for the mismatch factor $\mu = 1.0$ (the detailed study of the halo extent on a mismatch factor was presented in [13, 15]).

The redistribution process in a non-stationary beam with initial zero mismatch causes the core to perform an oscillation about its initial distribution which is equivalent to introducing a relatively small mismatch for the stationary distributions. The important consequence is that the redistribution process by itself (zero initial rms mismatch) does

not lead to significant emittance growth [15].

5.2 Initially mismatched beam

Numerical 3-D simulations with the initially mismatched non-stationary distributions [15] confirmed all the characteristics of halos observed for the stationary distribution [13]. The main difference is that for a non-stationary distribution the halo extent is larger (especially for the Gaussian) than the halo extent of the stationary distribution with the same initial mismatch parameters.

6 HALO FORMATION IN A PERIODIC FOCUSING CHANNEL

The halo properties in periodically focused cases have been also extensively studied [21]-[27]. Apart from the instabilities due to the structure-driven resonances, these studies showed a close resemblance to the continuous focusing channel results.

7 OTHER ISSUES INVOLVING HALO FORMATION

7.1 Coulomb scattering

Various mechanisms can potentially cause beam halo. Some recent studies suggested that Coulomb collisions in the beam bunch can contribute significantly to beam bunch growth and halo development in linear accelerators. Despite the general belief that collisions are not important it is clear that a rigorous treatment of this question is needed. In an effort to explore this issue in detail we have undertaken an analysis of the effects of Coulomb scattering between ions in a self-consistent spherical bunch [28].

We have calculated the effect of single Coulomb scattering of a self-consistent 6-D distribution for a spherical beam bunch. In this calculation we found that single collisions are capable of populating a thin spherical shell around the beam bunch. This result is for the stationary phase space distribution with $n = -1/2$, but it is probably quantitatively similar for other higher values of n. When the beam is non-equipartitioned or the beam with the stationary distribution is rms mismatched, the thickness of the shell can be significantly larger, depending on the equipartitioning factor. However, the rate of this process is very small. For the relatively singular distribution with $n = -1/2$, a proton bunch with a normalized emittance $\epsilon_N \sim 10^{-6}$ [m rad] and a radius of 1 cm will populate the shell with a probability of 10^{-11} per kilometer of linac. For distributions with $n > 0$, this rate of population is further reduced by a factor 10^{-4}.

Our conclusion is that the effect of single Coulomb collisions on halo development in high current ion linear accelerators is not important. A similar analysis for non-stationary distributions was performed by N. Pichoff [29], who arrived at the same conclusions.

We then related our analysis to diffusion caused by many small angle Coulomb collisions, with the conclusion that the effect of multiple Coulomb collisions in halo development in high current ion accelerators is also expected not to be important [28].

7.2 Halo formation in circular accelerators

Space-charge can also lead to emittance growth and halo generation in circular accelerators. In undertaking a study of the space-charge dynamics in high intensity rings one needs to consider two different effects.

The first one is associated with the intrinsic halo formation due to the core mismatch, corresponding to a parametric resonance of the coherent frequency with twice the incoherent depressed tune of individual ions. Although the tune depression in the ring is very small compared with high intensity linacs this effect will still generate a halo of significant size around the beam core.

The second effect is associated with the machine resonances due to the magnet imperfections, and is governed by the resonant effect of different coherent mode frequencies [30]-[31].

8 SUMMARY

Analytic models have been developed to study halo development in both 2-D beams and 3-D beam bunches in a linac. The detailed study requires both an analytical model which explains available observations as well as computer simulations to verify both the assumptions of the model and its predictions.

Our recent contributions to these efforts have been the construction of a model which identifies a major mechanism for transverse halo formation [4], followed by the construction of a self-consistent 6-D phase space distribution for studies of halo formation in spheroidal bunches in a linear external confining field [13]. What we found [4] is that halo formation appears to arise from a parametric resonant coupling of individual particle oscillations with collective oscillation of the charged bunch, primarily those describing the breathing modes. We explored the dependence of the halo properties (extent, rate of growth, intensity, etc.) on the longitudinal and transverse rms tune depressions and mismatches [13]. These studies automatically assumed equipartition of kinetic energy between the longitudinal and two transverse directions. We then performed numerical studies with an rms matched, but otherwise non-self-consistent 6-D distribution [15]. In these studies we found that starting with a non-self-consistent distribution altered the parameters for halo formation obtained for the self-consistent distribution only slightly.

Our main conclusion is that the longitudinal halo in a linac is of great importance. The control of the longitudinal halo could be challenging if the phase width of a beam bunch in the RF bucket cannot be made sufficiently small.

9 REFERENCES

[1] I.M. Kapchinsky, Theory of Resonance Linear Accelerators, Harwood Academic Publishers, New York, 1985.

[2] Any distribution which is only a function of the Hamiltonian will be self-consistent.

[3] M. Reiser, Theory and Design of Charged Particle Beams, Wiley, New York (1994).

[4] R.L. Gluckstern, Phys. Rev. Letters 73, 1247 (1994).

[5] J.S. O'Connell, T.P. Wangler, R.S. Mills, and K.R. Crandall, in Proceedings of the 1993 Particle Accelerator Conference (IEEE, Washington, DC, 1993), p. 3657.

[6] R.A. Jameson, in 'Frontiers of Accelerator Technology' (Proceed. of the Joint US-CERN-Japan Intern'l School, 1994), World Scient., Singapore (1996).

[7] J.M. Lagniel, Nucl. Inst. Meth. A345 (1994) 46; A345 (1994) 405.

[8] A. Riabko, M. Ellison, X. Kang, S.Y. Lee, D. Li, J.Y. Liu, X. Pei, and L. Wang, Phys. Rev. E 51, 3529 (1995).

[9] H. Okamoto and M. Ikegami, Phys. Rev. E 55, 4694 (1997).

[10] R.L. Gluckstern, W-H. Cheng, and H. Ye, Phys. Rev. Letters 75, 2835 (1995); R.L. Gluckstern, W-H. Cheng, S.S. Kurennoy and H. Ye, Phys Rev. E 54, 6788 (1996).

[11] R.L. Gluckstern and S.S. Kurennoy, in Proceedings of the 1997 Particle Accelerator Conference, Vancouver, Canada (IEEE, Piscataway, NJ, 1998), p. 1950.

[12] J.J. Barnard and S.M. Lund, in Proceedings of the 1997 Particle Accelerator Conference, Vancouver, Canada (IEEE, Piscataway, NJ, 1998), p. 1929; S.M. Lund and J.J. Barnard, ibid., p. 1932.

[13] R.L. Gluckstern, A.V. Fedotov, S. Kurennoy and R. Ryne, Phys. Rev. E 58, 4977 (1998).

[14] J.J. Barnard, S.M. Lund and R.D. Ryne, in Proceedings of the 1998 Linear Accelerator Conference, Chicago, IL (1998).

[15] A.V. Fedotov, R.L. Gluckstern, S.S. Kurennoy and R.D. Ryne, Phys. Rev. ST Accel. Beams, 2, 014201 (1999).

[16] E. Forest, J. Bengtsson, and M.F. Reusch, Phys. Lett. A 158, 99 (1991).

[17] R.W. Hockney and J.W. Eastwood, Computer Simulation Using Particles, Adam Hilger, NY (1988).

[18] R. Ferrell and E. Bertschinger, Int. J. Mod. Phys. C 5, 933 (1994).

[19] R. Ryne, S. Habib, J. Qiang, K. Ko, Z. Li, B. McCandless, W. Mi, C. Ng, M. Saparov, V. Strinivas, Y. Sun, X. Zhan, V. Decyk, G. Golub, in Proceedings of the 1998 Linear Accelerator Conference, Chicago, IL (1998).

[20] APT Conceptual Design Report, Los Alamos Report No. LA-UR-97-1329, 1997.

[21] C. Chen and R.C. Davidson, Phys. Rev. E 49, 5679 (1994).

[22] C. Chen and R.C. Davidson, Phys. Rev. Lett. 72, 2195 (1994).

[23] Q. Qian, R.C. Davidson and C. Chen, Phys. Plasmas 1, 3104 (1994).

[24] S.Y. Lee and A. Riabko, Phys. Rev. E 51, 1609 (1995).

[25] Q. Qian and R.C. Davidson, Phys. Rev. E 53, 5349 (1996).

[26] M. Ikegami and H. Okamoto, Jpn. J. Appl. Phys. 36, 7028 (1997).

[27] M. Pabst, K. Bongardt and A. Letchford, in Proceedings of the 1998 EPAC (Stockholm, Sweden, 1998), p. 146.

[28] R.L Gluckstern and A.V. Fedotov, Coulomb Scattering Within a Spherical Beam Bunch in a High Current Linear Accelerator, these Proceedings; submitted for publication in Phys. Rev. ST Accel. Beams, 1999.

[29] N. Pichoff, DAPNIA/SEA Report 98-46, France (1998).

[30] R.L. Gluckstern, in Proceedings of the 1970 Linear Accelerator Conference, edited by M.R. Tracy (Fermilab, Batavia, IL), p. 811.

[31] R. Baartman, AIP Conference Proceeding 448, edited by A.U. Luccio and W.T. Weng (AIP, N.Y., 1998), p. 56; and references therein.

BEAM DYNAMICS DESIGN AND SIMULATION STUDIES OF THE APT SUPERCONDUCTING LINAC

T. P. Wangler, B. Blind, S. Nath, R. D. Ryne, and K. R. Crandall*

Los Alamos National Laboratory, Los Alamos, NM 87545 USA
*Techsource, Santa Fe, NM 87594-1057

1 APT LINAC

The 100-mA Accelerator for Production of Tritium (APT) nominal design[1],[2] consists of a normal-conducting proton linac to 211-MeV, followed by a 700-MHz, cw superconducting linac to 1030 MeV. The APT superconducting linac accelerates the beam using two distinct 5-cell elliptical superconducting-cavity shapes, designed with cell lengths corresponding to two different geometric beta values β_G=0.64 and 0.82. A summary of the main parameters is shown in Table 1, and the beam-dynamics parameters are given in Table 2.

Table 1. APT Superconducting Linac Parameters

Parameter	β_G=0.64 section 1a	β_G=0.64 section 1b	β_G=0.82 section 2
Input energy	211	242	471
β_{MIN}	0.578	0.607	0.746
β_{MAX}	0.607	0.746	0.879
E_A(MV/m)	6.1 to 5.4	5.1 to 5.3	7.1 to 5.3
E_{PK}/E_A	3.12	3.12	2.77
B_{PK}/E_A(G/MV/m)	69.3	69.3	62.7
Bore radius (mm)	65	65	80
Cavs./klystron	2	3	2
Cavs./cryomod.	2	3	4
No. cryomods.	6	30	35
P_{BEAM}/cav. (MW)	0.28	0.28	0.42
$P_{COUPLER}$ (MW)	0.14	0.14	0.21

2 LINAC PARAMETER ISSUES

Our design approach takes advantage of the large velocity acceptance of the superconducting cavities. As a guide to an initial layout, an analytic model of multi-cell cavities excited in a π-mode was used to provide an expression for the transit-time factor T as a function of particle velocity. A simple cavity-field distribution was assumed where the fields are uniform in the accelerating gaps and zero immediately outside the gaps. For a cavity with N identical cells, T can be expressed as a product of two separate factors $T=T_G T_S$. The gap factor T_G, which is also the transit-time factor for a single gap of length g, RF wavelength λ, and particle-velocity β, is given by the expression $T_G =\sin(\pi g/\beta\lambda)/(\pi g/\beta\lambda)$. The synchronism factor T_S is a function of N and of the ratio of the local velocity, β, to the cavity geometric velocity, $\beta_G =2L/\lambda$,

where L is the cell length. The synchronism factor is given by:

$$T_S = \begin{cases} (-1)^{\frac{N-1}{2}} \cos(N\pi\beta_G/2\beta)/N\cos(\pi\beta_G/2\beta), N\,odd \\ (-1)^{\frac{N}{2}+1} \sin(N\pi\beta_G/2\beta)/N\cos(\pi\beta_G/2\beta), N\,even \end{cases} \quad (1)$$

Equation 1 can be compared with direct numerical computation of T for the real cell shape. We find that the velocity dependence in the model is modified when penetration of the fields into the beam pipe on the end cells is included. For the two 5-cell APT elliptical cavities, the model gives a good fit to the numerical results when we choose $g=0.463\beta_G\lambda$ in the expression for T_G, and we replace β_G by $1.04\beta_G$ in Eq.1.

Table 2. Beam Dynamics Parameters*

Parameter	β_G=0.64 sect. 1a	β_G=0.64 sect. 1b	β_G=0.82 sect. 2
Quad lattice type	Doublet	Doublet	Doublet
Lattice period (m)	4.88	6.18	8.54
Synch. phase (deg)	-30 to -35	-30 to -42	-30
I=0 transv. phase adv./period (deg)	78 to 63	80 to 58	81 to 72
I=0 long. phase adv./period (deg)	46	56 to 40	53 to 25
Transverse tune-depression ratio	0.43 to 0.37	0.39 to 0.42	0.44 to 0.62
Longitudinal tune-depression ratio	0.33 to 0.37	0.36 to 0.40	0.39 to 0.34
Trans. rms norm. emittance (mm-mrad)	0.23 to 0.24	0.24 to 0.26	0.26 to 0.25
Long. rms norm. emittance (deg-MeV)	0.38 to 0.36	0.36 to 0.42	0.42 to 0.58
Rms phase width (deg)	4.1 to 2.9	3.5 to 2.4	2.5 to 2.1
Aperture radius/max rms beam size	24 to 30	22 to 31	33 to 51

* Values are quoted for zero machine errors. Including realistic machine errors typically doubles the emittances, and gives tune depressions greater than 0.5.

For APT the RF power delivered to the beam greatly exceeds the power dissipated in the superconducting walls. Then, the rf power required per cavity, P_C, is approximately equal to the beam power, which is given as the product of the beam current times the particle energy gain ΔW per cavity, as:

$$P_C = I\Delta W / q = IE_A \frac{T(\beta)}{T_{MAX}} \cos(\phi) N\beta_G \lambda / 2 \qquad (2)$$

The beam current I is averaged over an RF period, E_A is the accelerating gradient defined as the product of the spatial average of the axial accelerating field times the transit-time factor $T_{MAX}=T(\beta_T)$, where the velocity β_T gives the maximum transit-time factor. $T(\beta)$ is the transit-time factor at the local velocity β of the beam centroid, ϕ is the phase of the field when the beam centroid is at the center of a cavity, and N is the number of cells per cavity. The velocities, β_T and β_G, are not exactly equal because of the gap factor T_G, which increases with increasing particle velocity.

Among the design parameters that must be chosen for each section (each section uses identical cavity shapes) of a proton superconducting linac include N, β_G, E_A and ϕ. One must also choose the number of sections, and the minimum and maximum velocities β_{MIN} and β_{MAX} for each section. These parameters must be chosen consistent with the design objectives, and for APT there were five goals. 1) Deliver the maximum usable power per klystron. 2) Maximize the number of cavities that are able to perform within the design specifications of accelerating gradient and peak surface fields. 3) Provide acceptable beam-dynamics performance. 4) Minimize the overall accelerator length. 5) Minimize the number of sections to reduce the overall cavity-development effort. These requirements cannot all be satisfied simultaneously. The best that can be done is to find an acceptable compromise.

In searching for a choice of β_G that satisfies the first and second criteria, we were initially influenced by the following considerations. From Eq.2, it can be seen that to maintain constant beam power for each cavity in a constant-β_G section, the value of E_A can be chosen to compensate for the variations in $T(\beta)$. The largest values of E_A and of the peak surface fields will be at the ends of each section where $T(\beta)$ is lowest. If the strategy to satisfy the second criterion is to minimize the highest peak surface field in a section, defined by fixed minimum and maximum velocity values β_{MIN} and β_{MAX}, the optimum choice of β_G would be the value that provides equal values of $T(\beta)$ at both β_{MIN} and β_{MAX}.

However, a better procedure for satisfying the second criterion is suggested by considering what happens to the accelerating gradient distribution over the same fixed velocity range if β_G is increased by a small amount. Because the cavities become longer, over most of the range the first-order effect is that for fixed input power the accelerating gradients and peak surface fields will decrease. An exception is at the low-velocity end of the section, where the gradients and peak fields will increase because of the decrease in transit-time factor. The result of a small increase in β_G is that most cavities will require lower gradient and peak surface fields, while a few cavities at the low-velocity end of the section will require higher values. If the objective of the second criterion was better achieved by reducing the average peak surface field

rather than just the maximum values, a better strategy would be to increase β_G.

To decide on the best strategy, we compared the required or design distribution of peak surface electric fields with an estimate of the expected peak surface field distribution (see Fig.1), based on the approximately three hundred 1500-MHz superconducting cavities in the CEBAF linac. These data were reduced by an empirical field-emission factor, assumed to equal the ratio of surface areas to the minus one fourth power, and increased by a factor 1.3 to account for technology improvements since CEBAF was constructed.[3] We concluded that the strategy of a modest increase of β_G to reduce the average value of the peak surface field is a better approach, because it allows us to increase the number of cavities that can reach usable fields, resulting in fewer cavities that have to be rebuilt or sent back for reprocessing.

3 APT LINAC PARAMETER CHOICES

Assuming that the electromagnetic properties of the cavities have been determined so that $T(\beta)$ is known, we must choose values of N, β_{MIN}/β_G and β_{MAX}/β_G for each section. For APT we chose N=5 as a trial value. To define the constant-β_G sections in a way that addresses the second criterion described above, we chose non-symmetric values $T(\beta_{MIN}/\beta_G)=0.7T_{MAX}$ and $T(\beta_{MAX}/\beta_G)=0.95T_{MAX}$, corresponding to $\beta_{MIN}/\beta_G=0.908$ and $\beta_{MAX}/\beta_G=1.174$. These choices allow us to cover the full velocity range with two constant-β_G sections, which satisfies the fifth criterion. The value of $\beta_{MIN}=0.578$ for the first section, known as the medium-beta section (later divided into two subsections), corresponds to the output velocity of the normal-conducting linac. The value of β_{MIN} for the second or high-beta section was chosen to equal $\beta_{MAX}=0.747$ of the medium-beta section. The two resulting values of β_G are 0.64 and 0.82, respectively.

To satisfy the first criterion, we want to use all the available RF power per klystron, which is 0.84MW. Equation 2 may be used to choose parameter values that make use of all the power. For the medium-beta section, assuming trial values N=5 and $\phi=-30°$, we find that one klystron can deliver 0.28 MW to three cavities if $E_A=4.72MV/m$. For the high-beta cavities, assuming N=5 and $\phi=-30$ deg, Eq. 2 shows that one klystron can deliver 0.42 MW to two cavities, if $E_A=5.52$ MV/m. The electromagnetic field-solver codes yield corresponding values of the peak surface fields for the two cavities, 14.7MV/m and 15.3 MV/m, respectively, for electric fields, and 346G and 327G, respectively, for magnetic fields. These are conservative peak surface field values. Conservative power coupler values can be obtained by using two couplers per cavity. The values of ϕ are adjusted to provide optimum focusing and matching, as we discuss in the next section.

The choices for β_{MIN}/β_G and β_{MAX}/β_G produce a distribution of the peak surface field that is maximum at the low-velocity end of each section (see Fig. 1). The relatively small value of β_{MAX} allows us to switch at

612

relatively low velocity from the medium-beta to the longer high-beta cavities, which improves the real-estate gradient and shortens the linac (fourth criterion).

The choice of N=5 for APT led to practical values for accelerating gradients and peak surface fields. Generally, varying N causes several changes. A larger N reduces the velocity acceptance of the transit-time factor, as described by Eq.1. Additionally, for larger N at fixed beam power, the average accelerating gradient and peak surface electric field are reduced, but the longer cryomodule means that the average or real-estate gradient is also reduced, lengthening the linac. The longer cryomodule also increases the focusing period, which may increase the beam size. For APT we found no significant improvement from choices other than N=5.

Figure 1: Comparison of the APT design and the scaled CEBAF experimental peak surface electric-field distributions.

4 APT FOCUSING DESIGN

The transverse focusing in APT is obtained using room-temperature quadrupole doublets installed between the cryomodules. This approach was preferred over the use of superconducting quadrupoles to simplify the cryomodule design. Doublets were favored over a FODO singlet lattice to reduce the focusing period and the maximum rms beam size. The medium-beta cryomodules in subsection 1b contain three cavities driven by a single klystron. Each high-beta cryomodule in section 2 contains four cavities and uses two klystrons. To reduce the focusing period and provide better beam matching to the normal-conducting linac, which has a very short focusing period, we began with a medium-beta transition subsection (subsection 1a), consisting of six shorter 2-cavity cryomodules.

Current-independent matching [4] was used at all focusing transitions, and is achieved by maintaining equal values of the zero-current phase-advance per unit length on each side of every focusing transition. The zero-current phase advance per focusing period after each transition was chosen near 80° to provide the strongest transverse focusing, while staying safely below the envelope instability at 90°. At 1030 MeV, it was constrained to equal 72° to provide a current-independent match to the high-energy transport line. The quadrupole gradients in the FODO lattice of the normal-conducting linac were

decreased smoothly from 100 to 211 MeV to help achieve the 211-MeV match. As a second step, small adjustments were applied to the gradients of the two quadrupoles on each side of that transition. The quadrupole gradients in each superconducting section were varied smoothly from beginning to end to accomplish the match into the next section.

With fixed accelerating gradients, longitudinal matching was achieved by adjusting the synchronous phase ϕ in the superconducting cavities, so that the longitudinal phase advance per unit length was equal on both sides of every focusing transition, while maintaining the constant energy gain ΔW per cavity that is characteristic of each section. This results in equal values of $\Delta W \tan(\phi)/D$ on each side of a transition, where D is the period length. The values of ϕ were ramped smoothly in each section to achieve the matches.

Our choice of quadrupole gradients is not the only one we could have made. For example, we could have chosen the gradients to equipartition the beam in section 2, but this choice had the disadvantage of weakening the transverse focusing and increasing the transverse beam sizes. The resulting tune-depression ratios, when machine errors are included, are well above a value of 0.4, where chaos is observed in beam-halo models. Multiparticle simulation studies confirm that the design procedures provide good current-independent matches, and good overall beam-dynamics performance with a low risk of beam loss. Also, since the quadrupole gradients and phases are adjustable, experimental optimization is possible during the commissioning.

In spite of the large velocity acceptance of the cavities, one may wonder whether operation at velocities far from β_G might cause large longitudinal emittance growth, associated with a large cell-to-cell variation of the phase throughout the five cells of a cavity. For the APT design, we found that the maximum beam-phase slip between the first and fifth cells was about 100 degrees (for the $\beta_G=0.82$ cavity at 471 MeV). Nevertheless, the beam-dynamics code showed no significant effect caused by this phase slip. The results of a detailed cell-by-cell treatment are indistinguishable from the simpler approach of calculating the dynamics using a single equivalent gap, using the phase of the middle cell.

5 ACKNOWLEDGMENTS

6 REFERENCES

[1] G. P. Lawrence and T. P. Wangler, Proc. 1997 Particle Accelerator Conf., Vancouver, B.C., Canada (May, 1997).

[2] G.P. Lawrence, XIX International Linear Accelerator Conf. Chicago, Ill. (August, 1998).

[3] These empirical factors were recommended by participants at the CEBAF Workshop on the APT Design, April, 1977.

[4] R.S.Mills, K.R.Crandall, and J.A.Farrell, Proc. 1984 Linac Conf., Seeheim, Germany(May, 1984).

HIGH INTENSITY PERFORMANCE OF THE BROOKHAVEN AGS*,

L.A. Ahrens, J. Alessi, M. Blaskiewicz, J.M. Brennan#, K. Brown,
C. Gardner, J.W. Glenn, T. Roser, K. S. Smith, W. VanAsselt, S.Y. Zhang, BNL, Upton, NY

Abstract

The Brookhaven AGS provides 24 GeV protons for a multi-user program of fixed-target high energy physics experiments, such as the study of extremely rare Kaon decays. Up to 7×10^{13} protons are slowly extracted over 2.2 seconds each 5.1 seconds. The muon storage ring of the g-2 experiment is supplied with bunches of 7×10^{12} protons. Since the completion of the a 1.9 GeV Booster synchrotron and installation of a new high-power rf system and transition jump system in the AGS various modes of operation have been explored to overcome space charge limits and beam instabilities at these extreme beam intensities. Experiments have been done using barrier cavities to enable accumulation of de-bunched beam in the AGS as a potential path to significantly higher intensities. We report on the present understanding of intensity limitations and prospects for overcoming them.

Run Year	Harmonic Numbers		Booster Cycles	Intensity $\times 10^{12}$
	Booster	AGS		
94	3	12	4	40
95,96, 97	2 & 4	8	4	63
98 SEB	1 & 2	6	6	71
98 g-2	1 & 2	6→12	6	58

Table 1. Development of harmonic number and intensity for the last five runs. SEB is slowly extracted beam to the fixed targets. g-2 is fast bunch extraction to the muon storage ring.

1. INTRODUCTION

Very high intensity operation of the AGS began in 1994 after the completion of an extensive upgrade program. The AGS injection energy was increased from 200 to 1900 MeV by the 7.5 Hz Booster which is ¼ of its circumference.[1] As series of harmonic numbers have been used in attempt improve peak intensity and efficiency. The trend to fewer and longer bunches makes more stable beam with less tune spread. Bunches are made longer by; emittance dilution[2], double harmonic rf, and controlled bunch shape oscillations. Emittance dilution is limited by a constriction in the momentum aperture when the transition jump system operates. A low impedance rf system allows low voltage at high beam current during accumulation in the AGS.

With one bunch in the Booster six loads are put into the AGS, thus removing the need for the highest intensities in the Booster. Table 1 summarizes the configurations of several runs.

2. BOOSTER INJECTION

Experience shows that Booster injection is pivotal for good performance throughout the cycle. Up to 33 mA of 200 MeV H⁻ is injected for 300 turns as the dipole field rises corresponding to 8.7 GeV/s. A fast chopper after the 750 keV RFQ cuts the beam to phase bites of about 180° of the rf bucket. The chopper can also skip turns to make 10:1 intensity changes without changing the linac macro pulse length. This is useful for studying intensity-driven effects without changing transverse phase painting parameters that determine beam emittance and distribution. Making long smooth bunches is essential for achieving high intensity. Somewhat smoother bunches are produced by ramping the linac energy by 1% to match the Booster field ramp. Attempts to flatten the bunches by chopping two pulses into one bucket thus making a smoke-ring distribution in longitudinal phase space were unsuccessful. At 1.5×10^{13} protons the Lasslett tune shift reaches $\Delta v = 0.5$ and up to 15% beam loss occurs within the first 10 ms.

Figure 1 Mountain range view of the first millisecond of injection. The 300 injected bunches are 180 degrees long. The vector sum of the h=1 and h=2 rf cavities is shown on right. By careful choice of the phase and pulse width of the rf chopper smooth bunches can be obtained.

3. BOOSTER ACCELERATION

The Booster accelerates to 1.9 GeV in 75 ms. The rf voltage is a composite of the first and second harmonics at up to 60% amplitude of the fundamental. Two adjustable functions of time control the relative amplitude (by counter phasing) and phase of the harmonics. These functions are empirically tuned for best intensity and efficiency. The bunches are made longer at extraction by pumping the longitudinal quadrupole bunch-shape oscillation by modulating the rf voltage at $\pm10\%$ at twice the synchrotron frequency, figure 2. The phase of the h=2 voltage is adjusted to linearize the bucket for this operation. Feedforward beam loading compensation on these cavities is necessary.

Figure 2 Pumping the coherent quadrupole mode in the Booster to make the bunches longer (x2) before transfer to the AGS. Left, envelope of pick up and rf voltage, 1ms/division. Right, mountain range view of last oscillation cycle.

4. AGS INJECTION

Most of the beam loss in the AGS (up to 20%) occurs during the injection and accumulation process which lasts for 750 ms. Here the Lasslett tune shift is significant $\Delta\nu$ = 0.3) and tune is set just below the integer, ν_x=8.9. The

Booster output energy was increased from 1.5 to 1.9 GeV kinetic to reduce the tune spread of the accumulating beam.

Figure 3 Current transformer and longitudinal pick-up (wall current monitor) in AGS. Fast loss is seen at each injection pulse. A 5% loss at transition can also be seen

Significant beam loss occurs in the first 1 ms, figure 3. A plausible conjecture for the mechanism of loss is halo (which scrapes vertically) formed by the space charge coupling of coherent center of mass motion to particles at the fringe of the phase space distribution. The coherent motion arises from injection dipole and quadrupole mismatch. Intensity dependent tune along the bunch creates de-phasing, making wiggles in bunch centeroid that develop more rapidly as intensity increases, figure 4. Synchrotron motion and chromaticity mixes particles with different tunes and dissipates the coherent motion, thereby stopping halo pumping and loss. The benefit from high synchrotron frequency (500 Hz) during accumulation outweighs the penalty at transition for longitudinal emittance growth due to exceeding the matching voltage for the long Booster bunches.

Figure 4 Coherent within-the-bunch vertical motion at AGS injection. Each trace is a new turn. Different parts of the bunch oscillate at different frequencies because of different local coherent tune shift. (because the intensity varies along the bunch) Left is low intensity, 3×10^{12}. Right is high intensity, 10^{13} per bunch.

Figure 5 shows a single bunch when the first bunch is stored. The wakefield must be of order the bunch length since no coupling between bunches is seen. The head of the bunch is undisturbed. The oscillation of the center of the bunch grows until beam loss reduces the intensity and the instability self-limits.

Figure 5. Single bunch vertical instability in the AGS, 10^{13} protons per bunch, 1.9 GeV kinetic. Top trace is sum of up & down pickups, bottom are difference.

5. AGS ACCELERATION

The only significant beam loss (<5%) during acceleration occurs at transition crossing. [3] The high power (>2 MW) rf system is stabilized by rf feedback against beam loading instabilities. [4] At intensities above $5x10^{13}$ beam image currents that escape the vacuum chamber are a serious noise problem. It was necessary to short chambers together in groups of five to minimize the quantity of rf bypasses between chambers.

6. SLOW SPILL

A smooth 2.2 second spill is achieved by ramping the dipole field by –1% by a time varying reference function augmented with feedback on the extraction rate. [5] Controlled de-bunching spreads and flattens the momentum distribution. Maintaining homogeneity of the longitudinal phase space distribution is difficult at high intensity. A high harmonic (h=270) cavity operates continuously after transition to drive emittance blow up. The cavity is also used during the spill to reduce fast (>100 Hz) rate fluctuations (x10 improvement) by quickly accelerating beam micro-bunches into the 3rd order extraction resonance.[5, 6]

7. G-2 EXPERIMENT

The AGS fills the muon storage ring of the g-2 experiment [7] by single-bunch extraction. The accelerator repetition period is 2.5 seconds. Both 6 and 12 bunches per cycle were provided. To extract 12 bunches the 6 injected bunches were split in two at injection energy and accelerated on h=12, figure 6. The splitting technique was recently developed at CERN [8].

Bunches were shortened by a factor of two in a similar way to Booster extraction. The key difference being the sustained (200 ms) bunch shape oscillations without emittance growth which was accomplished by the adiabatic nature of the rf voltage modulation.[9]

8. BARRIER BUCKET INJECTION

A novel type of beam accumulation was tested using barrier bucket rf cavities in a collaboration experiment with KEK. The barrier cavities allowed accumulation of de-bunched beam.[10] One of the two cavities, developed by KEK, [11] employed a new magnetic material, FINEMET, which surpasses ferrite in peak rf magnetic field achievable. The experiments showed that de-bunched beam can be accumulated, rebunched and accelerated and that details of the barrier waveform are important.

Figure 6. Splitting (h: 6→12) of 10^{13} bunches at 1.9 GeV with little emittance growth. Horizontal scale 1.5 µs. Vertical scale is 50 ms.

ACKNOWLEDGEMENTS

REFERENCES

1. R.K. Reece, et al PAC 93, pp3763, L. A. Ahrens , et al EPAC 94, p485 M. Blaskiewicz, et al PAC 95, p383, J.M. Brennan and T. Roser, EPAC 96, p530
2. R.K. Reece et al, PAC 89 Chicago, p1934
3. W.K. van Asselt et al, PAC 95 Dallas, p3022, J. Wei et al PAC 95 Dallas p 3334, L.A. Ahrens et al, Performance of the AGS Transition Jump System, these proceedings
4. J.M. Brennan, PAC 95 Dallas, p1489.
5. L. Ahrens et al AGS Resonant Extraction with High Intensity Beams, these proceedings
6. R. Cappi and C. Steinbach, PAC NS-28, 1981, p2806.
7. Phys. Rev. Lett. paper 82, 1632 (99)
8. Bunch Merging and Splitting Techniques in the Injectors for High Energy Hadron Colliders", R. Garoby, CERN/PS 98-048, 17th Int1 Conf. on High Energy Accelerators (HEACC'98), September 7-12, 1998, Dubna, Russia.
9. Beam Manipulations by and RF Dipole, M. Bai, et al, these proceedings.
10. M. Blaskiewicz et al, Barrier Cavities in the Brookhaven AGS, these proceedings. M. Blaskiewicz and J.M. Brennan , EPAC 96 p2373.
11. M. Fujieda et al, these proceedings.

DARHT ACCELERATORS UPDATE AND PLANS FOR INITIAL OPERATION*

M.J. Burns, B.E. Carlsten, T.J.T. Kwan, D.C. Moir, D.S. Prono, S.A. Watson
Los Alamos National Laboratory, P.O Box 1663, Los Alamos, NM 87544

E.L. Burgess, H.L. Rutkowski
E.O. Lawrence Berkeley National Laboratory, 1 Cyclotron Rd., Berkeley, CA 94720

G.J. Caporaso, Y.-J. Chen, Y. J. (Judy) Chen, S. Sampayan and G. Westenskow
Lawrence Livermore National Laboratory, 7000 East Ave., Livermore, CA 94550

Abstract

The Dual-Axis Radiographic Hydrodynamics Test (DARHT) facility will use two perpendicular electron Linear Induction Accelerators to produce intense, bremsstrahlung x-ray pulses for flash radiography. We intend to produce measurements containing three-dimensional information with sub-millimeter spatial resolution of the interior features of very dense explosively driven objects. The facility will be completed in two phases with the first operational by June 1999 utilizing a single-pulse, 19.8-MeV, 2 to 4-kA, 60-ns accelerator (activated in March 1999), a high-resolution electro-optical x-ray imaging system, and other hydrodynamics testing systems. The second phase will be operational by Sept. 2002 and features the addition of a 20-MeV, 2 to 4-kA, 2-microsecond accelerator. Four short electron micropulses of variable pulse-width and spacing will be chopped out of the original, long accelerator pulse for producing time-resolved x-ray images. The second phase also features an extended, high-resolution electro-optical x-ray system with a framing speed of about 2-Mhz. In this paper we will present a Figure-Of-Merit for a x-ray based flash radiography system to motivate the selection of accelerator parameters. We will then present sub-system performance measurements from Phase 1, the physics of the interaction of our high-intensity beams with the x-ray conversion target, initial Phase 1 accelerator measurements (if available), and plans for operation. We will also discuss designs and prototype testing results for the 2-microsecond Phase 2 accelerator, including prototype induction cells and pulsed power, prototype kicker magnet performance to chop the beam, and design considerations for a multipulse x-ray conversion target.

1 INTRODUCTION

Maintenance of a smaller, aging U.S. nuclear weapons stockpile without underground nuclear testing (UGT) requires the capability to verify and benchmark the complex computer calculations on which stockpile confidence will be based. A key to this capability will be evaluation of the primaries of U.S. nuclear weapons through non-nuclear hydrodynamic testing, or "hydrotesting". These tests utilize very powerful x-ray sources to radiograph a full-scale, non-nuclear mock-up of a nuclear weapon primary during the late stages of the implosion, returning data on shapes, densities, and edge locations. (In the future, other probes such as tens-of-GeV-energy proton beams may also be used.) DARHT will be the first hydrotesting facility in the post-UGT era and will address evolving DOE requirements by developing images with sub-millimeter resolution, from two views (the minimum for large-scale three-dimensional information), and with multiple views along one axis.

Figure 1: Artist's rendition of the DARHT facility

We will present the current status of DARHT by first describing in Section 2 a Figure-of-Merit for radiographic hydrotesting that motivates parameter selection for the DARHT accelerators. In Section 3 we will present the status of Phase 1 of DARHT. In Section 4 we will discuss Phase 2, featuring the second x-ray system with multipulsing capability. Section 5 discusses the schedules and plans for initial operations of both phases.

2 RADIOGRAPHIC FOM

Each leg of DARHT is a x-ray imaging system. Two simultaneous images from perpendicular directions are the minimum required for 3D data and thus the essential layout of the facility is determined. An information theory based Figure-of-Merit (FOM), using the general radiographic system schematic shown in Fig. 2, has been developed to help describe the design of DARHT.

Radiographic magnification, M = (b/a) + 1

Figure 2: Radiographic system schematic

We tightly focus the electron beam from the accelerator onto a high-Z x-ray conversion target. X-rays are attenuated through the object that has been explosively compressed at velocities of many km/sec. An ~250,000 element segmented scintillator that converts x-rays to light, which is lens-coupled onto a mosaic of large-area charge-coupled devices (CCD).

A minimum description of the x-ray system must consist of parameters describing the source, object, detector, and experimental geometry. Source parameters are the spot size (S, mm, the diameter of an equivalent, uniformly illuminated disk at 50% modulation, or about 1.6 times greater than a Gaussian FWHM description [1]), the x-ray dose (D, Roentgens, R, @ 1-m distance from the source), the number, N(E), of x-ray photons per square-mm per R @ 1-m (a function of the electron beam energy, E), and the x-ray pulse width, τ, μsec. The object parameters are the average object transmission, T, and the characteristic velocity, V (km/sec. The detector parameters are the detective quantum efficiency, QE, the cut-off frequency (detector blur), F_c (cycles/mm at 50% modulation), and the scintillator pixel size in the object plane, P (mm). Finally, the first radiographic conjugate, a (m), and the radiographic magnification, M (see Fig. 2), describe the geometry.

The FOM is developed as the product of the system blur (characterized by the MTFA [2], or area under Modulation Transfer Function curve for the system) and the amplitude signal-to-noise ratio (SNR). Our simple SNR model assumes Poisson counting statistics and is proportional to the square root of the number of recorded quanta. This model neglects noise from situation-dependent sources (such as x-ray scatter, see below). Every doubling of the amplitude SNR doubles the quantization levels and thus increases the dynamic range by one-bit. Thus, information (in bits) increases as the base-2 logarithm of the amplitude SNR.

The MTFA is inversely proportional to the three principal blurs (source blur, detector blur, and object motion blur) added in quadrature. We approximate the 50% modulation frequency of each blur, convert to an equivalent spatial blur (strictly valid only for Gaussian blurs), and assume no aliasing effects.

Our system FOM (proportional to bits/pixel) is:

$$FOM = (MFTA)\, Log_2(1 + SNR)$$

$$= \frac{Log_2\left(1 + \dfrac{P}{a}\sqrt{N(E)\, D\, T\, QE}\right)}{\sqrt{2\left[\dfrac{(M-1)S}{M}\right]^2 + \left[\dfrac{1}{M\, F_c}\right]^2 + 2[V\tau]^2}}$$

This is a slowly varying quantity with a larger FOM value indicative of a higher quality x-ray system.

Although this FOM is useful for general comparisons of x-ray imaging systems, quantitative system design is also "task" dependent. For DARHT, the task is to precisely identify edges within the object. Other tasks could result in different system parameter optimization than selected for DARHT.

In the past, x-ray scatter has limited the resolution of dense-object images using MeV-radiography. Generally, x-ray scatter causes a background noise in the image and has been partially mitigated by "graded collimation" (being thick where the object is thin and thin where the object is thick. This helps to control scatter and also reduces the dynamic ranger required in the detector). Proper electron beam energy selection has been required to best match the bremsstrahlung spectrum with the objects of interest. We find an optimum electron beam energy between 12-20 MeV that balances photoelectric absorption and Thompson scattering (the predominant scatter mechanisms at low energy) with Compton scattering and pair production (more important at high energies). X-ray dose is almost a cubic power of the beam energy and therefore we pick the highest energy practicable with respect to scatter, or 20-MeV.

A short pulse-width is needed to reduce motion blur. High peak currents are then required to generate sufficient x-ray dose (dose being proportional to the total charge striking the conversion target). We selected a Linear Induction Accelerator to provide the required high dose at moderate energy with short pulse length. Consideration of the FOM shows that a preoccupation with dose is not warranted because the spot blurs and detector blurs are dominant. Therefore, the design of the DARHT accelerators is driven most by the need to generate a small spot size and with a sensitive detector design of high cut-off frequency. Table 1 lists the design parameters.

Table 1: DARHT system parameters		
Parameter	*Phase 1*	*Phase 2*
Spot size (mm)	1.2 - 2.0	1.2 - 2.0
Dose (R@1m)	500 - 1000	Max. 650-1000
Pulse width (ns)	60	variable to 80
DQE (%)	≥30	≥20
F_c (cycles/mm)	≥0.3 (-3dB)	≥0.3 (-3dB)
Pixel Size (mm)	0.9 x 0.9	1 x 1
1st conjugate (m)	0.8 to 1.5	1.1
Magnification	≤ 4	≤ 4
Accelerator Parameters		
Energy (MeV)	19.8	20.0
Current (kA)	2 - 4	2 – 4
Pulse width (ns)	60	2000
Energy spread	< ± 1%	< ± 1%
Norm. emittance (4-rms, πcm-rad)	0.15	0.15
Grad. (MeV/m)	0.47	0.35

3   PHASE 1

Phase 1 accelerator components (Fig. 3) have been tested on the Integrated Test Stand, or ITS [3], consisting of the injector and 8 induction cells. Other principal components for the full system include 56 additional cells, the single-pulse detector and high-explosive containment structures.

Figure 3: Phase 1 injector and accelerator

The 60-ft. long Phase 1 injector [4] consists of a prime power supply (a 3.0-µF/120-kV capacitor bank switched through the primary of a 1:15 Stangenes iron-core autotransformer by an air-blown spark gap) that pulse-charges a glycol Blumlein. The 6-ft. diam. Blumlein (7.65-Ω inner line, 7.3-Ω outer line, pulse-charged to 1.5-MV in 4.6-µs) discharges via 4 laser-

triggered spark gaps (0.7-ns 1-σ jitter) into a series of three transmission lines with impedance changes to step-up the voltage to 4-MV at the diode. The vacuum diode consists of a 170-Ω liquid resistor load in parallel with the 181-mm A-K gap and has a 10-90% risetime of 20-ns. A flat, 64-mm diameter velvet emitter is used to produce 2-kA at 3.75-MeV. A 90-mm cathode is used to generate 4-kA.

The accelerator consists of 64, 0.25-MV induction cells [5]. Each has a 148.2-mm-diam. bore, a 19.1-mm accelerating gap, 11 oil-insulated TDK PE16B nickel-iron-zinc ferrite toroids (237-mm ID, 503-mm OD, 25.4-mm thick), a cross-linked polystyrene insulator (ε=2.5), a quadrufilar-wound solenoid magnet with homogenizer rings [6], two cosine-wound dipole trim magnets, and a cosine-wound quadrupole magnet (to compensate for the weak quadrupole field introduced on-axis by the pulse-power feed to the cells). 818 individual ferrite toroids were measured and sorted into individual cell groupings resulting in each cell having 27.93-mV-s with σ=0.61%. 66 solenoids (64 plus spares) were measured to have an average maximum tilt (defined at the largest transverse magnetic field on axis divided by the axial field at that point) of 0.35-mrad (σ=0.17-mrad) and 0.90-mrad (σ=0.48-mrad) after installation in the cells. Beam Break-Up parameters have been measured with both the TSD method and by measuring transverse oscillations on the ITS beam [7]. At the principal resonant frequency of 790-MHz, the real (reZ) and imaginary (imZ) parts of the transverse impedance in the horizontal (X) and vertical (Y) planes are reZ_X=6.03Ω/cm±5%, reZ_Y= 6.45Ω/cm±5%, imZ_X=-1.0Ω/cm±1.0Ω/cm, imZ_Y= 5.5Ω/cm±1.0Ω/cm. The quality factors are Q_X=4.6 and Q_Y=5.5.

Thirty-two water-insulated, 11-Ω, 0.25-MV Blumleins with coaxial midplane-triggered switches operating in SF_6 drive two cells each through four DS 2158 44-Ω cables. Each Blumlein charging unit has two 1.4-µF/40-kV capacitors switched via two parallel EEV CS-1722 thyratrons into a 1:11 step-up transformer to pulse-charge the line in 5-µs. An independent trigger is supplied for each Blumlein consisting of two 30-nF/70-kV capacitors switched by a EEV CX-1725 thyratron into a 1:4 step-up transformer to drive a magnetic pulse-compressor to supply a 200-kV/10-ns risetime pulse to the trigger cable. Typical system jitter is <1-ns (1σ) for any consecutive 100 shots. The Blumleins provide a 67-ns pulse to the cells with a 0.6%-rms variation over the beam pulse-width of 60-ns.

Beam is transported to the x-ray conversion target via simple solenoid transport. Maintenance of a 1.2-2.0-mm electron beam spot with a front surface power density of 0.3-1.7 TW/cm² is one of the principal design challenges. At these energy density levels the target material or surface contaminants may be ionized and the ions accelerated into the beam due to space charge forces. This can partially charge neutralize the beam, causing a pinch upstream of the target and subsequent overforcing at the

target [8] leading to x-ray spot size growth as the pinch point moves upstream. Experiments at the ITS (Fig. 4) showed a growth in the radiographic spot size at 3.3-mm, 5.5-MeV, 2.8-kA, and 60-ns. Other experiments [9] at 5-MeV, 2-kA, 40-ns, and 2-3-mm focus have not observed the effect. When the phenomena is present, resistively isolating the target from ground has been found to be effective (see Fig. 4 and Ref. [8]). The intercepted charge "self-biases" the target, overcoming the beam self-field and trapping ions within about 1-cm of the target surface.

One theory explaining the ITS results [8] requires

Figure 4 : Time-resolved radiographic spot size measurements from the ITS

sufficient energy be deposited in the target material to cause boiling. Therefore target material with a high specific heat and high boiling point, while maintaining the high-atomic number and high density required for efficient x-ray production, may also be of use. Tantalum silicide ($TaSi_2$) and a Ta-Nb-V alloy (62.5Ta-30Nb-7.5V) are two such materials. Experiments at DARHT will begin initially at 2-kA/2-mm and focus on the use of special target material and a clean environment. As current density is increased, a barrier upstream of the target to limit ion migration and the biased-target may be used.

The phase 1 detector consists of a 55-cm-diam. x 2-cm-thick segmented BGO scintillator array with 250,000 polished 1mm x 1mm x 20mm pixels [10]. The x-ray scintillation light is lens coupled with 5, fixed conjugate, 165mm, f1.1 lenses [11] to a mosaic of 5, SITe SI424A [12], back-thinned CCD's (125cm² effective area). This combination results in a highly quantum efficient, linear detector (DQE > 30%) with better than 20uR sensitivity.

4 PHASE 2

Phase 2 is a collaboration between LANL, LBNL, and LLNL. It will produce the second x-ray system necessary to generate 3D data. This system will also produce four high-resolution images within a 2-μs time window. We will generate a 2-μs, 20-MeV, 2-4-kA LIA electron beam and use a fast deflection system to select four short (<80-ns) micropulses to be focused on a 4-pulse target system.

The resulting x-ray images will be captured on a 4-pulse extension of the Phase 1 detector.

Space restrictions within the existing DARHT facility force the injector to occupy two levels. On the bottom level is the Marx prime power feeding a vertical insulating column that drives a flat, 16.5-cm dia. dispenser-cathode with polished stainless steel electrodes. The Marx consists of 88 type E PFN stages driving a matched load at 3.2-MV with a 400-ns rise, 2-μs flat pulse. The 444.5-cm tall, oil-filled insulator column has both alumina and Mycalex insulating rings. The peak electric field stress on the cathode shroud is 120-kV/cm with 2-kA beam current. The design beam emittance (norm,4-rms) is 0.05-πcm-rad.

There are two types of induction cells. The first eight have a 35.56-cm dia. beam pipe and run at 173-kV while the remaining 80 have a 25.40-cm dia. pipe and supply 193-kV. The larger bore cells intercept essentially no beam from the injector rise time and reduce transverse impedance in a region susceptible to BBU because of the low transport field. All of the oil insulated cells use 4 individual cores of Allied Signal 2605SC Metglas with either 0.48 V-sec core capacity or 0.43 V-sec in the large bore cells. A 200-ns rise-time leads to a 2.02-μs flattop. A Mycalex conical insulator is used in each cell is for its excellent breakdown and mechanical properties. Each individually mounted cell contains a transport solenoid and a steering coil. Ferrite damping is employed to reduce the cell quality factor.

Each induction cell has an individual cell-driver which contains 4, 7-section E-network PFNs in a Marx configuration. Each driver has a 20-Ω impedance and will deliver a 2.4-μs flattop into a resistive load of 5-Ω for a total drive current of 10-kA at 200kV. To compensate for the non-linear magnetization current of the Metglass cores, the PFN impedance varies from front to back. The impedance of each PFN can also be reduced 20% to tune for a ±0.5% flattop.

The principal element of the beam transport section is the fast deflector, or kicker system [13], used to generate four micropulses from the primary accelerator beam. It is similar in design to stripline beam position monitors. There are four equal size electrodes enclosed within a vacuum housing that has a DC bias magnetic dipole wound over the enclosure. An opposite pair of electrodes is driven by a fast amplifier through transit time isolated 50-Ω cables to provide beam deflection. The other two electrodes are terminated at their 50-Ω matched impedance. A subsequent drift space of several meters allows a substantial relative deflection to develop between the output beam positions of the kicker and drift. A DC septum magnet allows the separation of the two output beams. The bias dipole will deflect the beam off-axis into a dipole field region of the septum that will transport the beam into a dump. When an x-ray pulse is desired the kicker pulsers are activated and overcome the bias field allowing a short segment of beam to travel down the axis through a null field region of the septum and on to the x-

ray converter target.

The initial 4-pulse target will consist of a large number (of order 20) of thin (approximately .05 mm) tungsten sheets separated by vacuum gaps with an overall thickness of about 1 cm (we are also exploring the use of a low density "foamed" target). The sheets are held within a tungsten cylinder that provides radial confinement of the target. Distributing the target over an extended distance delays the axial outflow of plasma and permits the generation of four x-ray pulses over a period of 2-μs. Operating the target in good vacuum ($< 10^{-7}$ Torr) will reduce the light contaminants on the surface to the level that the first pulse to disrupt the target focus will generate insufficient ions. Typically the first pulse will convert much of the target into a plasma. Subsequent pulses can be protected from backstreaming ions by using either a target bias or an inductive ion trap placed immediately upstream of the target. Plasma lengths over 2-μs (< 2 cm.) will not significantly disrupt the focal spot.

Prototype accelerator components will be evaluated on a long-pulse electron beam test stand assembled around the THOR [14] diode. THOR generates a 2-μs, ≤4-MeV, and ≤3.2-kA beam with an integrated beam emittance of 0.5-1.0 cm-rad, sufficient for evaluating long-pulse DARHT components. Two prototype induction cells will be tested through September 1999, to investigate effects of beam interception on the cell insulator, including breakdown and focusing/steering effects due to plasma generation. Then

Figure 5: A Phase 2 induction cell on the THOR diode

8 induction cells, kicker, and multiple-pulse target components will be evaluated. In addition long-pulse beam current, centroid, and profile measurement diagnostics will be evaluated.

The phase 2 detector is an extension of the single pulse BGO detector. It utilizes a 40cm diam. x 3cm thick, segmented LSO scintillator array. LSO [15] was chosen because of its unique combination of high brightness, high density, and fast time constant. This array will also be lens coupled to a variety of special purpose frame shuttered CCD's under development at MIT-

LL, Princeton Instruments, and SITe.

5. PLANS FOR INITIAL OPERATIONS

Phase 1 injector start-up has begun with full accelerator operation by May 1999. By June 1999 we expect a 2-mm (1.3-mm FWHM) x-ray spot and 500 R @ 1-m, sufficient to meet the project's radiographic resolution requirements. Increased beam current and advanced target designs will be introduced later with the goal of achieving a 1.2-mm spot and 1000 R @1-m.

Phase 2 prototype testing is underway. Injector installation during the second half of 2000 will be followed by phased accelerator operation for the next year. A year of full system commissioning is planned ending in Phase 2 hydrotesting operations by the end of Sept. 2002. The Initial Operating Capability will be at 2-kA using a simple target system. The beam current will be increased and more advanced target designs introduced during the operations. The installation of additional beamlines utilizing the dumped fraction of the beam for more views of the object and higher order 3D data may also be considered at that time.

6 REFERENCES

[1] Mueller, K., "Measurement and Characterization of X-Ray Spot Size", *Proceedings of the Flash Radiology Topical*, American Defense Preparedness Assoc., 1989.

[2] Holst, G.C., *Sampling, Aliasing, and Data Fidelity for Electronic Imaging Systems, Communications, and Data Acquisition*, SPIE JCD Publishing, 1998.

[3] Burns, M.J. et al, "Status of the Dual-Axis Radiographic Hydrotest Facility", *Proc. of the XVIII Intl. Linear Accel. Conf.*, Geneva, Switzerland, 1996

[4] Downing, J.N. et al, "Pulsed Power Systems for the DARHT Accelerators", *IEEE 1991 Part. Accel. Conf.*, San Francisco, CA, 1991

[5] Burns, M.J. et al, "Cell Design for the DARHT Linear Induction Accelerators", ", *IEEE 1991 Part. Accel. Conf.*, San Francisco, CA

[6] Burns, M.J. et al, "Magnet Design for the DARHT Linear Induction Accelerators", ", *IEEE 1991 Part. Accel. Conf.*, San Francisco, CA

[7] Alison, P. and Moir, D.C., "BBU Gain Measurements on the ITS 6-MeV, 4-kA Linac", *Proc. of the 1997 Part. Accel. Conf.*, Vancouver, Canada, 1997

[8] Kwan, T.J.T, "Electron Beam-Target Interaction in X-Ray Radiography", LA-UR-98-4802, submitted to *Physics of Plasmas*, 1998

[9] Sampayan, S., et al,"Experimental Investigation of Beam Optics Issues at the Bremsstrahlung Converters for Radiographic Applications", *Proc. of the 1998 Linear Accelerator Conference*

[10] Watson, S.A. et al, "Solid and Segmented Scintillator Performance in a Co60 Test Stand", *DARHT Tech. Memo. No. 93*, Los Alamos National Laboratory, 1998

[11] Watson, S.A. et al, "The DARHT Radiographic Camera Lenses: Design and Performance", *DARHT Tech. Memo. No. 98*, 1998

[12] Scientific Imaging Technologies, Inc., "SITe 2048 x 2048 Scientific-Grade CCD", 1994

[13] Chen, Y.J.(Judy), et al, "Precision Fast Kickers For Kiloampere Electron Beams", proceedings of this conference.

[14] R. F. Schneider, J. D. Miller, W. C. Freeman, M. J. Rhee, D. J. Weidman, J. Pasour, and K. T. Nguyen, "THOR, a long-pulse electron beam generator design and performance characteristics," 8th IEEE Pulsed Power Conference, San Diego, 1991

[15] Melcher, C.L. et al, "Cerium-doped Lutetium Oxyorthosilicate: A Fast, Efficient New Scintillator", *IEEE Trans. Nucl. Sci.*, NS-39, 1992.

PRECISION FAST KICKERS FOR KILOAMPERE ELECTRON BEAMS

Y. J. (Judy) Chen[2], G. J. Caporaso, J. T. Weir, LLNL, Livermore, CA

Abstract

These kickers will be used to make fast dipoles and quadrupoles which are driven by sharp risetime pulsers to provide precision beam manipulation for high current kA electron beams. This technology will be used on the 2nd axis of the DARHT linac at LANL. It will be used to provide 4 micropulses of pulse width up to 120 nsec. selected from a 2 μsec., 2kA, 20MeV macropulse. The fast pulsers will have amplitude modulation capability [1][2] to compensate for beam-induced steering effects [3] and other slow beam centroid motion to within the bandwidth of the kicker system [4]. Scaling laws derived from theory will be presented along with extensive experimental data obtained on the test bed ETA-II [5].

1 INTRODUCTION

The kicker system is the principal element of the beam transport section of DARHT-II. It is similar in design to stripline beam position monitors. There are four equal size electrodes enclosed within a vacuum housing that has a DC bias magnetic dipole wound over the enclosure as shown in fig. 1. An opposite pair of electrodes is driven by fast amplifiers through transit time isolated cables to provide beam deflection. The other two electrodes are terminated at their matched impedance. A drift space between the kicker and a DC septum magnet provides additional separation between the switch positions. The bias dipole is turned on at all times to deflect the beam into a dump. When an x-ray pulse is desired the pulsers activate and overcome the bias dipole force allowing the beam to steer straight ahead through the rest of the transport section and on to the converter target (see fig. 2).

Figure 1: Cross-sectional view of kicker and completed assembly on beam line. The red tape holds the bias dipole windings.

Fig. 2 Kicker system beam line layout

2 SCALING LAWS

The following is a list of scaling laws that relate performance of the system to the kicker geometry, pulser performance, and beam parameters.

2.1 Applied "kick"

The complete treatment of dipole steering through the kicker has no analytic closed form solution. However, a numerical particle code treatment can be found in [6]. If we assume negligible beam-induced steering effects, we have a solution to the differential-integral equation of the kicker as a function of time [4].

$$x(z = l, t) = \frac{c^2}{4V_0 l} \int_{t-2l/c}^{t} V_p(t')(t - t')dt' \qquad (1)$$

where $V_p(t)$ is the applied voltage and c is the speed of light in free space. This equation yields for an ideal square pulse

$$x(z = l) = \frac{V_p}{2V_0} l$$

where V_p is a square output from the pulsers. The characteristic voltage V_0 is a parameter used in determining the amount of kick. It is given by

$$V_0 = \frac{1}{32} \frac{b}{l} \frac{\gamma\beta^2 I_0 Z_0}{\sin^2 45°}$$

where I_0=17kA and Z_0=377Ω. The following proportionalities relate the amount of output displacement and angle to the dimensions of the kicker.

$$x \propto \frac{l^2}{b}$$

$$\angle \propto \frac{l}{b}$$

2.2 Rise time of beam

Assume that the pulsers have a linear rising edge with a rise time (from 0 to maximum) of τ_{pulser}. Using eqn. (1), the rise time of the beam as it switches from one position to another is

$$\tau_{beam} = \tau_{pulser} + 2l/c \qquad (2)$$

2.3 Beam-induced steering effects

The critical current, I_c, as derived in [3], is a parameter used to measure the amount of beam-induced steering the kicker adds to the beam. One generally would like to design it such that $I_b \ll I_c$ to minimize this effect where I_b is the beam current. Assuming that this is true, the following laws can be used.

$$I_c \propto \frac{b^2}{l^2 Z_k}$$

$$\text{amplification in input } x \propto 1 + \frac{I_b}{I_c}$$

$$\text{amplification in input } \angle \propto 1 + \frac{I_b}{3 I_c}$$

$$\text{amplification in } k_\perp \propto 1 + \frac{I_b}{6 I_c}$$

where Z_k is the dipole impedance of the kicker and determined by the radius of the striplines and outer vacuum chamber.

2.4 Quadrupole shaping

The kicker can act like a quadrupole lens, shaping the beam with a dynamically controlled quadrupole electric field. Two pulsers connected on opposite plates similar to the dipole configuration excite the plates with the same polarity voltage signals. The strength which is defined to be the field gradient multiplied by the length of the lens can also be applied here.

$$\frac{dE}{dx} l \propto \frac{l}{b^2}$$

2.5 Emittance

If we assumed a small perturbation from the particle trajectory due to sextupole fields that exist in an activated kicker, we can deduce a simple scaling law for emittance growth through the kicker structure.

$$\Delta \varepsilon \propto \left(\frac{l}{b^3} \right)^2 R_0^6$$

R_0 is the beam radius assumed to be constant through the kicker (no space charge effect included). One can see that the distance of the strip lines from the center and the beam size dominate the emittance growth through the kicker.

3 NEW EXPERIMENTAL DATA

A review of the landmark data [1] acquired during testing of the kicker structure is presented alongside new data on emittance and the control system. Septum data is not included due to lack of space.

3.1 Kicker dipole measurements

(a)

(b)

Fig. 3 (a) Photo of beam switching from one position to another. I_b=1200A, V_p=±9kV, camera gated over entire beam pulse, and Δx=4cm. (b) Further downstream sat a resistive wall monitor (a.k.a. beam bug) to measure beam centroid motion. One can see that the risetime of the switched beam is about 20nsec. which matches eqn. (2).

3.2 Kicker quadrupole measurement

Fig. 4 When the polarity of the pulser signals are the same, a quadrupole instead of a dipole field is formed. The photo is for a beam current of 1200A, V_p=-10kV and the ratio of major to minor axes is 2:1.

3.3 Kicker emittance measurements

Emittance measurements use a pepper pot method [7] whereby the beam impinges on a grid of holes (the pepper pot mask) and the beamlets which survive are allowed to drift a distance. The amount the beamlets expand is used to calculate beam emittance.

Fig. 5 A large beam being switched from one position to another has a triangular shape due to the sextupole moment in the powered kicker. Sextupole fields, due to their nonlinearity, contribute to emittance growth.

(a)

(b)

Fig. 6 Emittance measured downstream of the kicker with and without an applied voltage. (a) A round beam at the output yielded no emittance growth. (b) A larger beam yielded some emittance growth. The y-emittance is slightly larger than in x which is predicted by theory.

3.4 Kicker control system

A kicker control system that attempts to regulate beam motion with the dynamics of the kicker has been designed and tested on ETA-II. As shown in Fig. 7, the outer loop takes beam position data and calculates a desired pulser voltage waveform. The inner loop then attempts to match actual output of the pulser to the desired waveform.

Fig. 7 The beam control algorithm (BCA) takes measured beam location to find the desired voltage needed for the next correction. It then feeds into the pulser control algorithm (PCA) which trys to produce the desired waveform at the output of the pulsers via the arbitrary waveform generators (AWG). The pulses are then sent to the kicker and beam position data is acquired from beam bugs (BB). Each pulser is controlled independently.

Fig. 8 The desired voltage is achieved at the output of the positive pulser (similar for the negative pulser) to within 2%. Notice the tail end of the waveform has a steep slope that the pulser cannot physically meet.

3.5 The septum magnet and split beam pipe

A septum magnet which is capable of generating two opposing dipole field regions was designed and built [6]. A split beam line and the transport section for two diverging beamlines, one straight-ahead and one at 15° were designed and tested in conjunction with the septum. Results of the experiment have lead us to believe that the aperture of the magnet is too restrictive for a low repetition rate machine such as DARHT. Hence, it is decided that a quad septum will be used in it's place (see fig. 2).

4 CONCLUSION

Development of a complete kicker system is well underway. The kicker structure itself and the septum magnet have been designed and tested on ETA-II. The two components are well-characterized. The kicker structure itself has shown success in beam switching and little emittance growth. The control system has been implemented and is undergoing further refinements. A new generation of solid state pulsers is being pursued. Long pulse precision beam position monitors for beam steering throughout the kicker system have been developed and scheduled to be tested on ETA-II later this year [9].

5 ACKNOWLEDGEMENTS

6 REFERENCES

[1] Chen, Judy, presented at LINAC98, Chicago, Aug. 1998.
[2] DeHope, W.J. et. al, to be presented at the 12 th IEEE Int l. Pulsed Power Conf., Monterey, June 1999.
[3] Caporaso, G.J. et. al, 1997 Particle Accelerator Conference, 1861-3, Vancouver, May 1997.
[4] Chen, Judy et. al, "Fast kicker for high current, continuous beam", to be submitted, preprint avail. upon request.
[5] Weir, J.T. et al., this conference.
[6] Poole, B.D., et al., this conference.
[7] Paul, A.C.
[8] Wang, L.F. et al., this conference.
[9] Nelson, S.D. et al., this conference.

MHZ REPETITION RATE SOLID-STATE DRIVER FOR HIGH CURRENT INDUCTION ACCELERATORS*

H. Kirbie, G. Caporaso, D. Goerz, R. Hanks, B. Hickman, B. Lee,
Lawrence Livermore National Laboratory, Livermore, CA
C. Brooksby, R. Saethre, Bechtel Nevada, Livermore, CA

Abstract

A research team from the Lawrence Livermore National Laboratory and Bechtel Nevada Corporation is developing an all solid-state power source for high-current induction accelerators. The original power system design, developed for heavy-ion fusion accelerators, is based on the simple idea of using an array of field effect transistors (FETs) to switch energy from a pre-charged capacitor bank to an induction accelerator cell. Recently, that idea has been expanded to accommodate the greater power needs of a new class of high-current electron accelerators for advanced radiography. For this purpose, we developed a 3-stage induction adder that uses over 4000 field effect transistors to switch peak voltages of 45 kV at currents up to 4.8 kA, with pulse repetition rates of up to 2 MHz. This radically advanced power system can generate a burst of five or more pulses that vary from 200 ns to 2 μs at a duty cycle of up to 25%. Our new source is precise, robust, flexible, and exceeds all previous drivers for induction machines by a factor of 400 in repetition rate and a factor of 1000 in duty cycle [1].

1 INTRODUCTION

We are developing a radiographic concept for Stockpile Stewardship that is based on a single, high-current induction accelerator driven by solid-state power. The accelerator will produce bursts of 16–20 MeV, 3–6 kA electron beams in long pulses that may vary from 200 ns to 2 μs. Each beam will be cleaved by an electromagnetic "kicker" device that directs the divided beam portions down separate pathways [2]. The chopping action of the kicker may be repeated on the remaining portions of the beam until the desired number of beam segments arrive at a test chamber where they are converted into x-ray sources for radiography. The solid-state driven accelerator enables the viewing process to be repeated at rates exceeding a megahertz, while resetting the magnetic material in each accelerator core between pulses. Further information about this and other advanced radiographic methods for Stockpile Stewardship is available in the literature [3].

The two power sources illustrated in Figure 1(a) are inductive voltage adders that sum the voltage contributions from three solid-state modulators. The output voltage from the adders is multiplied by three at the accelerating gap due to the transformer action of three induction cores within the cell. Figure 1(b) is a conceptual design of a three-core cell. Details concerning

the operation of an induction accelerator and the behavior of a multicore cell can also be found in the literature [4,5]. Figure 2(a) depicts the basic elements of our prototype induction adder, which contains three ARM-II solid state modulators surrounding a voltage summing stalk. When stacked together, the modulators act as independent pulse transformers linked by a common secondary winding.

Figure 1: (a) Illustration of a solid-state power system for an induction accelerator. (b) Computer design of a long-pulse, three-core induction cell.

Figure 2: (a) Simple diagram showing the internal elements of a three-stage voltage adder plus (b) a photograph and specifications for an ARM-II solid-state modulator.

2 ARM-II MODULATOR

The ARM-II modulators each contain four 20-kV, 4-μF capacitor banks that are switched across a tape-wound magnetic core using a modular array FETs. Each modulator also contains a reset system that uses insulated gate bipolar transistors (IGBTs) to switch four 10-kV, 4-μF capacitor banks across the same magnetic core. The goal of the reset system is to control the magnetic states of the modulator and accelerator cell so that a long burst of pulses can be sustained without saturating the magnetic core material.

Figure 3(a) is a simplified circuit diagram of an ARM-II modulator. When the FETs are commanded to close, the 15-kV capacitor voltage is applied across the induction core and remains there until the FETs are opened. At that time, the core voltage reverses and is held at the 7.5-kV level by the IGBT switches. One should note that the core is loaded by a 3-Ω resistor in series with a diode that acts to load the modulator during the acceleration pulse (negative) but not during the reset pulse (positive). The polarity-dependent loading imitates the effect of an electron beam that is present during acceleration but not during reset. Figures 3(b)–(d) are modulator test data showing a 2-μs pulse. Figure 3(b) shows a voltage waveform with the reset pulse adjusted to match the volt-second value of the acceleration pulse (flux balanced). Figure 3(c) is an expansion of the acceleration pulse showing that the core voltage is well shaped, but less than 15 kV due to the 0.75-Ω on-state impedance of the FET array.

Figure 3: ARM-II performance data showing (a) an idealized ARM-II circuit diagram with (b) reset pulse matching the volt-second value of the acceleration pulse, (c) expanded voltage wave form and (d) total FET switch current.

3 INDUCTION ADDER AND CABLE-COUPLED POWER

The ARM-II modulators are built to stack on top of each other as shown in Figure 4.

Figure 4: Adder photograph showing three ARM-II modulators.

Voltage from each modulator is gathered by a voltage-summing stalk and delivered to a set of 50-Ω cable connections that enable us to power an accelerator cell at some remote location. Unfortunately, we have no long-pulse electron beam to accelerate nor a large three-core induction cell, as previously shown. What we have managed to do is scale the original concept, shown in Figure 1(a), down to the power level of the prototype adder, which is able to drive the smallest of the three accelerator cores shown in the figure. The loading effect of a single core, combined with an electron beam, is modeled by the simple network shown in Figure 5(a). In this model, the capacitor represents the lumped effect of the gap, gap insulator, and oil-cavity capacitances. The inductor accounts for the unsaturated inductance of the core, while magnetization losses in the core during acceleration are attributed to one of the five 50-Ω resistors. The remaining four 50-Ω resistors imitate the loading effect of a 2.8-kA electron beam. The 110-Ω resistor and reversed diode embody the magnetization losses in the core during the reset pulse. Figure 5(b) shows the oil-immersed cell model connected to the adder via 50-Ω, high-voltage cables.

Figure 5: (a) Lumped-element model of an accelerator cell and beam load that is scaled to match the prototype adder and (b) photograph of the lumped-element network immersed in a tank of insulating oil.

Figure 6 shows the voltage and current response of the cell load to a burst of 1-µs pulses at a pulse rate of 200 kHz. The adder is adjusted to provide the appropriate amount of reset voltage after each acceleration pulse. Figure 6(c) compares cell voltages for the first and fifth pulses, which shows a voltage drop on the fifth pulse due to capacitor bank droop. Later versions of the adder will eliminate this effect by actively regulating the adder output voltage to the value of the last pulse. The FET switch currents in Figure 6(d) show a peak value of 4.3 kA. Figure 7 illustrates the great flexibility that solid-state power affords an induction accelerator by showing a pulse schedule that changes from pulse to pulse. One should note that the final long pulse (or long burst) avoids saturation by controlling the reset conditions of earlier pulses.

(a)

(b) V_cell—flux balanced
8 kV/d, 5 µs/d

(c) V_cell—1st and 5th pulses
8 kV/d, 200 ns/d

(d) I_SW
800 A/d, 5 µs/d

Figure 6: 200-kHz burst data showing (b) five voltage pulses with active reset, (c) comparison of first and fifth voltage pulse at the cell, and (d) burst of FET current pulses with a peak value of 4.3 kA on the first pulse.

(a) 1.96 MHz finish
8 kV/d, 2 µs/d

(b) 2.0 µs finish
8 kV/d, 2 µs/d

Cell voltage

10-Ω cell load

Figure 7: An arbitrary pulse schedule showing (a) cell voltage for a pulse train that finishes with five, 200-ns pulses at 1.96 MHz and (b) cell voltage showing a pulse train that finishes with a 2-µs pulse.

Figure 8 compares a network simulation of the cell voltage with measured data. The network model uses linear circuit elements to represent the separate ARM-II modulators, power transmission lines, and accelerator cell

load. The simulation network is derived from series/parallel component values from each modulator combined with calculated values of inductance and capacitance for structure elements and transmission lines.

Figure 8: Comparison between measured and simulated cell voltage at the accelerator cell load.

4 SUMMARY AND OUTLOOK

Experiments involving an all solid-state voltage adder and lumped-element cell load have demonstrated the feasibility of powering a high-current induction accelerator at pulse rates beyond a megahertz. Further encouragement for solid-state accelerator power is provided by electronic manufacturers who produce devices that continue to increase in speed and power while falling in cost. For example, the estimated cost of powering the accelerator depicted in Figure 1(a) has fallen by a factor of five since work began on the ARM-II modulator. Our latest estimates indicate that solid-state power is approaching the cost of conventional accelerator power but with much greater performance and flexibility.

5 REFERENCES

[1] H. Kirbie, et al., "An All Solid State Pulse Power Source for High PRF Induction Accelerators," (Invited) Proceedings of the Twenty-Third International Power Modulator Symposium, Rancho Mirage, CA, June 22–25, 1998, p. 6.

[2] Y. J. (Judy) Chen, G. J. Caporaso, J. T. Weir, "Precision Fast Kickers for Kiloampere Electron Beams," Proceedings of the 1999 Particle Accelerator Conference, New York, NY, March 29–April 2, 1999, (proceedings awaiting publication).

[3] A. J. Toepfer, "A Review of Accelerator Concepts for the Advanced Hydrotest Facility," (Invited) Proceedings of the XIX International Linac Conference, LINAC98, Chicago, IL, August 23–28, 1998, (proceedings awaiting publication).

[4] S. Humphries, Jr., Principles of Charged Particle Acceleration, John Wiley & Sons, New York, 1986, ISBN 0-471-87878-2.

[5] J. E. Leiss, N. J. Norris, and M. A. Wilson, "The Design and Performance of a Long-Pulse High-Current Linear Induction Accelerator at the National Bureau of Standards," Particle Accelerators 10, 223 (1980).

CURES OF COUPLED BUNCH INSTABILITIES

A. Mosnier, SOLEIL, Gif/Yvette (France)

Abstract

To achieve the desired luminosities and brilliances in future storage rings for colliders and synchrotron light sources, very large beam currents need to be stored in many tightly spaced bunches. A serious limitation of the performances comes then from the conventional coupled bunch instabilities (CBI). Energy oscillations and transverse ocillations are mainly driven by high-Q structures and the resistivity of the vacuum chamber. Control of these multibunch instabilities has become a critical issue and various strategies are considered to push up the instability thresholds : HOM frequency control to avoid the overlap of dangerous modes with beam spectrum, heavy mode damping to reduce the resonant buildup of the fields, Landau damping to destroy the coherence of the beam and lastly strong feedback systems operating either in the frequency or time domains. These different cures and their technological developments are reviewed in this short paper, more details can be found in [1].

1 INTRODUCTION

The common approach of both synchrotron light sources and e^+e^- circular colliders to achieve the desired luminosities and brilliances consists in storing high beam currents in many tightly spaced bunches. Control of coupled-bunch oscillations, excited by the long-range parasitic modes of the vacuum chamber, mainly of the *rf* cavities, has become accordingly a critical issue. Energy or position oscillations spoil the luminosity in colliders, because beams don't collide properly any more, in time or in position, and the spectral brilliance in synchrotron light sources, because undulators are strongly sensitive to any increase in effective energy spread and emittance. Figure 1 shows for example the effect of longitudinal CBI on the brightness of a typical undulator in the SOLEIL light source for different energy oscillation amplitudes.

Figure 1: Effect of longitudinal oscillation on the 7th harmonic of SOLEIL U34 undulator spectrum.

When we are interested in the coherent motion of a bunch as a whole, the one-particle model, also named rigid bunch approximation, leads to a well-known system of linear equations (see [2,3,4] for example). For a beam interacting with its environment, the single particle equation of longitudinal motion is given by:

$$\ddot{\tau}_k(t) + 2\alpha_s \dot{\tau}_k(t) + \omega_{sk}^2 \tau_k(t) = \frac{\alpha}{T_0\, E/e} V_k(t) \qquad (1)$$

where τ_k and ω_{sk} are the time displacement with respect to the synchronous particle and the synchrotron frequency of particle index k; T_0, E and α are the revolution period, the beam energy and the momentum compaction; $\alpha_s = 1/\tau_s$ is the synchrotron damping rate; V_k is the total induced voltage by all circulating particles, seen by bunch k.

For M equally spaced and equally populated rigid bunches, a coherent oscillation of the k-th bunch is described by:

$$\tau_k(t) = \hat{\tau}\, e^{j(\Omega t + k\Delta\phi)}$$

Signals add up coherently and provide synchrotron sidebands if the bunch-to-bunch phase shift satisfies $\Delta\phi = 2\pi n/M$, where n is called the coupled-bunch mode number. The total induced voltage is then obtained by summing the currents of the M individual bunches of current I_b:

$$V_k(t) = j\, M\, I_b \sum_p \omega_p\, Z(\omega_p) \times e^{jk\Delta\phi} \langle\tau\rangle(t) \qquad (2)$$

$\langle\tau\rangle(t) = \hat{\tau}\, e^{j\Omega t}$ is the mean displacement of the bunches and can be understood either as the average over all particles of a same bunch or as the average over all bunches of the train; Impedance is sampled at frequencies $\omega_p = (pM + n)\omega_0 + \Omega$.

When all particles have the same incoherent synchrotron frequency, we obtain the well-known growth rate of the nth mode, after substitution of the induced voltage (2) into the single particle equation of motion (1):

$$\frac{1}{\tau} = \frac{\alpha I_0}{4\pi\, E/e\, Q_s} \sum_p \omega_p\, \Re e\left[Z(\omega_p)\right] e^{-(\omega_p \sigma_t)^2} - \frac{1}{\tau_s} \qquad (3)$$

In a similar way, we obtain the well-known result for the transverse multi-bunch instability:

$$\frac{1}{\tau} = -\frac{\beta_\perp\, \omega_0 I_0}{4\pi\, E/e} \sum_p \Re e\left[Z_\perp(\omega_p)\right] e^{-(\omega_p \sigma_t)^2} - \frac{1}{\tau_\perp} \qquad (4)$$

with the longitudinal and transverse damping times τ_s and $\tau_\perp$, and the mode spectrum lines $\omega_p = (pM + n)\omega_0 + \omega_s$ and $\omega_p = (pM + n)\omega_0 + \omega_\beta$ for longitudinal dipole mode and rigid dipole transverse oscillations, respectively.

Independently of the vacuum chamber impedance, we

can compare the sensitivity of different machines to longitudinal or transverse CBI by means of the parameters:

$$S_{LCBI} = \frac{\alpha \tau_s}{2 E / e Q_s} \quad \text{and} \quad S_{TCBI} = \frac{\beta_\perp f_0 \tau_\perp}{2 E / e}$$

The sensitivity is of course inversely proportional to the beam energy and to the longitudinal or transverse focusing strength. Table 1 gives parameter values in the longitudinal plane for some colliders and synchrotron light sources.

Table 1: LCBI sensitivity parameter for some machines

	KEK-B	PEP-II	CESR III	DAΦNE
E (GeV)	3.5	3.1	5.3	0.510
S_L	3.7	22.7	41.4	3141
	ESRF	ELETTRA	ALS	SOLEIL
E (GeV)	6	2	1.9	2.5
S_L	1	32.2	34.7	6.2

The cures against CBI, developed at various places, are reviewed hereafter and systematically applied to the SOLEIL synchrotron light source for illustration.

2 LANDAU DAMPING

Landau damping proved to be an efficient tool in stabilizing multi-bunch instabilities, especially at ESRF, where this method is successfully used for the operation [5]. When the oscillators, which represent either the particles in a bunch or the different bunches in the train, have a finite spectrum of natural frequency with a distribution $\rho(\omega)$, the net response of the beam to the driving force due to wakefields in (1) is failing and the beam can be stable again if the frequency spread is large enough. The substitution of the induced voltage (2) by all oscillators with different frequencies into the single particle equation of motion (1) leads to the dispersion relation

$$-\Delta\Omega_0 \times 2\omega_s \int \frac{\rho(\omega)\, d\omega}{\omega^2 + 2 j \alpha_s \Omega - \Omega^2} = 1 \quad (5)$$

with $\quad \Delta\Omega_0 = -\dfrac{\alpha I_0}{4\pi E / e Q_s} \sum_p j \omega_p Z(\omega_p),$

the coherent frequency shift in the absence of Landau and synchrotron dampings. When frequency spread is provided by point-like bunches in the train, the integral should be replaced by a summation over the individual bunches, though the integral might be kept for many bunches.

2.1 rf voltage modulation

A first source of bunch frequency spread can come from the modulation of the rf voltage, easily provided by beam loading in the rf cavity with partial filling of the ring. In the steady-state, the phase of the bunches grows about linearly. As a result, the frequency distribution consists in a nearly rectangular spectrum, with total spread and phase

modulation

$$\frac{\Delta\omega}{\omega} = \frac{1}{2}\frac{\Delta V}{V} = \tan \Delta\phi \cdot \tan \phi_s \,,$$

$$\Delta\phi = \frac{\omega}{2V} R/Q\, I_0\, \Delta T_{gap}$$

At ESRF, the instability threshold has been increased by this way, from about 60 mA to beyond the nominal intensity of 200 mA with a 1/3 filling.

A stability diagram, corresponding to the dispersion relation (5), is usually defined in the complex plane by plotting on the one hand the locus of the inverse of the integral as Ω is swept from $-\infty$ to $+\infty$, and the frequency shift $\Delta\Omega_0$ without Landau and radiation dampings on the other hand. Figure 2 shows for example the stability diagram of the SOLEIL ring, assuming LEP Cu cavities, operating at 352 MHz and having a first HOM at about 500 MHz (R/Q=75Ω and Q=3.10⁴). As the frequency of the cavity mode is not exactly known, it is also scanned and the frequency shift $\Delta\Omega_0$ just looks like the resonance curve of the HOM. Without Landau damping, the instability threshold is 14 mA, assuming perfect overlap of the HOM with a spectral line of the beam. To achieve a threshold I_{th}, a rectangular spectrum must have a total frequency spread $\Delta\omega$ given by

$$\frac{\alpha I_{th} \omega_r R_s}{4\pi E / e Q_s} = \frac{\Delta\omega}{\pi/2 - ArcTan(\alpha_s/\Delta\omega)}$$

For 100 mA, the required spread is larger than 6 %, whereas the frequency spread provided by the fractional filling is only 0.3 % for a current of 100 mA and a 2/3 filling of the SOLEIL ring, making this method impractical in this case.

Figure 2: Stability diagram for the SOLEIL ring
- radiation damping only + HOM with 16 mA
- rectangular spectrum (spread = 6.3 %) + HOM (100mA).

Synchrotron frequency splitting can also be achieved by driving the normal RF cavities at a frequency $(h \pm 1)f_0$ and was used at CERN to suppress longitudinal instability [6].

In a similar way, aiming at producing a frequency spread even for an homogenous filling, an active rf modulation has been tested in the ESRF storage ring by driving two of the four installed cavities at one revolution harmonic above the rf frequency. The modulation frequency must be precisely f_0 to avoid longitudinal excitation of the beam. All the HOMs could be made in principle harmless well beyond the nominal intensity of 200 mA. However, the n=1 instability prevents the cavities from being tuned close to the h+1 revolution

harmonic. The trade-off between the modulation level and the reflected power due to detuning, results in a maximum current of 170 mA.

2.2 Landau cavity

Since an harmonic cavity introduces non-linearities in the focusing force and thus some spread in synchrotron frequency, it has been proposed [7,8,9] for stabilizing multi-bunch instabilities. The maximum frequency spread is achieved in bunchlengthening mode, when the slope of the total voltage is zero at the bunch location. With this quartic bucket potential, the distribution has the form [10]

$$\rho(\omega) = K\omega^2 e^{-\frac{1}{2}(\omega/\omega_n)^4},$$

and has a maximum at $\omega = \omega_n$ which is generally much lower than the natural synchrotron frequency. A 3rd harmonic cavity in the SOLEIL ring provides in this way a relative frequency spread of about 200%, but since the center-frequency has been dramatically decreased, the net result is a poor improvement in the stabilization. The stability diagram with and without Landau cavity are shown in Fig.3. The gain on the instability threshold is only 30%. We note that, operating in the bunch-shortening mode, the same harmonic cavity would give a gain of about $\sqrt{2}$ on the threshold (the same as the synchrotron frequency enhancement) with a same voltage, about one third of the main rf voltage.

Figure 3: Stability diagram for the SOLEIL ring
- radiation damping only + HOM with 16 mA
- spread from a 3rd harmonic cavity + HOM with 18 mA.

2.3 Betatron tune spread

Conversely to the longitudinal case, a significant spread in betatron frequency is easily obtained because of the non-linearities in the focusing system or with a non-zero chromaticity, together with an energy spread in the beam. For that reason essentially, transverse multi-bunch instability occurs after longitudinal instability on most of the existing rings, whereas a crude threshold calculation gives generally the inverse. With Gaussian distribution in energy and betatron frequency spectrum $\sigma_\omega = Q_\perp\omega_0\xi\sigma_E/E$, the dispersion relation can be analytically calculated. Neglecting the transverse damping rate $\alpha_\perp$, the required spread is simply:

$$\sigma_\omega > -\sqrt{\frac{\pi}{2}}\,\Im m(\Delta\Omega_0)$$

For example, the transverse instability, excited by the most dangerous dipole HOM of the LEP Cu cavity

(f_r=614 MHz, $R_\perp/Q$=360 Ω/m, Q=6.10⁴) has a current threshold of only 6 mA. A chomaticity of only $\xi = 0.1$ pushes away the onset of the instability to 240 mA. The corresponding stability diagram is shown in Fig.4.

Figure 4: Stability diagram for the SOLEIL ring Gaussian betatron spread with chromaticity $\xi = 0.1$ and energy spread $\sigma_E/E < 10^{-3}$.

3 MODE FREQUENCY CONTROL

As the coupled-bunch modes are spaced one revolution frequency apart, there is some latitude in relatively small rings to escape the sharp HOMs from the beam spectrum lines, provided that they are not damped. This method was developed and is routinely used at ELETTRA [11], where the HOMs are tuned by precise cavity temperature control. Temperature windows, in which the growth rates of all modes are below the radiation damping rate, are first calculated. These stability windows can be checked and refined by a direct measurement of the coupled bunch mode spectrum on the machine. The growth rate of all longitudinal and transverse modes are calculated according to the expressions (3,4) by summing the contribution of all cavities present in the machine. The resonance frequency ω_k of cavity mode k is then a function of temperature T and fundamental mode tuning ω_f, being itself function of beam current; at first order :

$$\omega_k(T,\omega_f) = \omega_k(T_0) + \frac{\partial\omega_k}{\partial T}(T - T_0) + \frac{\partial\omega_k}{\partial\omega_f}(\omega_f - \omega_{f0})$$

Since it was difficult at ELETTRA to find temperature intervals, stable for both longitudinal and transverse planes, movable plungers were designed for allowing an additional degree of freedom [11]. Assuming six Elettra-type cavities installed in the SOLEIL ring to provide 5 MV rf voltage and 400 kW rf power to the beam, the cavity temperatures have been optimized by taking into account the nine longitudinal modes below the cut-off frequency of the beam tubes. The HOM spectrum has been randomly generated with a frequency spread of a few MHz for each cavity. Fig.5 shows for example one stability window of one cavity after optimization, for a temperature scan of 30°C. Only the growth rates above the radiation damping rate are plotted. However, it was not always possible to find stability intervals for some HOM spectra (25% over 100 seeds) and movable plungers would be also required for that cases.

Figure 5: Example of stability window for one of the Elettra-type cavities in the SOLEIL ring.

4 HEAVY MODE DAMPING

The other way to combate CBI consists in grappling directly with the source of the instabilities, i.e. in damping as much as possible the HOMs in order to lower the resonant buildup of the fields. Once the deQing requirements are determined so that growth rates do not exceed the radiation or eventually feedback damping rates, dampers must be designed and their effectiveness checked with bench measurements. Various designs for superconducting and normal conducting cavities have been developed to meet high power and low impedance challenges. SC technology offers many advantages:

- Fewer cells, and thus lower overall impedance, for a given voltage, due to the high CW gradient capability
- Higher achievable deQing, because large beam holes are allowed, while keeping a very high accelerating mode shunt-impedance, through which HOMs can propagate out and be easily damped.

The drawbacks of SC systems are nevertheless a larger complexity, owing mainly to the cryogenic system, and the precautions that have to be taken against the risk of pollution of coupler and cavities, which could result in Q_0 degradation or even quenches.

For NC cavities, dampers are mounted directly on the cavity walls at proper locations, where the coupling to the most troublesome modes is maximum. HOM power is carried out and dissipated on external rf loads. Waveguide couplers, with a cut-off frequency slightly above the fundamental mode frequency, offer a natural FM rejection and provide higher deQing than coaxial couplers. Three ridged waveguides are generally placed symetrically around the nose-cone shaped cell to provide heavy damping [12,13]. Care must be paid to the additional power dissipation, due to field penetration into the waveguide, in the estimation of the thermal stress of the cavity wall at high field level.

Dampers cannot be directly mounted on the cavity walls of SC cavities (risk of multipactor, magnetic quench and surface contamination), but beam tubes can be made large enough for efficient coupling to the cavity modes.

Two approaches have been considered so far :

- Dampers are formed by the beam pipes themselves, by

bonding rf lossy material (ferrite) to the inner surface of both pipes, outside the cyostat (CESR, KEK-B)
- More classical HOM dampers are mounted on the beam pipes, in the vicinity of the cavity (LHC, SOLEIL)

The first option [14,15] needs very large openings to ensure the propagation of all modes and the high HOM powers require that special attention be paid to the outgassing rate of the ferrite for preventing surface contamination. The second option allows the housing of several cells in a single cryostat, but puts more the issue on the HOM couplers, which must be optimized in combination with the string of cavities. A special arrangement, proposed for SOLEIL [16] and shown in Fig. 6 involves pairs of cavities, linked with large beam tubes in-between, but terminated on smaller outer pipes, featuring strong coupling for the HOMs and weak coupling for the accelerating mode.

Figure 6: Cavity-pair arrangement for SOLEIL featuring weak coupling for the accelerating mode (top) and strong coupling for HOMs (bottom).

HOM dampers are mounted on the wide tubes, where the standing-wave HOM fields have large peaks. Inner tube diameter and cavity spacing have been numerically optimized and checked by bench measurements. Two coaxial couplers per cell, tailored to the deQing requirement of each HOM, are enough to meet the SOLEIL specifications, with a safety margin of the order of 10 for both planes.

5 FEEDBACK SYSTEMS

Active feedback systems have been developed for more than 20 years [17], first in the frequency domain, on a mode-by-mode basis, and more recently in the time domain [18,19,20], on a bunch-by-bunch basis, thanks to the advent of commercially available fast Digital Signal Processors. They are complementary to passive mode damping in the sense that they can damp definitely all coupled bunch modes, so long as impedances arising from strong HOMs have been first sufficiently reduced. Otherwise, and assuming that the coherent frequency shifts are smaller than the synchrotron frequency to prevent any coupling of internal modes, a huge broadband and very expensive power would be required at the kicker. The

correction kick voltage needed to just cancel the beam-induced voltage causing growth of a coupled-bunch mode is

$$\Delta V = I_0 \, \Delta\phi \sum_p \frac{\omega_p}{\omega_{rf}} \Re e\left[Z(\omega_p)\right]$$

where $\Delta\phi$ is the amplitude of phase modulation at the rf frequency for the coupled-bunch mode.

Let's consider again with the first HOM of two LEP Cu cavities in the SOLEIL storage ring (f_r=500 MHz, R/Q=75Ω and Q=3.10^4), full coupling would call for a longitudinal kick of 84 kV/turn, assuming a mode amplitude of 1.5°. The power required $P = \Delta V^2 / 2 R_s$, would be more than 5 MW, assuming a DAΦNE type kicker (low-Q resonator loaded with ridged waveguides, shunt impedance of about 700 Ω). In order to make the feedback damping rate practical, cavity modes must then be firstly reduced by nearly two orders of magnitude.

Any feedback system consists mainly of three parts:
- A detector for beam oscillations measurement
- A filter, analog or digital, for providing the proper time delay, corresponding to a $\pi/2$ phase rotation, while suppressing the dc component in the error signal
- A broadband amplifier and kicker for imparting the correction kick

The mode-by-mode feedback is generally used when only a few troublesome coupled-bunch modes have been identified. For a very large number of bunches, the bunch-by-bunch approach is more attractive. In the latter case, the bunches are treated as individual oscillators and the minimum bandwidth of the feedback system must be, from the Nyquist theorem, half the bunch frequency to be able to damp all coupled-bunch modes. PEP-II, ALS and DAΦNE have adopted a common longitudinal feedback system design, based on fast ADC/DAC converters and DSP chips for digital filtering. After digitizing of the baseband error signal, a N-taps FIR (Finite Impulse Response) filter, which performs a discrete-time convolution over N prior values of the error signal, is used for providing maximum gain at the synchrotron frequency and zero dc response. Taking advantage of the relatively low synchrotron frequency, the number of processors needed is reduced by sampling at a rate slower than the revolution frequency. A detailed hardware description can be found in [19]. In addition, the DSP architecture revealed to be an efficient diagnostics tool, such as measurements of growth and damping rates by means of time domain transient techniques [21]. For KEK-B, the oscillation is damped simultaneously at both phase shifts $\pi/2$ and $3\pi/2$, with gains of inverted signs, by using a simple and very fast (no multiplications) 2-tap digital filter [22]. Transverse feedback systems usually combine the signals of two PU, placed approximately 90° in betatron phase apart, with appropriate coefficients to produce the $\pi/2$ betatron phase shift for any kicker location and betatron tune. Signal processing (PU signals

combining and time delaying) is preferably performed at baseband by a digital system [23].

REFERENCES

[1] A. Mosnier, "Cures of Coupled-Bunch Instabilities : Landau Damping, HOM Frequency Control, HOM Free Cavities and Feedbacks", SOLEIL Report 99-3, 1999.

[2] F.J. Sacherer, "A Longitudinal Stability Criterion for Bunches Beams", IEEE Trans. Nucl. Sci., NS-20, 825, 1973.

[3] J.L. Laclare, "Bunched Beam Coherent Instabilities", CERN 87-03, Vol. I, pp. 264-326, 1987.

[4] A.W. Chao, "Physics of Collective Beam Instabilities in High Energy Accelerators", J. Wiley & Sons, 1993.

[5] O. Naumann and J. Jacob, "Landau Damping of Longitudinal Instabilities for the Operation of the ESRF Storage Ring", Proc. of the 6th European Part. Acc. Conf., Stockholm, June 1998.

[6] D. Boussard and J. Gareyte, "Damping of the Longitudinal Instability in the CERN PS", Proc. of 8th Int. Conf. of High Energy Acc., CERN 1971.

[7] R. Bosch and C. Hsue,"Suppression of Longitudinal Coupled-Bunch Instabilities by a Passive Higher Harmonic Cavity", Proc. of Part. Acc. Conf., 1993, Vol. 42(2), pp. 81-99.

[8] S. Bartalucci et al, "A 3rd Harmonic Cavity for DAΦNE", Proc. of the 4th European Part. Acc. Conf., London, June 1994.

[9] Å. Andersson et al, "Landau Cavities at MAX II", Proc. of the 6th European Part. Acc. Conf., Stockholm, June 1998.

[10] A. Hofmann, S. Myers, "Beam Dynamics in a Double RF System", Proc. of the 11th Int. Conf. on High-Energy Acc., Geneva, 1980.

[11] M. Svanderlik et al, "Improved Methods of Measuring and Curing Multibunch Instabilities in ELETTRA", Proc. of the 5th European Part. Acc. Conf., Sitges, June 1996.

[12] R. Boni, "High Power Test of the Waveguide Loaded RF cavity for the Frascati$I$ Φ–Factory Main Rings", Proc. of the 5th European Part. Acc. Conf., Sitges, June 1996.

[13] R. Rimmer et al, "Higher Order Modes Damping Studies on the PEP-II B-Factory RF Cavity", Proc. of the 3rd European Part. Acc. Conf., Berlin, March 1992.

[14] T. Furuya et al, "Superconducting Accelerating Cavity for KEK B-Factory", Proc. of the 7th Workshop on RF Superconductivity, Gif-sur-Yvette, October 1995.

[15] S. Belomestnykh et al, "Development of Superconducting RF for CESR", Proc. of the 1997 Part. Acc. Conf., Vancouver.

[16] A. Mosnier et al, "Design of a Heavily Damped Superconducting Cavity for SOLEIL", Proc. of the 1997 Part. Acc. Conf., Vancouver.

[17] F. Pedersen and F. Sacherer, "Theory and Performance of the Longitudinal Active Damping System for the CERN PS Booster", IEEE NS-24, No 3, 1396 (1977).

[18] M. Bassetti et al, "DAΦNE Longitudinal Feedback", Proc. of the 3th European Part. Acc. Conf., Berlin, June 1992.

[19] G. Oxoby et al, "Bunch-by-bunch Longitudinal Feedback System for PEP-II", Proc. of the 4th European Part. Acc. Conf., London, 1994.

[20] D. Teylerman et al, "Operation and Performance of the PEP-II Prototype Longitudinal Damping System at the ALS", Proc. of the 1995 Part. Acc. Conf., Dallas.

[21] S. Prabhakar, "Observation and Modal Analysis of Coupled-Bunch Longitudinal Instabilities via a Digital Feedback Control System", pub. in Particle Accelerators, 57/3, 1997.

[22] E. Kikutani, "Strategy for Developing Fast Bunch Feedback Systems for KEKB", Proc. of the 1997 Part. Acc. Conf., Vancouver.

[23] W. Barry et al, "Initial Commissioning Results from the PEP-II Transverse Coupled-Bunch Feedabck Systems", Proc. of the 6th European Part. Acc. Conf., Stockholm, June 1998.

RECENT STUDIES ON BEAM-PHOTOELECTRON INSTABILITY IN BEPC

Z. Y. Guo, H. Huang, S. P. Li, D. K. Liu, Y. Luo, L. Ma, Q. Qin, L. F. Wang, J. Q. Wang, S. H. Wang, J. W. Xu, K. R. Ye, C. Zhang, F. Zhou, IHEP, Beijing China

Y. H. Chin, H. Fukuma, S. Hiramatsu, M. Izawa, T. Kasuga, E. Kikutani, Y. Kobayashi, S. Kurokawa, K. Ohmi, Y. Sato, Y. Suetsugu, M. Tobiyama, K. Tsukamoto, K. Yokoya, KEK, Japan

Abstract

An experiment investigating the photoelectron instability has been performed in BEPC at IHEP, China. The betatron oscillation of each bunch was observed and recorded by a single pass beam position monitor system which has a capability to measure the transverse position of every bunch over 16000 turns. The effect of an octupole magnet on the instability was also studied. This paper describes results of those observations and analyses.

Table 1: Main parameters in the experiment

Beam energy	1.3 GeV
Nominal betatron tune	5.82 (H) and 6.74 (V)
Natural emittance	0.134 mm mr
RF frequency	200MHz
Rad. damping time (trans.)	86 ms
Harmonic number	160
Minimum bunch spacing	5 nsec

1 INTRODUCTION

Several years ago, an anomalous vertical coupled-bunch instability was observed[1] in PF at KEK, Japan. It occurs only with the positron beam and the threshold current is rather low. K. Ohmi proposed a physics model[2] which can qualitatively reproduce the phenomenon. According to this model, the instability is caused by the cloud of an enormous number of electrons which are produced by synchrotron light hitting the inner surface of the beam chamber. With reference to this mechanism, we call the instability, the *Photo Electron Instability* (PEI).

In order to investigate the nature of the PEI, a series of experiments have been carried out in BEPC since 1996 under the collaboration of IHEP, China and KEK, Japan. At the early stage of these experiments, we found an instability in BEPC, which was very similar to that observed in PF. After that we studied the dependence of the instability on several parameters such as chromaticity, bunch spacing, emittance, beam energy, RF frequency, on/off status of distributed ion bumps, betatron tunes, magnetic field, RF voltage and so forth. Results of these experiments were published in the Proceedings of PAC97[3], EPAC98[4] and APAC98[5].

The recent experiment was carried out in May 1998. Aims of this experiment were (1) measurement of vertical damping time, (2) time domain analysis of the oscillations with a single-pass beam position monitor (SPBPM) and (3) investigation the effect of an octupole field on the instability. In this paper, we report the results of these investigations.

2 EXPERIMENTAL SETUP

The main parameters in the experiment are given in Table1. Basic beam-diagnostics tools for the experiment are pickup electrode connected to a spectrum analyzer HP8568B and a synchrotron light monitor, which is very useful to confirm the occurrence of the instability visually. Also a wall current monitor is indispensable for checking the relative population of particles in each RF bucket.

Another beam-diagnostic device, which was added this time, is the SPBPM developed at KEK[6]. This is a very powerful tool for investigating the nature of instabilities. Traditionally, the mode analysis of the instability has been done with a spectrum analyzer, which is essentially narrow-band device. However, when the bunch spacing in the beam is very short, for instance, a few nano seconds, observing the spectrum around each revolution harmonic is very time-consuming. Conditions of the instability may be changed during data acquisition due to a change of beam parameters, such as the beam current. The SPBPM system, in contrast to a spectrum analyzer, enables us to acquire data in a very short time, owing to its wide band-width. In addition, with this system we can study the time development of the instability.

The SPBPM system consists of (1) front-end electronics as a bunch position detector, (2) a fast A-to-D converter (FADC) and (3) a memory system which can store data up to 20 MB. A diagram of the FADC-memory system is shown in Fig. 1.

One set of the BPM electrodes are connected to the front-end electronics, and the position of every bunch was recorded turn by turn. Out of 20 MB memory capacity, only 2.6 MB was used in each file. This corresponds to 16384 (2^{14}) turns of 160 bunches (full bucket filling). The number of the turns 16384 was supposed to be large enough for the analysis of the phenomenon and was reasonable for quick semi-real-time analysis.

Another newly installed device is an octupole magnet to control the damping time of beam oscillation. Experience in PF showed that the octupole field introduces the damping to the instability.

Figure 1: Block diagram of the FADC and the memory system.

Figure 2: Damping rate as a function of bunch current.

3 RESULTS AND DISCUSSIONS

3.1 Measurement of damping time in vertical plane

The purpose of the damping time measurement is to estimate the growth time of the PEI at its threshold current. A single bunch with very low current which is at the level of the PEI threshold was stored in the ring, and betatron oscillation was resonantly excited by a stripline kicker. Just before the excitation is turned off, the data acquisition by the SPBPM system starts to record the damping behavior of the bunch.

The damping rate was obtained as follows. The 16384-point data were divided into 64 sub-data each of which contains 256-point. Each sub-data was processed by Fourier transformation and amplitude corresponding to the tune was picked up. Then we have the amplitude as a function of time. When we fit this function with an exponentially damped function plus an offset, we get the damping rate.

The damping rate was measured for several values of the bunch current and the result is shown in Fig. 2. It shows us that the damping rate linearly increases as a function of bunch current. The line can be extrapolated to zero-current and is consistent with the radiation damping rate of 12 s^{-1}. No Landau damping was observed in the experiment.

3.2 Mode analysis

A basic method of investigating coupled-bunch instabilities is the mode analysis, because the mode distribution holds the information on wake force which causes the instabilities. In this experiment we have done this mode analysis using the SPBPM data, which can track the behavior of the modes as a function of time.

The 160 × 16384-point data are divided into sub-data of 160 × 256-point data. The discrete Fourier transform was performed for each of the sub-data. The signal corresponding the tune (6.75) is picked up. Then we obtain mode spectra as a function of time.

Applying this method we analyzed a number of data taken for 160 positron bunches. One example of the time variation of mode amplitude is shown in Fig. 3. From this graph, we recognize two broad peaks within which many modes are growing and damping. It is a common characteristic of all the positron multi-bunch data. From the analysis results in this way, one can confirm the results obtained before with the spectrum analyzer[3].

Figure 3: Behavior of the modes for positron bunches.

Two broad peaks in the mode distributions can be reproduced by a simple phenomenological model, with which the growth time τ_s is given by

$$\tau_s^{-1} = Im \left[A \sum_{p=1}^{l} F(-pD) \exp\left[2p\pi i(m + \nu_\beta)/M\right] \right] \quad (1)$$

where A is a positive constant, F a transverse wake which affects on the next l bunches, m the mode number, ν_β the betatron tune, D the bunch spacing, and M the bunch number. The growth rate in the mode distribution and position of the peaks of Fig. 4 are similar to that of the

observation as shown in Fig. 3. This analysis shows us that the range of the wake is a few RF buckets. We adopted the rigid bunch simulation method in reference[4], in which the nonlinear wake force is involved, to track the behavior of the coherent coupled bunch oscillation. The simulation results show the same characteristic of the mode distribution as in Fig. 5.

Figure 4: Growth rate calculated by a simple step-function wake.

Figure 5: Mode distribution of the PEI

Fig. 6 depicts the time variation of the mode amplitude of electron beam which is totally different from that of the positron. There is one dominant mode whose mode number is 153. In the two beam model of the ion trapping[7], this mode can be excited if the ion tune ν_i is near $1 - \delta\nu_\beta$, where $\delta\nu_\beta$ is a fractional tune. Under our experimental condition, the condition $1 - \delta\nu_\beta$ is fulfilled if the beam current is 8.4 mA, which is not so far from the beam current of 11.8 mA where data were taken.

3.3 Effects of the octupole magnet

An octupole magnet was installed in BEPC ring to observe its effect on the the instability. When the octupole was excited to $K_3 = -33\text{m}^{-3}$, the instability was suppressed. The Landau damping rate by the octupole was calculated by the canonical perturbation theory[8] and it shows the damping time of 6.5 ms which should be the estimate of the growth time of the instability. A simulation based on the PEI model gives the growth time of about 3 ms which is close to the estimated growth time due to the octupole effect observation.

Figure 6: Behavior of modes for electron bunches.

4 SUMMARY

The photoelectron instability was studied in BEPC at IHEP, China. The SPBPM system was used to measure the bunch oscillation in the instability. Obtained mode spectrum shows two broad peaks. This has the same feature as the simulation based on the PEI model. The growth time of the instability was measured by exciting the octupole magnet. Estimated growth time by the measurement is 6.5 ms which is consistent with the result by the PEI simulation. The model of the beam-photoelectron instability is further confirmed by the recent studies on this phenomena in BEPC. No Landau was observed in the experiment. The reason why it was not observed is not understood yet.

5 ACKNOWLEDGMENT

6 REFERENCES

[1] M. Izawa et al., Phys. Rev. Lett. 74, 5044 (1995).

[2] K. Ohmi, Phys. Rev. Lett. 75, 1526 (1995).

[3] Z.Y. Guo et al., Proceedings of 17th PAC, Vancouver, B.C., Canada, 1566(1997).

[4] Z. Y. Guo et al., Proceedings of EPAC98, Stockholm, Sweden, 957(1998).

[5] Z. Y. Guo et al. Proceedings of 1st APAC98, KEK, Tsukuba, Japan, 5d020(1998).

[6] E. Kikutani et al., Proceedings of EPAC96, Barcelona, Spain, 1893(1996).

[7] E. Keil and B. Zotter, CERN-ISR-TH/71-58(1971); D.G. Koshkarev, P.R.Zenkevich, Particle Accelerators 3,1(1972).

[8] K. Ohmi, KEK Report 97-9, IHEP/BEPC/AP/97-09.

MULTI-BUNCH INSTABILITY DIAGNOSTICS VIA DIGITAL FEEDBACK SYSTEMS AT PEP-II, DAΦNE, ALS and SPEAR

J. Fox* R. Larsen, S. Prabhakar, D. Teytelman, A. Young, SLAC[†]
A. Drago, M. Serio, INFN Frascati; W. Barry, G. Stover, LBL

Abstract

Longitudinal feedback systems based on a common programmable DSP architecture have been commissioned at 4 laboratories. In addition to longitudinal feedback and beam diagnostics these flexible systems have been programmed to provide diagnostics for tranverse motion. The diagnostic functions are based on transient domain techniques which record the response of every bunch while the feedback system manipulates the beam. Operational experience from 4 installations is illustrated via experimental results from PEP-II, DAΦNE, ALS and SPEAR. Modal growth and damping rates for transverse and longitudinal planes are measured via short (20 ms) transient excitations for unstable and stable coupled-bunch modes. Data from steady-state measurements are used to identify unstable modes, noise-driven beam motion, and noise sources. Techniques are illustrated which allow the prediction of instability thresholds from low-current measurements of stable beams. Tranverse bunch train grow-damp sequences which measure the time evolution of instabilities along the bunch train are presented and compared to signatures expected from ion and fast ion instabilities.

1 TRANSIENT-DOMAIN DIAGNOSTICS

High current colliders such as the B Factories and Φ-factory, and high current light sources such as the ALS have pushed accelerator operation into regimes where coupled-bunch instabilities are operational concerns [1, 2]. Several of these facilities use active feedback to control longitudinal and transverse instabilities [3, 4]. Diagnostic techniques to understand thresholds for instability and diagnostics to understand the performance of the feedback systems have become important tools for operation of these facilities.

The longitudinal feedback systems developed for the PEP-II/DAΦNE/ALS machines use a digital processing architecture. This programmable processing block allows the recording of beam motion in conjunction with feedback or special diagnostic algorithms [5]. The information present in the oscillation co-ordinates is processed off-line to quantify the motion of the bunches. Information may be found in the steady-state controlled motion (information such as residual noise) or from dynamic sequences where the beam

might be excited to some amplitude, then damped back to the controlled state.

Our group has recently applied these transient-domain diagnostics to transverse instability measurements. We have used the existing ALS and PEP-II transverse feedback systems to control the beams in conjunction with the longitudinal processing hardware acting as a high-speed data recorder. In this scheme the digital processing block does not compute correction signals, though the digital hardware does control various gating functions in the transverse processing to synchronise the recording of excited/damped bunch motion. [6]

The longitudinal system design is based on downsampled processing, in which the sampling rate of the digital processing is matched to the oscillation frequency of the bunches, rather than the revolution frequency. Downsampled processing is advantageous for the longitudinal systems where the synchrotron oscillation frequency is significantly lower than the revolution frequency. The transverse systems operate as aliased sampling systems, as the revolution (sampling) frequency is lower than the natural betatron oscillation frequencies. The recording of this aliased information in the downsampled data recorder further aliases and folds the spectral information. However, if the machine tune is a known quantity and the downsampling factor is selected appropriately, downsampled recording loses no useful spectral information. The off-line data processing can completely recover the original oscillation frequencies and phase relationships in the bunches. Another way of thinking of the bandwidth required in the transverse motion recording process is that one must sample fast enough to unambiguously record the envelope of any signal modulation corresponding to bunch motion, though the carrier frequency of the bunch motion may not be recorded. The envelopes contain all the spectral information from which growth/damping rates may be calculated. Additionally, the sampling process correctly preserves the phase information in the bunch oscillations, so that the true modal information relating the phase relationships of the bunches is faithfully preserved in the analysis.

2 MODAL GROWTH AND DAMPING RATES FOR TRANSVERSE AND LONGITUDINAL PLANES

The most direct measurement of unstable motion is found from grow-damp sequences, in which a controlled beam is

a) Osc. Envelopes in Time Domain

Figure 1: . Grow-Damp sequence in the horizontal plane from the ALS. The envelope of the bunch motion shows the free growth ($0 < t < 6$ms), then damping under the action of feedback ($t > 6$ms)

b) Evolution of Modes

Figure 2: . The recorded bunch motion is Fourier transformed to reveal the growth of modes 326 and 327.

allowed to grow in amplitude without feedback for a short interval, followed by a damping transient as feedback control is re-applied. Fourier-transform techniques allow the identification of particular unstable modes of motion from the bunch data representation [7]. An example from the the ALS reveals the growth of two transverse unstable modes in figures #1 and #2. The resistive-wall impedance is the dominant mechanism driving this instability, as revealed in the strongest growth of modes 326 and 327. The damping transient in this figure directly reveals the available gain margin in the feedback channel, as the damping rates are seen to be roughly 10X the growth rates for this current. Figure #3 shows a longitudinal damp-grow transient from the DAΦNE machine , which shows a system controlled by feedback from which unstable mode zero (barycentric) motion rapidly grows as the feedback is turned off.

One important feature of these transient-domain techniques is that the full spectrum of bunch motion is recorded

Figure 3: Modal longitudinal grow-damp transient from DAΦNE. The feedback is turned off and mode 0 in the machine is unstable with a rapid growth rate of 11 ms^{-1}

in a single transient, unlike a narrowband measurement made with a traditional spectrum analyser. Another important feature of this technique is that motion can be studied in the small-oscillation (linear) situation before saturation and non-linear mechanisms appear.

3 NOISE-DRIVEN BEAM MOTION

Useful information can also be extracted from steady-state records of controlled motion. The controlled system will show the signature of any disturbances driving the beam, attenuated by the action of the feedback system. In the longitudinal plane, motion of the beam might be due to true unstable motion from HOMs, or motion might be due to noise injected from the RF system. Our experience from the PEP-II LER commissioning illustrates these issues. Figure #4 shows a plot of LER modal amplitude (feedback on) vs. time for a 291 bunch even fill. There is significant structure in the data, suggesting that whatever mechanism is driving the beam at mode zero is a noisy or non-stationary process. Further experiments with the RF system revealed a 10Hz periodic phase modulation of the master oscillator, which was first identified from the beam spectral information. After improvement of the master oscillator phase noise [8] and implementation of a low-mode "woofer" through the RF system [9], the resulting all-mode rms noise floor is seen in figure #5. With these improvements the residual noise level for mode zero is at the 0.03 degree rms(at 476 MHz) level, while higher modes fall to 0.005 degrees rms which is the electronic noise floor of the processing channel.

4 PREDICTION OF INSTABILITY THRESHOLDS

As the growth rates of these instabilities are proportional to current, a threshold current exists for each mode for which the difference between a growth rate, and damping rate (

Figure 4: . Steady state feedback-on record of LER motion at 110 mA, showing a disturbance which drives mode zero at roughly 0.3 degrees rms with significant time structure.

Figure 6: . PEP-II LER longitudinal growth rates vs. current for modes 780 - 800

Figure 5: Steady state feedback-on record of LER motion (873 bucket pattern) at 730 mA, after improvement of master oscillator phase noise. The mode zero motion is now roughly 0.03 degrees rms, while the remaining controlled bandwidth has residual noise of less than 0.005 degrees.

from radiation damping plus action of the feedback system) becomes positive. In an operational environment it is desirable to be able to predict the instability threshold (for example, to confirm the configuration of the RF system) without having to dedicate a fill to check a threshold directly. The grow-damp sequences, if measured above the no-feedback threshold, directly measure the gain margin at that specific current. If the measurements are repeated over a range of currents, a plot such as figure #6 can be made. This figure shows the free growth rate of the PEP-II LER for the most unstable band of cavity HOMs vs. current. The linear scaling of growth rate with current is seen, and the projection of the line to the zero current position reveals the radiation damping in the system (design value $\lambda_{rad} = 0.03\text{ms}^{-1}$). The threshold is clearly seen at 310 mA where the growth rate becomes positive. Related

techniques, examining fed-back damping rates vs. current, and quantifying the degree of saturation in the feedback channel allow the prediction of a maximum current that can be controlled with feedback from lower-current measurements. If the grow-damp sequences are performed with positive feedback, rather than no feedback for the exciting interval, these measurements can be made well below threshold and still predict the instability thresholds. Figure #7 shows this sort of positive feedback excitation from SPEAR, revealing the two modes closest to instability. In a commissioning environment, in which operating currents may be below the design current, it has proven very useful to be able to predict high-current behavior, and operating margins, before exploring the high-current operating points directly.

Figure 7: Grow-damp transient from SPEAR. The data is taken at 29 mA, for which the machine is below threshold. Positive feedback is used to excite the growing portion of the transient, revealing modes 65 and 67 as the two modes closest to instability.

hb

Figure 8: Vertical rms bunch motion for a 150 bucket train (150 buckets filled at 2 RF bucket spacing) for 10 successive instants during a 20 ms damp-grow measurement at 66 mA. In this case feedback is turned off at 1.3 ms. The first 20 bunches start out at a larger damped amplitude. The motion initially grows from the tail progressing towards the head of the train.

5 TRANSVERSE BUNCH TRAIN STUDIES

During the PEP-II HER comissioning a detailed series of transverse instability measurements was made to try to understand the mechanism which was producing unexpectedly rapid growth rates in both vertical and horizontal planes [10]. Measurements were performed on a variety of fill patterns, including various even-fill patterns, and very asymmetric train patterns. The impedance spectrum sampled by these varied patterns is quite different, and it is interesting to observe the evolution of instabilities in these bunch trains as a possible signature of ion instabilities [11]. Such a measurement from the PEP-II HER is shown in figure #8, which shows the vertical rms amplitude of bunch motion along a 150 bunch train at 10 intervals during a 20 ms damp-grow sequence. Motion is clearly seen to originate from the tail of the train and propogate back towards the head, with an interesting secondary growing structure appearing around bucket 90 roughly 10 ms into the sequence. Also seen is a growth of the leading bunches during the transient in isolation from the motion at the tail.

Figure #9 shows the average spectrum of each bunch during the transient. The motion is composed of a single eigenmode, and there is no measurable tune spread along the train. Such a tune spread would be strongly suggestive of a fast-ion type instability due to variations in the ion tune[12]. Figure #10 is a presentation showing the angular position in phase space of each bunch vs. time for this 20 ms damp-grow transient. The reference phase is taken from bunch 150 (the tail of the train). The figure shows several striking features. First, the anomalous amplitudes for the first 20 bunches are seen to be motion corresponding

Figure 9: Average spectrum vs. bunch number for the 150 bucket train transient. The figure suggests only a single eigenmode is present in this data.

to a 180 degree phase shift relative to the tail (other diagnostics indicate that these initial bunches are uncontrolled or driven by some mechanism, even in the damped state). The majority of the train of oscillators stays mostly fixed in phase space relationship during the growing transient. As the amplitude grows, the phase across the train uniformly shifts due to tune shifts with amplitude of motion. The unusual feature growing around bunch 90 after 10 ms is also seen as a phase perturbation in this figure, most likely from the same non-linear restoring mechanism which produces a tune shift with amplitude of motion.

Figure 10: Surface plot showing the phase of each bunch vs. time for this 20 ms dampgrow transient. The reference phase is taken from bunch 150 (the tail of the train). The figure shows several striking features. First, an anomalous 180 degree phase jump for the first 20 bunches. Second, as the bunch motion grows a general phase shift with amplitude is present, suggestive of some non-linear restoring potential which gives some tune dependence with amplitude. This non-linear amplitude effect is clearly seen in both the tail and around bunch 90 as the amplitudes of motion become large.

A series of bunch train and uniform fill studies, in conjunction with deliberate variations of ring vacuum produced evidence which could be interpreted as suggestive of both ion-driven and HOM driven instabilities. The tail to head growing motion observed in the figure can be obtained from a resonator mechanism if the Q of the resonator is such that the energy stored in it is largely dissipated between turns in the ring.

6 GAP TRANSIENTS AND COLLIDER OPERATION

To help prevent ion instabilities the PEP-II design uses a current distribution with an unfilled gap of 5 to 15% of a revolution. Such a gap produces a significant transient in the RF cavity voltage, so that along the turn the individual bunches ride on unique synchronous phases. This effect produces a DC shift in the synchronous phase of the bunches vs. bunch number, such that the luminous region of collision moves if the LER and HER transients are not identical. The time-domain data from the motion recording directly shows this synchronous position of each bunch in the mean oscillation co-ordinate of each bunch. Figure #10 shows the variation in synchronous phase for the PEP-II HER (at 319 mA) and LER (at 638 mA) machines in collision.

Figure 11: Synchronous phases of the LER (638 mA) and HER (319 mA) in collision (873 bucket pattern).

The variation in synchronous phase around the turn is associated with a variation in synchrotron frequency (tune) around the turn, which leads to a de-coupling of the bunches in the turn, and significantly raises the instability thresholds for such uneven fills [13, 14].

7 SUMMARY

The original PEP-II/ALS/DAΦNE longitudinal systems have been commissioned and we continue to develop longitudinal operating codes and longitudinal diagnostics. The programmable architecture and flexible structure of the longitudinal processing design has been extended to implement recording functions useful for transverse diagnostics. The information contained in the time-domain data, in conjunction with the development of new diagnostic codes, continues to suprise us with the variety and subtlety of the behavior of the beams.

8 ACKNOWLEDGMENTS

9 REFERENCES

[1] A. Mosnier, "Cures of Coupled-Bunch Instabilities: HOM Free Cavities, Feedbacks, Laudau Damping" Proc. IEEE Particle Accelerator Conference, 1999

[2] M. Serio "Multi-Bunch Instabilities and Cures," Proc. European Particle Accelerator Conference, 1996.

[3] M. Tobiyama and E. Kikutani, "Commissioning of the KEKB Bunch Feedback Systems" Proc. IEEE Particle Accelerator Conference, 1999

[4] S. Guiducci, "DAΦNE Operating Experience," Proc. IEEE Particle Accelerator Conference, 1999.

[5] D. Teytelman, et al, "Beam Diagnostics Based on Time Domain Bunch by Bunch Data," Proc. Beam Instrumentation Workshop, 1998

[6] W. Barry, et al, " Operational Experience with the PEP-II Transverse Coupled-Bunch Feedback Systems", Proc. IEEE Particle Accelerator Conference, 1999

[7] S. Prabhakar et al, "Observation and Modal Analysis of Coupled-Bunch Longitudinal Instabilities via a Digital Feedback Control System," Particle Accelerators, 57/3, (1997).

[8] R. Tighe, "A Sampled Master Oscillator for the PEP-II B Factory," Proc. IEEE Particle Accelerator Conference, 1999.

[9] P. Corredoura, "Architecture and Performance of the PEP-II Low Level RF System," Proc. IEEE Particle Accelerator Conference, 1999.

[10] H.U. Wienands, et al, "Beam Commissioning of the PEP-II High Energy Ring," Proc. IEEE Particle Accelerator Conference, 1999

[11] J. Y. Huang, et al "Study of the Fast Beam-Ion Instability in the Pohang Light Source," Proc. European Particle Accelerator Conference, 1998.

[12] G. Stupakov, T. Raubenheimer, F. Zimmermann, "Fast Beam Ion Instability," Phys.Rev.E 52, p. 5499, 1995.

[13] S. Prabhakar, et al. "Commissioning Experience from PEP-II HER Longitudinal Feedback," Proc. Beam Instrumentation Workshop, 1998

[14] S. Prabhakar, et al. "Calculation of Impedance from Multibunch Synchronous Phases: Theory and Experimental Results," Proc. European Particle Accelerator Conference, 1998

BEAM INSTABILITIES IN VERY LARGE HADRON COLLIDER

V. Shiltsev, J. Marriner, FNAL, Batavia, IL 60510
and V. Danilov, ORNL, Oak Ridge, TN 37831

Abstract

The Very Large Hadron Collider (VLHC) is a superconducting proton-proton collider with approximately 100 TeV cm and approximately $10^{34} \, s^{-1} cm^{-2}$ luminosity [1]. Currently, beam dynamics in this future accelerator is the subject of intensive studies within the framework of the US-wide VLHC R&D program. This presentation summarizes recent developments in the field. Besides general discussion on relevant VLHC parameters, we consider various beam instabilities and ways to avoid them. Finally, we outline possibilities for theoretical and experimental R&D.

1 COLLIDER PARAMETERS

At the energies contemplated, protons and anti-protons behave almost undistinguishably and the VLHC is foreseen as a pp collider. The 150 GeV rapid cycling Fermilab Main Injector produces a beam with the required quality to feed the 3 TeV VLHC Booster accelerator, followed by 50+50 TeV VLHC. The 3 TeV Booster has to be capable of cycling rapidity to fill the VLHC in a reasonable time. The parameters for the machine are not yet all fixed. The amount of freedom varies a lot from parameter to parameter. For example, the beam energy $E_b = 50$ TeV and the collider luminosity $L = 10^{34} \, s^{-1} cm^{-2}$ are fixed *a priori* by physics considerations [2]. The dipole magnetic field $B \approx 2$ T in the case of the low-field (LF) option, and $B = 10 - 14$ T for the high-field (HF) option are approximately fixed. Freedom in the dipole field is limited by the choice of magnet technology. Closely related to B, and also technology dependent, is the beam pipe aperture. It varies very little for LF - around $a = 9$ mm (half gap) and varies somewhat more for HF - $a = 10...20$ mm (radius). In the case of HF, the beam aperture is reduced from the physical coil aperture by the necessity of a synchrotron radiation beam screen. The choice of a significantly affects the magnet cost.

Another approximately fixed parameter is the bunch spacing. The first order assumption is $l_{bb} = 18.9$ ns which is the period of the 53 MHz RF system of the Fermilab Main Injector. Larger l_{bb} would increase the number of inelastic interactions/crossing $n_{int} \propto t_{bb}$ and would give a larger head-on beam-beam tune shift parameter $\xi \propto \sqrt{t_{bb}}$. Both are undesirable, but the total beam power decreases ($P_{stored} \propto 1/\sqrt{t_{bb}}$). LHC has $t_{bb} \approx 25$ ns. Present day detector triggering technology appears to disfavor bunch spacing of 10 ns or less.

Another detector-related requirement is to keep the number of interactions per unit length low (i.e. less than 0.2-0.3 int/mm would allow vertex recognition). This leads to the desire to a have longer luminous region, and therefore, bunch length. The latter could be as long as $\sigma_s = 5...10$cm

rms. One has aslo to consider the beta-function at the interaction point as an approximately fixed parameter. These considerations limit the minimum value of β^* to about 15 cm while the maximum value of about 50 cm is determined by the need for high luminosity.

Table 1: Zeroth order VLHC parameter list

Parameter, units	Low-field	High-field
Proton Energy, E_p, TeV	50	50
Luminosity, L, $s^{-1}cm^{-2}$	10^{34}	10^{34}
Injection Energy, E_{inj}, TeV	3	3
Dipole field , B, T	2.0	11.6
Circumference, C, km	520	95
Rev. frequency, f_0, Hz	577	3156
Bunch spacing, l_{bb}, ns	18.9	18.9
No. bunches, N_b	92000	16800
Bunch intensity, $N_p/10^{10}$	0.82	1.5
Total protons, $N_{tot}/10^{15}$	1.5	0.5
Tune, ν,	533.765	37.385
Slip factor, $\eta/10^{-5}$	0.4	72
No. half cells,	4200	350
1/2-cell length, L_{cell}, m	122	260
Phase/cell, μ, deg	90	60
Average beta, $< \beta >$, m	246	600
Max dispersion, D_x, m	0.5	23
Pipe 1/2 size, a, mm	9	16.5
RMS emittance, ε_n, $10^{-6} \, m$	1.0	2.5
Long. emitt.(rms), ε_L, eV·sec	.2	0.3
Mean beam current, I_B, mA	69	127
SR loss/turn, E_{SR}, MeV	0.6	3.4
Long. damping time, τ_l, hrs	40.4	1.3
RF frequency, f_{RF}, MHz	477	477
RF harmonic number, h_{RF}	$8.28 \cdot 10^5$	$1.5 \cdot 10^5$
RF voltage (inj), U_{RF}, MV	4(200)	7(40)
Acceleration time, T_{acc}, min	13	13
Bucket area (inj), A, eV·sec	18(31)	4(2.2)
Synchr. tune (inj), $\nu_s/10^{-3}$	0.2(5)	1 (14)
Bunch length (inj), σ_s, cm	7.6(5.5)	5.6(7.2)
Mom.spread (inj), $(\frac{\delta P}{P})/10^{-5}$	3.5 (100)	0.9 (9.1)
IP focus, β^*, cm	15	50
Head-on b.b. tune shift, ξ	0.001	0.0007
Int./crossing (max) n_{int}	24.7	31
Vertices/mm, $n_{int}/\sqrt{\sqrt{2\pi}\sigma_s}$	0.16	0.26

Transverse beam emittance at injection is thought to be somewhat fixed by the injector chain but depending on the bunch population it may vary within the range $\varepsilon_n = 1...3$ mm·mrad (normalized, in FNAL units 6-18 π). The emittance evolution at the collider energy depends on the choice of B, e.g., the HF option is less dependent on the injection emittance because of synchrotron radiation damping.

RF frequency f_{RF} also is "an approximately free parameter". To make synchronization and injection easier, the frequency should be a multiple of the FNAL Main Injector RF frequency of 53 MHz. Multi MV 477 MHz (=9×53 MHz) superconducting RF is considered for the VLHC [3].

Longitudinal emittance ε_L and the lattice are thought to be free parameters. Longitudinal emittance in the range of $0.2 - 3\,eV \cdot sec$ rms does not affect the luminosity and the other parameters too much, while larger emittances can help to damp instabilities. As for the lattice, it is relevant that numerous transverse instabilities have longer risetime in a lattice with smaller average beta-function. On the other hand, choice of the lattice must be done taking into account many other physical considerations as well as cost saving arguments. Table 1 presents the VLHC 0th order parameter list that is used for further analysis of instabilities.

2 BEAM INSTABILITIES

There are several instabilities which may take place in the VLHC. Some of them are rather "weak" in the sense that they do not lead to beam loss (e.g., coherent synchrotron tune shift, longitudinal microwave instability) or have slow growth rates (instability due to photoelectrons). Others are "strong" - like TMCI or the resistive wall coupled-bunch instability. All the effects are more severe in the low-field option of the VLHC. Nevertheless, we have found that **none of the instabilities can be considered as a "show-stopper" for either the low-field or high-field VLHC. Even at the current status of accelerator physics and technology there appear to be enough tools to damp/eliminate all of the instabilities.**

Transverse mode coupling instability at 3 TeV. This is also known as "strong head-tail" (in contrast to "weak head-tail" which is due to chromaticity). Frequencies of coherent bunch motion (mode 0) and head-tail motion (mode 1) are shifted by the transverse wide-band impedance toward each other. Above a threshold the frequencies become equal and instability occurs with characteristic growth time of a fraction of a synchrotron period.

TMCI in the LF VLHC is mostly due to RW impedance (>90% contribution) and has a threshold of [5]:

$$N_{thr} \approx 1.24 \cdot 10^{10} \times$$

$$\times \sqrt{\frac{\sigma_s}{.1m}} \cdot \frac{E}{3TeV} \cdot \frac{\nu_s}{0.005} \cdot \left(\frac{a}{0.9cm}\right)^3 \cdot \frac{520km}{C} \cdot \frac{250m}{<\beta>}. \quad (1)$$

Fig.1 demonstrates coupling of 0 and -1 azimuthal modes due to resistive wall wake $W_1(s) = -2C/\pi a^3 \cdot \sqrt{c/\sigma s}$ in the low-field VLHC. Five azimuthal modes and four radial modes are taking into account. The presented multimode analysis (see details in [5]). shows that above $N_p = 1.8 \cdot 10^{10}$ a positive imaginary part of the eigenfrequency appears (see lines marked by), that corresponds to unstable motion. Paramters of simulations are $<\beta> = 320$m, $\nu_s = 0.01, \sigma_s = 0.1$m, $E = 3$TeV, $C = 550$km, and round Al vacuum pipe with radius $a = 9$ mm is considered.

Comparison of the number of protons per bunch from Table 1 and the TMCI threshold is given below:

	Low Field	High Field
Protons/bunch, $N_p/10^{10}$	0.82	1.5
TMCI Threshold, $N_{thr}/10^{10}$	1.1	28.

Note, that for HF, most of the impedance (about 90%) comes from bellows, BPMs, RF, kickers, etc., and RW contribution is only about 10%. One can see that the safety factor $S = N_{thr}/N_p$ is about 1 in the LF VLHC, i.e., not large enough.

Figure 1: Beam eigenfrequencies vs. number of protons per bunch. Dots are for real part of frequency, stars are for imaginary part.

This instability was observed at many electron storage rings (PETRA, PEP, VEPP-4, LEP) which usually increase the synchrotron tune ν_s in order to increase the TMCI threshold. To date there is no solid evidence of the "strong-head tail" instability in proton machines. For example, there is a large spread of the Tevatron transverse broadband impedance estimates $Z_\perp = (3-10)$ MΩ/m (the resistive wall contributes about 0.8 MΩ/m) [5]. That yields threshold bunch populations of $N_{th}^{TeV} = (12 - 3.7) \cdot 10^{11}$. Since the maximum number of protons per bunch in the Tevatron to date has not exceeded $3.3 \cdot 10^{11}$, the Tevatron intensity is below the threshold. It is expected the proton TMCI will be important at injection into the SPS, when it works with LHC parameters [6] and in the VLHC.

Ways to increase the TMCI threshold. There are "trivial" ideas of increasing the TMCI threshold by decreasing C, or increasing aperture a, injection energy E_{inj} or bunch length σ_s. Unfortunately, most of these parameters are fixed or approximately fixed. A smaller beta function $<\beta>$ and larger synchrotron tune can help, see Eq.1, but may cause a significant cost increase (more quadrupoles, more powerful RF system). Less obvious and more interesting approaches are:

method	threshold increase
coalescing at 50 TeV	2-9
thin Cu, Ag coating	$\simeq 1.3$
asymmetric beam pipe	1.5-3
RF quadrupole	4
AC chromaticity	$\simeq 10$
Feedback system	5-more

Let us consider these techniques. Instead of injection into every 9th RF bucket (if $f_{RF} = 477MHz = 9 \cdot f_{MIRF}$), one can fill more buckets and thus, reduce the single bunch intensity (up to) 9 times. Of course, after acceleration to the top energy of 50 TeV one needs to coalesce every 9 bunches into one in order to get the design luminosity. To be effective, the coalescing process must not cause a significant increase in transverse emittance (while the longitudinal emittance requirement is not strong - see discussion above). The technique is routinely used in the Tevatron collider injector chain.

The use of a thin coating of conducting material with conductivity better than Al alloy can help as $N_{thr} \propto \sqrt{conductivity}$. For example, a 10 μm layer of copper or silver (2-3 times the skin-depth at bunch frequencies of about 3 GHz) will give a 30-40% threshold increase.

Recently, it was demonstrated in Ref.[9], that the absence of axial symmetry of the beam pipe leads to the appearance of an additional wake-force component which is proportional to the coordinate of the trailing particle in the bunch (while in axisymmetric structures, the force has a component which is proportional to the leading particle coordinate only). As a result, betatron oscillation frequencies of the head and tail of the bunch become unequal, and such a detuning leads to an increase of the TMCI threshold. For example, in a flat beam chamber geometry with half-gap a, one can expect a threshold increase of the order of 3-3.5 with respect to a round beam pipe with radius a (that factor consists of a factor of 2 in geometrical wake reduction and about 1.5-1.75 of improvement due to the detuning wake effect). However, it may be that the transverse coupled-bunch instability would require a round vacuum chamber, i.e., in contradiction to the TMCI consideration. Further studies and numerical simulations of the detuning wakes in elliptic chambers are under way.

One more opportunity to counteract effectively TMCI was considered recently in Ref.[10]. Introduction of a correlated tune spread from the head to the tail of the bunch using RF quadrupoles has shown a significant increase of the threshold if the spread is several times the synchrotron tune ν_s. The idea is similar to BNS-damping in linear electron-positron colliders which was experimentally proven as an effective way to counteract beam break-up in the SLAC Linear Collider. Figure 2 below shows an increase of the TMCI threshold in the LF VLHC driven by resistive wall wake with a head-tail tune spread generated by an RF quadrupole. The RF quadrupole for the VLHC seems to be a rather feasible technique as it requires only 20 m of superconducting RF cavities (or about 50 m of copper cavities) with a quadrupole mode excited. A major concern is

that the beam footprint due to RFQ induced incoherent tune spread can be too large to tolerate.

Figure 2: The TMCI threshold vs RF quadrupole tune spread parameter $\left(\frac{\Delta\nu_{RFQ}(1\cdot\sigma_s)}{\nu_s}\right)$.

A similar effect can be obtained by increasing lattice chromaticity ξ. It was suggested in [11] to have a time-variable chromaticity $\xi = (\Delta\nu/\nu)/(\Delta p/p)$ in the ring:

$$\xi(s) = \xi_0 + \xi_1 * sin(\omega_s s/c). \qquad (2)$$

The AC scheme not only provides damping of the weak head-tail instability but also increases the TMCI threshold due to Landau damping and rotation of the head-tail phase. Possible TMCI threshold increase is given by

$$N_{thr}/N_{thr}(\xi_1 = 0) \simeq 1 + 0.6 \cdot \xi_1 \nu(\delta p/p)/\nu_s. \qquad (3)$$

E.g., for parameters of the LF VLHC with $\xi_1 = 2$ (i.e., AC chromaticity about twice the natural one) we get a threshold increase at injection of about 9. As with the RF quadrupole, a foreseeable limitation would be reduction of dynamic aperture due to resonances. There is the possibility to reduce resonance excitation with very fast chromaticity modulation when different parts of the ring have different but constant in time $\xi(s)$.

The TMCI threshold can be increased with use of a feedback system. Resistive feedback doubles the threshold in PEP (see [7] and references therein) and in the VEPP-4M storage rings [8]. Relevant VLHC parameters (bunch length, synchrotron tune) are close to the VEPP-4M parameters. So, it can be assumed, that conventional feedback has to help at VLHC, as it does at the VEPP-4M collider.

A special kind of the "head-tail" feedback can further increase the TMCI threshold. Essentially, it is based on high-frequency pick-up(s) and kicker(s) which distinguishing "head-tail" motion (azimuthal modes) or portions of 10 cm long bunches (rms). After amplification, one turn delay and 90° betatron phase adjustment, the signal goes

into the kicker, that results in mode "-1" suppression. The tune shift of mode "0" is suppressed by a conventional resistive/reactive feedback system, and as a result, the mode coupling takes place at larger N_{thr}. Though preliminary results are very promising (4-10 times threshold increase), the method needs more analytical and numerical studies.

Generally speaking, the threshold increase factors for the different methods listed above can not be multiplied, e.g., RF quadrupole can not provide much TMCI damping in addition to the AC chromaticity scheme if the latter is implemented and generates the maximum allowable tune spread. Nevertheless, a combination of two or three appropriate methods can give safety factors in LF VLHC of the order of $S \simeq 6 - 20$ (which corresponds to a luminosity enhancement of S^2).

Coupled-bunch instability at 3 TeV This effect is proportional to the total beam current and is driven by the low-frequency transverse impedance due to the finite conductivity of the beam pipe walls. Instability growth time can be expressed in number of turns:

$$N^{RW} \equiv \tau_{RW} \cdot f_0 = \frac{\sqrt{2\pi}(E_p/e)a^3}{I_B Z_0 <\beta>} \sqrt{\frac{\Delta\nu\sigma_{Al}}{cR^3}}. \quad (4)$$

Rough estimates of N^{RW} at the injection energy of 3TeV are given below:

	Low Field	High Field
Mean beam current, I_B, mA	69	127
Risetime N^{RW}, turns	1.5	180

At first glance, these numbers look somewhat scary especially in the LF option. Nevertheless, taking into account that one turn is equal to approximately 500 km of the ring circumference, we conclud that such increments can be (easily) damped with use of distributed feedback systems. A general view of the system is presented in Fig.3. The system is based on the installation of several, e.g., 10, separate feedback systems around the ring. Each of the feedback systems provide strong damping of low-frequency coupled-bunch modes (bandwidth of 100-200 kHz) by transmitting a pick-up signal to the kicker via coaxial cable. Naturally, the signal propagates slower than protons in the ring and, therefore, the kick is applied to succeeding bunches. For example, using foam cable with $\beta \simeq 0.8$ to transmit the signal over 500 m (corresponds to $90°$ phase advance between pickup and kicker), the system will introduce a delay of about $(1-\beta)\cdot500 = 100$ m. The latter is much less than the lowest mode wavelength of about $\Delta\nu \cdot C \simeq 200$ km; thus, the relevant phase shift is very small $\phi = 100m/200km = 5 \cdot 10^{-4}$rad and will not affect the feedback operation. Of course, it will not be true for higher order coupled-bunch modes with frequencies $f_n = |\nu - n|f_0$ above 200-300 kHz, and one has to take care of these modes with the use of an additional standard one-turn-delay feedback system with lower gain (the instability growth time $N^{RW} \propto \sqrt{f_n}$).

Electron cloud instability at 50TeV arises due to a combination of photoemission and secondary emission from the vacuum chamber wall, by which, for each passing bunch

VLHC coupled-bunch instability damping scheme

Figure 3: Principle of the VLHC resistive wall coupled bunch instability damper.

train, an electron cloud builds up in the beam pipe. Interaction with this electron cloud can amplify small perturbation in the orbit of the individual bunches which results in transverse multi-bunch instability. The instability growth time can be estimated as [14]:

$$\tau \approx \frac{4\pi\gamma\nu}{N_p r_p c W_1(l_{bb})}, \quad (5)$$

where $W_1(l_{bb})$ is the transverse wake due to electrons. Only a few neighboring bunches can interact via the cloud. Eq.(5) gives $\tau \approx 10 - 15$ s for LF and about 0.5 s (1600 turns) for HF. In HF the instability is stronger than the resistive wall instability at 50 TeV and has to be damped by a bunch-by-bunch feedback system.

Coherent synchrotron tune shift at 50 TeV The coherent synchrotron tune shift is driven by inductive longitudinal broad band impedance. To preserve Landau damping, the synchrotron tune shift must remain smaller than the synchrotron tune spread. This leads to an upper limit for the impedance:

$$Im(Z/n)_{eff} \leq \frac{6}{\pi^3}\frac{h_{RF}^3 U_{RF}}{I_{bunch}}\left(\frac{\sigma_s}{R}\right)^5. \quad (6)$$

The instability is rather weak and can be eliminated by any of the following: a) increasing the bunch length, b) reducing the slope of the RF wave with a second RF system at a higher frequency, c) low-power longitudinal feedback for the first modes (e.g., quadrupole, sextupole, etc; dipole mode will be damped anyway by a mandatory phase locked loop). Such an instability was observed at the SPS [4]. Comparison of the impedance estimates and

threshold numbers is given below:

	Low Field	High Field
Estimated Im(Z/n)	0.1 Ohm	0.03 Ohm
Threshold CSTSI	0.4 Ohm	0.4 Ohm

The VLHC intensity is below threshold in both cases. Note that the longitudinal emittance $\varepsilon_l = 2$ eV·s for the LF case [1] and $\varepsilon_l = 0.3$ eV·s for the HF case.

Longitudinal microwave instability at 50 TeV Also known as "turbulent bunch lengthening", the instability leads to a blow-up of the longitudinal emittance above a certain threshold (instead of just distortion of the RF potential well). The instability is caused by coupling of the beam to the very high frequency part of the impedance, and does not lead to beam loss (see Ref. [4] for observations in the ISR). The threshold is given by:

$$|Z/n|_{eff} \leq \frac{1}{\sqrt{2\pi}} \frac{h_{RF} U_{RF}}{I_{bunch}} \left(\frac{\sigma_s}{R}\right)^3. \qquad (7)$$

Comparison of the impedance estimates and threshold numbers is given below:

	Low Field	High Field
Estimated $|Z/n|$	0.2 Ohm	0.05 Ohm
Threshold TMWI	1.4 Ohm	0.9 Ohm

Again, the longitudinal emittance of 2 eV·sec in the LF case leads to an acceptable safety factor. The threshold would be about 0.2 Ohm in LF for $\varepsilon_l = 0.5$ eV·sec, i.e. close to the machine impedance.

Feedback systems There are several feedback systems to be implement in the VLHC:

- transverse narrow band system (100-200 kHz) to damp resistive wall coupled bunch modes, injection errors, and the emittance growth;

- transverse one turn delay 26 MHz bandwidth feedback system for damping high frequency bunch-to-bunch modes and mode 0 of single bunch motion;

- transverse very wide band (3GHz) feedback is needed to damp the first head-tail mode of the single bunch motion;

- longitudinal feedback.

3 R&D OPPORTUNITIES

The question why TMCI has not been observed at proton machines should be studied in detail. In particular, we propose a measurement of the tune shift vs bunch intensity at the Tevatron. Existing data on the weak head-tail instability (due to chromaticity) at the Tevatron can be analyzed in order to get an estimate of the transverse impedance of the ring.

TMCI can be intentionally excited by a controlled increase of the Tevatron impedance due to "an electron lens" being constructed for beam-beam compensation in the Tevatron [12]. Wake fields due to the electron beam can cause the instability if the solenoid magnetic field is less than some threshold value (of the order of 17 kG) [13].

Detuning wake studies can include a) simulation of the detuning wakes in realistic geometry with available codes, like TBCI, ABCI; b) on-bench measurements of the detuning wake excitation at high frequencies in beam pipes; c) detuning wake measurements with use of short intense electron beams (from a photoinjector) traveling in an asymmetric environment (e.g. in between two parallel ceramic plates).

An RF quadrupole can be designed, fabricated and tested at an existing electron machine. A good candidate is VEPP-4M (Novosibirsk, Russia) where TMCI limits single bunch intensity, and bunch length and synchrotron frequency are comparable with the VLHC design parameters.

Evaluation of different kinds of feedback systems for TMCI suppression can be done with numerical codes, and a prototype feedback system could be built and tested.

Coupled-bunch instabilities suppression: the effectiveness of multistage feedback system with small delay (to damp the resistive wall coupled-bunch instability) has to be studied numerically. Experimental studies could concentrate on gain limitations in these systems. Another subject of studies can be the detuning wake effect on the coupled bunch instability in the VLHC.

4 REFERENCES

[1] see VLHC Web page *http://vlhc.org*; also G.Dugan, "VLHC R&D", these Proceedings.

[2] *Proc. VLHC Physics and Detector Workshop, FNAL, March 1997*, FNAL-Conf-97-318-T (1997).

[3] J.Marriner, V.Shiltsev, "Accelerator Technology for the VLHC", these Proceedings.

[4] L.Evans, AIP Conf. Proc. 127 (1985).

[5] V.Danilov, V.Shiltsev, FNAL-TM-2042 (1998).

[6] S.Peggs, Part. Accel., **50**, 19 (1995).

[7] S.Mayers, in *Proc. PAC'87, Washington*, 503.

[8] M.M.Karliner, *et al.*, in *Proc. EPAC'96, Barcelona*, 1009.

[9] A.Burov, V.Danilov, *Phys. Rev. Letters, vol. 82* (1999), 2286.

[10] V.V.Danilov, *Phys. Rev. ST - Accel. Beams, 1*, 041301 (1998).

[11] W.H.Cheng, A.M.Sessler, J.S.Wurtele, *Phys. Rev. E*, **56**, No.4 (1997), 4695.

[12] V.Shiltsev, *et.al*, FNAL-Pub-98/260 (1998).

[13] A.Burov, V.Danilov, V.Shiltsev *Phys. Rev. E*, **59** (1999).

[14] F.Zimmermann, CERN-LHC-95 (1997).

---

[1] the Main Injector can provide beams with smaller longitudinal emittance, e.g., $\varepsilon_l = 0.5$ eV·s, that would lead to the threshold as low as 0.01 Ohm that is 10 times less than the machine impedance in the LF.

FAST DIGITAL FEEDBACK SYSTEM FOR ENERGY AND BEAM POSITION STABILIZATION*

R. Dickson, V. A. Lebedev#, Jefferson Lab, Newport News, VA

Abstract

A digital fast feedback system for beam energy and position stabilization at the target of the CEBAF accelerator is capable of suppressing beam motion in the frequency band from 0 to 80 Hz and also performs narrow band suppression at the first twelve power line harmonics. The system utilizes two VME computers and runs at a 2.4 kHz sampling rate. The numerical algorithm is based on a recursive digital filter with an additional feedforward loop for suppression of high power line harmonics. The system suppresses beam motion by a factor greater than ten, thus achieving the stabilization of relative beam energy fluctuations to better than 10^{-5} and stabilization of beam position on the target to better than 20 μm.

1. INTRODUCTION

Study of the beam motion at different locations in the CEBAF accelerator [1] has shown that the beam has excursions in energy and in both transverse planes. The amplitude of the motion is roughly the same along the machine and is about $(0.5 - 2) \cdot 10^{-4}$ for relative energy change and 0.2 - 0.5 mm for transverse beam motion. The motion spectral density can be separated into two main regions: the low frequency region (0 - 80 Hz), and the high frequency region (below 1 kHz) where the beam motion mainly occurs at power line harmonics. The first three power line harmonics make the main contribution to beam motion at short time intervals, ≤ 1 min, while the contribution from harmonics higher than 12 can be neglected. The sources of the perturbation are scattered along the entire machine and it is almost impossible to correct them locally for each of 320 superconducting cavities and 1800 magnets.

While such beam motion does not cause a problem for beam transport, many experiments require better accuracy for beam energy and position stabilization on the target. A digital beam based feedback system has been chosen as the best candidate to resolve the problem. Such a system has significantly better flexibility than an analog system, and did not require significant changes in hardware.

2. CHOICE OF THE SYSTEM

Achieving the best possible beam stabilization in the framework of existing hardware was the main requirement

we set for the system. SEE beam position monitors (BPM) [2] were already installed for the beam lines of two experimental halls which required beam stabilization. The BPM resolution is about 20 μm per single measurement for beam current more than 10 μA and grows approximately inversely proportionally to the current below 10 μA. Maximum sampling rate determined by the BPM hardware is about 3 kHz. As can be seen below, that implies that the resolution of BPM measurements is a significant factor in determining the beam stabilization.

2.1. Beam Line Optics

The layout of the accelerator is shown in Figure 1. The beam starts in the injector. After acceleration to a required pass number, a fraction of the beam (or the whole beam) can be split by RF separator and sent to one of three experimental halls. Normally the beam is simultaneously delivered to all three experimental halls.

Figure 1: Layout of CEBAF recirculator.

Fast feedback systems are installed in the lines leading to Halls A and C. Each system consists of actuators (energy corrector, two horizontal and two vertical correctors) and a set of responders (BPMs) installed down-stream of the actuators. Taking into account that both halls have common energy regulation, only one of them can be used for energy stabilization. Each beam line has a string of dipoles bending the beam horizontally by 37.5 deg with achromatic optics. The bending creates the dispersion, which allows us to perform the energy stabilization. The beam position change at the responders can be expressed through optical functions of the transfer line and values of actuators,

$$\mathbf{x} = \mathbf{Ac} . \qquad (1)$$

Here $\mathbf{x}$ is the vector of BPM measurements $\mathbf{x}^T = (x_1, ..., x_N)$, and $\mathbf{c}$ is the vector of corrections $\mathbf{c}^T = (x_1, ..., x_M)$. To get a single solution for vector $\mathbf{c}$, the number of responders

should be more than or equal to the number of actuators, $N \geq M$. Below we will consider a system with four transverse correctors, c_1, c_2, c_3, c_4 and, if the energy correction is on, the energy corrector c_5. To compute values of actuators which will minimize the beam displacement the SVD (single value decomposition) algorithm [3] is used, so that

$$\mathbf{c} = \mathbf{Bx} \ , \qquad (2)$$

$$\mathbf{B} = \left(\mathbf{A}^T \mathbf{A}\right)^{-1} \mathbf{A}^T \ . \qquad (3)$$

To achieve maximum resolution the optics of the beam lines was altered. First, the focusing inside arcs was changed to attain maximum dispersion, which is compatible with achromatic transport. Second, the beta-functions through the arcs were adjusted to obtain optimum phase advances in between correctors and active BPMs. To maximize the sampling frequency only five BPM positions (three horizontal and two vertical) are usually used. In this case the optimum betatron phase advance is $\pi(n +1/2)$ for each pair of correctors and each pair of BPMs. The horizontal beta-function for the third horizontal BPM, which sits at the top of the dispersion function, was reduced to achieve better energy resolution. It yields a momentum resolution of $6.6 \cdot 10^{-6}$ for 20 μm BPM resolution. The use of all BPMs of the arc (six horizontal and six vertical) improves the system resolution by only about 10%. That justifies the reduced set of BPMs.

Figure 2: Dependence of the transfer function on frequency; the sampling frequency is 2.4 kHz, the low pass filter bandwidth is 1.5 kHz, $k_0 = 0.07$, $|k_1| = 0.05$, $|k_2| = 0.01$, $|k_3| = 0.01$, $\arg(k_1) = 0$, $\arg(k_2) = 0.5$, $\arg(k_3) = 0.5$; dashed line - the uncorrected transfer function, solid line - the transfer function corrected for low pass filter bandwidth.

2.2. Digital Filter

Noise in measurements causes the system to excite undesirable beam motion. For a generic single channel feedback system the noise drives the beam motion equal to

$$\overline{x_{output}^2} = \frac{\overline{x_{meas}^2}}{\pi f_s} \int_0^{\pi f_s} |K(\omega) - 1|^2 d\omega \ , \qquad (4)$$

where f_s is the sampling frequency, $\overline{x_{meas}^2}$ is the single measurement accuracy, and $K(\omega)$ is the transfer function

for a harmonic signal, $K(\omega) = x_{output_\omega} / x_{input_\omega}$.

The condition of the system stability also imposes a limitation for $K(\omega)$,

$$\frac{1}{\pi f_s} \int_0^{\pi f_s} \mathrm{Re}(K(\omega)) d\omega = 1 \ . \qquad (5)$$

This implies that if at some frequency the system strongly suppresses the input signal, $|K(\omega)| \ll 1$, it should amplify the signal at a different frequency, $|K(\omega)| > 1$. Thus to achieve optimum system performance, one needs to suppress the beam motion only in frequency ranges where the motion spectral density is significant.

The choice of digital filter parameters has been determined by necessity to suppress the beam motion at low frequency and the first three power line harmonics,

$$K(\omega) = \frac{e^{i\omega T} - 1}{e^{i\omega T} - (1 - k_0)}$$

$$\prod_{n=1}^{3} \frac{e^{i\omega T} - e^{in\omega_l T}}{e^{i\omega T} - (1 - k_n)e^{in\omega_l T}} \frac{e^{i\omega T} - e^{-in\omega_l T}}{e^{i\omega T} - (1 - k_n^*)e^{-in\omega_l T}} , \quad (6)$$

$$\equiv \frac{e^{i\omega T} - \sum_{k=0}^{6} a_n e^{-in\omega T}}{e^{i\omega T} - \sum_{k=0}^{6} (a_n + b_n) e^{-in\omega T}}$$

where * denotes complex conjugation, $\omega_l = 2\pi \cdot 60$ Hz, k_0 and $|k_n|$ are the system gains at zero and first three power line harmonics, $\arg(k_n)$ are the gain angles and coefficients a_n and b_n are determined by expanding the numerator and denominator of the first part of the equation into a series. An example of $K(\omega)$ is shown in Figure 2. A numerical algorithm realizing the transfer function of Eq. (6) can be written in the following form

$$\mathbf{c}_{k+1} = \sum_{n=0}^{6} \left(a_n \mathbf{c}_{k-n} + b_n \mathbf{y}_{k-n}\right) \ , \qquad (7)$$

where $\mathbf{c}_k$ is the vector of corrections at step k,

$$\mathbf{y}_k = \mathbf{Bx}_k \qquad (8)$$

is the state vector at step k, and $\mathbf{x}_k$ is the vector of measurements at step k.

3. SYSTEM IMPLEMENTATION AND EXPERIMENTAL RESULTS

The system layout is shown in Figure 3. To maximize speed, all digital hardware is concentrated in one VME crate. The system utilizes two CPUs. The first CPU runs the feedback system algorithm and the second provides system control and interface with operators using EPICS software [4]. ADC data acquisition is triggered by the timing module, which sets a series of pulses for multiplexing BPM electrodes. The measurement results are stored in ADC memory and are read after measurement

completion. The timing module is driven by the frequency multiplier, which is phase locked to the power line and creates a series of pulses at a desired power line harmonic. Normally the 40th harmonic (2.4 kHz) is used.

Figure 3: Feedback system schematic

Figure 4: Time domain signals to suppress 180 Hz harmonic perturbation; dotted line - DAC voltage, solid line - post filter correcting signal, dashed line - residual beam motion increased by three times; crosses show beam positions at data acquisition time. The system parameters are similar to Figure 2.

Different halls use different types of BPMs. Hall A uses BPMs with data acquisition time of 2.7 μs per electrode. To reduce measurement noise every electrode is read eight times. That yields a total data acquisition time of about 90 μs. To accelerate data transfer into the computer memory, Direct Memory Access (DMA) is used. This allows reading of data from one ADC in about 70 μs. The CPU starts calculations of beam positions measured by the first ADC while DMA supplies measurement results of the second ADC. Hall C has BPMs with 16 times longer integration time. This yields a total data acquisition time of about 200 μs, and only one reading of each electrode is used. That reduces data flux and allows one to avoid DMA transfer.

After data acquisition is performed, the system computes the required corrections and writes new corrector values into the DACs. Analog low pass filters are used to smooth DAC voltage. Reducing the filter cutoff frequency allows one to get a better approximation of a sinusoid, but is limited by system instability. Usually a bandwidth of

1.5 kHz is used. Figure 2 demonstrates the effect of filter bandwidth on the transfer function. It is important to note that although for the first three power line harmonics the system perfectly conceals the beam motion at the time when data acquisition is performed, it fails to conceal it in between data acquisitions. This is because the sinusoid is approximated by DAC voltage with finite accuracy. Figure 4 demonstrates this for 180 Hz beam motion. As one can see, the suppression factor is only about ten.

To improve the suppression of beam motion for the first three power line harmonics and suppress higher harmonics, a feedforward system was built on the top of the feedback system. To implement it the DACs are run at a frequency three times higher than the data acquisition from the BPMs. DAC corrections are summed from the feedback system predictions and data coming from a circular feedforward array. The length of the feedforward array is set such that after one power line period, the feedforward array is completely traversed. To match DAC and ADC frequencies, every feedback system prediction is propagated for three consecutive DAC corrections. Computation of the feedforward array data is performed by a UNIX process which reads time domain data from the correctors and BPMs, computes amplitudes and phases of power line harmonics present in the beam motion, and then calculates time domain signals for the feedforward array. The amplitudes and phases of power line harmonics are relatively stable, and therefore good suppression for the first twelve power line harmonics is achieved with comparatively modest sampling frequency. Figure 5 demonstrates the beam motion spectrum with the system on.

Figure 5: Spectrum of the beam motion with fast feedback system on in frequency range of 0 – 1.2 kHz. If the system is off, the amplitude of the first power line harmonic is about 30 times the vertical scale.

4. REFERENCES

[1] D.Douglas,*et al.*,CEBAF-PR-89-008;*Proc. of the 1989 Particle Accelerator Conference*, pp. 557-559 (1989).

[2] T. Powers, *Proc. of the 1998 Beam Inst. Workshop*, pp.256-265.

[3] W.Press, B.Flannery, *et al, Numerical Recipes in C*, Cambridge University Press, 1988.

[4] L.Dalesio, *et al., Proc.of the Intl. Conf. on Accel. and Large Exptl.Phys.ControlSystems*, pp.278-282(1992).

Author Index

Abe, Hiroshi **2015, 2749**
Aberle, Oliver **949**
Abo-Bakr, Michael **2385**
Acharya, R. **1393**
Adachi, Toshikazu **2271, 3348, 3752**
Adamenko, Stanislav V. **3269, 3271**
Adams, D.J. **2199**
Adderley, P. **1991**
Adolphsen, Christopher D. **253, 777, 3411, 3423, 3477**
Afonin, A.G. **53**
Agafonov, Alexey V. **1731, 1734**
Agematsu, Takashi **2259**
Ahle, Larry **1937, 3248**
Ahn, Hyo-Eun **875, 1255**
Ahrens, Leif A. **614, 1276, 1746, 2063, 2286, 2918, 3291, 3294**
Akagi, Hirofumi **3749**
Akai, Kazunori **440, 1132, 2731**
Akaoka, Nobuo **3546**
Akasaka, Nobumasa **1132, 2238, 2731, 3411**
Akemoto, Mitsuo **3414**
Akiyama, Atsuyoshi **343, 3158**
Akre, Ronald A. **2846**
Alai Tafti, A. **2722**
Alba, Rosa **2578**
Aleksandrov, A. **237, 3321**
Aleksandrov, Aleksander V. **78, 2948**
Aleksandrov, Vladimir S. **3501**
Alekseev, Nicolay N. **1479**
Aleshaev, Alexander N. **750**
Alessi, James G. **106, 614, 1297, 1902, 1964, 3300**
Alexahin, Yuri **1527**
Alford, Owen J. **2590, 3251**
Alimov, Andrey S. **2301, 2555**
Alonso, Jose **574**
Alton, Gerald D. **1878, 1881**
Alton, William J. **845**
Altuna, Xavier **2617**
Amano, Daizo **2403, 2689**
Amatuni, Andrey Ts. **3657, 3660**
Ambrosio, G. **174**
Ames, Friedhelm **1955**
Anderegg, Jim **1402**
Anders, W. **197, 2385**
Anderson, David E. **3390**
Anderson, Edwin B. **1686**
Anderson, James L. **571**
Anderson, Oscar **1908, 1937**
Anderson, Scott **217, 2006, 2039, 2042, 2045**
Andersson, Ake **2945**
Andreev, N. **174, 3194, 3197**
Andreev, Nikolai **154**
Andreev, V.A. **2256**
Andrianov, Serge N. **1866, 2701**
Anerella, Michael D. **185, 3161, 3170**
Anferov, Vladimir A **392**
Anguelov, Vladimir **2289**
Anthouard, Philippe **3260**
Antoine, Claire **919**
Antonello, M. **1324**
Antonsen Jr., Thomas M. **360**
Aoki, Yasushi **2018, 2036**
Apel, Ruediger **812, 818**

Arakawa, Dai **1141, 1653, 1821**
Arakawa, Kazuo **2259**
Araki, Sakae **343**
Arapov, L. **237**
Arcan, T. **174, 3197**
Archambault, L. **325, 3705**
Arduini, Gianluigi **1282, 1285, 2617, 2996**
Argan, Andrea **1599**
Arimatea, Claudio **2617**
Arkan, T. **3194**
Arkan, Tug T. **3242**
Arnett, Don **1390**
Arnold, Ned D. **2024**
Aronson, A **548**
Artoos, Kurt **154**
Arutunian, Suren G. **1468, 2105, 3657**
Arvin, Adrian H. **1444, 1447, 1929, 1946**
Arvin, Andy **349**
Asaka, Takao **2015, 2749, 3507**
Asano, K. **777, 3417, 3423**
Asaoka, Seiji **667, 670**
Aspenleiter, Jeffrey **1390, 2698**
Assadi, Saeed **711, 720, 1082, 1085, 2719**
Assmann, Ralph **330, 2996, 2999, 3002**
Aston, David **2990**
Atencio, Samuel J. **965**
Aune, Bernard **432**
Autin, Bruno **3071**
Autrey, Daryl **3248**
Avilov, Alexandr M. **2549**
Ayers, James J. **1961**
Baartman, Richard A. **128, 3534, 3537**
Babayan, Ruben A. **2424**
Baboi, N. **922**
Babzien, Marcus **2024, 2158, 2471, 2480, 3722**
Bach, H. **2427**
Backe, H. **165**
Badan, L. **1324**
Badea, V. **3767**
Bae, Young-Soon **3525**
Bai, Mei **387, 471, 2725, 3336**
Bailey, Roger **2617, 2996**
Bak, J. S. **1384**
Bak, Peter A. **2167**
Bakker, Rene J. **197, 726, 2078, 2379, 2382**
Baklakov, Boris **1387**
Balakin, Vladimir **461**
Balbekov, Valeri I. **315, 3062, 3146**
Baldis, Hector A. **2000**
Ball, M. **498, 1545, 1548**
Ball, Millicent J. **3245**
Ballarino, Amalia **1405**
Balleyguier, Pascal P. **1444, 1447, 1946**
Baltadoros, D. **1037**
Bane, Karl F. **3432, 3486**
Bane, Karl L.F. **1725, 1728, 2822, 3423, 3453, 3474, 3477**
Bangerter, Roger O. **3215**
Banks, Thomas I. **1686**
Banna, S. **3600, 3606, 3609**
Bannon, M. **3767**
Baptiste, Ken **1471, 3131**
Baranauskas, V. **2811**
Barber, D. P. **2635**
Bardy, Jacques **3260**

Barklow, Timothy L. **307, 3489**
Barlow, D. **3576**
Barnard, John J. **1761, 1803, 1830, 3248**
Barnes, C. **321**
Barnes, Michael J. **1509, 3378**
Barnes, Peter D. **2590**
Barnes, Phil **980**
Barnett, Ian **3743**
Barone Tonghi, L. **2578**
Barov, N. **2027**
Barr, Dean S. **2214, 2241**
Barraza, Juan **2090**
Barry, Walter C. **636, 1207**
Barsotti, E.L. **2146, 2211**
Bartolini, R. **1557**
Barzi, E. **174, 3330**
Bassalleck, B. **471**
Batchelor, Kenneth **75**
Batskikh, Gennady I. **2564**
Battle, Chris **2936**
Batygin, Yuri K. **1737, 1740**
Bauda, B. **197**
Bauer, P. **3194**
Baumann, C. A. **2659**
Bayanov, Boris F. **3086**
Bazhan, Anatoli **461**
Bazzani, Armando **1773**
Bechstedt, Ulf **1701, 2292**
Bechtold, Alexander **530**
Beck, David **1937, 2849**
Beck, U. **206**
Becker, R. **1899**
Becker, T. **197**
Becker, Ulrich **2951**
Beczek, Kevin J. **1378**
Beebe, E. **1902**
Beebe-Wang, Joanne J. **1743, 2843, 3143, 3185**
Beetham, C.Gary **765**
Behne, Dan **1333**
Beinhauer, Wolfgang **1647**
Bellavia, S. **1902**
Bellomo, Giovanni **1776**
Bellomo, Paul **206, 3429**
Belomestnykh, Sergey A. **272, 980, 1112**
Belousov, Ilja V. **750**
Belov, Victor P. **3086**
Ben-Zvi, Ilan **75, 2018, 2158, 2471, 2480, 2552, 3495, 3722**
Benabed, Karim **2990**
Benjamin, John **2277**
Benjegerdes, R. **3233**
Benson, S.V. **212, 2456**
Bent, Bruce **931**
Berg, Georg P. A. **2519**
Berg, J. Scott **3152**
Berg, Jeff **1333**
Berg, William J. **2024, 2134**
Berger, Christoph **2172**
Bergstrom, Paul M. **1827**
Bernal, Santiago **234, 1749, 1758, 1970, 2102, 3372**
Bernard, Michel **922**
Bertolini, Louis R. **2477, 3251**
Besnier, Gilbert **1192, 1195**
Besson, Jean-Claude **1569, 2686**

Conference Chairman
W.T. Weng, BNL
Telephone: 516-344-2135
Fax: 516-344-5954
E-mail: weng@bnl.gov

Program Chairman
I. Ben-Zvi, BNL
Telephone: 516-344-5143
Fax: 516-344-3029
E-mail: ilan@bnl.gov

Organizing Committee
M. Allen, SLAC (NPSS)
J. Ball, ORNL
W. Barletta, LBNL
I. Ben-Zvi, BNL
Y. Cho, ANL
L. Costrell, NIST
M. K. Craddock, UBC & Triumf
W.K. Dawson, TRIUMF (IEEE)
D. Finley, FNAL
D. Friesel, IUCF
D. Hartill, Cornell U.
C. Joshi, UCLA
M. Kihara, KEK (APAC)
S. Krinsky, BNL
C. Leemann, TJNAF
J. Peoples, FNAL (DPB)
M. Reiser, U. Maryland
B. Ripin, APS
C. Roberson, ONR
S. Schriber, LANL
R. Siemann, SLAC
D. Sutter, DOE
S. Tazzari, U. Roma &
    INFN-LNF (EPAC)
W.T. Weng, BNL, Chairman
G. Westenkow, LLNL
R. York, NSCL

Conference Secretary
M. Campbell, BNL
Telephone: 516-344-5458
Fax: 516-344-5954
E-mail: pac99@bnl.gov

Local Committee, BNL
J. Becker, *Treasurer*
H. Kirk, *Coordinator, Poster & Exhibits*
J. Laurie, *Printing*
E. Lowenstein, *BNL Tour*
P. Lucas, *Publishing (FNAL)*
A. Luccio, *Editor*
W. MacKay, *Editor*
C. Ronick, *Hotel Coordinator*
J. Smith, *Electronic Publishing*
P. Yamin, *Social & Spouse Activities*

The
American
Physical
Society   **IEEE**

BROOKHAVEN NATIONAL LABORATORY
BROOKHAVEN SCIENCE ASSOCIATES

February 23, 2000

DTIC
8725 John J Kingman Road
Ste. 0944
Ft. Belvoir, VA 22060-6218

Dear Sir,

The 1999 Particle Accelerator Conference (PAC'99) took place on March 29 - April 2, 1999 at the New York Marriott Marquis. We had approximately 1,195 registrants, 76 invited speakers and 1,528 abstracts covering all aspects of accelerator science, technology and applications. Among the registrants, approximately 2/3 were from the United States, 1/3 from abroad - truly an international conference in its scope and participation. Concurrent with the conference, there were 40 industrial firms participating in the exhibition.

The proceedings of PAC'99 were published and distributed in November 1999. Total published papers are 1,223 which are published in a 5 volume set with the total pages numbering 3,779.

The total amount of the ONR grant of $10,000.00 was all used in the support of the expense of junior staff, graduate students, and scientists from the developing nations and former Soviet Union.

As requested form SF298 is enclosed, and shipped separately is one set of the PAC '99 proceedings.

I would like to express my sincere thanks to ONR for its support to PAC'99 which is a very effective vehicle for the development and communication in the accelerator profession.

Sincerely yours,

Wu-Tsung Weng
Chair, PAC'99

attachment: Form SF298

cc: K. Galuchie, IEEE
       Grant Administrator - ONR

WTW:mc